

Landfalling tropical cyclones: Physical processes, forecasting and impacts

Edited by

Yihong Duan, Qingqing Li, Guanghua Chen, Hui Yu,
Da-Lin Zhang and Kun Zhao

Published in

Frontiers in Earth Science



FRONTIERS EBOOK COPYRIGHT STATEMENT

The copyright in the text of individual articles in this ebook is the property of their respective authors or their respective institutions or funders. The copyright in graphics and images within each article may be subject to copyright of other parties. In both cases this is subject to a license granted to Frontiers.

The compilation of articles constituting this ebook is the property of Frontiers.

Each article within this ebook, and the ebook itself, are published under the most recent version of the Creative Commons CC-BY licence. The version current at the date of publication of this ebook is CC-BY 4.0. If the CC-BY licence is updated, the licence granted by Frontiers is automatically updated to the new version.

When exercising any right under the CC-BY licence, Frontiers must be attributed as the original publisher of the article or ebook, as applicable.

Authors have the responsibility of ensuring that any graphics or other materials which are the property of others may be included in the CC-BY licence, but this should be checked before relying on the CC-BY licence to reproduce those materials. Any copyright notices relating to those materials must be complied with.

Copyright and source acknowledgement notices may not be removed and must be displayed in any copy, derivative work or partial copy which includes the elements in question.

All copyright, and all rights therein, are protected by national and international copyright laws. The above represents a summary only. For further information please read Frontiers' Conditions for Website Use and Copyright Statement, and the applicable CC-BY licence.

ISSN 1664-8714
ISBN 978-2-83251-007-0
DOI 10.3389/978-2-83251-007-0

About Frontiers

Frontiers is more than just an open access publisher of scholarly articles: it is a pioneering approach to the world of academia, radically improving the way scholarly research is managed. The grand vision of Frontiers is a world where all people have an equal opportunity to seek, share and generate knowledge. Frontiers provides immediate and permanent online open access to all its publications, but this alone is not enough to realize our grand goals.

Frontiers journal series

The Frontiers journal series is a multi-tier and interdisciplinary set of open-access, online journals, promising a paradigm shift from the current review, selection and dissemination processes in academic publishing. All Frontiers journals are driven by researchers for researchers; therefore, they constitute a service to the scholarly community. At the same time, the *Frontiers journal series* operates on a revolutionary invention, the tiered publishing system, initially addressing specific communities of scholars, and gradually climbing up to broader public understanding, thus serving the interests of the lay society, too.

Dedication to quality

Each Frontiers article is a landmark of the highest quality, thanks to genuinely collaborative interactions between authors and review editors, who include some of the world's best academicians. Research must be certified by peers before entering a stream of knowledge that may eventually reach the public - and shape society; therefore, Frontiers only applies the most rigorous and unbiased reviews. Frontiers revolutionizes research publishing by freely delivering the most outstanding research, evaluated with no bias from both the academic and social point of view. By applying the most advanced information technologies, Frontiers is catapulting scholarly publishing into a new generation.

What are Frontiers Research Topics?

Frontiers Research Topics are very popular trademarks of the *Frontiers journals series*: they are collections of at least ten articles, all centered on a particular subject. With their unique mix of varied contributions from Original Research to Review Articles, Frontiers Research Topics unify the most influential researchers, the latest key findings and historical advances in a hot research area.

Find out more on how to host your own Frontiers Research Topic or contribute to one as an author by contacting the Frontiers editorial office: frontiersin.org/about/contact

Landfalling tropical cyclones: Physical processes, forecasting and impacts

Topic editors

Yihong Duan — Chinese Academy of Meteorological Sciences, China

Qingqing Li — Nanjing University of Information Science and Technology, China

Guanghua Chen — Institute of Atmospheric Physics, Chinese Academy of Sciences, China

Hui Yu — Shanghai Typhoon Institute, China Meteorological Administration, China

Da-Lin Zhang — University of Maryland, College Park, United States

Kun Zhao — Nanjing University, China

Citation

Duan, Y., Li, Q., Chen, G., Yu, H., Zhang, D.-L., Zhao, K., eds. (2022). *Landfalling tropical cyclones: Physical processes, forecasting and impacts*.

Lausanne: Frontiers Media SA. doi: 10.3389/978-2-83251-007-0

Table of contents

- 06 Editorial: Landfalling tropical cyclones: Physical processes, forecasting, and impacts
Yihong Duan and Qingqing Li
- 08 High-Wind Drag Coefficient Based on the Tropical Cyclone Simulated With the WRF-LES Framework
Wenrui Jiang, Liguang Wu and Qingyuan Liu
- 13 Sensitivity of Fine-Scale Structure in Tropical Cyclone Boundary Layer to Model Horizontal Resolution at Sub-Kilometer Grid Spacing
Hongxiong Xu and Yuqing Wang
- 30 Possible Environmental Influence on Eyewall Expansion During the Rapid Intensification of Hurricane Helene (2006)
Nannan Qin and Liguang Wu
- 42 Monsoon Surges Enhance Extreme Rainfall by Maintaining the Circulation of Landfalling Tropical Cyclones and Slowing Down Their Movement
Dajun Zhao, Lianshou Chen and Yubin Yu
- 57 Slowdown in the Decay of Western North Pacific Tropical Cyclones Making Landfall on the Asian Continent
Jinjie Song, Philip J. Klotzbach, Haikun Zhao and Yihong Duan
- 68 Simulation of Rapid Intensification of Super Typhoon Lekima (2019). Part I: Evolution Characteristics of Asymmetric Convection Under Upper-Level Vertical Wind Shear
Qijun Huang, Xuyang Ge and Melinda Peng
- 85 Trends in Western North Pacific Tropical Cyclone Intensity Change Before Landfall
Qingyuan Liu, Jinjie Song and Philip J. Klotzbach
- 92 The Asymmetric Precipitation Evolution in Weak Landfalling Tropical Cyclone Rumbia (2018) Over East China
Lichun Tang, Yuqing Wang, Zifeng Yu and Lan Wang
- 111 The Cold Avoidance of Typhoons in Their North Turning Over the South China Sea
Shaojun Lai, Ying Li, Fen He, Yufei Wang and Yan Chen
- 124 The Performance of Three Exponential Decay Models in Estimating Tropical Cyclone Intensity Change After Landfall Over China
Lu Liu, Yuqing Wang and Hui Wang
- 136 DSAEF_LTP Model Experiment to Forecast the Accumulated Precipitation of Landfalling Northward-Moving Typhoons in China
Mei Yao, Yunqi Ma, Li Jia, Fumin Ren, Guoping Li, Chenchen Ding, Mingyang Wang and John L. McBride

- 149 **Factors Controlling Tropical Cyclone Intensification Over the Marginal Seas of China**
Xiaomeng Li, Ruifen Zhan, Yuqing Wang and Jing Xu
- 165 **Statistical Seasonal Forecasting of Tropical Cyclone Landfall on South China Utilizing Preseason Predictors**
Oscar Y. W. Zhang, Kelvin T. F. Chan, Lifeng Xu and Zhenzhen Wu
- 178 **Fine-Scale Structures in the Mid-Level Eyewall of Super Typhoon Rammasun (2014) Simulated With the WRF-LES Framework**
Zhen Gao, Liguang Wu and Xingyang Zhou
- 196 **Modulation of Pacific Sea Surface Temperatures on the Late-Season Tropical Cyclone Tracks Over the Western North Pacific and its Implication for Seasonal Forecasting**
Hua Yu, Chao Wang and Xuyang Ge
- 186 **Detecting Interdecadal Change in Western North Pacific Tropical Cyclone Genesis Based on Cluster Analysis Using pHash + Kmeans**
Ye Tian, Wen Zhou and W. K. Wong
- 204 **Simulation of Rapid Intensification of Super Typhoon Lekima (2019). Part II: The Critical Role of Cloud-Radiation Interaction of Asymmetric Convection**
Qijun Huang, Xuyang Ge and Mingyu Bi
- 218 **Impacts of El Niño Diversity on Tropical Cyclone Activity in the Bay of Bengal**
W. A. E. Lakshani, Wen Zhou and Paxson K. Y. Cheung
- 235 **A Machine-Learning Based Tool for Diagnosing Inland Tropical Cyclone Maintenance or Intensification Events**
Andrew Michael Thomas and James Marshall Shepherd
- 248 **Impact of the Spring North Atlantic Oscillation on the Northern Hemisphere Tropical Cyclone Genesis Frequency**
Leying Zhang, Xiting Yang and Jiuwei Zhao
- 256 **Risk Assessment of Typhoon Disaster Chains in the Guangdong–Hong Kong–Macau Greater Bay Area, China**
Yujie Wang, Yizhou Yin and Lianchun Song
- 273 **Sea Surface Height Changes due to the Tropical Cyclone-Induced Water Mixing in the Yellow Sea, Korea**
KiRyong Kang and Il-Ju Moon
- 283 **Estimation of Dissipative Heating Properties Above the Internal Boundary Layer in Landfalling Typhoons Using Multi-Layer Tower Observations**
Kang Zhou, Qingqing Li and Jie Tang

- 293 **Modulation of Pacific Sea Surface Temperature on Two Types of Tropical Cyclone Tracks Affecting Northeast China**
Yiqiu Yu, Yihe Fang, Chunyu Zhao, Yi Lin, Yitong Lin, Zhiqiang Gong and Yang Li
- 308 **Enhanced understanding of changes in tropical cyclones' landfall frequency over mainland China**
Guangxin Li, Qinglan Li, Wei Zhao, Guanbo Zhou, Qifeng Qian, Chuanhai Qian and Lunkai He



OPEN ACCESS

EDITED AND REVIEWED BY
Kevin Cheung,
E3-Complexity Consultant, Sydney,
Australia

*CORRESPONDENCE

Qingqing Li,
liqq@nuist.edu.cn

SPECIALTY SECTION

This article was submitted to
Atmospheric Science,
a section of the journal
Frontiers in Earth Science

RECEIVED 15 October 2022

ACCEPTED 31 October 2022

PUBLISHED 25 November 2022

CITATION

Duan Y and Li Q (2022), Editorial:
Landfalling tropical cyclones: Physical
processes, forecasting, and impacts.
Front. Earth Sci. 10:1071061.
doi: 10.3389/feart.2022.1071061

COPYRIGHT

© 2022 Duan and Li. This is an open-
access article distributed under the
terms of the [Creative Commons
Attribution License \(CC BY\)](#). The use,
distribution or reproduction in other
forums is permitted, provided the
original author(s) and the copyright
owner(s) are credited and that the
original publication in this journal is
cited, in accordance with accepted
academic practice. No use, distribution
or reproduction is permitted which does
not comply with these terms.

Editorial: Landfalling tropical cyclones: Physical processes, forecasting, and impacts

Yihong Duan¹ and Qingqing Li^{2,3*}

¹State Key Laboratory of Severe Weather, Chinese Academy of Meteorological Sciences, Beijing, China,

²Nanjing University of Information Science and Technology, Nanjing, China, ³Pacific Typhoon
Research Center, Key Laboratory of Meteorological Disaster of the Ministry of Education, Nanjing
University of Information Science and Technology, Nanjing, China

KEYWORDS

landfall, tropical cyclone, physical process, forecasting, impact

Editorial on the Research Topic

[Landfalling tropical cyclones: Physical processes, forecasting, and impacts](#)

Tropical cyclones (TCs) are one of the most catastrophic weather systems, regularly causing severe winds, torrential rainfall, and secondary disasters such as storm surges, mudslides, and municipal flooding. Particularly during landfall, the threats to lives and properties become even greater with TCs. It has been widely recognized that the risks induced by landfalling TCs are tightly linked to changes in TC track, intensity, and structure. In addition, on a longer temporal scale, variations in TC activity can also significantly modulate the possible menace triggered by TC landfalls. The multi-scale physical processes controlling TC track, intensity, and structure changes are complicated, and there remain quite a few hanging questions concerning these processes. Therefore, a Research Topic, Landfalling Tropical Cyclones: Physical Processes, Forecasting, and Impacts, was featured in Frontiers in Earth Science–Atmospheric Science. Recent related research advances are presented in this Research Topic.

Interactions between the TC circulation, ambient weather systems, and the underlying surface complicate the TC intensity change during landfall. These complex processes were discussed in the Topic. A study by [Qing and Wu](#) examined the possible environmental influence on the eyewall expansion during Hurricane Helene (2006)'s rapid intensification (RI) and found that the synoptic-scale features resulted in additional low-level inflow and upper-level outflow that contributed mainly to the eyewall expansion. [Gao et al.](#) investigated the strong turbulent kinetic energy within the eyewall of Super Typhoon Rammasun (2014), pointing out that the strong turbulent kinetic energy was involved in horizontal rolls. A series of studies of the RI of Super Typhoon Lekima (2019) indicated that deep convection contributed to the development of the upper-level outflow, thus, decreasing the upper-level vertical wind shear (VWS) and that the cloud–radiation interaction also furnished positive feedback between the tilting-induced convective asymmetry and the build-up of the upper-level outflow channel ([Huang et al.](#); [Huang et al.](#)). [Liu et al.](#) assessed the performance of three exponential decay

models in estimating post-landfall TC intensity change over China and suggested that the TC intensity at landfall contributed approximately 18% to the model errors. [Thomas and Shepherd](#) utilized a machine-learning method to diagnose inland TC maintenance and intensification and found that the variables that were important at the time of TC's arrival were also important the day before.

Along with the structure and intensity changes, landfalling TC rainfall is also characterized by a complex nature. [Zhao et al.](#) addressed extreme rainfall events induced by landfalling TCs in China and showed that monsoonal surges regulate the TC-associated extreme rainfall by directly influencing the maintenance of the TC circulation and slowing down TC movement. An observational study of Tropical Storm Rumbia (2018), which made landfall in Shanghai, China, showed that the low-level convective instability and deep-layer environmental VWS tended to deepen the inflow boundary layer and contribute to the redevelopment of the secondary circulation. As a result, heavy rainfall was enhanced in the northeast quadrant of Rumbia after landfall ([Tang et al.](#)). [Yao et al.](#) evaluated the Dynamical-Statistical-Analog Ensemble Forecast model's precipitation forecasts of landfalling northward-moving typhoons and indicated that the model could capture reasonably well the distribution of precipitation in most cases, with better forecasts of typhoons hitting the southern coast of China.

The boundary-layer processes and dynamics are essential for the structure and intensity changes of landfalling TCs. [Jiang et al.](#) employed a large-eddy simulation technique to evaluate the drag coefficient within TCs. The results show that the drag coefficient leveling off or decreases, which is observed in strong wind conditions, are not produced when TC-ocean interactions are excluded in the model. [Xu and Wang](#) documented that a grid spacing of sub-100-m in a large-eddy simulation is required to capture more fine-scale structures of horizontal rolls and tornado-scale vortices within the TC boundary layer. Tower observations showed the presence of a stress internal boundary layer within the circulation of landfalling typhoons, and integrated dissipative heating increased with increasing wind speed above the internal boundary layer ([Zhou et al.](#)).

Variations of landfalling TC activities are also investigated in the Topic from a climatological perspective. The spring North Atlantic Oscillation was found to have cross-basin impacts on the summer and autumn TC genesis frequency in the North Hemisphere ([Zhang et al.](#)). A slowdown in the decay of landfalling TCs in the Asian continent was revealed from 1966 to 2018 ([Song et al.](#)), and a significant increasing trend in the average 24-h intensity change of western North Pacific TCs before landfall was found between June and November during the period 1970 to 2019 ([Liu et al.](#)). It is also indicated that TC intensification over the marginal seas of China likely occurred when TCs underwent relatively large intensity, weak VWS, small translation perpendicular to the coastline, relatively large fullness, strong upper-level divergence, low-level relative vorticity, and high inner-core precipitation rate ([Li et al.](#)). Cluster analysis

showed that an abrupt decrease in western North Pacific TC formation after 1998 was related mainly to a decrease in the class located in the southern and eastern parts of the western North Pacific, and an increase after 2010 occurred due to the class located in the northwestern part of the western North Pacific ([Tian et al.](#)). [Yu et al.](#) classified the tracks of northward-moving TCs that hit Northeast China during July–September into two groupings based on a machine learning algorithm. They further examined the characteristics of large-scale factors associated with each grouping. [Lakshan et al.](#) examined the variation in large-scale parameters associated with two types of El Niño and their impacts on TC activity over the Bay of Bengal from 1980 to 2019. It is shown that the relationship between the genesis potential index and El Niño–Southern Oscillation (ENSO) in the primary TC peak season exhibits a distinct meridional feature over the southwestern to northeastern parts of the Bay of Bengal, with the ENSO-modulated VWS contributing the most to increasing the likelihood of TC genesis over the southwestern portion of the Bay of Bengal. [Yu et al.](#) identified two leading modes of the late-season TC track frequency and indicated that the circulation anomalies associated with the two modes are relevant to the concurrent ENSO but with different locations of the warmest sea surface temperature. [Li et al.](#) examined the climatological characteristics and interannual variations of TCs making landfall in mainland China in the peak TC seasons from 1980 to 2020. They found that the TC landfall frequency in mainland China and South China decreased significantly in 1995/1996 and 1996/1997, respectively. A statistical seasonal forecasting model was developed by [Zhang et al.](#) to predict the number of TC landfalls in South China based on pre-season environmental conditions, and the hit rate could be up to 90% during the period 1979–2020.

Author contributions

YH conceptualized the idea of the Research Topic. QQ wrote the first draft of this editorial with editing and additional contributions from YH.

Conflict of interest

The authors declare that the research was conducted in the absence of any commercial or financial relationships that could be construed as a potential conflict of interest.

Publisher's note

All claims expressed in this article are solely those of the authors and do not necessarily represent those of their affiliated organizations, or those of the publisher, the editors and the reviewers. Any product that may be evaluated in this article, or claim that may be made by its manufacturer, is not guaranteed or endorsed by the publisher.



High-Wind Drag Coefficient Based on the Tropical Cyclone Simulated With the WRF-LES Framework

Wenrui Jiang^{1,2}, Liguang Wu^{1,3*} and Qingyuan Liu⁴

¹Department of Atmospheric and Oceanic Sciences and Institute of Atmospheric Sciences, Fudan University, Shanghai, China,

²Innovation Center of Ocean and Atmosphere System, Zhuhai Fudan Innovation Research Institute, Zhuhai, China, ³State Key Laboratory of Severe Weather, Chinese Academy of Meteorological Sciences, Beijing, China, ⁴Nanjing Joint Institute for Atmospheric Sciences, Nanjing, China

OPEN ACCESS

Edited by:

Qingqing Li,
Nanjing University of Information
Science and Technology, China

Reviewed by:

Zhanhong Ma,
National University of Defense
Technology, China
Jie Tang,
China Meteorological Administration,
China

*Correspondence:

Liguang Wu
liguangwu@fudan.edu.cn

Specialty section:

This article was submitted to
Atmospheric Science,
a section of the journal
Frontiers in Earth Science

Received: 12 April 2021

Accepted: 05 May 2021

Published: 20 May 2021

Citation:

Jiang W, Wu L and Liu Q (2021) High-
Wind Drag Coefficient Based on the
Tropical Cyclone Simulated With the
WRF-LES Framework.
Front. Earth Sci. 9:694314.
doi: 10.3389/feart.2021.694314

The numerical simulation of tropical cyclones has been increasingly conducted using the advanced Weather Research and Forecast (WRF) model with the large-eddy simulation (LES) technique. Given the importance of the boundary wind profile for the vertical exchange of horizontal momentum between the atmosphere and the ocean, the drag coefficient was evaluated in the numerical simulation with the WRF-LES framework at the finest horizontal grid spacing of 37 m. In the absence of the TC–ocean interaction, the drag coefficient derived from the simulated wind profile does not show the leveling off or decrease in the strong wind conditions. The drag coefficient increases with the increasing near-surface wind speed and agrees well with the extrapolation of the Large and Pond formula in the strong wind conditions. It is suggested that the boundary wind structure simulated with the LES technique may be unrealistic when the TC–ocean interaction is not fully considered.

Keywords: drag coefficient, tropical cyclone, numerical simulation, large-eddy simulation, air–sea interaction

INTRODUCTION

Numerical simulation has been a powerful tool for studying tropical cyclones (TCs). In numerical models for TC simulation, the drag coefficient (C_d) is important for determining the vertical exchange of horizontal momentum between the atmosphere and the ocean. Great effort has been made to evaluating the drag coefficient through observational analysis (Powell et al., 2003; Jarosz et al., 2007; Vickery et al., 2009; Bell et al., 2012) and theoretical studies (Donelan et al., 2004; Donelan, 2018), especially as wind speed is stronger than 30 ms^{-1} (French et al., 2007; Jarosz et al., 2007; Bell et al., 2012; Edson et al., 2013). It is generally believed that the drag coefficient in high-wind condition does not increase linearly with surface wind speed although the mechanisms responsible for the reduction of the drag coefficient have not been fully understood (Donelan, 2018). However, relatively few studies have been conducted to examine the drag coefficient in the numerical simulation, while the fine-scale (less than 1,000 m) features have been explicitly simulated over the past decade (Zhu, 2008; Rotunno et al., 2009; Zhu, 2013; Green and Zhang, 2015; Wu et al., 2018, Wu et al., 2019; Jiang et al., 2020; Zheng et al., 2020; Zhou et al., 2020).

The large-eddy simulation (LES) technique has been incorporated into the Weather Research and Forecast (WRF) model (Mirocha et al., 2010). The WRF-LES framework has been used to conduct TC simulation with a horizontal grid spacing less than 1,000 m. For example, (Zhu, 2008) simulated the fine-scale structures in the TC boundary layer with the 300-m and 100-m spacings. Rotunno et al. (2009) conducted idealized experiments on the f-plane and found a sharp increase in randomly

distributed fine-scale turbulent eddies or gusts when the horizontal grid spacing was decreased from 185 to 62 m. Recently, the WRF-LES framework has been used to simulate fine-scale structures such as horizontal rolls and tornado-scale vortex in the TC boundary layer, and extreme wind gusts have been simulated (Ito et al., 2017; Wu et al., 2018; Wu et al., 2019; Cécé et al., 2021).

With the LES technique, the energy-producing scales of three-dimensional atmospheric turbulence are explicitly resolved, while the smaller-scale portion of the turbulence spectrum is removed from the flow field using a spatial filter. In other words, the vertical exchange of horizontal momentum between the atmosphere and the ocean, which is otherwise parameterized without the LES technique, is partially resolved in the WRF-LES framework. Many studies have demonstrated that the WRF-LES framework can reasonably well simulate the boundary layer structure of TCs; it is unknown whether the drag coefficient in simulated TCs is reasonably comparable to the observation (e.g., Powell et al., 2003). These fine-scale structures are closely associated with the wind profile and the vertical momentum transfer in the boundary layer (e.g., Zhu, 2008, 2013; Ito et al., 2017; Wu et al., 2018; Wu et al., 2019); it is necessary to examine the drag coefficient based on the TC simulation with the WRF-LES framework.

THE WIND PROFILE METHOD

Following Powell et al. (2003), we use the wind profile method to estimate the drag coefficient, which is based on the log-profile of wind at the bottom of the marine atmospheric boundary layer. The wind profile in neutral conditions can be written as

$$\bar{U} = (U_*/k) \ln(z/z_0), \quad (1)$$

or

$$\ln z = \frac{k}{U_*} \bar{U} + \ln z_0, \quad (2)$$

where \bar{U} is the wind speed at altitude z and the Karman constant k is set to be 0.41. The remaining variables in Eq 2, namely, the friction velocity U_* and the roughness length z_0 can be estimated through logarithmic linear regression. Then C_d can be derived from

$$\tau = \rho U_*^2 = \rho C_d U_{10}^2, \quad (3)$$

where U_{10} and ρ are the wind speed and air density at the 10-m altitude.

DATA

For comparison with the simulation, we use wind profiles from the GPS dropsondes deployed in 120 TCs over 17 years (Wang et al., 2015). There are over 12,000 quality-controlled data profiles. In this study, we used 1,003 profiles that were measured in high wind. Examination indicates that most of

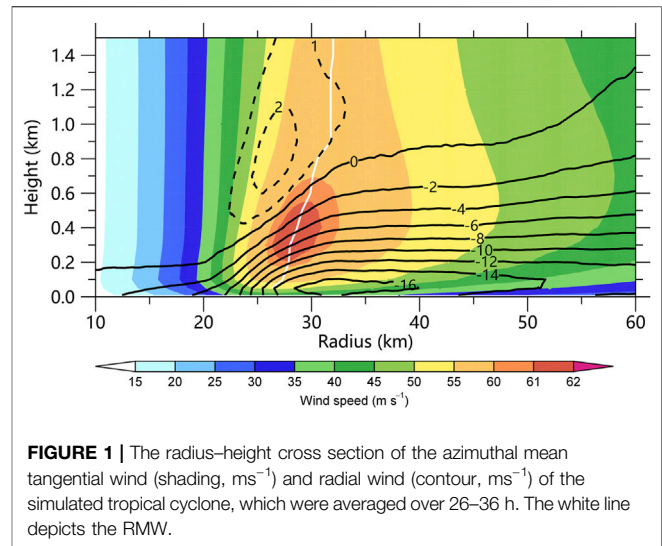


FIGURE 1 | The radius–height cross section of the azimuthal mean tangential wind (shading, ms^{-1}) and radial wind (contour, ms^{-1}) of the simulated tropical cyclone, which were averaged over 26–36 h. The white line depicts the RMW.

the GPS real dropsondes (RDs) were deployed at the altitude of ~6,000 m or below within a radius of less than 30 km from the TC center. The individual wind profiles are categorized into five groups based on the mean boundary layer wind (MBW), which is defined as the mean wind speed below 1,200 m. The five high-wind groups correspond to MBW in the ranges of 20–29 ms^{-1} (531 profiles), 30–39 ms^{-1} (247 profiles), 40–49 ms^{-1} (104 profiles), 50–59 ms^{-1} (68 profiles), and 60–69 ms^{-1} (53 profiles).

The simulation data used in the study are from a numerical simulation conducted with the WRF-LES system (Wu et al., 2018; Wu et al., 2019). The simulated TC evolves over the open ocean in the large-scale background of Typhoon Matsa (2005). Note that there was no TC–ocean interaction in this simulation. Six two-way interactive domains are embedded in the outermost domain. The finest grid spacing is 1/27 km (or about 37 m) and the model consists of 75 vertical levels with 19 levels below 2 km. The domains with the grid spacing less than 1 km move with the TC. In this study, a 22-min subset at 3-s intervals from the 30th hour of wind field data (in steady state) is used (Wu et al., 2018). The data cover an area of $90 \times 90 \text{ km}^2$ in the inner core region (the eye and eyewall).

Figure 1 shows the radius–height cross section of the azimuthal mean tangential and radial winds of the simulated TC. The tangential and radial winds are averaged over 26–36 h with the data in the 1/9-km domain. The maximum tangential wind occurs around the height of 400 m and the radius of maximum wind is ~27 km. Comparing to Zhang et al. (2011) and Ren et al. (2020), the altitude of the boundary layer jet in the simulated TCs is lower than the observation. The strongest boundary layer inflow of more than 16 ms^{-1} can be found at ~32 km near the surface, and the outflow above the inflow is much weaker. In the composite of Zhang et al. (2011) and Ren et al. (2020), the strongest inflow is between 1 and 2 times RMW. Ren et al. (2020) found that the strongest inflow is 20.7 ms^{-1} for major hurricanes. We can see that the wind structures of the wind in the TC boundary layer are well comparable to the observation.

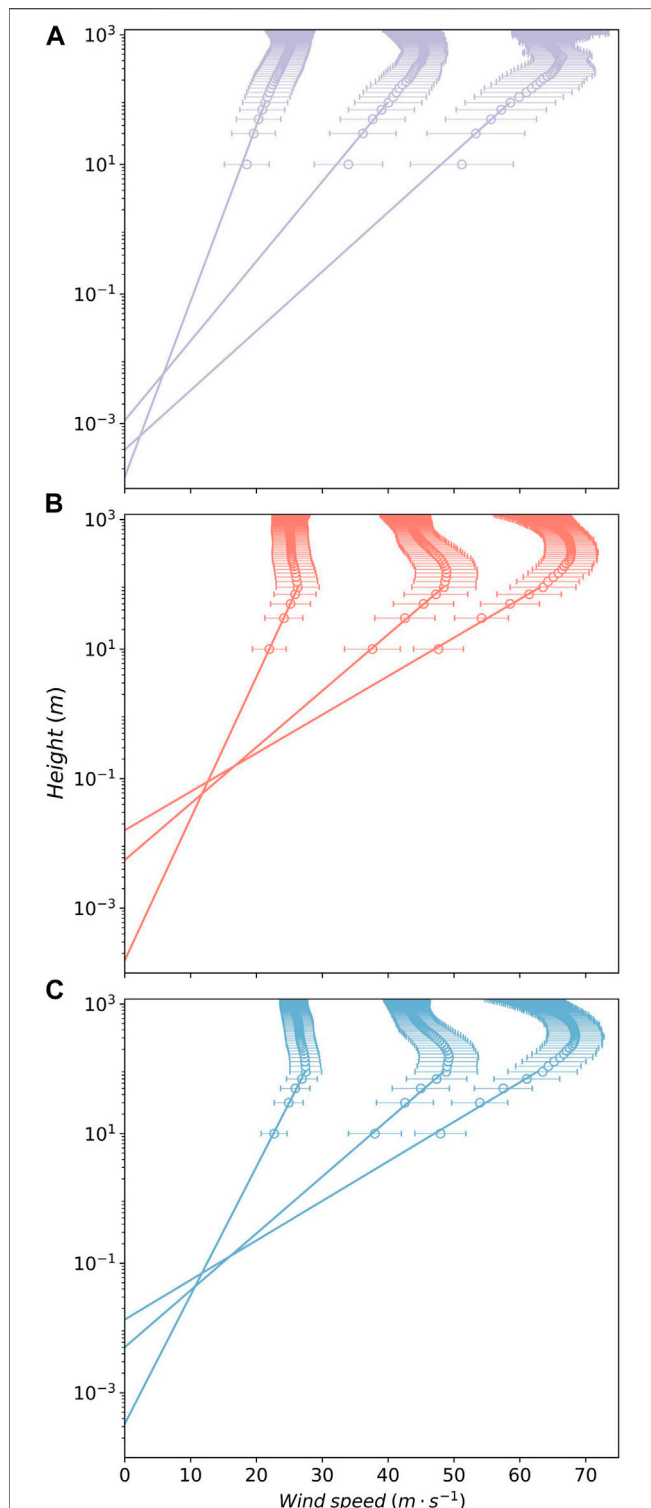


FIGURE 2 | The RD (A), SD (B), and ID (C) wind profiles for the MBW categories of 20–29 ms^{-1} , 40–49 ms^{-1} , and 60–69 ms^{-1} . The line in (B) and (C) is regressed using wind from 10 to 100 m, while the lowest level in (A) was not used for regression.

Two types of wind profiles are derived from the 22-min wind data at 3-s intervals. The first kind of profiles is simultaneously collected in a vertical column of the wind field. To mimic the real GPS dropsonde profiles and make more direct comparison, we construct the second kind of dropsonde profiles by simulating the dropsonde falling in the simulation. The simulated dropsonde (SD) falls only in response to gravity and drag force from the wind, and the latter is given by Hane (1975), Hock and Franklin (1999), and Stern and Bryan (2018)

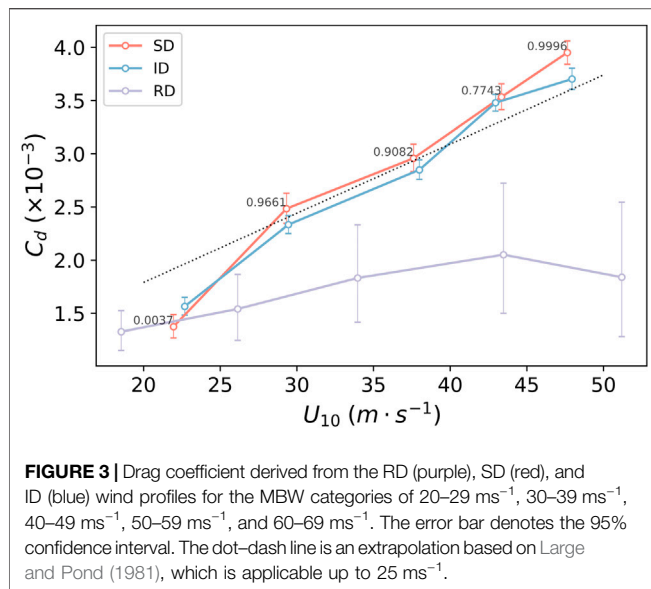
$$\vec{F}_s = -C_{ds}A_p\rho_a|\vec{V}_r|\vec{V}_r, \quad (4)$$

where \vec{V}_r denotes the relative speed of dropsonde to the wind, A_p is the area of the parachute, ρ_a is the density of surrounding air, and C_{ds} is the drag coefficient of the dropsonde. Stern and Bryan (2018) noted that the horizontal velocity of the dropsonde is almost the same as the surrounding wind speed. Therefore, the wind drag is almost only in the vertical direction. Like the GPS dropsondes in the real TCs, the simulated dropsonde is released at the altitude of 6,000 m during the first 10 min of the simulated data. The horizontal locations and time are randomly selected in the eyewall (17.5–30 km). The drag force in Eq 4 is set to be the same as the weight of the dropsonde, leading to the dropsonde falling at the speed of the real GPS dropsonde. Then the dropsonde locations at various vertical levels can be obtained by integrating a trajectory model.

A total of 3,895 dropsondes are effectively constructed for high-wind conditions. Similar to the GPS dropsondes, the individual wind profiles are also categorized into five categories. The five high-wind groups correspond to MBW in the ranges of 20–29 ms^{-1} (316 profiles), 30–39 ms^{-1} (565 profiles), 40–49 ms^{-1} (660 profiles), 50–59 ms^{-1} (1,064 profiles), and 60–69 ms^{-1} (1,290 profiles). The second type of wind profile is simultaneously collected in the vertical. Unlike the RD and SD profiles, the wind data at various altitudes are simultaneous and there are no horizontal drifts. The horizontal locations and time are also selected randomly. There are 7,151 wind profiles in high-wind conditions in the ranges of 20–29 ms^{-1} (495 profiles), 30–39 ms^{-1} (1,138 profiles), 40–49 ms^{-1} (1,335 profiles), 50–59 ms^{-1} (2,448 profiles), and 60–69 ms^{-1} (1,735 profiles). For convenience, we call the second type the idealized dropsonde (ID) profiles. The purpose of the ID profiles is to evaluate the sampling error in the SD wind profiles.

THE ESTIMATED DRAG COEFFICIENT

In this study, we linearly interpolate wind profile (horizontal component) with height onto every level that is 20 m apart and starts with 10 m. For the model output, the height is calculated from the geopotential height. For the observational data, the GPS height is used when estimating the altitude of the dropsonde. For simplicity, following Powell et al., 2003, we set the boundary layer to be 1200 m thick. Taking the categories of 20–29 ms^{-1} , 40–49 ms^{-1} , and



60–69 ms⁻¹ as an example, **Figure 2** shows the mean horizontal wind and their variance of ID, SD, and RD from the same MBW bins. The fitting of the logarithmic linear regression is also plotted in **Figure 2**. Since the dropsondes data are known to be heavily contaminated at the 10-m level (Jarosz et al., 2007), they were not included in the regression. **Figure 2** indicates that the simulated wind profiles (SD and ID) generally follow the log-profile, as shown in **Figure 2A**. The boundary layer jet in the model as shown in **Figures 2B,C** is lower than that observed, which is likely a result of the simulated TC being stronger than most TCs observed using dropsondes (Kepert and Wang, 2001).

The drag coefficient derived from the three types of wind profiles is shown in **Figure 3**. We used a bootstrap method to calculate the error bar. That is, a sampling with replacement of the same size as the dataset used was conducted. We calculated drag coefficients from each sample and used their 2.5 and 97.5% percentile as the boundaries of the 95% confidence interval. The drag coefficient based on the RD profile is between 1.0×10^{-3} and 2.0×10^{-3} and peaks for the category of 40–49 ms⁻¹. For comparison with the previous studies, note that horizontal coordinate is the wind speed at 10 m. The resulting drag coefficient agrees very well with the result in Powell et al. (2003).

For the SD and ID profiles, as shown in **Figure 3**, the derived drag coefficient increases with the increasing MBW speed, although it is close to the drag coefficient of the RD for the category of 20–29 ms⁻¹. One may be wondering about the large spread of the derived drag coefficient from the RD profiles. One possible reason is that the RD profiles were from different TCs, while the SD and ID profiles are from the same TC. An important feature of the derived drag coefficient from the SD and ID profiles is that it increases linearly with the MBW or near-surface wind speed. For the category of 60–69 ms⁻¹, it can be as large as 4×10^{-3} , almost twice as much as the typical observation. It is interesting that the drag coefficient in the simulation is in good agreement with the extrapolated classic Large and Pond formula (Large and Pond, 1981). Note that the formula of Large and Pond (1981) is only valid for wind speed less than 25 ms⁻¹.

As mentioned above, the wind data of the SD profiles at various altitudes are not simultaneous and there are horizontal drifts. In addition, the sampling bias may be due to the boundary layer inflow or the presence of small-scale coherent structures, such as tornado-scale vortices and boundary layer rolls since the dropsondes can be repelled from strong updrafts in the boundary layer. For most of the MBW bins as shown in **Figure 3**, the differences in the drag coefficient between the SD and ID profiles can be 8% in the high-wind condition. Given the same MBW, the drag coefficient of the SD profiles has a smaller u_{10} and larger C_d . It is suggested that the sampling bias has some influence on the derived drag coefficient, but the sampling bias has little influence on the increasing drag coefficient with the increase of the MBW speed.

SUMMARY

In this study, based on the high-resolution simulation of the TC, the drag coefficient is calculated with the wind profile method (Powell et al., 2003). The numerical experiment was conducted over the open ocean using the WRF-LES model at the finest grid spacing of 37 m. While the simulated drag coefficient is similar to the observation in the category of 20–29 ms⁻¹, it does not show the leveling off or decrease in the strong wind conditions, likely due to the fact that in LES framework cannot take the complicated response from the sea surface, including sea foam, wave-breaking, and sheltering effect. For the strong wind conditions, the drag coefficient can be as large as 4×10^{-3} , almost twice as much as the typical observation. It is interesting that the drag coefficient in the simulation is in strong agreement with the extrapolated classic Large and Pond formula (Large and Pond, 1981). Since it has been demonstrated that the drag coefficient in high-wind condition does not increase linearly with surface wind speed (Powell et al., 2003), this study suggests that the boundary wind structure of the TC simulated with the LES technique may be unrealistic when the TC–ocean interaction is not fully considered.

DATA AVAILABILITY STATEMENT

The raw data supporting the conclusions of this article will be made available by the authors, without undue reservation.

AUTHOR CONTRIBUTIONS

LW conducted analysis and writing. WJ conducted analysis and writing. QL conducted the numerical experiment.

ACKNOWLEDGMENTS

The authors thank X. Qiu and W. Lin for many helpful discussions and advice. This study was jointly supported by the National Natural Science Foundation of China (41730961, 61827901, 41905001), and the scientific Research Program of Shanghai Municipal Science and Technology Commission (19dz1200101).

REFERENCES

- Bell, M. M., Montgomery, M. T., and Emanuel, K. A. (2012). Air-Sea Enthalpy and Momentum Exchange at Major Hurricane Wind Speeds Observed during CBLAST. *J. Atmos. Sci.* 69 (11), 3197–3222. doi:10.1175/JAS-D-11-0276.1
- Cécé, R., Bernard, D., Krien, Y., Leone, F., Candela, T., Péroche, M., et al. (2021). A 30 M Scale Modeling of Extreme Gusts during Hurricane Irma (2017) Landfall on Very Small Mountainous Islands in the Lesser Antilles. *Nat. Hazards Earth Syst. Sci.* 21 (1), 129–145. doi:10.5194/nhess-21-129-2021
- Donelan, M. A., Haus, B. K., Reul, N., Plant, W. J., Stiassnie, M., Graber, H. C., et al. (2004). On the Limiting Aerodynamic Roughness of the Ocean in Very Strong Winds. *Geophys. Res. Lett.* 31 (18). doi:10.1029/2004GL019460
- Donelan, M. A. (2018). On the Decrease of the Oceanic Drag Coefficient in High Winds. *J. Geophys. Res. Oceans* 123 (2), 1485–1501. doi:10.1002/2017JC013394
- Edson, J. B., Jampana, V., Weller, R. A., Bigorre, S. P., Plueddemann, A. J., Fairall, C. W., et al. (2013). On the Exchange of Momentum over the Open Ocean. *J. Phys. Oceanogr.* 43 (8), 1589–1610. doi:10.1175/JPO-D-12-0173.1
- French, J. R., Drennan, W. M., Zhang, J. A., and Black, P. G. (2007). Turbulent Fluxes in the Hurricane Boundary Layer. Part I: Momentum Flux. *J. Atmos. Sci.* 64 (4), 1089–1102. doi:10.1175/JAS3887.1
- Green, B. W., and Zhang, F. (2015). Numerical Simulations of Hurricane Katrina (2005) in the Turbulent Gray Zone. *J. Adv. Model. Earth Syst.* 7, 142–161. doi:10.1002/2014MS000399
- Hane, C. E. (1975). The Trajectories of Dropsondes in Simulated Thunderstorm Circulations. *Mon. Weather Rev.* 103 (8), 709–716. doi:10.1175/1520-0493(1975)103<0709:TTODIS>2.0.CO;2
- Hock, T. F., and Franklin, J. L. (1999). The NCAR GPS Dropwindsonde. *Bull. Am. Meteorol. Soc.* 80 (3), 407–420. doi:10.1175/1520-0477(1999)080<0407:TNGD>2.0.CO;2
- Ito, J., Oizumi, T., and Niino, H. (2017). Near-surface Coherent Structures Explored by Large Eddy Simulation of Entire Tropical Cyclones. *Sci. Rep.* 7 (1), 3798. doi:10.1038/s41598-017-03848-w
- Jarosch, E., Mitchell, D. A., Wang, D. W., and Teague, W. J. (2007). Bottom-Up Determination of Air-Sea Momentum Exchange under a Major Tropical Cyclone. *Science* 315 (5819), 1707–1709. doi:10.1126/science.1136466
- Jiang, Y., Wu, L., Zhao, H., Zhou, X., and Liu, Q. (2020). Azimuthal Variations of the Convective-Scale Structure in a Simulated Tropical Cyclone Principal Rainband. *Adv. Atmos. Sci.* 37 (11), 1239–1255. doi:10.1007/s00376-020-9248-x
- Kepert, J., and Wang, Y. (2001). The Dynamics of Boundary Layer Jets within the Tropical Cyclone Core. Part II: Nonlinear Enhancement. *J. Atmos. Sci.* 58 (17), 2485–2501. doi:10.1175/1520-0469(2001)058<2485:TDOBLJ>2.0.CO;2
- Large, W. G., and Pond, S. (1981). Open Ocean Momentum Flux Measurements in Moderate to Strong Winds. *J. Phys. Oceanogr.* 11 (3), 324–336. doi:10.1175/1520-0485(1981)011<0324:OOMFMI>2.0.CO;2
- Mirocha, J. D., Lundquist, J. K., and Kosović, B. (2010). Implementation of a Nonlinear Subfilter Turbulence Stress Model for Large-Eddy Simulation in the Advanced Research WRF Model. *Mon. Weather Rev.* 138 (11), 4212–4228. doi:10.1175/2010MWR3286.1
- Powell, M. D., Vickery, P. J., and Reinhold, T. A. (2003). Reduced Drag Coefficient for High Wind Speeds in Tropical Cyclones. *Nature* 422 (6929), 279–283. doi:10.1038/nature01481
- Ren, Y., Zhang, J. A., Vigh, J. L., Zhu, P., Liu, H., Wang, X., et al. (2020). An Observational Study of the Symmetric Boundary Layer Structure and Tropical Cyclone Intensity. *Atmosphere* 11 (2), 158. doi:10.3390/atmos11020158
- Rotunno, R., Chen, Y., Wang, W., Davis, C., Dudhia, J., and Holland, G. J. (2009). Large-Eddy Simulation of an Idealized Tropical Cyclone. *Bull. Amer. Meteorol. Soc.* 90 (12), 1783–1788. doi:10.1175/2009bams2884.1
- Stern, D. P., and Bryan, G. H. (2018). Using Simulated Dropsondes to Understand Extreme Updrafts and Wind Speeds in Tropical Cyclones. *Mon. Weather Rev.* 146 (11), 3901–3925. doi:10.1175/MWR-D-18-0041.1
- Vickery, P. J., Wadhera, D., Powell, M. D., and Chen, Y. (2009). A Hurricane Boundary Layer and Wind Field Model for Use in Engineering Applications. *J. Appl. Meteorol. Climatol.* 48 (2), 381–405. doi:10.1175/2008JAMC1841.1
- Wang, J., Young, K., Hock, T., Lauritsen, D., Behringer, D., Black, M., et al. (2015). A Long-Term, High-Quality, High-Vertical-Resolution GPS Dropsonde Dataset for Hurricane and Other Studies. *Bull. Am. Meteorol. Soc.* 96 (6), 961–973. doi:10.1175/BAMS-D-13-00203.1
- Wu, L., Liu, Q., and Li, Y. (2018). Prevalence of Tornado-Scale Vortices in the Tropical Cyclone Eyewall. *Proc. Natl. Acad. Sci. USA* 115 (33), 8307–8310. doi:10.1073/pnas.1807217115
- Wu, L., Liu, Q., and Li, Y. (2019). Tornado-scale Vortices in the Tropical Cyclone Boundary Layer: Numerical Simulation with the WRF-LES Framework. *Atmos. Chem. Phys.* 19, 2477–2487. doi:10.5194/acp-19-2477-2019
- Zhang, J. A., Rogers, R. F., Nolan, D. S., and Marks, F. D. (2011). On the Characteristic Height Scales of the Hurricane Boundary Layer. *Mon. Weather Rev.* 139 (8), 2523–2535. doi:10.1175/MWR-D-10-05017.1
- Zheng, Y., Wu, L., Zhao, H., Zhou, X., and Liu, Q. (2020). Simulation of Extreme Updrafts in the Tropical Cyclone Eyewall. *Adv. Atmos. Sci.* 37 (7), 781–792. doi:10.1007/s00376-020-9197-4
- Zhou, X., Wu, L., Liu, Q., and Zheng, Y. (2020). Influence of Low-Level, High-Entropy Air in the Eye on Tropical Cyclone Intensity: A Trajectory Analysis. *J. Meteorol. Soc. Jpn.* 98, 1231–1243. doi:10.2151/jmsj.2020-063
- Zhu, P. (2008). Simulation and Parameterization of the Turbulent Transport in the Hurricane Boundary Layer by Large Eddies. *J. Geophys. Res.* 113, D17104. doi:10.1029/2007JD009643
- Zhu, P., Menelaou, K., and Zhu, Z. (2013). Impact of subgrid-scale vertical turbulent mixing on eyewall asymmetric structures and mesovortices of hurricanes. *Q. J. R. Meteorol. Soc.* 140, 416–438. doi:10.1002/qj.2147

Conflict of Interest: The authors declare that the research was conducted in the absence of any commercial or financial relationships that could be construed as a potential conflict of interest.

Copyright © 2021 Jiang, Wu and Liu. This is an open-access article distributed under the terms of the Creative Commons Attribution License (CC BY). The use, distribution or reproduction in other forums is permitted, provided the original author(s) and the copyright owner(s) are credited and that the original publication in this journal is cited, in accordance with accepted academic practice. No use, distribution or reproduction is permitted which does not comply with these terms.



Sensitivity of Fine-Scale Structure in Tropical Cyclone Boundary Layer to Model Horizontal Resolution at Sub-Kilometer Grid Spacing

Hongxiong Xu^{1*} and Yuqing Wang²

¹State Key Laboratory of Severe Weather, Chinese Academy of Meteorological Sciences, China Meteorological Administration, Beijing, China, ²International Pacific Research Center and Department of Atmospheric Sciences, School of Ocean and Earth Science and Technology, University of Hawaii at Manoa, Honolulu, HI, United States

OPEN ACCESS

Edited by:

Da-Lin Zhang,
University of Maryland, United States

Reviewed by:

Liguang Wu,
Fudan University, China
Yubin Li,
Nanjing University of Information
Science and Technology, China

*Correspondence:

Hongxiong Xu
xuhx@cma.gov.cn

Specialty section:

This article was submitted to
Atmospheric Science,
a section of the journal
Frontiers in Earth Science

Received: 09 May 2021

Accepted: 07 June 2021

Published: 21 June 2021

Citation:

Xu H and Wang Y (2021) Sensitivity of
Fine-Scale Structure in Tropical
Cyclone Boundary Layer to Model
Horizontal Resolution at Sub-Kilometer
Grid Spacing.
Front. Earth Sci. 9:707274.
doi: 10.3389/feart.2021.707274

In view of the increasing interest in the explicit simulation of fine-scale features in the tropical cyclone (TC) boundary layer (TCBL), the effects of horizontal grid spacing on a 7–10 h simulation of an idealized TC are examined using the Weather Research and Forecast (ARW-WRF) mesoscale model with one-way moving nests and the nonlinear backscatter with anisotropy (NBA) sub-grid-scale (SGS) scheme. In general, reducing the horizontal grid spacing from 2 km to 500 m tends to produce a stronger TC with lower minimum sea level pressure (MSLP), stronger surface winds, and smaller TC inner core size. However, large eddies cannot be resolved at these grid spacings. In contrast, reducing the horizontal grid spacing from 500 to 166 m and further to 55 m leads to a decrease in TC intensity and an increase in the inner-core TC size. Moreover, although the 166-m grid spacing starts to resolve large eddies in terms of TCBL horizontal rolls and tornado-scale vortex, the use of the finest grid spacing of 55 m tends to produce shorter wavelengths in the turbulent motion and stronger multi-scale turbulence interaction. It is concluded that a grid spacing of sub-100-meters is desirable to produce more detailed and fine-scale structure of TCBL horizontal rolls and tornado-scale vortices, while the relatively coarse sub-kilometer grid spacing (e.g., 500 m) is more cost-effective and feasible for research that is not interested in the turbulence processes and for real-time operational TC forecasting in the near future.

Keywords: tropical cyclones, grid spacing, Boundary layer rolls, tornado-scale vortices, TC forecasting

INTRODUCTION

Tropical cyclones (TCs) are among the strongest atmospheric vortices in nature, which often bring about heavy rainfall and damaging winds on their paths (Chen and Meng, 2001; Chen et al., 2019), and induce storm surge and other natural disasters in coastal regions when they make landfall (Duan et al., 2020). The accurate forecast of TC track and intensity are important for preparedness for disaster prevention and reduction of damages potentially induced by a coming TC. How to improve the understanding and prediction skill of TC track and intensity has received great attention by both research and operational communities (Chen and Meng, 2001; Wang and Wu, 2004; Emanuel, 2018). Although the forecast of TC track has made remarkable progress in the last 3 decades or so, the research and forecast of TC intensity change are well behind and need to be improved. TC intensity change involves the interaction of multi-scale and nonlinear dynamical/physical processes that are

often poorly resolved or parameterized by global and regional models (Wang et al., 2001; Wang and Wu, 2004; Bao et al., 2012; Xu et al., 2013; Bu et al., 2017). The TC planetary boundary layer (TCBL) turbulent processes belong to these crucial physical processes and can significantly influence the intensification and maintenance of a TC by turbulent surface flux and vertical mixing of heat, moisture and momentum (Hill and Lackmann, 2009; Gopalakrishnan et al., 2013; Zhang et al., 2017).

In the numerical model, TCBL turbulent processes are either parameterized, such as those in mesoscale regional and global models, or explicitly represented, such as in large eddy simulations (Zhu, 2008; Rotunno et al., 2009; Wu et al., 2018). These two approaches are different strategies and depend on the model resolution. In mesoscale simulations (>1 km), all turbulent processes are parameterized using the resolved parameters/processes. In LESs (<100 m), large turbulent motions are explicitly resolved, while the subgrid scale, smaller turbulent motions are still parameterized. In general, contributions by the resolved (parameterized) turbulence increase (decrease) with increasing model resolution (Bryan and Morrison, 2011).

Previous studies (Fierro et al., 2009; Gentry and Lackmann, 2010) showed that the simulated TC structure could be greatly affected by the grid spacing (>1 km) in mesoscale models. These studies demonstrated that higher resolution would produce narrower eyewalls, smaller radii of maximum wind speed, higher vertical wind speeds, and more symmetric structure of the eyewall with high-wavenumber asymmetries. They recommended that a grid spacing less than 2 km or 3 km can be used in research or operational forecast models in order to better represent physical processes of rainband and eyewall structures. Fierro et al. (2009) focused on the influence of grid spacing in the range of 1–5 km on TC simulations using the Weather Research and Forecasting (WRF) model with two-way nesting. Their results showed no systematic trend in TC intensity with change in model resolution. However, Gentry and Lackmann (2010) suggested that simulations with higher resolution could significantly reduce the minimum sea level pressure (MSLP) and increase the magnitude of the resolved vertical motion. Although a grid spacing about 1 km starts to partially resolve downdraft and updraft cores in the eyewall, mesoscale models are still unable to explicitly resolve the planetary boundary layer (PBL) turbulent processes (Smith et al., 2012), suggesting that more adequate treatment of turbulent processes is important to better represent the atmospheric state and the TC intensity and structure changes.

The development of computing power and advanced numerical technique have greatly contributed to the efforts of very high-resolution simulations to study the small-scale features in the TCBL. More studies on TCs (Zhu, 2008; Rotunno et al., 2009; Green and Zhang, 2015; Wu et al., 2018; Zhu et al., 2019; Zheng et al., 2020) have run models on sub-kilometer or even sub-100-meters resolutions, by which turbulence can be reasonably resolved. Rotunno et al. (2009) suggested that a model cannot resolve turbulence until reducing the grid spacing to sub-100-meters. The explicitly resolved turbulent mean TC intensity began to decrease with a sharp increase in gusts with sub-100-meters resolutions. Green and Zhang (2015)

suggested that the turbulent structure of a TC can exist in hundreds meter simulations (111, 222, and 333 m) with LESs. They attributed this discrepancy to the use of the nonlinear backscatter with anisotropy (NBA) scheme in the newer version of the WRF model as documented by Mirocha et al. (2010). Furthermore, they also found that the scales of turbulent motion vary with model resolution. In TCs, tornado-scale vortices and boundary layer rolls are considered being important fine-scale features of TCBL. It is necessary for a numerical models to have sufficiently high model resolution and adequate parametrization of smaller scales to reasonably represent the two fine-scale features in TCBL (Zhu et al., 2019).

Frequently observed TCBL rolls, can lead to small-scale swath of damage, and are important small-scale features that can affect the turbulent transport/mixing in the TCBL (Wurman and Winslow, 1998; Wurman and Kosiba, 2018). Zhu (2008) configured a nested WRF-LES with the innermost grid spacing of 100 m to simulate the landfall of Hurricane Ivan (2004). They found that the boundary layer rolls play an important role in enhancing exchanges of momentum, heat, and moisture. The resolved turbulence resulted from the boundary layer rolls is considerably underestimated by the current commonly used PBL schemes. Both observations and numerical simulations show that the wavelength of the boundary layer rolls are affected by the TC size. Their wavelengths are only several hundred meters within the radius of maximum wind speed of a TC but can reach 1–2 km outside the eyewall (Foster, 2005; Morrison et al., 2005). Similarly, Gao and Ginis (2014) found that the wavelength and the growth rate of the boundary layer rolls are affected by the PBL height and the magnitude of the sustained wind shear, respectively. Tornado-scale vortices near the eyewall are another small-scale feature of TCBL. Observational analyses (Marks et al., 2008; Zhang et al., 2011a; Wurman and Kosiba, 2018) suggested the existence of tornado-scale vortices prevail in TCBL with maximum vertical vorticity maximum greater than 0.15 s^{-1} and diameters of 1–2 km. Wu et al. (2018); Wu et al. (2019) simulated tornado-scale vortices using the WRF-LES simulations with grid spacing of 37 m. They found that tornado-scale vortices have significant influences on extreme updrafts and surface wind gusts.

Although depending on the numerical precision of finite-differencing schemes, in general, the grid spacing can marginally resolve about 1/4 of the wavelength of a wave (Grasso, 2000), 1/7 of the wavelength reasonably well (Skamarock, 2004) to match the observed power spectrum, and 1/10 of the wavelength almost completely (Walters, 2000).

TCBL rolls, which have linear shaped coherent structures, are aligned nearly with the background flow direction with the scale ranges from 600 m to 2 km (Wurman and Winslow, 1998; Foster, 2005; Morrison et al., 2005), while tornado-scale vortices are vortices with the scale ranges from 1 to 2 km often embedded within the TC eyewall (Marks et al., 2008; Zhang et al., 2011a; Wurman and Kosiba, 2018). Note that tornado-scale vortices are one of the fine-scale features found near the inner edge of the TC eyewall, and their scales are much larger than tornados (~200 m; Rotunno, 2013). Based on these criteria, the minimum grid spacing to resolve these two phenomena needs to reach at

least 150–500 and 250–500 m, and to completely resolve these phenomena, the minimum grid spacing needs to reach 60–200 m and 100–200 m, respectively. Therefore, it seems that the grid spacing from 500 to 60 m is crucial to resolve the fine-scale structure of TCBL rolls and tornado-scale vortices. However, it is still infeasible to use a grid spacing of sub-hundred meters for either global and regional models for routinely operational forecasts. For example, the grid spacing of the current operational HWRF (Hurricane WRF) model at the National Centers for Environmental Prediction (NCEP) is 1.5 km. Nevertheless, the TC operational forecasting systems and research models at sub-kilometer or even sub-hundred meters will not be achievable soon. Therefore, a study on the influence of model grid spacing from sub-kilometer to sub-hundred meters on TC simulations/predictions can help guide future developments of operational TC forecasting models.

In this study, a high-resolution idealized simulation of a TC is conducted using the WRF-LES model with one-way nesting and a grid spacing varying from kilometers to sub-kilometer to sub-hundred-meters. The following questions will be addressed: 1) do the simulated fine-scale structures of boundary layer rolls and tornado-scale vortices strongly depend on the model grid spacing in the range of sub-kilometer and sub-hundred-meters? and 2) will TC intensity continue to increase and eyewall size of the simulated TC continue to decrease with the increasing model resolution (decreasing the grid spacing), or will a convergence occurs at a certain grid spacing? The rest of the paper is organized as follows. *Model and Experimental Setup* section briefly describe the model and experimental setup. The results are discussed in *Results* section. Our main conclusions are drawn in *Discussion* section.

MODEL AND EXPERIMENTAL SETUP

To investigate the effects of horizontal grid spacing on the simulated fine-scale TC structure and intensity, the Advanced Research Weather Research and Forecasting model (Skamarock et al., 2019) version 4.1.5 was used to simulate a TC with the grid spacing varying from kilometers through sub-kilometer to sub-100-meters. The six one-way moving (vortex-following) nested domains (d01–d06) had horizontal grid spacings of 6 km, 2 km, 500 m, 166 m and 55 m, and domain sizes of 311×325 , 271×271 , 211×211 , 721×721 , $1,501 \times 1,501$ and $1,501 \times 1,501$. The model atmosphere was discretized in the vertical with 72 vertical levels from the sea surface to 20 km. In addition to the model horizontal resolution, the vertical resolution in the numerical simulation is also suggested to play an important role in simulating TC intensities and inner-core structures (Zhang and Wang, 2003; Zhang et al., 2015). Despite the importance of vertical resolution, this study used 72 levels in the vertical for all grid spacings because of the limitation of our existing computing resources. To minimize the impact of vertical resolution on the simulated TCBL, we set 19 vertical levels below 1 km height to provide finer resolution in the PBL. This gives the ratio of horizontal and vertical grid spacing around 1.0 in the boundary layer for the finest horizontal grid spacing in this study. Nevertheless, the

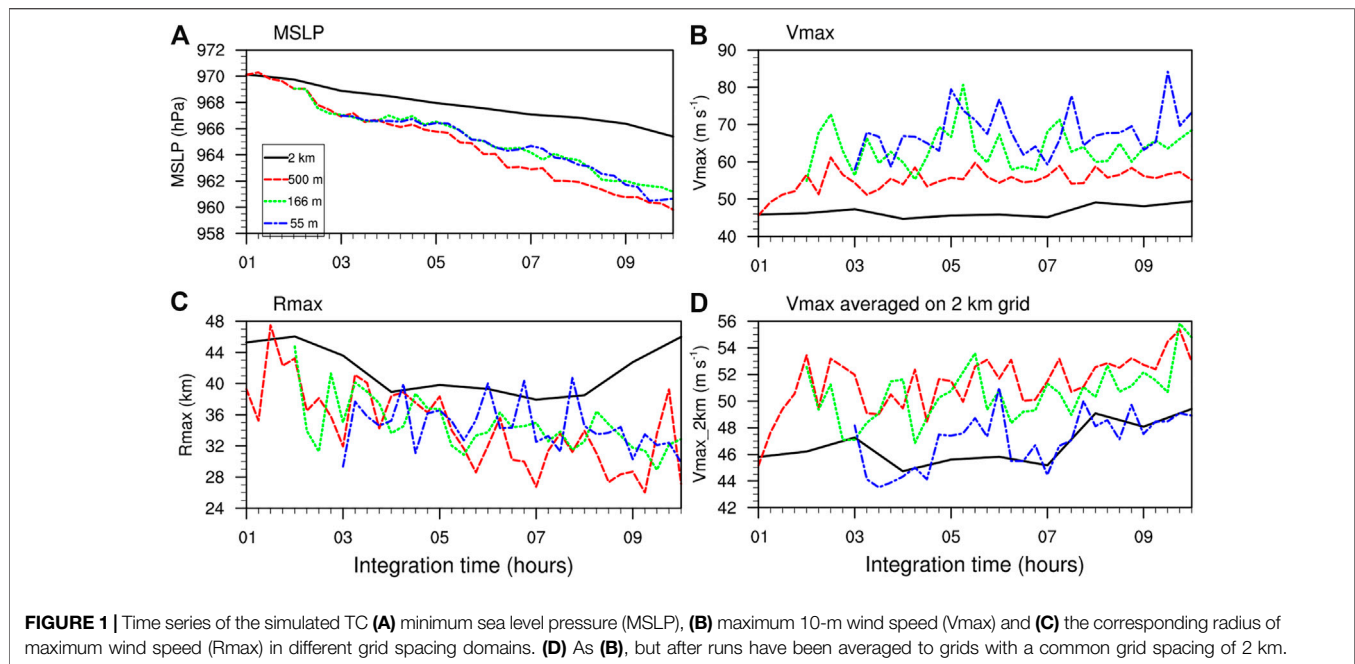
vertical grid spacing above the boundary layer is relatively larger than the finest horizontal grid spacing and could be reduced in future studies. Note that Rotunno et al. (2009) pointed out that the horizontal grid spacing of 67 m still cannot fully resolve the TCBL turbulence. This seems to suggest that the smallest grid spacing of 55 m used in this study may be still not fine enough to fully resolve the TCBL turbulence. However, it is near the limit of our existing computing resources. Therefore, the horizontal grid spacing of the innermost domain in our simulation will be limited to 55 m, which covers the inner core (in a radius of 41.25 km from the storm center) of the simulated TC.

The model was calculated with a constant sea surface temperature of 301 K on an f -plane at 20°N (with $f = 5 \times 10^{-5} \text{ s}^{-1}$). The model was initialized with a Rankine vortex of maximum surface tangential wind speed of 20 m s^{-1} at a radius of 85 km from the vortex center embedded in a quiescent environment. The Jordan's Caribbean sounding (Gray et al., 1975) was used as the input profiles of humidity and temperature for the unperturbed tropical environment. In the simulation, d01–d03, d04, and d05 was initiated at 27-h, 2-h, and 1-h prior to the initiation of the d06, which was integrated for 7-hours. This period was selected because the simulated TC was in its rapid intensification stage, which was distinguished from the mature stage in previous studies (Rotunno et al., 2009; Green and Zhang, 2015; Zheng et al., 2020), so that we can examine the effects of horizontal grid spacing on the intensification of the model TC.

The following schemes for model physics were used in our simulation. The revised MM5 Monin-Obukhov surface layer scheme, WSM6 microphysics scheme (Hong and Lim, 2006), the Dudhia shortwave radiation scheme (Dudhia, 1989) and the Rapid Radiative Transfer Model (RRTM) for longwave radiation (Mlawer et al., 1997) were selected for all six domains (d01–d06). The Kain–Fritsch cumulus parameterization scheme (Kain, 1993; Kain, 2004) was used only in d01 (18 km). The Yonsei University (YSU) PBL scheme (Hong and Pan, 1996) was applied to d01–d03 and while the large eddy simulation (LES) option was used in the three innermost domains (d04–d06) to allow explicit simulation of the most energetic turbulence at sub-kilometer and sub-100-meters grid spacings. In the LES domains, the sub-grid scale (SGS) turbulence was parameterized by the Nonlinear Backscatter and Anisotropy (NBA) sub-filter-scale (SFS) stress scheme (Mirocha et al., 2010) with diagnostic stress terms ($\text{sfs_opt} = 1$ in WRF namelist).

RESULTS

In this section, we examine the impact of one-way nested domains with different grid spacings on the simulated TC under idealized conditions in terms of the intensity, inner-core size, and overall structure, and fine-scale features in TCBL. Note that since the similar sensitivity of the simulated TC to the grid spacing in the d01–d03 (18–2 km) domains was also conducted and discussed by Fierro et al. (2009) and Gentry and Lackmann (2010), we will focus mainly on the sensitivity of the simulated storm to the grid spacing in the d04–d06 (2 km–55 m) domains.



For convenience of discussions, we refer to d03, d04, d05, and d06 domains as the 2-km, 500-m, 166-m, and 55-m domains, respectively.

Intensity and Overall Structure of the Simulated Storm

Figure 1 shows the time series of the TC intensity and inner-core size in terms of the minimum sea level pressure (MSLP), instantaneous 10-m maximum wind speed (Vmax) and the radius of 10-m maximum wind speed (Rmax) for the 10-hour simulation after the initial 24-h model integration/spinup. The TC intensity in the 500-m grid spacing is the lowest MSLP (959.4 hPa), followed by the 166-m (961.1 hPa) and 55-m (960.5 hPa) grid spacings by the end of the 10-h simulation (**Figure 1A**). The largest increment of TC intensity is between the 2-km and 500-m grid spacings, followed by the second increment from the 500-m to 166-m grid spacings. The simulated TC intensity with the 55-m grid spacing shows little difference from that with the 166-m grid spacing. As the grid spacing increases, the instantaneous Vmax increases significantly, namely by about 36 m s^{-1} from the 55-m grid spacing to the 2-km grid spacing in the 9.5-h simulation, although the increase in the instantaneous Vmax is not a linear response to the reduction in grid spacing (**Figure 1B**). Of interest is small fluctuation in the instantaneous Vmax shown with 500-m grid spacing while much stronger fluctuations occur in the 166-m and 55-m grid spacing domains. This seems to suggest that even the 500-m grid spacing may not be able to explicitly resolve the turbulent eddies to any considerable extent. The increase in the instantaneous Vmax from the 2-km grid spacing to the 500-m grid spacing could be mainly attributed to the increase in the simulated TC sustained intensity. However, the large difference in the instantaneous

Vmax between the 500-m grid spacing and the 166-m or 55-m grid spacing is systematic and is mainly due to the fact that turbulent eddies can be explicitly resolved in the latter but not in the former. On the other hand, the Rmax shows a general decrease with reducing the grid spacing from 2 km to 500 m but then an increase with further reducing the grid spacing from 500 to 55 m (**Figure 1C**), namely showing a trend similar to that for the MSLP. To further investigate the sustained surface maximum wind, three LES simulations are averaged to grids with a common grid spacing of 2 km (**Figure 1D**). Of interest is that the sustained Vmax in $2 \text{ km} \times 2 \text{ km}$ box with the YSU PBL scheme shows similar value with 55-m grid spacing. Similar to that in Green and Zhang (2015), the difference of the sustained Vmax among the sub-kilometer grid spacing is also systematic and the sustained Vmax shows a decrease with reducing the grid spacing from 500 to 55 m.

To confirm the impact of the resolved turbulent eddies on the simulated TC, we show in **Figure 2** the horizontal distribution of instantaneous 10-m wind speed (m s^{-1}). In addition to the three coarse domains with the size the same as the domain d05 (166 m; **Figures 2A,B,C**), **Figures 2D,E** also show results from d05 and d06 with the size the same as the domain d6 to further distinguish the difference. First, the 166-m grid spacing starts to resolve roll-like turbulence but are less detailed with longer wavelengths. Second, consistent with Rmax, the 500-m grid spacing simulates the smallest eyewall size. This indicates that the size of the eyewall starts to converge at this sub-kilometer resolution. Third, because d06 only covers the eyewall region, we further compare the differences between the 500-m and 166-m grid spacings out of the eyewall later (see **Figure 8**). In addition to changes in the eyewall size, there are also significant differences among different domains. The 500-m and 166-m grid domain show some turbulence structure at a

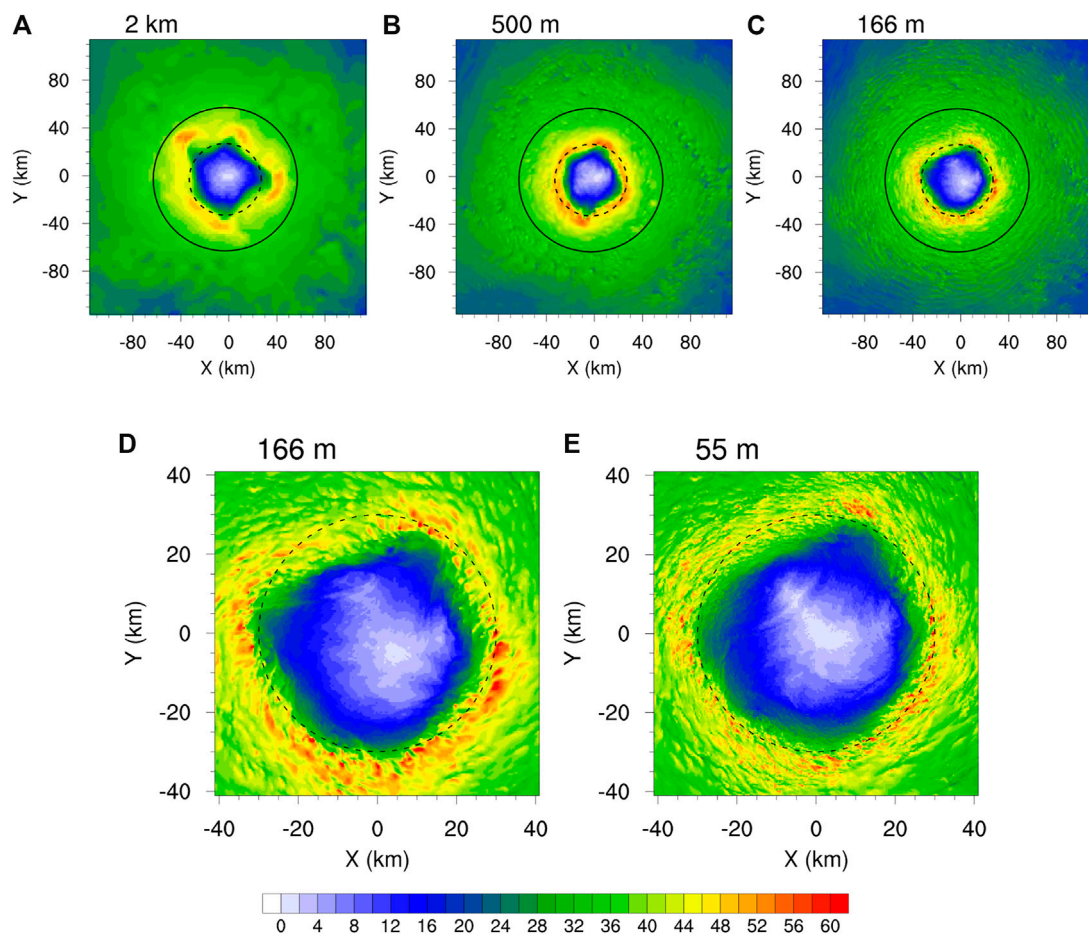


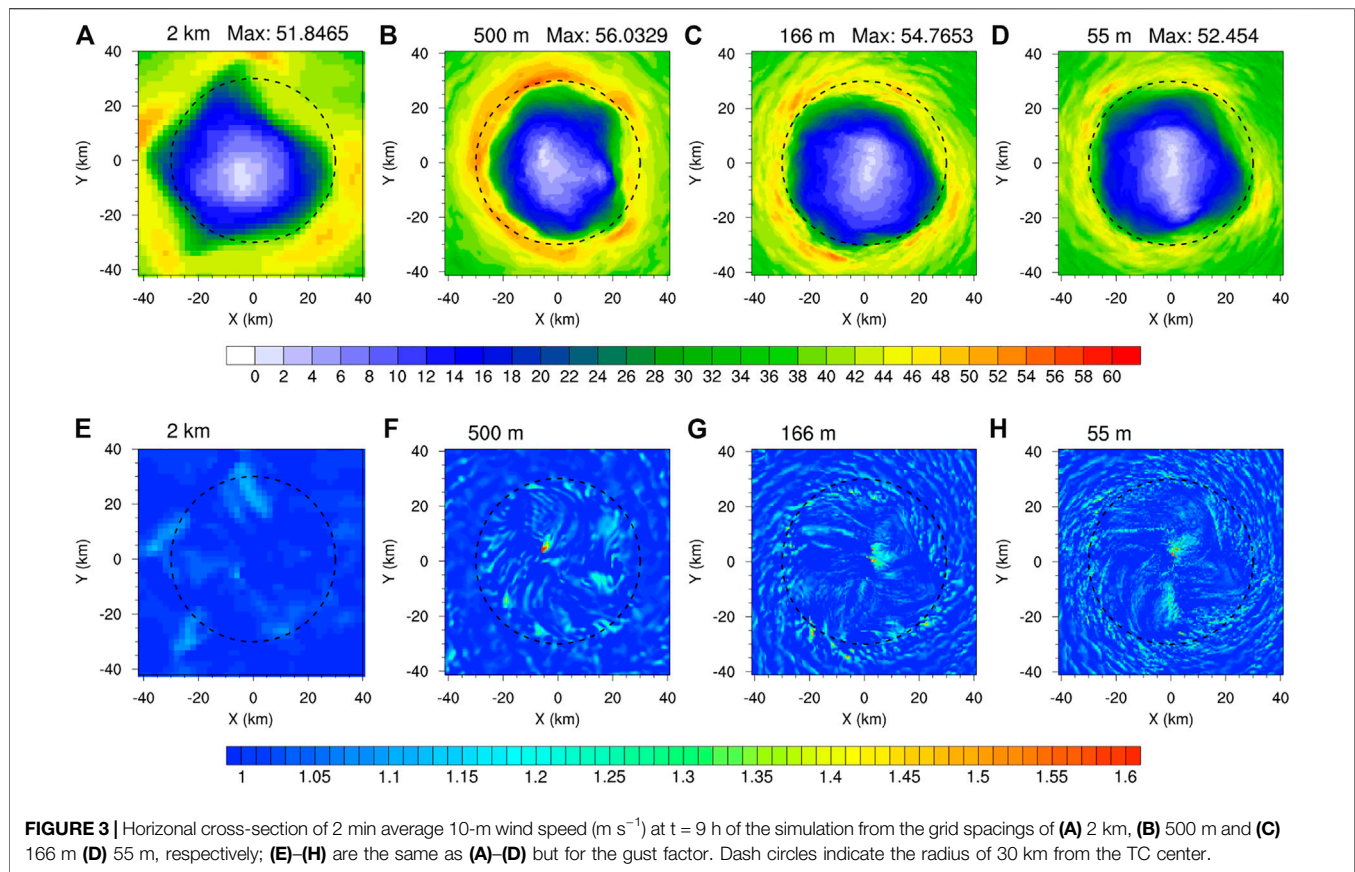
FIGURE 2 | Horizontal cross-section of instantaneous 10-m wind speed (m s^{-1}) at $t = 9$ h of the simulation from the grid spacings of (A) 2 km, (B) 500 m, and (C) 166 m with the domain size the same as d05; (D) and (E) are as in (C) but with the domain size the same as d06. Dash and solid circles indicate the radii of 30 and 60 km from the TC center, respectively.

radius of 40–60 km. Detailed analyses on these small-scale features will be given in sections 3b and 3c below.

In addition to the instantaneous wind distribution, we also analyzed the time averaged wind and gust factor distributions in the inner-core region of the simulated TC. This allows an examination of the impact of grid spacing on sustained winds (and also intensity). The sustained wind is 2-minutes average in the best-track data of CMA (China Meteorological Administrator) but 1-minutes average in that of JTWC (Joint Typhoon Warning Center). We calculated 2-minutes average 10-m wind speed (m s^{-1}) and the gust factor for domains with the grid spacing less than 2 km, with the results shown in Figures 3A,B,C,D and E,F,G,H respectively. Consistent with the MSLP, the sustained wind from the 55-m grid spacing is generally weaker than that from the 166-m grid spacing (Figures 3C,D). Interestingly, the domain with 500-m grid spacing begins to resolve gust wind in the inner-core region (cf. Figures 3E,F). Relatively large gust factors expand radially outward with as the grid spacing decreases because more energetic large eddies (fine-scale turbulence) can be resolved by the model resolution. Although both the finest resolution (166 and 55 m) domains

show similar structure and peak values in gust factor, the domain with the 55-m grid spacing still shows more detailed structure and stronger gusty winds that expand more outward than the domain with the 166-m grid spacing (Figures 3G,H).

Our results show a high degree of consistency with those of Ito et al. (2017). Their study examined structure of TCBL rolls by large eddy simulation of an entire TC. Although findings related to TCBL rolls were highly consistent, a nonnegligible difference is that Ito et al. (2017) showed most of the large gust factors located near the RMW, whereas our results clearly show large gust factors outside of the RMW. This may be attributed to the use of domain size for the entire TC, differences in the model configuration and physics parametrization in their study. For example, One possible reason for this difference is the choice of SGS scheme; Green and Zhang (2015) suggested that the use of NBA scheme reproduced better fine-scale than the TKE-based scheme. Figure 2 of this study can be directly compared with Figures 3E,F of Green and Zhang (2015) and Figure 3 of Zhu et al. (2019). The ability of the NBA scheme in the WRF model used in these studies and our results to resolve fine scale features guarantees that the horizontal wind would become widely



distributed, which may extend large gust factor to the outside of the RMW.

Note that although the 500-m grid spacing did not resolve the PBL turbulence, it still shows marked differences in the PBL turbulence from the 2-km grid spacing. The discrepancy in gust wind between the 500 and 166-m or 55-m grid spacings arises mainly from the difference in explicitly resolving the large eddies in PBL turbulence. The discrepancy between the 166 and 55-m grid spacings is due to the different scale in the resolved eddies in PBL turbulence. Namely, the 55-m grid spacing can explicitly resolve eddies with finer structure and shorter wavelength, and thus producing gust factors with more detailed structures (Figure 3H).

The azimuthal mean boundary layer structures of the simulated TC in 2-km, 500-m, 166-m, and 55-m domains are compared in Figure 4. Note that the 55-m domain only covers the eyewall region (Figure 4D), nevertheless, we don't see any noises near its lateral boundary, suggesting that the one-way nesting is successful in terms of the simulated azimuthal mean vortex-scale structure. The overall distributions of tangential and radial winds in the boundary layer are quite similar as the grid spacing decreased from 2 km to 55 m. However, the maximum inflow in the lower part of the boundary layer occurred at a slightly larger radius in the 2-km domain with slightly deeper and stronger inflow (Figure 4A). The radius of the maximum azimuthal mean tangential wind in the boundary layer is also larger in the 2-km domain than in

the 500 (Figure 4B), 166 m (Figure 4C) and 500 m (Figure 4D) domains. The azimuthal mean tangential wind is slightly stronger with a slightly deeper inflow layer in the 55-m domain than in the 500-m and 166-m domains.

To more clearly isolate the variations between the experiments attributable to the difference in horizontal grid spacing, the simulated height of maximum tangential wind is compared with observations (e.g., Zhang et al., 2011b and Franklin et al., 2003). Overall, there is a decrease in the height of the azimuthally averaged maximum tangential wind as the grid spacing decreases. The height of maximum tangential wind in the eyewall is above 600 m in all simulations with the horizontal grid spacing greater than 500 m. There is an evident decrease in the height of the azimuthal mean maximum tangential wind from the 166- to 55-m grid spacings, with the height between 400 and 600 m, slightly higher in the eyewall. The 55-m domain has the lowest height of the azimuthal mean maximum tangential wind, with a height of about 400 m. This is consistent with observations in Zhang et al. (2011b), who composited more than 793 dropsondes in TCs and showed that the maximum boundary layer tangential wind in the eyewall occurred between 400–1,300 m height. Franklin et al. (2003) also found that for an individual hurricane, the height of maximum tangential wind could be even lower than 400 m.

All domains exhibited a low frequency ($>0.05\%$) of strong updrafts ($>9 \text{ m s}^{-1}$) in the eyewall at about 4-km altitude as we can see from the contoured frequency by altitude diagrams (CFADs) in Figure 5, which is similar to the findings in

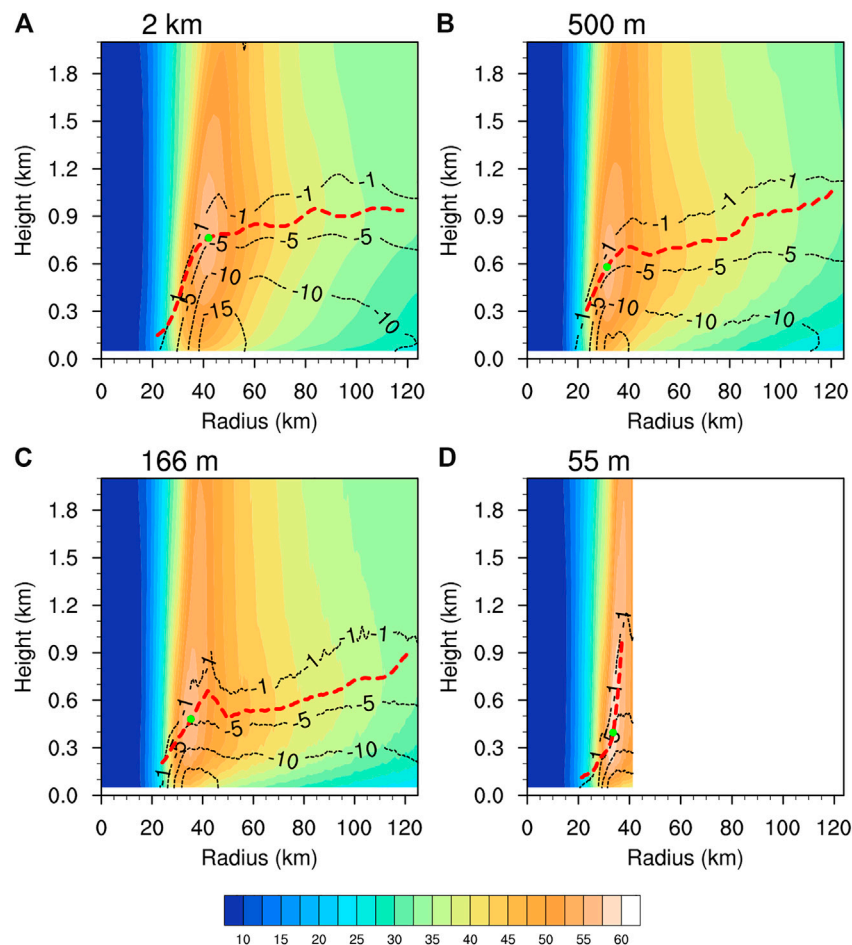


FIGURE 4 | Azimuth mean tangential (shaded, m s^{-1}) and radial (contour, m s^{-1}) winds at $t = 9$ h of the simulation from the grid spacings of (A) 2 km, (B) 500 m, (C) 166 m, and (D) 55 m, respectively. The red lines indicate the heights of the maximum tangential wind varying with radius. The green dot represents the location of the maximum tangential wind.

previous mesoscale model simulations (e.g., Fierro et al., 2009; Wang and Wang, 2014). Although the updraft distribution in the domain with the 2-km grid spacing did not show large differences, the strongest updrafts (near 9 m s^{-1} ; Figure 5A) are considerably less frequent than those simulated in the domain with the 500-m grid spacing (greater than 10% updrafts reached 12 m s^{-1} at 2–6 km altitude; Figure 5B). Note that only the 55-m and 166-m domains (Figures 5C,D) show another two low frequency of strong updrafts in the boundary layer at 300–400 m height and in the upper troposphere at about 11 km height, respectively, with maximum values increasing with decreasing of grid spacing, consistent with the LES simulations in Wu et al. (2019) and Zheng et al. (2020). The large difference in vertical motion in the boundary layer is mainly attributed to the resolved large eddies, corresponding the PBL rolls and tornado-scale vortices in the eyewall, which often result in extreme updrafts and increase both updrafts and downdrafts between (>3 and $<-3 \text{ m s}^{-1}$). In contrast, the 500-m domain produced a wider distribution of updraft at middle altitude although it started to show some weak updraft and downdrafts in the boundary

layer, an improvement compared to the 2-km domain. Nevertheless, compared to 166 and 55-m domains, the 500-m grid spacing is not high enough to resolve the strong turbulent eddy motion and the related updrafts and downdrafts in the TCBL boundary layer. We will show below that the resolved eddy-related strong updrafts and downdrafts in the boundary layer are related to the boundary layer horizontal rolls and tornado-scale vortices and they play important roles in enhancing vertical mixing, affecting both the structure and intensity of the simulated TC.

TCBL Horizontal Rolls

Figure 6 compares the horizontal distributions of vertical velocity at the 183-m height in the northeast quadrant at 8.75 h of the simulation from the three inner nest LES domains. Results from the 2-km grid spacing are not shown because there are little small-scale features in the 2-km domain. Note that the updraft-downdraft couplets along the azimuthal direction reflect the TCBL horizontal rolls. We can see from Figure 6 that the horizontal structure of the simulated TCBL horizontal depends

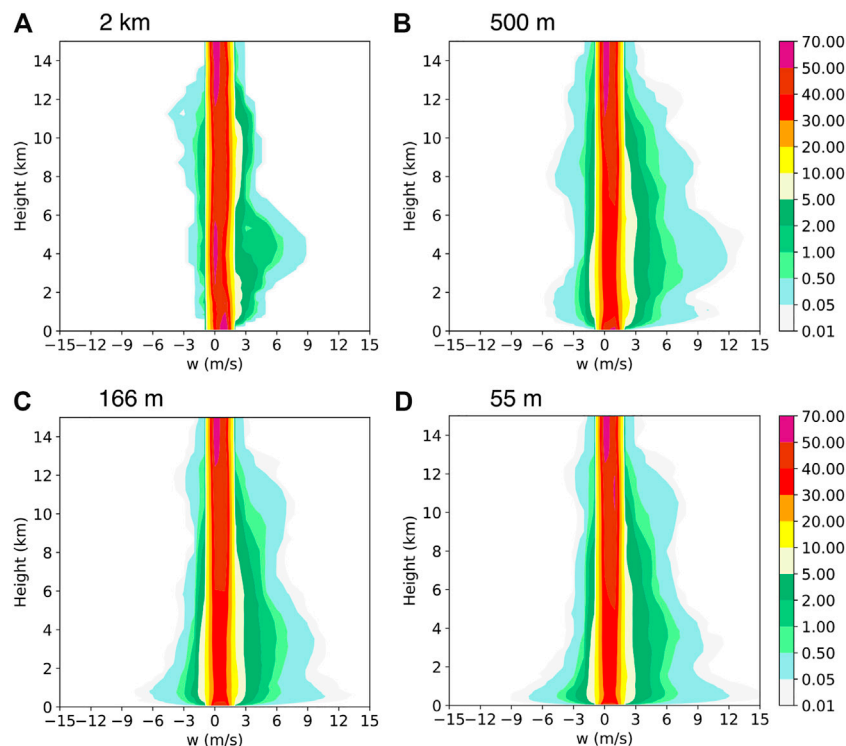


FIGURE 5 | CFADs of the simulated vertical velocity (w ; m s^{-1}) in the radius of 41.25 km from the storm center (namely in the d06 domain) at $t = 9$ h of the simulation from the grid spacings of **(A)** 2 km, **(B)** 500 m and **(C)** 166 m **(D)** 55 m, respectively.

strongly on model grid spacing. The 500-m grid spacing did not reproduce the line or banded structures in vertical motion, although it produced some fine-scale features of updraft and downdraft in the TCBL (**Figure 6A**), similar to those shown in Gentry and Lackmann (2010). The 166-m grid spacing produced two or three banded vertical motion between 6 and 8 m s^{-1} along the R_{max} in the eyewall region (**Figure 6B**), suggesting that this grid spacing starts to resolve the TCBL horizontal rolls. The 55-m domain produced shorter wavelength, stronger vertical motion and more lines along the R_{max} than the 166-m domain, also with some large difference in the structure of the simulated TCBL horizontal rolls. This indicates that the structure of the simulated TCBL rolls may be very sensitive to the horizontal grid spacing. It seems to suggest that sub-100-meters grid spacing is required to fully resolve fine-scale features of TCBL rolls.

To examine the different characteristics of the simulated large eddies and the resolved small turbulence in the 166-m and 55-m domains, we decomposed the model vertical motion at 183-m height in **Figures 6A–C** into scales with the wavelengths larger than 1,600 m (about 10 times of the 166-m grid spacing) as filtered and those with wavelengths less than 1,600 m as residual with the results shown in **Figures 6D–I**, respectively. Since the 500-m grid spacing can hardly resolve turbulent eddies, the filtered field is nearly the same as the original field. The filtered field in the 166-m domain shows similar magnitude of updraft and turbulent structure in the inner edge of the eyewall to that in the 55-m domain. However, compared to those in the 166-

m domain, the TCBL rolls in the 55-m domain extend much more radially outward and show much clearer banded and linearly shaped structure in the outer edge of the eyewall with much longer azimuthal length scales along the roll but shorter wavelengths cross the rolls in the radial direction. These features of the simulated TCBL rolls in the 55-m domain are more comparable with those in observations (Wurman and Winslow, 1998) than those simulated in the 166-m domain. In addition, larger discrepancies can be seen in the vertical motion with wavelength less than 1,600 m (**Figures 6G–I**) as the 55-m domain can resolve finer and stronger turbulent motions in addition to the TCBL rolls. These results demonstrate that even though the use of the recently updated NBA scheme for subgrid-scale turbulent processes, the 166-m grid spacing is not high enough to realistically resolve TCBL rolls and the fine turbulence structure in the LESs.

To have quick look at the vertical structure of TCBL rolls, we show in **Figure 7** the vertical cross section of vertical velocity and the perturbation horizontal winds along the line segment given in **Figure 6**. As we see from the horizontal distribution of vertical velocity in **Figure 6A**, the 500-m domain still cannot resolve TCBL rolls well either in the vertical cross-section (**Figure 7A**). Both the 166-m and 55-m domains simulated the roll structure typical of TCBL rolls: including intense updrafts from the surface to the top of the TCBL, downdrafts, which brought high momentum from top down, a cyclonic-anticyclonic couplet along rolls (**Figures 7B,C**). However, as the roll

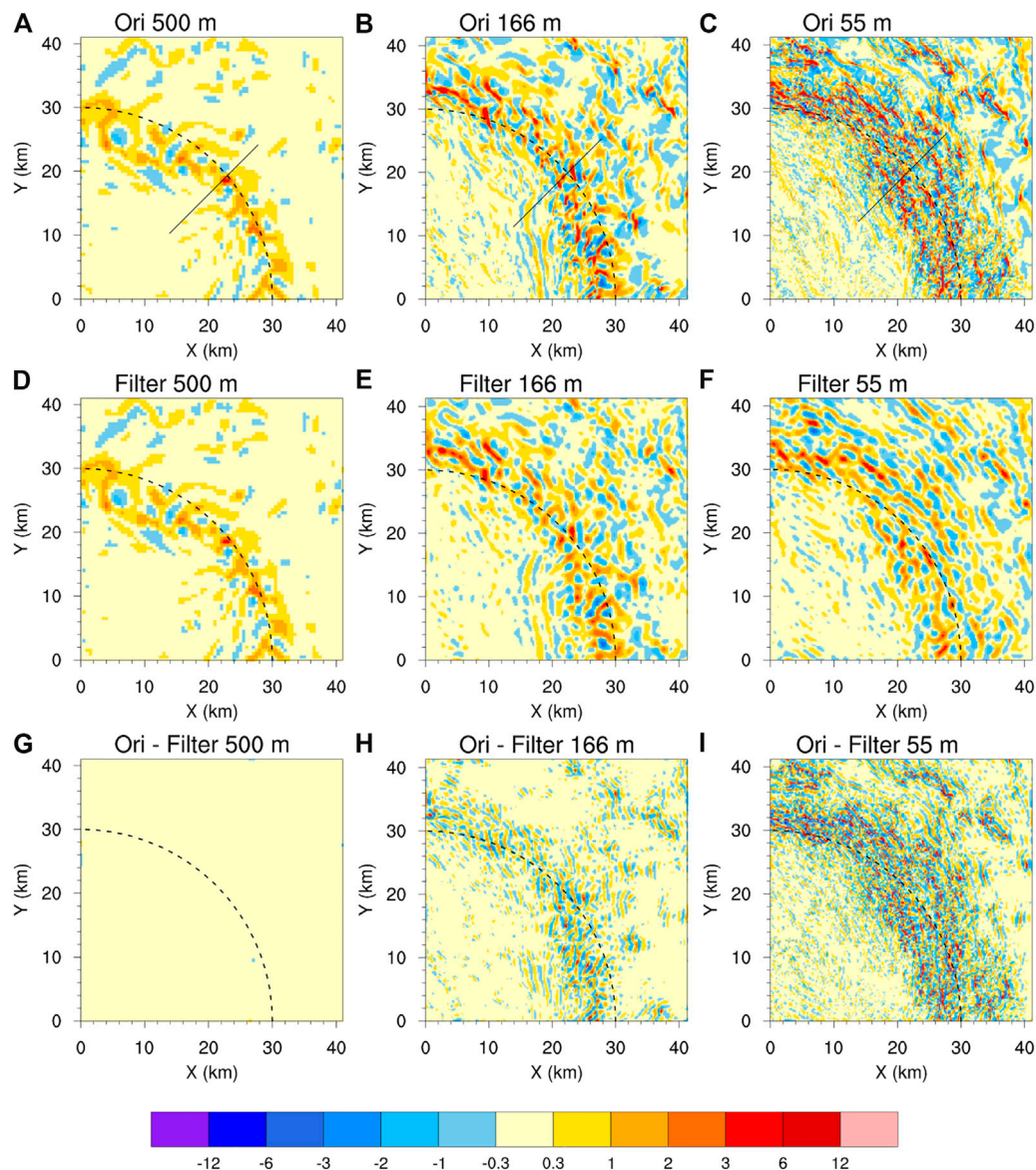
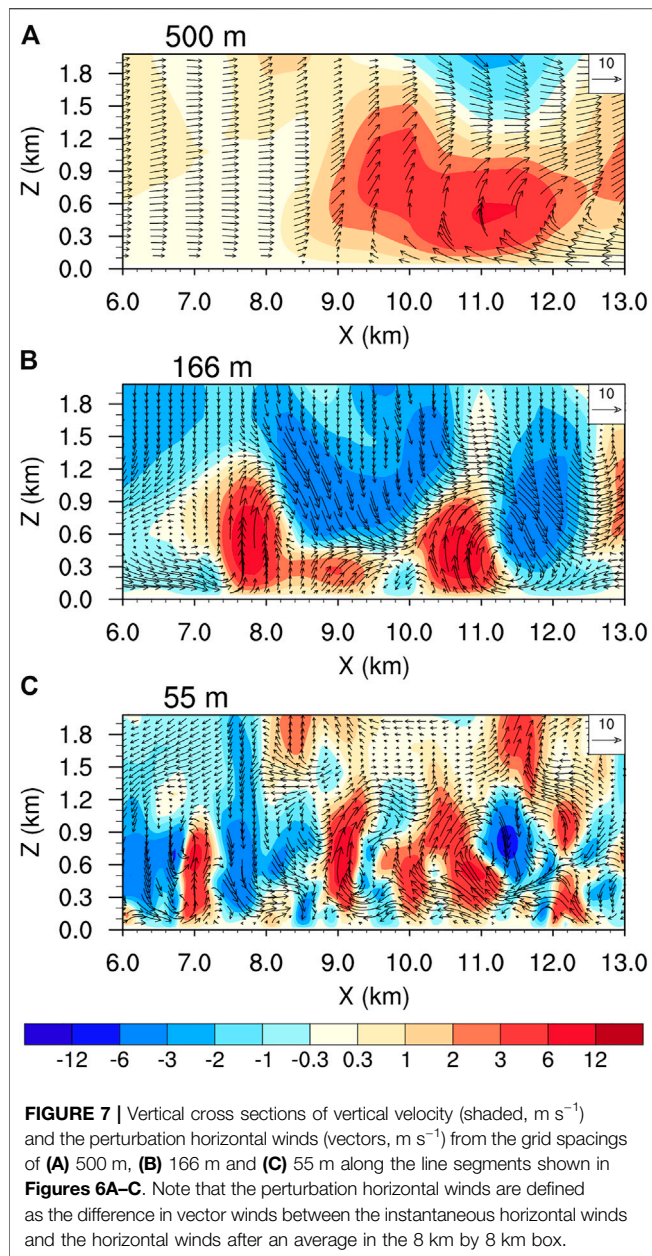


FIGURE 6 | Horizontal distributions of vertical velocity (m s^{-1}) at the 183-m height in the northeast quadrant at $t = 8.75$ h of the simulation from the grid spacings of (A) 500 m, (B) 166 m, and (C) 55 m. (D)–(F) and (G)–(I) are the same as (A)–(C) but for scales with the wavelengths larger than 1,600 m and those with wavelengths less than 1,600 m, respectively.

wavelength ranged from hundreds to several kilometers and was much shorter in the eyewall, for example, with a wavelength of 600 m in Wurman and Winslow (1998), not all TCBL rolls were reproduced by the 166-m grid spacing. Nevertheless, in terms of the updraft magnitude ($>12 \text{ m s}^{-1}$) and vertical extent ($\sim 1.2 \text{ km}$) of rolls, the 166-m domain still showed roll structure as fine as the 55-m domain.

In agreement with observations (Wurman and Winslow, 1998; Foster, 2005), the simulated wavelengths of the TCBL rolls in the 55-m domain are about 800–1,200 m (Figure 7C), much shorter than that in the 166-m domain ($>2000 \text{ m}$; Figure 7B). Another important feature is that smaller-scale rolls can be resolved and coexist in the 55-m domain

(Figure 7C). Nakanishi and Niino (2012) suggested that the roll vortices can be partly coupled with other processes, such as entrainments (ET), internal gravity waves (GW), and Kelvin–Helmholtz (KH) waves above the boundary layer. Compared with Fig. 12 in Nakanishi and Niino (2012), the characteristics of the rolls from the surface to about 300 m altitude is similar to their inflection point (IP) mode. The rolls at $x = 7 \text{ km}$ or 9 km are similar to their KH-IP mode and the roll at $x = 11 \text{ km}$ is similar to their ET mode. This suggests that the model can resolve the essential aspect of TCBL rolls as the grid spacing is sub-100-meters (reduced from 166 to 55 m). On the other hand, of interesting is that the 166-m grid spacing can produce better fine-scale rolls (Figure 8) in the outer core region



than that in inner core of the TC. This is possibly due to the fact that rolls in the outer core region may have relatively longer wavelength than those in the eyewall, as in observation.

Tornado Scale Vortices

As in (Wu et al., 2019), tornado scale vortex are defined as $w > 20 \text{ m s}^{-1}$ or $> 15 \text{ m s}^{-1}$ and vertical maximum vorticity $> 0.2 \text{ s}^{-1}$ (for 55 m) or $> 0.1 \text{ s}^{-1}$ (for 166 and 500 m). A comparison between the 500-m, 166-m and 55-m domains (Figures 9A–C) shows that there are only four extreme updrafts with $w > 20 \text{ m s}^{-1}$ and two of them with $w > 20 \text{ m s}^{-1}$ and vorticity $> 0.2 \text{ s}^{-1}$, which can be defined as tornado-scale vortices in the 55-m domain (Figure 9). The number of the extreme updrafts ($w > 20 \text{ m s}^{-1}$) in both the 166-m and 55-m domains are very

small. In the study of Wu et al. (2019), they show that there are 24 tornado-scale vortices found at the 11 h period (in their Table 1). Except for the 10 tornado-scale vortices at 27 h, 1–4 occur during 26–31 and 36 h. This indicate that there were 1–4 tornado-scale vortices for most of the time, when a LES is used to simulate the fine-scale features in TCBL from a single snapshot. The relatively small number of tornado-scale vortices is in agreement with Wu et al. (2019), and may be due to the relatively weak intensity of the simulated TC in this study. The count of vertical velocity $> 15 \text{ m s}^{-1}$ in the 166-m domain is remarkably less than that in the 55-m domain. The 55-m grid spacing produced much stronger updrafts and simulated tornado-scale vortices with less restrict criteria than the 166-m grid spacing.

The local surface wind and perturbation winds shown in Figure 10 suggested the small-scale boundary layer features of about $10 \text{ km} \times 10 \text{ km}$ box on the inner edge of the eyewall prevailed extreme updraft and vorticity at the 500-m altitude. It is important to note that tornado-scale vortices in the 55 m-domain (cf. Figures 10A,B) are surrounded by banded relative higher wind speed, which could be associated with TCBL rolls. The vertical structure around a tornado-scale vortex shown in Figure 11 reveals that updraft in the 166-m domain is much weaker ($\sim 22 \text{ m s}^{-1}$) than that of ($> 30 \text{ m s}^{-1}$) in the 55-m domain, and the wind field is smoother because it could not resolve smaller scale features. Moreover, the 3D structure (Figure 12) reveals the presence of boundary layer rolls under tornado-scale vortices near the surface. Previous studies (Wu et al., 2018; Wu et al., 2019) suggested that extreme updrafts are mainly attributed to tornado-scale vortices, while strong updrafts could result from boundary layer rolls. Our results suggest, however, that multi-scale interaction between boundary layer rolls and tornado-scale vortices might play important roles in producing extreme updrafts in TCBL as well. Unlike those in the 55-m domain, the tornado-scale vortices in the 166-m domain do not show multi-scale interaction between boundary layer rolls and tornado-scale vortices (cf. Figures 12A,B). The result seems to suggest that the interaction between boundary layer rolls and tornado-scale vortices could result in more extreme updrafts and stronger maximum winds, such as that we see from the 55-m grid spacing. The simulated TCBL roll and tornado-scale vortices are sensitive to the grid spacing.

The interaction between boundary layer rolls and tornado-scale vortices are show similar characteristics with airborne observations in the inner core of Hurricane Hugo first discussed by Marks et al. (2008). Marks et al. (2008) showed that the eyewall vorticity maximum (EVM) along the inner edge of the eyewall, which were similar to tornado-scale vortices seen in this study, were embedded within the boundary layer roll-like structures on the inner edge of the eyewall. Zhang et al. (2011a) suggested that this kind of features were considered to have short time-scale but showed very intense signatures locally. The magnitude and the heights of boundary layer rolls they observed in Hurricane Hugo indicate that they might be evidence of interaction between boundary layer rolls and tornado-scale vortices from 55-m grid spacing in our results.

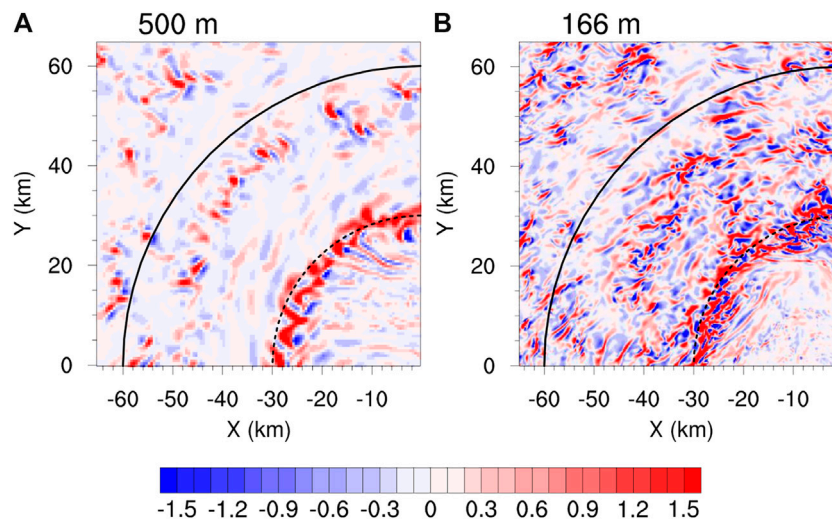


FIGURE 8 | Horizontal distribution of vertical velocity (m s^{-1}) at the 183-m height in the northwest quadrant at $t = 8.75$ h of the simulation from the grid spacings of (A) 500 m and (B) 166 m, respectively.

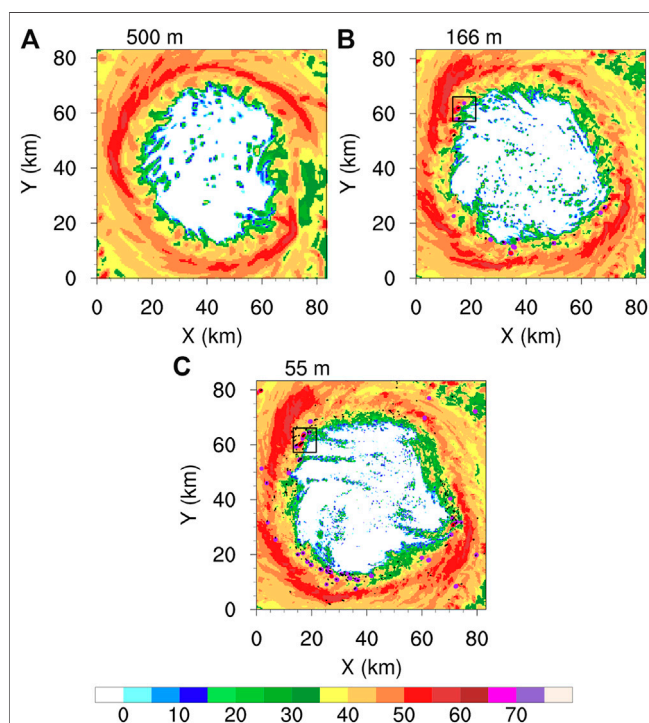


FIGURE 9 | The simulated radar reflectivity (dBZ) with vertical maximum vorticity $>0.2 \text{ m s}^{-1}$ or 0.1 m s^{-1} (black contour), $w > 15 \text{ m s}^{-1}$ (purple contour) and $w > 20 \text{ m s}^{-1}$ (red contour) at $t = 9$ h of the simulation from the grid spacings of (A) 500 m, (B) 166 m and (C) 55 m, respectively.

Vertical Momentum Flux and Energy Spectra

To further show the impact of grid spacing on the simulated TC inner-core turbulent processes, we examined the vertical momentum fluxes from different grid spacings with the results

shown in **Figure 13**. There are two components of the vertical momentum fluxes from, respectively, the parameterized sub-grid scale (SGS) and the resolved eddy processes. The vertical momentum fluxes are calculated following Green and Zhang (2015) and Zhu et al. (2019). Specifically, the resolved fluxes are estimated by the resolved turbulences with scales smaller than 2 km. The SGS fluxes directly output by WRF model are calculated from Eq. 7 of Mirocha et al. (2010). The SGS momentum fluxes in the TCBL decrease as the grid spacing decreases. The SGS momentum fluxes in the 55-m domain is very smaller than those in the 166-m and 500-m domains. In contrast to the SGS vertical momentum fluxes, the vertical momentum fluxes by the resolved eddy motions increase as the grid spacing decreases. Importantly, the total vertical momentum fluxes also decrease as the grid spacing decreases in the boundary layer. For example, the vertical momentum fluxes in the boundary layer from the 55-m grid spacing is much larger than that from the 500-m grid spacing, but show less discrepancies between the heights of 50 and 200 m. Furthermore, although the difference in the total vertical momentum fluxes between the 166-m and 55-m grid spacings are much closer, the 55-m grid spacing still produces slightly larger vertical momentum fluxes in middle and smaller in the lower boundary layer. This means that the relatively coarse horizontal resolution may considerably underestimate (overestimate) the middle (lower) boundary layer vertical mixing in the simulated TCs. Note that the vertical distributions of both the resolved and SGS momentum fluxes are similar to those in previous studies (Green and Zhang, 2015; Zhu et al., 2019), but with much smaller magnitude mainly because the intensity of the storm (with MSLP of 960–965 hPa) in this study is much weaker than that in their studies.

The coarser resolution with the NBA SGS parameterization scheme overestimates and underestimates the vertical momentum fluxes in the lower and middle boundary layer, respectively. In the coarse resolution simulation (e.g., 500 m), the total momentum fluxes are mainly determined by the SGS fluxes. Therefore, simulations of a coarse resolution would be

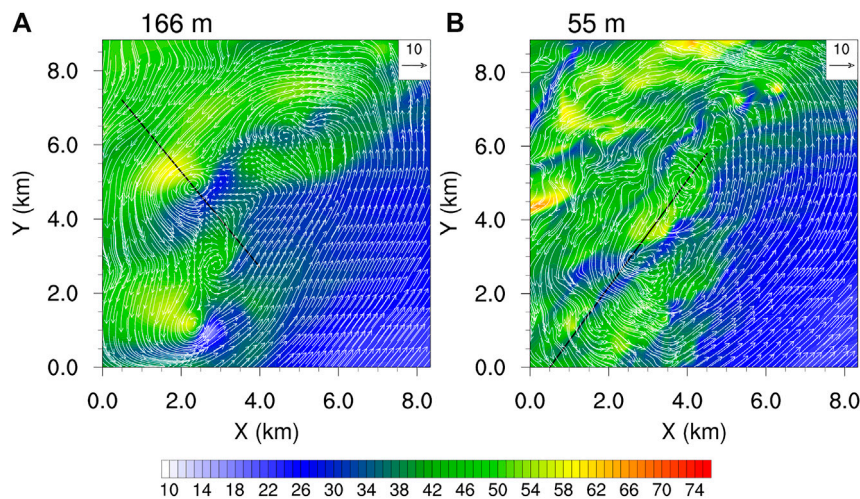


FIGURE 10 | Horizontal distributions of perturbational winds (vector, m s^{-1}) at 512 m height and surface wind speed (shaded, m s^{-1}) at $t = 9$ h of the simulation from the grid spacings of (A) 166 m and (B) 55 m in the rectangle shown in **Figures 9B,C**, respectively.

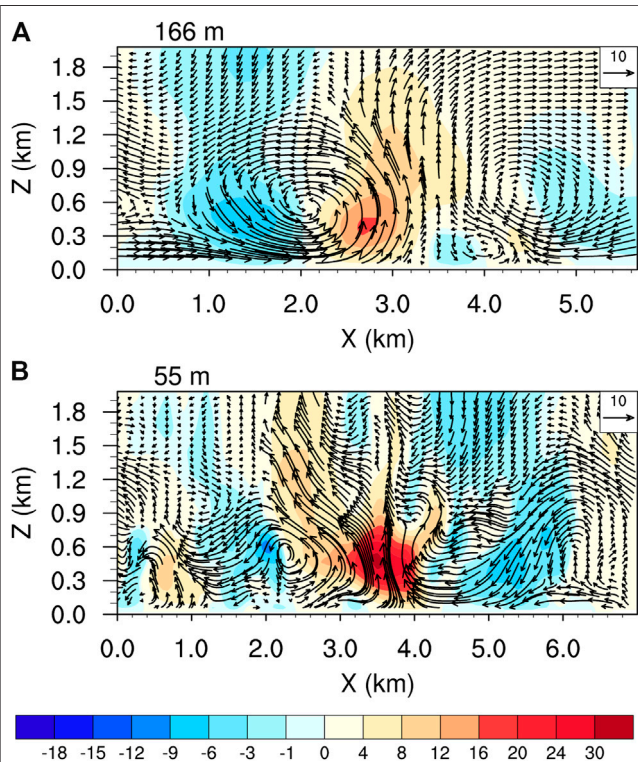


FIGURE 11 | Vertical cross sections of vertical velocity (shaded, m s^{-1}) and the perturbation winds (vectors, m s^{-1}) along the line segment in **Figure 10** from the grid spacings of (A) 166 m and (B) 55 m, respectively.

more sensitive to the SGS scheme used in the model than those of a fine resolution. The simulated total momentum fluxes do not monotonically increase or decrease with the grid spacing in the vertical. These analyses strongly suggest that the representation of SGS vertical mixing in the gray zone is still

an issue, especially in high turbulent TC conditions, even the recently updated NBA SGS scheme are used. Furthermore, recent modifications to the SGS boundary layer parameterization, such as the scale-aware schemes (Shin and Hong, 2015) in which the vertical profile of diffusion are multiplied by a factor estimated based on the PBL height and grid spacing may still not solve the problem. Therefore, more endeavor should be given to improve the parameterization of subgrid-scale boundary layer processes so that the effect of the unresolved fine-scale motions in the TC boundary layer can be reasonably represented.

The dependence of the vertical momentum fluxes on grid spacing can be understood by the difference in the resolved scales from different grid spacings. As we can see from **Figure 14**, which shows the energy spectra of vertical velocity at the 183-m altitude from different grid spacings in the radius of 41.25 km, namely in the d06 domain. As expected, the resolved scales strongly depend on the grid spacing. Given the ratio between the wavelength and grid spacing in the order of 10, it seems that the 55-m grid spacing is close to provide the convergence toward the TCBL horizontal rolls. This is because their wavelengths of 800–1,200 m are much longer than 10 times of the grid spacing of 55 m while the 166-m grid spacing could not resolve these fine-scale TCBL rolls. This suggests that a sub-100-meters grid spacing is required to realistically resolve TCBL rolls and tornado-scale vortices.

Note that in the study of Rotunno et al. (2009), the grid spacing of 67 m still cannot completely resolve TCBL turbulence. Due to the computational constraint, the horizontal grid spacing of the innermost domain in our simulation is limited to 55 m, slightly finer than that in Rotunno et al. (2009) but still coarser than 36 m in (Wu et al., 2018; Wu et al., 2019). It is still an open question what is the finest horizontal grid spacing that can be fine enough to fully resolve TCBL turbulence and provide the converged solution to their upscale impact on the fine-scale TC structure and intensity change.

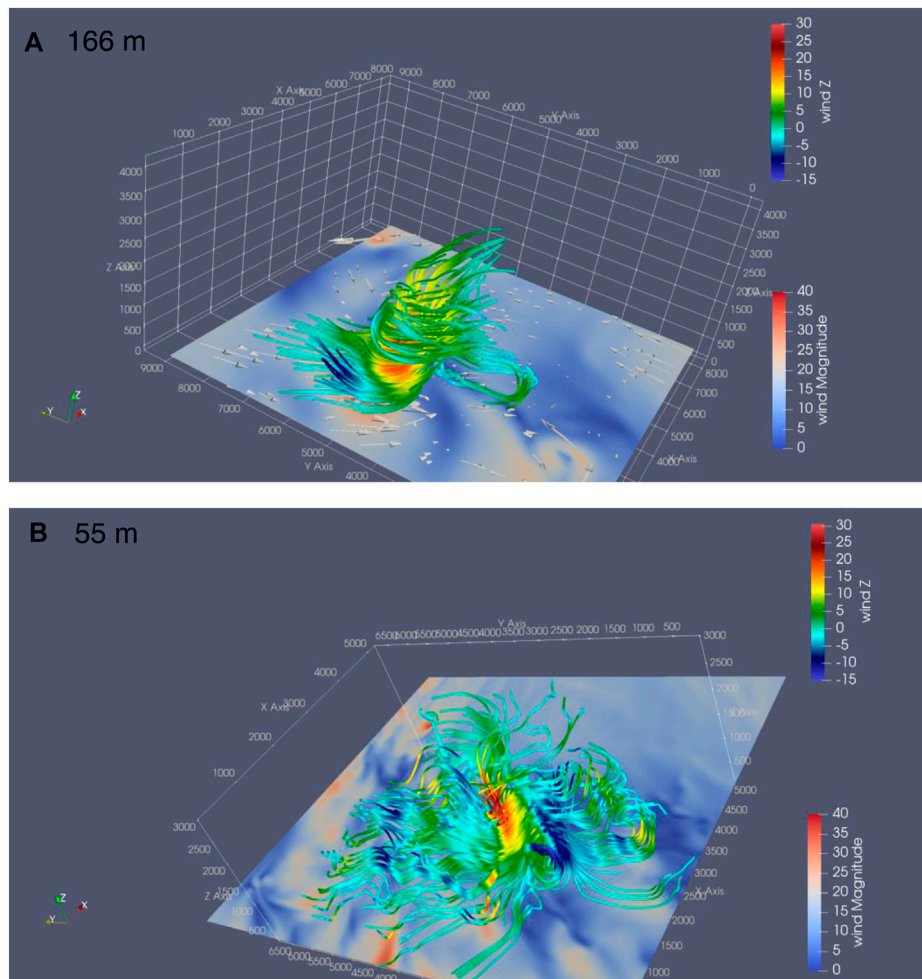
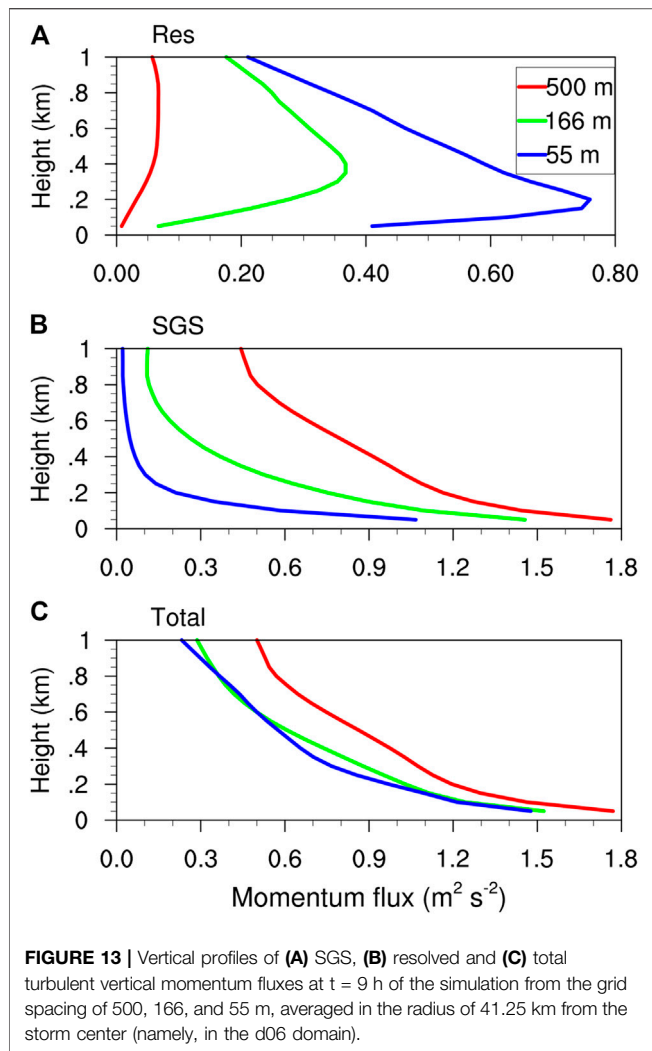


FIGURE 12 | Three-dimensional streamlines of perturbation wind (m s^{-1}) colored with vertical velocity (m s^{-1}) and surface perturbation wind speed (shaded, m s^{-1}) at $t = 9$ h of the simulation from the grid spacings of (A) 166 m and (B) 55 m. The scale of vertical coordinate is doubled as its size is much smaller than the horizontal coordinate.

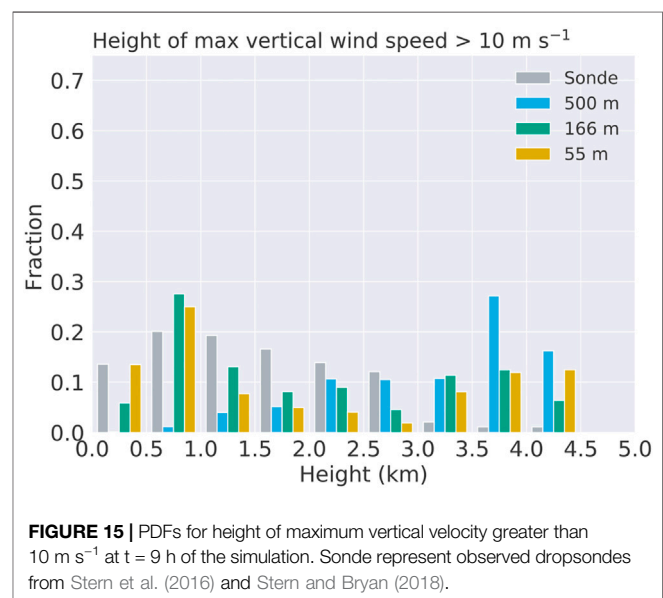
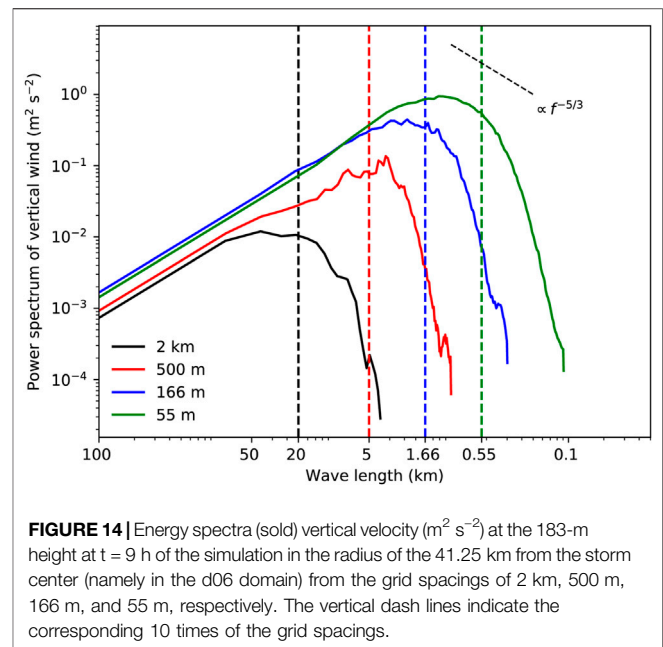
Figure 15 shows PDFs for the height of the simulated maximum vertical velocity and the height of the simulated maximum wind speed, along with the respective heights from dropsonde (Stern et al., 2016; Stern and Bryan, 2018). The heights of maximum vertical velocity decreases noticeably as grid spacing decreases. This is in agreement with the height of azimuthally averaged tangential winds, which indicate that, with smaller grid spacing, there is an evidently decrease in the height of the maximum horizontal and vertical winds. There is relatively good agreement between the finer grid spacing simulated and observed heights of the updrafts greater than 10 m/s, with extreme updrafts observed with similar frequencies within the lowest 500 m in the PBL (Figure 15). The peak frequency vertical motion is found at between 500 and 1,000 m in the 166 m, 55 m domains and observation, as opposed to 3,500–4,000 m in the 500 m domain. The presence of stronger vertical motion in the PBL at smaller grid spacing is physically attributable to the improved resolving of fine-scale features in the higher-resolution domains.

DISCUSSION

As TC research moves toward large eddy simulation, it is crucial that horizontal grid spacing smaller than 1 km are well examined in order to be a good reference for the development of future operational TC forecast and research models. We note that Rotunno et al. (2009) found that turbulence could only be resolved by a model at the finest resolution of 62 m in their simulation of an idealized TC. However, Green and Zhang (2015) showed that sub-kilometer grid spacing could start to be able to resolve turbulence consistent with observations. They attributed the discrepancy to the use of the NBA (nonlinear backscatter with anisotropy) SGS scheme. They showed that simulations with the NBA SGS scheme produced better small-scale features than the TKE scheme in the LES simulations with sub-kilometer grid spacings. Our results agree with those of Green and Zhang (2015); we also show that a grid spacing of 166 m can reasonably resolve the macro aspects of boundary layer rolls and tornado-scale vortices in the simulated TC, especially in the outer core region.



Previous studies (Walters, 2000; Gentry and Lackmann, 2010) have shown that grid spacing finer than $1/10$ of the wavelength is necessary to realistically reproduce the physical phenomena. Our results show that even for the wavelengths larger than 1,600 m, the 166-m grid spacing still cannot reproduce all important characteristics of TCBL roll structures (e.g., radial distribution and banded structure) that simulated in the 55-m domain. The ability to resolve the fine scales of turbulence at 55-m or smaller grid spacings seems to be important to resolve the rolls, multi-scale turbulent interaction, and tornado-scale vortices. One of the possible reasons could be related to the unrealistic representation of SGS parameterization. This is reported by previous non-TC studies (Muñoz-Esparza et al., 2014; Doubrawa and Muñoz-Esparza, 2020). For example, Muñoz-Esparza et al. (2014) suggested that energy cannot be dissipated by the SGS parameterization and can result in overestimate of the resolved motions. In our results, overestimates and underestimates the vertical momentum fluxes in the lower and middle boundary layer in the 166-m and 500-m domains are possibly caused by the unrealistic representation of SGS parameterization. Observations showed that the dominant wavelengths of turbulence near the



eyewall are very short [e.g., 600 m in Wurman and Winslow (1998)]. This may also explain why the 166-m grid spacing domain could not resolve the turbulence process in the eyewall region while can produce the broad turbulence features in the outer core region where the turbulent eddies have relatively longer wavelengths. Therefore, our results demonstrate that even the model grid spacing close to 100 m is still not fine enough to reproduce fine-scale features in the inner core region in TCBL and sub-100-m grid spacing is desired to realistically resolve TCBL fine-scale features in numerical models.

The 500-m grid spacing seems to be critical to whether a LES with NBA scheme is appropriate for TC simulations. This is

crucial for the operational TC numerical forecasting community, because the sub-kilometer grid spacing, such as 500 m, could be about to be affordable for real-time operational forecasting. Although the 500-m grid spacing cannot resolve fine-scale features of turbulent eddies, such as TCBL horizontal rolls and tornado-scale vortices as shown in this study, it can produce the TC-scale structure and intensity much better than kilometer grid spacings (Bryan et al., 2003).

An issue for a sub-kilometer grid spacing also arises as to the existence of the turbulent gray zone or “terra incognita,” or sub-100-meters. The relatively coarse grid spacing of around 500 m in the turbulent gray zone potentially benefits the conventional TC intensity and size forecasting. Therefore, future work will be done to determine what kind of the subgrid PBL scheme (e.g., convectional scheme, scale-aware scheme, or TKE scheme) can be used to achieve the optimal performance of the model at about 500-m grid spacing in simulating/predicting TC structure and intensity. It might be a good topic to develop new turbulent parameterization schemes that can include contributions by the organized large-eddies in TCBL and thus can be used in the models with grid spacings in the turbulent gray zone.

CONCLUSION

In the present study, the Weather Research and Forecast (ARW-WRF) mesoscale model with multiple one-way moving nests and nonlinear backscatter with anisotropy (NBA) sub-grid-scale (SGS) scheme was utilized to examine the sensitivity of TCBL fine-scale features to model grid spacing from kilometers through sub-kilometer to sub-100-meters. The focus is on the effects of horizontal grid spacing on the 7–10 h simulation of the boundary layer rolls and tornado-scale vortices in the inner core region of an intensifying TC under idealized conditions.

Results show that reducing the horizontal grid spacing from kilometers to sub-kilometer (e.g., 500 m) can reasonably capture the TC intensity change and TC-scale vortex structure, and further reducing the grid spacing from sub-kilometer to sub-100-meters can start to resolve well organized fine-scale eddies, including TCBL rolls and tornado-scale vortices. Furthermore, as the horizontal grid spacing decreases, increasingly more realistic fine structures in the TC eyewall can be simulated. However, because the resolved eddies at higher resolutions play an important role in enhancing the vertical momentum mixing, the simulated TC intensity often does not increase with the increasing model resolution and the eyewall size may increase a little bit as the grid spacing increases from about 500 m.

Compared with mesoscale simulations using grid spacings of kilometers, three innermost domains of sub-kilometer grid spacings with the use of an NBA SGS scheme show considerable improvements to the simulations of fine-scale features in TCBL. It is found that the 166-m grid spacing can simulate tornado-scale vortices, TCBL horizontal rolls and the

associated near surface instantaneous wind gust. However, the sub-100-meters grid spacing (55 m) seems to be necessary to simulate finer scale rolls with wavelengths about 400–800 m. More importantly, only the sub-100-meters grid spacing can simulate the multiscale interactions between boundary layer rolls and tornado-scale vortices, including extremely intense updrafts of greater than 30 m s^{-1} near the inner edge of the TC eyewall. Nevertheless, we also found that the wavelengths of TCBL rolls increase with increasing distance from the TC center and thus the 166-m grid spacing also simulated TCBL rolls outside the inner core better than in the eyewall. Considering the cost effectiveness, our results seem to suggest a grid spacing of sub-100-meters is desirable to produce more detailed and fine-scale structure of TCBL horizontal rolls and tornado-scale vortices, while the relative coarse grid spacing of sub-kilometer (e.g., 500 m) is more cost-effective and feasible for research and operational forecasts if the major interests are not on the turbulence processes in the inner-core region of TCs.

In addition, constrained by computational resource, the innermost domain with the 55-m grid spacing only covered the inner core of the simulated TC. We showed that the 166-m grid spacing can marginally resolve boundary layer rolls outside the inner core (Figure 8) and could partially resolve the rolls and tornado-scale vortices in the eyewall region. However, it is unclear whether the boundary layer rolls in the outer core display any different characteristics of those in the eyewall because our finest grid spacing only covered the inner core region. This may be a topic for a future study examine the performance of different horizontal grid spacing in simulating the fine-scale features in the outer core region of a TCs.

DATA AVAILABILITY STATEMENT

The datasets presented in this study can be found in online repositories. The names of the repository/repositories and accession number(s) can be found below: <https://zenodo.org/badge/latestdoi/10.5281/zenodo.305684938>.

AUTHOR CONTRIBUTIONS

HX contributed to figures included in this manuscript. HX and YW wrote the manuscript. All authors contributed to the article and approved the submitted version.

FUNDING

This study was supported in part by the National Key R&D Program of China under grant 2017YFC1501602 and in part by the National Natural Science Foundation of China under grants 41730960, 41905095 and 61827901.

REFERENCES

- Bao, J.-W., Gopalakrishnan, S. G., Michelson, S. A., Marks, F. D., and Montgomery, M. T. (2012). Impact of Physics Representations in the HWRF on Simulated Hurricane Structure and Pressure-Wind Relationships. *Monthly Weather Rev.* 140, 3278–3299. doi:10.1175/mwr-d-11-00332.1
- Bryan, G. H., and Morrison, H. (2012). Sensitivity of a Simulated Squall Line to Horizontal Resolution and Parameterization of Microphysics. *Monthly Weather Rev.* 140, 202–225. doi:10.1175/MWR-D-11-00046.1
- Bryan, G. H., Wyngaard, J. C., and Fritsch, J. M. (2003). Resolution Requirements for the Simulation of Deep Moist Convection. *Monthly Weather Rev.* 131, 2394–2416. doi:10.1175/1520-0493(2003)131<2394:Rrftso>2.0.CO;2
- Bu, Y. P., Fovell, R. G., and Corbosiero, K. L. (2017). The Influences of Boundary Layer Mixing and Cloud-Radiative Forcing on Tropical Cyclone Size. *J. Atmos. Sci.* 74, 1273–1292. doi:10.1175/jas-d-16-0231.1
- Chen, L., and Meng, Z. (2001). An Overview on Tropical Cyclone Research Progress in China during the Past Ten Years. *Chin. J. Atmos. Sci.* 5, 420–432. doi:10.3878/j.issn.1006-9895.2001.03.11
- Chen, P., Yu, H., Xu, M., Lei, X., and Zeng, F. (2019). A Simplified index to Assess the Combined Impact of Tropical Cyclone Precipitation and Wind on China. *Front. Earth Sci.* 13, 672–681. doi:10.1007/s11707-019-0793-5
- Doubrawa, P., and Muñoz-Esparza, D. (2020). Simulating Real Atmospheric Boundary Layers at gray-zone Resolutions: How Do Currently Available Turbulence Parameterizations Perform? *Atmosphere* 11, 345. doi:10.3390/atmos11040345
- Duan, Y., Wan, Q., Huang, J., Zhao, K., Yu, H., Wang, Y., et al. (2019). Landfalling Tropical Cyclone Research Project (LTCRP) in China. *Bull. Am. Meteorol. Soc.* 100, ES447–ES472. doi:10.1175/BAMS-D-18-0241.1
- Dudhia, J. (1989). Numerical Study of Convection Observed during the winter Monsoon experiment using a Mesoscale Two-Dimensional Model. *J. Atmos. Sci.* 46, 3077–3107. doi:10.1175/1520-0469(1989)046<3077:nsocod>2.0.co;2
- Emanuel, K. (2018). 100 Years of Progress in Tropical Cyclone Research. *Meteorol. Monogr.* 59, 151–168. doi:10.1175/amsmonographs-d-18-0016.1
- Fierro, A. O., Rogers, R. F., Marks, F. D., and Nolan, D. S. (2009). The Impact of Horizontal Grid Spacing on the Microphysical and Kinematic Structures of strong Tropical Cyclones Simulated with the WRF-ARW Model. *Monthly Weather Rev.* 137, 3717–3743. doi:10.1175/2009mwr2946.1
- Foster, R. C. (2005). Why Rolls Are Prevalent in the hurricane Boundary Layer. *J. Atmos. Sci.* 62, 2647–2661. doi:10.1175/jas3475.1
- Franklin, J. L., Black, M. L., and Valde, K. (2003). GPS Dropwindsonde Wind Profiles in Hurricanes and Their Operational Implications. *Weather Forecast.* 18, 32–44. doi:10.1175/1520-0434(2003)018<0032:GDWPIH>2.0.CO;2
- Gao, K., and Ginis, I. (2014). On the Generation of Roll Vortices Due to the Inflection point Instability of the hurricane Boundary Layer Flow. *J. Atmos. Sci.* 71, 4292–4307. doi:10.1175/jas-d-13-0362.1
- Gentry, M. S., and Lackmann, G. M. (2010). Sensitivity of Simulated Tropical Cyclone Structure and Intensity to Horizontal Resolution. *Monthly Weather Rev.* 138, 688–704. doi:10.1175/2009mwr2976.1
- Gopalakrishnan, S. G., Marks, F., Zhang, J. A., Zhang, X., Bao, J.-W., and Tallapragada, V. (2013). A Study of the Impacts of Vertical Diffusion on the Structure and Intensity of the Tropical Cyclones Using the High-Resolution HWRF System. *J. Atmos. Sci.* 70, 524–541. doi:10.1175/jas-d-11-0340.1
- Grasso, L. D. (2000). The Differentiation between Grid Spacing and Resolution and Their Application to Numerical Modeling. *Bull. Am. Meteorol. Soc.* 81, 579–580. doi:10.1175/1520-0477(2000)081<0579:CAA>2.3.CO;2
- Gray, W. M., Ruprecht, E., and Phelps, R. (1975). Relative Humidity in Tropical Weather Systems. *Monthly Weather Rev.* 103, 685–690. doi:10.1175/1520-0493(1975)103<0685:RHITWS>2.0.CO;2
- Green, B. W., and Zhang, F. (2015). Numerical Simulations of hurricane Katrina (2005) in the Turbulent gray Zone. *J. Adv. Model. Earth Syst.* 7, 142–161. doi:10.1002/2014ms000399
- Hill, K. A., and Lackmann, G. M. (2009). Analysis of Idealized Tropical Cyclone Simulations Using the Weather Research and Forecasting Model: Sensitivity to Turbulence Parameterization and Grid Spacing. *Monthly Weather Rev.* 137, 745–765. doi:10.1175/2008mwr2220.1
- Hong, S.-Y., and Lim, J.-O. J. (2006). The WRF Single-Moment 6-class Microphysics Scheme (WSM6). *Asia Pac. J. Atmos. Sci.* 42, 129–151.
- Hong, S.-Y., and Pan, H.-L. (1996). Nonlocal Boundary Layer Vertical Diffusion in a Medium-Range Forecast Model. *Mon. Wea. Rev.* 124, 2322–2339. doi:10.1175/1520-0493(1996)124<2322:nblvdi>2.0.co;2
- Ito, J., Oizumi, T., and Niino, H. (2017). Near-surface Coherent Structures Explored by Large Eddy Simulation of Entire Tropical Cyclones. *Sci. Rep.* 7, 3798. doi:10.1038/s41598-017-03848-w
- Kain, J. S., and Fritsch, J. M. (1993). Convective Parameterization for Mesoscale Models: The Kain-Fritsch Scheme. *Meteorol. Monogr.* 46, 165–170. doi:10.1007/978-1-935704-13-3_16
- Kain, J. S. (2004). The Kain-Fritsch Convective Parameterization: An Update. *J. Appl. Meteorol.* 43, 170–181. doi:10.1175/1520-0450(2004)043<0170:Tkcpau>2.0.CO;2
- Marks, F. D., Black, P. G., Montgomery, M. T., and Burpee, R. W. (2008). Structure of the Eye and Eyewall of Hurricane Hugo (1989). *Monthly Weather Rev.* 136, 1237–1259. doi:10.1175/2007MWR2073.1
- Mirocha, J. D., Lundquist, J. K., and Kosović, B. (2010). Implementation of a Nonlinear Subfilter Turbulence Stress Model for Large-Eddy Simulation in the Advanced Research WRF Model. *Monthly Weather Rev.* 138, 4212–4228. doi:10.1175/2010mwr3286.1
- Mlawer, E. J., Taubman, S. J., Brown, P. D., Iacono, M. J., and Clough, S. A. (1997). Radiative Transfer for Inhomogeneous Atmospheres: RRTM, a Validated Correlated-K Model for the Longwave. *J. Geophys. Res.* 102, 16663–16682. doi:10.1029/97jd00237
- Morrison, I., Businger, S., Marks, F., Dodge, P., and Businger, J. A. (2005). An Observational Case for the Prevalence of Roll Vortices in the Hurricane Boundary Layer*. *J. Atmos. Sci.* 62, 2662–2673. doi:10.1175/jas3508.1
- Muñoz-Esparza, D., Kosović, B., García-Sánchez, C., and Van Beeck, J. (2014). Nesting Turbulence in an Offshore Convective Boundary Layer Using Large-Eddy Simulations. *Boundary-layer Meteorol.* 151, 453–478. doi:10.1007/s10546-014-9911-9
- Nakanishi, M., and Niino, H. (2012). Large-eddy Simulation of Roll Vortices in a hurricane Boundary Layer. *J. Atmos. Sci.* 69, 3558–3575. doi:10.1175/jas-d-11-0237.1
- Rotunno, R., Chen, Y., Wang, W., Davis, C., Dudhia, J., and Holland, G. J. (2009). Large-eddy Simulation of an Idealized Tropical Cyclone. *Bull. Amer. Meteorol. Soc.* 90, 1783–1788. doi:10.1175/2009bams2884.1
- Rotunno, R. (2013). The Fluid Dynamics of Tornadoes. *Annu. Rev. Fluid Mech.* 45, 59–84. doi:10.1146/annurev-fluid-011212-140639
- Shin, H. H., and Hong, S.-Y. (2015). Representation of the Subgrid-Scale Turbulent Transport in Convective Boundary Layers at gray-zone Resolutions. *Monthly Weather Rev.* 143, 250–271. doi:10.1175/mwr-d-14-00116.1
- Skamarock, W. C. (2004). Evaluating Mesoscale NWP Models Using Kinetic Energy Spectra. *Mon. Wea. Rev.* 132, 3019–3032. doi:10.1175/Mwr2830.1
- Skamarock, W. C., Klemp, J. B., Dudhia, J., Gill, D. O., Liu, Z., Berner, J., et al. (2019). A Description of the Advanced Research WRF Model Version 4. NCAR Tech. Notes NCAR/TN-556+STR. doi:10.5065/1dfh-6p97
- Smith, J., Bou-Zeid, E., and Talbot, C. (2012). Nested Mesoscale Large-Eddy Simulations with WRF: Performance in Real Test Cases. *J. Hydrometeorology* 13, 1421–1441. doi:10.1175/jhm-d-11-048.1
- Stern, D. P., Bryan, G. H., and Abersson, S. D. (2016). Extreme Low-Level Updrafts and Wind Speeds Measured by Dropsondes in Tropical Cyclones. *Monthly Weather Rev.* 144, 2177–2204. doi:10.1175/MWR-D-15-0313.1
- Stern, D. P., and Bryan, G. H. (2018). Using Simulated Dropsondes to Understand Extreme Updrafts and Wind Speeds in Tropical Cyclones. *Monthly Weather Rev.* 146, 3901–3925. doi:10.1175/MWR-D-18-0041.1
- Walters, M. K. (2000). Comments of the Differentiation between Grid Spacing and Resolution and Their Application to Numerical Modeling. *Bull. Am. Meteorol. Soc.*
- Wang, H., and Wang, Y. (2014). A Numerical Study of Typhoon Megi (2010). Part I: Rapid Intensification. *Monthly Weather Rev.* 142, 29–48. doi:10.1175/MWR-D-13-00070.1
- Wang, Y., Kepert, J. D., and Holland, G. J. (2001). The Effect of Sea spray Evaporation on Tropical Cyclone Boundary Layer Structure and Intensity. *Monthly Weather Rev.* 129, 2481–2500. doi:10.1175/1520-0493(2001)129<2481:Teosse>2.0.CO;2

- Wang, Y., and Wu, C.-C. (2004). Current Understanding of Tropical Cyclone Structure and Intensity Changes ? a Review. *Meteorol. Atmos. Phys.* 87, 257–278. doi:10.1007/s00703-003-0055-6
- Wu, L., Liu, Q., and Li, Y. (2018). Prevalence of Tornado-Scale Vortices in the Tropical Cyclone Eyewall. *Proc. Natl. Acad. Sci. USA* 115, 8307–8310. doi:10.1073/pnas.1807217115
- Wu, L., Liu, Q., and Li, Y. (2019). Tornado-scale Vortices in the Tropical Cyclone Boundary Layer: Numerical Simulation with the WRF-LES Framework. *Atmos. Chem. Phys.* 19, 2477–2487. doi:10.5194/acp-19-2477-2019
- Wurman, J., and Kosiba, K. (2018). The Role of Small-Scale Vortices in Enhancing Surface Winds and Damage in hurricane Harvey (2017). *Mon. Wea. Rev.* 146, 713–722. doi:10.1175/mwr-d-17-0327.1
- Wurman, J., and Winslow, J. (1998). Intense Sub-kilometer-scale Boundary Layer Rolls Observed in hurricane Fran. *Science* 280, 555–557. doi:10.1126/science.280.5363.555
- Xu, H., Zhang, X., and Xu, X. (2013). Impact of Tropical Storm Bopha on the Intensity Change of Super Typhoon Saomai in the 2006 Typhoon Season. *Adv. Meteorology* 2013, 1–13. doi:10.1155/2013/487010
- Zhang, D.-L., and Wang, X. (2003). Dependence of Hurricane Intensity and Structures on Vertical Resolution and Time-step Size. *Adv. Atmos. Sci.* 20, 711–725. doi:10.1007/bf02915397
- Zhang, D.-L., Zhu, L., Zhang, X., and Tallapragada, V. (2015). Sensitivity of Idealized Hurricane Intensity and Structures under Varying Background Flows and Initial Vortex Intensities to Different Vertical Resolutions in HWRF. *Monthly Weather Rev.* 143, 914–932. doi:10.1175/MWR-D-14-00102.1
- Zhang, J. A., Marks, F. D., Montgomery, M. T., and Lorsolo, S. (2011a). An Estimation of Turbulent Characteristics in the Low-Level Region of Intense Hurricanes Allen (1980) and Hugo (1989). *Mon. Wea. Rev.* 139, 1447–1462. doi:10.1175/2010mwr3435.1
- Zhang, J. A., Rogers, R. F., Nolan, D. S., and Marks, F. D. (2011b). On the Characteristic Height Scales of the Hurricane Boundary Layer. *Monthly Weather Rev.* 139, 2523–2535. doi:10.1175/mwr-d-10-05017.1
- Zhang, J. A., Rogers, R. F., and Tallapragada, V. (2017). Impact of Parameterized Boundary Layer Structure on Tropical Cyclone Rapid Intensification Forecasts in HWRF. *Monthly Weather Rev.* 145, 1413–1426. doi:10.1175/mwr-d-16-0129.1
- Zheng, Y., Wu, L., Zhao, H., Zhou, X., and Liu, Q. (2020). Simulation of Extreme Updrafts in the Tropical Cyclone Eyewall. *Adv. Atmos. Sci.* 37, 781–792. doi:10.1007/s00376-020-9197-4
- Zhu, P. (2008). Simulation and Parameterization of the Turbulent Transport in the hurricane Boundary Layer by Large Eddies. *J. Geophys. Res.* 113, D17104. doi:10.1029/2007jd009643
- Zhu, P., Tyner, B., Zhang, J. A., Aligo, E., Gopalakrishnan, S., Marks, F. D., et al. (2019). Role of Eyewall and Rainband Eddy Forcing in Tropical Cyclone Intensification. *Atmos. Chem. Phys.* 19, 14289–14310. doi:10.5194/acp-19-14289-2019

Conflict of Interest: The authors declare that the research was conducted in the absence of any commercial or financial relationships that could be construed as a potential conflict of interest.

Copyright © 2021 Xu and Wang. This is an open-access article distributed under the terms of the Creative Commons Attribution License (CC BY). The use, distribution or reproduction in other forums is permitted, provided the original author(s) and the copyright owner(s) are credited and that the original publication in this journal is cited, in accordance with accepted academic practice. No use, distribution or reproduction is permitted which does not comply with these terms.



Possible Environmental Influence on Eyewall Expansion During the Rapid Intensification of Hurricane Helene (2006)

Nannan Qin^{1,2,3} and Liguang Wu^{1,2*}

¹Department of Atmospheric and Oceanic Sciences and Institute of Atmospheric Sciences, Fudan University, Shanghai, China,

²State Key Laboratory of Severe Weather, Chinese Academy of Meteorological Sciences, Beijing, China, ³Innovation Center of Ocean and Atmosphere System, Zhuhai Fudan Innovation Research Institute, Zhuhai, China

OPEN ACCESS

Edited by:

Qingqing Li,
Nanjing University of Information
Science and Technology, China

Reviewed by:

Jian-Feng Gu,
University of Reading, United Kingdom
Xiaoping Cheng,
National University of Defense
Technology, China

*Correspondence:

Liguang Wu
liguangwu@fudan.edu.cn

Specialty section:

This article was submitted to
Atmospheric Science,
a section of the journal
Frontiers in Earth Science

Received: 26 May 2021

Accepted: 22 July 2021

Published: 29 July 2021

Citation:

Qin N and Wu L (2021) Possible
Environmental Influence on
Eyewall Expansion During the
Rapid Intensification of
Hurricane Helene (2006).
Front. Earth Sci. 9:715012.
doi: 10.3389/feart.2021.715012

Tropical cyclone (TC) rapid intensification (RI) is usually accompanied by a rapid eyewall contraction, followed by a slow contraction, and then a nearly steady eyewall. However, this study shows that Hurricane Helene (2006) exhibited an eyewall expansion during its 30-h rapid intensification period. The possible environmental influence on the eyewall expansion during the RI of Helene is examined. It is found that the synoptic-scale circulations led to additional low-level inflows and upper-level outflows that may play an important role in the eyewall expansion during the RI of Helene. Examination of the divergence of the absolute angular momentum flux (AAMF) associated with the environmental circulation suggests that the synoptic-scale atmospheric circulation played an important role in the eyewall expansion during the RI of Helene. In the lower and middle troposphere, the synoptic-scale cross-equatorial flow, which was enhanced by the Helene-induced wave train, led to the horizontal convergence of absolute angular momentum flux, while the TC-trough interaction and the related outflow in the upper troposphere resulted in the divergence of AAMF. The environment-induced low-level convergence and upper-level divergence of AAMF were superimposed on the secondary circulation of Helene and may be important to the eyewall expansion during the RI by accelerating the tangential wind outside of the eyewall. This study suggests that RI can occur with an eyewall expansion.

Keywords: hurricane, expanding eyewall, rapid intensification, environmental influence, tropical cyclone

INTRODUCTION

The improvement of tropical cyclone (TC) intensity forecast is lagging far behind the improvement of the TC track forecast (Kaplan and DeMaria 2003; Rogers et al., 2006; Rogers et al., 2013; Huang et al., 2021), especially when TCs undergo rapid intensification (RI), which is defined by Kaplan and DeMaria (2003) as an intensification rate of not less than $15.4 \text{ m s}^{-1} (24 \text{ h})^{-1}$ in the maximum surface wind (V_{MAX}). It has been found that TC intensification is accompanied by the contraction of the eyewall and radius of maximum wind (RMW) (Willoughby et al., 1982; Hack and Schubert 1986; Willoughby 1990; Willoughby and Rahn 2004; Knaff and Zehr 2007; Rogers 2010). Modeling and observational studies further indicate that the TC intensification process is accompanied by a rapid contraction of the RMW, followed by a slow contraction, and then a nearly steady stage (Hill and

Lackmann 2009; Vigh 2010; Kieu 2012; Chen and Zhang 2013; Wang and Wang 2014; Qin et al., 2018). Based on the analysis of a 25-years dataset, Qin et al. (2016) indicated that nearly 60% of RI events exhibited a steady RMW phenomenon, that is, the RMW stops contracting but keeps nearly constant. So far, it is not known whether the RI can occur with the expansion of the TC eyewall.

Early theoretical and observational studies proposed that diabatic heating that maximizes within the RMW will lead to the contraction of the eyewall because the maximum tendency of the tangential wind is located inside the RMW (Shapiro and Willoughby 1982; Willoughby et al., 1982; Hack and Schubert 1986). Based on a kinematic model, Kieu (2012) suggested that the inward momentum transport contributes to the RMW contraction by intensifying tangential wind further inward, while the frictional dissipation prevents the RMW from contracting in the boundary layer. Qin et al. (2018) obtained similar conclusions to Kieu (2012), in which the radial momentum advection indeed contributes to the RMW contraction, while the frictional diffusion leads to the cessation of the RMW within the boundary layer. Above the boundary layer, Qin et al. (2018) also emphasized that the vertical momentum advection promotes the RMW contraction by amplifying tangential wind, while the radial momentum advection inhibits the RMW contraction by inhibiting the tangential wind. The RMW contraction rate is also sensitive to the tangential wind profile. Stern et al. (2015) proposed that an increase in the sharpness of the tangential wind profile prevents the RMW from contracting, while the negative gradient of tangential wind tendency with the maximum inside of the RMW is favorable for RMW contraction. In consideration of the tangential wind tendency, Li et al. (2019) proposed that the radial gradient of the tangential wind tendency and the radial curvature of the tangential wind are influenced by the tangential wind budget terms. Therefore, factors that can change the tangential wind tendency will affect the RMW changes. Since an enlarging RMW generally occurs during the weakening stage of TCs, the expansion of the eyewall and RMW during the RI stage has not been discussed in previous studies.

Environmental factors favorable for RI have been revealed, including weaker vertical wind shear (VWS), warmer sea surface temperature (SST), higher oceanic heat content, higher relative humidity in the low-to mid-troposphere, and the external forcing from upper-level systems (Gray 1968; Holliday and Thompson 1979; Chen and Gray 1985; Kaplan and DeMaria 2003; Kaplan et al., 2010; Shieh et al., 2013; Chen et al., 2015). The environmental factors also do impact on TC size changes. Hill and Lackmann (2009) found that high relative humidity around the environment favors the outer rainband formation and the increase of TC size. Xu and Wang (2010) demonstrated that the surface entropy flux outside the eyewall contributes to the enhancement of the outer rainbands and thus affects the TC size. The TC intensity and size changes are associated with the radial transport of the absolute angular momentum (AAM). Montgomery and Smith (2011) emphasized that the tangential wind above the boundary layer intensifies by the inward transport of the material conservation of the AAM. Within the boundary

layer, the amplifying tangential wind results from the convergence of the AAM with a minimal loss of frictional momentum diffusion. By examining the changes of the radius of the 34-kt ($1 \text{ kt} = 0.514 \text{ m s}^{-1}$) wind (R17) in TC, Chan and Chan (2013) emphasized that TC size (R17) is positively related to the import of the low-level AAM, i.e., the increasing low-level AAM import increases the TC size. However, the influences of the AAM transport induced separately by the environment and by the TC itself on the intensity and size changes are not discussed.

In this study, we show that Hurricane Helene (2006) experienced an expansion of the eyewall and RMW during its RI stage based on observational analysis. The environmental factors responsible for the eyewall expansion during the RI of Helene are discussed. The data and analysis methods used are described in *Data and Methods* section. *Overview of Hurricane Helene* section gives a brief overview of the intensity and size evolution of Hurricane Helene (2006). *Environmental Influences on the Eyewall Expansion of Helene* section identifies possible environmental influences by diagnosing the divergence of the AAM flux (AAMFD) in terms of the low-frequency and synoptic-scale wind fields, respectively, followed by a summary in *Summary* Section.

DATA AND METHODS

The environmental wind field, temperature, and relative humidity are based on the National Centers for Environmental Prediction (NCEP) Climate Forecast System Reanalysis (CFSR) data (Saha et al., 2010), which are available at 37 vertical levels from 1,000 hPa up to 1 hPa with the grid spacing of $0.5^\circ \text{ latitude} \times 0.5^\circ \text{ longitude}$ at 6-h intervals. The CFSR data are also used for calculating the AAM transports since the CFSR data contain all available conventional and satellite data (Saha et al., 2010; Chan and Chan 2013). Based on the method proposed by Kurihara et al. (1993, 1995), the TC vortex is removed from the CFSR data to exclude the influence of TC circulation since we focus on the environmental factors and the TC circulation is inaccurately represented in the coarse data. The TC circulation within 600-km-radius circular area is removed from the CFSR wind field using the procedure proposed by Kurihara et al. (1993, 1995). Readers are referred to Kurihara et al. (1993, 1995). In addition, our results are independent on the removing circular area of TC with a radius of from 600 to 1,000 km. In addition, a low-pass Lanczos filter with a 10-day period is applied to the wind field to analyze the synoptic-scale and low-frequency systems (Duchon 1979; Wu et al., 2011, Wu et al., 2013a; Liang et al., 2016, 2018).

The 3-h brightness temperature with the horizontal spatial resolution of $0.07^\circ \text{ latitude} \times 0.07^\circ \text{ longitude}$ was from the fundamental climate data record (FCDR, Knapp et al., 2011) sponsored by the National Oceanic and Atmospheric Administration (NOAA). The NOAA 42 Airborne Doppler radar observation is used to show the observed near-surface wind structure. The SST data are from the National Oceanic and Atmospheric Administration Advanced Very High Resolution Radiometer (AVHRR) daily data at a spatial grid spacing of 0.25° .

The hurricane information, including the central position (latitude and longitude) and intensities including the 1-min

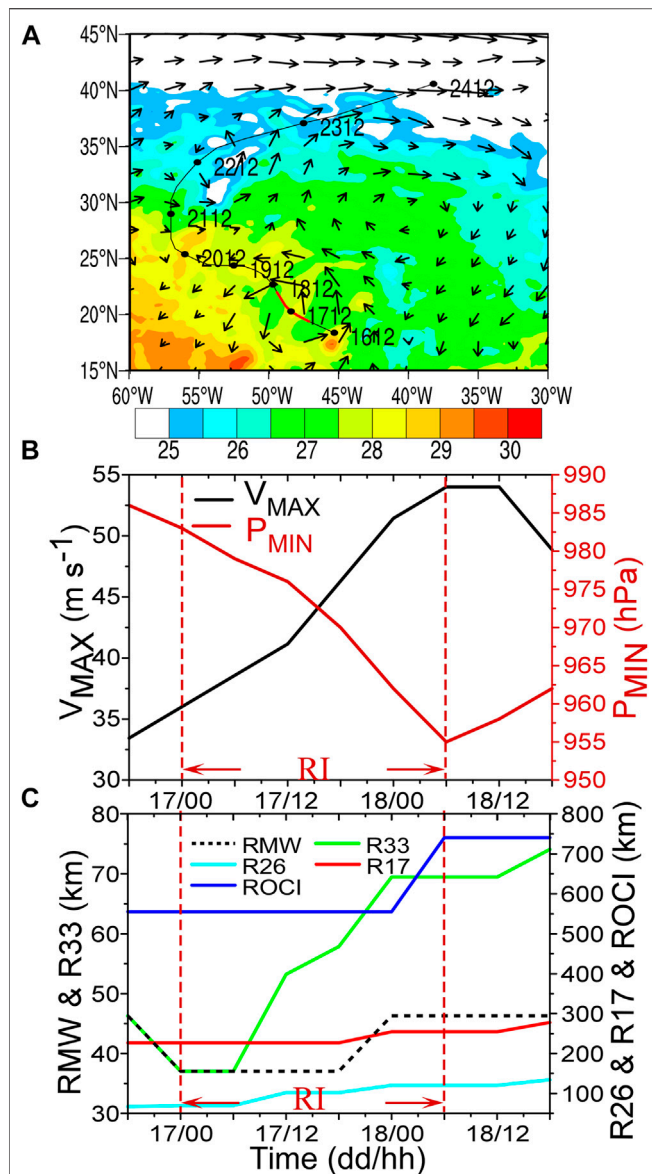


FIGURE 1 | (A) Best track (black contour) of Hurricane Helene from 1200 UTC 16 to 1200 UTC Sep 24, 2006 superimposed with the sea surface temperature (shaded, °C) at 0000 UTC 17 and the 500-hPa wind vector ($m s^{-1}$) at 1200 UTC Sep 17, 2006. Time series of **(B)** the maximum sustained surface wind (V_{MAX} , black solid contour, $m s^{-1}$) and the minimum sea-level pressure (P_{MIN} , red contour, hPa) from the National Hurricane Center (NHC) dataset, and **(C)** the radii of the V_{MAX} (RMW, black dashed lines, km), 34 kt wind (R17, red solid line, km), 50 kt wind (R26, cyan line, km) and 64 kt wind (R33, green line, km) from 1800 UTC 16 to 1,800 UTC Sep 18, 2006. The red solid line in **(A)** and red dashed lines in **(B, C)** indicate the RI period.

sustained maximum winds (V_{MAX}) and the minimum central pressure (P_{MIN}) at 6-h intervals, is from the revised Atlantic hurricane dataset conducted by the National Hurricane Center (NHC). The extended best-track (EBT) dataset (Demuth et al., 2006) at 6-h intervals is used for the size parameters of Hurricane Helene (2006), including the RMW, the R17, the radii of the 50 kt wind (R26), 64 kt wind (R33) and the outer closed isobar (ROCI).

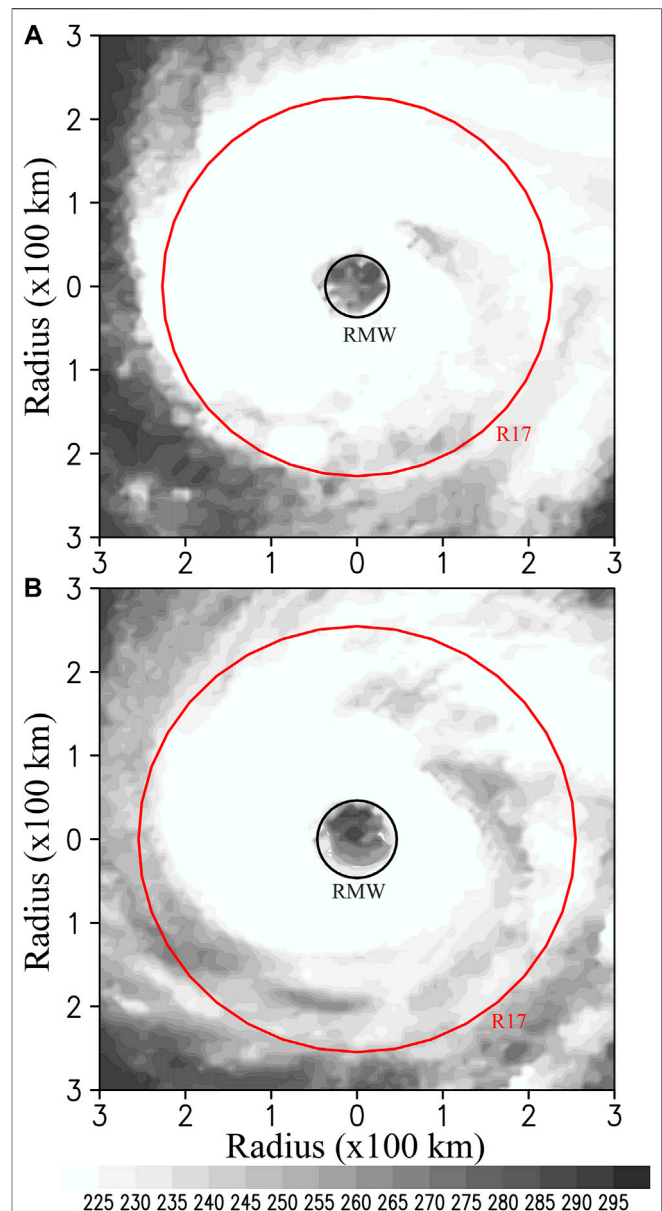
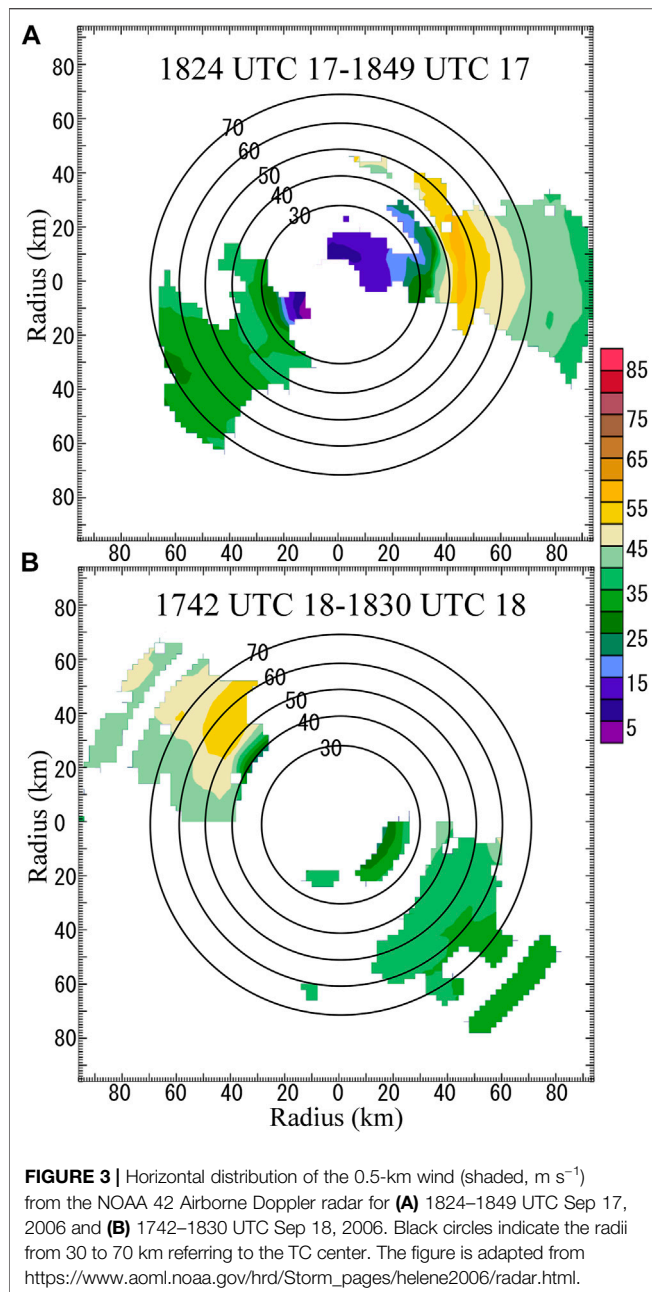


FIGURE 2 | Horizontal distribution of the infrared brightness temperature (shaded, K) from NOAA FCDR at **(A)** 1800 UTC Sep 17, 2006 and **(B)** 0000 UTC Sep 18, 2006. The black and red circles indicate the RMW and the radius of the 34-kt wind (R17).

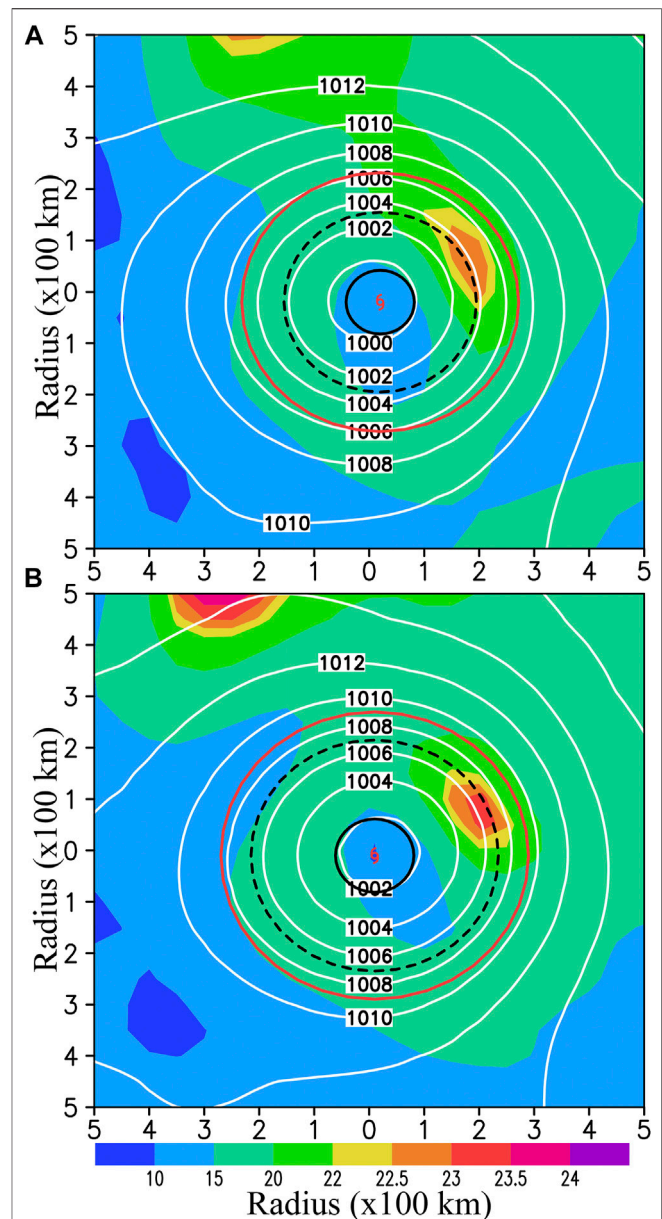
The radii parameters in EBT dataset are provided in four quadrants, i.e., the northeast, southeast, northwest, and southwest quadrants. The radii used in this study is calculated by averaging the radii from these four quadrants with the requirement that no undefined values are included.

OVERVIEW OF HURRICANE HELENE

Hurricane Helene (2006) can be traced back to a tropical wave near the coast of Africa in early September. This tropical wave



developed into a tropical depression by 1200 UTC 12 September. The tropical depression intensified into Tropical Storm Helene in an easterly shear environment by 0000 UTC 14 September. Around 1200 UTC 16 September, Helene strengthened to a hurricane. During the subsequent few days (from September 16–19), Helene moved northwestward affected by the subtropical high system that was located to the northeast of Helene (**Figure 1A**). Helene experienced an RI period from 0000 UTC 17 to 0600 UTC 18, September, with its V_{MAX} (P_{MIN}) increasing (deepening) from 36 m s^{-1} (983 hPa) to the peak intensity of 54 m s^{-1} (955 hPa) (**Figure 1B**). During this period, SST was around $27\text{--}28^\circ\text{C}$ (**Figure 1A**), which is favorable for TC intensification (Holliday and Thompson,



1979). The magnitude of VWS, which is calculated using the 1,000-km area-averaged wind between 200 hPa and 850 hPa, was below 7 m s^{-1} during the RI period of Helene. This weak VWS favors for the RI of Helene since strong VWS tends to weaken the TC intensity through the injection of dry and low entropy air (Frank and Ritchie 2001; Tang and Emanuel 2010). We examined the evolution of environmental potential vorticity around Helene (not shown) and found that strong environmental potential vorticity anomalies approached Helene from the northwest

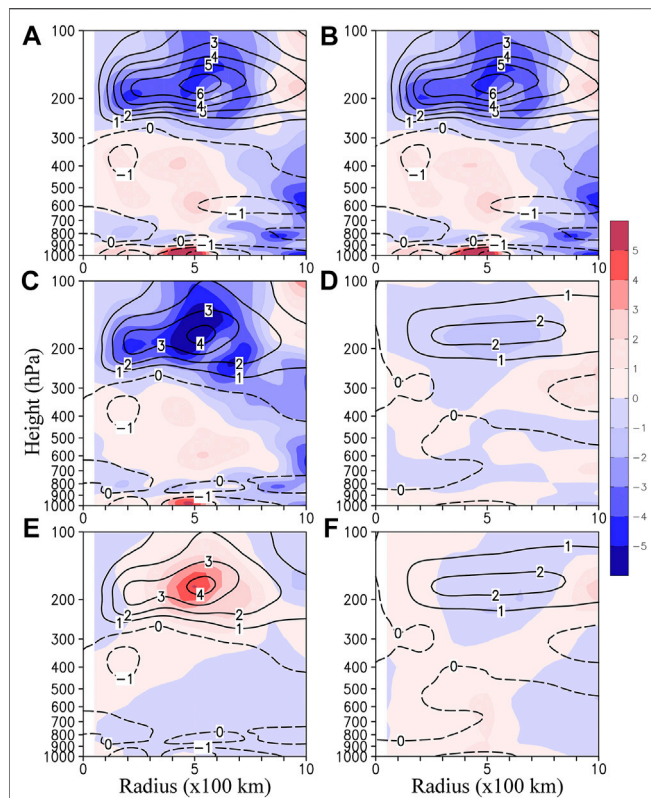


FIGURE 5 | Radius-height cross-sections of the azimuthal-mean horizontal flux divergence of AAM (AAMFD, shaded, $10^5 \text{ m}^3 \text{ s}^{-1} \text{ h}^{-1}$) and radial wind (contours, m s^{-1} , solid and dashed lines are for outflow and inflow, respectively) at 1800 UTC Sep 17, 2006 **(A)** total AAMFD and radial wind **(B)** sum of the RHS AAMFD terms of Eq. 4 and total radial wind **(C)** AAMFD and radial wind associated with the synoptic-scale circulation **(D)** AAMFD and radial wind associated with the low-frequency circulation **(E)** the divergence of low-frequency AAM flux by the radial wind associated with the synoptic-scale circulation, and **(F)** the divergence of synoptic-scale AAM flux by the radial wind associated with the low-frequency circulation.

with a radial distance of less than 500 km from 1800 UTC 17 to 0600 UTC 18. The interaction of environmental potential vorticity anomalies with TC circulation may contribute to the intensification of Helene according to the finding by other studies (Molinari et al., 1995; Hanley et al., 2001). After that, Helene weakened and dissipated at 0000 UTC 28 September when it moved over the cold ocean.

The size changes of Helene are examined in Figure 1C. Before the RI onset, the intensifying Helene was featured with a contracting RMW. Then, the RMW kept steady from 0000 UTC 17 to 1800 UTC 17 and increased from around 37 km at 1800 UTC 17 to about 46 km at 0000 UTC 18. After that, the RMW of 46 km was maintained till 1800 UTC 18. Meanwhile, the R33, R26, R17, and the ROCI also were enlarged during the RI. These changes in the eyewall and RMW were also reflected in the cloud features (Figure 2). The convection indicated by the satellite brightness temperature exhibited an expanding eye. The NOAA aircraft was flown into Helene during 17–20 September. The near-surface wind observed by the Airborne

Doppler radar is shown in Figure 3 at the closest time when the eyewall expansion occurred. Around 1800 UTC 17, the maximum near-surface wind of over 55 m s^{-1} was located to the northeast-east of TC with a radius of about 43 km, while the maximum wind to the southwest of the TC was located around a radius of 35 km. The averaged radius was about 39 km around 1800 UTC 17, close to the RMW shown in Figure 1C. Unfortunately, no aircraft data were available for the period from 0000 UTC 18 to 1700 UTC 18. We show the wind at another time in Figure 3B for these reasons: 1) the EBT data show that the RMW kept steady from 0000 UTC 18 to 1800 UTC 18; 2) the intensity at 1800 UTC 18 was similar to that at 0000 UTC 18; 3) there was aircraft observation around 1800 UTC 18. Figure 3B shows that the maximum wind was located at a radius of about 60 km to the northwest of Helene. The maximum wind to the southeast of Helene is hard to be recognized in Figure 3B. But the radius of the southeastern maximum wind was about 35 km when we check the observed wind structure near 1900 UTC 18. The observed wind structure presented that the eyewall was expanded from about 39 km to about 48 km. Therefore, the intensity and RMW changes are not simply negatively correlated, which is consistent with other studies (Qin et al., 2016; Kieu 2012; Knaff et al., 2015; Xu and Wang 2015, 2018). Although TC intensities are significantly underestimated and the RMW is systematically overestimated in the reanalysis data (Hodges et al., 2018), the eyewall expansion is also present in the CFSR data. The surface wind and the azimuthal-mean RMW obtained from the CFSR data are shown in Figure 4. It is noted that the azimuthal-mean RMW in the CFSR data increased from 150 to 200 km from 1800 UTC 17 to 0000 UTC 18, which confirmed the eyewall expansion shown in Figures 1–3.

ENVIRONMENTAL INFLUENCES ON THE EYEWALL EXPANSION OF HELENE

Divergence of the Environmental AAMflux

Since the conservation of AAM is generally a constrain for mature TCs, the AAM transport can be used to understand the changes in TC intensity and size (Merrill 1984; Liu and Chan 2002; Montgomery and Smith 2011; Chan and Chan 2013). The AAM in the cylindrical coordinate (λ, r, z, t) can be written as

$$\text{AAM} = v_t r + \frac{f r^2}{2}, \quad (1)$$

where r is the radius to the TC center; f is the Coriolis parameter; v_t is the tangential wind. Since the horizontal AAMFD is a major contributor to the intensification of the tangential wind within the boundary layer where the RMW expansion occurred, only the horizontal AAMFD is examined here. The AAMFD in the cylindrical coordinates is given by

$$\text{AAMFD} = -\frac{1}{r} \frac{\partial}{\partial r} \left[r v_r \left(v_t r + \frac{f r^2}{2} \right) \right], \quad (2)$$

where λ indicates the azimuthal angle; v_r is the radial wind. The storm movement is removed from the wind field to avoid the

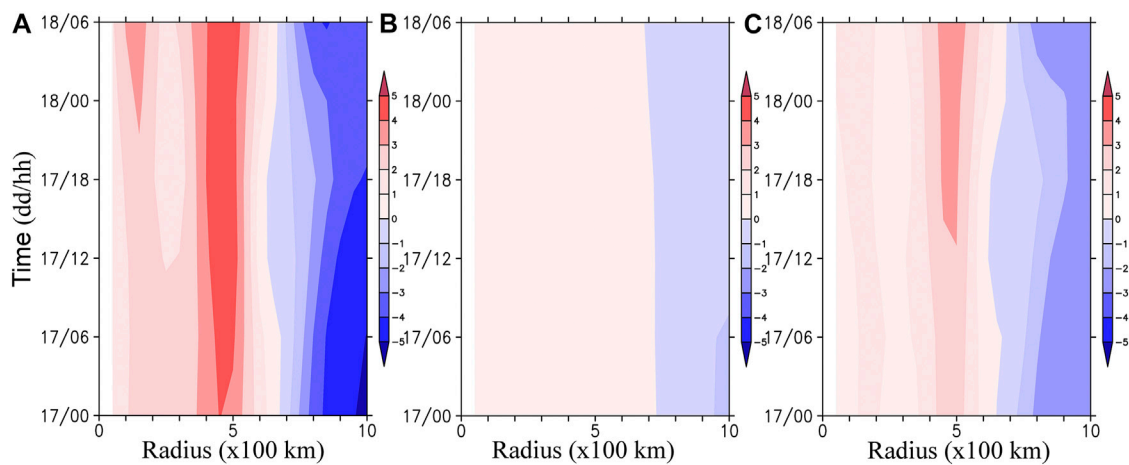


FIGURE 6 | Time-radius cross-section of the azimuthal-mean integrated divergence of the AAM flux (AAMFD, shaded, $10^5 \text{ m}^3 \text{ s}^{-1} \text{ h}^{-1}$) over low levels (averaged from 1,000 hPa to 900 hPa) during the RI period of Helene (A) total AAMFD (B) AAMFD associated with the low-frequency circulation, and (C) AAMFD associated with the synoptic-scale circulation.

advective effects associated with the TC movement. Note that the positive (negative) AAMFD indicates the convergence (divergence) of AAM flux (AAMF) due to the inclusion of a minus sign on the right-hand side of Eq. 2. In order to separate the influences of the low-frequency and synoptic-scale flows on Helene, v_t and v_r in Eq. 2 are decomposed into low-frequency and synoptic-scale components, and the wind speed with the subscripts L and H stands for the low-frequency and the synoptic-scale components, respectively. Eq. 2 can be rewritten as:

$$\begin{aligned} \text{AAMFD} = & -\frac{1}{r} \frac{\partial}{\partial r} \left[r v_{rL} \left(r v_{tL} + \frac{r^2 f}{2} \right) \right] - \frac{1}{r} \frac{\partial}{\partial r} \left[r v_{rH} \left(r v_{tH} + \frac{r^2 f}{2} \right) \right] \\ & - \frac{1}{r} \frac{\partial}{\partial r} [r v_{rL} r v_{tH}] - \frac{1}{r} \frac{\partial}{\partial r} [r v_{rH} r v_{tL}]. \end{aligned} \quad (3)$$

The first term on the right-hand side (RHS) of Eq. 3 is the contribution from the low-frequency component (AAMFD_L). The second term is the contribution from the synoptic-scale component (AAMFD_H). The third term represents the divergence of the synoptic-scale AAMF by the low-frequency radial wind (AAMF_{LH}), while the last term is the divergence of the low-frequency AAMF by the synoptic-scale radial wind (AAMF_{HL}). After taking the azimuthal mean indicated by the overbars, Eq. 3 can be written as

$$\begin{aligned} \overline{\text{AAMFD}} = & -\frac{1}{r} \frac{\partial}{\partial r} \left[r v_{rL} \left(r v_{tL} + \frac{r^2 f}{2} \right) \right] - \frac{1}{r} \frac{\partial}{\partial r} \left[r v_{rH} \left(r v_{tH} + \frac{r^2 f}{2} \right) \right] \\ & - \frac{1}{r} \frac{\partial}{\partial r} [r v_{rL} r v_{tH}] - \frac{1}{r} \frac{\partial}{\partial r} [r v_{rH} r v_{tL}]. \end{aligned} \quad (4)$$

Note that the eddy terms are included in Eq. 4. Figure 5 shows the radius-height structures of azimuthal-averaged AAMFD, AAMFD_L , AAMFD_H , AAMFD_{LH} , AAMFD_{HL} , the sum of the

four terms on the RHS of Eq. 4, and the related inflows and outflows at the selected time. We can find that the sum of the four terms on the RHS is close to the total AAMFD (cf. Figures 5A,B). In the lower troposphere, the convergence of AAMF is dominant inside of the radius of 600 km, with the maxima located around the radius of 500 km, which is associated with low-level inflows. The convergence of AAMF also occurred with inflows at the middle levels (between 700 hPa and 300 hPa). In the upper troposphere, the divergence of AAMF occurred with the maximum core appearing near 175 hPa where the strong outflow ($>6 \text{ m s}^{-1}$) was located. The convergence of AAMF at low and middle levels tended to intensify the storm especially outside of the eyewall (Shapiro and Willoughby 1982; Montgomery and Smith 2011).

The low- and middle-level convergence of AAMF and the upper-level divergence of AAMF were mainly caused by the synoptic-scale circulation (Figure 5C) since the AAMFD caused by the low-frequency circulation was substantially small (Figure 5D and Figure 5F), and the divergence of the low-frequency AAMF caused by the synoptic-scale inflows (AAMF_{HL} , Figure 5E) performed almost oppositely to the structure of the total AAMFD. The AAMF transports were associated with the environmental inflows and outflows, which were superimposed on the secondary circulation of Helene and contributed to the intensification of Helene especially outside of the eyewall (Shapiro and Willoughby 1982). The environmental inflows/outflows were closely related to the synoptic-scale rather than the low-frequency circulation, suggesting that the synoptic-scale circulation played an important role in enlarging the RMW by changing the AAMFD during the RI period of Helene.

The Low-Level Synoptic-Scale Wind Field Associated with the AAMFD

Figure 6 shows the radius-time distribution of the azimuthally averaged AAMFD integrated over low levels. During the RI

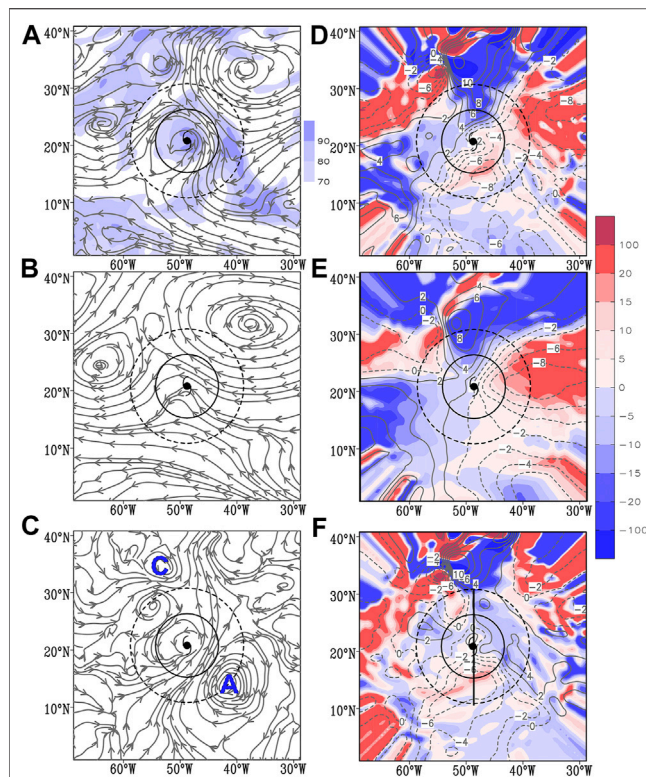


FIGURE 7 | (A, B, C) Streamlines with the shading in **(A)** indicating the relative humidity averaged from 850 hPa to 700 hPa and **(D, E, F)** the divergence of the environmental AAM flux (AAMFD, shaded, $10^6 \text{ m}^3 \text{ s}^{-2}$) superimposed with the radial flow [contours, solid (dashed) lines indicating the outflow (inflow) at 2 m s^{-1} intervals] **(A, D)** for the total field after removing the TC vortex **(B, E)** for low-frequency, and **(C, F)** for the synoptic-scale field at 900 hPa at 1800 UTC Sep 17, 2006. “A” and “C” in blue color in **(C)** indicate the synoptic-scale anticyclonic circulation and Hurricane Gordon. The black line in **(F)** denotes the location for the vertical cross-section in **Figure 9**. The black solid and dashed circles indicate the radius of the outer closed isobar (ROCI, with a radius of 555 km) and $R = 1,000 \text{ km}$.

period of Helene, the low-level convergence of AAMF maintains within the radius of 650 km (**Figure 6A**), which is mainly caused by the synoptic-scale circulation compared to that from the low-frequency circulation (**Figures 6B,C**). The maximum positive AAMFD is located at radii of 400–500 km, supporting that the intensification of the tangential wind outside the eyewall is persistent during the RI stage.

In order to investigate how the environmental circulation affected the convergence of AAMF in the lower troposphere, we examine the horizontal distribution of the 900-hPa total, synoptic-scale and low-frequency wind fields, as well as the related AAMFD in **Figure 7**. In the lower troposphere, Hurricane Helene was located to the south of the subtropical high, which was split into two parts with one over the eastern North Atlantic and the other near the Caribbean Sea (**Figure 7A**). While the eastern part of the subtropical high can be seen in the synoptic-scale wind field (**Figure 7C**), **Figure 7B** indicates that the two parts of the subtropical high are clear in the low-

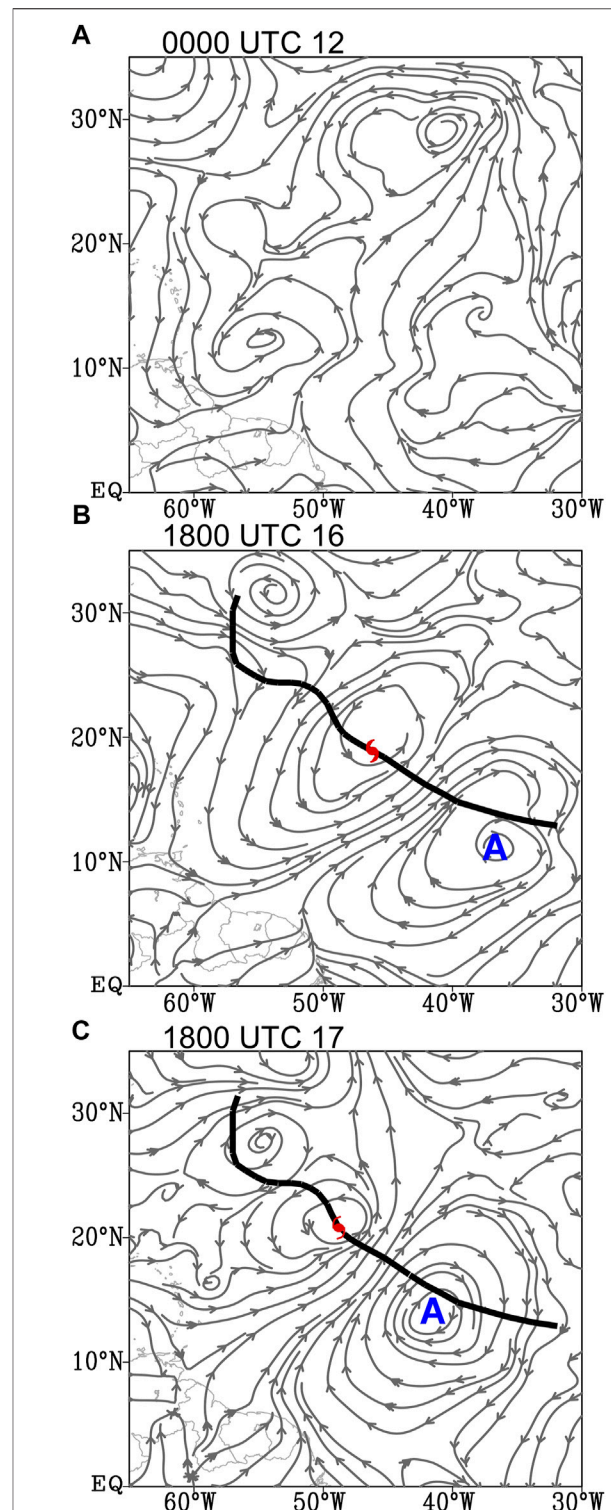
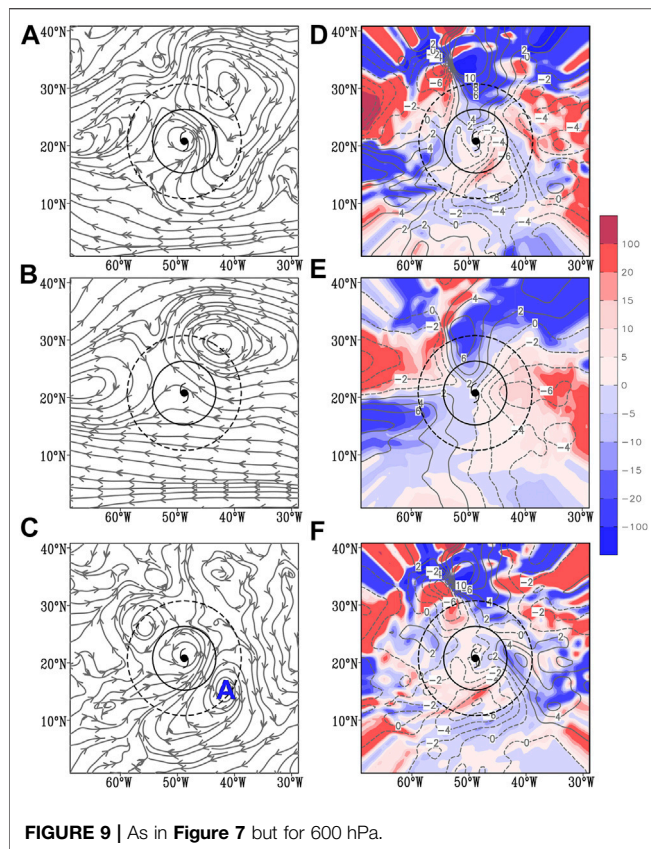
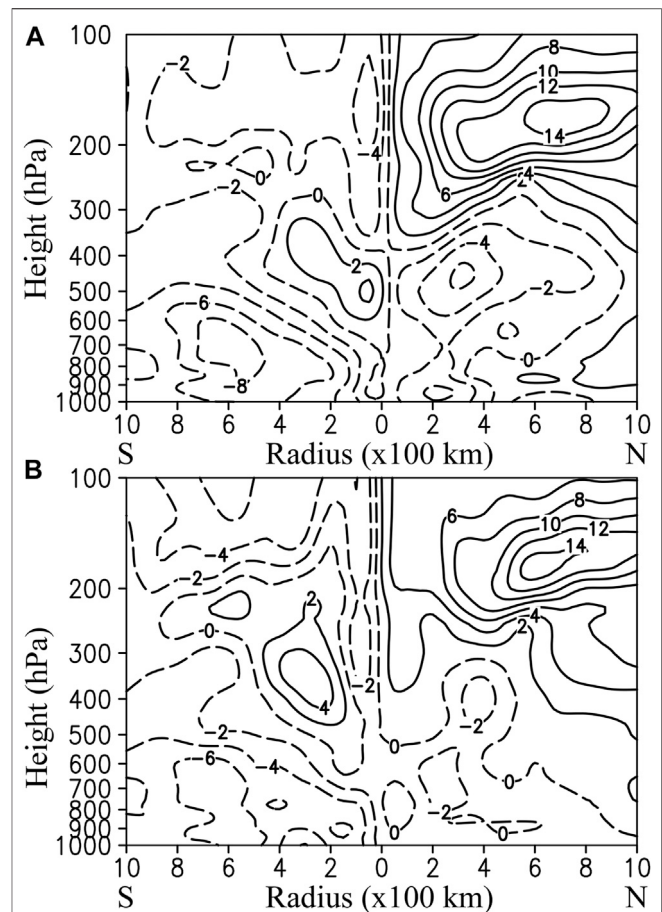


FIGURE 8 | 900-hPa streamline for the synoptic-scale field at (A) 0000 UTC 12 (B) 1800 UTC 16 and (C) 1800 UTC Sep 17, 2006. The thick black solid line indicates the track of Helene from 0000 UTC 14 to 0000 UTC Sep 22, 2006. The red symbol indicates the TC position at the selected times. The letter “A” in blue color represents the anticyclonic circulation.



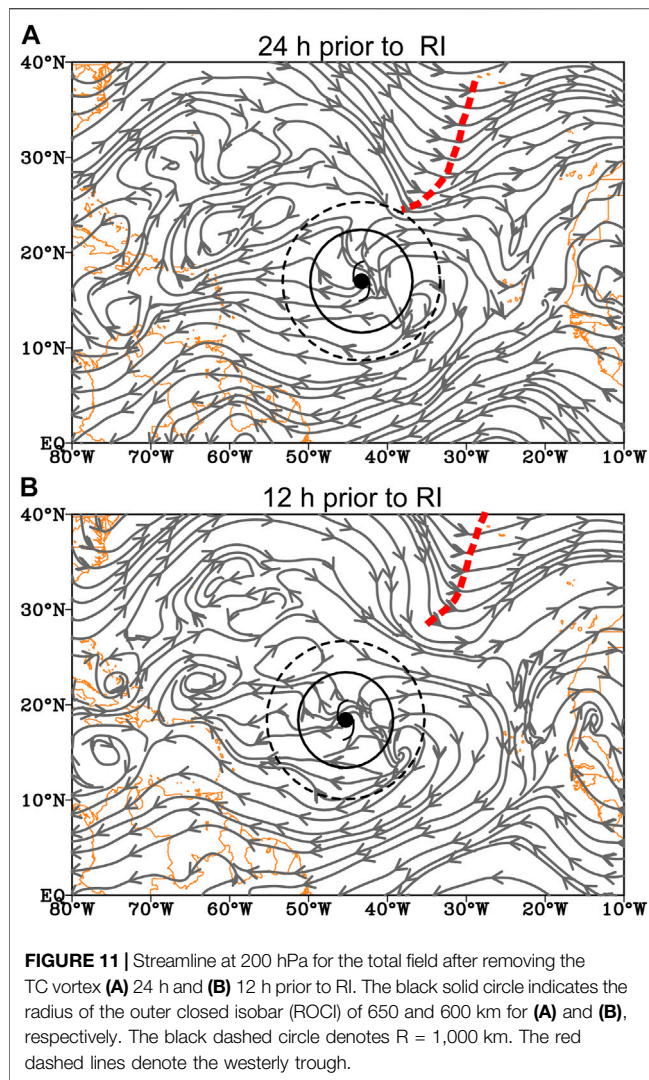
frequency wind field. The splitting of the subtropical high was coincident with the northward movement of Hurricane Gordon (marked by “C” in **Figure 7C**), which formed 2 days earlier than Helene. It is suggested that the northward movement of Helene was mainly affected by the eastern part of the subtropical high (**Figure 1A**).

In the 900-hPa wind field on the synoptic scale (**Figure 7C**), a pronounced feature is an anticyclonic circulation to the southeast of Helene. The strong anticyclone was centered near 14°N, with a horizontal scale of about 2000 km. Thus, the cross-equatorial flow to the west of the anticyclone was extended to the circulation of Helene, which led to the inflow of over 6 m s^{-1} located to the south of Helene (**Figure 7F**). This synoptic-scale anticyclonic circulation was further examined in **Figure 8** by showing the horizontal streamline before the formation of the tropical depression, prior to RI, and during the RI of Helene. It is noted that a synoptic-scale cross-equatorial flow existed between the longitude of 40°W and 55°W far before the formation of Hurricane Helene (**Figure 8A**). Prior to and during the RI of Helene, alternating regions of anticyclonic and cyclonic circulation appeared along the TC track in a northwest-southeast direction (**Figures 8B,C**), which is likely induced by the TC activity and called the Rossby train as proposed by previous studies (Carr and Elsberry 1995; Holland 1995; Wu et al., 2013b; Wu and Duan 2015). Of importance is that the anticyclonic circulation to the southeast of Helene strengthened during the RI of the eyewall expansion



stage (**Figure 8B**). This enhanced anticyclonic circulation might be caused by the interaction of the TC-induced Rossby train with the tropical wave. Therefore, the synoptic-scale cross-equatorial flow to the west of the anticyclone was enhanced and extended to the circulation of Helene introducing the convergence of AAMF.

The low-level convergence of the AAMF was related to the synoptic-scale circulation. **Figure 7D** shows that the low-level convergence of the AAMF prevailed in the southeast semicircle, while the divergence of the AAMF prevailed in the northwest semicircle within a radius of 1,000 km except for a small area with the convergence of the AAMF in the northwest of Helene. Specifically, the cross-equatorial flow from the synoptic-scale wind field played an important role in transporting AAMF inward to the southern area of Helene (**Figure 7F**). On the other hand, the low-level convergence of the AAMF in the northwest semicircle of Helene was generally caused by the low-frequency flow (cf., **Figure 7D** and **Figure 7E**). Since the convergence of the AAMF associated with the synoptic-scale wind field compensates for the low-level divergence of the AAMF, there was the net convergence of the AAMF after the azimuthal averaging (**Figure 5A**), suggesting that the synoptic-scale



circulation influenced the intensity and size changes of Helene by changing the convergence of the AAMF.

The Middle-Level Synoptic-Scale Wind Field Associated With the AAMFD

The synoptic-scale anticyclonic circulation is also important to the middle-level convergence of the AAMF, which determines the intensification of the middle-level wind of Helene, especially outside the eyewall since the AAM is materially conserved (Shapiro and Willoughby 1982; Montgomery and Smith 2011). Figure 9 shows the 600-hPa wind field and AAMFD, and their synoptic-scale and the low-frequency components. As discussed in *The Low-Level Synoptic-Scale Wind Field Associated with the AAMFD* section, the pattern of the middle-level wind field was similar to the low-level wind structure. The strong cross-equatorial flow to the southeast of Helene was closely related to the synoptic-scale anticyclonic circulation (Figure 9C). As a result, the inflow induced by the synoptic-scale circulation was maximized to the south of Helene, which agrees with the convergence of AAMF at

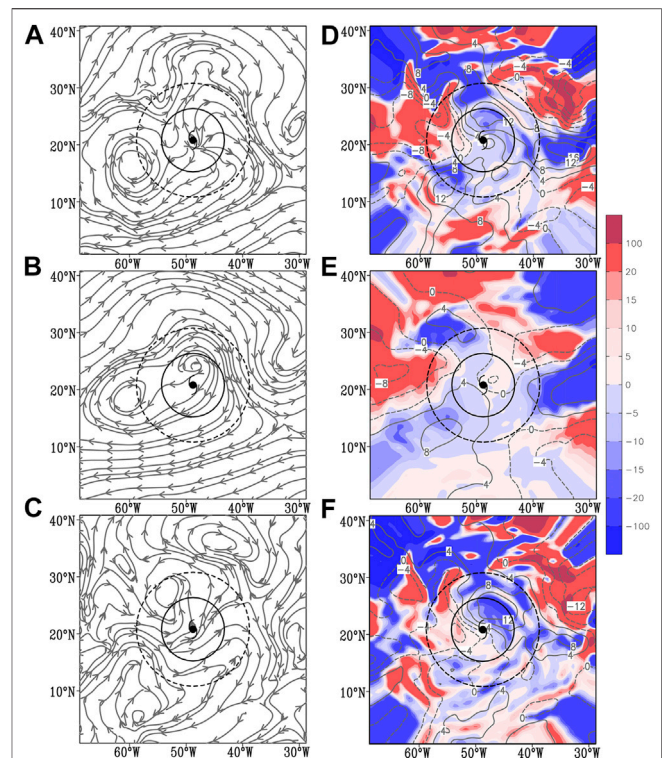


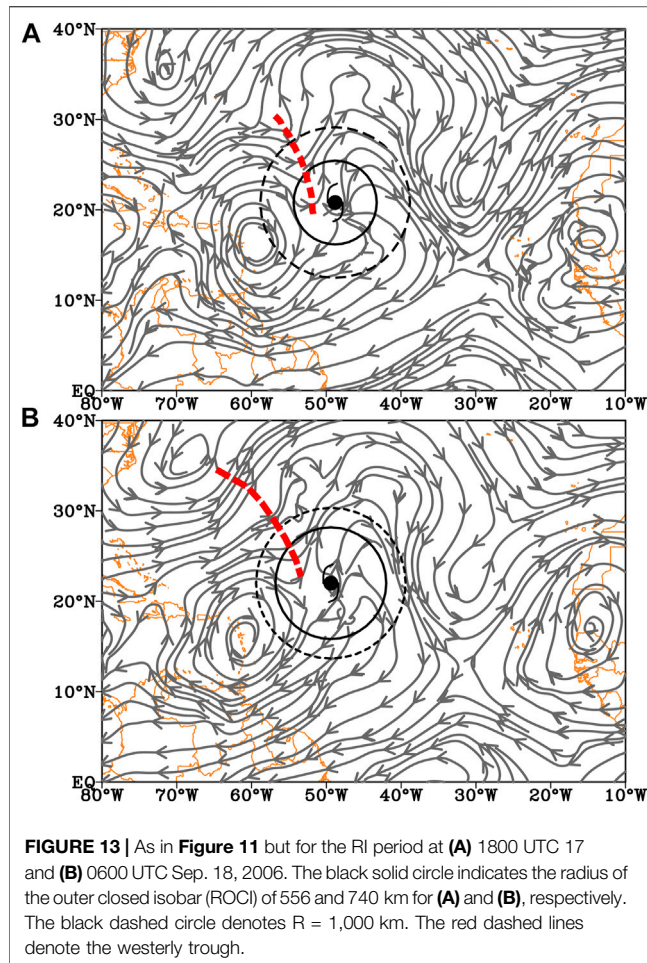
FIGURE 12 | As in Figure 7 but for 200 hPa.

middle levels (Figures 9D,F). Without consideration of the friction diffusion, the convergence of AAMF at middle levels tended to intensify the storm especially outside of the eyewall where the maximum convergence of AAMF was located.

The vertical structures of the inflow/outflow induced by the synoptic-scale circulation are examined in Figure 10. It is confirmed that the inflow to the south of Helene was stronger than that to the north of Helene below the layer of 500 hPa. The low-to-middle-level inflow prevailed and maintained during the RI with the expansion of the eyewall. Note that the maximum inflow was located near the radius of 600 km, which influenced the location of the maximum convergence of AAMF (Figures 7E,9F) that contributed to the intensification of the tangential wind outside of the eyewall.

The Upper-Level Helene-Trough Interaction and AAMFD

In the upper troposphere, Helene was located to the south of the westerly trough before the RI onset (Figures 11A,B). The TC-trough interaction can be measured by the eddy flux convergence of relative angular momentum (EFC, DeMaria et al., 1993; Molinari et al., 1995; Chen et al., 2015; Qiu et al., 2020). Following DeMaria et al. (1993), EFC is defined as $EFC = -r^2 \partial / \partial r (r^2 \bar{u}_r' \bar{v}_t')$, where \bar{u}_r' and \bar{v}_t' are the deviate radial and tangential wind from the azimuthal average, r is the radius from the TC center, and the overbar represents the azimuthal mean. DeMaria et al. (1993) found that RI cases usually featured



with a value of $2\text{--}3 \text{ m s}^{-1} \text{ day}^{-1}$ of the EFC over a 300–600-km radial range at 200 hPa. The 200-hPa EFC over a 300–600-km radial range for Helene was about $3.5 \text{ m s}^{-1} \text{ day}^{-1}$ prior to the RI onset, indicating a significant TC-trough interaction and a favorable environment for the RI onset.

During the RI period, a synoptic-scale circulation contributed to the intense northeastward outflow and the outward transport of AAM at upper levels, which intensified the secondary circulation as well as the intensity of Helene. **Figure 12** shows the horizontal distributions of the upper-level wind field and the AAMFD of Helene. The upper-level outflow with a value over 12 m s^{-1} was located to the north-northeast of Helene (**Figure 12D**). This outflow was largely induced by the synoptic-scale circulation, which was found in **Figure 12C** as a synoptic-scale cyclonic circulation that was located to the northwest of Helene. The synoptic-scale cyclonic circulation was associated with a westerly trough that was seen in **Figure 13**. During the RI period with the eyewall expansion, the westerly trough moved eastward and became closer to Helene, leading to a cyclonic circulation to the northwest quadrant of Helene. Thus, the upper-level outflow was enhanced with the maximum outflow core located around the radius of 500 km, which favors TC intensification especially outside of the eyewall.

The upper-level divergence of AAMF that was influenced by the synoptic-scale circulation is further examined by showing the horizontal distribution of the AAMFD in **Figure 12F**. In agreement with the upper-level outflow, the divergence of AAMF was located to the northeast of Helene. Moreover, the upper-level divergence of AAMF was maximized at a similar radius as the maxima of the upper-level outflow within a radius of 1,000 km. The outflow prevailed and maintained in the upper troposphere during the eyewall expansion stage, which was a manifestation of the divergence of AAMF and the TC size expansion. While the low-frequency circulation presented a divergent wind field at upper levels, the divergence of AAMF associated with the low-frequency circulation was relatively weak (**Figures 5, 11**), suggesting that the synoptic-scale circulation determined the divergence of AAMF.

SUMMARY

Hurricane Helene (2006) experienced a 30-h RI under favorable environmental conditions, including the warm SST, high low-level humidity, weak large-scale VWS, and the upper-level TC-trough interaction. Under the environmental influence, Helene intensified rapidly with an expansion of the eyewall, suggesting that the intensity and inner-core size changes are not negatively correlated.

This study reveals that the synoptic-scale atmospheric circulation was likely responsible for the eyewall expansion during the RI of Helene through the environmental influences on the AAM transport. In the low and middle troposphere, the cross-equatorial flow associated with a synoptic-scale anticyclonic circulation was enhanced due to the intensifying TC and/or its interaction with the tropical wave. The enhanced inflow penetrated the Helene circulation and caused the convergence of AAMF, accelerating the tangential wind outside of the eyewall. In the upper troposphere, the divergence of AAMF was enhanced by a synoptic-scale cyclonic circulation associated with a westerly trough located to the northwest of Helene. Consequently, the environmental influences led to the low-level convergence and upper-level divergence of AAMF, which was superimposed on the secondary circulation of Helene, likely being important to the eyewall expansion during the RI of Helene.

In this study, for the first time we show that the RI can occur with the eyewall expansion. Hurricane Helene (2006) is such a case. The increase of the RMW of Helene is found in both the best-track data and the CFSR data, although the RMW is systematically overestimated in the CFSR data. Note that the expansion in Helene was also indicated in R33, R26, R17, and the ROCI. It is suggested that a TC can indeed experience the eyewall expansion during its RI. As a first step, we investigated the possible influences of the environmental flows on the phenomena of the size expansion using the CFSR data. The environmental influences are important to the eyewall expansion but more work in terms of the high-resolution simulation is necessary to understand the inner-core dynamics on the eyewall expansion for RI cases.

DATA AVAILABILITY STATEMENT

The original contributions presented in the study are included in the article/supplementary material, further inquiries can be directed to the corresponding author.

AUTHOR CONTRIBUTIONS

LW designed research. NQ conceptualized the analysis and wrote the manuscript. All authors were involved in helpful discussions and contributions to the manuscript.

REFERENCES

- Carr, L. E., III, and Elsberry, R. L. (1995). Monsoonal Interactions Leading to Sudden Tropical Cyclone Track Changes. *Mon. Wea. Rev.* 123, 265–290. doi:10.1175/1520-0493(1995)123<0265:MILTST>2.0.CO;2
- Chan, K. T. F., and Chan, J. C. L. (2013). Angular Momentum Transports and Synoptic Flow Patterns Associated with Tropical Cyclone Size Change. *Mon. Wea. Rev.* 141, 3985–4007. doi:10.1175/MWR-D-12-00204.1
- Chen, H., and Zhang, D.-L. (2013). On the Rapid Intensification of Hurricane Wilma (2005). Part II: Convective Bursts and the Upper-Level Warm Core. *J. Atmos. Sci.* 70, 146–162. doi:10.1175/JAS-D-12-062.1
- Chen, L., and Gray, W. M. (1985). “Global View of the Upper Level Outflow Patterns Associated with Tropical Cyclone Intensity Change during FGGE,” in *Dept. Of Atmospheric Science Paper 392* (Colorado state: Colorado State University), 126.
- Chen, X., Wang, Y., and Zhao, K. (2015). Synoptic Flow Patterns and Large-Scale Characteristics Associated with Rapidly Intensifying Tropical Cyclones in the South China Sea. *Mon. Weather Rev.* 143, 64–87. doi:10.1175/MWR-D-13-00338.1
- DeMaria, M., Baik, J.-J., and Kaplan, J. (1993). Upper-level Eddy Angular Momentum Fluxes and Tropical Cyclone Intensity Change. *J. Atmos. Sci.* 50, 1133–1147. doi:10.1175/1520-0469(1993)050<1133:ULEAMF>2.0.CO;2
- Demuth, J. L., DeMaria, M., and Knaff, J. A. (2006). Improvement of Advanced Microwave Sounding Unit Tropical Cyclone Intensity and Size Estimation Algorithms. *J. Appl. Meteorol. Climatol.* 45, 1573–1581. doi:10.1175/JAM2429.1
- Duchon, C. E. (1979). Lanczos Filtering in One and Two Dimensions. *J. Appl. Meteorol. Climatol.* 18, 1016–1022. doi:10.1175/1520-0450(1979)018<1016:LFIOT>2.0.CO;2
- Frank, W. M., and Ritchie, E. A. (2001). Effects of Vertical Wind Shear on the Intensity and Structure of Numerically Simulated Hurricanes. *Mon. Wea. Rev.* 129, 2249–2269. doi:10.1175/1520-0493(2001)129<2249:EOVWSO>2.0.CO;2
- Gray, M. W. (1968). Global View of the Origin of Tropical Disturbances and Storms. *Mon. Weather Rev.* 96, 669–700. doi:10.1175/1520-0493(1968)096<0669:GVOTOO>2.0.CO;2
- Hack, J. J., and Schubert, W. H. (1986). Nonlinear Response of Atmospheric Vortices to Heating by Organized Cumulus Convection. *J. Atmos. Sci.* 43, 1559–1573. doi:10.1175/1520-0469(1986)043<1559:NROAVT>2.0.CO;2
- Hanley, D. D., Molinari, J., and Keyser, D. (2001). A Composite Study of the Interactions between Tropical Cyclones and Upper Tropospheric Troughs. *Mon. Weather Rev.* 129, 2570–2584. doi:10.1175/1520-0493(2001)129<2570:ACSOTI>2.0.CO;2
- Hill, K. A., and Lackmann, G. M. (2009). Influence of Environmental Humidity on Tropical Cyclone Size. *Mon. Wea. Rev.* 137, 3294–3315. doi:10.1175/2009MWR2679.1
- Hodges, K., Cobb, A., and Vidale, P. L. (2017). How Well Are Tropical Cyclones Represented in Reanalysis Datasets? *J. Clim.* 30, 5243–5264. doi:10.1175/JCLI-D-16-0557.1
- Holland, G. J. (1995). Scale Interaction in the Western Pacific Monsoon. *Meteorol. Atmos. Phys.* 56, 57–79. doi:10.1007/BF01022521
- Holliday, C. R., and Thompson, A. H. (1979). Climatological Characteristics of Rapidly Intensifying Typhoons. *Mon. Wea. Rev.* 107, 1022–1034. doi:10.1175/1520-0493(1979)107<1022:ccorit>2.0.co;2
- Huang, X., Peng, X., Fei, J., Cheng, X., Ding, J., and Yu, D. (2021). Evaluation and Error Analysis of Official Tropical Cyclone Intensity Forecasts during 2005–2018 for the Western North Pacific. *J. Meteorol. Soc. Jpn.* 99, 139–163. doi:10.2151/jmsj.2021-008
- Kaplan, J., DeMaria, M., and Knaff, J. A. (2010). A Revised Tropical Cyclone Rapid Intensification index for the Atlantic and Eastern North Pacific Basins. *Wea. Forecast.* 25, 220–241. doi:10.1175/2009WAF2222280.1
- Kaplan, J., and DeMaria, M. (2003). Large-scale Characteristics of Rapidly Intensifying Tropical Cyclones in the north Atlantic basin. *Wea. Forecast.* 18, 1093–1108. doi:10.1175/1520-0434(2003)018<1093:LCORIT>2.0.CO;2
- Kieu, C. Q. (2012). An Investigation into the Contraction of the hurricane Radius of Maximum Wind. *Meteorol. Atmos. Phys.* 115, 47–56. doi:10.1007/s00703-011-0171-7
- Knaff, J. A., Longmore, S. P., DeMaria, R. T., and Molinar, D. A. (2015). Improved Tropical-Cyclone Flight-Level Wind Estimates Using Routine Infrared Satellite Reconnaissance. *J. Appl. Meteorol. Climatol.* 54, 463–478. doi:10.1175/JAMC-D-14-0112.1
- Knaff, J. A., and Zehr, R. M. (2007). Reexamination of Tropical Cyclone Wind-Pressure Relationships. *Wea. Forecast.* 22, 71–88. doi:10.1175/WAF965.1
- Knapp, K. R., Ansari, S., Bain, C. L., Bourassa, M. A., Dickinson, M. J., Funk, C., et al. (2011). Globally Gridded Satellite Observations for Climate Studies. *Bull. Amer. Meteorol. Soc.* 92, 893–907. doi:10.1175/2011BAMS3039.1
- Kurihara, Y., Bender, M. A., and Ross, R. J. (1993). An Initialization Scheme of hurricane Models by Vortex Specification. *Mon. Wea. Rev.* 121, 2030–2045. doi:10.1175/1520-0493(1993)121<2030:AISOHM>2.0.CO;2
- Kurihara, Y., Bender, M. A., Tuleya, R. E., and Ross, R. J. (1995). Improvements in the GFDL hurricane Prediction System. *Mon. Wea. Rev.* 123, 2791–2801. doi:10.1175/1520-0493(1995)123<2791:IITGHP>2.0.CO;2
- Li, Y., Wang, Y., and Lin, Y. (2019). Revisiting the Dynamics of Eyewall Contraction of Tropical Cyclones. *J. Atmos. Sci.* 76, 3229–3245. doi:10.1175/JAS-D-19-0076.1
- Liang, J., Wu, L., Gu, G., and Liu, Q. (2016). Rapid Weakening of Typhoon Chan-Hom (2015) in a Monsoon Gyre. *J. Geophys. Res. Atmos.* 121, 9508–9520. doi:10.1002/2016JD025214
- Liang, J., Wu, L., and Gu, G. (2018). Rapid Weakening of Tropical Cyclones in Monsoon Gyres over the Tropical Western North Pacific. *J. Clim.* 31, 1015–1028. doi:10.1175/JCLI-D-16-0784.1
- Liu, K. S., and Chan, J. C. L. (2002). Synoptic Flow Patterns Associated with Small and Large Tropical Cyclones over the Western North Pacific. *Mon. Wea. Rev.* 130, 2134–2142. doi:10.1175/1520-0493(2002)130<2134:SFPAWS>2.0.CO;2
- Merrill, R. T. (1984). A Comparison of Large and Small Tropical Cyclones. *Mon. Wea. Rev.* 112, 1408–1418. doi:10.1175/1520-0493(1984)112<1408:ACOLAS>2.0.CO;2
- Molinari, J., Skubis, S., and Vollar, D. (1995). External Influences on hurricane Intensity. Part III: Potential Vorticity Structure. *J. Atmos. Sci.* 52, 3593–3606. doi:10.1175/1520-0469(1995)052<3593:EIOHIP>2.0.CO;2
- Montgomery, M. T., and Smith, R. (2011). Paradigms for Tropical-Cyclone Intensification. *Q. J. R. Meteorol. Soc.* 137, 1–31. doi:10.1002/qj.000
- Qin, N., Zhang, D.-L., and Li, Y. (2016). A Statistical Analysis of Steady Eyewall Sizes Associated with Rapidly Intensifying Hurricanes. *Wea. Forecast.* 31, 737–742. doi:10.1175/waf-d-16-0016.1
- Qin, N., Zhang, D. L., Miller, W., and Kieu, C. Q. (2018). On the Rapid Intensification of Hurricane Wilma (2005). Part IV: Inner-core Dynamics

FUNDING

This work was jointly supported by the National Natural Science Foundation of China (41730961, 41675051, 41675009, 42075072, 41905001, 42005007), the Postdoctoral Science Foundation of China (2019M661342), the National Key R&D Program of China (2019YFC1510201), the Natural Science Foundation of Jiangsu Province (BK20201505), the Open Research Program of the State Key Laboratory of Severe Weather (2019LASW-A02), and the Open Grants of the State Key Laboratory of Severe Weather (2021LASW-B11).

- during the Steady Radius of Maximum Wind Stage. *Q.J.R. Meteorol. Soc.* 144, 2508–2523. doi:10.1002/qj.3339
- Qiu, W., Wu, L., and Ren, F. (2020). Monsoonal Influences on Offshore Rapid Intensification of Landfalling Typhoons in a Sheared Environment over the South China Sea. *Wea. Forecast.* 35, 623–634. doi:10.1175/WAF-D-19-0134.1
- Rogers, R., Aberson, S., Aksoy, A., Annane, B., Black, M., Cione, J., et al. (2013). NOAA'S Hurricane Intensity Forecasting Experiment: A Progress Report. *Bull. Amer. Meteorol. Soc.* 94, 859–882. doi:10.1175/BAMS-D-12-00089.1
- Rogers, R., Aberson, S., Black, M., Black, P., Cione, J., Dodge, P., et al. (2006). The Intensity Forecasting Experiment: A NOAA Multiyear Field Program for Improving Tropical Cyclone Intensity Forecasts. *Bull. Amer. Meteorol. Soc.* 87, 1523–1538. doi:10.1175/BAMS-87-11-1523
- Rogers, R. (2010). Convective-scale Structure and Evolution during a High-Resolution Simulation of Tropical Cyclone Rapid Intensification. *J. Atmos. Sci.* 67, 44–70. doi:10.1175/2009JAS3122.1
- Saha, S., Moorthi, S., Pan, H.-L., Wu, X., Wang, J., Nadiga, S., et al. (2010). The NCEP Climate Forecast System Reanalysis. *Bull. Amer. Meteorol. Soc.* 91, 1015–1058. doi:10.1175/2010BAMS3001.1
- Shapiro, L. J., and Willoughby, H. E. (1982). The Response of Balanced Hurricanes to Local Sources of Heat and Momentum. *J. Atmos. Sci.* 39, 378–394. doi:10.1175/1520-0469(1982)039<0378:TROBHT>2.0.CO;2
- Shieh, O. H., Fiorino, M., Kucas, M. E., and Wang, B. (2013). Extreme Rapid Intensification of Typhoon Vicente (2012) in the South China Sea. *Wea. Forecast.* 28, 1578–1587. doi:10.1175/WAF-D-13-00076.1
- Stern, D. P., Vigh, J. L., Nolan, D. S., and Zhang, F. (2015). Revisiting the Relationship between Eyewall Contraction and Intensification. *J. Atmos. Sci.* 72, 1283–1306. doi:10.1175/JAS-D-14-0261.1
- Tang, B., and Emanuel, K. (2010). Midlevel Ventilation's Constraint on Tropical Cyclone Intensity. *J. Atmos. Sci.* 67, 1817–1830. doi:10.1175/2010JAS3318.1
- Vigh, J. L. (2010). *Formation of the hurricane Eye*. Ph.D. dissertation. Colorado State University, 378, 473–498pp. [Available online at http://www.ral.ucar.edu/staff/jvigh/documents/vigh2010_dissertation_corrected_color_hyperlinks.pdf]
- Wang, H., and Wang, Y. (2014). A Numerical Study of Typhoon Megi (2010). Part I: Rapid Intensification. *Mon. Wea. Rev.* 142, 29–48. doi:10.1175/MWR-D-13-00070.1
- Willoughby, H. E., Clos, J. A., and Shoreibah, M. G. (1982). Concentric Eye walls, Secondary Wind Maxima, and the Evolution of the hurricane Vortex. *J. Atmos. Sci.* 39, 395–411. doi:10.1175/1520-0469(1982)039<0395:CEWSWM>2.0.CO;2
- Willoughby, H. E., and Rahn, M. E. (2004). Parametric Representation of the Primary Hurricane Vortex. Part I: Observations and Evaluation of the Holland (1980) Model. *Mon. Wea. Rev.* 132, 3033–3048. doi:10.1175/MWR2831.1
- Willoughby, H. E. (1990). Temporal Changes of the Primary Circulation in Tropical Cyclones. *J. Atmos. Sci.* 47, 242–264. doi:10.1175/1520-0469(1990)047<0242:TCOTPC>2.0.CO;2
- Wu, L., and Duan, J. (2015). Extended Simulation of Tropical Cyclone Formation in the Western North Pacific Monsoon Trough. *J. Atmos. Sci.* 72, 4469–4485. doi:10.1175/JAS-D-14-0375.1
- Wu, L., Liang, J., and Wu, C.-C. (2011). Monsoonal Influence on Typhoon Morakot (2009). Part I: Observational Analysis. *J. Atmos. Sci.* 68, 2208–2221. doi:10.1175/2011JAS3730.1
- Wu, L., Ni, Z., Duan, J., and Zong, H. (2013a). Sudden Tropical Cyclone Track Changes over the Western North Pacific: A Composite Study. *Mon. Wea. Rev.* 141, 2597–2610. doi:10.1175/MWR-D-12-00224.1
- Wu, L., Zong, H., and Liang, J. (2013b). Observational Analysis of Tropical Cyclone Formation Associated with Monsoon Gyres. *J. Atmos. Sci.* 70, 1023–1034. doi:10.1175/JAS-D-12-0117.1
- Xu, J., and Wang, Y. (2015). A Statistical Analysis on the Dependence of Tropical Cyclone Intensification Rate on the Storm Intensity and Size in the North Atlantic. *Wea. Forecast.* 30, 692–701. doi:10.1175/WAF-D-14-00141.1
- Xu, J., and Wang, Y. (2018). Dependence of Tropical Cyclone Intensification Rate on Sea Surface Temperature, Storm Intensity, and Size in the Western North Pacific. *Forecasting* 33, 523–537. doi:10.1175/WAF-D-17-0095.1
- Xu, J., and Wang, Y. (2010). Sensitivity of the Simulated Tropical Cyclone Inner-Core Size to the Initial Vortex Size*. *Mon. Wea. Rev.* 138, 4135–4157. doi:10.1175/2010MWR3335.1

Conflict of Interest: The authors declare that the research was conducted in the absence of any commercial or financial relationships that could be construed as a potential conflict of interest.

Publisher's Note: All claims expressed in this article are solely those of the authors and do not necessarily represent those of their affiliated organizations, or those of the publisher, the editors and the reviewers. Any product that may be evaluated in this article, or claim that may be made by its manufacturer, is not guaranteed or endorsed by the publisher.

Copyright © 2021 Qin and Wu. This is an open-access article distributed under the terms of the Creative Commons Attribution License (CC BY). The use, distribution or reproduction in other forums is permitted, provided the original author(s) and the copyright owner(s) are credited and that the original publication in this journal is cited, in accordance with accepted academic practice. No use, distribution or reproduction is permitted which does not comply with these terms.



Monsoon Surges Enhance Extreme Rainfall by Maintaining the Circulation of Landfalling Tropical Cyclones and Slowing Down Their Movement

Dajun Zhao^{1,2}, Lianshou Chen^{1*} and Yubin Yu¹

¹State Key Laboratory of Severe Weather, Chinese Academy of Meteorological Sciences, Beijing, China, ²University of Chinese Academy of Sciences, Beijing, China

OPEN ACCESS

Edited by:

Qingqing Li,
Nanjing University of Information
Science and Technology, China

Reviewed by:

Mingyu Bi,
Nanjing University of Information
Science and Technology, China
Qingyuan Liu,
Chinese Academy of Meteorological
Sciences, China

*Correspondence:

Lianshou Chen
chenls@cma.gov.cn

Specialty section:

This article was submitted to
Atmospheric Science,
a section of the journal
Frontiers in Earth Science

Received: 31 May 2021

Accepted: 11 August 2021

Published: 23 August 2021

Citation:

Zhao D, Chen L and Yu Y (2021)
Monsoon Surges Enhance Extreme
Rainfall by Maintaining the Circulation
of Landfalling Tropical Cyclones and
Slowing Down Their Movement.
Front. Earth Sci. 9:717447.
doi: 10.3389/feart.2021.717447

Extreme rainfall induced by landfalling tropical cyclones (ERLTCs) in China can cause flash floods and other disastrous impacts, so investigating their genesis and mechanism of enhancement has been attracting considerable attention. This study demonstrates that the extreme rainfall of landfalling tropical cyclones (LTCs) possesses two key properties—namely, maintenance of the LTC circulation and a lagging (slowing down or looping) of its movement, and the monsoon surge can provide a positive contribution to these properties. Specifically, diagnostics show that the low-level cyclonic vorticity and upper-level divergence of ERLTCs are significantly stronger than those of NERLTCs (non-extreme-rainfall-producing LTCs). The continuous intensification of the cyclonic rotation in the lower troposphere before the occurrence of extreme rainfall is a significant feature that distinguishes ERLTCs from NERLTCs. Vorticity budget analysis further shows that the relative vorticity advection term contributes the most to the local increase and maintenance of vorticity in the middle and lower troposphere of ERLTCs under the influence of the southwest monsoonal surge, thus demonstrating that the monsoonal surge favors the maintenance of LTC circulation. On the other hand, the activity of the southwest monsoonal surge is mainly manifested in the zonal wind anomaly, and the corresponding strong westerly transport can significantly reduce the zonal component of the steering flow. As a result, the total steering flow can be weakened, which decreases the northwestward translation speed of ERLTCs, and thus the monsoonal surge favors a lagging (slowing down or looping) of LTC movement. These results reveal the mechanism of influence through which the monsoonal surge affects ERLTCs via its direct impacts on the maintenance of their circulation and lagging of their movement—two distinct evolutionary characteristics.

Keywords: extreme rainfall, tropical cyclones, monsoon surge, maintenance, lagging

INTRODUCTION

Among all the countries in the world, China experiences the largest numbers of landfalling tropical cyclones (TC). As such, its coastal provinces, including districts and cities, and relevant inland areas of the country often suffer from the effects of TC-related disasters (Duan et al., 2019). The range of influence and losses caused by secondary disasters after a TC makes landfall, such as flash flooding

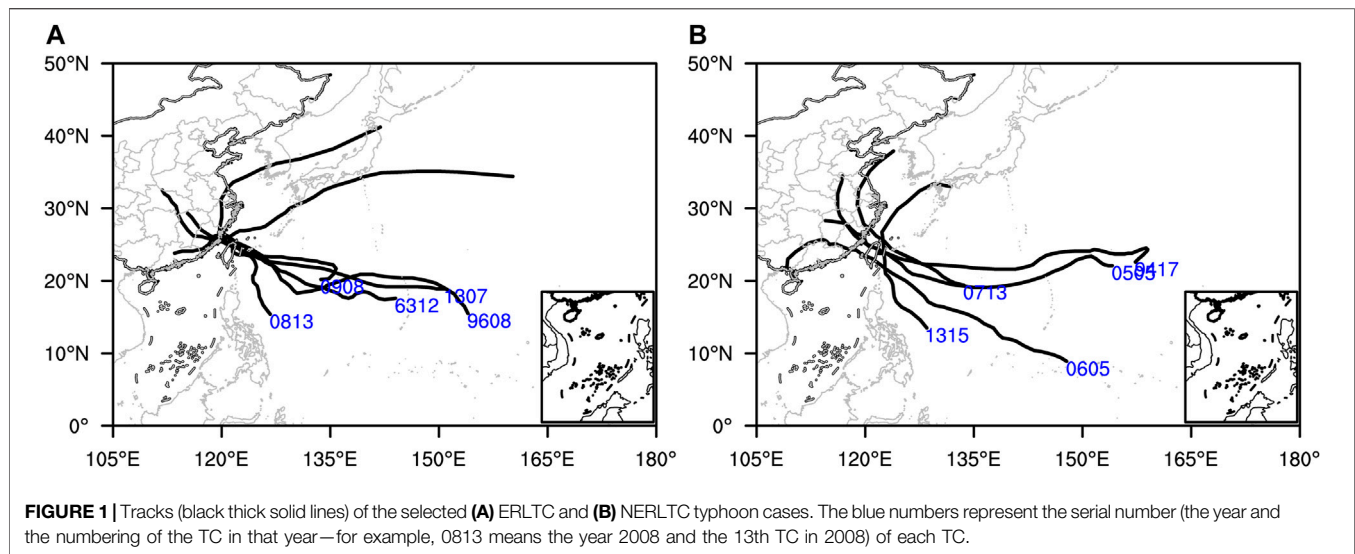
and debris flow, are often larger than those of the TC rainfall in its inner-core region (Duan et al., 2014). Statistics have shown that TCs in China cause direct economic losses of about 0.4% of GDP and more than 9,000 casualties each year (Lei, 2020). Therefore, it is of great significance for disaster prevention in China to improve the forecasting skill for TCs and provide timely warnings of their arrival. China is heavily influenced by the East Asian summer monsoon in terms of the transportation of water vapor and rainfall—especially the eastern part of the country, where the monsoon and TCs have more opportunities to interact with each other (Chen and Xu, 2017). The interaction between TCs and monsoon circulation has a considerable influence on their precipitation. For instance, when the remnant vortex of a TC combines with the southwest monsoonal surge from the South China Sea to the mainland, the remnant vortex can acquire a large amount of water vapor and latent heat, enabling it to sustain over land for a long time and produce heavy rainstorms (Cheng et al., 2012). A famous example was the strong tropical storm Bilis (0604), which, after making landfall, maintained a long period of connection with the southwest monsoon flow, leading to continuous torrential rainfall in many provinces in Southeast China (Gao et al., 2009; Dong et al., 2010; Lu et al., 2012).

The intensity and frequency of extreme precipitation in China have shown increasing trends under global warming, especially since the 1990s (Xia et al., 2019), and extreme precipitation has become a hot topic in scientific research internationally (Gu and Zhang, 2020). As the strongest type of precipitation-related weather system, TCs often bring extreme precipitation, leading to serious secondary disasters. For example, the 24-h rainfall amount reached 1,062 mm after TC Nina (7503) made landfall, breaking the existing record of maximum daily rainfall over the mainland China held by the famous “75•8” extremely severe rainfall in Henan Province (Ding et al., 1978). Another very famous example is TC Morakot (0908), which landed in Taiwan Province and Fujian Province successively, and the associated extreme rainfall caused 673 deaths and 26 missing persons in Taiwan, and affected 14.3 million people on the mainland China. The direct economic losses reached 12.7 billion yuan (Chen et al., 2012). Recently, TC Lekima (1909) landed in Zhejiang Province of China with a double-eyewall structure (Dai et al., 2021), heavy rainfall, and a wide range of impact. It produced rainfall amounting to 488.1 mm over Shanghe, exceeding the maximum precipitation record produced by landfalling TCs (LTCs) since 1960 in Shandong Province (Jia et al., 2020). Therefore, research on the rainstorms of LTCs has always been of critical importance for TC research in China, and a wide range of results have been obtained from different perspectives (Ding, 2015; Chen and Xu, 2017; Ren and Yang, 2019; Lei, 2020).

Chen (1977), Chen and Xu (2017) analyzed the most extreme rainstorm processes of TCs throughout the history of China in which the 24-h accumulated rainfall exceeded 1,000 mm, and found that their maintenance and stagnation were the two most important conditions for the occurrence of extreme rainstorms. The extreme precipitation of TCs is associated mainly with the convective rain caused by the interaction of TC circulation and other weather systems (Bao et al., 2020). Cheng et al. (2012)

carried out a systematic study on the torrential rainfall associated with LTCs and revealed that the southwest monsoon transported the water vapor and unstable energy to TC Bilis (2006) *via* the low-level jet stream, which was highly beneficial to its maintenance and severe torrential rainfall. Dong et al. (2010) pointed out that the interaction between the southwest monsoonal surge and LTCs can sustain the low-level jet in the lower troposphere and intensify the shear line convergence, leading to rainfall reinforcement. China is located in a typical monsoon climate region. On the synoptic scale, the summer monsoon is characterized by the low-level jet streams carrying large quantities of water vapor and unstable energy. The process of severe torrential rainfall is closely related to the low-level jet (Cheng et al., 2012). Lu et al. (2012) compared the mechanisms of how the low-latitude monsoonal surge affected the intensification of the torrential rainfall of LTCs Durian (0103) and Bilis (0604). They pointed out that the low-latitude monsoonal surges, represented by different low-frequency oscillation cycles, moved significantly northwards. When the low-frequency oscillation was in an extremely active phase, the monsoonal surge peaked and invaded the circulation, corresponding to the intensification of the TC rainstorms. Zhou and Wu (2019) compared the difference in rainfall area and intensity among westward LTCs against the background of strong and weak summer monsoons. The results showed that a strong summer monsoon tends to correspond to westward LTCs featuring heavy rainfall and is conducive to the maintenance of the warm-core structure of a TC after it has made landfall. Therefore, a strong summer monsoon enables the maintenance of TC circulation and the intensification of its associated rainfall. The above studies have laid the foundation for us to further understand TC-related torrential rainfall, as well as provide multiple research perspectives for us to further investigate the extreme rainfall of LTCs. However, the very recent study by Yu et al. (2020) showed that, when the precipitation of a LTC meets the criteria of extremely severe rainfall (≥ 250 mm/24 h), the ETS (equitable threat score) of the 24-h rainfall forecast can be as low as < 0.1 , indicating that operational forecasting remains difficult. Therefore, it is necessary to carry out research on the extreme rainfall of LTCs (including offshore-affecting TCs) over China.

In the first part (Zhao et al., 2021) of this series of studies, we focused on the water vapor budget analysis of the ERLTC under the influence of monsoon surges, and preliminarily exploring impact of the zonal component of monsoonal surges on the slower translational speed of ERLTCs on the rainfall occurrence day. We further proposed a new dynamic monsoon surge index (DMSI) to characterize the intensity of monsoon surge quantitatively. Results showed that the monsoonal surges could enhance the convergence of horizontal wind and water vapor fluxes by strengthening the water vapor input at the western and southern boundaries of ERLTCs. Besides, the zonal component of monsoonal surges could also weaken the background zonal steering flow and decelerate the translation of ERLTCs. The present study is a further extension of Zhao et al. (2021). It attempts to comprehensively summarize the distinct evolution characteristics of ERLTCs (NERLTCs) during the whole rainfall process (3 days ago to the occurrence of rainfall)



and investigate the mechanisms of monsoon surges for these evolution characteristics of the LTCs. In particular, the relative importance of zonal and meridional components of the monsoon surges and their influences on the steering flow will be examined in some detail. These investigations will further enrich our understanding of the role of monsoon surges impact on ERLTCs.

The rest of this paper is arranged as follows: *Data and methods* introduces the data and methods. *Evolutionary characteristics of ERLTCs in terms of maintenance and lagging* presents the characteristics of the circulation and translational-speed evolution of ERLTCs and NERLTCs. *Mechanisms through which the monsoonal surge influences the maintenance and lagging of ERLTCs* analyzes the mechanisms of influence of the monsoonal surge on the maintenance of ERLTCs (NERLTCs) circulation and the lagging (slowing down or looping) of its movement from the perspectives of the vorticity budget and environmental steering flow, respectively. Further presented in this section is a conceptual physical model of how the monsoonal surge influences ERLTCs, based on the present findings. Finally, conclusions and some further discussion around future work are provided in *Conclusions and future work*.

DATA AND METHODS

Data

The six-hourly reanalysis dataset with a spatial resolution of 2.5° latitude \times 2.5° longitude from the NCEP–NCAR (National Centers for Environmental Prediction–National Center for Atmospheric Research) and the TC best-track database developed by the Shanghai Typhoon Institute of the China Meteorological Administration (Ying et al., 2014; Lu et al., 2021) are employed in this study. The cloud-top brightness temperature (TBB, also named black body temperature) datasets obtained from the infrared channel of the FY-2 satellite are used. In addition, TC-induced precipitation data obtained by OSAT (the objective synoptic analysis technique)

are also used (Ren et al., 2007), which cover 1888 stations affected by TC precipitation over China, including 21 stations in Taiwan. The composite analysis methods adopted in this work are introduced in detail in Zhao et al. (2021). **Figures 1A,B** show the entire tracks of ERLTC and NERLTC cases in the composite analyses. It can be seen that these TCs generated in the Northwest Pacific, landfalling in or affecting Taiwan Province and the mainland China following the northwestward track.

Methods

Following Chen and Xu (2017), an absolute threshold method is used to define the ERLTCs, except the number of ERLTC samples and the representativeness of the ERLTCs are further taken into consideration. Thus, 24-h accumulated rainfall ≥ 600 mm at a single rain gauge station over China is defined as an ERLTC event; otherwise, it is an NERLTC event under the influence of an LTC. The evolution of the vertical component of the vorticity is often used to characterize the intensity and structural evolution of a weather system. The vertical vorticity equation in the p -coordinate system is as follows (Yang et al., 1983):

$$\frac{\partial \zeta}{\partial t} = - \left(u \frac{\partial \zeta}{\partial x} + v \frac{\partial \zeta}{\partial y} \right) - \omega \frac{\partial \zeta}{\partial p} - \beta v - (\zeta + f) \left(\frac{\partial u}{\partial x} + \frac{\partial v}{\partial y} \right) + \left(\frac{\partial u}{\partial p} \frac{\partial \omega}{\partial y} - \frac{\partial v}{\partial p} \frac{\partial \omega}{\partial x} \right) \quad (1)$$

where

$$- \left(u \frac{\partial \zeta}{\partial x} + v \frac{\partial \zeta}{\partial y} \right)$$

is the advection variation term of the relative vorticity, which is caused by the uneven horizontal distribution of the relative vorticity;

$$- \omega \frac{\partial \zeta}{\partial p}$$

is the convective variation term of the relative vorticity, which is caused by the uneven vertical distribution of relative vorticity; $-\beta v$ is the advection term of the geostrophic vorticity, which represents the variability of the relative vorticity induced by the

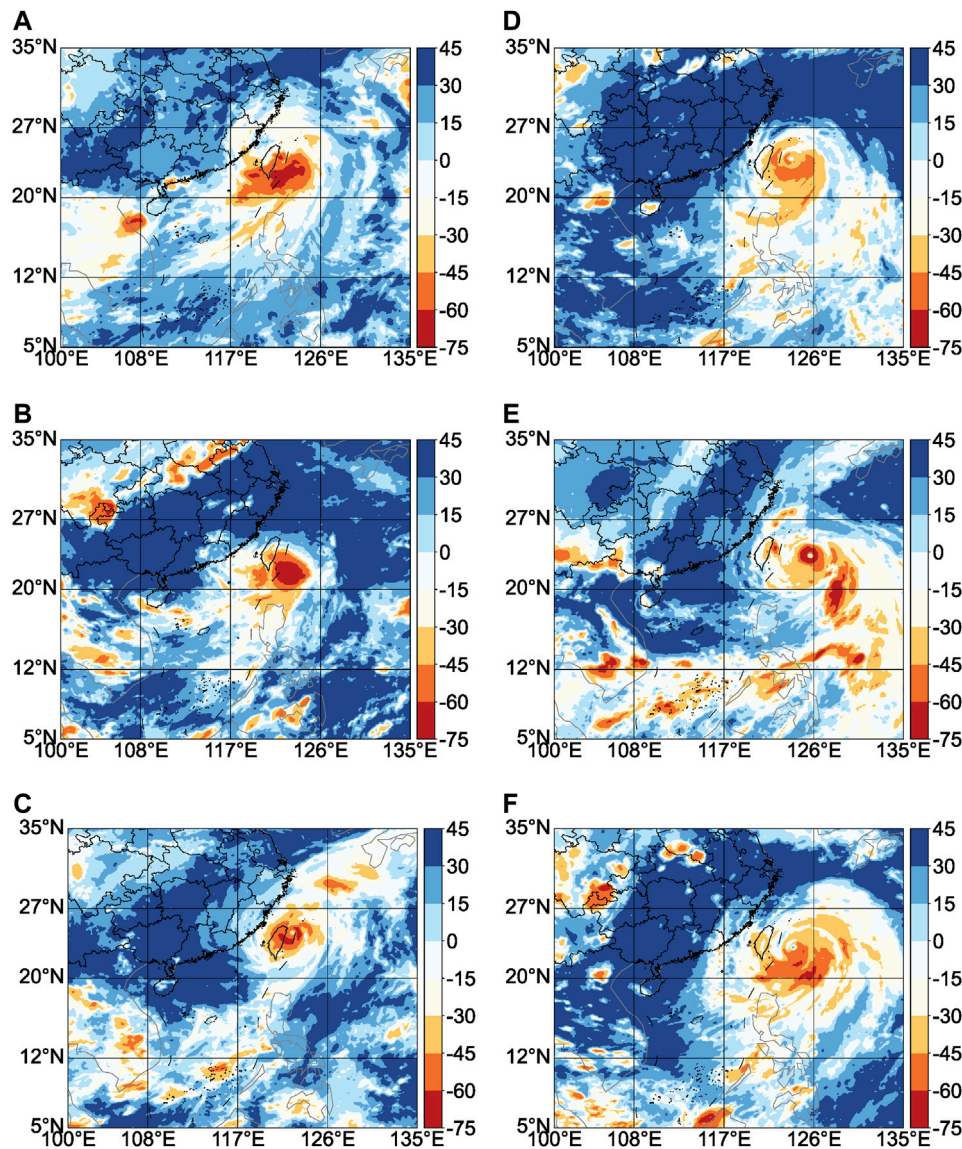


FIGURE 2 | The cloud top brightness temperature (Unit: °C) from the Chinese geostationary meteorological satellite FY-2 for the ERLTC cases [(A–C) indicate Morakot, Soulik and Hagupit, respectively] and NERLTC cases [(D–F) indicate Kong-Rey, Wipha and Haitang respectively] 1 day before the extreme or non-extreme rainfall. Data for Herb, Gloria, Fred and Kaemi are unavailable, the corresponding figures omitted here.

different geostrophic vorticities during the north–south movement of the air parcel;

$$-(\zeta + f) \left(\frac{\partial u}{\partial x} + \frac{\partial v}{\partial y} \right)$$

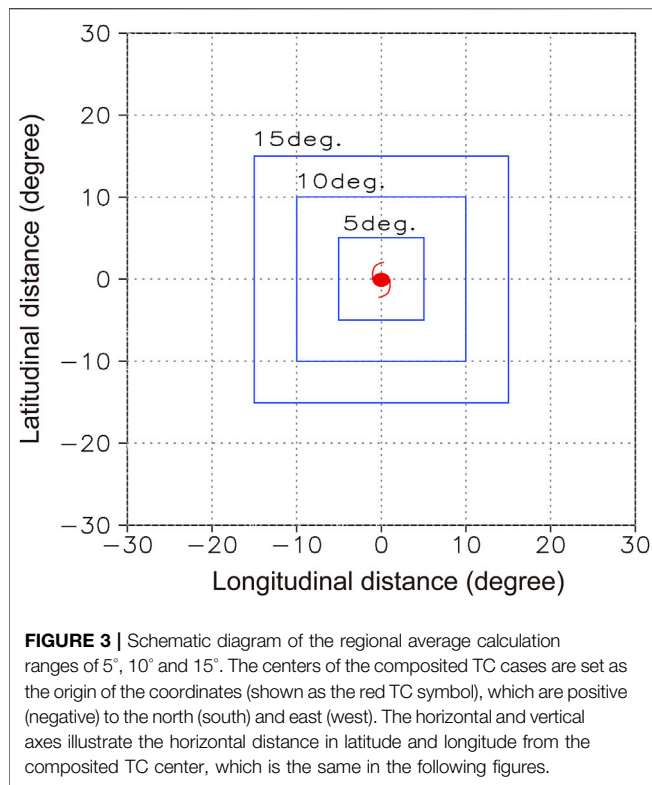
is the horizontal divergence or convergence term, indicating that the horizontal divergence will reduce the absolute vorticity;

$$\frac{\partial u}{\partial p} \frac{\partial \omega}{\partial y} - \frac{\partial v}{\partial p} \frac{\partial \omega}{\partial x}$$

is the tilting term, which represents the conversion of the horizontal vorticity to the vertical vorticity. In this study, the

vertical vorticity equation in the p -coordinate system is used to further diagnose the physical processes that determine the maintenance of ERLTC (NERLTC) circulation under the influencing of the monsoonal surge, which has been widely used in previous diagnostic studies on TC structure and intensity evolution (Li et al., 2019; Rantanen et al., 2020).

The whole-layer steering airflow of the TC environmental field is calculated based on the mass-weighted average scheme recommended by the World Meteorological Organization (Kimberlain and Breman, 2017). This scheme can be calculated approximately based on several typical pressure layers, which is simplified as follows:



$$S_x = [(U_{850} + U_{500})/2 * 350mb + (U_{500} + U_{200})/2 * 300mb]/650mb \quad (2)$$

$$S_y = [(V_{850} + V_{500})/2 * 350mb + (V_{500} + V_{200})/2 * 300mb]/650mb \quad (3)$$

Here, S_x and S_y represent the zonal and meridional steering flows of the whole layer, respectively. Hereafter, U_{850} (V_{850}), U_{500} (V_{500}) and U_{200} (V_{200}) on the right-hand side of Eqs 2, 3 describe the zonal (meridional) wind at the lower (850 hPa), middle (500 hPa) and upper (200 hPa) levels of the troposphere. The deep layer mean (DLM) of the environmental steering flow of a TC is

$$DLM = (S_x, S_y)$$

Figure 2 shows the infrared cloud images on the day before the extreme or non-extreme rainfall of ERLTC (**Figures 2A–C**) and NERLTC (**Figures 2D–F**) cases. **Figures 2A–C** show that the convection to the southwest of the ERLTC is strong. At the same time, there are significant cloud-band activities in the environmental field to the southwest of the TC, which can be seen in the area to the southwest of the TCs in the figure. It is difficult to strictly distinguish the ERLTC from the southwest monsoonal surge in the cloud image, and there is a clear connection between the two cloud bands. In comparison, the cloud-band activity in the environmental field to the southwest of the NERLTC (**Figures 2D–F**) is much weaker. In particular, there is a clearer boundary between this band and the cloud band to the southwest of the TC, and there

is even a clear-sky area. Thus, the satellite cloud image can qualitatively reflect the interaction between the monsoonal surge and the typhoon. Further quantitative analyses of the contribution of monsoonal surges to the ERLTC based on meteorological data are carried out in the following analysis. A schematic diagram of the regional average calculation ranges of 5°, 10°, and 15° are shown in **Figure 3**.

EVOLUTIONARY CHARACTERISTICS OF ERLTCS IN TERMS OF MAINTENANCE AND LAGGING

Maintenance of ERLTC Vorticity and Divergence

Figure 4 shows the temporal variation of the relative vorticity at 850-hPa (**Figures 4A,B**) and divergence at 200-hPa (**Figures 4C,D**) in the rectangular area around the composited ERLTC (**Figures 4A,C**) and NERLTC (**Figures 4B,D**) center with side lengths of 5°, 10° and 15°, as well as at the typhoon center. The rectangular areas of different sizes represent the evolution of the low-level vorticity and upper-level divergence of the TC and its surrounding environmental field. **Figure 4** shows that the evolutionary trends of the low-level vorticity and upper-level divergence are basically the same for the regional average of the different rectangles.

The relative vorticity at 850-hPa (**Figures 4A,B**) shows fluctuating increases before the extreme or non-extreme rainfall and reaches its maximum one to 2 days before the extreme rainfall. It then decreases rapidly with the occurrence of the extreme or non-extreme rainfall. This evolutionary trend is most significant in the typhoon center, followed by the regional average in the 5° rectangle, while the variations of the regional average in the 10° and 15° rectangles are non-significant. This indicates that the low-level cyclonic rotation of the ERLTC is stronger than that of the NERLTC, and this difference is significant in the typhoon center and in the regional average of the 5° rectangle. Similarly, the temporal variations of the divergence at 200-hPa (**Figures 4C,D**) of these two types of TCs are significant in the typhoon center and in the regional average of the 5° rectangle, while those of the regional average of the 10° and 15° rectangles are non-significant. Compared with the NERLTC (**Figure 4D**), the upper-level divergence of the ERLTC is maintained at a high value before the extreme rainfall, which then decreases rapidly on the day of the extreme rainfall, indicating that the upper-level divergence of the ERLTC is significantly stronger than that of the NERLTC. Thus, the low-level cyclonic rotation and upper-level divergence of the ERLTC are significantly stronger than those of the NERLTC. The ERLTC differs from the NERLTC in that the cyclonic rotation at 850 hPa continuously intensifies before the extreme rainfall and the divergence at 200 hPa decreases sharply on the day of the extreme rainfall.

Figure 5 shows the height–time evolution of the relative vorticity (**Figures 5A,B**) and divergence (**Figures 5C,D**) of the composited ERLTC (**Figures 5A,C**) and NERLTC (**Figures**

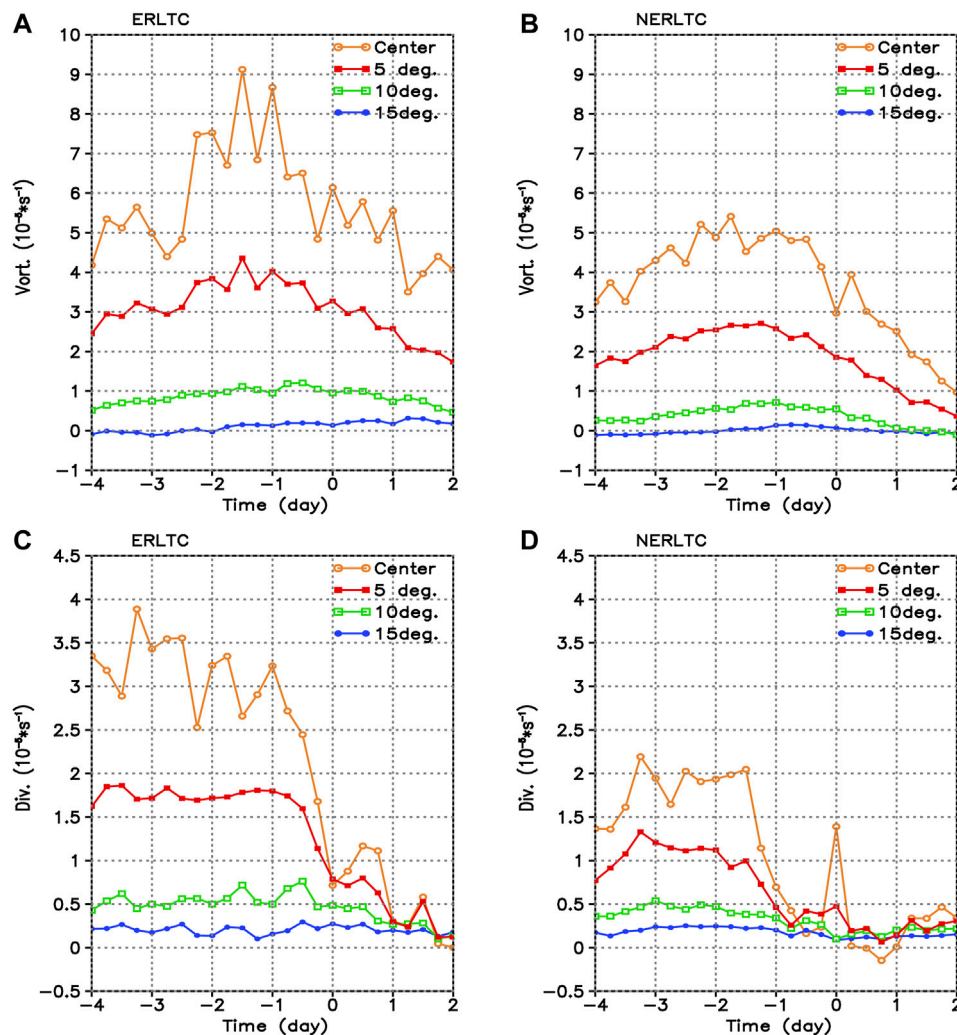


FIGURE 4 | Temporal variations of the regional-average relative vorticity (units: 10^{-5} s^{-1}) at 850 hPa (A, B) and the divergence (units: 10^{-5} s^{-1}) at 200 hPa (C, D) for ERLTCs (A, C) and NERLTCs (B, D). The abscissa represents the relative time in days to the occurrence of the rainfall during the study period (unit: days), which is the same in the following figures.

5B,D) across the TC center to further illustrate the evolution of the vorticity and divergence at different heights. Before the extreme rainfall occurs, the high-value area of the ERLTC's relative vorticity (Figure 5A) gradually descends from the middle and upper troposphere at 400–500 hPa to the lower troposphere at 800–900 hPa. On the day before the extreme rainfall, the relative vorticity near 850 hPa in the lower troposphere reaches its maximum. In comparison, the high-value area of the NERLTC's relative vorticity (Figure 5B) is smaller and the vertical extent is lower than that of the ERLTC, which reaches its maximum 2 days before the non-extreme rainfall. The height–time evolution of the divergence shows that both the upper-level divergence and lower-level convergence of the ERLTC (Figure 5C) are stronger than those of the NERLTC (Figure 5D), and the lower-level convergence of the two types reaches its maximum before the rainfall. Combining the above analyses of the temporal evolution

of the relative vorticity at 850 hPa and the divergence at 200 hPa in different regions, it can be seen that, before the extreme rainfall, the cyclonic rotation in the lower levels and the divergence in the upper levels are both strong in the case of the ERLTC. In general, the characteristics of the ERLTC's structure are more similar to those of “strong typhoons” than those of the NERLTC. The reasons are explored in the next section based on the similarities and differences between the environmental fields of the two types of TC.

Basic Circulation Configuration of ERLTCs

Figure 6 shows the wind field and water vapor flux at 850 hPa of the composited ERLTC and NERLTC superimposed onto the 588-dagpm contour at the 500-hPa isobaric surface. Compared with the NERLTC (Figures 6C,D), the water vapor flux to the southwest of the ERLTC (Figures 6A,B) is much stronger. At the same time, this southwest water vapor is continuously

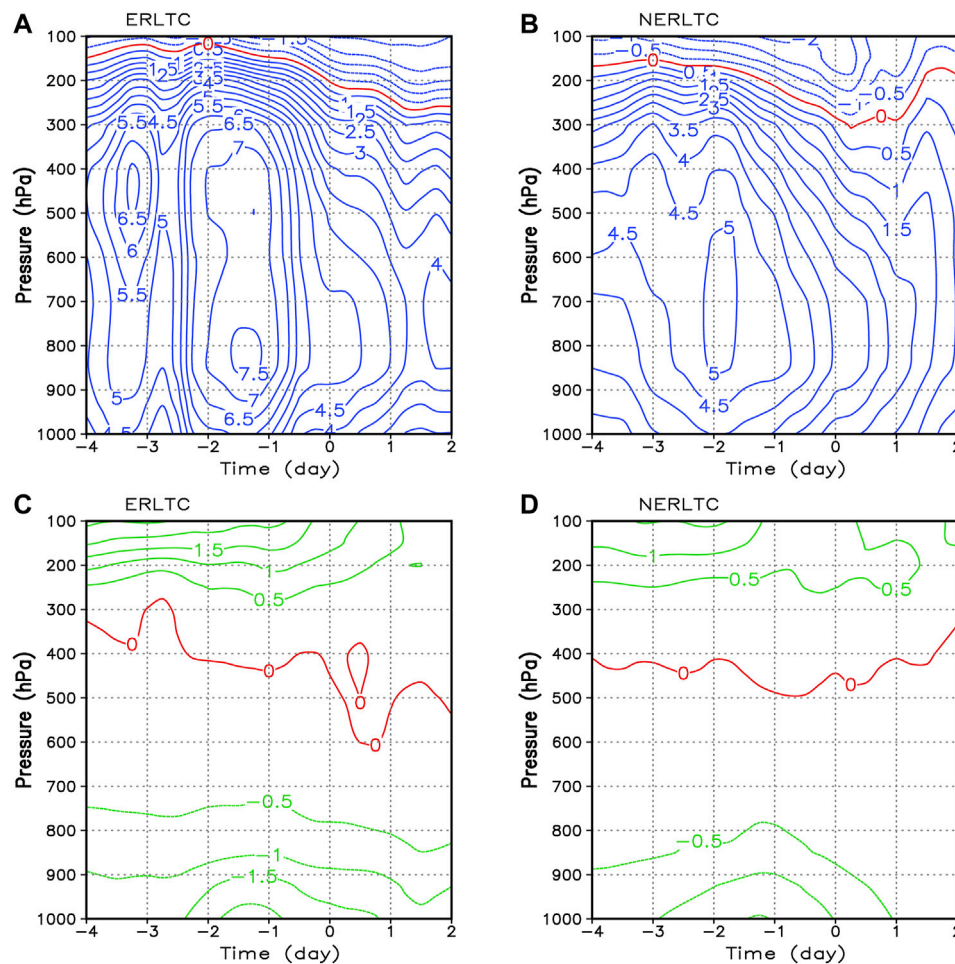
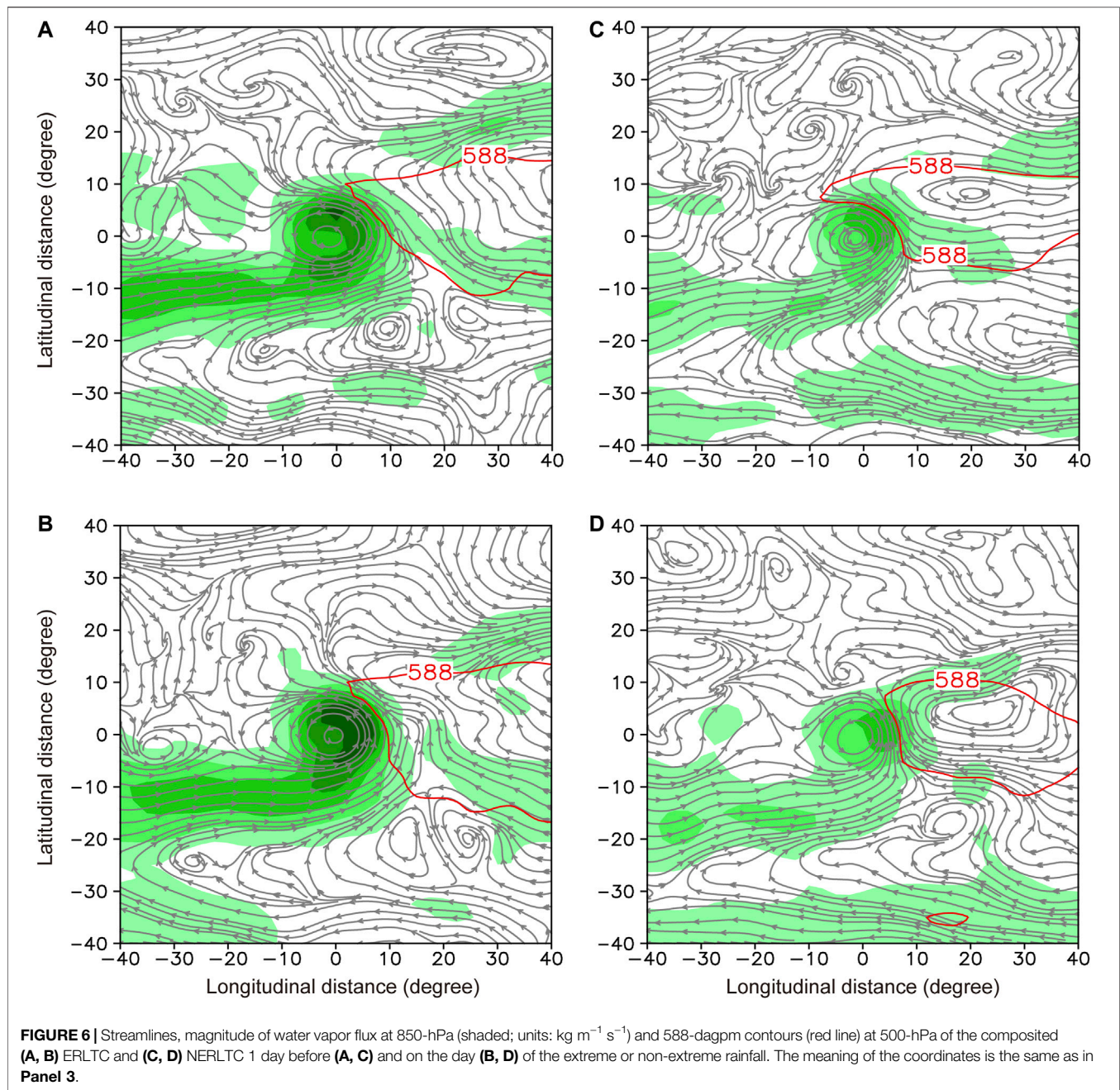


FIGURE 5 | Height-time evolution of the (A,B) relative vorticity (units: 10^{-5} s^{-1}) and (C,D) divergence (units: 10^{-5} s^{-1}) for (A,C) ERLTCs and (B,D) NERLTCs across the typhoon center.

transported from the environmental field, which can be seen 4 days before the extreme rainstorm (figures not shown). Therefore, the continuous and strong southwest water vapor transport in the ERLTC's environmental field is an important feature that distinguishes it from the NERLTC, which is the southwest monsoonal surge activity discussed in this paper. The 588-dagpm contour on the 500-hPa isobaric surface represents the activity of the subtropical high, indicating a strong subtropical high to the east of the ERLTC. Thus, the joint effects of the strong monsoonal surge to the southwest and the strong activity of the subtropical high to the east of the ERLTC lead to a stronger lower-level cyclonic rotation and upper-level divergence of the ERLTC compared to those of the NERLTC.

Figure 7 shows the height-time evolution of the water vapor flux and horizontal wind of the composited ERLTC and NERLTC to further explore the vertical structure characteristics of the southwest monsoonal surge. **Figures 7D–F** show that, although there are also high water vapor flux values to the west of the NERLTC before the non-extreme rainstorm, they are not connected to the TC.

Combined with the horizontal wind, it can be seen that northerly wind prevails in the middle and lower troposphere between the TC and the high-value area of the water vapor flux, which is not conducive to the transport of water vapor from the environmental field in the southwest to the TC. On the contrary, **Figures 7A–C** show that the high-value area of the water vapor flux to the west of the ERLTC has an enduring connection to the TC, and southwesterly wind prevails between them, indicating strong southwest monsoonal surge activity. Two days before the extreme rainstorm (**Figure 7A**), there are two peaks of water vapor flux near 20° and 40° west of the TC center. One day before the extreme rainstorm (**Figure 7B**), the peak of the water vapor flux near 20° west of the TC center merges with the TC; and with the expansion of the high-value water vapor flux area in the TC, it further extends vertically on the day of the extreme rainstorm (**Figure 7C**). In addition, there are differences in the vertical structures of the TC and the southwest monsoonal surge, even though both are warm and wet weather systems. **Figure 7** shows that the high-value area of the water vapor flux of the southwest monsoonal surge is located in the lower troposphere and reaches



the underlying surface. However, the high-value area of the water vapor flux of the TC is located in the middle and lower troposphere, which cannot reach the underlying surface. This feature is determined by the wind structure in the TC boundary layer.

Lagging of the ERLTC

Figure 8 shows the translational speed of the selected cases of ERLTCs and NERLTCs and their relative average translational speeds, which were calculated by the great circle distance between two latitudinal and longitudinal points in the best-track dataset at 6-h intervals. The results show that the average translational

speeds of ERLTCs (NERLTCs) remains slower (faster) from 3 days before to the day when the rainfall occurs. During this 3-day period of rainfall, the average translational speed of the ERLTCs and NERLTCs in our study is 14.7 km h^{-1} and 20.4 km h^{-1} , respectively. From this, we can see that the average translational speed of the ERLTCs is nearly a quarter slower than that of the NERLTCs, which is in consistent with previous conclusions (Chen, 1977; Wu, 2013; Chen and Xu, 2017) that the maintenance and stagnation of TCs are important characteristics for LTC extreme rainfall. We believe that the monsoonal surge is an important factor of influence for the lagging of ERLTCs. A detailed mechanistic analysis in this

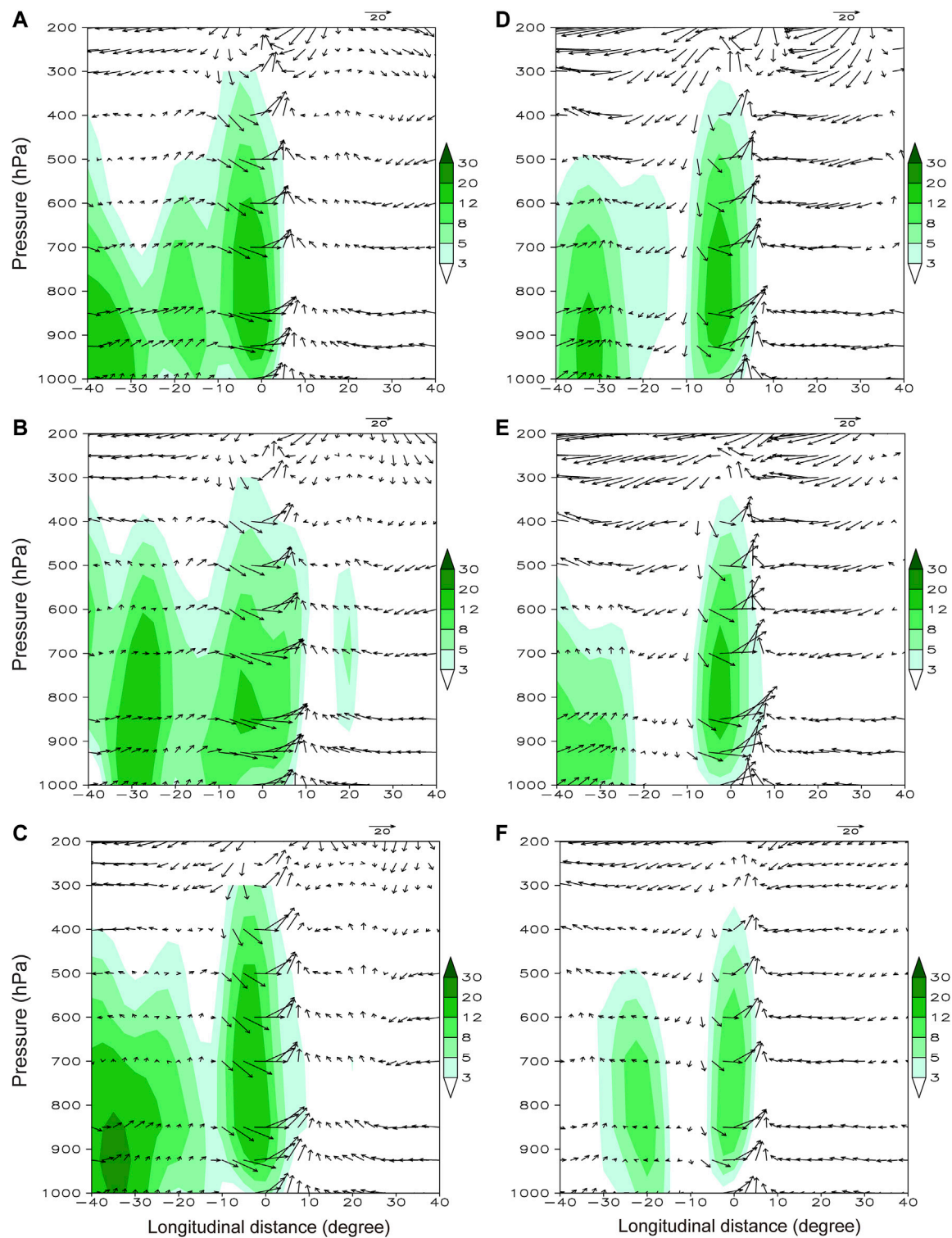
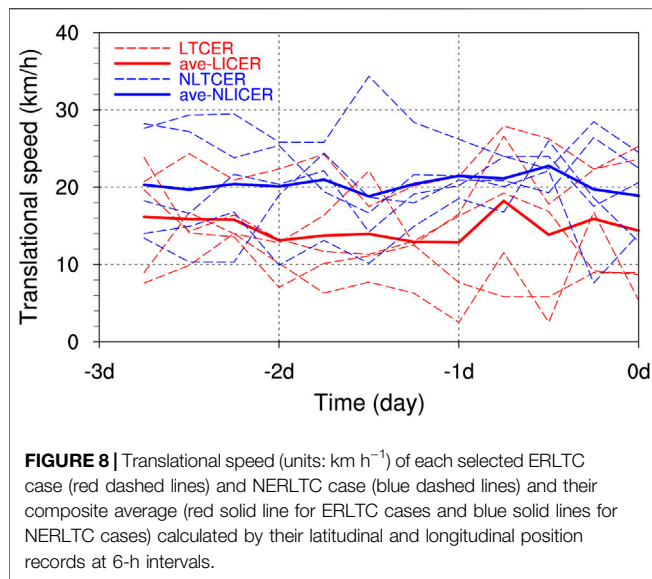


FIGURE 7 | Height-time evolution of the magnitude of water vapor flux (shaded; units: $\text{kg m}^{-1} \text{s}^{-1}$) and horizontal wind (vectors; units: m s^{-1}) of the composited (A–C) ERLTC and (D–F) NERLTC 2 days before (A, D), 1 day before (B, E), and on the day (C, F) of the extreme or non-extreme rainfall.



respect is further given in *Lagging mechanism revealed by the environmental steering flow*.

MECHANISMS THROUGH WHICH THE MONSOONAL SURGE INFLUENCES THE MAINTENANCE AND LAGGING OF ERLTCS

Maintenance Mechanism Revealed by Vorticity Budget Analysis

Rotation is one of the most basic characteristics of the TC system. A TC is often considered as a flat cyclonic vortex, and the ratio of its vertical to horizontal scale is about 1:50 (Chen and Ding, 1979). The vorticity budget equation can be used to describe the characteristics of a TC's vortex motion. Based on our earlier qualitative analyses, we next quantitatively analyze the vertical vorticity budgets of the ERLTC and NERLTC cases by focusing on the contribution of the southwest monsoonal surge to the ERLTC vorticity budget.

One day before the extreme rainfall (Figure 9A), the total vorticity tendency of the composited ERLTC is positive below 250 hPa and negative above 250 hPa, indicating that its vorticity increases below 250 hPa and decreases above 250 hPa. The horizontal divergence term contributes the most to the vorticity tendency, followed by the vorticity advection term. For the composited NERLTC (Figure 9C), the total vorticity tendency is positive (negative) below (above) 300 hPa, indicating that its vorticity increases below 300 hPa and decreases above 300 hPa. The horizontal divergence term also contributes the most to the vorticity tendency, but the vorticity advection term below 300 hPa has a negative contribution in general. Thus, the most significant difference in the vorticity budgets between the two types of LTC is the relative vorticity advection term between 700 hPa and 400 hPa in the middle and upper troposphere. The contributions of other terms are small. On the day of the extreme rainfall (Figure 9C), the peak total vorticity tendency of the

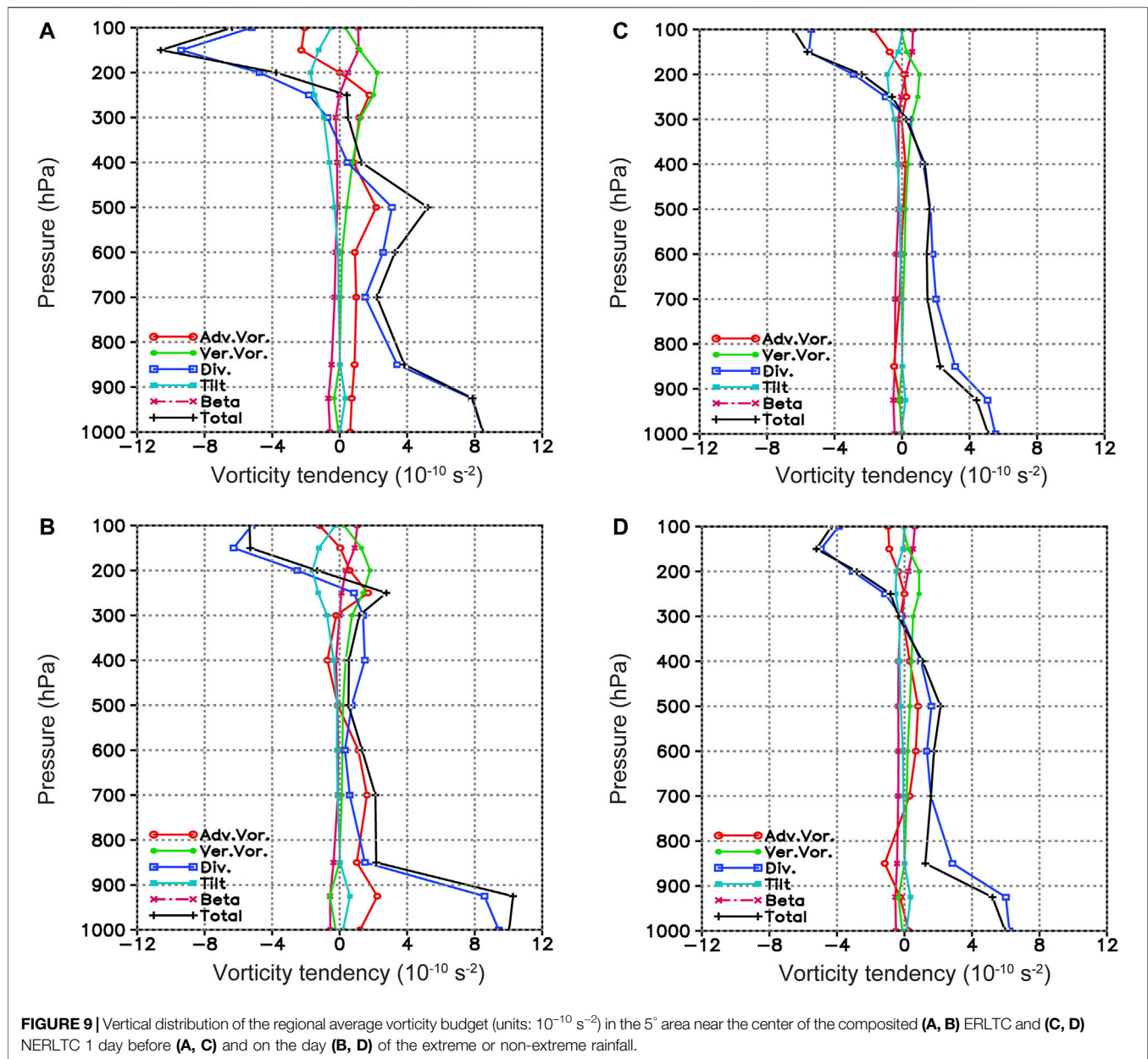
ERLTC decreases near 500 hPa and increases significantly below 850 hPa, indicating that the vorticity decreases in the middle troposphere and increases in the lower troposphere. These analyses of the contributions of different terms show that the increase in the relative vorticity advection term in the lower troposphere plays an important role. However, the variations in total vorticity tendency and the budgets of the terms of the NERLTC (Figure 9D) are non-significant.

The vorticity of the ERLTC increases more significantly in the middle and lower troposphere compared with that of the NERLTC, especially in the lower troposphere on the day of the extreme rainfall. Although the vertical variational trends of the vorticity tendency of the two types of LTC are basically consistent with those of the horizontal divergence term, the relative vorticity advection term contributes significantly to the ERLTC in the middle and lower troposphere, indicating an important contribution of the southwest monsoonal surge to ERLTCs.

The height–time evolution of the average vorticity budgets in the 5° region near the center of the ERLTC (Figures 10A–F) and NERLTC (Figures 10G–L) before and after the extreme or non-extreme rainfall are given below. The patterns of the horizontal divergence terms (Figures 10C,I) of the ERLTC and NERLTC are similar, in which the convergence gradually intensifies in the lower troposphere before the extreme or non-extreme rainfall. The difference is that the convergence of the ERLTC is stronger than that of the NERLTC. The relative vorticity advection term (Figures 10B,H) shows the high-value area to be located in the middle and lower troposphere. The difference is that the value of the ERLTC is one order of magnitude larger than that of the NERLTC, which further proves that the relative vorticity advection term in the middle and lower troposphere makes an important contribution to ERLTCs. The vertical transport terms of the relative vorticity (Figures 10E,K) of the ERLTC and NERLTC are very similar, with both having peaks near 200 hPa in the upper troposphere. In addition, the β -effect terms (Figures 10D,J) and the tilting terms (Figures 10F,L) of the two types of typhoons are one order of magnitude smaller than the total vorticity tendency, horizontal divergence, and relative vorticity advection terms. Their contributions are relatively small, which is consistent with the dimensional analysis results of the TC system. All in all, the vorticity in the middle troposphere begins to increase and gradually extends to the lower troposphere before the extreme rainfall, and is contributed significantly by the relative vorticity advection term in the middle and lower troposphere.

Lagging Mechanism Revealed by the Environmental Steering Flow

Figure 11 shows the DLM of the environmental steering flow, which is the southeasterly wind for both the composited ERLTC and NERLTC, thus explaining why the TC cases selected in this study all follow the northwestward track. In Zhao et al. (2021), the influence of the zonal component of the monsoonal surge on the zonal steering flow was discussed. Here, Figure 11 further shows the meridional component of the monsoonal surge and its influence on



the meridional steering flow and the total DLM. Comparison between the ERLTC and NERLTC shows that the patterns of the meridional wind at different levels of the environmental field are similar to each other, with southerly wind in the lower levels, northerly wind in the upper levels, and weak southerly wind in the DLM. Thus, the magnitude of the DLM is mainly determined by the zonal component. Therefore, the activity of the southwest monsoonal surge is mainly manifested in the zonal anomaly, and the corresponding strong westerly wind transport can significantly reduce the zonal component of the TC steering flow. Subsequently, the TC steering flow can be weakened and the northwestward speed of movement of the ERLTC decreases, generating the favorable conditions for extreme rainfall.

Conceptual Model of the Impacts of the Monsoonal Surge on ERLTCs

Combining the findings of Zhao et al. (2021) and the main conclusions of the present study, a complete conceptual model of the impacts of the monsoonal surge on ERLTCs is presented in **Figure 12**. Against the background of the East Asian summer monsoon, monsoonal surge with favorable underlying surface conditions play important roles in the evolution and characteristics of ERLTCs. Specifically, the impacts can be summarized into three aspects: Firstly, the monsoonal surge can continuously transport water vapor to the ERLTC. Secondly, the activities of the monsoonal surge can significantly reduce the ERLTC's steering flow and TC

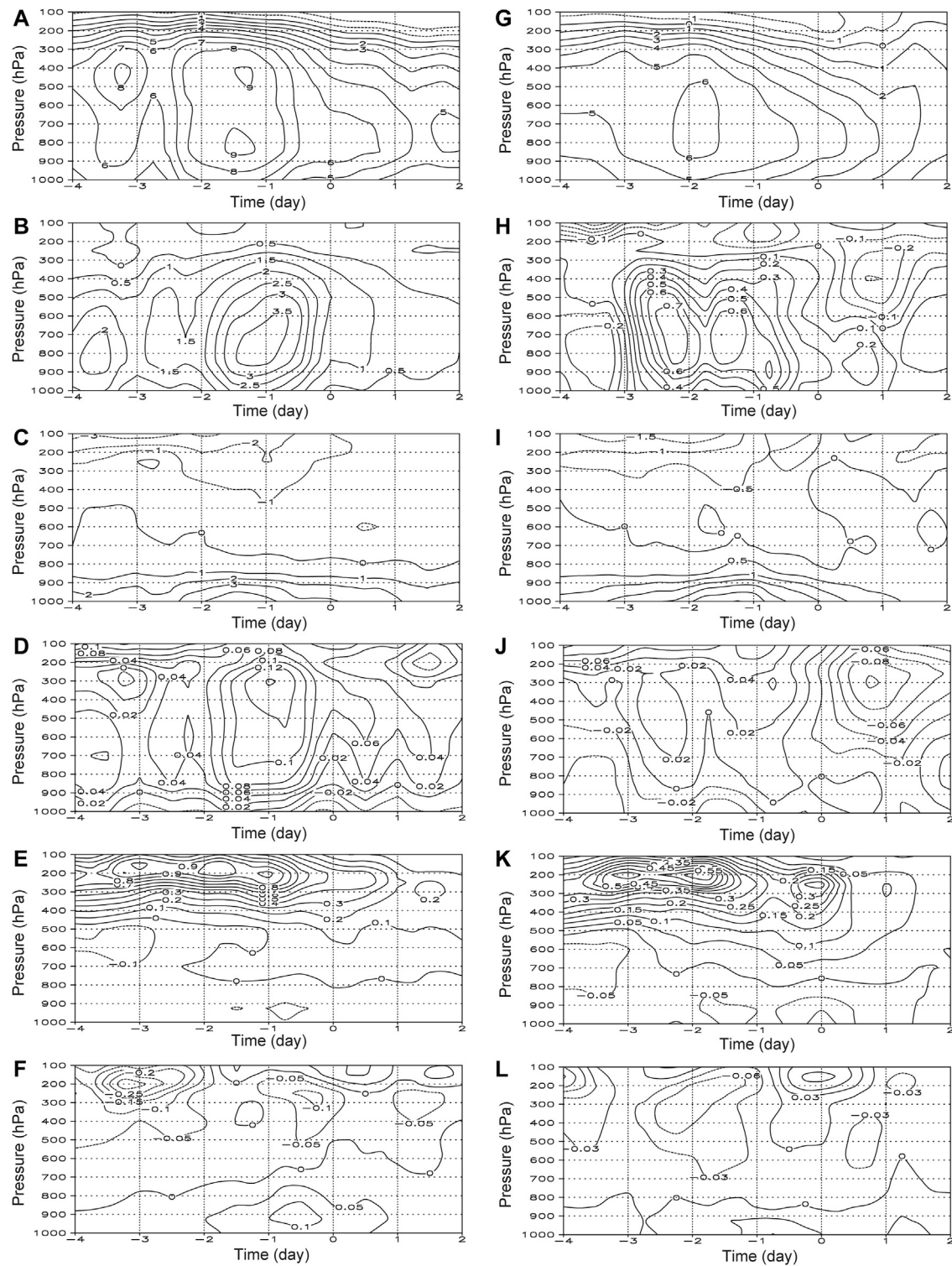


FIGURE 10 | Height-time evolution of the regional-average vorticity budget terms (units: 10^{-10} s^{-2}) in the 5° area near the centers of the **(A–F)** ERLTCs and **(G–L)** NERLTCs: **(A, G)** temporal vorticity evolution; **(B, H)** relative vorticity advection term; **(C, I)** horizontal divergence term; **(D, J)** β -effect term; **(E, K)** vertical transport term of the relative vorticity; **(F, L)** tilting term.

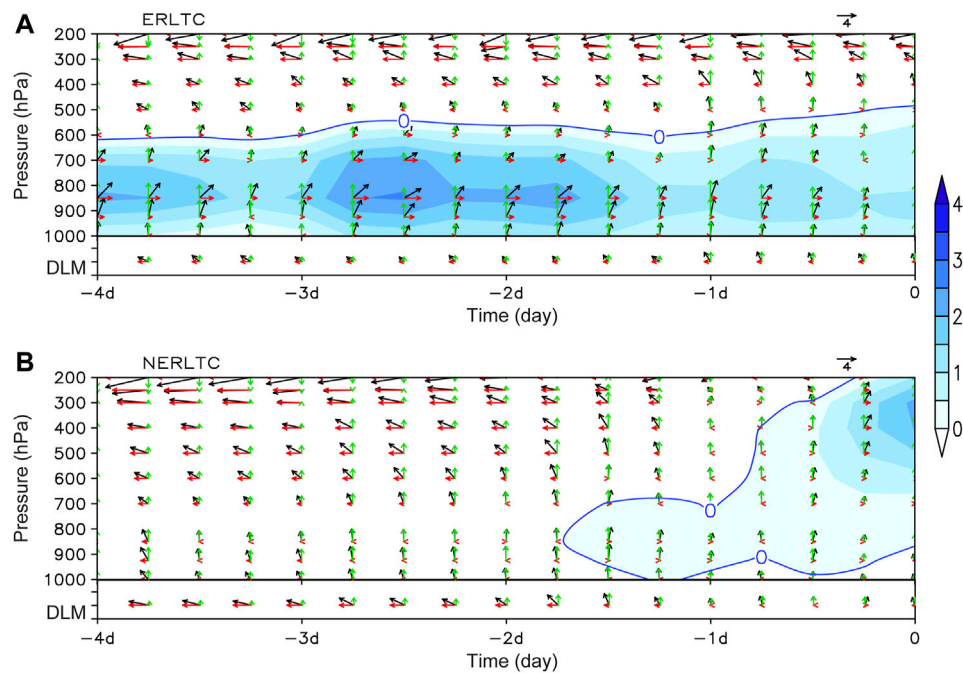


FIGURE 11 | Environmental steering flow at different heights and the DLM for the **(A)** ERLTCs and **(B)** NERLTCs, including the total wind speed (black vectors; units: m s^{-1}) the meridional (green vectors; unit: m s^{-1}) and zonal (red vectors; units: m s^{-1}) components of the steering flow and the DLM superimposed on the temporal evolution of the zonal zero wind-speed line (blue line; units: m s^{-1}). Areas with zonal steering airflow greater than zero are shaded.

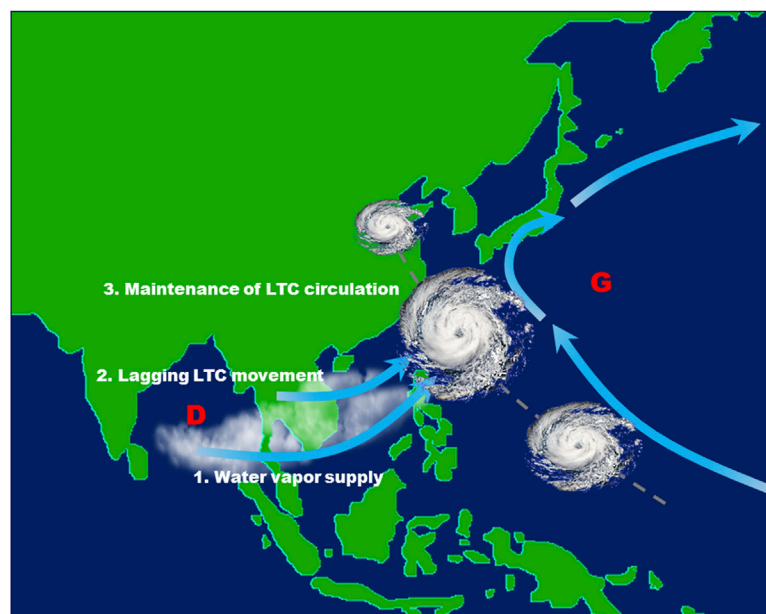


FIGURE 12 | Conceptual model for the influence of the monsoonal surge on ERLTCs. The thick blue arrows represent the directions of the airflow; G and D represent the high pressure and low pressure associated with the anticyclonic circulation and cyclonic circulation, respectively; the grey dashed line indicates the track of the TC; and the cloud cluster to the southwest of the TC indicates the activity of the monsoonal surge.

translational speed. And thirdly, the monsoonal surge transports vorticity to the ERLTC via horizontal vorticity advection, which effectively increases the cyclonic vorticity in the middle and lower levels of the ERLTC and markedly affects the maintenance of the strong cyclonic circulation in the ERLTC.

CONCLUSION AND FUTURE WORK

In this study, five typical ERLTC cases and five typical NERLTC cases were composited and compared in terms of the evolutionary characteristics of their circulation and their translational speed under the influence of a strong or weak monsoonal surge. Combined with our previous findings (Zhao et al., 2021), the mechanism through which the monsoonal surge influences ERLTCs is further discussed from a new perspective. The results can be summarized as follows:

- 1) Compared with NERLTCs, ERLTCs have two distinct characteristics—namely, maintenance of the LTC circulation and a lagging (slowing down or looping) of their movement. The monsoonal surge can provide a direct positive contribution to these two distinct characteristics of ERLTCs via two different mechanisms.
- 2) The low-level cyclonic rotation and upper-level divergence of an ERLTC are significantly stronger than those of an NERLTC, and the characteristics of an ERLTC's structure are more similar to those of “strong typhoons” than they are for an NERLTC. The continuous intensification of the cyclonic rotation in the lower troposphere before the extreme rainfall is a significant feature that distinguishes ERLTCs from NERLTCs. Analysis of the vorticity budget shows that the total vorticity of ERLTCs increases significantly in the middle and lower levels, especially on the day of their extreme rainfall, when the high-value vorticity area in the middle troposphere gradually extends to the lower level and the vorticity increases more significantly in the lower troposphere. The relative vorticity advection in the middle and lower levels under the influence of the southwest monsoonal surge contributes greatly to the increased vorticity in the middle and lower levels of an ERLTC. Thus, a strong monsoonal surge is conducive to the maintenance of ERLTC circulation.
- 3) The magnitude of the DLM is mainly determined by the zonal wind. Thus, the activity of the southwest monsoonal surge is mainly manifested in the zonal wind anomaly, and the corresponding strong westerly transport can significantly reduce the zonal component of the TC's steering flow. Hence, the TC steering flow can be weakened and the northwestward speed of movement decreases and favors the occurrence of extreme rainfall. Thus, the monsoonal surge contributes to a lagging (slowing down or looping) of ERLTC movement.
- 4) Strong monsoonal surge activity to the southwest of an ERLTC and strong activity of the subtropical high to the east jointly make the low-level cyclonic rotation and upper-level divergence of an ERLTC stronger than those of an NERLTC. The two types of LTC differ from

the southwest monsoonal surge in vertical structure, even though they are both warm and wet weather systems. The high-value area of water vapor flux of the southwest monsoonal surge (TC) is located in the lower (middle and lower) troposphere, which can (cannot) extend to the underlying surface.

The above conclusions show that the activity of the monsoonal surge plays an important role in maintaining the cyclonic circulation of ERLTCs and slowing down their translational speed. This further enriches our previous understanding of the role played by the impact of the monsoonal surge on ERLTCs, which was already well known to relate to the supply and transportation of water vapor (Gao et al., 2009; Zhao et al., 2021) and their coupling with the low-level jet (Dong et al., 2010; Cheng et al., 2012). It also shows that the monsoonal surge plays an important role in ERLTCs with a northwestern track, i.e., not only those with a western track (Zhou and Wu, 2019). In terms of the synoptic-scale activity of the East Asian summer monsoon, the southwest monsoonal surge is universal in its interaction with LTCs in China. Our study shows that the intensity of the monsoonal surge differs significantly between ERLTCs and NERLTCs. Therefore, real-time quantitative monitoring of the activity of the monsoonal surge is of great significance towards improving the forecast skill for ERLTCs. It should be noted that some typical cases have shown ERLTCs to result from the optimal configuration and synergistic effects of multi-scale systems, such as the “75•8” extremely severe rainfall (Ding, 2015) in Henan Province and the extreme rainfall of TC Morakot (Lee et al., 2011). The mechanisms of influence on ERLTCs relating to the characteristics of the underlying surface, the TC structure, mid-latitude trough, binary TC interaction, and other environmental factors need to be further studied based on multi-source observational data derived from satellites and radar, as well as high-resolution numerical simulations.

DATA AVAILABILITY STATEMENT

The original contributions presented in the study are included in the article/supplementary material, further inquiries can be directed to the corresponding author.

AUTHOR CONTRIBUTIONS

LC designed the study. DZ analyzed the datasets and generated figures. DZ and LC wrote the paper with contributions from YY.

FUNDING

This study was supported by the National Key R&D Program of China (2017YFC1501602), National Science Foundation of China (41775048), National Basic Research Program of China

(2015CB452804), Huafeng Meteorological Media Group Essential Research Project (CY-J2020002) and the Open Grants of the State Key Laboratory of Severe Weather (2020LASW-B06).

REFERENCES

- Bao, X., Wu, L., Zhang, S., Yuan, H., and Wang, H. (2020). A Comparison of Convective Raindrop Size Distributions in the Eyewall and Spiral Rainbands of Typhoon Lekima (2019). *Geophys. Res. Lett.* 47, e2020GL090729. doi:10.1029/2020GL090729
- Chen, L. S., and Ding, Y. H. (1979). *Overview of the Typhoons in Northwest Pacific*. Beijing: Science Press, 491pp. (in Chinese).
- Chen, L. S., Duan, Y. H., Song, L. L., and Xu, Y. L. (2012). *Typhoon Forecast and Disaster*. Beijing: China Meteorological Press, 370. (in Chinese).
- Chen, L. S. (1977). Origin Analysis for Landfalling Typhoon Heavy Rainstorm. *Meteorol. Mon* 3 (11), 10–12. (in Chinese). doi:10.7519/j.issn.1000-0526.1977.11.007
- Chen, L. S., and Xu, Y. L. (2017). Review of Typhoon Very Heavy Rainfall in China. *Meteorol. Environ. Sci.* 40 (1), 3–10. (in Chinese with English abstract). doi:10.16765/j.cnki.1673-7148.2017.01.001
- Cheng, Z. Q., Chen, L. S., and Li, Y. (2012). Interaction between Landfalling Tropical Cyclone and Summer Monsoon with Influences on Torrential Rain. *J. Appl. Meteorol. Sci* 23 (6), 660–671. (in Chinese with English abstract).
- Dai, H., Zhao, K., Li, Q., Lee, W. C., Ming, J., Zhou, A., et al. (2021). Quasi-Periodic Intensification of Convective Asymmetries in the Outer Eyewall of Typhoon Lekima (2019). *Geophys. Res. Lett.* 48, e2020GL091633. doi:10.1029/2020GL091633
- Ding, Y. H., Cai, Z. Y., and Li, J. S. (1978). 9. Demobilization. *Chin. J Atmos Sci* 2, 276–301. (in Chinese with English abstract). doi:10.1525/9780520310148-013
- Ding, Y. H. (2015). On the Study of the Unprecedented Heavy Rainfall in Henan Province during 4–8 August 1975: Review and Assessment. *Acta Meteorologica Sinica* 73, 411–424. (in Chinese with English abstract). doi:10.11676/qxxb2015.067
- Dong, M., Chen, L., Li, Y., and Lu, C. (2010). Rainfall Reinforcement Associated with Landfalling Tropical Cyclones. *J. Atmos. Sci.* 67, 3541–3558. doi:10.1175/2010JAS3268.1
- Duan, Y. H., Chen, L. S., Liang, J. Y., Wang, Y., Wu, L. G., Cui, X. P., et al. (2014). Research Progresses in Abnormal Changes before and after Typhoon Landfall. *J. Meteorol. Res.* 72, 969–986. (in Chinese with English abstract).
- Duan, Y., Wan, Q., Huang, J., Zhao, K., Yu, H., Wang, Y., et al. (2019). Landfalling Tropical Cyclone Research Project (LTCRP) in China. *Bull. Am. Meteorol. Soc.* 100 (12), ES447–ES472. doi:10.1175/BAMS-D-18-0241.1
- Gao, S., Meng, Z., Zhang, F., and Bosart, L. F. (2009). Observational Analysis of Heavy Rainfall Mechanisms Associated with Severe Tropical Storm Bilis (2006) after its Landfall. *Monthly Weather Rev.* 137 (6), 1881–1897. doi:10.1175/2008MWR2669.1
- Gu, X. H., and Zhang, Q. (2020). *Statistical Characteristics of Extreme Precipitation Events and Associated Mechanisms*. Beijing: Science Press, 185. (in Chinese).
- Jia, L., Jia, Z., Ren, F., Ding, C., Wang, M., and Feng, T. (2020). Introducing TC Intensity into the DSAEF_LTP Model and Simulating Precipitation of Super-typhoon Lekima (2019). *Q.J.R. Meteorol. Soc.* 146, 3965–3979. doi:10.1002/qj.3882
- Kimberlain, T. B., and Breman, M. J. (2017). “Chapter 3: Tropical Cyclone Motion,” in *Global Guide to Tropical Cyclone Forecasting*. Editor C. C. Guard. 2nd ed. (Geneva, Switzerland: WMO), 63–125. 978-92-63-11194-4.
- Lee, C.-S., Wu, C.-C., Wang, T.-C. C., and Elsberry, R. L. (2011). Advances in Understanding the “Perfect Monsoon-Influenced Typhoon”: Summary from International Conference on Typhoon Morakot (2009). *Asia-Pacific J. Atmos. Sci.* 47 (3), 213–222. doi:10.1007/s13143-011-0010-2
- Lei, X. (2020). Overview of the Development History of China’s Typhoon Research and Operational Work in the Past century. *Sci. China Earth Sci.* 63, 362–383. doi:10.1007/s11430-018-9379-8
- Li, Z., Yu, W., Li, K., Wang, H., and Liu, Y. (2019). Environmental Conditions Modulating Tropical Cyclone Formation over the Bay of Bengal during the Pre-monsoon Transition Period. *J. Clim.* 32 (14), 4387–4394. doi:10.1175/JCLI-D-18-0620.1
- Lu, S., Wang, L. J., Guan, Z. Y., He, J. L., and Song, H. (2012). Comparison of Impacts of Low-Latitude Monsoon Surge on the Enhanced Rainstorm from landing Typhoons Dorian and Bilis. *Trans. Atmos. Sci.* 35 (2), 175–185. (in Chinese with English abstract).
- Lu, X., Yu, H., Ying, M., Zhao, B., Zhang, S., Lin, L., et al. (2021). Western North Pacific Tropical Cyclone Database Created by the China Meteorological Administration. *Adv. Atmos. Sci.* 38 (4), 690–699. doi:10.1007/s00376-020-0211-7
- Rantanen, M., Räisänen, J., Sinclair, V. A., Lento, J., and Järvinen, H. (2020). The Extratropical Transition of Hurricane Ophelia (2017) as Diagnosed with a Generalized omega Equation and Vorticity Equation. *Tellus A: Dynamic Meteorology and Oceanography* 72 (1), 1–26. doi:10.1080/16000870.2020.1721215
- Ren, F. M., and Yang, H. (2019). An Overview of Advances in Typhoon Rainfall and its Forecasting Researches in China during the Past 70 Years and Future Prospects. *Torrential Rain and Disasters* 38 (5), 526–540. (in Chinese with English abstract).
- Ren, F., Wang, Y., Wang, X., and Li, W. (2007). Estimating Tropical Cyclone Precipitation from Station Observations. *Adv. Atmos. Sci.* 24, 700–711. doi:10.1007/s00376-007-0700-y
- Wu, C.-C. (2013). Typhoon Morakot: Key Findings from the Journal TAO for Improving Prediction of Extreme rains at Landfall. *Bull. Amer. Meteorol. Soc.* 94, 155–160. doi:10.1175/BAMS-D-11-00155.1
- Xia, J., Wang, H. Y., Gan, Y. Y., and Zhang, L. P. (2019). Research Progress in Forecasting Methods of Rainstorm and Flood Disaster in China. *Torrential Rain and Disasters* 38, 416–421. (in Chinese with English abstract). doi:10.3969/j.issn.1004-9045.2019.05.003
- Yang, D. S., Liu, Y. B., and Liu, S. G. (1983). *Dynamic Meteorology*. Beijing: China Meteorological Press, 423. (in Chinese).
- Ying, M., Zhang, W., Yu, H., Lu, X. Q., Feng, J. X., Fan, Y. X., et al. (2014). An Overview of the China Meteorological Administration Tropical Cyclone Database. *J. Atmos. Ocean. Technol.* 31, 287–301. doi:10.1175/JTECH-D-12-00119.1
- Yu, Z., Chen, Y. J., Ebert, B., Davidson, N., Xiao, Y., Yu, H., et al. (2020). Benchmark Rainfall Verification of Landfall Tropical Cyclone Forecasts by Operational ACCESS-TC over China. *Meteorol. Appl.* 27, e1842. doi:10.1002/met.1842
- Zhao, D., Yu, Y., and Chen, L. (2021). Impact of the Monsoonal Surge on Extreme Rainfall of Landfalling Tropical Cyclones. *Adv. Atmos. Sci.*, 38(5), 771–784. doi:10.1007/s00376-021-0281-1
- Zhou, Y., and Wu, T. (2019). Composite Analysis of Precipitation Intensity and Distribution Characteristics of Western Track Landfall Typhoons over China under strong and Weak Monsoon Conditions. *Atmos. Res.* 225, 131–143. doi:10.1016/j.atmosres.2019.03.037

ACKNOWLEDGMENTS

The authors thank Fumin Ren for providing the TC-induced OSAT precipitation dataset over China in this study.

Conflict of Interest: The authors declare that the research was conducted in the absence of any commercial or financial relationships that could be construed as a potential conflict of interest.

Publisher’s Note: All claims expressed in this article are solely those of the authors and do not necessarily represent those of their affiliated organizations, or those of the publisher, the editors and the reviewers. Any product that may be evaluated in this article, or claim that may be made by its manufacturer, is not guaranteed or endorsed by the publisher.

Copyright © 2021 Zhao, Chen and Yu. This is an open-access article distributed under the terms of the Creative Commons Attribution License (CC BY). The use, distribution or reproduction in other forums is permitted, provided the original author(s) and the copyright owner(s) are credited and that the original publication in this journal is cited, in accordance with accepted academic practice. No use, distribution or reproduction is permitted which does not comply with these terms.



Slowdown in the Decay of Western North Pacific Tropical Cyclones Making Landfall on the Asian Continent

Jinjie Song^{1,2*}, Philip J. Klotzbach³, Haikun Zhao⁴ and Yihong Duan²

¹Nanjing Joint Institute for Atmospheric Sciences, Chinese Academy of Meteorological Sciences, Nanjing, China, ²State Key Laboratory of Severe Weather, Chinese Academy of Meteorological Sciences, Beijing, China, ³Department of Atmospheric Science, Colorado State University, Fort Collins, CO, United States, ⁴School of Atmospheric Sciences, Nanjing University of Information Science and Technology, Nanjing, China

OPEN ACCESS

Edited by:

Hui Yu,
China Meteorological Administration,
China

Reviewed by:

Shuai Wang,
Princeton University, United States
Yuan Sun,
National University of Defense
Technology, China

*Correspondence:

Jinjie Song
songjinjie@qq.com

Specialty section:

This article was submitted to
Atmospheric Science,
a section of the journal
Frontiers in Earth Science

Received: 29 July 2021

Accepted: 01 September 2021

Published: 15 September 2021

Citation:

Song J, Klotzbach PJ, Zhao H and
Duan Y (2021) Slowdown in the Decay
of Western North Pacific Tropical
Cyclones Making Landfall on the
Asian Continent.
Front. Earth Sci. 9:749287.
doi: 10.3389/feart.2021.749287

This study finds an increasing trend in the decay timescale (τ) of western North Pacific (WNP) tropical cyclone (TCs) making landfall on the Asian continent from 1966–2018. Statistical analysis of individual landfalling TCs shows that τ is significantly positively linked to soil wetness, 850-hPa relative vorticity and 200-hPa divergence, whereas it is weakly correlated with 700–500-hPa relative humidity and 850–200-hPa vertical wind shear. For TCs hitting southeastern China, the observed increasing τ is likely caused by enhanced 850-hPa vorticity and 200-hPa divergence. For TCs hitting southern China, increasing τ is likely driven by increased 850-hPa vorticity. By comparison, there are no significant trends in environmental variables over the eastern Indo-China Peninsula, and τ has not significantly changed in this region. Our results imply that the increasing τ of WNP landfalling TCs on the Asian continent are more likely caused by changes in dynamic variables than changes in thermodynamic variables.

Keywords: tropical cyclone, Western North Pacific, decay timescale, making landfall, environmental changes

INTRODUCTION

Tropical cyclones (TCs) are among the most destructive and deadliest natural disasters around the world, causing significant economic losses and casualties to coastal and adjacent inland regions when these TCs make landfall (Chen et al., 2011). Most TCs weaken rapidly after landfall, due to various TC-unfavorable conditions including increased friction, enhanced baroclinicity, decreased moisture and most importantly, significant reductions in latent and sensible heat fluxes (Kaplan and DeMaria, 1995). Li and Chakraborty (2020) recently found that the inland decay rate of North Atlantic TCs slowed during the period from 1967–2018. By using statistical analysis and numerical simulations, they found that warmer SSTs increased the moisture supply transported by a TC, providing additional heat that helped to sustain the warm-core structure leading to a slower decay. Compared with the North Atlantic the number of TC landfalls over the western North Pacific (WNP) is much greater, accounting for more than 50% of global TC landfalls from 1970–2010 (Weinkle et al., 2012). Nonetheless, it remains unclear how the inland decay of WNP TCs has changed during the past few decades. Chen et al. (2011) reported an increasing duration of TCs over China from 1975 to 2009, possibly due to decreasing VWS over southeastern China. Given that TCs with a higher landfall intensity usually survive longer (Liu et al., 2020), this increasing duration over land does not necessarily imply a slower inland decay.

Previous publications (e.g. Wood and Ritchie, 2015; Ma et al., 2019; Fei et al., 2020; Song et al., 2020) have found several environmental conditions responsible for the rate of WNP TC weakening over water. A larger weakening rate is statistically correlated with lower sea surface temperatures (SSTs), increased SST gradients, larger vertical wind shear (VWS) and a drier mid-troposphere. By contrast, there are fewer papers investigating the relationship between the underlying surface and the inland decay rate of TCs. Some inland TCs maintain their strength or even intensify without transitioning to extratropical systems. This phenomena has been linked to anomalously wet soils over which the TCs track (Andersen and Shepherd, 2013). Wet soils can create an environment with increased moist static energy and latent heat that inhibits TC decay (Arndt et al., 2009; Kellner et al., 2012; Evans et al., 2011). In addition, wet soils can delay the weakening of TCs following landfall by providing them with additional energy due to enhanced heat and moisture transfers (Emanuel et al., 2008; Kishtawal et al., 2012). However, whether atmospheric variables modulate the inland decay of TCs remains unknown.

To resolve this issue, this study not only investigates long-term trends in the decay of inland WNP TCs, but also provides statistical linkages between various environmental factors and the inland decay timescale. The remainder of this paper is arranged as follows. *Data and methods* discusses the data and methods for identifying and classifying landfalling TCs over the WNP. This section also includes the computation of the decay timescale metric that serves as a single parameter characterizing TC decay (Li and Chakraborty, 2020). *Results* discusses the long-term tendency in the decay timescale of WNP landfalling TCs as well as the potential environmental contributors to this observed change. A summary is given in the last section.

DATA AND METHODS

The 3-hourly WNP TC best track data from the China Meteorological Administration (CMA) used in this study are provided by the International Best Track Archive for Climate Stewardship (IBTrACS) v04r00 (Knapp et al., 2010), including TC center position and 2-min maximum sustained wind. There are three other agencies compiling best track data over the WNP, including the Joint Typhoon Warning Center (JTWC), the Japan Meteorological Agency (JMA) and the Hong Kong Observatory (HKO). Compared with other coastal countries in the WNP, more TCs hit China climatologically. The CMA data is primarily applied in this study because relatively more observational data are available over China from CMA than from these other agencies (Chen et al., 2011). The JTWC, JMA and HKO data are used to validate the results. We analyze TC best track data during the period of 1966–2018, which tend to be of higher quality and are therefore more reliable due to the use of polar-orbiting and geostationary satellites starting in 1966 (Moon et al., 2019). Owing to the uncertainty in detecting weak TCs such as tropical depressions (Klotzbach and Landsea, 2015), TCs with a lifetime maximum intensity less than 34 kt are excluded in this study.

We investigate all landfall cases that are not excluded by the criteria that are now presented. First, landfalls on large islands (e.g. Hainan, Taiwan, Philippines, Japan) are not considered, since the environmental conditions for these landfalls are more characteristic of an oceanic environment. Second, TCs that survived less than 12 h after landfall (e.g., fewer than four continuous inland TC records with non-zero estimates of maximum sustained wind) are excluded. The remaining sample is further subdivided to identify TCs surviving at least 24 h after landfall. Third, cases completing extratropical transition as recorded in the best track during landfall are not considered, in order to minimize the influence of extratropical transition. In total, there are 375, 322, 114, and 256 (190, 147, 13, 58) 12-h (24-h) landfall cases identified from the CMA, JTWC, JMA, and HKO best track data, respectively, during 1966–2018 (**Figure 1**). Similar TC tracks and landfall tracks occur in all four datasets.

Ren et al. (2011) reported that there were many more landfalling TCs in the CMA dataset than in other WNP best track data. Also, because CMA usually tracks the overland portion of TCs making landfall on China for a longer time than other agencies, this study also identifies more landfall cases from CMA than for other agencies. Relatively few landfall cases are identified in the JMA data using our methodology, partly because JMA only started to estimate wind speeds after 1977. Given that the numbers of identified landfalls in the JMA and HKO data are much smaller than those in the CMA and JTWC data, we primarily use the CMA data in the following analysis, while the JTWC data are applied to cross check the results.

After landfall, the TC intensity (V) exhibits an exponential decay as $V(t) = V(0)e^{-t/\tau}$, where t is the time past landfall and τ is the decay timescale (Kaplan and DeMaria, 1995; Li and Chakraborty, 2020). A larger τ indicates a slower inland decay. For each case, τ is statistically estimated by regression over the first 24-h or 12-h period after landfall, similar to Li and Chakraborty (2020). Among the 190 24-h landfalls and 375 12-h landfalls in the CMA data, there are only two and five cases with a regression that fails to pass the 0.05 significance test. In addition to τ , a decaying rate (DR) from landfall to dissipation is also estimated, by regressing 3-hourly maximum sustained winds on time.

Monthly mean atmospheric and surface data are provided by the Japanese 55-year Reanalysis (JRA-55) on a 1.25×1.25 grid (Kobayashi et al., 2015). The JRA-55 land-sea mask is applied to determine whether the TC center is over water or land. Five factors are considered here for their potential impact on TC inland decay: soil wetness, 700–500-hPa relative humidity (RH), 850–200-hPa vertical wind shear (VWS), 850-hPa relative vorticity (VOR) and 200-hPa divergence (DIV). Furthermore, to investigate the relationship between inland decay and environmental variables on a case by case basis, these reanalysis fields are cubically interpolated in space to the mean location during the 24-h period after landfall and in time to the actual day, assigning the monthly mean climatology to the middle day of each month as was done by Emanuel et al. (2004) and Lee et al. (2016).

Monthly Pacific Decadal Oscillation (PDO) index values are obtained from the National Oceanic and Atmospheric

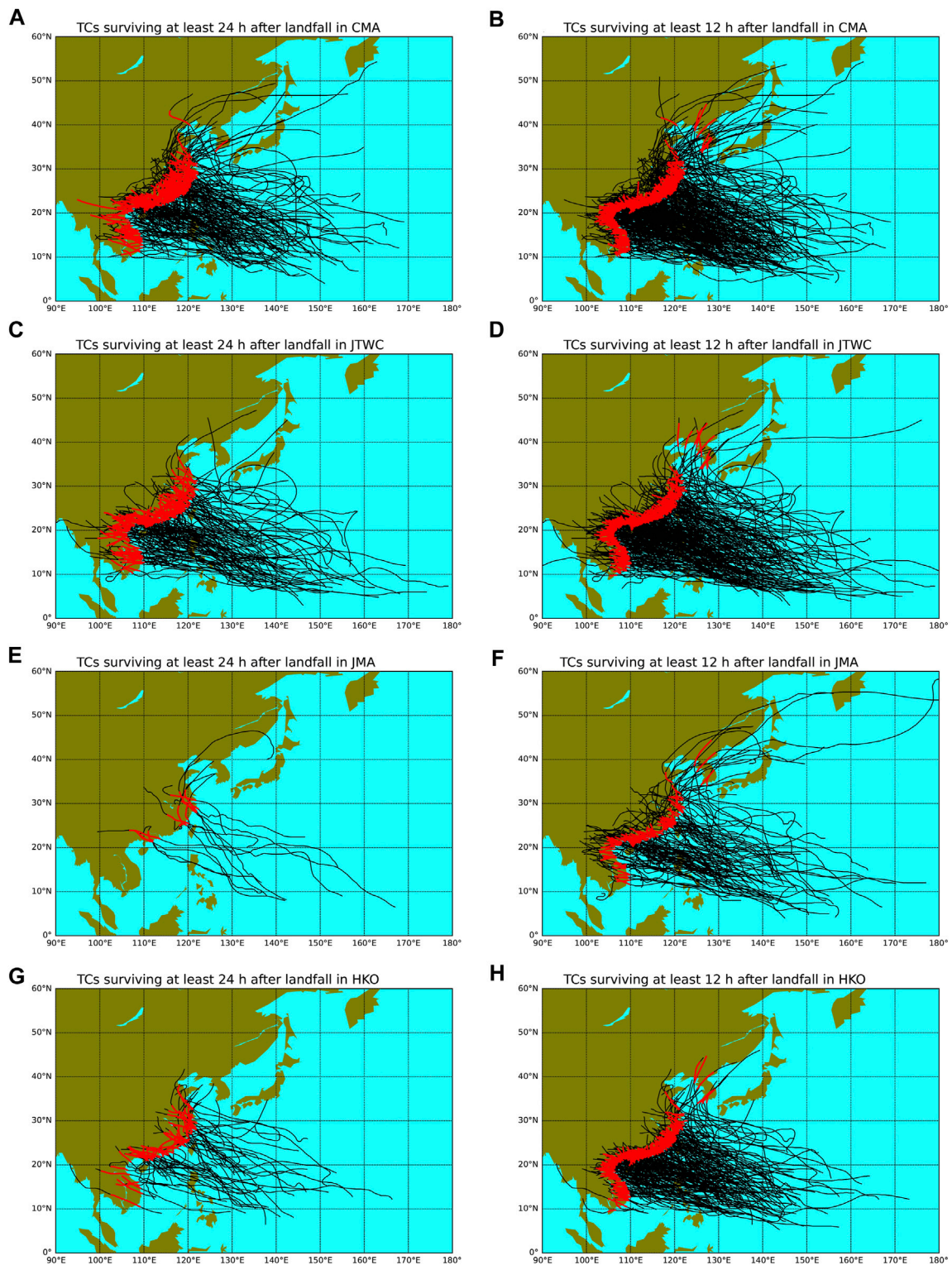


FIGURE 1 | Tracks of landfalling WNP TCs identified from the (A,B) CMA (C,D) JTWC (E,F) JMA and (G,H) HKO dataset from 1966 to 2018. The trajectories during the first 24 and 12 h after landfall are represented as red thick lines in the **left** and **right** columns, respectively.

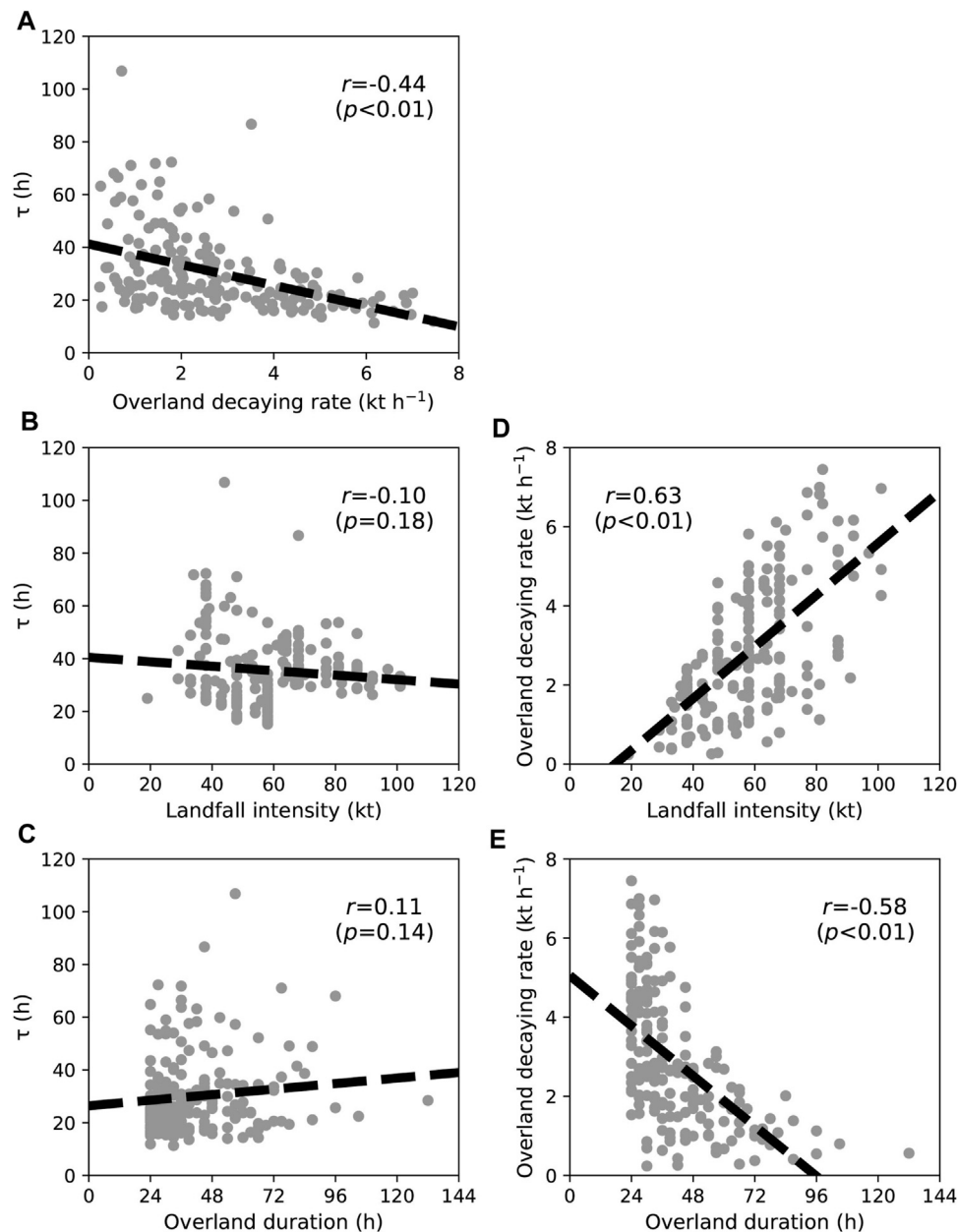


FIGURE 2 | Relationship of τ versus (A) overland decaying rate, (B) landfall intensity, (C) overland duration and relationship of overland decaying rate versus (D) landfall intensity, and (E) overland duration. The dashed lines are obtained by least squares, while the correlation coefficients and their significance levels are given in the panels.

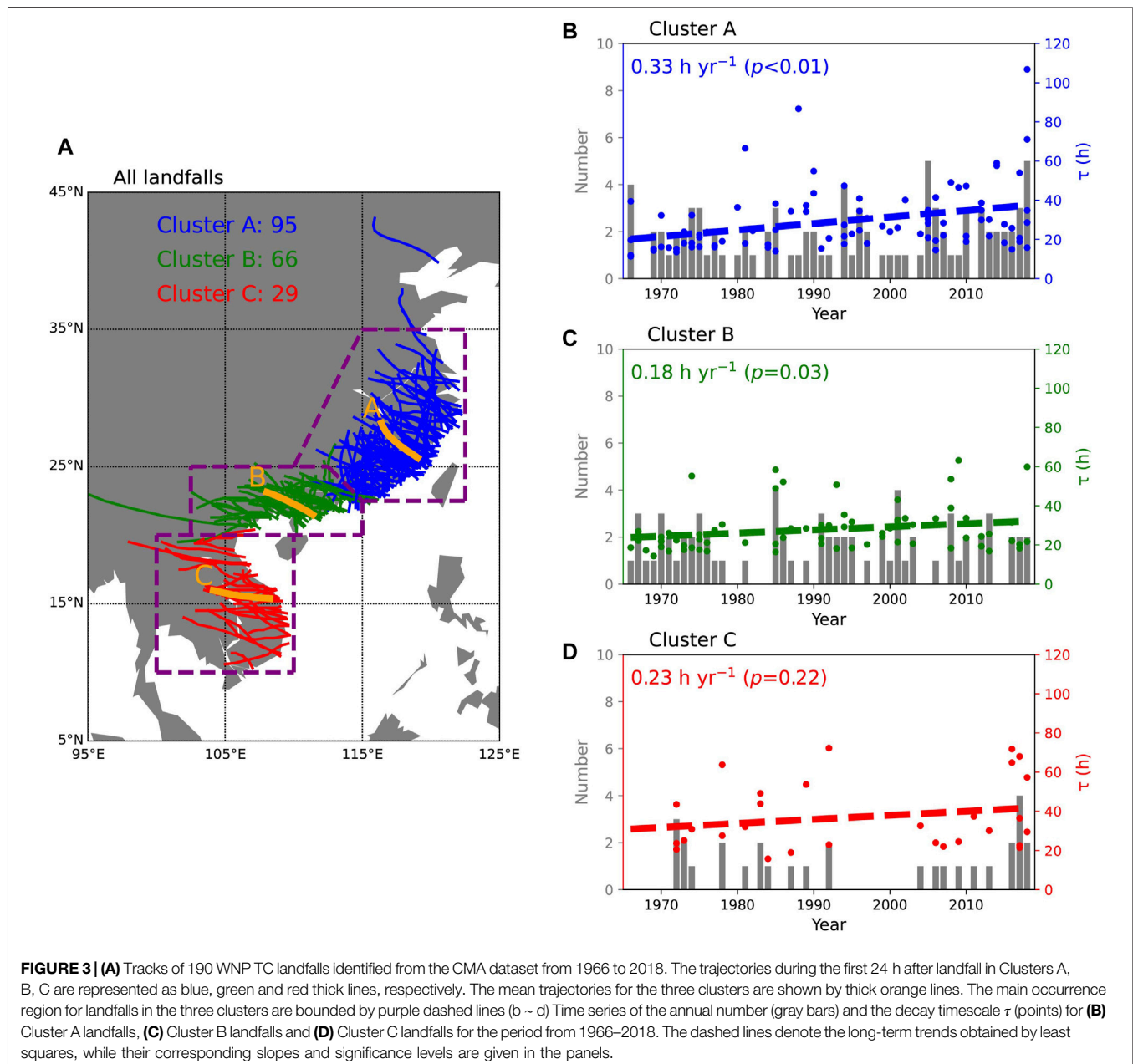
Administration (NOAA) Earth System Research Laboratory's Physical Sciences Division (PSD).

RESULTS

Increasing Trend in Decay Timescale

During 1966–2018, in the CMA data, although there is no significant trend in the annual frequency of landfalls, there are significant increasing tendencies in τ of 0.26 h yr^{-1} ($p < 0.01$) for

24-h landfalls (Figure 1A) and 0.20 h yr^{-1} ($p < 0.01$) for 12-h landfalls (Figure 1B). These τ trends become 0.24 h yr^{-1} ($p = 0.02$) and 0.19 h yr^{-1} ($p = 0.01$), when using a weighted linear regression model (Wang et al., 2020) in which annual τ is weighted by the corresponding landfall frequency. There are also significant increasing τ trends in the JTWC data, which show similar rates to those in the CMA data. These results mean that the τ trend is not significantly changed, regardless of different landfall durations or different best track datasets. Hereafter, we focus on the 24-h landfalls recorded by CMA. Over these

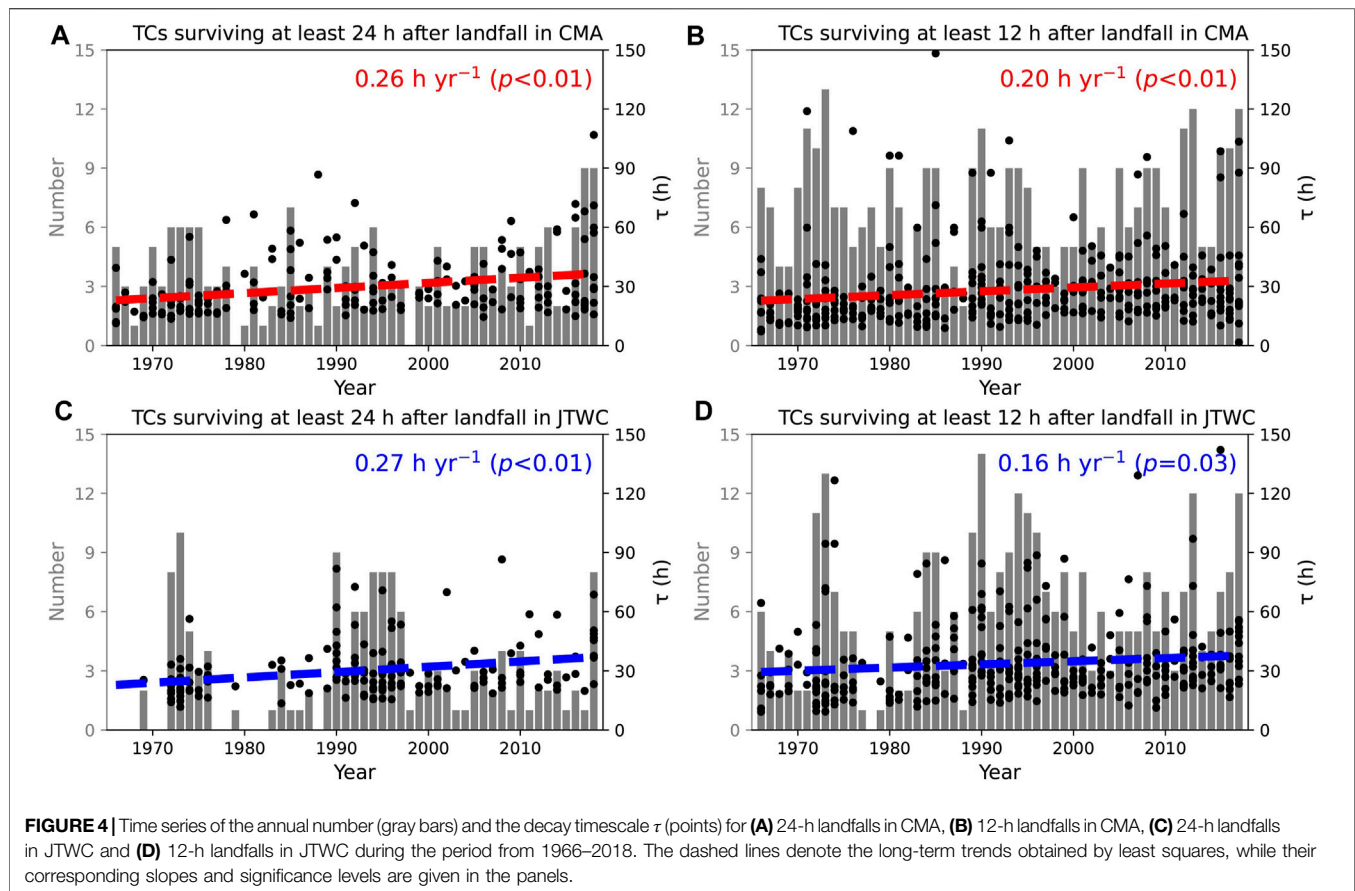


53 years, τ has increased by 57% over the WNP (from 23 to 36 h), which is lower than the 94% increase in τ over the North Atlantic (Li and Chakraborty, 2020). These findings mean that over land, WNP TCs are now decaying at a slower rate and may consequently survive for a longer time, similar to what was found for North Atlantic TCs (Li and Chakraborty, 2020).

As another decaying metric, DR shows a significant inverse relation with τ ($r = -0.44$; $p < 0.01$), implying that TCs weakening at a lower rate usually undergo a slower decay (Figure 2A). Consistent with the increasing τ trend, there is a significant decreasing DR trend of $-2.0 \times 10^{-2} \text{ kt h}^{-1} \text{ yr}^{-1}$ ($p = 0.04$) during 1966–2018 (figures not shown). However, DR is very sensitive to the landfall intensity and the overland duration

(Figures 2D,E), meaning that TCs landfalling at a higher intensity or surviving at a shorter duration typically exhibit a greater DR. By contrast, τ is independent of both the landfall intensity ($r = -0.10$; $p = 0.18$) and the overland duration ($r = 0.11$; $p = 0.14$) (Figures 2B,C). The estimation of τ minimizes the linkage between the landfall intensity/overland duration and the TC decay rate.

We now expand upon these results by categorizing the 24-h tracks after landfall into three clusters using the *K*-means method (Nakamura et al., 2009). 95, 66, and 29 TCs are classified into Clusters A, B and C, respectively. These clusters make landfall in southeastern China, southern China and in other Southeast Asian countries, respectively (Figure 3A). We classify three clusters



here. These clusters identify TCs hitting different areas but also include enough TC samples in each cluster.

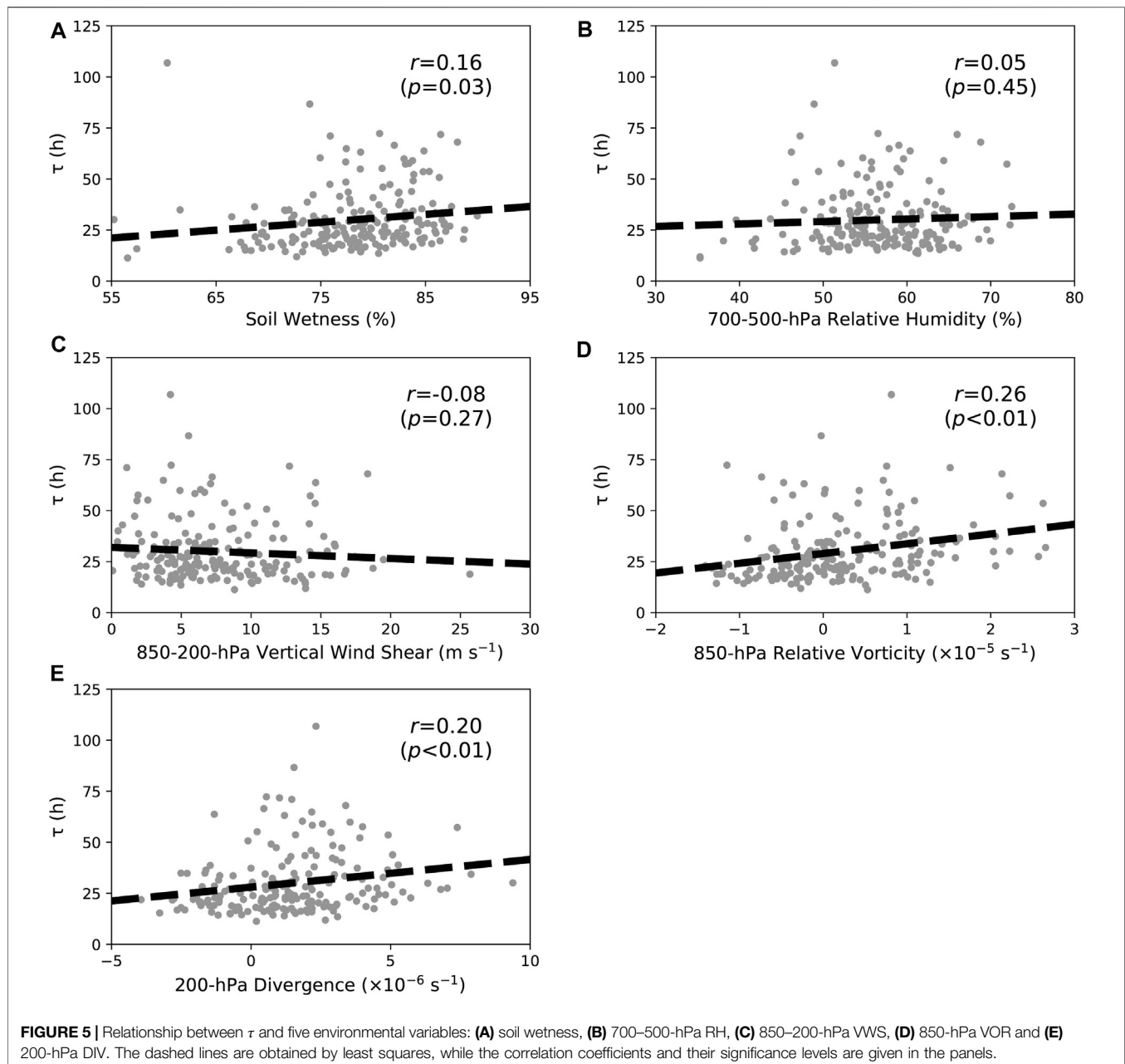
The change in τ is not uniform along the Asian coast, with different long-term τ trends from 1966 to 2018 for the three landfall clusters (Figure 3 b–d). Landfalls in Cluster A have the largest increase in τ , with a slope of 0.33 h yr^{-1} ($p < 0.01$), while landfalls in Cluster B show a smaller but significant increasing τ of 0.18 h yr^{-1} ($p = 0.03$). By comparison, there is no significant τ trend (0.23 h yr^{-1} ; $p = 0.22$) for landfalls in Cluster C. While the increasing trend for Cluster C is larger than Cluster B, the relatively small sample size of landfalls in Cluster C is the reason why the trend in that region is not significant. Since 85% (161 out of 190) of the observed landfalls in this study occur in Clusters A and B, the increasing τ of Clusters A and B landfalls are primarily responsible for the increasing trend in τ for all landfalls as shown in Figure 4A.

Environmental Factors Influencing WNP Decay Timescale

Li and Chakraborty (2020) attributed the increasing τ over the North Atlantic to warmer SSTs, which then increased the available moisture carried by a TC after making landfall. Their findings were based on a correlation analysis of smoothed annual timeseries of landfalls and SST. By comparison, we examine the statistical relationship between several environmental variables

and τ from individual cases (Figure 5). Figure 5A highlights a significant positive relationship between τ and soil wetness ($r = 0.16$; $p = 0.03$), implying that a moist underlying land surface can slow TC weakening. This result is consistent with previous studies (e.g. Emanuel et al., 2008; Arndt et al., 2009; Kellner et al., 2012; Evans et al., 2011; Kishtawal et al., 2012; Andersen and Shepherd, 2013). Wet soils supply additional energy to TCs post-landfall via vertical transport of heat and moisture (Emanuel et al., 2008; Kishtawal et al., 2012). By contrast, in Figure 5B, there is no significant linkage between τ and 700–500-hPa RH ($r = 0.05$; $p = 0.45$). Although changes in atmospheric moisture have had a considerable impact on the WNP TC weakening rate over water (Fei et al., 2020), it appears to have had less of an impact on inland wind decay over the Asian continent. These results imply that surface thermodynamic factors play a larger role in modulating the decay of inland TCs over the Asian continent than those in the atmosphere.

Figure 5C displays a weak inverse relationship between τ and 850–200-hPa VWS ($r = -0.08$; $p = 0.27$), indicating that VWS only has a minor influence on TC inland decay. Note that this result is inconsistent with Chen et al. (2011) who concluded that decreasing VWS led to an increasing TC survival time over land. Because of the weak linkage between τ and the actual overland duration, an increasing TC duration over land does not necessarily mean an increasing τ . We speculate that less VWS likely results in a longer duration over land because TCs



encountering less VWS shear before landfall are likely to be stronger at the time of landfall. The relationship between VWS and TC decay seems to play a lesser role after landfall. This result is also different from the observed strong relationship between the weakening rate of WNP TCs and VWS over water (Fei et al., 2020). Two other dynamic factors, 850-hPa VOR and 200-hPa DIV, both exhibit significant positive connections with τ (Figures 5D,E), with correlation coefficients of 0.26 ($p < 0.01$) and 0.20 ($p < 0.01$), respectively. These results imply that an environment characterized by an anomalous lower-level cyclonic circulation and anomalous upper-level divergent flow favors a slower weakening of TCs over land. By contrast, these two variables are not strongly correlated with the WNP TC weakening rate over

water (Fei et al., 2020). The above results imply that the environmental elements significantly influencing WNP TC decay over the Asian continent differ from those influencing WNP TC decay over water.

When dividing total landfalls into different clusters (Figure 4A), the statistical relationship between environmental variables and τ remains of the same sign (figures not shown). However, the significant positive relationship between τ and soil wetness is only found in Cluster C ($r = 0.37$; $p = 0.04$). The significant positive relationship between τ and 850-hPa VOR is found in Cluster A ($r = 0.33$; $p < 0.01$) and in Cluster B ($r = 0.25$; $p = 0.04$), while the significant positive relationship between τ and 200-hPa DIV is only observed in Cluster A ($r = 0.29$; $p < 0.01$).

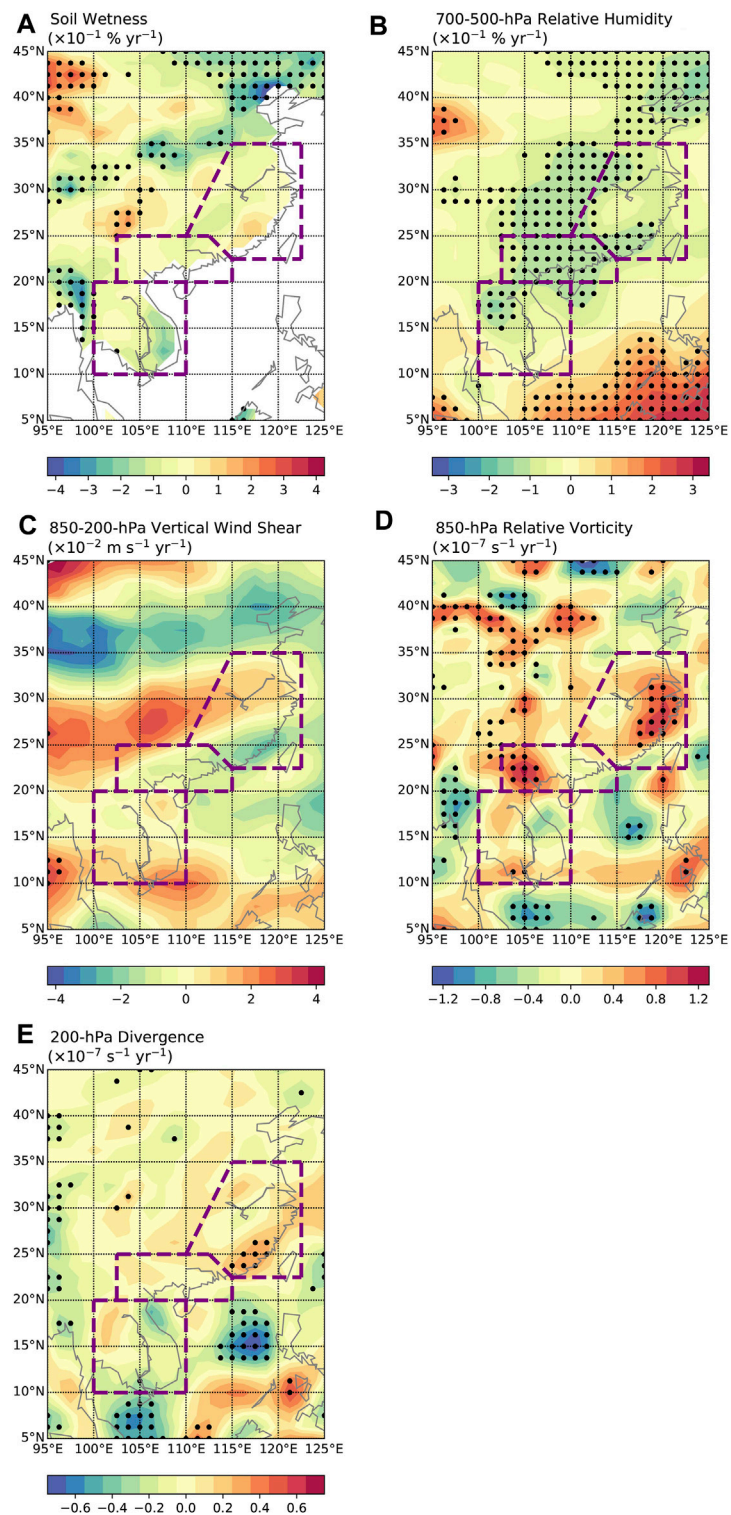
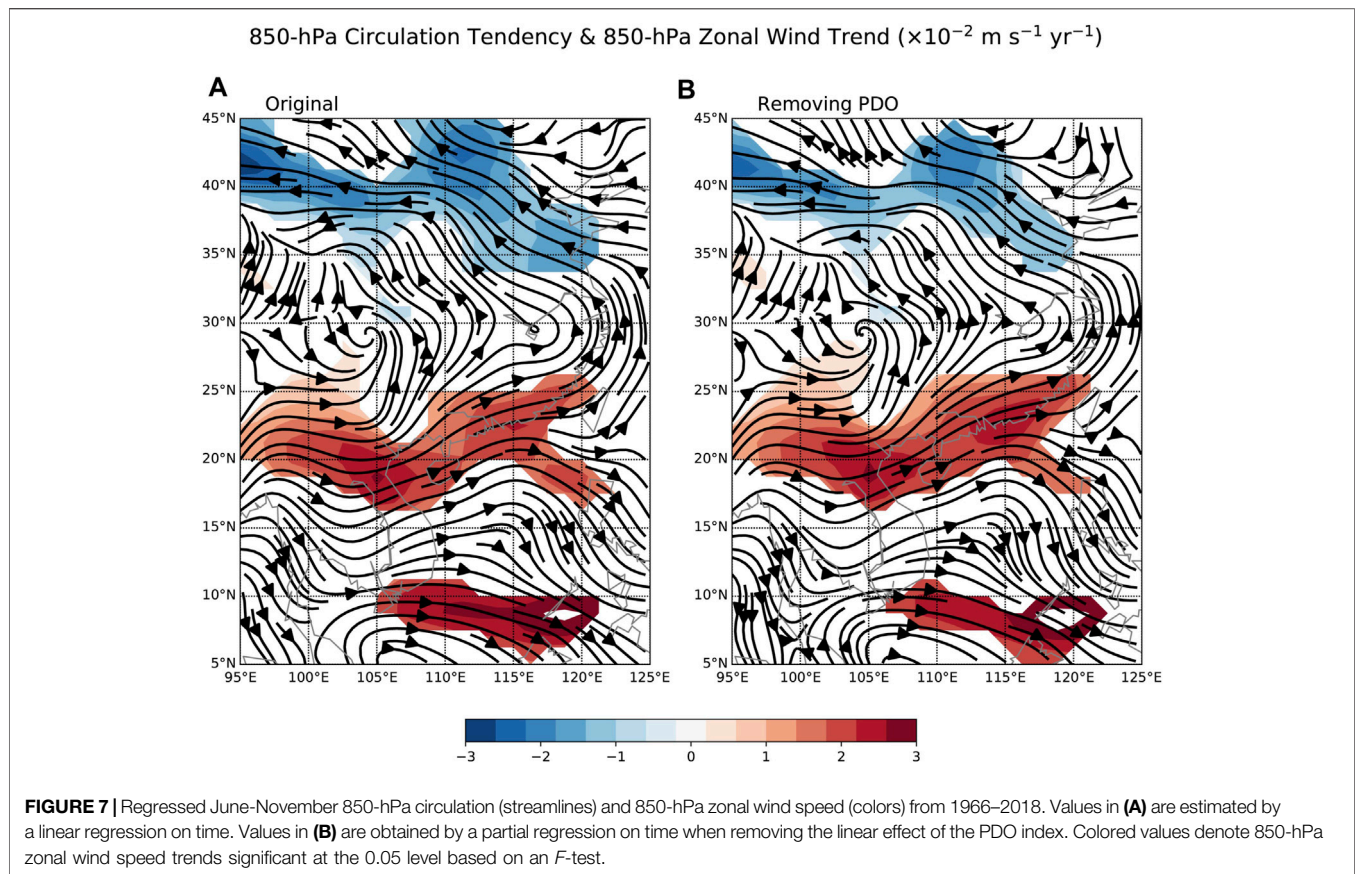


FIGURE 6 | Long-terms trends (1966–2018) in June–November averages of environmental variables: **(A)** soil wetness, **(B)** 700–500-hPa RH, **(C)** 850–200-hPa VWS, **(D)** 850-hPa VOR and **(E)** 200-hPa Div. Circles denote values significant at the 0.05 level based on an *F*-test. Areas bounded by purple dashed lines refer to the main occurrence region of landfalls for the three clusters, as was demarcated in **Figure 1A**.



Long-Term Trends in Environmental Variables

To investigate whether trends in environmental variables are inducing the increasing τ , we calculate the long-term trends in the June–November averages of the five aforementioned factors during 1966–2018 (**Figure 6**). There are no significant trends in soil wetness over the main occurrence regions for landfalls (**Figure 6A**). Although soil wetness is significantly correlated with τ , long-term changes in soil wetness do not appear to be contributing to the long-term increase in τ . By comparison, significant decreasing and increasing trends in 700–500-hPa RH are observed over the Asian continent and over the ocean, respectively (**Figure 6B**). Although drier conditions are found over the main landfall regions, these drier conditions do not appear to significantly impact long-term changes in τ , since the linkage between τ and atmospheric moisture is weak.

Figure 6C shows only a very small region between 95 and 100°E with significant changes in 850–200-hPa VWS from 1966 to 2018. Although weaker VWSs are observed over southern China, the trends in VWS are not as significant as those found in Chen et al. (2011). This difference is likely caused by the different periods analyzed in Chen et al. (2011) and in our study. There are significantly enhanced 850-hPa VORs over the main landfall regions of Clusters A and B, with the two largest increasing regions centered over Zhejiang Province and Guangxi Province

(**Figure 6D**). No significant changes in 850-hPa VOR are found over the eastern part of the Indo-China Peninsula, where landfalls in Cluster C mainly occur. In addition, there are significantly enhanced 200-hPa DIVs over southeastern China that are concentrated in Fujian Province (**Figure 6F**). Over southern China and the Indo-China Peninsula, 200-hPa DIVs remain nearly unchanged.

Summarizing the above analysis, we conclude that the increasing τ of WNP TC landfalls on the Asian continent are more linked to changes in dynamic factors than changes in thermodynamic factors. The increasing τ for Cluster A is likely induced by both increasing 850-hPa VOR and 200-hPa DIV over southeastern China, while the increasing τ for Cluster B appears to be primarily driven by increasing 850-hPa VOR over southern China. By contrast, there are no significant environmental changes over the eastern Indo-China Peninsula, and we found no significant changes in τ for Cluster C.

Figure 7 examines trends in the June–November 850-hPa circulation during 1966–2018. There is a large-scale anomalous cyclonic flow trend over the Chinese mainland, with significantly increased westerlies and easterlies over the southern portion and the northern portion, respectively (**Figure 7A**). These enhanced westerlies along the southern coastline of China provide anomalously positive 850-hPa VOR over southeastern and southern China due to the shear effect. This anomalous cyclonic flow over China is consistent with an enhanced East

Asian summer monsoon circulation during recent decades, which has been linked to global warming (Zhu et al., 2011; He et al., 2019). **Figure 7B** highlights these same trends in the 850-hPa circulation after removing the influence of the PDO *via* partial regression. We find similar flow patterns in **Figure 7B**, highlighting that these results remain mostly unchanged, regardless of whether the influence of decadal changes is considered.

SUMMARY

This study investigates long-term trends in the decay timescale (τ) of WNP TCs making landfall on the Asian continent. We find a significant increasing τ for the period of 1966–2018, indicating a slower decay of inland TCs over the WNP. This increasing tendency is primarily caused by a significantly increasing τ of TCs hitting southeastern and southern China (Clusters A and B), while the τ of TCs striking the Indo-China Peninsula (Cluster C) has not increased significantly.

Compared with the WNP TC weakening rate over water, which is predominately determined by SST gradients and VWS (Fei et al., 2020), we find that TC inland decay over the Asian continent is modulated by different environmental variables. We find *via* statistical analysis that τ is significantly positively correlated with soil wetness, 850-hPa VOR and 200-hPa DIV. Wetter soils, greater lower-level cyclonic flow and upper-level divergent flow are expected to provide additional energy allowing TCs to survive for a longer time over land, further leading to a slower inland decay. By contrast, atmospheric moisture and VWS appear to play a lesser role in the modulation of the TC decay rate over land, due to their weak correlations with τ .

Changes in τ during 1966–2018 appear to be caused by different environmental factors over different regions over the WNP. For TCs hitting southeastern China (Cluster A), increasing τ is jointly induced by increased 850-hPa VOR and 200-hPa DIV. For TCs hitting southern China (Cluster B), increasing τ appears to be primarily due to increasing 850-hPa VOR. The increase in 850-hPa VOR is caused by the shear effect of an enhanced large-scale low-level cyclonic circulation over China. Due to global warming, an enhanced East Asian summer monsoon circulation is projected by climate models as global surface temperature increases, leading to anomalous low-level cyclonic flow over East Asia (Zhu et al., 2011; He et al., 2019; Li et al., 2019). These results imply that WNP inland TCs are likely to decay more slowly in the future. By comparison, we find little trend in environmental conditions over the eastern Indo-China Peninsula. This region (Cluster C) also exhibited an insignificant change in τ . Despite the linkage between τ and soil wetness, no significant trends in soil wetness are observed over the main occurrence region for

landfalls along the Asian continent. These results imply that the increasing τ of WNP landfalling TCs is more likely caused by changes in dynamic variables than changes in thermodynamic variables.

Our results are based on a statistical analysis of a limited number of samples. The main findings need to be verified by numerical sensitivity experiments using different large-scale environmental forcings. These experiments will be designed and conducted in future research.

DATA AVAILABILITY STATEMENT

The original contributions presented in the study are included in the article/supplementary material, further inquiries can be directed to the corresponding author.

AUTHOR CONTRIBUTIONS

JS, PK, and YD contributed to conception and design of the study. JS organized the database and performed the statistical analysis. JS wrote the first draft of the article. PK, HZ, and YD revised the article. All authors contributed to manuscript revision, read, and approved the submitted version.

FUNDING

This work was jointly funded by the National Key Research and Development Program of China (2018YFC1507103), the National Natural Science Foundation of China (61827901 and 41922033), the China Postdoctoral Science Foundation (2020M680789) and the Natural Science Foundation of Jiangsu Province, China (BK20181412).

ACKNOWLEDGMENTS

We would like to express our sincere thanks to two reviewers for their helpful comments on an earlier version of this manuscript. WNP TC best track data provided by CMA, JTWC, JMA and HKO and archived in IBTrACS are downloaded from <https://www.ncdc.noaa.gov/ibtracs/index.php?name=ib-v4-access>. The monthly timeseries of the PDO index is obtained from <https://psl.noaa.gov/data/climateindices/>. The Japanese 55-years Reanalysis (JRA-55) data are available at <http://search.diasjp.net/en/dataset/JRA55>. Klotzbach would like to acknowledge financial support from the G. Unger Vetlesen Foundation.

REFERENCES

- Andersen, T. K., and Shepherd, J. M. (2013). A global spatiotemporal analysis of inland tropical cyclone maintenance or intensification. *Int. J. Climatol.* 34, 391–402. doi:10.1002/joc.3693
- Chen, X., Wu, L., and Zhang, J. (2011). Increasing duration of tropical cyclones over China. *Geophys. Res. Lett.* 38, L02708. doi:10.1029/2010gl046137
- Emanuel, K., DesAutels, C., Holloway, C., and Korty, R. (2004). Environmental Control of Tropical Cyclone Intensity. *J. Atmos. Sci.* 61, 843–858. doi:10.1175/1520-0469(2004)061<0843:ecotci>2.0.co;2

- Fei, R., Xu, J., Wang, Y., and Yang, C. (2020). Factors Affecting the Weakening Rate of Tropical Cyclones over the Western North Pacific. *Mon. Wea. Rev.* 148, 3693–3712. doi:10.1175/mwr-d-19-0356.1
- He, C., Wang, Z., Zhou, T., and Li, T. (2019). Enhanced Latent Heating over the Tibetan Plateau as a Key to the Enhanced East Asian Summer Monsoon Circulation under a Warming Climate. *J. Clim.* 32, 3373–3388. doi:10.1175/jcli-d-18-0427.1
- Kaplan, J., and DeMaria, M. (1995). A Simple Empirical Model for Predicting the Decay of Tropical Cyclone Winds after Landfall. *J. Appl. Meteorol.* 34, 2499–2512. doi:10.1175/1520-0450(1995)034<2499:asemp>2.0.co;2
- Klotzbach, P. J., and Landsea, C. W. (2015). Extremely intense hurricanes: Revisiting Webster et al. (2005) after 10 years. *J. Clim.* 28, 7621–7629. doi:10.1175/jcli-d-15-0188.1
- Knapp, K. R., Kruk, M. C., Levinson, D. H., Diamond, H. J., and Neumann, C. J. (2010). The International Best Track Archive for Climate Stewardship (IBTrACS). *Bull. Amer. Meteorol. Soc.* 91, 363–376. doi:10.1175/2009bams2755.1
- Kobayashi, S., Ota, Y., Harada, Y., Ebata, A., Moriya, M., Onoda, H., et al. (2015). The JRA-55 Reanalysis: General specifications and basic characteristics. *J. Meteorol. Soc. Jpn.* 93, 5–48. doi:10.2151/jmsj.2015-001
- Lee, C.-Y., Tippet, M. K., Sobel, A. H., and Camargo, S. J. (2016). Autoregressive Modeling for Tropical Cyclone Intensity Climatology. *J. Clim.* 29, 7815–7830. doi:10.1175/jcli-d-15-0909.1
- Li, L., and Chakraborty, P. (2020). Slower decay of landfalling hurricanes in a warming world. *Nature* 587, 230–234. doi:10.1038/s41586-020-2867-7
- Li, Z., Sun, Y., Li, T., Ding, Y., and Hu, T. (2019). Future Changes in East Asian Summer Monsoon Circulation and Precipitation under 1.5 to 5 °C of Warming. *Earth's Future* 7, 1391–1406. doi:10.1029/2019ef001276
- Liu, L., Wang, Y., Zhan, R., Xu, J., and Duan, Y. (2020). Increasing destructive potential of landfalling tropical cyclones over China. *J. Clim.* 33, 3731–3743. doi:10.1175/jcli-d-19-0451.1
- Ma, Z., Fei, J., and Huang, X. (2019). A definition of rapid weakening for tropical cyclones over the western North Pacific. *Geophys. Res. Lett.* 46, 11471–11478. doi:10.1029/2019gl085090
- Moon, I.-J., Kim, S.-H., and Chan, J. C. L. (2019). Climate change and tropical cyclone trend. *Nature* 570, E3–E5. doi:10.1038/s41586-019-1222-3
- Nakamura, J., Lall, U., Kushnir, Y., and Camargo, S. J. (2009). Classifying North Atlantic Tropical Cyclone Tracks by Mass Moments*. *J. Clim.* 22, 5481–5494. doi:10.1175/2009jcli2828.1
- Ren, F., Liang, J., Wu, G., Dong, W., and Yang, X. (2011). Reliability Analysis of Climate Change of Tropical Cyclone Activity over the Western North Pacific. *J. Clim.* 24, 5887–5898. doi:10.1175/2011jcli3996.1
- Song, J., Klotzbach, P. J., Duan, Y., and Guo, H. (2020). Recent increase in tropical cyclone weakening rates over the western North Pacific. *Geophys. Res. Lett.* 47, e2020GL090337. doi:10.1029/2020gl090337
- Wang, S., Rashid, T., Throp, H., and Toumi, R. (2020). A shortening of the life cycle of major tropical cyclones. *Geophys. Res. Lett.* 47, e2020GL088589. doi:10.1029/2020gl088589
- Weinkle, J., Maue, R., and Pielke, R., Jr. (2012). Historical Global Tropical Cyclone Landfalls*. *J. Clim.* 25, 4729–4735. doi:10.1175/jcli-d-11-00719.1
- Wood, K. M., and Ritchie, E. A. (2015). A definition for rapid weakening of North Atlantic and eastern North Pacific tropical cyclones. *Geophys. Res. Lett.* 42, 10091–10097. doi:10.1002/2015gl066697
- Zhu, Y., Wang, H., Zhou, W., and Ma, J. (2011). Recent changes in the summer precipitation pattern in East China and the background circulation. *Clim. Dyn.* 36, 1463–1473. doi:10.1007/s00382-010-0852-9

Conflict of Interest: The authors declare that the research was conducted in the absence of any commercial or financial relationships that could be construed as a potential conflict of interest.

The handling editor declared a shared affiliation with one of the authors HZ at time of review.

Publisher's Note: All claims expressed in this article are solely those of the authors and do not necessarily represent those of their affiliated organizations, or those of the publisher, the editors and the reviewers. Any product that may be evaluated in this article, or claim that may be made by its manufacturer, is not guaranteed or endorsed by the publisher.

Copyright © 2021 Song, Klotzbach, Zhao and Duan. This is an open-access article distributed under the terms of the Creative Commons Attribution License (CC BY). The use, distribution or reproduction in other forums is permitted, provided the original author(s) and the copyright owner(s) are credited and that the original publication in this journal is cited, in accordance with accepted academic practice. No use, distribution or reproduction is permitted which does not comply with these terms.



Simulation of Rapid Intensification of Super Typhoon Lekima (2019). Part I: Evolution Characteristics of Asymmetric Convection Under Upper-Level Vertical Wind Shear

Qijun Huang¹, Xuyang Ge^{1*} and Melinda Peng²

¹Key Laboratory of Meteorological Disaster of Ministry of Education, Joint International Research Laboratory of Climate and Environment Change, Collaborative Innovation Center on Forecast and Evaluation of Meteorological Disasters, Nanjing University of Information Science and Technology, Nanjing, China, ²University of Colorado, Denver, CO, United States

OPEN ACCESS

Edited by:

Guanghua Chen,
Institute of Atmospheric Physics,
Chinese Academy of Sciences, China

Reviewed by:

Donglei Shi,
Institute of Atmospheric Physics
(CAS), China
Eric Hendricks,
National Center for Atmospheric
Research (UCAR), United States

*Correspondence:

Xuyang Ge
xuyang@nuist.edu.cn

Specialty section:

This article was submitted to
Atmospheric Science,
a section of the journal
Frontiers in Earth Science

Received: 11 July 2021

Accepted: 17 August 2021

Published: 29 September 2021

Citation:

Huang Q, Ge X and Peng M (2021)
Simulation of Rapid Intensification of
Super Typhoon Lekima (2019). Part I:
Evolution Characteristics of
Asymmetric Convection Under Upper-
Level Vertical Wind Shear.
Front. Earth Sci. 9:739507.
doi: 10.3389/feart.2021.739507

The role of the upper-level vertical wind shear (VWS) on the rapid intensification (RI) of super typhoon Lekima (2019) is investigated with a high-resolution numerical simulation. Our simulation shows that under moderate upper-level easterly VWS, the tilting-induced convective asymmetry is transported from the initially downshear quadrant to the upshear quadrant and wrapped around the storm center by the cyclonic flow of the storm while moving inward. This process enhances upward motions at the upshear flank and creates upper-level divergent flow. As such, the establishment of outflow acts against the environmental flow to reduce the VWS, allowing vertical alignment of the storm. The organized outflow plays an important role in sustaining the inner-core deep convection by modulating the environmental upper-level thermal structure. Accompanying deep convective bursts (CBs), cold anomalies are generated in the tropopause layer due to the adiabatic cooling by the upward motion and radiative process associated with the cloud anvil. Physically, cold anomalies at the tropopause locally destabilize the atmosphere and enhance the convections and the secondary circulation. The CBs continue to develop episodically through this process as they wrap around the storm center to form a symmetric eyewall. The results suggest that deep convections are capable of reducing the upper-level VWS, promoting the development of upper-level outflow. Lekima overcame the less favorable environment and eventually intensified to become a super typhoon.

Keywords: tropical cyclone, rapid intensification, upper vertical shear, outflow pattern, asymmetric convection

INTRODUCTION

Although the track forecasts of tropical cyclones (TCs) have been improved progressively, intensity prediction remains as a big challenge for the TC community (DeMaria et al., 2014), particularly during the rapid intensification (RI) with winds increased by at least 30 knots in a 24-hour period. The operational prediction of RI is particularly difficult (Titley and Elsberry, 2000; Elsberry et al., 2007). It has been well realized that the RI is ascribed to the multi-scale interactions, involving environmental, oceanic, and inner-core processes (Kaplan and DeMaria, 2003; Emanuel et al., 2004;

Kaplan et al., 2015). Statistical studies reveal that there are significant differences in both oceanic conditions (Wang and Wu, 2004; Zeng et al., 2010; Zhang et al., 2017) and atmospheric conditions for developing versus non-developing TCs (Ge et al., 2013; Zhang and Tao, 2013; Gu et al., 2015). Among them, the environmental vertical wind shear (VWS) has long been considered as one of the key factors controlling the intensity of TCs (Emanuel et al., 2004; Zeng et al., 2007; Zeng et al., 2008; Wang et al., 2015; Chen et al., 2017). Several negative effects of VWS on the intensification have been proposed, including: 1) upper-level dilution of the TC warm core (Frank and Ritchie, 2001); 2) dry intrusion of mid-level air into the TC eyewall (Tang and Emanuel, 2010; Ge et al., 2013; Kanada and Wada, 2015); and 3) the so-called mid-level “ventilation” effect (Riemer et al., 2010; Tang and Emanuel, 2010; Tang and Emanuel, 2012; Riemer and Laliberté, 2015). In short, these studies suggest that due to the evaporation of precipitation or ambient intrusion from outside the storm’s inner region, the air with low equivalent potential temperature (θ_e) reduces eyewall moist entropy located downshear-left and suppresses convection within the eyewall.

In general, the VWS acts to tilt the TC vortex, creating pronounced asymmetries in TC structure and rainfall pattern and thus is not favorable for TC development. Statistically, there exists a wavenumber one convective asymmetry with strong updrafts in the downshear-left flank during the intensifying period under the vertical wind shear (Rogers 2016). The linkage between convective updrafts around the storm center and the RI process has been widely examined. From both observation and numerical simulations, TCs experiencing RI episodes usually have a relatively large amount of deep and vigorous convective bursts (CBs) inside the radius of maximum wind (RMW) (Braun, 2013; Chen and Zhang, 2013; Rogers et al., 2013; Sanger et al., 2014; Chen and Gopalakrishnan, 2015; Rogers et al., 2015; Smith and Montgomery, 2015; Rogers et al., 2016). The axisymmetrization process associated with these rotating convective updrafts in and around the developing eyewall region also contributes to TC intensification. For instance, Bhalachandran et al. (2020) found that certain aspects of eddy energetics can potentially serve as early-warning indicators of TC rapid intensity changes. However, different types of downdrafts have different impacts on the TC intensity (Wadler et al., 2018).

The complex interactions between VWS with different structures and convective patterns likely will result in different outcomes for TC intensification. Finocchio et al. (2016) found that the development of a TC is highly sensitive to the shear height and depth. The shear height appears to affect the response of a TC to the tilt by modifying its thermodynamics, while the shear depth controls the height of TC in responding to the tilt. Generally, the shallower and lower the VWS, the more destructive it is to TC’s intensification. TC vortices tilt the most under lower-level VWS and are unable to process upshear and realign, thus fail to intensify. Some recent observational and numerical studies (Leighton et al., 2018; Ryglicki et al., 2018a; Ryglicki et al., 2018b; Li et al., 2020) found that TCs can experience an RI under moderate VWS (e.g., 5–10 m s⁻¹). For this atypical class of TCs underwent RI, it is hypothesized that they are closely

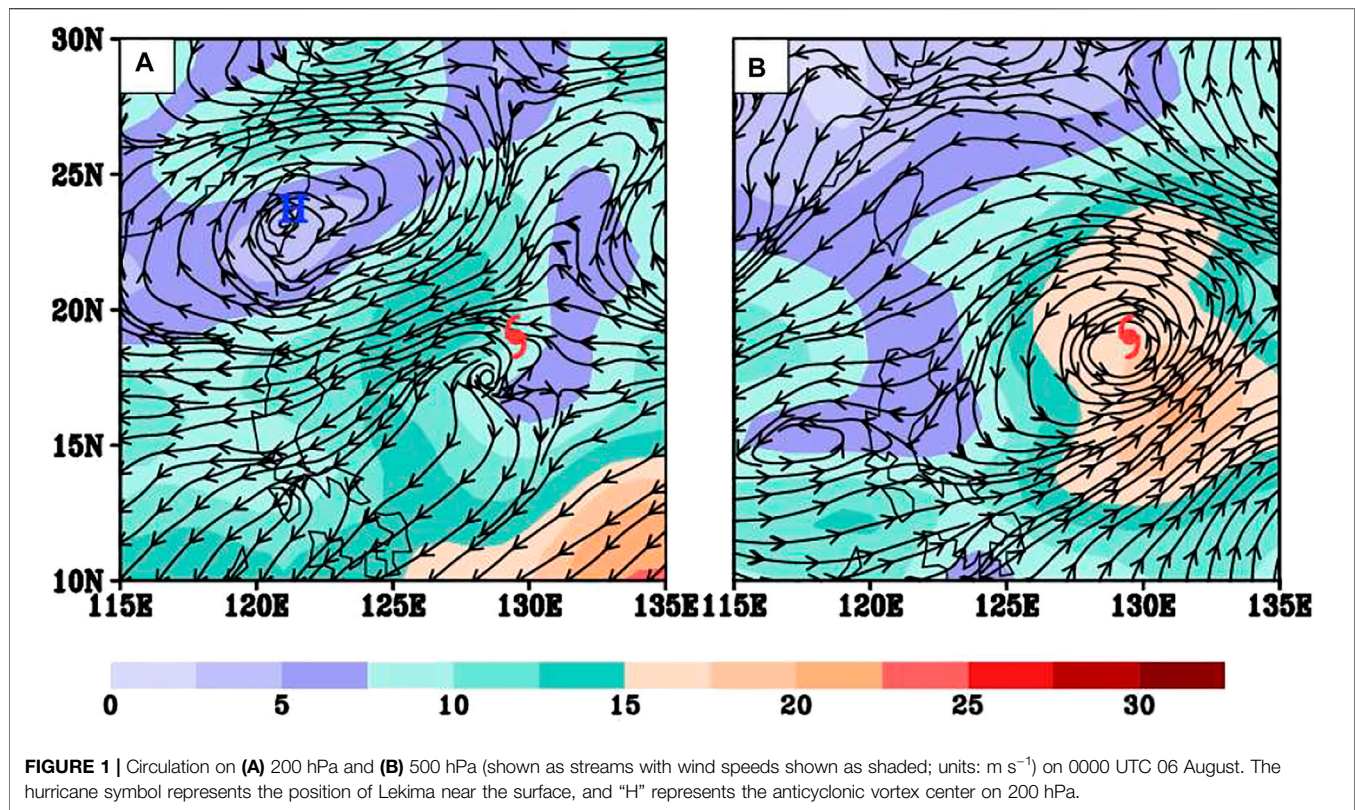
associated with the tilt-modulated convective asymmetries (TCA). The TCAs, characterized as collections of updrafts, move towards upshear flank to enhance upper-level outflow. The enhanced outflow converges with the environmental winds, creating a dynamic high pressure to decelerate the environmental winds and thus reduced the VWS. Corbosiero and Molinari (2002) suggested that the deep divergent circulations in the active TC can reduce the VWS and act to minimize the tilt of the TC.

Under various VWSs, TC intensity is largely determined by the vertical alignment of TC circulations (Zhang and Tao, 2013) with some conceptual models for the interpretations (Wong and Chan, 2004; Zhang and Kieu, 2006). However, how the VWS precisely influences the convection pattern, and thus the vertical alignment remains unclear. For example, Molinari et al. (2006) pointed out that TC intensification can be promoted under a sheared environment when a TC undergoes a “downshear reformation” to suppress the ventilation effect. This differs from the “upshear realignment” process discussed above. We attempt to explore this scientific question by investigating super typhoon (STY) Lekima (2019) through numerical simulation. As will be shown later, Lekima underwent an RI under moderate upper-level VWS. Some recent studies (Dai et al., 2021; Shi and Chen, 2021) have focused on the different aspects of these particular TC structures (i.e., warm core and asymmetric rainbands). Dai et al. (2021) investigated the quasi-periodic intensification of convective asymmetries in the outer eyewall during the mature stage. In this study, we focus on an early stage (during the period of RI), and the main focus is on the possible interaction between upper outflow and TCA.

The article is organized as follows. In *Model Configurations* section, the numerical model used for the simulation and its configuration are described. The simulated results are presented in *Environment of Lekima* section. The physical understanding is given in *Simulated Results* section. Finally, discussion and summary are given in the last section.

MODEL CONFIGURATIONS

In this study, the Advanced Research Weather Research and Forecasting model (WRF-ARW; version 3.9.1; Davis et al., 2008) is used. Four-nested domains with the horizontal grid spacings of 27, 9, 3, and 1 km, respectively, are configured with two-way interactions between each domain. The outermost domain covers a region of (90°E–155°E, 0°–40°N) (not shown). The vortex-following technique is used to allow the TC-vortex to be always located near the center for the second and the innermost moving-nested domain. There are 45 uneven σ levels in the vertical using terrain-following extending from the surface to the model top at 10 hPa. The model physics includes a Lin microphysics scheme (Lin et al., 1983), including six classes of hydrometeors about water vapor, cloud water, rain, cloud ice, snow, and graupel. Kain–Fritsch convective scheme (Kain and Fritsch, 1993) is applied for the outermost domain only, and YSU turbulent mixing scheme for boundary layer parameterization. For the radiation process, Dudhia



shortwave radiation (Dudhia, 1989) and Rapid Radiation Transfer Model (RRTM) longwave radiation parameterization scheme (Mlawer et al., 1997) are used.

The initial and boundary conditions are obtained from $1^\circ \times 1^\circ$ National Centers for Environmental Prediction/Final Analysis data (NCEP/FNL), which has 34 layers from 1,000 to 40 hPa at 6-hour intervals. The RI period of TC is from 1200 UTC 06 to 1200 UTC 08 August. The initial time of the numerical simulation is at 0000 UTC 06 August 2019. The integration lasts for 3 days from 06 to 08 August, which covers the period of RI for Lekima.

ENVIRONMENT OF LEKIMA

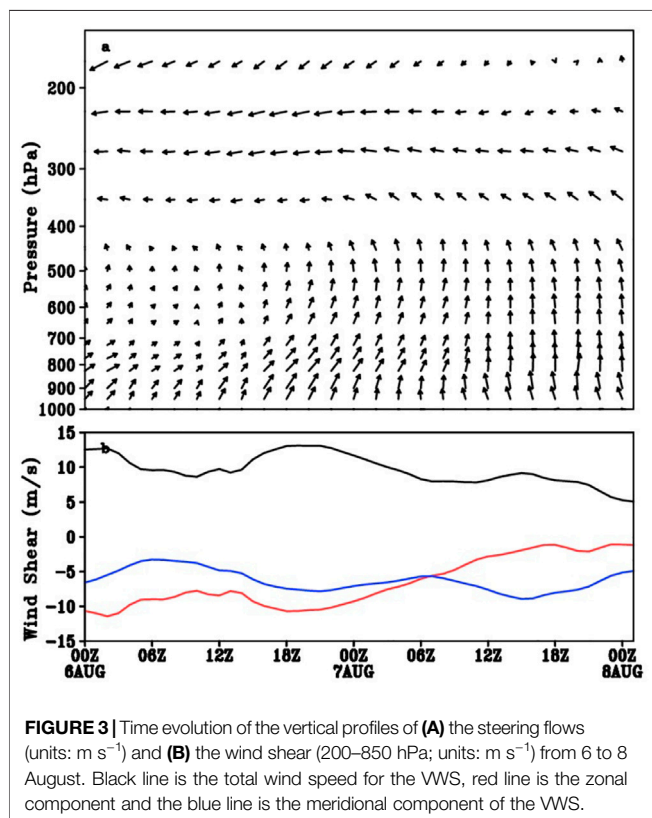
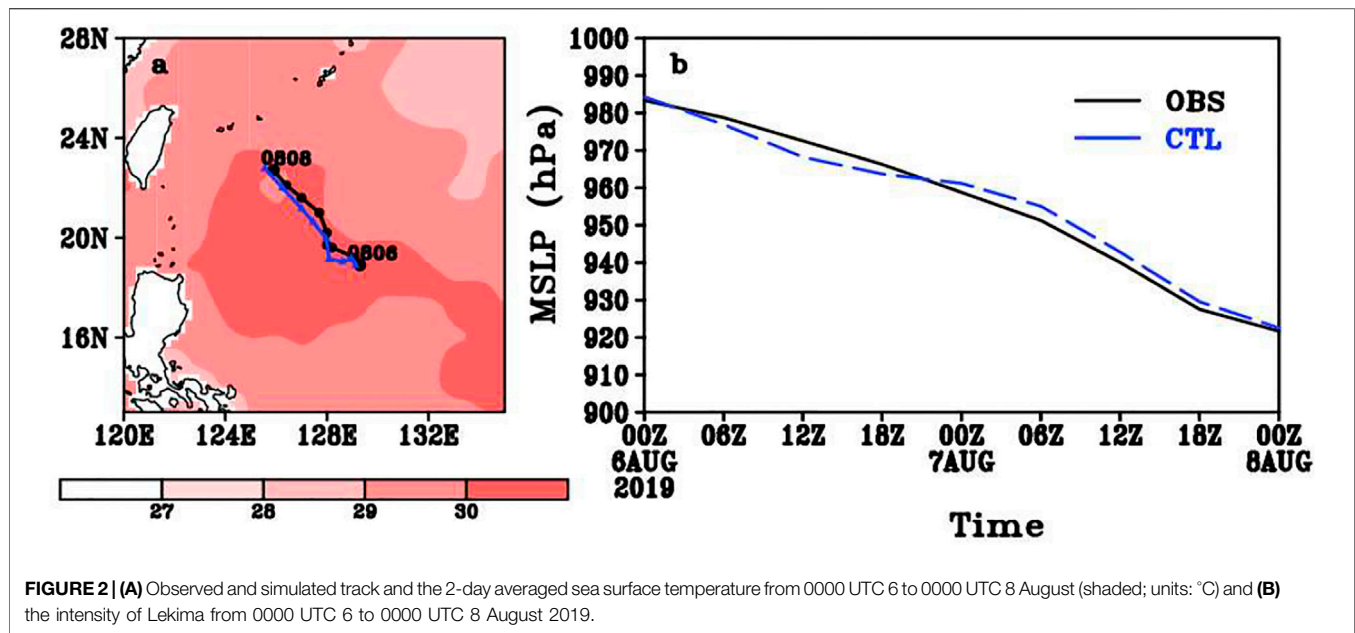
Lekima (2019, 09W) was first monitored as a tropical disturbance by the Joint Typhoon Warning center (JTWC) on 0600 UTC 04 August 2019. The storm strengthened and became a typhoon on 1200 UTC 06 August. At that time, the minimum central pressure was estimated to be 985 hPa. The intensity of the typhoon continued to develop. On 0600 UTC 08 August, it reached STY category with a minimum central pressure of 912 hPa and maximum wind speed of 75 m s^{-1} . The typhoon weakened slightly on 1800 UTC 08 August. **Figure 1** presents the circulations on 200 and 500 hPa at the initial time of our simulation on 0000 UTC 6 August. TC is located to the southern-east flank of the upper-level anticyclone on 200 hPa. **Figure 1B** shows that TC is mainly embedded in the cyclonic circulation on 500 hPa. And the typhoon was affected by the straight east wind located to the north flank of the typhoon on

500 hPa. The vertical structure of the anticyclone is shallow and is confined in the upper level.

The simulated track and intensity are compared against the Japan Meteorological Administration (JMA) best-track data (**Figure 2**). Generally, the simulation captures reasonably well the storm's northwestward movement. Furthermore, the intensity forecast is very close to the best track estimate. The averaged sea surface temperature from 0000 UTC 6 August to 0000 UTC 8 August is relatively high (above 29°C) which is beneficial to the development of the typhoon (**Figure 2A**). During the integration period from 0000 UTC 6 August to 0000 UTC 8 August, the central pressure of the storm fell 65 hPa within a 48-h period, which satisfies the criteria for RI for western North Pacific TCs (Wang and Zhou, 2008). With the good track and intensity prediction, the RI processes can be analyzed with detailed structure using the simulation as the proxy of the real atmosphere.

Upper-Level VWS

There is an asymmetry of Rossby waves under the vertical shear (Wang and Xie, 1996). That is, the amplitude of wave is enhanced (weakened) at the lower troposphere under easterly (westerly) shear. With this regard, the easterly shear favors a greater amplitude of wave at the lower level and thus a stronger air-sea interaction. We define the wind difference between 200 and 500 hPa as the upper-level shear. **Figure 3** presents the time evolution of the vertical profiles of the steering flows and the evolution of VWS in the vicinity of Lekima averaged within a 500-km radius centered on the storm and with the TC vortex



removed. The spatial filtering technique (Hendricks et al., 2011) was used to separate the TC-scale circulation and the large-scale circulation. Specifically, the component with wavenumber greater than 500 km is used to present the environmental flows. The initial magnitude of VWS from 850 to 200 hPa is 12 m s^{-1} , which is

in the range of moderate-to-strong shear (Molinari et al., 2004; Molinari et al., 2006; Ryglicki et al., 2019). During the period of interest, the magnitude of VWS progressively decreases, albeit with some oscillations. The environmental winds change from southwesterly to southerly below about 500 hPa to nearly uniform easterly above. To further investigate the vertical structure of the VWS (not shown), the vertical profiles of the zonal components of the VWS show a prevailing easterly (westerly) wind appears at the upper (lower) level with a transition layer at about 500 hPa on 0000 UTC 06 August and 0000 UTC 07 August. The upper level VWS from 500–200 hPa is about 6 m s^{-1} and the lower level VWS from 900–500 hPa is about 4 m s^{-1} . On 0000 UTC 08 August, the easterly wind became very small at lower levels so that the VWS is mainly located in upper levels. During the first 48 simulation hours, a southerly wind appears below 350 hPa and a weak northerly wind appears up to 350 hPa. The northerly wind changed to the weak southerly wind on 0000 UTC 08 August. In short, the meridional component of the VWS is about 6 m s^{-1} during the whole integration.

What kind of synoptic weather pattern results in such upper-level VWS? To answer this question, we go back to the 200 and 500 hPa circulation presented in Figure 1. The anticyclone is confined in the upper level and disappears on 500 hPa. Hoskins et al. (1985) shows that the lowest vertical extent of the upper-level cyclonic potential vorticity (PV) anomaly is 800 hPa, while the lowest vertical extent of the upper-level anticyclonic PV anomaly is 300 hPa. Notice that the TC is located to the southern flank of the upper-level anticyclone. This pattern agrees well with the findings by Ryglicki et al. (2018a) and Ryglicki et al. (2018b). The authors pointed out that, the upper-level anticyclone generally creates moderate upper-level VWS, and TCs embedded in such environment likely have a potential to undergo RI. Compared with upper-level VWS, a

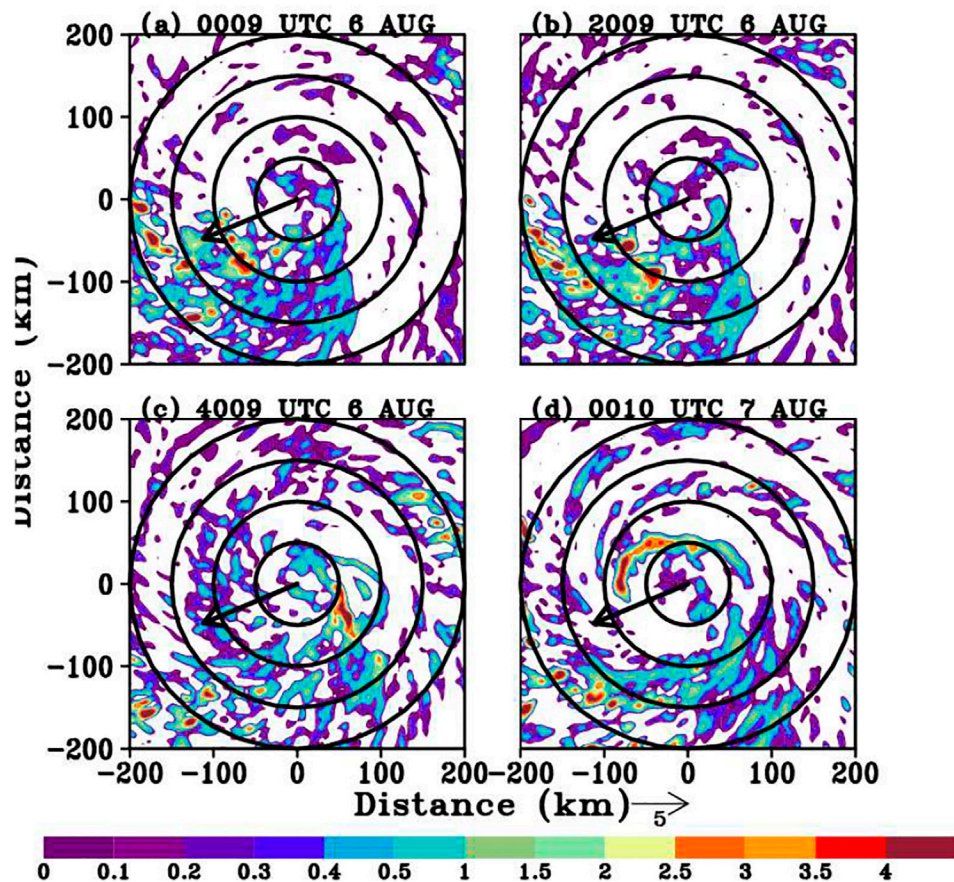


FIGURE 4 | Time evolution of the 10-km vertical velocity (shaded; units: m s^{-1}) from 0900 UTC 6 August to 1000 UTC 7 August every 20 min. Black circles are radii at every 50 km. Black arrows are the shear direction.

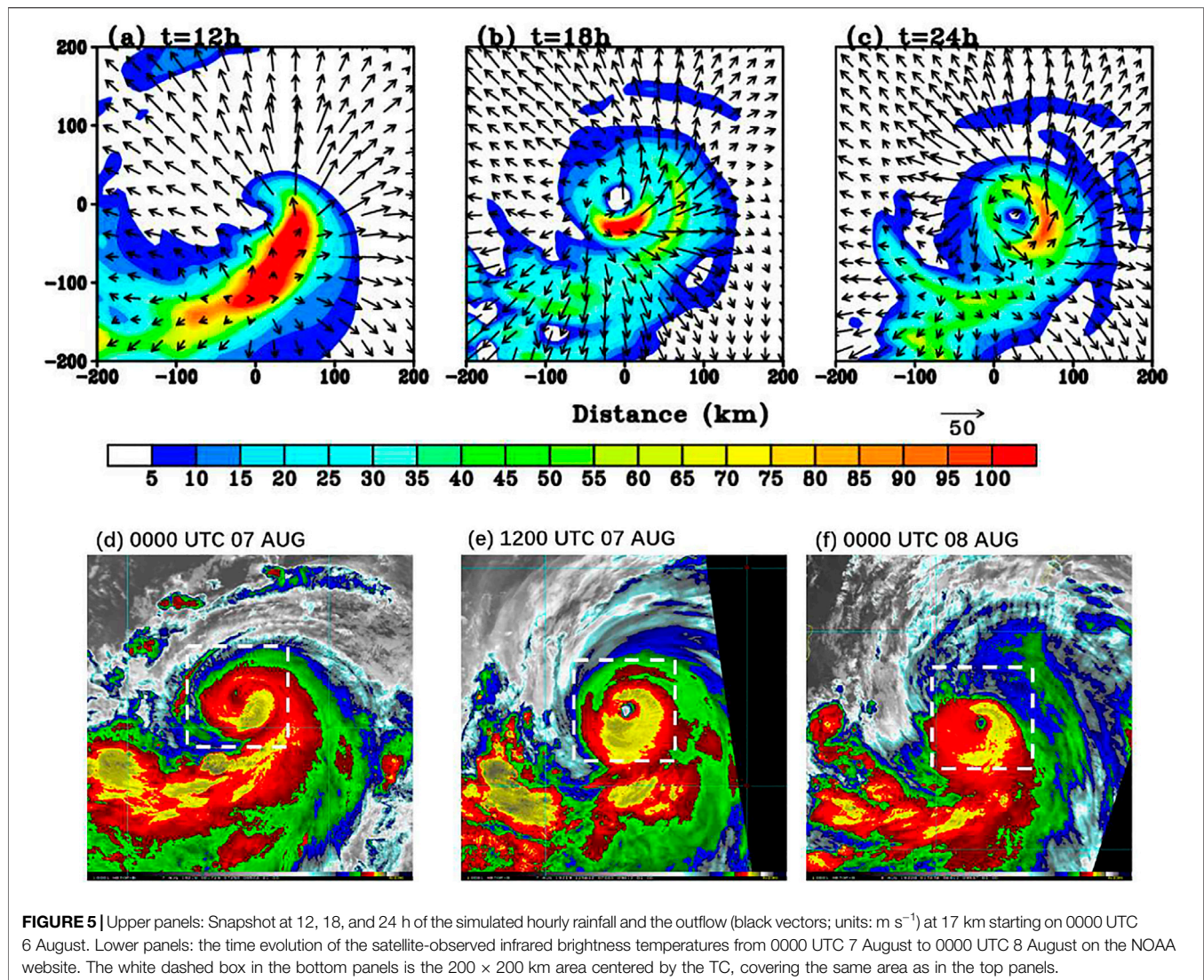
lower-level shear is more detrimental to TCs (Rhome et al., 2006; Zeng et al., 2010; Wang et al., 2015; Finocchio et al., 2016). Since Lekima undergoes a RI process under moderate upper-level VWS, a question arises here is what processes account for the RI of STY Lekima in the presence of the VWS? To address this, we will focus on the realignment process and the tilt-modulated convective asymmetries during the RI period.

SIMULATED RESULTS

Evolution of Convective Asymmetries

As shown in **Figure 2**, the intensity change of Lekima is fairly well captured in our numerical simulation. In this section, we examine the evolution of storm structure and convective activity during the period of the RI. In the presence of VWS, the tilted vortex generally induces asymmetric wavenumber one structure of convection. That is, a prolific convection usually occurs at the downshear-left quadrant in the Northern Hemisphere. To illustrate such asymmetric feature, **Figure 4** displays the distribution of the convection represented by the simulated vertical velocity from 0900 UTC 6 August to 1000 UTC 7 August every 20 min. The CBs are defined as the cells with

vertical velocity greater than 2 m s^{-1} from 0.5 to 10 km in each level. Here the vertical velocity field at the height of 10 km is selected to represent the CBs. The VWS is mainly the northeast easterly vertical wind shear. The simulated convective asymmetries are evident, with more extensive, more active convection located to the southwest of the storm center, and the convection moves inward and counterclockwise with time. **Figure 5** presents the simulated hourly rainfall and the satellite-observed infrared brightness temperatures for comparison during the simulated RI period. The asymmetry distribution of the hourly rainfall is located in the downshear-left quadrant near the storm center at the simulation of 12 h. The distribution of the hourly rainfall becomes more symmetric with time. Initially, the strong convective cloud band represented by the coldest temperature occurs to the southwest section of TC center. During the period of interest, the strongest convection is expanded to the upshear side, and the eyewall cloud becomes more symmetric. Meanwhile, the inner cloud band within 200 km from the center of the TC extends southeastward, and it corresponds with the outflow at the top; both move upshear flank with time. In general, the simulated asymmetry agrees fairly well with the satellite-observed infrared brightness temperatures (**Figures 5D–F**).

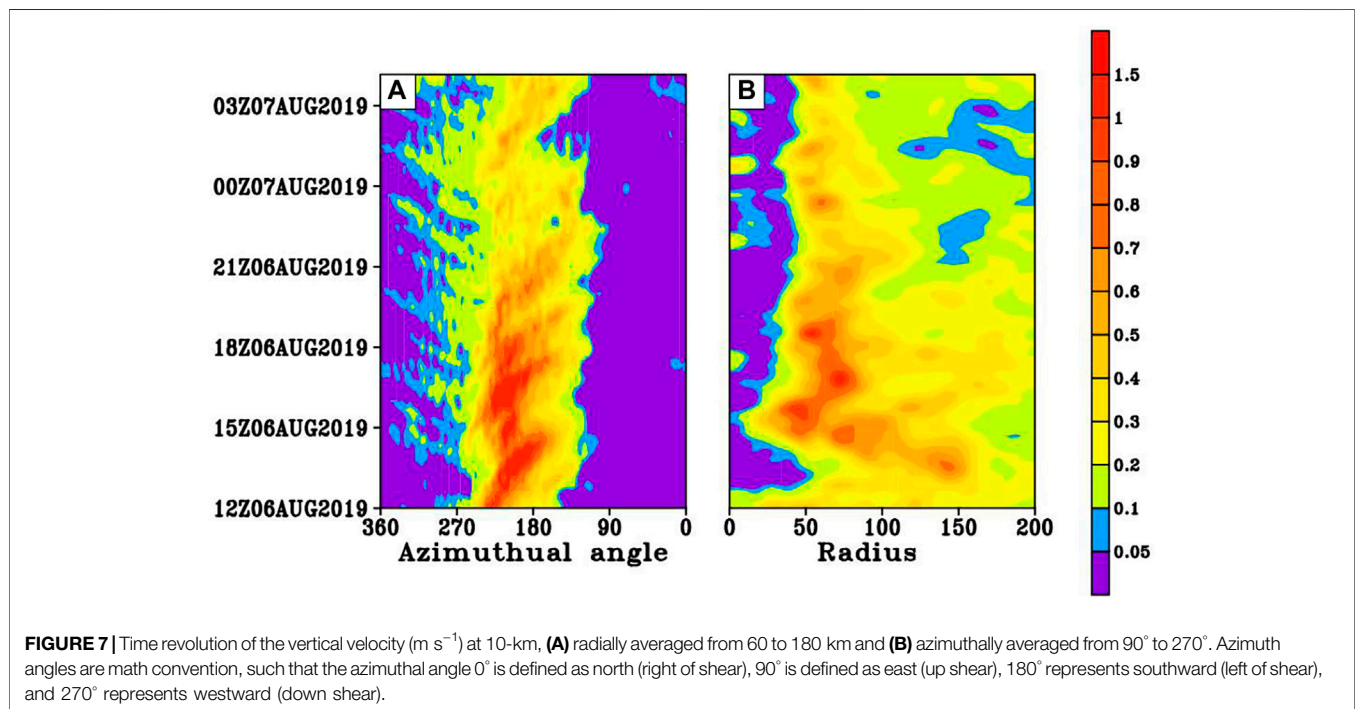
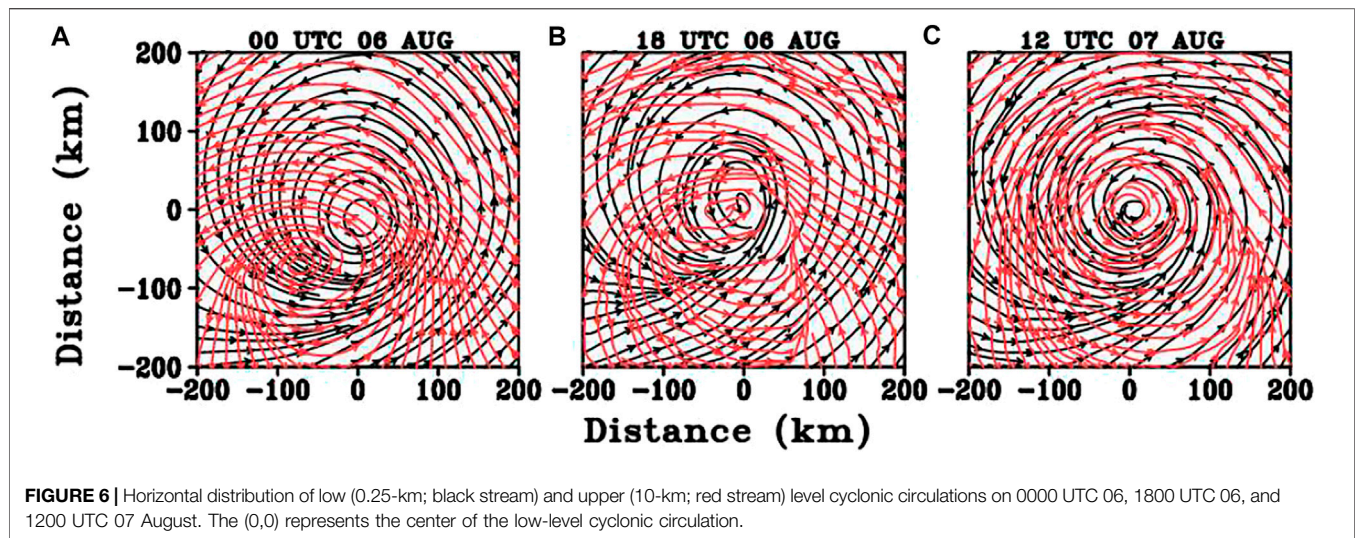


The deep convection represented by the CBs is akin to the so-called vortical hot towers (VHTs) described in Hendricks et al. (2004) and Montgomery et al. (2006). During the early development stage of Lekima (i.e., 1200 UTC 06 August 2019), the convective asymmetry originates over the southwest sector to the storm center. With times, the most active convection moves anticlockwise, and approaches to east flank of the storm (Figure 5). This evolution feature bears many similarities as previous studies (Ryglicki et al., 2018a; Ryglicki et al., 2018b; Li et al., 2020), indicating that an inward-spiraling inner cloud band moves to upshear flank to form the eyewall cloud. This process agrees with Moon and Nolan (2010), in which they proposed a hypothesis that inner rainbands are simply convective clouds advected by the rapidly rotating TC wind, and then likely deformed into spiral shapes. Through axisymmetrization, the entity likely provides a source of vorticity for the developing inner core.

In short, the simulation demonstrates that in the presence of the VWS, strong CBs occur at the left-downshear section and

then are transported cyclonically into the upshear section to form the eyewall. During this period, the magnitude of VWS is gradually reduced (Figure 3). In response to the shear reduction, the tilting of vortex is reduced and becomes almost vertically realigned. To demonstrate this feature, Figure 6 displays the horizontal distribution of low and upper-level circulations in the simulation. Initially, there is an obvious displacement between the lower-level and upper-level circulation centers (i.e., 00 UTC 06 August), with the upper-level circulation center located about 80 km southwest of the lower-level center. During the period from 6 to 7 August, along with the reduction of VWS, the horizontal displacement between mid- and upper-level centers becomes quite small (i.e., less than 10 km), indicating a vertical realignment process.

Ryglicki et al. (2018a) and Ryglicki et al. (2018b) pointed out that, while the TCA moves towards upshear flank, the cumulative effect of the continuous convective events is to push the upper-level upshear environmental winds away from the TC center. As a result, this dynamical process reduces the local wind shear and



helps vortex realignment. To illustrate the evolution features of TCA, **Figure 7A** displays the time-azimuthal cross section of vertical velocity averaged within the radius of 60–180 km. The azimuthal angle 0° is defined here as due north, and 180° represents southward since it rotates clockwise. It is apparent that the strong vertical motion originates constantly around the azimuthal angle of 270° (downshear flank) and then propagates counterclockwise to about 90° (upshear flank). **Figure 7B** presents the time-radius cross section of the vertical velocity azimuthally averaged from 90° to 270° . It shows that strong ascending motion moves radially inward from 1300 UTC 6 August to 1500 UTC 6 August and then stays close to the

RMW, reflecting that the CBs moves closer to the RMW before and during RI.

In short, our simulation shows the evolution characteristics of Lekima in which periodically generated asymmetric convective cloud bands are wrapped cyclonically into the upshear flank of the eyewall. To reveal their possible roles on the RI, Fourier decomposition is used to extract the azimuthal wavenumber-1 component of vertical mass fluxes at 17 km from 0800 UTC 06 August to 1900 UTC 06 August (not shown). Clearly, the asymmetry maximum is initially located in the downshear-left quadrant, which is outside the RMW (about 60 km). With time, the maximum shows a cyclonic movement and approaches the

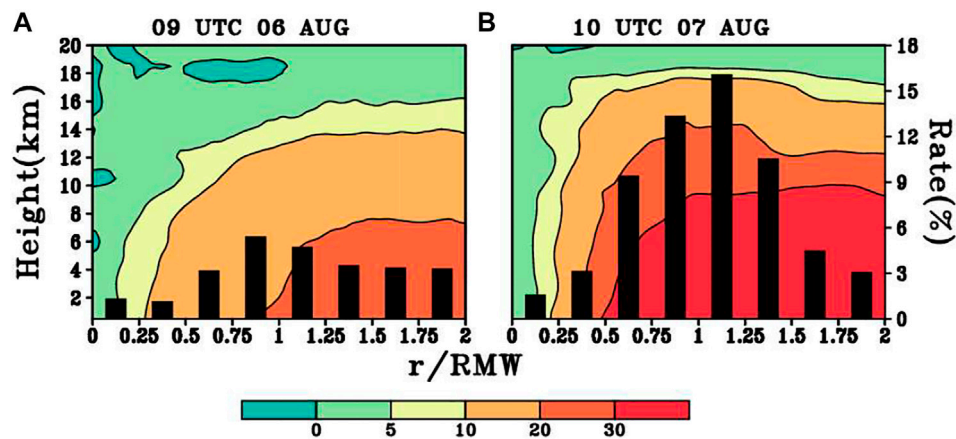


FIGURE 8 | Radial distribution of CBs, shown as which shows the percentage of the CBs at each radial distance (bar; $w > 2 m s^{-1}$; units: %) and the tangential wind (shaded; units: $m s^{-1}$) with respect to the RMW on 0900 UTC 06 and 1000 UTC 07 August.

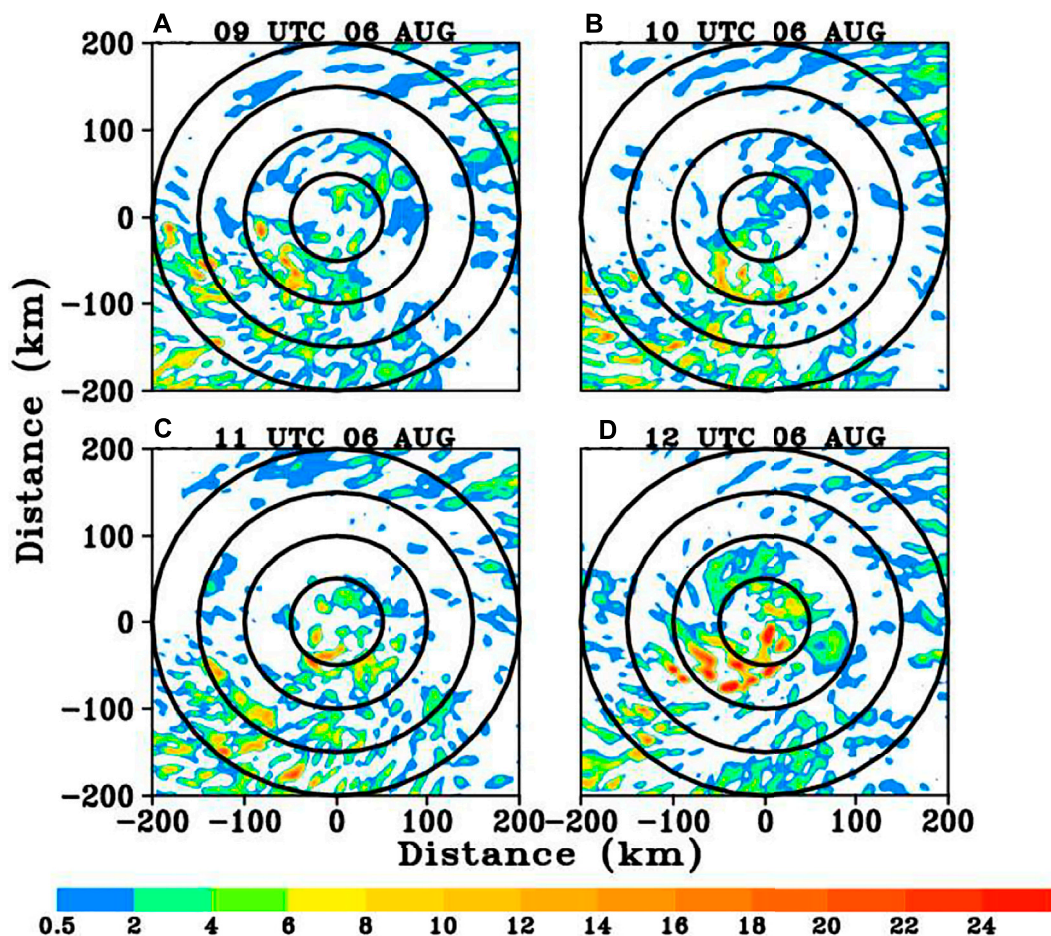


FIGURE 9 | Time evolution of radial eddy vorticity flux ($-V_r \zeta_r'$, shading; units: $1 \times 10^{-3}, m s^{-2}$) at 17-km from 0900 UTC to 1200 UTC 06 August.

RMW. This reflects the progressive cyclonic precession of the convective complex and more active convection near or within the inertially stable TC core for TC intensification, consistent

with previous studies (Nolan et al., 2007; Vigh and Schubert, 2009; Finocchio et al., 2016). By comparing the composites for the relatively early onset of RI members and the late onset of RI

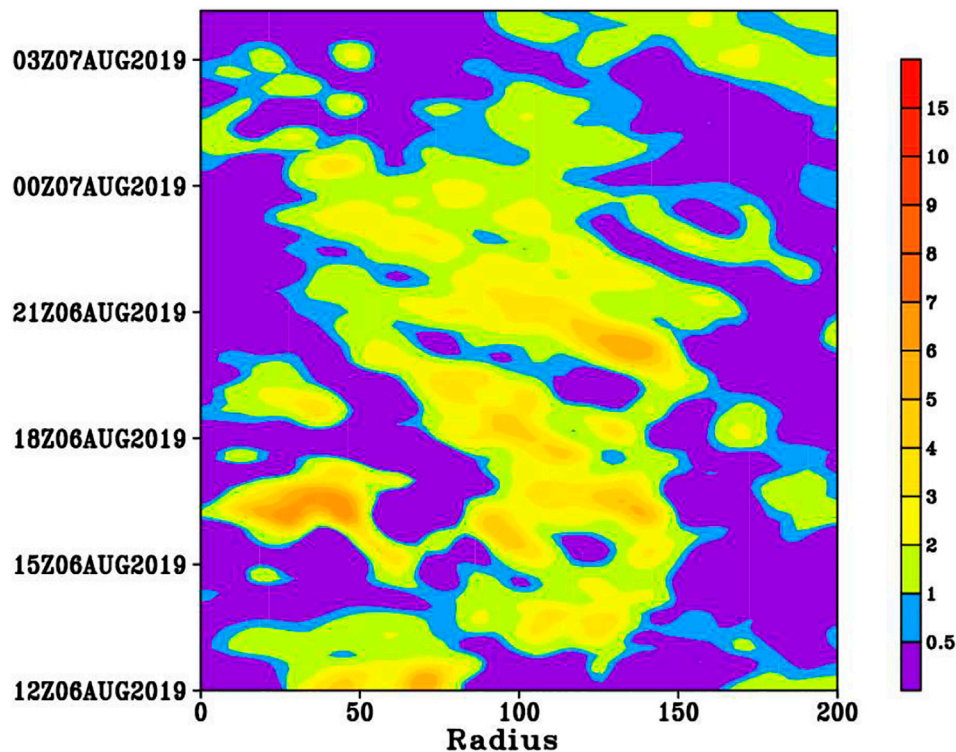


FIGURE 10 | Time-radius cross section of radial eddy vorticity flux ($-V_r'\zeta'$, shading units: 1×10^{-3} , m s^{-2}) at 17-km from 1200 UTC 06 to 0400 UTC 07 August.

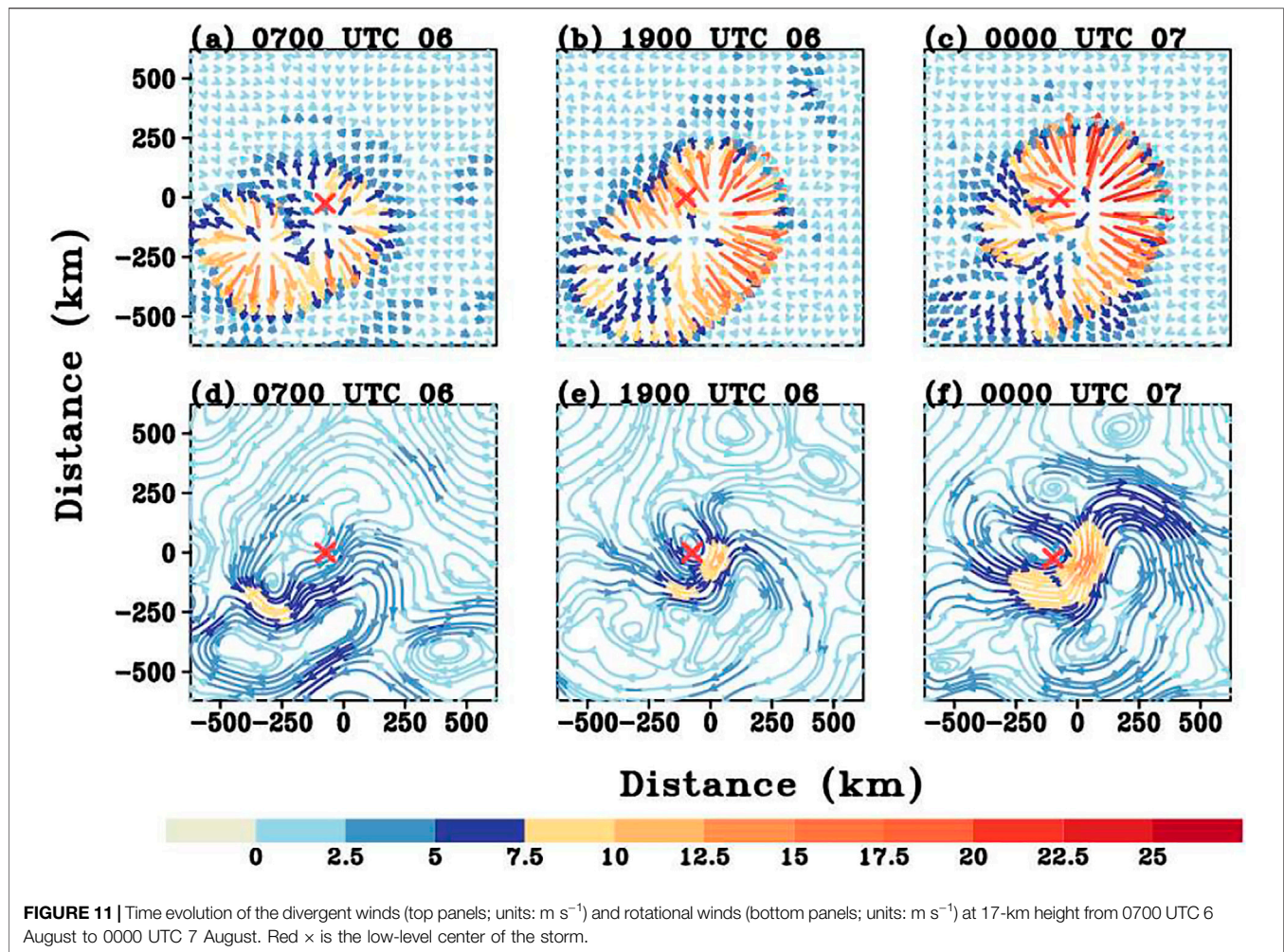
members, Li et al. (2020) suggested the early RI members with high environmental moisture and weak ventilation show the asymmetric convection develops actively and moves from the downshear side to the inner core to reduce the tilting of the TC. However, the late RI members under the stronger VWS show larger ventilation that is not conducive to TC intensity.

From a physical perspective, a larger vertical mass flux implies more pronounced diabatic heating. Furthermore, the closer the diabatic heating to the RMW where the inertial stability is the largest, the larger the conversion rate of heating to the kinetic energy. To understand this dynamic and thermodynamic aspect, the radial distributions of CBs relative to the RMW are plotted at two given times from our simulations (Figure 8). The radial distribution of CBs shows the percentage of the CBs at each radial distance normalized by the RMW at the height of 1.5 km. Since the RMW evolves with time, the CBs distribution is displayed with the x -axis normalized by the corresponding RMW at each time snapshot. Notice that the radial distributions of CBs exhibit a marked difference with respect to RMW between these two times. At the early stage (i.e., 0900 UTC 06 August), the radial distribution of strong convection mostly stays away the RMW. With time, CBs near the RMW increase, and start to move inward and closer to the RMW as shown on 1000 UTC 07 August. This agrees with previous studies (Rogers et al., 2016; Hazelton et al., 2017), namely, CBs need to occur inside, not outside the RMW, in sufficient numbers for genesis and intensification (Braun, 2013).

The axisymmetrization processes associated with rotating convective updrafts in and around the developing eyewall

region have been shown to contribute to an enhanced secondary circulation (Montgomery et al., 2014; Montgomery and Smith, 2014; Smith et al., 2017; Chen et al., 2018). To further assess the dynamical influences of these eddies on the TC intensification, we calculate the term $-V_r'\zeta'$ at 17 km (Figure 9), where V_r' is radial inflow anomaly and ζ' is the vorticity anomaly. Dynamically, the positive value implies that the eddies will enhance the mean circulation. These eddies are defined as the positive cyclonic vorticity. The positive vertical velocity is mainly located in the downshear-left quadrant and moves to the upshear quadrant (Figure 4). As expected, the spatial pattern clearly shows the asymmetric structure with the positive value dominated in the downshear-left section. Figure 10 displays the time-radius cross section of eddy vorticity fluxes at the height of 17 km. Once again, the positive value exhibits consistent and periodic inward propagation, coinciding with the inward propagation of asymmetric convective band. Consequently, the positive value helps spin up the upper-level inner-core circulation.

To summarize, under moderate upper-level easterly VWS, TC exhibits a wavenumber-one TCA indicated by strong upward motion to the downshear-left side of the storm. This tilting-induced convective asymmetry, which resembles the inner convective bands (ICBs), is then transported and/or wrapped inwards to the upshear quadrant to form an eyewall. Along with the continuous development of inward-penetrating ICBs, the vortex starts to undergo vertical realignment. Since the deep



CBs are the nature source to drive TC outflow, we will examine the evolution of TC outflow structure in the following section.

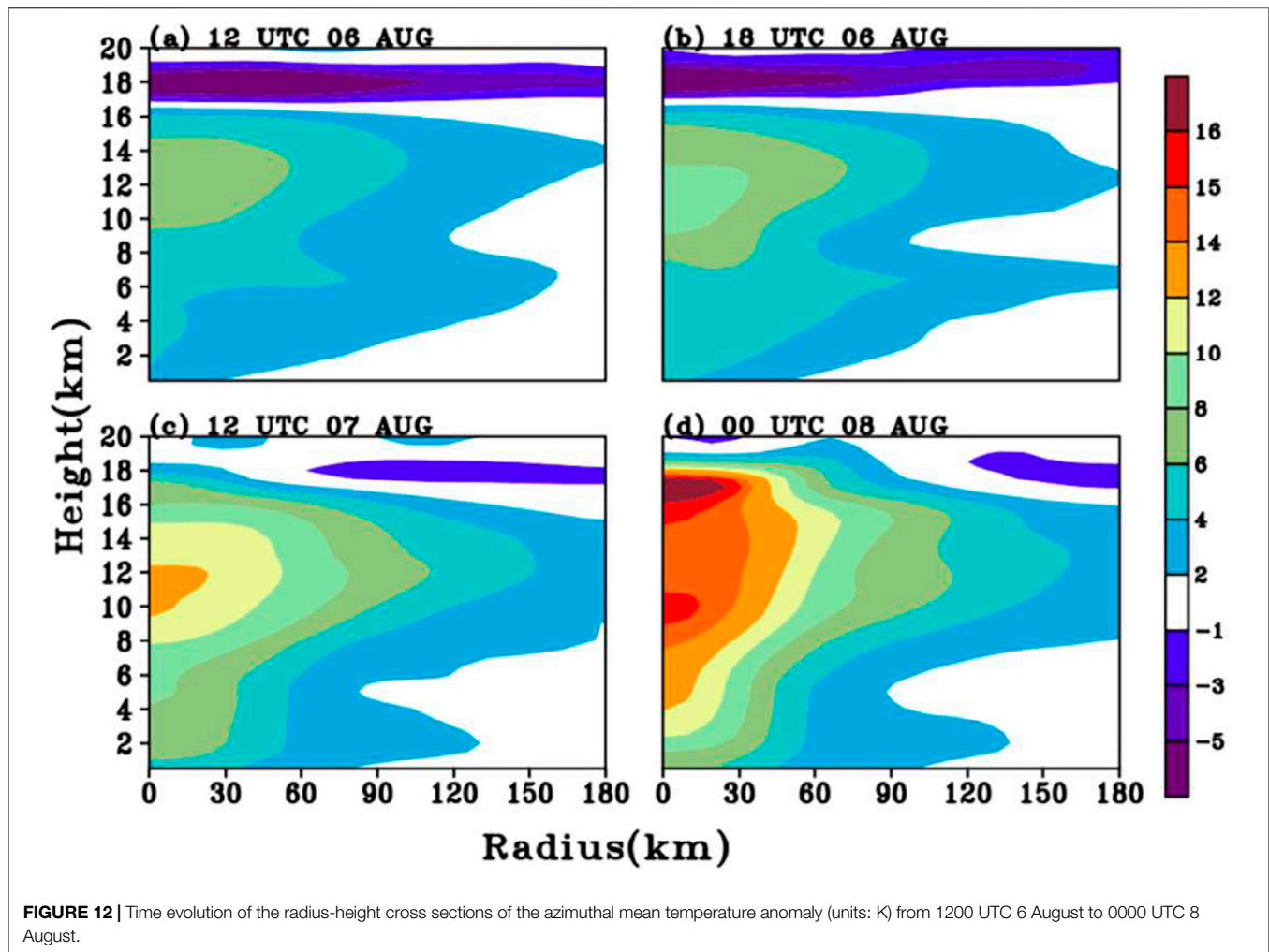
Evolution of Outflow Structure

For a TC with RI, one pronounced feature is a strong upper-level outflow jet with an open circulation (Merrill, 1988). Generally, a strong outflow channel will efficiently ventilate the mass from storm center, resulting in a rapid falling of sea-level pressure. Previous studies suggested that outflow serves to divert and to block the environmental flow at upper levels (Elsberry and Jeffries, 1996; Ryglicki et al., 2019). Under favorable circumstances, the outflow could reduce VWS in the upper levels near the storm, allowing it to intensify.

Following Finocchio et al. (2016), the upper-level horizontal circulation is decomposed into the divergent and rotational components, respectively. **Figure 11** presents the time evolution of divergent wind (top panels) and rotational wind (bottom panels) at the height of 17 km. Initially, two divergent flows occur at this level: one is close to the storm center and the other is located to the downshear-left region, coinciding with the TCA. With time, the latter appears to approach the vortex center so that the strongest divergent winds are concentrated in the

upshear flank. The repeated generation of TCA moving cyclonically and forming an eyewall is speculated that this process greatly enhances the upper divergent flows. The enhanced divergent flow acts as an important source of the blocking to the environmental flow and thus the reduction of VWS (Ryglicki et al., 2018a, Ryglicki et al., 2018b). Meanwhile, the rotational wind is reinforced as part of an anticyclonic circulation to the eastern flank of the storm center. Accordingly, an open outflow channel is established.

In the presence of outflow channels in the vicinity of the TC, it is reasonable to expect less energy expenditures since the outflow channels can provide low inertial stability so that minimal work is required to vent the outflow against the radial pressure gradient. Furthermore, as the outflow channels extend outward to a wider area, it may change the environmental conditions and thus their effect on core convection and tropical cyclone intensity. We will examine the relationship of the ambient upper-level outflow and the organization of TC convective entities. Two possible mechanisms may account for their interactions. On the one hand, the organized outflow plays an important role in sustaining the inner-core deep convection in developing TCs. It stands to reason that, as a branch of the secondary circulation,



strong outflow would curtail subsidence adjacent to the updrafts in the storm core. As such, this ventilation away from the core would promote compensating subsidence farther away from TC center (Pratt and Evans, 2009). On the other hand, this setup promotes a prolific deep convection, which is the natural source to drive the outflow. With these regards, it is important to understand how the outflow channel influences the convective activity by modulating the environmental conditions. To address this question, we take a close look at the storm's structure at upper levels.

Figure 12 displays the radius-height cross sections of the azimuthal mean temperature anomaly at four snapshots during the RI period. The temperature anomaly is relative to the area average between 300 and 500 km away from the storm center at each level. In early stage, there is an intense cold anomaly at the upper troposphere just above 17 km (**Figures 12A,B**). With time, this cold anomaly extends outward and gradually weakens and is replaced by the warm anomaly when the storm intensifies. Along with the rapid intensification, both the magnitude and height of the warm core increase. By 0000 UTC 8 August, the warm core is well established throughout the troposphere (**Figure 12D**). This is consistent with the finding by Rivoire et al. (2016).

Using temperature retrievals from the remote sensing platforms, Rivoire et al. (2016) examined the evolution of the fine-scale temperature structure within TCs. The authors found that the convective structure evolves highly asymmetrically with respect to the lifetime maximum intensity (LMI). More specifically, relative to the far-field structure, tropopause-level cooling occurs before a tropospheric TC warm core is established. In the present study, we also identify similar evolution feature. That is, the tropopause-level cooling precedes the warm core signal and move away from the storm during the RI period. Rogers et al. (2013) found that, the complex relation between the tropopause level cooling and the convective bursts is beneficial to intensifying TCs. We will investigate the possible processes leading to such cold anomalies.

Physically, both the long wave radiation due to the cloud anvils and the adiabatic cooling associated with deep CBs can contribute to the upper-level cooling. It is likely that, when the upper-level outflow jet channel is established and extends to a broader horizontal area, it can carry the hydrometers away from the storm center and forms a large cloud anvil. Gao et al. (2020) suggested that, compared with lower-layer VWS, upper-layer VWS is apt to produce stronger upper-level outflow in the downshear-left quadrant. This stronger

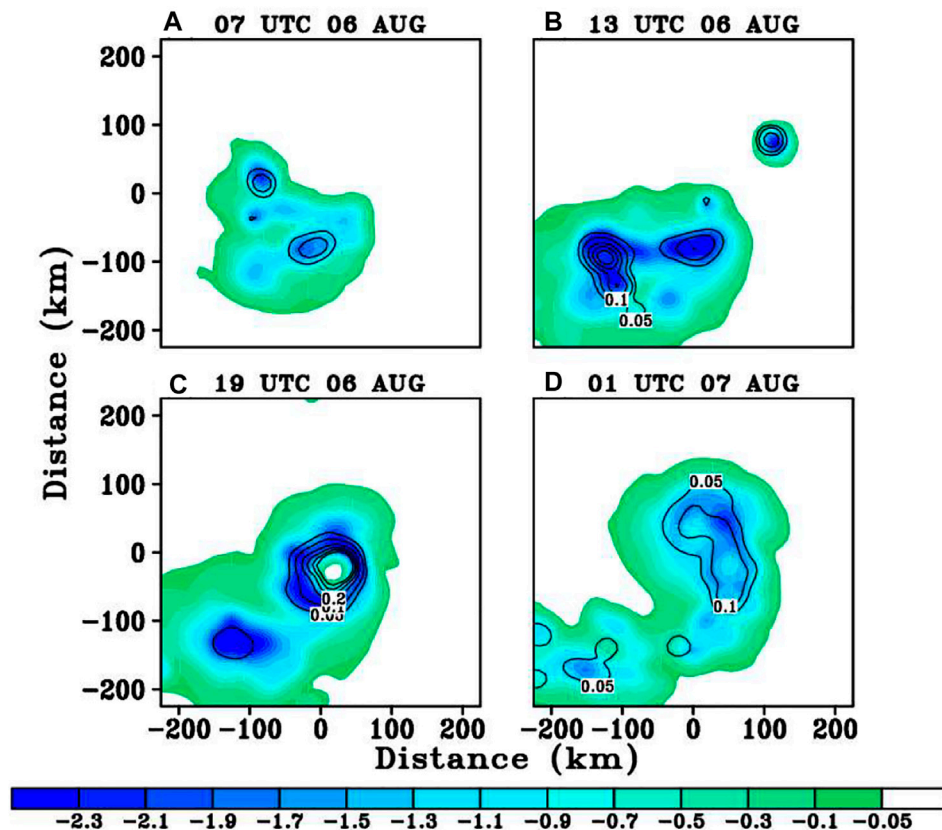


FIGURE 13 | Time evolution of the hydrometers (contour; units: g/kg) and temperature tendency due to radiation (Q_r , shaded; units: K/h) at 18-km from 0700 UTC 06 to 0100 UTC on 07 August.

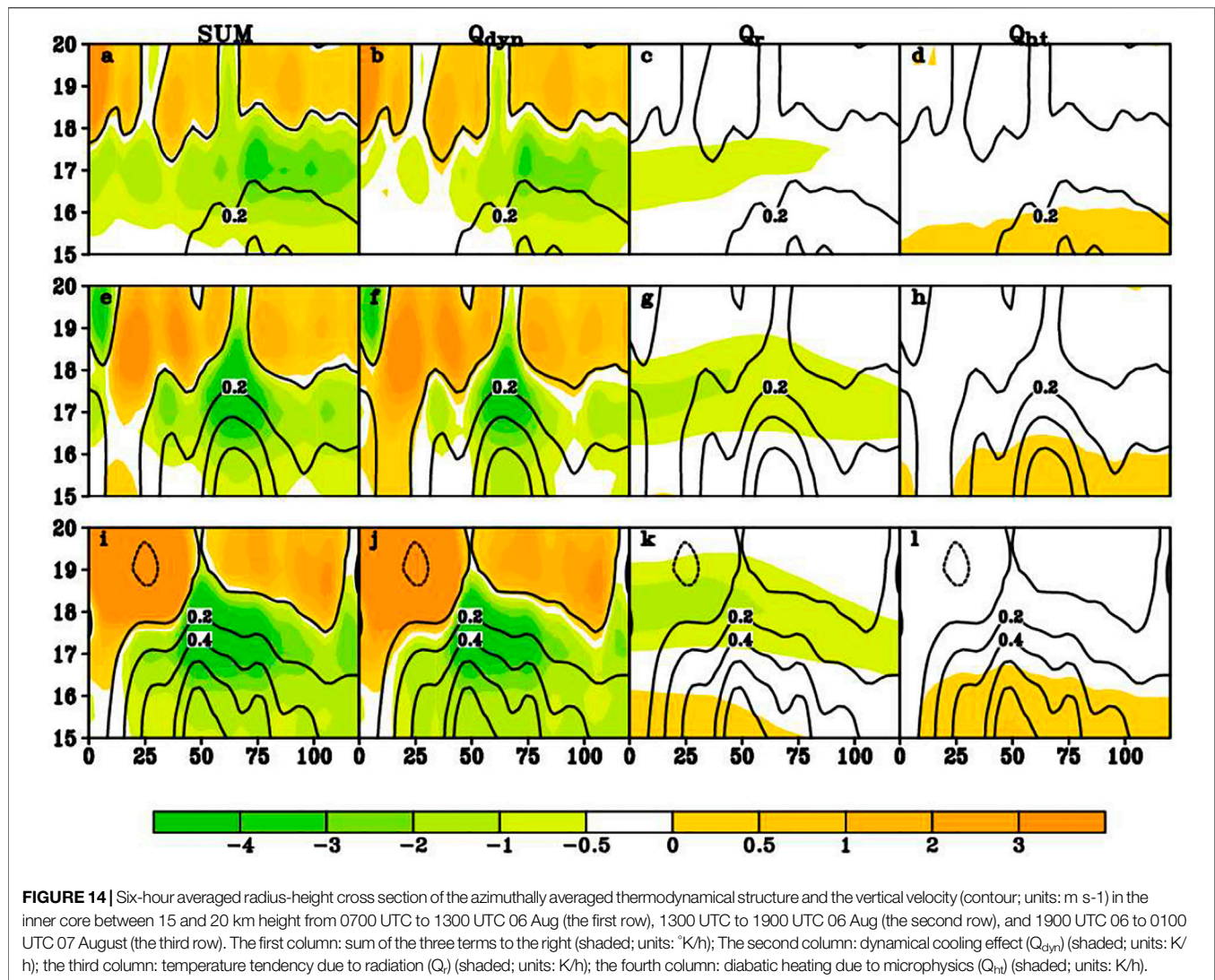
outflow transports more water vapor radially outward from the inner core to the outer core in the downshear-left quadrant, resulting in an organized stratiform cloud in the outer rainbands. The cloud avail will bring about a cooling due to the longwave radiation process. For further understanding, the upper-level hydrometers and temperature tendency due to radiation (Q_r) at 18 km are examined in **Figure 13**. As anticipated, there exists a large portion of hydrometers (mostly are ice and snow) in the downshear-left quadrant, since the outflow channel goes southwestward. Furthermore, there is an asymmetric pattern in Q_r with the minimum located in the downshear-left quadrant. These radiative patterns are consistent with the signatures of thick anvils.

Using a cloud-resolving model, Kuang and Hartmann (2007) demonstrated that convection has a cooling effect in the tropopause layer that significantly affects the thermal structure of the environment. In particular, the cold anomaly in the tropopause layer is found to be strongly tied to the convective cooling maximum. Here we calculate the dynamical cooling effect, which is formulated as follows:

$$Q_{dyn} = -\bar{w} \left(\partial_z T + \frac{g}{C_p} \right), \quad (1)$$

where \bar{w} is the vertical velocity, T is temperature, C_p is the specific heat of dry air at constant pressure, g is the gravity constant, $-\partial_z T$ represents the environmental lapse rate (γ), and $\frac{g}{C_p}$ is the dry adiabatic lapse rate (γ_d).

Figure 14 presents the time evolution of the averaged 6 h radius-height cross section of the azimuthally averaged dynamical cooling effect (Q_{dyn}), the temperature tendency due to the radiation (Q_r), and the diabatic heating due to the microphysics (Q_{ht}) and sum of the three terms from the height of 15–20 km from 0700 UTC 06 to 1300 UTC 06, 1300 UTC 06 to 1900 UTC 06, and 1900 UTC 06 to 0100 UTC 07 August. There is a dynamical cooling corresponding to the deep CBs. Conversely, the sinking motion may produce a dynamical warming in association with a warm anomaly. In the tropopause layer, there is indeed pronounced dynamical cooling at the storm center, which is closely associated with the updrafts of the deep CBs. The dynamical cooling by the inner updrafts is gradually increasing from 0700 UTC 06 to 0100 UTC 07 August, and the adiabatic cooling extends outward from the inner core with time. However, the microphysics heating remains basically stable. It is possible that, due to the scarcity of upper-level moisture supplies, the diabatic heating due to the microphysics cannot offset the adiabatic cooling and thus partially accounts for the upper-level cooling anomalies. Furthermore, the upper-level thermodynamical structure will modify



the static stability, which is possibly the primary driver of the invigoration of deep convection (Willoughby, 1998; Ruppert and Hohenegger, 2018), namely, cold anomalies at the tropopause locally destabilize the atmosphere, which enhances the deep convection and thus promote the development of outflow channels.

In short, the cold anomalies precede the establishment of a strong warm core, and this might reinforce the secondary circulation and indirectly stiffen the vortex against VWS. Recall that the strong deep CBs are mainly located to the downshear-left section, collocated with the outflow channel. To better understand the origin of convective updrafts, we now calculate the vertical velocity tendency due to the local buoyancy production, which is defined as follows:

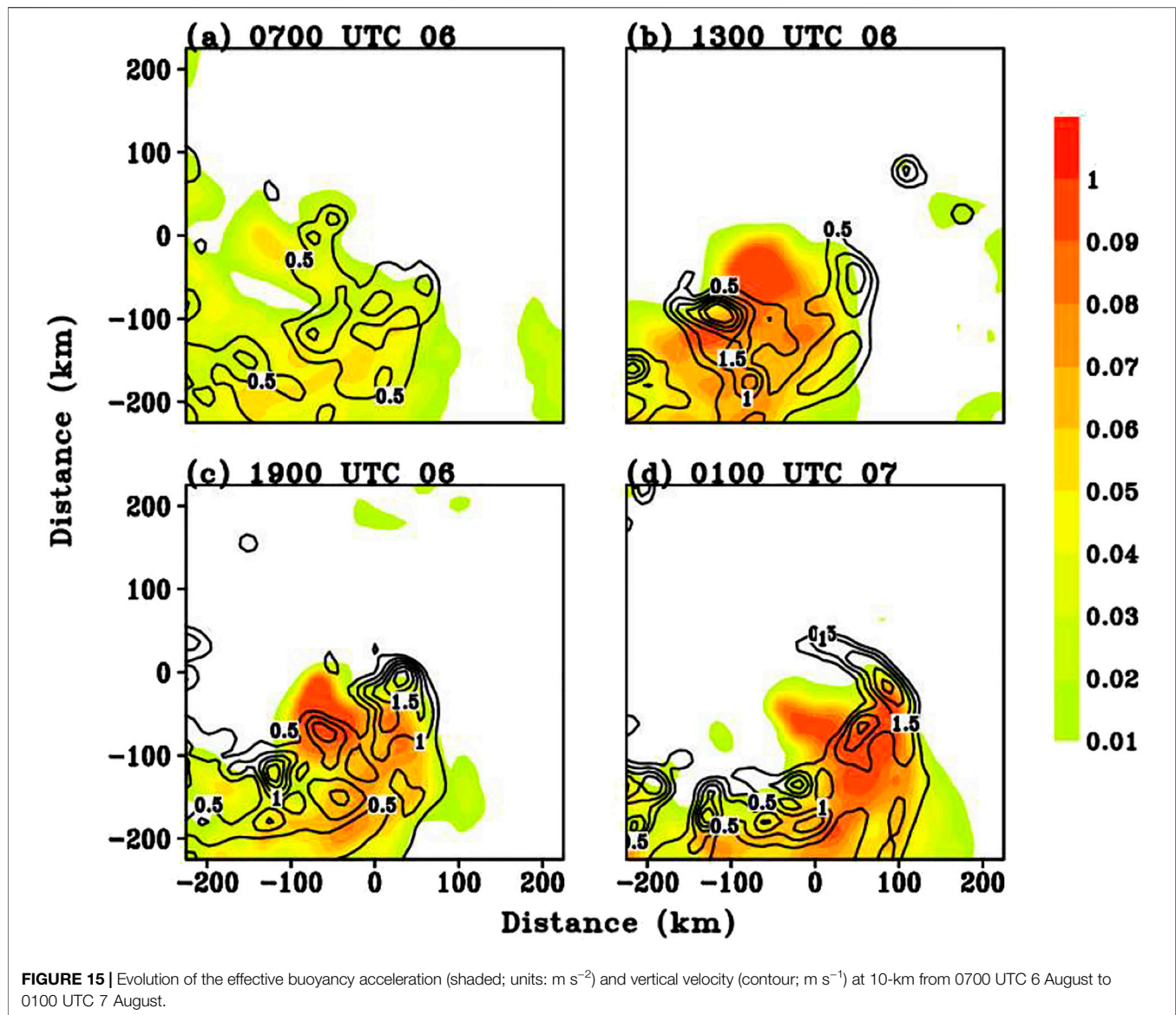
$$\frac{dw}{dt} = g \frac{T'}{\bar{T}}, \quad (2)$$

where the bar represents the azimuthal-mean, and the prime indicates the asymmetric component deviated from the

azimuthally averaged. Figure 15 presents the snapshots of spatial pattern of acceleration of vertical velocity due to the buoyancy. The largest vertical accelerations are confined at the southwestern flank of the storm center, where largely underneath the strongest upper-level cooling anomalies (Figure 13). To summarize, the upper-level thermal structure has shown a modulating effect on the TC intensification. However, the detailed underlying processes are less apparent. This interesting topic awaits for further studies.

CONCLUSION AND DISCUSSION

Finocchio et al. (2016) showed that, as with many other studies, the vertical wind shear (VWS) is in general not favorable for the TC intensification. However, the upper-level VWS has slightly less influence on the TC intensity than the low-level VWS. Super typhoon Lekima (2019) in the western North Pacific went through RI under an upper-



level VWS, defined between 500 and 200 hPa. In this study, a comprehensive analysis of Lekima is conducted using a numerical simulation. The focus is on the inner convection process and its relation with the cold anomalies at the tropopause under the upper level VWS during the RI process of Lekima. The main findings are summarized as the follows:

- 1) Under moderate upper-level easterly VWS, a wavenumber-one convective asymmetry indicated by strong upward motion and large reflectivity occur to the downshear-left side of the storm center in the initial stage. This tilting-induced convective asymmetry, constituted by ICBs, is then transported cyclonically to the upshear quadrant and wraps around the storm center and becomes as part of the eyewall. The upward motion is further enhanced, particularly in the upshear flank, to create upper-level divergent flow. As such,
- 2) In turn, upper-level conditions exert a modulating effect on the TC intensification, specifically the development of an outflow channel that evacuates mass from the storm center. The organized outflow plays an important role in sustaining the inner core deep convection via modulating the upper-level thermal structure. In the early stage, cold anomalies are generated in the tropopause layer, mainly due to the adiabatic cooling by the deep ICBs and radiative process associated with the cloud anvil. Physically, cold anomalies at the tropopause locally destabilize the atmosphere, enhance the deep convection, and thus promote the development of outflow

channels. The eyewall cloud continues to develop episodically through this process as it wrapped around the storm.

Our simulation reveals that the development of the eyewall occurred as a convective band wrapped inward from the downshear-left sector, which is closely related to the vertical realignment of the sheared vortex, in particular the alignment vertically over the upshear quadrants. This process suggests a different pathway of TC RI from the one described by Molinari et al. (2006), in which TC intensification under a sheared environment can be promoted when a TC vortex undergoes a “downshear reformation” to suppress the ventilation effect. Specifically, a new vortex is generated by the downshear convection, becomes the new storm center, and then intensifies through the combination of surface enthalpy fluxes and the absence of penetrative downshear-right downdrafts. It is argued that this intensification process was set into motion by the vertical wind shear in the presence of an environment with upward motion forced by the approaching upper tropospheric trough.

Finocchio et al. (2016) indicates the complexity of different VWS patterns, and different convective asymmetric structures likely result in different outcomes for the intensification of a TC. To gain better understanding, simulations with different initial vortex structures and environmental conditions will be conducted in the future. For instance, the different structure of initial vortices (i.e., sizes and vertical depths) may provide sources of uncertainty for RI, since the vertical realignment will depend

on these size factors. Furthermore, the heterogeneous environmental moisture conditions are also important for the asymmetric convective structure. More future works will focus on these topics.

DATA AVAILABILITY STATEMENT

The original contributions presented in the study are included in the article/Supplementary Material; further inquiries can be directed to the corresponding author.

AUTHOR CONTRIBUTIONS

QH and XG designed and executed field experiments. XG and MP analyzed data and wrote the article.

FUNDING

This work was jointly sponsored by the National Natural Science Foundation of China (42088101; 42175003) and the Science and Technology Innovation Project of Ningbo (Grant No. 2019B10025). The numerical calculations are performed on the supercomputing system in the Supercomputing Center of Nanjing University of Information Science & Technology.

REFERENCES

- Bhalachandran, S., Chavas, D. R., Marks, F. D., Jr., Dubey, S., Shreevastava, A., and Krishnamurti, T. N. (2020). Characterizing the Energetics of Vortex-Scale and Sub-vortex-scale Asymmetries during Tropical Cyclone Rapid Intensification Changes. *J. Atmos. Sci.* 77, 315–336. doi:10.1175/jas-d-19-0067.1
- Braun, S. A., Kakar, R., Zipser, E., Heymsfield, G., Albers, C., Brown, S., et al. (2013). NASA's Genesis and Rapid Intensification Processes (GRIP) Field Experiment. *Bull. Amer. Meteorol. Soc.* 94, 345–363. doi:10.1175/bams-d-11-00232.1
- Chen, H., and Gopalakrishnan, S. G. (2015). A Study on the Asymmetric Rapid Intensification of Hurricane Earl (2010) Using the HWRF System. *J. Atmos. Sci.* 72, 531–550. doi:10.1175/jas-d-14-0097.1
- Chen, H., and Zhang, D.-L. (2013). On the Rapid Intensification of Hurricane Wilma (2005). Part II: Convective Bursts and the Upper-Level Warm Core. *J. Atmos. Sci.* 70, 146–162. doi:10.1175/jas-d-12-062.1
- Chen, X., Wang, Y., Fang, J., and Xue, M. (2018). A Numerical Study on Rapid Intensification of Typhoon Vicente (2012) in the South China Sea. Part II: Roles of Inner-Core Processes. *J. Atmos. Sci.* 75, 235–255. doi:10.1175/jas-d-17-0129.1
- Chen, X., Wang, Y., Zhao, K., and Wu, D. (2017). A Numerical Study on Rapid Intensification of Typhoon Vicente (2012) in the South China Sea. Part I: Verification of Simulation, Storm-Scale Evolution, and Environmental Contribution. *Mon. Wea. Rev.* 145, 877–898. doi:10.1175/mwr-d-16-0147.1
- Corbosiero, K. L., and Molinari, J. (2002). The Effects of Vertical Wind Shear on the Distribution of Convection in Tropical Cyclones. *Mon. Wea. Rev.* 130, 2110–2123. doi:10.1175/1520-0493(2002)130<2110:teovws>2.0.co;2
- Dai, H., Zhao, K., Li, Q., Lee, W.-C., Ming, J., and Zhou, A. (2021). Quasi-periodic Intensification of Convective Asymmetries in the Outer Eyewall of Typhoon Lekima (2019). *Geophys. Res. Lett.* 48, e2020GL091633. doi:10.1029/2020gl091633
- Davis, C. A., Wang, W., Chen, S. S., Chen, Y., Corbosiero, K., DeMaria, M., et al. (2008). Prediction of Landfalling Hurricanes with the Advanced Hurricane WRF Model. *Mon. Wea. Rev.* 136 (6), 1990–2005. doi:10.1175/2007mwr2085.1
- DeMaria, M., Sampson, C. R., Knaff, J. A., and Musgrave, K. D. (2014). Is Tropical Cyclone Intensity Guidance Improving?. *Bull. Amer. Meteorol. Soc.* 95, 387–398. doi:10.1175/bams-d-12-00240.1
- Dudhia, J. (1989). Numerical Study of Convection Observed during the Winter Monsoon Experiment Using a Mesoscale Two-Dimensional Model. *J. Atmos. Sci.* 46, 3077–3107. doi:10.1175/1520-0469(1989)046<3077:nsocod>2.0.co;2
- Elsberry, R. L., and Jeffries, R. A. (1996). Vertical Wind Shear Influences on Tropical Cyclone Formation and Intensification during TCM-92 and TCM-93. *Mon. Wea. Rev.* 124, 1374–1387. doi:10.1175/1520-0493(1996)124<1374:vwsiot>2.0.co;2
- Elsberry, R. L., Lambert, T. D. B., and Boothe, M. A. (2007). Accuracy of Atlantic and Eastern North Pacific Tropical Cyclone Intensity Forecast Guidance. *Wea. Forecast.* 22, 747–762. doi:10.1175/waf1015.1
- Emanuel, K., DesAutels, C., Holloway, C., and Korty, R. (2004). Environmental Control of Tropical Cyclone Intensity. *J. Atmos. Sci.* 61, 843–858. doi:10.1175/1520-0469(2004)061<0843:ecotci>2.0.co;2
- Finocchio, P. M., Majumdar, S. J., Nolan, D. S., and Iskandarani, M. (2016). Idealized Tropical Cyclone Responses to the Height and Depth of Environmental Vertical Wind Shear. *Mon. Wea. Rev.* 144, 2155–2175. doi:10.1175/mwr-d-15-0320.1
- Frank, W. M., and Ritchie, E. A. (2001). Effects of Vertical Wind Shear on the Intensity and Structure of Numerically Simulated Hurricanes. *Mon. Wea. Rev.* 129, 2249–2269. doi:10.1175/1520-0493(2001)129<2249:eovwsi>2.0.co;2
- Gao, Q., Li, Q., and Dai, Y. (2020). Characteristics of the Outer Rainband Stratiform Sector in Numerically Simulated Tropical Cyclones: Lower-Layer Shear versus Upper-Layer Shear. *Adv. Atmos. Sci.* 37, 399–419. doi:10.1007/s00376-020-9202-y
- Ge, X., Li, T., and Peng, M. (2013). Effects of Vertical Shears and Midlevel Dry Air on Tropical Cyclone Developments*. *J. Atmos. Sci.* 70, 3859–3875. doi:10.1175/jas-d-13-066.1
- Gu, J.-F., Tan, Z.-M., and Qiu, X. (2015). Effects of Vertical Wind Shear on Inner-Core Thermodynamics of an Idealized Simulated Tropical Cyclone. *J. Atmos. Sci.* 72, 511–530. doi:10.1175/jas-d-14-0050.1
- Hazelon, A. T., Rogers, R. F., and Hart, R. E. (2017). Analyzing Simulated Convective Bursts in Two Atlantic Hurricanes. Part I: Burst Formation and Development. *Mon. Wea. Rev.* 145, 3073–3094. doi:10.1175/mwr-d-16-0267.1

- Hendricks, E. A., Montgomery, M. T., and Davis, C. A. (2004). The Role of “Vortical” Hot Towers in the Formation of Tropical Cyclone Diana (1984). *J. Atmos. Sci.* 61, 1209–1232. doi:10.1175/1520-0469(2004)061<1209:trovht>2.0.co;2
- Hendricks, E. A., Peng, M. S., Ge, X., and Li, T. (2011). Performance of a Dynamic Initialization Scheme in the Coupled Ocean-Atmosphere Mesoscale Prediction System for Tropical Cyclones (COAMPS-TC). *Wea. Forecast.* 26, 650–663. doi:10.1175/waf-d-10-05051.1
- Hoskins, B. J., McIntyre, M. E., and Robertson, A. W. (1985). On the Use and Significance of Isentropic Potential Vorticity Maps. *Quart. J. Roy. Meteorol. Soc.* 111, 877–946.
- Kain, J., and Fritsch, J. M. (1993). “Convective Parameterization for Mesoscale Models: The Kain-Fritsch Scheme,” in *The Representation of Cumulus Convection in Numerical Models*. Meteor. Monographs, 24. Editors K. A. Emanuel and D. J. Raymond (Boston, MA: American Meteorological Society), 246.
- Kanada, S., and Wada, A. (2015). Numerical Study on the Extremely Rapid Intensification of an Intense Tropical Cyclone: Typhoon Ida (1958). *J. Atmos. Sci.* 72, 4194–4217. doi:10.1175/jas-d-14-0247.1
- Kaplan, J., and DeMaria, M. (2003). Large-scale Characteristics of Rapidly Intensifying Tropical Cyclones in the North Atlantic basin. *Wea. Forecast.* 18, 1093–1108. doi:10.1175/1520-0434(2003)018<1093:lcorit>2.0.co;2
- Kaplan, J., Rozoff, C. M., DeMaria, M., Sampson, C. R., Kossin, J. P., Velden, C. S., et al. (2015). Evaluating Environmental Impacts on Tropical Cyclone Rapid Intensification Predictability Utilizing Statistical Models. *Wea. Forecast.* 30, 1374–1396. doi:10.1175/waf-d-15-0032.1
- Kuang, Z., and Hartmann, D. L. (2007). Testing the Fixed Anvil Temperature Hypothesis in a Cloud-Resolving Model. *J. Clim.* 20, 2051–2057. doi:10.1175/jcli4124.1
- Leighton, H., Gopalakrishnan, S., Zhang, J. A., Rogers, R. F., Zhang, Z., and Tallapragada, V. (2018). Azimuthal Distribution of Deep Convection, Environmental Factors, and Tropical Cyclone Rapid Intensification: A Perspective from HWRF Ensemble Forecasts of Hurricane Doudard (2014). *J. Atmos. Sci.* 75, 203–227. doi:10.1175/jas-d-17-0171.1
- Li, X., Davidson, N. E., Duan, Y., Tory, K. J., Sun, Z., and Cai, Q. (2020). Analysis of an Ensemble of High-Resolution WRF Simulations for the Rapid Intensification of Super Typhoon Rammasun (2014). *Adv. Atmos. Sci.* 37, 187–210. doi:10.1007/s00376-019-8274-z
- Lin, Y.-L., Farley, R. D., and Orville, H. D. (1983). Bulk Parameterization of the Snow Field in a Cloud Model. *J. Clim. Appl. Meteorol.* 22, 1065–1092. doi:10.1175/1520-0450(1983)022<1065:bpotsf>2.0.co;2
- Merrill, R. T. (1988). Characteristics of the Upper-Tropospheric Environmental Flow Around Hurricanes. *J. Atmos. Sci.* 45, 1665–1677. doi:10.1175/1520-0469(1988)045<1665:cotute>2.0.co;2
- Mlawer, E. J., Taubman, S. J., Brown, P. D., Iacono, M. J., and Clough, S. A. (1997). Radiative Transfer for Inhomogeneous Atmospheres: RRTM, a Validated Correlated-K Model for the Longwave. *J. Geophys. Res.* 102, 16663–16682. doi:10.1029/97jd00237
- Molinari, J., Dodge, P., Vollaro, D., Corbosiero, K. L., Jr., and Marks, F. (2006). Mesoscale Aspects of the Downshear Reformation of a Tropical Cyclone. *J. Atmos. Sci.* 63, 341–354. doi:10.1175/jas3591.1
- Molinari, J., Vollaro, D., and Corbosiero, K. L. (2004). Tropical Cyclone Formation in a Sheared Environment: A Case Study. *J. Atmos. Sci.* 61, 2493–2509. doi:10.1175/jas3291.1
- Montgomery, M., and Smith, R. (2014). Paradigms for Tropical Cyclone Intensification. *AmoJ* 64, 37–66. doi:10.22499/2.6401.005
- Montgomery, M. T., Nicholls, M. E., Cram, T. A., and Saunders, A. B. (2006). A Vortical Hot Tower Route to Tropical Cyclogenesis. *J. Atmos. Sci.* 63, 355–386. doi:10.1175/jas3604.1
- Montgomery, M. T., Zhang, J. A., and Smith, R. K. (2014). An Analysis of the Observed Low-Level Structure of Rapidly Intensifying and Mature Hurricane Earl (2010). *Q.J.R. Meteorol. Soc.* 140, 2132–2146. doi:10.1002/qj.2283
- Moon, Y., and Nolan, D. S. (2010). The Dynamic Response of the hurricane Wind Field to Spiral Rainband Heating. *J. Atmos. Sci.* 67, 1779–1805. doi:10.1175/2010jas3171.1
- Nolan, D. S., Moon, Y., and Stern, D. P. (2007). Tropical Cyclone Intensification from Asymmetric Convection: Energetics and Efficiency. *J. Atmos. Sci.* 64, 3377–3405. doi:10.1175/jas3988.1
- Pratt, A. S., and Evans, J. L. (2009). Potential Impacts of the Saharan Air Layer on Numerical Model Forecasts of North Atlantic Tropical Cyclogenesis. *Wea. Forecast.* 24, 420–435. doi:10.1175/2008waf2007090.1
- Rheme, J. R., Sisko, C. A., and Knabb, R. D. (2006). “On the Calculation of Vertical Shear: An Operational Perspective,” in 27th Conference. On Hurricanes And Tropical Meteorology, Monterey, CA, April 27, 2006. American Meteorological Society. Available at: https://ams.confex.com/ams/27Hurricanes/techprogram/paper_108724.htm
- Riemer, M., and Laliberté, F. (2015). Secondary Circulation of Tropical Cyclones in Vertical Wind Shear: Lagrangian Diagnostic and Pathways of Environmental Interaction. *J. Atmos. Sci.* 72, 3517–3536. doi:10.1175/jas-d-14-0350.1
- Riemer, M., Montgomery, M. T., and Nicholls, M. E. (2010). A New Paradigm for Intensity Modification of Tropical Cyclones: Thermodynamic Impact of Vertical Wind Shear on the Inflow Layer. *Atmos. Chem. Phys.* 10, 3163–3188. doi:10.5194/acp-10-3163-2010
- Rivoire, L., Birner, T., and Knaff, J. (2016). Evolution of the Upper-Level thermal Structure in Tropical Cyclones. *Geophys. Res. Lett.* 43 (10), 530–537. doi:10.1002/2016gl070622
- Rogers, R. F., Reasor, P. D., and Zhang, J. A. (2015). Multiscale Structure and Evolution of Hurricane Earl (2010) during Rapid Intensification. *Mon. Wea. Rev.* 143, 536–562. doi:10.1175/mwr-d-14-00175.1
- Rogers, R. F., Zhang, J. A., Zawislak, J., Jiang, H., Alvey, G. R., Zipser, E. J., et al. (2016). Observations of the Structure and Evolution of hurricane Edouard (2014) during Intensity Change. Part II: Kinematic Structure and the Distribution of Deep Convection. *Mon. Wea. Rev.* 144, 3355–3376. doi:10.1175/mwr-d-16-0017.1
- Rogers, R., Reasor, P., and Lorsolo, S. (2013). Airborne Doppler Observations of the Inner-Core Structural Differences between Intensifying and Steady-State Tropical Cyclones. *Mon. Wea. Rev.* 141, 2970–2991. doi:10.1175/mwr-d-12-00357.1
- Ruppert, J. H., and Hohenegger, C. (2018). Diurnal Circulation Adjustment and Organized Deep Convection. *J. Clim.* 31, 4899–4916. doi:10.1175/jcli-d-17-0693.1
- Ryglicki, D. R., Cossuth, J. H., Hodyss, D., and Doyle, J. D. (2018a). The Unexpected Rapid Intensification of Tropical Cyclones in Moderate Vertical Wind Shear. Part I: Overview and Observations. *Mon. Wea. Rev.* 146, 3773–3800. doi:10.1175/mwr-d-18-0020.1
- Ryglicki, D. R., Doyle, J. D., Hodyss, D. H., Cossuth, J. H., Jin, Y., Viner, K. C., et al. (2019). The Unexpected Rapid Intensification of Tropical Cyclones in Moderate Vertical Wind Shear Part III: Outflow-Environment Interaction. *Mon. Wea. Rev.* 147 (8), 2919–2940. doi:10.1175/mwr-d-18-0370.1
- Ryglicki, D. R., Doyle, J. D., Jin, Y., Hodyss, D., and Cossuth, J. H. (2018b). The Unexpected Rapid Intensification of Tropical Cyclones in Moderate Vertical Wind Shear. Part II: Vortex Tilt. *Mon. Wea. Rev.* 146, 3801–3825. doi:10.1175/mwr-d-18-0021.1
- Sanger, N. T., Montgomery, M. T., Smith, R. K., and Bell, M. M. (2014). An Observational Study of Tropical Cyclone Spinup in Supertyphoon Jangmi (2008) from 24 to 27 September. *Mon. Wea. Rev.* 142, 3–28. doi:10.1175/mwr-d-12-00306.1
- Shi, D. L., and Chen, G. H. (2021). Double Warm-Core Structure and Potential Vorticity Diagnosis during the Rapid Intensification of Supertyphoon Lekima (2019). *J. Atmos. Sci.* 78 (8), 2471–2492. doi:10.1175/jas-d-20-0383.1
- Smith, R. K., and Montgomery, M. T. (2015). Toward Clarity on Understanding Tropical Cyclone Intensification. *J. Atmos. Sci.* 72, 3020–3031. doi:10.1175/jas-d-15-0017.1
- Smith, R. K., Zhang, J. A., and Montgomery, M. T. (2017). The Dynamics of Intensification in a Hurricane Weather Research and Forecasting Simulation of Hurricane Earl (2010). *Q.J.R. Meteorol. Soc.* 143, 293–308. doi:10.1002/qj.2922
- Tang, B., and Emanuel, K. (2010). Midlevel Ventilation’s Constraint on Tropical Cyclone Intensity. *J. Atmos. Sci.* 67, 1817–1830. doi:10.1175/2010jas3318.1
- Tang, B., and Emanuel, K. (2012). Sensitivity of Tropical Cyclone Intensity to Ventilation in an Axisymmetric Model. *J. Atmos. Sci.* 69, 2394–2413. doi:10.1175/jas-d-11-0232.1
- Titley, D. W., and Elsberry, R. L. (2000). Large Intensity Changes in Tropical Cyclones: A Case Study of Supertyphoon Flo during TCM-90. *Mon. Wea. Rev.* 128, 3356–3573. doi:10.1175/1520-0493(2000)128<3556:licitc>2.0.co;2
- Vigh, J. L., and Schubert, W. H. (2009). Rapid Development of the Tropical Cyclone Warm Core. *J. Atmos. Sci.* 66, 3335–3350. doi:10.1175/2009jas3092.1

- Wadler, J. B., Zhang, J. A., Jaimes, B., and Shay, L. K. (2018). Downdrafts and the Evolution of Boundary Layer Thermodynamics in Hurricane Earl (2010) before and during Rapid Intensification. *Mon. Wea. Rev.* 146, 3534–3565. doi:10.1175/mwr-d-18-0090.1
- Wang, B., and Xie, X. (1996). Low-Frequency Equatorial Waves in Vertically Sheared Zonal Flow. Part I: Stable Waves. *J. Atmos. Sci.* 53 (3), 449–467. doi:10.1175/1520-0469(1996)053<0449:lfewiv>2.0.co;2
- Wang, B., and Zhou, X. (2008). Climate Variation and Prediction of Rapid Intensification in Tropical Cyclones in the Western North Pacific. *Meteorol. Atmos. Phys.* 99, 1–16. doi:10.1007/s00703-006-0238-z
- Wang, Y., Rao, Y., Tan, Z.-M., and Schönmann, D. (2015). A Statistical Analysis of the Effects of Vertical Wind Shear on Tropical Cyclone Intensity Change over the Western North Pacific. *Mon. Wea. Rev.* 143, 3434–3453. doi:10.1175/mwr-d-15-0049.1
- Wang, Y., and Wu, C.-C. (2004). Current Understanding of Tropical Cyclone Structure and Intensity Changes? a Review. *Meteorol. Atmos. Phys.* 87, 257–278. doi:10.1007/s00703-003-0055-6
- Willoughby, H. E. (1998). Tropical Cyclone Eye Thermodynamics. *Mon. Wea. Rev.* 126, 3053–3067. doi:10.1175/1520-0493(1998)126<3053:tcet>2.0.co;2
- Wong, M. L. M., and Chan, J. C. L. (2004). Tropical Cyclone Intensity in Vertical Wind Shear. *J. Atmos. Sci.* 61, 1859–1876. doi:10.1175/1520-0469(2004)061<1859:tciiwv>2.0.co;2
- Zeng, Z., Chen, L., and Wang, Y. (2008). An Observational Study of Environmental Dynamical Control of Tropical Cyclone Intensity in the Atlantic. *Mon. Wea. Rev.* 136, 3307–3322. doi:10.1175/2008mwr2388.1
- Zeng, Z., Wang, Y., Duan, Y., Chen, L., and Gao, Z. (2010). On Sea Surface Roughness Parameterization and its Effect on Tropical Cyclone Structure and Intensity. *Adv. Atmos. Sci.* 27, 337–355. doi:10.1007/s00376-009-8209-1
- Zeng, Z., Wang, Y., and Wu, C.-C. (2007). Environmental Dynamical Control of Tropical Cyclone Intensity-An Observational Study. *Mon. Wea. Rev.* 135, 38–59. doi:10.1175/mwr3278.1
- Zhang, D.-L., and Kieu, C. Q. (2006). Potential Vorticity Diagnosis of a Simulated Hurricane. Part II: Quasi-Balanced Contributions to Forced Secondary Circulations. *J. Atmos. Sci.* 63, 2898–2914. doi:10.1175/jas3790.1
- Zhang, F., and Tao, D. (2013). Effects of Vertical Wind Shear on the Predictability of Tropical Cyclones. *J. Atmos. Sci.* 70, 975–983. doi:10.1175/jas-d-12-0133.1
- Zhang, X., Duan, Y., Wang, Y., Wei, N., and Hu, H. (2017). A High-Resolution Simulation of Supertyphoon Rammasun (2014)-Part I: Model Verification and Surface Energetics Analysis. *Adv. Atmos. Sci.* 34, 757–770. doi:10.1007/s00376-017-6255-7

Conflict of Interest: The authors declare that the research was conducted in the absence of any commercial or financial relationships that could be construed as a potential conflict of interest.

Publisher's Note: All claims expressed in this article are solely those of the authors and do not necessarily represent those of their affiliated organizations, or those of the publisher, the editors and the reviewers. Any product that may be evaluated in this article, or claim that may be made by its manufacturer, is not guaranteed or endorsed by the publisher.

Copyright © 2021 Huang, Ge and Peng. This is an open-access article distributed under the terms of the Creative Commons Attribution License (CC BY). The use, distribution or reproduction in other forums is permitted, provided the original author(s) and the copyright owner(s) are credited and that the original publication in this journal is cited, in accordance with accepted academic practice. No use, distribution or reproduction is permitted which does not comply with these terms.



Trends in Western North Pacific Tropical Cyclone Intensity Change Before Landfall

Qingyuan Liu¹, Jinjie Song^{*1,2} and Philip J. Klotzbach³

¹Nanjing Joint Institute for Atmospheric Sciences, Chinese Academy of Meteorological Sciences, Nanjing, China, ²State Key Laboratory of Severe Weather, Chinese Academy of Meteorological Sciences, Beijing, China, ³Department of Atmospheric Science, Colorado State University, Fort Collins, CO, United States

OPEN ACCESS

Edited by:

Qingqing Li,
Nanjing University of Information
Science and Technology, China

Reviewed by:

Jiuwei Zhao,
Nanjing University of Information
Science and Technology, China
Si Gao,
Sun Yat-sen University, China

*Correspondence:

Jinjie Song
songjinjie@qq.com

Specialty section:

This article was submitted to
Atmospheric Science,
a section of the journal
Frontiers in Earth Science

Received: 20 September 2021

Accepted: 14 October 2021

Published: 03 November 2021

Citation:

Liu Q, Song J and Klotzbach PJ (2021)
Trends in Western North Pacific
Tropical Cyclone Intensity Change
Before Landfall.
Front. Earth Sci. 9:780353.
doi: 10.3389/feart.2021.780353

This study investigates the long-term trend in the average 24-h intensity change (ΔV_{24}) of western North Pacific (WNP) tropical cyclones (TCs) before landfall during June–November for the period from 1970–2019. We find a significant increasing trend in basin-averaged ΔV_{24} during 1970–2019. The increase in ΔV_{24} is significant over the northern South China Sea (17.5°–25°N, 107.5°–120°E) and to the east of the Philippines (7.5°–15°N, 122.5°–132.5°E), implying a slower weakening rate before landfall for the South China Sea and an increased intensification rate before landfall for the region east of the Philippines. We find a significant linkage between changes in ΔV_{24} and several large-scale environmental conditions. The increased ΔV_{24} before landfall in the above two regions is induced by a warmer ocean (e.g., higher sea surface temperatures, maximum potential intensity and TC heat potential) and greater upper-level divergence, with a moister mid-level atmosphere also aiding the ΔV_{24} increase east of the Philippines. Our study highlights an increasing tendency of ΔV_{24} before landfall, consistent with trends in ΔV_{24} over water and over land as found in previous publications.

Keywords: tropical cyclone, intensity change, western North Pacific, before landfall, environmental changes

INTRODUCTION

Tropical cyclones (TCs) are one of the most devastating global natural disasters, inducing large economic losses as well as fatalities for various coastal regions. Among TC metrics, TC intensity change has long been regarded as a major challenge for both the scientific research and operational forecasting communities (Courtney et al., 2019; Hendricks et al., 2019). TC intensity change is the result of a complex interaction between various internal influences that are related to the structure and internal processes of the TC itself and various external influences that are controlled by the large-scale atmospheric and oceanic environment (Hendricks et al., 2019).

Given active research on the relationship between TCs and climate change, there has been an increasing focus on temporal variations in TC intensity change. Bhatia et al. (2019) reported an increasing trend in the mean TC 24-h intensity change (ΔV_{24}) over the globe and for the Atlantic basin specifically since the 1980s. They also found a broadening distribution of ΔV_{24} , due to increasing intensification and weakening rates. Similar changes in the ΔV_{24} distribution from 1982 to 2019 were shown over the western North Pacific (WNP) in Song et al. (2020). The increasing intensification rate is associated with an increasing proportion of rapid intensification (RI) cases that likely has an anthropogenic warming component (Bhatia et al., 2019). By comparison, there is a linkage between the increasing weakening rate and the increasing proportion of rapid weakening

(RW) cases, possibly resulting from increasing sea surface temperature (SST) gradients in the subtropics (Song et al., 2020). Note that all of the above findings are only based on TC records over the open ocean.

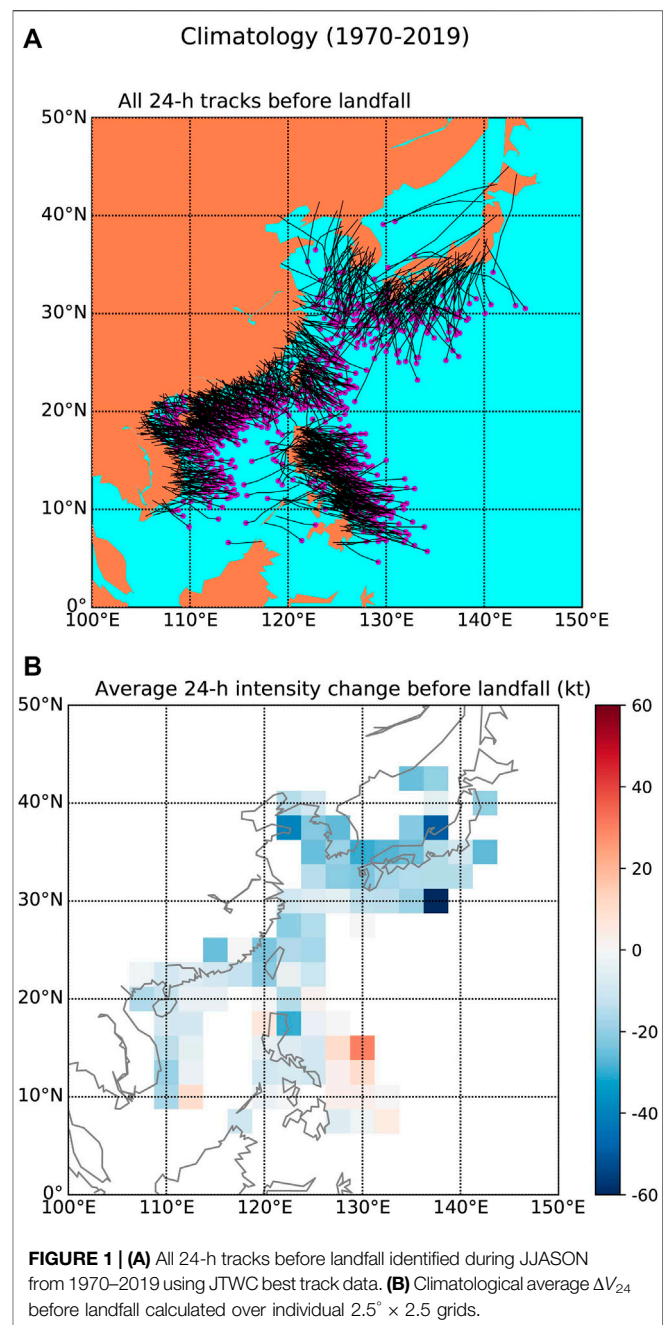
By analyzing TC samples over land, Liu et al. (2020) demonstrated a slight decreasing trend in the TC weakening rate after landfall in mainland China during 1980–2018, implying an increasing trend in overland ΔV_{24} . This was attributed to decreasing vertical wind shear (VWS), increasing upper-level divergence and increasing mid-level upward motion (Liu et al., 2020). Over mainland China, the decreasing TC weakening rate is consistent with the increasing decaying timescale of landfalling TCs, as shown in Song et al. (2021). They found a slower decay in the first 24 h after landfall, primarily driven by increasing low-level vorticity in coastal regions of China (Song et al., 2021). Additionally, Li and Chakraborty (2020) reported a slowing trend in the decay of landfalling TCs over the North Atlantic, mainly from a contemporaneous increase in SST.

There are still 24-h TC tracks excluded from consideration in the aforementioned previous publications, which examined either five 6-hourly records occurring over water or five 6-hourly records over land. The samples that have been excluded in previous publications move from water to land during the 24-h period, and are consequently expected to have complex ΔV_{24} s, due to multiple environmental and land surface changes that occur during the 24-h period. The most important of these intensity change questions is the ΔV_{24} before landfall, which is critical for reducing damage and loss of life. Rappaport et al. (2010) studied the intensity change of TCs making landfall along the U.S. Gulf Coast, in which TC tracks in the 48 h prior to landfall were considered. They found that, on average, category 1–2 (category 3–5) hurricanes strengthened (weakened) before landfall, and this observed trend could be partially explained by environmental conditions.

Up until now, it is still unclear what environmental conditions are related to ΔV_{24} before landfall over the WNP and their potential long-term trends. The reminder of this study is arranged as follow. **Data** introduces the data used in this study. **Trends in ΔV_{24} Before Landfall** examines the long-term trends in the average ΔV_{24} before landfall and its contributors. **Changes in Environmental Conditions** highlights changes in environmental variables and their links to changes in ΔV_{24} before landfall. A summary is given in **Summary**.

DATA

WNP TC best track data used in this study are given by the Joint Typhoon Warning Center (JTWC), the Japan Meteorological Agency (JMA), the China Meteorological Administration (CMA) and the Hong Kong Observatory (HKO) including 6-hourly TC central positions and maximum sustained winds, as compiled in the International Best Track Archive for Climate Stewardship (IBTrACS) v04r00 (Knapp et al., 2010). Owing to the relatively low quality of the TC intensity estimates in the best track data prior to the 1970s (Camargo and Sobel, 2005), we focus on the period from 1970–2019. To reduce the uncertainty in detecting weak TCs (e.g., tropical depressions) that are induced by changing observational platforms (Klotzbach and Landsea,



2015), we only consider TCs with a lifetime maximum intensity of at least 34 kt. TCs forming during June–November (JJASON) are analyzed here, accounting for ~85% of the annual total number of WNP TCs (Song and Klotzbach, 2019). Similar to Rappaport et al. (2010) and Zhu et al. (2021), a 24-h track before landfall is identified in this study as when the last record is over land and the previous four 6-h records are all over water. Any 24-h tracks with records labeled as extratropical cyclones in the best track data are removed, in order to minimize the influence of extratropical transition on intensity change. In total, there are 4307 identified 24-h tracks before landfall over the WNP (Figure 1A). The mid-points of these tracks are further

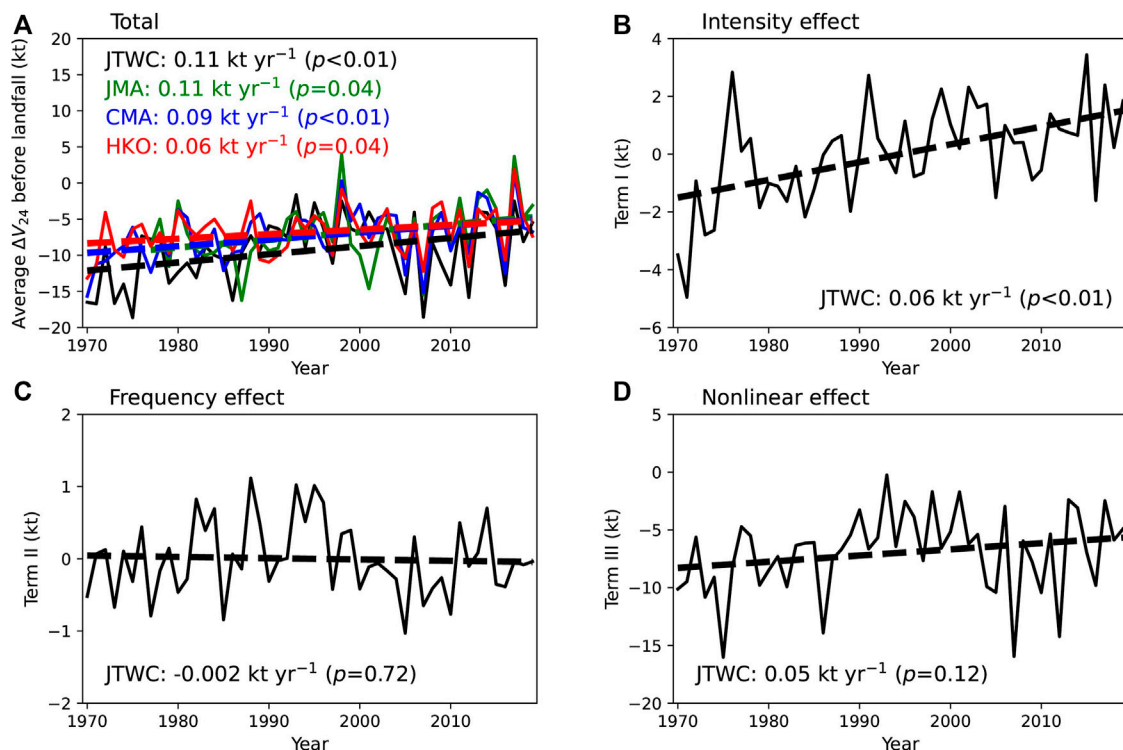


FIGURE 2 | Annual averages of ΔV_{24} before landfall during JJASON for the period from 1970–2019. Black, green, blue, and red lines in (A) are for JTWC, JMA, CMA, and HKO, respectively. The original values and their three components are shown in (A) and in (B–D), respectively. The dashed lines are obtained by least squares, while the trends and their respective significance levels are shown in the panels.

interpolated onto a $2.5^\circ \times 2.5^\circ$ grid. Our results are not significantly changed if a $5^\circ \times 5^\circ$ resolution is used instead (figure not shown).

Monthly large-scale environmental conditions are provided by the fifth generation European Centre for Medium-Range Weather Forecasts (ECMWF) reanalysis of the global climate (ERA5; Hersbach and Bell, 2020), including SST, 200-hPa temperature, 700–500-hPa relative humidity, 850-hPa relative vorticity, 200-hPa divergence and 850–200-hPa VWS. The original ERA5 data over a grid of $0.25^\circ \times 0.25^\circ$ are re-gridded to a resolution of $2.5^\circ \times 2.5^\circ$, in order to highlight large-scale features. Maximum potential intensity (MPI; Emanuel, 1988) is calculated from monthly ERA5 data. TC heat potential (TCHP), which measures ocean heat content that is warmer than 26°C (DeMaria et al., 2005), is estimated using monthly subsurface temperature profiles from the ECMWF Ocean Reanalysis System 5 (ORAS5; Zuo et al., 2019) with a resolution of $1^\circ \times 1^\circ$.

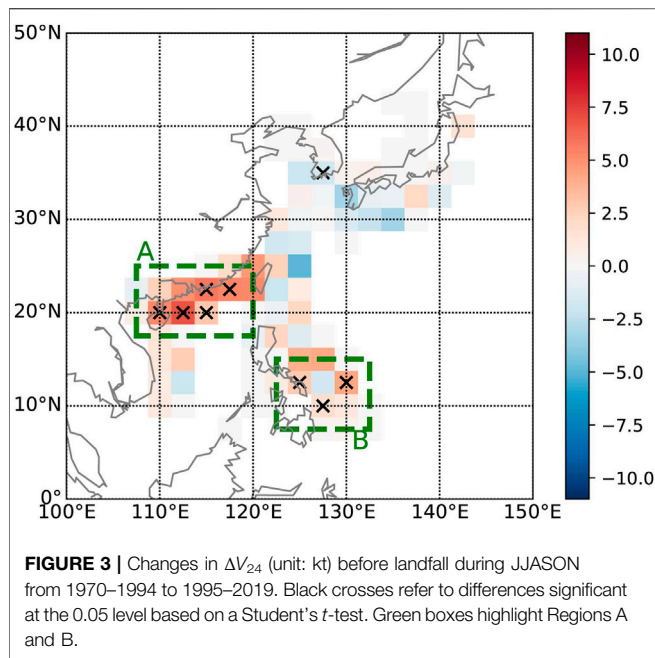
TRENDS IN ΔV_{24} BEFORE LANDFALL

Figure 1A shows all of the 24-h tracks before landfall over the WNP during JJASON between 1970 and 2019. These tracks are located near the coasts of most East Asian and Southeast Asian countries. While it is typically viewed that TCs weaken as they approach land due to interactions with topography, the average

ΔV_{24} before landfall exhibits obvious spatial inhomogeneities (**Figure 1B**). There are positive average ΔV_{24} s near the Philippines and to the southeast of Vietnam, indicating that TCs, on average, intensify within 24 h prior to landfall in these regions. While Brand and Brelloch (1973) only examined a limited number of TCs, they reported an average TC intensity increase prior to hitting the Philippines. This TC intensity increase is likely caused by environmental conditions near the Philippines being more characteristic of an oceanic environment. Furthermore, negative average ΔV_{24} s are observed along other WNP coastlines, and the magnitude of the negative ΔV_{24} s generally increases with latitude. This result implies that TCs tend to weaken at a greater rate prior to landfall at higher latitudes, possibly as a result of both lower SSTs and increased VWS at higher latitudes.

Figure 2A displays a significant increasing trend for the JJASON average ΔV_{24} during 1970–2019, with increasing trends of 0.11 kt yr^{-1} ($p < 0.01$), 0.11 kt yr^{-1} ($p = 0.04$), 0.09 kt yr^{-1} ($p < 0.01$) and 0.06 kt yr^{-1} ($p = 0.04$) for the best track data from the JTWC, the JMA, the CMA and the HKO, respectively. Given that these increasing trends are relatively consistent between the four agencies, we use the JTWC dataset for all of the remaining analysis.

To examine the relative contributions of incorporated variables to the overall ΔV_{24} change, a decomposition of the average ΔV_{24} in each year ($\overline{\Delta V_{24m}}$) is performed as:



$$\overline{\Delta V}_{24m}(t) = \sum_{\lambda, \varphi} p(\lambda, \varphi, t) \times \overline{\Delta V}_{24}(\lambda, \varphi, t). \quad (1)$$

Here, λ , φ and t refer to latitude, longitude and year, respectively. $p(\lambda, \varphi, t)$ denotes the spatial distribution of TC occurrence over a $2.5^\circ \times 2.5^\circ$ grid, while $\overline{\Delta V}_{24}(\lambda, \varphi, t)$ represents the average ΔV_{24} in the corresponding grid. Eq. 1 can be further written as:

$$\overline{\Delta V}_{24m}(t) = \sum_{\lambda, \varphi} [p^c(\lambda, \varphi) + p^a(\lambda, \varphi, t)] \times [\overline{\Delta V}_{24}^c(\lambda, \varphi) + \overline{\Delta V}_{24}^a(\lambda, \varphi, t)]. \quad (2)$$

The superscripts “c” and “a” refer to the climatological average value and the anomaly relative to the climatology, respectively. Finally, Eq. 2 is decomposed as:

$$\begin{aligned} \overline{\Delta V}_{24m}(t) = & \underbrace{\sum_{\lambda, \varphi} p^c(\lambda, \varphi) \times \overline{\Delta V}_{24}^c(\lambda, \varphi)}_{\text{climatology}} \\ & + \underbrace{\sum_{\lambda, \varphi} p^c(\lambda, \varphi) \times \overline{\Delta V}_{24}^a(\lambda, \varphi, t)}_{\text{Term I: intensity effect}} + \underbrace{\sum_{\lambda, \varphi} p^a(\lambda, \varphi, t) \times \overline{\Delta V}_{24}^c(\lambda, \varphi)}_{\text{Term II: frequency effect}} \\ & + \underbrace{\sum_{\lambda, \varphi} p^a(\lambda, \varphi, t) \times \overline{\Delta V}_{24}^a(\lambda, \varphi, t)}_{\text{Term III: nonlinear effect}}. \end{aligned} \quad (3)$$

In Eq. 3, because the climatology term does not vary with time, the temporal change in the average ΔV_{24} can only be influenced by the three other terms, namely the frequency effect, the intensity effect and the nonlinear effect.

There is a significant increasing trend in ΔV_{24} related to the intensity effect, with a slope of 0.06 kt yr^{-1} ($p < 0.01$), accounting for approximately one-half of the total ΔV_{24} trend (Figure 2B). By contrast, we find no significant trend in ΔV_{24} related to the frequency effect, whose rate is lower than the total ΔV_{24} trend by one order of magnitude (Figure 2C). The trend in ΔV_{24} related to the nonlinear effect is not significant, although its magnitude is comparable to that related to the intensity effect (Figure 2D). The

reason that the nonlinear trend is not significant may be due to the larger standard deviation of this term (3.5 kt) relative to the intensity effect (1.7 kt). These results indicate that the intensity effect is the primary driver of the long-term changes in the total ΔV_{24} , while the frequency effect and the nonlinear effect have a lesser impact.

Figure 3 displays the differences in ΔV_{24} before landfall during JJASON between two sub-periods (1970–1994 and 1995–2019). Similar features are obtained if long-term ΔV_{24} trends from 1970–2019 are displayed instead (figure not shown). Significant increases in ΔV_{24} are concentrated over two regions: one is located over the northern South China Sea (SCS) (Region A: 17.5° – 25° N, 107.5° – 120° E), while the other is located to the east of the Philippines (Region B: 7.5° – 15° N, 122.5° – 132.5° E). Given the climatological ΔV_{24} distribution in Figure 1A, the ΔV_{24} increase in Region A (Region B) implies a slower weakening (stronger intensification) of TCs before landfall. By comparison, changes in ΔV_{24} over other regions are of a lower magnitude and are less significant. We thus conclude that the increase in basin-averaged ΔV_{24} is primarily induced by the ΔV_{24} increases over Regions A and B.

CHANGES IN ENVIRONMENTAL CONDITIONS

Although TCs make landfall near the end of the identified 24-h tracks, they are over the ocean during most of the 24-h period. Consequently, these 24-h tracks are more likely influenced by the environment over water than over land. Figures 4A–E illustrates changes in thermodynamic conditions during JJASON from 1970–1994 to 1995–2019. There are significant increases in SST, MPI and TCHP over almost all of the WNP (Figures 4A–C), consistent with the global warming that has occurred since the middle of the last century. Compared with the period from 1970–1994, higher SST, MPI and TCHP in 1995–2019 inhibit the decaying of TCs before landfall over Region A and favor the intensification of TCs before landfall over Region B. There are no significant changes in 200-hPa temperature over Regions A and B from 1970–1994 to 1995–2019 (Figure 4D). While 200-hPa temperature has also increased, the increases in SST and 200-hPa temperature are of comparable magnitude, yielding a thermodynamic environment that is more favorable for TC intensification (Tuleya et al., 2016). In general, the mid-level atmosphere has become moister over the ocean and drier over land from 1995–2019 relative to 1970–1994 (Figure 4E). Although the 700–500-hPa relative humidity has only changed slightly over Region A, relative humidity has increased significantly over Region B. A moister environment is favorable for TC development and intensification, helping to increase the TC intensification rate before landfall over Region B. Given that MPI is a function of SST and the profiles of atmospheric temperature and humidity (Emanuel, 1988), the increasing MPI over Region A is primarily induced by increasing SST, while the increasing MPI over Region B is jointly driven by increasing SST and the moistening atmosphere.

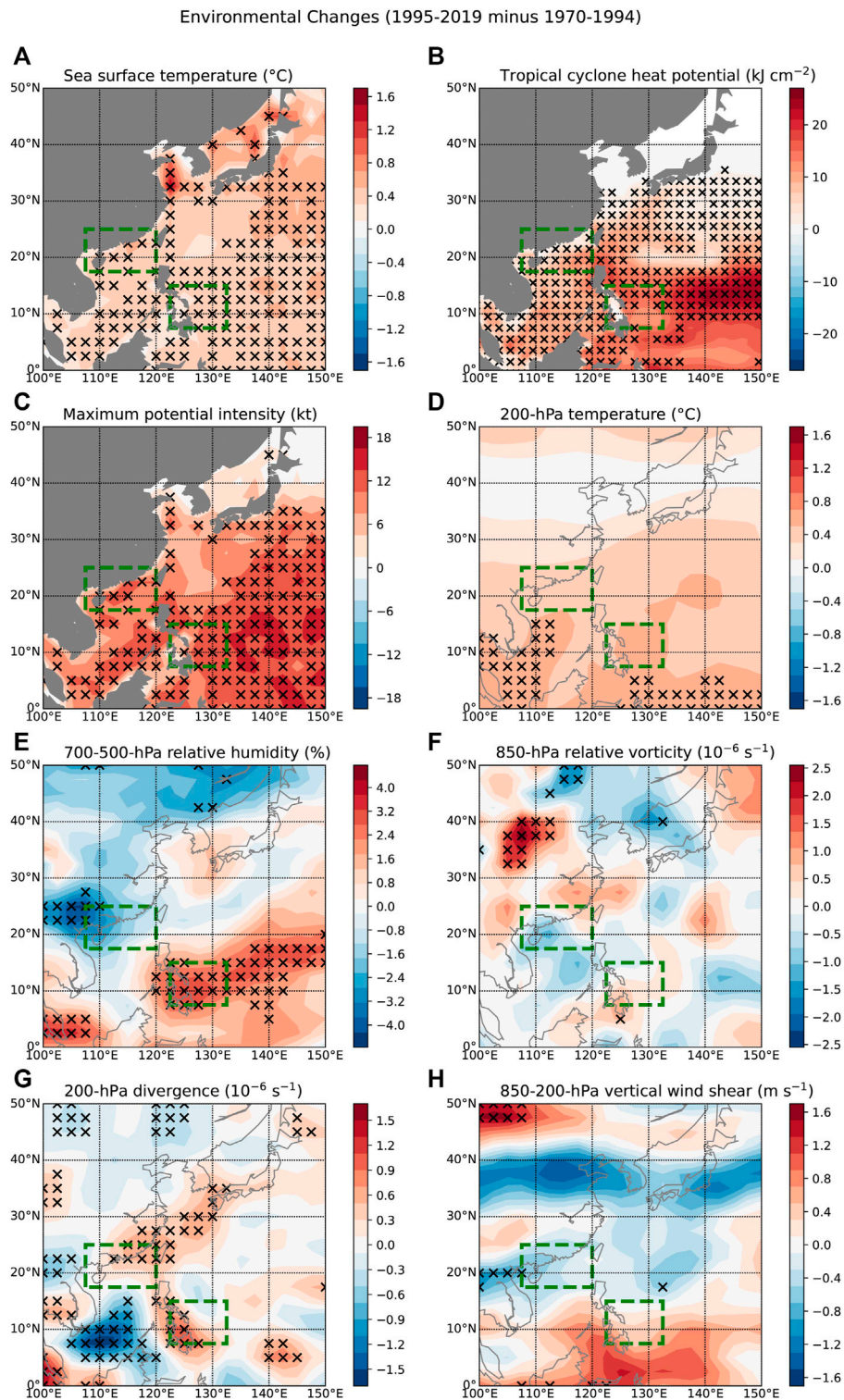


FIGURE 4 | Changes from 1970–1994 to 1995–2019 for JJASON averages of the following environmental variables: **(A)** SST, **(B)** TCHP, **(C)** MPI, **(D)** 200-hPa temperature, **(E)** 700–500-hPa relative humidity, **(F)** 850-hPa relative vorticity, **(G)** 200-hPa divergence, and **(H)** 850–200-hPa VWS. Black crosses denote values significant at the 0.05 level based on a Student's *t*-test. Green boxes denote the two focus regions of this study.

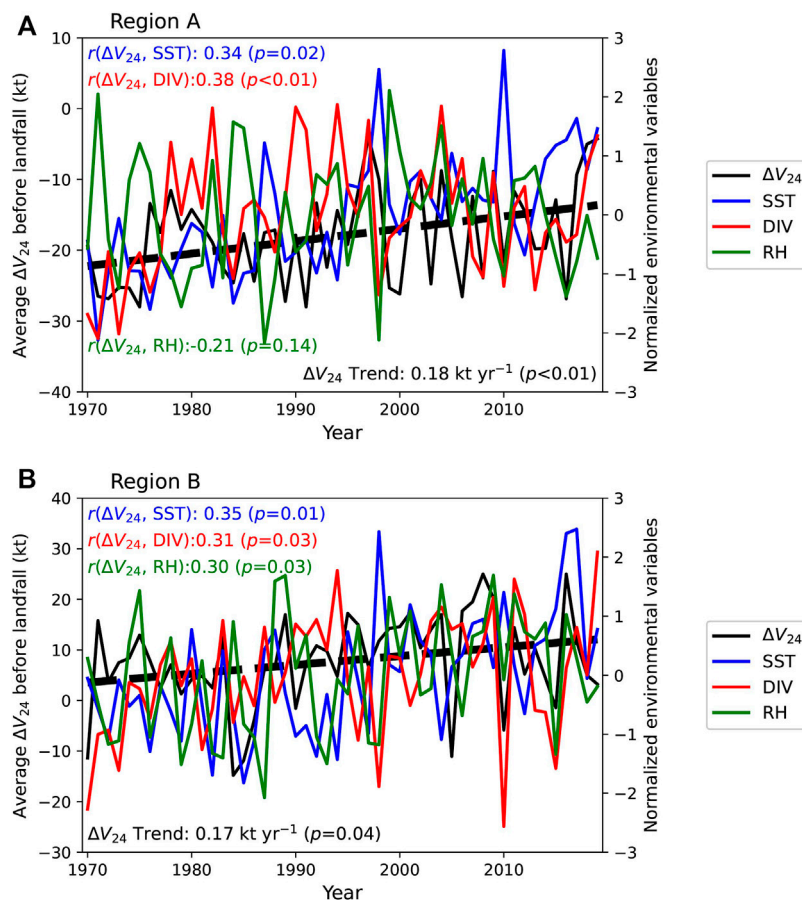


FIGURE 5 | JJASON averages of ΔV_{24} before landfall and environmental variables (SST, 700–500-hPa relative humidity and 200-hPa divergence) from 1970 to 2019 over (A) Region A and (B) Region B. The black dashed lines denote linear trends in the average ΔV_{24} , which are obtained through least squares, while their rates and respective significance levels are shown in the panels.

Figures 4F–H displays differences in dynamic variables during JJASON between 1970–1994 and 1995–2019. There are no significant changes in 850-hPa relative vorticity and 850–200-hPa VWS over Regions A and B (Figures 4F,H), indicating that changes in these variables related to the low-level environmental circulation have only had minor impacts on TC intensity changes before landfall. By contrast, significant increases in 200-hPa divergence are found over both Regions A and B (Figure 4G). The enhanced upper-level divergence favors TC development and subsequently increases ΔV_{24} before landfall. The above environmental variables exhibit similar features if their long-term trends from 1970–2019 are displayed (figure not shown).

To confirm the relationship between ΔV_{24} before landfall and environmental variables over Regions A and B, Figure 5 examines JJASON correlations between ΔV_{24} and environmental variables from 1970 to 2019. Over Region A, there is a significant increasing trend in the average ΔV_{24} , with a slope of 0.18 kt yr^{-1} ($p < 0.01$). This increasing trend is much larger than the trend in the basinwide average ΔV_{24} . Changes in average ΔV_{24} significantly correlate with changes in SST and 200-hPa divergence, with correlation coefficients of 0.34 ($p = 0.02$) and 0.38 ($p < 0.01$), respectively (Figure 5A).

However, there is no significant correlation between the changes in average ΔV_{24} and 700–500-hPa relative humidity ($r = -0.21$; $p = 0.14$).

By comparison, over Region B, the average ΔV_{24} shows a significant increasing trend of 0.17 kt yr^{-1} ($p = 0.04$). The change in average ΔV_{24} is significantly correlated with changes in SST, 700–500-hPa relative humidity and 200-hPa divergence, with correlation coefficients of 0.35 ($p = 0.01$), 0.31 ($p = 0.03$) and 0.30 ($p = 0.03$), respectively (Figure 5A). Additionally, although SST, MPI, TCHP and 200-hPa divergence significantly increase to the south of Japan (27.5° – 35° N, 127.5° – 135° E), there are no significant changes in the average ΔV_{24} before landfall. The lack of trend may be related to the low number of TCs occurring over this region (1.2 TCs per year on average). This low TC frequency can lead to large variability in the annual change of average ΔV_{24} , subsequently reducing the significance of the long-term trend.

SUMMARY

This study investigates long-term trends in average ΔV_{24} before landfall during June–November from 1970–2019. After

identifying 4307 24-h tracks before landfall, we display the climatological spatial distribution of their ΔV_{24} s. On average, TCs intensify before landfall near the Philippines and to the southeast of Vietnam, while they weaken before landfall over other coastal regions. There is a significant increasing trend in basin-averaged ΔV_{24} during 1970–2019, regardless of best track dataset used to identify TCs. This increasing trend is primarily caused by changes in ΔV_{24} over individual grids, while it is only weakly influenced by changes in the TC occurrence distribution. We find that ΔV_{24} before landfall increases significantly over the northern SCS (Region A: 17.5°–25°N, 107.5°–120°E) and to the east of the Philippines (Region B: 7.5°–15°N, 122.5°–132.5°E). This implies a weakening decay rate over Region A and an increased intensification rate over Region B for WNP TCs before landfall.

The changes in ΔV_{24} before landfall over Regions A and B correlate well with changes in several large-scale environmental variables. The greater ΔV_{24} before landfall over Regions A and B can be linked to a warmer ocean (e.g., higher SST, MPI and TCHP) and greater upper-level divergence in 1995–2019 than in 1970–1994. By comparison, the greater ΔV_{24} before landfall over Region B is likely also a result of a moister mid-level atmosphere. Our study highlights an increasing tendency of ΔV_{24} in the WNP before landfall, consistent with trends in ΔV_{24} over water and over land (Bhatia et al., 2019; Liu et al., 2020).

REFERENCES

- Bhatia, K. T., Vecchi, G. A., Knutson, T. R., Murakami, H., Kossin, J., Dixon, K. W., et al. (2019). Recent Increases in Tropical Cyclone Intensification Rates. *Nat. Commun.* 10, 635. doi:10.1038/s41467-019-08471-z
- Brand, S., and Blueloch, J. W. (1973). Changes in the Characteristics of Typhoons Crossing the Philippines. *J. Appl. Meteorol.* 12, 104–109. doi:10.1175/1520-0450(1973)012<0104:citcot>2.0.co;2
- Camargo, S. J., and Sobel, A. H. (2005). Western North Pacific Tropical Cyclone Intensity and ENSO. *J. Clim.* 18, 2996–3006. doi:10.1175/jcli3457.1
- Courtney, J. B., Sampson, C. R., Knaff, J. A., Birchard, T., Barlow, S., Kotal, S. D., et al. (2019). Operational Perspectives on Tropical Cyclone Intensity Change Part 1: Recent Advances in Intensity Guidance. *Trop. Cyclone Res. Rev.* 8, 123–133. doi:10.1016/j.tcr.2019.10.002
- DeMaria, M., Mainelli, M., Shay, L. K., and Kaplan, J. A. (2005). Further Improvements to the Statistical Hurricane Intensity Prediction Scheme (SHIPS). *Wea. Forecast.* 20, 531–543. doi:10.1175/waf862.1
- Emanuel, K. A. (1988). The Maximum Intensity of Hurricanes. *J. Atmos. Sci.* 45, 1143–1155. doi:10.1175/1520-0469(1988)045<1143:tmioh>2.0.co;2
- Hendricks, E. A., Braun, S. A., Vigh, J. L., and Courtney, J. B. (2019). A Summary of Research Advances on Tropical Cyclone Intensity Change from 2014–2018. *Trop. Cyclone Res. Rev.* 8, 219–225. doi:10.1016/j.tcr.2020.01.002
- Hersbach, H., and Bell, B. (2020). The ERA5 Global Reanalysis. *Quart. J. Roy. Meteorol. Soc.* 146, 1999–2049.
- Klotzbach, P. J., and Landsea, C. W. (2015). Extremely intense hurricanes: Revisiting Webster et al. (2005) after 10 years. *J. Clim.* 28, 7621–7629. doi:10.1175/jcli-d-15-0188.1
- Knapp, K. R., Kruk, M. C., Levinson, D. H., Diamond, H. J., and Neumann, C. J. (2010). The International Best Track Archive for Climate Stewardship (IBTrACS). *Bull. Amer. Meteorol. Soc.* 91, 363–376. doi:10.1175/2009bams2755.1
- Li, L., and Chakraborty, P. (2020). Slower Decay of Landfalling Hurricanes in a Warming World. *Nature* 587, 230–234. doi:10.1038/s41586-020-2867-7
- Liu, L., Wang, Y., Zhan, R., Xu, J., and Duan, Y. (2020). Increasing Destructive Potential of Landfalling Tropical Cyclones over China. *J. Clim.* 33, 3731–3743. doi:10.1175/jcli-d-19-0451.1
- Rappaport, E. N., Franklin, J. L., Schumacher, A. B., DeMaria, M., Shay, L. K., and Gibney, E. J. (2010). Tropical Cyclone Intensity Change before U.S. Gulf Coast Landfall. *Wea. Forecast.* 25, 1380–1396. doi:10.1175/2010waf2222369.1

DATA AVAILABILITY STATEMENT

The original contributions presented in the study are included in the article/Supplementary Material, further inquiries can be directed to the corresponding author.

AUTHOR CONTRIBUTIONS

QL, JS, and PK contributed to conception and design of the study. QL and JS organized the database and performed the statistical analysis. QL wrote the first draft of the article. JS and PK revised the article. All authors contributed to manuscript and approved the submitted version.

FUNDING

This work was jointly funded by the National Key Research and Development Program of China (2018YFC1507305), the National Natural Science Foundation of China (61827901 and 42175007) and the China Postdoctoral Science Foundation (2020M680789). Klotzbach would like to acknowledge financial support from the G. Unger Vetlesen Foundation.

- Song, J., Klotzbach, P. J., Duan, Y., and Guo, H. (2020). Recent Increase in Tropical Cyclone Weakening Rates over the Western North Pacific. *Geophys. Res. Lett.* 47, e2020GL090337. doi:10.1029/2020gl090337
- Song, J., and Klotzbach, P. J. (2019). Relationship between the Pacific-North American Pattern and the Frequency of Tropical Cyclones over the Western North Pacific. *Geophys. Res. Lett.* 46, 6118–6127. doi:10.1029/2019gl082925
- Song, J., Klotzbach, P. J., Zhao, H., and Duan, Y. (2021). Slowdown in the Decay of Western North Pacific Tropical Cyclones Making Landfall on the Asian Continent. *Front. Earth Sci.* 9, 749287. doi:10.3389/feart.2021.749287
- Tuleya, R. E., Bender, M., Knutson, T. R., Sirutis, J. J., Thomas, B., and Ginis, I. (2016). Impact of Upper-Tropospheric Temperature Anomalies and Vertical Wind Shear on Tropical Cyclone Evolution Using an Idealized Version of the Operational GFDL hurricane Model. *J. Atmos. Sci.* 73, 3803–3820. doi:10.1175/jas-d-16-0045.1
- Zhu, Y. -J., Collins, J. M., and Klotzbach, P. J. (2021). Nearshore hurricane Intensity Change and post-landfall Dissipation along the United States Gulf and East Coasts. *Geophys. Res. Lett.* 48, e2021GL094680. doi:10.1029/2021gl094680
- Zuo, H., Balmaseda, M. A., Tietche, S., Mogensen, K., and Mayer, M. (2019). The ECMWF Operational Ensemble Reanalysis-Analysis System for Ocean and Sea Ice: a Description of the System and Assessment. *Ocean Sci.* 15, 779–808. doi:10.5194/os-15-779-2019

Conflict of Interest: The authors declare that the research was conducted in the absence of any commercial or financial relationships that could be construed as a potential conflict of interest.

Publisher's Note: All claims expressed in this article are solely those of the authors and do not necessarily represent those of their affiliated organizations, or those of the publisher, the editors and the reviewers. Any product that may be evaluated in this article, or claim that may be made by its manufacturer, is not guaranteed or endorsed by the publisher.

Copyright © 2021 Liu, Song and Klotzbach. This is an open-access article distributed under the terms of the Creative Commons Attribution License (CC BY). The use, distribution or reproduction in other forums is permitted, provided the original author(s) and the copyright owner(s) are credited and that the original publication in this journal is cited, in accordance with accepted academic practice. No use, distribution or reproduction is permitted which does not comply with these terms.



The Asymmetric Precipitation Evolution in Weak Landfalling Tropical Cyclone Rumbia (2018) Over East China

Lichun Tang^{1,2}, Yuqing Wang¹, Zifeng Yu^{2,3*} and Lan Wang³

¹International Pacific Research Center and Department of Atmospheric Sciences, University of Hawaii at Manoa, Honolulu, HI, United States, ²Shanghai Typhoon Institute, and Key Laboratory of Numerical Modeling for Tropical Cyclone of China Meteorological Administration, Shanghai, China, ³Fujian Key Laboratory of Severe Weather of China Meteorological Administration, Fuzhou, China

OPEN ACCESS

Edited by:

Kun Zhao,
Nanjing University, China

Reviewed by:

Li Tao,
Nanjing University of Information
Science and Technology, China

Bo-Wen Shen,
San Diego State University,
United States

*Correspondence:

Zifeng Yu
yuzf@typhoon.org.cn

Specialty section:

This article was submitted to
Atmospheric Science,
a section of the journal
Frontiers in Earth Science

Received: 26 July 2021

Accepted: 08 October 2021

Published: 09 November 2021

Citation:

Tang L, Wang Y, Yu Z and Wang L
(2021) The Asymmetric Precipitation
Evolution in Weak Landfalling Tropical
Cyclone Rumbia (2018) Over
East China.
Front. Earth Sci. 9:747271.
doi: 10.3389/feart.2021.747271

The rainfall in landfalling TC is not always correlated with the storm intensity. Some weak landfalling TCs could bring extremely heavy rainfall during and after landfall. Such extreme events are very challenging to operational forecasts and often lead to disasters in the affected regions. Tropical storm Rumbia (2018) made its landfall in Shanghai with weak intensity but led to long-lasting and increasing rainfall to East China. The asymmetric rainfall evolution of Rumbia during and after its landfall was diagnosed based on the fifth generation European Centre for Medium-Range Weather Forecasting (ECMWF) reanalysis (ERA5) data, the tropical cyclone (TC) best-track data, and rainfall observations from China Meteorological Administration (CMA). Results showed that Rumbia was embedded in an environment with a deep-layer (300–850 hPa) southwesterly vertical wind shear (VWS). The maximum rainfall mostly occurred downshear-left in its inner-core region and downshear-right in the outer-core region. The translation of Rumbia also contributed to the rainfall distribution to some extent, especially prior to and just after its landfall. The strong southwesterly-southeasterly summer monsoon flow transported water vapor from the tropical ocean and the East China Sea to the TC core region, providing moisture and convective instability conditions in the mid-lower troposphere for the sustained rainfall even after Rumbia moved well inland. The results also showed that the low-level convective instability and the deep-layer environmental VWS played an important role in deepening the inflow boundary layer and the redevelopment of the secondary circulation, thus contributing to the heavy rainfall in the northeast quadrant of Rumbia after its landfall. However, further in-depth studies are recommended in regard of the rainfall evolution in the weak TCs. This study further calls for a continuous understanding of the involved physical processes/mechanisms that are responsible for the extreme rainfall induced by landfalling TCs, which can help improve the rainfall forecast skills and support damage mitigation in the future.

Keywords: landfalling tropical cyclone, vertical wind shear, boundary layer, secondary circulation, heavy rainfall, asymmetric structure, instability

INTRODUCTION

Tropical cyclones (TCs) are synoptic systems that form over the tropical oceans by the energy supply from the underlying warm ocean. They display cyclonic circulations with low central pressure. TCs are one of the most destructive weather systems and often produce storm surge, strong winds, heavy rainfall, and severe flooding, inducing tremendous economic loss and deaths each year during and after landfall (Chen and Ding, 1979). According to Zhang et al. (2009), landfalling TCs in China always brought torrential rainfall to most coastal provinces and imposed great economic losses every year. Zhejiang Province got the most direct economic loss on average at 6960 million RMB Yuans per year, and Guangdong Province had the most significant number of landfalling TCs at 2.9 TCs per year on average. Therefore, it is important for China to accurately forecast rainfall induced by landfalling TCs. However, even though the TC track forecast has been improved continuously in the past decades, the skill in TC precipitation forecast is still low and far behind the track forecast (Yu et al., 2020). Wang et al. (2012) showed that the threat score (TS) of a 24-h forecast for 25 mm-rainfall in landfalling TCs over China was only 0.2. Hence, TC rainfall forecasts remain challenging because precipitation processes associated with landfalling TCs are complicated and involve multi-scale interactions (Yu and Wang 2018).

The regions suffering from TC rainfall are largely determined by the rainfall distribution in the TC circulation. The spatial distribution of rainfall in TCs is particularly important for rainfall forecast (Yu et al., 2015). The rainfall distribution in a TC can be decomposed into a wavenumber-0 component or the axisymmetric component and a series of lower-wavenumber components (Lonfat et al., 2004). Many efforts have been devoted to revealing the mechanisms of the asymmetric rainfall distribution (Rogers et al., 2003; Lonfat et al., 2004; Chen et al., 2006; Lonfat et al., 2007; Wingo and Cecil 2010; Reasor et al., 2013; Jiang and Ramirez 2013). Environmental vertical wind shear (VWS) is widely known as one of the important factors affecting TC rainfall asymmetric distribution, which is defined as the vector difference of the horizontal winds averaged within a radius such as 500 km between 200 and 850 hPa. Results from statistical and composite analyses indicate that heavy rainfall is mainly located downshear-left in the inner-core region and downshear-right in the outer-core region in a TC (Chen et al., 2006; Reasor et al., 2013). The TC translation is another important factor affecting TC rainfall distribution. Chen et al. (2006) found that heavy rainfall often occurs in the front quadrants of the storm center in the low shear environment, and when the direction of VWS is the same as that of TC translation, the TC would have the largest rainfall asymmetry. Previous studies also found that interactions between a TC and its other surrounding environments, such as an upper-level jet, monsoon flow, and a mid-latitude trough, may impose significant impacts on rainfall intensity and distribution in TCs as well (Atallah et al., 2007; Deng and Ritchie, 2020; Meng and Wang 2016a; Meng and Wang 2016b).

Most of the previous studies mentioned above have mainly focused on TC rainfall distribution over open oceans. The complex underlying surface forcing and interactions, such as inland water surface, terrain, and mesoscale convective activities, may play significant roles in shaping rainfall distribution in a landfalling TC (Yu J. et al., 2010; Yu et al., 2017). The asymmetric rainfall distribution in landfalling TC is closely related to the asymmetric convergence and vertical motion associated with the surface friction, forcing due to environmental VWS, and the asymmetric distribution and transport of environmental water vapor, or the embedded convective system (Shapiro 1983; Chen and Yau 2001; Yu et al., 2015, 2017). For example, Yu et al. (2017) examined the relationship between TC intensity and rainfall distribution in landfalling TCs over China. They found that the rainfall axisymmetry is closely related to the landfalling TC intensity. Stronger TCs have higher rain rates and higher amplitude of axisymmetric rainfall in general, while rapid decaying TCs show the most rapid decrease in total rainfall and axisymmetric rainfall relative to the total rain. Nevertheless, it is not the case for the maximum rain rate. Feng and Shu (2018) reported no significant relationship between TC intensity and rainfall frequency in the outer-core region, and heavy rainfall may also result from weak TCs due to the influence of VWS.

Some studies have been devoted to understanding torrential rainfall processes induced by individual landfalling TCs. For example, Tropical Storm Bilis (2006) made landfall in Zhejiang Province of China, and remained inland for days and produced excessively heavy rainfall, causing at least 843 deaths and a direct economic loss of up to five billion U.S. dollars (Deng et al., 2017). The heavy rainfall commenced after about 7 h after landfall and occurred about 400 km southwest of the circulation center. The southwesterly monsoon flow was the major carrier of water vapor and energy. The cold air intrusion from the northwest in the lower troposphere helped release the potential instability energy, triggered convective activities and substantially enhanced the rainstorm intensity (Kang et al., 2008). Yu Z. et al. (2010) demonstrated that the environmental VWS largely triggered the rainfall asymmetries in Bilis. Jiang et al. (2008) compared the rainfall resulting from Tropical Storm Isidore (2002) and Category-1 Hurricane Lili (2002) based on satellite observations and found that Isidore produced a much larger total volumetric rainfall in the same area both over the open gulf and during landfall. Tropical Storm Swan (2009) is another weak landfalling TC making landfall in Guangdong Province of China and producing extremely heavy rainfall. Huang et al. (2010) claimed that the torrential rainfall associated with Swan was mainly due to strong convergence and water vapor transport from the Bay of Bengal. Tropical Storm Goni (2015) and Super Typhoon Shanshan (2006) shared similar tracks, but Goni brought more than 100 mm rainfall from southern Jiangsu Province to northern Zhejiang Province of China while rainfall from Shanshan was below 30 mm. That was because Goni had a more stable upper-level trough and continuous water vapor supply (Cao et al., 2018).

Rumbia (2018) was another weak TC, which made its landfall in Shanghai, China at 2004 UTC on August 16, 2018. This is a case

worthy of being studied because only a very small part of TC cases made their landfalls north of Zhejiang Province, China, in the past 3 decades. Besides, the rainfall kept increasing after landfall while the TC was continuously weakening. After landfall, Rumbia moved inland and induced heavy rainfall and severe flooding along its track in East China. At about 1800 UTC on 18 August, Rumbia tracked northeastward and transited into an extratropical cyclone at about 0000 UTC on 20 August. The rainfall brought by Rumbia kept increasing while Rumbia was weakening. The heavy rainfall in Rumbia was mostly located on the right of its track, causing a great loss of human lives and property.

The primary goal of this study is to reveal the physical process of asymmetric precipitation evolution in Rumbia (2018) during and after its landfall. The study focuses on the rainfall evolution right after Rumbia just made landfall but before it turned to its northeastward movement. The rest of the paper is organized as follows. The data used are described in *Data and Methods*. Main results are discussed in *Results*, including an overview of Rumbia's rainfall and the synoptic evolution and the diagnostic analysis of the related dynamic and thermodynamic processes. Conclusions are summarized in the last section.

DATA AND METHODS

The hourly gauge-radar-satellite merged precipitation data from China Meteorological Administration (CMA) with a spatial resolution of $0.05^\circ \times 0.05^\circ$ were used to give an overview of observed rainfall evolution of Rumbia. The three-hourly TC best-track data, which include the intensity and central location (longitude and latitude) of the TC, were obtained from the Shanghai Typhoon Institute of CMA (STI/CMA).

The fifth generation European Centre for Medium-range Weather Forecasting (ECMWF) global reanalysis (ERA5, 0.25° , 1-hourly, Hersbach et al., 2020) dataset. ERA5 is based on the Integrated Forecasting System (IFS) Cy41r2 (which was operational in 2016) and benefits from a decade of developments in model physics, core dynamics and data assimilation. Since this study focuses on the rainfall evolution in Rumbia, we compared the precipitation from ERA5 with observations. Results showed that although ERA5 shows considerable discrepancies in precipitation over ocean prior to landfall of Rumbia, it captures well the temporal evolution and spatial distribution of precipitation over land in observations (Figure ignored). This indicates that ERA5 can be used to examine the synoptic evolution associated with the precipitation process in Rumbia after landfall. The ERA5 data used here has the horizontal resolution of $0.25^\circ \times 0.25^\circ$ with 1-h intervals at 23 pressure levels (1,000, 975, 950, 925, 900, 875, 850, 825, 800, 775, 750, 700, 650, 600, 550, 500, 450, 400, 350, 300, 250, 225, and 200 hPa), which includes geopotential height, zonal and meridional components of horizontal winds, vertical motion, temperature, relative humidity, potential vorticity, and boundary layer height.

RESULTS

An Overview of Rumbia (2018) Rainfall Evolution

Figure 1A shows the observed rainfall distribution of Rumbia accumulated from 0600 UTC 14 to 1800 UTC 20 August in 2018. Rumbia intensified prior to its landfall, with the central pressure reaching the minimum of about 982 hPa and the maximum sustained 10-m wind speed of 25 m s^{-1} (Figure 1B). Rumbia produced a large amount of precipitation after its landfall at 2000 UTC on 16 August although its intensity just reached strong tropical storm at landfall and soon weakened to a tropical storm after landfall. By about 1800 UTC 18 August, Rumbia turned its motion from northwestward to northeastward and then weakened into a tropical depression. At about 0000 UTC 20 August, Rumbia entered the Bohai Sea and transited into an extratropical cyclone. The rainfall induced by Rumbia was enhanced after landfall, with the heavy rainfall always located to the right of its track and kept increasing as it moved further inland (Figure 1A). In this study, we will mainly focus on the heavy rainfall after landfall when Rumbia moved northwestward but before it turned northeastward.

Figure 2 shows the observed 6-hourly total rainfall evolution during and after landfall of Rumbia. Before Rumbia made landfall in Shanghai, only scattered rainfall appeared over the East China Sea or even near the TC center (Figure 2A). At 2000 UTC on 16 August, when Rumbia made landfall, the rainfall strengthened compared to that 6 h ago but was still distributed discretely (Figure 2B). The rainfall area quickly enlarged from 0200 to 1400 UTC on 17 August (Figures 2C–I). At 0800 UTC on 17 August, the heavy rainfall mainly occurred in the northeast quadrant of Rumbia and kept increasing and became more concentrated afterward. The rainfall showed an obvious wavenumber-1 asymmetric distribution after landfall, particularly from 0800 UTC on 17 August (Figure 2D), which will be the focus of this study. This might be due to the influence of change in the environmental VWS as discussed extensively in many previous studies (e.g., Lonfat et al., 2004; Chen et al., 2006). The detailed analyses will be discussed below.

Synoptic Evolution

The rainfall distribution and intensity in a TC is often largely affected by the large-scale environment the TC is embedded. Therefore, to understand the mechanism behind the heavy rainfall in Rumbia, we briefly discuss the synoptic evolution based on the ERA5 reanalysis. Figures 3A–F illustrate the evolutions of the 200-hPa geopotential height and wind fields after landfall of Rumbia. It can be seen that an upper-level jet appeared near 45°N to the north of Rumbia at 2000 UTC 16 August, which was far away from Rumbia, and thus its influence on the rainfall of Rumbia should be very limited. There was a weak divergent anticyclonic circulation at 200 hPa over Rumbia, which strengthened as the rainfall increased after the landfall of Rumbia.

An outflow jet to the northeast of Rumbia showed a strengthening after 0800 UTC on August 17. This outflow jet may reflect the enhanced convective heating related to the enhanced rainfall on one hand and increased the upper-level divergence and thus favorable for the rainfall enhancement on the other hand. Besides, a cyclonic circulation occurred near 30°N

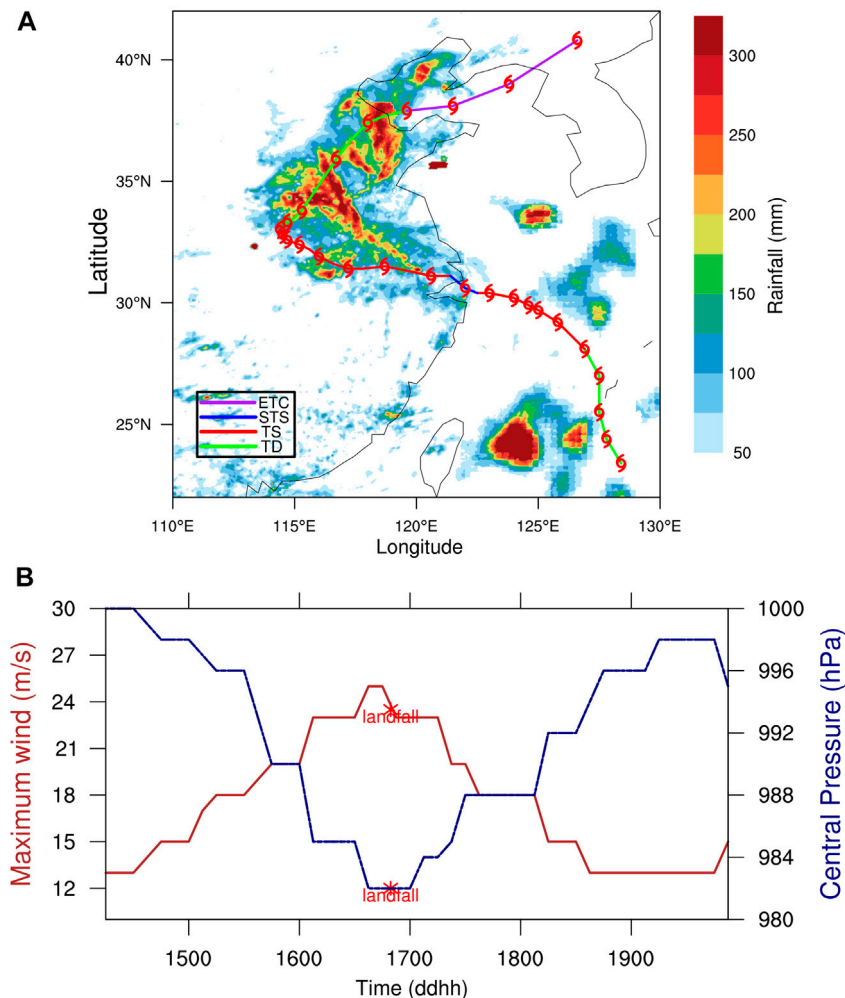


FIGURE 1 | (A) Observed storm track (solid line) and accumulated total rainfall (shading, mm). **(B)** Observed evolution of the central pressure (blue polyline, hPa) and maximum 10-m height wind speed (red polyline, m/s) from 0600 UTC 14 (1406, in the form of ddhh on the x-axis) August to 1800 UTC 20 (2018, in the form of ddhh on the x-axis) August 2018.

to the west of the outflow of Rumbia. The southwesterly flow to the southeast of the cyclonic circulation, together with the northeasterly outflow jet to the northeast of Rumbia in the upper troposphere, contributed to the establishment of a large-scale moderate southwesterly VWS over Rumbia. As we will discuss in the next subsection. And it was this VWS that was largely responsible for the observed rainfall asymmetry in Rumbia after its landfall.

Figures 3G–L display the evolution of the 500-hPa geopotential height and wind fields. On 2000 UTC 16 August, there was a weak western North Pacific subtropical high (WNPSH) to the north of Rumbia (**Figure 3G**). Rumbia moved northwestward inland along the southwestern edge of the WNPSH from 2000 UTC 16 to 0200 UTC 18 August. As a result of the existence of the WNPSH, the winds in the northeast quadrant of Rumbia were much larger than in the southwest quadrant, leading to a wavenumber-1 asymmetric structure in the wind fields in the mid-lower troposphere. Note that there was a

new TC formed far away to the southeast over the western North Pacific, which seemed not to play any role in affecting the rainfall of Rumbia. As we mentioned earlier, the upper-level westerly jet in the midlatitude might not interact directly with Rumbia and thus should not affect the rainfall distribution of Rumbia. This is mainly because the jet seemed to be far away from the outflow of Rumbia (**Figures 3A–F**).

The possible interaction between a TC and the midlatitude system is often examined by the potential vorticity (PV) distribution (e.g., Wang et al., 2009; Meng and Wang 2016a,b). Here we also checked the evolution of the meridional and vertical cross-section of PV through the center of Rumbia corresponding to the synoptic evolution with the results shown in **Figure 4**. We can see that Rumbia was characterized by a high PV column up to 200–300 hPa from the lower troposphere. The downward dip contours of potential temperature in the high PV column indicates the warm core structure of Rumbia. This seems to suggest that

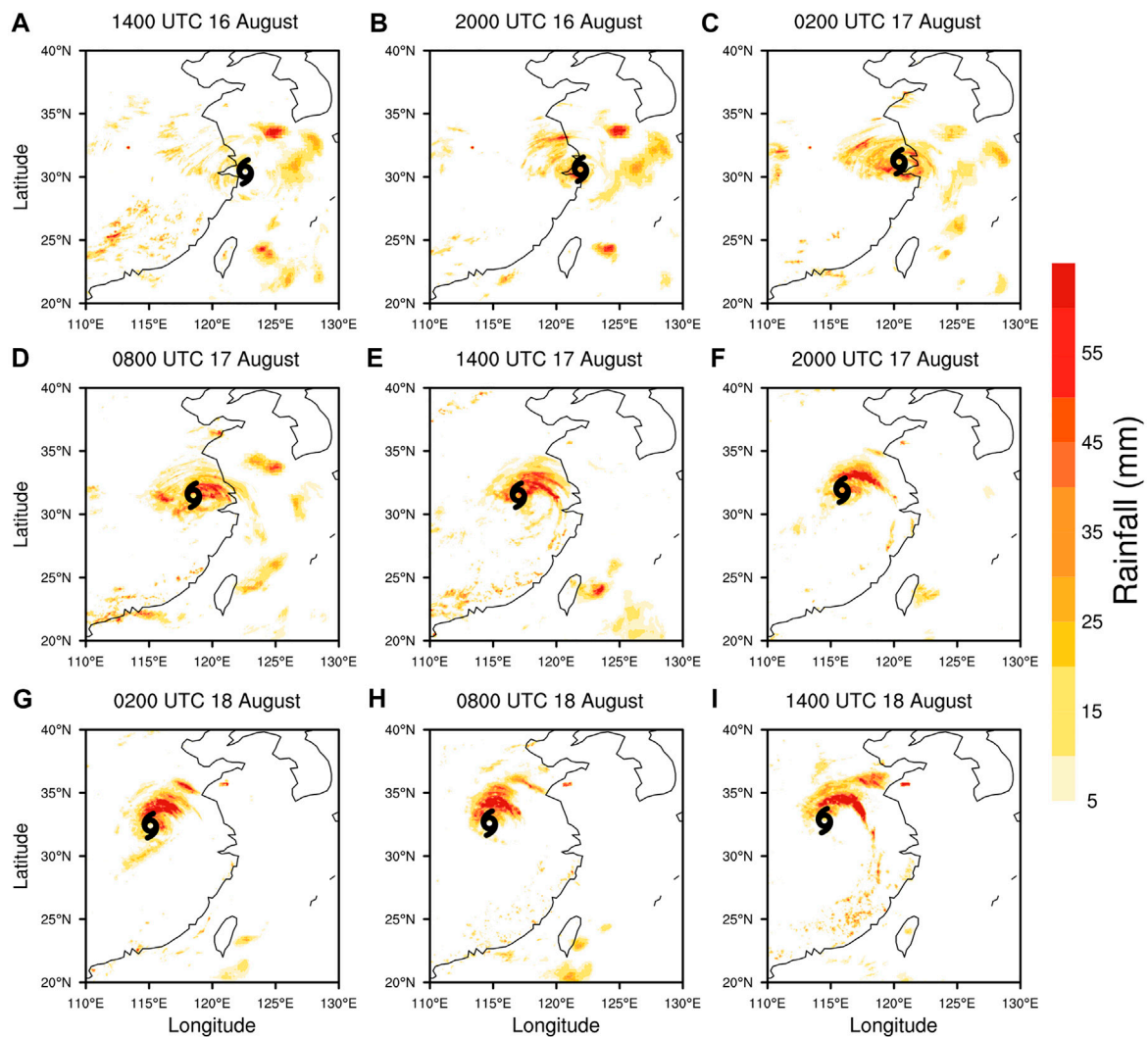


FIGURE 2 | Evolution of the observed 6-hourly rainfall distribution (mm) at (A) 1,400, (B) 2000 UTC 16 August, (C) 0200, (D) 0800, (E) 1,400, (F) 2000 UTC 17 August, (G) 0200, (H) 0800, (I) 1400 UTC August 18, 2018.

although Rumbia was a strong tropical storm at landfall and weakened to a tropical storm in the study period, it showed the feature of a typical TC. The high PV in the upper troposphere far to the north was associated with the mid-latitude westerly trough, which was well isolated from the high PV of Rumbia, further suggesting that the mid-latitude interaction might be secondary to the heavy rainfall of Rumbia at least before August 18. At the same time, from **Figures 4G–L**, we can prove that the high PV was also far from the TC center and did not have a noticeable contribution to the storm's heavy rainfall.

Effects of Vertical Wind Shear and Storm Motion

As mentioned earlier, rainfall in Rumbia after landfall shows an asymmetric distribution, which was dominated by the wavenumber-1 structure. Similar wavenumber-1 rainfall

distribution in landfalling TCs over China has been extensively studied in previous studies (Yu J. et al., 2010; Yu et al., 2015; Meng and Wang 2016a). Several factors responsible for the observed rainfall asymmetries have been identified, including the land-sea contrast, translation of the TC, and environmental VWS. In the Rumbia case, the rainfall near the landfall did not show a systematic rainfall asymmetric distribution. This seems to suggest that the land-sea contrast is secondary to the observed rainfall asymmetric distribution in Rumbia, in particularly after its core moved inland. Therefore, we will focus on the analysis of the effects of environmental VWS and the translation on the rainfall asymmetry in Rumbia first.

Figure 5 shows the hourly environmental VWS evolution in three different vertical layers, that is 200–850 hPa, 300–850 hPa, and 500–950 hPa VWSs. The environmental VWS was defined as the difference of wind vectors averaged within a radius of 500 km

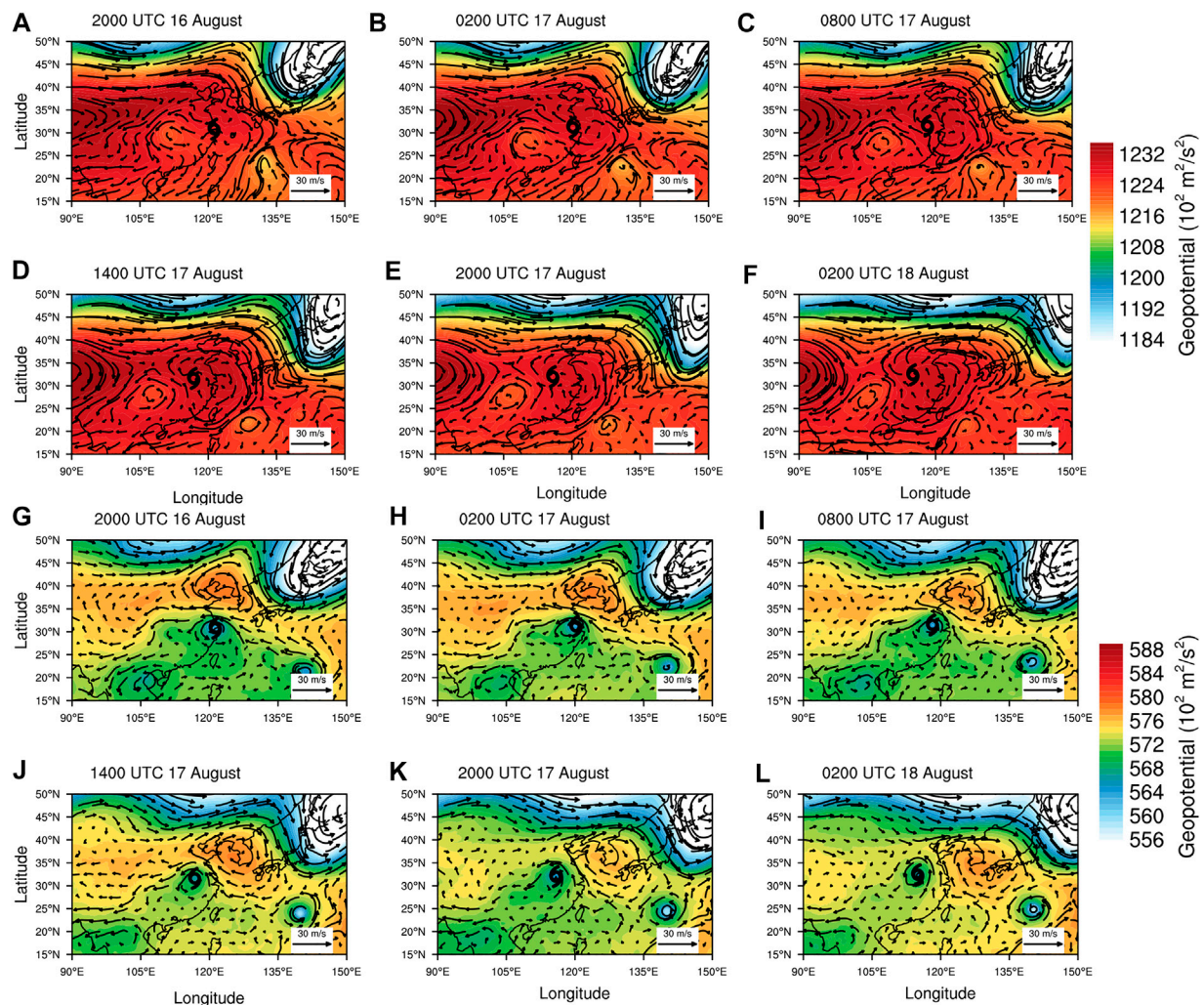


FIGURE 3 | Geopotential height (shading, 10 geopotential meters) and wind vectors (m s^{-1}) at 200 hPa: (A) 2000 UTC 16 August, (B) 0200, (C) 0800, (D) 1,400, (E) 2000 UTC 17 August, (F) 0200 UTC August 18, 2018, and at 500 hPa: (G) 2000 UTC 16 August, (H) 0200, (I) 0800, (J) 1,400, (K) 2000 UTC 17 August, (L) 0200 UTC August 18, 2018.

from the TC center between two given levels (e.g., 300–850 hPa VWS is defined as the difference of wind vectors averaged within a radius of 500 km from the TC center between 300 hPa and 850 hPa). In previous studies, 200–850 hPa VWS is always used to diagnose rainfall distribution, and heavy rainfall often occurs downshear-left in the inner-core region and downshear-right in the outer-core region (e.g., Chen et al., 2006). Because Rumbia was a relatively weak TC with shallower convection than an intense TC, 300–850 hPa VWS is given here as well as 200–850 hPa VWS. In addition, a weak TC is often shallower with a weaker and lower warm core, and the lower-layer shear (e.g., 1.3–5.8 km) might be more likely to affect the TC intensity (Finocchio et al., 2016; Fu et al., 2019). Therefore, we also examined the lower-level VWS between 500–950 hPa.

We can find in **Figure 5A** that after 0600 UTC 17 August, the 500–950 hPa VWS was relatively stable while the rainfall distribution varies greatly, suggesting that the lower-level VWS

had very limited influence on the rainfall evolution in Rumbia. The 300–850 hPa and 200–850 hPa VWS shared a similar tendency, and the deeper VWS was 3 m s^{-1} larger at most. As we can see from **Figure 5B**, although the shear magnitude varied with time during the study period, the shear direction was very stable. The deep-layer environmental VWS was northeasterly between 300–850 hPa and 200–850 hPa. Since the rainfall in Rumbia was scattered in the early stage after landfall and then concentrated in the northeast quadrant in the inner-core region, the southwesterly VWS must have contributed the most to the rainfall distribution, consistent with the conclusion of Chen et al. (2006).

To further examine the relationship between the TC rainfall and the environmental VWS, we analyzed the hourly rainfall distribution, storm motion vector, and 300–850 hPa VWS. **Figure 6** gives the hourly rainfall evolution from 1400 UTC 16 to 0100 UTC 17 August. As we can see, the environmental

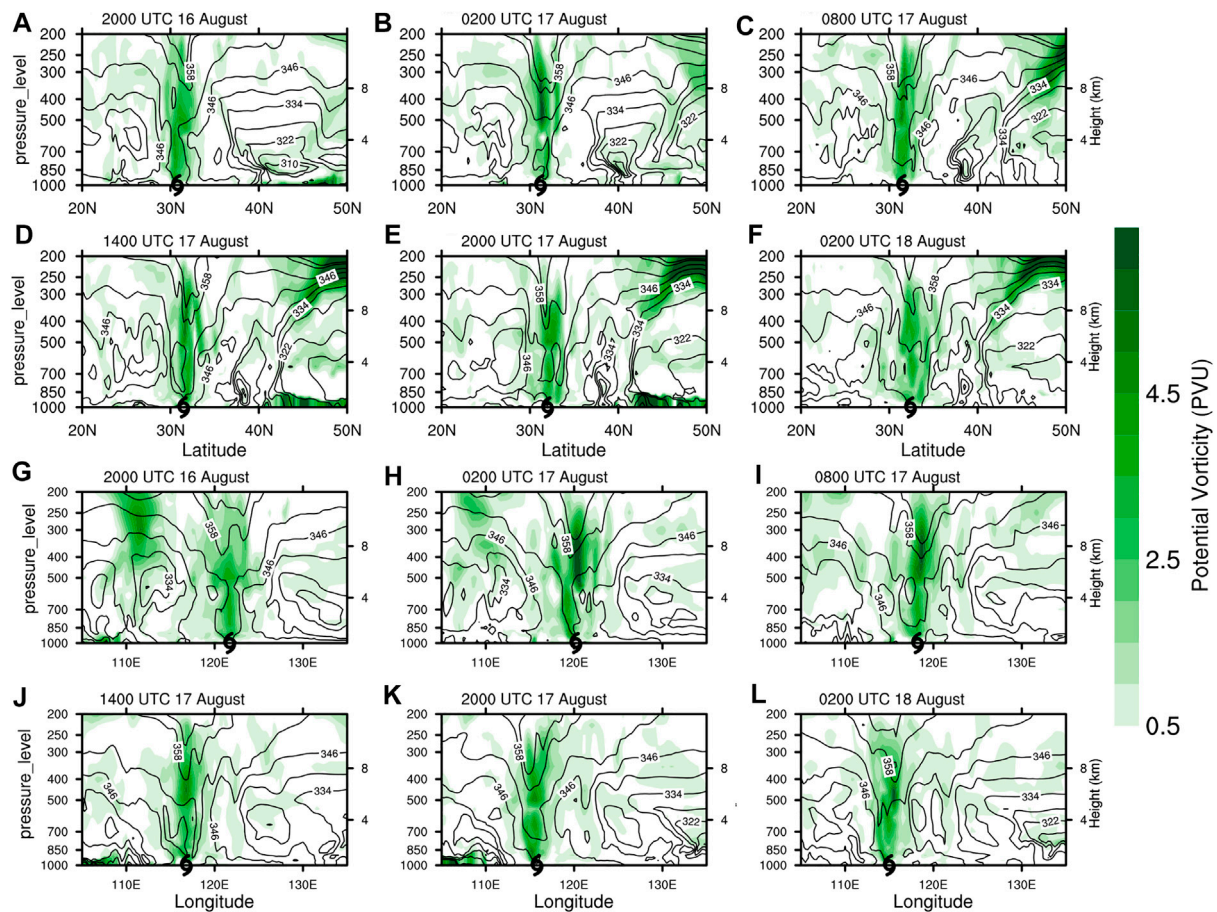


FIGURE 4 | South-north (A–F) and west-east (G–L) vertical cross-sections of potential vorticity (shading, PVU) and potential temperature (contours, K) across the center of Rumbia: (A, G) 2000 UTC 16 August, (B, H) 0200, (C, I) 0800, (D, J) 1,400, (E, K) 2000 UTC 17 August, (F, L) 0200 UTC August 18, 2018.

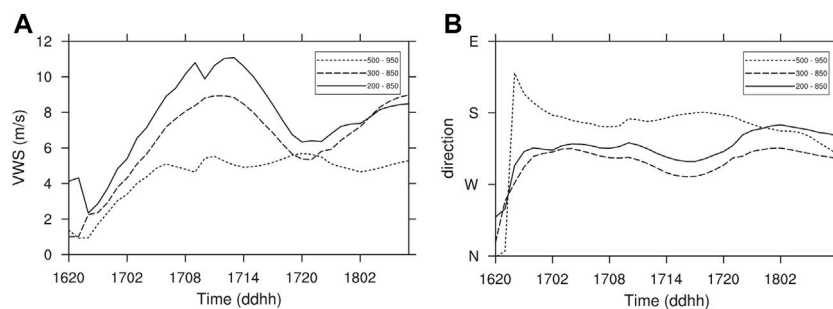


FIGURE 5 | Time evolution of environmental VWS magnitude (A) and direction (B) in different vertical layers over Rumbia. Here the VWS is defined as the difference between the horizontal mean wind vector averaged within a radius of 500 km from the storm center at two given pressure levels.

VWS was small (less than 5 m s^{-1}), and the TC translational speed showed an apparent acceleration as Rumbia was approaching the coast. By 1900 UTC 16 August, the rainfall occurred mainly to the north of Rumbia along the coastline, and scattered over the sea, suggesting that the land-sea contrast dominated the rainfall distribution when Rumbia moved toward the land. Many previous studies indicate that some

intense outer convective spiral bands may form ahead of the TC center when it approaches the land (e.g., Parrish et al., 1982). When interacting with the inner core, such enhanced convective bands may interact with the inner core and accelerate the TC motion (Willoughby 1992). In the Rumbia case, we can find that as Rumbia moved across the coastline, the translational speed increased to reach 11.8 m s^{-1} at 2100 UTC 16 August after

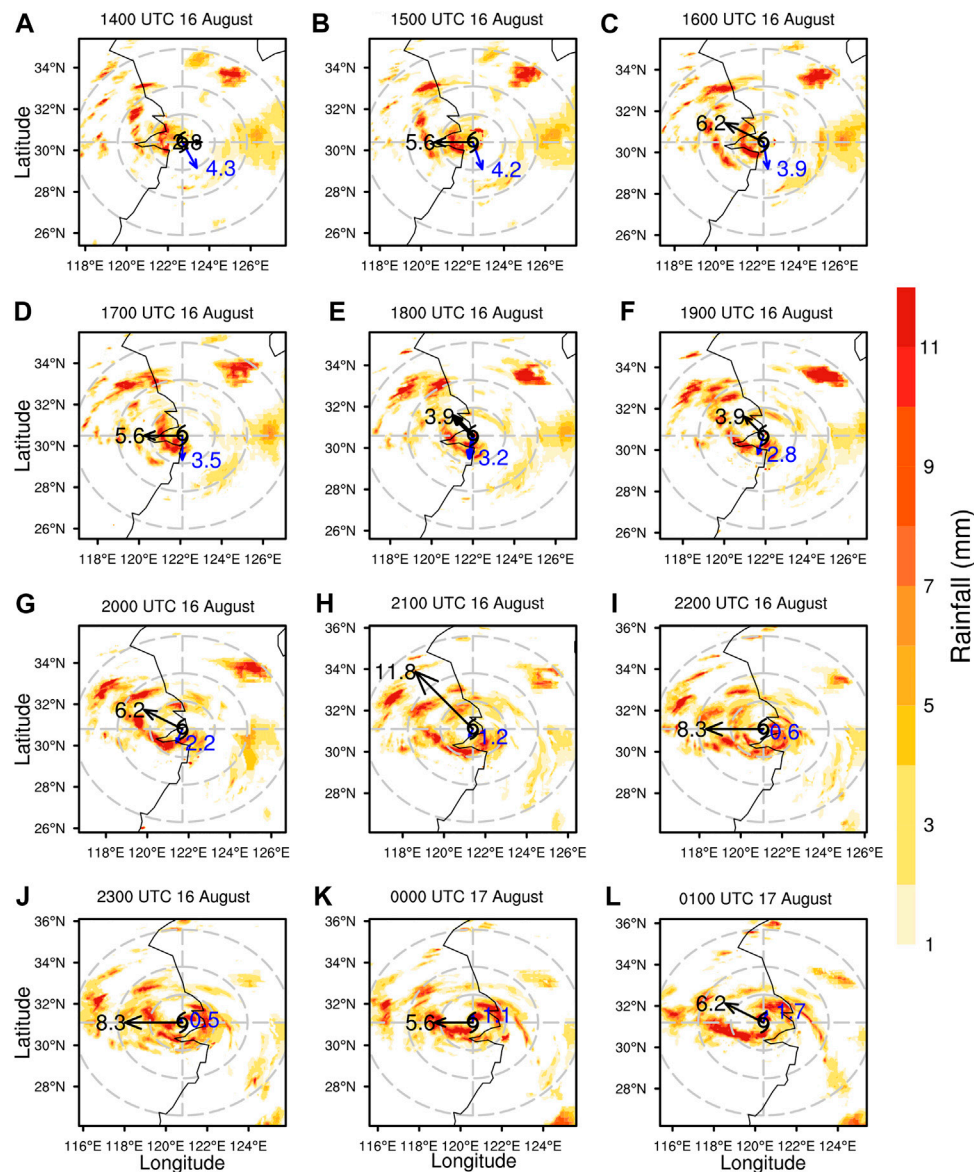


FIGURE 6 | Hourly rainfall evolution (shading, mm) at (A) 1,400, (B) 1,500, (C) 1,600, (D) 1700, (E) 1800, (F) 1900, (G) 2000, (H) 2,100, (I) 2,200, (J) 2300 UTC 16 August, (K) 0000 (L) 0100 UTC 17 August. Grey dashed concentric circles are 150, 300, and 500 km from the storm center. Black arrows and numbers denote the storm motion vectors and speeds (m s^{-1}). Blue arrows and numbers refer to the directions and magnitudes (m s^{-1}) of the deep layer VWS between 300 and 850 hPa. The cyclone symbol indicates the storm center at the given time.

landfall. This is consistent with the finding in Chen and Yau (2001) and Willoughby (1992).

Figure 7 shows the temporal evolution of the variables mentioned above from 0200 to 0700 UTC 17 August. The environmental VWS increased during this period while the TC translational speed decreased to some extent. By 0400 UTC 17 August, rainfall occurred not only downshear-left, but also downshear right in the inner-core region, and rainfall even occurred in the upshear-left quadrant in the outer-core region. From 0500 UTC on 17 August, the downshear-right rainfall in the inner-core region gradually weakened and eventually disappeared. The rainfall distribution began to

display an obvious wavenumber-1 asymmetric structure in the inner-core region, with the heavy rainfall occurring downshear-left in the inner-core region while downshear-right in the outer-core region in terms of the deep-layer environmental VWS. This seems to suggest that from 0500 UTC on 17 August, the 300–850 hPa VWS dominated the rainfall asymmetric distribution in Rumbia after its landfall (**Figure 5**), consistent with many previous studies as mentioned earlier.

During the 6 h period from 0900 to 1,400 August 17 (**Figures 7H, 8A**), a rainband developed in the southeast quadrant in the outer-core region and spiraled cyclonically inward and connected

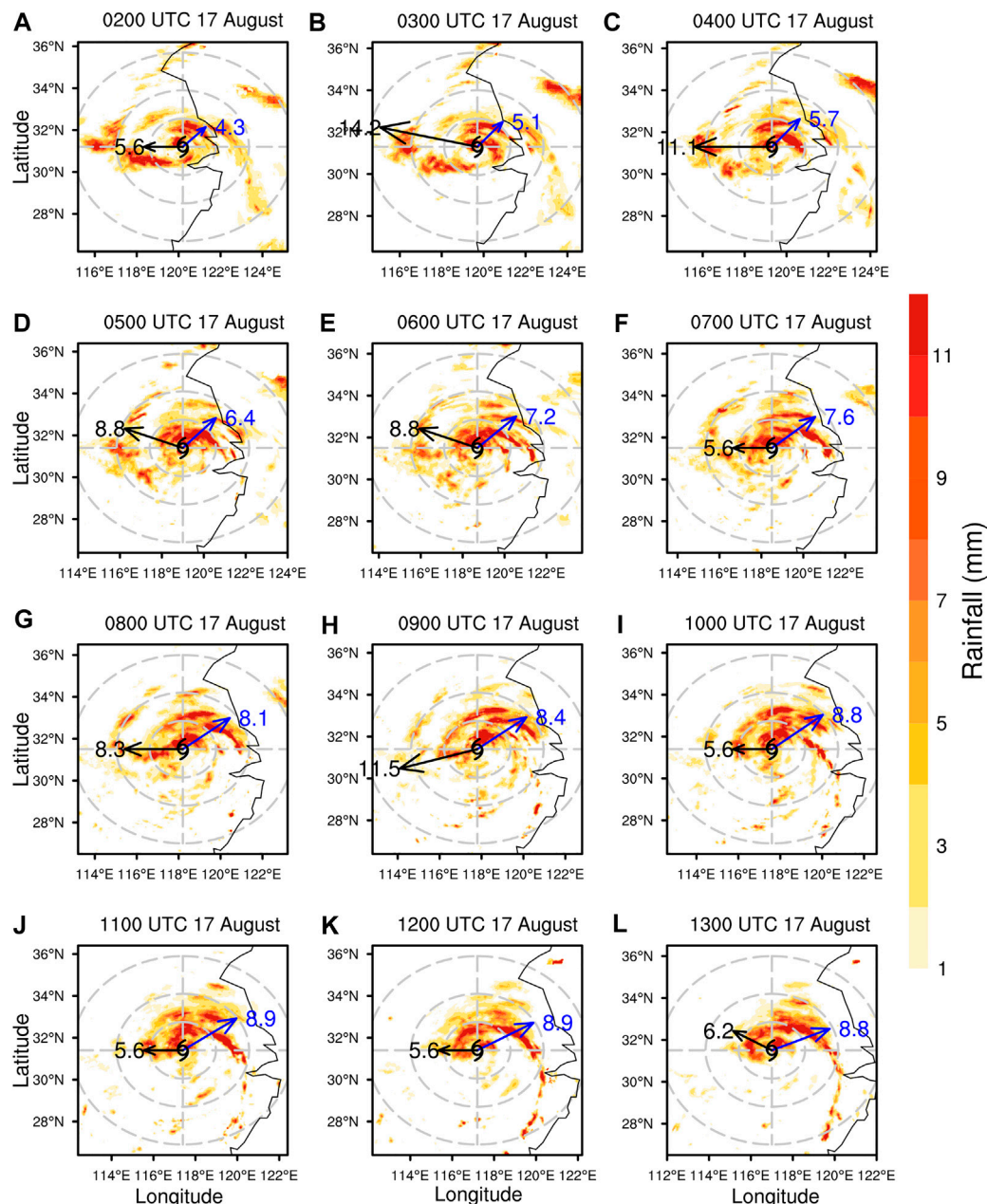


FIGURE 7 | Same as **Figure 6**, but at (A) 0200, (B) 0300, (C) 0400, (D) 0500, (E) 0600, (F) 0700, (G) 0800, (H) 0900, (I) 1,000, (J) 1,100, (K) 1,200, (L) 1300 UTC 17 August.

to the heavy rainfall in the inner core. The rainband possessed a quite stable pattern and intensified and elongated further outward in the upwind section. The stable evolution of the rainband was consistent with the quasi-steady evolution of the environmental VWS. The spiral rainband featured the quasi-stationary primary rainband in a TC embedded in a sheared environment, as discussed in Willoughby et al. (1984) and Li et al. (2017). Note that the TC translational speed was relatively large at 0800 UTC on 17 August, but decreased and almost remained unchanged at the speed of about 5.6–6.2 m s^{-1} during this period.

This suggests that although the translation of the storm might also contribute to the rainfall asymmetry, the environmental VWS dominantly controlled the asymmetric rainfall distribution, in particular the development of the quasi-steady primary rainband in the Rumbia case.

The deep-layer environmental VWS experienced a considerable weakening from 1,400 to 1900 UTC on 17 August, although the low-level shear showed little change (**Figure 5A**). As the deep-layer VWS was gradually weakening, the spiral rainband outside of 300 km radius from the storm

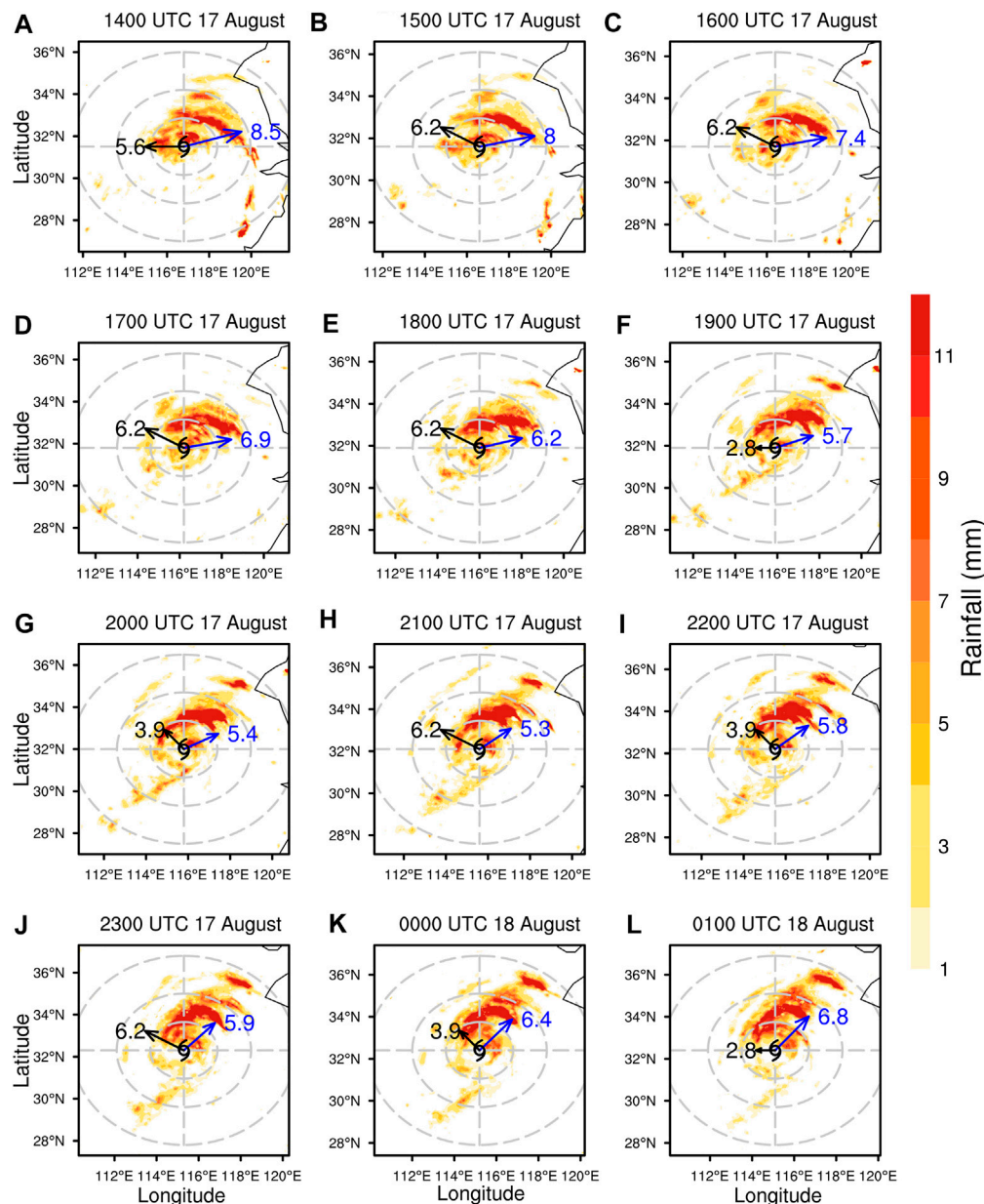


FIGURE 8 | Same as **Figure 6**, but at (A) 1,400, (B) 1,500, (C) 1,600, (D) 1700, (E) 1800, (F) 1900, (G) 2000, (H) 2,100, (I) 2,200, (J) 2300 UTC 17 August, (K) 0000, (L) 0100 UTC August 18.

center also experienced a drastic weakening and faded away quickly in an hour or so (**Figures 8A–F**). The rainfall mainly occurred to the north of the storm center and was still located to the right of the storm track and downshear-left of the environmental VWS. Note that the rainfall was distributed in an arc-shaped band mainly between radii of 150–300 km. In the meantime, some rainfall appeared near the storm center but became less organized after 1,600 August 17.

From 2100 UTC 17 August to 0100 UTC 18 August, the deep-layer VWS showed a slight increase with time, and the rainfall extended a little bit more northeastward with several

rainband segments developed in parallel (**Figures 8H–L**). With the increasing deep-layer VWS and the slowing down of the storm motion, relatively strong rainfall appeared in the inner-core region downshear-left again, indicating that the deep-layer VWS played a critical role in shaping the rainfall pattern during this period. The persistent downshear-left rainfall pattern with heavy rainfall further away from the storm center resulted in the accumulated heavy rainfall region some distance from the storm track, as we can see from **Figure 1A**. After the storm further slowed down and turned northeastward, strong rainfall remained to the

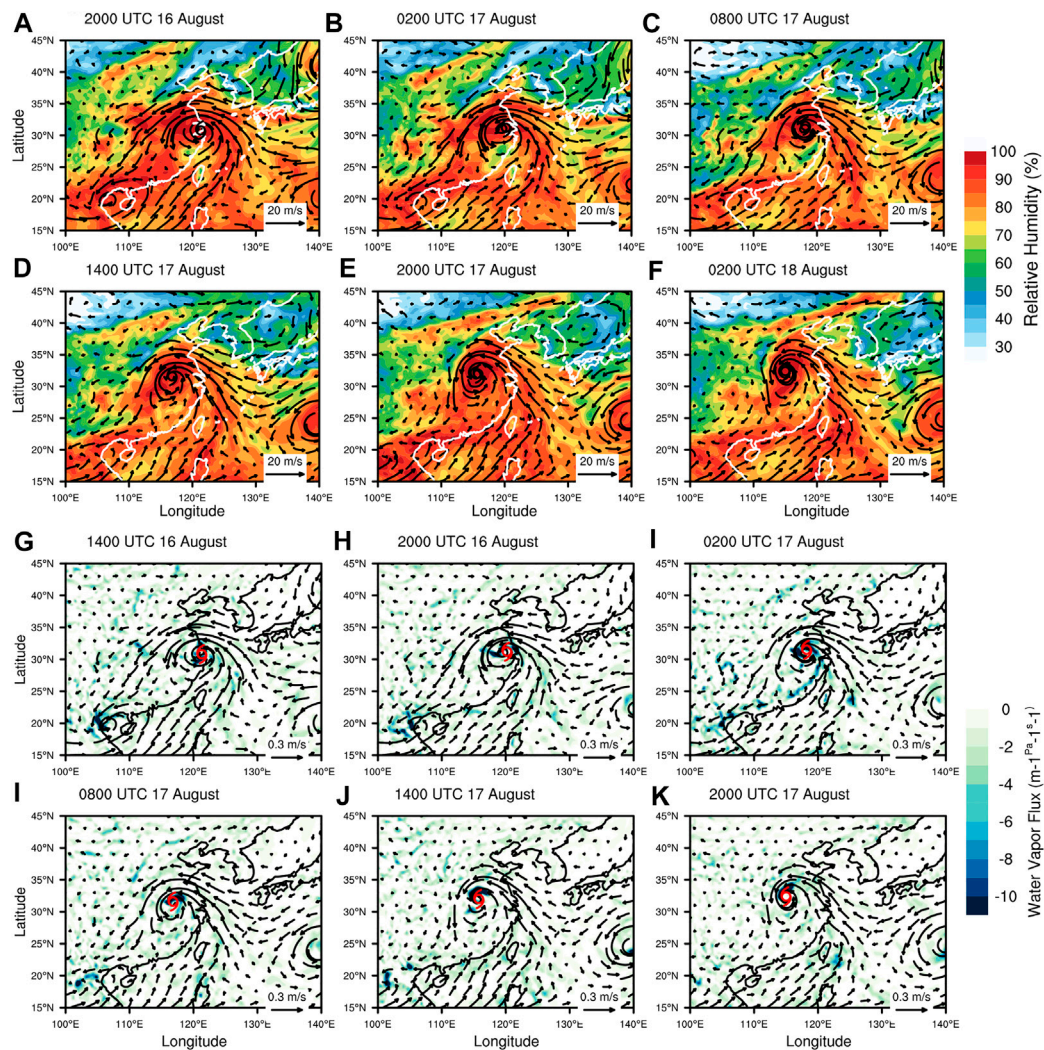


FIGURE 9 | The evolution of the lower tropospheric relative humidity (shading, %) and wind vectors (m s^{-1}), both averaged between 700 and 1,000 hPa: **(A)** 2000 UTC 16 August, **(B)** 0200, **(C)** 0800, **(D)** 1,400, **(E)** 2000 UTC 17 August, **(F)** 0200 UTC August 18, 2018. The lower tropospheric water vapor flux (arrows, $\text{m}^{-1} \text{Pa}^{-1} \text{s}^{-1}$) and vapor flux divergence (shading, $\text{m}^{-2} \text{Pa}^{-1} \text{s}^{-1}$), both averaged between 700 and 1,000 hPa: **(G)** 2000 UTC 16 August, **(H)** 0200, **(I)** 0800, **(J)** 1,400, **(K)** 2000 UTC 17 August, **(L)** 0200 UTC August 18, 2018. The cyclone symbol indicates the storm center at the given time.

northeast quadrant, or downshear-left and right-front of the storm motion (**Figure 1A**).

Water Vapor Supply

One of the necessary conditions for heavy rainfall induced by landfalling TCs (and also any other weather systems) is the water vapor supply. Therefore, it is important to examine the water vapor transport following the storm. Here, we analyzed the moisture conditions first and then the water vapor flux and water vapor flux divergence in the Rumbia case. This may help identify the water vapor sources of heavy rainfall induced by Rumbia. **Figures 9A–F** show the relative humidity and horizontal wind fields, both averaged in the lower troposphere between 700 and 1,000 hPa. The lower tropospheric relative humidity in the inner-core region of Rumbia was very high, mostly over 95% or even nearly

saturated near the storm center, in particular in the region with heavy rainfall. An interesting feature is the strong southwesterly-southeasterly monsoon flow with relatively high relative humidity to the southeast and northeast of the storm center, which can be traced upstream to the tropical western Pacific and South China Sea. This indicates that moisture transport by the monsoon flow is key to the water vapor supply to the rainfall of Rumbia.

To illustrate the water vapor transport more explicitly, we show the water vapor flux and vapor flux divergence, both were averaged between 700 and 1,000 hPa in **Figures 9G–L**. Consistent with the evolution of the layer averaged relative humidity and wind distributions in the lower troposphere, the water vapor flux and the vapor flux divergence fields show the major water vapor transport channel toward the storm's inner-core region with vapor flux convergence in the areas with high relative

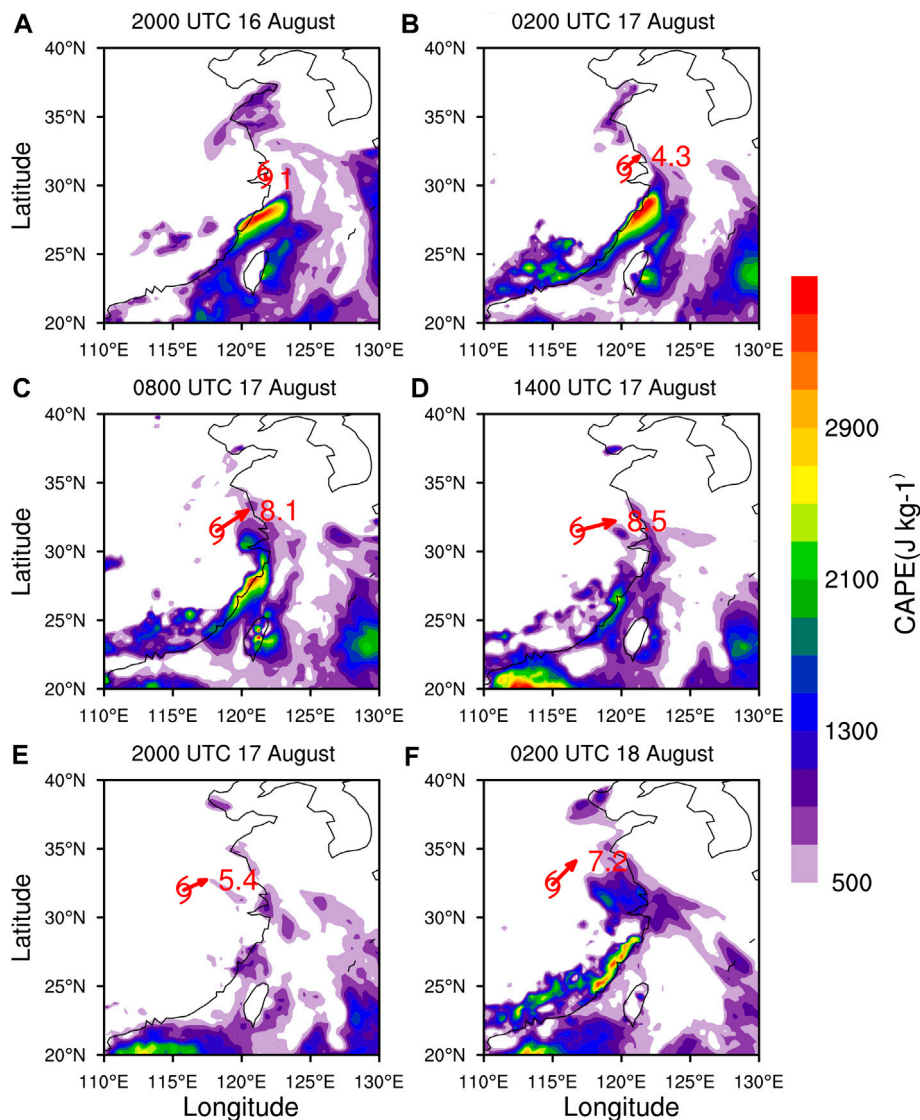


FIGURE 10 | Convective Available Potential Energy (CAPE, shading, J kg^{-1}) with the deep layer VWS vectors given at the storm center (red arrows): (A) 2000 UTC 16 August, (B) 0200, (C) 0800, (D) 1,400, (E) 2000 UTC 17 August, (F) 0200 UTC August 18, 2018. The cyclone symbol indicates the storm center at the given time. The red arrows and numbers show the 300–850 hPa VWS directions and magnitudes (m s^{-1}).

humidity. Particularly, the large vapor flux convergence is consistent with the large rainfall to the northeast quadrant of the storm or downshear-left (Figures 7, 8). Note that as the storm moved inland, the main water vapor transport channel was always strong in the southeast and northeast quadrants of the storm. In addition, a narrow vapor flux convergence zone corresponds to the primary spiral rainband discussed earlier in the 6 h from 0800 UTC August 17 (Figures 9I,J). In addition to the effect of the environmental VWS, the formation of the rainband seemed also to substantially contributed by the topographic effect since the spiral rainband was close to the terrain along the southeastern coastal region of China. After Rumbia moved further inland, the water vapor supply to the rainband was cut off and the rainband weakened (Figure 9J).

Nevertheless, the result suggests that the transport of water vapor by the southwesterly and southeasterly monsoon flow provided the necessary moisture conditions not only to the heavy rainfall downshear-left but also to the rainfall in the primary spiral rainband associated with Rumbia. The latter was obviously forced by not only the environmental VWS but also the orographic effect in Southeast China.

Convective Instability

Convective instability is key to convection and convective rainfall. Several measures are often used to imply the convective instability, including the convective available potential energy (CAPE), minimum in equivalent potential temperature in the mid-troposphere. We first examined the evolution of CAPE

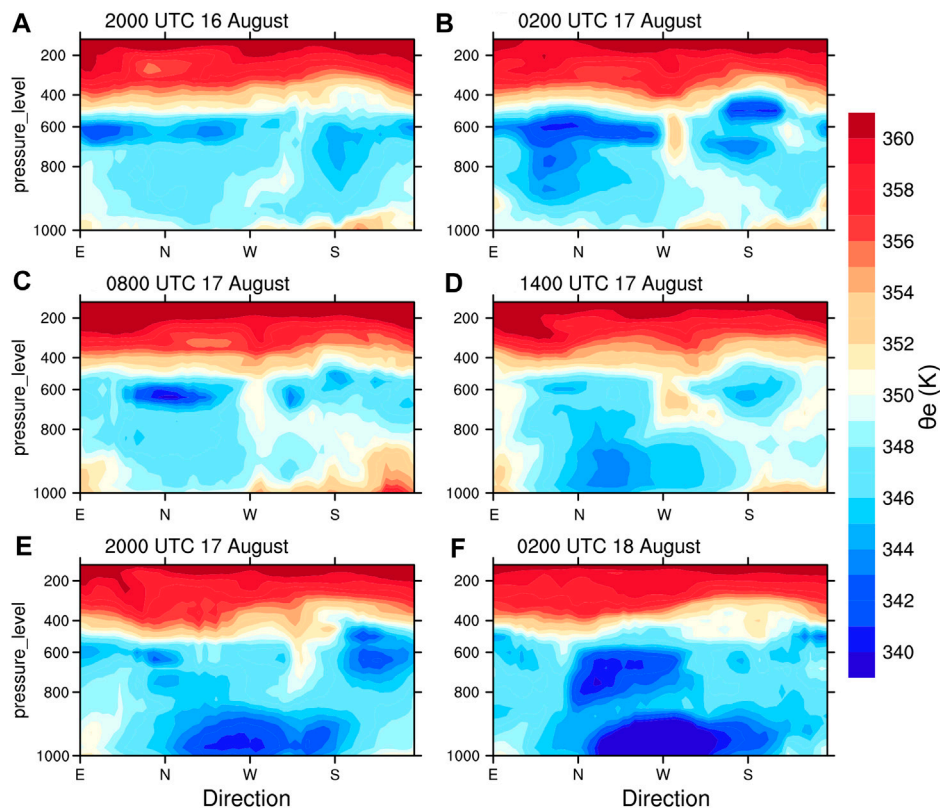


FIGURE 11 | The vertical cross-section of equivalent potential temperature (shading, K) averaged in an annulus between the radii of 150 and 300 km from the storm center: **(A)** 2000 UTC 16 August, **(B)** 0200, **(C)** 0800, **(D)** 1,400, **(E)** 2000 UTC 17 August, **(F)** 0200 UTC August 18, 2018.

distribution in **Figure 10**. In general, high CAPE was located over the tropical ocean and in the coastal region along Southeast China. Although the CAPE was not high in the inner-core region of Rumbia, the CAPE was relatively high to the southeast of the storm center, namely upstream of the rainfall region or in the downshear-right quadrant. This strongly suggests that high CAPE air with high moisture content was transported to the rainfall region, where the CAPE was quickly consumed by deep convection. **Figure 11** gives the vertical cross-section of equivalent potential temperature averaged in an annulus between the radii of 150 and 300 km from the storm center. This annulus mean was chosen to illustrate the difference in the vertical structure of convective stability in different quadrants of the storm. At the time of landfall and shortly after landfall of Rumbia, the equivalent potential temperature was relatively low in the lower troposphere in both the northwest and southwest quadrants while relatively high in both the southeast and northeast quadrants (**Figures 11A–D**). As Rumbia moved further inland, the equivalent potential temperature became much lower to the west of the storm, mainly because of the dry air intrusion from the north (**Figures 11E,F**). To the northeast-east of the storm center, the lower troposphere in which the equivalent potential temperature decreased with increasing height shows weak

convective instability (**Figures 11D–F**). The evolution of equivalent potential temperature is generally consistent with the horizontal distribution in CAPE shown in **Figure 10**.

Since the convective instability occurred mainly in the northeast quadrant of the storm, it is our interest to see the radial variation of convective instability in the northeast quadrant. **Figure 12** shows the evolutions of the quadrant-mean equivalent potential temperature and its vertical gradient ($\frac{\partial \theta_e}{\partial z}$). We can see that the region within about 200 km from the storm center shows a convectively stable layer near 950 hPa while the region outside the radius of 200 km was convectively unstable below 600 hPa in the mid-lower troposphere at the time of and shortly after the landfall of Rumbia (**Figures 12A–C**). Although the convective instability weakened somehow in the 6-h period from 08 UTC to 14 UTC 17 August, it strengthened again afterwards (**Figures 12E,F**) and could contribute to the enhancement of rainfall in the northeast quadrant as shown in **Figure 8**. The maintenance of convective instability in the northeast quadrant could be attributed to the warm and moist air transported from the warm tropical ocean as discussed in the last subsection.

The Secondary Circulation

The secondary circulation is key to both the intensity and heavy rainfall in a TC. Although being main driven by both boundary

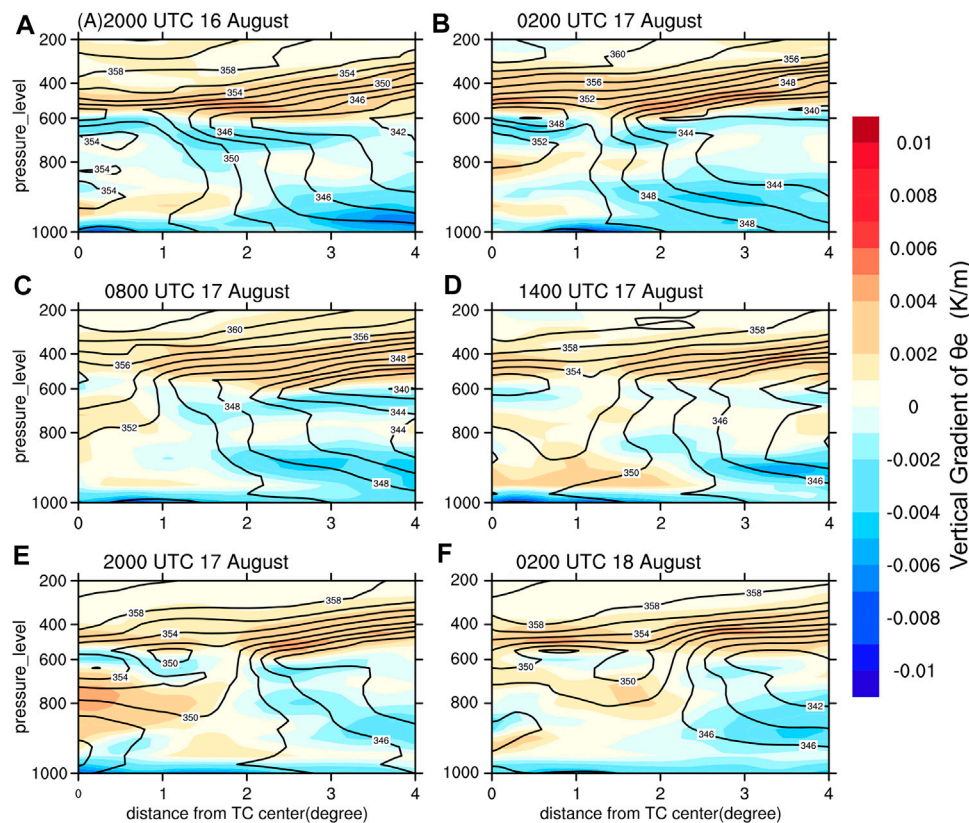


FIGURE 12 | Vertical-radius cross section of equivalent potential temperature (contours, K) and its vertical gradient ($\partial\theta/\partial z$) (shading, K/m). Both averaged in the northeast quadrant of the storm: (A) 2000 UTC 16 August, (B) 0200, (C) 0800, (D) 1,400, (E) 2000 UTC 17 August, (F) 0200 UTC August 18, 2018.

layer dynamics and diabatic heating in the eyewall for a well-developed TC, the secondary circulation in a weak and landfalling TC often does not develop well (e.g., Yu Z. et al., 2010). We have already discussed the evolution of environmental VWS and convective instability during and after the landfall of Rumbia above. We found that the northeast quadrant was convectively unstable in the mid-lower troposphere and Rumbia was mostly embedded in a deep-layer southwesterly VWS after its landfall. It is our interest to further examine the evolution of the secondary circulation in the northeast quadrant and its connection to the rainfall. Note that the resolution of the reanalysis data was not high enough to fully resolve the secondary circulation in a TC. However, Rumbia did not develop a compact inner-core structure and kept a tropical storm intensity at its landfall. Therefore, we examined the secondary circulation in the northeast quadrant of Rumbia based on the ERA5 reanalysis.

Figure 13 shows the radial wind and vertical motion averaged in the northeast quadrant, where the heavy rainfall occurred after Rumbia made landfall over East China. At the time of landfall, the secondary circulation in the northeast quadrant of Rumbia shows a deep inflow layer through the troposphere, but the upward motion was broad and quite weak. The maximum inflow occurred in the boundary layer

between 200 and 300 km radii from the storm center with the maximum upward motion in the upper troposphere (**Figure 13A**). Note that the deep-layer environmental VWS between 300 and 850 hPa was quite weak at the time when Rumbia made its landfall but substantially increased thereafter as it moved inland shortly after landfall (**Figure 5**). The secondary circulation in the northeast quadrant shows an inward shift of the maximum inflow in the boundary layer with substantially enhanced upward motion (**Figures 13B–D**). This suggests that the environmental VWS played a critical role in forcing the secondary circulation in the downshear quadrant of Rumbia during this time period when environmental VWS increased. Note that although the rainfall distribution shows two separate rainfall regions: one near the storm center and one near the radius of 200 km from the storm center in the northeast quadrant (**Figure 8A**), the secondary circulation based on the coarse resolution reanalysis data could not reflect the separate vertical motion center associated with the two separate rainfall regions (**Figures 13C,D**).

From 1400 UTC 17 August, the secondary circulation in the northeast quadrant shows some weakening with the maximum inflow and upward motion shifting radially outward compared with the previous 12 h. The inflow layer also became shallower

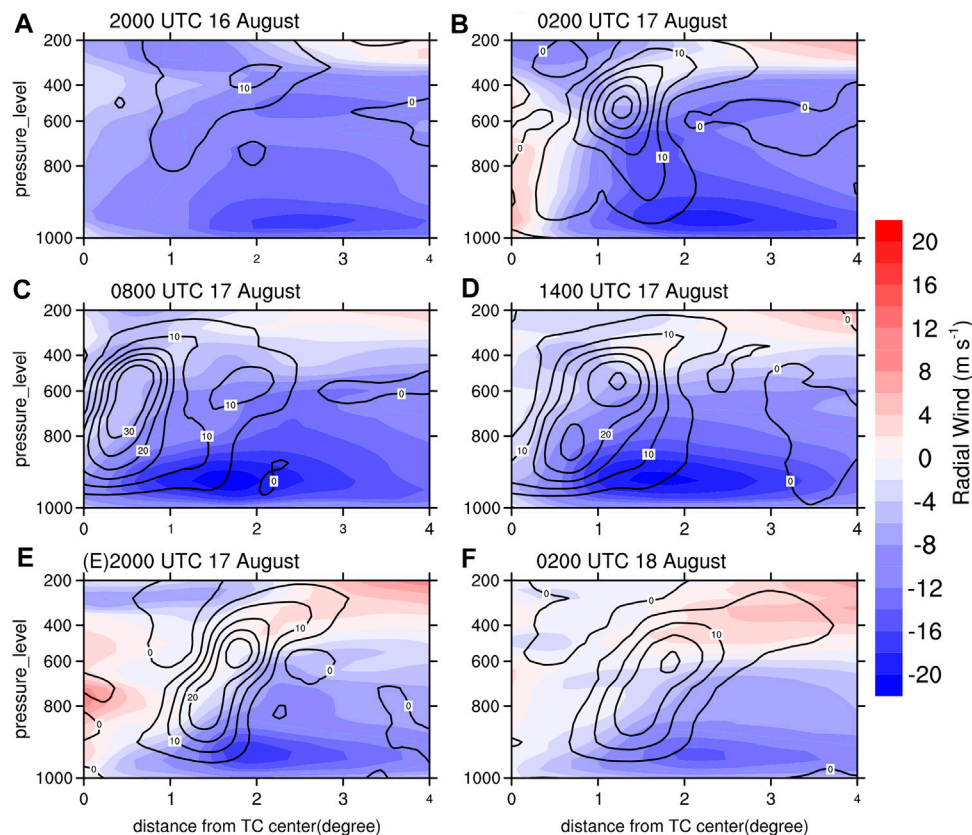


FIGURE 13 | Northeast quadrant mean radial wind (shading, m s^{-1}) and vertical motion (contours, m s^{-1}): (A) 2000 UTC 16 August, (B) 0200, (C) 0800, (D) 1,400, (E) 2000 UTC 17 August, (F) 0200 UTC August 18, 2018.

compared with that of the previous 6 h (**Figures 13E,F**). This change is roughly consistent with the weakening of rainfall near the storm center and the slightly outward shift of the rainband near the radius of 200 km mentioned above (**Figure 8**). During this time period, the deep-layer environmental VWS experienced some weakening (**Figure 5**) but remained still relatively strong, indicating that the environmental VWS still dominantly controlled the asymmetric structure of vertical motion and rainfall of Rumbia.

Zhang et al. (2013) found that the boundary layer is higher in the downshear side for a TC embedded in deep-layer environmental VWS. Ren et al. (2019) pointed out a front-rear asymmetric distribution of the TC boundary layer height. Since the depth of the inflow layer varied greatly in Rumbia after landfall (**Figure 13**), partially due to the variation of environmental VWS, we also looked at the evolution of the boundary layer height during the same time period. **Figure 14** presents the distribution and evolution of the boundary layer height. At the time of landfall, the deep-layer environmental VWS was very weak while the storm moved northwestward, and the boundary layer was high to the right of the storm track, mainly over the ocean (**Figure 14A**). With the rainfall increasing, the boundary layer showed to the right front of the storm

motion, now mainly over the land (**Figure 14B**). As the deep-layer VWS increased and the storm turned to the west-southwest, the area with a relatively high boundary layer increased and appeared still to the right of the storm track and also to the downshear and downshear left (**Figure 14C**). Finally, as the storm moved further inland and the decrease in the deep-layer VWS, the boundary layer became shallower to the right of the storm track and downshear-left while some increases appeared to the front and front-left of the storm motion (**Figures 14E,F**). The shallowing of the boundary layer seems to be consistent with the shallowing of the inflow boundary layer in the northeast quadrant as shown in **Figures 13E,F**. The above results are consistent with the finding of Reasor et al. (2013), who found that the boundary layer depth is higher where strong convection occurs. Therefore, it seems that the asymmetric distribution of the boundary layer height could be associated with the asymmetric distribution of convection.

DISCUSSION

Tropical Storm Rumbia (2018) resulted in long-lasting, heavy rainfall to East China after its landfall in Shanghai on August 16, 2018, although it had a weak intensity at

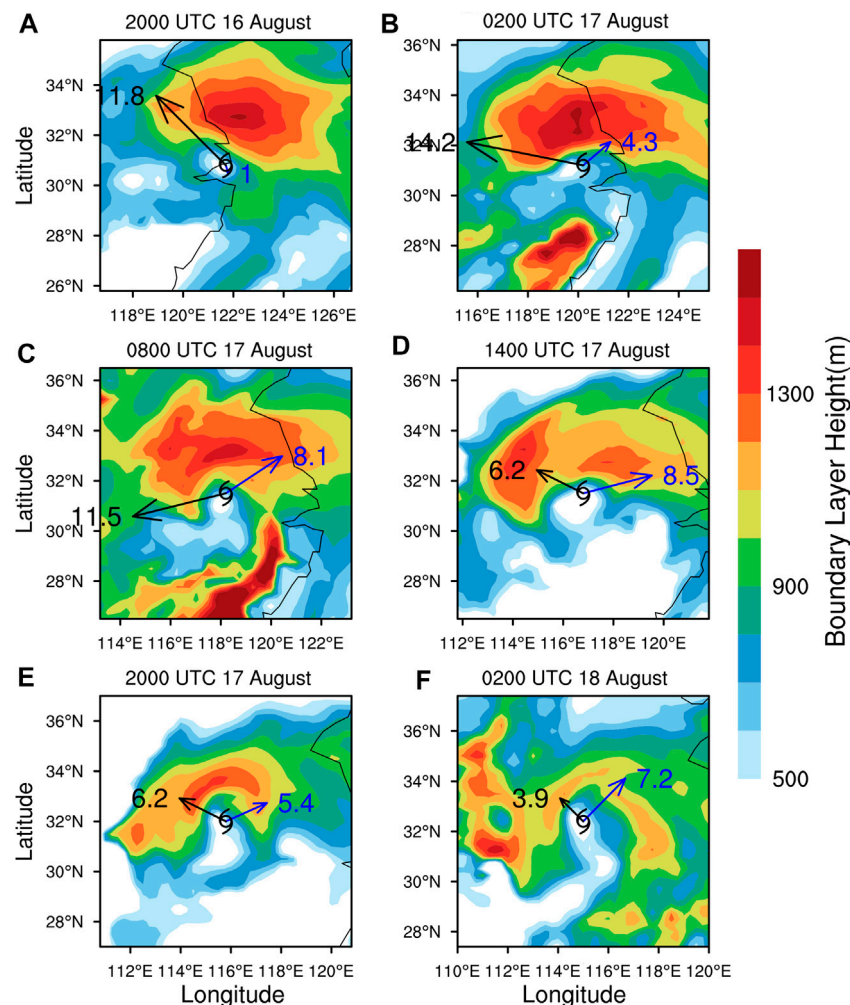


FIGURE 14 | Boundary layer height (shading, m): (A) 2000 UTC 16 August, (B) 0200, (C) 0800, (D) 1,400, (E) 2000 UTC 17 August, (F) 0200 UTC 18 August. Black arrows and numbers denote the storm motion vectors and speeds. Blue arrows and numbers refer to the directions and magnitudes of the deep layer VWS between 300 and 850 hPa.

its landfall. In this study, the ERA5 reanalysis data, the best-track TC data of STI/CMA, and rainfall observations from CMA were used to examine the rainfall evolution of Rumbia after its landfall. The ERA5 reanalysis was chosen because it captures the observed hourly rainfall evolution over land.

This study mainly analyzed the rainfall induced by Rumbia qualitatively. As illustrated in a schematic **Figure 15**, Rumbia was embedded in an environment with a deep-layer (300–850 hPa) southwesterly vertical wind shear. The translation of Rumbia also contributed to the inner-core rainfall distribution to some extent. The strong southwesterly-southeasterly summer monsoon flow (**Figures 10–12**) provided moisture, convective instability conditions, and some dynamical effect partially by modifying the VWS. The low-level convective instability and the deep-layer environmental VWS were important to the asymmetric rainfall evolution after landfall.

The use of relatively coarse resolution reanalysis data did not allow for a detailed quantitative budget analysis to understand the relative importance of various processes in controlling the observed rainfall distribution and evolution. In a future study, high-resolution numerical experiments can be conducted to simulate the rainfall of Rumbia and help quantify contributions of various physical and dynamical processes to the asymmetric rainfall distribution and understand the involved dynamical mechanisms. In particular, the short-lived primary rainband in the observation is another topic that could be further investigated. It is unclear whether the orographic effect or the land-sea contrast played any important roles in initiating and shaping the rainband. Also, we have only analyzed the possible rainfall processes before Rumbia turned northeastward. Observations showed that another period of heavy rainfall occurred after Rumbia turned northeastward. Therefore, future studies may also extend the analysis to the

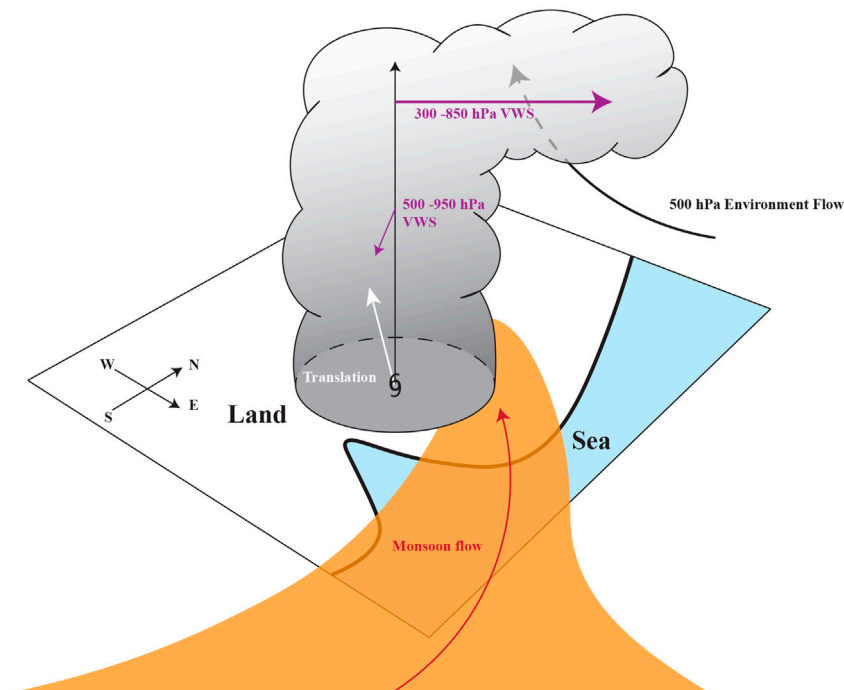


FIGURE 15 | Schematic illustration of asymmetric rainfall evolution in Rumbia. The purple arrows indicate the 300–850 hPa VWS and 500–950 hPa VWS. The white arrow shows the TC translation direction. The black and red streamlines represent the 500 hPa environmental flow and the 850 hPa monsoon flow, respectively. The yellow area indicates the high energy air mass transported into the heavy rainfall region from the South China Sea and the western North Pacific by the low-level monsoon flow.

second rainfall period because the heavy rainfall also induced great economic loss in China.

CONCLUSION

Rumbia was embedded in an environment with a substantially increasing deep-layer southwesterly VWS during landfall. Compared to the VWSs in the layers of 200–850 hPa and 500–950 hPa, heavy rainfall occurred mostly downshear-left in its inner-core region and downshear-right in the outer-core region, relative to the 300–850 hPa VWS. In the study period, the heavy rainfall in the inner-core region was also located mainly to the right of the storm track, suggesting that the storm motion might also have contributed partly to the asymmetric rainfall distribution in Rumbia, especially when the VWS was very weak (<5 m/s) before its landfall.

The strong southwesterly-southeasterly summer monsoon flow over the western North Pacific transported warm and moist air from the tropical ocean and the East China Sea to the core region of Rumbia, providing moisture and convective instability conditions for the sustained rainfall even after Rumbia moved well inland. This low-level moist monsoon flow also caused VWS change and thus imposed an impact on TC precipitation, in addition to increasing convection instability in the TC rain area. Both the convective instability in the mid-lower troposphere and the deep-layer environmental VWS played

important roles in deepening the inflow boundary layer and the development of the secondary circulation and the heavy rainfall in the northeast quadrant of Rumbia.

Such extreme events as in this study are very challenging to operational forecasts and often lead to disasters in the affected regions. Further in-depth studies are recommended in regard of the rainfall evolution in the weak TCs. This study further calls for an understanding of the involved physical processes/mechanisms that are responsible for the extreme rainfall induced by landfalling TCs, which can help improve the rainfall forecast skills and support damage mitigation in the future.

DATA AVAILABILITY STATEMENT

The original contributions presented in the study are included in the article/Supplementary Material, further inquiries can be directed to the corresponding author.

AUTHOR CONTRIBUTIONS

LT and ZY conceived the study and wrote the article. YW provided critical feedback and helped shape the research and article. LW helped the data analysis. All authors contributed to the article and approved the submitted version.

FUNDING

The work was supported in part by Key Program for International S&T Cooperation Projects of China (No. 2017YFE0107700), the National Natural Science Foundation of China (41875080), Scientific Research Program of Shanghai Science and

Technology Commission (19dz1200101), and in part by Shanghai Talent Development Fund, Program of Shanghai Academic/Technology Research Leader (21XD1404500), Fujian Key Laboratory of Severe Weather Open Foundation (2020TFS01), and Typhoon Scientific and Technological Innovation group of Shanghai Meteorological Service.

REFERENCES

- Atallah, E., Bosart, L. F., and Ayyer, A. R. (2007). Precipitation Distribution Associated with Landfalling Tropical Cyclones over the Eastern United States. *Mon. Weather Rev.* 135 (6), 2185–2206. doi:10.1175/mwr3382.1
- Cao, L., Qiao, D., Chen, X., and Dai, W. (2018). Laplace ℓ_1 Huber Based Cubature Kalman Filter for Attitude Estimation of Small Satellite. *Acta Astronaut.* 148, 48–56. doi:10.1016/j.actaastro.2018.04.020
- Chen, L. S., and Ding, Y. H. (1979). *An Introduction to Typhoons in West Pacific*. Beijing: Science Press.
- Chen, Y., and Yau, M. K. (2001). Spiral Bands in a Simulated hurricane. Part I: Vortex Rossby Wave Verification. *J. Atmos. Sci.* 58 (15), 2128–2145. doi:10.1175/1520-0469(2001)058<2128:sbiash>2.0.co;2
- Chen, S. S., Knaff, J. A., and Marks, F. D., Jr (2006). Effects of Vertical Wind Shear and Storm Motion on Tropical Cyclone Rainfall Asymmetries Deduced from TRMM. *Mon. Weather Rev.* 134 (11), 3190–3208. doi:10.1175/mwr3245.1
- Deng, D., and Ritchie, E. A. (2020). Rainfall Mechanisms for One of the Wettest Tropical Cyclones on Record in Australia-Oswald (2013). *Mon. Weather Rev.* 148 (6), 2503–2525. doi:10.1175/mwr-d-19-0168.1
- Deng, D., Davidson, N. E., Hu, L., Tory, K. J., Hankinson, M. C. N., and Gao, S. (2017). Potential Vorticity Perspective of Vortex Structure Changes of Tropical Cyclone Bilis (2006) during a Heavy Rain Event Following Landfall. *Mon. Weather Rev.* 145 (5), 1875–1895. doi:10.1175/mwr-d-16-0276.1
- Feng, X., and Shu, S. (2018). How Do Weak Tropical Cyclones Produce Heavy Rainfall when Making Landfall over China. *J. Geophys. Res. Atmos.* 123 (21), 11–830. doi:10.1029/2018jd029228
- Finocchio, P. M., Majumdar, S. J., Nolan, D. S., and Iskandarani, M. (2016). Idealized Tropical Cyclone Responses to the Height and Depth of Environmental Vertical Wind Shear. *Mon. Weather Rev.* 144 (6), 2155–2175. doi:10.1175/mwr-d-15-0320.1
- Fu, H., Wang, Y., Riemer, M., and Li, Q. (2019). Effect of Unidirectional Vertical Wind Shear on Tropical Cyclone Intensity Change-Lower-Layer Shear versus Upper-Layer Shear. *J. Geophys. Res. Atmos.* 124 (12), 6265–6282. doi:10.1029/2019jd030586
- Hersbach, H., Bell, B., Berrisford, P., Hirahara, S., Horányi, A., Muñoz-Sabater, J., et al. (2020). The ERA5 Global Reanalysis. *Q.J.R. Meteorol. Soc.* 146 (730), 1999–2049. doi:10.1002/qj.3803
- Huang, P., Huang, H. P., Chen, H. J., and Zheng, Y. (2010). Analysis on Moving Path of Tropical Storm “SWAN”(No. 0907) and its Torrential Rain. *J. Meteorol. Res. Appl.* 31, 5–8. doi:10.1002/chin.200034171
- Jiang, H., and Ramirez, E. M. (2013). Necessary Conditions for Tropical Cyclone Rapid Intensification as Derived from 11 Years of TRMM Data. *J. Clim.* 26 (17), 6459–6470. doi:10.1175/jcli-d-12-00432.1
- Jiang, H., Halverson, J. B., and Simpson, J. (2008). On the Differences in Storm Rainfall from Hurricanes Isidore and Lili. Part I: Satellite Observations and Rain Potential. *Weather Forecast.* 23 (1), 29–43. doi:10.1175/2007waf2005096.1
- Kang, Z. M., Chen, T., Qian, C. H., and Yang, K. M. (2008). Diagnostic Analysis on Torrential Rain Caused by the Tropical Storm Bilis (0604). *Plateau Meteorol.* 27 (3), 596–607.
- Li, Q., Wang, Y., and Duan, Y. (2017). A Numerical Study of Outer Rainband Formation in a Sheared Tropical Cyclone. *J. Atmos. Sci.* 74 (1), 203–227. doi:10.1175/jas-d-16-0123.1
- Lonfat, M., Marks, F. D., Jr, and Chen, S. S. (2004). Precipitation Distribution in Tropical Cyclones Using the Tropical Rainfall Measuring Mission (TRMM) Microwave Imager: A Global Perspective. *Mon. Weather Rev.* 132 (7), 1645–1660. doi:10.1175/1520-0493(2004)132<1645:pditcu>2.0.co;2
- Lonfat, M., Rogers, R., Marchok, T., and Marks, F. D., Jr (2007). A Parametric Model for Predicting hurricane Rainfall. *Mon. Weather Rev.* 135 (9), 3086–3097. doi:10.1175/mwr3433.1
- Meng, W., and Wang, Y. (2016a). A Diagnostic Study on Heavy Rainfall Induced by Typhoon Utor (2013) in South China: 1. Rainfall Asymmetry at Landfall. *J. Geophys. Res. Atmos.* 121 (21), 12–781. doi:10.1002/2015jd024646
- Meng, W., and Wang, Y. (2016b). A Diagnostic Study on Heavy Rainfall Induced by Landfalling Typhoon Utor (2013) in South China: 2. Postlandfall Rainfall. *J. Geophys. Res. Atmos.* 121 (21), 12–803. doi:10.1002/2015jd024647
- Parrish, J. R., Burpee, R. W., Marks, F. D., Jr, and Grebe, R. (1982). Rainfall Patterns Observed by Digitized Radar during the Landfall of Hurricane Frederic (1979). *Mon. Wea. Rev.* 110 (12), 1933–1944. doi:10.1175/1520-0493(1982)110<1933:rpbdr>2.0.co;2
- Reasor, P. D., Rogers, R., and Lorsolo, S. (2013). Environmental Flow Impacts on Tropical Cyclone Structure Diagnosed from Airborne Doppler Radar Composites. *Mon. Weather Rev.* 141 (9), 2949–2969. doi:10.1175/mwr-d-12-00334.1
- Ren, Y., Zhang, J. A., Guimond, S. R., and Wang, X. (2019). Hurricane Boundary Layer Height Relative to Storm Motion from GPS Dropsonde Composites. *Atmosphere* 10 (6), 339. doi:10.3390/atmos10060339
- Rogers, R., Chen, S., Tenerelli, J., and Willoughby, H. (2003). A Numerical Study of the Impact of Vertical Shear on the Distribution of Rainfall in Hurricane Bonnie (1998). *Mon. Weather Rev.* 131 (8), 1577–1599. doi:10.1175//2546.1
- Shapiro, L. J. (1983). The Asymmetric Boundary Layer Flow under a Translating hurricane. *J. Atmos. Sci.* 40 (8), 1984–1998. doi:10.1175/1520-0469(1983)040<1984:tblfu>2.0.co;2
- Wang, Y., Wang, Y., and Fudeyasu, H. (2009). The Role of Typhoon Songda (2004) in Producing Distantly Located Heavy Rainfall in Japan*. *Mon. Weather Rev.* 137 (11), 3699–3716. doi:10.1175/2009mwr2933.1
- Wang, Y., Shen, X., and Chen, D. (2012). Verification of Tropical Cyclone Rainfall Predictions from CMA and JMA Global Models. *J. Trop. Meteorol.* 18, 537–542. doi:10.16555/j.1006-8775.2012.04.014
- Willoughby, H. E., Marks, F. D., Jr, and Feinberg, R. J. (1984). Stationary and Moving Convective Bands in Hurricanes. *J. Atmos. Sci.* 41 (22), 3189–3211. doi:10.1175/1520-0469(1984)041<3189:samcbi>2.0.co;2
- Willoughby, H. E. (1992). Linear Motion of a Shallow-Water Barotropic Vortex as an Initial-Value Problem. *J. Atmos. Sci.* 49 (21), 2015–2031.
- Wingo, M. T., and Cecil, D. J. (2010). Effects of Vertical Wind Shear on Tropical Cyclone Precipitation. *Mon. Weather Rev.* 138 (3), 645–662. doi:10.1175/2009mwr2921.1
- Yu, Z., and Wang, Y. (2018). “Rainfall Distribution in Landfalling Tropical Cyclones,” in *Extreme Weather*. Editors P. J. Sallis (IntechOpen). doi:10.5772/intechopen.75910
- Yu, J., Tan, Z., and Wang, Y. (2010a). Effects of Vertical Wind Shear on Intensity and Rainfall Asymmetries of strong Tropical Storm Bilis (2006). *Adv. Atmos. Sci.* 27 (3), 552–561. doi:10.1007/s00376-009-9030-6
- Yu, Z., Liang, X., Yu, H., and Chan, J. C. L. (2010b). Mesoscale Vortex Generation and Merging Process: A Case Study Associated with a post-landfall Tropical Depression. *Adv. Atmos. Sci.* 27 (2), 356–370. doi:10.1007/s00376-009-8091-x
- Yu, Z., Wang, Y., and Xu, H. (2015). Observed Rainfall Asymmetry in Tropical Cyclones Making Landfall over China. *J. Appl. Meteorol. Climatol.* 54 (1), 117–136. doi:10.1175/jamc-d-13-0359.1
- Yu, Z., Wang, Y., Xu, H., Davidson, N., Chen, Y., Chen, Y., et al. (2017). On the Relationship between Intensity and Rainfall Distribution in Tropical Cyclones Making Landfall over China. *J. Appl. Meteorol. Climatol.* 56 (10), 2883–2901. doi:10.1175/jamc-d-16-0334.1
- Yu, Z., Chen, Y. J., Ebert, B., Davidson, N. E., Xiao, Y., Yu, H., et al. (2020). Benchmark Rainfall Verification of Landfall Tropical Cyclone Forecasts by

- Operational ACCESS-TC over China. *Meteorol. Appl.* 27 (1), e1842. doi:10.1002/met.1842
- Zhang, Q., Wu, L., and Liu, Q. (2009). Tropical Cyclone Damages in China 1983–2006. *Bull. Amer. Meteorol. Soc.* 90 (4), 489–496. doi:10.1175/2008bams2631.1
- Zhang, J. A., Rogers, R. F., Reasor, P. D., Uhlhorn, E. W., and Marks, F. D., Jr (2013). Asymmetric hurricane Boundary Layer Structure from Dropsonde Composites in Relation to the Environmental Vertical Wind Shear. *Mon. Weather Rev.* 141 (11), 3968–3984. doi:10.1175/mwr-d-12-00335.1

Conflict of Interest: The authors declare that the research was conducted in the absence of any commercial or financial relationships that could be construed as a potential conflict of interest.

Publisher's Note: All claims expressed in this article are solely those of the authors and do not necessarily represent those of their affiliated organizations, or those of the publisher, the editors and the reviewers. Any product that may be evaluated in this article, or claim that may be made by its manufacturer, is not guaranteed or endorsed by the publisher.

Copyright © 2021 Tang, Wang, Yu and Wang. This is an open-access article distributed under the terms of the Creative Commons Attribution License (CC BY). The use, distribution or reproduction in other forums is permitted, provided the original author(s) and the copyright owner(s) are credited and that the original publication in this journal is cited, in accordance with accepted academic practice. No use, distribution or reproduction is permitted which does not comply with these terms.



The Cold Avoidance of Typhoons in Their North Turning Over the South China Sea

Shaojun Lai^{1,2,3}, Ying Li^{1*}, Fen He⁴, Yufei Wang³ and Yan Chen³

¹State Key Laboratory of Severe Weather, Chinese Academy of Meteorological Sciences, Beijing, China, ²Fujian Key Laboratory of Severe Weather, Fuzhou, China, ³Fuzhou Meteorological Bureau, Fuzhou, China, ⁴Fujian Climate Center, Fuzhou, China

OPEN ACCESS

Edited by:

Hui Yu,
China Meteorological Administration,
China

Reviewed by:

Nannan Qin,
Fudan University, China
Jia Liang,
Nanjing University of Information
Science and Technology, China

*Correspondence:

Ying Li
yli@cma.gov.cn

Specialty section:

This article was submitted to
Atmospheric Science,
a section of the journal
Frontiers in Earth Science

Received: 24 September 2021

Accepted: 01 November 2021

Published: 03 December 2021

Citation:

Lai S, Li Y, He F, Wang Y and Chen Y
(2021) The Cold Avoidance of
Typhoons in Their North Turning Over
the South China Sea.
Front. Earth Sci. 9:782195.
doi: 10.3389/feart.2021.782195

Based on the typhoon best tracks of the China Meteorological Administration (CMA), ERA5 reanalysis data of ECMWF at 0.25 degrees horizontal resolution, and NOAA optimal interpolated sea surface temperature (OISST V2) data, the dynamical compositing analysis is used to study the north turning at nearly 90 degrees of 4 westward typhoons over the South China Sea (SCS). The composite analysis results show that: (1) As the typhoon goes westward into the SCS, the upper-level westerly trough moves eastward to the vicinity of 110°E in the mainland of China, and the western North Pacific subtropical high (SH) retreats eastward at the same time, which weakens the steering flow of typhoon and slows down its movement. (2) The cold air guided by the westerly trough invades southwardly into the western part of SCS from the mainland leading to a descending and divergent airflow in the lower-to-middle atmospheric layers and enhancing the eastward pressure gradient force (PGF) in the west quadrant of the typhoon, which blocks and repels the typhoon from moving any further westward. (3) Due to the cold air intrusion, the vertical atmospheric stratification in the west quadrant of the typhoon becomes static and stable, which may suppress the convection, impeding a typhoon's westward motion. (4) With the cold air involving to the south of the typhoon, the direction of the PGF on the typhoon switches from eastward to northward, and the SH falling southward enhances the southwesterly airflow on the south of the typhoon at the same time. The remarkable increase of the northward steering airflows of the typhoon results in an abrupt northward turn. (5) In addition, the sea surface temperature (SST) and the ocean heat content (OHC) on the western part of the SCS is also reduced, attributed to the cold air cooling, and the typhoon is likely to avoid the cold ocean and approach a relatively warmer region. This study suggests that cold avoidance during the westward movement of typhoons is worthy of consideration in the operational forecast of typhoon tracks.

Keywords: typhoon, cold avoidance, north turning, motion change, asymmetric structure

INTRODUCTION

A tropical cyclone (TC) is a kind of severe weather system which can cause tremendous loss of human life and social property through excessive torrential rainfall, flash floods, and strong winds, etc. The western North Pacific (WNP) basin experiences on average 26 TCs each year, accounting for about 33% of the global total, and is the most active region of TCs on the Earth (Yumoto and Matsuura, 2001; Wu and Wang, 2004). What is more, 13% of TCs are generated in the South China

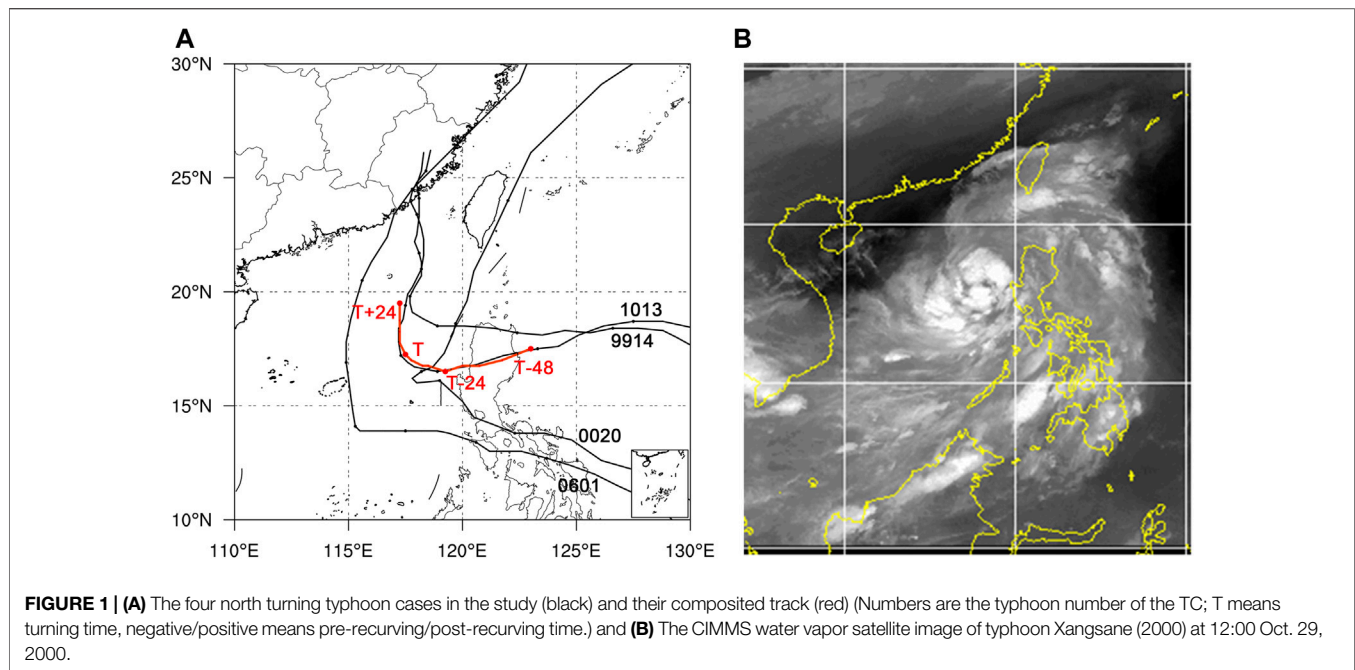
Sea (SCS) (Wang and Fei, 1987). TCs can bring enormous disasters to the Pacific islands and coastal regions, and an average of 472 people were killed each year by TCs making landfall during the period 1983–2006, with the greatest casualties occurring in coastal cities in Zhejiang, Fujian, and Guangdong Provinces (Zhang et al., 2009). In general, a TC generating in the WNP takes one of the three typical tracks: westward, northwestward, and northeastward recurving (Wu and Wang, 2004; Wu et al., 2005a) and may affect the SCS region (including the Philippines), the coastal region of China (including the island of Taiwan), and the region of Japan (Wu and Wang, 2004) accordingly. It is very important to make accurate forecasts of TC motion to prevent and defend against TC disasters.

In the past few decades, dramatic improvements have been made in the forecasting performance of TC tracks, which could be attributed to two major developments (Elsberry, 2007). One is the forecasting performance of numerical weather prediction (NWP) models by the rapid advances in computing power, higher weather prediction models resolutions, and data assimilation, and rapid growth in available remote sensing observations (Rappaport et al., 2009; Abernethy, 2010). The other is the operational application of the multi-model consensus technique (Goerss, 2000; Goerss et al., 2004; Elsberry, 2014), which helps to improve short-range track forecasts greatly (Gall et al., 2013). As a result, it is possible to provide 3-days, 5-days, or even longer track forecast products for many operational centers. However, it is still difficult to make accurate forecasting on unusual TC tracks (UNTK) in terms of both numerical prediction and subjective forecast. Zhang et al. (2018) identified 1,059 typhoons over the WNP in the past 65 years and found that the UNTK events could be categorized into seven types, in which the sharply north turning typhoons accounted for more than 20%, and all of the UNTK events tended to take place in the areas to the south of 30°N with the most frequency in the SCS and the east of the Philippines. Based on operational track forecasts from the NMC/CMA for seven sudden north-turning cases during 2005–2010, the average 24- and 48-h forecast errors in distance increased by 29.3 and 68.3%, respectively, compared to the average errors for all TCs (Wu et al., 2013).

It is well known that TCs exhibited a wide variety of motions influenced by environmental large-scale systems as steering flow (Chen and Ding, 1979; Neumann, 1992), beta effect (e.g., Chan and Williams, 1987; Wang and Holland, 1996), the spatial distribution of SST (Chan, 1995), diabatic heating (Wu and Wang, 2001), asymmetric structure (Liang and Wu, 2015), orographic effects (Brand and Blelloch, 1974; Wang, 1980; Yeh and Elsberry, 1993a; Yeh and Elsberry, 1993b; Xu et al., 2013), and so on. Based on the statistics presented by Elsberry (1995), the TCs motion is mainly controlled by the environmental steering flow (Chan and Gray, 1980; Holland, 1983; Carr and Elsberry, 1990; Harr and Elsberry, 1995; Berger et al., 2011; Choi et al., 2013; Wu et al., 2013), composed of the subtropical ridges, midlatitude troughs, and cyclonic circulations. The TCs may be slow, stagnated, or recurved because of the change of the steering flow related to the large-scale systems surrounding them, such as relatively weaker SH, the stronger westerlies and continent high over China, or the presence of a deep midlatitude baroclinic wave/trough during the season of late summer (Wu et al., 2004).

In terms of the research of abruptly northward turning tracks, consensus analysis indicates the approach of a deep westerly trough and the eastward retreat of the SH are found to be favorable to a northward shift (Shi et al., 2014). Holland and Wang (1995) found that typhoons tended to recurve into the midlatitudes when a synoptic-scale trough moved away from East Asia into the subtropical ocean. Relevant research shows that the northward track deflection is attributed to the combined effects of the mid- and low-latitude systems (Kieu et al., 2012; Qian et al., 2013; Shi et al., 2014). Li et al. (2012) found that a sharp northward turning of Typhoon (Meranti, 2010) was associated with a northwestward-moving cold vortex on the northern side of the storm. Carr and Elsberry (1995) conducted a pioneering study on the sudden TC track change embedded in monsoon gyres (MGs) over the WNP. In fact, nearly 70% of TCs over the WNP are associated with a monsoon gyre (MG, Chen et al., 2004). Monsoonal influences on TC westward or sharp northward turnings over the SCS and the WNP have been examined in various time scales of the Madden–Julian oscillation (MJO), quasi-biweekly oscillation (QBW), and synoptic-scale flow (Wu et al., 2011; Wu et al., 2013; Liang and Wu, 2015). Typhoon Megi (2010) is a typical north-turning example, Bi et al. (2015) found that the low-frequency (10–60 days) MG interacted with Megi and affected its track change. Peng et al. (2014) revealed the cold-air intrusion from the northwest played a key role in the big turn of Megi through its adjustment to the large-scale circulation. In the lower layers, the northerly inflow of cold air tends to destroy the axisymmetric thermal structure of the TC, which may reduce the moving speed of the TC (Chou et al., 2008). Chen et al. (1997) revealed that the asymmetry of the thermal structure and the strength of the thermal instability layer of the TCs could lead to the significant anomaly of the TC track.

Underlying conditions also are important factors impacting the abnormal motions of TCs. Topographic effects can influence low-level flows and induce significant asymmetric diabatic heating resulting in TC track changes (Fiorino and Elsberry, 1989; Yeh and Elsberry, 1993a; Yeh and Elsberry, 1993b; Elsberry, 1995; Wang et al., 2012). TCs tend to move into a region with a higher SST value and a favorable condition for TC deflection could be established when the SST gradient is perpendicular to the mean flow (Chang and Madala, 1980). The positive SST anomalies (SSTA) over the equatorial western and central Pacific appear to be a major factor contributing to a northward-shifted typhoon track (Tu et al., 2009). Yun et al. (2012) studied a northeastward-moving TC demonstrating that the TC motion was sensitive to the SST magnitude and gradient. Xu et al. (2013) conducted a 60-years (1950–2009) survey on TCs that made landfall on China's mainland and performed a set of numerical experiments. They proposed that the warmer land surface, with intense moisture supply from the summer Asian monsoon, was conducive to deep convection that attracts supertyphoons. The straight-moving (i.e., northward moving) TC will deflect toward the region of warmer SST when SST is zonally asymmetric (Choi et al., 2013). The slowdown of motion and the asymmetric latent heating are the main reasons why the typhoon Morakot (2009) caused extreme rainfall in Taiwan (Liang et al., 2011; Wu et al., 2011; Wang et al., 2012).



Although a great deal of work has been carried out on TC motion anomalies from different aspects, there is still a larger error in the prediction of abruptly turning TC tracks due to the lack of mechanism recognition. In particular, over the SCS, a high-frequency area of TC sharp turning is renowned for complicated interactions between TCs and mid-latitude systems (Shi et al., 2014). More importantly, there is only a limited time to make a prediction on TC motion change and landfalling site for the TCs over the SCS because of a short distance to the coasts (Ling et al., 2016). Therefore, it is a challenge to make accurate forecasting on abnormal changes in motion of TCs over the SCS. This study aims to gain a better understanding of the relationship between TC north turning and cold air intrusion in order to promote TC track forecasting technique over the SCS. The description of the data and methods are given in “Data and Methods” section. Section three presents the evolution of the synoptical circulation background for the north turning briefly. Section four demonstrates the cold avoidance characteristics during the north turning of TCs, followed by a summary and discussion in section five.

DATA AND METHODS

Data

The TCs track data downloaded from (<http://tcdata.typhoon.org.cn/en/index.html>) the Shanghai Typhoon Institute of the China Meteorological Administration (CMA-STI; Ying et al., 2014) are in 6-h intervals with position, minimum sea level pressure, and maximum wind speed near the TC center. ERA5 is the fifth generation of the European Centre for Medium-Range Weather Forecasts (ECMWF) atmospheric analysis of the global climate

(Hennermann and Berrisford, 2018). ERA5 datasets employed in this paper include 37 pressure levels and surface hourly grid data with a spatial resolution of 0.25° longitude \times 0.25° latitude from 1979 to the present. The data can be accessed easily from the Climate Data Store (CDS) cloud server (Hersbach et al., 2019). The OISSTV2 data (Banzon et al., 2021) from the National Oceanic and Atmospheric Administration (NOAA) is utilized, which is a series of global and spatially gridded products created by interpolating and extrapolating data, including the weekly SST on a 1° grid and daily on a 0.25° grid. In addition, the ocean heat content (OHC) data from the National Centers for Environmental Prediction (NCEP) Climate Forecast System Reanalysis (CFSR) data (Saha et al., 2010) with the grid spacing of 0.5° latitude \times 0.5° longitude at 6-h intervals are used to investigate the ocean characteristic affected by the cold air.

Methods

So far, there is not a uniform standard definition for sudden TC track changes. Chan et al. (1980) defined the left- and right-turning tracks by a minimum direction change of 20° within 12 h. Wu et al. (2011) indicated the sharp track direction change exceeded 60° over a 24-h period, and the standard derivation of direction changes were about 28.5° and 24.2° for 12- and 6-h periods, respectively. Wu et al. (2013) defined a track direction change exceeding 40° (37°) during the 12-h (6 h) period as a sudden northward-turning track change. In this study, in order to highlight the northward movement trend of the TC, the threshold of TC track sharpening north changing directions is 45° and 40° for 12-h and 6-h, respectively.

A survey of historical TC tracks over the WNP in the past 30 years indicates that there are about 10 west-moving TCs which experienced sudden northward turning after moving into the

TABLE 1 | The information of four typhoon cases over the south China sea.

Code	Name	Maximum speed (m s^{-1})	Minimum pressure (hPa)	Maximum category	Life time (duration hours)	Turning time (UTC)	Landing mainland
9914	Dan	40	965	TY	162	1999.10.06.12	Y
0020	Xangsane	40	965	TY	168	2000.10.29.18	N
0601	Chanchu	45	945	STY	270	2006.05.15.00	Y
1013	Megi	52	940	Super TY	270	2010.10.20.00	Y

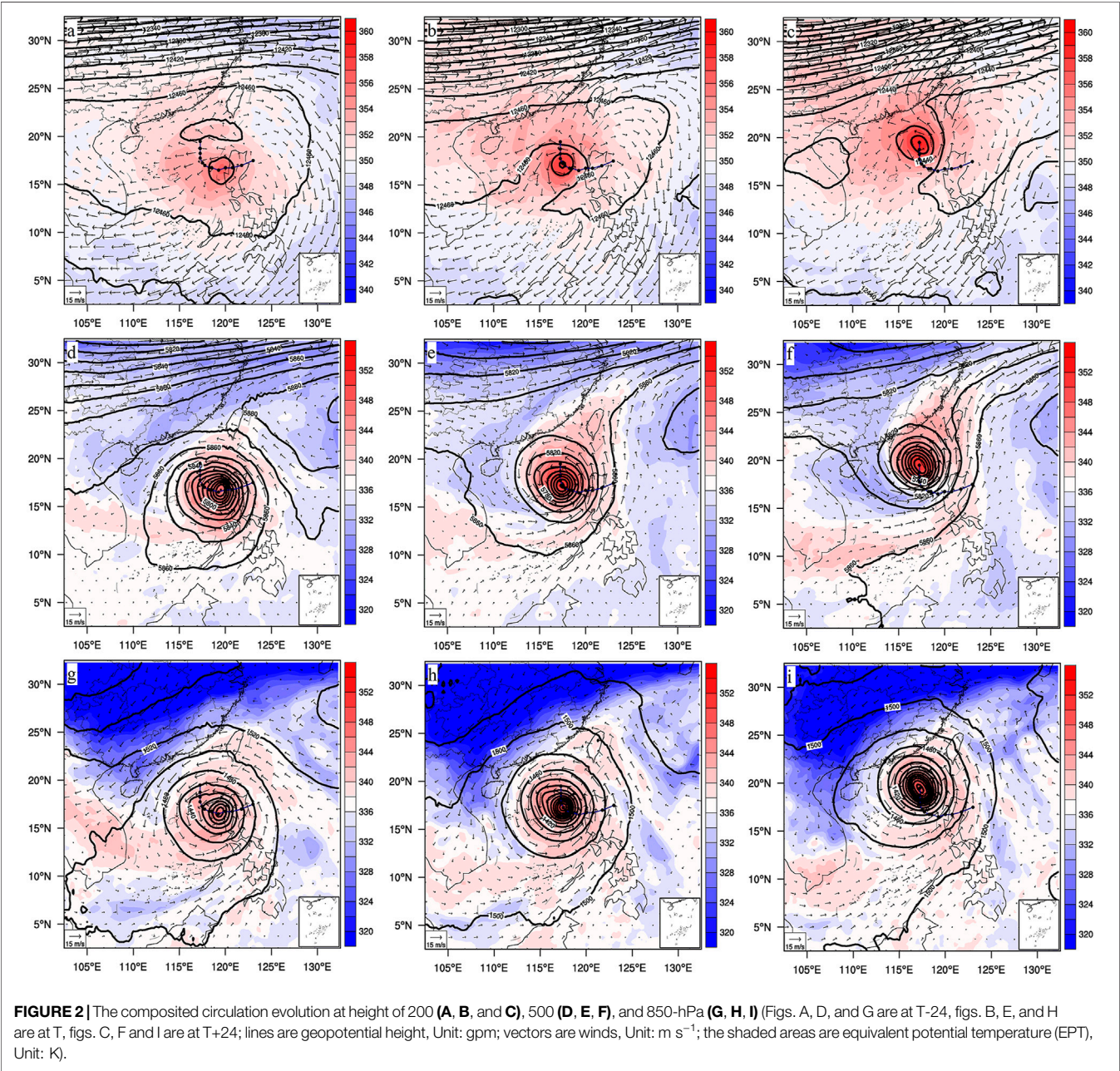


FIGURE 2 | The composited circulation evolution at height of 200 (A, B, and C), 500 (D, E, F), and 850-hPa (G, H, I) (Figs. A, D, and G are at T-24, figs. B, E, and H are at T, figs. C, F and I are at T+24; lines are geopotential height, Unit: gpm; vectors are winds, Unit: m s^{-1} ; the shaded areas are equivalent potential temperature (EPT), Unit: K).

SCS, among which 6 cases are accompanied by the low-level cold air intruding southward to the SCS. Excluding the possibility of orographic influence during the north turning, the four typhoons, Dan (1999), Xangsane (2000), Chanchu (2006), and Megi (2010), were chosen as the samples for this study (Figure 1A). All the selected cases reached typhoon intensity (32.7 m s^{-1}), especially,

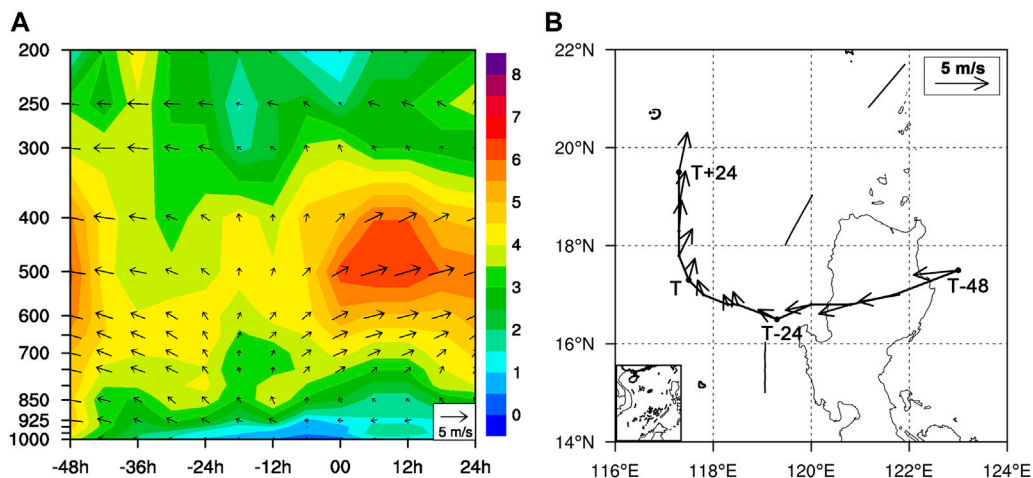


FIGURE 3 | (A) The time series of the vertical distribution of the mass-weighted mean steering flow (averaged in a region of a radius of 400 km from the TC center) (Vectors are wind speed and direction, shaded means magnitude of wind speed, Unit: m s^{-1} .) and **(B)** the averaged steering flow vectors between 850 hPa and 300 hPa.

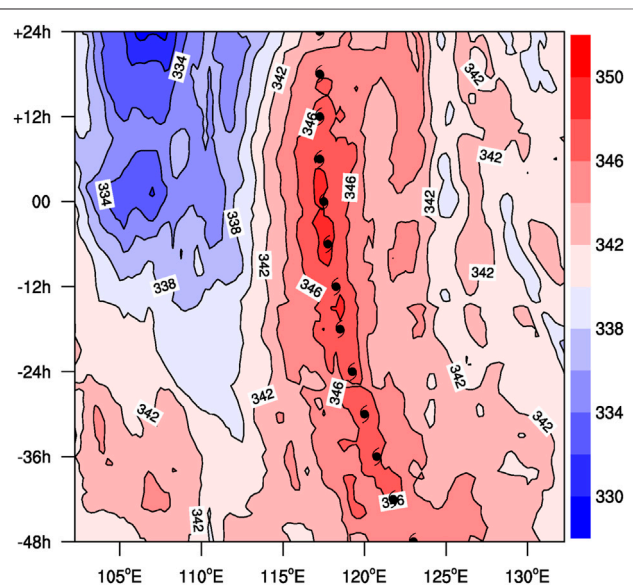


FIGURE 4 | The temporal-longitude variation of EPT at 925-hPa averaged on 15.5–17.5°N across the TC centers (Contours with shaded are the EPT, Unit: K) (Symbols indicate the longitude position of typhoon centers).

the maximum sustained wind speed of Megi exceeded 51 m s^{-1} (reaching Super TY category). The four typhoons all originated in the seasonal transition period when the cold air was active with three in October and one in May. (Table 1).

Figure 1B shows the satellite water vapor (WV) image of typhoon Xangsane (2000) at 12:00 October 29, 2000, obtained from the Cooperative Institute for Meteorological Satellite Studies (CIMSS) at the University of Wisconsin-Madison (available online at <http://tropic.ssec.wisc.edu/archive/>). The bright and white cloud of the typhoon is located in the SCS, while a large dark area appears in the southeast coastal region to the northwest

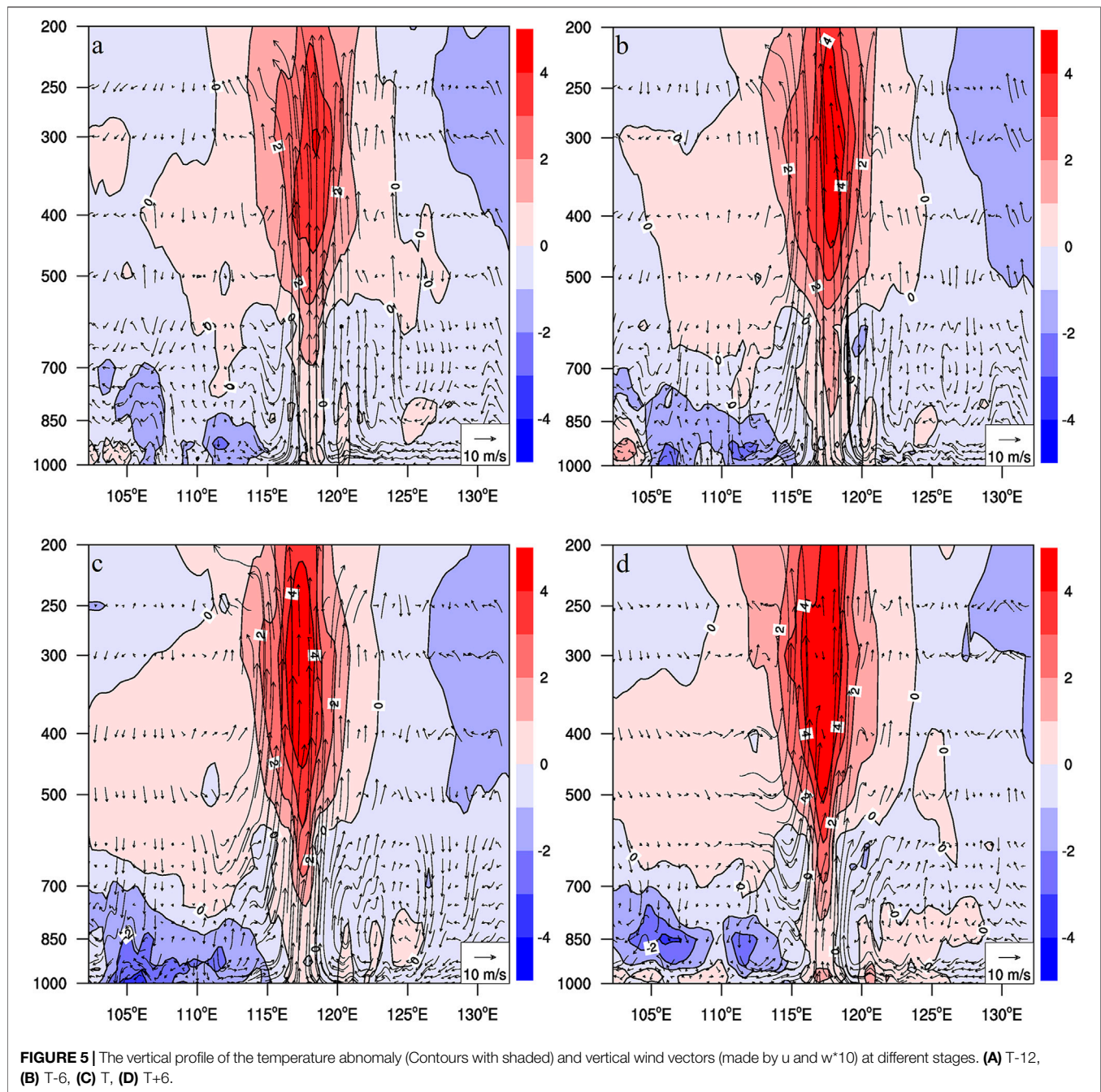
side of the typhoon. The dark area stretches southward and meets with the typhoon cloud, which means that the dry and cold air sinks southward and affects the periphery of the typhoon. The WV imageries of other selected cases also have a similar dark area in coordination with the cold air.

In order to analyze the comprehensive effects of cold air on the north turnings of four typhoons and keep a relatively intact typhoon circulation, the dynamic composite technique (Li et al., 2004) is used in the study. In this method, the composite region moves with the TC, and the center of the region is located at the TC center. At any given time, the value of a composite variable at a particular grid is calculated in the composite region. This procedure can be carried out for a set of times, from which each composite variable with time series can be obtained easily (Dong et al., 2010). In this study, it takes the turning position (time) as turning time (T) with 48 timesteps backward (T-48) and 24 timesteps forward (T+24), and slices the 15 longitudes and latitudes around the TC center in space cube respectively. The analysis and discussions in this paper are based on these composed data of four typhoon samples. The tracks of four typhoons (black lines) and their composited track (red line) are shown in Figure 1. In the figure, T means the turning time (T), negative values indicate pre-recurving, and a positive value means post-recurving. From the composed track, the turning begins at T-18 and basically completes at T time (Figure 1A).

SYNOPTIC CIRCULATION AND STEERING FLOW

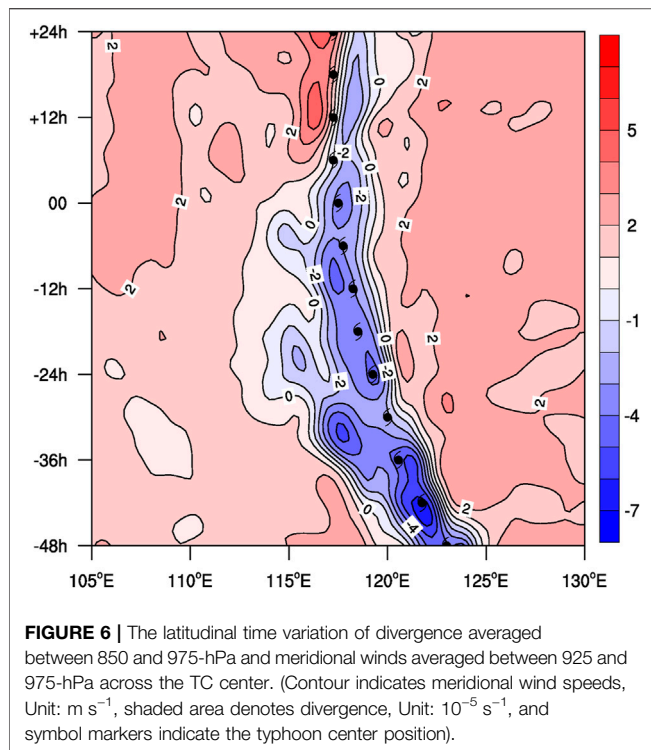
Synoptic Circulation

The prevailing TC tracks are intimately linked to the large-scale circulation patterns (Wu and Wang, 2004). TC track with a sudden turning usually is related to the common effect of multiple



synoptic systems. Before the turning (T-24), the composed TC moves westward with a relatively higher speed across Luzon Island, Philippines, and then into the SCS steadily, after generating to the east of the islands of the Philippines. During the turning (from T-24 to T), there was a major adjustment in the synoptic circulation. The SAH 200-hPa begins to weaken and splits into western and eastern parts over the Indo-China Peninsula and the western North Pacific, respectively (Figures 2A–C). The SH retreats eastward to the east of Taiwan island and a westerly trough moves eastward to about 105°E in the mid-

latitude (Figures 2D–F). In this connection, the cold air with lower equivalent potential temperature ($\theta_e < 324$ K; hereafter LEPT) is entangled into the western circulation of the typhoon at 500-hPa. At the same time, the LEPT invades southward from the mainland of China to the west side of the SCS in the lower layer at 850-hPa (Figures 2G–I). At T-24 time, the southwest jet stream to the southeast of the TC has not yet been established (Figure 2G). The TC slows down and shows a tendency of northward turning gradually. At T time, as the westerly trough moving at about 110°E and the cold air is involved southwardly



into the TC circulation, the SH falls southward to the southeast part of the TC (**Figure 2E**) with strengthened southwest airflow on the southeast side of the TC (**Figures 2E,H**), the track of the TC bends significantly and accelerates northward (**Figure 2H**). Then ($T+24$), the TC almost completes the north turn and keeps moving northward (**Figure 2I**).

It is evident that the synoptic patterns become complex during the TC deflection, including the weakening SAH, the passing midlatitude westerly trough with down south cold air, the retreating SH, and enhanced southwesterly flow in the southeast of TC, et al., thus resulting in a sudden changing of TC motion.

Steering Flow

George and Gray (1976) suggested that TC track was primarily a function of the steering flow and the advection of planetary vorticity by the TC circulation. The TC is primarily advected by the mean large-scale circulation patterns with a steering level ranging from 500 to 700-hPa (Holland, 1983). More studies have suggested that the deep-layer mean wind is the best discriminator for the motion of well-developed TCs (e.g., Sanders et al., 1980; Dong and Neumann, 1986; Velden and Leslie, 1991), however, individual cases can exhibit large variability in the steering flow depth (e.g., George and Gray, 1976; Dong and Neumann, 1986; Velden and Leslie, 1991; Aberson and DeMaria, 1994).

As suggested by Wu et al. (2011), the steering flow profiles are calculated as the mass-weighted mean wind averaged across the TC center, and the horizontal steering flows are averaged between 850- and 300-hPa within a domain with a radius of 400 km from the TC center in this study. **Figure 3A** shows the steering flow vertical profiles variation with time. Starting from $T-48$, the

directions of steering flow shift from westward to northwestward, especially in layers below 500-hPa, and the magnitude decreases gradually reaching the minimum (about 2 m s^{-1}) of northerly at $T-18$ related to the SH retreating eastward. After then, the northeastward steering flows of TC increased significantly near 500-hPa reaching $5\text{--}6 \text{ m s}^{-1}$ and the TC motion shifts northward. These variations agree with the results of Carr and Elsberry (1995) and Wu et al. (2011).

Horizontally (**Figure 3B**), prior to the sudden track change, the TC keeps moving westward by the strong westward steering flows. However, the average speed of TC movement slows from about 6 m s^{-1} (before $T-24$) down to about 2 m s^{-1} (around $T-12$) gradually after moving across the Philippine Islands. Especially, from $T-24$, the westward component of the steering flow keeps decreasing, the TC motion speed slows down to about 1 m s^{-1} and shows a trend of turning. While the northward component of the TC motion increases with the influence of the strengthening of southwest airflow. At T time, the steering flow shifts to the northward and keeps growing, and the northward turning of the TC almost fulfills. Then, the speed of the TC movement rapidly increases and moves northward continuously.

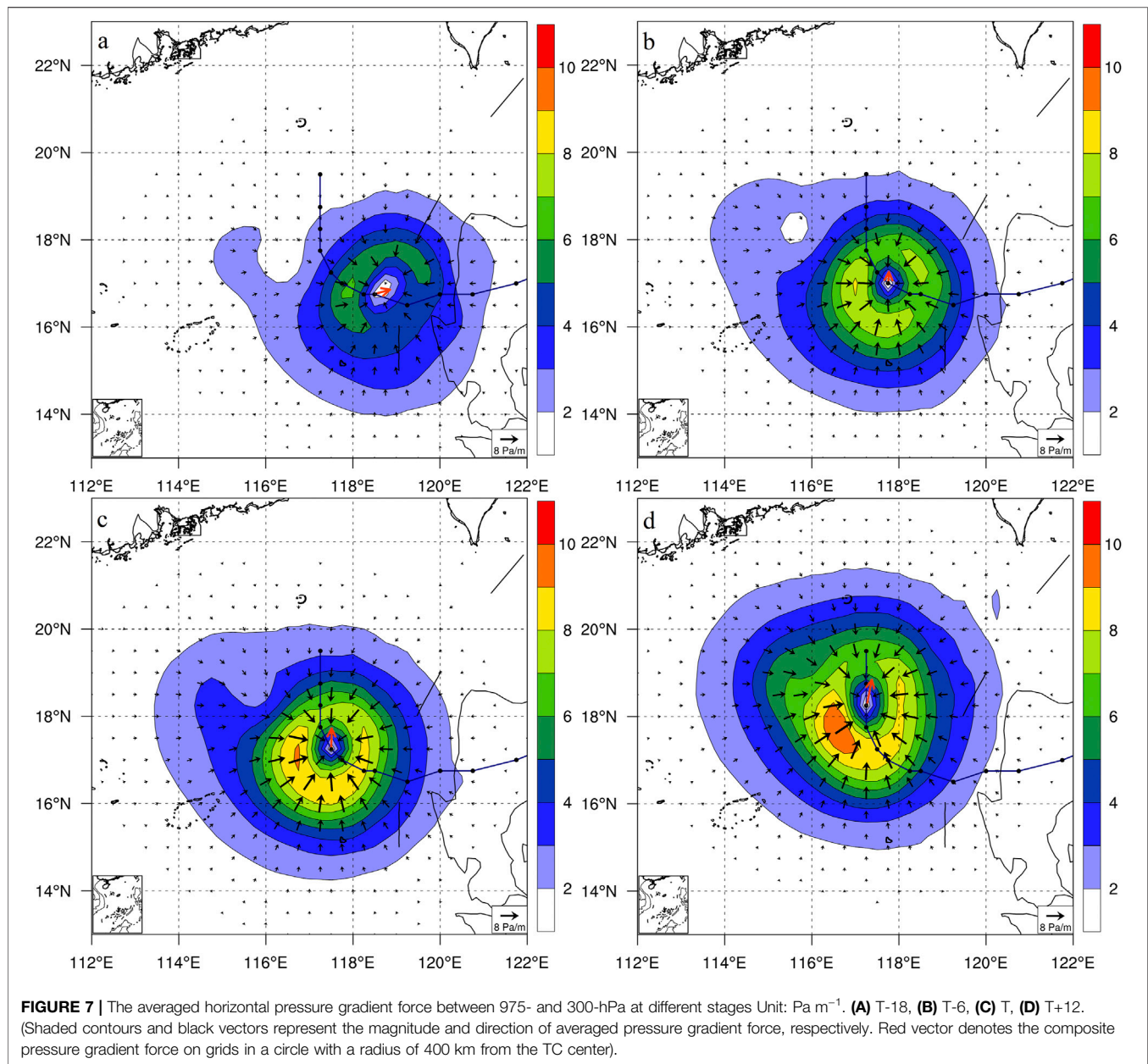
COLD AVOIDANCE AND WARM TENDENCY OF TC MOTION

Asymmetric Structure Induced by Cold Air Intrusion

Thermal Asymmetry

The TC motion is dominantly guided by the steering flow, however, when the synoptic-scale steering flow is weak, the β -effect propagation will contribute significantly to the TC motion (Fiorino and Elsberry, 1989). The difference of gyres between lower and upper layers may lead to the asymmetric structure or circulation of TC, and hence it, in turn, affects the TC motion. The asymmetric divergent flow associated with convective asymmetries within the vortex core region deflects the vortex center toward the region with maximum convection and results in meandering vortex tracks (Wang and Holland, 1996). The TC motion is also directly influenced by the asymmetric component of diabatic heating (Wu and Wang, 2001). Chen et al. (1997) revealed that the asymmetry of the thermal structure and the strength of the thermal instability layer of the TCs could lead to the significant anomaly of the TC track (e.g. Holland, 1983; Chan and Williams, 1987).

The temporal-longitude variation of the EPT averaged on $15.5\text{--}17.5^\circ\text{N}$ across the TC center at the height of 925-hPa is shown in **Figure 4**. It is obvious that there is a region higher than 344 K near 105°E before the cold air invades southward ($T-24$). From $T-24$, there exists a region with the values of EPT lower than 340 K on western of 115°E when the cold air coming from the Chinese mainland invades southward. Starting from this time, the values of LEPT on TC western side get much lower than those on the eastern side, with the center of LEPT around 105°E . There forms a region with a larger gradient of LEPT located around 115°E which indicates the cold air intrusion resulting in an asymmetric thermal structure of the TC. As the cold air continuously invades southward into the west of the SCS, the



values of LEPT on the west of the TC continue to get lower and the thermal structure of TC becomes more asymmetric (at T time). The motion of TC shows the characteristics of deceleration to the west and acceleration to the north denoting the cold avoidance in TC motion.

The vertical distribution of the temperature anomaly can be found in **Figure 5**. In the figure, there is a positive temperature anomaly center above 500-hPa embodying the basic warm-core characteristic of the TC vertical profile. What is more important is there exists a negative temperature anomaly region below 700-hPa on the west side of the TC starting from T-24 for the cold air invading. As the cold air invades into the west of the TC circulation further, the intensity of negative temperature anomaly keeps increasing gradually (**Figures 5A,B**) and extends to the edge of

TC center, particularly at T time (**Figure 5C**). On the contrary, there is a small range of weak positive temperature anomalies occurring on the east of the TC center in the lower layer. It represents clearly the vertical thermal structure asymmetric of the TC caused by the cold air from the China mainland.

Combined with **Figure 4**, it can be found that the increasing of negative temperature anomaly induced by the cold air with LEPT intrusion, is opposite to the direction of the TC movement, like a barrier blocking and preventing the TC from moving further westward.

Dynamical Asymmetry

The asymmetric structure forced by dynamics related to the interaction between the TC circulation and the cold air advection on the west side of the TC can also be found in

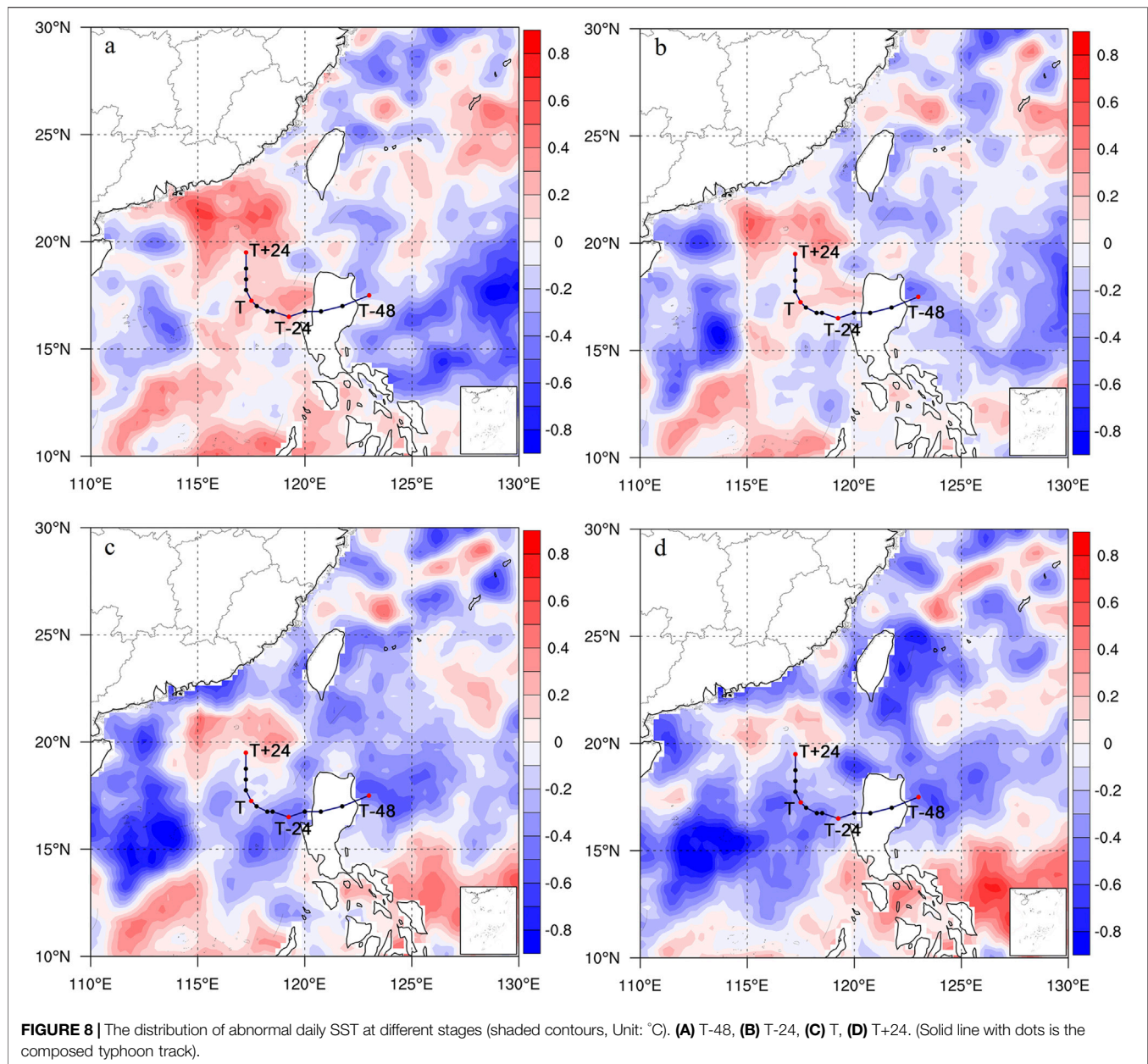
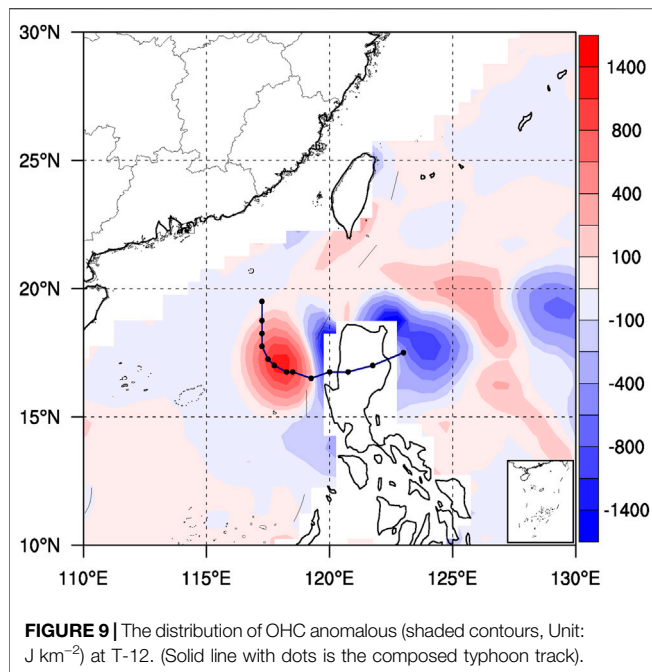


Figure 5. The intrusion of LEPT air (**Figure 2**) indicated by the relative dark region a few degrees west (**Figure 1B**) below 500-hPa may cause the isentropic descent of the drier, colder air (Ritchie and Elsberry, 2001). The negative temperature anomaly generates a direct thermal circulation with downdraft near 117°E below 500-hPa (**Figure 5A**), which is consistent with the results of Harr and Elsberry (2000). As the negative temperature anomaly increases, the downdrafts from levels of 500-hPa to the sea surface are also enhanced obviously (**Figures 5B,C**), which causes divergent flows enhancing inflows toward the TC center in lower layers over 110–115°E.

Figure 6 presents the time variation of averaged divergence between 850 and 975-hPa and meridional wind between 925 and

975-hPa. Before the TC turning (at about T-36), the negative meridional wind center over -12 m s^{-1} is located on the east of the TC center, and there exists the convergence center with a value less than $-5 \times 10^{-5} \text{ s}^{-1}$ located near the negative meridional wind center. The meridional winds on the west of TC are also negative. The TC keeps moving westward. As the cold air continues to invade into the west and south sides of the TC from T-36 to T, the divergence motion on 110°E is strengthened gradually both in values and scope extending to the TC center, while the convergence near the TC center is suppressed and weakened. In addition, the cold air sinking and diverging on the west of the TC can increase the low layer positive meridional winds pointing to the TC center, while weakening negative meridional winds on



the east of the TC center. The westward motion of the TC is impeded showing a tendency of recurving in its track. After T time, the divergence on the west of the TC enhances greatly, and extends into the vicinity of the TC center with the center value over $4 \times 10^{-5} \text{ s}^{-1}$, even stronger than the convergence center near the TC center on the eastern side. The meridional winds are positive at the TC center and its west quadrant. It can be inferred that the divergence formed by the cold air sinking on the west side of the TC may block the TC from moving westward further.

In circumstances with weak steering airflow, the PGF may highlight its influence on TC movement (Chen et al., 1997). The flow associated with large northward pressure gradients could push the TC northward (Chen et al., 2021). At T-18 (Figure 7A), due to the invasion of cold air on the west quadrant of TC, TC enters into an environment with weak guiding airflow. The direction of the resultant PGF on TC shifts eastward, and its magnitude also decreases to about 1 Pa m^{-1} . From this moment, the TC begins to slow down (Figure 7A). Starting from T-12 to T-6 (Figure 7B), as the cold air keeps entangling southward into the southwest part of TC, the larger PGF occurs on the west and then the south sides of TC, which makes the resultant of PGF on TC decrease further to about 0.3 Pa m^{-1} and point to the north. The TC westward movement is suppressed with the northward motion promoted gradually, and the TC appears to deflect to the north obviously. The PGF continues to increase to 1 Pa m^{-1} and about 10 Pa m^{-1} at T (Figure 7C) and T+12 (Figure 7D) respectively, benefiting the TC moving northward obviously and accelerating gradually. Due to the strengthening of cold air intrusion from the mainland, the direction of the resultant PGF on TC is opposite to its movement direction, which prevents the TC from moving westward and is favorable to turning.

When a TC enters an environment with weak steering airflow and slows down, the thermal asymmetric structure of TC induced by the cold air intrusion may project an impact on TC motion. The cold air sinking on the west of the TC center may lead to the divergent drafts, and form a pressure gradient force opposite to the direction of TC movement, which is unfavorable for a TC keeping its original moving direction.

Approaching Warm

Tuleya and Kurihara (1982) reported that a warm SST increases the TC intensity and induces a northwestward shift of the northwestward-moving TC related to the beta effect (sensitive to the intensity and size of the TC). Wu et al. (2005b) showed the relative contribution of the symmetric and asymmetric SST components to TC motion. They demonstrated that the asymmetric SST component modulates the TC motion by changing the asymmetry in rainfall and vertical motion, while the symmetric component is related to the beta effect. This result indicates the importance of the asymmetric distributions of SST on TC motion. Chang and Madala (1980) presented evidence that the spatial distribution of SST influences the TC motion, a warm SST to the right of the mean flow is more favorable for the northwest drift of westward-moving TCs than a warm SST on the left side.

In this study, the TC also has the characteristics of approaching to warm region. Figure 8 shows the daily SSTA distributions at variant stages during the TC turning. During the stage of westward travel across the Luzon Island (Figure 8A), the negative SSTA is located west of 115°E . The TC keeps on moving westward approaching the SCS, because the sea surface of the region ahead of the TC track is still controlled by the positive SSTA over 0.4°C , the TC keeps moving westward approaching the region with positive SSTA in the SCS. Starting from T-24 (Figure 8B), the range of negative SSTA region on west of 115°E continues to expand. As the cold air heads southward further, the negative SSTA region with center values becomes lower than 0.6°C to the west of 115°E . It is notable that the negative SST anomaly occurring in the south and near the center of TC gets stronger, while the positive SSTA region is weakened and squeezed to the north of the TC (Figures 8C,D). It also finds that there is a negative SSTA region appearing near and on the south of the center of the TC, which is the typical response of SST caused by the cold wake of TC (Ma et al., 2013). In addition, the cooling of SST increases the asymmetry of the TC thermodynamic and dynamic structures (Zhu et al., 2004; Chen et al., 2010) and affects the track of the TC further.

Although SST has been used widely to represent the ocean state in studies on air-sea interaction, Deser et al. (2003) have suggested that the OHC can also better reflect the heat storage of the ocean than the SST. The anomalous upper OHC indicates the total amount of heat that the ocean can release to the atmosphere (Dong and Kelly 2004). The anomalous of upper OHC at T-12 is shown in Figure 9. The cold air cools the SST to the west of the TC (Figure 8), which decreases the OHC of the upper surface. The presence of negative inconsistencies of OHC locating inhibits the TC from developing and moving westward, while the positive OHC anomalous is located on the north of the TC, which is favorable for the TC turning north.

Mesoscale variability in SST affects sea surface heat fluxes, which then alters the boundary layer, leading to convective activity (Skylvingstad et al., 2019). Latent and sensible heat transfer from the ocean surface along with potential energy, increasing the moist static energy of the boundary layer (Andersen et al., 2013). The increasing moist static energy (MSE) in the lower troposphere leads to an establishment of convective instability, producing a high CAPE value (Chen and Qin 2016). In this study, the MSE also has a similar distribution to that of the SST (figures not shown). The region with an MSE less than 334 K is on the west and south sides of the TC, and the region with higher values (greater than 346 K) on the north side of TC due to the cold air intrusion.

It is found that convective heating can significantly affect TC motion through the direct asymmetric heating and the asymmetric flow caused by diabatic heating (Flatau et al., 1994; Wu et al., 2005b). Fiorino and Elsberry (1989) established a concept that the asymmetric flow induced by diabatic heating associated with the convection within a TC can significantly affect TC motion and vertical coupling. The asymmetric diabatic heating tends to move vortices to the region downstream of the maximum gradient of asymmetric diabatic heating (Wu and Wang, 2001). **Figure 5** and **Figure 8** represent a downdraft and colder ocean surface on the west side of the TC generated by the invasion of the cold air, which may suppress the convective activity there. While the convection may be promoted over a warmer underlying surface on the north side of the TC. Such the inhomogeneity of convection makes the TC present asymmetric diabatic heating. There is a convergent center downstream of the diabatic heating center located at the north side of the TC in lower layers (figure not shown), which is favorable for the TC vortex to turn northward. These are consistent with the results of Wu and Wang (2001).

According to the abovementioned, the asymmetric distribution of SSTA, OHC, or diabatic heating are all related to the cold air intrusion. The warm approaching of TC reflects its avoidance feature from the cold air in another way.

DISCUSSION AND SUMMARY

The effects of cold air during the north turning of the TCs over the SCS are studied in this paper. The compositive analysis attributes the north turning of TCs mainly to their characteristic of avoidance from the cold air under circumstances with weakened steering flows.

The cold air from the northern mainland may result in thermal and dynamical asymmetry of TCs exerting an influence on TC motion. On one hand, the negative temperature anomaly occurring below the mid-levels on the west and south sides of the TC may lead to stable atmospheric stratification and lower SST and OHC restraining convection development. On another hand, the cold air

descending can generate diverging outflows opposite to the movement direction of TC, which slows and blocks the TC from moving westward further. Plus, the PGF related to the cold intrusion highlights its influence on the north turning in a weak steering flow field. Besides, the underlying warm region (including the SST and the OHC) are found occurring on the north side with the influence by the cold air and the cold wake of the TC, which is beneficial to the north turning.

In a word, when a westward-moving TC encounters cold air intruding from mid-latitude over the SCS, it may show a sharp north turn to avoid the cold air area, especially in weak steering flows. However, it should be noted the factors causing the recurvature of a TC can be various and complex, such as the low-latitude monsoon trough, binary tropical cyclone interaction, the tropical upper-tropospheric trough, diabatic heating, orographic effects, and so on. The role of cold avoidance should be discussed in detail. The cold avoidance characteristics need to be considered quantitatively in further study.

DATA AVAILABILITY STATEMENT

The original contributions presented in the study can be inquired to the corresponding author directly.

AUTHOR CONTRIBUTIONS

SL and YL conducted analysis and writing in the paper. SL contributed to the figures included in this manuscript. All of the authors were contributed to the article and approved to submit the paper.

FUNDING

This work was jointly funded by the National Natural Science Foundation of China (Grants Nos. 41930972 and 51778617), Fujian Key Laboratory of Severe Weather (Grants Nos.2020TF10).

ACKNOWLEDGMENTS

We thank reviewers for their critical comments that helped to improve the presentation of our results. Thanks also go to the graphic software packages, i.e., NCAR Command Language (NCL, doi: 10.5065/D6WD3XH5), which is employed to plot the figures.

REFERENCES

- Aberson, S. D. (2010). 10 Years of Hurricane Synoptic Surveillance (1997–2006). *Mon. Wea. Rev.* 138, 1536–1549. doi:10.1175/2009MWR3090.1
- Aberson, S. D., and DeMaria, M. (1994). Verification of a Nested Barotropic hurricane Track Forecast Model (VICBAR). *Mon. Wea. Rev.* 122, 2804–2815. doi:10.1175/1520-0493(1994)122<2804:voanbh>2.0.co;2
- Andersen, T. K., Radcliffe, D. E., and Shepherd, J. M. (2013). Quantifying Surface Energy Fluxes in the Vicinity of Inland-Tracking Tropical

- Cyclones. *J. Appl. Meteorology Climatology* 52, 2797–2808. doi:10.1175/JAMC-D-13-035.1
- Banzon, V., and Reynolds, R. National Center for Atmospheric Research Staff (Editors) (2021). *The Climate Data Guide: SST Data: NOAA High-Resolution (0.25×0.25) Blended Analysis of Daily SST and Ice, OISSTv2*. Retrieved from <https://climatedataguide.ucar.edu/climate-data/sst-data-noaa-high-resolution-025x025-blended-analysis-daily-sst-and-ice-oisstv2>
- Berger, H., Langland, R., Velden, C. S., Reynolds, C. A., and Pauley, P. M. (2011). Impact of Enhanced Satellite-Derived Atmospheric Motion Vector Observations on Numerical Tropical Cyclone Track Forecasts in the Western North Pacific during TPARC/TCS-08. *J. Appl. Meteorol. Climatol.* 50, 2309–2318. doi:10.1175/JAMC-D-11-019.1
- Bi, M., Li, T., Peng, M., and Shen, X. (2015). Interactions between Typhoon Megi (2010) and a Low-Frequency Monsoon Gyre. *J. Atmos. Sci.* 72, 2682–2702. doi:10.1175/JAS-D-14-0269.1
- Brand, S., and Blueloch, J. W. (1974). Changes in the Characteristics of Typhoons Crossing the Island of Taiwan. *Mon. Wea. Rev.* 102, 708–713. doi:10.1175/1520-0493(1974)102<0708:citcot>2.0.co;2
- Carr, L. E., and Elsberry, R. L. (1995). Monsoonal Interactions Leading to Sudden Tropical Cyclone Track Changes. *Mon. Wea. Rev.* 123, 265–290. doi:10.1175/1520-0493(1995)123<0265:miltst>2.0.co;2
- Carr, L. E., and Elsberry, R. L. (1990). Observational Evidence for Predictions of Tropical Cyclone Propagation Relative to Environmental Steering. *J. Atmos. Sci.* 47, 542–546. doi:10.1175/1520-0469(1990)047<0542:oeftot>2.0.co;2
- Chan, J. C. L., Gray, W. M., and Kidder, S. Q. (1980). Forecasting Tropical Cyclone Turning Motion from Surrounding Wind and Temperature fields. *Mon. Wea. Rev.* 108, 778–792. doi:10.1175/1520-0493(1980)108<0778:ftctmf>2.0.co;2
- Chan, J. C. L. (1995). Prediction of Annual Tropical Cyclone Activity over the Western North Pacific and the South China Sea. *Int. J. Climatol.* 15, 1011–1019. doi:10.1002/joc.3370150907
- Chan, J. C. L., and Williams, R. T. (1987). Analytical and Numerical Studies of the Beta-Effect in Tropical Cyclone Motion. Part I: Zero Mean Flow. *J. Atmos. Sci.* 44, 1257–1265. doi:10.1175/1520-0469(1987)044<1257:aansot>2.0.co;2
- Chang, S. W., and Madala, R. V. (1980). Numerical Simulation of the Influence of Sea Surface Temperature on Translating Tropical Cyclones. *J. Atmos. Sci.* 37, 2617–2630. doi:10.1175/1520-0469(1980)037<2617:nsotio>2.0.co;2
- Chen, G., and Qin, H. (2016). Strong Ocean-Atmosphere Interactions during a Short-Term Hot Event over the Western Pacific Warm Pool in Response to El Niño. *J. Clim.* 29 (10), 3841–3865. doi:10.1175/JCLI-D-15-0595.1
- Chen, L. S., Xu, X. D., Xie, Y. Y., and Li, W. H. (1997). The Effect of Tropical Cyclone Asymmetric Thermodynamic Structure on its Unusual Motion. *Chin. J. Atmos. Sci. (Scientia Atmospherica Sinica) (in Chinese)* 21 (1), 83–90. doi:10.3878/j.issn.1006-9895.1997.01.09
- Chen, L. S., and Ding, Y. H. (1979). *An Introduction to Typhoons over the Western North Pacific (In Chinese)*. Beijing: Science Press, 491.
- Chen, S.-Y., Shih, C.-P., Huang, C.-Y., and Teng, W.-H. (2021). An Impact Study of GNSS RO Data on the Prediction of Typhoon Nepartak (2016) Using a Multi-Resolution Global Model with 3D-Hybrid Data Assimilation. *Wea. Forecast.* 36 (3), 957–977. doi:10.1175/WAF-D-20-0175.1
- Chen, S., Campbell, T. J., Jin, H., Gaberšek, S., Hodur, R. M., and Martin, P. (2010). Effect of Two-Way Air-Sea Coupling in High and Low Wind Speed Regimes. *Mon. Wea. Rev.* 138, 3579–3602. doi:10.1175/2009MWR3119.1
- Chen, T.-C., Wang, S.-Y., Yen, M.-C., and Gallus, W. A. (2004). Role of the Monsoon Gyre in the Interannual Variation of Tropical Cyclone Formation over the Western North Pacific. *Wea. Forecast.* 19, 776–785. doi:10.1175/1520-0434(2004)019<0776:rotmgi>2.0.co;2
- Choi, Y., Yun, K.-S., Ha, K.-J., Kim, K.-Y., Yoon, S.-J., and Chan, J. C. L. (2013). Effects of Asymmetric SST Distribution on Straight-Moving Typhoon Ewiniar (2006) and Recurring Typhoon Maemi (2003). *Mon. Wea. Rev.* 141, 3950–3967. doi:10.1175/MWR-D-12-00207.1
- Chou, C.-B., Huang, C.-Y., Huang, H.-P., Wang, K.-H., and Yeh, T.-C. (2008). The Analysis of Typhoon Structures Using Advanced Microwave Sounding Unit Data and its Application to Prediction. *J. Appl. Meteorol. Climatol.* 47, 1476–1492. doi:10.1175/2007JAMC1577.1
- Deser, C., Alexander, M. A., and Timlin, M. S. (2003). Understanding the Persistence of Sea Surface Temperature Anomalies in Midlatitudes. *J. Clim.* 16, 57–72. doi:10.1175/1520-0442(2003)016<0057:utpos>2.0.co;2
- Dong, K., and Neumann, C. J. (1986). The Relationship between Tropical Cyclone Motion and Environmental Geostrophic Flows. *Mon. Wea. Rev.* 114, 115–122. doi:10.1175/1520-0493(1986)114<0115:trbtcm>2.0.co;2
- Dong, M., Chen, L., Li, Y., and Lu, C. (2010). Rainfall Reinforcement Associated with Landfalling Tropical Cyclones. *J. Atmos. Sci.* 67, 3541–3558. doi:10.1175/2010JAS3268.1
- Dong, S., and Kelly, K. A. (2004). Heat Budget in the Gulf Stream Region: The Importance of Heat Storage and Advection. *J. Phys. Oceanogr.* 34, 1214–1231. doi:10.1175/1520-0485(2004)034<1214:hbtgs>2.0.co;2
- Elsberry, R. L. (2014). Advances in Research and Forecasting of Tropical Cyclones from 1963–2013. *Asia-Pacific J. Atmos. Sci.* 50, 3–16. doi:10.1007/s13143-014-0001-1
- Elsberry, R. L. (2007). Advances in Tropical Cyclone Motion Prediction and Recommendations for the Future. *WMO Bull.* 56, 131–134.
- Elsberry, R. L. (1995). “Tropical Cyclone Motion. Global Perspectives on Tropical Cyclones,” in *WMO Tech. Doc. WMO/TD-693*. Editor R. L. Elsberry (Geneva, Switzerland: World Meteorological Organization), 106–197.
- Fiorino, M., and Elsberry, R. L. (1989). Some Aspects of Vortex Structure Related to Tropical Cyclone Motion. *J. Atmos. Sci.* 46, 975–990. doi:10.1175/1520-0469(1989)046<0975:saovsr>2.0.co;2
- Flatau, M., Schubert, W. H., and Stevens, D. E. (1994). The Role of Baroclinic Processes in Tropical Cyclone Motion: The Influence of Vertical Tilt. *J. Atmos. Sci.* 51, 2589–2601. doi:10.1175/1520-0469(1994)051<2589:trobpi>2.0.co;2
- Gall, R., Franklin, J., Marks, F., Rappaport, E. N., and Toepfer, F. (2013). The Hurricane Forecast Improvement Project. *Bull. Amer. Meteorol. Soc.* 94, 329–343. doi:10.1175/BAMS-D-12-00071.1
- George, J. E., and Gray, W. M. (1976). Tropical Cyclone Motion and Surrounding Parameter Relationships. *J. Appl. Meteorol.* 15, 1252–1264. doi:10.1175/1520-0450(1976)015<1252:tcmap>2.0.co;2
- Goerss, J. S. (2000). Tropical Cyclone Track Forecasts Using an Ensemble of Dynamical Models. *Mon. Wea. Rev.* 128, 1187–1193. doi:10.1175/1520-0493(2000)128
- Goerss, J. S., Sampson, C. R., and Gross, J. (2004). A History of Western North Pacific Tropical Cyclone Track Forecast Skill. *Wea. Forecasting* 19, 633–638. doi:10.1175/1520-0434(2004)019<0633:AHOWNP>2.0.CO;2
- Harr, P. A., and Elsberry, R. L. (2000). Extratropical Transition of Tropical Cyclones over the Western North Pacific. Part I: Evolution of Structural Characteristics during the Transition Process. *Mon. Wea. Rev.* 128, 2613–2633. doi:10.1175/1520-0493(2000)128<2613:etotco>2.0.co;2
- Harr, P. A., and Elsberry, R. L. (1995). Large-scale Circulation Variability over the Tropical Western North Pacific. Part I: Spatial Patterns and Tropical Cyclone Characteristics. *Mon. Wea. Rev.* 123, 1225–1246. doi:10.1175/1520-0493(1995)123<1225:lscvot>2.0.co;2
- Hennermann, K., and Berrisford, P. (2018). What Are the Changes from ERA-Interim to ERA5? ECMWF. Available at: <https://confluence.ecmwf.int/pages/viewpage.action?pageId=74764925>.
- Hersbach, H., Bell, W., Berrisford, P., Horányi, A. J., Nicolas, J., Radu, R., et al. (2019). *Global Reanalysis: Goodbye Era-Interim, Hello ERA5*. ECMWF Newsletter, No. 159. Reading, United Kingdom: ECMWF, 17–24. Available at: <https://www.ecmwf.int/node/19027>.
- Holland, G. J. (1983). Tropical Cyclone Motion: Environmental Interaction Plus a Beta Effect. *J. Atmos. Sci.* 40, 328–342. doi:10.1175/1520-0469(1983)040<0328:tcmeip>2.0.co;2
- Holland, G. J., and Wang, Y. (1995). Baroclinic Dynamics of Simulated Tropical Cyclone Recurvature. *J. Atmos. Sci.* 52, 410–426. doi:10.1175/1520-0469(1995)052<0410:bdostc>2.0.co;2
- Kieu, C. Q., Truong, N. M., Mai, H. T., and Ngo-Duc, T. (2012). Sensitivity of the Track and Intensity Forecasts of Typhoon Megi (2010) to Satellite-Derived Atmospheric Motion Vectors with the Ensemble Kalman Filter. *J. Atmos. Oceanic Technol.* 29, 1794–1810. doi:10.1175/JTECH-D-12-00020.1
- Li, Y., Chen, L. S., and Wang, J. Z. (2004). The Diagnostic Analysis on the Characteristics of Large Scale Circulation Corresponding to the Sustaining and Decaying of Tropical Cyclone after it's Landfall. *Acta Meteorol. Sin.* 62, 167–179. doi:10.3321/j.issn:0577-6619.2004.02.004
- Li, Y., Guo, L., Ying, Y., and Hu, S. (2012). Impacts of Upper-Level Cold Vortex on the Rapid Change of Intensity and Motion of Typhoon Meranti (2010). *J. Trop. Meteorol.* 18, 207–219.
- Liang, J., Wu, L., Ge, X., and Wu, C.-C. (2011). Monsoonal Influence on Typhoon Morakot (2009). Part II: Numerical Study. *J. Atmos. Sci.* 68, 2222–2235. doi:10.1175/2011JAS3731.1

- Liang, J., and Wu, L. (2015). Sudden Track Changes of Tropical Cyclones in Monsoon Gyres: Full-Physics, Idealized Numerical Experiments*. *J. Atmos. Sci.* 72, 1307–1322. doi:10.1175/JAS-D-13-0393.1
- Ling, Z., Wang, Y., and Wang, G. (2016). Impact of Intraseasonal Oscillations on the Activity of Tropical Cyclones in Summer over the South China Sea. Part I: Local Tropical Cyclones. *J. Clim.* 29, 855–868. doi:10.1175/JCLI-D-15-0617.1
- Ma, Z., Fei, J., Liu, L., Huang, X., and Cheng, X. (2013). Effects of the Cold Core Eddy on Tropical Cyclone Intensity and Structure under Idealized Air-Sea Interaction Conditions. *Mon. Wea. Rev.* 141, 1285–1303. doi:10.1175/MWR-D-12-00123.1
- Neumann, C. (1992). Final Report: Joint Typhoon Warning Center (JTWC92) Model. SAIC Contract Rep. N00014-90-C-6042 (Part 2), 41.
- Peng, S., Qian, Y.-K., Lai, Z., Hao, S., Chen, S., Xu, H., et al. (2014). On the Mechanisms of the Recurviture of Super Typhoon Megi. *Sci. Rep.* 4, 4451. doi:10.1038/srep04451
- Qian, C., Zhang, F., Green, B. W., Zhang, J., and Zhou, X. (2013). Probabilistic Evaluation of the Dynamics and Prediction of Supertyphoon Megi (2010). *Wea. Forecast.* 28, 1562–1577. doi:10.1175/WAF-D-12-00121.1
- Rappaport, E. N., Franklin, J. L., Avila, L. A., Baig, S. R., Beven, J. L., Blake, E. S., et al. (2009). Advances and Challenges at the National Hurricane Center. *Wea. Forecast.* 24, 395–419. doi:10.1175/2008WAF2222128.1
- Ritchie, E. A., and Elsberry, R. L. (2001). Simulations of the Transformation Stage of the Extratropical Transition of Tropical Cyclones. *Mon. Wea. Rev.* 129, 1462–1480. doi:10.1175/1520-0493(2001)129<1462:sottso>2.0.co;2
- Saha, S., Moorthi, S., Pan, H.-L., Wu, X., Wang, J., Nadiga, S., et al. (2010). The NCEP Climate Forecast System Reanalysis. *Bull. Amer. Meteorol. Soc.* 91, 1015–1058. doi:10.1175/2010BAMS3001.1
- Sanders, F., Adams, A. L., Gordon, N. J. B., and Jensen, W. D. (1980). Further Development of a Barotropic Operational Model for Predicting Paths of Tropical Storms. *Mon. Wea. Rev.* 108, 642–654. doi:10.1175/1520-0493(1980)108<0642:fdoabo>2.0.co;2
- Shi, W., Fei, J., Huang, X., Cheng, X., Ding, J., and He, Y. (2014). A Numerical Study on the Combined Effect of Midlatitude and Low-Latitude Systems on the Abrupt Track Deflection of Typhoon Megi (2010). *Mon. Wea. Rev.* 142, 2483–2501. doi:10.1175/MWR-D-13-00283.1
- Skyllingstad, E. D., de Szoeke, S. P., and O'Neill, L. W. (2019). Modeling the Transient Response of Tropical Convection to Mesoscale SST Variations. *J. Atmos. Sci.* 76, 1227–1244. doi:10.1175/JAS-D-18-0079.1
- Tu, J.-Y., Chou, C., and Chu, P.-S. (2009). The Abrupt Shift of Typhoon Activity in the Vicinity of Taiwan and its Association with Western North Pacific-East Asian Climate Change. *J. Clim.* 22, 3617–3628. doi:10.1175/2009JCLI2411.1
- Tuleya, R. E., and Kurihara, Y. (1982). A Note on the Sea Surface Temperature Sensitivity of a Numerical Model of Tropical Storm Genesis. *Mon. Wea. Rev.* 110, 2063–2069. doi:10.1175/1520-0493(1982)110<2063:anotss>2.0.co;2
- Velden, C. S., and Leslie, L. M. (1991). The Basic Relationship between Tropical Cyclone Intensity and the Depth of the Environmental Steering Layer in the Australian Region. *Wea. Forecast.* 6, 244–253. doi:10.1175/1520-0434(1991)006<0244:tbrbrc>2.0.co;2
- Wang, C.-C., Kuo, H.-C., Chen, Y.-H., Huang, H.-L., Chung, C.-H., and Tsuboki, K. (2012). Effects of Asymmetric Latent Heating on Typhoon Movement Crossing Taiwan: The Case of Morakot (2009) with Extreme Rainfall. *J. Atmos. Sci.* 69, 3172–3196. doi:10.1175/JAS-D-11-0346.1
- Wang, S.-T. (1980). Prediction of the Movement and Strength of Typhoons in Taiwan and its Vicinity (In Chinese). *Natl. Sci. Counc. Res. Rep.* 108, 100.
- Wang, Y., and Holland, G. J. (1996). The Beta Drift of Baroclinic Vortices. Part II: Diabatic Vortices. *J. Atmos. Sci.* 53, 3737–3756. doi:10.1175/1520-0469(1996)053<3737:tbdobv>2.0.co;2
- Wang, Z., and Fei, L. (1987). *Manual for Typhoon Prediction (In Chinese)*. Beijing, China: China Meteorological Press, 360.
- Wu, L., Ni, Z., Duan, J., and Zong, H. (2013). Sudden Tropical Cyclone Track Changes over the Western North Pacific: A Composite Study. *Mon. Wea. Rev.* 141, 2597–2610. doi:10.1175/MWR-D-12-00224.1
- Wu, L., and Wang, B. (2004). Assessing Impacts of Global Warming on Tropical Cyclone Tracks*. *J. Clim.* 17, 1686–1698. doi:10.1175/1520-0442(2004)017<1686:aigwo>2.0.co;2
- Wu, L., Wang, B., and Braun, S. A. (2005b). Impacts of Air-Sea Interaction on Tropical Cyclone Track and Intensity. *Mon. Wea. Rev.* 133, 3299–3314. doi:10.1175/MWR3030.1
- Wu, L., and Wang, B. (2001). Effects of Convective Heating on Movement and Vertical Coupling of Tropical Cyclones: A Numerical Study*. *J. Atmos. Sci.* 58, 3639–3649. doi:10.1175/1520-0469(2001)058<3639:eochoh>2.0.co;2
- Wu, L., Wang, B., and Geng, S. (2005a). Growing Typhoon Influence on East Asia. *Geophys. Res. Lett.* 32, a–n. doi:10.1029/2005GL022937
- Wu, L., Zong, H., and Liang, J. (2011). Observational Analysis of Sudden Tropical Cyclone Track Changes in the Vicinity of the East China Sea. *J. Atmos. Sci.* 68, 3012–3031. doi:10.1175/2010JAS3559.1
- Xu, X., Peng, S., Yang, X., Xu, H., Tong, D. Q., Wang, D., et al. (2013). Does Warmer China Land Attract More Super Typhoons? *Sci. Rep.* 3, 1522. doi:10.1038/srep01522
- Yeh, T.-C., and Elsberry, R. L. (1993a). Interaction of Typhoons with the Taiwan Orography. Part I: Upstream Track Deflections. *Mon. Wea. Rev.* 121, 3193–3212. doi:10.1175/1520-0493(1993)121<3193:iotwt>2.0.co;2
- Yeh, T.-C., and Elsberry, R. L. (1993b). Interaction of Typhoons with the Taiwan Orography. Part II: Continuous and Discontinuous Tracks across the Island. *Mon. Wea. Rev.* 121, 3213–3233. doi:10.1175/1520-0493(1993)121<3213:iotwt>2.0.co;2
- Ying, M., Zhang, W., Yu, H., Lu, X., Feng, J., Fan, Y., et al. (2014). An Overview of the China Meteorological Administration Tropical Cyclone Database. *J. Atmos. Oceanic Technol.* 31, 287–301. doi:10.1175/JTECH-D-12-00119.1
- Yumoto, M., and Matsuura, T. (2001). Interdecadal Variability of Tropical Cyclone Activity in the Western North Pacific. *J. Meteorol. Soc. Jpn.* 79, 23–35. doi:10.2151/jmsj.79.23
- Yun, K.-S., Chan, J. C. L., and Ha, K.-J. (2012). Effects of SST Magnitude and Gradient on Typhoon Tracks Around East Asia: A Case Study for Typhoon Maemi (2003). *Atmos. Res.* 109–110, 36–51. doi:10.1016/j.atmosres.2012.02.012
- Zhang, Q., Wu, L., and Liu, Q. (2009). Tropical Cyclone Damages in China 1983–2006. *Bull. Amer. Meteorol. Soc.* 90, 489–496. doi:10.1175/2008BAMS2631.1
- Zhang, X., Li, Y., Zhang, D.-L., and Chen, L. (2018). A 65-yr Climatology of Unusual Tracks of Tropical Cyclones in the Vicinity of China's Coastal Waters during 1949–2013. *J. Appl. Meteorol. Climatol.* 57, 155–170. doi:10.1175/JAMC-D-16-0392.1
- Zhu, H., Ulrich, W., and Smith, R. K. (2004). Ocean Effects on Tropical Cyclone Intensification and Inner-Core Asymmetries. *J. Atmos. Sci.* 61, 1245–1258. doi:10.1175/1520-0469(2004)061<1245:oeotci>2.0.co;2

Conflict of Interest: The authors declare that the research was conducted in the absence of any commercial or financial relationships that could be construed as a potential conflict of interest.

Publisher's Note: All claims expressed in this article are solely those of the authors and do not necessarily represent those of their affiliated organizations, or those of the publisher, the editors and the reviewers. Any product that may be evaluated in this article, or claim that may be made by its manufacturer, is not guaranteed or endorsed by the publisher.

Copyright © 2021 Lai, Li, He, Wang and Chen. This is an open-access article distributed under the terms of the Creative Commons Attribution License (CC BY). The use, distribution or reproduction in other forums is permitted, provided the original author(s) and the copyright owner(s) are credited and that the original publication in this journal is cited, in accordance with accepted academic practice. No use, distribution or reproduction is permitted which does not comply with these terms.



The Performance of Three Exponential Decay Models in Estimating Tropical Cyclone Intensity Change After Landfall Over China

Lu Liu^{1*}, Yuqing Wang^{1,2} and Hui Wang¹

¹State Key Laboratory of Severe Weather, Chinese Academy of Meteorological Sciences, Beijing, China, ²International Pacific Research Center and Department of Atmospheric Sciences, School of Ocean and Earth Science and Technology, University of Hawaii at Manoa, Honolulu, China

OPEN ACCESS

Edited by:

Qingqing Li,
Nanjing University of Information
Science and Technology, China

Reviewed by:

Li Tao,
Nanjing University of Information
Science and Technology, China
Kevin Cheung,
Macquarie University, Australia

*Correspondence:

Lu Liu
liulu@cma.gov.cn

Specialty section:

This article was submitted to
Atmospheric Science,
a section of the journal
Frontiers in Earth Science

Received: 09 October 2021

Accepted: 19 November 2021

Published: 10 December 2021

Citation:

Liu L, Wang Y and Wang H (2021) The
Performance of Three Exponential
Decay Models in Estimating Tropical
Cyclone Intensity Change After
Landfall Over China.
Front. Earth Sci. 9:792005.
doi: 10.3389/feart.2021.792005

In this study, the performance of three exponential decay models in estimating intensity change of tropical cyclones (TCs) after landfall over China is evaluated based on the best-track TC data during 1980–2018. Results indicate that the three models evaluated can reproduce the weakening trend of TCs after landfall, but two of them (M1 and M2) tend to overestimate TC intensity and one (M3) tends to overestimate TC intensity in the first 12 h and underestimate TC intensity afterwards. M2 has the best performance with the smallest errors among the three models within 24 h after landfall. M3 has better performance than M1 in the first 20 h after landfall, but its errors increase largely afterwards. M1 and M2 show systematic positive biases in the southeastern China likely due to the fact that they have not explicitly included any topographic effect. M3 has better performance in the southeastern China, where it was originally attempted, but shows negative biases in the eastern China. The relative contributions of different factors, including landfall intensity, translational speed, 850-hPa moist static energy, and topography, to model errors are examined based on classification analyses. Results indicate that the landfall intensity contributes about 18%, translational speed, moist static energy and topography contribute equally about 15% to the model errors. It is strongly suggested that the TC characteristics and the time-dependent decay constant determined by environmental conditions, topography and land cover properties, should be considered in a good exponential decay model of TC weakening after landfall.

Keywords: landfalling tropical cyclones, exponential decay model, model performance, tropical cyclone intensity, error analysis

INTRODUCTION

Tropical cyclones (TCs) can exert severe destructive potential and impacts on human activities and often cause substantial property damage and loss of life after their landfall, particularly in a well-populated area with high economic development. The disaster potential caused by extremely strong winds, torrential rainfall, and storm surge is largely related to the intensity of a TC during and after its landfall. Therefore, understanding and forecasting the weakening rate of TCs after landfall are of critical importance for disaster prevention by estimating the potential inland penetration of the TC-induced hazards. Although TCs mostly experience a rapid weakening after landfall, the rate of the

weakening is determined by many factors, including the large-scale atmospheric circulation, the internal dynamics of the TC itself (such as size and intensity, etc.), the near-shore sea surface temperature (SST), and the land surface properties (such as the land cover, soil moisture and temperature, orography, etc.). These processes may interact nonlinearly with each other, leading to large variability in the weakening rate of TCs during and after landfall. This also makes the intensity forecasts of landfalling TCs even more challenging than the intensity forecasts of TCs over open oceans (e.g., Duan et al., 2019).

In the last 3 decades or so, considerable efforts have been devoted to understanding the processes that lead to TC weakening after landfall. The basic principle behind the TC weakening after landfall is known to be mainly due to the decrease in sensible and latent heat fluxes and the increase in surface friction over land (Tuleya and Kurihara, 1978; Tuleya et al., 1984; Tuleya, 1994). However, the detailed dynamic and thermodynamic processes involved are multiple, highly nonlinear, and varying in both time and space. Nevertheless, still considerable progress has been made to quantify the weakening rate of landfalling TCs. One of the efforts is to construct empirical models to fit the decay rate of maximum sustained near-surface wind speed (MSSW) of a TC after landfall (Schwerdt et al., 1979; Batts et al., 1980; Georgiou, 1985; Ho et al., 1987; Kaplan and DeMaria, 1995; Kaplan and DeMaria, 2001; Vickery and Twisdale, 1995; Knaff et al., 2005; Colette et al., 2010). Schwerdt et al. (1979) first showed that the decay of a TC after landfall in terms of central sea level pressure depended on the region where the TC made landfall. Batts et al. (1980) proposed a decay model for a TC over land with a decaying constant that varies with the angle at which the TC crosses the coastline. Georgiou (1985) modeled the decay of a TC after landfall as a function of the distance from the landfalling point. Ho et al. (1987) found that the decay rate was a function of the TC intensity at landfall.

The most promising decay models are the so-called exponential decay models, which are shown to be better than other decay models and will be evaluated in this study. Kaplan and DeMaria (1995) developed a simple empirical decay model to estimate TC intensity change after landfall over the United States, which is an exponential decay equation in terms of the MSSW as a function of time after landfall. The model was later extended and refined for TCs making landfall in the New England area (north of 37°N) by (Kaplan and DeMaria, 2001) and for TCs making landfall over narrow landmasses by DeMaria et al. (2006). This decay model of landfalling TC intensity is used in the Statistical Hurricane Intensity Prediction Scheme (SHIPS, DeMaria and Kaplan, 1994; Demaria and Kaplan, 1999) for TC intensity forecasts over the North Atlantic and the Eastern Pacific (DeMaria et al., 2005), and have been shown to have good skills in predicting TC intensity after landfall. Bhowmik et al. (2005) further improved the decay model of Kaplan and DeMaria (1995) for TCs making landfall over India by considering different decay constants for two periods: the first 6 h after landfall and the remaining 12 h over land. Vickery (2005) proposed a decay model of TC intensity in terms of the increase in central sea level pressure after landfall over the

United States by considering the exponential decaying constant as a function of three factors: the landfall intensity, the radius of maximum wind, and the translational speed of the TC at landfall. These factors are believed to considerably affect the TC weakening rate after landfall. Wong et al. (2008) constructed an empirical decay model for estimating TC intensity change after landfall along the South China coast. In this empirical decay model, the exponential decay constant is a function of TC intensity, the landward translational speed of the TC, and the 850-hPa moist static energy at the time of landfall.

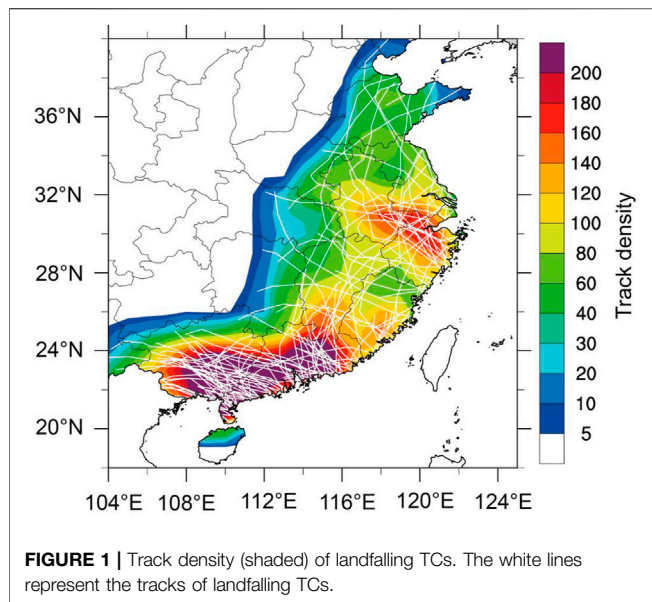
Because all existing decay models of TC intensity change after landfall were developed for a particular region, it is unclear how well these models estimate TC intensity after landfall in other regions. To address this issue, in this study we evaluated and compared the performance of three previously developed decay models in estimating TC intensity change in terms of the MSSW after landfall over China [namely, those developed, respectively, by Kaplan and DeMaria (1995), Bhowmik et al. (2005), Wong et al. (2008)]. We paid special attention to the relative contributions of various factors to the model errors and to identify the error sources and their regional dependence and various parameters, including the TC intensity at landfall, translational speed at landfall, and landfall latitude. Results from this study can help future improvements of the decay models for estimating and forecasting TC intensity change after landfall over China. The rest of the paper is organized as follows. *Data and Decay Models* describes the data and exponential decay models evaluated in this study. The performances of the three decay models are evaluated in *Evaluation of Model Performance*. *Model Error Analysis* examines the impact of different factors on the weakening rate of TC intensity after landfall and model errors. A brief discussion and major conclusions are given in the last section.

DATA AND DECAY MODELS

Data

The best-track TC data during 1980–2018 used in this study were acquired from the China Meteorological Administration–Shanghai Typhoon Institute (CMA/STI), which include latitude and longitude of the TC center, TC intensity in terms of the MSSW (2-min mean), and minimum sea level pressure at 6-h intervals. Note that the 6 hourly best-track data were linearly interpolated into 1-h intervals in the following analyses. The CMA/STI best-track data were used as the primary TC data because relatively more observational data were available over mainland China when the postseason TC analysis was conducted to generate the best-track TC data [see Ying et al. (2014) for more details]. The European Centre for Medium-Range Weather Forecasts (ECMWF) interim reanalysis (ERA-Interim) data at the horizontal resolution of $0.75^\circ \times 0.75^\circ$ (Dee et al., 2011) were used to calculate the parameters in the decay models as described in the next subsection.

We only considered TCs making landfall over mainland China (excluding those making landfall over Taiwan or Hainan Islands)



during 1980–2018. A landfalling TC is referred to a TC whose center crossed the coastline of mainland China at least once during its lifetime. Only TCs that made landfall and remained over land for at least three subsequent hours during the peak TC season (June–October) were included. If a TC re-entered the sea after landfall, we only considered the time period when the TC moved over land. The data period includes 135 cases of landfalling TCs over mainland China, with the average post-landfall duration of 32.6 h per TC. The tracks of these TCs are depicted in **Figure 1**. Here the track density is defined as the occurrence frequency of TCs that made landfall over mainland China and passed through a $2^\circ \times 2^\circ$ grid box. Note that when two time (1 hourly) points from one TC that occurred in one grid box, we counted them twice in the track density.

Description of Three Decay Models

As mentioned in *Introduction*, the performance of the most recent three exponential decay models for estimating the time evolution of MSSW of TCs after landfall are evaluated and compared in this study. They are developed by Kaplan and DeMaria (1995), Bhowmik et al. (2005), and Wong et al. (2008), respectively, and named in short M1, M2, and M3 for convenient discussions below. Each of the three decay models is briefly described below to allow readers to know the similarities and differences among these models.

The first model (M1) is that developed by Kaplan and DeMaria (1995), which is a simple exponential decay model for estimating the MSSW for TCs after landfall south of 37°N over the United States. Kaplan and DeMaria (1995) found that the decay rate of MSSW of a TC after landfall is proportional to the MSSW of the TC at the time of landfall, and the MSSW decreases with time to a background wind speed. The decay model is mathematically expressed by

$$V(t) = V_b + (V_0 - V_b) \exp(-\alpha t), \quad (1)$$

where V is MSSW of the TC after landfall and V_0 is V at the time of landfall, α is the decay constant, V_b is the background wind speed, t is the time after landfall. The background wind speed, V_b , is assumed to be 12 m s^{-1} in this study. The TC intensity at the time of landfall of each TC was provided by the National Meteorological Center (NMC) of CMA. The landfall intensity dataset is consistent with the CMA/STI best-track dataset. The decay constant α in **Eq. 1** was determined by minimizing the errors of the estimated against the observed values of V using the method of least squares from all samples of landfalling TCs in the study period, which resulted in the values of α of 0.0768 h^{-1} . In Kaplan and DeMaria (1995), the intensity at landfall was assumed to be the MSSW at the time closest to but preceding landfall. Powell et al. (1991) noted that the rapid decrease in MSSW of a landfalling TC occurs within a few kilometers of the coastline as onshore winds quickly adjust to the increased roughness of the underlying land surface. Therefore, a reduction factor R was considered into the decay model by Kaplan and DeMaria (1995). However, in our study, the intensity at landfall is defined as that at the time when the TC center crossed the coastline of mainland China. Therefore, the factor R is not necessary here. The decay constant α for TCs making landfall over China is smaller than that of 0.95 h^{-1} for TCs making landfall over the United States (Kaplan and DeMaria 1995). The difference in the decay constant could be partly due to the small samples of landfalling TCs in Kaplan and DeMaria (1995) and partly due to the different large-scale environmental conditions in the two basins.

The second model (M2) is the empirical decay model developed by Bhowmik et al. (2005) for estimating TC intensity crossing the east coast of India. They found that the decay rate during the first 6 h after landfall is more than doubled than that of the next 6 h in the region. Therefore, they used the same exponential decay model of **Eq. 1** but they allowed the decay constant to be different in the two time periods. The decay constant becomes,

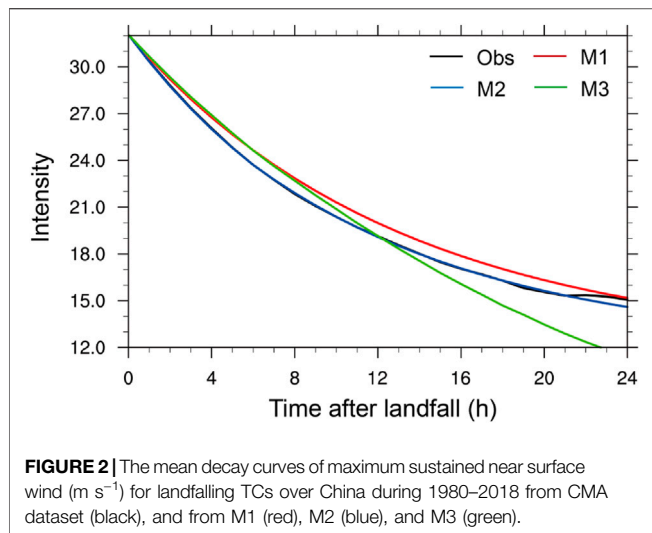
$$\alpha = \begin{cases} \{\ln[(V_0 - V_b)/(V_6 - V_b)]\}/6, & t \leq 6 \text{ h}, \\ \{\ln[(V_6 - V_b)/(V_{18} - V_b)]\}/12, & t > 6 \text{ h}, \end{cases} \quad (2)$$

where V_6 and V_{18} are MSSWs at 6 and 18 h after landfall, respectively. The decay constant α was calibrated based on the mean decay curve from all samples of landfalling TCs. The decay constant α in M2 is 0.09 h^{-1} in the first 6 h and 0.084 h^{-1} in the following 18 h for TCs making landfall over China. It is worth noting that we didn't take the correction procedure as done in Bhowmik et al. (2005) for simplicity.

The third model (M3) is the intensity decay model for TCs making landfall along the south coast of mainland China ($110.5^\circ\text{--}117.5^\circ\text{E}$) developed by Wong et al. (2008). Different from the above two decay models, based on an analysis of various factors, Wong et al. (2008) found that the landfall intensity, landward translational speed, and 850-hPa moist static energy of the TC at landfall had significant impact on the decay constant. They constructed the following decay model

$$V(t) = V_0 \exp(-\alpha t), \quad (3)$$

$$\alpha = \alpha_0 + \alpha_1 V_0 + \alpha_2 c + \alpha_3 / \Delta \phi_m, \quad (4)$$



where c is the landward translational speed of the TC at landfall, and ϕ_m is the 850-hPa moist static energy ($\Delta\phi_m = \phi_m - 335$) at the time of landfall, which is defined as the 9-point average (i.e., a square box with sides of 7.5 latitudes) around the TC center as used by Wong et al. (2008) and was calculated using the ERA-Interim data. The constant coefficients of α_0 , α_1 , α_2 , and α_3 in the decay constant α are determined using the method of least squares from all samples of landfalling TCs over mainland China in the study period. The average α obtained for M3 is 0.042 h^{-1} , with α_0 of -0.01495 , α_1 of -0.00085 , α_2 of -0.00012 , and α_3 of 2.9319 . Different from M1, M2, and M3 includes the possible effects of environmental conditions and TC characteristics at the time of landfall on the decay rate of the TC weakening rate after landfall. Note that α in M3 is much smaller than that in M1 and M2, this is mainly because there is no V_b in the decay equation of M3.

EVALUATION OF MODEL PERFORMANCE

We first examine the averaged intensity of landfalling TCs as a function of time after landfall (black curve in Figure 2). We can see from Figure 2 that rapid weakening of TCs occurs during the first 12 h after landfall. The weakening slows down afterwards. Eventually, the MSSW weakens to the background wind speed (about 30–40 h after landfall). Consistent with previous studies (Kaplan and DeMaria, 1995; Bhowmik et al., 2005; Vickery, 2005; Wong et al., 2008), TCs after landfall weaken roughly exponentially with time in terms of the MSSW. This explains why the existing decay models are based on the exponential function of time as summarized in *Description of Three Decay Models*.

The performances of the three decay models in estimating TC intensity change within 24 h after landfall are evaluated based on the basic statistical analysis of the model errors applied to all samples of landfalling cases over China during 1980–2018. Figure 2 compares the overall performances of the three models in terms of the mean intensity evolution after landfall

against the CMA best-track data during 1980–2018. All three models can produce the overall weakening of TCs after landfall, but with considerable mean errors. In M1, the decay constant is assumed to be independent of time (Kaplan and DeMaria, 1995). Therefore, it can only roughly model the overall weakening trend of landfalling TCs but with relatively larger mean errors. On average, M1 overestimates the intensity of landfalling TCs in the first 24 h after landfall. This is similar to the result in Kaplan and DeMaria (1995), who also found that on average the decay model tends to overpredict the MSSWs of TCs inland. Different from M1, M2 uses two decay constants for two different time periods after landfall (Bhowmik et al., 2005). The use of different decay constants largely improves the model performance in estimating the weakening of TCs after landfall, especially during the first 12 h after landfall. Particularly, the overall rapid weakening of TCs in the first 6 h after landfall is well captured by M2. Although the mean error from M2 increases for the following 18 h (Figure 3A), the mean errors are much smaller than those from M1. Different from those in M1 and M2, the decay constant in M3 is determined by considering the TC intensity, landward translational speed, and 850-hPa moist static energy of the TC at the time of landfall. As a result, in M3, different TCs possess different decay constants determined by different environmental conditions and characteristics of the landfalling TCs. In this sense, M3 can reflect the different characteristics of each TC to some extent. On average, M3 overestimates the intensity of landfalling TCs in the first 12 h after landfall while underestimates the intensity after TCs move further inland. The mean error increases largely as TC move further inland.

In addition to the mean intensity evolution, we also analyzed biases and mean absolute errors (MAEs) of the three decay models in estimating intensity of landfalling TCs after landfall during 1980–2018 with the results shown in Figure 3. Here, bias is defined as the estimated intensity minus the observed intensity in terms of the MSSW. On average, M1 and M2 tend to overestimate the intensity of landfalling TCs with positive biases during the whole period, while M3 tends to overestimate the intensity with positive biases during the first 12 h after landfall and underestimate the intensity with negative biases afterwards (Figures 3A,B). The average biases of M1 are generally larger than those of M2, with the mean bias of 0.82 m s^{-1} for M1 versus that of 0.05 m s^{-1} for M2. The errors of the two models initially increase with time, reach the peak of 1.17 m s^{-1} at 9 h after landfall for M1 and 0.24 m s^{-1} at 19 h after landfall for M2, and then turn to decrease with time for both models. As a result, the smallest biases of M1 and M2 occur in the beginning and at the end of the evaluated time period, with larger errors in between. M3 has the moderate biases of -0.56 m s^{-1} during the first 24 h after landfall, but the bias of M3 increases with time afterwards. The large increase in model error was consistent with the results in Wong et al. (2008), who mentioned that the MAE error and root-mean-square error (RMSE) increase with time after 12 h after landfall.

Compared the MAEs among the three decay models (Figures 3C,D), the increasing MAEs with time after landfall is similar. Among them, M2 has the lowest averaged MAE of 3.02 m s^{-1} during the whole period, while M1 has the highest averaged MAE

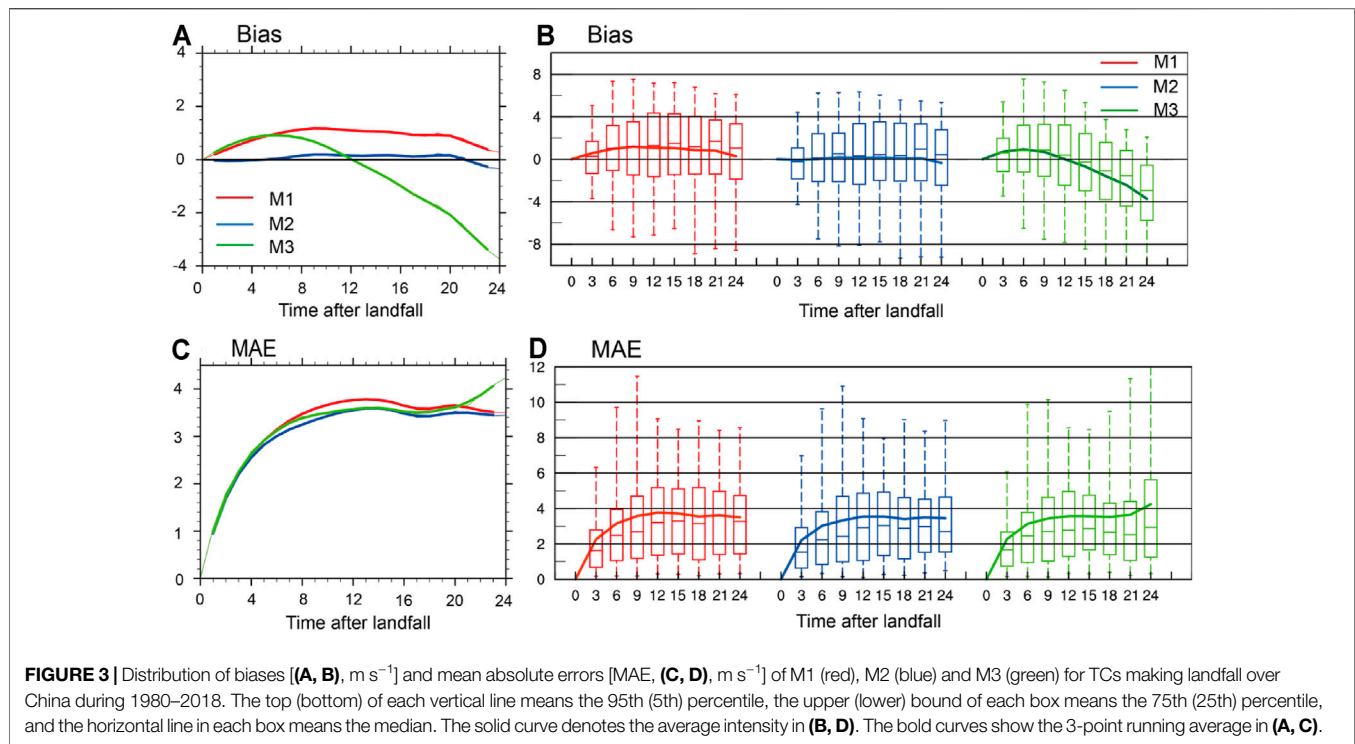


TABLE 1 | The decay rate, mean absolute error (MAE), bias and root-mean-square error (RMSE) from M1, M2, and M3 during the first 12 h or 24 h after landfall.

Decay rate ($\text{m s}^{-1} \text{ h}^{-1}$)	α (h^{-1})	MAE		Bias		RMSE	
		12 h	24 h	12 h	24 h	12 h	24 h
M1	0.0768	2.72	3.16	0.81	0.82	3.74	4.15
M2	0.09 0.084	2.60	3.02	0.06	0.05	3.6	4.02
M3	0.042	2.66	3.16	0.57	-0.56	3.66	4.29

of 3.16 m s^{-1} . M3 has the better performance during the first 20 h after landfall than M1 and M2. However, after 20 h after landfall, the MAE of M3 significantly increases with time, resulting in the largest RMSE among the three models during 24 h after landfall (Table 1). In Wong et al. (2008), the averaged MAE and RMSE are 1.8 and 2.67 m s^{-1} at 12 h after landfall, which are a little bit lower than 2.66 and 3.66 m s^{-1} in ours. This is mainly because M3 was originally developed for estimating intensity change of TCs making landfall along the southern coast of China (Wong et al., 2008), while here we considered all samples of TCs making landfall over both southern and eastern coasts of mainland China. In additions, the rapid increase in the MAE of M3 with time is likely because the decay coefficient in M3 is determined with factors at the time of landfall, but the changes in both dynamic and thermodynamic processes after landfall are not considered. This strongly suggests that the time independent decay coefficient can't reflect the intensity change after TCs move further inland, thus leading to the rapid error growth for M3.

The method proposed by Aberson (2008) was adopted to further evaluate the model skills in estimating the landfalling

TC intensity. By this method, all estimates and observations of the MSSWs are binned by certain intervals. At each forecast (estimate) time, a contingency table (or matrix) is filled with the count of each forecast-verification pair in the sample. The row and column in the table represent the number of times in intensity during certain intervals. Perfect forecasts/estimates are along the contingency table's diagonal. The farther each forecast is from the diagonal, the larger the forecast error is. The skill score (S) is then calculated using the following equation,

$$S = (C - E)/(T - E)$$

$$E = \sum (R_i C_i)/T$$

where C is the number of correct forecasts, T is the total number of forecasts, and E is the number of forecasts expected to be correct, which is calculated for each contingency table. R_i and C_i are the total counts of cases in the i^{th} row and i^{th} column, respectively. Based on this equation, the skill scores of the three decay models are calculated. Here, we choose 3 m s^{-1} as intervals instead of five knots used in Aberson (2008). The skill

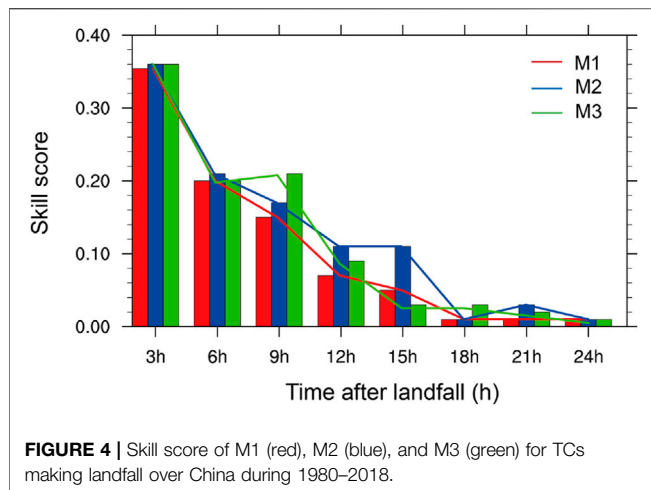


FIGURE 4 | Skill score of M1 (red), M2 (blue), and M3 (green) for TCs making landfall over China during 1980–2018.

score is 1.0 if all forecasts are correct and equals to zero or negative if the forecasts have no skill.

Figure 4 illustrates the skill scores of the three decay models for the period 1980–2018. The skill scores of all models almost decrease linearly with time, with the highest skill score of approximately 0.36 in the beginning, and become nearly zero or negative by 24 h after landfall and afterwards. This means that the effective forecast time of the three decay models are approximately 24 h, especially for M3. Note that the skill score

of M2 and M3 decreases steadily during the whole period with relatively higher values than M1, indicating that M2 and M3 outperforms M1 during this period, especially the period between 6 and 18 h after landfall. This is consistent with the above conclusion.

We further examine the spatial distribution of biases of the three decay models with the results shown in **Figure 5**. To help see any orographic dependence of model errors, the topographic map of China is given in **Figure 5D**. The distributions of biases of M1 and M2 are similar (**Figures 5A,B**), with large positive biases primarily in the southeastern China, where the Wuyi Mountains in Fujian Province are located (**Figure 5D**), and slightly negative biases in the eastern China. The large positive bias is likely due to the topographic effect, which may enhance the weakening of a TC when it moves inland. The rough surface and the blocking effect of mountains in the southeastern China can impose considerable effects on TC motion, structure, precipitation, and intensity (Duan et al., 2019; Lin et al., 2018). These effects often enhance the weakening of a TC and slow down the TC motion, leading to the enhancement of local torrential rainfall (e.g., Dong et al., 2019; Li et al., 2019). Because the decay constants in the decay models are obtained based on the fitting of landfalling TC samples, the orographic/terrain effects are not explicitly considered in the current decay models.

Both M1 and M2 can't reflect the effect of mountains along the coastal areas and, thus, overestimate TC intensity after landfall with positive biases over the southeastern China (**Figures 5A,B**).

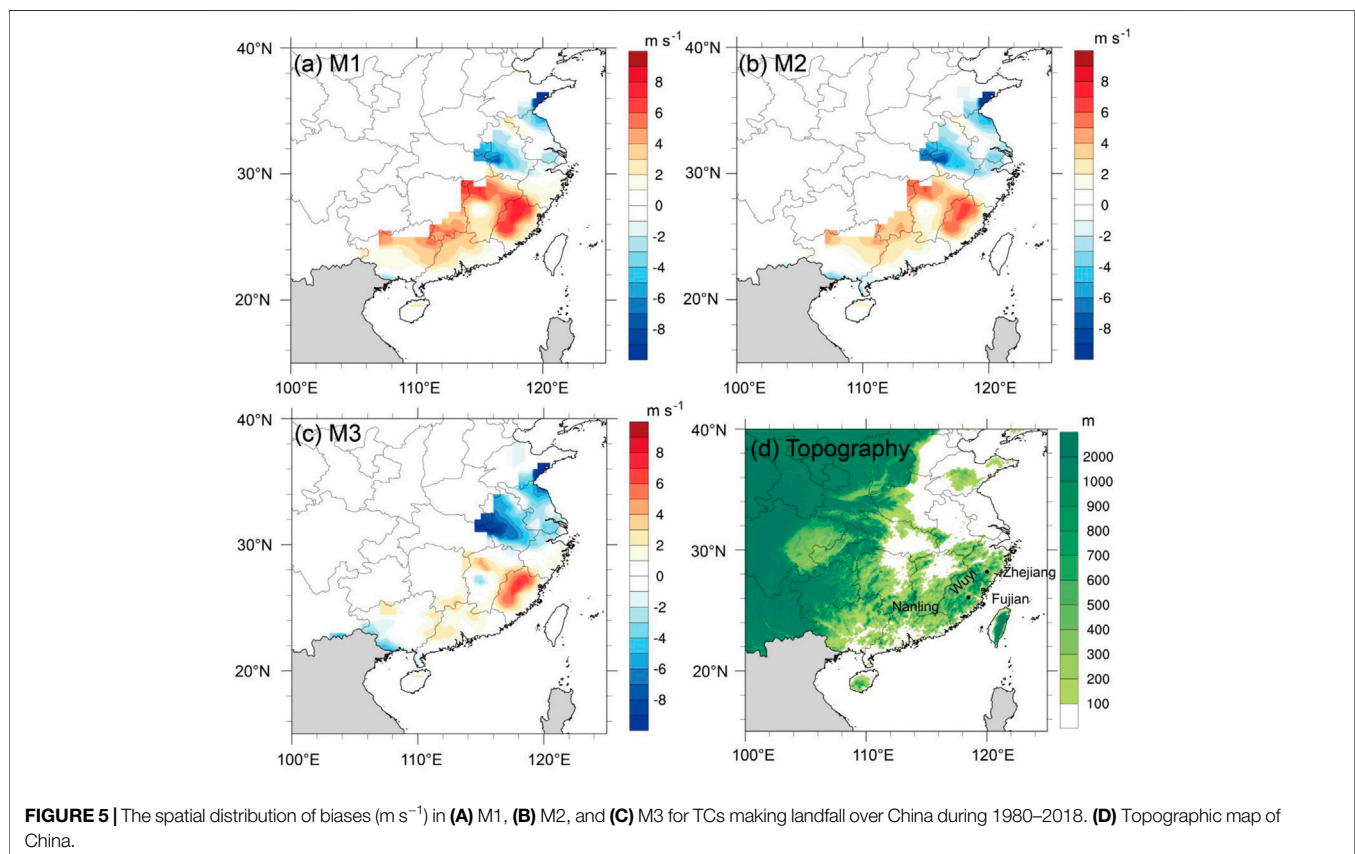
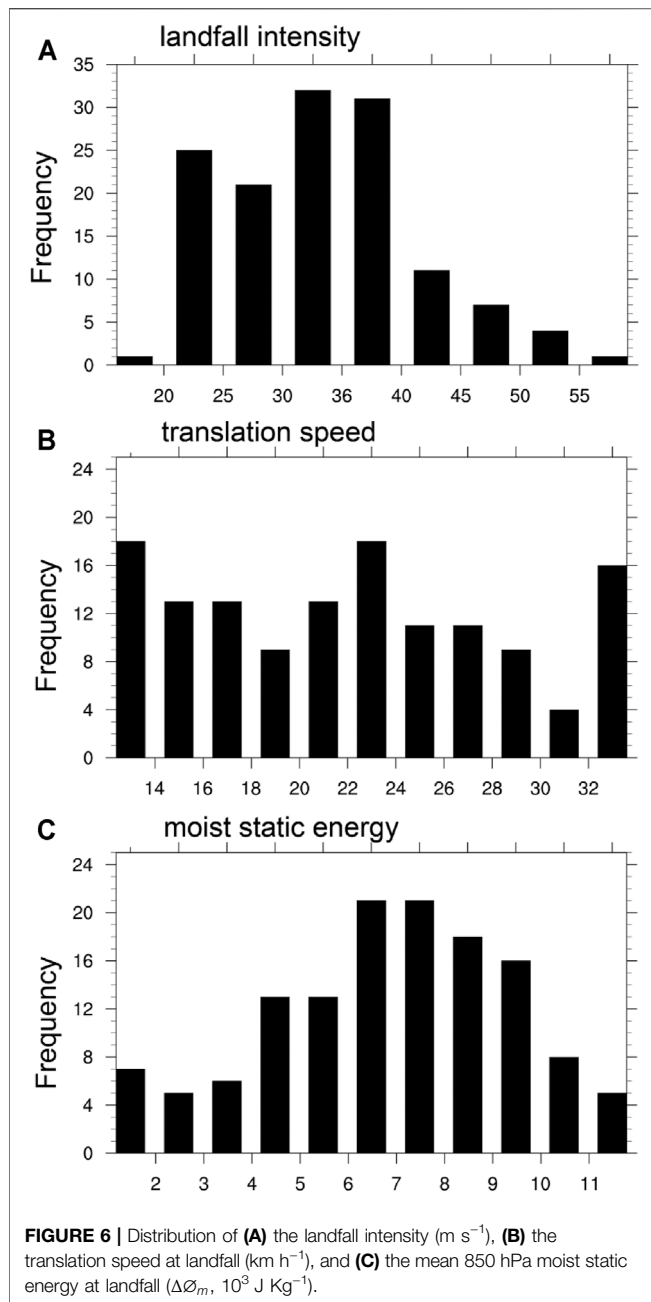


FIGURE 5 | The spatial distribution of biases (m s^{-1}) in (A) M1, (B) M2, and (C) M3 for TCs making landfall over China during 1980–2018. (D) Topographic map of China.



By contrast, M3 performs relatively better in the southeastern China with a small area of positive biases, but it shows large negative biases in the eastern China (Figure 5C), where the land is dominated by flat plain (Figure 5D). This is mainly because M3 was originally developed for estimating intensity change of TCs making landfall along the southern coast of China (Wong et al., 2008). Since mesoscale mountains exist in the southern coastal regions of China and the effect of atmospheric environmental conditions along the southern coast of China at the time of landfall are partly considered. This explains why M3 performs the best for the intensity change of TCs making landfall in the southeastern China. However, the environmental atmospheric

conditions with negligible terrain effects in the eastern China are different from those in the southern China. As a result, M3 overestimates the weakening rate of landfalling TCs in the eastern China with negative intensity biases.

MODEL ERROR ANALYSIS

To identify the main error sources in the three decay models discussed above, we further analyzed three critical factors, namely TC intensity and translational speed, and the 850-hPa moist static energy for landfalling TCs, all at the time of landfall, to quantify contributions by different factors to the model errors. Since the topography may affect the model performance as well, the topography is also selected as the fourth critical factor for our analysis. Figure 6 illustrates the distributions of the key variables, including the landfall intensity, the landfall translational speed, and the 850 hPa moist static energy $\Delta\phi_m$ at the time of landfall. The majority of landfall TC intensity is between 20–45 m s⁻¹, with the mean landfall intensity of 31.82 m s⁻¹. The translational speed at the time of landfall is mainly between 14 and 32 km h⁻¹ with the mean value of 22.3 km h⁻¹. The mean $\Delta\phi_m$ is primarily between 6×10^3 – 10×10^3 J Kg⁻¹, with the mean value of 6.8×10^3 J Kg⁻¹.

We then examine the dependences of TC weakening rate after landfall on the four critical factors mentioned above. Firstly, we classified landfalling TCs into strong TCs (STCs, with MSSW ≥ 32 m s⁻¹) and weak TCs (WTCs, with MSSW < 32 m s⁻¹) at the time of landfall. The weakening rate of STCs is much higher than that of WTCs (Figure 7A). The difference in the decay rates between STCs and WTCs is statistically significant over 99% confidence level during the whole period up to 24 h after landfall (Table 2). After 24 h after landfall, the intensity of landfalling TCs continue to weaken but more slowly. Secondly, we classified the landfalling TCs into fast moving TCs (Fast, with translational speed ≥ 20 km h⁻¹) and slow moving TCs (Slow, with translational speed < 20 km h⁻¹) at the time of landfall. Here, the translational speed of a TC at the time of landfall was calculated as the distance traveled between 3 h prior to landfall and 3 h after landfall. The slow-moving TCs are generally weaker at the time of landfall and, thus, show lower weakening rate than the fast-moving TCs (Figure 7B). Such a difference is significant over 90% confidence level (Table 2) during the first 12 h after landfall. This means that the slow moving TCs at the time of landfall is more favorable for the maintenance of their intensity after landfall. Thirdly, we classified the landfalling TCs into high moist static energy (Em_h, with $\Delta\phi_m \geq 7.5 \times 10^3$ J Kg⁻¹) and low moist static energy (Em_l, with $\Delta\phi_m < 7.5 \times 10^3$ J Kg⁻¹) at the time of landfall. Although the initial intensity at landfall shows little difference between high and low $\Delta\phi_m$ groups (Figure 7C), landfalling TCs in the Em_h group weaken more slowly than those in the Em_l group, especially during the first 12 h after landfall. The difference in the weakening rate between the Em_h and Em_l groups is statistically significant over 90% confidence level in the first 12 h after landfall (Table 2). This indicates that TCs with high moist static energy at landfall is more favorable for the maintenance of TC intensity after landfall. Finally, according

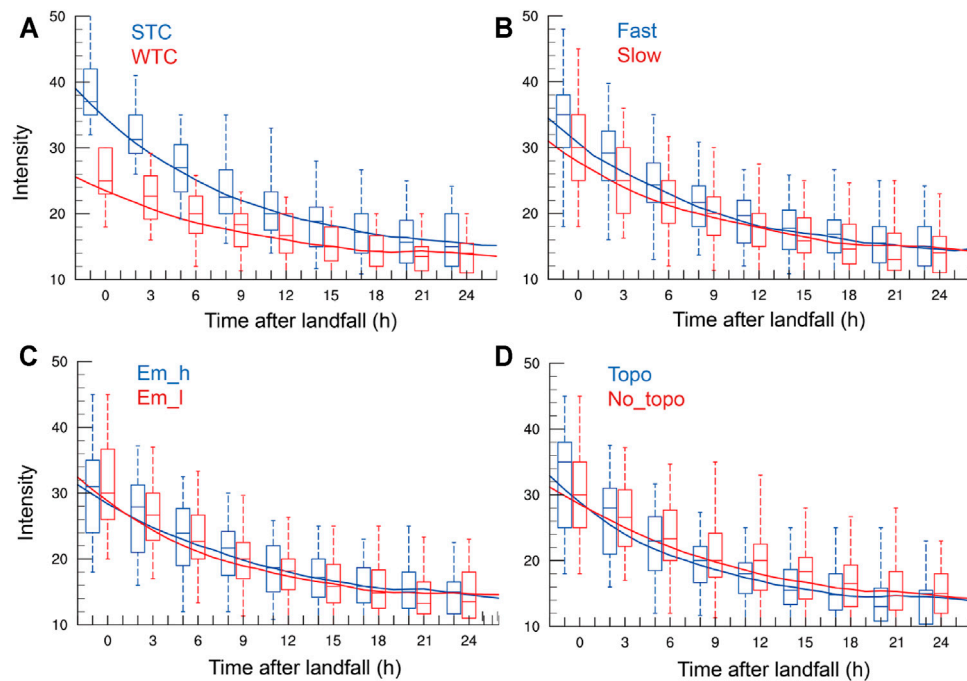


FIGURE 7 | As in **Figure 3B**, but for **(A)** STC (blue) vs. WTC (red), **(B)** Fast (blue) vs. Slow (red), **(C)** Em_h (blue) vs. Em_l (red), and **(D)** Topo (blue) vs. No_topo (red), see text for details.

TABLE 2 | Decay rates ($\text{m s}^{-1} \text{h}^{-1}$) during different periods (0–6, 0–12, 0–18, and 0–24 h) after landfall for different classification groups (STC/WTC, Topo/No_topo, Fast/Slow, Em_h/Em_l). Boldface and italic fonts indicate the differences being statistically significant over the 90 and 99% confidence level, respectively, based on the Student's *t* test.

Decay rate ($\text{m s}^{-1} \text{h}^{-1}$)	Intensity		Topography		Speed		$\Delta\theta_m$	
	STC	WTC	Topo	No_topo	Fast	Slow	Em_h	Em_l
6	<i>-1.89</i>	<i>-0.94</i>	<i>-1.69</i>	<i>-1.11</i>	<i>-1.55</i>	<i>-1.29</i>	<i>-1.24</i>	<i>-1.56</i>
12	<i>-1.48</i>	<i>-0.73</i>	<i>-1.24</i>	<i>-0.92</i>	<i>-1.18</i>	<i>-0.98</i>	<i>-1.01</i>	<i>-1.16</i>
18	<i>-1.18</i>	<i>-0.6</i>	<i>-0.98</i>	<i>-0.79</i>	-0.93	-0.83	-0.83	-0.92
24	<i>-0.96</i>	<i>-0.47</i>	-0.76	-0.65	-0.77	-0.66	-0.67	-0.73

to the topographic distribution along the coastal regions of mainland China given in **Figure 5D**, we divided landfalling TCs into those making landfall in regions with visible topography (Topo, between 22 and 29°N) and those without visible topography (No_topo, south of 22°N or north of 29°N). TCs in the two groups show little difference in intensity at the time of landfall, however, TCs in the Topo group weaken more rapidly during the first 18 h after landfall than those in the No_topo group (**Figure 7D**, **Table 2**). These results strongly suggest that the topographic effect is an indispensable factor affecting the decay rate of landfalling TC over China.

We see in *Evaluation of Model Performance* that M1 and M3 have relatively larger errors than M2 and both show geographical dependences of model errors, where we speculated the larger errors could be related to terrain effect for M1 and the time-independent decay coefficient for M3. To confirm those speculations, we did some further analyses. We

separately analyzed TC samples making landfall north of 29°N over China, where there are no visible terrains, and compared the errors with those for all samples of TCs making landfall over China (**Figure 8**). As expected, the decay rate for all TC samples is larger than that for TCs making landfall north of 29°N in the first 10 h after landfall and then becomes smaller afterwards (**Figures 8A,B**). Both MAE and bias (**Figures 8C,D**) for TCs making landfall north of 29°N are much smaller than those for all samples of landfalling TCs over China in the whole period, with MAE of 3.16 m s^{-1} and bias of 0.82 m s^{-1} for all samples and 2.98 and 0.4 m s^{-1} for TCs making landfall north of 29°N, especially when TC moved farther inland. This indicates that errors for TCs north of 29°N with little terrain effect are close to or even smaller than those in Kaplan and DeMaria (1995). Therefore, the relatively large errors in M1 results partially from the ignorance of terrain effects as mentioned above.

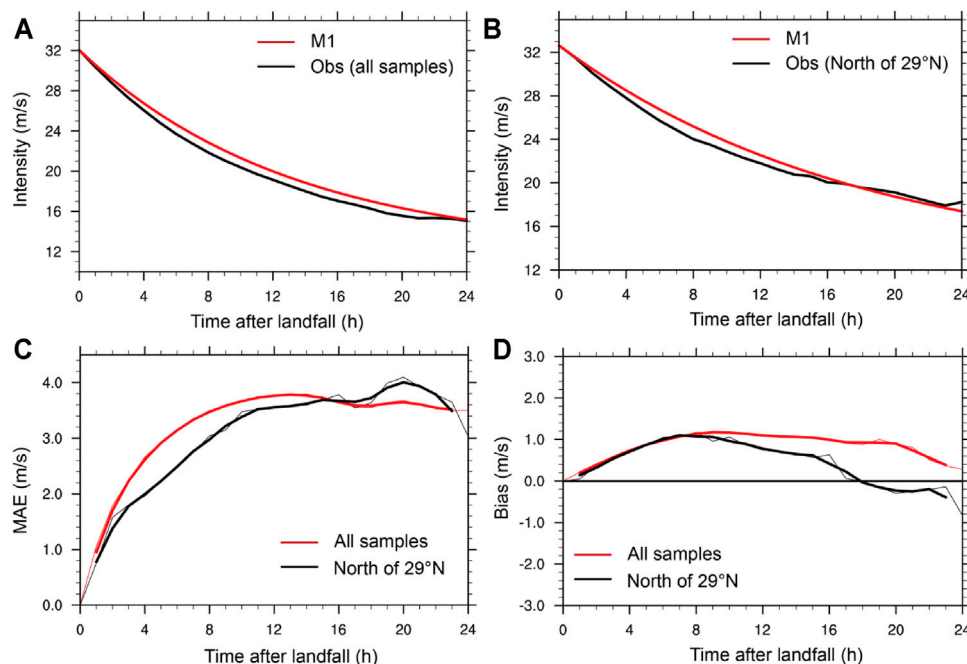


FIGURE 8 | The mean decay curves of maximum sustained near-surface wind (m s^{-1}) (A) for all samples of landfalling TCs, and (B) for TCs making landfall north of 29°N over China. Distribution of (C) MAE (m s^{-1}) and (D) biases (m s^{-1}) of all samples of landfalling TCs (red lines) and TCs making landfall north of 29°N (black lines) over China during 1980–2018.

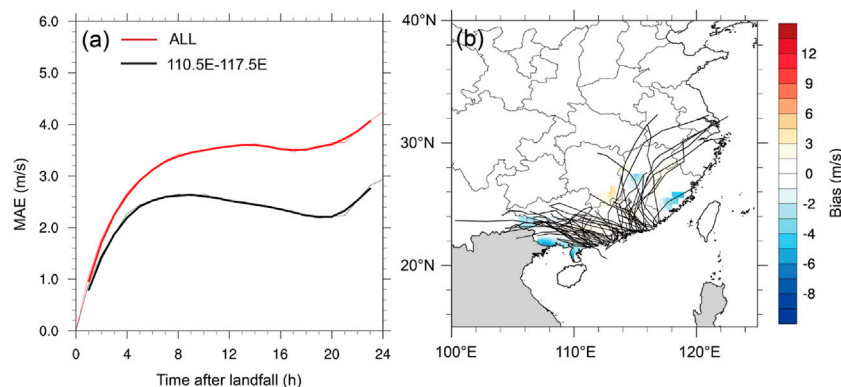


FIGURE 9 | (A) Distribution of MAE (m s^{-1}) of M3 for all samples of landfalling TCs (red line) and for TCs making landfall along the South China coast (110.5°–117.5°, black line). (B) The spatial distribution of biases (m s^{-1}) in M3 for TCs making landfall along the South China coast. The black lines in (B) represent the tracks of landfalling TCs.

Since M3 was originally attempted for TCs making landfall over the South China coast, we show in **Figure 9A** the MAEs for all TCs samples and samples of TCs making landfall along the South China coast (110.5–117.5°), and in **Figure 9B** the spatial distribution of biases and tracks for TCs making landfall along the South China coast. MAE for TCs making landfall along the South China coast is much smaller than that for all TC samples, with MAE of 3.16 m s^{-1} for all TC samples and MAE of 2.25 m s^{-1} for TC samples making landfall along the South China coast. Compared with the MAE of 1.8 m s^{-1} and RMSE of 2.67 m s^{-1} at 12 h after landfall in Wong et al. (2008), the MAE of 2.08 m

s^{-1} and RMSE of 2.7 m s^{-1} in our study are very close to those at 12 h after landfall. Nevertheless, although the error for TCs making landfall along the South China coast increases more slowly with the time after landfall than that for all samples of landfalling TCs over China, the error still grows rapidly after TCs move further inland. This suggests that the rapid error growth in M3 can be largely attributed to the fact that the decay coefficient in M3 is determined by factors at the time of landfall only. As TCs move further inland, the decay rate should be adjusted with changes in both dynamic and thermodynamic environmental conditions after landfall. This suggests that the time independent

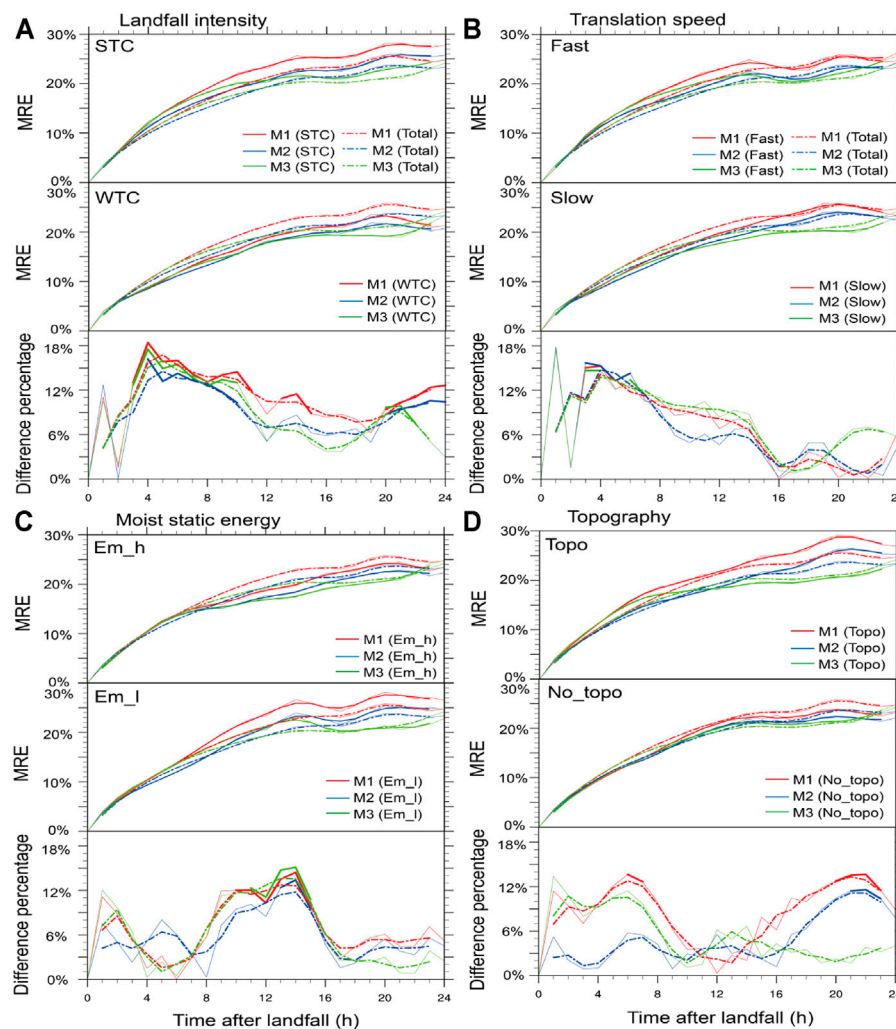


FIGURE 10 | Mean relative errors (MRE) of all samples of landfalling TCs (dashed) and the MREs of different classification groups (solid) in the upper and middle part of each panel, and the percentage of difference in MREs between different groups and all TCs in the lower panels. The solid portions in the lower panels indicating the difference being statistically significant over 90% confidence level, for (A) landfall intensity, (B) translation speed, (C) moist static energy, (D) topography.

decay coefficient can't reflect the intensity change of TCs that move further inland, thus leading to the rapid error growth for M3. Note that the error evolution in **Figure 9A** is very similar to that in Wong et al. (2008, see their **Figure 10B**). The above analysis confirms that the terrain effect and the time independent decay coefficient are two essential factors responsible for the relatively large errors in M1 and M3.

To further examine the relative contributions of different key factors to model errors, we compared the mean relative errors (MREs) of different groups (STC/WTC, Fast/Slow, Em_h/Em_l, Topo/No_topo) and the percentage of difference in the model errors between different groups and all TCs. Here, the relative error is defined as the absolute error divided by the TC intensity at the evaluation time. We used the relative errors instead of the absolute errors to reduce the influence of TC intensity on model errors because strong TCs often have larger absolute errors than weak TCs. The percentage of difference is defined as the percentage of the difference in the MREs between one group

and all landfalling TCs divided by the MRE of all landfalling TCs. The solid curves in the upper and middle parts of different panels in **Figure 10** represent the MREs of TCs in different groups, and the dashed curves represent the MREs of all samples of landfalling TCs from M1, M2 and M3, respectively. The dashed curves in the lower parts of different panels in **Figure 10** indicate the percentages of differences between MREs for TCs in different groups and MREs for all landfalling TCs, and the corresponding solid portions indicate the differences that are statistically significant over 90% confidence level between different groups.

Compared MREs of all TC samples among M1, M2 and M3 (dashed lines in the upper part of each panel in **Figure 10**), MREs of M2 and M3 are relatively smaller than that of M1 during the whole period, and the averaged MRE of M3 is the smallest. In **Figure 10A**, the MREs of M1, M2, and M3 are significantly larger for STCs than for all TC samples during the whole period after landfall. On the contrary, the MRE for WTCs is significantly smaller than that for all samples of TCs. This indicates that all

three models have larger relative errors for strong TCs than weak TCs. Note that the difference in MREs between STCs and WTCs becomes statistically significant during 3–10 h after landfall, with the largest contribution of about 18% from the initial TC intensity. Among them, the difference percentage in M1 is the largest, indicating that M1 is less stable than other two models. The MREs of the three models are larger for fast moving TCs than for all sample TCs during the first 16 h after landfall and are smaller for slow moving TCs, especially during the first 2–6 h after landfall, with the largest contribution over 15% (**Figure 10B**). This means that the forecast errors for landfalling TCs with faster translational speeds would be larger in the early stage after landfall. However, the MREs are similar between fast TCs/slow TCs and all samples of TCs in the later stage. This indicates that the impact of translational speed at the time of landfall on model errors is negligible except for the period shortly after landfall. The MREs for landfalling TCs with high moist static energy are smaller than landfalling TCs with low moist static energy in all three models (**Figure 10C**), which is statistically significant for about 10–15 h after landfall, with the largest contribution over 15%. The MREs of M1 and M2 are larger for TCs in the Topo group than in the No_topo group almost for the whole period after landfall (**Figure 10D**), with the largest contribution up to 15% between 4 and 8 h and after 18 h after landfall. However, the MRE of M3 is slightly lower for TCs in the Topo group and slightly higher for TCs in the No_topo group than that for all landfalling TCs with no significant difference between the Topo and No_topo groups, suggesting that the topography has some minor effects on the performance of M3 (**Figure 10D**).

DISCUSSION AND CONCLUSION

In this study, the performances of three exponential decay models (M1, M2, and M3) in estimating the intensity change in terms of the MSSW of TCs after landfall over China are evaluated and compared. The three models are developed by, respectively, Kaplan and DeMaria (1995), Bhowmik et al. (2005), and Wong et al. (2008). The decay constants in M1 and M2 are obtained by fitting the mean MSSWs of all TC samples making landfall over mainland China. The difference between M1 and M2 is in that only one decay constant is fitted in M1 but two different decay constants are fitted in M2 for different time periods after landfall. The decay constant in M3 is determined by several factors, including the TC intensity, landward translational speed, and 850-hPa moist static energy, all at the time of landfall. The performances of the three models are evaluated based on all TC samples making landfall over mainland China during 1980–2018.

Results indicate that these models can reproduce the weakening trend of TCs after landfall and have reasonable skills in estimating/predicting TC intensity change after landfall. On average, M1 and M2 tend to overestimate TC intensity after landfall, while M3 overestimates the TC intensity in the first 12 h after landfall and underestimates the intensity after TCs moving further inland. M2 has the best

performance with the smallest mean errors among the three models within 24 h after landfall, which is mainly due to the fact that two decay constants are fitted for two different time periods in M2 based on the mean intensity change of all TC samples after landfall. M3 shows relatively better performance than M1 in the first 20 h after landfall, but its errors increase largely after TCs move further inland. This is because M3 considers several environmental factors and/or the characteristics of the TCs only at the time of landfall in determining the decay constant.

M1 and M2 have similar spatial error distributions with large positive biases primarily in the southeastern coastal regions of China, where the Wuyi Mountains in Fujian Province are located. Because the possible orographic effects are not explicitly considered in M1 and M2, both models overestimate TC intensity with positive biases in the southeastern China. M3 performs better in the southeastern China, but shows negative biases in the eastern China. This is because M3 was originally developed to estimate the intensity change of TCs making landfall along the southern coast of China (Wong et al., 2008). Since both the terrain and the environmental conditions in the eastern China coast are different from those in the southeastern China coast, it is not surprising that M3 performs better over the southeastern China than over the eastern China. The classification analyses based on landfall intensity, translational speed, and 850-hPa moist static energy of the TCs at the time of landfall, and topography of the landfalling region are conducted to examine the relative contributions of different factors to model errors. Results demonstrate that these four factors all contribute to model errors of M1, M2, and M3, with the maximum contribution of about 18% by landfall intensity, and about 15% equally by translational speed, moist static energy and topography during different periods after landfall.

Although the three exponential decay models evaluated in this study can reproduce the weakening trends of TCs after landfall, their performances are not perfect. Based on results from this study, we can recommend several aspects for future development/improvement of the decay model of landfalling TC intensity. First, topography could have a significant effect on the model performance as inferred from the spatial error distribution. However, such an effect has not been explicitly considered in the current intensity decay models. Second, different performances of M1 and M2 indicate the importance of the time-dependent decay constant in a decay model. TCs often have a larger decay rate in the first period than in the second period after landfall. Third, including the effects of environmental conditions and TC characteristics as factors in determining the decay constant has some benefits to the performance of a decay model. However, only the conditions at the time of landfall might be not enough. Future efforts may consider changes in the environmental conditions based on forecast of numerical weather prediction models and also the land surface properties, such as the effect of large lakes and so on. In addition, the inner core size of a TC at the time of landfall may affect the decay rate of the TC intensity after landfall as well (Vickery, 2005). Therefore, the time-dependent decay constant determined by environmental conditions, topography and land cover properties, and the TC characteristics (including the inner core size) is necessary to further improve the exponential decay

models for estimating TC intensity change after landfall. Efforts in this direction are under way and the results will be reported in a future publication in due course.

DATA AVAILABILITY STATEMENT

The ERA-Interim data used in this study were downloaded from <https://apps.ecmwf.int/datasets/data/interim-full-daily/levtype=pl/>. The TC best track datasets were obtained from STI/CMA (<http://tcdata.typhoon.org.cn>). Further inquiries can be directed to the corresponding author.

REFERENCES

- Aberson, S. D. (2008). An Alternative Tropical Cyclone Intensity Forecast Verification Technique. *Wea. Forecast.* 23, 1304–1310. doi:10.1175/2008WAF2222123.1
- Batts, M. E., Simiu, E., and Russell, L. R. (1980). *Hurricane Wind Speeds in the United States*. J. Struct. Div. 106, 2001–2016. doi:10.1061/JSEAG.0005541
- Bhowmik, S. K. R., Kotal, S. D., and Kalsi, S. R. (2005). An Empirical Model for Predicting the Decay of Tropical Cyclone Wind Speed after Landfall over the Indian Region. *J. Appl. Meteorol.* 44, 179–185. doi:10.1175/JAM-2190.1
- Colette, A., Leith, N., Daniel, V., Bellone, E., and Nolan, D. S. (2010). Using Mesoscale Simulations to Train Statistical Models of Tropical Cyclone Intensity over Land. *Mon. Wea. Rev.* 138, 2058–2073. doi:10.1175/2010MWR3079.1
- Dee, D. P., Uppala, S. M., Simmons, A. J., Berrisford, P., Poli, P., Kobayashi, S., et al. (2011). The ERA-Interim Reanalysis: Configuration and Performance of the Data Assimilation System. *Q.J.R. Meteorol. Soc.* 137, 553–597. doi:10.1002/qj.828
- Demaria, M., and Kaplan, J. (1994). A Statistical hurricane Intensity Prediction Scheme (SHIPS) for the Atlantic basin. *Wea. Forecast.* 9, 209–220. doi:10.1175/1520-0434(1994)009<0209:aships>2.0.co;2
- Demaria, M., and Kaplan, J. (1999). An Updated Statistical hurricane Intensity Prediction Scheme (SHIPS) for the Atlantic and Eastern North Pacific Basins. *Wea. Forecast.* 14, 326–337. doi:10.1175/1520-0434(1999)014<0326:auship>2.0.co;2
- DeMaria, M., Knaff, J. A., and Kaplan, J. (2006). On the Decay of Tropical Cyclone Winds Crossing Narrow Landmasses. *J. Appl. Meteorol. Climatol.* 45, 491–499. doi:10.1175/JAM2351.1
- Demaria, M., Mainelli, M., Shay, L. K., Knaff, J. A., and Kaplan, J. (2005). Further Improvements to the Statistical hurricane Intensity Prediction Scheme (SHIPS). *Wea. Forecast.* 20, 531–543. doi:10.1175/WAF862.1
- Dong, M., Ji, C., Chen, F., and Wang, Y. (2019). Numerical Study of Boundary Layer Structure and Rainfall after Landfall of Typhoon Fitow (2013): Sensitivity to Planetary Boundary Layer Parameterization. *Adv. Atmos. Sci.* 36 (4), 431–450. doi:10.1007/s00376-018-7281-9
- Duan, Y., Wan, Q., Huang, J., Zhao, K., Yu, H., Wang, Y., et al. (2019). Landfalling Tropical Cyclone Research Project (LTCRP) in China. *Bull. Amer. Meteorol. Soc.* 100 (12), ES447–ES472. doi:10.1175/bams-d-18-0241.1
- Georgiou, P. N. (1985). *Design Windspeeds in Tropical Cyclone-Prone Regions*. London, ON, Canada: Ph.D. thesis, University of Western Ontario, 295. Available at: <https://ir.lib.uwo.ca/digitizedtheses/1523>.
- Ho, F. P., Su, J. C., Hanevich, K. L., Smith, R. J., and Richards, F. P. (1987). *Hurricane Climatology for the Atlantic and Gulf Coasts of the United States*. Washington, DC: NOAA Tech. Rep. NWS38, Federal Emergency Management Agency, 195. Available at: https://coast.noaa.gov/data/hes/images/pdf/ATL_GULF_HURR_CLIMATOLOGY.pdf.
- Kaplan, J., and DeMaria, M. (1995). A Simple Empirical Model for Predicting the Decay of Tropical Cyclone Winds after Landfall. *J. Appl. Meteorol.* 34, 2499–2512. doi:10.1175/1520-0450(1995)034<2499:asemp>2.0.co;2
- Kaplan, J., and Demaria, M. (2001). On the Decay of Tropical Cyclone Winds after Landfall in the New England Area. *J. Appl. Meteorol.* 40, 2802–2826. doi:10.1175/1520-0450(2001)040<0280:OTDOTC>2.0.CO10.1175/1520-0450(2001)040<0280:otdotc>2.0.co;2
- Knaff, J. A., Sampson, C. R., and Demaria, M. (2005). An Operational Statistical Typhoon Intensity Prediction Scheme for the Western North Pacific. *Wea. Forecast.* 20, 688–699. doi:10.1175/WAF863.1
- Li, Y., Lin, Y., and Wang, Y. (2019). A Numerical Study on the Formation and Maintenance of a Long-Lived Rainband in Typhoon Longwang (2005). *J. Geophys. Res. Atmos.* 124 (19), 10401–10426. doi:10.1029/2019jd030600
- Lin, Y., Li, Y., Li, Q., Chen, M., Xu, F., Wang, Y., et al. (2018). A Long-Lasting Vortex Rossby Wave-Induced Rainband of Typhoon Longwang (2005). *Bull. Amer. Meteorol. Soc.* 99, 1127–1134. doi:10.1175/BAMS-D-17-0122.1
- Schwerdt, R. W., Ho, F. P., and Watkins, R. R. (1979). *Meteorological Criteria for Standard Project hurricane and Probable Maximum hurricane Wind fields, Gulf and East Coasts of the United States*. MD: NOAA Tech. Rep. NWS23, Silver Spring, 317.
- Tuleya, R. E., Bender, M. A., and Kurihara, Y. (1984). A Simulation Study of the Landfall of Tropical Cyclones. *Mon. Wea. Rev.* 112, 124–136. doi:10.1175/1520-0493(1984)112<0124:assotl>2.0.co;2
- Tuleya, R. E., and Kurihara, Y. (1978). A Numerical Simulation of the Landfall of Tropical Cyclones. *J. Atmos. Sci.* 35, 242–257. doi:10.1175/1520-0469(1978)035<0242:ANSOTL>2.0.CO;2
- Tuleya, R. E. (1994). Tropical Storm Development and Decay: Sensitivity to Surface Boundary Conditions. *Mon. Wea. Rev.* 122, 291–304. doi:10.1175/1520-0493(1994)122<0291:tsdads>2.0.co;2
- Vickery, P. J. (2005). Simple Empirical Models for Estimating the Increase in the central Pressure of Tropical Cyclones after Landfall along the Coastline of the United States. *J. Appl. Meteorol.* 44, 1807–1826. doi:10.1175/JAM2310.1
- Vickery, P. J., and Twisdale, L. A. (1995). Wind-field and Filling Models for hurricane Wind-Speed Predictions. *J. Struct. Eng.* 121, 1700–1709. doi:10.1061/(asce)0733-9445(1995)121:11(1700)
- Wong, M. L. M., Chan, J. C. L., and Zhou, W. (2008). A Simple Empirical Model for Estimating the Intensity Change of Tropical Cyclones after Landfall along the South China Coast. *J. Appl. Meteorol. Climatol.* 47, 326–338. doi:10.1175/2007JAMC1633.1
- Ying, M., Zhang, W., Yu, H., Lu, X., Feng, J., Fan, Y., et al. (2014). An Overview of the China Meteorological Administration Tropical Cyclone Database. *J. Atmos. Oceanic Technol.* 31, 287–301. doi:10.1175/JTECH-D-12-00119.1

AUTHOR CONTRIBUTIONS

YW designed the study. LL analyzed the datasets and generated figures. YW and LL wrote the paper with contributions from HW.

FUNDING

This study has been supported by National Natural Science Foundation of China under grants 41730960, 42175011 and in part by the National Key R&D Program of China under grant 2017YFC1501602. YW was supported in part by NSF grant AGS-1834300.

Conflict of Interest: The authors declare that the research was conducted in the absence of any commercial or financial relationships that could be construed as a potential conflict of interest.

Publisher's Note: All claims expressed in this article are solely those of the authors and do not necessarily represent those of their affiliated organizations, or those of the publisher, the editors and the reviewers. Any product that may be evaluated in this article, or claim that may be made by its manufacturer, is not guaranteed or endorsed by the publisher.

Copyright © 2021 Liu, Wang and Wang. This is an open-access article distributed under the terms of the Creative Commons Attribution License (CC BY). The use, distribution or reproduction in other forums is permitted, provided the original author(s) and the copyright owner(s) are credited and that the original publication in this journal is cited, in accordance with accepted academic practice. No use, distribution or reproduction is permitted which does not comply with these terms.



DSAEF_LTP Model Experiment to Forecast the Accumulated Precipitation of Landfalling Northward-Moving Typhoons in China

Mei Yao^{1,2}, Yunqi Ma², Li Jia², Fumin Ren^{2*}, Guoping Li¹, Chenchen Ding², Mingyang Wang² and John L. McBride^{3,4}

¹School of Atmospheric Sciences, Chengdu University of Information Technology, Chengdu, China, ²State Key Laboratory of Severe Weather/Chinese Academy of Meteorological Sciences, Beijing, China, ³School of Earth Science, University of Melbourne, Melbourne, VIC, Australia, ⁴Research and Development Division, Bureau of Meteorology, Melbourne, VIC, Australia

OPEN ACCESS

Edited by:

Hui Yu,
China Meteorological Administration,
China

Reviewed by:

Jia Liang,
Nanjing University of Information
Science and Technology, China
Chao Wang,
Nanjing University of Information
Science and Technology, China

*Correspondence:

Fumin Ren
fmren@163.com

Specialty section:

This article was submitted to
Atmospheric Science,
a section of the journal
Frontiers in Earth Science

Received: 27 August 2021

Accepted: 22 November 2021

Published: 17 December 2021

Citation:

Yao M, Ma Y, Jia L, Ren F, Li G, Ding C,
Wang M and McBride JL (2021)
DSAEF_LTP Model Experiment to
Forecast the Accumulated
Precipitation of Landfalling Northward-
Moving Typhoons in China.
Front. Earth Sci. 9:765532.
doi: 10.3389/feart.2021.765532

We designed two groups of experiments to test the forecast performance of the Dynamical-Statistical-Analog Ensemble Forecast (DSAEF_LTP) model for precipitation caused by landfalling northward-moving typhoons. The first group DSAEF_LTP-1 had the generalized initial value containing three factors (tropical cyclone track, landfall season and tropical cyclone intensity) while the second group DSAEF_LTP-2 added multiple choices of similarity regions. We selected 33 typhoons that brought about maximum daily precipitation ≥ 100 mm to the area north of the Yangtze River from 2004–2019. We used 22 tropical cyclones from 2004–2015 as training samples to identify the best scheme, which was then used to conduct independent sample forecasting experiments for 11 tropical cyclones from 2016–2019. The results were compared with those of four numerical models (ECMWF, GFS, GRAPES and SMS-WARMS). The simulation ability of the DSAEF_LTP model was significantly improved after adding the similarity regions. The TSsum (TS250 + TS100) for accumulated precipitation ≥ 250 and ≥ 100 mm increased from 0.1239 (0 + 0.1239) to 0.1883 (0.0526 + 0.1357). The forecast performance of the DSAEF_LTP for TS100 was 0.1355 for DSAEF_LTP-1 and 0.099 for DSAEF_LTP-2. Both exceeded the scores for two of the operational Numerical Models, GRAPES (0.0798) and SMS-WARMS (0.0943). The DSAEF_LTP model can capture the distribution patterns of the observed precipitation in most cases. The forecasting performance was good over the southern coast of China but was limited in the north. The development of vortex identification technology for residual vortices and the introduction of new environmental factors into the generalized initial value are required to improve the DSAEF_LTP model.

Keywords: landfalling northward-moving typhoons, accumulated precipitation, forecasts, DSAEF_LTP model, improve

1 INTRODUCTION

Typhoons (or tropical cyclones) frequently produce severe catastrophic weather (Cai et al., 1994; Liang et al., 1995; Zhou et al., 2004). Typhoon rainstorms often bring about disasters (Cheng et al., 2005, 2007; Chen et al., 2010), and many records of extreme rainstorms are related to typhoon activity (Chen and Ding, 1979)—For example, Typhoon Nina caused daily precipitation of 1,062 mm in Zhumadian, Henan Province in 1975 and destroyed 102 km of the Beijing–Guangzhou railway. Traffic was interrupted for 18 days and at least 26,000 people died. Precipitation from Typhoon Morakot in 2009 reached 3,059.8 mm, causing a major disaster in southern Taiwan and resulting in about 700 people being reported as missing or dead. In 2013, Typhoon Fitow brought extreme precipitation to the north-central coastal areas of Zhejiang Province, causing cities such as Yuyao to be flooded for more than a week; the direct economic loss exceeded 60 billion yuan. Strengthening the forecasts of tropical cyclone rainstorms is therefore of great practical significance in improving our ability to prevent tropical cyclone rainstorm disasters.

Research on precipitation forecasts of landfalling tropical cyclones (LTCs) has attracted much attention (Chen et al., 2006; Woo et al., 2014; Rogers, 2018). Numerical models for the prediction of LTC precipitation are being improved (Ma and Tan, 2009; Zhu et al., 2016; Chen et al., 2016) and dynamical–statistical models (Ren et al., 2020) have been shown to improve forecasting by numerical models. Dynamical–statistical forecasting methods can be divided into three categories: 1) models that forecast tropical cyclone precipitation from the perspective of the climate-mean by combining the tropical cyclone track predicted by the numerical model with the historical observed precipitation (Marks et al., 2002; Lee et al., 2006; Lonfat et al., 2007); 2) models that predict tropical cyclone precipitation from the tropical cyclone track and the distribution of rainfall intensity at the initial time (Kidder et al., 2005; Liu, 2009; Ebert et al., 2011); and 3) models that construct a dynamical–statistical similarity scheme based on the forecast element field of the numerical model to predict tropical cyclone precipitation (Li and Zhao, 2009; Zhong et al., 2009).

Ren et al. (2020) proposed the Dynamical-Statistical-Analog Ensemble Forecast (DSAEF_LTP) model for predicting the precipitation of landfalling typhoons based on an exploration of new ideas of ensemble forecasts with a perfect model. The generalized initial value (GIV) is the most important concept in this model and is composed of physical factors that have a clear influence on typhoon precipitation. In the early stage of model development, the GIV introduces only two physical factors: the tropical cyclone track and the landfall season. Ding et al. (2020) added a tropical cyclone intensity factor in an experiment to forecast the accumulated precipitation in South China, resulting in improved forecast performance. Jia et al. (2020) used this model to conduct a simulation experiment

on Typhoon Lekima and improved the simulation ability of the model by including the tropical cyclone intensity and by improving the specification of the parameters for the similarity region (the area over which the forecast track is compared with historic tracks for the choice of analogs).

Research on the DSAEF_LTP model is aimed mainly at experiments with landfalling typhoons in southern China, and is restricted by small sample numbers. However, landfalling northward-moving typhoons have frequently occurred in China in recent years and it is unclear whether this model is suitable for forecasting precipitation from these systems. In this paper, we carry out an experiment with a large number of samples to investigate this issue.

Section 2 introduces the data and methods. **Section 3** describes the design of the experiment and the steps used to obtain the “best scheme”. **Section 4** compares the performance of the DSAEF_LTP model under the best scheme in predicting precipitation for landfalling northward-moving tropical cyclones and compares the results with those from four numerical models. **Section 5** summarizes and discusses our results.

2 DATA AND METHODOLOGY

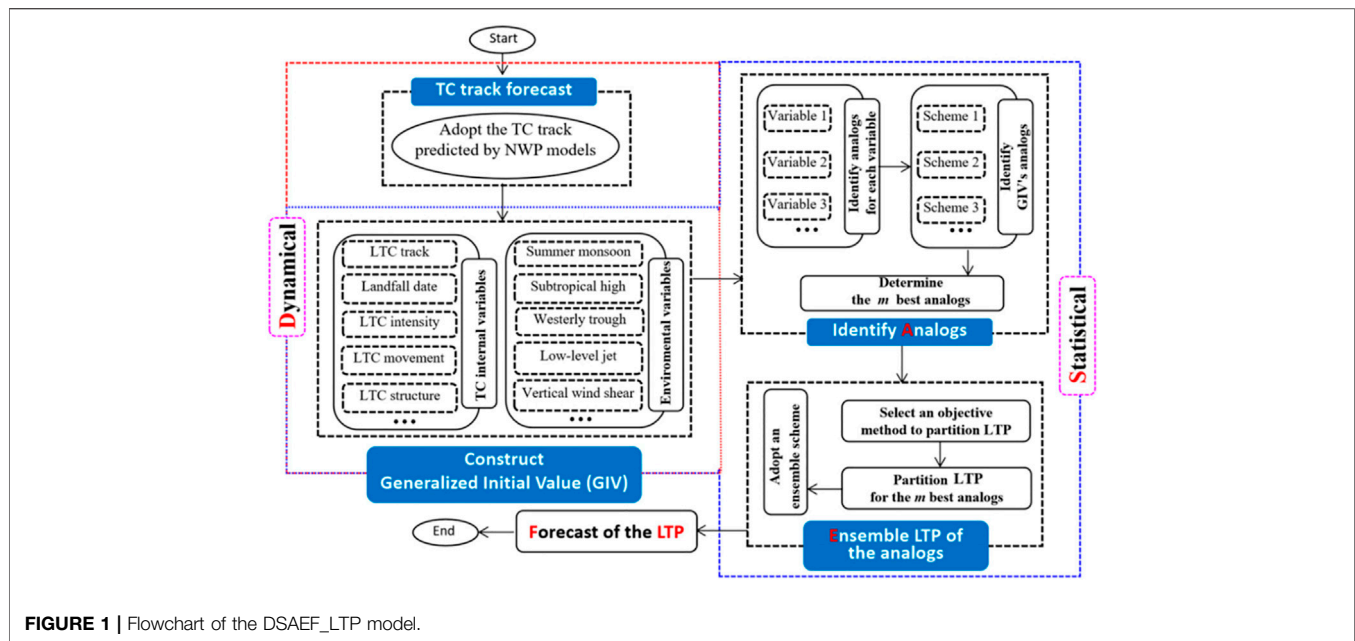
2.1 Data

We used daily precipitation data from 2027 rain gage stations in China from 1960 to 2019 provided by the National Meteorological Information Center (NMIC) of the China Meteorological Administration (CMA). The daily data period was from 12:00 UTC on the previous day to 12:00 UTC on the same day. The tropical cyclone track data were from the best-track dataset for 1960–2019 provided by the Shanghai Typhoon Research Institute. The dataset included the measured position and intensity of each tropical cyclone at intervals of 6 h (Ying et al., 2014). The analysis period was 2004–2019, chosen according to availability of forecast tracks of the target TCs based on the numerical weather prediction model in the NMIC of the CMA.

We used precipitation forecast data from four numerical models to test the precipitation prediction performance of the DSAEF_LTP model: the European Centre for Medium-Range Weather Forecasting (ECMWF), the China Meteorological Administration Global/Regional Assimilation and Prediction System (GRAPES), the Global Forecast System (GFS) of the U.S. National Center for Environmental Prediction and the Shanghai Meteorological Service WRF ADAS Real-Time Modeling System (SMS-WARMS). The horizontal resolution of the models were $(0.125^\circ \times 0.125^\circ)$, $(0.25^\circ \times 0.25^\circ)$, $(0.25^\circ \times 0.25^\circ)$ and $(0.09^\circ \times 0.09^\circ)$ respectively.

2.2 DSAEF_LTP Model

Ren et al. (2020) developed the DSAEF model and applied it to the prediction of precipitation caused by LTCs (**Figure 1**). The forecast procedure of the DSAEF_LTP model is divided into four steps: 1) obtain the tropical cyclone track predicted by numerical weather prediction models; 2) construct the GIV, including the internal variables of the tropical cyclone and environmental variables; 3)



identify analogs for the GIV—in this study, this included identifying the similarity of the track using the tropical cyclone track similarity area index (TSAI) (Ren et al., 2018) and also identifying the similarity of the landfalling dates and intensity; and 4) construct the “ensemble LTP of the analogs” to forecast the accumulated rainfall field of the target tropical cyclone.

2.3 Other Algorithms

1) Objective synoptic analysis technique

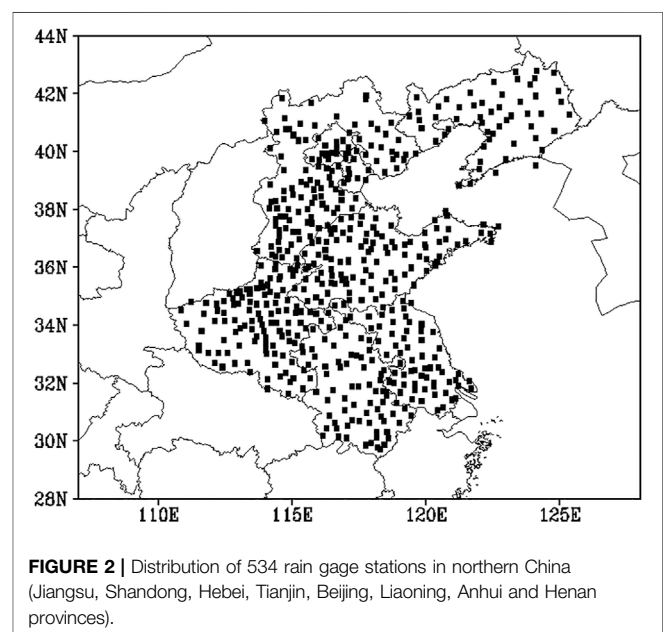
The objective synoptic analysis technique was used to separate and obtain the precipitation caused by the tropical cyclone (Ren et al., 2001; Ren et al., 2007; Wang et al., 2006). It was divided into four steps: 1) division of the precipitation field into independent natural rainbands; 2) identification of potential tropical cyclone rainbands; 3) discrimination of the precipitation of each station; and 4) combination of the complete tropical cyclone rainband.

2) Objective tropical cyclone track similarity area index

The objective tropical cyclone TSAI refers to the geometric area enclosed by any two typhoon tracks. This was used to determine the similarity of two tropical cyclone tracks (Ren et al., 2018). The smaller the TSAI index value, the higher the degree of similarity between the two tropical cyclone tracks.

3) Threat score

We used the threat score, a commonly used test index for the evaluation of weather forecast accuracy, to evaluate the prediction performance of the DSAEF_LTP model. The calculation formula is:



$$\text{Threat score} = \frac{\text{hits}}{\text{hits} + \text{misses} + \text{false alarms}}$$

where “hits” is the number of stations at which the prediction is the same as the reality, “misses” is the number of stations where precipitation is not predicted but does occur, and “false alarms” is the number of stations at which precipitation is predicted but does not occur. The value range of threat score is 0–1. The larger the value, the higher the accuracy.

4) Threat score of rain gage stations

TABLE 1 | Names of tropical cyclones used for training and as independent samples.

Sample classification	Date and name of typhoon
Training samples	2004 Mindulle, Rananim 2005 Matsa, Khanun 2006 Ewiniar 2007 Wipha, Krosa 2008 Kalmaegi, Fung-Wong 2009 Morakot 2010 Kompasu 2011 Meari, Muifa 2012 Damrey, Haikui, Bolaven 2013 Fitow, Danas 2014 Matmo 2015 Chan-hom, Soudelor, Goni 2016 Meranti, Megi 2017 Haitang 2018 Prapiroom, Maria, Ampil, Jongdari, Yagi, Rumbia 2019 Lekima, Lingling
Independent samples	

TABLE 2 | Parameter table for the DSAEF_LTP model.

Parameter (1–8)	Description	Number of parameter values
Initial time (P1)	12.00 UTC or 00.00 UTC on the day tropical cyclone precipitation first occurs on the land surface or 12:00 UTC on the previous day	3
Similarity region (P2)	A parameter of TSAI. The position of the tropical cyclone at the start time and the maximum prediction time are selected as the two diagonal points of the similarity region (rectangular box). The vertex corresponding to the start time can be changed to the tropical cyclone observation position 12, 24, 36 or 48 h in advance, and the other vertex can be changed to the tropical cyclone forecast position with a time reduction of 6 or 12 h (1–15). The vertex corresponding to the start time is taken as the southeast vertex with a side length of 2000 km square, which is taken as the 16th similarity region scheme. We take the midpoint of the southwest corner of this similarity region and the first type of similarity region as point A, and the midpoint of the northeast corner as point B, where A and B are the two diagonal points of the 17th similarity region. We move the 16th similarity region as a whole until its southeast corner reaches point A as the 18th similarity region. The 16th similarity region is fixed as a whole until its northwest corner reaches point B as the 19th similarity region. We make a straight line through A and B in the north–south and east–west directions, respectively; the intersection point is C and we take C as the northwest vertex and make a square with a side length of 2000 km, which is the 20th similarity region (16–20)	15 + 5
Threshold of the segmentation ratio of a latitude extreme point (P3)	A parameter of TSAI: 0.1, 0.2 and 0.3	3
Overlapping percentage threshold of two tropical cyclone tracks (P4)	A parameter of TSAI: 0.4, 0.5, 0.6, 0.7, 0.8 and 0.9	6
Seasonal similarity (P5)	The whole year, May–November, July–September, the same landfall month as the target tropical cyclone and within 15 days of the target tropical cyclone landfall time	5
Intensity similarity (P6)	Four types of intensity indexes: (land) the average and maximum intensity of the first day of the tropical cyclone precipitation process and the average and maximum intensity of the process (wind speed) Five kinds of strength similarity values: all levels; the same level and above; the same level and below; only the same level; and the maximum difference of one level	4 × 5
Number of tropical cyclones with the top closest similarity (P7)	1, 2, 3, 4, 5, 6, 7, 8, 9 and 10	10
Ensemble forecast scheme (P8)	Mean and maximum	2
Total number of schemes	3 × 20 × 3 × 6 × 5 × 4 × 5 × 10 × 2	2,160,000

The precipitation sequence at each rain gage station as forecast by the DSAEF_LTP model was evaluated against the observed tropical cyclone precipitation to obtain the threat score for each

station (STS or Station Threat Score). The distribution of the STS reflects the variations in forecasting performance of the DSAEF_LTP model across different regions.

3 EXPERIMENTAL DESIGN OF THE DSEAF_LTP MODEL

3.1 Experimental Samples

We carried out a precipitation prediction experiment with the DSEAF_LTP model using data for northward-moving typhoons that caused maximum daily precipitation ≥ 100 mm at stations in northern China (Jiangsu, Shandong, Hebei, Tianjin, Beijing, Liaoning, Anhui and Henan provinces north of the Yangtze River) (Figure 2). Table 1 lists the 33 northward-moving typhoon samples selected from 2004 to 2019, from which we used 22 tropical cyclones from 2004 to 2015 as training samples and 11 tropical cyclones from 2016 to 2019 as independent samples.

3.2 Experimental Design

Table 2 lists the eight characteristic parameters used in the DSEAF_LTP model and their corresponding physical meanings. The parameters specifying the similarity regions had 15 values in the early stage of model development; we added a further five similarity regions, which were the 16th–20th values of the similarity region in Table 2, based on the results of Jia et al. (2020). The number of values of each parameter is listed in the last column of the table, and the total number of combinations used for the ensemble forecast is given at the bottom of the table. Each combination constituted a forecasting scheme. From comparison of the threat score for each scheme, we determined the “best scheme” for forecasting the accumulated precipitation of LTCs.

We designed two groups of experiments. The first group introduced three factors (the tropical cyclone track, the landfall season and the intensity) (Ding et al., 2020) and the first 15 types of similarity region were selected and recorded as DSEAF_LTP-1. There were 1,620,000 schemes in this group of experiments under ideal conditions. The new similarity regions were added in the second group of experiments—that is, the similarity regions had a total of 20 values, recorded as DSEAF_LTP-2, and there were 2,160,000 prediction schemes in the ideal state. Because the values corresponding to the similarity regions and the number of similar tropical cyclones were not always available, the ensemble size for actual prediction scheme was often smaller than for the ideal scheme.

We focused on the threshold of accumulated precipitation at 100 and 250 mm. The threat score of accumulated precipitation ≥ 100 mm was defined as TS100 and the threat score of accumulated precipitation ≥ 250 mm was TS250. The sum of the two was TSsum (TSsum = TS250 + TS100) and the best scheme was the scheme with the largest TSsum. The 22 training samples were used in simulation experiments to screen out the best schemes and then these best schemes were used to carry out the forecast experiments on the 11 independent samples. The results of the forecast were compared with those of the four numerical models (ECMWF, GFS, GRAPES and SMS-WARMS).

4 RESULTS

4.1 Simulation Experiment of Training Samples

The DSEAF_LTP model was used to forecast accumulated precipitation ≥ 100 and ≥ 250 mm for the 22 training sample tropical cyclones for the two configurations DSEAF_LTP-1 and DSEAF_LTP-2. Figure 3 shows the distribution of the threat score for the two groups of experiments, where the abscissa (TS250) is the threat score of accumulated precipitation ≥ 250 mm and the ordinate (TS100) is the threat score of accumulated precipitation ≥ 100 mm. Each point represents a forecast scheme and the red point is the maximum TSsum, which is defined as the best scheme.

Table 3 gives the parameter values of the best schemes for the two groups of experiments. According to Figure 3, TSsum (TS250 + TS100) of the best scheme of DSEAF_LTP-1 was 0.1239 (0 + 0.1239) and TSsum (TS250 + TS100) of the best scheme of DSEAF_LTP-2 was 0.1883 (0.0526 + 0.1357). The overall simulation ability was improved after adding new similarity regions for both accumulated precipitation ≥ 250 and ≥ 100 mm.

4.2 Independent Sample Forecast Experiment

4.2.1 Comparison Between Methods

To test the forecasting performance of the DSEAF_LTP model, accumulated landfall precipitation was predicted with the best schemes of the two groups of simulation experiments for 11 independent tropical cyclone samples from 2016 to 2019. The prediction results were compared with those of the four numerical models (ECMWF, GFS, GRAPES and SMS-WARMS). Figure 4 shows that the forecasting performance of the DSEAF_LTP model was acceptable for accumulated precipitation ≥ 100 mm, ranking in the middle position compared with the four dynamic models. The TSsum of DSEAF_LTP-1 was 0.1355, which was better than scores for the GRAPES (0.1131) and SMS-WARMS (0.0943) models.

Figure 5 shows the threat score for each independent sample forecast by the DSEAF_LTP model and the four numerical models. Figure 5A shows that the DSEAF_LTP model has no forecasting performance for northward-moving typhoons for the accumulated precipitation threshold ≥ 250 mm: the TS250 being 0 for both model DSEAF_LTP configurations. Among the 11 independent samples only four tropical cyclones (TC1619, TC 1817, TC1821 and TC 1912) had an accumulated precipitation ≥ 250 mm. The northward-moving typhoons brought less accumulated precipitation ≥ 250 mm to the north of the Yangtze River, with only one and two stations with accumulated precipitation ≥ 250 mm (TC1619 and TC 1817, respectively). It was therefore difficult to accurately forecast precipitation ≥ 250 mm.

Figure 5B shows the threat scores for precipitation ≥ 100 mm. For TC1808 and TC1809, there were only three and two stations,

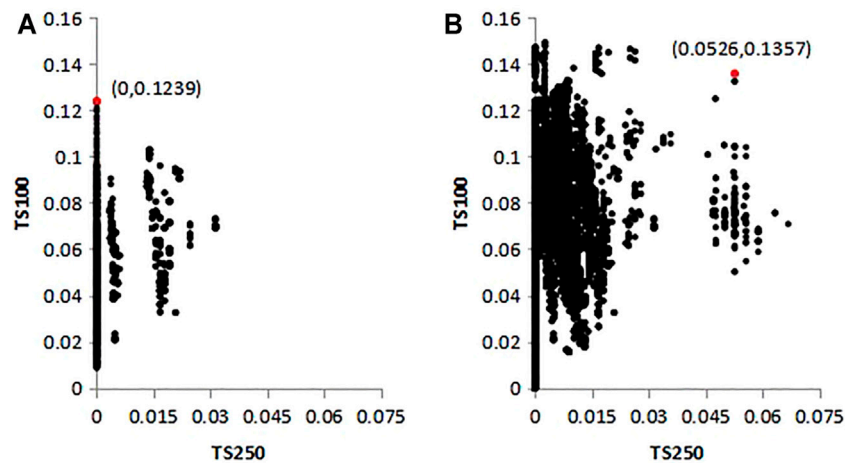


FIGURE 3 | Scatter plots of the threat scores for (A) DSAEF_LTP-1 and (B) DSAEF_LTP-2.

TABLE 3 | Parameter values of the best schemes.

	DSAEF_LTP-1	DSAEF_LTP-2
Initial time	1	1
Similarity region	2	20
Threshold of the segmentation ratio of a latitude extreme point	1	3
Overlapping percentage threshold of two tropical cyclone tracks	4	6
Seasonal similarity	1/2	1/2
Intensity similarity	(4, 5)	(2, 5)
Number of tropical cyclones with the top closest similarity	3	7
Ensemble forecast scheme	2	2

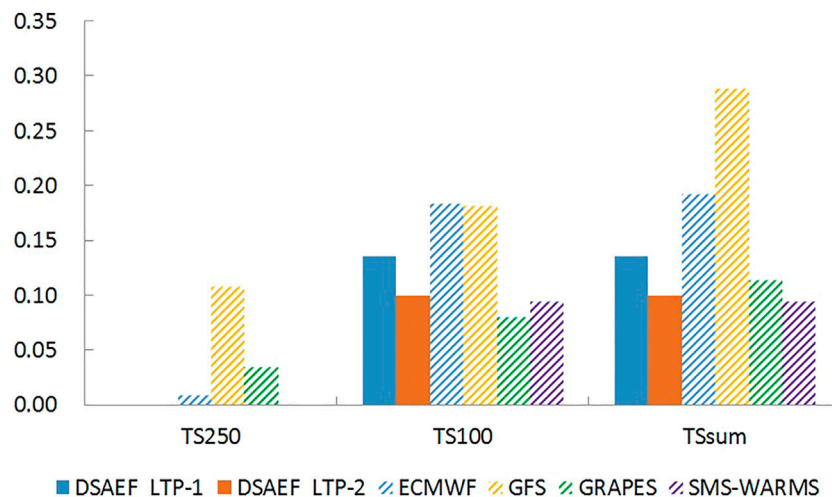


FIGURE 4 | Comparison of the average threat score of different models for independent sample precipitation forecasts.

respectively, with accumulated precipitation ≥ 100 mm and none of the models successfully predicted this precipitation threshold. The DSAEF_LTP model was better than the four numerical models in predicting landfalling typhoon precipitation for

TC1616, TC1711, TC1814 and TC 1817. Only the DSAEF_LTP model predicted ≥ 100 mm precipitation for TC 1814. For the predictions of TC1619, TC 1811, TC1821 and TC 1912, the models with the highest threat score were GRAPES,

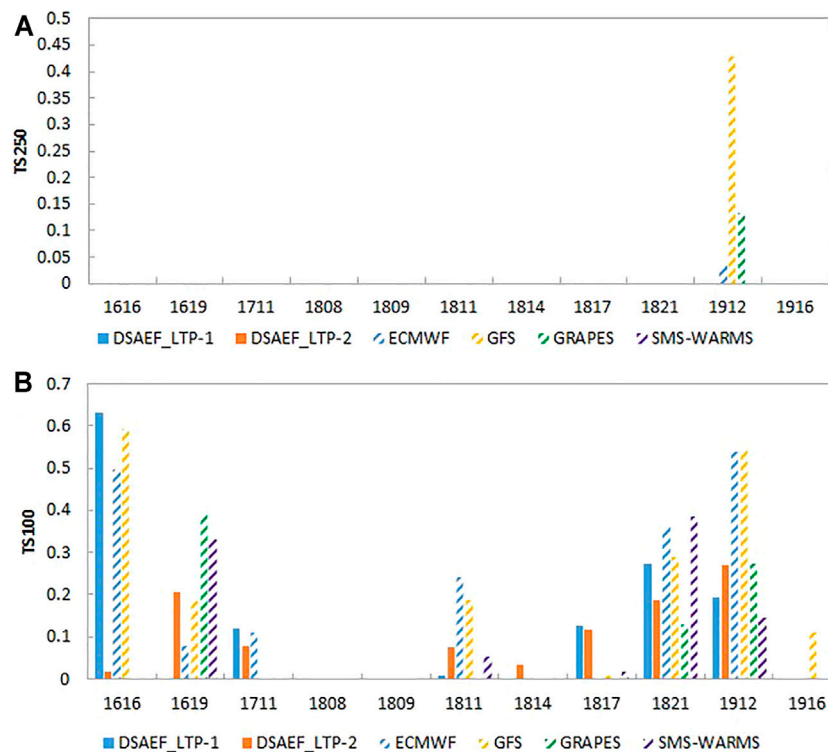


FIGURE 5 | Comparison of the threat score of different models for the precipitation forecasts of individual tropical cyclones **(A)** ≥ 250 and **(B)** ≥ 100 mm.

ECMWF, SMS-WARMS and GFS, respectively; the threshold for TC1916 was predicted by the GFS model only. The number of TCs for which the DSAEF_LTP model threat score ranked highest exceeded that of the four dynamic models. For the two sets of experiments, DSAEF_LTP-1 was better than DSAEF_LTP-2 in predicting TC1616, TC1711, TC1817 and TC 1821. The forecast performance was improved in the predictions of TC1619, TC 1811, TC1814 and TC1912 after adding the new similarity regions.

4.2.2 Analysis of Typical Examples

To better compare the prediction performance of the DSAEF_LTP model with the four numerical models, we selected two typhoons for in-depth analysis: TC1616 with the largest difference in threat score between DSAEF_LTP-1 and DSAEF_LTP-2; and TC 1912 for which the forecast performance of the numerical model was better than the DSAEF_LTP model. The maximum accumulated precipitation of TC1616 was in the range 100–250 mm and the threat score of DSAEF_LTP-1 ($TS_{sum} = 0.6308$) was better than that of the four numerical models and of DSAEF_LTP-2 ($TS_{sum} = 0.0189$). The threat score of the DSAEF_LTP-2 model for TC1912 was higher than that of the DSAEF_LTP-1 model, but the prediction performance was poor compared with the ECMWF, GFS and GRAPES models. **Figure 6** (TC1616) and **Figure 7** (TC 1912) show the field distribution of precipitation for these two tropical cyclones for observations and as predicted by the two DSAEF_LTP configurations and the four numerical models.

Compared with the observations (**Figure 6A**), the DSAEF_LTP-1, ECMWF and GFS models (**Figures 6B,D,E**) all capture precipitation ≥ 100 mm well for TC1616. The DSAEF_LTP-1 model performs best in all models, and the distribution of the precipitation fields was more similar to the observations than other models. The DSAEF_LTP-2 model (**Figure 6C**) does not show the heavy precipitation center, and the GRAPES (**Figure 6F**) and SMS-WARMS (**Figure 6G**) models have no forecasting performance for the higher precipitation thresholds.

Figure 6A shows that the northernmost end of the forecast track corresponding to the best scheme of the DSAEF_LTP model reaches only the northern part of Jiangxi and does not enter the northern region. Due to the increased number of similarity regions for the DSAEF_LTP-2 model, the selected historically similar tropical cyclones of DSAEF_LTP-2 also increase. The tropical cyclones with high similarity are mainly concentrated in the southeastern coastal area and do not penetrate into the northern region. These tropical cyclones are therefore not sufficiently representative to forecast the precipitation of northward-moving typhoons, leading to a poor precipitation forecast performance. This is the reason the average threat score of the DSAEF_LTP-2 model was lower than that of the DSAEF_LTP-1 model in the forecast experiment. Extending the track of typhoons to select more representative historically similar tropical cyclones will help to improve the forecasting performance of the DSAEF_LTP model if we use vortex identification technology for the residual vortices.

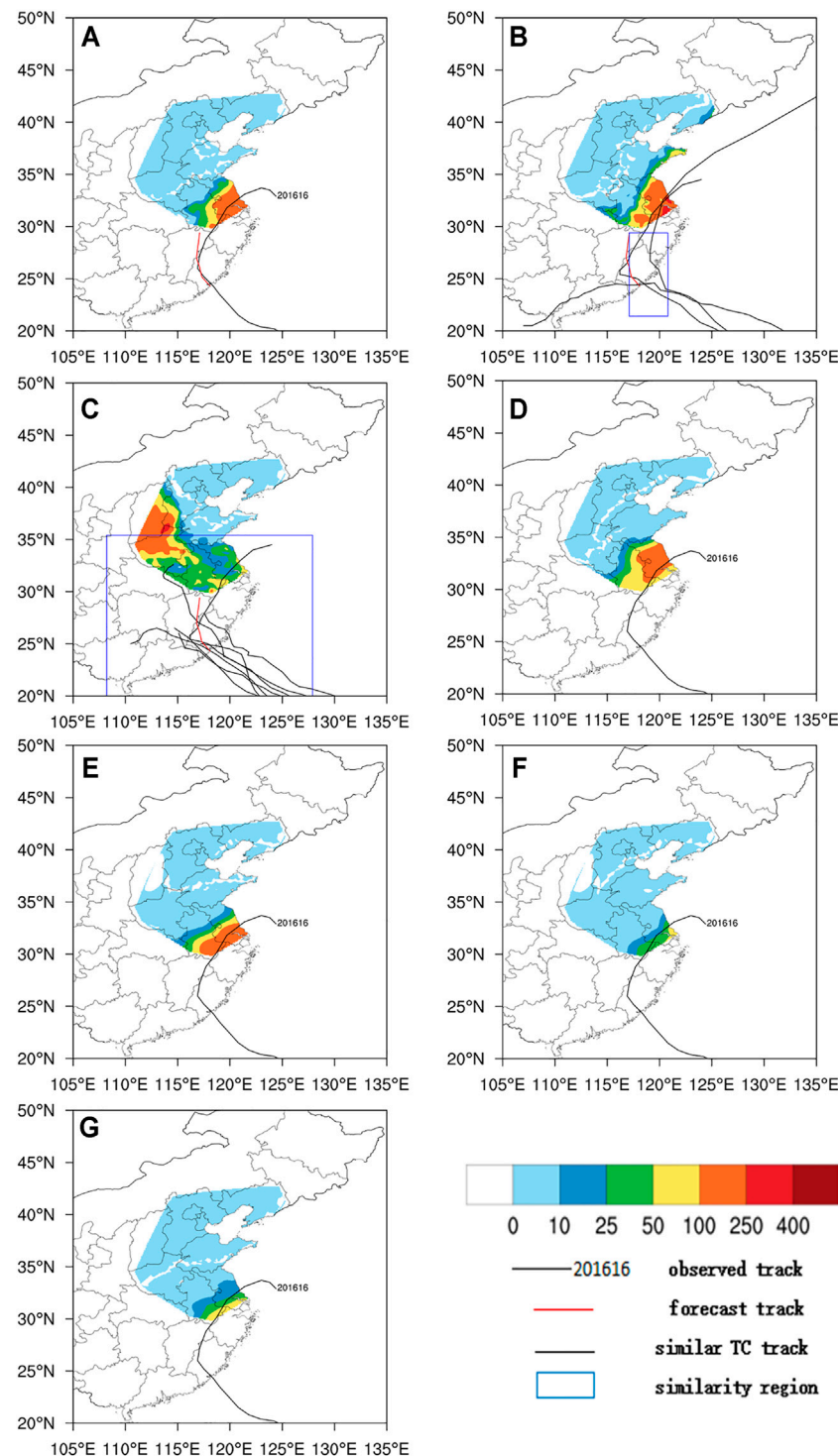


FIGURE 6 | Distribution of the accumulated precipitation field for TC1616 (Typhoon Meranti). (A) Observed track and the (B) DSAEF_LTP-1, (C) DSAEF_LTP-2, (D) ECMWF, (E) GFS, (F) GRAPES and (G) SMS-WARMS models.

For TC 1912, the DSAEF_LTP and SMS-WARMS model (Figures 7B,C,G) did not capture the precipitation field ≥ 250 mm. The patterns of the DSAEF_LTP model were relatively consistent with the observations in the precipitation

field ≥ 100 mm (Figure 7A), but there were many forecast misses and the forecast range for heavy rainfall was relatively small. However, the occurrence of forecast misses of the DSAEF_LTP-2 model was improved compared with the DSAEF_LTP-1 model.

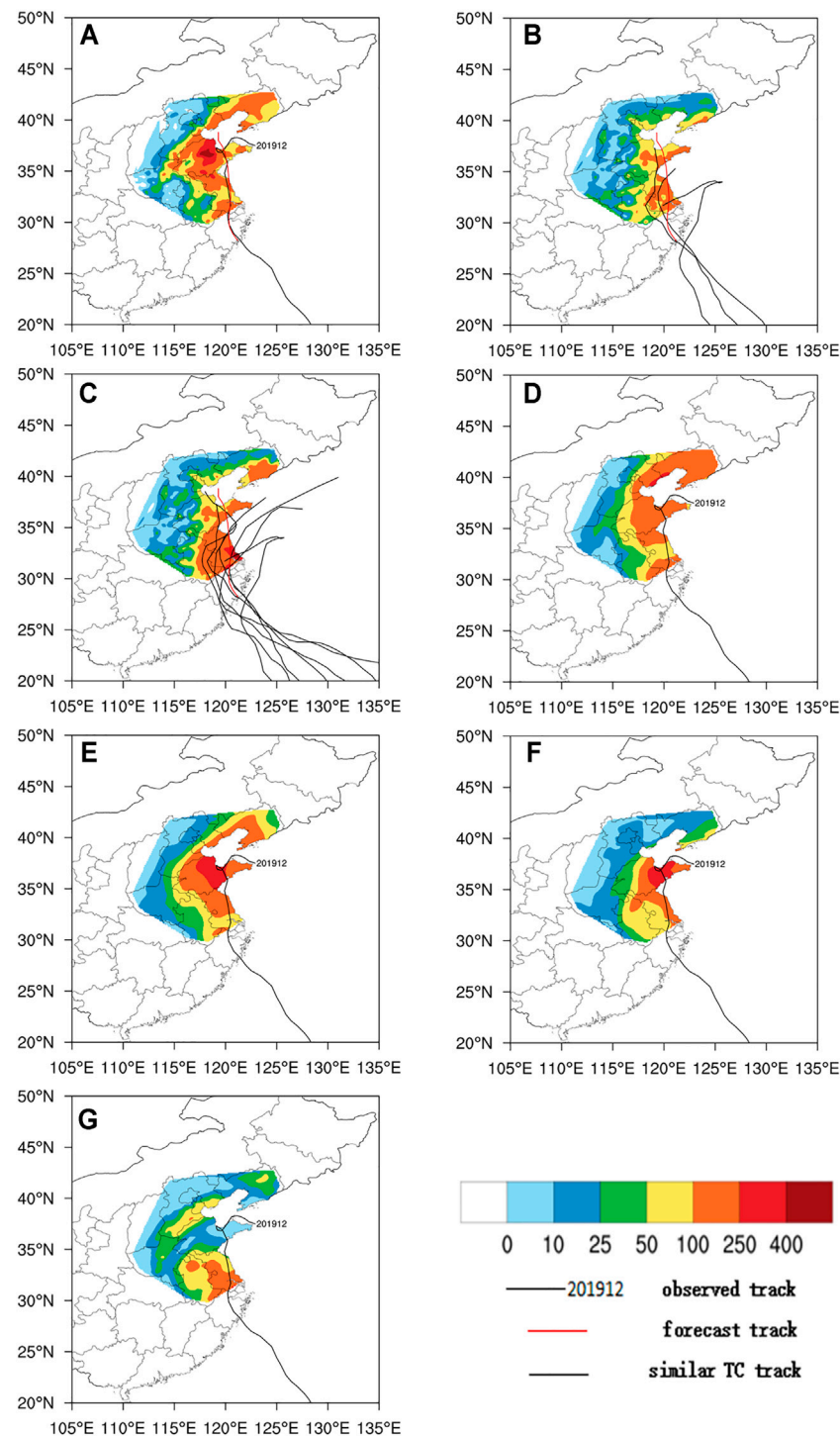


FIGURE 7 | Distribution of the accumulated precipitation field of TC 1912 (Typhoon Lekima). **(A)** Observed track and the **(B)** DSAEF_LTP-1, **(C)** DSAEF_LTP-2, **(D)** ECMWF, **(E)** GFS, **(F)** GRAPES and **(G)** SMS-WARMS models.

Overall, the GFS model (**Figure 7E**) performed best and the SMS-WARMS model (**Figure 7G**) had the poorest performance.

Figure 8 shows the track and precipitation field distribution of the historical similar tropical cyclones corresponding to the best

scheme for TC 1912. **Figures 8A–C** show the best similar tropical cyclones corresponding to the DSAEF_LTP-1 model and **Figures 8A–G** show the seven best similar tropical cyclones corresponding to the DSAEF_LTP-2 model. TC1912 Lekima was a rare

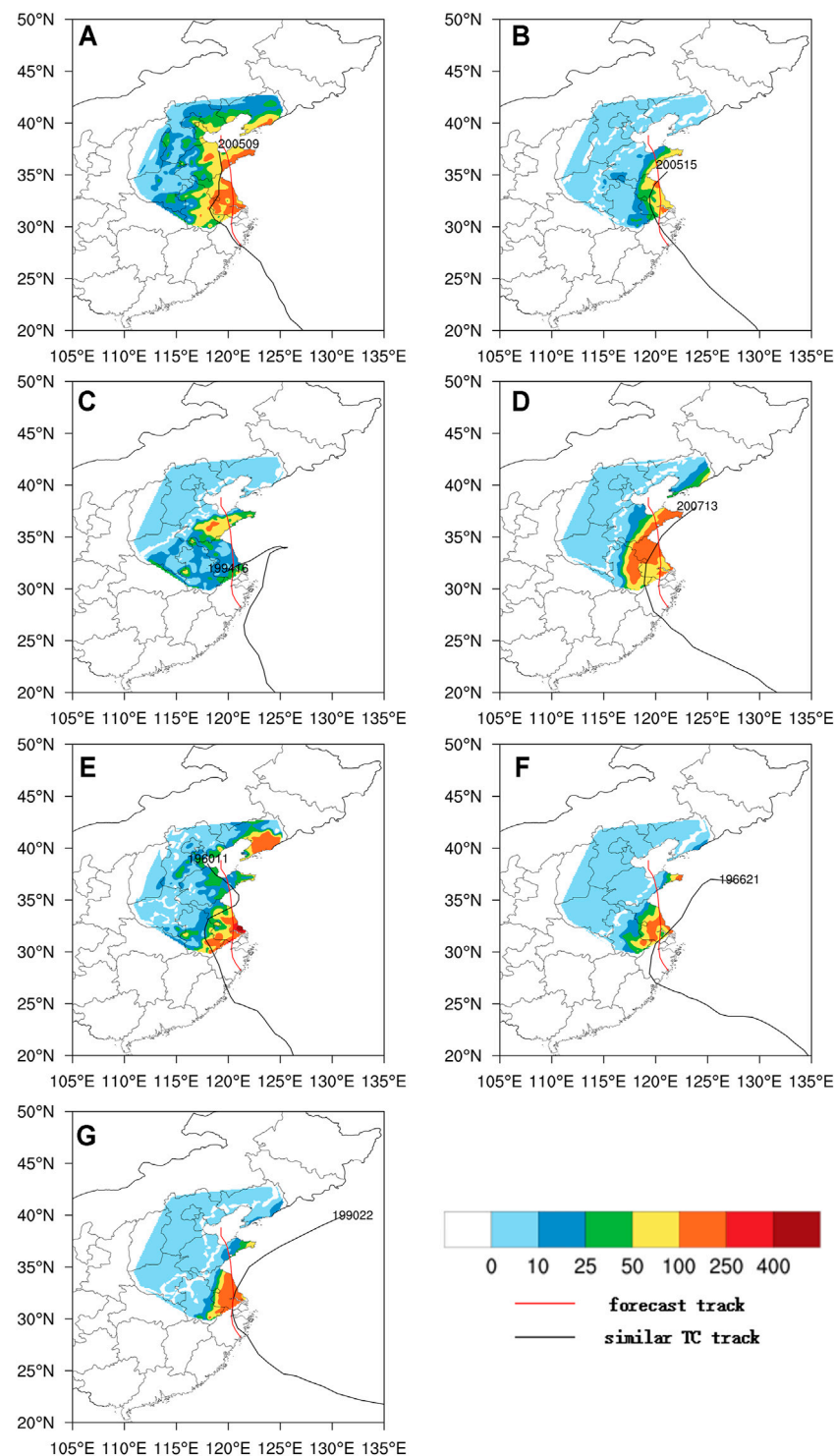


FIGURE 8 | Track and precipitation field distribution of the best tropical cyclones similar to TC 1912 (Typhoon Lekima).

northward-moving strong tropical cyclone. After entering Laizhou Bay, Shandong, it rotated and moved less. It was affected by the continuous transport of water vapor by the tropical cyclone circulation and cold air flowing southward under the guidance

of an inverted trough, which brought a large amount of heavy precipitation to the northern region. However, **Figure 8** shows that the aerial range of heavy precipitation brought to the northern region by the best similar tropical cyclones was generally not large.

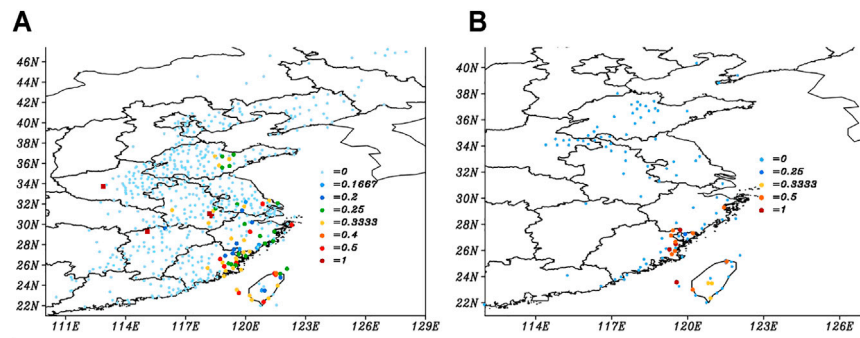


FIGURE 9 | STS distribution of the forecast for independent samples with DSAEF_LTP-1 (A) ≥ 100 and (B) ≥ 250 mm.

Few historical strong tropical cyclones with ≥ 250 mm precipitation moved northward to Shandong and none of the optimum similar tropical cyclones produced heavy precipitation ≥ 250 mm in Shandong. This is the reason the DSAEF_LTP model does not report a heavy precipitation center with accumulated precipitation ≥ 250 mm in Shandong and the accumulated precipitation forecast for the northern region was generally poor.

4.2.3 Forecast Score of STS

Figure 9 shows that the largest value of the STS was mainly in the southern coastal area in the forecast of accumulated precipitation in the DSAEF_LTP model for both ≥ 100 or ≥ 250 mm precipitation, whereas the STS in the northern area was generally not high. This indicates that the forecast performance of the DSAEF_LTP model was better for typhoon precipitation in the southern region. We need to further analyze the possible causes of extreme precipitation caused by northward-moving typhoons and improve the DSAEF_LTP model to make it suitable for the forecast of precipitation caused by these typhoons.

This analysis shows that the DSAEF_LTP model can generally predict the morphological distribution of the precipitation field. The DSAEF_LTP-2 model, which has an increased number of similarity regions compared with the DSAEF_LTP-1 model, improved the issue of forecast misses. The poor landfall rainfall prediction for some tropical cyclones by the DSAEF_LTP model may be because the prediction track of the target tropical cyclone and the official track of the best historical similar tropical cyclones do not penetrate the northern region. Also the historical tropical cyclone may have different background conditions (such as the westerly trough, vertical wind shear or water vapor transport) from the target tropical cyclone, leading to a lack of representativeness of the best similar tropical cyclones. We could extend the tropical cyclone track and introduce these background conditions into the DSAEF_LTP model as similarity variables to further improve the prediction performance of the model.

5 SUMMARY AND DISCUSSION

We carried out two groups of simulation experiments with (DSAEF_LTP-2) and without (DSAEF_LTP-1) new similarity

regions based on the DSAEF_LTP model with GIV including tropical cyclone track, landfall season and tropical cyclone intensity. We selected the northern region of the Yangtze River (including Jiangsu, Shandong, Hebei, Tianjin, Beijing, Liaoning, Anhui and Henan provinces) for the experiments. We selected 22 typhoons from 2004–2015 as training samples to identify the best schemes for the two groups of experiments. The best schemes were then used to predict the precipitation of 11 typhoons from 2016–2019. The forecast results were compared with those of four numerical models (ECMWF, GFS, GRAPES and SMS-WARMS). Our main results can be summarized as follows.

- 1) The simulation ability of the DSAEF_LTP model for northward-moving typhoons improves after adding new similarity regions; the simulation of TS250 and TS100 increased from 0 to 0.1239 to 0.0526 and 0.1357, respectively.
- 2) In the forecast experiment, the threat scores of the DSAEF_LTP-1 and DSAEF_LTP-2 models for accumulated precipitation ≥ 250 mm were both 0 and for accumulated precipitation ≥ 100 mm were 0.1355 and 0.099, respectively. The forecasting performance of the DSAEF_LTP model for TS100 was better than that of the GRAPES and SMS-WARMS models.
- 3) The analysis of typical typhoons (TC1616 and TC 1912) and comparison with the four numerical models showed the DSAEF_LTP model can predict the distribution of precipitation fields similar to the observations. However, because the forecast track and the tracks of similar historical tropical cyclones do not penetrate north and there were few historical northward-moving strong typhoons, the selected best historical tropical cyclones were not sufficiently representative and it was difficult to capture the heavy precipitation center. This restricted the prediction performance of the DSAEF_LTP model.

For the DSAEF_LTP model, it was the first time it has been applied to a large-sample experiment of northward-moving typhoons. It has shown that the prediction performance of the DSAEF_LTP model was comparable to that of the dynamic models. For the number of TCs with the highest threat score

generated by the models, the DSEAF_LTP model exceeded that of dynamical models. The prediction performance of the DSEAF_LTP model has been affirmed and is expected to be further improved.

Jia et al. (2020) used the DSEAF_LTP model to conduct a simulation experiment for TC1912 Lekima and showed that the simulation ability of the DSEAF_LTP model ranked second in the prediction models, whereas the threat score for Lekima ranked fourth in our study. However, the best scheme in our study was selected through a large sample simulation experiment and is different from that of Jia et al. (2020). In addition, Jia et al. (2020) considered the whole of China, whereas we considered only northern China. This explains why the prediction performance for TC1912 Lekima was different in the two studies.

The best scheme in the simulation experiment performed well in the DSEAF_LTP model and, with the improvement in the similarity regions, the simulation ability of the model also increased significantly. However, it did not show any advantages over the dynamic model of the simulation stage in the independent sample forecast experiment. After adding similarity regions, its prediction performance was lower than before the improvement. This may be because the prediction performance of the DSEAF_LTP model depends on the independent samples and the scheme selected.

Considering that the forecast performance of DSEAF_LTP model was good over the southern coast, but limited over northern China, further research is required to improve the model's forecast performance in the north. It is important to develop vortex identification technology for residual vortices to extend the tropical cyclone track data because a residual vortex from not recorded in the tropical cyclone dataset can generally produce

heavy rainfall in the north. The GIV of the DSEAF_LTP model currently includes only three factors, and no environmental factors. Considering that environmental factors (e.g., mid-latitude systems and subtropical highs) are important for the precipitation of northward-moving typhoons in the north, we need to introduce environmental factors into the GIV. These modifications should produce a better prediction performance of the DSEAF_LTP model.

DATA AVAILABILITY STATEMENT

The original contributions presented in the study are included in the article/Supplementary Material, further inquiries can be directed to the corresponding author.

AUTHOR CONTRIBUTIONS

FR designed research. MY conceptualized the analysis and wrote the manuscript. All authors were involved in helpful discussions and contributions to the manuscript.

FUNDING

This work was supported by the National Key R&D Program of China (Grant No. 2019YFC1510205), the Hainan Provincial Key R&D Program of China (Grant No. SQ2019KJHZ0028), the National Natural Science Foundation of China (Grant No. 41675042) and the Climate Change Cooperation and Innovation Center of Jiangsu Province.

REFERENCES

- Cai, Z. Y., Xu, L. Y., and Xu, Y. T. (1994). A Study on the Tropical Cyclone Disasters in China. *Atmos. Sci.* 18, 826–836. (in Chinese).
- Chen, B., Guo, Y., Dai, K., and Qian, Q. (2016). Research for the Ensemble Member Optimization Correction Technique on Typhoon Rainstorm Forecast and its Application Experiment. *Meteorol. Mon* 42 (12), 1465–1475. (in Chinese).
- Chen, L. S., and Ding, Y. H. (1979). *Introduction to Typhoons in the Western North Pacific*. Beijing: Science Press. (in Chinese).
- Chen, L. S., Li, Y., and Cheng, Z. (2010). An Overview of Research and Forecasting on Rainfall Associated with Landfalling Tropical Cyclones. *Adv. Atmos. Sci.* [J], 27. doi:10.1007/s00376-010-8171-y
- Chen, S. S., Knaff, J. A., and Marks, F. D. (2006). Effects of Vertical Wind Shear and Storm Motion on Tropical Cyclone Rainfall Asymmetries Deduced from TRMM. *Monthly Weather Rev.* [J] 134, 3190–3208. doi:10.1175/mwr3245.1
- Cheng, Z. Q., Chen, L. S., Liu, Y., and Peng, T. Y. (2007). The Spatial and Temporal Characteristics of Tropical Cyclone-Induced Rainfall in China during 1960–2003. *J. Appl. Meteorol. Sci.* 18 (4), 427–434. (in Chinese).
- Cheng, Z. Q., Chen, L. S., Xu, X. D., and Peng, T. Y. (2005). Research Progress on Typhoon Heavy Rainfall in China for Last Ten Years. *Meteorol. Monthly* 31 (12), 3–9. doi:10.3969/j.issn.1000-0526.2005.12.001
- Ding, C. C., Ren, F. M., Liu, Y., McBride, J. L., and Feng, T. (2020). Improvement in the Forecasting of Heavy Rainfall over South China in the DSEAF_LTP Model by Introducing the Intensity of the Tropical Cyclone[J]. *Weather Forecast.* 35 (5), 1967–1980.
- Ebert, E. E., Turk, M., Kusselson, S. J., Yang, J., Seybold, M., Keehn, P. R., et al. (2011). Ensemble Tropical Rainfall Potential (eTRaP) Forecasts. *Weather Forecast.* 26, 213–224. doi:10.1175/2010waf222443.1
- Jia, L., Jia, Z., Ren, F., Ding, C., Wang, M., and Feng, T. (2020). *Introducing TC Intensity into the DSEAF_LTP Model and Simulating Precipitation of Super-typhoon Lekima(2019) [J]. Quarterly Journal of the Royal Meteorological Society*, 1–15. doi:10.1002/qj.3882
- Kidder, S. Q., Knaff, J. A., Kusselson, S. J., Turk, M., Ferraro, R. R., and Kuligowski, R. J. (2005). The Tropical Rainfall Potential (TRaP) Technique. Part I: Description and Examples. *Wea Forecast.* 20 (4), 456–464. doi:10.1175/waf860.1
- Lee, C. S., Huang, L. R., Shen, H. S., and Wang, S. T. (2006). A Climatology Model for Forecasting Typhoon Rainfall in Taiwan. *Nat. Hazards* 37 (1), 87–105. doi:10.1007/s11069-005-4658-8
- Li, B., and Zhao, S. X. (2009). Development of Forecasting Model of Typhoon Type Rainstorm by Using SMAT. *Meteorol. Monthly* 35 (6), 3–12. (in Chinese).
- Liang, B. Q., Liang, J. P., and Wen, Z. P. (1995). Study of Typhoon Disasters and its Affects in china. *J. Nat. Disasters* 4 (1), 84–91. (in Chinese).
- Liu, C.-C. (2009). The Influence of Terrain on the Tropical Rainfall Potential Technique in Taiwan. *Weather Forecast.* 24, 785–799. doi:10.1175/2008waf2222135.1
- Lonfat, M., Rogers, R., Marchok, T., and Marks, F. D. (2007). A Parametric Model for Predicting hurricane Rainfall. *Monthly Weather Rev.* 135, 3086–3097. doi:10.1175/mwr3433.1
- Ma, L.-M., and Tan, Z.-M. (2009). Improving the Behavior of the Cumulus Parameterization for Tropical Cyclone Prediction: Convection Trigger. *Atmos. Res.* 92 (2), 190–211. doi:10.1016/j.atmosres.2008.09.022
- Marks, F. D., Kappler, G., and DeMaria, M. (2002). *Development of a Tropical Cyclone Rainfall Climatology and Persistence (RCLIPER) Model*. San Diego: Preprints, 25th Conference on Hurricanes and Tropical Meteorology, 327–328.
- Ren, F. M., Gleason, B., and Easterling, D. R. (2001). A Technique for Partitioning Tropical Cyclone Precipitation. *J. Trop. Meteorology* 17 (3), 308–313. (in Chinese).
- Ren, F., Ding, C., Zhang, D.-L., Chen, D., Ren, H.-I., and Qiu, W. (2020). A Dynamical-Statistical-Analog Ensemble Forecast Model: Theory and an

- Application to Heavy Rainfall Forecasts of Landfalling Tropical Cyclones. *Monthly Weather Rev.* 148 (4), 1503–1517. doi:10.1175/mwr-d-19-0174.1
- Ren, F., Qiu, W., Ding, C., Jiang, X., Wu, L., Xu, Y., et al. (2018). An Objective Track Similarity Index and its Preliminary Application to Predicting Precipitation of Landfalling Tropical Cyclones. *Weather Forecast.* 33, 1725–1742. doi:10.1175/waf-d-18-0007.1
- Ren, F., Wang, Y., Wang, X., and Li, W. (2007). Estimating Tropical Cyclone Precipitation from Station Observations. *Adv. Atmos. Sci.* 24 (4), 700–711. doi:10.1007/s00376-007-0700-y
- Rogers, R. (2018). *Summary of Fourth International Workshop on Tropical Cyclone Landfall Processes (IWTCLP-4)*. Honolulu, Hawaii, December: WMO/IWTC-9, 3–7.
- Wang, Y. M., Ren, F. M., Wang, X. L., Li, W. J., and Shao, Z. M. (2006). The Study on the Objective Technique for Partitioning Tropical Cyclone Precipitation in China. *Meteorol. Monthly* 32 (3), 6–10. (in Chinese).
- Woo, W. C., Hogsett, W., Mohapatra, M., Nagata, K., Otto, P., Qi, L., et al. (2014). “Challenges and Advances Related to TC Rainfall Forecast,” in The Third International Workshop on Tropical Cyclone Landfall Processes (IWTCLP-III), Jeju, November 8–10.
- Ying, M., Zhang, W., Yu, H., Lu, X., Feng, J., Fan, Y., et al. (2014). An Overview of the China Meteorological Administration Tropical Cyclone Database. *J. Atmos. Oceanic Techn.* 31, 287–301. doi:10.1175/jtech-d-12-00119.1
- Zhong, Y., Yu, H., Teng, W., and Chen, P. (2009). A Dynamic Simulated Scheme for Tropical Cyclone Quantitative Precipitation Forecast. *J. Appl. Meteorol. Sci.* 20 (01), 17–27. (in Chinese).
- Zhou, J. H., Shi, D. P., Fan, Y. D., and Xu, W. (2004). Risk Analysis of Tropical Cyclones in the Northwestern Pacific. *J. Nat. Disasters* 13 (3), 146–151. (in Chinese).
- Zhu, L., Wan, Q., Shen, X., Meng, Z., Zhang, F., Weng, Y., et al. (2016). Prediction and Predictability of High-Impact Western Pacific Landfalling Tropical Cyclone Vicente (2012) through Convection-Permitting Ensemble Assimilation of Doppler Radar Velocity. *Mon. Wea. Rev.* 144, 21–43. doi:10.1175/mwr-d-14-00403.1

Conflict of Interest: The authors declare that the research was conducted in the absence of any commercial or financial relationships that could be construed as a potential conflict of interest.

Publisher’s Note: All claims expressed in this article are solely those of the authors and do not necessarily represent those of their affiliated organizations, or those of the publisher, the editors and the reviewers. Any product that may be evaluated in this article, or claim that may be made by its manufacturer, is not guaranteed or endorsed by the publisher.

Copyright © 2021 Yao, Ma, Jia, Ren, Li, Ding, Wang and McBride. This is an open-access article distributed under the terms of the Creative Commons Attribution License (CC BY). The use, distribution or reproduction in other forums is permitted, provided the original author(s) and the copyright owner(s) are credited and that the original publication in this journal is cited, in accordance with accepted academic practice. No use, distribution or reproduction is permitted which does not comply with these terms.



Factors Controlling Tropical Cyclone Intensification Over the Marginal Seas of China

Xiaomeng Li^{1,2}, Ruifen Zhan^{1,3*}, Yuqing Wang⁴ and Jing Xu²

¹Department of Atmospheric and Oceanic Sciences/Institute of Atmospheric Sciences, Fudan University, Shanghai, China, ²State Key Laboratory of Severe Weather, Chinese Academy of Meteorological Sciences, China Meteorological Administration, Beijing, China, ³CMA-FDU Joint Laboratory of Marine Meteorology, Shanghai, China, ⁴International Pacific Research Center and Department of Atmospheric Sciences, University of Hawaii at Manoa, Honolulu, HI, United States

OPEN ACCESS

Edited by:

Kun Zhao,
Nanjing University, China

Reviewed by:

Si Gao,
Sun Yat-sen University, China
Chao Wang,
Nanjing University of Information
Science and Technology, China

*Correspondence:

Ruifen Zhan
zhanrf@fudan.edu.cn
orcid.org/0000-0001-7209-0904

Specialty section:

This article was submitted to
Atmospheric Science,
a section of the journal
Frontiers in Earth Science

Received: 14 October 2021

Accepted: 22 November 2021

Published: 23 December 2021

Citation:

Li X, Zhan R, Wang Y and Xu J (2021)
Factors Controlling Tropical Cyclone
Intensification Over the Marginal Seas
of China.
Front. Earth Sci. 9:795186.
doi: 10.3389/feart.2021.795186

Tropical cyclone (TC) intensification over marginal seas, especially rapid intensification (RI), often poses great threat to lives and properties in coastal regions and is subject to large forecast errors. It is thus important to understand the characteristics of TC intensification and the involved key factors affecting TC intensification over marginal seas. In this study, the 6-hourly TC best-track data from Shanghai Typhoon Institute of China Meteorological Administration, ERA-Interim reanalysis data, and TRMM satellite rainfall products are used to analyze and compare the climatological characteristics and key factors of different intensification stratifications over the marginal seas of China (MSC) and the western North Pacific (WNP) during 1980–2018. The statistical results show that TC intensification over the MSC is more likely to occur when TCs experience relatively large intensities, weak vertical wind shear, small translation perpendicular to the coastline, relatively high fullness, strong upper-level divergence, low-level relative vorticity, and high inner-core precipitation rate. The box difference index method is used to quantify the relative contributions of these factors to TC RI. Results show that the initial (relative) intensity contributes the most to TC RI over both the MSC and the WNP. The inner-core precipitation rate and translation perpendicular to the coastline are of second importance to TC RI over the MSC, while both vertical wind shear and TC fullness are crucial to TC RI over the WNP. These findings may help understand TC activity over the MSC and provide a basis for improving intensity prediction of TCs in the MSC.

Keywords: tropical cyclones, rapid intensification, marginal seas, relative contribution, internal factor

SIGNIFICANCE STATEMENTS

It is important to understand the characteristics of tropical cyclone (TC) intensification and the involved key factors affecting TC intensification over marginal seas, since TCs that intensify in the coastal regions often pose a more serious threat. Most previous studies have qualitatively examined the environmental factors influencing rapid intensification (RI) of TCs over the SCS or the MSC. This study focuses on a quantitative study about the influence of the TC internal and environmental factors on TC intensification and RI over all marginal seas of China, including the SCS. Results indicate that the RI occurrence over the MSC strongly depends on the characteristics of the TC itself, such as its intensity, inner-core precipitation rate and the degree of axisymmetry, and its motion component toward the coastline. In addition, the threshold of each factor at the time of the onset of

RI over the MSC is also identified. These findings may help understand TC activity over the MSC and provide a basis for improving intensity prediction of TCs in the MSC.

INTRODUCTION

Tropical cyclone (TC) intensification in marginal seas, especially rapid intensification (RI), is a critical and difficult problem in the operational forecast of TCs. It poses a serious threat to the lives and property in coastal regions. For instance, Supertyphoon Rammasun (1409) experienced two unexpectedly RI periods in the near-coastal regions of the central Philippines and the eastern China, respectively, causing at least 206 deaths and more than \$6.5 billion in economic loss. It is, thus, important to understand the characteristics of TC intensification and the key factors affecting TC intensification in marginal seas. This cannot only help disaster prevention and mitigation but also reduce unnecessary preparedness caused by fault alarms.

Previous studies have stressed the importance of the inner-core process and the interaction between the TC circulation and both the underlying ocean and the large-scale environmental field to TC intensification and intensity changes (Wang, 2002a; Wang, 2002b; Wang and Wu, 2004). Sea surface temperature (SST) is a key in determining the surface enthalpy flux from the underlying ocean to the atmosphere, providing the energy for TC intensification and maintenance (Gao et al., 2016). SST also primarily determines the maximum potential intensity (MPI) of a TC (Emanuel, 1995; Emanuel, 1997; Emanuel, 1988; Holland, 1997). In recent studies, Wang et al. (2021a, b) have demonstrated that TC intensification rate depends predominantly on the MPI and, thus, SST. In addition to SST, the upper ocean heat content (TCHP), the sea temperature averaged in a depth of 0–100 m, the depth of ocean temperature of 26°C isotherm, and the TC-induced ocean cooling may also affect TC intensification and maintenance (Lin et al., 2008; Wada, 2015; Miyamoto et al., 2017; Fudeyasu et al., 2018).

The environmental atmospheric conditions have been found to play key roles in affecting TC intensification and intensity (Wu and Cheng, 1999; Bosart et al., 2000; Hong et al., 2000; Emanuel et al., 2004; Wang and Wu, 2004). The statistical results have shown that TC RI occurs in favorable environmental conditions, including weak vertical wind shear (VWS), strong upper-tropospheric divergence, high mid-lower tropospheric relative humidity (RH), and high convective available potential energy and TCHP (Kaplan and Demaria, 2003; Hendricks et al., 2010; Kaplan et al., 2010; Shu et al., 2012; Wang et al., 2015). Wang et al. (2015) found that the environmental VWS between 300 and 1,000 hPa is more representative than the commonly used VWS between 200 and 850 hPa in suppressing TC intensification in the western North Pacific (WNP).

In addition to the environmental conditions, TC structure also has an important impact on TC intensification. Xu and Wang (2015, 2018) used the radius of maximum wind (RMW), the radius of 34-kt wind (AR34), and the outer-core wind skirt parameter ($DR34 = AR34 - RMW$) to characterize the storm size and found that RI occurs only in a relatively narrow

range of parameter space in TC intensity and both inner- and outer-core sizes. Guo and Tan (2017) proposed the concept of TC fullness (TCF), which is defined as the ratio of the extent of the outer-core wind skirt to the outer-core size of a TC ($TCF = DR34/AR34$). They found that the correlation between TC intensity and fullness is stronger than other measures that only contain a single size parameter. Some other studies have also indicated the importance of convective processes in TC intensity change. For example, convective bursts in the eyewall are shown to play important roles in the onset of RI (Chen and Zhang, 2013; Wang and Wang, 2014). Previous studies have also revealed that TC intensity change rate is linearly correlated with the departures in the inner-core precipitation, and RI TCs usually correspond to relatively high core precipitation rates (Gao and Chiu, 2010; Su et al., 2020).

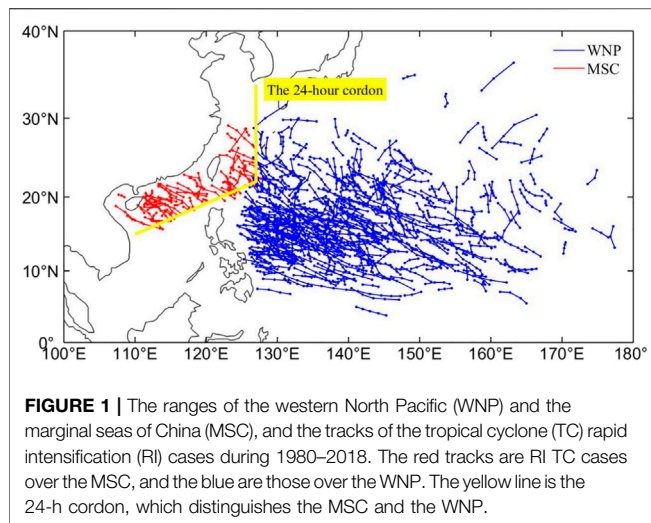
The marginal seas of China (MSC), including the Bohai Sea, the Yellow Sea, the East China Sea, and the South China Sea (SCS), are extremely vulnerable to TC activity, especially to RI TCs. Most previous studies have focused on RI over the SCS. Liang et al. (2020) indicated that most of RI cases over the SCS occur in the post-monsoon season, during which the mid-latitude westerly trough often reaches the northern SCS and the southwest monsoon flow retreats to the southern SCS but is still strong (Chen et al., 2015). Among various environmental conditions, VWS, low-level convergence, and low-level moist convergence are particularly important (Hu and Duan, 2016). A recent study also emphasized the role of fast storm translation speed and high TC intensification potential north of the storm center at the previous 24 h in TC RI over the SCS (Chen et al., 2021). Some studies have also examined TC RI over the MSC as a whole. It has been shown that the environmental conditions in the RI composite over the MSC exhibit weak VWS, plentiful moisture transport, strong low-level convergence and ascending motion, all being favorable for TC RI (Huang and Lei, 2010; Zheng et al., 2016). Chen et al. (2014) have compared the differences in intensity characteristics between Supertyphoons Rammasun (1409) and Damrey (0518) and found that weak downstream vertical shear of zonal wind, and high temperature in the northern SCS were key factors to the RI of the two supertyphoons.

Most previous studies have qualitatively examined the environmental factors influencing RI of TCs over the SCS or the MSC. A systematic analysis and quantitative investigation on TC intensification rate (IR) over the MSC and its relationship with the environmental factors and the TC metrics itself have not yet been conducted. Therefore, the main objectives of this study are 1) to compare the climatological characteristics of TC intensification and RI events over the MSC and the WNP; 2) to determine the key factors that affect TC IR over the MSC and the WNP; 3) to quantify the relative contributions of the associated factors to TC RI based on the box difference index (BDI) method and identify the threshold of each factor at the time of the onset of RI over the MSC.

DATA AND METHODS

Data and Definitions

The 6-hourly TC best-track data during 1980–2018 used in this study were obtained from the Shanghai Typhoon Institute of

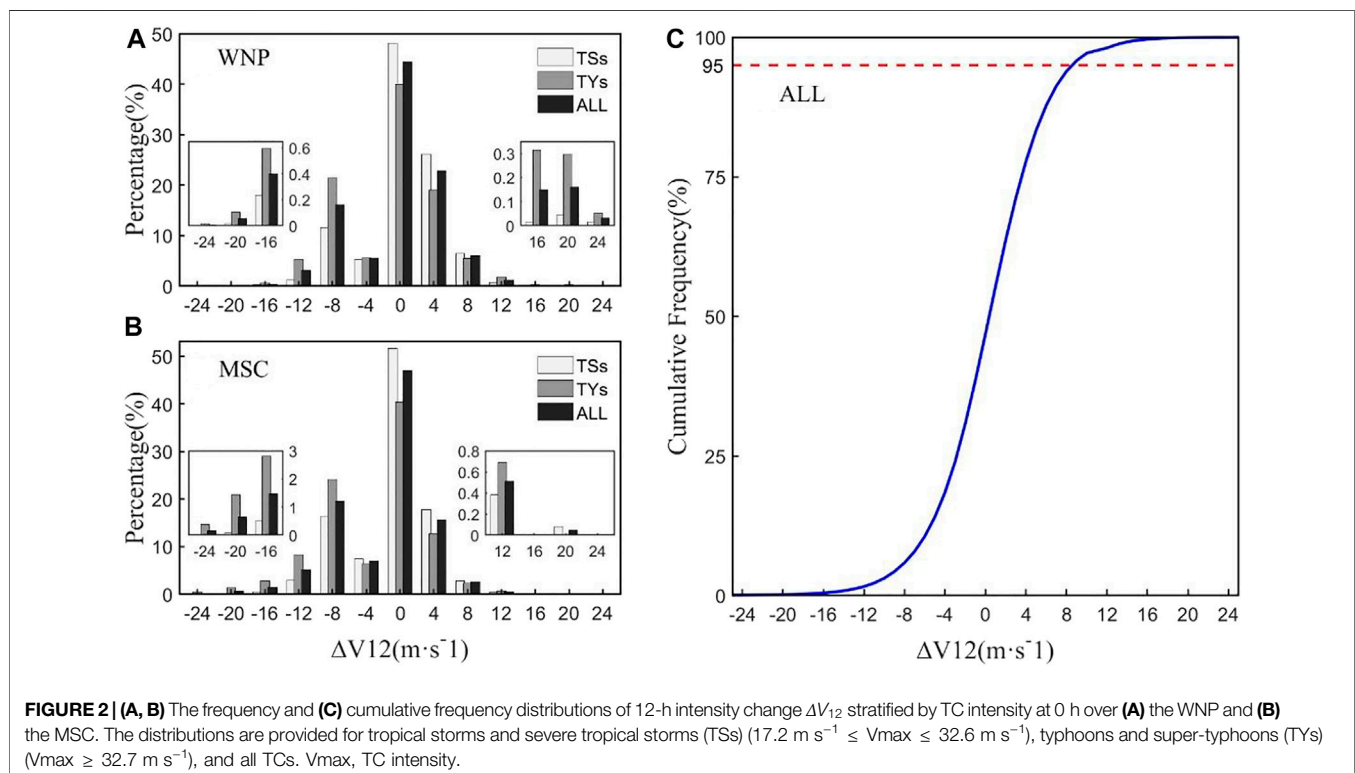


China Meteorological Administration (CMA), which consist of TC central location (longitude and latitude), maximum 2-min mean sustained surface wind speed (V_{max}), and minimum central sea level pressure. Based on the TC best-track data, RMW, TC intensity change, and translation speed were calculated. We calculated translation components parallel and perpendicular to the coastline closest to the TC center, SPD_x and SPD_y, respectively. The 6-hourly TC size data were also from the CMA (Lu et al., 2017), in which the AR34 data were used in this study. Here, we mainly focused on TC activity over the MSC. For comparison, TC activity over the WNP was also examined. The

MSC is defined as the areas inside the 24-h cordon according to TC Operation and Service Criterion of China Meteorological Administration (2012), while the WNP is defined as the region 0–40°N, 127–180°E excluding the MSC, as shown in **Figure 1**. Only TCs with V_{max} greater than 17.2 m s^{-1} were considered in our analysis, and the data for offshore distance $\leq 50 \text{ km}$ were removed to avoid the land effect.

The 24-h intensity changes are often used to define TC RI over the WNP and the North Atlantic (Kaplan and Demaria, 2003; Shu et al., 2012). Considering the relatively short duration of TCs in the MSC before making landfall and the size of RI samples, here 12-h intensity changes are considered as in previous studies (Yan, 1996; Zheng et al., 2016). According to the 12-h TC intensity change (ΔV_{12}), $\Delta V_{12} > 0$ was defined as the intensification case with ΔV_{12} as IR. Based on the 95th percentile of ΔV_{12} for all TC cases, we further defined $\Delta V_{12} \geq 8 \text{ m s}^{-1}$ as the RI case, and $0 < \Delta V_{12} < 8 \text{ m s}^{-1}$ as non-RI cases (**Figure 2C**). For a comparison, TC weakening cases were defined as $\Delta V_{12} \leq -4 \text{ m s}^{-1}$ based on 20th percentile of ΔV_{12} for all TC cases. Unless otherwise stated, this study focuses on TC intensification cases.

The environmental factors were calculated using ERA-Interim reanalysis data with a $1 \times 1^\circ$ horizontal resolution and 37 vertical pressure levels. Following Kurihara et al. (1993), the environmental fields including winds, vorticity, divergence, relative humidity were filtered to remove all disturbances with wavelengths less than 1,000 km. We calculated the correlation between the 12-h TC IR and VWS between two given pressure levels over the WNP and the MSC during 1980–2018. We found



that the deep-layer shear between 300 and 850 hPa is more representative than the shear between any other two pressure levels in affecting TC intensity in both the WNP and the MSC, which is consistent with the findings of Wang et al. (2015). Therefore, the environmental VWS between 300 and 850 hPa is used as VWS in our following analysis.

In addition, the core precipitation rate and TC fullness were considered as potential factors to study the influence of the TC inner-core size on its intensity change. The core precipitation rate was calculated based on surface precipitation taken from the Tropical Rainfall Measuring Mission (TRMM) 3B42 precipitation product (Huffman et al., 2007), with a 3-h temporal resolution and $0.25 \times 0.25^\circ$ spatial resolution from 1998 to 2018. TC fullness was calculated based on the TC best-track data and TC size data mentioned above.

METHODS

The TC MPI was calculated using the algorithm of Bister and Emanuel (2002), which is expressed as

$$V_{mpi} = \alpha \sqrt{\frac{T_s}{T_o} \frac{C_k}{C_d} [CAPE^* - CAPE]_{rm}} \quad (1)$$

where C_k is the surface exchange coefficient, C_d is the surface drag coefficient, T_s is the SST, and T_o is the outflow layer air temperature. $CAPE^*$ is the convective available potential energy of the air being saturated at SST and lifted upward from the sea level through the environmental sounding, and $CAPE$ is that of the air in the boundary layer. The code is publicly available at <ftp://texmex.mit.edu/pub/emanuel/TCMAX/>.

The box difference index (BDI) method (Fu et al., 2012) was used to distinguish the differences between the two sets of factor samples in the TC RI cases and non-RI cases and to rank the importance of the factors. The BDI was given by

$$BDI = \frac{M_A - M_B}{\sigma_A + \sigma_B} \quad (2)$$

where M_A and σ_A (M_B and σ_B) represent the mean and standard deviation of the variable for the RI (non-RI) cases. The sign of the BDI reflects the nature of the variable, and the BDI value measures how well the variable can differentiate between the RI cases and the non-RI cases. The greater the BDI value is, the better the variable can be used to predict the occurrence of TC RI.

The factor threshold for the onset of RI was determined following Hu and Duan (2016). First, the Kolmogorov–Smirnov (KS) test method was used to determine whether the factor X obeys a normal distribution (Yap and Sim, 2011). Second, the threshold range of the factor X was determined based on its average value \bar{X} and the standard deviation S . To ensure that the factor X meets the threshold conditions in most of RI cases and to exclude abnormal values, the range was taken between \bar{X} and $\bar{X} \pm 2S$. Finally, the corresponding X value at the time of maximum RI probability (P_{RI}) was taken as the threshold of the factor X triggering the onset of RI. Here, the formula for the RI probability is given as (Kaplan and Demaria, 2003)

TABLE 1 | The distribution of 12-h intensity change (ΔV_{12}) over the MSC, the number of cases in each stratified intensification category in each intensity class and their percentages in the 1,261 intensification cases, and the percentage of RI cases in each intensity class to the corresponding intensification cases in that category (RI/I).

ΔV_{12} ($m s^{-1}$)	TS	TY	All TCs	Percentage (%)
(0–4)	346	69	415	32.91
(4–8)	464	240	704	55.83
(8–12)	74	43	117	9.28
(≥12)	12	13	25	1.98
Total cases	896	365	1261	100
Percentage (%)	71.05	28.95	100	—
RI/I (%)	9.60	15.34	11.26	—

$$P_{RI} = \frac{N_{RI}}{N_{RI} + N_{non-RI}} \quad (3)$$

where P_{RI} represents the RI probability, N_{RI} represents the number of RI cases that meet the threshold condition, and N_{non-RI} represents the number of non-RI cases that meet the corresponding threshold condition. The greater the P_{RI} is, the greater is the probability of RI occurrence when the threshold condition is met. When calculating the threshold, the factor threshold and the corresponding RI probability were calculated at 6-h intervals for 24 h before the onset of TC RI.

RESULTS AND DISCUSSION

Characteristics of Intensifying Tropical Cyclones Over the Western North Pacific and The Marginal Seas of China

During 1980–2018, there were a total of 1,012 TCs, with 4,897 intensification cases and 960 RI cases over the WNP and 1,261 intensification cases and 142 RI cases in the MSC (Figure 1).

Figure 2 shows the frequency and cumulative frequency distributions of 12-h intensity change (ΔV_{12}) stratified by TC intensity. As expected, the frequency of slow intensification ($0 \leq \Delta V_{12} < 4 m s^{-1}$) is the highest for all categories of TCs over the WNP and the MSC, namely, most TCs intensified slowly in their lifetimes. Compared with weak TCs (tropical storms and severe tropical storms, TSs) with V_{max} between 17.2 and $32.6 m s^{-1}$, intense TCs (typhoons and super-typhoons, TYs) with intensity greater than $32.6 m s^{-1}$ have relatively lower (higher) frequency of intensification cases for intensifying rate smaller than (larger than) $12 m s^{-1}$ ($12 h^{-1}$), but a larger weakening rate. This suggests that a TC with weak intensity is more likely to experience a relatively lower intensification rate, while a TC with high intensity increases the potential for weakening, consistent with previous studies (Shu et al., 2012; Xu and Wang, 2018; Fei et al., 2020). The distribution of TC intensity change rate over the MSC is generally consistent with those over the WNP. Based on the cumulative frequency distributions of TC intensity change over the WNP (Figure 2C), the intensity change rate at the 95th percentile of all

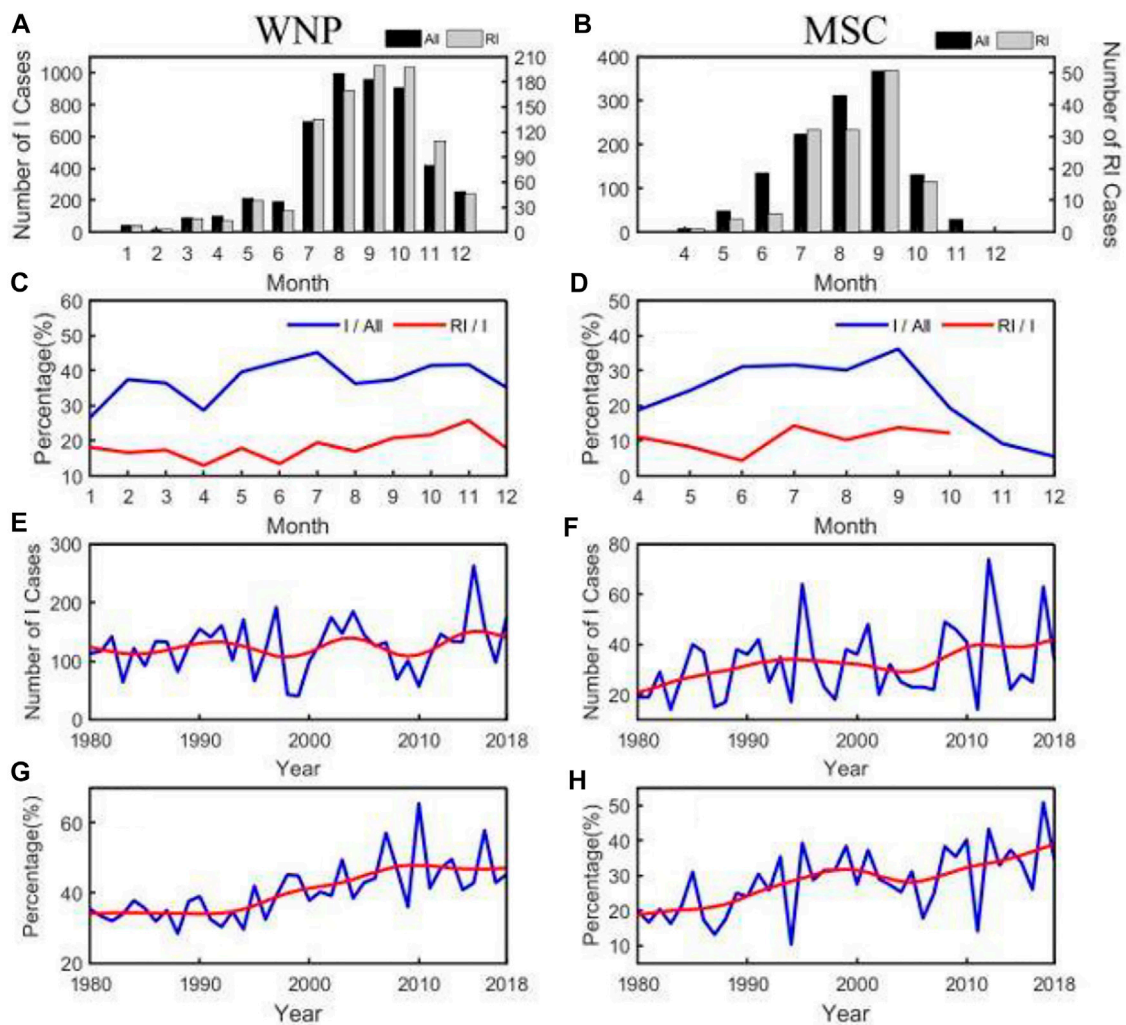


FIGURE 3 | The monthly frequencies of all intensification (black) and RI (gray) cases (A,B) and their proportions (%) to the frequency of all TC cases (blue) and all intensification (red) cases (C,D), and the interannual variability of TC intensification frequency (blue) (E,F) and its proportions to the frequency of all TC intensity changes (blue) (G,H) over the WNP (A,C,E,G) and the MSC (B,D,F,H). E–H The red curves indicate after a 5-point smoothing.

TCs is $8 \text{ m s}^{-1} (12 \text{ h})^{-1}$. Since the 95th percentile of intensity change rate cases is representative of RI (Kaplan and Demaria, 2003), $8 \text{ m s}^{-1} (12 \text{ h})^{-1}$ is used as the RI threshold in this study.

We further statistically analyzed the TC IR over the MSC. Table 1 shows the IR distribution of the 1,261 TC intensification cases stratified by intensity category over the MSC. We can see that TSs accounted for the higher proportion of all intensification cases by 71.05%, and TYs for the lower proportion by 28.95%. Among the different IR ranges, the proportion is the highest in the range of $4\text{--}8 \text{ m s}^{-1} (12 \text{ h})^{-1}$ with 55.83%. For TYs, the frequency of RI cases among the intensification cases is the highest, with 15.34%, followed by TSs with 9.60%. This strongly indicates that the RI cases over the MSC depend on the TC intensity.

Figures 3A–D present the monthly frequency of all intensification cases and RI cases, and their proportions to total cases and all intensification cases over the WNP and the

MSC, respectively. Over the WNP (Figures 3A, C), the TC intensification and RI mostly occurred in July–October, with the peak for intensification cases in August and for RI cases in September, respectively (Figure 3A). The proportions of intensification cases to total TC cases do not show significant difference in 12 months, while the monthly proportion of the frequency of RI cases to all intensification cases exhibits the peak in November (Figure 3C). In contrast, over the MSC (Figures 3B, D), the TC intensification and RI mainly occurred in July–September, with the peak in September (Figure 3C). This may be due to the active southwest monsoon in the MSC during this period (Hu and Duan, 2016). The monthly proportions decrease rapidly in November and December (Figure 3D). Figures 3E–H show interannual variabilities of the frequency of all intensification cases and its proportions to the frequency of all TC intensity changes over the WNP and the MSC, respectively. A prominent feature is a significant upward trend in the

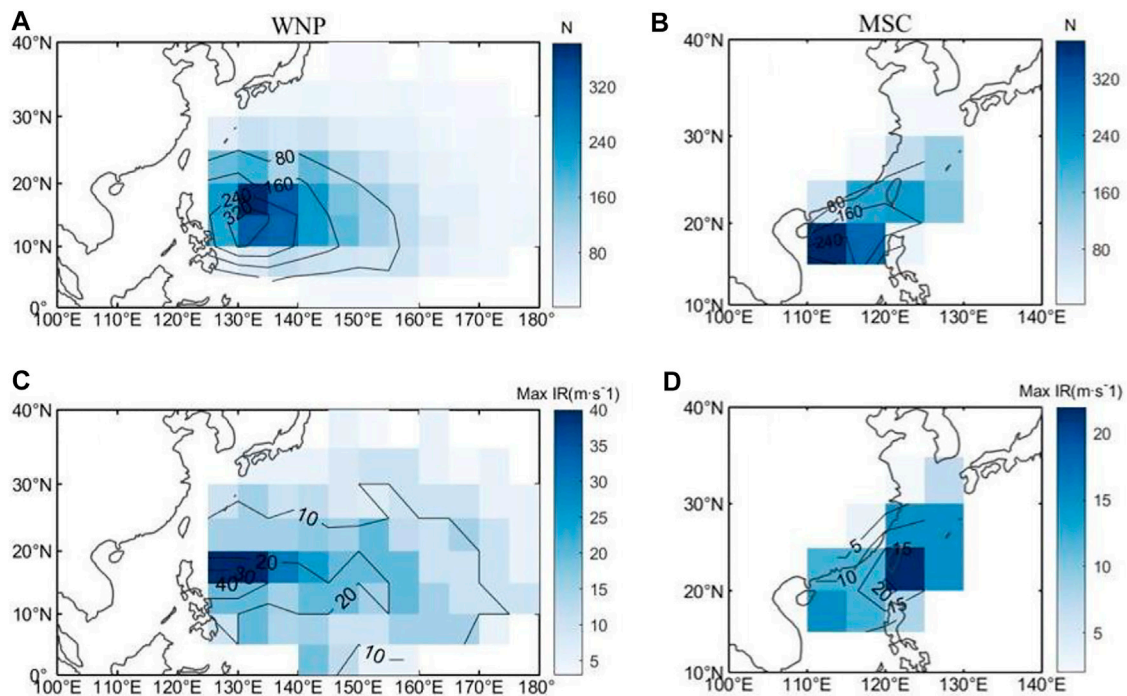


FIGURE 4 | Spatial distributions of frequency of (A,B) all intensification cases and (C,D) maximum intensification rate (Max IR; m s^{-1}) in each $5^\circ \times 5^\circ$ grid box over the WNP (A,C) and the MSC (B,D). IR, TC in intensification rate.

frequency of TC intensification cases over the MSC, from 21 cases per year in 1980 up to more than 42 cases per year in 2018, namely, with a doubling in 39 years (Figure 3F). In contrast, the trend in the frequency of TC intensification cases over the WNP during 1980–2018 is not significant. Similar to the frequency of TC intensification cases over the MSC, the ratio of the intensification cases to all cases over both the WNP and the MSC also shows a robust increasing trend (Figures 3G, H). The ratio over the WNP increased from 34% to 47% (Figure 3G), and from 19% to 39% over the MSC (Figure 3H) during 1980–2018. This indicates that the frequency and probability of TC intensification over the MSC is increasing, which may pose greater challenges to operational forecasting and a more serious threat to coastal areas of China.

Figure 4 shows the spatial distributions of the frequency of all TC intensification cases and the maximum IR in the two sub-basins. Most of the intensification cases over the WNP occurred east of the Philippines (10° – 25°N , 125° – 155°E), centered in the region 10° – 20°N , 130° – 140°E . Over the MSC, the intensification cases mostly occurred in the northern SCS and the East China Sea, with a maximum in the central and eastern SCS (15° – 20°N , 110° – 120°E) and second maximum in the east coasts of the northern Philippines and Taiwan. In contrast, the positions of the maximum IR are widely distributed. The two maximum areas are located east of the northern Philippines (15° – 20°N , 125° – 135°E) with the maximum 40 m s^{-1} (12 h) $^{-1}$ and over the southern East China Sea with the peak 20 m s^{-1} (12 h) $^{-1}$, respectively. Note that intensification cases with IR greater than 10 m s^{-1} (12 h) $^{-1}$ occurred along the China coast.

Factors Affecting Tropical Cyclone Intensification Rate and Rapid Intensification Over the Marginal Seas of China

TC intensification often occurs in a favorable environment. Based on previous studies, potential factors affecting TC intensity change over the WNP and the MSC include climatology and persistence factors, large-scale environmental factors, ocean forcing factors, and TC structure factors (Table 2). In the following, we discuss these factors over the MSC. The corresponding factors over the WNP are also examined for a comparison.

Correlation Analyses

Figure 5 shows the scatter diagrams of TC IR against TC intensity (V_{max}), relative intensity (the ratio of V_{max} to its theoretical MPI abbreviated as POT), TCF, and environmental VWS between 300 and 850 hPa over the WNP and the MSC, respectively, together with their corresponding fitted 50th and 95th percentiles of IRs. TC IR shows an approximately linear dependence on V_{max} , with a positive correlation over both sub-basins (Figures 5A, B), with the correlation coefficients of 0.36 and 0.28, respectively. It can be seen from the fitted 95th percentile curve that over the WNP (Figure 5A), the TC IR increases with the increase of V_{max} initially and peaks at V_{max} of around 40 m s^{-1} , and then decreases with increasing TC intensity afterward, which is consistent with the results of Xu and Wang (2018). Over the MSC, the IR- V_{max} relationship is similar to that

TABLE 2 | List of the factors (their unit and description) analyzed in this study.

Variables	Unit	Description
Vmax	m s^{-1}	Current intensity
VWS	m s^{-1}	Vertical shear of horizontal winds averaged within a radius of 5 degrees of the TC center between 300 and 850 hPa
SPDx	m s^{-1}	Component of TC translation parallel to the coastline (x)
SPDy	m s^{-1}	Component of TC translation perpendicular to the coastline (y)
SST	$^{\circ}\text{C}$	Sea surface temperature at the TC center
MPI	m s^{-1}	Maximum potential intensity
POT	—	Vmax/MPI (relative intensity defined as the ratio of the current TC intensity to its theoretical MPI)
RH600	%	600-hPa relative humidity averaged within a radius of 5 degrees of the TC center
PRE	mm h^{-1}	Precipitation rate averaged within a radius of 5 degrees of the TC center
DIV200	s^{-1}	200-hPa Divergence averaged within a radius of 5 degrees of the TC center
VOR850	s^{-1}	850-hPa relative vorticity averaged within a radius of 5 degrees of the TC center
TCF	—	DR34/AR34 (TC fullness, defined as the ratio of the extent of the outer-core wind skirt to the outer-core size of the TC)

over the WNP, except that the IR peaks at Vmax of 35 m s^{-1} (**Figure 5B**). Since the 95th percentile of IR can roughly represent RI, the results suggest that TCs with Vmax of $40\text{--}45 \text{ m s}^{-1}$ over the WNP and Vmax of $30\text{--}35 \text{ m s}^{-1}$ over the MSC are the most conducive to the occurrence of TC RI. We further examined the relationship between TC IR and TC relative intensity, which represents how far the current TC intensity is from its MPI. The IR also shows an approximately positive correlation with POT. For the fitted 95th percentile curve, when $\text{POT} < 0.45$, the IR increases with the increase of POT, reaches the peak at $\text{POT} = 0.45$ and then decreases with increasing POT over the WNP (**Figure 5C**). However, the IR reaches the peak when $\text{POT} = 0.35$ over the MSC (**Figure 5D**). This indicates that when the intensity of a TC reaches 45% (35%) of its corresponding MPI, the TC has the greatest potential to intensify and, thus, is favorable for RI in the WNP (MSC). The IR over the WNP is highly correlated with TCF, but IR does not linearly depend on TCF over the MSC. In fact, when the $\text{TCF} < 0.7$, TC IR increases with increasing TCF, but decreases with TCF when $\text{TCF} > 0.7$ over the MSC, suggesting that the TCF between 0.6 and 0.8 is the most conducive to TC RI (**Figure 5F**). In general, consistent with previous studies, there is a negative correlation between VWS and TC IR. Namely, the environmental VWS significantly suppresses the occurrence of TC RI over the MSC.

Composite Analyses

We further divided the intensity changes into four categories as listed in **Table 3**. They are weakening cases with $\Delta V_{12} \leq -4 \text{ m s}^{-1}$, neutral cases with $0 < \Delta V_{12} < 4 \text{ m s}^{-1}$, intensifying cases with $4 \text{ m s}^{-1} < \Delta V_{12} < 8 \text{ m s}^{-1}$, and rapidly intensifying cases with $\Delta V_{12} \geq 8 \text{ m s}^{-1}$. Here, we compare the differences in various factors listed in **Table 2** among the four intensity change categories. **Figure 6** shows the box plots of Vmax, POT, TCF, VWS, SPDy, and 200-hPa divergence in the four intensity change categories for TCs over the WNP and the MSC, respectively. The two-sided Student's test is used to examine whether the differences between RI and non-RI (including neutral and intensifying categories) are statistically significant. There are large differences in these factors between the weakening and intensifying composites over the WNP and the MSC. Weakening TCs correspond to larger Vmax, POT, TCF, VWS, and SPDy, and

smaller upper-level divergence than all other categories. This indicates that intense TCs with strong VWS, rapid SPDy and weak upper-level divergence are prone to weakening, and they are close to their corresponding theoretical MPI.

Factors important to the three intensity change categories over the MSC show similar characteristics to those over the WNP except for TCF (**Figure 6**). Vmax, POT, 200-hPa divergence increase, while VWS and SPDy decrease from neutral to RI. TCF in the weakening composites has the largest median value exceeding 0.8, and the median in the other three composites is between 0.6 and 0.8. TCF over the WNP generally increases from the neutral to RI, but the increase from the intensifying composite to RI composite is relatively small. However, TCF over the MSC shows a change from increasing to decreasing, with a slightly smaller TCF in the RI composite than in the intensifying composite. This leads to the statistically insignificant difference in TCF between the RI and non-RI composites over the MSC. These results indicate that a TC over the MSC has the potential to intensify rapidly when it is embedded in the favorable environment with small VWS, slow-moving component perpendicular to the coastline (SPDy), and strong upper-level divergence, and has a relatively large Vmax but far from its MPI.

In general, a fast-moving TCs tend to develop large inner-core asymmetries, which is often unfavorable for TC RI (Peng et al., 1999; Wang and Wu, 2004). Meanwhile, the slow-moving TCs could reduce the intensification of a strong TC due to SST cooling induced by ocean upwelling and turbulent mixing and, thus, unfavorable for TC intensification. However, in the MSC, the ocean temperature is often well mixed compared with the open tropical oceans. As a result, slow translation toward the coastline (small SPDy) often leads insignificant SST cooling and even causes coastal warming in some cases and, thus, favorable for RI (Zhang et al., 2019). In addition, the strong upper-level divergent environment can provide a favorable “pumping” effect, which is conducive to the occurrence of TC RI (Mei and Yu, 2016).

We further examined the spatial distribution of the composite 600-hPa relative humidity and 850-hPa vertical relative vorticity for the four intensity change categories over the MSC (**Figure 7**). Note that the TC vortex has been removed as mentioned in the *Data and methods* section. As expected, the weakening composite shows the driest in the northwest quadrant and near the TC core

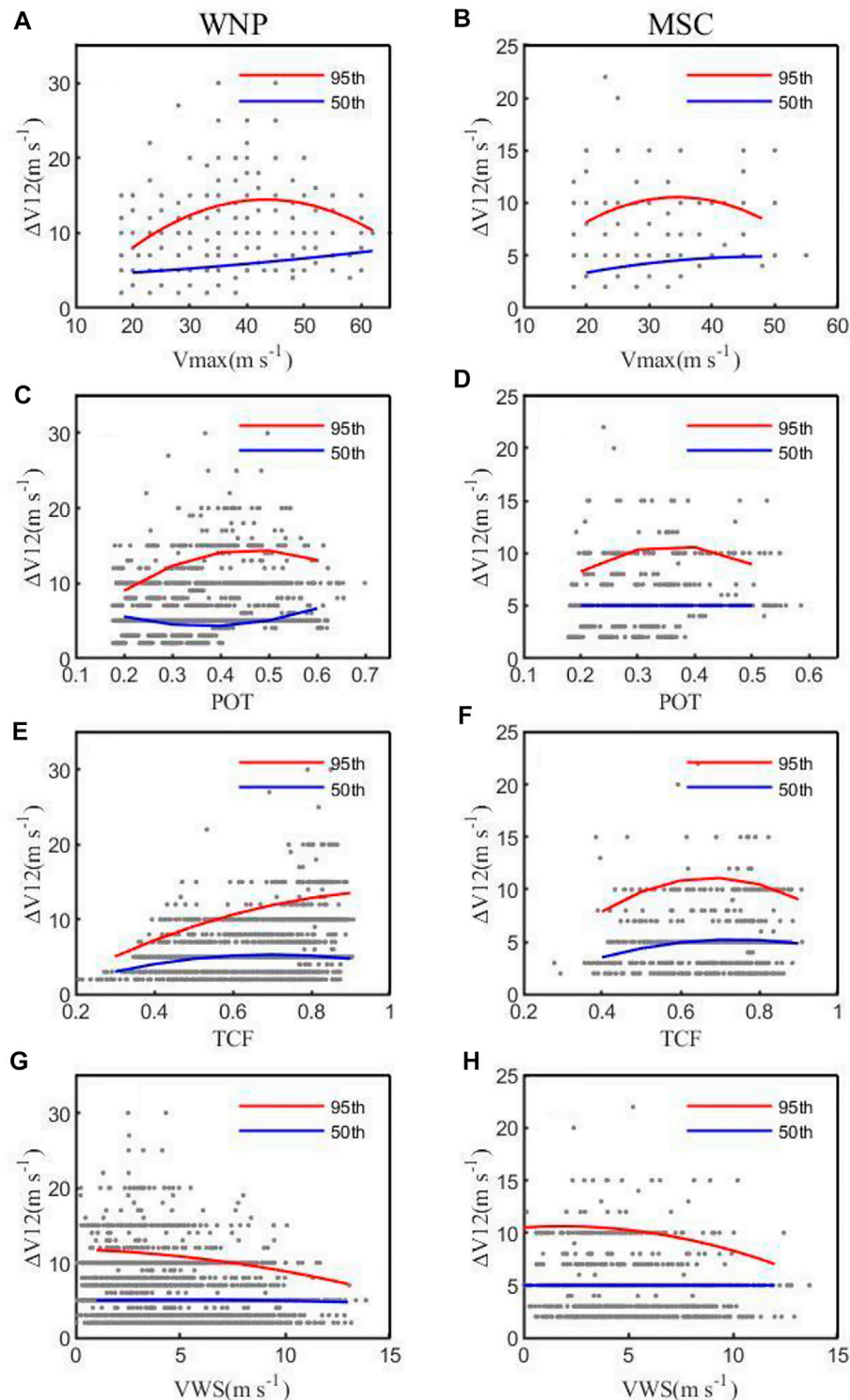


FIGURE 5 | Scatter diagrams of TC intensification rate (IR) against (A,B) V_{max} (m s^{-1}), (C,D) POT, (E,F) TCF, and (G,H) VWS between 300 and 850 hPa (m s^{-1}) over (A,C,E,G) the WNP and (B,D,F,H) the MSC. The red and blue curves are the 95th and 50th percentiles of IR for the given storm intensity, respectively, for the corresponding sample sizes. POT, the ratio of V_{max} to its theoretical MPI; TCF, TC fullness; VWS, vertical wind shear.

among all intensity change composites (Figures 7A–D). However, there is little difference in the mid-level relative humidity for three intensifying composites, which is different

from those over the WNP where the RI composite is slightly moister than both the intensifying and neutral composites (Hendricks et al., 2010), but similar to those over the SCS

TABLE 3 | Intensity change categories, definitions, and sample sizes for TCs over the WNP and the MSC, respectively.

Category (m s^{-1})	WNP	MSC
Weakening (W) $\Delta V_{12} \leq -4$	2,496	1233
Neutral (N) $0 < \Delta V_{12} < 4$	1,057	415
Intensifying (I) $4 \leq \Delta V_{12} < 8$	2,879	704
Rapidly intensifying (RI) $\Delta V_{12} \geq 8$	961	142

Note. WNP, western North Pacific; MSC, marginal seas of China.

(Hu and Duan, 2016). The weakening composite shows the background relative vorticity in similar magnitudes to the intensifying and the RI composites, while the neutral composite has the smallest relative vorticity in the TC core (Figures 7E–H). The large background vorticity still occurs in the weakening composite likely because considerable weakening cases are embedded in monsoon gyres with relatively large positive vorticity over the WNP, as documented by Liang et al. (2018) and more recently by Song et al. (2021). In contrast, the neutral composite TCs are often in their slow intensification stage with relatively low intensification rate, and the background circulations are often stable and unfavorable for either RI or weakening of TCs. The RI composite is quite similar to the intensifying composite in terms of the spatial structure and magnitude of the background vorticity. Note that part of the positive vorticity in the composite could be due to the deficiency in the vortex filtering algorithm used. The RI cases could be more likely to be embedded in monsoon trough with relatively high background vorticity over the WNP but are at their intermediate intensity as previously documented based on observations (Xu and Wang, 2015; Xu and Wang, 2018) and recent theoretical studies (Wang et al., 2021a; Wang et al., 2021b). However, the weakening cases often occur after TCs pass their lifetime maximum intensity and, thus, are at relatively high intensity with large size, leading to the remnant of the low wavenumber component of the TC vortex in the filtered field. These results are in general consistent with the frequency distributions of TC intensity for the four intensity change categories shown in Figure 6A and also similar to those found for TCs over the WNP by Hendricks et al. (2010). This suggests that although the mid-level relative humidity and low-level relative vorticity are important for TC intensification, they could not be considered as critical factors affecting TC RI because they are strongly dependent on TC intensity itself.

Finally, we examined the spatial distributions of the composite SST and precipitation rate for each of the intensity change categories over the MSC (Figure 8). There is a remarkable meridional SST gradient across the TC center in all categories with cold to the north and warm to the south (Figures 8A–D). The meridional SST gradient is the largest in the weakening TC composite while smallest in the RI composite. The SST near the TC center increases monotonously from weakening (27.6°C) to RI composites (28.6°C) over the MSC, consistent with that over

the WNP (Hendricks et al., 2010). This is mainly because most RI cases occurred in the tropics, while the weakening cases often moved out of the deep tropics. Unlike SST, the TC core precipitation rate tends to be the least in neutral composite and the most in intensifying and RI composites (Figures 8E–H), again likely related to TC intensity (Cecil and Zipser, 1999; Hoshino and Nakazawa, 2007). Nevertheless, the composite inner-core precipitation rate shows a more axisymmetric structure in the RI composite while a more asymmetric structure in the weakening composites than in all other intensity change composites.

The above analyses demonstrate that TC intensification over the MSC is more likely to occur when TCs have relatively large and relative intensities, small translation component perpendicular to the coastline, and high core precipitation rate, and are embedded in an environment with warm SST, weak vertical wind shear, and strong upper-level divergence. Especially, TC relative intensity, VWS, 200-hPa divergence, and axisymmetric inner-core structure are key factors affecting TC RI over the MSC. However, we note that these factors might not be independent of each other and their relative importance is different. Therefore, it is important to examine the relative importance of these factors and their thresholds in determining TC RI over the MSC, which will be discussed in the next section.

Relative Importance and Thresholds of Factors Affecting Tropical Cyclone Rapid Intensification Over the Marginal Seas of China

The BDI method described earlier in the *Method* section is used to quantify the relative importance of factors to TC RI over the MSC, including TC persistent factors (V_{max} , POT, SPDy), environmental factors [SST, VWS, middle-level relative humidity (RH600), low-level vorticity at 850 hPa (VOR850), and upper-level divergence (DIV200)], and TC structure factors (TCF and precipitation rate, PRE). For a comparison, the corresponding factors affecting TC RI over the WNP are also discussed.

Figure 9 shows the relative importance of all abovementioned factors to RI over the WNP and the MSC, respectively. The results show that the most important factors distinguishing RI and non-RI cases over the WNP are POT, V_{max} , and VWS with the BDI values 0.28, 0.27, and -0.13 , respectively, followed by TCF (0.10), SPDy (-0.08), DIV200 (0.07), SST (0.07), PRE (0.06), VOR850 (0.06), and RH600 (0.002). For the MSC, the most important factors distinguishing RI and non-RI cases are V_{max} , POT, core PRE with the BDI values being 0.18, 0.17, and 0.13, respectively, followed by SPDy (-0.12), VWS (-0.11), TCF (0.09), SST (0.07), DIV200 (0.06), VOR850 (0.03), and RH600 (0.02). Compared with the environmental factors, V_{max} and POT contribute greater to TC RI over both the MSC and the WNP, which is consistent with the results shown in Figure 6. More interestingly, PRE and SPDy play a key role in TC RI over the MSC, while VWS and TCF are two critical factors to TC RI over the WNP. This suggests that TC RI over the MSC is more

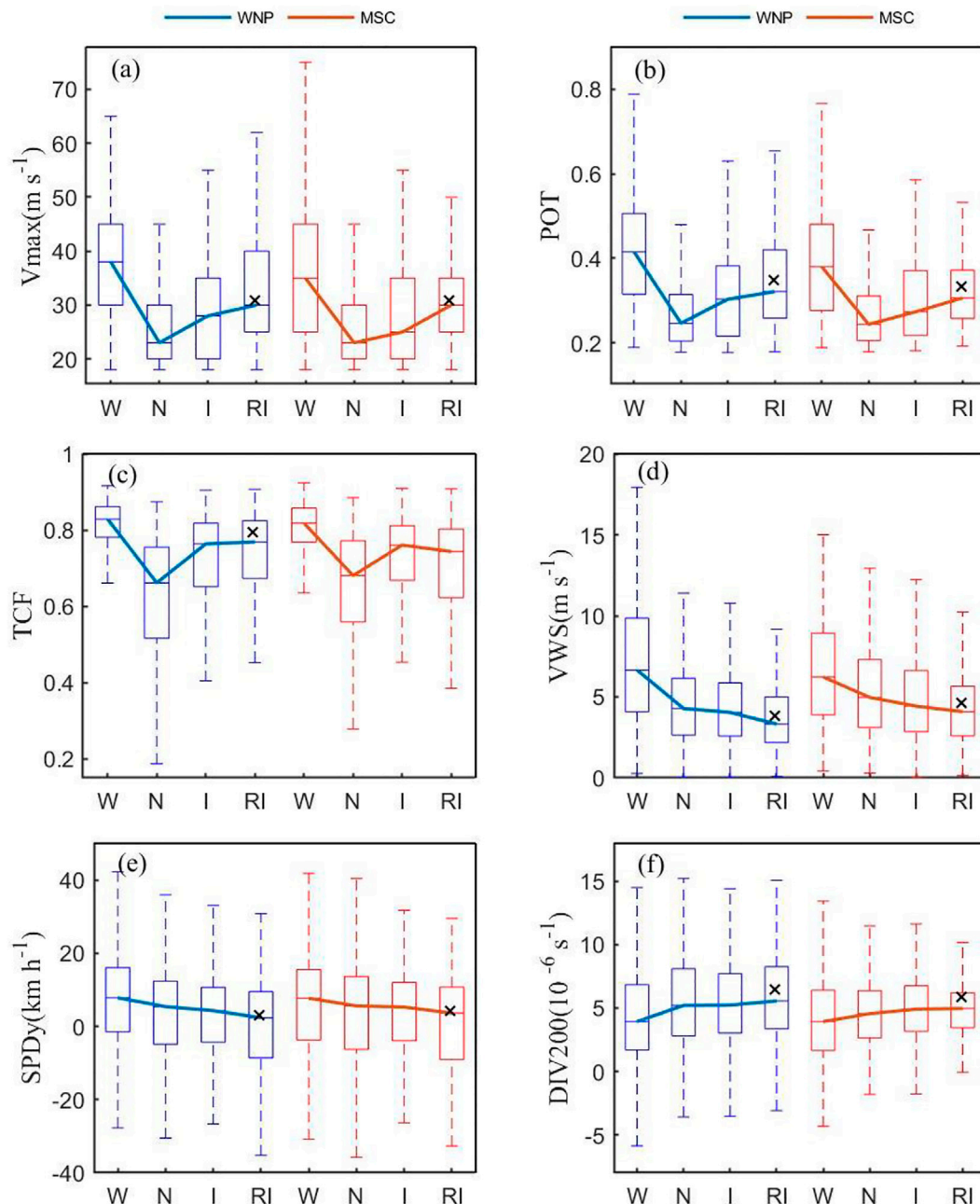


FIGURE 6 | Box plots and median lines of (A) Vmax (m s^{-1}), (B) POT, (C) TCF, (D) VWS (m s^{-1}), (E) SPDy (m s^{-1}), and (F) 200 hPa divergence (DIV200, 10^{-6} s^{-1}) for different TC intensification rates over the WNP (A,C,E) and the MSC (B,D,F). The blue represents WNP, and the red represents MSC. "x" shows differences between RI and non-RI being statistically significant above 95% confidence level based on the two-sided Student's *t* test. SPDy, slow moving component perpendicular to the coastline.

likely related to the TC itself and the coastal air-sea interaction implied by the slow translation component perpendicular to the coastline. It is also shown that the impacts of low-level vorticity and mid-level relative humidity on RI are not significant over the MSC, which is consistent with the results shown in Figure 7.

Finally, the threshold determination method is applied to calculate the threshold of each factor triggering the onset of RI

and the corresponding RI probability, with the results shown in Table 4. Vmax and POT have a greater probability to the RI occurrence than other factors over the MSC. Vmax greater than 33.45 m s^{-1} and POT greater than 0.35 are especially conducive to TC RI occurrence, with the RI probabilities of 16.23% and 16.20%, respectively, which is consistent with the results in Figure 9. When the precipitation rate and TCF meet the thresholds of $\text{PRE} \geq 1.87 \text{ mm h}^{-1}$ and $\text{TCF} \geq 0.58$, the

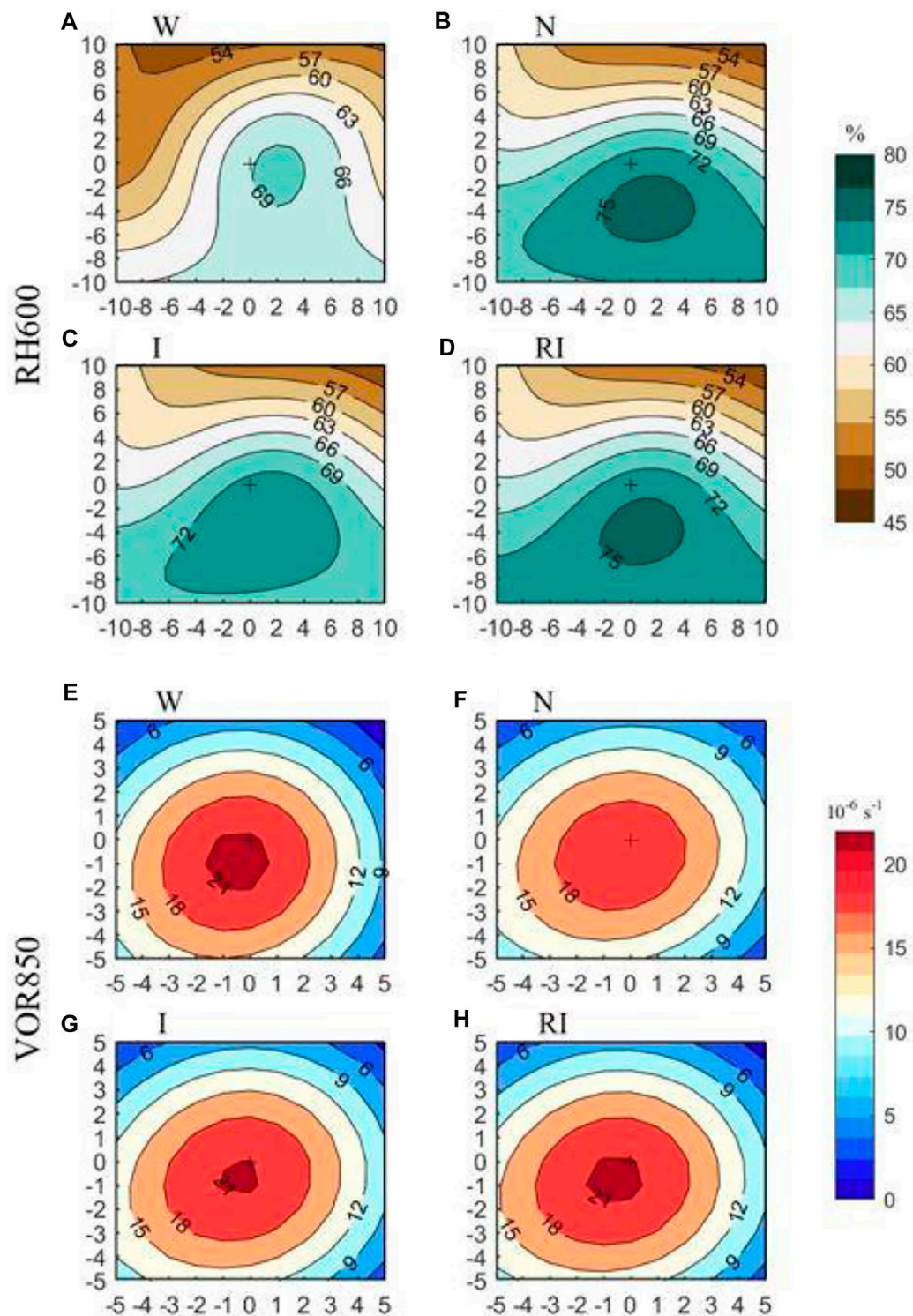


FIGURE 7 | The composites of (A–D) 600-hPa relative humidity (RH600, %) and (E–H) 850-hPa relative vorticity (VOR850, 10^{-6} s^{-1}) for four intensity change categories over the MSC described in Table 3. In each category, the top-left panel is the weakening (W) composite, the top-right panel is the neutral (N) composite, the bottom-left panel is the intensifying (I) composite, and the bottom-right panel is the rapidly intensifying (RI) composite. “+” represents the TC center, and the horizontal and vertical coordinates are the latitude and longitude (°) to the TC center.

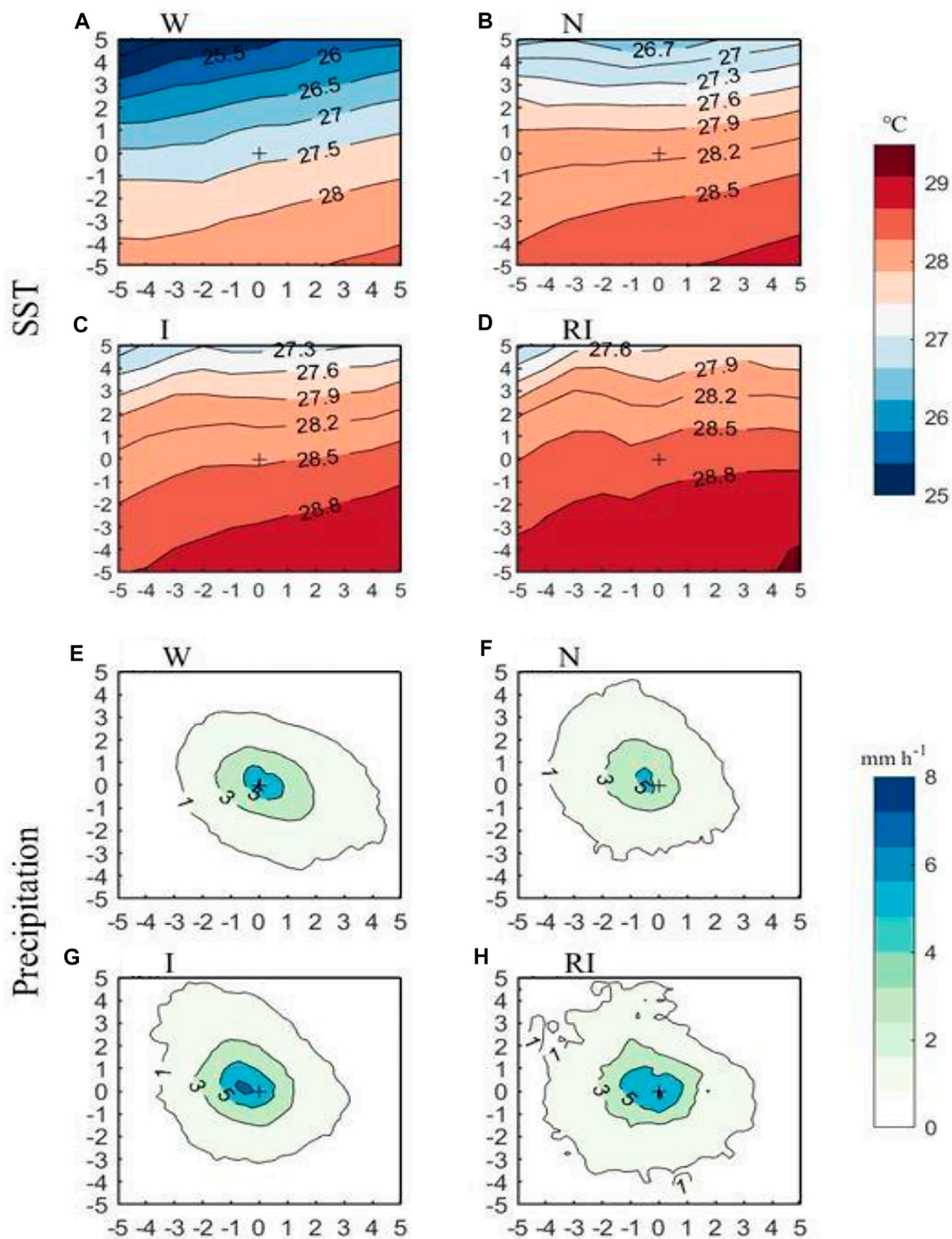


FIGURE 8 | As in **Figure 7**, but for **(A–D)** sea surface temperature (SST) in °C and **(E–H)** precipitation rate in mm h⁻¹.

probabilities of RI occurrence are also relatively large, reaching 14.39% and 13.61%, respectively. The rest in order are VWS ($\leq 5.02 \text{ m s}^{-1}$), SPDy ($\leq 14.84 \text{ km h}^{-1}$), upper-level divergence ($\geq 7.35 \text{ s}^{-1}$), and SST ($\geq 28.57^\circ\text{C}$), with the RI probabilities of

12.47%, 11.84%, 11.74%, and 11.39%, respectively. Note that although high SST is considered as favorable underlying surface conditions, SST does not show a high probability to RI occurrence, also consistent with the insignificant contribution

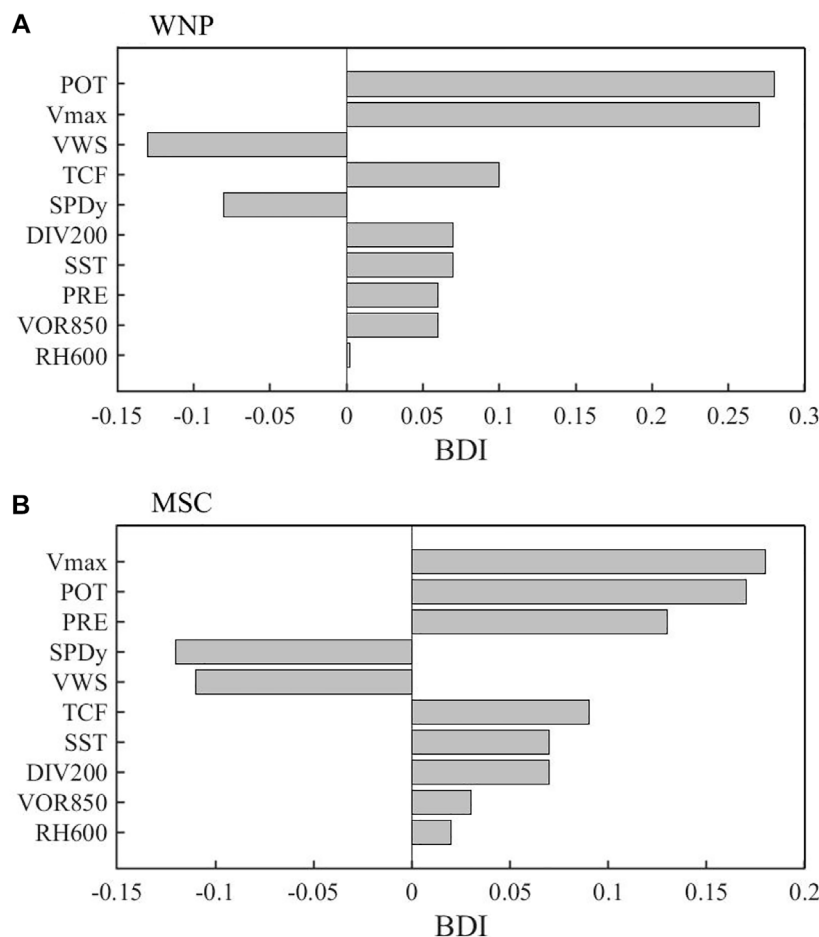


FIGURE 9 | Key factors in the TC RI and their corresponding box difference index (BDI) values over **(A)** the WNP and **(B)** the MSC. The factors have been ordered based on the BDI absolute value.

TABLE 4 | The threshold of each factor, the corresponding RI probability, and the lead time for TC RI over the MSC.

Variables	Threshold	P _{RI} (%)	T(h)
Vmax (m s ⁻¹)	≥33.45	16.23	00
POT	≥0.35	16.20	00
PRE (mm h ⁻¹)	≥1.87	14.39	24
TCF	≥0.58	13.61	00
VWS (m s ⁻¹)	≤5.02	12.47	06
SPDy (km h ⁻¹)	≤14.84	11.84	00
DIV200 (s ⁻¹)	≥7.35	11.74	00
RH600 (%)	≥69.05	11.68	12
SST (°C)	≥28.57	11.39	24
VOR850 (s ⁻¹)	≥14.00	11.25	00

shown in **Figure 9B** and previous studies (Hendricks et al., 2010; Hu and Duan, 2016).

It is also interesting to see whether a factor is meaningful for forecasting or, alternatively, whether a factor has any leading signal. As we see from **Table 4**, the factors with the earliest signal

are PRE and SST with a leading time of 24 h, followed by VWS with the leading time of 6 h, but other factors seem to show no leading signals. These results indicate that when Vmax, POT, PRE, and TCF meet the thresholds, it is most beneficial for the TC RI over the MSC, and other factors are often secondary and partly associated with the consequence of TC intensity change. In terms of prediction, only the inner-core precipitation rate, SST, mid-level RH, and VWS show good lead time signal and, thus, meaningful for TC RI prediction over the MSC.

CONCLUSION

In this study, we have compared the climatological characteristics of TC intensification and RI over the MSC and the WNP, and determined the key factors that affect TC IR and RI over the MSC based on the best-track TC data, ERA-Interim global reanalysis, and TRMM precipitation products during 1980–2018. Particularly, we have quantified the relative contributions of various factors to TC RI based on the box difference index

(BDI) method and identified the threshold of each factor at the time of the RI onset over the MSC.

The statistical results show that strong TCs have relatively lower (higher) frequency of intensification with IR less than (greater than) 12 m s^{-1} (12 h^{-1}) than weak TCs, but they often have faster weakening rates. The frequency of RI is higher for strong TCs than for weak TCs, indicating that TC RI over the MSC strongly depends on the intensity of the TC itself. Furthermore, TC intensification and RI show a distinct seasonal variation over the WNP and the MSC. Over the WNP, TC intensification and RI mostly occurred in July–October, with the peaks for intensification in August and for RI in September, respectively. In contrast, over the MSC, TC intensification and RI mainly occurred in July–September, both with the peak in September. It is worth noting that both the frequency of the intensifying cases and the ratio of the intensifying cases to all cases over the MSC show an increasing trend during 1980–2018. A similar trend has also been found in a recent study by Liu et al. (2021). If the trend continues, it may impose increasing challenges to forecasting and warning associated with landfalling TCs over China coast.

We have also analyzed and evaluated the climatological and persistence factors, large-scale environmental factors, ocean forcing factors, and TC structure factors that affect TC intensity changes over the MSC. Results from correlation and composite analyses demonstrate that TC intensification over the MSC is more likely to occur when a TC has relatively large initial and relative intensities, weak VWS, small TC translation component perpendicular to the coastline, relatively high TCF, strong upper-level divergence, warm SST and high core precipitation rate. A comparison of all these factors with TC RI indicates that Vmax and POT contribute the greatest to TC RI over both the MSC and the WNP among all factors examined. More interestingly, both PRE and SPDy are of the second importance to TC RI over the MSC, while both VWS and TCF are crucial to TC RI over the WNP. Furthermore, when Vmax, POT, precipitation rate, and TCF meet the thresholds with $V_{\max} \geq 33.45 \text{ m s}^{-1}$, $POT \geq 0.35$, $PRE \geq 1.87 \text{ mm h}^{-1}$, and $TCF \geq 0.58$, the probabilities of RI occurrence over the MSC are relatively large. In addition, precipitation rate, SST, and VWS show good leading signal to TC RI occurrence over the MSC.

Compared with previous studies (Chen et al., 2015; Hu and Duan, 2016; Liang et al., 2020), this study has focused on TC intensification and RI over all marginal seas of China, including the SCS. In addition, the TC internal factors including TCF and

precipitation rate, and the translation component perpendicular to the coastline have also been analyzed. Both qualitative and quantitative analysis results indicate that the RI occurrence over the MSC strongly depends on the characteristics of the TC itself, such as its intensity, inner-core precipitation rate, the degree of axisymmetry, and its motion component toward the coastline. Although high SST is favorable for TC intensification, its effect on TC RI is not statistically significant, consistent with previous studies (Hendricks et al., 2010; Hu and Duan, 2016).

Finally, we should point out that more factors, such as the upper ocean heat content (TCHP), atmospheric moisture transport flux, and the upper-tropospheric momentum flux, could also affect TC intensity change and RI, and can be examined in future studies. In addition, it should be noticed that some key factors discussed in this study are not independent of each other but are interrelated. How the independency may affect the results discussed in this study is unknown. Therefore, it is necessary to find a better algorithm that can provide a more accurate estimate of relative importance of key factors in future studies. Nevertheless, the findings in this study provide a basis for future research to improve the understanding and forecasting of TC intensity change in the MSC.

DATA AVAILABILITY STATEMENT

The original contributions presented in the study are included in the article/Supplementary Material, further inquiries can be directed to the corresponding author.

AUTHOR CONTRIBUTIONS

RZ developed the main idea. XL performed the analysis of observations. XL and RZ wrote the manuscript. YW and JX provided critical feedback. YW helped shape the research and manuscript.

FUNDING

This study is supported by the National Key R&D Program of China (2017YFC1501604) and the National Natural Science Foundation of China (41730960, 41875114, and 41875057).

REFERENCES

- Bister, M., and Emanuel, K. A. (2002). Low Frequency Variability of Tropical Cyclone Potential Intensity 1. Interannual to Interdecadal Variability. *J. Geophys. Res.* 107 (D24), 4801. doi:10.1029/2001jd000776
- Bosart, L. F., Velden, C. S., Bracken, W. E., Molinari, J., and Black, P. G. (2000). Environmental Influences on the Rapid Intensification of Hurricane Opal (1995) over the Gulf of Mexico. *Monthly Weather Rev.* 128, 322–325. doi:10.1175/1520-0493(2000)128<0322:eiotri>2.0.co;2
- Cecil, D. J., and Zipser, E. J. (1999). Relationships between Tropical Cyclone Intensity and Satellite-Based Indicators of Inner Core Convection: 85-GHz Ice-Scattering Signature and Lightning. *Mon. Wea. Rev.* 127, 103–123. doi:10.1175/1520-0493(1999)127<0103:rbcia>2.0.co;2
- Chen, H., and Zhang, D.-L. (2013). On the Rapid Intensification of Hurricane Wilma (2005). Part II: Convective Bursts and the Upper-Level Warm Core. *J. Atmos. Sci.* 70, 146–162. doi:10.1175/jas-d-12-062.1
- Chen, J., Sun, H., Gao, A., Lin, Z., and Huang, M. (2014). Comparative Analysis of Intensity Changes between Super Typhoons Rammasun (1409) and Damrey (0518) during the Period of Entering the Beibu Gulf. *Torrential Rain Disasters* 33, 392–400. [in Chinese, with English abstract]. doi:10.3969/j.issn.1004-9045.2014.04.012

- Chen, X., Wang, Y., and Zhao, K. (2015). Synoptic Flow Patterns and Large-Scale Characteristics Associated with Rapidly Intensifying Tropical Cyclones in the South China Sea. *Mon. Weather Rev.* 143, 64–87. doi:10.1175/mwr-d-13-00338.1
- Chen, Y., Gao, S., Li, X., and Shen, X. (2021). Key Environmental Factors for Rapid Intensification of the South China Sea Tropical Cyclones. *Front. Earth Sci.* 8, 609727. doi:10.3389/feart.2020.609727
- China Meteorological Administration (2012). *Tropical Cyclone Operation and Service Criterion (Fourth Version)*. Beijing: China Meteorological Press, 92.
- Emanuel, K. A. (1995). Sensitivity of Tropical Cyclones to Surface Exchange Coefficients and a Revised Steady-State Model Incorporating Eye Dynamics. *J. Atmos. Sci.* 52, 3969–3976. doi:10.1175/1520-0469(1995)052<3969:soctcs>2.0.co;2
- Emanuel, K. A. (1997). Some Aspects of hurricane Inner-Core Dynamics and Energetics. *J. Atmos. Sci.* 54, 1014–1026. doi:10.1175/1520-0469(1997)054<1014:saohic>2.0.co;2
- Emanuel, K. A. (1988). The Maximum Intensity of Hurricanes. *J. Atmos. Sci.* 45, 1143–1155. doi:10.1175/1520-0469(1988)045<1143:tmioh>2.0.co;2
- Emanuel, K., DesAutels, C., Holloway, C., and Korty, R. (2004). Environmental Control of Tropical Cyclone Intensity. *J. Atmos. Sci.* 61, 843–858. doi:10.1175/1520-0469(2004)061<0843:ecotci>2.0.co;2
- Fei, R., Xu, J., Wang, Y., and Yang, C. (2020). Factors Affecting the Weakening Rate of Tropical Cyclones over the Western North Pacific. *Mon. Weather Rev.* 148, 3693–3712. doi:10.1175/mwr-d-19-0356.1
- Fu, B., Peng, M. S., Li, T., and Stevens, D. E. (2012). Developing versus Nondeveloping Disturbances for Tropical Cyclone Formation. Part II: Western North Pacific. *Mon. Wea. Rev.* 140, 1067–1080. doi:10.1175/2011mwr3618.1
- Fudeyasu, H., Ito, K., and Miyamoto, Y. (2018). Characteristics of Tropical Cyclone Rapid Intensification over the Western North Pacific. *J. Clim.* 31, 8917–8930. doi:10.1175/jcli-d-17-0653.1
- Gao, S., and Chiu, L. S. (2010). Surface Latent Heat Flux and Rainfall Associated with Rapidly Intensifying Tropical Cyclones over the Western North Pacific. *Int. J. Remote Sensing* 31, 4699–4710. doi:10.1080/01431161.2010.485149
- Gao, S., Zhai, S., Chiu, L. S., and Xia, D. (2016). Satellite Air-Sea Enthalpy Flux and Intensity Change of Tropical Cyclones over the Western North Pacific. *J. Atmos. Sci.* 55, 425–444. doi:10.1175/jamc-d-15-0171.1
- Guo, X., and Tan, Z.-M. (2017). Tropical Cyclone Fullness: A New Concept for Interpreting Storm Intensity. *Geophys. Res. Lett.* 44, 4324–4331. doi:10.1002/2017gl073680
- Hendricks, E. A., Peng, M. S., Fu, B., and Li, T. (2010). Quantifying Environmental Control on Tropical Cyclone Intensity Change. *Mon. Weather Rev.* 138, 3243–3271. doi:10.1175/2010mwr3185.1
- Holland, G. J. (1997). The Maximum Potential Intensity of Tropical Cyclones. *J. Atmos. Sci.* 54, 2519–2541. doi:10.1175/1520-0469(1997)054<2519:tmptot>2.0.co;2
- Hong, X., Chang, S. W., Raman, S., Shay, L. K., and Hodur, R. (2000). The Interaction between Hurricane Opal (1995) and a Warm Core Ring in the Gulf of Mexico. *Mon. Wea. Rev.* 128, 1347–1365. doi:10.1175/1520-0493(2000)128<1347:tibhoa>2.0.co;2
- Hoshino, S., and Nakazawa, T. (2007). Estimation of Tropical Cyclone's Intensity Using TRMM/TMI Brightness Temperature Data. *J. Meteorol. Soc. Jpn.* 85, 437–454. doi:10.2151/jmsj.85.437
- Hu, H., and Duan, Y. (2016). Analysis of Environmental Variables of Rapidly Intensifying Tropical Cyclones in the South China Sea. *J. Trop. Meteorol.* 32, 299–310. [in Chinese, with English abstract]. doi:10.16032/j.issn.1004-4965.2016.03.002
- Huang, R., and Lei, X. (2010). Comparative Analysis of the Influence of Environment Field on Rapid Intensifying and Weakening of Tropical Cyclones over Offshore Waters of China. *J. Trop. Meteorol.* 26, 129–137. doi:10.3969/j.issn.1004-4965.2010.02.001 [in Chinese, with English abstract]
- Huffman, G. J., Bolvin, D. T., Nelkin, E. J., Wolff, D. B., Adler, R. F., Gu, G., et al. (2007). The TRMM Multisatellite Precipitation Analysis (TMPA): Quasi-Global, Multiyear, Combined-Sensor Precipitation Estimates at fine Scales. *J. Hydrol.* 8, 38–55. doi:10.1175/jhm560.1
- Kaplan, J., DeMaria, M., and Knaff, J. A. (2010). A Revised Tropical Cyclone Rapid Intensification index for the Atlantic and Eastern North Pacific Basins. *Wea. Forecast.* 25, 220–241. doi:10.1175/2009waf2222280.1
- Kaplan, J., and Demaria, M. (2003). Large-scale Characteristics of Rapidly Intensifying Tropical Cyclones in the North Atlantic basin. *Wea. Forecast.* 18, 1093–1108. doi:10.1175/1520-0434(2003)018<1093:lcort>2.0.co;2
- Kurihara, Y., Bender, M. A., and Ross, R. J. (1993). An Initialization Scheme of hurricane Models by Vortex Specification. *Mon. Wea. Rev.* 121, 2030–2045. doi:10.1175/1520-0493(1993)121<2030:aisohm>2.0.co;2
- Liang, J., Wu, L., and Gu, G. (2018). Rapid Weakening of Tropical Cyclones in Monsoon Gyres over the Tropical Western North Pacific. *J. Clim.* 31, 1015–1028. doi:10.1175/JCLI-D-16-0784.1
- Liang, M., Zhong, X., Xu, J., and Xu, F. (2020). Sudden Changes in Tropical Cyclone Intensity in South China Sea from 1960 to 2017. *J. Guangdong Ocean Uni.* 40, 83–91. [in Chinese, with English abstract]. doi:10.3969/j.issn.1673-9159.2020.03.011
- Lin, I.-I., Wu, C.-C., Pun, I.-F., and Ko, D.-S. (2008). Upper-Ocean Thermal Structure and the Western North Pacific Category 5 Typhoons. Part I: Ocean Features and the Category 5 Typhoons' Intensification. *Mon. Wea. Rev.* 136, 3288–3306. doi:10.1175/2008mwr2277.1
- Liu, Q., Song, J., and Klotzbach, P. J. (2021). Trends in Western North Pacific Tropical Cyclone Intensity Change before Landfall. *Front. Earth Sci.* 9, 780353. doi:10.3389/feart.2021.780353
- Lu, X., Yu, H., Yang, X., and Li, X. (2017). Estimating Tropical Cyclone Size in the Northwestern Pacific from Geostationary Satellite Infrared Images. *Remote Sensing* 9, 728. doi:10.3390/rs9070728
- Mei, Y., and Yu, J. (2016). Effect of Environment Field on Rapid Intensification Process of Tropical Cyclones over the Western North Pacific. *J. Atmos. Sci.* 36, 770–778. [in Chinese, with English abstract]. doi:10.3969/2016jms.0006
- Miyamoto, Y., Bryan, G. H., and Rotunno, R. (2017). An Analytical Model of Maximum Potential Intensity for Tropical Cyclones Incorporating the Effect of Ocean Mixing. *Geophys. Res. Lett.* 44, 5826–5835. doi:10.1002/2017gl073670
- Peng, M. S., Jeng, B.-F., and Williams, R. T. (1999). A Numerical Study On Tropical Cyclone Intensification. Part I: Beta Effect And Mean Flow Effect. *J. Atmos. Sci.* 56, 1404–1423. doi:10.1175/1520-0469(1999)056<1404:ansotc>2.0.co;2
- Shu, S., Ming, J., and Chi, P. (2012). Large-scale Characteristics and Probability of Rapidly Intensifying Tropical Cyclones in the Western North Pacific basin. *Wea. Forecast.* 27, 411–423. doi:10.1175/waf-d-11-00042.1
- Song, K., Tao, L., and Gao, J. (2021). Rapid Weakening of Tropical Cyclones in Monsoon Gyres over the Western North Pacific: A Revisit. *Front. Earth Sci.* 9, 688613. doi:10.3389/feart.2021.688613
- Su, H., Wu, L., Jiang, J. H., Pai, R., Liu, A., Zhai, A. J., et al. (2020). Applying Satellite Observations of Tropical Cyclone Internal Structures to Rapid Intensification Forecast with Machine Learning. *Geophys. Res. Lett.* 47. doi:10.1029/2020gl089102
- Wada, A. (2015). Verification of Tropical Cyclone Heat Potential for Tropical Cyclone Intensity Forecasting in the Western North Pacific. *J. Oceanogr.* 71, 373–387. doi:10.1007/s10872-015-0298-0
- Wang, H., and Wang, Y. (2014). A Numerical Study of Typhoon Megi (2010). Part I: Rapid Intensification. *Mon. Wea. Rev.* 142, 29–48. doi:10.1175/mwr-d-13-00070.1
- Wang, Y., Li, Y. L., and Xu, J. (2021b). A New Time-dependent Theory of Tropical Cyclone Intensification. *J. Atmos. Sci.* 78, 3855–3865. doi:10.1075/jas-d-21-0169.1
- Wang, Y., Li, Y. L., Xu, J., Tan, Z. T., and Lin, Y. L. (2021a). The Intensity-Dependence of Tropical Cyclone Intensification Rate in a Simplified Energetically Based Dynamical System Model. *J. Atmos. Sci.* 78, 2033–2045. doi:10.1175/jas-d-20-0393.1
- Wang, Y., Rao, Y., Tan, Z.-M., and Schönmann, D. (2015). A Statistical Analysis of the Effects of Vertical Wind Shear on Tropical Cyclone Intensity Change over the Western North Pacific. *Mon. Weather Rev.* 143, 3434–3453. doi:10.1175/mwr-d-15-0049.1
- Wang, Y. (2002a). Vortex Rossby Waves in a Numerically Simulated Tropical Cyclone. Part I: Overall Structure, Potential Vorticity, and Kinetic Energy Budgets*. *J. Atmos. Sci.* 59, 1213–1238. doi:10.1175/1520-0469(2002)059<1213:vrwian>2.0.co;2
- Wang, Y. (2002b). Vortex Rossby Waves in a Numerically Simulated Tropical Cyclone. Part II: The Role in Tropical Cyclone Structure and Intensity Changes*. *J. Atmos. Sci.* 59, 1239–1262. doi:10.1175/1520-0469(2002)059<1239:vrwian>2.0.co;2

- Wang, Y., and Wu, C.-C. (2004). Current Understanding of Tropical Cyclone Structure and Intensity Changes ? a Review. *Meteorol. Atmos. Phys.* 87, 257–278. doi:10.1007/s00703-003-0055-6
- Wu, C.-C., and Cheng, H.-J. (1999). An Observational Study of Environmental Influences on the Intensity Changes of Typhoons Flo (1990) and Gene (1990). *Mon. Wea. Rev.* 127, 3003–3031. doi:10.1175/1520-0493(1999)127<3003:aosoei>2.0.co;2
- Xu, J., and Wang, Y. (2015). A Statistical Analysis on the Dependence of Tropical Cyclone Intensification Rate on the Storm Intensity and Size in the North Atlantic. *Wea. Forecast.* 30, 692–701. doi:10.1175/waf-d-14-00141.1
- Xu, J., and Wang, Y. (2018). Dependence of Tropical Cyclone Intensification Rate on Sea Surface Temperature, Storm Intensity, and Size in the Western North Pacific. *Wea. Forecast.* 33, 523–537. doi:10.1175/waf-d-17-0095.1
- Yan, J. (1996). Climatological Characteristics of Rapidly Intensifying Tropical Cyclones over the Offshore of China. *J. Appl. Meteorol. Sci.* 1, 28–35.
- Yap, B. W., and Sim, C. H. (2011). Comparisons of Various Types of Normality Tests. *J. Stat. Comput. Simulation* 81, 2141–2155. doi:10.1080/00949655.2010.520163
- Zhang, Z., Wang, Y., Zhang, W., and Xu, J. (2019). Coastal Ocean Response and its Feedback to Typhoon Hato (2017) over the South China Sea: A Numerical Study. *J. Geophys. Res. Atmos.* 124, 13731–13749. doi:10.1029/2019jd031377
- Zheng, F., Zeng, Z., Lei, X., and Chen, L. (2016). A Statistical Study of Rapid Intensification of Typhoons over Coastal Water of China. *Plateau Meteorol.* 35, 198–210. [in Chinese, with English abstract]. doi:10.7522/j.issn.1000-0534.2014.00148

Conflict of Interest: The authors declare that the research was conducted in the absence of any commercial or financial relationships that could be construed as a potential conflict of interest.

The handling Editor declared a past co-authorship with one of the authors, JX.

Publisher's Note: All claims expressed in this article are solely those of the authors and do not necessarily represent those of their affiliated organizations, or those of the publisher, the editors, and the reviewers. Any product that may be evaluated in this article, or claim that may be made by its manufacturer, is not guaranteed or endorsed by the publisher.

Copyright © 2021 Li, Zhan, Wang and Xu. This is an open-access article distributed under the terms of the Creative Commons Attribution License (CC BY). The use, distribution or reproduction in other forums is permitted, provided the original author(s) and the copyright owner(s) are credited and that the original publication in this journal is cited, in accordance with accepted academic practice. No use, distribution or reproduction is permitted which does not comply with these terms.



Statistical Seasonal Forecasting of Tropical Cyclone Landfall on South China Utilizing Preseason Predictors

Oscar Y. W. Zhang¹, Kelvin T. F. Chan^{1,2,3*}, Lifeng Xu¹ and Zhenzhen Wu¹

¹School of Atmospheric Sciences, Sun Yat-sen University, and Southern Marine Science and Engineering Guangdong Laboratory (Zhuhai), Zhuhai, China, ²Guangdong Province Key Laboratory for Climate Change and Natural Disaster Studies, Sun Yat-sen University, Zhuhai, China, ³Key Laboratory of Tropical Atmosphere-Ocean System, Ministry of Education, Sun Yat-sen University, Zhuhai, China

OPEN ACCESS

Edited by:

Guanghua Chen,
Institute of Atmospheric Physics
(CAS), China

Reviewed by:

Xi Cao,
Chinese Academy of Sciences, China
Rui Jin,
China Meteorological Administration,
China

*Correspondence:

Kelvin T. F. Chan
chent25@mail.sysu.edu.cn

Specialty section:

This article was submitted to
Atmospheric Science,
a section of the journal
Frontiers in Earth Science

Received: 31 October 2021

Accepted: 25 November 2021

Published: 10 January 2022

Citation:

Zhang OYW, Chan KTF, Xu L and Wu Z
(2022) Statistical Seasonal Forecasting
of Tropical Cyclone Landfall on South
China Utilizing Preseason Predictors.
Front. Earth Sci. 9:806204.
doi: 10.3389/feart.2021.806204

Predicting tropical cyclone (TC) activities has been a topic of great interest and research. Many existing seasonal forecasting models of TC predict the numbers of TC geneses and landfalls based on the environmental factors in the peak TC season. Here, we utilize the mainstream reanalysis datasets in 1979–2005 and propose a statistical seasonal forecasting model, namely the SYSU model, for predicting the number of TC landfalls on South China based on the preseason environmental factors. The multiple linear regression analysis shows that the April sea level pressure over the tropical central Pacific, the March–April mean sea surface temperature southwest to Australia, the March 850-hPa zonal wind east to Japan, and the April 500-hPa zonal wind over Bay of Bengal are the significant predictors. The model is validated by the leave-one-out cross validation and recent 15-year observations (2006–2020). The correlation coefficient between the modeled results and observations reaches 0.87 ($p < 0.01$). The SYSU model exhibits 90% hit rate (38 out of 42) in 1979–2020. The Antarctic Oscillation, and the variations of the western North Pacific subtropical high and Intertropical Convergence Zone could be the possible physical linkages or mechanisms. The model demonstrates an operational potential in the seasonal forecasting of TC landfall on South China.

Keywords: seasonal forecast, South China, landfall, preseason predictors, tropical cyclone

INTRODUCTION

Tropical cyclone (TC) is one of the most devastating natural phenomena in the world. It could lead to heavy precipitation, flooding, strong winds, and storm surges to the coastal regions (Zhang et al., 2018), causing great economic and human losses. On average, about 80 TCs form globally per year. Among the basins, the western North Pacific (WNP) is a region with the most active tropical cyclogenesis. About one-third of global TCs, 26 on annual average, formed in the WNP during 1975–2011 (Liu and Chan, 2012; Hu et al., 2017), which could make landfall on Southeast Asia and East Asia. East Asia, including China, Korea, and Japan, etc., accommodates around 25% of the world's total population with a large portion dwelling in coastal regions. South China is one of these regions mostly affected by TCs. Thus, the accurate seasonal forecasting on predicting the seasonal or annual TC landfall numbers on South China is indispensable for disaster prevention and mitigation.

Many studies have made contributions to the prediction of TC activities in the past decades. In the early 1980s, the statistical seasonal forecasts of TC activities have been developed in the Australian (Nicholls, 1979), and dynamical forecast in North Atlantic (Gray, 1984a, b). Subsequently, the

statistical models of TC tracks (e.g., Hall et al., 2007), and annual TC frequency (e.g., Fan, 2010; Xie and Liu, 2014) in North Atlantic and North Indian Ocean (e.g., Wahiduzzaman et al., 2019) have also been proposed. The statistical forecasts in different parts of Pacific are also studied. For example, Nicholls (1992) forecasts for the Australian–southwest Pacific, while numbers of studies (e.g., Chan et al., 1998; Au-Yeung and Chan, 2012; Zhang and Villarini, 2019; Chan et al., 2021) work for the WNP. Apart from the statistical forecastings, the dynamical and hybrid statistical-dynamical forecastings (e.g., Huang and Chan, 2014; Ham and Kug, 2015; Zhang et al., 2017; Camp et al., 2019) have also been introduced. The hybrid models are built using climate indices as predictors to train the Poisson regression models. Using climate indices (e.g., subtropical high index) to build the model is apparent because it is much easier to deduce the physical linkages. Camargo et al. (2007), Zhan et al. (2012), and Klotzbach et al. (2019) reviewed the existing models all over the world. Among the studies above, most of them focus on the TC activities over the open oceans (e.g., Liu and Chan, 2003; Wang et al., 2007; Choi et al., 2010), while those focusing on the TC landfall activities (e.g., Fan, 2009; Goh and Chan, 2010), which is more beneficial with socioeconomic value, are rather less. Recently, studies by Gao et al. (2018) and Gao et al. (2020) identify the relationship between the tropical North Atlantic sea surface temperature (SST), and the TC landfalls on East Asia (including mainland China). Furthermore, Zhang and Villarini (2019) have built a simple model for the TC frequency in the WNP using only predictors based on SST. They suggested that using the SST-based predictors gives better predictability than the atmospheric-based predictors. However, although consistent increasing trends in frequency and intensity of landfalling TCs in East China were found, Gao et al. (2020) reviewed that the reported trends in landfalling TC activity in South China were divergent. Some studies (Zhang et al., 2012; Li et al., 2017; Zhang et al., 2019) showed no significant trend in landfalling TC intensity or frequency in South China. Park et al. (2014) suggested no trend in landfalling TC frequency, but a downward trend in landfalling TC intensity in South China, while Mei and Xie (2016) found a counter upward trend in landfalling TC intensity in South China. In addition, Lok and Chan (2017) projected fewer but stronger TCs could make landfall on South China in the late 21st century.

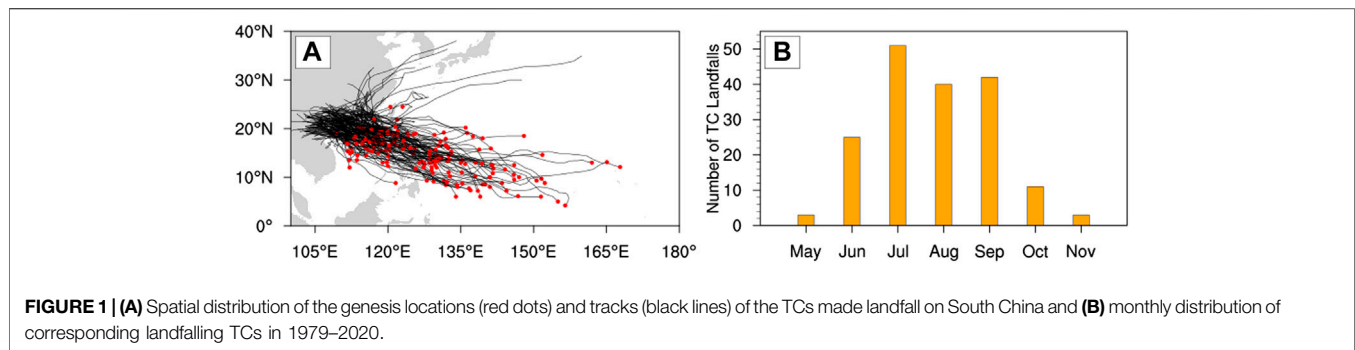
Notably, although the statistical seasonal forecasting of TC has therefore been a hot topic for decades, there is still a lot of rooms to improve. Some of them used a lot of predictors to build their models which could cause model overfitting and complexity. What is more, many forecasts are closed-source, internal use only, and provide little understanding of the physical linkages or mechanisms (see Klotzbach et al., 2019). Another deficiency of the existing models is that, numbers of studies mainly make use of the environmental factors in the peak TC season to make prediction (e.g., Au-Yeung and Chan, 2012; Wang et al., 2012; Zhang et al., 2017; Camp et al., 2019), while very less achieve this using the pre-season environmental factors (Chan et al., 2021). Choi et al. (2010) and Chen et al. (2015) suggested that the North Pacific Oscillation (NPO) index in spring could be a reliable predictor for predicting the TC activity over the WNP. Tian and

Fan (2019) utilized the predictors in preceding year (e.g., the preceding boreal summer SST) and adopted year-to-year increment method to predict the number of landfalling TCs on China during June to August. Chan et al. (2021) built a statistical seasonal forecasting model for predicting the TC activity over the WNP using the pre-season factors including both the dynamics and thermodynamics factors. Practically, due to the quasi-periodic or persistent anomalies, or the delayed memory due to the oceanic processes, some of the pre-season environmental factors could have “memory effect”, suggesting that their seasonal or annual characteristics are relatively sustainable and transmittable through certain time periods. Thereby, through selecting the particular factors in the pre-season, it is plausible to predict the landfall number in the upcoming TC season.

This study, therefore, aims 1) to establish an effective (not more than 4 predictors), open-source, and competitive (at least 80% hit rate) statistical seasonal forecasting model to predict the number of TC landfalls on South China in the upcoming TC season (May to December) using pre-season environmental factors, and 2) to propose possible physical linkages or mechanisms advancing the predictability and understanding of the seasonal forecasting. The paper is organized as follows: **section 2** describes the data and methodology. **Section 3** raises four potential predictors of the model. **Section 4** introduces our statistical seasonal forecasting model with the model validation. **Section 5** proposes the possible physical linkages or mechanisms. **Section 6** summarizes the study with discussion.

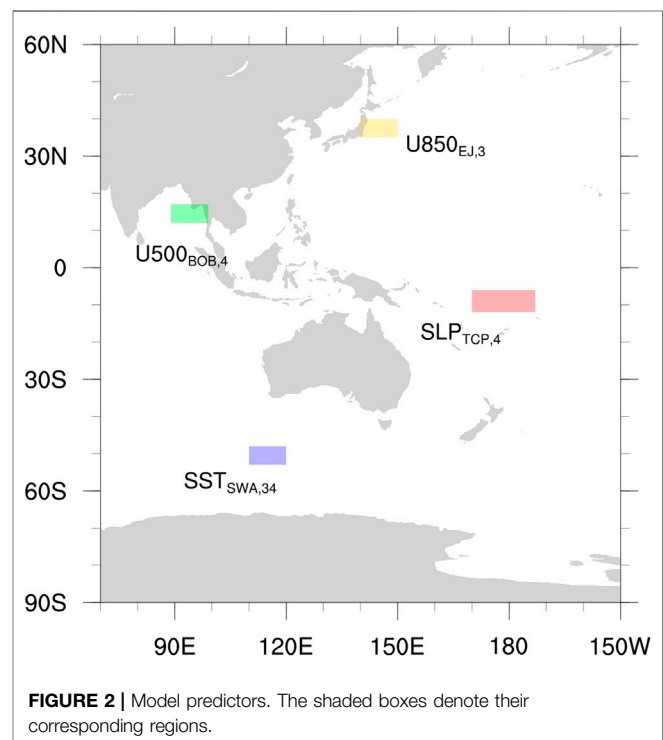
DATA AND METHODOLOGY

The best-track data from the China Meteorological Administration, including TC positions, and maximum 2-min average winds are adopted. The TCs that made landfall on South China in 1979–2020 are retrieved. Given that the benchmarks of the number of typhoons (TCs reaching typhoon intensity or above $\geq 34 \text{ m s}^{-1}$) from different meteorological centers are divergent (Chan et al., 2021), only those reaching tropical storm intensity or above (maximum sustained wind speed $\geq 17 \text{ m s}^{-1}$) are examined. In this study, South China includes Hainan, Guangxi, Guangdong, Hong Kong, and Macau. It is noted that those made landfall on East China or Vietnam at first and then moved to South China over land are not counted. In other words, only the “sea-to-land” attacks are focused. Those “land-to-land” attacks, which are relatively less destructive, are not considered. In addition, for the TC made several landfalls on South China counts once only. The TC that skirts along the coastal line, which has almost the same impacts as the narrow sense of landfalling TC, is also counted. From 1979 to 2020, there are 175 TCs made landfall on South China in total, that is, 4.2 TC landfalls per year on average. Most of them formed over the north of South China Sea (12–25°N, 105–122°E) and Philippine Sea (5–20°N, 122–142°E) then moved northwestward (**Figure 1A**). They mostly appeared in July, August, and September (**Figure 1B**). No TC made landfall on South China in December in 1979–2020.



The monthly fifth generation of European Centre for Medium-Range Weather Forecasts (ECMWF) atmospheric reanalysis of the global climate (ERA5; $0.25^\circ \times 0.25^\circ$, 1979–2020), the National Centers for Environmental Prediction—Climate Forecast System Reanalysis (NCEP-CFSR; $0.5^\circ \times 0.5^\circ$, 1982–2020), and the National Oceanic and Atmospheric Administration—Optimal Interpolation SST analysis version 2 (NOAA-OISSTv2; $1^\circ \times 1^\circ$, 1982–2020) are used for identifying the predictors and examining the possible physical linkages or mechanisms. These data are the mainstreams with high recognition and confidence nowadays. It is noted that two sets of reanalysis data (first: ERA5 from ECMWF; second: CFSR and OISSTv2 from NOAA) are employed in this study because this can avoid the uncertainties or arbitrary conclusions given by the single data source, and hence, increases the robustness of the model. The meteorological quantities like zonal wind, meridional wind, geopotential height, temperature, relative vorticity, sea level pressure (SLP), SST, and relative humidity in the preseason (i.e., January to April) are examined. The Antarctic Oscillation (AAO) index and the outgoing longwave radiation (OLR) data from the NOAA Climate Prediction Center (NCPCC) are also examined in this study.

DelSole and Shukla (2009) pointed out that during the screening of predictors, numbers of artificial skills could involve in the model. Therefore, to justifiably train and validate the model, the data before 2006 (24 years +) are used for the model training, while those in the recent 15 years (2006–2020) are used for the model validation in this study. The sampling ratio of the training set to validation set is approximately 2:1. The dozens of candidates from the typical aforementioned meteorological quantities at typical levels (surface, lower, mid, and upper troposphere) are selected by picking the high and significant regions from the correlation maps. Various areas of any significant regions (area $\geq 50^\circ$ latitude \times longitude) are extracted. The mutual correlations and collinearities between the predictors are then considered. The combination of four predictors (see next section) has the highest correlation with the number of TC landfalls is adopted to build the model. Standardizations of the predictors (by z-score) are applied in the multiple linear regression analysis so that all the predictors are in form of indices. To test whether there exists collinearity between predictors, the Variance Inflating Factor (VIF) method is performed. If the VIFs ($VIF = 1/(1-r_i^2)$) of predictors are less than $1/(1-R_i^2)$, where r_i is the correlation coefficient between the selected predictor and observed TC landfalls, and R_i is the correlation coefficient between the modeled and observed TC landfalls, then the multicollinearity is weak to affect



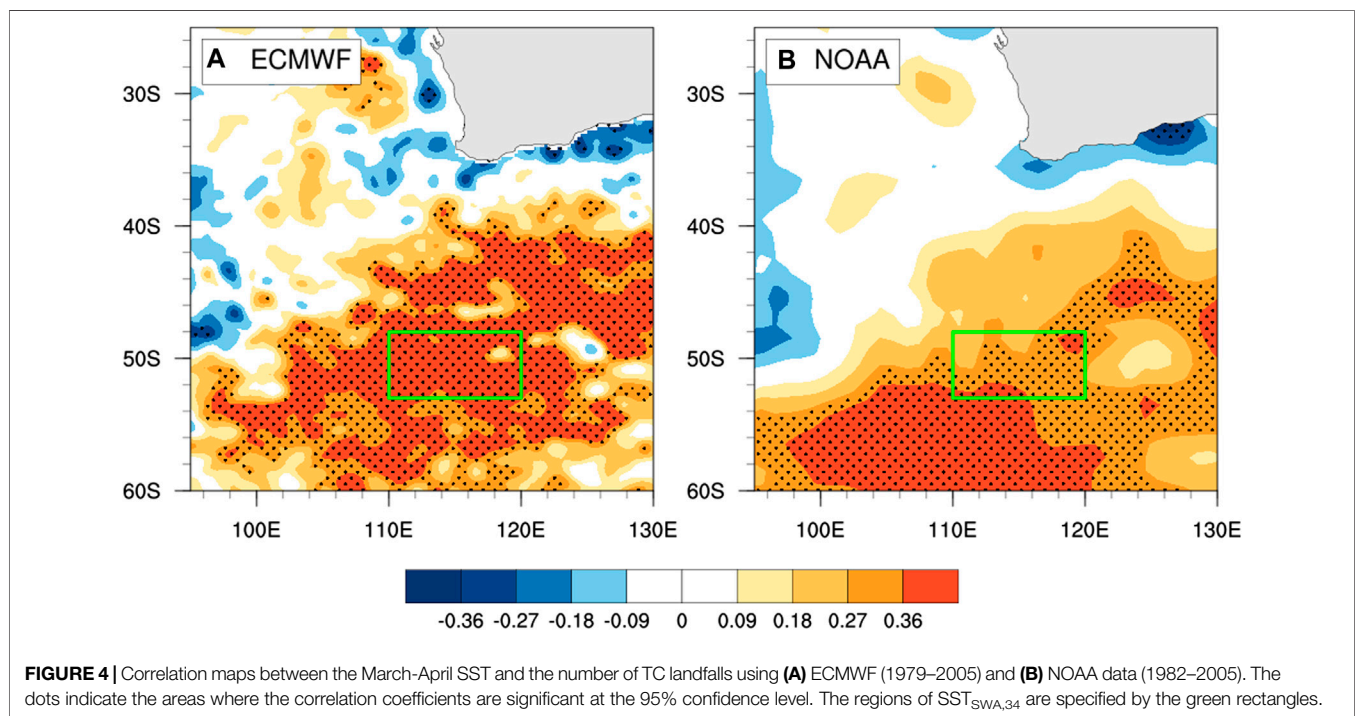
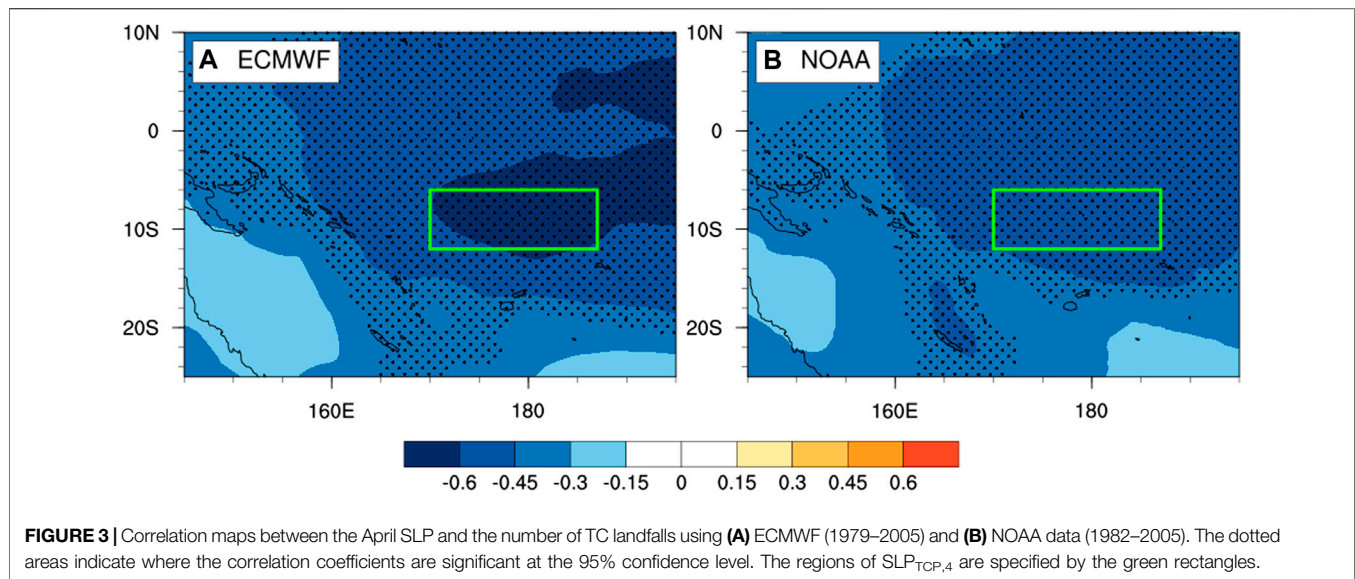
the coefficient estimates. In order to further validate the model skills, the leave-one-out cross validation has also been performed.

POTENTIAL PREDICTORS

In this study, four predictors are optimally selected. They are the April SLP over the tropical central Pacific ($SLP_{TCP,4}$), the March–April mean SST southwest to Australia ($SST_{SWA,34}$), the March 850-hPa zonal wind east to Japan ($U850_{EJ,3}$), and the April 500-hPa zonal wind over Bay of Bengal ($U500_{BOB,4}$). The corresponding geophysical regions are shown in Figure 2.

Sea Level Pressure

The regional SLP anomalies have been widely employed to reflect the teleconnections and oscillations (e.g., AAO, El Niño Southern



Oscillation (ENSO), and NPO) in both the ocean and atmosphere, which have close relationships with TC activities (e.g., Chen et al., 2015). In April, the region over the tropical central Pacific (12–6°S, 170°E–173°W, green rectangles in **Figure 3**) shows a high correlation ($r = -0.65$ and -0.52 for ECMWF, and NOAA data, respectively) between the SLP (hereafter $SLP_{TCP,4}$) and TC landfalls, suggesting that the $SLP_{TCP,4}$ could be an important potential predictor for the seasonal forecasting model.

Sea Surface Temperature

The SST anomalies over the main development region is known as one of the necessary thermodynamic factors for TC formation and development, where it determines the heat flux and moisture flux exchanges between the sea surface and atmosphere. The remote SST might impact on TC activities by causing anomalies of upper and lower tropospheric circulations (Zhan, 2011; Gao et al., 2018; Zhang and Villarini, 2019). **Figure 4** shows that the March-April SST southwest to

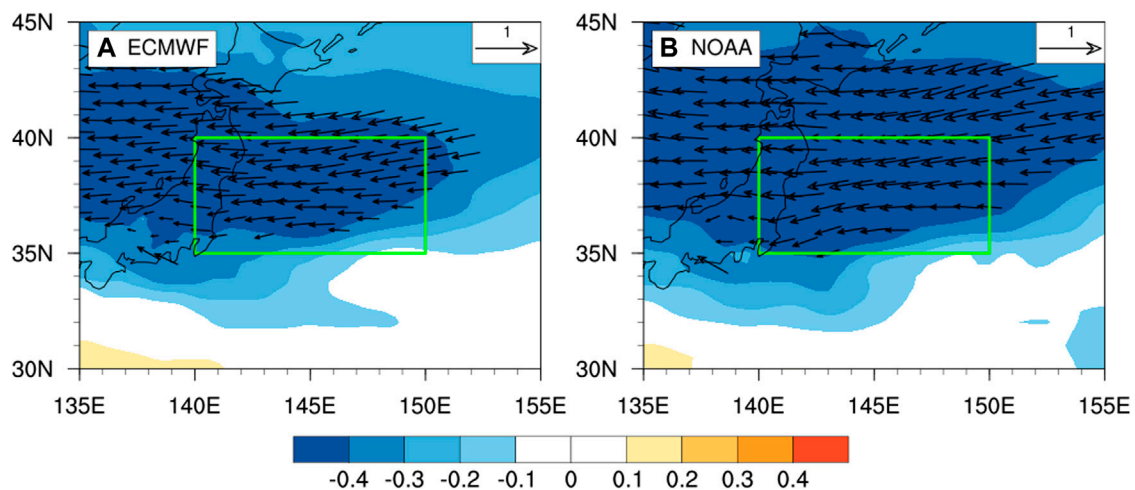


FIGURE 5 | Regression (vector; unit: m s^{-1}) and correlation (shading) of the March 850-hPa wind anomalies on the number of TC landfalls using (A) ECMWF (1979–2005) and (B) NOAA data (1982–2005). Either zonal wind or meridional wind statistically significant at the 95% confidence level are shown. Shading indicates the areas where the correlation coefficients of the zonal wind anomalies are significant at the 95% confidence level. The regions of $U850_{EJ,3}$ are specified by the green rectangles.

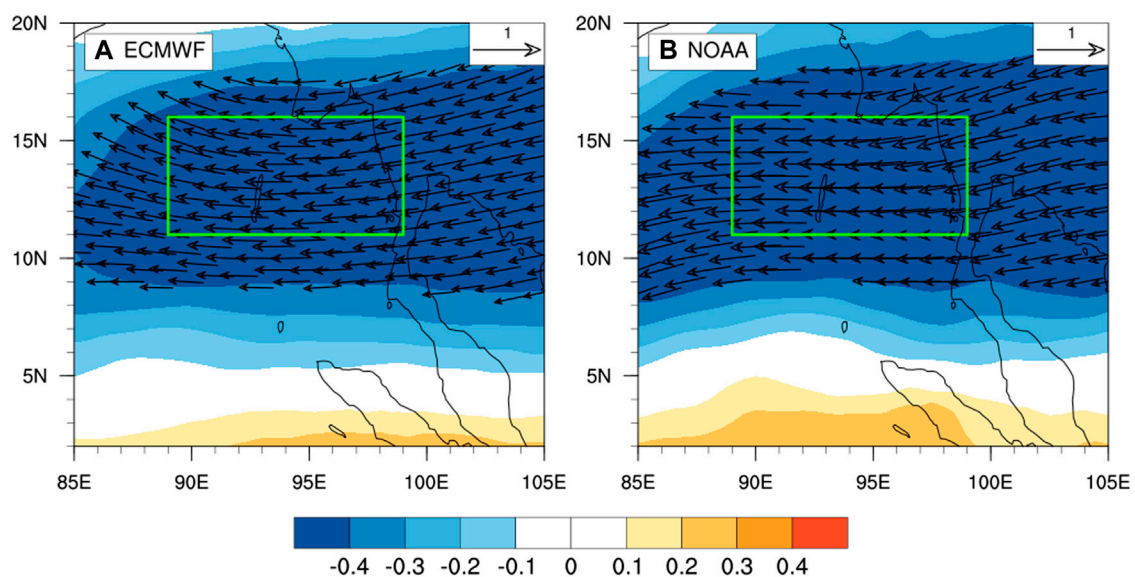


FIGURE 6 | Regression (vector; unit: m s^{-1}) and correlation (shading) of the April 500-hPa wind anomalies on the number of TC landfalls using (A) ECMWF (1979–2005) and (B) NOAA data (1982–2005). Either zonal wind or meridional wind statistically significant at the 95% confidence level are shown. Shading indicates the areas where the correlation coefficients of the zonal wind anomalies are significant at the 95% confidence level. The regions of $U500_{BOB,4}$ are specified by the green rectangles.

TABLE 1 | Mutual correlation coefficients among the $SLP_{TCP,4}$, $SST_{SWA,34}$, $U850_{EJ,3}$, and $U500_{BOB,4}$ in the ECMWF and NOAA data.

	ECMWF (1979–2005)				NOAA (1982–2005)			
	$SLP_{TCP,4}$	$SST_{SWA,34}$	$U850_{EJ,3}$	$U500_{BOB,4}$	$SLP_{TCP,4}$	$SST_{SWA,34}$	$U850_{EJ,3}$	$U500_{BOB,4}$
$SLP_{TCP,4}$	1	−0.242	−0.394*	−0.282	1	−0.010	−0.123	−0.069
$SST_{SWA,34}$		1	0.164	0.377		1	0.244	0.316
$U850_{EJ,3}$			1	0.040			1	0.284
$U500_{BOB,4}$				1				1

Values with single asterisk represent they are significant at the 95% confidence levels.

TABLE 2 | Correlation coefficients, RMSEs, MAEs, intercepts, and regression coefficients of the Model E and Model N.

	Model E (based on ECMWF, 1979–2005)	Model N (based on NOAA, 1982–2005)
r	0.87**	0.85**
RMSE	0.95	1.02
MAE	0.59	0.58
Intercept	4.12	4.04
SLP _{TCP,4}	−0.80**	−0.52*
SST _{SWA,34}	0.62**	0.45**
U850 _{EJ,3}	−0.51*	−0.66**
U500 _{BOB,4}	−0.42*	−0.69**

Values with single asterisk and double asterisks represent they are significant at the 95 and 99% confidence levels, respectively.

Australia (48–53°S, 110–120°E; indicated by the green rectangles) positively correlates with the TC landfalls ($r = 0.63$ and 0.44 for ECMWF, and NOAA data, respectively). The observable difference of SST correlations found in **Figure 4** is likely due to the heterogeneities of data sources and resolutions (ERA5: $0.25^\circ \times 0.25^\circ$; NOAA-OISSTv2: $1^\circ \times 1^\circ$), and the data periods (ERA5 starts from 1979, while NOAA-OISSTv2 starts from 1982; see next section). The positive correlation implies the higher SST in this region (hereafter SST_{SWA,34}) links to more TC landfalls. Thus, it could be a viable predictor to help establishing the forecasting model via the teleconnection.

Zonal Wind

Although lots of environmental factors (e.g., SST, pressure, and geopotential height) are commonly employed in various statistical forecasting models, the zonal and meridional winds, which are the important components of atmospheric circulations, are seldom adopted. Here we find that the 850-hPa zonal wind east to Japan in March (hereafter U850_{EJ,3}; 35–40°N, 140–150°E; green rectangles in **Figure 5**) and the 500-hPa zonal wind over Bay of Bengal in April (hereafter U500_{BOB,4}; 12–17°N, 89–99°E; green

rectangles in **Figure 6**) have significant correlations and regressions on the TC landfalls. The correlation coefficients between the U850_{EJ,3} and the number of TC landfalls are respectively -0.51 and -0.61 for ECMWF, and NOAA data, while those between the U500_{BOB,4} and TC landfalls are -0.50 and -0.62 , correspondingly. The negative correlations suggest that these two easterly anomalies link to a decrease in TC landfalls.

STATISTICAL SEASONAL FORECASTING MODEL

Table 1 shows that the mutual correlations among the aforementioned predictors are weak. These imply the predictors are mostly independent of each other. Although that between the SST_{SWA,34} and U850_{EJ,3} in the ECMWF dataset is a bit higher, the VIF values of all predictors are less than 4.1 (result of $1/(1-R_i^2)$; see **section 2**), suggesting that there exists no multicollinearity between predictors. The multiple linear regression analyses further confirm this, in which the regression coefficients of the four predictors all pass the significance test (**Table 2**).

In this study, the multiple linear regression model based on the ECMWF data is named as Model E, while that based on the NOAA data is named as Model N. **Table 2** shows that both models are primarily consistent with each other, suggesting that the robustness of predictors are strong. The correlation coefficients between the modeled TC landfalls and observed TC landfalls reach 0.85–0.87. The corresponding root mean squared errors (RMSEs) are close to 1. After performing the leave-one-out cross validation, the correlation coefficients between the modeled TC landfalls, and observed TC landfalls become 0.79–0.82, while the corresponding RMSEs are 1.02 and 1.10 for Model E and Model N, respectively. These results demonstrate that both models have a competitively high potential on predicting seasonal TC landfalls on South China.

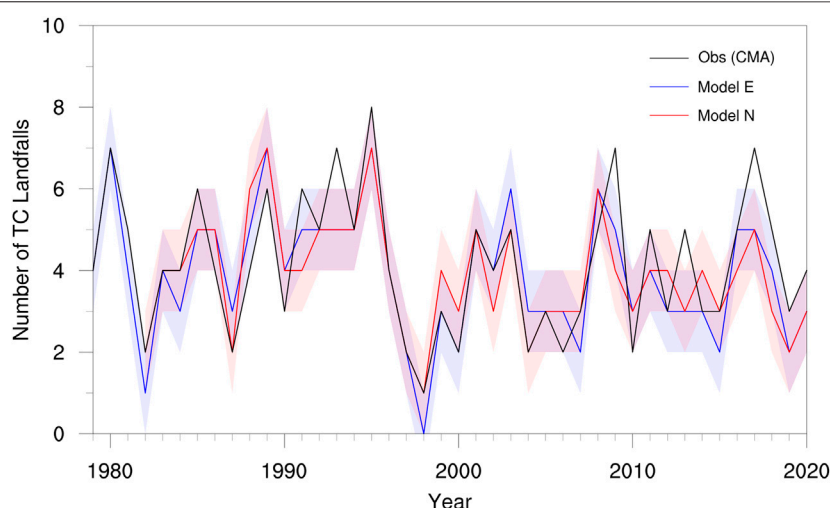


FIGURE 7 | Time series of the observed (black line) and modeled TC landfalls on South China based on the ECMWF (Model E; blue line) and NOAA (Model N; red line) data. The blue and red shadings indicate the model uncertainties (denoted by ± 1 of corresponding RMSE in Model E and Model N, and then rounded to the nearest integers, respectively). Note that the modeled results before 2006 are based on the model training, those after are for the model validation.

TABLE 3 | Extreme high years (>1) and low years (<-1) of four predictors based on the respective standardized values of predictors in 1979–2020.

	Extreme high years	Extreme low years
SST _{SWA,34}	1980, 1983, 1989, 2003, and 2020	1982, 1987, 2000, 2015, and 2019
SLP _{TCP,4}	1983, 1998, 2007, 2010, 2012, and 2020	1980, 1986, and 1995
U850 _{EJ,3}	2000, 2002, 2005, 2013, and 2014	1983, 1989, 1995, 2008, and 2017
U500 _{BOB,4}	1982, 1990, 1997, 1998, 2018, and 2020	1989, 1999, 2000, 2001, and 2008

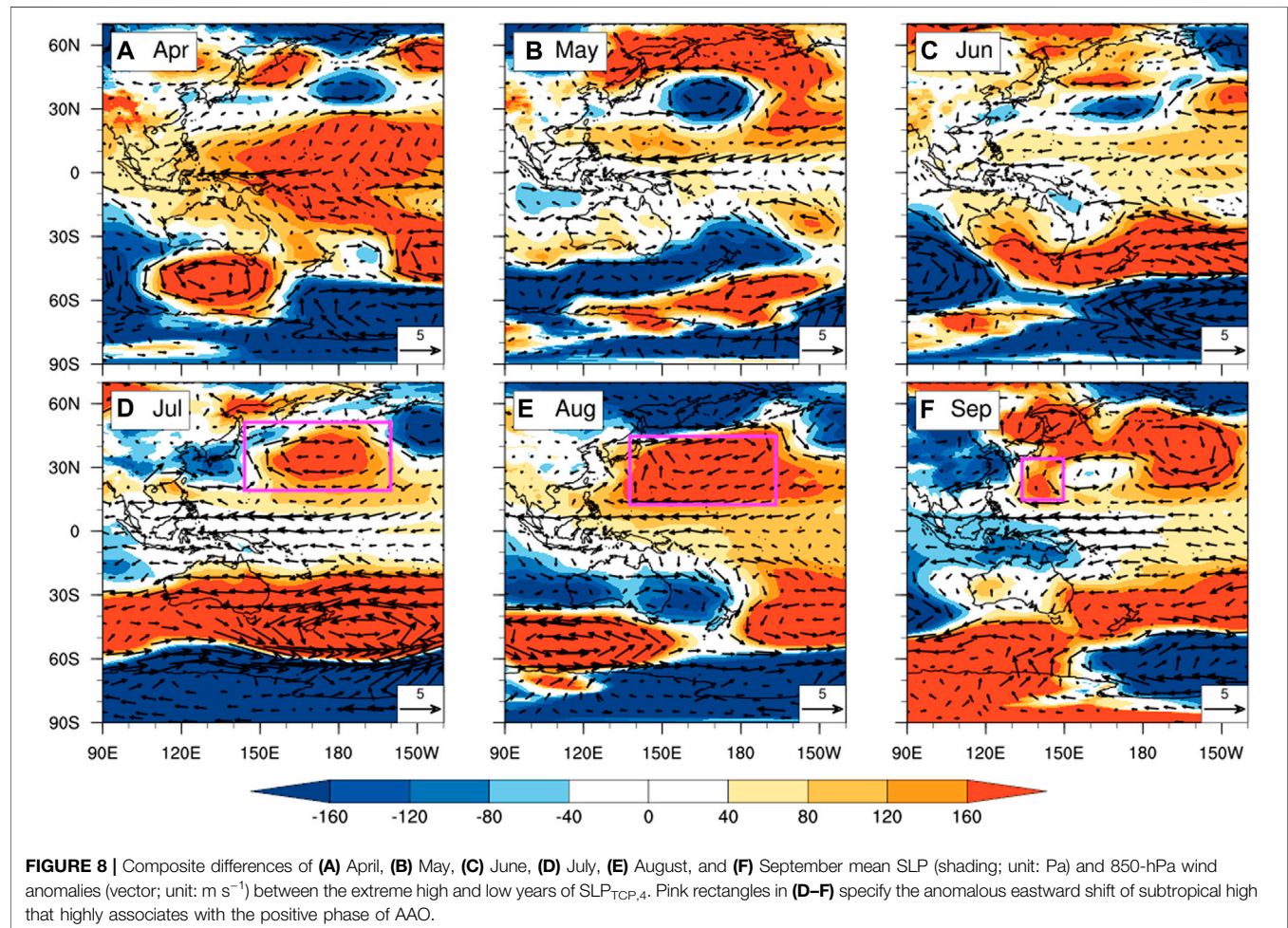
Figure 7 shows that the modeled landfall number matches well with the observations in 1979–2005. The errors are generally within ± 1 . The mean absolute errors (MAEs) of Model E and Model N are 0.59 and 0.58, respectively (**Table 2**). Notably, besides the leave-one-out cross validation, the models are further validated by the recent 15-year (2006–2020) observations. The corresponding absolute errors are ≤ 2 .

To bring the results from research into practice and application, a new model, namely the Sun Yat-sen University (SYSU) model, is proposed. The SYSU model takes both the Model E and Model N into consideration. The prediction range of the SYSU model is defined as the maximum range of both the modeled landfall numbers ± 1 of their corresponding RMSEs, and then rounded to the nearest integers. Visually, it is exactly the all-

inclusive shadings shown in **Figure 7**. Once the observed landfall number falls within the prediction range, we call the model hits. **Figure 7** shows that the SYSU model exhibits a 90% hit rate in 1979–2020 (38 out of 42). This is promising for a statistical model which only utilizes 4 preseason factors.

POSSIBLE PHYSICAL LINKAGES OR MECHANISMS

In order to figure out the possible physical linkages or mechanisms of the model, based on the standardized predictors, the corresponding meteorological quantities in the extreme high years (>1) and low years (<-1) are investigated



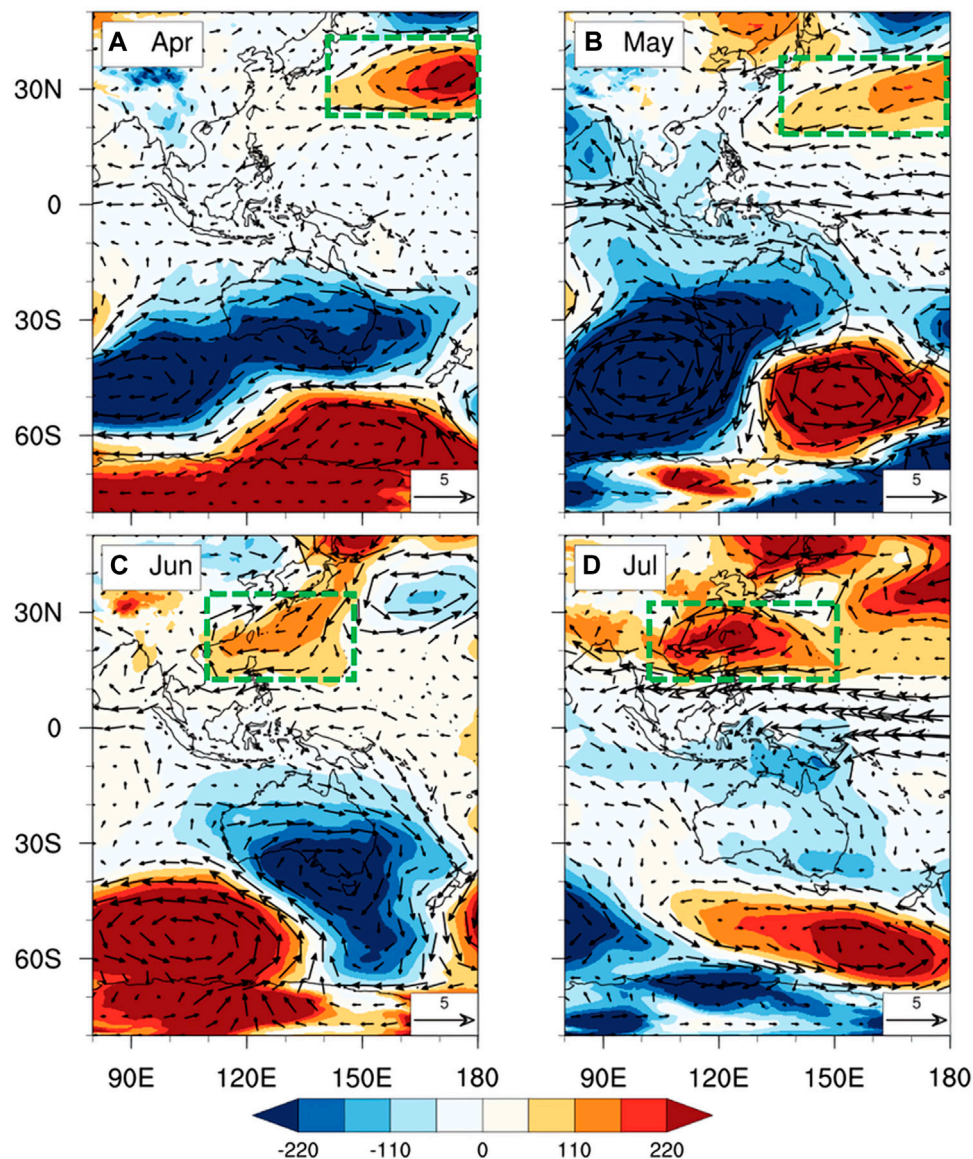


FIGURE 9 | Composite differences of (A) April, (B) May, (C) June, and (D) July mean SLP (shading; unit: Pa) and 850-hPa wind anomalies (vector; unit: m s^{-1}) between the extreme high and low years of $\text{SST}_{\text{SWA},34}$. Green dash rectangles in (A–D) indicate the seasonal shift of anomalous westward or southwestward shift of subtropical high that highly associates with the negative phase of AAO.

(Table 3). Examining the composite difference between the extreme high and low years can magnify the signals which help the identification. Meanwhile, incorporating what have found in previous studies, three possible physical linkages or mechanisms are proposed.

Antarctic Oscillation

The Antarctic Oscillation (AAO), a dominant low frequency mode of atmospheric variability in the Southern Hemisphere, also known as Southern Annular Mode, is suspected to be a possible mechanism affecting landfalling TC activity. The AAO index could be measured by the zonal mean SLP difference

between 40°S and 65°S (Gong and Wang, 1999). Fan et al. (2003) studied the annual variations of AAO and the distribution of correlation coefficient between AAO index and monthly mean SLP anomalies in each month, and proposed series of conclusions. From January to December, the areas of negative correlation are basically the same, located from 60°S to 90°S . During austral winter, the areas of positive correlation could expand from 50°S to 30°N , and even to 60°N during June, July, and August. These suggest that the impacts of AAO could persist and even enhance from boreal spring to summer. Yuan et al. (2021) further found that the AAO in boreal spring can influence the zonal wind and meridional circulation in the Northern

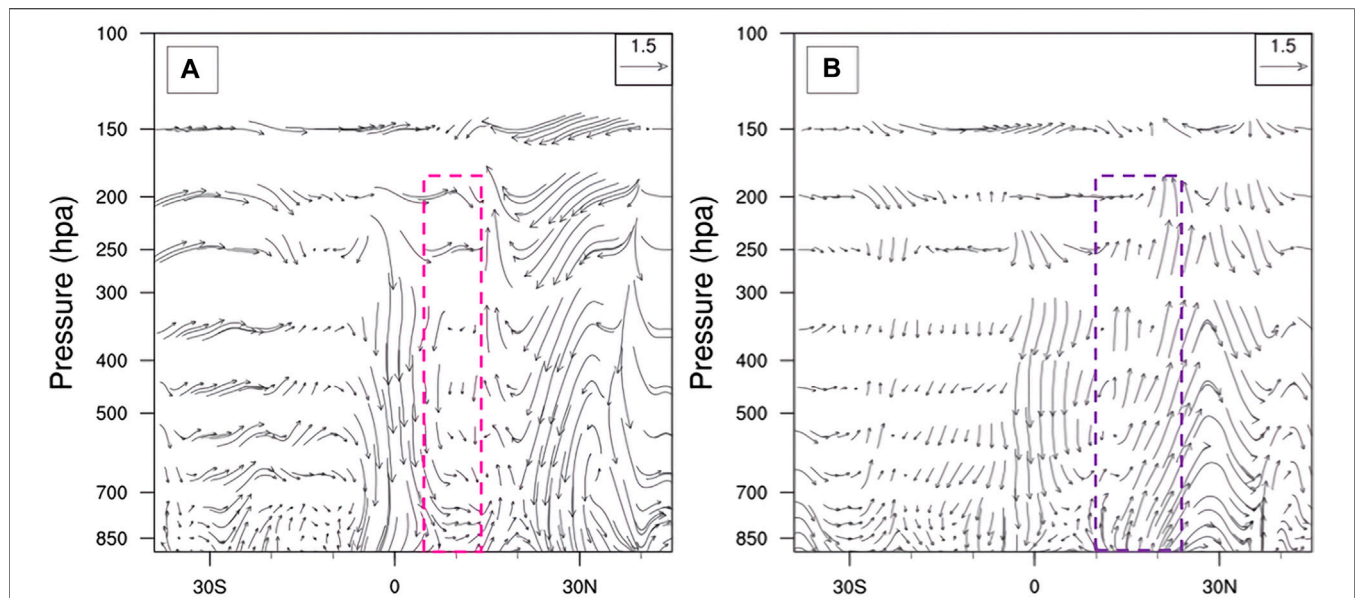


FIGURE 10 | Height-latitude cross sections of the composite difference of anomalous meridional circulation (**A**: 123–128°E; **B**: 110–120°E; unit: m s^{-1}) between the extreme high years and low years of (**A**) $\text{SLP}_{\text{TCP},4}$ in July, August, and September and (**B**) $\text{SST}_{\text{SWA},34}$ in June, July, and August. Vertical velocity is multiplied by 100. The pink (purple) dash rectangle specifies the anomalous downdraft (updraft) in the 5–13°N (10–25°N) band in positive $\text{SLP}_{\text{TCP},4}$ ($\text{SST}_{\text{SWA},34}$).

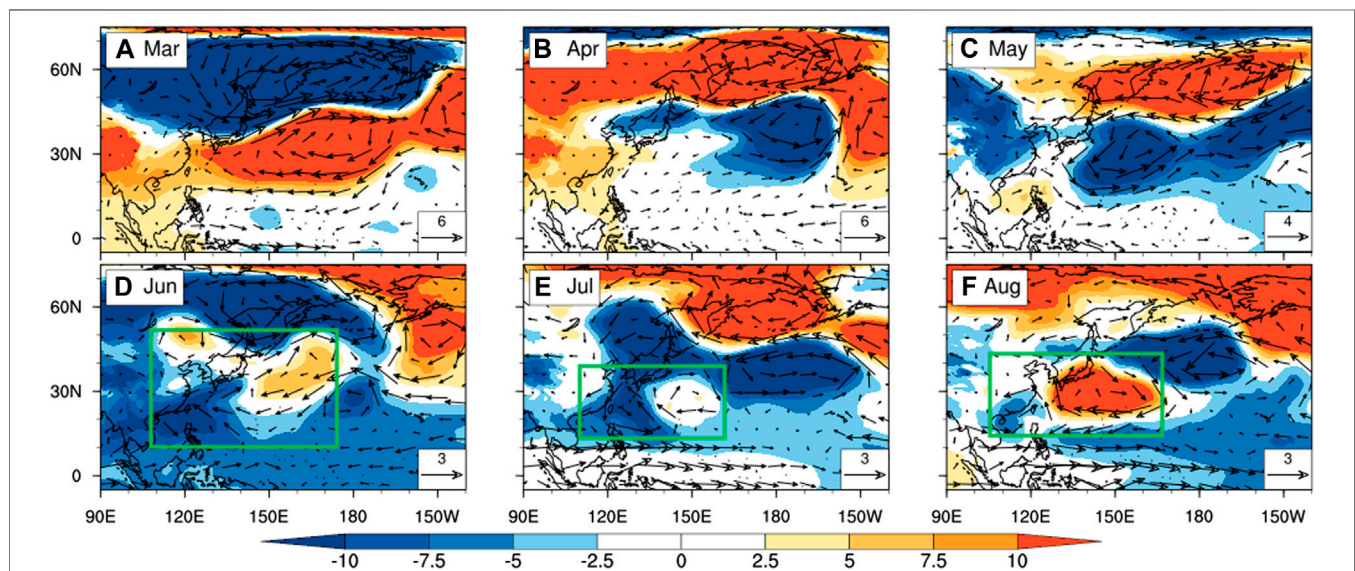
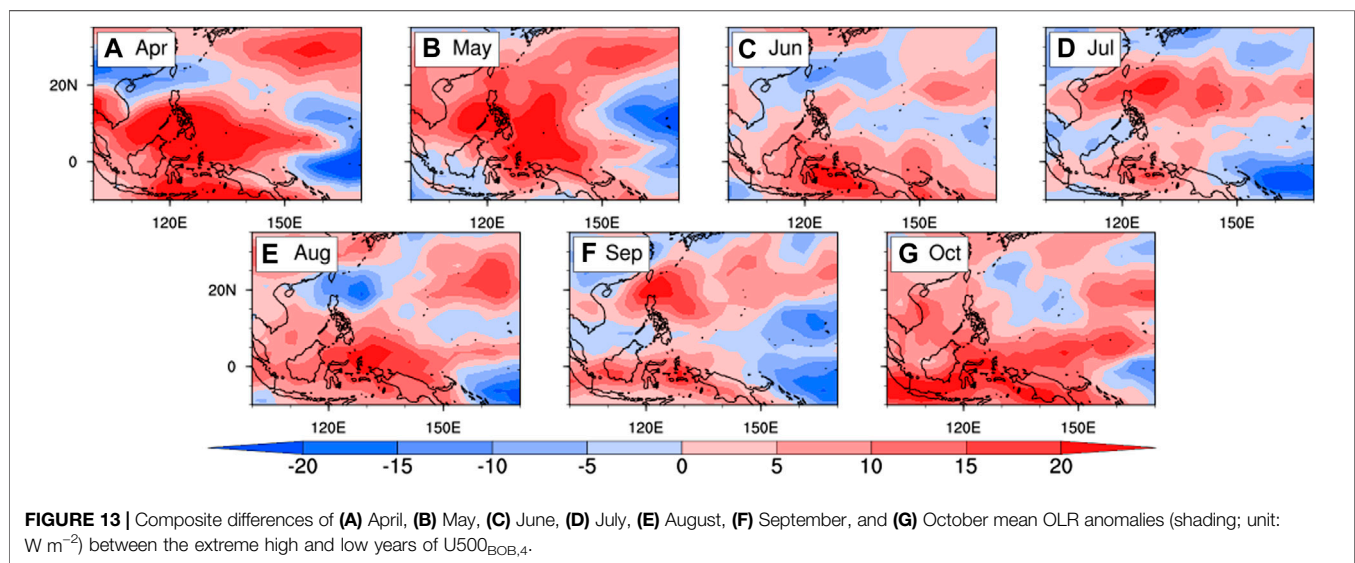
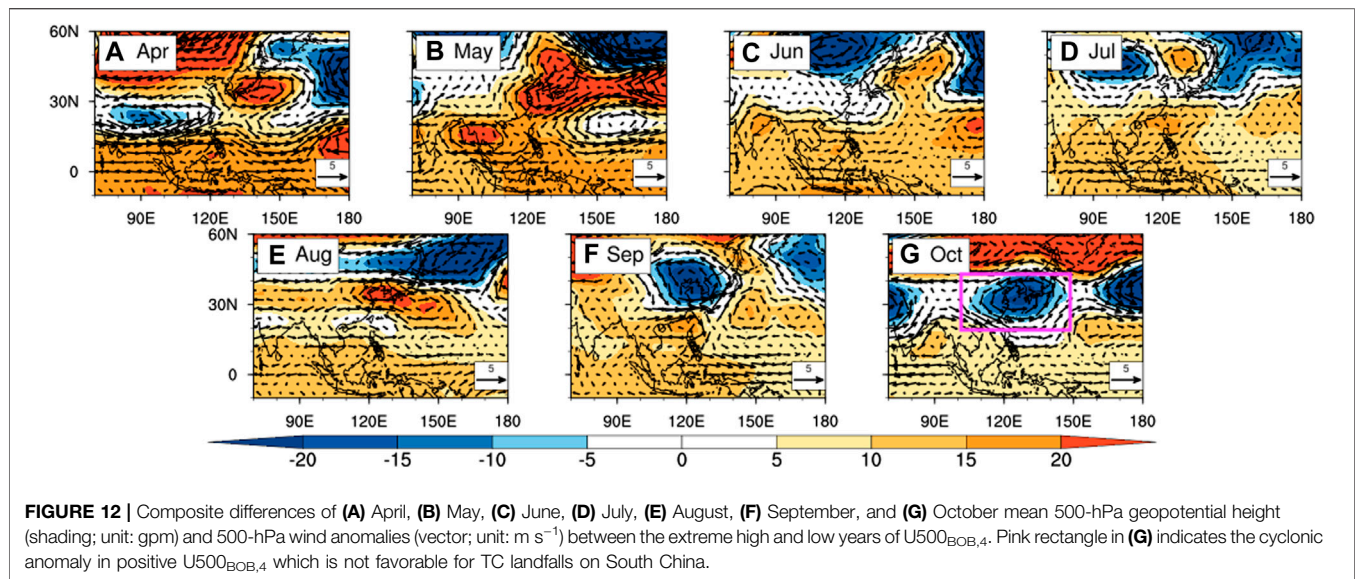


FIGURE 11 | Composite differences of (**A**) March, (**B**) April, (**C**) May, (**D**) June, (**E**) July, and (**F**) August mean 850-hPa geopotential height (shading; unit: gpm) and 850-hPa wind anomalies (vector; unit: m s^{-1}) between the extreme high and low years of $\text{U850}_{\text{EJ},3}$. Green rectangles in (**D–F**) indicate the anomalous eastward shift of subtropical high over the WNP in positive $\text{U850}_{\text{EJ},3}$.

Hemisphere, leading to the southeasterly and ascending motion anomalies, and thus, the precipitation anomaly in North China during boreal summer. In this study, we find that the correlation coefficient between $\text{SLP}_{\text{TCP},4}$ and April AAO index is about 0.56, while the correlation coefficient between $\text{SST}_{\text{SWA},34}$ and March–April AAO index is -0.42 . The results suggest that these two

predictors are highly associated with the positive and negative phases of AAO, respectively.

Ho et al. (2005) and Wang and Fan (2007) suggested that the AAO would lead to anomalous anticyclonic circulation over the WNP during boreal summer. During positive phase of AAO, the subtropical high in the WNP is weaker and retreats eastward



(pink rectangles in **Figures 8D–F**), leading to an unfavorable condition for TC activity in the proximity of South China, but favorable for TC passage or landfall to East China and Japan. On the contrary, during the negative phase of AAO, the subtropical high is stronger over the WNP and extends westward (**Figure 9**). In addition, a seasonal southwestward shift of anomalous anticyclone from April to July (green dash rectangles in **Figures 9A–D**) takes place. These two together favor more landfalling TCs on South China.

Meanwhile, Wang and Fan (2007) and Choi et al. (2010) also suggested that AAO might impact on the WNP TC activity through the teleconnection of meridional circulation anomaly from the middle latitudes in the Southern Hemisphere to the

tropical WNP. As the region of $\text{SST}_{\text{SWA},34}$ has similar longitude range with that of South China Sea, the way how the AAO modifies the later meridional circulation could be another possible mechanism. The composite difference of anomalous meridional circulation shows that there is an anomalous downdraft in $5\text{--}13^\circ\text{N}$ during July to September (pink dash rectangle in **Figure 10A**), which highly associates with the positive phase of AAO and is unfavorable for convective activity over Philippines Sea. On the contrary, the anomalous updraft in $10\text{--}25^\circ\text{N}$ during peak TC season (purple dash rectangle in **Figure 10B**) is favorable for convective activity over the north of South China Sea. These results are highly consistent with Choi et al. (2010).

Subtropical High

The composite differences of the 850-hPa geopotential height and wind anomalies between the extreme high years and low years of $U850_{EJ,3}$ show that there exists a persistent anomalous anticyclone southeast to Japan and an anomalous cyclone to its west in the June, July, and August (green rectangles in **Figure 11**). These imply there is an anomalous eastward shift of subtropical high over the WNP in positive $U850_{EJ,3}$. As TC generally moves along the western and southern periphery of the WNP subtropical high, the anomalous eastward shift could steer more TCs towards East China, and Korea, or Japan in positive $U850_{EJ,3}$. Although how the $U850_{EJ,3}$ propagates signals and affects the subtropical high activity from March to the peak TC season in the WNP remain unclear, it shows a strong linkage with the variation of subtropical high that is physically indicative of the TC landfall on South China. There might be signal transformation and/or propagation process (es) from the boreal spring. For example, Hu et al. (2020) performed 10-year high-pass filtering method to show significant signals of heat flux during March and April over the WNP, which results in anticyclonic anomaly over low latitudes of the WNP and impacts on the East Asia monsoon onset in May. Though it is not suitable to employ high-pass filtering in real-time forecasting because this requires the data beyond the time series (Wheeler and Hendon, 2004), it provides an idea to understand the processes. More investigations are warranted.

Intertropical Convergence Zone

About 80% of TCs form and develop in ITCZ (Chen and Ding, 1979). The position and intensity of ITCZ are important in TC activities (Zhang et al., 1995; Liu et al., 2007; Liu et al., 2009; Cao et al., 2015). It has been found that the stronger ITCZ favors more cyclogenesis, and vice versa. **Figure 12** shows that there is the persistent positive geopotential height anomaly in 0–30°N from April to October, suggesting that during positive $U500_{BOB,4}$ the convection over ITCZ is weaker, and thus unfavorable for cyclogenesis activity. This is evident by the persistent positive OLR (proxy of convection) anomaly over low latitudes west of 150°E (**Figure 13**). Meanwhile, the persistent anomalous westerly in the proximity of South China is not favorable for TC landfalls. In addition, the westerly and northwesterly associated with the anomalous low (pink rectangle in **Figure 12G**) could be detrimental to TC landfalls on South China in October. Although how the $U500_{BOB,4}$ results in or impacts on the persistence of ITCZ activity from pre-season to late season are unclear, it demonstrates an evident linkage with the variation of ITCZ intensity that is physically indicative of the TC landfalls on South China. More work on this is also needed.

SUMMARY AND DISCUSSION

In this study, an effective, open source, and competitive statistical seasonal forecasting model, namely the SYSU model, for predicting the annual TC landfall (reaching tropical storm intensity or above) on South China is proposed. Different from most of the existing seasonal forecasting models that consider the peak-season environment, we make use of pre-season environmental factors to build the model. The April SLP over the tropical central Pacific, the March–April mean SST

southwest to Australia, the March 850-hPa zonal wind east to Japan, and the April 500-hPa zonal wind over Bay of Bengal are found to be the key predictors. The models based on the ECMWF (Model E) and NOAA (Model N) reanalysis data show high correlations with the observations ($r = 0.85\text{--}0.87$, $p < 0.01$). Here, we combine the predictions from Model E and Model N to establish the SYSU model. The advantages of this approach can minimize the uncertainties and risks introduced by the single source of data, and thus, increases the robustness of the model predictability. The SYSU model is justifiably validated by the leave-one-out cross validation and recent 15-year observations (2006–2020). It exhibits 90% hit rate in 1979–2020 and demonstrates a promising potential in the seasonal forecasting of TC landfall on South China.

Deduced from the four predictors and previous literature, the AAO, and the variations of subtropical high and ITCZ over the WNP are proposed to be the possible physical linkages or mechanisms underlying the SYSU model. The main idea is that these predictors highly relate to the changes in atmospheric circulation (i.e., steering and convective activity) over South China Sea and the WNP in the TC season via sequences of thermodynamic and dynamic teleconnections. Although these possible linkages and mechanisms are yet not systematically validated, they are physically meaningful and evidently indicative. In this study, the proposed physical linkages and mechanisms are the auxiliary aiming to demonstrate the possible physics behind the model. Doing comprehensive mechanism validations requires a lot of sophisticated modeling work and are left for future study.

No model is perfect. Although the SYSU model proposed in this study shows potentials in the seasonal forecasting of TC landfall on South China, there are always rooms to improve. For instance, why the model misses in 1993, 2009, 2013, and 2017 (see **Figure 7**)? There may be better predictors and matrices to improve the accuracy, but it requires further research. Last but not least, we would officially implement and keep updating this model targeting to provide the seasonal forecasting products for the public access and monitoring by every mid of May in the near future.

DATA AVAILABILITY STATEMENT

The CMA best-track data was extracted from <http://tcdata.typhoon.org.cn>. The ERA5 reanalysis data was retrieved from <https://www.ecmwf.int/en/forecasts/datasets/reanalysis-datasets/era5>. The NCEP-CFSR reanalysis data was downloaded from <https://rda.ucar.edu/datasets/ds094.0>. The OISSTv2 data was obtained from <https://psl.noaa.gov/data/gridded/data.noaa.oisst.v2.html>. The OLR data was retrieved from <https://climatedataguide.ucar.edu/climate-data/outgoing-longwave-radiation-olr-avhrr>. The AAO index data is available at https://www.cpc.ncep.noaa.gov/products/precip/CWlink/daily_ao_index/ao/ao_index.html. Further inquiries can be directed to the corresponding author.

AUTHOR CONTRIBUTIONS

OZ performed the analysis. OZ and LX did the visualization. OZ and KC wrote the manuscript. OZ, KC, and LX contributed to the

editing. KC and ZW supervised the study. All authors participated in the discussion.

FUNDING

This study was supported by the National Key R&D Program of China (2019YFC1510400), the National Natural Science Foundation of China and Macau Science and Technology Development Joint Fund (41861164027), the Innovation Group Project of the Southern Marine Science and Engineering Guangdong Laboratory (Zhuhai) (311021001), the Guangdong Province Key Laboratory for Climate Change and

Natural Disaster Studies (2020B1212060025), and the Fundamental Research Funds for the Central Universities, Sun Yat-sen University (2021qntd29).

ACKNOWLEDGMENTS

The authors gratefully thank Dr. Dongxiao Wang, Dr. Ke Fan, Dr. Si Gao, Dr. Marco Y.-T. Leung, Dr. Peng Hu, Mr. Zhenyuan Dong, and Miss Minglin Zheng for the valuable discussions. Besides, we thank the anonymous reviewers for the helpful comments and suggestions that significantly improve the manuscript.

REFERENCES

- Au-Yeung, A. Y. M., and Chan, J. C. L. (2012). Potential Use of a Regional Climate Model in Seasonal Tropical Cyclone Activity Predictions in the Western North Pacific. *Clim. Dyn.* 39, 783–794. doi:10.1007/s00382-011-1268-x
- Camargo, S. J., Barnston, A. G., Klotzbach, P. J., and Landsea, C. W. (2007). Seasonal Tropical Cyclone Forecasts. *WMO Bull.* 56, 297–309.
- Camp, J., Roberts, M. J., Comer, R. E., Wu, P., MacLachlan, C., Bett, P. E., et al. (2019). The Western Pacific Subtropical High and Tropical Cyclone Landfall: Seasonal Forecasts Using the Met Office GloSea5 System. *Q. J. R. Meteorol. Soc.* 145, 105–116. doi:10.1002/qj.3407
- Cao, X., Chen, G.-H., Huang, R.-H., and Chen, W. (2014). The Intensity Variation of the Summer Intertropical Convergence Zone in Western North Pacific and its Impact on Tropical Cyclone. *J. Trop. Meteorology* 20, 193–201. doi:10.16555/j.1006-8775.2014.03.001
- Chan, J. C. L., Shi, J.-E., and Lam, C.-M. (1998). Seasonal Forecasting of Tropical Cyclone Activity over the Western North Pacific and the South China Sea. *Weather Forecast.* 13, 997–1004. doi:10.1175/1520-0434(1998)013<0997:sfotca>2.0.co;2
- Chan, K. T. F., Dong, Z., and Zheng, M. (2021). Statistical Seasonal Forecasting of Tropical Cyclones over the Western North Pacific. *Environ. Res. Lett.* 16, 074027. doi:10.1088/1748-9326/ac05f1
- Chen, D., Wang, H., Liu, J., and Li, G. (2015). Why the Spring North Pacific Oscillation Is a Predictor of Typhoon Activity over the Western North Pacific. *Int. J. Climatol.* 35, 3353–3361. doi:10.1002/joc.4213
- Chen, L., and Ding, Y. (1979). *The Conspectus of Western Pacific Typhoon*. Beijing: Science Press, 107–109.
- Choi, K.-S., Moon, J.-Y., Kim, D.-W., and Chu, P.-S. (2010). Seasonal Prediction of Tropical Cyclone Genesis Frequency over the Western North Pacific Using Teleconnection Patterns. *Theor. Appl. Climatol.* 100, 191–206. doi:10.1007/s00704-009-0182-1
- DelSole, T., and Shukla, J. (2009). Artificial Skill Due to Predictor Screening. *J. Clim.* 22, 331–345. doi:10.1175/2008JCLI2414.1
- Fan, K. (2009). Seasonal Forecast Model for the Number of Tropical Cyclones to Make Landfall in China. *Atmos. Oceanic Sci. Lett.* 2, 251–254. doi:10.1080/16742834.2009.11446811
- Fan, K. (2010). A Prediction Model for Atlantic Named Storm Frequency Using a Year-By-Year Increment Approach. *Weather Forecast.* 25, 1842–1851. doi:10.1175/2010WAF2222406.1
- Fan, L., Li, J., Wei, Z., Dong, W., and Wang, J. (2003). Annual Variations of the Arctic Oscillation and the Antarctic Oscillation. *Chin. J. Atmos. Sci.* 27, 419–424.
- Gao, S., Chen, Z., and Zhang, W. (2018). Impacts of Tropical North Atlantic SST on Western North Pacific Landfalling Tropical Cyclones. *J. Clim.* 31, 853–862. doi:10.1175/JCLI-D-17-0325.1
- Gao, S., Chen, Z., Zhang, W., and Shen, X. (2020). Effects of Tropical North Atlantic Sea Surface Temperature on Intense Tropical Cyclones Landfalling in China. *Int. J. Climatol.* 41, 1056–1065. doi:10.1002/joc.6732
- Goh, A. Z.-C., and Chan, J. C. L. (2010). An Improved Statistical Scheme for the Prediction of Tropical Cyclones Making Landfall in South China. *Weather Forecast.* 25, 587–593. doi:10.1175/2009WAF2222305.1
- Gong, D., and Wang, S. (1999). Definition of Antarctic Oscillation index. *Geophys. Res. Lett.* 26, 459–462. doi:10.1029/1999GL900003
- Gray, W. M. (1984a). Atlantic Seasonal Hurricane Frequency. Part I: El Niño and 30 mb Quasi-Biennial Oscillation Influences. *Mon. Weather Rev.* 112, 1649–1668. doi:10.1175/1520-0493(1984)112<1649:ashfpi>2.0.co;2
- Gray, W. M. (1984b). Atlantic Seasonal Hurricane Frequency. Part II: Forecasting its Variability. *Mon. Weather Rev.* 112, 1669–1683. doi:10.1175/1520-0493(1984)112<1669:ashfpi>2.0.co;2
- Hall, T. M., and Jewson, S. (2007). Statistical Modelling of North Atlantic Tropical Cyclone Tracks. *Tellus A: Dynamic Meteorology and Oceanography* 59, 486–498. doi:10.1111/j.1600-0870.2007.00240.x
- Ham, Y.-G., and Kug, J.-S. (2015). Role of north Tropical Atlantic SST on the ENSO Simulated Using CMIP3 and CMIP5 Models. *Clim. Dyn.* 45, 3103–3117. doi:10.1007/s00382-015-2527-z
- Ho, C.-H., Kim, J.-H., Kim, H.-S., Sui, C.-H., and Gong, D.-Y. (2005). Possible Influence of the Antarctic Oscillation on Tropical Cyclone Activity in the Western North Pacific. *J. Geophys. Res.* 110, D19104. doi:10.1029/2005JD005766
- Hu, F., Li, T., Liu, J., Bi, M., and Peng, M. (2018). Decrease of Tropical Cyclone Genesis Frequency in the Western North Pacific since 1960s. *Dyn. Atmospheres Oceans* 81, 42–50. doi:10.1016/j.dynatmoce.2017.11.003
- Hu, P., Chen, W., Chen, S., Liu, Y., Wang, L., and Huang, R. (2020). Impact of the March Arctic Oscillation on the South China Sea Summer Monsoon Onset. *Int. J. Climatol.* 41, 3239–3248. doi:10.1002/joc.6920
- Huang, W.-R., and Chan, J. C. L. (2014). Dynamical Downscaling Forecasts of Western North Pacific Tropical Cyclone Genesis and Landfall. *Clim. Dyn.* 42, 2227–2237. doi:10.1007/s00382-013-1747-3
- Klotzbach, P., Blake, E., Camp, J., Caron, L.-P., Chan, J. C. L., Kang, N.-Y., et al. (2019). Seasonal Tropical Cyclone Forecasting. *Trop. Cyclone Res. Rev.* 8, 134–149. doi:10.1016/j.tcr.2019.10.003
- Li, R. C. Y., Zhou, W., Shun, C. M., and Lee, T. C. (2017). Change in Destructiveness of Landfalling Tropical Cyclones over China in Recent Decades. *J. Clim.* 30, 3367–3379. doi:10.1175/JCLI-D-16-0258.1
- Liu, G., Sun, S., and Zhang, Q. (2009). Characteristics of the Intraseasonal Oscillation of Intertropical Convergence Zone and its Influence on the Periodical Tropical Cyclogenesis. *Chin. J. Atmos. Sci.* 33, 879–889.
- Liu, G., Zhang, Q., and Sun, S. (2007). A Preliminary Study on Activities of Tropical Cyclones over the Western North Pacific during the Summer of 2006. *Climatic Environ. Res.* 12, 738–750. doi:10.3969/j.issn.1006-9585.2007.06.004
- Liu, K. S., and Chan, J. C. L. (2003). Climatological Characteristics and Seasonal Forecasting of Tropical Cyclones Making Landfall along the South China Coast. *Mon. Weather Rev.* 131, 1650–1662. doi:10.1175/2554.1
- Liu, K. S., and Chan, J. C. L. (2013). Inactive Period of Western North Pacific Tropical Cyclone Activity in 1998–2011. *J. Clim.* 26, 2614–2630. doi:10.1175/JCLI-D-12-00053.1
- Lok, C. C. F., and Chan, J. C. L. (2017). Changes of Tropical Cyclone Landfalls in South China throughout the Twenty-First Century. *Clim. Dyn.* 51, 2467–2483. doi:10.1007/s00382-017-4023-0
- Mei, W., and Xie, S.-P. (2016). Intensification of Landfalling Typhoons over the Northwest Pacific since the Late 1970s. *Nat. Geosci.* 9, 753–757. doi:10.1038/ngeo2792

- Nicholls, N. (1979). A Possible Method for Predicting Seasonal Tropical Cyclone Activity in the Australian Region. *Mon. Weather Rev.* 107, 1221–1224. doi:10.1175/1520-0493(1979)107<1221:apmfps>2.0.co;2
- Nicholls, N. (1992). Recent Performance of a Method for Forecasting Australian Seasonal Tropical Cyclone Activity. *Aust. Meteorol. Mag.* 40, 105–110.
- Park, D.-S. R., Ho, C.-H., and Kim, J.-H. (2014). Growing Threat of Intense Tropical Cyclones to East Asia over the Period 1977–2010. *Environ. Res. Lett.* 9, 014008. doi:10.1088/1748-9326/9/1/014008
- Tian, B., and Fan, K. (2019). Seasonal Climate Prediction Models for the Number of Landfalling Tropical Cyclones in China. *J. Meteorol. Res.* 33, 837–850. doi:10.1007/s13351-019-8187-x
- Wahiduzzaman, M., Oliver, E. C. J., Klotzbach, P. J., Wotherspoon, S. J., and Holbrook, N. J. (2019). A Statistical Seasonal Forecast Model of North Indian Ocean Tropical Cyclones Using the Quasi-Biennial Oscillation. *Int. J. Climatol.* 39, 934–952. doi:10.1002/joc.5853
- Wang, G., Su, J., Ding, Y., and Chen, D. (2007). Tropical Cyclone Genesis over the South China Sea. *J. Mar. Syst.* 68, 318–326. doi:10.1016/j.jmarsys.2006.12.002
- Wang, H., and Fan, K. (2007). Relationship between the Antarctic Oscillation in the Western North Pacific Typhoon Frequency. *Chin. Sci. Bull.* 52, 561–565. doi:10.1007/s11434-007-0040-4
- Wang, Y., Song, T., Liang, J., and Pan, W. (2012). Simulation of Seasonal Tropical Cyclone Activity over the Western North Pacific by Using the WRF Model. *Trans. Atmos. Sci.* 35, 24–31. doi:10.13878/j.cnki.dqkxb.2012.01.011
- Wheeler, M. C., and Hendon, H. H. (2004). An All-Season Real-Time Multivariate MJO index: Development of an index for Monitoring and Prediction. *Mon. Weather Rev.* 132, 1917–1932. doi:10.1175/1520-0493(2004)132<1917:aarmmi>2.0.co;2
- Xie, K., and Liu, B. (2014). An ENSO-Forecast Independent Statistical Model for the Prediction of Annual Atlantic Tropical Cyclone Frequency in April. *Adv. Meteorology* 2014, 1–11. doi:10.1155/2014/248148
- Yuan, Z., Qin, J., Li, S., Huang, S., and Mbululo, Y. (2021). Impact of Spring AAO on Summertime Precipitation in the North China Part: Observational Analysis. *Asia-Pacific J. Atmos. Sci.* 57, 1–16. doi:10.1007/s13143-019-00157-2
- Zhan, R., Wang, Y., and Lei, X. (2011). Contributions of ENSO and East Indian Ocean SSTA to the Interannual Variability of Northwest Pacific Tropical Cyclone Frequency. *J. Clim.* 24, 509–521. doi:10.1175/2010JCLI3808.1
- Zhan, R., Wang, Y., and Ying, M. (2012). Seasonal Forecasts of Tropical Cyclone Activity over the Western North Pacific: A Review. *Trop. Cyclone Res. Rev.* 1, 307–324. doi:10.6057/2012TCRR03.07
- Zhang, C., Hu, C., Huang, G., Yao, C., Zheng, Z., Wang, T., et al. (2019). Perspective on Landfalling Frequency and Genesis Location Variations of Southern China Typhoon during Peak Summer. *Geophys. Res. Lett.* 46, 6830–6838. doi:10.1029/2019GL083420
- Zhang, G., Zhang, X., and Wei, F. (1995). A Study on the Variations of Annual Frequency for Tropical Cyclone in Northwest Pacific during the Last Hundred Years. *J. Trop. Meteorology* 11, 315–323.
- Zhang, Q., Zhang, W., Lu, X., and Chen, Y. D. (2012). Landfalling Tropical Cyclones Activities in the South China: Intensifying or Weakening? *Int. J. Climatol.* 32, 1815–1824. doi:10.1002/joc.2396
- Zhang, W., Vecchi, G. A., Villarini, G., Murakami, H., Gudgel, R., and Yang, X. (2017). Statistical-Dynamical Seasonal Forecast of Western North Pacific and East Asia Landfalling Tropical Cyclones Using the GFDL FLOR Coupled Climate Model. *J. Clim.* 30, 2209–2232. doi:10.1175/JCLI-D-16-0487.1
- Zhang, W., and Villarini, G. (2019). Seasonal Forecasting of Western North Pacific Tropical Cyclone Frequency Using the North American Multi-Model Ensemble. *Clim. Dyn.* 52, 5985–5997. doi:10.1007/s00382-018-4490-y
- Zhang, W., Villarini, G., Vecchi, G. A., and Smith, J. A. (2018). Urbanization Exacerbated the Rainfall and Flooding Caused by Hurricane Harvey in Houston. *Nature* 563, 384–388. doi:10.1038/s41586-018-0676-z

Conflict of Interest: The authors declare that the research was conducted in the absence of any commercial or financial relationships that could be construed as a potential conflict of interest.

Publisher's Note: All claims expressed in this article are solely those of the authors and do not necessarily represent those of their affiliated organizations, or those of the publisher, the editors and the reviewers. Any product that may be evaluated in this article, or claim that may be made by its manufacturer, is not guaranteed or endorsed by the publisher.

Copyright © 2022 Zhang, Chan, Xu and Wu. This is an open-access article distributed under the terms of the Creative Commons Attribution License (CC BY). The use, distribution or reproduction in other forums is permitted, provided the original author(s) and the copyright owner(s) are credited and that the original publication in this journal is cited, in accordance with accepted academic practice. No use, distribution or reproduction is permitted which does not comply with these terms.



Fine-Scale Structures in the Mid-Level Eyewall of Super Typhoon Rammasun (2014) Simulated With the WRF-LES Framework

Zhen Gao^{1,2}, Liguang Wu^{1,3*} and Xingyang Zhou^{1,4}

¹Department of Atmospheric and Oceanic Sciences, Institute of Atmospheric Sciences, Fudan University, Shanghai, China,

²State Key Laboratory of Severe Weather, Chinese Academy of Meteorological Sciences, Beijing, China, ³Innovation Center of Ocean and Atmosphere System, Zhuhai Fudan Innovation Research Institute, Zhuhai, China, ⁴IRDRI CoE on Risk Interconnectivity and Governance on Weather/Climate Extreme Impact and Public Health, Fudan University, Shanghai, China

OPEN ACCESS

Edited by:

Qingqing Li,
Nanjing University of Information
Science and Technology, China

Reviewed by:

Xin Qiu,
Nanjing University, China
Hehe Ren,
Nanjing University of Aeronautics and
Astronautics, China

*Correspondence:

Liguang Wu
liguangwu@fudan.edu.cn

Specialty section:

This article was submitted to
Atmospheric Science,
a section of the journal
Frontiers in Earth Science

Received: 14 November 2021

Accepted: 23 December 2021

Published: 12 January 2022

Citation:

Gao Z, Wu L and Zhou X (2022) Fine-Scale Structures in the Mid-Level Eyewall of Super Typhoon Rammasun (2014) Simulated With the WRF-LES Framework.
Front. Earth Sci. 9:814785.
doi: 10.3389/feart.2021.814785

It has been numerically demonstrated that the turbulence above the boundary is important to tropical cyclone intensification and rapid intensification, but the three-dimensional structures of the sub-grid-scale (SGS) eddy have not been revealed due to the lack of observational data. In this study, two numerical simulations of Super Typhoon Rammasun (2014) were conducted with the Advanced Weather Research and Forecast (WRF) model by incorporating the large-eddy simulation (LES) technique, in which the enhanced eyewall convection and the process of rapid intensification are captured. Consistent with previous observational studies, the strong turbulent kinetic energy (TKE) is found throughout the whole eyewall inside of the radius of maximum wind in both experiments. The simulations indicate that the strong TKE is associated with horizontal rolls with the horizontal extent of 2–4 km, which are aligned azimuthally in the intense eyewall convection. It is indicated that the three-dimensional structures of the SGS eddy can be simulated with the vertical grid spacing of ~100 m when the horizontal grid spacing is 74 m. It is suggested that there is considerable turbulence associated with azimuthally-aligned horizontal rolls in the mid-level eyewall of tropical cyclone.

Keywords: tropical cyclone eyewall, turbulent kinetic energy, large-eddy simulation, horizontal rolls, sub-grid-scale eddy

INTRODUCTION

Intensity change is currently one of the most difficult challenges in tropical cyclone (TC) forecast (Rogers et al., 2006; Rogers et al., 2013). While the strong turbulence in the traditional intensity theories is usually regarded as a flow feature pertaining to the planetary boundary layer (PBL) (Charney and Eliassen, 1964; Ooyama, 1964; Ooyama, 1969; Emanuel, 1986; Emanuel, 1995), a few studies suggested that intense turbulent mixing generated by cloud processes also exists above the PBL in the eyewall and rainbands of a TC (Lorsolo et al., 2010; Rogers et al., 2012; Zhu et al., 2019; Chen and Bryan, 2021; Zhu et al., 2021). Using airborne Doppler measurements, Lorsolo et al. (2010) and Rogers et al. (2012) found strong turbulence in the convective eyewall throughout the troposphere mainly within the radius of maximum wind. Incorporating an in-cloud turbulent-mixing parameterization in the vertical turbulent-mixing scheme of the Hurricane Weather Research and Forecasting (HWRF) model, Zhu et al. (2019) numerically demonstrated the importance of

eyewall and rainband sub-grid-scale (SGS) eddy forcing to numerical prediction of TC intensification and rapid intensification, but the three-dimensional structures of the SGS eddy have not been revealed due to the lack of observational data. Thus, to better understand the in-cloud turbulent mixing and improve the TC intensity forecasts, it is necessary to understand the fine-scale features of the TC eyewall.

Previous studies focused mostly on fine-scale structures in the TC boundary layer. Two coherent structures have already been revealed. One is roll vortices (Foster, 2005; Nolan, 2005; Gao and Ginis, 2016; Wang and Jiang, 2016; Gao et al., 2017; Gao and Ginis, 2018), which tend to align with the tangential winds with sub-kilometer to multi-kilometer wavelengths (Wurman and Winslow, 1998; Morrison et al., 2005; Lorsolo et al., 2008; Ellis and Businger, 2010). The other is called tornado-scale vortices, which are associated with extreme updrafts and downdrafts, strong vertical vorticity, and huge near-surface gusts (Aberson et al., 2006; Marks et al., 2008; Wurman and Kosiba, 2018; Wu et al., 2018, 2019). Relatively little is known about the fine-scale structures in the mid-level eyewall of TCs although the extreme updrafts beyond the TC boundary layer were observed (Guimond et al., 2010; Heymsfield et al., 2010). Recently, Zheng et al. (2020) examined two numerical experiments conducted with the Advanced Weather Research and Forecast (WRF) model, in which the large-eddy simulation (LES) technique is used with the finest grid spacing of 37 and 111 m. They found that the simulated extreme updraft in the TC eyewall exhibited relatively high frequencies in the lower, middle and upper troposphere, suggesting different types of fine-scale structures associated with the extreme updrafts. Following Zheng et al. (2020), the numerical simulation of Typhoon Rammasun (2014) was conducted with the WRF-LES framework. In this study, our focus is on the vertical distribution of turbulent kinetic energy (TKE) and the associated fine-scale structures in the mid-level eyewall.

EXPERIMENTAL DESIGN

Super Typhoon Rammasun (2014) formed to the east of the Philippines on 12 July 2014, became a super typhoon in the South China Sea on 17 July, and reached its peak intensity at 0600 UTC 18 July after 36 h of rapid intensification (Qiu et al., 2020). Rammasun made its first landfall over Hainan Island at 0730 UTC 18 July 2014. Based on the China Meteorological Administration (CMA) best track dataset, the lifetime maximum intensity is 888 hPa in the sea-level pressure and 71.4 m s^{-1} in the maximum wind speed at 10 m, while the peak intensity is 918 hPa and 72.0 m s^{-1} in the Joint Typhoon Warning Center (JTWC) best track dataset.

In this study, two numerical experiments were designed to simulate the rapid intensification of Super Typhoon Rammasun (2014) in the South China Sea and its subsequent landfall process using version 3.2.1 of the WRF model. The outermost domain (centered at 18.9°N , 116.9°E) covered an area of $5,600 \text{ km} \times 4,500 \text{ km}$ with a horizontal grid spacing of 18 km. The horizontal grid spacings of the five nested domains were 6 km,

2 km, $2/3 \text{ km}$ ($\sim 667 \text{ m}$), $2/9 \text{ km}$ ($\sim 222 \text{ m}$), and $2/27 \text{ km}$ ($\sim 74 \text{ m}$), respectively. There were 251×311 , 271×271 , 211×211 , 541×541 , 802×802 , 1801×1801 grid points, respectively. Two different vertical spacings are used in the numerical simulations. Vertical grid spacing in LES75 increases rapidly from 40 to $\sim 350 \text{ m}$ at 5 km and shows decline to 250 m at top of the model (50 hPa). The second experiment (LES151) is designed to increase from 40 to 100 m at 200 m, sustain $\sim 100 \text{ m}$ until 12 km and experience a steady growth to more than 250 m at 50 hPa. The model tops in two experiments were 50 hPa.

The simulations were initialized at 1800 UTC 15 July 2014 when it was over the Philippines and integrated for 72 h to 1800 UTC 18 July 2014 when it made the second landfall in Guangxi, China. The spun-up vortex was initially located at the center of Super Typhoon Rammasun (13.6°N , 121.9°E). The two innermost domains were activated at 0000 UTC 18 July after the third and fourth domains were activated at 2100 UTC 15 July. The Kain–Fritsch cumulus parameterization scheme was used in the outermost domain (Kain and Fritsch, 1993), and the WRF six-class scheme was selected in the nested domains (Hong and Lim, 2006). The Rapid Radiative Transfer Model (RRTM) and the Dudhia shortwave radiation scheme were used for calculating long-wave radiation and shortwave radiation (Dudhia, 1989; Mlawer et al., 1997). The LES technique is adopted in the sub-kilometer domains (Mirocha et al., 2010) and the Yonsei University scheme is selected for PBL parameterization in the other domains (Noh et al., 2003).

The purpose of two experiments is to compare the influence of the vertical spacing on the TKE at the middle levels. In the following analysis, we will focus on the hourly output from 0300 UTC to 0700 UTC 18 July (3 h after the activation of the innermost domain and before landfall in Hainan Island at 0700 UTC 18 July). The TC center is defined as the minimum pressure variance center (Yang et al., 2020).

OVERVIEW OF THE SIMULATED TYPHOON

Figure 1 shows the comparisons of the track and intensity between the observation and the simulation. The simulated tracks in LES75 and LES151 are very close to the observation (**Figure 1A**). The mean errors between the observed and simulated tracks are about 30 km in LES75 and 33 km in LES151, respectively. The landfall time of the simulated TCs is 0700 UTC 18 July. Considering the 1-h output interval, it is consistent with the observed landfall time of 0730 UTC 18 July.

The simulated intensity is measured with the minimum sea-level pressure and the maximum instantaneous 10 m wind speed. Note that the simulated intensity is always derived from the innermost domain. The intensity evolution of Rammasun (2014) is well simulated in LES75 and LES151, except the abrupt increase of the maximum instantaneous 10 m wind speed immediately after the fifth and sixth domains are activated at 0000 UTC 18 July. For this reason, our analysis covers a 4-h period from 0300 UTC to 0700 UTC on 18 July. As shown in **Figure 1B**, both two simulations capture the observed rapid intensification processes.

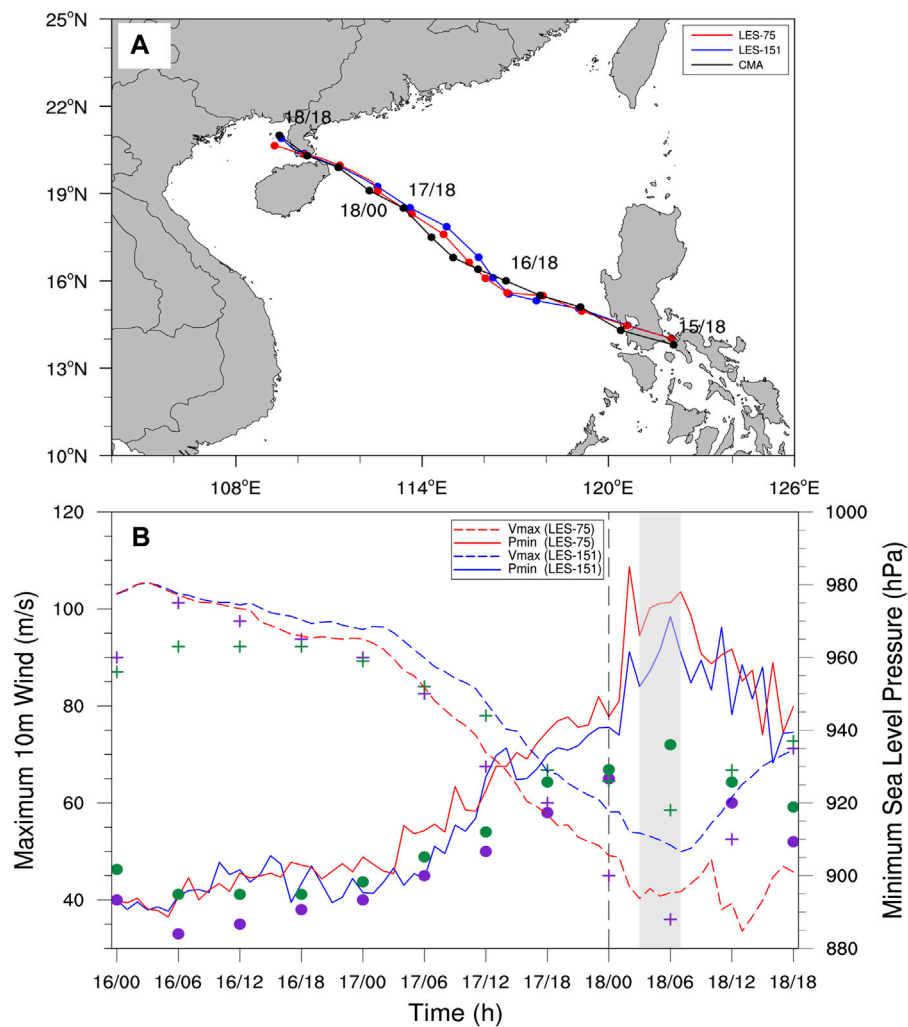


FIGURE 1 | Comparisons of the observed and simulated (A) tracks and (B) intensities of Super Typhoon Rammasun (2014). The time is in the dd/hh format. The observed track is from the CMA best track dataset, while the observed intensities are from the CMA best track dataset (purple dots and crosses) and the JTWC best track dataset (green dots and crosses) in terms of minimum sea-level pressure (crosses, units: hPa) and maximum instantaneous wind speed at 10 m (dots, units: m s^{-1}). The time intervals are 6 h from the observation and 1 h for the simulation. The gray shading area is the range of analysis times and the black dashed line indicates the activation of D05 and D06 domains.

The minimum sea-level pressure fluctuates between 893.7 (906.6) and 896.4 (911.7) hPa during 4 h in LES75 (LES151) (**Figure 1B**). They are higher than the minimum sea-level pressure of 888 hPa in the CMA dataset, and lower than the minimum sea-level pressure of 918 hPa in the JTWC dataset. The minimum pressure of 888 hPa in the CMA dataset was estimated by observation from Qizhou Island station in the eyewall (Cai and Xu, 2016). Feng et al. (2021) argued that the minimum sea-level pressure resulted from the tornado-scale vortex that is prevalent near the inner edge of the TC eyewall. During the 4-h period, the maximum instantaneous wind fluctuates between 94.5 (84.0) and 103.5 (98.4) m s^{-1} in LES75 (LES151). In Cai and Xu (2016), the maximum instantaneous wind of 72.4 m s^{-1} at 0439 UTC 18 July was observed at Qizhou Island station just before the anemometer was destroyed. The station was then located at the inner edge of the eyewall. Considering lack of the observation and the influence

of the tornado-scale vortex on the simulated maximum instantaneous wind (Wu et al., 2018), the intensity of Rammasun (2014) in our simulations are generally comparable to that in the observation.

Figure 2 shows the comparison of the simulated radar reflectivity at 800 m at 0700 UTC 18 July in the D04 domain and the observation at Haikou station at 0659 UTC 18 July. The observed and simulated vertical shear vectors between 200 hPa and 850 hPa are also plotted. The magnitudes of the shear over the radius of 500 km are 6.0 m s^{-1} in the fifth generation European Centre for Medium-range Weather Forecasting (ECMWF) global reanalysis (ERA5, 0.25°, and 1-hourly) dataset and 7.2 (7.1) m s^{-1} in LES75 (LES151). The shear vectors in the simulations shift westward than the observation. Consistent with the observation, as shown in **Figure 2**, the eyewall convection and rainbands are enhanced generally on

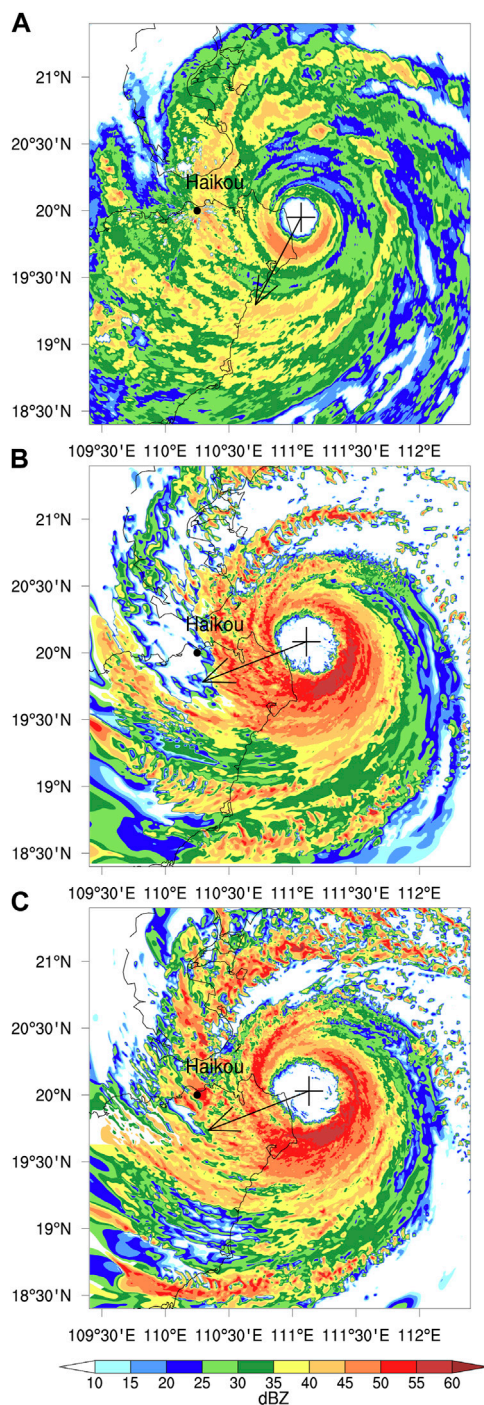


FIGURE 2 | The comparisons of the radar reflectivity (units: dBZ) from (A) Haikou station at 0659 UTC 18 July 2014 and the radar reflectivity at 800 m in (B) LES75 and (C) LES151 at 0700 UTC 18 July 2014 in the D04 domain. The arrow shows the vertical wind shear between 200 hPa and 850 hPa and plus signs indicate the TC center.

the southern side although the simulated eyes are larger than the observed one. Note that the eye in LES151 is larger than that in LES75.

THE SIMULATED TKE AND THE ASSOCIATED MID-LEVEL FINE STRUCTURES

Following previous studies (Green and Zhang, 2014; Wu et al., 2018, 2019), the mean wind fields are obtained by averaging in a moving box of $8 \times 8 \text{ km}^2$. The perturbation wind components are the differences between the total wind and the smoothed wind. Wu et al. (2019) examined the perturbation winds with different moving windows in size. They found that there is little difference in the resulting small-scale features with the finest grid spacing of 37 m as the window size is larger than $8 \times 8 \text{ km}^2$. The small-scale features are similar to those by subtracting the symmetric and wavenumber 1-3 components with respect to the TC center.

Following Zhang et al. (2011) and Liu et al. (2021), the TKE at a grid point is computed as follows:

$$e = \frac{1}{2} (u'^2 + v'^2 + w'^2), \quad (1)$$

where u' , v' , and w' are the perturbation wind components in the zonal, meridional and vertical directions. **Figure 3** shows the radius-height cross sections of TKE for the simulated TCs. The cross sections in **Figures 3A,B** are plotted in the enhanced eyewall convection along the azimuths of 185° at 0300 UTC 18 July in LES75 and 188° at 0400 UTC 18 July in LES151 (azimuthal positions shown in **Figure 4**). The selected time in the specific experiment corresponds to the highest TKE maximum during the 4-h period. We can see that the localized high TKE is roughly concentrated in three vertical layers: the boundary layer below 3 km, the middle levels between 3 and 12 km and the upper levels above 12 km. Consistent with Zheng et al. (2020), we suggest that the TKE in the three layers is associated with different fine-scale features. As indicated by the radar reflectivity contours, the relatively high TKE at the middle levels occurs in the tower of high radar reflectivity in the eyewall. The maximum TKE in the middle layer is $119 \text{ m}^2 \text{ s}^{-2}$ and $157 \text{ m}^2 \text{ s}^{-2}$ in LES75 and LES151, respectively, while the TKE maxima in the lower (upper) layer is 359 (97) $\text{m}^2 \text{ s}^{-2}$ in LES75 and 319 (257) $\text{m}^2 \text{ s}^{-2}$ in LES151. The TKE maximum at the middle levels is comparable in magnitude to the TKE maxima at the lower and upper levels.

To demonstrate the fine-scale wind structures associated with the localized high TKE, the sector radius-height cross sections in the vicinity of these in **Figures 3A,B** are averaged azimuthally in **Figures 3C,D**. The average covers an azimuthal range of 30° from 170° to 200° in LES75 and 173° – 203° in LES151 (azimuthal ranges shown in **Figure 4**). Both the experiments indicate that the high TKE at middle levels is associated with relatively horizontal rolls, which tilt radially outward with the increasing height. The radial extent of the horizontal rolls is 2–4 km, and the vertical extent is larger than the radial extent. The horizontal rolls occur in the eyewall vertical motion (white contours) smoothed with a $8 \times 8 \text{ km}^2$ moving box, suggesting that the horizontal rolls are associated with the eyewall convection (**Figures 3C,D**). The rolls are found on both the sides of the radius of maximum wind.

Lorsolo et al. (2010) retrieved the TKE using airborne Doppler measurements from Hurricanes Isabel (2003), Fabian (2003), Frances (2004), Katrina (2005), and Rita (2005) at various stages of their development. They constructed a mean cross

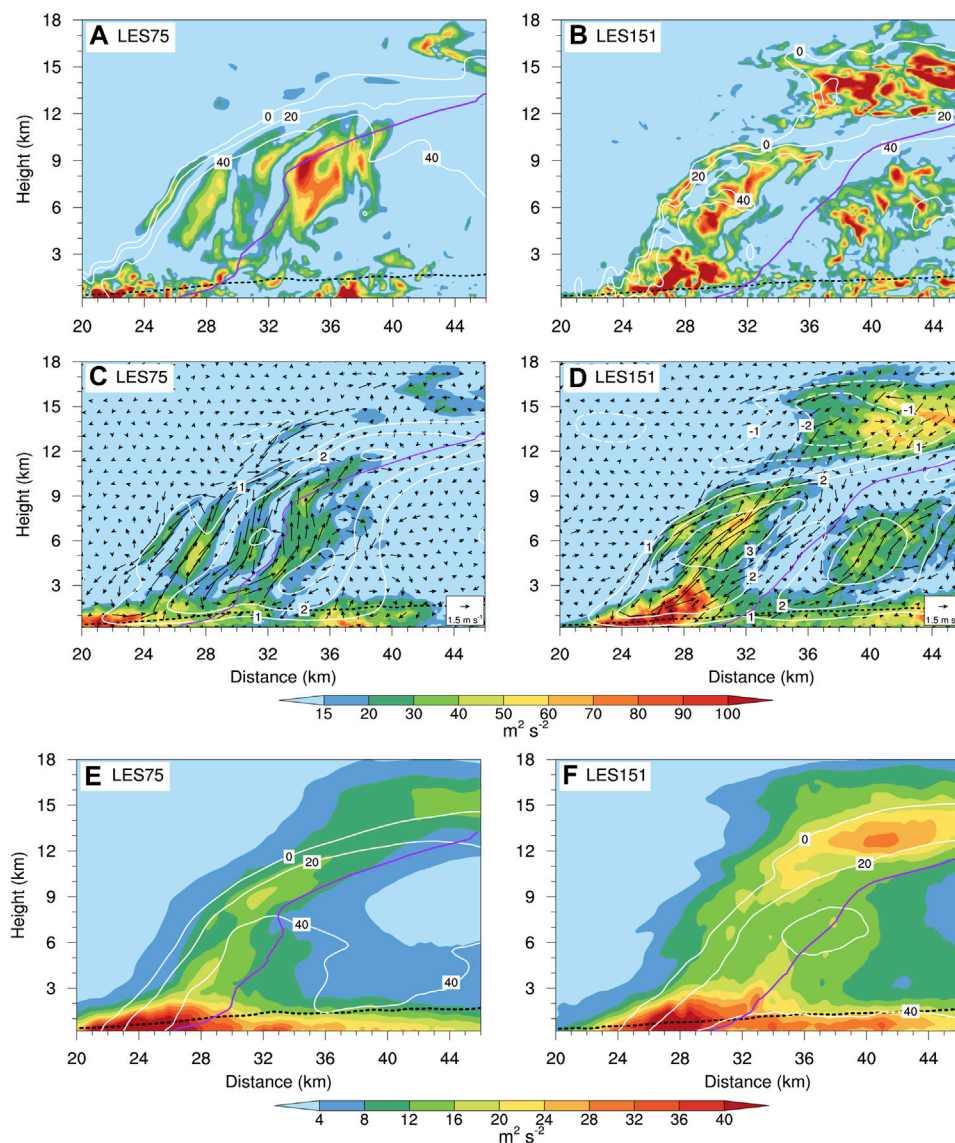


FIGURE 3 | (A, B) The radius-height cross sections of TKE (shading, units: $\text{m}^2 \text{s}^{-2}$) and radar reflectivity (contours, units: dBZ) simulated at 0300 UTC 18 July in LES75 (left) along the azimuth of 185° and at 0400 UTC 18 July in LES151 (right) along the azimuth of 188° with an interval of 20 dBZ. **(C, D)** The radius-height sector cross sections of TKE (shading), radial and vertical perturbation winds (vectors), and smoothed vertical motion (solid contours for upward motion and dashed contours for downward motion), which are averaged over 170°–200° in LES75 and averaged over 173°–203° in LES151. **(E, F)** Same as **(A, B)**, but averaged azimuthally over the whole eyewall. The radius of maximum wind is indicated with the solid purple lines and the dashed black lines indicate the height of the inflow layer.

section of TKE for all considered legs and proposed a conceptual model. The largest TKE is located inside of the radius of maximum wind. **Figures 3E,F** show the cross section of the mean TKE averaged azimuthally for the whole eyewall in LES75 and LES151. Consistent with Lorusso et al. (2010), both the two experiments successfully simulate “tower-like” structure of TKE, and the strongest TKE occurs inside of the radius of maximum wind. Also, the strong TKE exists in the boundary inflow outside of the radius of maximum wind. Compared with LES75, the region of azimuthally mean TKE $>12 \text{ m}^2 \text{s}^{-2}$ shows wider range at the middle level in LES151. Moreover, higher azimuthally mean TKE ($>20 \text{ m}^2 \text{s}^{-2}$) is simulated in LES151 at the upper levels (**Figures 3E,F**).

The horizontal rolls in **Figures 3C,D** actually represent azimuthally-aligned vortex rings in the three-dimensional streamlines of perturbation winds (**Figure 4**), which are located in the mid-level eyewall within the strong convection (**Figure 2**). In **Figure 4**, the simulated radar reflectivity at 7 km is also plotted to indicate the intense eyewall convection. As shown in **Figure 4**, horizontal rolls with the horizontal extent of 2–4 km in the mid-level eyewall are successfully simulated in LES75 and LES151 with vertical grid spacings of ~ 300 and $\sim 100 \text{ m}$. It is suggested that the simulation with the vertical grid spacings in LES75 and LES151 can resolve the vortex rings. We examine all the 4-h data and find that the azimuthally-aligned rolls are a common feature in the mid-level eyewall convection.

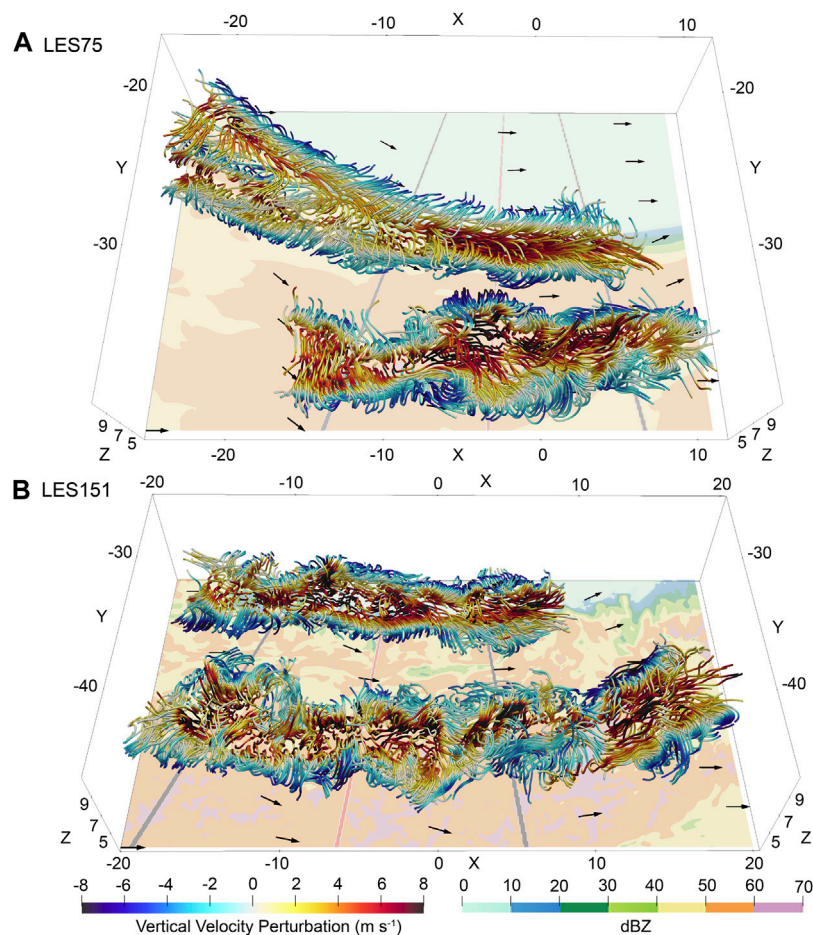


FIGURE 4 | The perturbation winds (three-dimensional streamlines), 7 km horizontal winds (vectors), and 7 km radar reflectivity (shading) at 0300 UTC 18 July in LES75 and at 0400 UTC 18 July in LES151. The streamlines with warm and cool colors indicate the upward and downward motion, respectively. The red and black lines indicate the position of the cross section in **Figures 3A,B** and the azimuthal range of the cross sections in **Figures 3C,D**, respectively.

SUMMARY

Previous studies indicated that strong turbulence could occur in the convective eyewall throughout the troposphere (Lorsolo et al., 2010; Rogers et al., 2012; Chen and Bryan, 2021). The importance of eyewall and rainband sub-grid-scale (SGS) eddy forcing to TC intensification and rapid intensification has been demonstrated numerically (Zhu et al., 2019). Jiang et al. (2020) and Zheng et al. (2020) have shown that the extreme updraft contained small-scale rolls within the eyewall and rainbands region. In addition, these small-scale turbulent mixing plays an important role in transporting heat, momentum and water vapor in deep convective clouds (LeMone and Zipser, 1980; Hogan et al., 2009). However, the three-dimensional structures of the fine-scale structures associated with strong TKE have not been revealed due to the lack of observational data.

In this study, two numerical simulations of Super Typhoon Rammasun (2014) were conducted with the LES technique in the WRF model. While the vertical spacing is ~ 300 m in LES75, the vertical spacing is ~ 100 m in LES151 at the middle levels

(3–11 km). Although the simulated intensity is different in terms of the minimum sea-level pressure and maximum instantaneous wind at 10 m, the enhanced eyewall convection and the process of rapid intensification are captured in two experiments. It is found that the azimuthally mean TKE simulated in both experiments consistent with the observation (Lorsolo et al., 2010; Rogers et al., 2012). That is, the strong TKE is found throughout the whole eyewall inside of the radius of maximum wind. Furthermore, the strong TKE is associated with horizontal rolls, and which are aligned azimuthally in the intense eyewall convection. The radial extent of the horizontal rolls is 2–4 km, and the vertical extent is larger than the radial extent. This study suggests that there is considerable turbulence associated with azimuthally-aligned horizontal rolls in the mid-level eyewall of tropical cyclone.

Although previous observations have studied the distributions of strong TKE in the eyewall (Lorsolo et al., 2010; Rogers et al., 2012), the associated mid-level fine-scale features remain unclear due to the limitation of the observations. The results presented in

this study should be useful for revealing the structures of fine-scale structures associated with strong TKE numerically. Future research effort should be continuously devoted to confirming the existence of mid-level horizontal rolls and improving in-cloud turbulent-mixing parameterization given the importance of the fine-scale systems on TC structure changes and intensity (Zhu et al., 2019, 2021).

DATA AVAILABILITY STATEMENT

The raw data supporting the conclusion of this article will be made available by the authors, without undue reservation.

REFERENCES

- Aberson, S. D., Montgomery, M. T., Bell, M., and Black, M. (2006). Hurricane Isabel (2003): New Insights into the Physics of Intense Storms. Part II: Extreme Localized Wind. *Bull. Am. Meteorol. Soc.* 87 (10), 1349–1354. doi:10.1175/BAMS-87-10-1349
- Cai, Q., and Xu, Y. “An Analysis of Super Typhoon Rammasun’s (2014) Peak Intensity,” in EGU general assembly conference abstracts, Vienna, Austria, April 2016, 13654. European Planetary Science Congress, EPSC2016-13654.
- Charney, J. G., and Eliassen, A. (1964). On the Growth of the Hurricane Depression. *J. Atmos. Sci.* 21 (1), 68–75. doi:10.1175/1520-0469(1964)021<0068:OTGOTH>2.0.CO;2
- Chen, X., and Bryan, G. H. (2021). Role of Advection of Parameterized Turbulence Kinetic Energy in Idealized Tropical Cyclone Simulations. *J. Atmos. Sci.* 1 (11), 3593–3611. doi:10.1175/JAS-D-21-0088.1
- Dudhia, J. (1989). Numerical Study of Convection Observed during the Winter Monsoon Experiment Using a Mesoscale Two-Dimensional Model. *J. Atmos. Sci.* 46 (20), 3077–3107. doi:10.1175/1520-0469(1989)046<3077:NSOCOD>2.0.CO;2
- Ellis, R., and Businger, S. (2010). Helical Circulations in the Typhoon Boundary Layer. *J. Geophys. Res.* 115, D06205. doi:10.1029/2009JD011819
- Emanuel, K. A. (1986). An Air-Sea Interaction Theory for Tropical Cyclones. Part I: Steady-State Maintenance. *J. Atmos. Sci.* 43 (6), 585–605. doi:10.1175/1520-0469(1986)043<0585:AASITF>2.0.CO;2
- Emanuel, K. A. (1995). Sensitivity of Tropical Cyclones to Surface Exchange Coefficients and a Revised Steady-State Model Incorporating Eye Dynamics. *J. Atmos. Sci.* 52 (22), 3969–3976. doi:10.1175/1520-0469(1995)052<3969:SOTCTS>2.0.CO;2
- Feng, Y., Wu, L., Liu, Q., and Zhou, W. (2021). Negative Pressure Perturbations Associated with Tornado-Scale Vortices in the Tropical Cyclone Boundary Layer. *Geophys. Res. Lett.* 48 (9). doi:10.1029/2020GL091339
- Foster, R. C. (2005). Why Rolls Are Prevalent in the Hurricane Boundary Layer. *J. Atmos. Sci.* 62 (8), 2647–2661. doi:10.1175/JAS3475.1
- Gao, K., Ginis, I., Doyle, J. D., and Jin, Y. (2017). Effect of Boundary Layer Roll Vortices on the Development of an Axisymmetric Tropical Cyclone. *J. Atmos. Sci.* 74 (9), 2737–2759. doi:10.1175/JAS-D-16-0222.1
- Gao, K., and Ginis, I. (2018). On the Characteristics of Linear-phase Roll Vortices under a Moving Hurricane Boundary Layer. *J. Atmos. Sci.* 75 (8), 2589–2598. doi:10.1175/JAS-D-17-0363.1
- Gao, K., and Ginis, I. (2016). On the Equilibrium-State Roll Vortices and Their Effects in the Hurricane Boundary Layer. *J. Atmos. Sci.* 73 (3), 1205–1222. doi:10.1175/JAS-D-15-0089.1
- Green, B. W., and Zhang, F. (2014). Sensitivity of Tropical Cyclone Simulations to Parametric Uncertainties in Air-Sea Fluxes and Implications for Parameter Estimation. *Monthly Weather Rev.* 142 (6), 2290–2308. doi:10.1175/mwr-d-13-00208.1
- Guimond, S. R., Heymsfield, G. M., and Turk, F. J. (2010). Multiscale Observations of Hurricane Dennis (2005): The Effects of Hot Towers on Rapid Intensification. *J. Atmos. Sci.* 67 (3), 633–654. doi:10.1175/2009JAS3119.1
- Heymsfield, G. M., Tian, L., Heymsfield, A. J., Li, L., and Guimond, S. (2010). Characteristics of Deep Tropical and Subtropical Convection from Nadir-

AUTHOR CONTRIBUTIONS

LW and ZG conducted analysis and writing. ZG contributed to figures included in this manuscript. XZ conducted the numerical experiment.

FUNDING

This study was jointly supported by the National Natural Science Foundation of China (41730961, 41930967, and 41905001) and the Scientific Research Program of Shanghai Municipal Science and Technology Commission (19dz1200101).

Viewing High-Altitude Airborne Doppler Radar. *J. Atmos. Sci.* 67 (2), 285–308. doi:10.1175/2009JAS3132.1

- Hogan, R. J., Grant, A. L. M., Illingworth, A. J., Pearson, G. N., and O’Connor, E. J. (2009). Vertical Velocity Variance and Skewness in clear and Cloud-Topped Boundary Layers as Revealed by Doppler Lidar. *Q.J.R. Meteorol. Soc.* 135 (640), 635–643. doi:10.1002/QJ.413
- Hong, S. Y., and Lim, J.-O. J. (2006). The WRF Single-Moment 6-Class Microphysics Scheme (WSM6). *Asia-Pacific J. Atmos. Sci.* 42 (2), 129–151.
- Jiang, Y., Wu, L., Zhao, H., Zhou, X., and Liu, Q. (2020). Azimuthal Variations of the Convective-Scale Structure in a Simulated Tropical Cyclone Principal Rainband. *Adv. Atmos. Sci.* 37 (11), 1239–1255. doi:10.1007/S00376-020-9248-X
- Kain, J. S., and Fritsch, J. M. (1993). “Convective Parameterization for Mesoscale Models: The Kain-Fritsch Scheme,” in *The Representation of Cumulus Convection in Numerical Models*. Editor K. Emanuel (New York, United States: Springer), 165–170. doi:10.1007/978-1-935704-13-3_16
- LeMone, M. A., and Zipser, E. J. (1980). Cumulonimbus Vertical Velocity Events in GATE. Part I: Diameter, Intensity and Mass Flux. *J. Atmos. Sci.* 37 (11), 2444–2457. doi:10.1175/1520-0469(1980)037<2444:CVVEIG>2.0.CO;2
- Liu, Q., Wu, L., Qin, N., and Li, Y. (2021). Storm-Scale and Fine-Scale Boundary Layer Structures of Tropical Cyclones Simulated with the WRF-LES Framework. *Geophys. Res. Atmos.* 126, e2021JD035511. doi:10.1029/2021JD035511
- Lorsolo, S., Schroeder, J. L., Dodge, P., and Marks, F. (2008). An Observational Study of Hurricane Boundary Layer Small-Scale Coherent Structures. *Monthly Weather Rev.* 136 (8), 2871–2893. doi:10.1175/2008MWR2273.1
- Lorsolo, S., Zhang, J. A., Marks, F., and Gamache, J. (2010). Estimation and Mapping of Hurricane Turbulent Energy Using Airborne Doppler Measurements. *Monthly Weather Rev.* 138 (9), 3656–3670. doi:10.1175/2010MWR3183.1
- Marks, F. D., Black, P. G., Montgomery, M. T., and Burpee, R. W. (2008). Structure of the Eye and Eyewall of Hurricane Hugo (1989). *Monthly Weather Rev.* 136 (4), 1237–1259. doi:10.1175/2007MWR2073.1
- Mirocha, J. D., Lundquist, J. K., and Kosović, B. (2010). Implementation of a Nonlinear Subfilter Turbulence Stress Model for Large-Eddy Simulation in the Advanced Research WRF Model. *Monthly Weather Rev.* 138 (11), 4212–4228. doi:10.1175/2010MWR3286.1
- Mlawer, E. J., Taubman, S. J., Brown, P. D., Iacono, M. J., and Clough, S. A. (1997). Radiative Transfer for Inhomogeneous Atmospheres: RRTM, a Validated Correlated-K Model for the Longwave. *J. Geophys. Res.* 102, 16663–16682. doi:10.1029/97JD00237
- Morrison, I., Businger, S., Marks, F., Dodge, P., and Businger, J. A. (2005). An Observational Case for the Prevalence of Roll Vortices in the Hurricane Boundary Layer*. *J. Atmos. Sci.* 62 (8), 2662–2673. doi:10.1175/JAS3508.1
- Noh, Y., Cheon, W. G., Hong, S. Y., and Raasch, S. (2003). Improvement of the K-Profile Model for the Planetary Boundary Layer Based on Large Eddy Simulation Data. *Boundary-Layer Meteorology* 107 (2), 401–427. doi:10.1023/A:1022146015946
- Nolan, D. S. (2005). Instabilities in hurricane-like Boundary Layers. *Dyn. Atmospheres Oceans* 40 (3), 209–236. doi:10.1016/J.DYNATMOCE.2005.03.002
- Ooyama, K. (1964). A Dynamical Model for the Study of Tropical Cyclone Development. *Geofisica Internacional (Mexico)* 4, 187–198.

- Ooyama, K. (1969). Numerical Simulation of the Life Cycle of Tropical Cyclones. *J. Atmos. Sci.* 26 (1), 3–40. doi:10.1175/1520-0469(1969)026<0003:NSOTLC>2.0.CO;2
- Qiu, W., Wu, L., and Ren, F. (2020). Monsoonal Influences on Offshore Rapid Intensification of Landfalling Typhoons in a Sheared Environment over the South China Sea. *Weather Forecast.* 35 (2), 623–634. doi:10.1175/WAF-D-19-0134.1
- Rogers, R., Aberson, S., Aksoy, A., Annane, B., Black, M., Cione, J., et al. (2013). NOAA'S Hurricane Intensity Forecasting Experiment: A Progress Report. *Bull. Am. Meteorol. Soc.* 94 (6), 859–882. doi:10.1175/BAMS-D-12-00089.1
- Rogers, R., Aberson, S., Black, M., Black, P., Cione, J., Dodge, P., et al. (2006). The Intensity Forecasting Experiment: A NOAA Multiyear Field Program for Improving Tropical Cyclone Intensity Forecasts. *Bull. Am. Meteorol. Soc.* 87 (11), 1523–1538. doi:10.1175/BAMS-87-11-1523
- Rogers, R., Lorusso, S., Reasor, P., Gamache, J., and Marks, F. (2012). Multiscale Analysis of Tropical Cyclone Kinematic Structure from Airborne Doppler Radar Composites. *Monthly Weather Rev.* 140 (1), 77–99. doi:10.1175/MWR-D-10-05075.1
- Wang, S., and Jiang, Q. (2016). Impact of Vertical Wind Shear on Roll Structure in Idealized hurricane Boundary Layers. *Atmos. Chem. Phys.* 17 (5), 3507–3524. doi:10.5194/ACP-17-3507-2017
- Wu, L., Liu, Q., and Li, Y. (2018). Prevalence of Tornado-Scale Vortices in the Tropical Cyclone Eyewall. *Proc. Natl. Acad. Sci. USA* 115 (33), 8307–8310. doi:10.1073/PNAS.1807217115
- Wu, L., Liu, Q., and Li, Y. (2019). Tornado-scale Vortices in the Tropical Cyclone Boundary Layer: Numerical Simulation with the WRF-LES Framework. *Atmos. Chem. Phys.* 19 (4), 2477–2487. doi:10.5194/ACP-19-2477-2019
- Wurman, J., and Kosiba, K. (2018). The Role of Small-Scale Vortices in Enhancing Surface Winds and Damage in Hurricane Harvey (2017). *Mon. Wea. Rev.* 146 (3), 713–722. doi:10.1175/MWR-D-17-0327.1
- Wurman, J., and Winslow, J. (1998). Intense Sub-kilometer-scale Boundary Layer Rolls Observed in hurricane Fran. *Science* 280 (5363), 555–557. doi:10.1126/SCIENCE.280.5363.555
- Yang, H., Wu, L., and Xie, T. (2020). Comparisons of Four Methods for Tropical Cyclone Center Detection in a High-Resolution Simulation. *J. Meteorol. Soc. Jpn.* 98 (2), 379–393. doi:10.2151/JMSJ.2020-020
- Zhang, J. A., Marks, F. D., Montgomery, M. T., and Lorusso, S. (2011). An Estimation of Turbulent Characteristics in the Low-Level Region of Intense Hurricanes Allen (1980) and Hugo (1989). *Mon. Wea. Rev.* 139 (5), 1447–1462. doi:10.1175/2010MWR3435.1
- Zheng, Y., Wu, L., Zhao, H., Zhou, X., and Liu, Q. (2020). Simulation of Extreme Updrafts in the Tropical Cyclone Eyewall. *Adv. Atmos. Sci.* 37 (7), 781–792. doi:10.1007/S00376-020-9197-4
- Zhu, P., Hazelton, A., Zhang, Z., Marks, F. D., and Tallapragada, V. (2021). The Role of Eyewall Turbulent Transport in the Pathway to Intensification of Tropical Cyclones. *Geophys. Res. Atmos.* 126, e2021JD034983. doi:10.1029/2021JD034983
- Zhu, P., Tyner, B., Zhang, J. A., Aligo, E., Gopalakrishnan, S., Marks, F. D., et al. (2019). Role of Eyewall and Rainband Eddy Forcing in Tropical Cyclone Intensification. *Atmos. Chem. Phys.* 19 (22), 14289–14310. doi:10.5194/ACP-19-14289-2019

Conflict of Interest: The authors declare that the research was conducted in the absence of any commercial or financial relationships that could be construed as a potential conflict of interest.

Publisher's Note: All claims expressed in this article are solely those of the authors and do not necessarily represent those of their affiliated organizations, or those of the publisher, the editors and the reviewers. Any product that may be evaluated in this article, or claim that may be made by its manufacturer, is not guaranteed or endorsed by the publisher.

Copyright © 2022 Gao, Wu and Zhou. This is an open-access article distributed under the terms of the Creative Commons Attribution License (CC BY). The use, distribution or reproduction in other forums is permitted, provided the original author(s) and the copyright owner(s) are credited and that the original publication in this journal is cited, in accordance with accepted academic practice. No use, distribution or reproduction is permitted which does not comply with these terms.



Modulation of Pacific Sea Surface Temperatures on the Late-Season Tropical Cyclone Tracks Over the Western North Pacific and its Implication for Seasonal Forecasting

Hua Yu, Chao Wang and Xuyang Ge*

Key Laboratory of Meteorological Disaster of Ministry of Education, Joint International Research Laboratory of Climate and Environment Change and Collaborative Innovation Center on Forecast and Evaluation of Meteorological Disasters, Nanjing University of Information Science and Technology, Nanjing, China

OPEN ACCESS

Edited by:

Guanghua Chen,
Institute of Atmospheric Physics
(CAS), China

Reviewed by:

Chundi Hu,
Sun Yat-sen University, China
Gen Li,
Hohai University, China

*Correspondence:

Xuyang Ge
xuyang@nuist.edu.cn

Specialty section:

This article was submitted to
Atmospheric Science,
a section of the journal
Frontiers in Earth Science

Received: 14 December 2021

Accepted: 07 January 2022

Published: 07 February 2022

Citation:

Yu H, Wang C and Ge X (2022)
Modulation of Pacific Sea Surface
Temperatures on the Late-Season
Tropical Cyclone Tracks Over the
Western North Pacific and its
Implication for Seasonal Forecasting.
Front. Earth Sci. 10:835001.
doi: 10.3389/feart.2022.835001

In this study, two leading modes of the late season (October–December) TC track frequency are identified with the empirical orthogonal function analysis. It is found that circulation anomalies associated with the two modes are linked to the concurrent El Niño–Southern Oscillation (ENSO), but with distinct locations of maximum sea surface temperature (SST). For the first mode, the maximum SST warming and the resulted heating can extend to the equatorial central Pacific, which emanates a cyclonic circulation extending to the east of the Philippines, and then generates an anti-cyclonic circulation to the west of the Philippines by dry advection and local air–sea interaction. In contrast, for the second mode, the maximum SST warming and the corresponding heating shift eastward to the equatorial eastern Pacific, the related cyclonic circulation, and the compensation descending motion migrate eastward and are confined to the east of 150°E. The associated suppressed heating then emanates an anti-cyclonic circulation to the west of 150°E. These anomalous circulations can modulate TC genesis and steering flow and thus contribute to variations in the two modes. A set of physics-based empirical models is further built, which shows a promising pathway for the seasonal forecasting of the two modes and the basin-wide total TC track frequency. The results highlight the importance of the location of ENSO maximum SST in understanding and seasonal prediction of the late-season TC tracks over the WNP.

Keywords: seasonal forecast, El Niño/Southern Oscillation, climate variability, tropical cyclone track, Western North Pacific

INTRODUCTION

Understanding the climate variabilities in tropical cyclone (TC) track over the western North Pacific (WNP) is of great importance owing to enormous TC-generated disasters (Zhang et al., 2009; Peduzzi et al., 2012). Variabilities in the WNP TC tracks are modulated by multi-timescale oscillations. The intra-seasonal oscillation has been known to be important to TC track through modulating large-scale steering flow and TC genesis location owing to the distinct convection and circulation features in its different phases (Li and Zhou 2013; Kim and Seo 2016). As the dominant

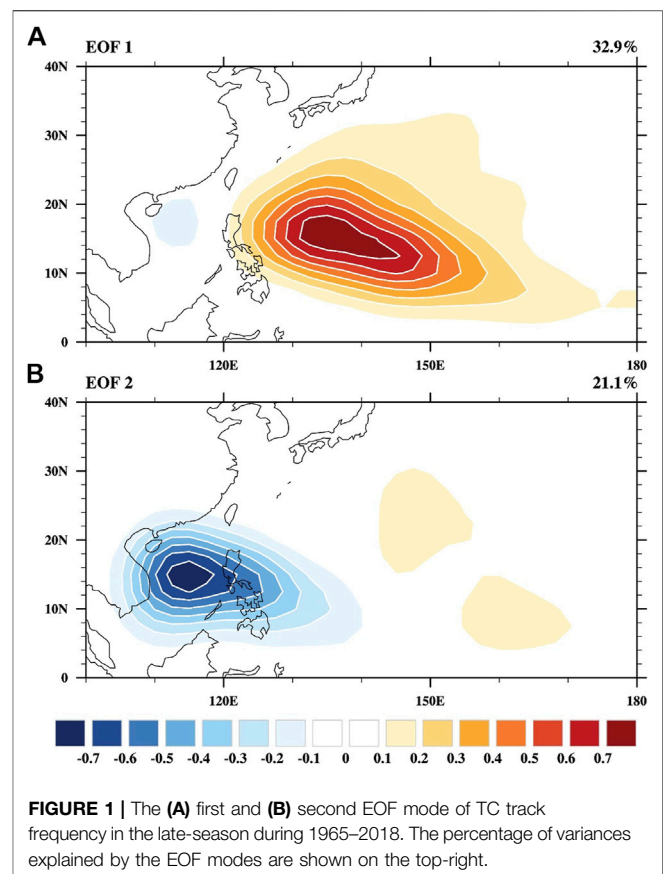
mode on the interannual time scale, El Niño–Southern Oscillation (ENSO) serves as a major driver of the interannual variability in the WNP TC tracks (Wang and Chan 2002; Wu and Wang 2004; Camargo et al., 2007; Hu et al., 2018). TC genesis locations tend to shift eastward during the warm phase of ENSO, leading to more TCs reaching the subtropical WNP (Zhao et al., 2010). However, the recently emerged central Pacific ENSO shows a distinct impact on the WNP TC tracks compared to the eastern Pacific ENSO (Chen and Tam 2010; Hong et al., 2011). The WNP subtropical high was suggested to play an essential role in the connection between ENSO and TC tracks through modulating the TC genesis location and steering flow (Wang and Wang 2019). In addition, the stratospheric quasi-biennial oscillation was found to be important for TC tracks in the subtropical WNP (Ho et al., 2009). On the decadal time scale, zonal migration of the WNP subtropical high can inhibit or favor TCs influencing the subtropical WNP, resulting in notable variability in TC tracks over the WNP (Ho et al., 2004; Wu et al., 2005; Liu and Chan 2008; Zhao and Wu 2014). The inter-decadal variability in the subtropical high is partially attributed to the Pacific Decadal Oscillation (Liu and Chan 2008). Zhao et al. (2020) found that the ENSO-like sea surface temperature (SST) pattern and the global warming collectively contribute to the inter-decadal variability in TC tracks over the WNP.

Most previous studies focus on the peak season (July–September) and TC track variability in the late season (October–December) remains unclear. In the late season, TCs at the lower latitudes have a greater potential to experience rapid intensification and thus to attain stronger intensity [e.g. Haiyan (2013) and Hagibis (2019)], which cause catastrophic disasters to the Pacific coastal regions. Specifically, in the late season, the ratio of TCs developing into typhoons is about 70%, which is much higher than that during the peak season (Hsu et al., 2014). Moreover, TC track change acts as a main driver of variations in the basin-wide translation speed in the late season (Wang et al., 2020; 2021b). In this regard, it motivates us to examine and understand the climate variability of late-season TC tracks over the WNP.

The paper is organized as follows. *Data and method* describes the data and methods, and *Two dominant modes of late-season track frequency* illustrates the two leading modes of late-season TC track frequency. *Origins of the two leading modes* interprets the mechanisms associated with the two leading modes. *Potential utility for the seasonal forecasting of late-season TC track* attempts to establish the seasonal forecasting scheme for the late-season TC track. A summary is presented in *Conclusion*.

DATA AND METHOD

TC track information was obtained from the Joint Typhoon Warning Center (JTWC). TCs are defined as those in the datasets with maximum wind speed exceeding the tropical storm intensity (35 knots). Monthly SST (Huang et al., 2017) and outgoing longwave radiation (OLR, Lee et al., 2007) were obtained from the National Oceanic and Atmospheric Administration. Atmospheric variables from the National

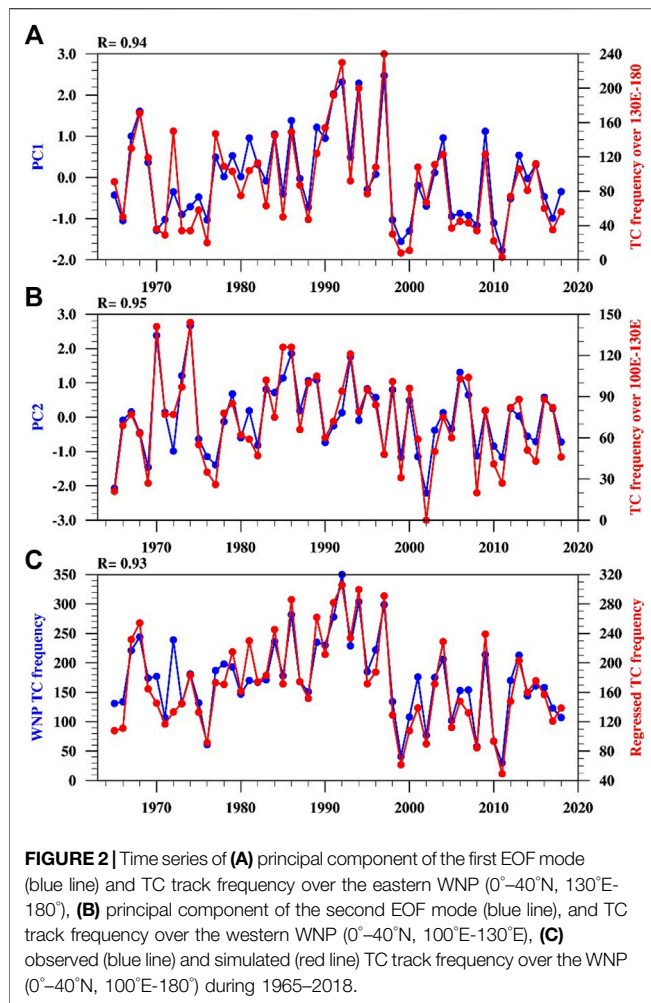


Centers for Environmental Prediction (NCEP) National Center for Atmospheric Research (NCAR) reanalysis (Kalnay et al., 1996) were used to demonstrate the anomalous large-scale circulation.

TC track is estimated by the occurrence frequency at each 2.5 latitude–longitude grid box (Wu and Wang 2004; Liu and Chan 2008). The conventional empirical orthogonal function (EOF) method was used to extract the dominant mode of the late-season TC track. Large-scale steering flow was defined as the pressure-weighted mean flow between 850 and 300 hPa (Wu and Wang 2004). Statistical significance was assessed using the two-tailed Student's *t*-test (Wilks 2006). In this study, we focus on TC activity in the late season (i.e., October–December) over the WNP (0°–40° N, 100° E–180°), and the period of interest covers from 1965 to 2018.

To estimate the overall effects of large-scale conditions on TC genesis, a newly developed dynamic genesis potential index (DGPI, Wang and Murakami 2020) was used. The formulation of the DGPI is defined as follows:

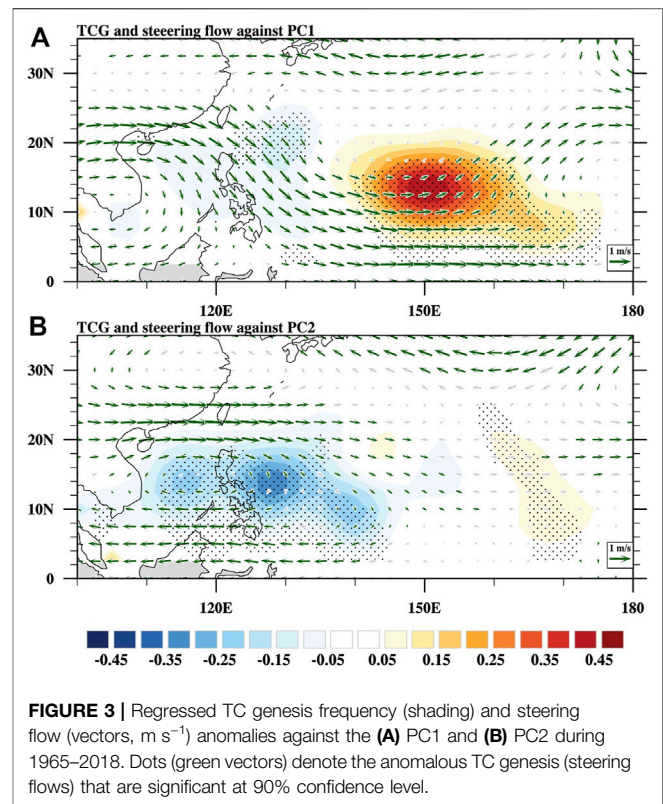
$$DGPI = (2 + 0.1V_s)^{-1.7} \left(5.5 - \frac{\partial u}{\partial y} 10^5 \right)^{2.3} (5 - 20\omega)^{3.3} \\ (5.5 + |10^5 \eta|)^{2.4} e^{-11.8} - 1$$



where V_s is the magnitude of the vertical wind shear (m s^{-1}) between 850 and 200 hPa, $\frac{\partial u}{\partial y}$ is the meridional gradient of zonal wind (s^{-1}) at 500 hPa, ω is the 500 hPa vertical pressure velocity (Pa s^{-1}), and η is the absolute vorticity (s^{-1}) at 850 hPa. The DGPI highlights the role of dynamical factors in TC genesis, which shows superior skill in representing temporal variability of TC genesis in the WNP compared to those empirical genesis indexes combining thermodynamic and dynamic factors (Wang and Murakami 2020).

TWO DOMINANT MODES OF LATE-SEASON TRACK FREQUENCY

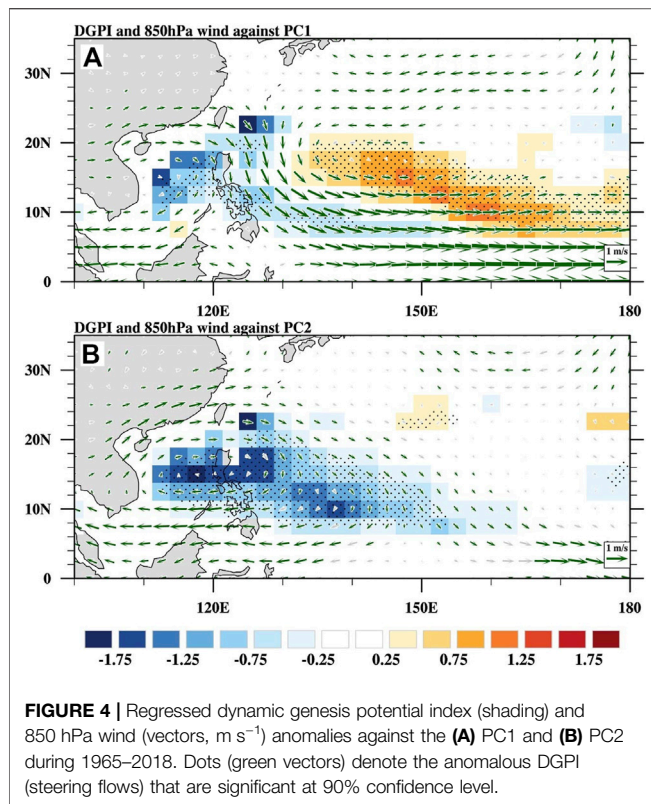
Figure 1 shows two leading EOF modes of late-season TC track frequency over the WNP. The first (second) mode can explain 32.9% (21.1%) of the total variance of late-season TC track frequency. Both modes show zonally distributed anomalies with different variability centers, indicating notable zonal variability in the late-season TC track. The first mode shows prominent positive anomalies occurring to the east of 120°E but weak anomalies in the South China Sea (Figure 1A). For the



second mode, marked positive anomalies occur to the west of 140°E with a center located at the South China Sea and weak negative anomalies to the east of 140°E (Figure 1B). Time series of principal components (PCs) of the two modes exhibit considerable interannual and inter-decadal variations (Figure 2). The temporal evolution of PC1 can largely reflect the variability of track frequency over the eastern WNP (0°–40°N, 130°E–180°), with a correlation coefficient of 0.94 during 1965–2018 (Figure 2A). Meanwhile, as shown in Figure 2B, the time series of PC2 is significantly correlated ($r = 0.95$) with the track frequency over the western WNP (0°–40°N, 100°E–130°E). By using multiple linear regression with these PCs of the two leading modes, we attempt to reproduce the temporal variations of total TC track frequency over the WNP. It is found that more than 85% of the variance of the late season can be reconstructed (Figure 2C), reflecting a close linkage between the two PCs and the late-season track frequency. To this end, we attempt to reveal the possible variability sources for the two leading modes.

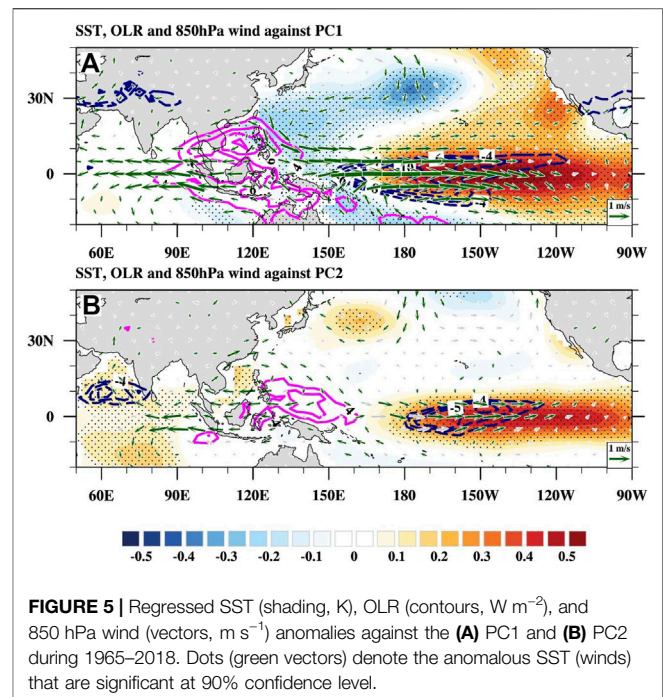
ORIGINS OF THE TWO LEADING MODES

In general, climate variability in TC track frequency is largely controlled by TC genesis location and large-scale steering flow (Wu and Wang 2004). Figure 3 shows the regressed TC genesis and large-scale steering flow anomalies against PCs of these two leading modes. The positive phase of the first mode corresponds to an enhanced TC genesis in the eastern WNP but relatively



weak negative anomalies of TC genesis to the west of 140°E (Figure 3A). Meanwhile, the westward steering tends to decelerate the climatological eastward steering and thus increase TC track frequency over the eastern WNP. The suppressed TC genesis to the west of 140°E contributes to the negative anomalies in track frequency therein (Figure 1A). For the second mode, the suppressed TC genesis to the west of 150°E and the westward steering to the south of 15°N collectively contribute the negative TC track frequency to the west of 140°E (Figure 3B). In short, the results suggest variability in two leading modes of TC track frequency is ascribed to TC genesis and large-scale steering.

It has been well realized that large-scale conditions are important for TC genesis (Gray 1968; Emanuel and Nolan 2004; Wang and Murakami 2020). Figure 4 shows the regressed DGPI and 850 hPa wind anomalies against PCs of the two leading modes. For the first mode, a cyclonic circulation occurs to the east of the Philippines, but anti-cyclonic circulation occupies the South China Sea (Figure 4A). Accordingly, the associated anomalies in large-scale parameters such as vorticity and mid-level vertical velocity show opposite anomalies to the east and west of 130°E , which are favorable for TC genesis to the east of 130°E but suppress TC genesis to the west of 130°E (figure not shown). Accordingly, DGPI shows positive (negative) anomalies to the east (west) of 130°E , which generally matches the observed distribution of TC genesis (Figure 3A). For the second mode, an anti-cyclonic circulation extends to about 150°E ; the associated anti-cyclonic vorticity is unfavorable for TC genesis (Figure 4B). As a result, the corresponding DGPI shows



negative anomalies to the west of 150°E , which is in accordance with the distribution of TC genesis (Figure 3B).

The aforementioned results suggest that large-scale circulations play an important role in the two modes. Namely, the key for the distinct large-scale conditions associated with the two modes lies in their different zonal ranges of the anomalous cyclonic circulation, which is speculated to be linked to the distinct maximum centers of SST anomalies over the equatorial Pacific associated with the two modes (Figure 5). Although the SST anomalies in both modes show an El Niño-like pattern, marked differences emanate in magnitude and zonal extension. For instance, compared with the second mode, the SST warming magnitude of the first mode is much greater. Furthermore, its maximum SST zone extends further westward. Specifically, the significant SST warming anomalies can extend to the west of the dateline and the maximum SST warming can extend to about 170°W (Figure 5A). The SST warming in the equatorial central Pacific acts to increase the convective heating (represented by lower OLR) and emanates a cyclonic circulation extending to the east of 120°E as a Rossby wave response. Moreover, the anomalous northerly to the western flank of the cyclonic circulation tends to cool the underlying SST by strengthening background winds and stabilize the tropical atmosphere by dry advection (Wang et al., 2000; Wu et al., 2017). The cold SST anomaly and reduced instability act to suppress convection, which can further emanate an anti-cyclonic circulation to the west of 120°E . The cyclonic (anti-cyclonic) circulation to the east (west) of 120°E is consistent with the distribution in TC genesis and anomalous large-scale steering flow shown in Figure 3A. In contrast, the maximum center of SST warming associated with the second mode shifts far eastward compared to that of the first mode, and the significant warming

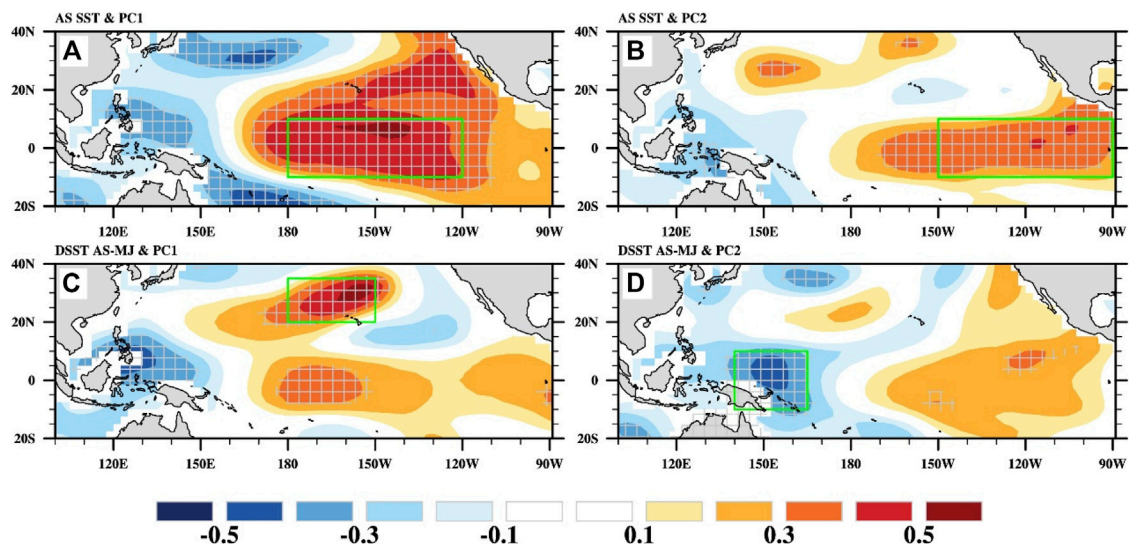


FIGURE 6 | Correlation map between PC1 and (A) August–September mean SST and (C) SST tendency from May–June to August–September during 1965–2018. (B) and (D) are the same as (A) and (C) but for PC2. Hatched areas denote regions with correlation coefficients that are significant at the 90% confidence level. The green boxes denote definition areas for the selected predictors.

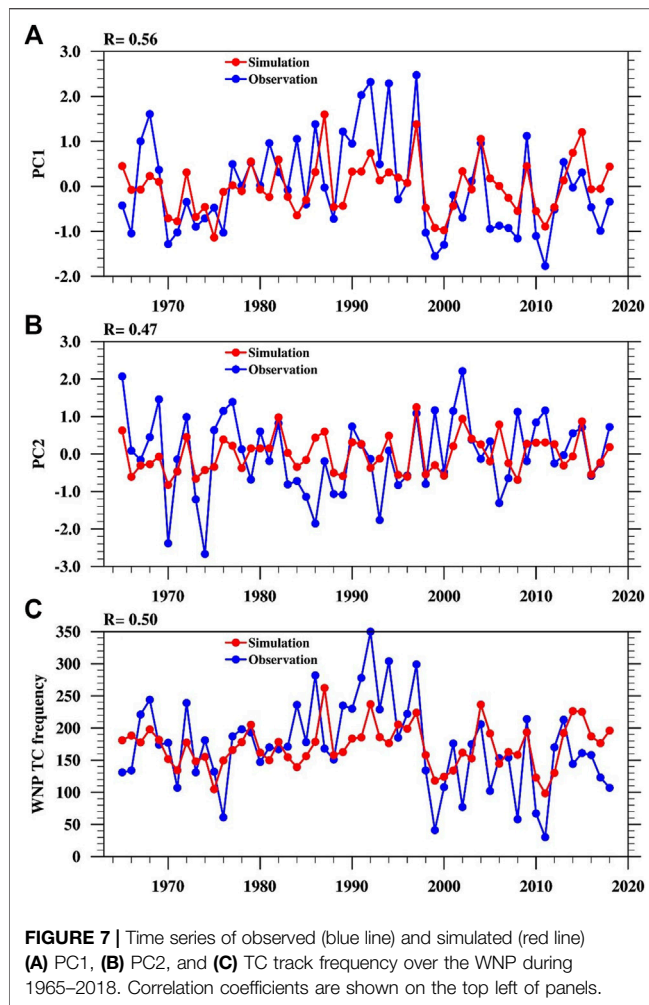
signal is confined to the east of the dateline. Accompanied with the eastward migration of SST warming-induced positive convective heating, the associated Rossby wave response (i.e., the cyclonic circulation) is confined to the east of 150°E, which is much more eastward compared with its counterpart for the first mode. Meanwhile, the SST warming induced ascending motion tends to generate an upper-level converge toward the tropical eastern WNP, leading to the suppressed convection in the tropical eastern WNP. Moreover, the anomalous northerly to the western flank of the cyclonic circulation acts to reinforce the suppressed convection in tropical WNP around 150°E by dry advection. Accordingly, the suppressed convective heating emanates an anti-cyclonic circulation to the west of 150°E as a Rossby response (Figure 5B). In addition, SST warming in the tropical western Indian ocean is likely conducive to the anti-cyclonic circulation to the west of 150°E through emanating the atmospheric Kelvin wave (Xie et al., 2009) or modulating zonal overturning circulation (Wang et al., 2021a). The anticyclonic circulation to the west of 150°E is unfavorable for TC genesis therein, which is consistent with the suppressed TC genesis shown in Figure 3B. The result suggests that the first mode is connected to strong ENSO events with an SST extremum center located in the equatorial central Pacific, while the second mode is closely linked to moderate/weak ENSO events with an equatorial eastern Pacific SST extremum center.

POTENTIAL UTILITY FOR THE SEASONAL FORECASTING OF LATE-SEASON TC TRACK

In this section, we built physical empirical models (PEMs, Wang et al., 2013; Wang et al., 2015) to predict the two modes of the

late-season track with a zero-month lead (i.e., starting from September 30th) by using SST predictors and linear regressions. Following Wang et al. (2015), two types of predictors were used in this study. The first type consists of the persistent predictors that suggest the relatively slow evolution of boundary anomalies that can persist into the forecasting season. The second type consists of the tendency signals that denote the evolution tendency of predictors. Persistent signals are defined as the 2-month mean (August–September) before the forecasting season (October–December), and tendency signals are defined as the difference between August and September mean and May–June mean.

Two predictors are used to construct the PEM for the first mode. The first is the August–September mean SST over the equatorial central Pacific (–10°S–10°N, 180°–120°W, Figure 6A). Physically, the August–September mean SST anomalies in the tropical central Pacific can foreshow their value in the late season due to the phase-locking property of ENSO (Rasmusson and Carpenter 1982). Additionally, a tendency predictor was identified over the subtropical North Pacific (20°N–32.5°N, 180°–150°W, Figure 6C), which indicates the development of SST warming in the equatorial central Pacific through the seasonal footprint mechanism (Vimont et al., 2001; Amaya 2019). For the second mode, two predictors are used to construct the PEM. The first is the August–September mean SST over the equatorial eastern Pacific (–10°S–10°N, 150°W–90°W, Figure 6B), which infers the SST anomalies in the late season by utilizing the phase-locking property of ENSO. Moreover, a tendency predictor over the equatorial central WNP (–10°S–10°N, 140°E–165°E, Figure 6D) was selected, which can infer the development of vertical motion in this region and thus the anti-cyclonic circulation to its west. Generally, all these selected



predictors are based on the physical processes that govern the large-scale circulations associated with the two modes.

Although the standard deviation of the predicted (simulated) TC track frequency is less than that of the observed, the PEMs using the identified SST predictors can reasonably reproduce the temporal variability of the two modes of late-season TC track frequency (Figure 7). The prediction (simulation) temporal correlation coefficient skills for the first and second modes are 0.56 and 0.47, respectively. These account for about 30% of the total variance, suggesting that these two modes are potentially predictable. Provided that these two leading modes can largely represent the variability of TC track frequency over the whole WNP in the late season, we further regressed the WNP TC track frequency with the predicted two modes (Figure 7C). The correlation between the regressed TC track frequency and observation is 0.50, which is significant at 95% confidence level. These results suggest a potential utility of our strategy for the seasonal forecasting of TC activity in the late season over the WNP.

CONCLUSION

In this study, two leading modes of the late-season TC track frequency are identified with the empirical orthogonal function analysis. The first mode features prominent positive anomalies to the east of the Philippines but weak negative anomalies to the west of the Philippines. From a dynamical viewpoint, the large-scale conditions associated with a cyclonic (anti-cyclonic) circulation to the east (west) of the Philippines act to enhance (suppress) TC genesis and thus contribute to the anomalous TC track frequency distribution. Additionally, the westward large-scale steering associated with the cyclonic circulation to the east of the Philippines tends to prevent westward TC move and contribute to the anomalous TC track frequency as well. For the second mode, it is characterized as notable negative (weak positive) anomalies in the western (eastern) WNP, respectively. Dynamically, a cyclonic (anticyclonic) circulation is confined to the east (west) of 150°E, which is favorable (unfavorable) to TC genesis to the east (west) of 150°E and eventually results in the negative (positive) anomalies of TC track frequency in the western (eastern) WNP.

Further analyses reveal that the circulations associated with two modes are both linked to the concurrent El Niño-Southern Oscillation (ENSO), but with different locations of maximum sea surface temperature (SST). For the first mode, the maximum SST warming can extend to about 170°W. The associated heating can emanate a cyclonic circulation extending to the east of the Philippines. Meanwhile, the anomalous northerly to the western flank of the cyclonic circulation can then generate cyclonic circulation to the west of 120°E through dry advection and local air-sea interaction. In contrast, the maximum center of SST warming and the corresponding increased convective heating associated with the second mode shift far eastward to the equatorial eastern Pacific. Accordingly, the associated Rossby wave response (i.e. the cyclonic circulation) migrates eastward and is confined to the east of 150°E. Meanwhile, the SST warming-induced ascending motion tends to generate an upper-level converge toward the tropical eastern WNP, leading to the suppressed convection in the tropical eastern WNP. Moreover, the anomalous northerly to the western flank of the cyclonic circulation acts to reinforce the suppressed convection in tropical WNP around 150°E by dry advection.

The suppressed heating around 150°E then emanates an anti-cyclonic circulation to the west of 150°E *via* the Gill-type response. The result suggests that the impacts of ENSO on the late-season TC tracks are sensitive to the location of the maximum SST anomaly.

A set of PEMs is further built to predict the two modes of late-season TC track frequency with the persistent and tendency SST predictors. The PEMs can reasonably reproduce the inter-annual variability of the two modes and the basin-wide total TC track frequency, suggesting that they are potentially predictable. The reasonable predicting skill here suggests that distinguishing the anomaly center of ENSO SST helps improve the seasonal prediction of the late-season TC tracks over the WNP.

DATA AVAILABILITY STATEMENT

The original contributions presented in the study are included in the article/supplementary material; further inquiries can be directed to the corresponding author.

AUTHOR CONTRIBUTIONS

HY, CW, and XG contributed to the conception and design of the study. HY, CW, and XG performed the analysis and wrote the

article. All authors contributed and approved the submitted version.

FUNDING

This study was jointly supported by the National Natural Science Foundation of China (Grant Nos. 42175003 and 42075031) and the National Key Research and Development Program of China (Grant Nos. 2019YFC1510201). All sources of funding were received for the research being submitted.

REFERENCES

- Amaya, D. J. (2019). The Pacific Meridional Mode and ENSO: a Review. *Curr. Clim. Change Rep.* 5, 296–307. doi:10.1007/s40641-019-00142-x
- Camargo, S. J., Robertson, A. W., Gaffney, S. J., Smyth, P., and Ghil, M. (2007). Cluster Analysis of Typhoon Tracks. Part II: Large-Scale Circulation and ENSO. *J. Clim.* 20, 3654–3676. doi:10.1175/jcli4203.1
- Chen, G., and Tam, C.-Y. (2010). Different Impacts of Two Kinds of Pacific Ocean Warming on Tropical Cyclone Frequency over the Western North Pacific. *Geophys. Res. Lett.* 37, L01803. doi:10.1029/2009gl014708
- Emanuel, K. A., and Nolan, D. S. (2004). "Tropical Cyclone Activity and the Global Climate System," in 26th Conf. on Hurricanes and Tropical Meteorology, Miami, FL, May 2–7, 2004 (Boston, Massachusetts, United States: Amer. Meteor. Soc.), 240–241. Preprints.
- Gray, W. M. (1968). Global View of the Origin of Tropical Disturbances and Storms. *Mon. Wea. Rev.* 96, 669–700. doi:10.1175/1520-0493(1968)096<0669:gvotoo>2.0.co;2
- Ho, C.-H., Kim, H.-S., Jeong, J.-H., and Son, S.-W. (2009). Influence of Stratospheric Quasi-Biennial Oscillation on Tropical Cyclone Tracks in the Western North Pacific. *Geophys. Res. Lett.* 36, L06702. doi:10.1029/2009gl037163
- Ho, C.-H., Baik, J.-J., Kim, J.-H., Gong, D.-Y., and Sui, C.-H. (2004). Interdecadal Changes in Summertime Typhoon Tracks. *J. Clim.* 17, 1767–1776. doi:10.1175/1520-0442(2004)017<1767:icistt>2.0.co;2
- Hong, C.-C., Li, Y.-H., Li, T., and Lee, M.-Y. (2011). Impacts of central Pacific and Eastern Pacific El Niños on Tropical Cyclone Tracks over the Western North Pacific. *Geophys. Res. Lett.* 38, L16712. doi:10.1029/2011gl048821
- Hsu, P.-C., Chu, P.-S., Murakami, H., and Zhao, X. (2014). An Abrupt Decrease in the Late-Season Typhoon Activity over the Western North Pacific*. *J. Clim.* 27, 4296–4312. doi:10.1175/jcli-d-13-00417.1
- Hu, C., Zhang, C., Yang, S., Chen, D., and He, S. (2018). Perspective on the Northwestward Shift of Autumn Tropical Cyclogenesis Locations over the Western North Pacific from Shifting ENSO. *Clim. Dyn.* 51, 2455–2465. doi:10.1007/s00382-017-4022-1
- Huang, B., Thorne, P. W., Banzon, V. F., Boyer, T., Chepurin, G., Lawrimore, J. H., et al. (2017). Extended Reconstructed Sea Surface Temperature, Version 5 (ERSSTv5): Upgrades, Validations, and Intercomparisons. *J. Clim.* 30, 8179–8205. doi:10.1175/jcli-d-16-0836.1
- Kalnay, E., Kanamitsu, M., Kistler, R., Collins, W., Deaven, D., Gandin, L., et al. (1996). The NCEP/NCAR 40-year Reanalysis Project. *Bull. Amer. Meteorol. Soc.* 77, 437–471. doi:10.1175/1520-0477(1996)077<0437:tnyrp>2.0.co;2
- Kim, H.-K., and Seo, K.-H. (2016). Cluster Analysis of Tropical Cyclone Tracks over the Western North Pacific Using a Self-Organizing Map. *J. Clim.* 29, 3731–3751. doi:10.1175/jcli-d-15-0380.1
- Lee, H.-T., Gruber, A., Ellingson, R. G., and Laszlo, I. (2007). Development of the HIRS Outgoing Longwave Radiation Climate Dataset. *J. Atmos. Ocean. Technol.* 24, 2029–2047. doi:10.1175/2007jtecha989.1
- Li, R. C. Y., and Zhou, W. (2013). Modulation of Western North Pacific Tropical Cyclone Activity by the ISO. Part I: Genesis and Intensity. *J. Clim.* 26, 2904–2918. doi:10.1175/jcli-d-12-00210.1
- Liu, K. S., and Chan, J. C. L. (2008). Interdecadal Variability of Western North Pacific Tropical Cyclone Tracks. *J. Clim.* 21, 4464–4476. doi:10.1175/2008jcli2207.1
- Peduzzi, P., Chatenoux, B., Dao, H., De Bono, A., Herold, C., Kossin, J., et al. (2012). Global Trends in Tropical Cyclone Risk. *Nat. Clim Change* 2, 289–294. doi:10.1038/nclimate1410
- Rasmusson, E. M., and Carpenter, T. H. (1982). Variations in Tropical Sea Surface Temperature and Surface Wind Fields Associated with the Southern Oscillation/El Niño. *Mon. Wea. Rev.* 110, 354–384. doi:10.1175/1520-0493(1982)110<0354:vitsst>2.0.co;2
- Vimont, D. J., Battisti, D. S., and Hirst, A. C. (2001). Footprinting: A Seasonal Connection between the Tropics and Mid-latitudes. *Geophys. Res. Lett.* 28, 3923–3926. doi:10.1029/2001gl013435
- Wang, B., and Chan, J. C. L. (2002). How Strong ENSO Events Affect Tropical Storm Activity over the Western North Pacific*. *J. Clim.* 15, 1643–1658. doi:10.1175/1520-0442(2002)015<1643:hseest>2.0.co;2
- Wang, B., and Murakami, H. (2020). Dynamic Genesis Potential index for Diagnosing Present-Day and Future Global Tropical Cyclone Genesis. *Environ. Res. Lett.* 15, 114008. doi:10.1088/1748-9326/abb01
- Wang, B., Wu, R., and Fu, X. (2000). Pacific-East Asian Teleconnection: How Does ENSO Affect East Asian Climate? *J. Clim.* 13, 1517–1536. doi:10.1175/1520-0442(2000)013<1517:peathd>2.0.co;2
- Wang, B., Xiang, B., and Lee, J.-Y. (2013). Subtropical High Predictability Establishes a Promising Way for Monsoon and Tropical Storm Predictions. *Proc. Natl. Acad. Sci.* 110, 2718–2722. doi:10.1073/pnas.1214626110
- Wang, B., Xiang, B., Li, J., Webster, P. J., Rajeevan, M. N., Liu, J., et al. (2015). Rethinking Indian Monsoon Rainfall Prediction in the Context of Recent Global Warming. *Nat. Commun.* 6, 7154. doi:10.1038/ncomms8154
- Wang, C., and Wang, B. (2019). Tropical Cyclone Predictability Shaped by Western Pacific Subtropical High: Integration of Trans-basin Sea Surface Temperature Effects. *Clim. Dyn.* 53, 2697–2714. doi:10.1007/s00382-019-04651-1
- Wang, C., Wu, K., Wu, L., Zhao, H., and Cao, J. (2021a). What Caused the Unprecedented Absence of Western North Pacific Tropical Cyclones in July 2020? *Geophys. Res. Lett.* 48, e2020GL092282. doi:10.1029/2020gl092282
- Wang, C., Wu, L., Lu, J., Liu, Q., Zhao, H., Tian, W., et al. (2020). Interannual Variability of the Basinwide Translation Speed of Tropical Cyclones in the Western North Pacific. *J. Clim.* 33, 8641–8650. doi:10.1175/jcli-d-19-0995.1
- Wang, C., Wu, L., Zhao, H., Liu, Q., and Wang, J. (2021b). An Abrupt Slowdown of Late Season Tropical Cyclone over the Western North Pacific in the Early 1980s. *J. Meteorol. Soc. Jpn. Ser.* 99 (6), 1413–1422. doi:10.2151/jmsj.2021-068
- Wilks, D. S. (2006). *Statistical Methods in the Atmospheric Sciences*. Cambridge, Massachusetts, United States: Academic Press, 676.
- Wu, B., Zhou, T., and Li, T. (2017). Atmospheric Dynamic and Thermodynamic Processes Driving the Western North Pacific Anomalous Anticyclone during El Niño. Part II: Formation Processes. *J. Clim.* 30, 9637–9650. doi:10.1175/jcli-d-16-0495.1
- Wu, L., and Wang, B. (2004). Assessing Impacts of Global Warming on Tropical Cyclone Tracks*. *J. Clim.* 17, 1686–1698. doi:10.1175/1520-0442(2004)017<1686:aioqwo>2.0.co;2
- Wu, L., Wang, B., and Geng, S. (2005). Growing Typhoon Influence on East Asia. *Geophys. Res. Lett.* 32, L18703. doi:10.1029/2005gl022937

- Xie, S.-P., Hu, K., Hafner, J., Tokinaga, H., Du, Y., Huang, G., et al. (2009). Indian Ocean Capacitor Effect on Indo-Western Pacific Climate during the Summer Following El Niño. *J. Clim.* 22, 730–747. doi:10.1175/2008jcli2544.1
- Zhang, Q., Wu, L., and Liu, Q. (2009). Tropical Cyclone Damages in China 1983–2006. *Bull. Amer. Meteorol. Soc.* 90, 489–496. doi:10.1175/2008bams2631.1
- Zhao, H., Klotzbach, P. J., and Chen, S. (2020). Dominant Influence of ENSO-like and Global Sea Surface Temperature Patterns on Changes in Prevailing Boreal Summer Tropical Cyclone Tracks over the Western North Pacific. *J. Clim.* 33, 9551–9565. doi:10.1175/jcli-d-19-0774.1
- Zhao, H., and Wu, L. (2014). Inter-decadal Shift of the Prevailing Tropical Cyclone Tracks over the Western North Pacific and its Mechanism Study. *Meteorol. Atmos. Phys.* 125, 89–101. doi:10.1007/s00703-014-0322-8
- Zhao, H., Wu, L., and Zhou, W. (2010). Assessing the Influence of the ENSO on Tropical Cyclone Prevailing Tracks in the Western North Pacific. *Adv. Atmos. Sci.* 27, 1361–1371. doi:10.1007/s00376-010-9161-9

Conflict of Interest: The authors declare that the research was conducted in the absence of any commercial or financial relationships that could be construed as a potential conflict of interest.

Publisher's Note: All claims expressed in this article are solely those of the authors and do not necessarily represent those of their affiliated organizations, or those of the publisher, the editors, and the reviewers. Any product that may be evaluated in this article, or claim that may be made by its manufacturer, is not guaranteed or endorsed by the publisher.

Copyright © 2022 Yu, Wang and Ge. This is an open-access article distributed under the terms of the Creative Commons Attribution License (CC BY). The use, distribution or reproduction in other forums is permitted, provided the original author(s) and the copyright owner(s) are credited and that the original publication in this journal is cited, in accordance with accepted academic practice. No use, distribution or reproduction is permitted which does not comply with these terms.



Detecting Interdecadal Change in Western North Pacific Tropical Cyclone Genesis Based on Cluster Analysis Using pHash + Kmeans

Ye Tian¹, Wen Zhou^{1,2*} and W. K. Wong³

¹Guy Carpenter Asia-Pacific Climate Impact Centre, School of Energy and Environment, City University, Hong Kong, Hong Kong SAR, China, ²Department of Atmospheric and Oceanic Sciences & Institute of Atmospheric Sciences, Fudan University, Shanghai, China, ³Hong Kong Observatory, Hong Kong, Hong Kong SAR, China

OPEN ACCESS

Edited by:

Guanghua Chen,
Institute of Atmospheric Physics
(CAS), China

Reviewed by:

Yipeng Guo,
Nanjing University, Nanjing, China
Jingliang Huangfu,
Institute of Atmospheric Physics
(CAS), China

*Correspondence:

Wen Zhou
wenzhou@cityu.edu.hk

Specialty section:

This article was submitted to
Atmospheric Science,
a section of the journal
Frontiers in Earth Science

Received: 30 November 2021

Accepted: 27 December 2021

Published: 08 February 2022

Citation:

Tian Y, Zhou W and Wong WK (2022)
Detecting Interdecadal Change in
Western North Pacific Tropical Cyclone
Genesis Based on Cluster Analysis
Using pHash + Kmeans.
Front. Earth Sci. 9:825835.
doi: 10.3389/feart.2021.825835

Previous studies have noted an abrupt decrease in western North Pacific (WNP) tropical cyclone (TC) genesis frequency and a westward shift in genesis location since the late 1990s. The recent application of cluster analysis in TC research shows the effect of detecting the contribution of the Western North Pacific Subtropical High (WNPSH) and the interdecadal Pacific oscillation (IPO) on interdecadal change in WNP TCs. In this work, we also apply a clustering algorithm called pHash + Kmeans to group WNP TCs into three classes based on their genesis environmental conditions. The clustering results show that an abrupt decrease after 1998 is related primarily to a decrease in the dominant class (Class3, located mainly in the southern and eastern WNP), and an increase after 2010 occurs because of a new dominant class (Class1, located mainly in the northwestern WNP), which indicates that the WNP environment suppresses Class3 genesis after 1998 and enhances Class1 genesis after 2010. Three periods (P1: 1979–1997, P2: 1998–2010, and P3: 2011–2020) and three regions (SCS: 100°E–120°E, EQ–30°N; WNP1: 120°E–140°E, EQ–30°N; and WNP2: 140°E–160°W, EQ–30°N) are divided to further confirm the above findings. In P1, high (low) mid-level relative humidity (RH), intense (weak) low-level vorticity, and weak (strong) vertical wind shear (VWS) are distributed in WNP2 (SCS and WNP1), indicating suitable environmental conditions for TC genesis in WNP2 but unsuitable conditions in SCS and WNP1. This situation is the opposite in P2, leading to a decrease in genesis frequency and a westward shift in genesis location. In P3, strong low-pressure vorticity and thermodynamic conditions occur in SCS and WNP1, contributing to an increase in TC genesis frequency.

Keywords: clustering analysis, tropical cyclone genesis, interdecadal change, pHash, Kmeans

1 INTRODUCTION

In recent years, interdecadal variation in tropical cyclone (TC) activity over the western North Pacific (WNP) has been an area of active research. Numerous works have reported that a pronounced interdecadal change in WNP TC activity occurred in the late 1990s, including a decrease in genesis frequency and a westward shift in genesis location (Chan, 2008; Liu and Chan, 2008; Tu et al., 2011; Liu and Chan, 2013; Yokoi and Takayabu, 2013; He et al., 2015; Hong et al., 2016; Huangfu et al., 2017a; Huangfu et al., 2017b). These interdecadal changes are related to variations in environmental

conditions and are influenced by large-scale circulations. Several studies (Tu et al., 2011; Liu and Chan, 2013; Zhao et al., 2014; Choi et al., 2015; Liu et al., 2019) have indicated that the inactive period of WNP TC activity is closely related to strengthening of vertical wind shear (VWS) over the eastern tropical WNP, which plays a vital role. Following these conclusions, Zhang et al. (2017) and Zhang et al. (2018) noted that the enhancement of warming over the North Atlantic also influences interdecadal change in WNP TC frequency by intensifying VWS in the southeastern WNP through the Walker circulation. Variation of sea surface temperature (SST) is also an essential influence on interdecadal change in WNP TCs (Kubota and Chan, 2009; Choi et al., 2015; He et al., 2015; Hsu et al., 2017; Wu R. et al., 2020). Hong et al. (2016) indicated that the La Niña-type pattern during the late 1990s is associated with an increase in VWS, anomalous vertical transport of water vapour, and increasing mid-level moisture, which is responsible for the shift in WNP TC genesis position. Hu et al. (2018) analysed the change in WNP TC genesis longitude and latitude separately and found that the change in mean longitude is closely linked to ENSO diversity, and the change in mean latitude is dominated by a warming WNP, which is induced by an interdecadal tendency of central Pacific La Niña-like events. Cao et al. (2020) indicated that a La Niña event and warming over the North Atlantic occurred in the 1990s and caused a northwestward shift in autumn TCs over the WNP. Additionally, the Western North Pacific Subtropical High (WNPSH) (Kim and Seo, 2016; Wu Q. et al., 2020), the East Asia winter monsoon (Choi et al., 2017), the monsoon trough (MT) (Huangfu et al., 2017a; Huangfu et al., 2017b), and the tropical upper tropospheric trough (Wu et al., 2015) are also essential in modulating interdecadal change in WNP TCs.

Some recent studies have attempted to understand TC activity in detail with the help of cluster analysis (e.g., Choi and Kim, 2009; Kim et al., 2011; Daloz et al., 2015; Kim and Seo, 2016; Boudreault et al., 2017; Ramsay et al., 2012, 2018). Clustering algorithms were applied to group TC cases into several classes based on their tracks. The TC cases in the different classes vary in position, intensity, and timing. Analysis of the contributors to the different classes enables a deeper, more detailed understanding of TC activity. A recent work by Zhao et al. (2018) grouped WNP TC tracks into three classes, of which the dominant class was closely related to the interdecadal Pacific oscillation (IPO). The relationship between the IPO and the dominant class was then analysed. The results show that the negative phase of the IPO during the late 1990s corresponds to a La Niña pattern, which intensified the Walker circulation and weakened the WNP MT, suppressing subsequent WNP TC genesis. Wu et al. (2020) also focused on one dominant class from clustering results and found modulation by interdecadal change of the WNPSH on the longitudinal shift of WNP TC tracks. These two works show that cluster analysis can potentially increase our understanding of interdecadal change in TC activity by analysing the dominant classes.

Regarding previous research, changing environmental conditions like SST and VWS play essential roles in the interdecadal change in WNP TC activity. In this case, we assume that the TC genesis environment can play the same

role as TC tracks in clustering WNP TCs. Because of changes in environmental conditions, clustering results show distinct differences in time series. Different classes are concentrated in different periods, and analysing the dominant class in different periods helps indicate the interdecadal change in the WNP environment and WNP TC activity. According to previous works (e.g., Kim et al., 2011), clustering algorithms have limitations regarding TC tracks because the tracks have different shapes. However, selecting environmental fields of a fixed shape can avoid this problem. The properties and environmental conditions of each class are compared for further analysis of the interdecadal change in WNP TC genesis.

This paper is organized as follows: **Section 2** introduces the datasets, clustering algorithm, and analysis methods. **Section 3** contains the analysis of the clustering results. **Section 4** further analyses the decadal change in TC genesis in the WNP based on the clustering results; the environmental conditions for the decadal change are also discussed. A summary and conclusion are provided in **Section 5**.

2 DATA AND METHODS

2.1 Data

In this work, TC best-track data were obtained from the International Best Track Archive for Climate Stewardship (IBTrACS) dataset (Knapp et al., 2010; Knapp and Kruk, 2010), including the time, position, and intensity (maximum sustained wind speed, MSWS) of TCs at 6-h intervals. Here we used data during 1979–2020 to remove any questionable data from the pre-satellite era, and only TC cases of tropical depression intensity (MSWS > 23 kts) were selected.

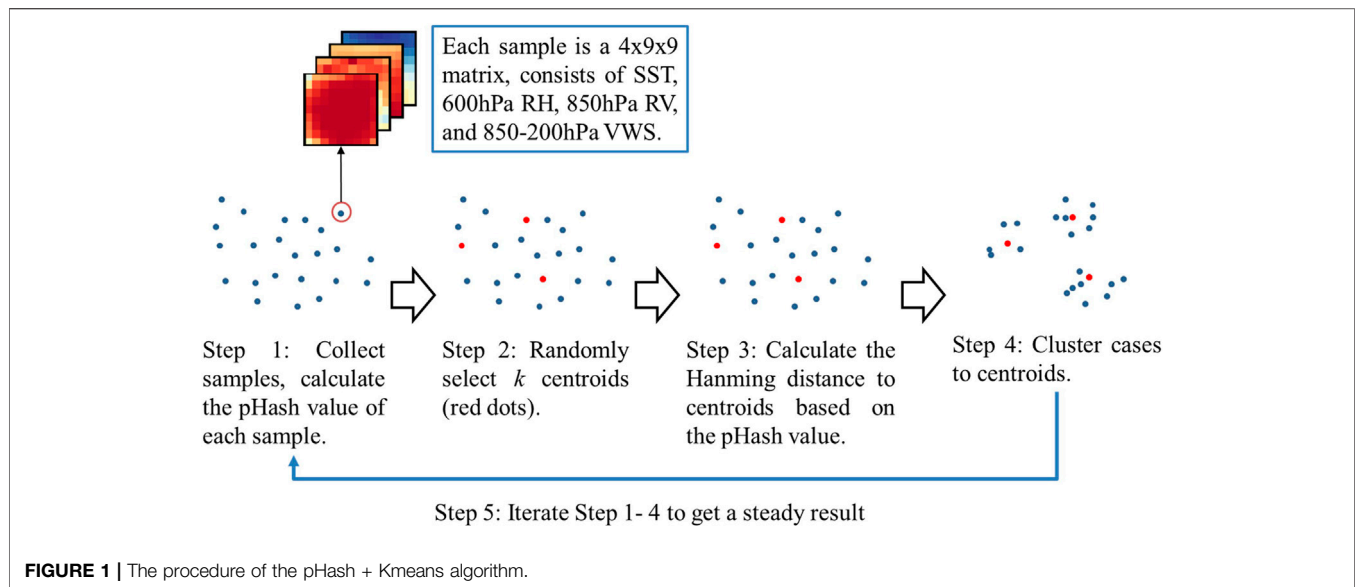
Several atmospheric and oceanic variables were used for clustering, including 6-hourly SST, 600 hPa relative humidity (RH), 850 hPa relative vorticity (RV), and wind at 850 and 200 hPa from the European Centre for Medium-Range Weather Forecasts (ECMWF) Reanalysis v5 (ERA5) hourly dataset (Hersbach et al., 2020). Wind data were used for calculating VWS between 850 and 200 hPa. For each TC case, we selected $9^\circ \times 9^\circ$ environmental fields centred on the TC genesis position. The environmental fields consist of SST, RH, RV, and VWS with a spatial resolution of $1^\circ \times 1^\circ$, which refers to one sample as a $4 \times 9 \times 9$ matrix. Accordingly, we built a dataset consisting of 1,081 TC genesis samples.

For further analysis of the interdecadal change in WNP TCs, monthly data for SST, 600 hPa RH, 850 hPa RV, specific humidity, and temperature at all profiles, wind at 850 hPa and 200 hPa, mean sea level pressure, and geopotential were also derived from the ERA5 monthly dataset.

2.2 Methods

2.2.1 PHash + Kmeans Clustering Algorithm

The clustering algorithm used in this study is the K-means clustering algorithm (Jain, 2010), one of the most widely used. It is an unsupervised machine learning algorithm, which means it can learn characteristics from data without external help. Its procedure is as follows: K centroids are randomly selected from



the whole dataset to cluster data into different classes. The distance between each sample and the centroids is calculated for each sample in the dataset. Then based on the distance, different samples are allocated into the closest centroid, and k clusters are formed. In each cluster, a new centroid is then selected. This process is iterated to update the centroids and clusters until all centroids have little change.

In K-means, the distance is used to distinguish the similarity between samples and cluster centroids, by which the algorithm can group samples to the closest cluster. The classical K-means algorithm usually uses the Euclidean distance:

$$distance = \frac{1}{n} \sqrt{\sum_{i=1}^n (A_i - B_i)^2}$$

where n refers to the data count in one sample, and A_i and B_i refer to the i th data in samples A and B. The Euclidean distance focuses on the similarity of the value and ignores the global characteristics of the data. Therefore, although it has worked well in previous studies using clustered TC tracks, it is not suitable for the 3-dimensional environmental field data in our work. To prevent this, we propose the pHash + Kmeans algorithm, in which we select the perceptual hashing (pHash) value with the Hamming distance (Venkatesan et al., 2000) to replace the Euclidean distance.

The pHash algorithm derives the fingerprint of image data and is popular for distinguishing different images. Its procedure is as follows, for each matrix: 1) perform the discrete cosine transform (DCT) and get the DCT matrix; 2) calculate the mean value of the DCT matrix; and 3) calculate the pHash value: compare each data point in the DCT matrix with the mean value; greater than or equal to the mean value is recorded as 1, and less than the mean value is recorded as 0. The new matrix of 0 and 1 is called the pHash value. After getting the pHash value of each matrix, the Hamming distance (the Hamming distance between two matrices is the number of positions in which the values are different) of

different matrices is calculated. The samples in our work are $4 \times 9 \times 9$ matrices with four variables, so we first calculate the pHash value matrix of each variable, then concatenate all matrices into one to represent the pHash value of one sample. **Figure 1** shows the detailed procedure of the pHash + Kmeans algorithm.

The Dunn index (Dunn, 1973) and Separation index (Xie and Beni, 1991) are calculated to evaluate clustering results and determine the optimal cluster numbers. The Separation index is defined as the average distance between the cluster centroids, and the Dunn index refers to the ratio of the shortest distance between two samples from different clusters and the largest distance between two samples in the same cluster. For each number of classes, clustering is repeated five times and the average value of the indexes is calculated.

2.2.2 Analysis Methods

The number of TC genesis cases in each $2.5^\circ \times 2.5^\circ$ grid over the WNP is counted. Spatial TC genesis frequency is defined as the average annual count for each grid. The position of TC genesis is defined as the first recorded position of each track in the IBTrACS dataset.

We also calculate the Genesis Potential Index (GPI) and the moist static energy (MSE) to help diagnose the variation in environmental conditions over the WNP. Emanuel and Nolan (2004) developed the GPI, defined as:

$$GPI = |10^5 \eta|^{\frac{3}{2}} \left(\frac{H}{50} \right)^3 \left(\frac{V_{pot}}{70} \right)^3 (1 + 0.1 V_{shear})^{-2}$$

where η is the absolute vorticity at 850 hPa, H is the relative humidity at 600 hPa in percent, V_{pot} is the potential intensity, and V_{shear} is the VWS magnitude between 850 and 200 hPa. The V_{pot} can be calculated based on the work of Bister and Emanuel (2002), as follows:

$$V_{pot}^2 = \frac{T_s}{T_o} \frac{C_k}{C_D} (CAPE^* - CAPE^b)$$

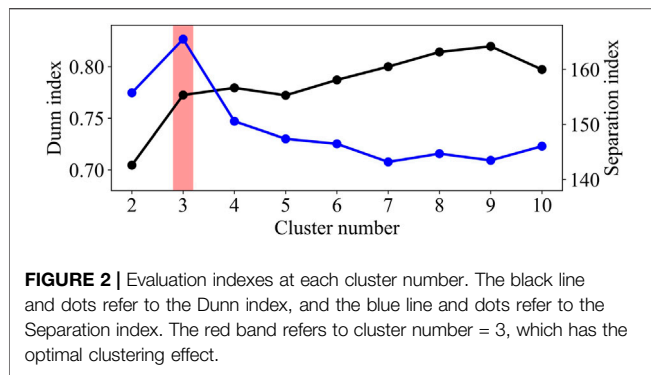


FIGURE 2 | Evaluation indexes at each cluster number. The black line and dots refer to the Dunn index, and the blue line and dots refer to the Separation index. The red band refers to cluster number = 3, which has the optimal clustering effect.

where T_s is SST, T_o is the mean outflow temperature, C_k is the exchange coefficient for enthalpy, C_D is the drag coefficient, $CAPE^*$ is the convective available potential energy (CAPE) of air lifted from saturation at sea level in reference to the environmental sounding, and $CAPE^b$ is the CAPE of the boundary layer air.

MSE is defined as:

$$MSE = C_p T + gz + L_v r$$

where g is the gravitational acceleration, L_v is the latent heat of vaporisation, C_p is the specific heat at constant pressure for air, T is the absolute temperature, z is the height above some reference level (either the local surface at $z = 0$ or the height where the ambient pressure is 100 kPa), and r is the water vapour mixing ratio in the air.

3 ANALYSIS OF CLUSTERING RESULTS AND DETECTION OF INTERDECADAL CHANGE IN WNP TC GENESIS

The clustering results from the genesis environment will show different characteristics due to the close relationship between interdecadal change in WNP TCs and changes in the WNP environment. As the WNP environment changes, the dominant class will also change. Therefore, the clustering results will reflect the interdecadal change in TC genesis. **Figure 2** gives the Dunn index and Separation index of the different class numbers. The Dunn index shows that the clustering results are steady, with more than two classes, and the Separation index indicates that clustering with three classes will achieve the best separation. Zhao et al. (2018) also indicated that some classes will share similar characteristics if the cluster number is too large and found that three clusters can have their own characteristics. Therefore, we clustered TCs into three classes named Class1, Class2, and Class3, with 256, 314, and 511 samples, respectively.

Figures 3A–C shows the spatial genesis frequency. Class2 and Class3 are mainly in the southern and eastern WNP, while Class1 is farther north than Class2 and Class3, mainly in the northern South China Sea (SCS) and the northern Philippine Sea (PS).

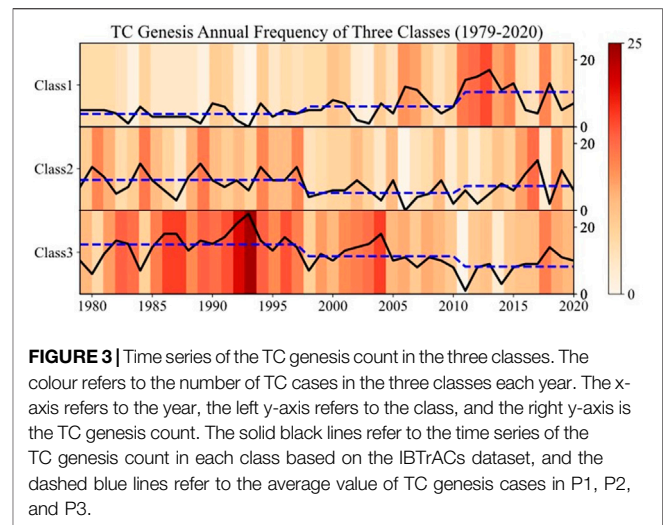
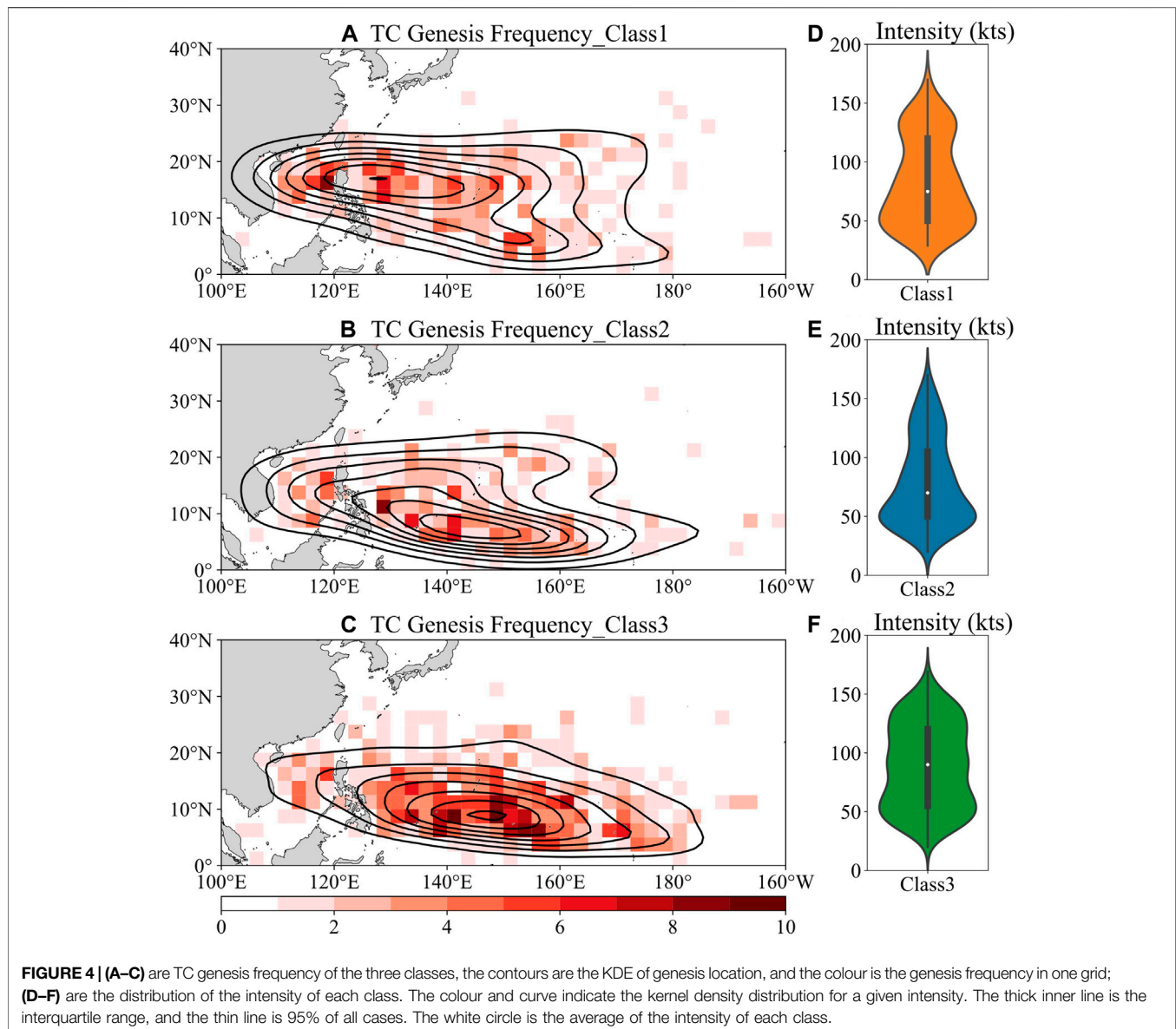


FIGURE 3 | Time series of the TC genesis count in the three classes. The colour refers to the number of TC cases in the three classes each year. The x-axis refers to the year, the left y-axis refers to the class, and the right y-axis is the TC genesis count. The solid black lines refer to the time series of the TC genesis count in each class based on the IBTrACs dataset, and the dashed blue lines refer to the average value of TC genesis cases in P1, P2, and P3.

Figures 3D–F give the distribution of TC intensity of the three classes. Compared with Class1 and Class3, Class2 has more low-intensity cases, as its density peak is distributed at 50 kts. The white dot for the average value and the inner boxplot also indicate this. Class1 has an intensity distribution similar to that of Class2 but has more cases with intensity >100 kts. Class3 has an evenly distributed intensity, and its proportion of high-intensity cases is also higher than in Class1 or Class2, along with the highest average intensity.

Figure 4 shows the time series of TC genesis counts in the three classes during 1979–2020. The heatmap gives the annual count of samples of each class, and the solid black lines present the time series of the three classes during 1979–2020. Class3 has a much higher proportion than the other classes in most years. After 1997, all three classes are inactive, and the most significant decrease occurs in Class3. This inactive period lasts until 2011, as Class1 increases and becomes the dominant class. The average value of the TC case count in 1979–1997, 1998–2010, and 2011–2020 is plotted as the blue dashed line, showing an increasing trend of Class1 and a decreasing trend of Class3. The sudden decrease of Class3 in 1998 corresponds to previous works showing that WNP TCs have been inactive since the late 1990s (e.g., Liu and Chan, 2013). According to Tang et al. (2020), a warming reacceleration trend has occurred in the northwestern WNP since 2011, possibly contributing to the increasing trend of Class1 during 2011–2020. These similarities show that the inactive period of WNP TCs after the late 1990s is possibly an inactive period of Class3, and the end of this inactive period after 2010 is related to the increase in Class1. Therefore, we infer that 1997 and 2010 are two important time nodes indicating interdecadal change in WNP TCs.

In this work, the clustering results come mainly from the surrounding environmental fields of TC genesis. Therefore, the differences between classes result from variations in the WNP environment. Here we compare the composite fields of SST, RH, RV, and VWS of each class over the WNP in **Figure 5**. Suitable environmental conditions for TC genesis are highlighted by



colours ($SST > 26^{\circ}\text{C}$ and positive RV) and thick solid lines ($RH > 60\%$ and $VWS < 14\text{ m s}^{-1}$). The figure shows that the genesis environments of Class2 and Class3 are similar, while that of Class1 shows apparent differences. For thermodynamic conditions, compared with Class2 and Class3, Class1 has a wider suitable area for TC genesis, including higher SST and RH, especially in SCS and PS. The area with suitable dynamic conditions in Class1 is farther north than in Class2 and Class3. The difference in RV is apparent west of 140°E , especially in SCS and PS. Combined with the intensity distribution in Figures 3E,F, we conclude that Class2 and Class3 share a similar WNP environment and have similar temporal and spatial distributions. Class2 contains mainly low-intensity cases with a lower proportion, and Class3 is mainly high-intensity cases with a dominant status.

WNP TC genesis cases can be clustered into three classes with different spatial and temporal characteristics based on environmental conditions. In different periods, the dominant class also changes. Before 1998, Class3 is the dominant class, but it substantially decreases after 1997. Then after the inactive period of all three classes in 1998–2010, Class1 becomes dominant after 2010. From Figures 3, 5, we find that the three classes have a noticeable difference in spatial distribution, which is related to the spatial distribution of environmental conditions. Class2 and Class3 may require a similar WNP environment, while the requirement of Class1 is different. Before 1998, the WNP environment is suitable for Class2 and Class3 but not for Class1. The southern and eastern WNP has more areas with suitable TC genesis conditions, thereby concentrating Class2 and Class3. We conclude that Class3 shows dominance during

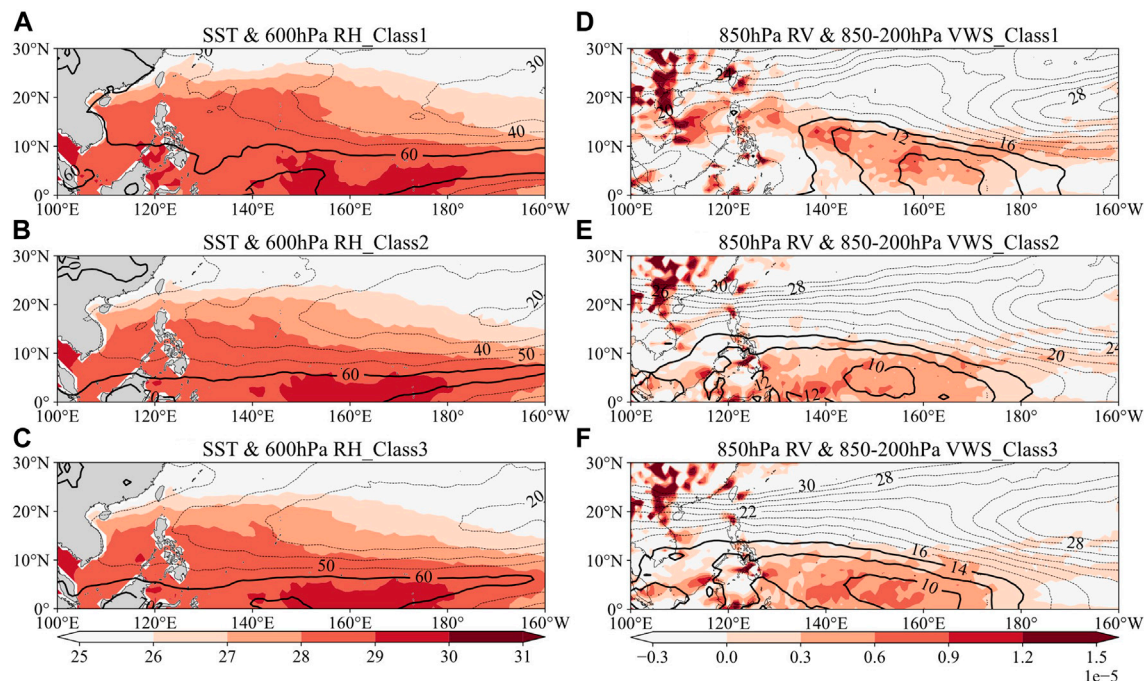


FIGURE 5 | Composite environmental field of the three classes. (A–C) are the SST and 600 hPa RH. The solid thick lines refer to RH ≥ 60%, and the dashed thin line refers to RH < 60%. The colours refer to the SST, and only SST > 26°C is plotted; (D–F) are the 850 hPa RV and 850–200 hPa VWS. The solid thick lines refer to VWS ≤ 14, and the dashed thin line refers to VWS > 14. The colours refer to RV, and only positive RV is plotted.

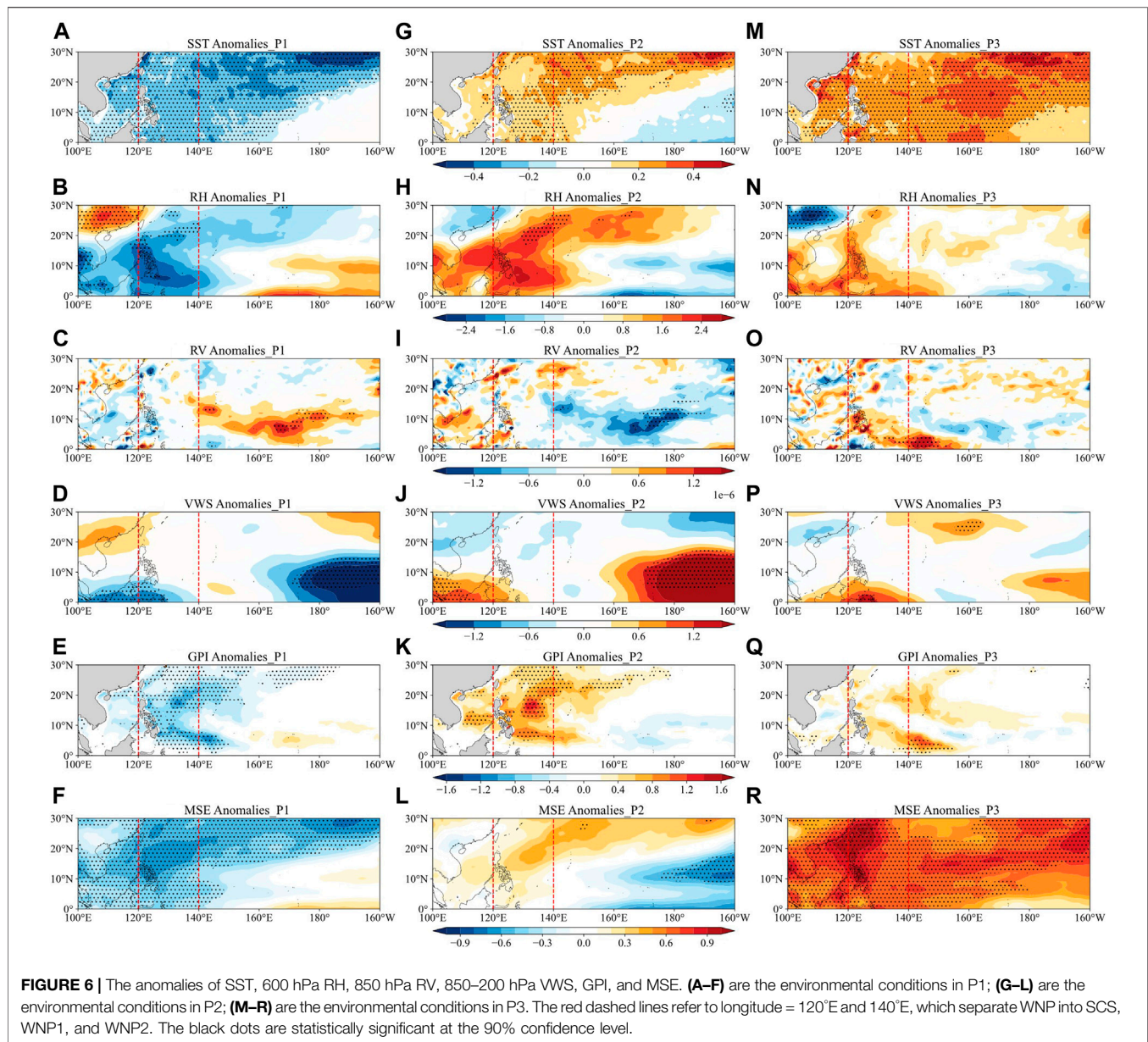
1979–1997, but after 1997, a less suitable environment for Class2 and Class3 causes the abrupt decrease in Class2 and Class3, leading to the inactive period of the three classes during 1998–2010. Then after 2010, the WNP environment becomes more favourable for Class1, and the northwestward shift of the suitable areas for TC genesis causes more Class1 to form in the northwestern WNP. Still, the environment is not suitable for Class2 and Class3, so Class1 increases and becomes the dominant class. In conclusion, variations in the WNP environment lead to interdecadal change in WNP TC genesis, which is shown by the differences in the three classes in our clustering results.

To prove our assumption from the clustering results and further analyse the interdecadal change in WNP TC genesis, in the next section, we will separate the research periods into 1979–1997 (P1), 1998–2010 (P2), and 2011–2020 (P3) and then compare WNP TC genesis in each period. To distinguish the changes in different areas over the WNP, we will also divide the WNP into three regions based on longitude: SCS (100°E–120°E, EQ–30°N), WNP1 (120°E–140°E, EQ–30°N), and WNP2 (140°E–160°W, EQ–30°N), and changes in the different regions will also be discussed.

4 THREE PERIODS OF INTERDECADAL CHANGE IN WNP TC GENESIS AND THEIR DIFFERENCES

To confirm the variation in the WNP environment in the three periods, we first compare the environmental conditions over the

WNP. The anomalies of SST, RH, RV, VWS, GPI, and MSE are shown in **Figure 6**. In P1, SST is negative in the WNP, except in southeastern WNP2, and RH also shows a similar distribution. The distribution of MSE also shows that the thermodynamic conditions are not favourable for TC genesis in SCS and WNP1. However, WNP2 has high positive RV and negative VWS, indicating suitable dynamic conditions. The WNP environment in P1 also shows similarities to the favourable environment of Class2 and Class3, as the suitable TC genesis conditions are concentrated mainly in WNP2. The environmental conditions in P2 are almost the opposite of those in P1 and become less favourable for Class2 and Class3. From P1 to P2, SST, RH, and MSE show an increase in SCS, WNP1, and northwestern WNP2 and a decrease in southeastern WNP2. Although the changes in RV and VWS are slight in SCS and WNP1, the high negative RV anomalies and positive VWS in WNP2 show that the dynamic conditions will suppress TC genesis in WNP2, which has also been reported in previous works (e.g., Zhang et al., 2017; Liu et al., 2019). GPI also shows that TCs are more likely to form in SCS and WNP1 than in WNP2. From P2 to P3, SST is still increasing and is positive at the basin scale. A slight decrease in RH occurs in SCS and WNP1, but RH is still positive in this area. The distribution of MSE also indicates a basin-wide strengthening of thermodynamic conditions from P2 to P3, similar to the Class1 genesis environment. Positive RV is distributed mainly in SCS and WNP1, much farther north and west than in P1 and P2, also showing similarities with Class1.



Given that the WNP environments in the three periods show apparent differences, we then further analyse the differences in WNP TCs in P1, P2, and P3, as shown in **Figure 7**. **Figures 7A–C** give the genesis frequency of each period. In P1, TCs form mainly in WNP2, and the highest KDE occurs around 150°E, 5°N, similar to Class2 and Class3. **Figures 6A–F** also show that in P1, WNP2 can provide a higher temperature, more mid-tropospheric moisture, stronger low-level vorticity, and weaker VWS than SCS and WNP1, indicating that more TCs can possibly form in WNP2 than in SCS or WNP1. From P1 to P2, the genesis frequency decreases in WNP2 but increases in SCS and WNP1. The KDE also shows a shift from WNP2 to WNP1, consistent with environmental conditions. From P2 to P3, TC genesis is still mainly in SCS and WNP1 but is more concentrated.

The TC genesis frequency in each grid shows that more TCs form in SCS during P2–P3, mainly due to the enhancement of RV and SST. **Figures 6G,M** also show a warming trend over SCS, similar to the result of Tang et al. (2020). **Figure 7D** gives the temporal change of WNP TC genesis, showing an increasing trend in P1, but after the abrupt decrease in 1997, WNP TCs are inactive in P2, and then WNP TC genesis shows another increasing trend in P3. **Figure 7E** gives the time series of TC genesis counts in the three regions. In P1, TC counts in SCS and WNP1 remain at a low level, but TCs in WNP2 are active and show an increasing trend. After a sudden decrease in WNP2 and an increase in WNP1 in 1997, TC genesis becomes active in WNP1 and inactive in WNP2 during P2, and SCS is still inactive. The TC genesis frequency remains steady and shows little change in WNP1 and WNP2

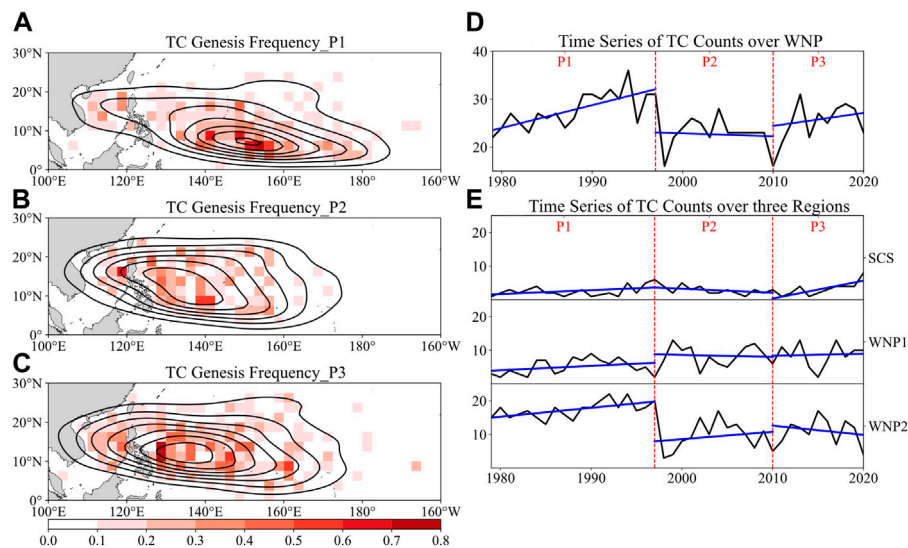


FIGURE 7 | (A–C) are the TC genesis frequency in the three periods, the contours are the KDE of genesis location, and the colour is the genesis frequency in one grid; (D) is the time series of TC genesis counts during 1979–2020, the black line refers to the count from the IBTrACs dataset, and the blue lines are the trend lines of TC count change in P1, P2, and P3. The red dashed lines refer to 1997 and 2010 to separate P1, P2, and P3; (E) is similar to (D), but for the time series of TC genesis counts in SCS, WNP1, and WNP2.

from P2 to P3, but it remains an increasing trend in SCS in P3. In summary, the abrupt decrease in WNP TCs is a combination of a slight increase in WNP1 TCs and a substantial decrease in WNP2 TCs, which also leads to the inactive period in P2, and the increase in WNP TCs in P3 occurs mainly in SCS.

5 SUMMARY AND DISCUSSION

Interdecadal change in WNP TCs has been a hot research topic in recent years. Many works have discussed how WNP TC activity has changed in recent decades and the possible reasons. Previous studies have widely reported that an abrupt decrease in TC genesis and a northwestward shift in the TC-active region occurred around the late 1990s (e.g., Chan, 2008; Tu et al., 2011; Liu and Chan, 2013; He et al., 2015; Hong et al., 2016; Huangfu et al., 2017a; Huangfu et al., 2017b). Cluster analysis is used to group TC tracks into different classes and can potentially lead to increased understanding of WNP TC interdecadal change by analysing the relationship between the dominant class and possible contributors like the WNPSH and PDO (Zhao et al., 2018; Wu Q. et al., 2020). In this work, we built a pHash + Kmean algorithm in which the pHash value was used to represent the genesis environmental conditions of TCs. This algorithm was used to cluster WNP TCs during 1979–2020 into three classes: Class1, Class2, and Class3, with 256, 314, and 511 cases, respectively.

The clustering result shows that the dominant class varies in the different periods. Class3 has the highest proportion before 1998 and then has an abrupt decrease, while Class1 has a low count until 2010 and then becomes the dominant class. The composite WNP environment fields of the three classes also show

differences: the environmental conditions of Class2 and Class3 are similar, with suitable genesis environmental conditions distributed in the southern and eastern WNP. In contrast, in the genesis environment for Class1, both high SST and RH have a broader distribution, and the area with positive RV and weak VWS also moves northward.

We found that the clustering results are closely related to changes in the WNP environment. The environmental conditions are more favourable for genesis in Class2 and Class3 during 1979–1997. The abrupt decrease in 1998 and the subsequent inactive period are caused by unfavourable environmental conditions for Class2 and Class3 genesis after 1997. After 2010, the WNP environment can lead to more Class1 genesis and less Class2 and Class3 genesis. To prove our assumption, we divided the study period into three periods (P1: 1979–1997, P2: 1998–2010, and P3: 2011–2020) and compared their differences. Additionally, as the three classes also show spatial differences, we divided the study region into three regions (SCS: 100°E–120°E, EQ–30°N; WNP1: 120°E–140°E, EQ–30°N; and WNP2: 140°E–180°W, EQ–30°N) for further analysis.

The environmental conditions in the three periods confirm our assumption that the clustering results come from changes in the WNP environment. In P1, positive (negative) RV anomalies and positive (negative) VWS anomalies are distributed in WNP2 (SCS and WNP1), and positive VWS anomalies are distributed in WNP2, indicating that TC genesis is enhanced in WNP2 and suppressed in SCS and WNP1. This situation is similar to the genesis environment for Class2 and Class3, creating a concentration of TC genesis in the southeastern WNP. The WNP environment in P2 is the opposite of that in P1. The WNP2 environment suppresses TC genesis, while the SCS and WNP1 environments enhance TC genesis. This change causes the environment to be unsuitable for Class2 and Class3

genesis, leading to decreased WNP TC genesis frequency and a westward shift in genesis location. From P2 to P3, a strengthening of RV in SCS and WNP1 and basin-wide warming of SST in the WNP occurs, making the WNP environment more suitable for Class1 and leading to an increase in TC genesis frequency in P3.

Figure 7E shows that interdecadal change in WNP TCs in the late 1990s is indicated by a decrease over WNP2 and an increase over the eastern WNP. Changing dynamic conditions, especially the intensification of VWS over the southern and southeastern WNP, are demonstrated to be the significant modulator for the sudden decrease in eastern WNP TCs (Liu and Chan, 2013; Choi et al., 2015). As revealed by previous studies (Zhang et al., 2017; Zhang et al., 2018; Cao et al., 2020), this intensification of VWS is related to a shift in the Walker circulation induced by enhanced SST warming in the North Atlantic. In the late 1990s, the SST over the Pacific showed a La Niña-like mean state, which could also enhance VWS over the eastern WNP (Hsu et al., 2014; Choi et al., 2015; Hong et al., 2016; Hu et al., 2018; Liu et al., 2019; Cao et al., 2020). Huangfu et al. (2018) pointed out that the negative RV anomalies and positive VWS anomalies are possibly associated with downward motion anomalies over the central Pacific. The weakening and westward shift of the monsoon trough are also related factors in the weakening of RV (Choi et al., 2017; Hsu et al., 2017; Huangfu et al., 2017). According to Hong et al. (2016), the increase in TC frequency in the western WNP is controlled by strengthened thermodynamic conditions (e.g., warming SST and increased mid-level relative humidity), which are induced by the K-sharp warming over the Pacific.

Moreover, our clustering results indicate that 2011–2020 is a reactive period of WNP TCs, which is probably connected with SST warming over the northwestern WNP and the strengthening RV over the western WNP. As Tang et al. (2020) investigated, after 2010, a noticeable reacceleration of SST warming occurred

in the northwestern WNP, especially offshore China. Zhang et al. (2019) also analysed the global annual mean surface temperature during 2014–2016, the recent warmest years on record, suggesting that global warming has accelerated since 2013. The variation trend of SST after 2010 may result in the interdecadal change in WNP TCs. We intend to examine the importance of different variables for the change in WNP TCs after 2010 and the physical mechanisms in follow-up research.

DATA AVAILABILITY STATEMENT

We are grateful to the institutions providing data for this study. TC best-track data were provided by the International Best Track Archive for Climate Stewardship (IBTrACS, <https://www.ncdc.noaa.gov/ibtracs/index.php?name=ib-v4-access>). Atmospheric data were taken from the European Centre for Medium-Range Weather Forecasts Reanalysis v5 (ERA5, <https://www.ecmwf.int/en/forecasts/datasets/reanalysis-datasets/era5>).

AUTHOR CONTRIBUTIONS

All authors listed have made a substantial, direct, and intellectual contribution to the work and approved it for publication.

FUNDING

This study is supported by the key project of National Natural Science Foundation of China (Grant 42192563 and Grant 42120104001), project of the Center for Ocean Research in Hong Kong and Macau (CORE), and the Hong Kong RGC General Research Fund (11300920).

REFERENCES

- Bister, M., and Emanuel, K. A. (2002). Low Frequency Variability of Tropical Cyclone Potential Intensity I. Interannual to Interdecadal Variability. *J. Geophys. Res. Atmospheres* 107, D24. ACL 26-1-ACL 26-15. doi:10.1029/2001jd000776.
- Boudreault, M., Caron, L. P., and Camargo, S. J. (2017). Reanalysis of Climate Influences on Atlantic Tropical Cyclone Activity Using Cluster Analysis. *J. Geophys. Res. Atmos.* 122 (8), 4258–4280. doi:10.1002/2016jd026103
- Cao, X., Liu, Y., Wu, R., Bi, M., Dai, Y., and Cai, Z. (2020). Northwestwards Shift of Tropical Cyclone Genesis Position during Autumn over the Western North Pacific after the Late 1990s. *Int. J. Climatol* 40 (3), 1885–1899. doi:10.1002/joc.6310
- Chan, J. C. L. (2008). Decadal Variations of Intense Typhoon Occurrence in the Western North Pacific. *Proc. R. Soc. A: Math. Phys. Eng. Sci.* 464 (2089), 249–272. doi:10.1098/rspa.2007.0183
- Choi, J. W., Cha, Y., Kim, T., and Kim, H. D. (2017). Interdecadal Variation of Tropical Cyclone Genesis Frequency in Late Season over the Western North Pacific. *Int. J. Climatol* 37 (12), 4335–4346. doi:10.1002/joc.5090
- Choi, K.-S., Kim, B.-J., Choi, C.-Y., and Nam, J.-C. (2009). Cluster Analysis of Tropical Cyclones Making Landfall on the Korean Peninsula. *Adv. Atmos. Sci.* 26 (2), 202–210. doi:10.1007/s00376-009-0202-1
- Choi, Y., Ha, K.-Ja., Ho, C.-Hoi., and Chung, C. E. (2015). Interdecadal Change in Typhoon Genesis Condition over the Western North Pacific. *Clim. Dyn.* 45 (11), 3243–3255. doi:10.1007/s00382-015-2536-y
- Daloz, A. S., Camargo, S. J., Kossin, J. P., Emanuel, K., Horn, M., Jonas, J. A., et al. (2015). Cluster Analysis of Downscaled and Explicitly Simulated North Atlantic Tropical Cyclone Tracks. *J. Clim.* 28 (4), 1333–1361. doi:10.1175/jcli-d-13-00646.1
- Dunn, J. C. (1973). A Fuzzy Relative of the Isodata Process and its Use in Detecting Compact Well-Separated Clusters. *J. Cybernetics* 3, 32–57. doi:10.1080/01969727308546046
- Emanuel, K., and Nolan, D. S. (2004). “Tropical Cyclone Activity and the Global Climate System”. in 26th Conference on Hurricanes and Tropical Meteorology (Miami, FL, United States: American Meteorological Society), 240–241.
- He, H., Yang, J., Gong, D., Mao, R., Wang, Y., and Gao, M. (2015). Decadal Changes in Tropical Cyclone Activity over the Western North Pacific in the Late 1990s. *Clim. Dyn.* 45 (11), 3317–3329. doi:10.1007/s00382-015-2541-1
- Hersbach, H., Bell, B., Paul, B., Hiraehara, S., Horányi, A., Muñoz-Sabater, J., et al. (2020). The Era5 Global Reanalysis. *Q. J. R. Meteorol. Soc.* 146 (730), 1999–2049. doi:10.1002/qj.3803
- Hong, C.-C., Wu, Y.-K., and Li, T. (2016). Influence of Climate Regime Shift on the Interdecadal Change in Tropical Cyclone Activity over the Pacific Basin during the Middle to Late 1990s. *Clim. Dyn.* 47 (7), 2587–2600. doi:10.1007/s00382-016-2986-X

- Hsu, P.-C., Lee, T.-H., Tsou, C.-H., Chu, P.-S., Qian, Y., and Bi, M. (2017). Role of Scale Interactions in the Abrupt Change of Tropical Cyclone in Autumn over the Western North Pacific. *Clim. Dyn.* 49 (9), 3175–3192. doi:10.1007/s00382-016-3504-X
- Hsu, P.-C., Chu, P.-S., Murakami, H., and Zhao, X. (2014). An Abrupt Decrease in the Late-Season Typhoon Activity over the Western North Pacific*. *J. Clim.* 27 (11), 4296–4312. doi:10.1175/jcli-d-13-00417.1
- Hu, C., Zhang, C., Yang, S., Chen, D., and He, S. (2018). Perspective on the Northwestward Shift of Autumn Tropical Cyclogenesis Locations over the Western North Pacific from Shifting ENSO. *Clim. Dyn.* 51 (7), 2455–2465. doi:10.1007/s00382-017-4022-1
- Huangfu, J., Huang, R., and Chen, W. (2017a). Interdecadal Increase of Tropical Cyclone Genesis Frequency over the Western North Pacific in May. *Int. J. Climatol.* 37 (2), 1127–1130. doi:10.1002/joc.4760
- Huangfu, J., Huang, R., Chen, W., Feng, T., and Wu, L. (2017b). Interdecadal Variation of Tropical Cyclone Genesis and its Relationship to the Monsoon Trough over the Western North Pacific. *Int. J. Climatol.* 37 (9), 3587–3596. doi:10.1002/joc.4939
- Huangfu, J., Huang, R., and Chen, W. (2018). Interdecadal Variation of Tropical Cyclone Genesis and its Relationship to the Convective Activities over the Central Pacific. *Clim. Dyn.* 50 (3), 1439–1450. doi:10.1007/s00382-017-3697-7
- Jain, A. K. (2010). Data Clustering: 50 Years beyond K-Means. *Pattern Recognition Lett.* 31 (8), 651–666. doi:10.1016/j.patrec.2009.09.011
- Kim, H.-K., and Seo, K.-H. (2016). Cluster Analysis of Tropical Cyclone Tracks over the Western North Pacific Using a Self-Organizing Map. *J. Clim.* 29 (10), 3731–3751. doi:10.1175/jcli-d-15-0380.1
- Kim, H.-S., Kim, J.-H., Ho, C.-H., and Chu, P.-S. (2011). Pattern Classification of Typhoon Tracks Using the Fuzzy C-Means Clustering Method. *J. Clim.* 24 (2), 488–508. doi:10.1175/2010jcli3751.1
- Knapp, K. R., Kruk, M. C., Levinson, D. H., Diamond, H. J., and Neumann, C. J. (2010). The International Best Track Archive for Climate Stewardship (IBTrACS). *Bull. Amer. Meteorol. Soc.* 91 (3), 363–376. doi:10.1175/2009bams2755.1
- Knapp, K. R., and Kruk, M. C. (2010). Quantifying Interagency Differences in Tropical Cyclone Best-Track Wind Speed Estimates. *Monthly Weather Rev.* 138 (4), 1459–1473. doi:10.1175/2009mwr3123.1
- Kubota, H., and Chan, J. C. L. (2009). Interdecadal Variability of Tropical Cyclone Landfall in the Philippines from 1902 to 2005. *Geophys. Res. Lett.* 36 (12). doi:10.1029/2009gl038108
- Liu, C., Zhang, W., Geng, X., Stuecker, M. F., and Jin, F.-F. (2019). Modulation of Tropical Cyclones in the Southeastern Part of Western North Pacific by Tropical Pacific Decadal Variability. *Clim. Dyn.* 53 (7), 4475–4488. doi:10.1007/s00382-019-04799-w
- Liu, K. S., and Chan, J. C. (2008). "Interdecadal Variability of Western North Pacific Tropical Cyclone Tracks. *J. Clim.* 21 (17), 4464–4476. doi:10.1175/2008jcli2207.1
- Liu, K. S., and Chan, J. C. (2013). Inactive Period of Western North Pacific Tropical Cyclone Activity in 1998–2011. *J. Clim.* 26 (8), 2614–2630. doi:10.1175/jcli-d-12-00053.1
- Ramsay, H. A., Camargo, S. J., and Kim, D. (2012). Cluster Analysis of Tropical Cyclone Tracks in the Southern Hemisphere. *Clim. Dyn.* 39 (3–4), 897–917. doi:10.1007/s00382-011-1225-8
- Ramsay, H. A., Chand, S. S., and Camargo, S. J. (2018). A Statistical Assessment of Southern Hemisphere Tropical Cyclone Tracks in Climate Models. *J. Clim.* 31 (24), 10081–10104. doi:10.1175/jcli-d-18-0377.1
- Tang, Y., Huangfu, J., Huang, R., and Chen, W. (2020). Surface Warming Reacceleration in Offshore China and its Interdecadal Effects on the East Asia-Pacific Climate. *Sci. Rep.* 10 (1), 14811. doi:10.1038/s41598-020-71862-6
- Tu, J.-Y., Chou, C., Huang, P., and Huang, R. (2011). An Abrupt Increase of Intense Typhoons over the Western North Pacific in Early Summer. *Environ. Res. Lett.* 6 (3), 034013. doi:10.1088/1748-9326/6/3/034013
- Venkatesan, R., Koon, S.-M., Jakubowski, M. H., and Moulin, P. (2000). "Robust Image Hashing", in Paper presented at the Proceedings 2000 International Conference on Image Processing (Vancouver, BC, Canada, IEEE).
- Wu, L., Wang, C., and Wang, B. (2015). Westward Shift of Western North Pacific Tropical Cyclogenesis. *Geophys. Res. Lett.* 42 (5), 1537–1542. doi:10.1002/2015gl063450
- Wu, Q., Wang, X., and Tao, L. (2020). Interannual and Interdecadal Impact of Western North Pacific Subtropical High on Tropical Cyclone Activity. *Clim. Dyn.* 54 (3), 2237–2248. doi:10.1007/s00382-019-05110-7
- Wu, R., Cao, X., and Yang, Y. (2020). Interdecadal Change in the Relationship of the Western North Pacific Tropical Cyclogenesis Frequency to Tropical Indian and North Atlantic Ocean SST in Early 1990s. *J. Geophys. Res. Atmospheres* 125 (2), e2019JD031493. doi:10.1029/2019jd031493
- Xie, X. L., and Beni, G. (1991). A Validity Measure for Fuzzy Clustering. *IEEE Trans. Pattern Anal. Machine Intell.* 13 (8), 841–847. doi:10.1109/34.85677
- Yokoi, S., and Takayabu, Y. N. (2013). Attribution of Decadal Variability in Tropical Cyclone Passage Frequency over the Western North Pacific: A New Approach Emphasizing the Genesis Location of Cyclones. *J. Clim.* 26 (3), 973–987. doi:10.1175/jcli-d-12-00060.1
- Zhang, C., Li, S., Luo, F., and Huang, Z. (2019). The Global Warming Hiatus Has Faded Away: An Analysis of 2014–2016 Global Surface Air Temperatures. *Int. J. Climatol.* 39 (12), 4853–4868. doi:10.1002/joc.6114
- Zhang, W., Vecchi, G. A., Villarini, G., Murakami, H., Rosati, A., Yang, X., et al. (2017). Modulation of Western North Pacific Tropical Cyclone Activity by the Atlantic Meridional Mode. *Clim. Dyn.* 48 (1–2), 631–647. doi:10.1007/s00382-016-3099-2
- Zhang, W., Vecchi, G. A., Murakami, H., Villarini, G., Delworth, T. L., Yang, X., et al. (2018). Dominant Role of Atlantic Multidecadal Oscillation in the Recent Decadal Changes in Western North Pacific Tropical Cyclone Activity. *Geophys. Res. Lett.* 45 (1), 354–362. doi:10.1002/2017gl076397
- Zhao, H., Chu, P.-S., Hsu, P.-C., and Murakami, H. (2014). Exploratory Analysis of Extremely Low Tropical Cyclone Activity during the Late-Season of 2010 and 1998 over the Western North Pacific and the South China Sea. *J. Adv. Model. Earth Syst.* 6 (4), 1141–1153. doi:10.1002/2014ms000381
- Zhao, J., Zhan, R., Wang, Y., and Xu, H. (2018). Contribution of the Interdecadal Pacific Oscillation to the Recent Abrupt Decrease in Tropical Cyclone Genesis Frequency over the Western North Pacific since 1998. *J. Clim.* 31 (20), 8211–8224. doi:10.1175/jcli-d-18-0202.1

Conflict of Interest: The authors declare that the research was conducted in the absence of any commercial or financial relationships that could be construed as a potential conflict of interest.

Publisher's Note: All claims expressed in this article are solely those of the authors and do not necessarily represent those of their affiliated organizations, or those of the publisher, the editors, and the reviewers. Any product that may be evaluated in this article, or claim that may be made by its manufacturer, is not guaranteed or endorsed by the publisher.

Copyright © 2022 Tian, Zhou and Wong. This is an open-access article distributed under the terms of the Creative Commons Attribution License (CC BY). The use, distribution or reproduction in other forums is permitted, provided the original author(s) and the copyright owner(s) are credited and that the original publication in this journal is cited, in accordance with accepted academic practice. No use, distribution or reproduction is permitted which does not comply with these terms.



Simulation of Rapid Intensification of Super Typhoon Lekima (2019). Part II: The Critical Role of Cloud-Radiation Interaction of Asymmetric Convection

Qijun Huang, Xuyang Ge* and Mingyu Bi

Key Laboratory of Meteorological Disaster of Ministry of Education, Joint International Research Laboratory of Climate and Environment Change, Collaborative Innovation Center on Forecast and Evaluation of Meteorological Disasters, Nanjing University of Information Science and Technology, Nanjing, China

OPEN ACCESS

Edited by:

Guanghua Chen,
Institute of Atmospheric Physics
(CAS), China

Reviewed by:

Nannan Qin,
Fudan University, China
Dajun Zhao,
State Key Laboratory of Severe
Weather, China

*Correspondence:

Xuyang Ge
xuyang@nuist.edu.cn

Specialty section:

This article was submitted to
Atmospheric Science,
a section of the journal
Frontiers in Earth Science

Received: 10 December 2021

Accepted: 27 December 2021

Published: 10 February 2022

Citation:

Huang Q, Ge X and Bi M (2022)
Simulation of Rapid Intensification of
Super Typhoon Lekima (2019). Part II:
The Critical Role of Cloud-Radiation
Interaction of Asymmetric Convection.
Front. Earth Sci. 9:832670.
doi: 10.3389/feart.2021.832670

In this study, super typhoon Lekima (2019) with an atypical rapid intensification (RI) episode is investigated by conducting a pair of experiments. In the control experiment, the model reproduces reasonably well the evolution characteristics of convective activity and intensity changes. That is, active downshear-left convection moved counterclockwise to the upshear flank. In the sensitivity experiment without the cloud-radiation feedback (CRF), the simulation fails to capture the observed upshear deep convection and the RI process. Our analyses suggest that the cloud-radiation interaction acts as positive feedback between the tilting-induced convective asymmetry (TCA) and outflow channel. On the one hand, the radiative process will induce upper (lower) cooling (warming) above (within) the cloud anvil of the outflow layer. This thermodynamical pattern locally destabilizes the upper troposphere and is conducive to enhance the deep convection. On the other hand, the enhanced deep convection provides the energy source to promote the upper divergent flows. The stronger divergent flow acts efficiently to block the vertical wind shear (VWS) and leads to a stronger outflow channel. This CRF assists in the development of a thicker and more radially extensive outflow than that CRF-off simulation. This study further confirms the outflow blocking effect, which gains insights on the evolution of upshear-left asymmetric convection and its role in the atypical RI event.

Keywords: tropical cyclone outflow layer, rapid intensification, asymmetric convection, cloud-radiation force, vertical wind shear

INTRODUCTION

The intensity prediction of tropical cyclone (TC) remains a big challenge for the operational centers (DeMaria et al., 2014), particularly during the rapid intensification (RI) with winds increased by at least 30 knots in a 24-h period. TC intensity change is affected by multiple-scale processes, including internal dynamics and external forcing. Among the external forcing, the environmental vertical wind shear (VWS) has been realized as one of the important factors in modulating TC intensification (Zeng et al., 2007; Zeng et al., 2008; Gu et al., 2015; Wang et al., 2015; Chen et al., 2017). In response to the VWS, the storm will exhibit significant structure change. For instance, the VWS can tilt the TC vortex, creating pronounced asymmetries in TC structure and rainfall pattern (Reasor et al., 2009; Molinari and Vollaro, 2010; Nguyen and Molinari, 2012). Specifically, the deep convection is mainly located at the downshear-left (DSL) quadrant, whereas it is greatly suppressed at the upshear (US)

quadrant under the VWS. Several paradigms are proposed to interpret the possible processes leading to such a wavenumber one asymmetry (Wong and Chan, 2004; Zhang and Kieu, 2006). Due to the superposition of the environmental flow and TC circulation, an asymmetric secondary circulation will be induced by an enhanced ascending (descending) at the downshear (US) flank (Wong and Chan, 2004), agreeing with the observed typical wavenumber-1 rainfall asymmetry (Rogers et al., 2003; Braun et al., 2006). By using the potential vorticity dynamics framework, Zhang and Kieu (2006) identified the so-called shear-forced secondary circulation (SFC), which acts to resist the influence of the environmental VWS. In short, for a sheared storm, the secondary circulation has a deep layer of low-level inflow on the downshear side (Reasor et al., 2013; DeHart et al., 2014).

Nevertheless, recent observational and numerical studies (Zhang and Tao, 2013; Tao and Jiang, 2015; Rogers et al., 2016; Munsell et al., 2017; Wadler et al., 2018; Ryglicki et al., 2019; Li et al., 2020; Huang et al., 2021) revealed that, under some circumstances, deep convection occurs mainly on the US side. For RI storms, Tao and Jiang (2015) observed that a cyclonic rotation of frequency peaks from shallow (downshear right; DSR) to moderately or/and very deep precipitation (upshear left; USL) and suggested that this feature is a potential indicator of a rapidly strengthening vortex. By conducting ensemble simulations of Hurricane Edouard, Leighton et al. (2018) illustrated that intensifying TC members have more actively convective bursts (CBs) on the US side, while the CBs with members that do not intensify remain on the downshear side. This result is supported by the analysis of aircraft observations (Wadler et al., 2018). This feature is different from the typical pattern with DSL deep convection. As such, the group of TCs with deep convection at the US flank is called atypical class (Ryglicki et al., 2019).

For a rapid development TC under ambient VWS, it must experience a quicker vertical alignment. Numerous studies have suggested a variety of mechanisms for the tilt realignment, including the evolution of vortex Rossby waves in the inner core (Smith and Montgomery, 2015), the SFC (Zhang and Kieu, 2006), vortex re-formation (Molinari et al., 2006), and an outflow in opposing and deflecting the environmental flow (e.g., Elsberry and Jeffries, 1996; Dai et al., 2019; Ryglicki et al., 2019; Dai et al., 2021). As an important branch of a TC, the upper-level outflow layer pattern potentially influences the storm's intensity and structure evolution (Merill, 1988). Elsberry and Jeffries (1996) suggested that the shallow outflow layer of TC could deflect the upper-level environmental flow. For this atypical class of TCs that underwent RI, the vertical realignment is closely associated with the tilt-modulated convective asymmetries (TCA) (Ryglicki et al., 2019). Once the TCA moves toward the US flank, it will greatly enhance the outflow layer and thus reduce the VWS. These results indicate the possible important role of the convective asymmetries in minimizing the TC tilting.

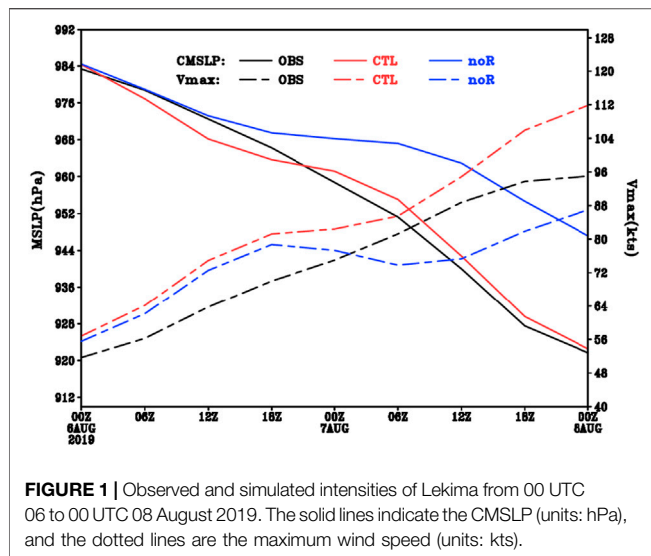
Previous studies suggested that TC intensification is strongly related to their upper-level clouds and stratiform precipitation (Tao et al., 2017; Fischer et al., 2018; Zhang and Xu, 2021). Recent theoretical and modeling studies have suggested that the crucial role of cloud-radiation feedback (CRF) in TC genesis and

development (Bu et al., 2014; Fovell et al., 2016; Wing et al., 2016; Ruppert et al., 2020; Smith et al., 2020; Yang and Tan, 2020; Yang et al., 2021). Ruppert et al. (2020) suggested that the intensification of the secondary circulation forced by the radiative warming anomaly might transport more moisture and low-level angular momentum into the disturbance region, which directly promotes TC development. Fovell et al. (2016) pointed out that the CRF processes may affect TC inner-core diabatic heating asymmetries, outer-core convective activity, and the characteristics of the anvil cloud. Due to the absorption and emission of longwave radiation in the cloud anvil, this encourages more extensive convective activity and thus helps a radial expansion of the TC wind field. Covered by a large area of cloud anvils, the outflow channel is believed to exert a significant CRF. In reality, the TC upper-level divergent flow is largely driven by the deep convection; it stimulates us to investigate the possible role of the TCA in the atypical RI process. Hence, several scientific issues will be addressed here: 1) What are the possible roles of US deep convection in modulating the TC outflow layer in the RI process? 2) What are the possible roles of the CRF in modulating TC outflow and asymmetric convection? To fulfill this goal, super typhoon Lekima (2019) is selected to represent an atypical RI case (Huang et al., 2021). The paper is organized as follows: in the *Experimental Designs* section, we briefly describe the experimental design and model setup. The results are presented in the *Simulation Results* section, and the conclusion and discussions are given in the *Conclusion and Discussion* section.

EXPERIMENTAL DESIGNS

In this study, the Advanced Research Weather Research and Forecasting model (WRF-AWR; version 3.9.1) is used. The model domains are two-way interactive and four-nested domains with the horizontal grid spacings of 27, 9, 3, and 1 km, respectively. There are 45 uneven σ levels in the vertical using terrain-following coordinates extending from the surface to the model top at 10 hPa. The vortex-following technique is used in the third and innermost moving-nested domains so that the TC vortex is always located near the center of the domain. The other model physics included the following: 1) the Lin microphysics scheme (Lin et al., 1983), including six classes of hydrometeors about water vapor, cloud water, rain, cloud ice, snow, and graupel; 2) the Dudhia scheme (Dudhia, 1989) for shortwave radiation calculations; 3) the rapid radiative transfer model (RRTM; Mlawer et al., 1997) for longwave radiation calculations; and 4) the YSU turbulent mixing scheme for boundary layer parameterization. The Kain-Fritsch convective scheme (Kain and Fritsch, 1993) is used for the outermost domain only.

The control experiment (CTL) is the same as that of Huang et al. (2021) for typhoon Lekima (2019), in which the evolution of TCA at the US quadrant is investigated. The simulation initial time is at 0000 UTC 6 August. Our previous work simulated well the observed atypical RI process. That is, under moderate upper-level easterly VWS, the TCA is transported from the initially



downshear quadrant to the US quadrant. This process enhances upward motions at the US flank and creates upper-level divergent flow. In this study, in order to gain insight on the possible roles of CRF in modulating the outflow, a sensitivity experiment (noR) is designed by turning off the cloud–radiation interaction feedback. The CRF functions as positive feedback, assisting in the development of a thicker and more radially extensive anvil. The details of the model strategy of the RRTMG scheme without CRF follow the previous studies (Bu et al., 2014; Ruppert et al., 2020). The CRF is the interaction of hydrometeors with radiation. The CRF-off removes the diurnal cycle in the radiative forcing and the period of the anvil development. In WRF, the CRF in the RRTMG scheme is controlled by the physics parameter “icloud” in the name list. The other model settings are the same as that of CTL. Consistent with CTL, noR was initialized at 0000 UTC 6 August, and the model was integrated for 48 h.

SIMULATION RESULTS

Intensity Simulations From Control and noR

Lekima (2019) was formed as a tropical depression on 0600 UTC 04 August, 2019, and strengthened into a typhoon in the following 2 days. At the initial time (i.e., 0000 UTC 6 August), the central minimum sea level pressure (CMSLP) was 985 hPa. Thereafter, an RI period was evident from 0000 UTC 6 August to 0000 UTC 8 August. **Figure 1** gives the simulated and observed TC intensities represented by the CMSLP and the maximum wind speed. The CTL simulation captures well the RI. Specifically, during the 48-h integration period, the CMSLP dropped by about 65 hPa to be 920 hPa and the maximum wind speed increased by about 60 kts to be 112 kts, which satisfy the criteria for RI for western North Pacific TCs (Wang and Zhou, 2008). In contrast, the entity in noR intensified slowly. Specifically, the CMSLP is about 952 hPa and the maximum wind speed is about 95 kts, which are much weaker than those in CTL at the end of integration.

Comparisons of the Tilting-Induced Convective Asymmetry

The VWS in this case is the northeasterly wind, determined by the difference between 2- and 16-km level wind fields. In general, a tilted vortex induces an asymmetric wavenumber one structure of convection under the VWS. To verify the simulated tilt-induced convective activity, **Figure 2** presents the simulated radar reflectivity at 5-km height in CTL (left panels) and the satellite-observed infrared brightness temperatures (right panels) during the RI period. In both CTL and observation, there exists a wavenumber one asymmetric convection distribution. Initially, the maximum radar reflectivity was located in the DSL quadrant and started to move counterclockwise to the US side shortly after a 12-h integration (**Figures 2A–C**). Initially, the strong convective cloud band, represented by the coldest temperature, occurs to the southwest section of the TC center. With time, the strongest convection is expanded to the US side, and the eyewall cloud becomes more symmetric. During the period of interest, the inner cloud band within 200 km from the TC center extends southeastward (US side). Overall, the simulated cloud asymmetry in CTL agrees fairly well with the satellite-observed infrared brightness temperatures (**Figures 2D–F**). Given the reasonably good performance of CTL, we use these simulated results as the proxy of the real atmosphere.

Figures 3, 4 compare the two snapshots of the distribution of the vertical velocity at different layers (i.e., $z = 1.5$ km, $z = 5$ km, and $z = 15$ km) in CTL and noR, respectively. In CTL (**Figure 3A**), a strong convective activity with vertical velocity greater than 2 m s^{-1} is initially located at the southwest quadrant at 06 UTC 6 August. During the time of interest, the CBs move counterclockwise to the US side at 00 UTC 7 August (**Figure 4B**), which is consistent with the atypical RI event reported in previous studies (Ryglicki et al., 2018a; Ryglicki et al., 2018b; Wadler et al., 2018; Li et al., 2020). The strong upward motion in the USL is mainly located at the upper level, which indicated that the cyclonic rotation developed to the deep convection during the RI period. **Figure 4** shows the vertical velocity in noR at three layers. Both experiments show similar patterns at the early stage, 6 h into the integration. That is, the convections were mainly located at the southwest flank of the storm (**Figures 3A, 4A**). It is likely that the model takes times to achieve CRF of comparable spatial extent and magnitude. With time, there are distinct differences in terms of the magnitude of the convection in two simulations. During the time of interest, the upward motion around RMW in noR is weaker than that in the CTL. The intensity of deep convection slightly weakened and did not show cyclonically inward propagation (**Figure 4B**).

To further demonstrate such differences, the contoured frequency by altitude diagrams (CFADs; Yuter and Houze, 1995) of vertical velocity for different quadrants within the 180-km radii is compared. The CFADs clearly illustrate the frequency distribution of vertical velocity of indicated values at different altitudes. In CTL, at 06 UTC 6 August, updrafts stronger than 2 m s^{-1} occur more frequently at the upper level in the DSL and DSR quadrants (**Figures 5A,D**). Initially, the strongest

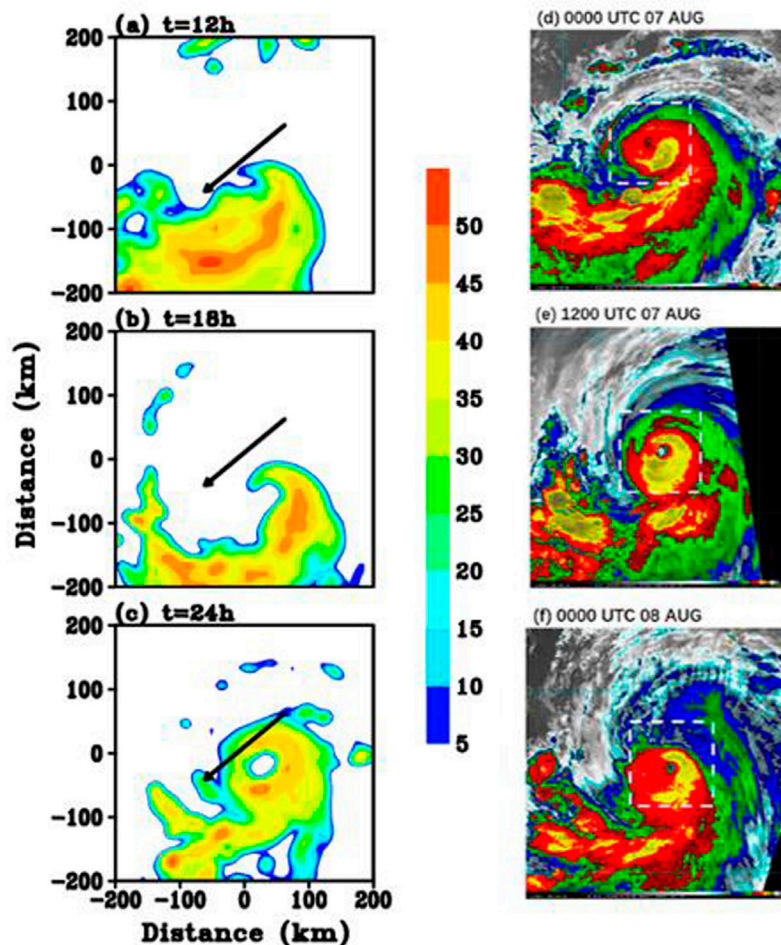
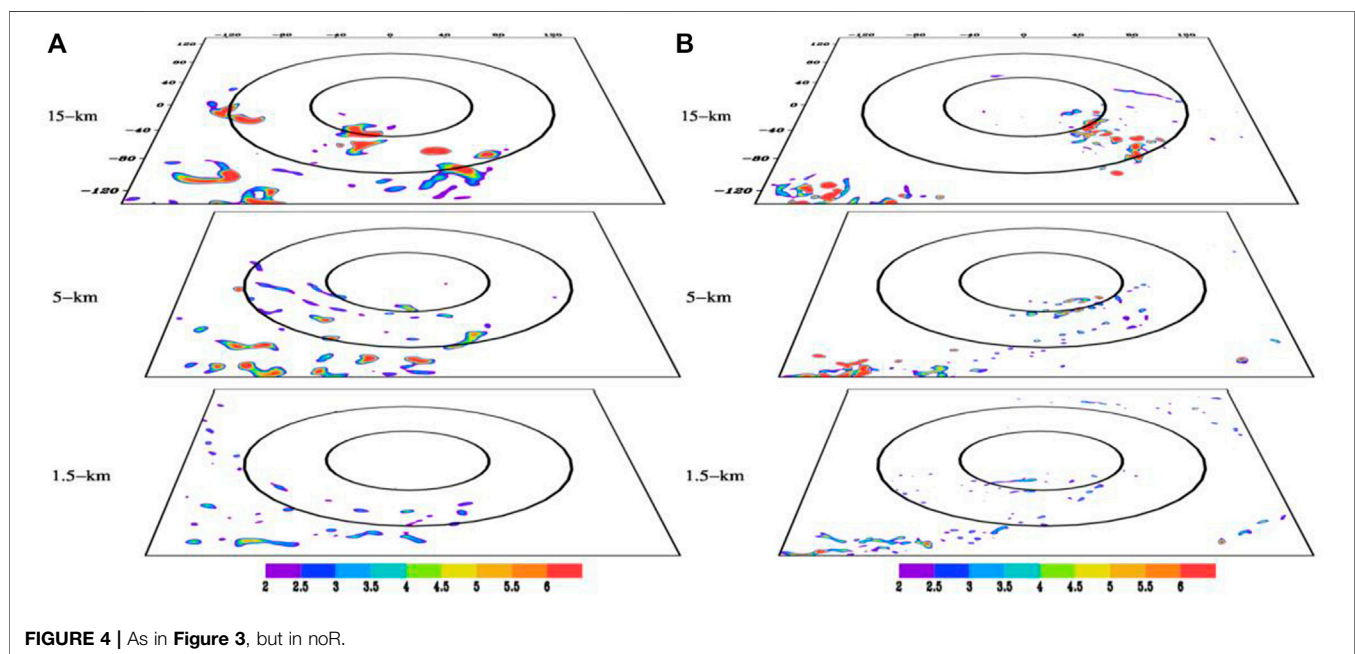
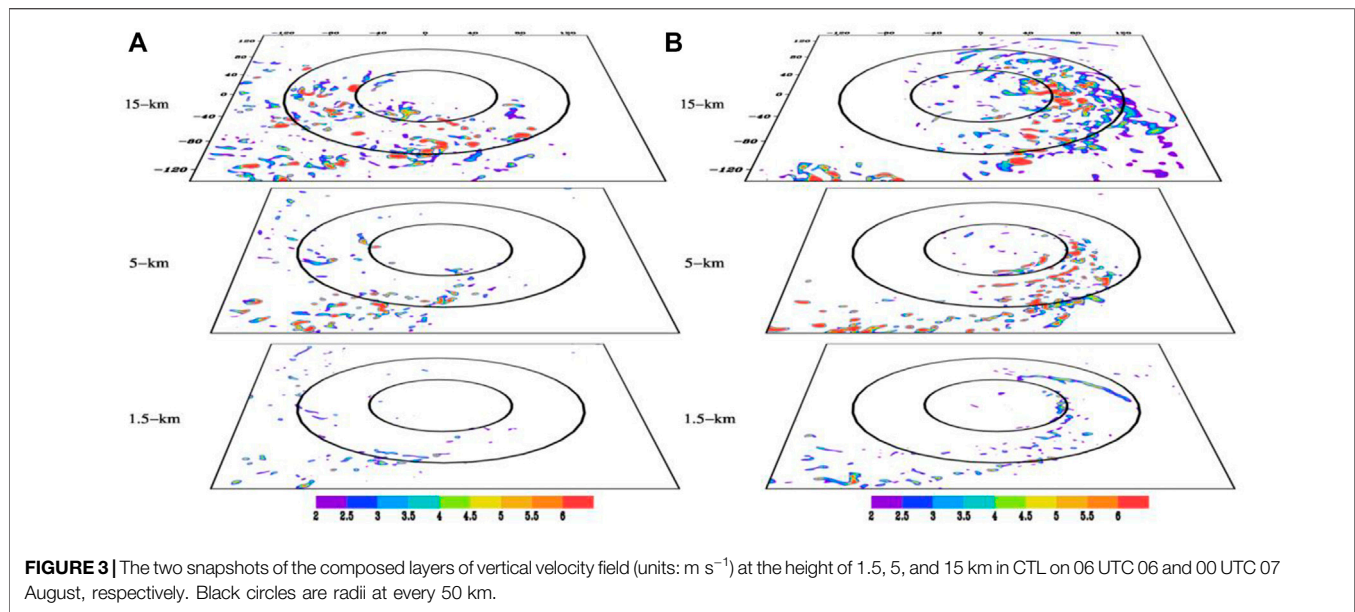


FIGURE 2 | Left panels: snapshot at 12, 18, and 24 h of the radar reflectivity at 5-km height (shaded; units: dBZ) and the VWS between 15 and 2 km (black vectors; units: m s^{-1}) at 17 km starting on 0000 UTC 6 August. Right panels: the time evolution of the satellite-observed infrared brightness temperatures from 0000 UTC 7 August to 0000 UTC 8 August on the NOAA website. The white dashed box in the right panels is the 200 × 200 km area centered by the TC, covering the same area as in the left panels.

convection is located around the DSL, indicating a convection initialization therein. In the US quadrants, there are no significant asymmetries, reflecting both weak ascending and descending motions. At 00 UTC 7 August, the modal distribution tilts toward stronger vertical velocity with height, implying that the strong upward motion is mainly located at the upper level. Notice that there are more substantial structural changes in the US side than in the downshear side (Figures 5E–H). Namely, the USL quadrant has more intense upper-level updrafts than the USR quadrant (Figures 5F,G).

Figure 6 displays the snapshots of CFAD of vertical velocity in noR. At the early stage, the vertical velocity is weaker in the US quadrants. Meanwhile, the strong updrafts are primarily located at the upper level in the DSL, which is similar to CTL. At 00 UTC 7 August, the portion of stronger vertical motion increases in both DSL and USL, but the stronger vertical velocity for the updrafts is mainly in the DSL. In USL, the peak occurs around the height of 15 km (Figure 6F), indicating an enhanced deep convection as well.

Nevertheless, the value of this peak is smaller than that in CTL (Figure 5F). To clearly illustrate the differences, Figure 7 presents the differences in CFADs of vertical velocity at four quadrants between CTL and noR. In this study, the values are obtained by CTL minus noR. Compared between CTL and noR, at 06 UTC 6 August, the vertical velocity for the updrafts was stronger in the former, except those larger than 3 m s^{-1} at the height between 8 and 16 km in DSL (Figure 7A). The ascending motion in DSR and USL is stronger in CTL than in noR (Figures 7B,D). The difference is more evident in the downshear quadrants. At 00 UTC 7 August, the most striking differences appear in the DSL and USL quadrants. As shown in Figure 7E, the value of the portion of weak ascending motion (i.e., $w < 2 \text{ m s}^{-1}$) is negative, indicating a weakening deep convection. Meanwhile, the difference of the strong updrafts (i.e., $w > 2 \text{ m s}^{-1}$) is insignificant in DSL. However, the value of such convection becomes positive in USL, especially above the height of 8 km, suggesting an enhanced upper-level deep convection therein. Recall that in CTL, the active activity initially appears in DSL and



then moves cyclonically toward USL. Accompanied by this transition, the upper-level upward motion becomes pronounced. Provided that a higher frequency of upper-level convection in USL as the storm development, the TC intensity in CTL is much stronger than that in noR, which agrees with Wadler et al. (2018). This result also agrees with Tao and Jiang (2015), who found that the intensifying TC has a large portion of CBs in the USL compared with the steady one.

To summarize, the results demonstrate that, in CTL, the asymmetric convection induced by VWS is transported from the initially downshear quadrant to the US quadrant, which is different from the general feature of the downshear convection under VWS. However, the active convection in noR is weaker

than that in CTL and mainly remained in DSL. In the next section, we will investigate the possible roles of different TCA in affecting the TC outflow layer.

Upper Outflow Layer

TC outflow is the dominant upper component of the TC secondary circulation. Generally, it has low inertial stability and thus expands radially thousands of kilometers and can interact with the environmental flow. The pattern of the outflow channel largely depends on the relative location of the TC and its environmental flow. Ryglicki et al. (2019) found that the divergent outflow forced by deep convection localized by the tilt of the vortex serves to divert the

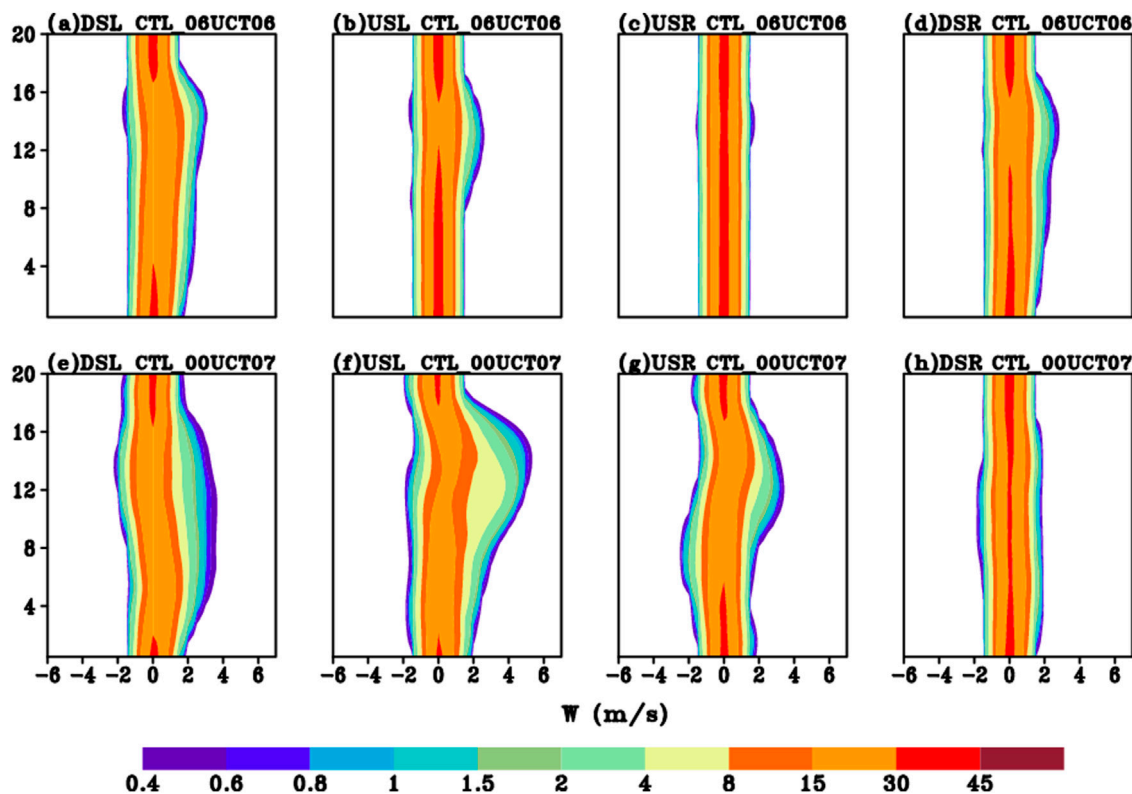


FIGURE 5 | Snapshots of 06 UTC 06 and 00 UTC 07 August of the contoured frequency by altitude diagrams (CFADs) of vertical velocity separated according to shear quadrant (units: %). With the shear vector pointing left, the quadrants are (A, E) DSL, (B, F) USL, (C, G) USR, (D, H) DSR in CTL.

background environmental flow around the TC, thus reducing the ambient VWS. Given the different convective activities between CTL and noR, it is inspiring to examine the upper outflow circulations.

To isolate the divergent flow induced by the diabatic heating, a PV- ω equation (Wang and Zhang, 2003) is applied. This dynamical framework is based on an equation system in three-dimensional pseudo-height coordinates, which considers the diabatic heating, the friction, and the dynamic forcing factors.

$$\begin{aligned}
 & \nabla_h^2 \left(\frac{\partial^2 \Phi}{\partial z^2} \omega \right) + f \eta \frac{\partial}{\partial z} \left\{ (Z_a - Z)^{-\mu} \frac{\partial}{\partial z} [(Z_a - Z)^\mu \omega] \right\} \\
 & - f \frac{\partial}{\partial z} \left(\frac{\partial \omega}{\partial x} \frac{\partial^2 \Psi}{\partial x \partial z} + \frac{\partial \omega}{\partial y} \frac{\partial^2 \Psi}{\partial y \partial z} \right) - f \frac{\partial}{\partial z} \left(\frac{\partial \omega}{\partial x} \frac{\partial^2 \chi}{\partial y \partial z} + \frac{\partial \omega}{\partial y} \frac{\partial^2 \chi}{\partial x \partial z} \right) \\
 & - \left(f \frac{\partial \eta}{\partial z} \frac{\mu}{Z_a - Z} + f \frac{\partial^2 \eta}{\partial z^2} \right) \omega \\
 & = f \frac{\partial}{\partial z} [V_h \cdot \nabla \eta] - \nabla_h^2 \left[V_h \cdot \nabla_h \frac{\partial \Phi}{\partial z} \right] - 2 \frac{\partial^2}{\partial t \partial z} \left[\frac{\partial^2 \Psi}{\partial x^2} \frac{\partial^2 \Psi}{\partial y^2} \right. \\
 & \quad \left. - \left(\frac{\partial^2 \Psi}{\partial x \partial y} \right)^2 \right] - \beta \frac{\partial^3 \Psi}{\partial t \partial y \partial z} + \frac{g}{\theta_0} \nabla_h^2 q_p - f \frac{\partial}{\partial z} \left(\frac{\partial f_y}{\partial x} - \frac{\partial f_x}{\partial y} \right) \\
 & \quad - \frac{\partial^2}{\partial t \partial z} \left(\frac{\partial f_x}{\partial x} + \frac{\partial f_y}{\partial y} \right)
 \end{aligned}
 \quad (1)$$

$$\nabla_h^2 \chi = -(\hat{z}_a - \hat{z})^{-\mu} \frac{\partial}{\partial z} [(\hat{z}_a - \hat{z})^\mu \omega] \quad (2)$$

where $z = [1 - (\frac{p}{p_0})^{\frac{\beta}{\gamma}}] (c_p \frac{\theta_0}{g})$ represents the vertical pseudo-height coordinate; $z_a = (\frac{c_p}{R_d}) H_s$; $H_s = \frac{p_0}{\rho_0 g} = \frac{R_d \theta_0}{g}$ is the characteristic height; $\mu = \frac{C_v}{R_d}$; $V_h = V_\psi + V_\chi$, χ is the velocity potential function; and η , Φ , and Ψ are the total absolute vorticity, stream function, and geopotential height, respectively. ω is the vertical velocity in the vertical pseudo-height coordinate. f_x and f_y are the latitudinal and meridional friction, respectively. θ_0 is the reference potential temperature, β is the beta parameter, p_0 is the surface pressure, and q_p is the diabatic heating. The vertical motion of the quasi-balanced model can be determined by Eq. 1, which, from left to right, shows the differential vorticity advection and the Laplacians of thermal advection by both non-divergent and divergent winds, the differential deformation or Jacobian term, the β effect, latent heating, and the effects of friction, respectively. In Eq. 1, the first four terms are the dynamic forcing factors. The last three terms are the thermodynamical forcing factors. The dynamic and thermodynamical forcing factors determine the magnitude of divergent winds and secondary circulations in TCs.

Figure 8 presents the simulated upper-level circulation at the height of 15 km and the diabatic heating in CTL. The simulated storm in CTL with CRF active has a large amount of convection and diabatic heating outside the radius of maximum wind (about

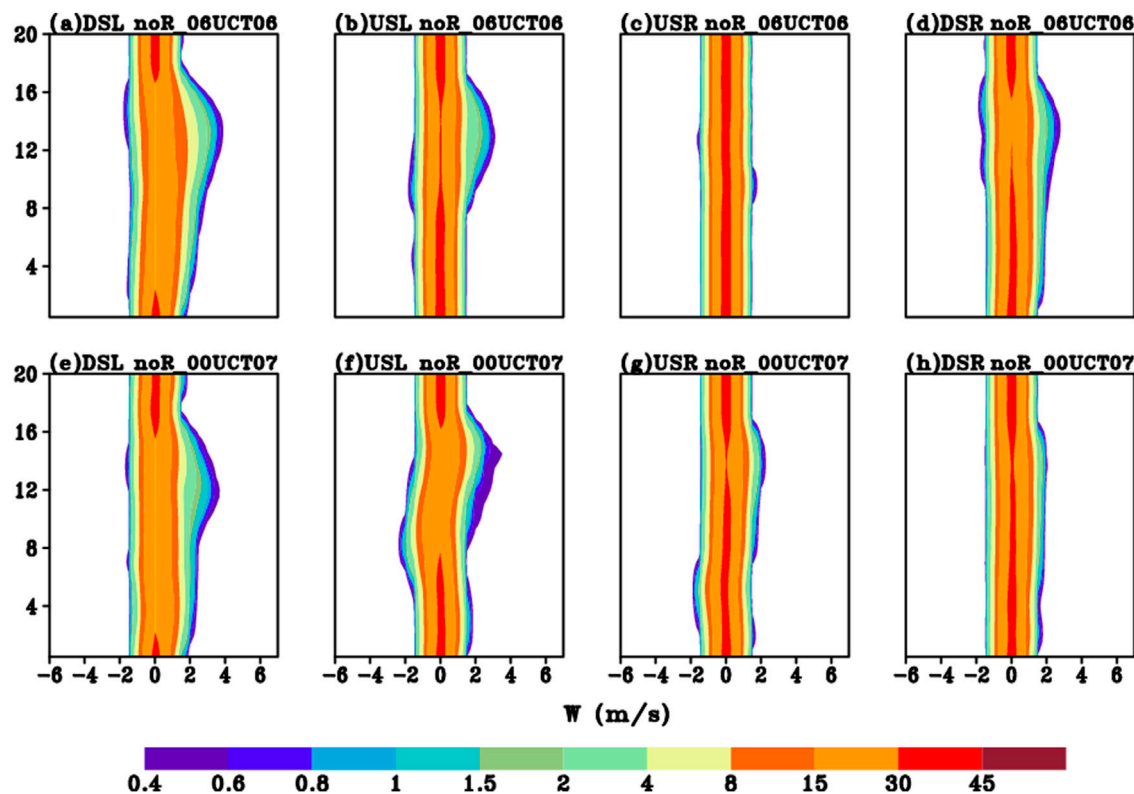


FIGURE 6 | As in Figure 5, but in noR.

60 km). There is a prevailing easterly flow, indicating an upper easterly VWS (Huang et al., 2021). Due to the model spin-up, it will take some time initially to trigger convection. As such, a weak divergent flow is forced by the weak diabatic heating in the beginning. Over time, the enhanced deep convection moves toward the US flank, and a pronounced divergent flow is evident. For instance, at 18 UTC 06 August, the strongest divergent winds are focused on the US flank, which meets with the environmental flow to generate a boundary referred to as the “outflow front” that exists about 200 km radially outward US of the storm center (Ryglicki et al., 2019). This front typically exists between 200 and 300 km radially outward US of the low-level center. Accordingly, the upper divergent flow is the dominated source of the blocking, whereas the rotational winds are largely deformed (not shown).

In noR (Figure 9), the early upper-level circulation is similar to that in CTL. Compared with that in CTL, the induced divergent flow is much weaker and occupies a relatively smaller area. It is likely due to the different magnitude of diabatic heating source that correlated with the convection. The smaller active convections and diabatic heating with CRF turned off compared to those with CTL. The comparison clearly demonstrates that the upper-level divergent flow is naturally driven by the diabatic heating. To emphasize the importance of deep convection, we further subdivide the diabatic heating source into upper- and lower-level components. Specifically, the heating rate above (below) the height of 8 km is taken as the upper

(lower)-level part. By applying these two separated forcings, the PV- ω method shows that the divergent outflow is primarily induced by the upper-level diabatic heating, whereas the lower-level diabatic heating plays a neglectable role (not shown). This result further suggests that the divergent wind in the outflow layer is mainly determined by the upper-level deep convection particularly in the USL quadrant in this case.

The PV- ω method clearly shows that the strengthening outflow forced by the diabatic heating plays an important role in blocking the environmental flow, reducing the upper-level environmental flow and thus the magnitude of VWS. To demonstrate this possibility, Figure 10 presents the time evolution of the vertical profiles of the steering flows in CTL and noR, respectively. Initially, the vertical profiles of the steering flows are nearly identical in both experiments. The environmental winds are southwesterly (northeasterly) below (above) about 8 km, indicating a moderate upper easterly shear. Compared with the large wind at the upper levels, the wind is relatively small at the lower levels, indicating an upper-level VWS. The difference is mainly located at the upper level during the time of interest. The easterly wind at the upper level decreases more largely with time in CTL than in noR resulting from the strong divergent wind at the outflow layer in the former. The initial VWS is a strong shear with the magnitude in 15 m s^{-1} (Figure 10B). Thereafter, albeit with some oscillations, the magnitude of VWS generally decreases with time, which is in the range of moderate-to-strong shear (Molinari et al., 2004;

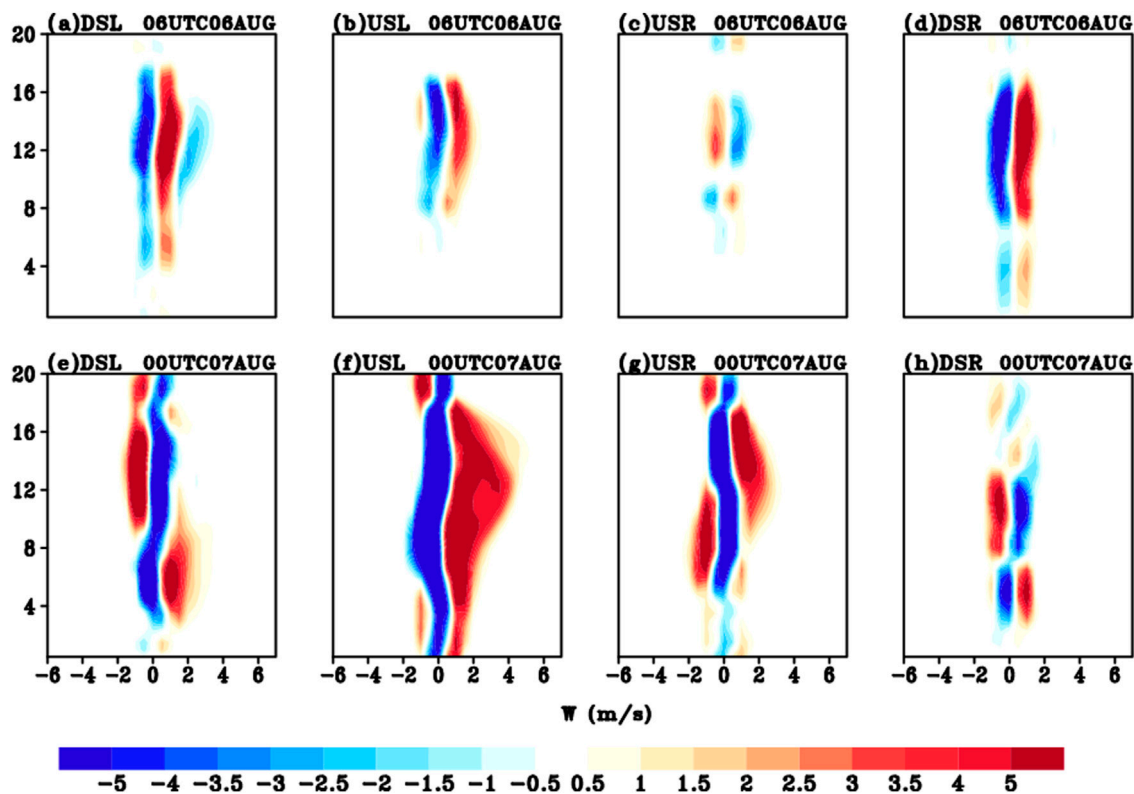


FIGURE 7 | The differences of CFADs of vertical velocity (units: %) for each shear quadrant between CTL and noR at 06 UTC 6 and 00 UTC 7 August.

Molinari et al., 2006; Ryglicki et al., 2019). More specifically, in CTL, the magnitude of VWS reached the minimum value (i.e., 7 m s^{-1}) about 12 UTC 06 August, which is smaller than its counterpart. That is, in noR, the VWS reduced much more slowly and the minimum value is about 10 m s^{-1} . A closer examination shows that the reduction of VWS is mainly ascribed to the weakening of environmental easterly at the upper level. The weakening of the easterly wind at the upper level is closely determined by the blocking effect of divergent flow. In short, a strong divergent flow exerts a greater blocking effect to resist the VWS and is favorable for TC intensification.

Physical Interpretations

The results above show marked differences in the evolution of deep convection between CTL and noR, especially in the USL region. Since the only difference is that the CRF is excluded in noR, it may help explain why the CRF-active storms possessed stronger convection maintained at the upper level. To this end, we will focus on its possible mechanisms in this section.

Previous studies (Bu et al., 2014; Fovell et al., 2016) pointed out that, in response to CRF that can influence the TC structure, TC is characterized by enhanced upper-tropospheric outflow. It is hypothesized that the TC outflow channel transports the hydrometeors outward, leading to a progressively wider cloud anvil, at least in the upper troposphere (Huang et al., 2021). The wider cloud anvil will have a greater potential to interact with the radiative processes. To demonstrate the radiative effect on the

outflow of TC, the Sawyer–Eliassen (SE) diagnosis is used to derive the transverse circulation forced by the radiation. The SE equation in the radius-pseudo-height coordinates (Hendricks et al., 2004) can be written as:

$$\frac{\partial}{\partial r} \left(\frac{A}{r} \frac{\partial \bar{\psi}}{\partial r} + \frac{B}{r} \frac{\partial \bar{\psi}}{\partial z} \right) + \frac{\partial}{\partial z} \left(\frac{C}{r} \frac{\partial \bar{\psi}}{\partial z} + \frac{B}{r} \frac{\partial \bar{\psi}}{\partial r} \right) = -\frac{\partial (\bar{\xi} \bar{F})}{\partial z} + \frac{\partial \bar{Q}}{\partial r} \quad (3)$$

where z is the pseudo height, r is the radius, and $\bar{\psi}$ represents the transverse stream function. The overbar denotes the azimuthal mean. Here, $A = (g/\theta_0)(\partial \bar{\theta}/\partial z)$ is the static stability, $B = -\bar{\xi}(\partial \bar{V}_t/\partial z)$ is the baroclinity, and $C = \bar{\xi} \bar{\eta}$ is the inertial stability, where $\bar{\theta}$, \bar{V}_t , $\bar{\xi}$, and $\bar{\eta}$ are the mean potential temperature, tangential wind, modified Coriolis parameter, and absolute vertical vorticity, respectively. The \bar{Q} and \bar{F} on the right-hand side of Eq. 3 represent the heating and momentum forcing, respectively. The diabatic heating associated with the ice phase is largely offset by the dynamical cooling process. In this study, since we focus on the impact of CRF, the temperature tendency due to the net radiative process (i.e., the sum of long-wave and short-wave radiation) is only taken as the heating forcing.

Figure 11 displays the forced transverse stream function and the associated secondary circulation by the temperature tendency due to radiation averaged from 07 UTC 6 to 18 UTC 6 August. Not surprisingly, there is a salient difference of the net radiative field in the two experiments. In CTL, the profile represents a

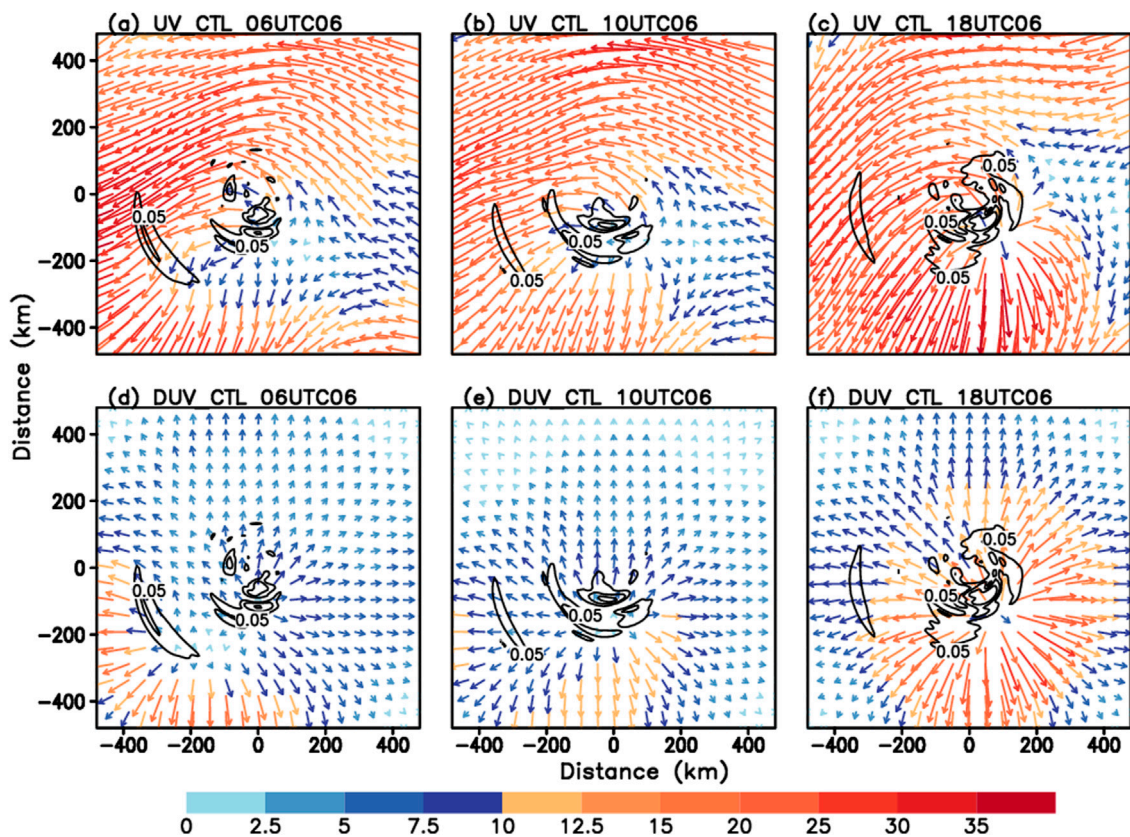


FIGURE 8 | Upper panels: the time evolution of the wind circulation (vector, units: m s^{-1}) and the diabatic heating (black contour, units: K/h) at 15-km height in CTL. Lower panels: the time evolution of the divergent wind (vector, units: m s^{-1}) and the diabatic heating (black contour, units: K/h) at 15-km height in CTL.

dipole with a cooling (warming) tendency above (below) the height of 16 km, where the top of the cloud anvil is located. This is a typical radiative heating structure of stratiform cloud cover (Tao et al., 1996; Yang and Tan, 2020). Huang et al. (2021) found that a large concentration of ice-phased particles is collocated with the cloud anvil of the outflow layer. Meanwhile, they suggested that this thermal pattern leads to a reduction of static stability in a larger area, favoring the development of deep convection. The large cooling (0.3 K/h) at the cloud top is likely due to the longwave (LW) radiative, the warming rate up to 0.3 K/h is situated between the height of 8 and 15 km, and a negative value is farther below. In contrast, there is generally an opposite tendency in noR with a cooling (warming) tendency below (above) the outflow layer. Furthermore, the magnitudes of both cooling and warming rates are weaker than those in CTL. Accordingly, the distinctly different distributions of the net radiative forcing will induce different secondary circulations.

In CTL, a transverse circulation is evident between the height of 8 and 16 km (Figure 11A). In general, a radial inflow occurs at around 12 km, and a radial outflow emanates at a higher altitude (i.e., the height of 16 km). In response to this circulation, the upper radial outflow will enhance the outflow channel. Furthermore, the radial inflow around the height of 12 km helps the development of the vortex and thus favors a deeper vertical structure of storm. Furthermore, an upward motion is induced in the inner core

region, bringing more upward water vapor flux and then resulting in more latent heating at upper levels. On the contrary, there is a weaker transverse circulation in noR with a weaker net radiative forcing. Yang and Tan (2020) found that the large concentration of ice-phased particles at high levels is critical to spinning up the midlevel vortex. The radiative interaction with upper-level hydrometers leads to an increase in the vertical diabatic heating gradient and then the intensification of the midlevel vortex. Previous studies (Ruppert and Hohenegger, 2018; Huang et al., 2021) also found that the temperature tendency change due to CRF will modify the static stability, which is possibly the primary driver of the invigoration of deep convection.

In short, the SE balanced dynamic framework illustrates that the CRF will impact the secondary circulation (i.e., outflow layer), which is consistent with Fovell et al. (2016). They also suggested that the upper-level thermal structure forced by the CRF likely has a certain effect on the TC intensification through modulating the outflow channel. Specifically, the CRF effect promotes the development of outflow channels and the TC secondary circulation. This CRF acts as positive feedback, assisting in the development of the outflow channel with a thicker and more radially extended anvil (see Huang et al., 2021 Figure 13). In turn, the wider cloud anvil has a greater potential to interact with the radiative process to modulate the upper thermal structure. Moreover, this impact can be simply understood in terms of

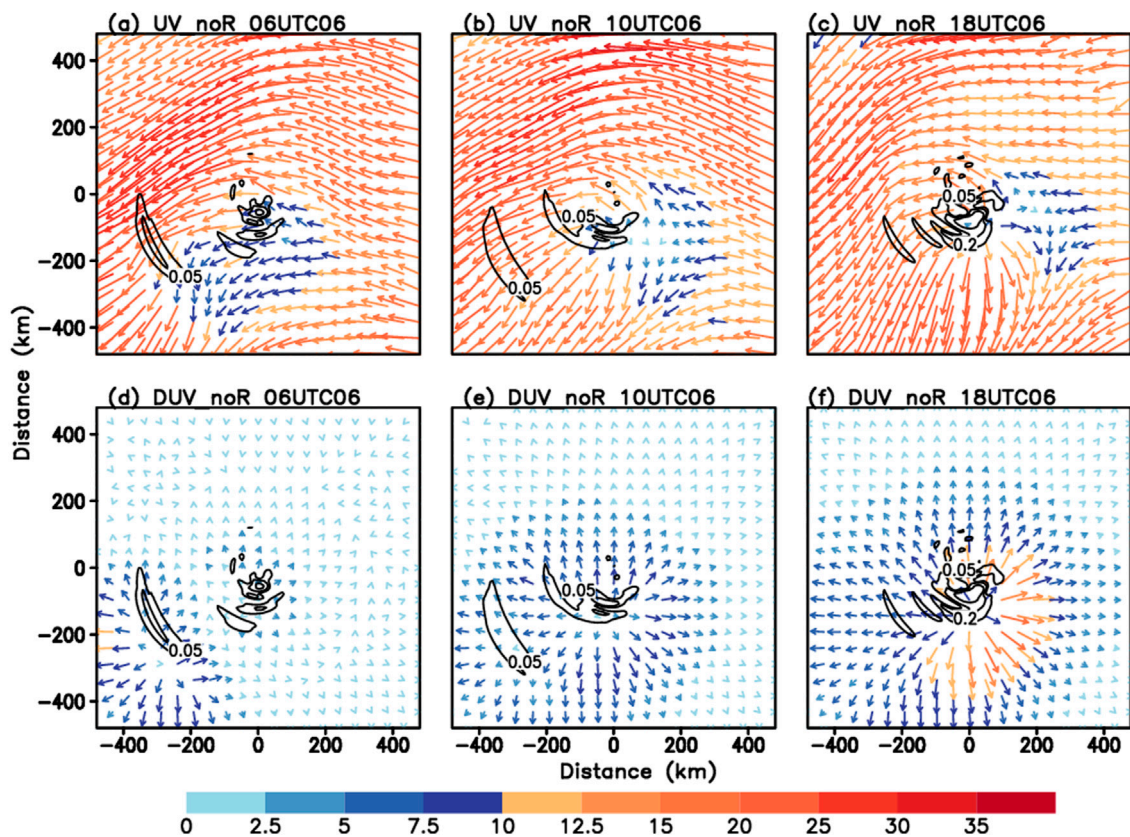


FIGURE 9 | As in Figure 8, but in noR.

the maximum potential intensity (MPI) theory (Emanuel, 1986), in which a lower outflow temperature implies a higher thermal efficiency and thus a stronger TC intensity. The CRF-on CTL experiment shows that the net radiative cooling is generated at the top of the cloud anvil associated with the outflow layer. Next, we will investigate the thermal efficiency in terms of energy budget.

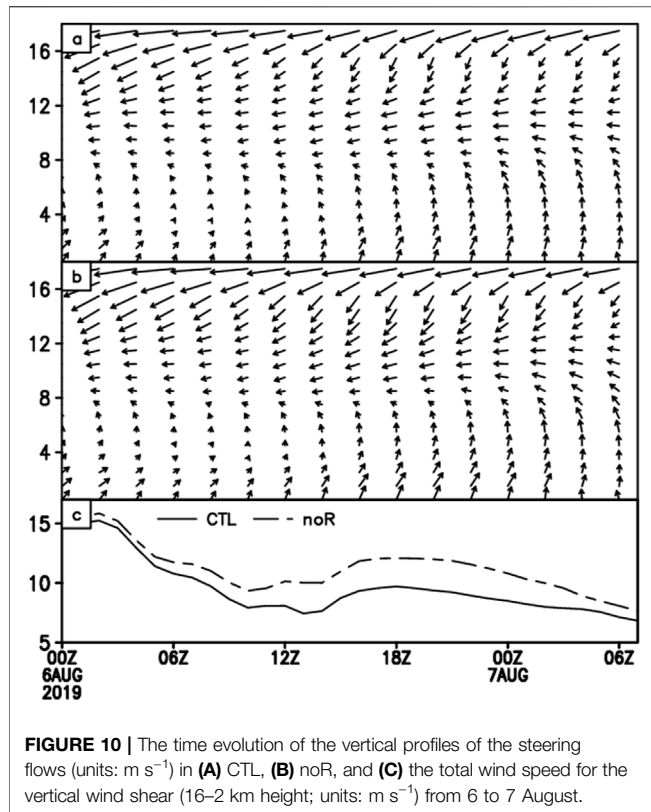
For a steady-state TC, the work done by the TC to spin up and expand the outflow anticyclone may have an impact on intensification rates or affect its ability to achieve MPI. The balance between total heating and dissipation in the inflow and outflow may be written symbolically:

$$\Delta Q = W_{in} + W_{out} \quad (4)$$

where W_{in} and W_{out} are the work done in the inflow layer and the outflow layer of TC, respectively. Rappin et al. (2009) suggested that the weak inertial stability in the outflow layer minimizes an energy sink of TC secondary circulation and leads to more RI to MPI. The work done in the outflow is the energy needed to restore the angular momentum of the outflow back to its ambient value:

$$\begin{aligned} W_{out} &= \frac{1}{2} \Delta V^2 = \frac{1}{2} \left[\left(\frac{M}{r_1} - \frac{1}{2} f r_1 \right)^2 - \left(\frac{M_a}{r_1} - \frac{1}{2} f r_1 \right)^2 \right] \\ &= \frac{1}{2} \left[\frac{M^2 - M_a^2}{r_1^2} + f (M_a - M) \right] \end{aligned} \quad (5)$$

where the definition of the absolute angular momentum is $M = rV + \frac{1}{2} f r^2$ and r_1 is the radius at which the angular momentum M_a along the tropopause becomes equal to the ambient value M . In this study, the azimuthal work done in the outflow layer of TCs is calculated. Figure 12 shows the evolution of the energy sinks and the radial wind speed at each azimuth in the outflow layer during the period of interest. The azimuthal angle 0° is defined here as due north, and 180° represents southward since it rotates counterclockwise. In CTL, the maximum radial wind greater than 30 m s^{-1} is located between the azimuthal angle of 120° and 180° which is the stronger outflow channel. Corresponding to the outflow channel, the outflow work down is relatively small (less than 130 J kg^{-1}). The small work down in the outflow originates constantly around the azimuthal angle of about 180° (left-of-shear side) and then propagates counterclockwise to about the region from 240° to 300° (US flank). The work done in the US left became smaller, which indicates the less energy expenditure in the outflow layer, corresponding well with the rapid establishment of the outflow jet therein. In noR, it bears many similarities as that in CTL, except that the work done at each azimuth is larger. This is likely ascribed to the different strength of outflow jets in both experiments. Given that the work done for its expansion is smaller, the earlier establishment of a stronger outflow jet in CTL than that in noR.



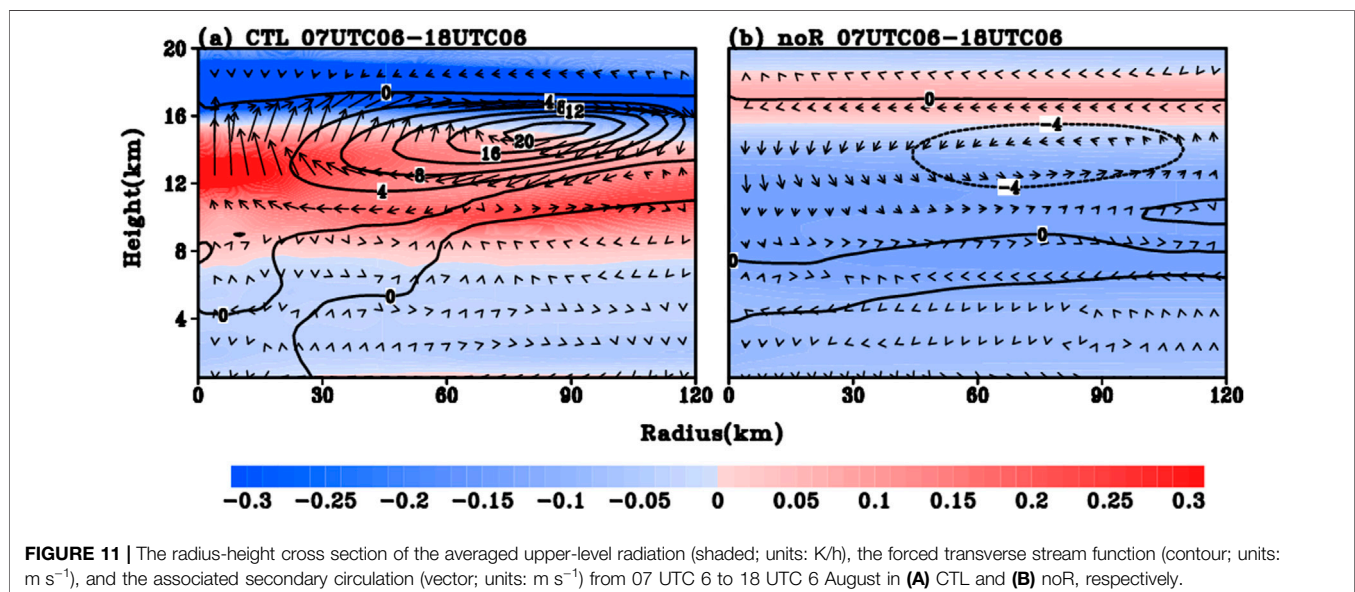
To further illustrate the evolution characteristics of the energy efficiency, **Figure 13** shows the ratio of the work done in the outflow layer to the net heat energy ($W_{out}/\Delta Q$). The smaller the ratio, the higher the efficiency of the TC strengthening is (Rappin et al., 2009). Namely, a smaller work (i.e., consumption kinetic energy) is needed to establish the outflow, and then more energy is input for TC

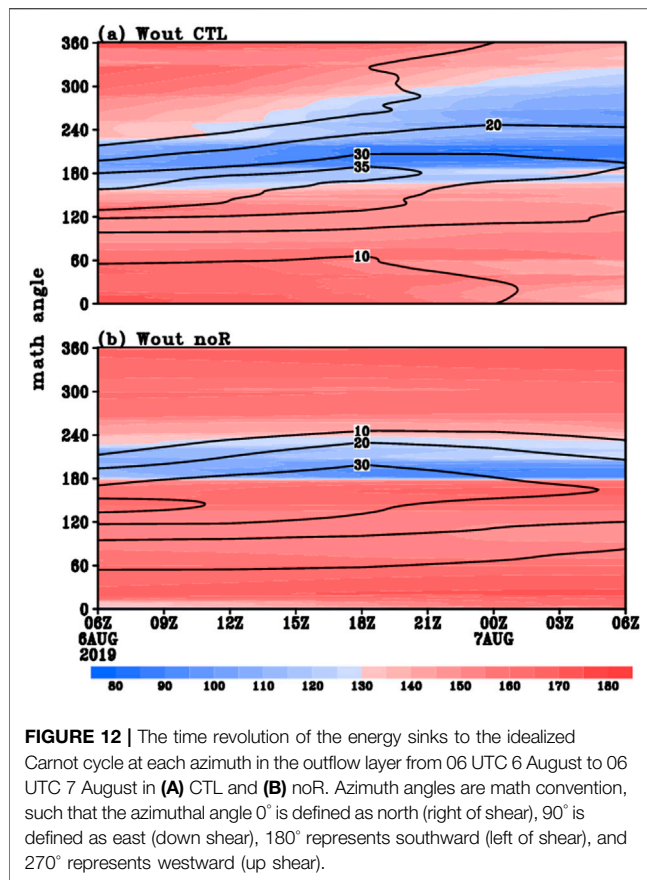
intensification. During the time of interest, the ratio steadily decreases with time in both experiments, reflecting a relatively weaker resistance to expand the outflow layer. Nevertheless, the ratio is consistently lower in CTL than that in noR, implying that more energy was transported to the outer region at the upper level in noR. Accordingly, the small amount of energy expended to expand the anticyclone in the outflow layer yields a RI in CTL. In short, the cloud–radiation interaction is conducive to expand the anticyclone in the outflow layer expending the small amount of energy so that only smaller work is required in the outflow layer; thus, the TC is able to achieve more energy to develop.

CONCLUSION AND DISCUSSION

Super typhoon Lekima (2019) in the western North Pacific went through an atypical RI under an upper-level VWS. During the period of RI, the initially DSL active convection moved counterclockwise to the US flank. In this study, a comprehensive analysis on the possible processes leading to the evolution of tilt-induced convective asymmetry is conducted by using a pair of numerical simulation. In the control experiment, the model reproduces reasonably well the evolution characteristics of convective activity. In the sensitivity experiment, the cloud–radiation interaction is artificially turned off. Accordingly, the model fails to capture the observed USL deep convection. The focus is on the possible role of cloud–radiation interaction forcing on the development of TCA and its relationship with upper outflow jet during the RI period. The main findings are summarized as the follows:

- 1) Under the VWS, a close relationship exists between the outflow layer and the deep convection in the US side. The enhanced upward motion on the US side favors the establishment of the outflow divergent flow. The strong

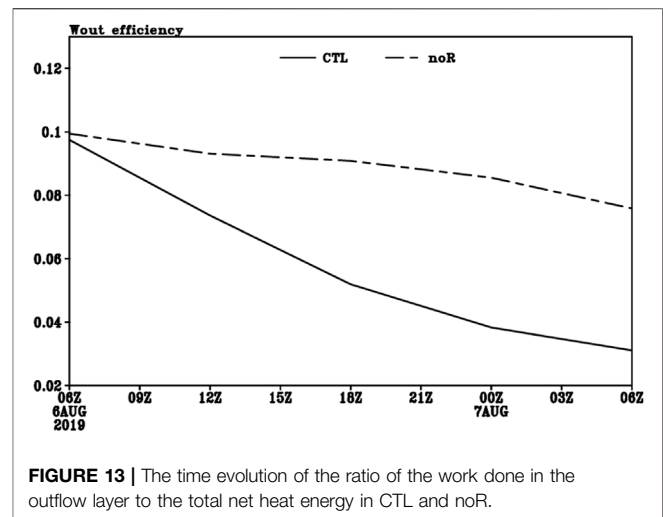




upper-level divergent flow acts against the environmental flow to reduce the VWS and thus helps in the sequential vertical realignment. This result supports previous studies that emphasized the important role of USL convection in RI.

- 2) The cloud-radiation interaction acts as positive feedback in the upper-level outflow layer. On the one hand, the radiative process associated with the cloud anvil will induce upper (lower) cooling (warming) above (within) the cloud anvil of the outflow layer. This thermodynamical pattern locally destabilizes the upper troposphere and is conducive to enhance the deep convection. On the other hand, the enhanced deep convection provides the energy source to promote the upper divergent flows. The stronger divergent flow acts efficiently to block the VWS and leads to a wider outflow channel. The larger outflow layer has a great influence due to the CRF.

Our simulations suggest that the cloud-radiation interaction feedback has a potential effect on the evolution of TCA that moves to the US side, which is an important driver for the divergent flow. The enhanced convective activity in the USL quadrant effectively leads to a stronger secondary circulation, a broader outflow layer circulation. With this regard, this CRF assists in the development of a thicker and more radially extensive anvil than that CRF-off simulation. This is consistent with Fovell et al. (2016). In addition to the



influence of the cloud-radiation interaction on the outflow layer to accelerate the TC development, our study reveals that CRF has effect on the evolution of asymmetric convection (i.e., magnitude and movement). The results help gain the insights on the prevailing USL convection and its role in the atypical RI event.

Different from the pathway of CRF which accelerates the TC development by accelerating the mid-level vortex (Ruppert et al., 2020; Yang et al., 2021), this study confirms the outflow blocking effect against the VWS. Physically, the CRF impact is closely associated with the distribution of cloud. With this regard, the CRF likely plays varied roles in the different regions or development stages. In the current study, the pronounced CRF effect is closely associated with TCA during the RI onset period. For the latter stage, along with the development of the inner-core convection, the CRF impact will be dominated in the inner region accordingly. Meanwhile, the different cloud types (i.e., convective and stratiform clouds) may induce different radiative impacts. These important issues need further investigation. Moreover, the formation of atypical TCA that moves to the US side is a complicated process, including both internal and external interactions. For instance, the southwesterly monsoon flow in the southeastern flank of TC provides abundant moisture and thus favors prolific convection. Moreover, the superposition monsoon flow and TC circulation is likely a potential factor in affecting TCA by changing the surface heat fluxes. As such, the enhanced surface heat fluxes will help the recovery of equivalent potential temperature from the DSL side, supporting the downstream development of deep convection in the USL side. Therefore, more future works will focus on these topics.

DATA AVAILABILITY STATEMENT

The raw data supporting the conclusions of this article will be made available by the authors, without undue reservation.

AUTHOR CONTRIBUTIONS

QH and XG designed and executed the experiments. XG and MB analyzed the data and wrote the article.

FUNDING

This work was jointly sponsored by the National Natural Science Foundation of China (42088101; 42175003; 41805039) and the

Science and Technology Innovation Project of Ningbo (Grant No. 2019B10025).

ACKNOWLEDGMENTS

The numerical calculations are performed on the supercomputing system in the Supercomputing Center of Nanjing University of Information Science & Technology.

REFERENCES

- Braun, S. A., Montgomery, M. T., and Pu, Z. (2006). High-resolution Simulation of Hurricane Bonnie (1998). Part I: The Organization of Eyewall Vertical Motion. *J. Atmos. Sci.* 63, 19–42. doi:10.1175/jas3598.1
- Bu, Y. P., Fovell, R. G., and Corbosiero, K. L. (2014). Influence of Cloud-Radiative Forcing on Tropical Cyclone Structure. *J. Atmos. Sci.* 71, 1644–1662. doi:10.1175/jas-d-13-0265.1
- Chen, X., Wang, Y., Zhao, K., and Wu, D. (2017). A Numerical Study on Rapid Intensification of Typhoon Vicente (2012) in the South China Sea. Part I: Verification of Simulation, Storm-Scale Evolution, and Environmental Contribution. *Mon. Wea. Rev.* 145, 877–898. doi:10.1175/mwr-d-16-0147.1
- Dai, Y., Majumdar, S. J., and Nolan, D. S. (2019). The Outflow-Rainband Relationship Induced by Environmental Flow Around Tropical Cyclones. *J. Atmos. Sci.* 76, 1845–1863. doi:10.1175/jas-d-18-0208.1
- Dai, Y., Majumdar, S. J., and Nolan, D. S. (2021). Tropical Cyclone Resistance to Strong Environmental Shear. *J. Atmos. Sci.* 78 (4), 1275–1293. doi:10.1175/jas-d-20-0231.1
- DeHart, J. C., Houze, R. A., Jr., and Rogers, R. F. (2014). Quadrant Distribution of Tropical Cyclone Inner-Core Kinematics in Relation to Environmental Shear. *J. Atmos. Sci.* 71, 2713–2732. doi:10.1175/jas-d-13-0298.1
- DeMaria, M., Sampson, C. R., Knaff, J. A., and Musgrave, K. D. (2014). Is Tropical Cyclone Intensity Guidance Improving? *Bull. Amer. Meteorol. Soc.* 95, 387–398. doi:10.1175/bams-d-12-00240.1
- Dudhia, J. (1989). Numerical Study of Convection Observed during the Winter Monsoon Experiment Using a Mesoscale Two-Dimensional Model. *J. Atmos. Sci.* 46, 3077–3107. doi:10.1175/1520-0469(1989)046<3077:nsocod>2.0.co;2
- Elsberry, R. L., and Jeffries, R. A. (1996). Vertical Wind Shear Influences on Tropical Cyclone Formation and Intensification during TCM-92 and TCM-93. *Mon. Wea. Rev.* 124, 1374–1387. doi:10.1175/1520-0493(1996)124<1374:vwsiot>2.0.co;2
- Emanuel, K. A. (1986). An Air-Sea Interaction Theory for Tropical Cyclones. Part I: Steady-State Maintenance. *J. Atmos. Sci.* 43, 585–605. doi:10.1175/1520-0469(1986)043<0585:aasitf>2.0.co;2
- Fischer, M. S., Tang, B. H., Corbosiero, K. L., and Rozoff, C. M. (2018). Normalized Convective Characteristics of Tropical Cyclone Rapid Intensification Events in the North Atlantic and Eastern North Pacific. *Mon. Wea. Rev.* 146 (4), 1133–1155. doi:10.1175/mwr-d-17-0239.1
- Fovell, R. G., Bu, Y. P., Kristen, L. C., Tung, W., Cao, Y., Kuo, H., et al. (2016). Influence of Cloud Microphysics and Radiation on Tropical Cyclone Structure and Motion. *Meteorol. Monogr.* 56, 11.1–11.27. doi:10.1175/amsmonographs-d-15-0006.1
- Gu, J.-F., Tan, Z.-M., and Qiu, X. (2015). Effects of Vertical Wind Shear on Inner-Core Thermodynamics of an Idealized Simulated Tropical Cyclone. *J. Atmos. Sci.* 72, 511–530. doi:10.1175/jas-d-14-0050.1
- Hendricks, E. A., Montgomery, M. T., and Davis, C. A. (2004). The Role of “Vortical” Hot Towers in the Formation of Tropical Cyclone Diana (1984). *J. Atmos. Sci.* 61, 1209–1232. doi:10.1175/1520-0469(2004)061<1209:trovht>2.0.co;2
- Huang, Q., Ge, X., and Peng, M. (2021). Simulation of Rapid Intensification of Super Typhoon Lekima (2019). Part I: Evolution Characteristics of Asymmetric Convection under Upper-Level Vertical Wind Shear. *Front. Earth Sci.* 9, 739507. doi:10.3389/feart.2021.739507
- Kain, J., and Fritsch, J. M. (1993). “Convective Parameterization for Mesoscale Models: The Kain-Fritsch Scheme,” in *The Representation of Cumulus Convection in Numerical Models*. Editors K. A. Emanuel and D. J. Raymond (Boston, MA: American Meteorological Society), 24, 246.
- Leighton, H., Gopalakrishnan, S., Zhang, J. A., Rogers, R. F., Zhang, Z., and Tallapragada, V. (2018). Azimuthal Distribution of Deep Convection, Environmental Factors, and Tropical Cyclone Rapid Intensification: A Perspective from HWRF Ensemble Forecasts of Hurricane Doudard (2014). *J. Atmos. Sci.* 75, 203–227. doi:10.1175/jas-d-17-0171.1
- Li, X., Davidson, N. E., Duan, Y., Tory, K. J., Sun, Z., and Cai, Q. (2020). Analysis of an Ensemble of High-Resolution WRF Simulations for the Rapid Intensification of Super Typhoon Rammasun (2014). *Adv. Atmos. Sci.* 37, 187–210. doi:10.1007/s00376-019-8274-z
- Lin, Y.-L., Farley, R. D., and Orville, H. D. (1983). Bulk Parameterization of the Snow Field in a Cloud Model. *J. Clim. Appl. Meteorol.* 22, 1065–1092. doi:10.1175/1520-0450(1983)022<1065:bpotsf>2.0.co;2
- Merrill, R. T. (1988). Characteristics of the Upper-Tropospheric Environmental Flow Around Hurricanes. *J. Atmos. Sci.* 45, 1665–1677. doi:10.1175/1520-0469(1988)045<1665:cotute>2.0.co;2
- Mlawer, E. J., Taubman, S. J., Brown, P. D., Iacono, M. J., and Clough, S. A. (1997). Radiative Transfer for Inhomogeneous Atmospheres: RRTM, a Validated Correlated-K Model for the Longwave. *J. Geophys. Res.* 102, 16663–16682. doi:10.1029/97jd00237
- Molinari, J., and Vollaro, D. (2010). Rapid Intensification of a Sheared Tropical Storm. *Mon. Wea. Rev.* 138, 3869–3885. doi:10.1175/2010mwr3378.1
- Molinari, J., Vollaro, D., and Corbosiero, K. L. (2004). Tropical Cyclone Formation in a Sheared Environment: A Case Study. *J. Atmos. Sci.* 61, 2493–2509. doi:10.1175/jas3291.1
- Molinari, J., Dodge, P., Vollaro, D., Corbosiero, K. L., Jr., and Marks, F. (2006). Mesoscale Aspects of the Downshear Reformation of a Tropical Cyclone. *J. Atmos. Sci.* 63, 341–354. doi:10.1175/jas3591.1
- Munsell, E. B., Zhang, F., Sippel, J. A., Braun, S. A., and Weng, Y. (2017). Dynamics and Predictability of the Intensification of Hurricane Edouard (2014). *J. Atmos. Sci.* 74, 573–595. doi:10.1175/jas-d-16-0018.1
- Nguyen, L. T., and Molinari, J. (2012). Rapid Intensification of a Sheared, Fast-Moving hurricane over the Gulf Stream. *Mon. Wea. Rev.* 140, 3361–3378. doi:10.1175/mwr-d-11-00293.1
- Rappin, E. D., Morgan, M. C., and Tripoli, G. J. (2009). The Impact of Outflow Environment on Tropical Cyclone Intensification and Structure. *J. Atmos. Sci.* 68, 179–194. doi:10.1175/2009JAS2970.1
- Reasor, P. D., Eastin, M. D., and Gamache, J. F. (2009). Rapidly Intensifying Hurricane Guillermo (1997). Part I: Low-Wavenumber Structure and Evolution. *Mon. Wea. Rev.* 137, 603–631. doi:10.1175/2008mwr2487.1
- Reasor, P. D., Rogers, R., and Lorsolo, S. (2013). Environmental Flow Impacts on Tropical Cyclone Structure Diagnosed from Airborne Doppler Radar Composites. *Mon. Wea. Rev.* 141, 2949–2969. doi:10.1175/mwr-d-12-00334.1
- Rogers, R., Chen, S., Tenerelli, J., and Willoughby, H. (2003). A Numerical Study of the Impact of Vertical Shear on the Distribution of Rainfall in Hurricane Bonnie (1998). *Mon. Wea. Rev.* 131, 1577–1599. doi:10.1175/2546.1
- Rogers, R. F., Zhang, J. A., Zawislak, J., Jiang, H., Alvey, G. R., Zipser, E. J., et al. (2016). Observations of the Structure and Evolution of hurricane Edouard (2014) during Intensity Change. Part II: Kinematic Structure and the Distribution of Deep Convection. *Mon. Wea. Rev.* 144, 3355–3376. doi:10.1175/mwr-d-16-0017.1

- Ruppert, J. H., and Hohenegger, C. (2018). Diurnal Circulation Adjustment and Organized Deep Convection. *J. Clim.* 31, 4899–4916. doi:10.1175/jcli-d-17-0693.1
- Ruppert, J. H., Wing, A. A., Tang, X., and Duran, E. L. (2020). The Critical Role of Cloud-Infrared Radiation Feedback in Tropical Cyclone Development. *Proc. Natl. Acad. Sci. USA* 117, 27884–27892. doi:10.1073/pnas.2013584117
- Ryglicki, D. R., Cossuth, J. H., Hodyss, D., and Doyle, J. D. (2018a). The Unexpected Rapid Intensification of Tropical Cyclones in Moderate Vertical Wind Shear. Part I: Overview and Observations. *Mon. Wea. Rev.* 146, 3773–3800. doi:10.1175/mwr-d-18-0020.1
- Ryglicki, D. R., Doyle, J. D., Jin, Y., Hodyss, D., and Cossuth, J. H. (2018b). The Unexpected Rapid Intensification of Tropical Cyclones in Moderate Vertical Wind Shear. Part II: Vortex Tilt. *Mon. Wea. Rev.* 146, 3801–3825. doi:10.1175/mwr-d-18-0021.1
- Ryglicki, D. R., Doyle, J. D., Hodyss, D., Cossuth, J. H., Jin, Y., Viner, K. C., et al. (2019). The Unexpected Rapid Intensification of Tropical Cyclones in Moderate Vertical Wind Shear. Part III: Outflow-Environment Interaction. *Mon. Wea. Rev.* 147, 2919–2940. doi:10.1175/mwr-d-18-0370.1
- Smith, R. K., and Montgomery, M. T. (2015). Toward Clarity on Understanding Tropical Cyclone Intensification. *J. Atmos. Sci.* 72, 3020–3031. doi:10.1175/jas-d-15-0017.1
- Smith, W. P., Nicholls, M. E., and Pielke, R. A., Sr (2020). The Role of Radiation in Accelerating Tropical Cyclogenesis in Idealized Simulations. *J. Atmos. Sci.* 77, 1261–1277. doi:10.1175/jas-d-19-0044.1
- Tao, C., and Jiang, H. (2015). Distributions of Shallow to Very Deep Precipitation-Convection in Rapidly Intensifying Tropical Cyclones. *J. Clim.* 28, 8791–8824. doi:10.1175/jcli-d-14-00448.1
- Tao, W.-K., Lang, S., Simpson, J., Sui, C.-H., Ferrier, B., and Chou, M.-D. (1996). Mechanisms of Cloud-Radiation Interaction in the Tropics and Midlatitudes. *J. Atmos. Sci.* 53, 2624–2651. doi:10.1175/1520-0469(1996)053<2624:mocrii>2.0.co;2
- Tao, C., Jiang, H., and Zawislak, J. (2017). The Relative Importance of Stratiform and Convective Rainfall in Rapidly Intensifying Tropical Cyclones. *Mon. Wea. Rev.* 145, 795–809. doi:10.1175/mwr-d-16-0316.1
- Wadler, J. B., Zhang, J. A., Jaimes, B., and Shay, L. K. (2018). Downdrafts and the Evolution of Boundary Layer Thermodynamics in Hurricane Earl (2010) before and during Rapid Intensification. *Mon. Wea. Rev.* 146, 3534–3565. doi:10.1175/mwr-d-18-0090.1
- Wang, X., and Zhang, D.-L. (2003). Potential Vorticity Diagnosis of a Simulated Hurricane. Part I: Formulation and Quasi-Balanced Flow. *J. Atmos. Sci.* 60, 1593–1607. doi:10.1175/2999.1
- Wang, B., and Zhou, X. (2008). Climate Variation and Prediction of Rapid Intensification in Tropical Cyclones in the Western North Pacific. *Meteorol. Atmos. Phys.* 99, 1–16. doi:10.1007/s00703-006-0238-z
- Wang, Y., Rao, Y., Tan, Z.-M., and Schönmann, D. (2015). A Statistical Analysis of the Effects of Vertical Wind Shear on Tropical Cyclone Intensity Change over the Western North Pacific. *Mon. Wea. Rev.* 143, 3434–3453. doi:10.1175/mwr-d-15-0049.1
- Wing, A. A., Camargo, S. J., and Sobel, A. H. (2016). Role of Radiative-Convective Feedbacks in Spontaneous Tropical Cyclogenesis in Idealized Numerical Simulations. *J. Atmos. Sci.* 73, 2633–2642. doi:10.1175/jas-d-15-0380.1
- Wong, M. L. M., and Chan, J. C. L. (2004). Tropical Cyclone Intensity in Vertical Wind Shear. *J. Atmos. Sci.* 61, 1859–1876. doi:10.1175/1520-0469(2004)061<1859:tciiwv>2.0.co;2
- Yang, B., and Tan, Z.-M. (2020). Interactive Radiation Accelerates the Intensification of the Midlevel Vortex for Tropical Cyclogenesis. *J. Atmos. Sci.* 77, 4051–4065. doi:10.1175/jas-d-20-0094.1
- Yang, B., Nie, J., and Tan, Z. M. (2021). Radiation Feedback Accelerates the Formation of Typhoon Haiyan (2013): The Critical Role of Mid-level Circulation. *Geo. Res. Let.* 48, e2021GL094168. doi:10.1029/2021gl094168
- Yuter, S. E., and Houze, R. A. (1995). Three-dimensional Kinematic and Microphysical Evolution of Florida Cumulonimbus. Part II: Frequency Distributions of Vertical Velocity, Reflectivity, and Differential Reflectivity. *Mon. Wea. Rev.* 123, 1941–1963. doi:10.1175/1520-0493(1995)123<1941:tdkame>2.0.co;2
- Zeng, Z., Wang, Y., and Wu, C.-C. (2007). Environmental Dynamical Control of Tropical Cyclone Intensity-An Observational Study. *Mon. Wea. Rev.* 135, 38–59. doi:10.1175/mwr3278.1
- Zeng, Z., Chen, L., and Wang, Y. (2008). An Observational Study of Environmental Dynamical Control of Tropical Cyclone Intensity in the Atlantic. *Mon. Wea. Rev.* 136, 3307–3322. doi:10.1175/2008mwr2388.1
- Zhang, D.-L., and Kieu, C. Q. (2006). Potential Vorticity Diagnosis of a Simulated Hurricane. Part II: Quasi-Balanced Contributions to Forced Secondary Circulations. *J. Atmos. Sci.* 63, 2898–2914. doi:10.1175/jas3790.1
- Zhang, F., and Tao, D. (2013). Effects of Vertical Wind Shear on the Predictability of Tropical Cyclones. *J. Atmos. Sci.* 70, 975–983. doi:10.1175/jas-d-12-0133.1
- Zhang, X., and Xu, W. (2021). Strong Diurnal Pulsing of Cold Clouds in Rapidly Intensifying Tropical Cyclones. *Geo. Res. Let.* 48, e2021GL094773. (in press). doi:10.1029/2021gl094773

Conflict of Interest: The authors declare that the research was conducted in the absence of any commercial or financial relationships that could be construed as a potential conflict of interest.

Publisher's Note: All claims expressed in this article are solely those of the authors and do not necessarily represent those of their affiliated organizations, or those of the publisher, the editors, and the reviewers. Any product that may be evaluated in this article, or claim that may be made by its manufacturer, is not guaranteed or endorsed by the publisher.

Copyright © 2022 Huang, Ge and Bi. This is an open-access article distributed under the terms of the Creative Commons Attribution License (CC BY). The use, distribution or reproduction in other forums is permitted, provided the original author(s) and the copyright owner(s) are credited and that the original publication in this journal is cited, in accordance with accepted academic practice. No use, distribution or reproduction is permitted which does not comply with these terms.



Impacts of El Niño Diversity on Tropical Cyclone Activity in the Bay of Bengal

W. A. E. Lakshani¹, Wen Zhou^{1,2*} and Paxson K. Y. Cheung¹

¹Guy Carpenter Asia-Pacific Climate Impact Centre, School of Energy and Environment, City University, Hong Kong, Hong Kong SAR, China, ²Department of Atmospheric and Oceanic Sciences and Institute of Atmospheric Sciences, Fudan University, Shanghai, China

OPEN ACCESS

Edited by:

Hui Yu,
China Meteorological Administration,
China

Reviewed by:

Ping Huang,
Institute of Atmospheric Physics
(CAS), China
Shangfeng Chen,
Institute of Atmospheric Physics
(CAS), China

*Correspondence:

Wen Zhou
wenzhou@cityu.edu.hk

Specialty section:

This article was submitted to
Atmospheric Science,
a section of the journal
Frontiers in Earth Science

Received: 29 November 2021

Accepted: 14 January 2022

Published: 10 February 2022

Citation:

Lakshani WAE, Zhou W and
Cheung PKY (2022) Impacts of El Niño
Diversity on Tropical Cyclone Activity in
the Bay of Bengal.
Front. Earth Sci. 10:824769.
doi: 10.3389/feart.2022.824769

This study investigates the variation in large-scale parameters associated with two types of El Niño and their impact on tropical cyclone (TC) activity over the Bay of Bengal (BoB) from 1980 to 2019. The Genesis Potential Index (GPI)-based quantitative evaluation was conducted to compute the relative contribution of ENSO and El Niño flavor-associated large-scale parameters. Relationship between the GPI and ENSO in the primary TC peak season (October–November; OND) exhibits a distinct meridional pattern over southwestern to northeastern parts of the BoB. Moreover, the results show that ENSO-modulated vertical wind shear (VWS) term (relative humidity; RH term) contributes the most to enhancing (suppressing) the GPI over the southwestern (northeastern) BoB during the primary TC peak season. The GPI exhibits a significantly positive (negative) dipole pattern with EP El Niño in the southern (northern) BoB, while CP El Niño shows a southwestern (positive)–northeastern (negative) meridional pattern. The increased GPI in the southern BoB with EP El Niño is due mainly to the VWS term, while RH term makes a minimal contribution. Similarly, during CP El Niño, VWS term contributes the most to the enhancement of the GPI, while the smallest contribution is from potential intensity (PI) term. Moreover, this study reveals that the thermodynamic (RH) factor is crucial in reducing TC genesis during CP El Niño in the northeastern BoB. On the other hand, the dynamic (VWS) and thermodynamic (RH) terms are almost equally important for suppressing TCs over the northern BoB in EP El Niño. Analysis of the secondary TC peak season (April–June; AMJ) demonstrates that CP El Niño and EP El Niño induce an increase and decrease in the GPI in the southern BoB mainly due to the dynamic factor (VWS term) and thermodynamic factor (RH term), respectively. On the other hand, TCs in AMJ are more favorable to occur in the south of BoB during CP El Niño events. The two types of El Niño-associated physical mechanisms are consistent with the diagnosed GPI changes, emphasizing the vital role of both EP and CP El Niño in influencing thermodynamic and dynamic parameters related to TC genesis over the BoB. Thus, the association of CP and EP El Niño with the GPI provides a valuable platform for studying El Niño-generated TC impacts over the BoB.

Keywords: the Bay of Bengal, El Niño diversity, eastern Pacific-type El Niño, central Pacific-type El Niño, genesis potential index, primary TC peak season, secondary TC peak season

INTRODUCTION

Tropical cyclones (TCs) are among the most destructive natural disasters in the world. The Bay of Bengal (BoB) accounts for an average of 5–6 cyclones among the world's TCs each year (Pal and Chatterjee, 2020). Though this is a low number, TCs in the BoB basin result in a massive death toll compared to other regions. For instance, the Great Bhola Cyclone in 1970 killed more than 300,000 people and remains one of the deadliest natural disasters in the world (Frank and Husain, 1971; Dube et al., 1997). Most recently, Cyclone Amphan killed 72 people in India and 112 people in Bangladesh (Halder et al., 2021). Due to the geographical location of the BoB, countries with highly populated coastal regions such as India, Sri Lanka, Bangladesh, and Myanmar are at risk from TCs. In addition, the BoB is an ideal site for studying variation in the large-scale environmental parameters that influence tropical cyclogenesis due to its isolation from other oceans by land on its western, eastern, and northern margins.

Researchers have therefore begun to assemble more data/observations of BoB TCs and have conducted more comprehensive studies to understand TC dynamics over the BoB on an interannual scale. These investigations illustrate that the El Niño–Southern Oscillation (ENSO) strongly influences TC activity over the BoB on an interannual time scale with variation in thermodynamic and dynamic factors (Girishkumar and Ravichandran 2012; Felton et al., 2013; Li et al., 2016). Moreover, it has been found that El Niño events suppress the formation of cyclones in the BoB while La Niña enhances TC genesis with changes in large-scale environmental conditions. Thus, to understand the influence of thermodynamic and dynamic factors on TC formation in detail, it is essential to identify the relative contribution of each parameter at different time scales.

Li et al. (2013) developed an advanced quantitative diagnosis method that can quantify the relative contributions of large-scale environmental parameters based on the modified GPI by Emanuel and Nolan (2004). Their findings indicate that GPI reduction is due mainly to vertical wind shear (VWS), while relative humidity (RH) enhances TCs in summer over the BoB. Hence, the empirical GPI method is a new approach to quantify the contribution of large-scale parameters to TC genesis under different climate modes. For instance, Girishkumar et al. (2015) used the same method to quantify the relative contribution of large-scale conditions responsible for TC activity under different phases of ENSO and Madden Julian oscillation (MJO) during the postmonsoon (October–December). Results show the importance of mid-tropospheric relative humidity, which is responsible for the enhancement (reduction) of the GPI during La Niña (El Niño) events over the BoB. Li et al. (2019) also used the quantitative method with another modified GPI (Kotal et al., 2009) to investigate the contribution of environmental parameters to TC formation in the BoB during the premonsoon transition period (PMT). They found that a significant difference in vorticity during the PMT contributed to TC development in the BoB. These previous studies on the relationship between TCs in the BoB and ENSO have been

conducted by defining ENSO with the Niño-3.4 index, focusing only on El Niño intensity and not pattern diversity.

El Niño is known to occur in two types according to the location of the SST anomaly center: namely central Pacific El Niño (CP-type) and eastern Pacific El Niño (EP-type) (Larkin and Harrison 2005; Ashok et al., 2007). Thus, the impact of EP and CP type El Niño on TC activity has become an interesting topic among the scientific community worldwide because of its conspicuous and unique influences on the relationship between ENSO and TC genesis (Chen and Tam, 2010; Yang, 2018; Choi et al., 2019). Most of these studies show the contribution of large-scale parameters in EP and CP El Niño to TC genesis based on the GPI. For instance, Xu and Huang (2015) found that more vigorous and intense TCs are more frequent in EP years over the western North Pacific and eastern North Pacific during July and August.

Overall, previous investigations of the impact of the two types of El Niño on TC variation in other ocean basins have shown more advanced and adequate results (Hong et al., 2011; Kim et al., 2011; Wang et al., 2013; Wu et al., 2018; Choi et al., 2019). However, the BoB basin has not received much attention, though it demonstrates the significant role of ENSO-induced large-scale parameters on TC activity. In addition, preliminary analysis of SST variation during the two types of El Niño shows different wave train patterns entering the Indian Ocean basin during EP El Niño but not CP El Niño. Yu et al. (2017) also explained that the more westward-located positive SST anomalies of the CP type might induce weaker SST anomalies in the Indian Ocean than the EP type. Hence, it is worth revisiting the ENSO influences on TC genesis in the BoB by investigating the impact of EP and CP type El Niño. The outcomes of this research will help answer the following questions: How does El Niño diversity (EP and CP type) impact TC variation in the BoB? How do CP and EP type El Niño modulate large-scale parameters and TC genesis (reduction/enhancement) in the BoB? Which factors are the most (least) important in TC formation during the two types of El Niño? The primary purpose of this study is to investigate the two types of El Niño–associated large-scale parameters and their impact on TC activity in the BoB.

The rest of the paper is organized as follows: the next section describes the data and analysis methods used, including the identified years of the two types of El Niño events. The results section first investigates the TC variation and relationship with ENSO on an interannual time scale as well as the relationship between the GPI and El Niño pattern diversity. Next, the relative contribution of large-scale parameters from the diagnosed GPI and possible physical mechanisms during the two types of El Niño are examined. Finally, the main conclusions of this study are drawn in the conclusions and discussion section.

DATA AND METHODS

Data

There are two TC peak seasons (bimodal distribution) over the BoB. Thus, the present study focuses on the primary TC peak

TABLE 1 | Identified EP El Niño and CP El Niño in AMJ and OND.

Type of El Niño	Pre-monsoon (AMJ)	Post-monsoon (OND)
CP El Niño (EMI > 1σ and Niño-4 > Niño-3)	1990, 1993, 1994, 2002, 2004	1990, 1991, 1994, 2004, 2009, 2019
EP El Niño (Niño-3.4 > 1σ and Niño-3 > 1σ)	1983, 1987, 1991, 1992, 1993, 1997, 2015	1982, 1987, 1997, 2015

season (postmonsoon) from October to December (OND) and the secondary TC peak season from April to June (AMJ) between 1980 and 2019. TC data from the Joint Typhoon Warning Center (JTWC) and the International Best-track Archive for Climate Stewardship (IBTrACS) are obtained for this study to investigate TC activity over the BoB. Atmospheric variables such as air temperature, wind, relative humidity, and specific humidity from the National Centers for Environmental Prediction (NCEP)–National Center for Atmospheric Research (NCAR) reanalysis from 1980 to 2019 are used for this study (Kalnay et al., 1996). For the Genesis Potential Index calculation (GPI), we use atmospheric data from ERA5 (Hersbach, et al., 2020), the latest global atmospheric reanalysis produced by the European Centre for Medium-Range Weather Forecasts (ECMWF). The monthly SST dataset is obtained from the Hadley Centre Sea Ice and Sea Surface Temperature dataset (HadISST) (Rayner et al., 2003).

The monthly Niño 3.4 SST indices from the NOAA Climate Prediction Center website (https://origin.cpc.ncep.noaa.gov/products/analysis_monitoring/ensostuff/ONIv5.php) and the monthly EP and CP El Niño indices from the (<https://www.ess.uci.edu/~yu/2OSC>) (Kao and Yu 2009; Yu and Kim 2011) are used for this study.

METHODOLOGY

EP El Niño and CP El Niño Events

First, the ENSO indices are defined as the averaged sea surface temperature anomalies of the Niño-3 (5°S–5°N, 150°–90°W), Niño-3.4 (5°S–5°N, 170°–120°W), and Niño-4 (5°S–5°N, 160°E–150°W) areas. The El Niño Modoki index (EMI) is also defined as the following (Ashok et al., 2007), where brackets indicate the area-averaged SST anomalies over the selected areas.

$$EMI = [10^{\circ}S - 10^{\circ}N, 165^{\circ}E - 140^{\circ}W]_{cp} - 0.5[10^{\circ}S - 20^{\circ}N, 125^{\circ}E - 145^{\circ}E]_{wp} - 0.5[15^{\circ}S - 5^{\circ}N, 110^{\circ}W - 70^{\circ}W]_{ep} \quad (1)$$

CP El Niño events are identified as those with the EMI higher than one standard deviation as well as the Niño-4 index higher than the Niño-3 index, and EP El Niño events are identified as those with both the Niño-3.4 and Niño-3 indices higher than one standard deviation, as shown in Table 1.

Quantitative Evaluation for Large-Scale Environmental Parameters

The Genesis Potential Index (GPI) was first developed by Gray (1979), representing the large-scale environmental conditions

that affect TC genesis. For this study, we used the GPI suggested by Emanuel and Nolan (2004), with absolute vorticity, mid-tropospheric humidity, potential intensity, and vertical wind shear. The GPI is defined as follows:

$$GPI = \underbrace{[10^5 \eta]^{3/2}}_{term1} \underbrace{\left(\frac{H}{50}\right)^3}_{term2} \underbrace{\left[\frac{V_{pot}}{70}\right]^3}_{term3} \underbrace{(1 + 0.1V_{shear})^{-2}}_{term4} \quad (2)$$

where η is the absolute vorticity in s^{-1} , H is the relative humidity at 700 hPa in percent, V_{pot} is the potential intensity in $m s^{-1}$ (Emanuel, 1995), and V_{shear} is the magnitude of the vertical wind shear from 850 to 200 hPa in $m s^{-1}$.

Quantitative evaluation (Li et al., 2013) was carried out to quantify the individual contributions from the four large-scale environmental parameters to changes in the GPI. The calculation of the diagnosed GPI is explained below. Eq. 2, two may obtain,

$$\begin{aligned} \delta GPI &= \delta Term1 \times (\overline{Term2 \times Term3 \times Term4}) + \delta Term2 \\ &\times (\overline{Term1 \times Term3 \times Term4}) \\ &+ \delta Term3 \times (\overline{Term1 \times Term2 \times Term4}) \\ &+ \delta Term4 \times (\overline{Term1 \times Term2 \times Term3}) \end{aligned} \quad (3)$$

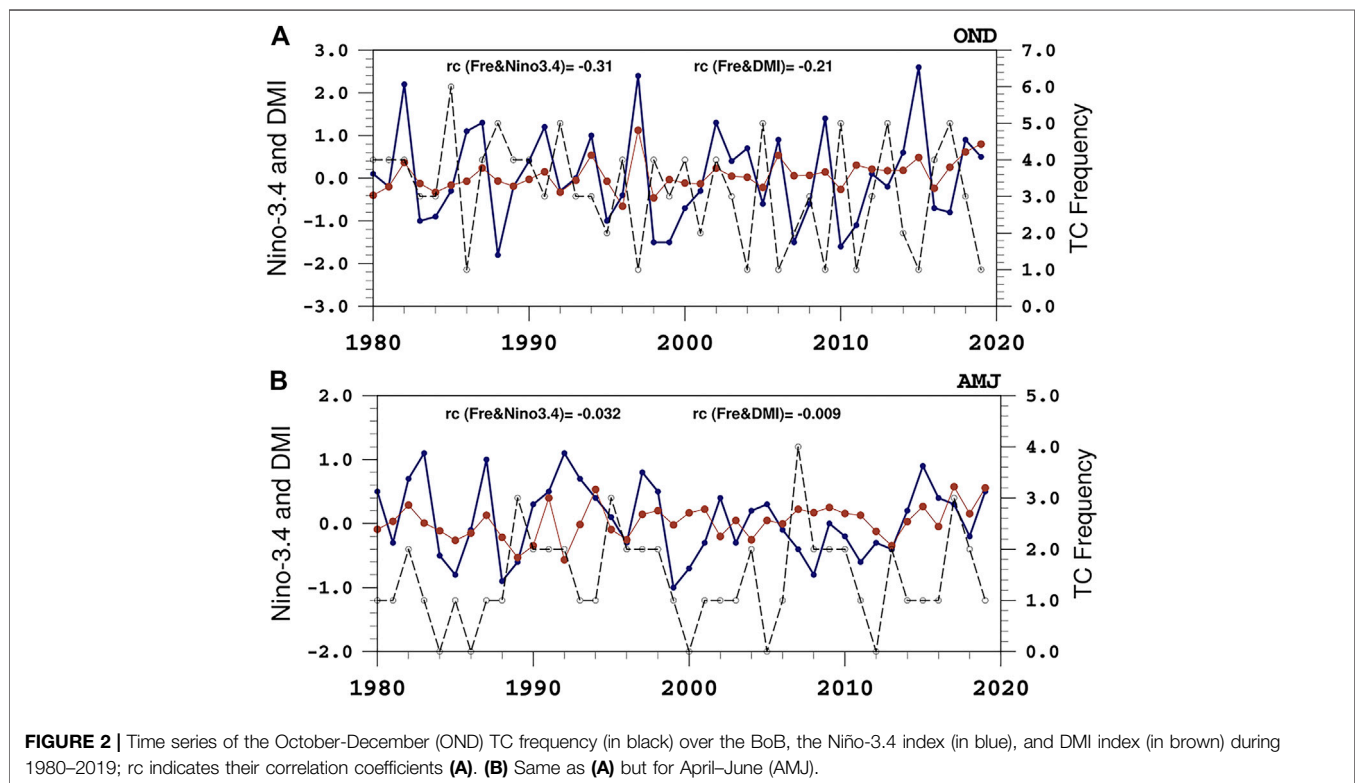
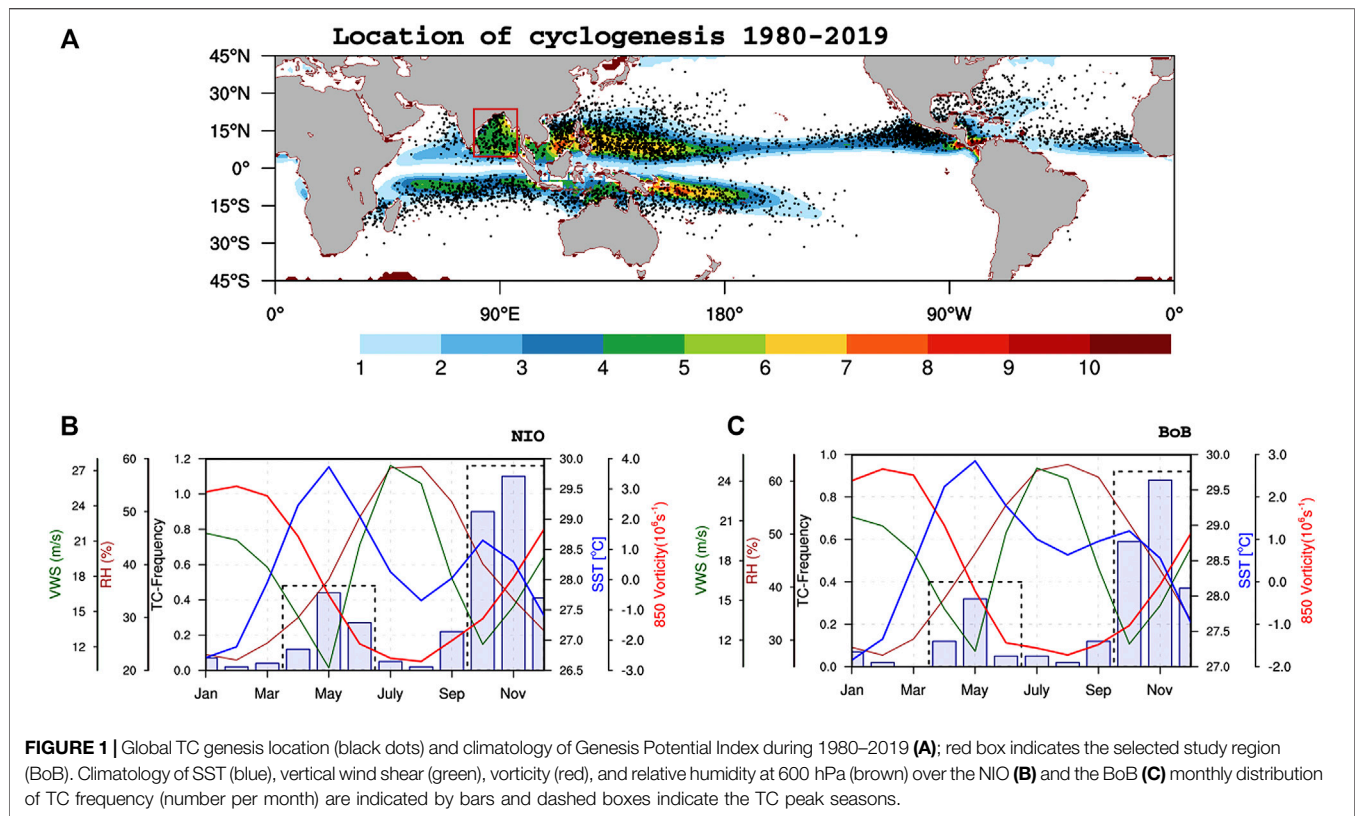
Where δ denotes the anomaly regressed onto the indices (Niño3.4, EP Type, CP Type) and the overbar represents the climatology of the other terms.

First, changes in the GPI are diagnosed at different time scales using Eq. 2. Each term's relative contributions (percentages) to the diagnosed GPI are then calculated by averaging each diagnosed term over the blue and red boxed regions in the regression maps. Student's t-tests are conducted to test the statistical significance of the regression analysis.

RESULTS

TC Variability and Interannual Relationship With ENSO

From a climatological perspective, we first examine the variation in large-scale parameters and TCs in the North Indian Ocean (NIO) and BoB over 40 years (1980–2019). Figure 1A shows the locations of TC genesis over the six major ocean basins, including NIO TC genesis. Compared to the Arabian Sea (AS), the BoB has more TC genesis locations, indicating the high productivity of TCs over the NIO. Similarly, the GPI also exhibits a higher potential of TC formation in our study region than in the AS. The TC climatology shows a bimodal distribution with two TC peak seasons, AMJ and OND (Figures 1B,C), which we will focus on in the coming sections. Notably, TC peak seasons have weak VWS,



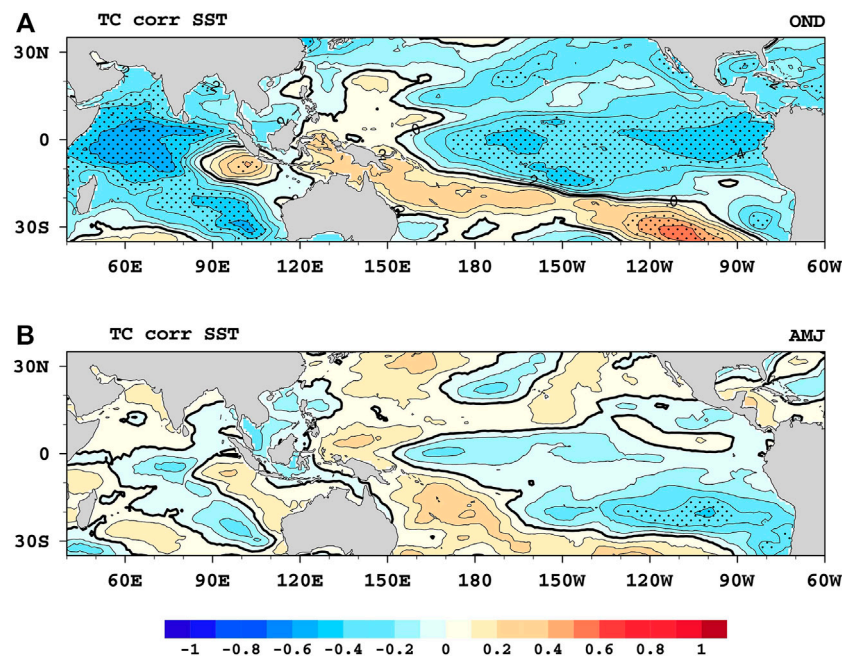


FIGURE 3 | Correlation of TC frequency and sea surface temperature (SST) OND during (A) and AMJ (B); Stipplings indicate that correlations are significant at the 95% confidence level.

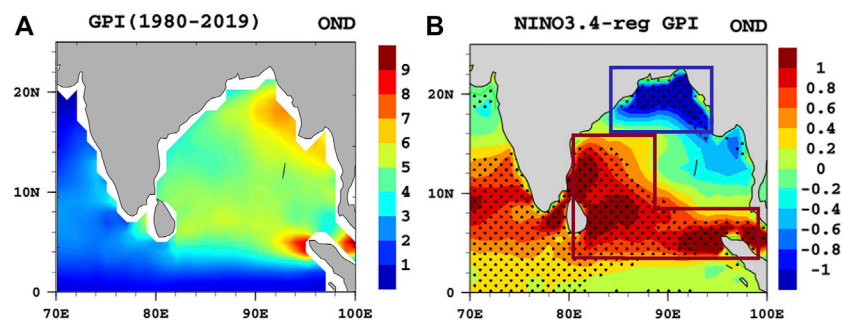
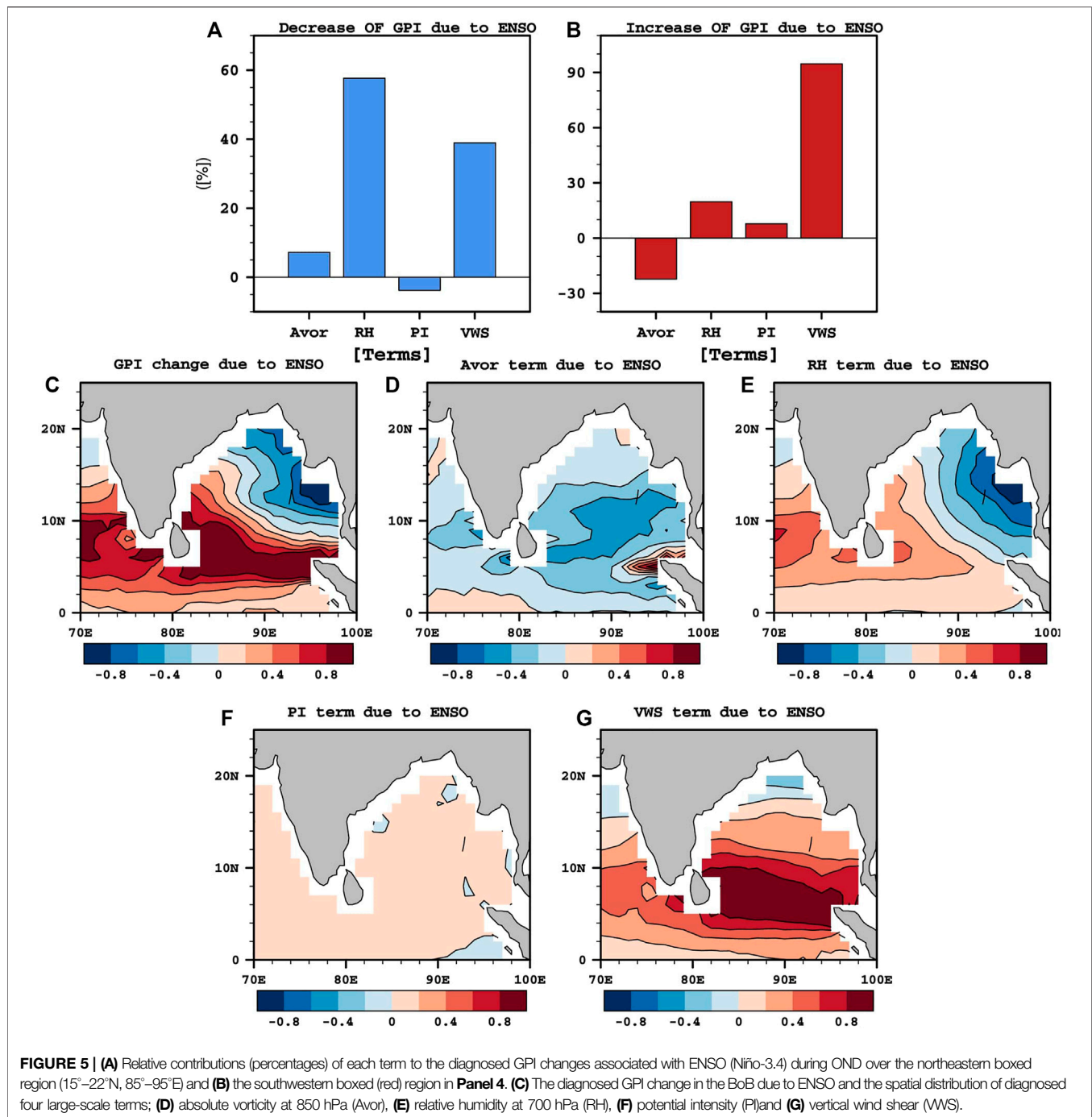


FIGURE 4 | (A) Seasonal average GPI and (B) spatial distribution of GPI anomalies regressed onto the Niño-3.4 index in OND. Stipplings indicate significant correlations exceeding the 95% confidence level. The red box indicates the GPI increase, while the blue indicates the reduction.

higher SST, and higher low-level vorticity, and RH shows lower values than during the summer monsoon. Though higher mid-tropospheric RH is supportive, strong VWS is unfavorable for TC genesis during summer. Li et al. (2013) explained the relationship between the climatological variation of these large-scale parameters and the bimodal distribution of BoB TCs using detailed GPI quantitative analysis. The BoB shows (Figure 1B) fluctuations of large-scale parameters similar to those in the NIO and accounts for more than half of the TC frequency. In addition, the postmonsoon (OND) season of the BoB accounts for a total of 126 TCs (mean = 3.27 and standard deviation = 1.42) with higher fluctuations, whereas AMJ records 57 TCs (mean = 1.42 and standard deviation = 0.89) during the selected period. Analyses are then conducted on the

interannual relationship of BoB TC frequency with ENSO and the Indian Ocean Dipole Index (IOD) during 1980–2019 for the two peak seasons. It is clear that BoB TCs (>17 knots) are significantly correlated with ENSO during the primary TC peak season with a slight influence of the IOD (Figure 2A). However, both indices show an insignificant relationship with BoB TCs in AMJ (Figure 2B). To further investigate the remote impact of SST on TC genesis in the BoB, spatial correlation maps are drawn between TC frequencies and tropical SSTs in AMJ and OND (Figure 3). A significant negative correlation (above the 95% confidence level) is found during OND over the eastern and central Pacific (Figure 3A), though AMJ TCs show a negative correlation with SST in the eastern to central Pacific, which is more concentrated in the eastern Pacific and less significant (Figure 3B). Analyses are



then conducted between the GPI and Niño 3.4 following the quantitative analysis to compare with the impacts of El Niño pattern diversity on BoB TCs and demonstrate the novelty of the present study.

GPI-ENSO Relationship in the Primary TC Peak Season

This study reveals a distinct meridional pattern of ENSO-associated GPI from the northeastern to southwestern BoB,

similar to the GPI variation (**Figures 4A,B**). Thus, the GPI can represent the linkage between ENSO and TC formation in the BoB during OND. The relative contributions of changes in the different terms in the GPI due to ENSO are computed based on Eq. 2, as described in the methods, and the results are shown in **Figures 5A–D**. VWS term is the most important contributor (94.70%) (**Figure 5B**) over the red box in **Figure 4B** for the increased GPI during the primary TC peak season, indicating the importance of dynamic factors in ENSO-associated TC genesis during OND.

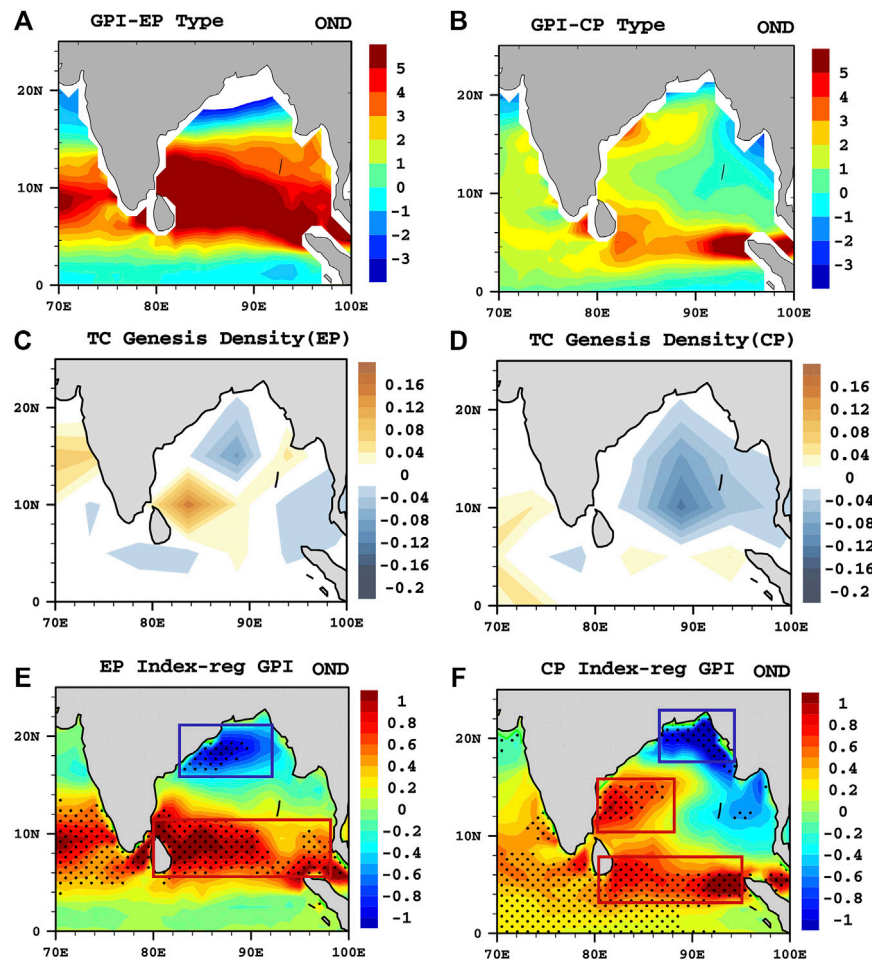


FIGURE 6 | (A) GPI anomalies during EP and **(B)** CP El Niño in OND. Genesis density in a $5^\circ \times 5^\circ$ grid in the EP **(C)** and CP types **(D)**. **(E)** Spatial patterns of GPI anomalies regressed onto the EP El Niño Index in OND and **(F)** for CP El Niño Index. Stipplings indicate significant anomalies exceeding the 95% confidence level. The red box indicates the GPI increase, while the blue indicates the reduction.

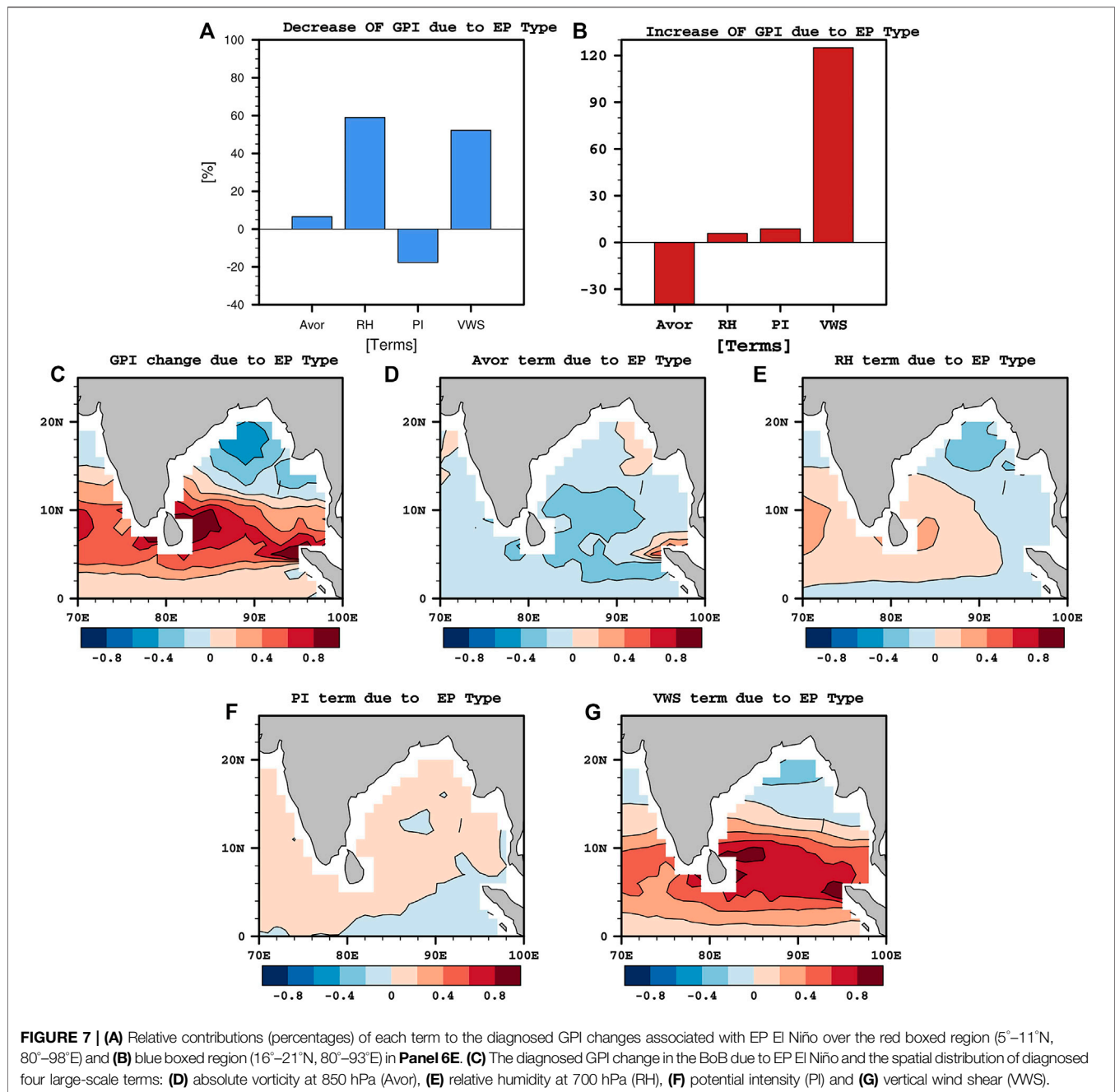
In contrast, RH term is the most important contributor (59.69%) (**Figure 5A**) over the selected blue box (**Figure 4B**), which suppresses the GPI in the northeastern BoB. Though the thermodynamic influence (RH) is prominent, VWS term is the second most significant contributor (36.32%) for the blue box in the northeastern BoB. The diagnosed change in the GPI due to ENSO (**Figure 5C**) exhibits a southwest-northeast dipole pattern more consistent with the ENSO-associated GPI. On the other hand, the spatial patterns of the diagnosed terms clearly show different contributions of GPI reduction and enhancement over the BoB (**Figures 5D–G**). Most importantly, the diagnosed VWS term shows a distinct south-north dipole pattern around 14°N over the BoB (**Figure 5G**).

Impacts of El Niño Pattern Diversity in the Primary TC Peak Season

Regression analyses are carried out between the seasonal average of the GPI anomalies and the two types of El Niño in OND to investigate the association between the GPI and El

Niño diversity. The GPI associated with both El Niño flavors illustrates a similar meridional distribution to GPI composites and TC genesis density (**Figures 6A–F**). In other words, the results show that the GPI increases south of the BoB and is suppressed over the northern BoB under EP El Niño. Significant GPI reduction is notably more concentrated in the northwestern BoB. In contrast, the relationship between the CP El Niño and the GPI is more analogous to the ENSO results, exhibiting a southwestern-northeastern meridional pattern.

Based on the spatial distribution of the significant regression anomalies, the area-averaged diagnosed GPI (blue and red boxes) is calculated to quantify the relative contribution of the four large-scale terms to the suppression and enhancement of the GPI. The decrease in the GPI in the northern BoB (blue box) during EP type El Niño is mainly due to RH (58.93%) and VWS term (51.77%) (**Figure 7A**). Moreover, absolute vorticity (Avor) (9.53%) makes a minor contribution to GPI reduction in the northern BoB. The increase in the GPI in the southern BoB in the EP type is



due to VWS (123.73%), and the RH term makes a minimal contribution (6.27%) (**Figure 7B**). Consistently with the EP El Niño-associated GPI, the diagnosed GPI change in EP El Niño exhibits a visible south-north dipole pattern during the primary TC peak season (**Figure 7C**). Moreover, the diagnosed results show that the VWS, RH, and potential intensity (PI) terms work together to increase the GPI, though the Avor term indicates an unsupportive environment (**Figures 7D–G**).

For CP El Niño, RH term is the main contributor (69.16%) to GPI suppression over the northeastern BoB (**Figure 8A**). However, VWS term (24.89%) is not higher than in EP El Niño, and Avor (9.81%) again makes a minor contribution to

GPI reduction. The above results indicate that the contribution of VWS term is more important over the northeastern BoB in CP El Niño, while both RH and VWS play an essential role in the northern BoB in EP type El Niño.

On the other hand, VWS (207.89, 101.33%) term is the main contributor to the increase in the GPI over the southern and western BoB during CP El Niño (**Figures 8B,C**). Nevertheless, RH makes a greater contribution (17.35%) in CP type El Niño in the southern BoB (red box 2) than in the EP type, and there is a minor contribution from PI term (8.49%). The diagnosed GPI change in CP El Niño exhibits a visible southwestern-northeastern dipole pattern (**Figure 8D**), indicating the

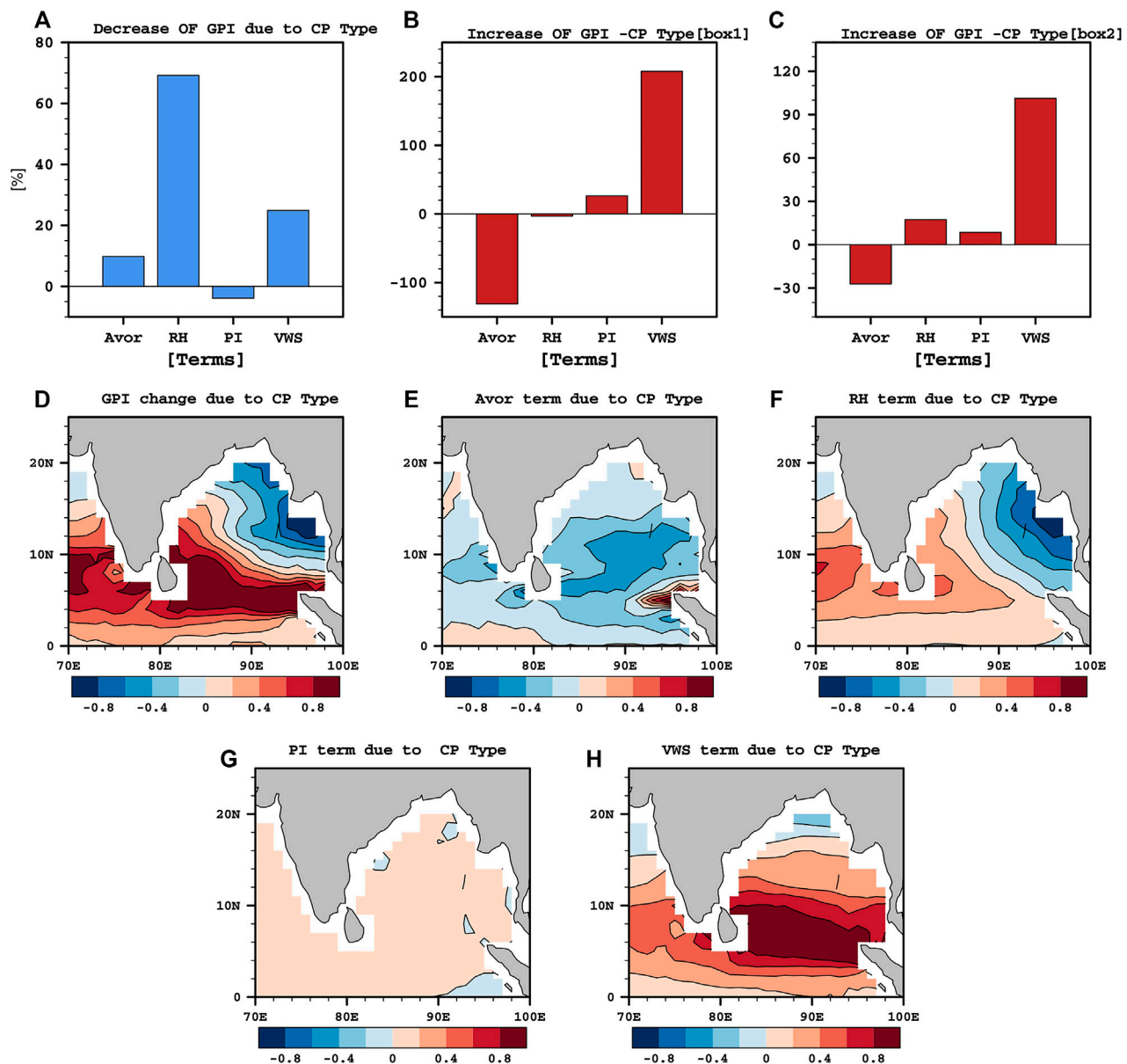


FIGURE 8 | (A) Relative contributions (percentages) of each term to the diagnosed GPI changes associated with CP El Niño during in OND over the northeastern boxed region (17° – 23° N, 87° – 95° E) and **(B)** in red box 1 (10° – 16° N, 81° – 90° E), **(C)** red box 2 (3° – 8° N, 82° – 96° E) in **Panel 6F**. **(D)** Diagnosed GPI change in the BoB due to CP El Niño and the spatial distribution of diagnosed four large-scale terms; **(E)** absolute vorticity at 850 hPa (Avor), **(F)** relative humidity at 700 hPa (RH), **(G)** potential intensity (PI) and **(H)** vertical wind shear (VWS).

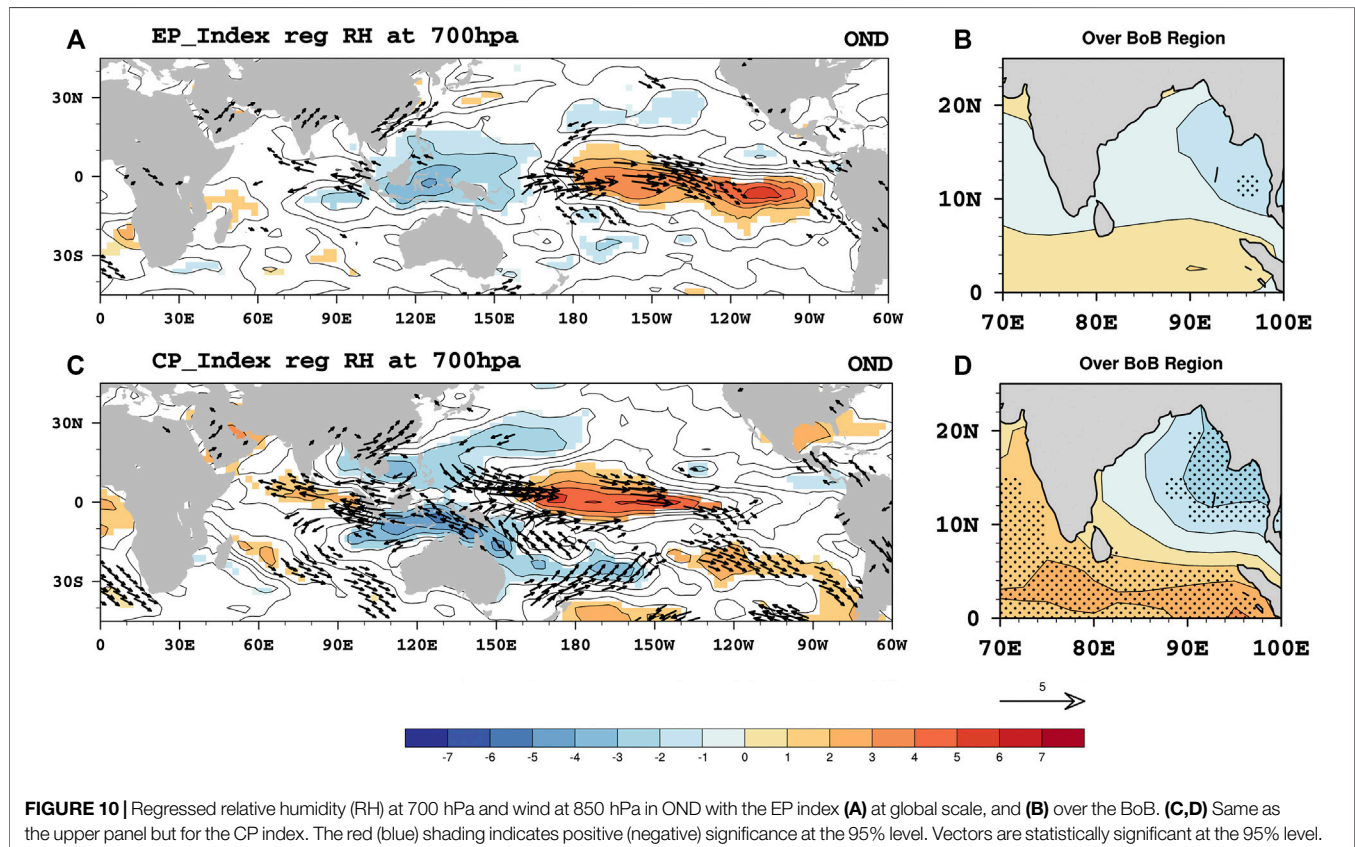
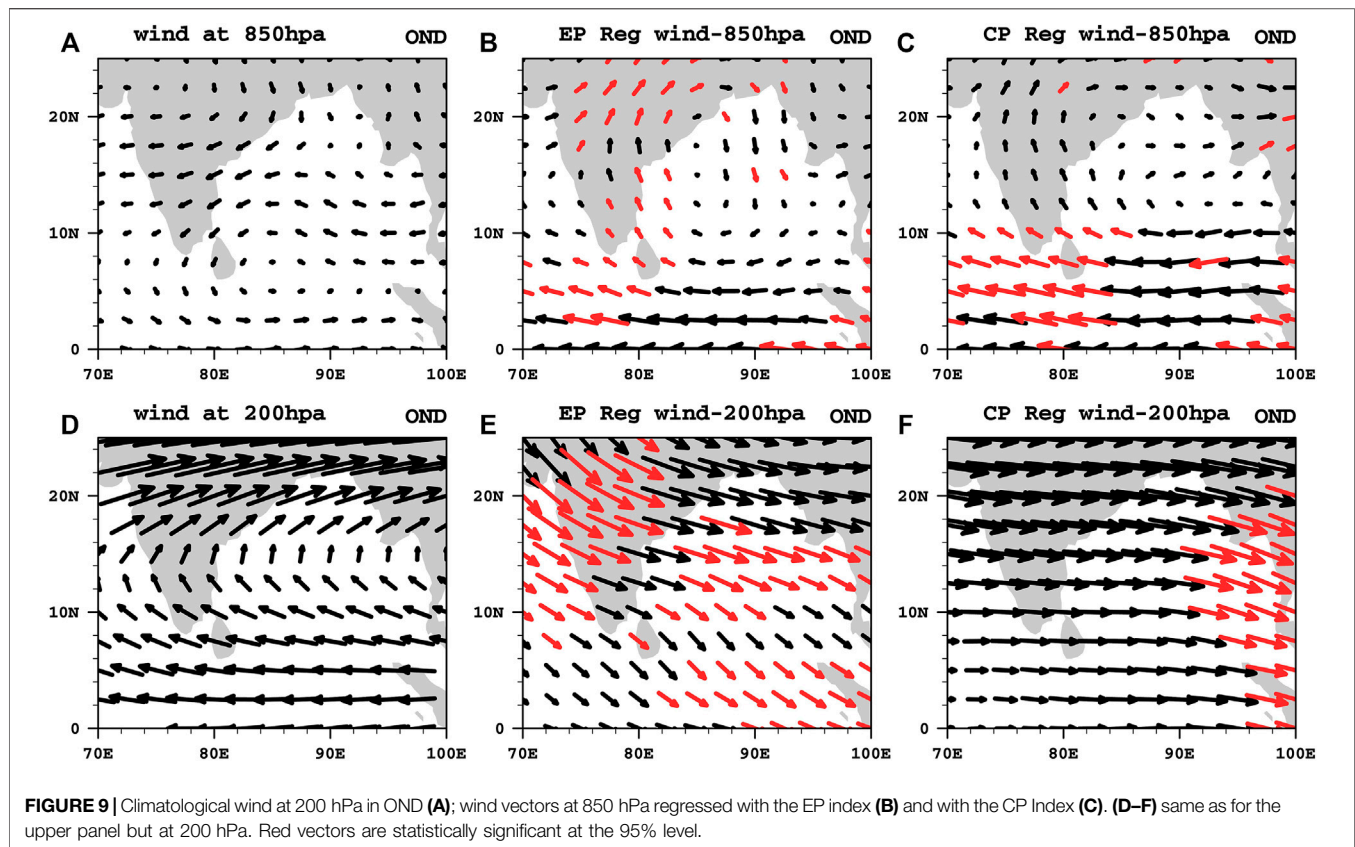
consistency with CP El Niño-associated GPI. In addition, the diagnosed results clearly illustrate that excluding absolute vorticity, the other three terms work together to enhance the GPI in the southern BoB (Figures 8E–H).

Possible Physical Mechanisms for GPI Changes During the Primary TC Peak Season

The previous section showed the relative contribution of large-scale environmental factors in EP and CP El Niño in

modulating TC genesis in the BoB during the primary TC peak season. Thus, regression analyses are conducted to understand the possible physical mechanisms for the diagnosed GPI changes.

First, the impact of VWS is revealed in detail by analyzing the two types of El Niño indices and the wind anomalies at 200 and 850 hPa. The result implies that an easterly VWS anomaly reduces the climatological VWS over the southern BoB (Figure 9) at 200 and 850 hPa because of EP and CP type El Niño, consistent with the diagnosed change in VWS term. In



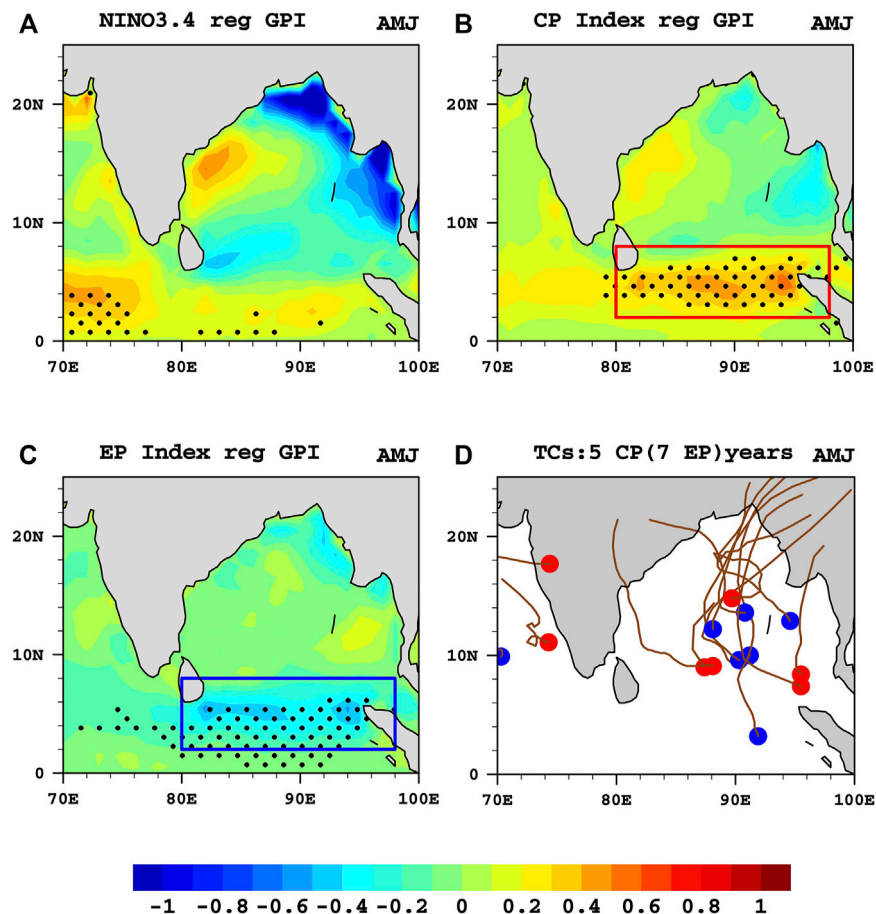


FIGURE 11 | (A) Spatial patterns of GPI anomalies regressed onto the normalized Niño-3.4 index in AMJ. **(B, C)** Same as **(A)**, but with the CP and EP indices; stippings indicate significant anomalies exceeding the 95% confidence level. The red box indicates a GPI increase, while the blue indicates a reduction. **(D)** TC genesis and tracks over the northern Indian Ocean during EP type (blue) and CP type El Niño (red); each dot represents a tropical cyclone genesis point.

other words, VWS is reduced at both levels due to the impact of the EP and CP types, indicating a positive contribution to the increase in the GPI. Moreover, regressed wind anomalies at the lower level (850 hPa) in EP type El Niño exhibit a conspicuous anticyclonic circulation near the northern BoB, causing the reduction in TC genesis.

On a global scale, both types of El Niño weaken the Walker circulation by strengthening westerly winds and weakening easterly winds over the equatorial Pacific Ocean (Figures 10A,C). In addition, significant wind divergence can be observed near northern Australia, which can induce air sinking and create opposing conditions for TC formation. Mid-level RH coincides with wind divergence due to subsidence over northern Australia, which enters the northern BoB, providing unfavorable conditions for TC genesis. A closer look at the BoB region (Figures 10B,D) shows that EP El Niño-associated RH explains the negative contribution to TC genesis over the northern BoB. On the other hand, CP El Niño-induced RH inhibits TC genesis over the northeastern BoB; nevertheless, the decrease in RH is more significant in CP El Niño than in EP El Niño. In addition, the Niño 3.4 regressed wind and mid-level RH display similar results to CP El Niño (Figure not shown). The

critical point from the above results is greater consistency between the relative contribution of each diagnosed term and the two CP and EP El Niño-associated large-scale parameters.

Impacts of El Niño Pattern Diversity During the Secondary TC Peak Season

We investigate the GPI and ENSO relationship before looking into how EP and CP El Niño impact TC formation. The GPI anomalies associated with the Niño.3.4 index display a less significant reduction (northeastern) and enhancement (western and southern) in the BoB (Figure 11A), as TC frequencies also show an insignificant relationship with ENSO in AMJ (Figure 2B). However, the CP type-associated GPI exhibits similar patterns to the Niño 3.4 index, with significant enhancement in the southern BoB (Figure 11B). In contrast, the EP El Niño-linked GPI shows a remarkable reduction in the southern BoB (Figure 11C). It is notable that during CP El Niño (5 years) TCs in BoB tend to genesis farther south (mean latitude of 9.27°N, (Figure 11D). TC geneses are recorded in EP El Niño (7 years) at central BoB (Mean Lat: 11.6°N), except one TC in more southward.

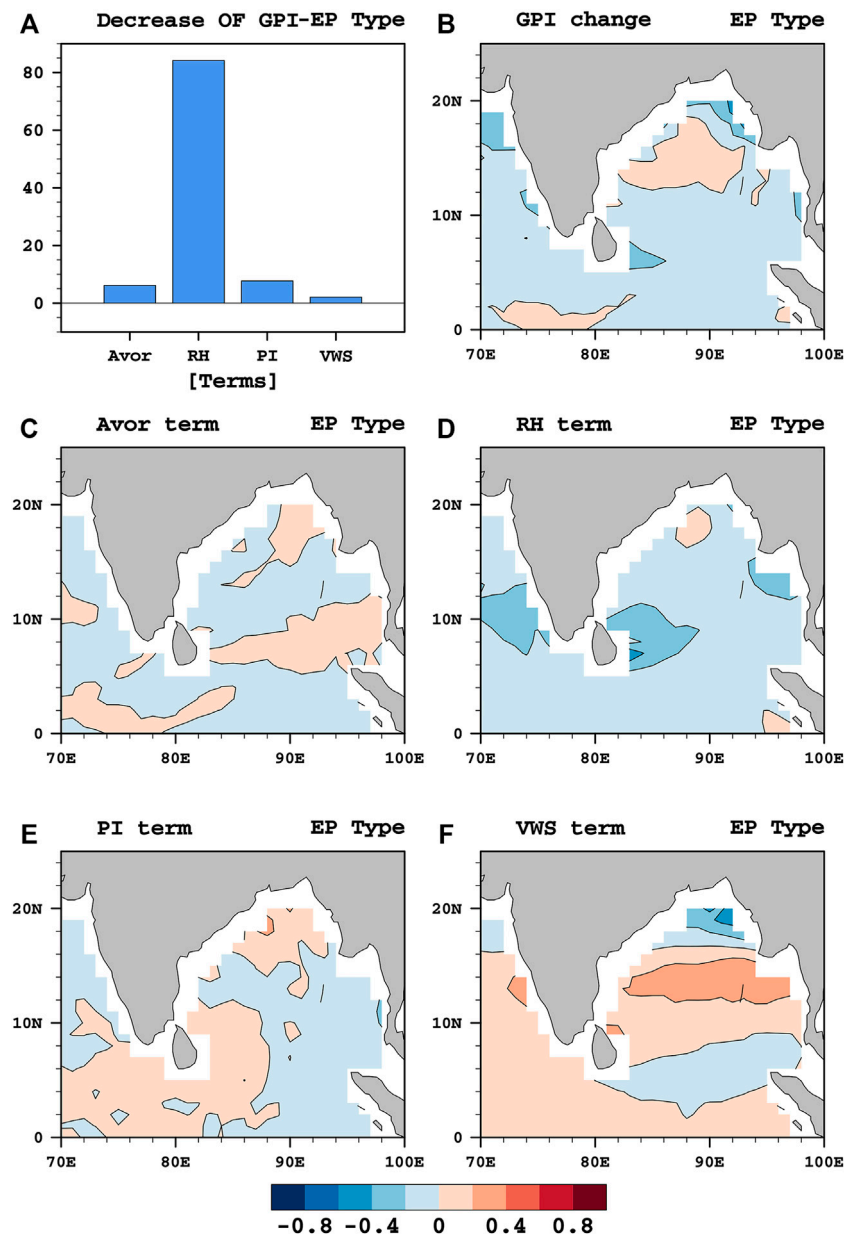


FIGURE 12 | (A) Relative contributions (percentages) of each term to the diagnosed GPI changes associated with EP El Niño during in AMJ over the southern boxed (blue box) (2° – 8° N, 80° – 98° E) region in **Panel 11C**. **(B)** The diagnosed GPI change and the spatial distribution of diagnosed four large-scale terms; **(C)** absolute vorticity at 850 hPa (Avor), **(D)** relative humidity at 700 hPa (RH), **(E)** potential intensity (PI), and **(F)** vertical wind shear (VWS).

Therefore, further investigation is conducted with GPI decomposition analyses in the selected region (2° – 8° N, 80° – 98° E) in the red and blue boxes where the GPI increases and decreases due to CP and EP El Niño, respectively. This study reveals that the decrease in the GPI in the southern BoB (blue box) during EP type El Niño is mainly due to RH term (84.15%) and PI (7.68%) (**Figure 12A**). Meanwhile, the VWS term (2.03%) contributes less to GPI change over the southern BoB. The diagnosed GPI change consistently illustrates GPI reduction in EP El Niño over the selected region (**Figure 12B**). Noticeably, all four terms contribute to TC

reduction in the southern BoB during EP type El Niño (**Figures 12C–F**).

In contrast, VWS term is the main contributor (79.8%) to GPI enhancement over the northeastern BoB in CP type El Niño (**Figure 13A**). Second, RH term (14.16%) affects the GPI increase, followed by PI (7.74%), while Avor term is unfavorable for GPI enhancement. The diagnosed GPI change in CP El Niño shows the GPI enhancement over the selected region in southern BoB (**Figure 13B**). Furthermore, the diagnosed results illustrate that the VWS, RH, and potential intensity (PI) terms work together to enhance the GPI, though the Avor term indicates an unfavorable

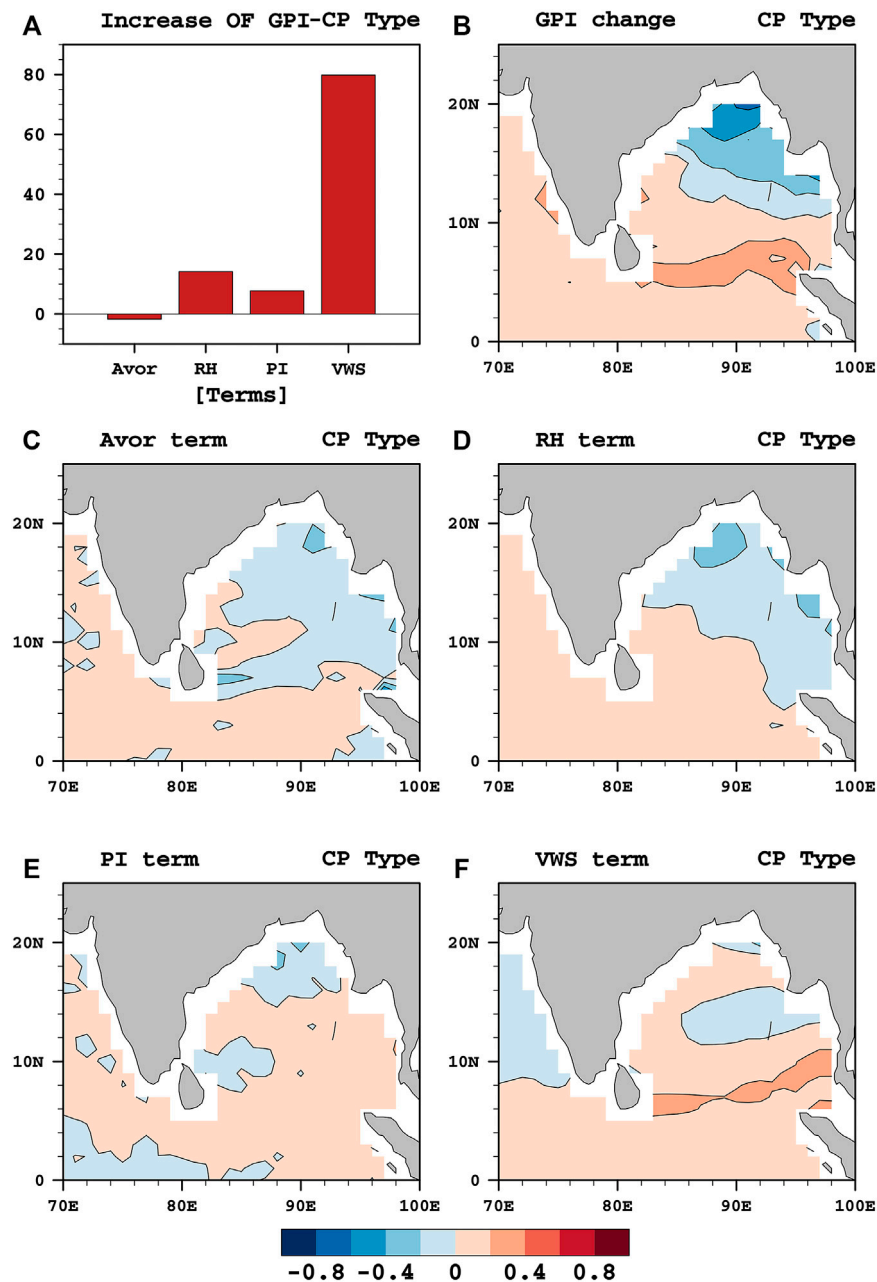


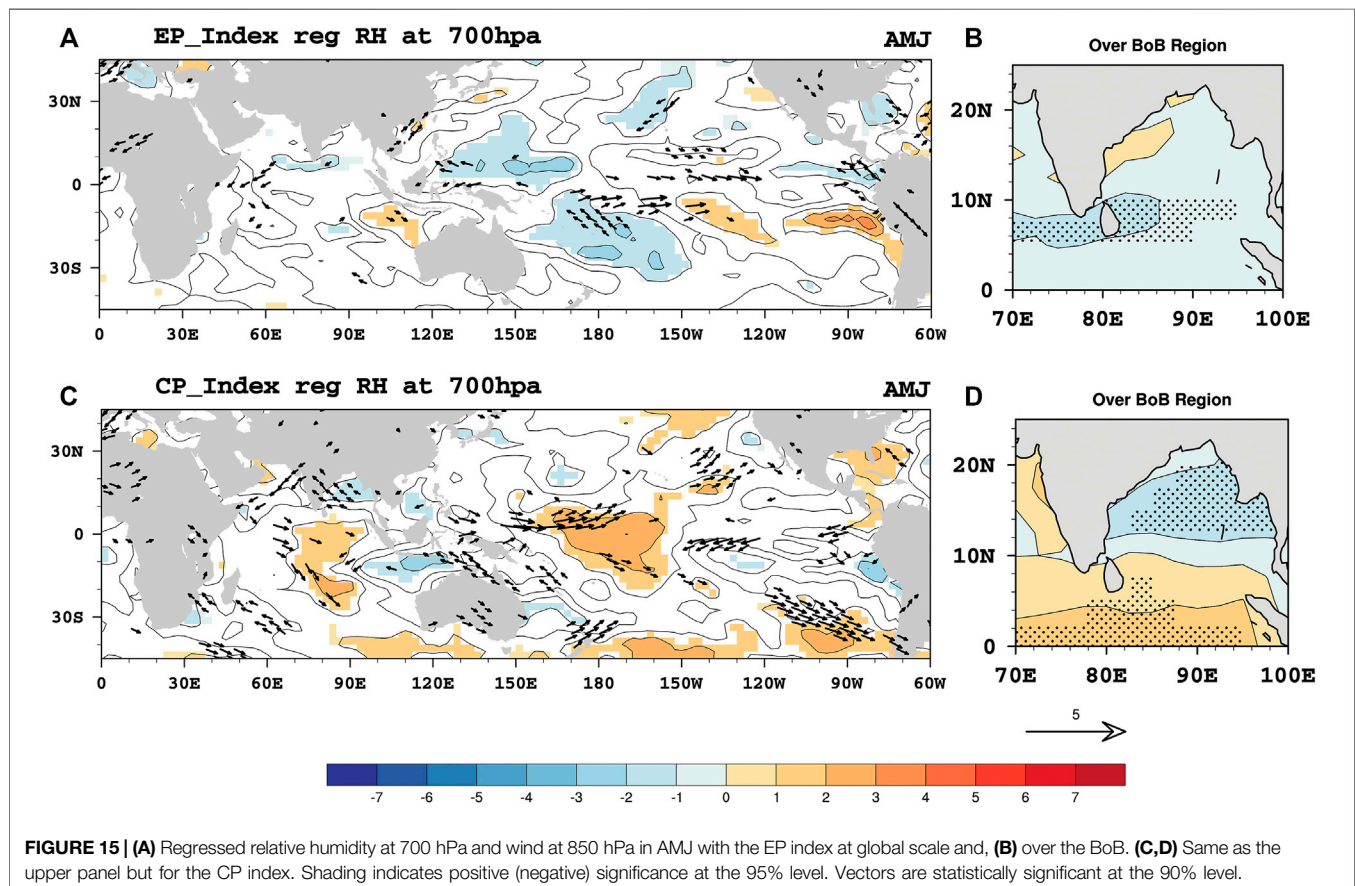
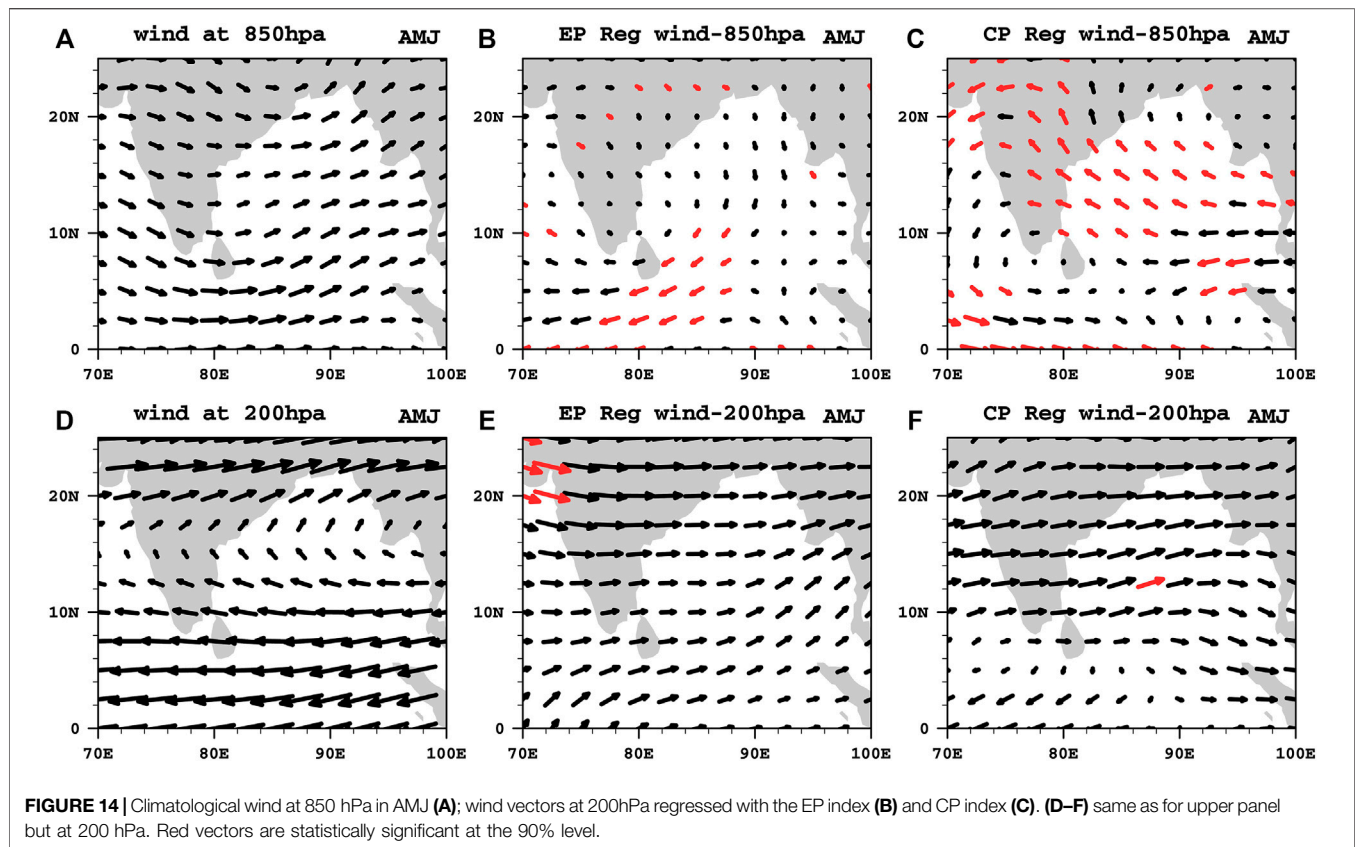
FIGURE 13 | (A) Relative contributions (percentages) of each term to the diagnosed GPI changes associated with CP El Niño during AMJ over the southern boxed (red box) (2°–8°N, 80°–98°E) region in **Panel 11B**. **(B)** Diagnosed GPI change and the spatial distribution of diagnosed four large-scale terms: **(C)** absolute vorticity at 850 hPa (Avor), **(D)** relative humidity at 700 hPa (RH), **(E)** potential intensity (PI), and **(F)** vertical wind shear (VWS).

environment (**Figures 13C–F**). Consequently, TC formation over the BoB has distinct responses to EP and CP events during AMJ.

Possible Physical Mechanisms for GPI Changes During the Secondary TC Peak Season

This section investigates the possible mechanisms responsible for TC genesis in AMJ to check the

consistency of the GPI-diagnosed results. The climatological state and the regressed wind anomalies with EP and CP El Niño indices are compared (**Figures 14A–F**). It is found that VWS is reduced at both 200 and 850 hPa due to CP type El Niño in the southern BoB (**Figures 14C,F**). Especially significant strengthened westerlies at the lower level (850 hPa) can be observed in the selected region consistent with the diagnosed change in VWS, indicating a positive contribution to the increase in the GPI.



We then examined the impacts of two types of El Niño on mid-tropospheric RH over the BoB (**Figures 15A–D**). The spatial patterns of EP El Niño-associated RH enter the southern NIO from the Pacific with more significant dry anomalies (**Figure 15A**). Moreover, wind at 850 hPa also shows significant divergence over the Maritime Continent, indicating sinking air extending toward the southern BoB. From a close look at the BoB (**Figure 15B**), EP El Niño-associated RH clearly shows dryer conditions over the southern BoB, which is more consistent with the diagnosed GPI results.

In contrast to the EP El Niño, the spatial patterns of RH in CP El Niño enter the Indian Ocean with significant wet anomalies in the southern BoB, which expand toward the southern Indian Ocean to a greater extent (**Figure 15C**). Correspondingly, significant wind convergence is observed over the same region in the Indian Ocean, indicating upward air motion and facilitating TC formation. Thus, mid-tropospheric relative humidity provides more favorable conditions for the formation of TCs in the southern BoB under CP El Niño (**Figure 15D**). This demonstrates the second large contribution of RH term to the increase in the GPI in CP type El Niño, as explained earlier in the GPI quantitative analysis. Though CP El Niño-related, large-scale circulation reduces VWS, EP El Niño strengthens the westerly wind shear in the southern BOB, inhibiting TC formation during AMJ (**Figures 14B,E**). In other words, VWS is the key factor causing positive GPI over southern BoB in CP El Niño, while the RH (700 hPa) plays a vital role in reducing GPI in EP El Niño.

CONCLUSION AND DISCUSSION

This study investigated the variation in large-scale parameters associated with the two types of El Niño and their impact on TC activity over the Bay of Bengal during the two TC peak seasons. We have shown that the contribution of the dynamic factor (VWS term) is more critical to the reduction of the GPI in CP El Niño over the northeastern BoB, while both the thermodynamic (RH term) and dynamic (VWS term) factors play an essential role in EP El Niño during the primary TC peak season (OND). In addition, the dynamic factor (VWS term) is the most critical contributor to the GPI enhancement induced by CP El Niño (EP El Niño) over the southwestern and southern (southern) BoB in OND. The relationship between the CP type and the GPI is more analogous to the ENSO results, exhibiting a southwestern-northeastern meridional pattern. Analysis of the secondary TC peak season (AMJ) demonstrates that CP El Niño and EP El Niño induce an increase and a decrease in the GPI, respectively, in the southern BoB mainly due to the dynamic factor (VWS term) and thermodynamic factor (RH term). In AMJ, on the other hand, TCs tend to genesis farther south during CP El Niño. Overall, our diagnosed GPI results for the two TC peak seasons are consistent with the two types of El Niño-associated physical mechanisms over the BoB.

To better understand the interannual variability of TCs in the BoB, we first investigate the correlation of BoB TCs with the

Niño3.4 and DMI indices in OND. In line with a previous study by Girishkumar and Ravichandran (2012), BoB TCs show a significant relationship with ENSO but an insignificant relationship with the IOD. Nevertheless, it is worth noting that the IOD can trigger extreme TCs (Girishkumar and Ravichandran 2012), and co-occurrence of the IOD and ENSO events has different impacts on BoB TC formation (Mahala et al., 2015) Meyers et al., 2007). However, this study focused on the effects of ENSO and El Niño pattern diversity on TC genesis in the BoB. The diagnosed GPI change due to ENSO demonstrates that a reduction (enhancement) in the GPI over the northeastern (southwestern) BoB is due mainly to RH (VWS). Fan et al. (2019) investigated a similar relationship between the GPI and Niño-3.4 (1998–2015) and illustrated the contribution of weak VWS to TC genesis in the southern BoB. Interestingly, at the same time, they observed an El Niño-like pattern in the equatorial Pacific region. Most importantly, our findings establish the enhancement of TC genesis in the southwestern and southern (southern) BoB due to CP type El Niño (EP type El Niño). In addition, consistent with the decomposed GPI analysis, CP El Niño and EP El Niño-related atmospheric circulations significantly reduce VWS over the southern BoB.

It should be noted that the combination of VWS, RH, and PI terms increases the GPI, while Avor has a negative influence (reduction in the GPI). This is because El Niño-associated 850-hPa relative vorticity is insignificant in the BoB (Figure not shown). This indicates that low-level relative vorticity is not vital for TC genesis over the southern BoB under El Niño diversity. Moreover, this study reveals that the thermodynamic (RH) factor is crucial in reducing TC genesis during CP El Niño in the northeastern BoB. On the other hand, the dynamic (VWS) and thermodynamic (RH) terms are almost equally important in suppressing TCs over the BoB in EP El Niño. This is because EP El Niño-associated anticyclone anomalies replace climatological winds at the lower level (850 hPa) over the northern BoB and enhance VWS, suppressing TCs in the northern BoB. Both types of El Niño-associated RH are reduced in the mid-troposphere over the northern BoB, indicating that lower RH values can inhibit TC genesis. Further, we noted that the diagnosed GPI change due to ENSO has similarities with CP El Niño compared to EP El Niño. Previously, the Niño-3.4 index has been used to classify El Niño and La Niña events and to investigate the relative contribution of large-scale parameters to TC genesis in the BoB (Girishkumar et al., 2015). Thus, this study emphasizes that investigations of El Niño pattern diversity effects on BoB TCs are greatly needed, rather than only studies limited to El Niño intensity.

Furthermore, the GPI and ENSO (Niño-3.4) in the secondary TC peak season (AMJ) exhibit a more similar but insignificant relationship than with CP El Niño. Remarkably, CP El Niño enhances the GPI in the southern BoB while EP El Niño decreases the GPI in the same region. As a result, we expect that the mean genesis location during CP El Niño would be farther south than that during EP El Niño. Although the sample is small, this is supported by the observed cyclogenesis. During CP El Niño, the mean genesis latitude is 9.27°N (4 TCs), which is about 1.83°

latitude south to that of EP El Niño (4 TCs, excluding the exceptional case that genesis around 2°N). In other words, more cyclogenesis seems to occur in the southern part of the BoB during CP type El Niño, and fewer TCs occur during EP type El Niño events. These TCs generated over the southern BoB have to travel farther over the ocean before they make landfall at the rim of the BoB. This increases the time they spend over water and therefore gives them more time to amplify. As a result, these TCs may tend to be more intense than those generated to the north. Consequently, by allowing TC genesis over the southern BoB, CP type El Niño may lead to more intense TCs than EP type El Niño. Hence, further investigations were carried out on large-scale parameters using GPI quantitative analysis. The findings reveal that GPI enhancement in the CP type is due mainly to VWS and the combination of RH and PI terms. This is because of the impact of reduced CP El Niño-associated VWS in the southern BoB, mainly due to the weakening of westerlies at lower levels (850 hPa). On the other hand, the significant increase in CP El Niño-associated mid-level RH indicates a supportive environment for TC genesis in the same region of the BoB. In contrast, EP El Niño-associated mid-tropospheric RH shows dryer conditions over the southern BoB and agrees better with the diagnosed GPI results.

This study suggests that further analysis is needed from the developing phase to the decaying phase of both types of El Niño since they have different life cycles and warming patterns (Kao and Yu, 2009; Sun et al., 2013). On the other hand, La Niña can be classified as EP and CP La Niña and has distinct influences on the tropical climate (Yuan and Yan, 2013). However, due to controversy and complexity, La Niña diversity and relationship with TCs gained less attention from scientists. Some studies illustrate that La Niña events cannot be divided into EP and CP La Niña due to similar distribution of SST and precipitations patterns (Kug and Ham, 2011; Shinoda et al., 2011). Nevertheless, most previous studies emphasized the distinct influence of the La Niña diversity on different climate impacts, such as rainfall variation (Song et al., 2017; Feng

and Wang, 2018). Thus, the effect of two types of La Niña on TC activity in BoB may become an interesting topic for future investigations.

On the other hand, according to previous studies, the two types of El Niño have different influences on the IOD. For instance, during CP El Niño events, the SST center is located farther west than the mean state, creating uncooperative conditions for the IOD (Zhang et al., 2015). Thus, one of our future studies will examine the co-occurrence of EP/CP El Niño and the IOD and their influence on BoB TC genesis. The overall findings of this study provide a valuable platform for studying El Niño-generated TC impacts over the BoB.

DATA AVAILABILITY STATEMENT

The original contributions presented in the study are included in the article/supplementary material, further inquiries can be directed to the corresponding author.

AUTHOR CONTRIBUTIONS

WL carried out the analysis and wrote the manuscript with the supervision of WZ. PC provided feedback and helped with the analysis. All authors discussed the results and commented on the manuscript.

FUNDING

This study is supported by the key project of National Natural Science Foundation of China (Grant 42192563 and Grant 42120104001), project of the Center for Ocean Research in Hong Kong and Macau (CORE), and the Hong Kong RGC General Research Fund (11300920).

REFERENCES

- Ashok, K., Behera, S. K., Rao, S. A., Weng, H., and Yamagata, T. (2007). El Niño Modoki and its Possible Teleconnection. *J. Geophys. Res.* 112 (11), 1–27. doi:10.1029/2006JC003798
- Chen, G., and Tam, C.-Y. (2010). Different Impacts of Two Kinds of Pacific Ocean Warming on Tropical Cyclone Frequency over the Western North Pacific. *Geophys. Res. Lett.* 37 (1), a–n. doi:10.1029/2009GL041708
- Choi, Y., Ha, K.-J., and Jin, F.-F. (2019). Seasonality and El Niño Diversity in the Relationship between ENSO and Western North Pacific Tropical Cyclone Activity. *J. Clim.* 32 (23), 8021–8045. doi:10.1175/JCLI-D-18-0736.1
- Dube, S. K., Rao, A. D., Sinha, P. C., Murty, T. S., and Bahulayan, N. (1997). Storm Surge in the Bay of Bengal and Arabian Sea: The Problem and its Prediction. *Mausam* 48, 283–304.
- Emanuel, K. A., and Nolan, D. S. (2004). “Tropical Cyclone Activity and Global Climate,” in Preprints, 26th Conf. on Hurricanes and Tropical Meteorology, Miami, FL, July 14 2004 (American Meteorological Society), 240–241.
- Emanuel, K. A. (1995). Sensitivity of Tropical Cyclones to Surface Exchange Coefficients and a Revised Steady-State Model Incorporating Eye Dynamics. *J. Atmos. Sci.* 52 (22), 3969–3976. doi:10.1175/1520-0469(1995)052<3969:soctcs>2.0.co;2
- Fan, K., Wang, X., Foltz, G. R., and Balaguru, K. (2019). Meridional Oscillation in Genesis Location of Tropical Cyclones in the Postmonsoon Bay of Bengal. *Clim. Dyn.* 53 (3–4), 2103–2118. doi:10.1007/s00382-019-04794-1
- Felton, C. S., Subrahmanyam, B., and Murty, V. S. N. (2013). ENSO-modulated Cyclogenesis over the Bay of Bengal. *J. Clim.* 26 (24), 9806–9818. doi:10.1175/JCLI-D-13-00134.1
- Feng, J., and Wang, X.-C. (2018). Impact of Two Types of La Niña on Boreal Autumn Rainfall Around Southeast Asia and Australia. *Atmos. Oceanic Sci. Lett.* 11 (1), 1–6. doi:10.1080/16742834.2018.1386538
- Frank, N. L., and Husain, S. A. (1971). The Deadliest Tropical Cyclone in History. *Bull. Amer. Meteorol. Soc.* 52, 438–445. doi:10.1175/1520-0477(1971)052<0438:tdctih>2.0.co;2
- Girishkumar, M. S., and Ravichandran, M. (2012). The Influences of ENSO on Tropical Cyclone Activity in the Bay of Bengal during October–December. *J. Geophys. Res.* 117 (2), a–n. doi:10.1029/2011JC007417
- Girishkumar, M. S., Suprit, K., Vishnu, S., Prakash, V. P. T., and Ravichandran, M. (2015). The Role of ENSO and MJO on Rapid Intensification of Tropical Cyclones in the Bay of Bengal during October–December. *Theor. Appl. Climatol.* 120 (3–4), 797–810. doi:10.1007/s00704-014-1214-z
- Gray, W. M. (1979). “Hurricanes: Their Formation, Structure, and Likely Role in the Tropical Circulation,” in *Meteorology over the Tropical Oceans*. Editor D. B. Shaw (London: Royal Meteorological Society), 155–218.

- Halder, B., Das, S., Bandyopadhyay, J., and Banik, P. (2021). The Deadliest Tropical Cyclone "Amphan": Investigate the Natural Flood Inundation over South 24 Parganas Using Google Earth Engine. *Saf. Extreme Environments* 3, 63–73. doi:10.1007/s42797-021-00035-z
- Hersbach, H., Bell, B., Berrisford, P., Hirahara, S., Horányi, A., Muñoz-Sabater, J., et al. (2020). The ERA5 Global Reanalysis. *Q. J. R. Meteorol. Soc.* 146 (730), 1999–2049. doi:10.1002/qj.3803
- Hong, C.-C., Li, Y.-H., Li, T., and Lee, M.-Y. (2011). Impacts of central Pacific and Eastern Pacific El Niños on Tropical Cyclone Tracks over the Western North Pacific. *Geophys. Res. Lett.* 38 (16), a–n. doi:10.1029/2011GL048821
- Kalnay, E., Kanamitsu, M., Kistler, R., Collins, W., Deaven, D., and Gandin, L. (1996). The NCEP/NCAR 40-Year Reanalysis Project. *Bull. Am. Meteorol. Soc.* 77, 437–472. doi:10.1175/1520-0477(1996)077<0437:TNYRP>2.0.CO;2
- Kao, H.-Y., and Yu, J.-Y. (2009). Contrasting Eastern-Pacific and Central-Pacific Types of ENSO. *J. Clim.* 22 (3), 615–632. doi:10.1175/2008JCLI2309.1
- Kim, H.-M., Webster, P. J., and Curry, J. A. (2011). Modulation of North Pacific Tropical Cyclone Activity by Three Phases of ENSO. *J. Clim.* 24 (6), 1839–1849. doi:10.1175/2010JCLI3939.1
- Kotal, S. D., Kundu, P. K., and Roy Bhowmik, S. K. (2009). Analysis of Cyclogenesis Parameter for Developing and Nondeveloping Low-Pressure Systems over the Indian Sea. *Nat. Hazards* 50 (2), 389–402. doi:10.1007/s11069-009-9348-5
- Kug, J.-S., and Ham, Y.-G. (2011). Are there two types of la Nina. *Geophys. Res. Lett.* 38 (16), a–n. doi:10.1029/2011GL048237
- Larkin, N. K., and Harrison, D. E. (2005). Global Seasonal Temperature and Precipitation Anomalies during El Niño Autumn and winter. *Geophys. Res. Lett.* 32 (16), 1–4. doi:10.1029/2005GL022860
- Li, Z., Li, T., Yu, W., Li, K., and Liu, Y. (2016). What Controls the Interannual Variation of Tropical Cyclone Genesis Frequency over Bay of Bengal in the post-monsoon Peak Season. *Atmos. Sci. Lett.* 17 (2), 148–154. doi:10.1002/asl.636
- Li, Z., Yu, W., Li, K., Wang, H., and Liu, Y. (2019). Environmental Conditions Modulating Tropical Cyclone Formation over the Bay of Bengal during the Pre-monsoon Transition Period. *J. Clim.* 32 (14), 4387–4394. doi:10.1175/JCLI-D-18-0620.1
- Li, Z., Yu, W., Li, T., Murty, V. S. N., and Tangang, F. (2013). Bimodal Character of Cyclone Climatology in the Bay of Bengal Modulated by Monsoon Seasonal Cycle*. *J. Clim.* 26 (3), 1033–1046. doi:10.1175/JCLI-D-11-00627.1
- Mahala, B. K., Nayak, B. K., and Mohanty, P. K. (2015). Impacts of ENSO and IOD on Tropical Cyclone Activity in the Bay of Bengal. *Nat. Hazards* 75 (2), 1105–1125. doi:10.1007/s11069-014-1360-8
- Meyers, G., McIntosh, P., Pigot, L., and Pook, M. (2007). The Years of El Niño, La Niña, and Interactions with the Tropical Indian Ocean. *J. Clim.* 20 (13), 2872–2880. doi:10.1175/JCLI4152.1
- Pal, A., and Chatterjee, S. (2020). Seasonal Nature and Trends of Tropical Cyclone Frequency and Intensity over the North Indian Ocean. *Curr. World Environ.* 15 (3), 526–534. doi:10.12944/cwe.15.3.16
- Rayner, N. A., Parker, D. E., Horton, E. B., Folland, C. K., Alexander, L. V., Rowell, D. P., et al. (2003). Global Analyses of Sea Surface Temperature, Sea Ice, and Night marine Air Temperature since the Late Nineteenth century. *J. Geophys. Res.* 108 (14). doi:10.1029/2002jd002670
- Shinoda, T., Hurlburt, H. E., and Metzger, E. J. (2011). Anomalous Tropical Ocean Circulation Associated with La Niña Modoki. *J. Geophys. Res.* 116 (12). doi:10.1029/2011JC007304
- Song, L., Chen, S., Chen, W., and Chen, X. (2017). Distinct Impacts of Two Types of La Niña Events on Australian Summer Rainfall. *Int. J. Climatol.* 37 (5), 2532–2544. doi:10.1002/joc.4863
- Sun, D., Xue, F., and Zhou, T. (2013). Impacts of Two Types of El Niño on Atmospheric Circulation in the Southern Hemisphere. *Adv. Atmos. Sci.* 30 (6), 1732–1742. doi:10.1007/s00376-013-2287-9
- Wang, C., Li, C., Mu, M., and Duan, W. (2013). Seasonal Modulations of Different Impacts of Two Types of ENSO Events on Tropical Cyclone Activity in the Western North Pacific. *Clim. Dyn.* 40 (11–12), 2887–2902. doi:10.1007/s00382-012-1434-9
- Wu, L., Zhang, H., Chen, J.-M., and Feng, T. (2018). Impact of Two Types of El Niño on Tropical Cyclones over the Western North Pacific: Sensitivity to Location and Intensity of Pacific Warming. *J. Clim.* 31 (5), 1725–1742. doi:10.1175/JCLI-D-17-0298.1
- Xu, S., and Huang, F. (2015). Impacts of the Two Types of El Niño on Pacific Tropical Cyclone Activity. *J. Ocean Univ. China* 14 (2), 191–198. doi:10.1007/s11802-015-2421-7
- Yang, S. (2018). Different Impacts of Two Kinds of Pacific Ocean Warming on Tropical Cyclone Frequency over the Western North Pacific. *Geophys. Res. Lett.* 31 (5), 1–6. doi:10.1175/JCLI-D-17-0298.1
- Yu, J.-Y., and Kim, S. T. (2011). Relationships between Extratropical Sea Level Pressure Variations and the central Pacific and Eastern Pacific Types of ENSO. *J. Clim.* 24 (3), 708–720. doi:10.1175/2010JCLI3688.1
- Yu, J.-Y., Wang, X., Yang, S., Paek, H., and Chen, M. (2017). The Changing El Niño-Southern Oscillation and Associated Climate Extremes. *Clim. Extremes, Geophysical Monogr. Ser.* 226, 1–38. doi:10.1002/9781119068020.ch1
- Yuan, Y., and Yan, H. (2013). Different Types of La Niña Events and Different Responses of the Tropical Atmosphere. *Chin. Sci. Bull.* 58 (3), 406–415. doi:10.1007/s11434-012-5423-5
- Zhang, W., Wang, Y., Jin, F.-F., Stuecker, M. F., and Turner, A. G. (2015). Impact of Different El Niño Types on the El Niño/IOD Relationship. *Geophys. Res. Lett.* 42 (20), 8570–8576. doi:10.1002/2015GL065703

Conflict of Interest: The authors declare that the research was conducted in the absence of any commercial or financial relationships that could be construed as a potential conflict of interest.

Publisher's Note: All claims expressed in this article are solely those of the authors and do not necessarily represent those of their affiliated organizations, or those of the publisher, the editors, and the reviewers. Any product that may be evaluated in this article, or claim that may be made by its manufacturer, is not guaranteed or endorsed by the publisher.

Copyright © 2022 Lakshani, Zhou and Cheung. This is an open-access article distributed under the terms of the Creative Commons Attribution License (CC BY). The use, distribution or reproduction in other forums is permitted, provided the original author(s) and the copyright owner(s) are credited and that the original publication in this journal is cited, in accordance with accepted academic practice. No use, distribution or reproduction is permitted which does not comply with these terms.



A Machine-Learning Based Tool for Diagnosing Inland Tropical Cyclone Maintenance or Intensification Events

Andrew Michael Thomas and James Marshall Shepherd*

Department of Geography, The University of Georgia, Athens, GA, United States

OPEN ACCESS

Edited by:

Qingqing Li,
Nanjing University of Information
Science and Technology, China

Reviewed by:

Ernesto Dos Santos Caetano Neto,
National Autonomous University of
Mexico, Mexico
Eric Hendricks,
National Center for Atmospheric
Research (UCAR), United States

*Correspondence:

James Marshall Shepherd
marshgeo@uga.edu

Specialty section:

This article was submitted to
Atmospheric Science,
a section of the journal
Frontiers in Earth Science

Received: 19 November 2021

Accepted: 25 January 2022

Published: 03 March 2022

Citation:

Thomas AM and Shepherd JM (2022)
A Machine-Learning Based Tool for
Diagnosing Inland Tropical Cyclone
Maintenance or Intensification Events.
Front. Earth Sci. 10:818671.
doi: 10.3389/feart.2022.818671

Tropical Cyclone Maintenance and Intensification (TCMI) is a generalized definition of tropical cyclones that strengthen or maintain intensity inland while maintaining tropical characteristics. Herein, a novel methodology, using a machine learning method was created to examine the tropical cyclone record to improve climatological representation of such cases. Using the International Best Track Archive for Climate Stewardship (IBTrACS) dataset, individual times of inland tropical cyclones were classified into TCMI and non-TCMI (weakening) events. The MERRA-2 dataset was applied to develop a prototypical machine-learning model to help diagnose future TCMI events. A list of possible TCMI storms for case studies in future analyses is provided. Two of these storms were examined for attributes characteristic of the Brown Ocean Effect, a hypothesized mechanism for TCMI centered on warm, moist soils. It was revealed that variables that were important at the time of storm arrival were important the prior day, which indicates that a TCMI event is a reaction to the environment. Moreover, the variables that were finally selected show a heavy emphasis on land-surface processes. This supports the idea that the accurate representation of the land surface state is critical to the accurate diagnosis of TCMI.

Keywords: tropical-cyclones, TCMI, machine-learning, reanalysis, ibtracs

1 INTRODUCTION

After tropical cyclones (TCs) make landfall, it is often assumed that the wind speeds decay, and damage is reduced. There are two types of progression that an inland tropical cyclone may take: extratropical transition (ET; Keller et al., 2018; Jones et al., 2003; Evans et al., 2017) or dissipation (Kaplan and Demaria, 2001; Shen et al., 2002). One exception to this categorization is the observation that some TCs intensify or maintain intensity while inland, albeit not indefinitely (Andersen and Shepherd, 2014; Brauer et al., 2021). These events are called TC Maintenance or Intensification (TCMI) events by Andersen and Shepherd (2014; hereafter referred to as AS14). Unlike AS14, the central pressure criteria was not considered. Decreases in pressure could be without meaning if the environmental pressure, which IBTrACS does not record, decreases proportionally thereby sustaining the pressure gradient. Often, the “Brown Ocean” effect (BOE), which hypothesizes that enhancements in surface enthalpy fluxes induced by antecedent soil moisture support the TC, is attributed or associated. Examples of these events include, but are not limited to, Tropical Storm Erin (2007; Evans et al., 2011; Kellner et al., 2012; Monteverdi and Edwards 2010), Tropical Storm Bill (2015), and an unnamed Tropical Depression in 2010 (Nair et al., 2019). The BOE may be a factor in non-TCMI events, as the surface roughness may reduce the intensity. That is, despite the presence of soil moisture and enhanced latent heat fluxes, the surface wind is still constrained by the properties of the surface.

TABLE 1 | Description of the machine-learning model and the constituent coefficients.

Variable Name	Variable	Coefficient	Standard Error	p-value	Coefficient units
Const	Constant	0.5955	1.051	0.571	N/A
BSTAR	Surface Buoyancy Scale	461.686	194.405	0.018	s ² m ⁻¹
PBLH	Planetary Boundary Layer Height	-0.0012	0.001	0.199	m ⁻¹
V250Prev	250 hPa Meridional Wind Velocity from the previous day	0.095	0.049	0.052	s m ⁻¹
PBLHPrev	Planetary Boundary Layer Height from the previous day	-0.0009	0.001	0.275	m ⁻¹
H1000Prev	Height of the 1,000 hPa level from the previous day	0.0076	0.008	0.323	m ⁻¹
BSTARPrev	Surface Buoyancy scale from the previous day	79.2888	119.757	0.508	s ² m ⁻¹
V250	250 hPa Meridional Wind velocity	-0.0826	0.06	0.167	s m ⁻¹
PRECTOTPrev	One hour accumulated precipitation from the previous day	1,597.887	911.807	0.08	kg ⁻¹ m ² s
U10M	10 m zonal wind velocity	0.1557	0.083	0.062	s m ⁻¹
LWLAND	Net longwave radiation from the land	0.0507	0.038	0.18	W ⁻¹ m ²
PRECTOT	One hour accumulated precipitation	370.3106	267.323	0.166	kg ⁻¹ m ² s

TABLE 2 | Contingency Analysis and Brier Score of the machine-learning model on the test dataset and training dataset.

Metric	Test	Train	References
Percentage of Hits (A)	25.24%	9.91%	N/A
Percentage of False Positives (B)	12.62%	1.8%	N/A
Percentage of Misses (C)	24.27%	17.12%	N/A
Percentage of Correct Negatives (D)	27.86%	71.17%	N/A
Climatological Probability of a Single TCMI event	49.51%	27.03%	N/A
Probability of Detection	51%	36.66%	Doswell et al. (1990); Wilks (2006)
False Alarm Rate	25%	2.5%	Wilks (2006)
Clayton Skill Score	0.276	0.6523	Clayton (1927), Clayton (1934), and Wilks (2006)
Brier Skill Score	0.2606	0.1566	Brier 1950; Wilks (2006)
Odds Ratio	3.12	22.87	Stephenson (2000)
Heidke Skill Score	0.1302	0.2081	Heidke (1926); Wilks (2006)
Peirce Skill Score	0.2598	0.342	Peirce 1884; Wilks (2006)
Equitable/Gilbert's Skill Score	0.1497	0.3827	Gilbert (1884); Wilks (2006)

The number of TCMI events is not limited to these studies. Rather, those studies are only instances of the BOE. AS14 examined previous TCs to identify characteristics of TCMI events not found in ET events. AS14 considered the 1-month antecedent values of latent heat flux and supporting components. However, the immediate surface conditions have a large impact on the resulting structure of the TCs not just the environment of the previous month. In this study, the analysis will focus on the immediate environment of each location that TCMI events occurred and did not occur.

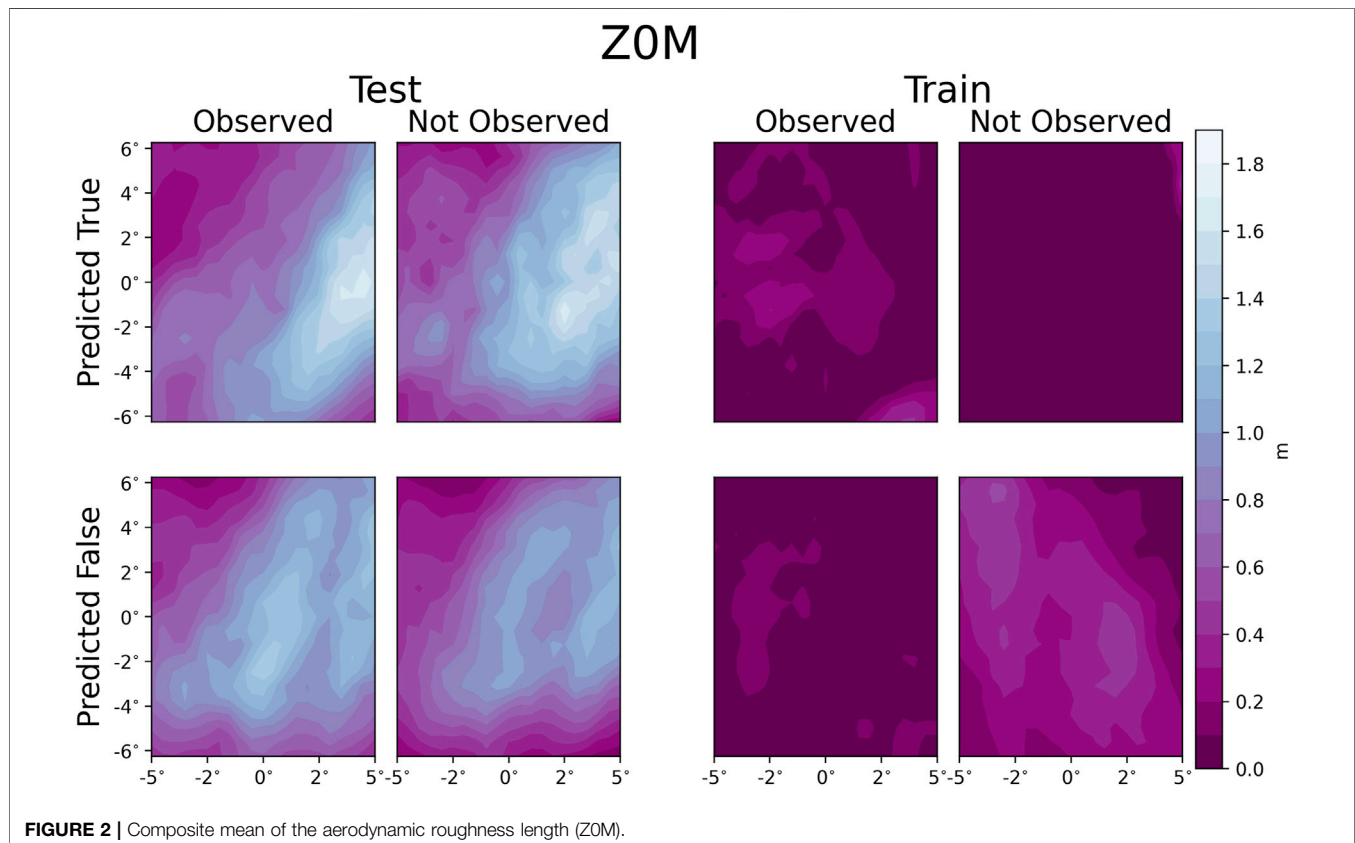
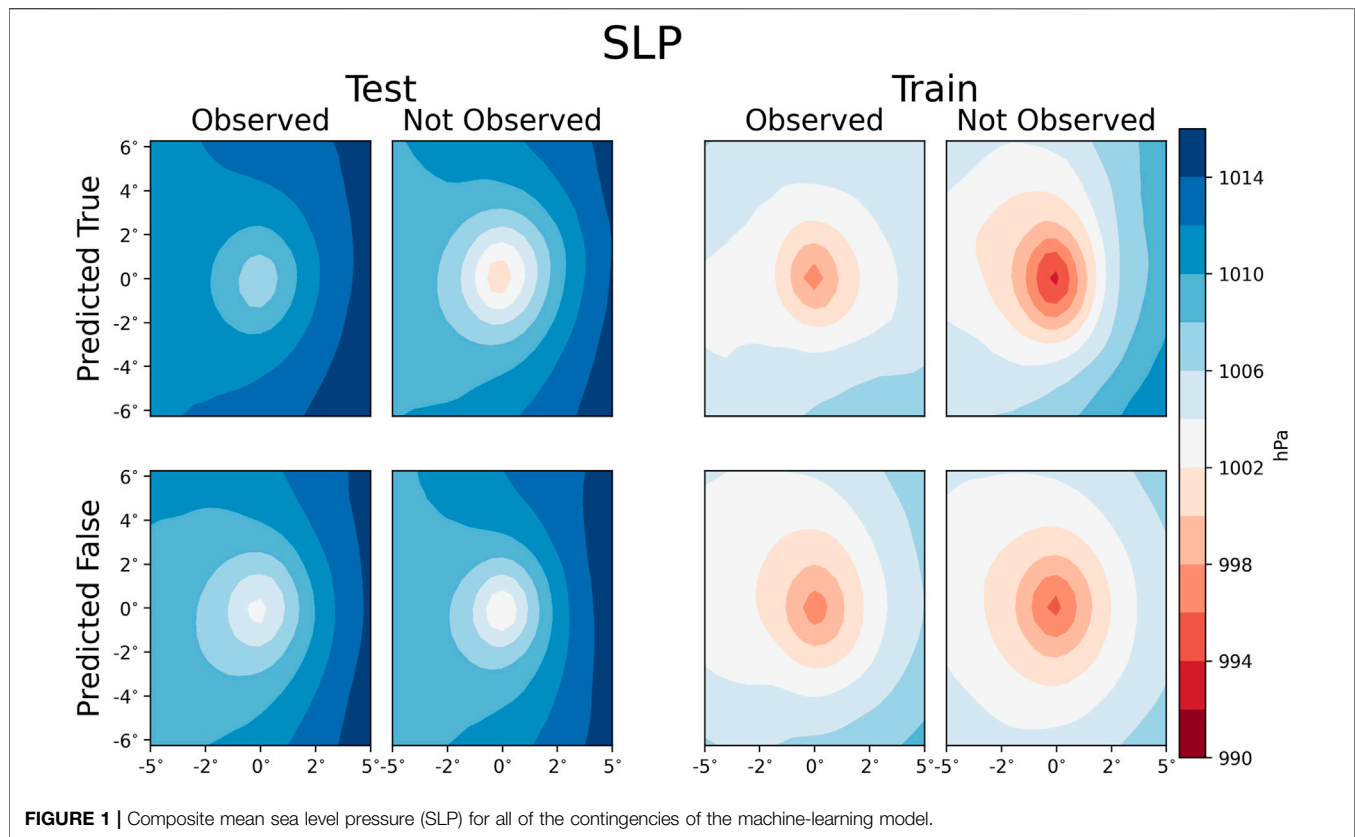
Section 2 describes the methodology used to identify TCMI events and describe a prototypical machine-learning model. **Section 3** investigates the cross-validation of similar machine-learning models, as well as instances where the prediction and dataset do not match. **Section 3** will also examine previously unexamined TCs. **Section 4** explores potential uses of the machine-learning model, as well as potential pitfalls of the model.

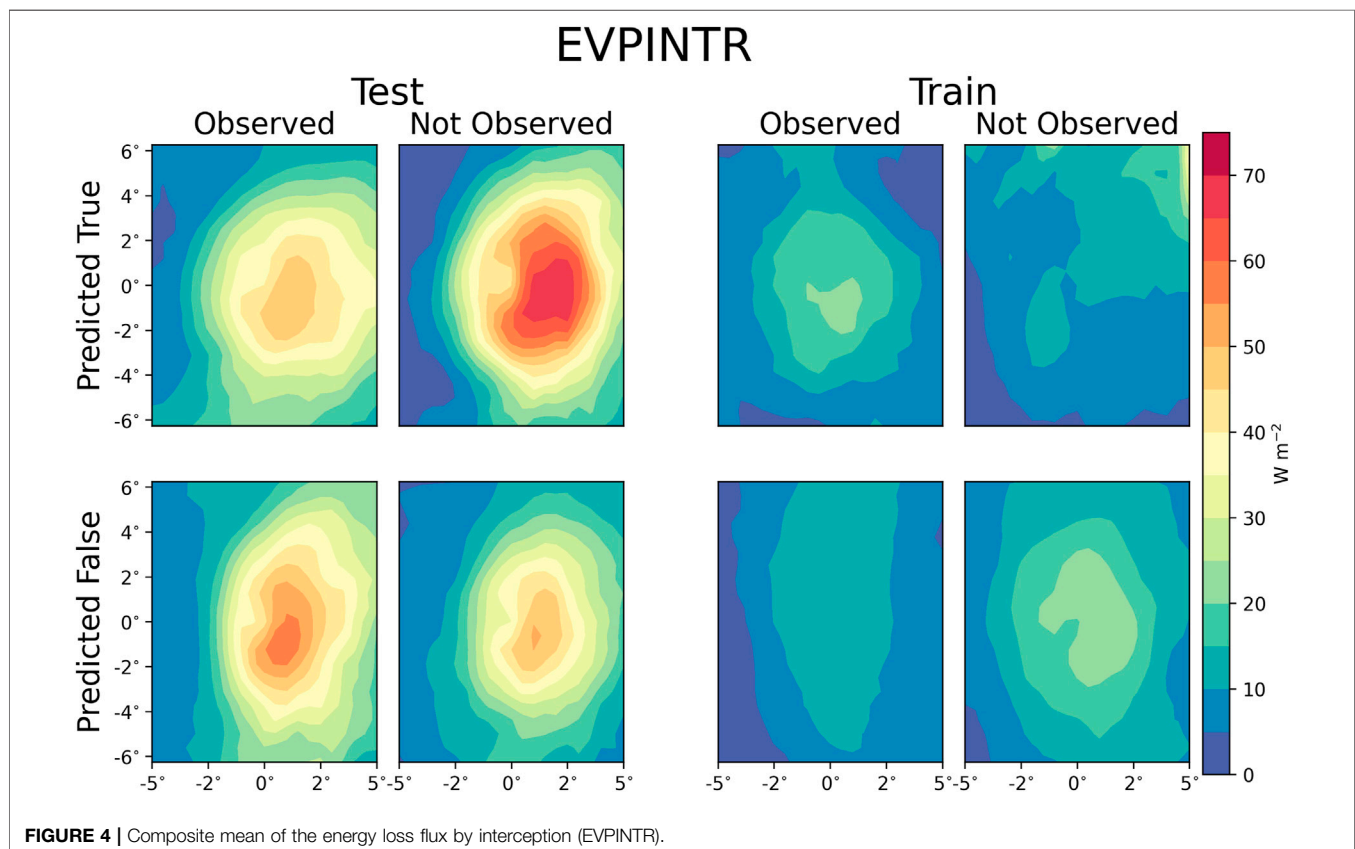
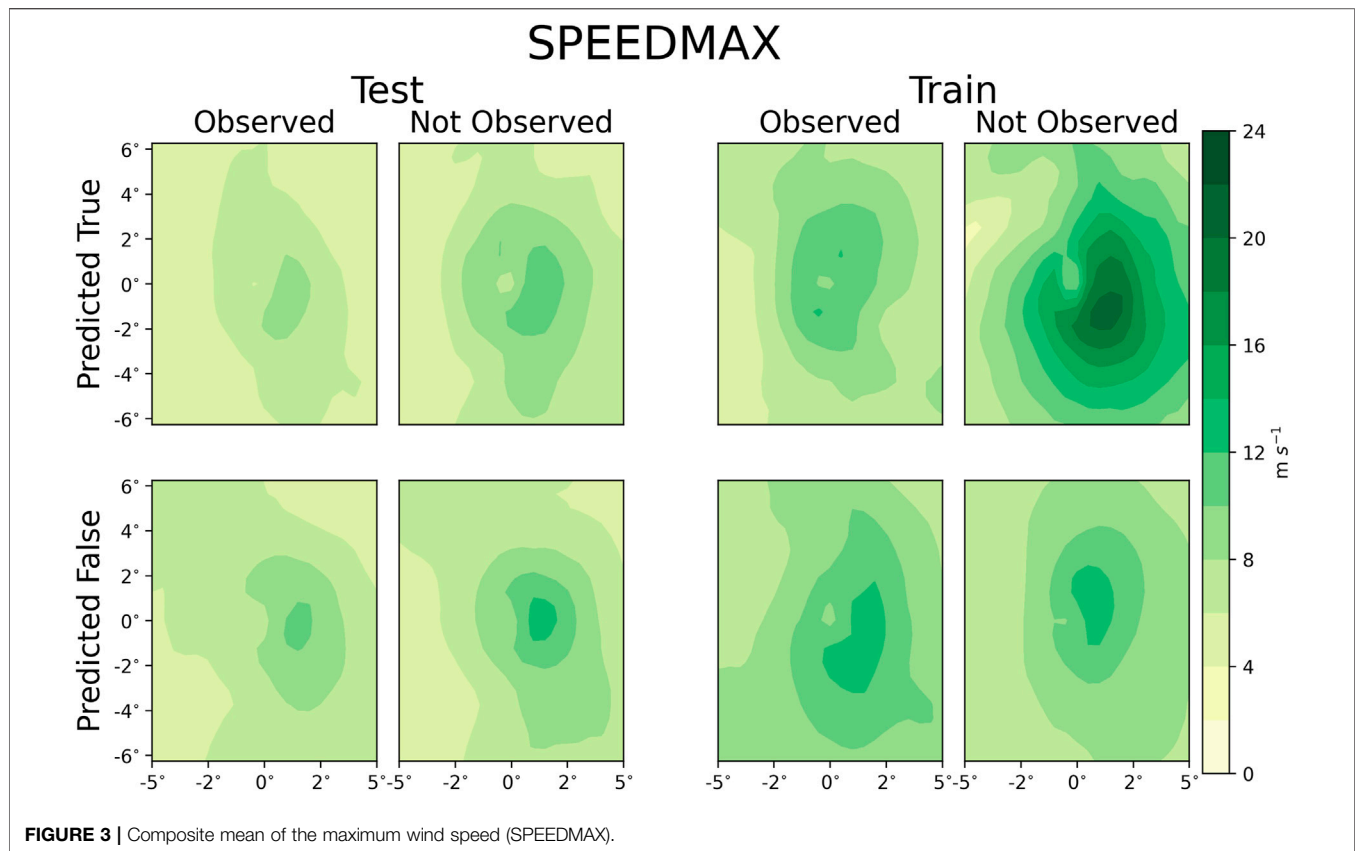
2 DATA AND METHODS

TC location and intensity data were obtained from the International Best Track Archive for Climate Stewardship dataset (IBTrACS; Knapp et al., 2010; Knapp et al., 2018). Of those TCs, only those that occurred since 1980 were considered as

that is the limit of the Modern-Era Retrospective analysis for Research and Applications, Version 2 (MERRA-2; Gelaro et al., 2017), which was used for the environmental conditions. Of the variables in MERRA-2, only the Single level variables (SLV), surface flux variables (FLX), and land-surface variables (LND) were considered. Not only were the variables at the time of the strike considered, but the variables 24 h prior were used. However, variables that were physically more relevant to reintensification, were more commonly measured, or more relevant to reintensification were considered. For example, total column ozone, a SLV variable was not considered as it is possibly unphysically related to tropical cyclones. Neither the root zone water content, a LND variable, nor the areal fraction of anvil showers, a FLX variable were considered, as both are undefinable outside of the model setting or are unmeasured.

Each datum that occurred 350 km away from the coast was considered, similar to AS14. Unlike AS14, however, this study does not compare ET events with TCMI events but rather TCMI events and TCs that decay. As long as the datum and the following datum's 'nature' were classified as a Tropical Storm or Disturbance, the datum was still categorized. The classification of the following datum is important as neglecting such a criterion may mean a miss-categorization of a TCMI storm as a TC undergoing ET. The change in the maximum wind speed (MUSD, or 'usa_wind' in IBTrACS) between the previous time





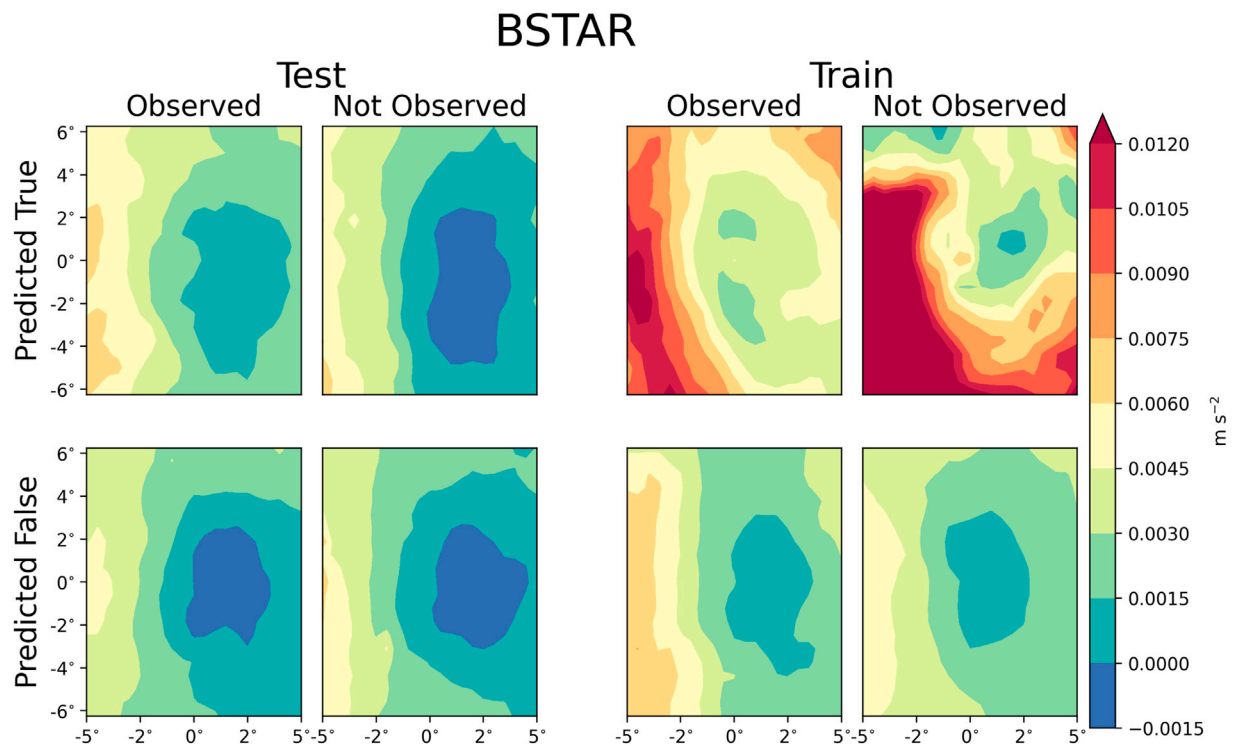


FIGURE 5 | Composite mean of the surface buoyancy scale (BSTAR).

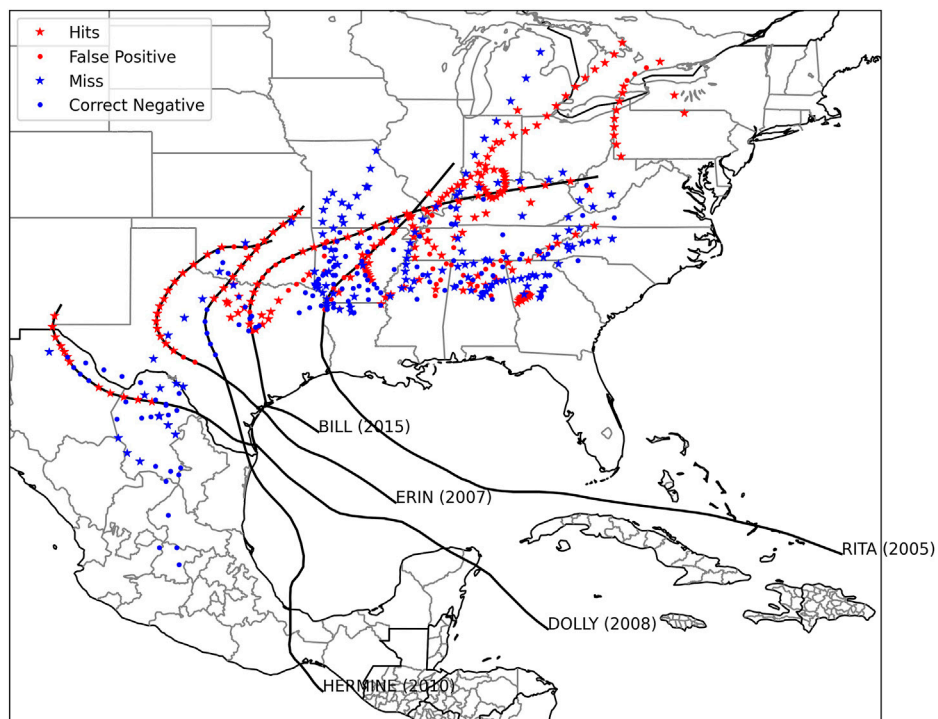


FIGURE 6 | Map of the performance of the machine-learning model. Tropical Storms Bill (2015) and Erin (2007) have been identified as TCMI events, while Hurricane Dolly (2008) and Tropical Storm Hermine (2010) are described in the text.

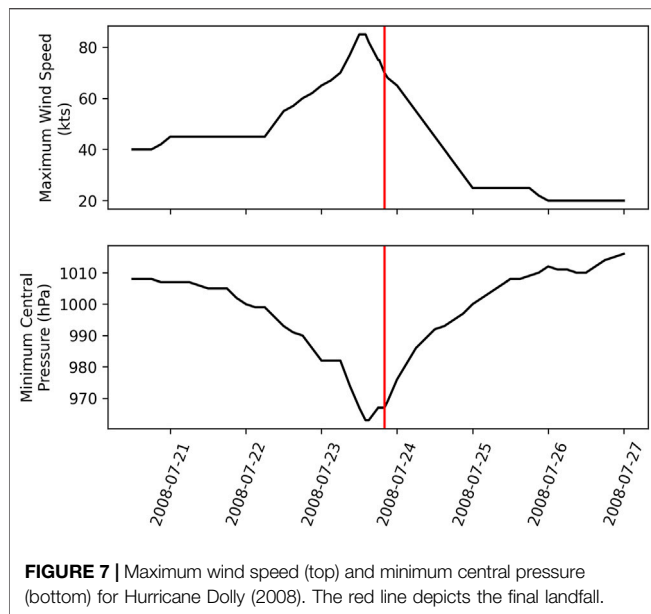
TABLE 3 | Tropical cyclones that Underwent TCMI.

Non-North Atlantic Storms			North Atlantic Storms		
Season	Name	Number of TCMI events	Season	Name	Number of TCMI events
1981	EDDIE	17	1980	ALLEN	1
1984	FREDA	7	1982	CHRIS	2
1987	IRMA	6	1983	ALICIA	1
1989	KEN-LOLA:LOLA	12	1985	DANNY	13
1990	LOLA	1	1985	ELENA	6
1991	DAPHNE	14	1986	BONNIE	2
1995	BOBBY	3	1988	FLORENCE	3
1996	JACOB	1	1988	GILBERT	11
1996	KIRSTY	18	1989	CHANTAL	3
1996	ETHEL	12	1992	ANDREW	1
1996	HERB	4	1994	ALBERTO	10
1997	RACHEL	22	1994	BERYL	5
1997	AMBER	2	1995	DEAN	13
1999	BILLY	1	1995	ERIN	15
2000	ROSITA	2	1995	JERRY	3
2001	WINSOME	5	1996	FRAN	10
2001	ABIGAIL	2	1997	DANNY	12
2002	SINLAKU	1	1998	CHARLEY	2
2003	DELFINA	2	1998	FRANCES	2
2005	SANJU	1	1999	BRET	1
2007	GEORGE	1	1999	DENNIS	2
2007	JACOB	1	2001	BARRY	6
2008	NOT_NAMED	1	2002	ISIDORE	4
2010	LAURENCE	4	2003	BILL	6
2010	PHET	1	2003	CLAUDETTE	2
2010	GIRI	1	2003	GRACE	4
2011	YASI	20	2004	FRANCES	7
2018	HILDA	8	2004	IVAN	3
2018	KELVIN	2	2005	ARLENE	8
2018	YAGI	1	2005	DENNIS	45
			2005	KATRINA	2
			2005	RITA	2
			2007	ERIN	14
			2008	DOLLY	12
			2008	EDOUARD	1
			2008	FAY	3
			2008	GUSTAV	9
			2008	IKE	2
			2010	NOT_NAMED	3
			2010	HERMINE	11
			2012	ISAAC	5
			2015	BILL	17
			2017	CINDY	6
			2017	HARVEY	4
			2017	IRMA	5
			2018	ALBERTO	15
			2018	FLORENCE	2
			2018	GORDON	10
			2019	BARRY	3
			2020	AMANDA:CRISTOBAL	6
			2020	LAURA	5

and next time, a time span typically of 6 h, were calculated using centered differencing. If the MWSPD difference was greater than or equal to 0, the datum was classified as a TCMI event. If the MWSPD-change criteria was not met, the datum was classified as a non-TCMI event. If the datum occurred in the North Atlantic basin, it was used to test the developed machine-learning model. Otherwise, the datum was used to train the model coefficients.

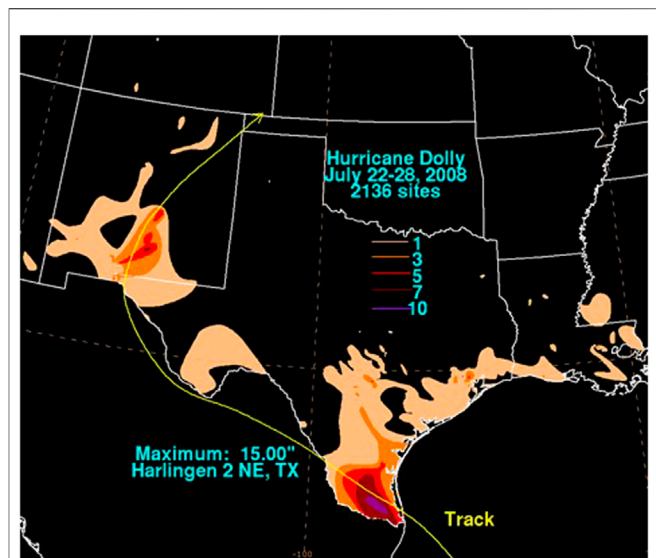
The data for TCMI and non-TCMI storms were consolidated by averaging the environmental variables of TCMI and non-TCMI events. This consolidation prevents the observational independence assumption of logistic regression models from being violated.

The function used to create the machine learning model was the “Logit,” a diminutive of logistic regression, function in



statsmodels (Seabold and Perktold, 2010). Logistic regression fits a likelihood function for a binary variable to a multivariate logistic equation. Another possible description for logistic regression is an estimate of the probability of a binary event by identifying the coefficients of a multivariate linear equation functionally composed within a logistic function. The statsmodels function allows for the statistical model to be trained, applied, and provides the contribution of each variable to the equation along with a statistical description of the fitness of the regression. Candidate machine-learning models were developed iteratively going through sets of unmatched, potentially relevant variables to identify independent candidate variables for a final prototype machine-learning model, which was initialized as an empty set. Then the accuracy of each variable pair for both the test and training dataset was evaluated and stored under the condition that the variance inflation factor (VIF) was less than or equal to 10 (O'Brien, 2007). If a variable in the variable pair is included in the candidate variables, it is excluded for the test.

Afterwards, the most accurate candidate machine-learning models were selected. The accuracy metric utilized is the average of the Peirce Skill Score (Peirce, 1884; Manzato, 2007) between the test and training dataset subtracted by the absolute difference, with the same process applied to the Clayton Skill Score. Optimizing the combined Peirce Skill Score with a difference penalty produced reasonable values of other skill scores with minimal difference between the testing and training datasets. The subtraction of the absolute difference is to penalize overfitting of the training dataset. The most frequent variable that was shown in the most accurate candidate machine-learning models was used to train the next iteration of candidate machine-learning models, though the variable was excluded if the most frequent variable appeared previously in the set of candidate variables. The exclusion of a candidate variable may not always indicate that the machine-learning model is necessarily less accurate but may be a result of a reduction in the VIF. After



the Peirce Skill Score was optimized, variables with a p -value greater than 0.6 were removed.

While the prototypical machine-learning model may be useful for identifying TCMI events, it is not without flaw. On a dynamic note, the machine-learning model does not account for external influences, including localized intensification due to surface features, or horizontal influences. For example, Cyclone Kelvin (2018) has been shown to have maintained a warm core (Shepherd et al., 2021) over land but was more influenced by the horizontal advection of moisture rather than the BOE (Yoo et al., 2020). This may be the reason that the prototypical machine-learning model missed the TCMI of Kelvin. Along a similar line, this prototypical machine-learning model does not include extratropical cyclones, which derive energy from baroclinicity (Evans et al., 2017; Keller et al., 2018). Intensification due to the influence of surface features and topography (Miller et al., 2013; Coch, 2020) are also not considered.

The criteria allowed for a small number of non-North Atlantic storms (93) and an even smaller number of North Atlantic TCs (65) so the amount of data used to train and test the machine-learning model is very limited. Of those limited number of TCs, there were 40 TCs in the North Atlantic basin and a total of 20 TCs in other basins that were counted as both non-TCMI and TCMI cyclones. This may mean that more stringent criteria for discriminating between TCMI and non-TCMI events, beyond wind speed, may be necessary. Other choices, such as excluding subtropical cyclones, is open for critique. One criteria for TCs to be consideration that may be relaxed is the 350 km buffer from the coast, suggested by Andersen and Shepherd (2014), which excluded TCs such as Hurricane Gaston (2004; Franklin et al.,

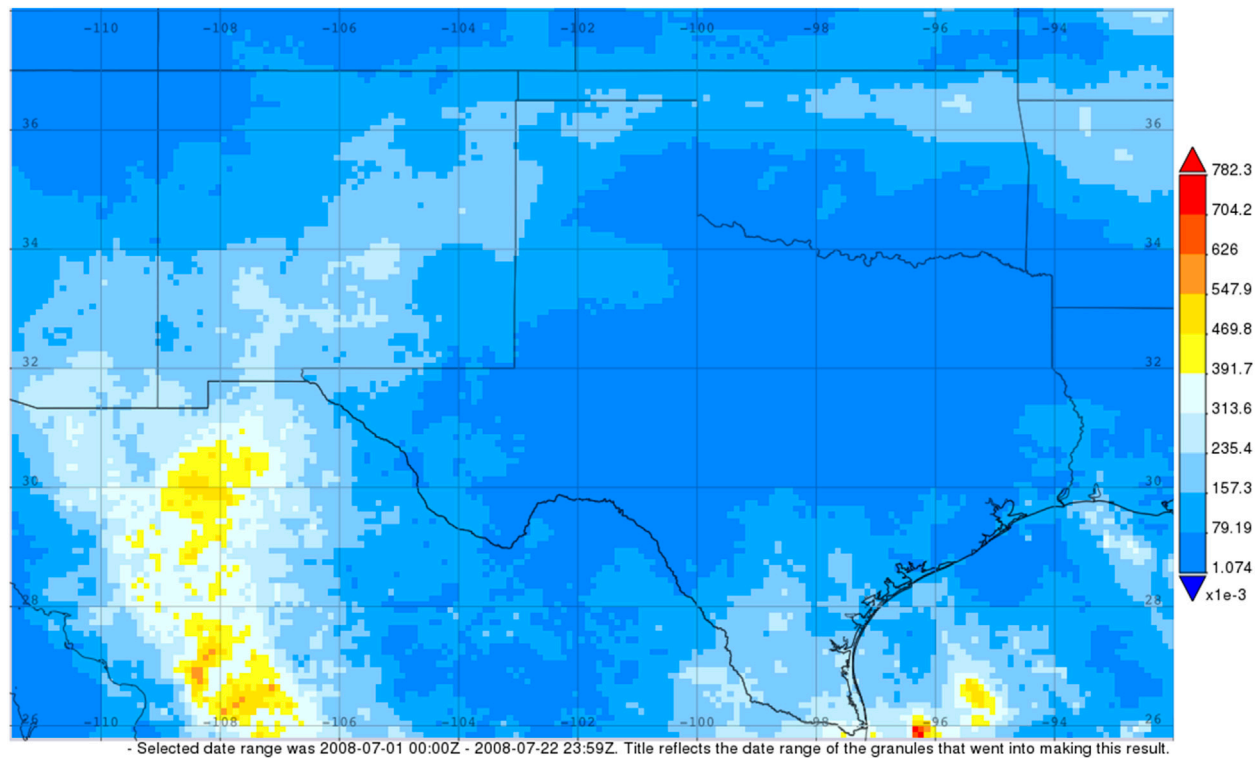


FIGURE 9 | Time-averaged map of the final run of multi-satellite precipitation estimate with gauge calibration prior to the landfall of Hurricane Dolly (2008). Source: NASA Giovanni (Berrick et al., 2009; Acker and Leptoukh, 2007).

2006) and Tropical Storm Helene (2000; Franklin et al., 2001) from being considered. The spatial criteria also does not prevent the TC under consideration from being influenced by the oceanic environment (Yoo et al., 2020).

3 RESULTS

3.1 Statistical Model

Table 1 provides a summary of the final statistical model. Variables ending with the suffix 'Prev' refer to variables from 24 h prior. For reference, the equation for a logistic regression model is

$$P = \left(1 + \exp \left[-\beta_0 - \sum_{i=1}^N \beta_i x_i \right] \right)^{-1}$$

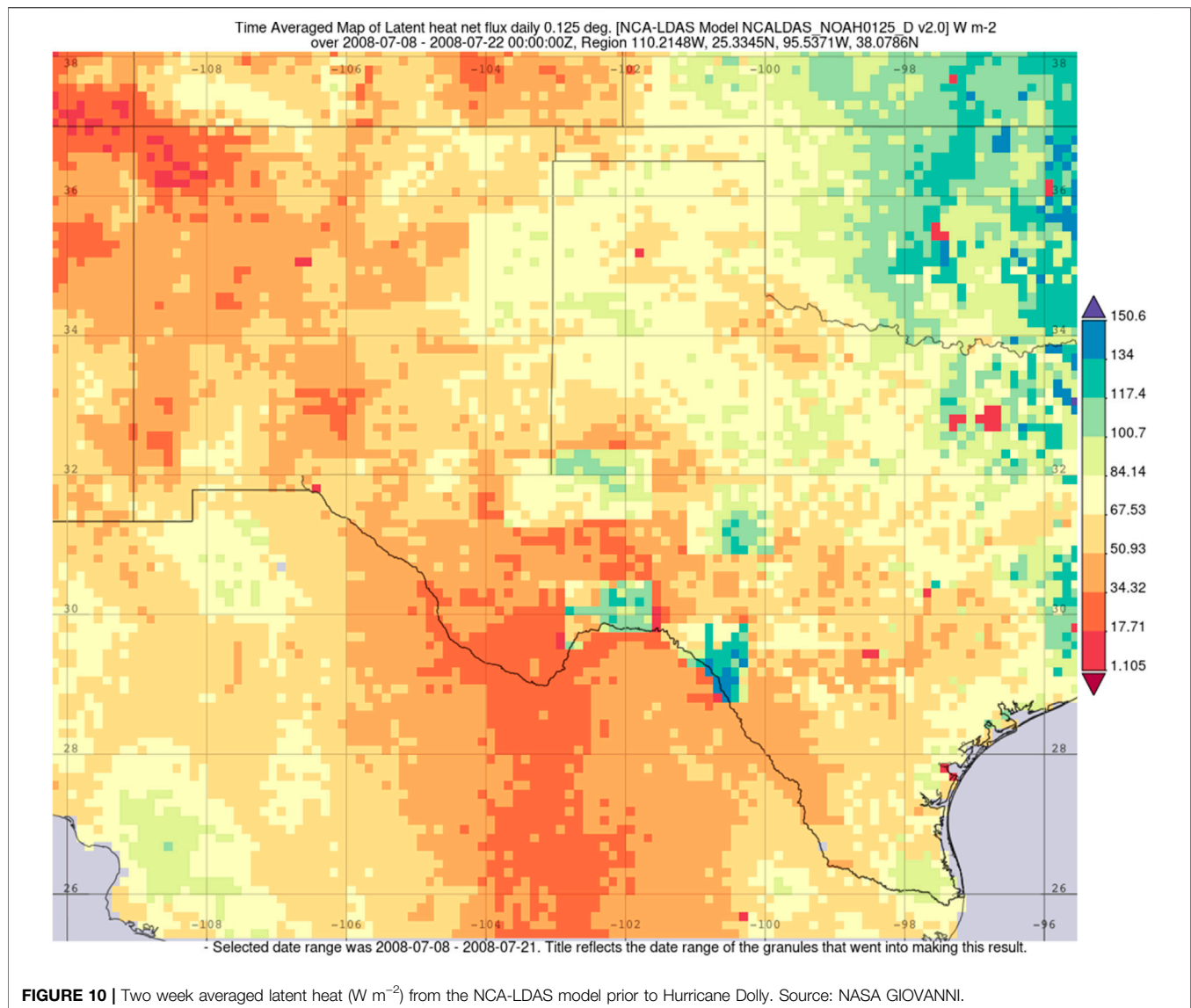
where P is the probability of an event occurring, β_0 is the constant, β_i is the i^{th} coefficient corresponding to the i^{th} variable. While the pseudo-R squared of 0.1727 may be underwhelming, the other statistical measures of accuracy, described in **Table 2** are more optimistic. The relatively small Brier Skill Score indicates the need to assign a reference probability to discriminate between TCMI and non-TCMI events. The probability that was used to discriminate between TCMI and non-TCMI events was a naïve probability of 50%. There is a bias towards overpredicting TCMI events, as indicated

by the False Alarm Rate for both datasets being over 50%. Adjustment of the naïve reference probability of 50% may change the Probability of Detection, but also may increase the False Alarm Rate.

A positive coefficient indicates that the variable has a tendency towards promoting a TCMI event, while a negative coefficient is indicative of a reduction in the likelihood to a TCMI event. The positive coefficient with buoyancy scale (BSTAR) is indicative of the influence of the WISHE mechanism on the occurrence of TCMI events. The coefficient associated with the previous day's accumulated precipitation (PRECTOTPrev) indicates recently wetted soil, which may be promoting the BOE. The coefficient associated with the planetary boundary layer height at the analysis (PBLH) implies that less turbulent mixing increases the probability of a TCMI event. The meaning of the opposite sign between the coefficients associated with the previous day's meridional wind and the meridional wind at the analysis time is unknown, but there may be some level of bias within the wind variables, based on the gradient wind balance and TCs in opposite hemispheres. The decrease in the coefficient with height for the previous day's meridional wind with height (V500Prev and V250Prev) can be reinterpreted as the positive contribution of the mean wind and the negative contribution of the shear.

3.2 Verification Composite

Figure 1 shows the sea level pressure (SLP) relative to the IBTrACS location averaged over the contingencies produced



by the prototype machine-learning model. The centeredness is indicative that the TC position is represented well by MERRA-2. The central and environmental pressures are lower in the non-North Atlantic dataset than the testing dataset, indicating a systematic difference between the datasets. There are a couple of other systematic differences between the training and testing datasets. Another systematic difference is the roughness length (**Figure 2**), which is larger in the North Atlantic basin than in the other basins. It should be noted that in both datasets but particularly the training dataset, the number of constituent storms that had false positives is limited, which emphasizes individual storm characteristics. Cyclone Naomi 1993) and Cyclone Yasi (2011), which progressed over the sparsely vegetated Australian interior, were the only TCs that were false positives in the training dataset leading to a systematic difference in the roughness length. Both the systematic difference in SLP and ZOM lead to systematic differences in the maximum

wind speed (SPEEDMAX; **Figure 3**). The average storm that underwent TCMI had a lower SPEEDMAX than the storms that did. The eastern maxima in SPEEDMAX is due to the compound effect of the translation velocity and gradient wind balance.

Figure 4 shows the energy loss flux from interception (EVPINTR). For the testing dataset, the average EVPINTR is a good metric for determining inaccurate diagnoses, while it may improve the accuracy in the training dataset. However, including EVPINTR in the machine-learning model produced a larger p -value than the threshold. From a physical interpretation, EVPINTR is the amount of energy constrained to the surface by the presence of objects on the surface. EVPINTR disrupts the surface energy flux and reduces the buoyancy. This is seen in **Figure 5**, which shows BSTAR. BSTAR is one of the criteria variables within the machine-learning model that describes the role of the WISHE/BOE mechanism. In the testing dataset, the average BSTAR near the center of the TC is positive only in the

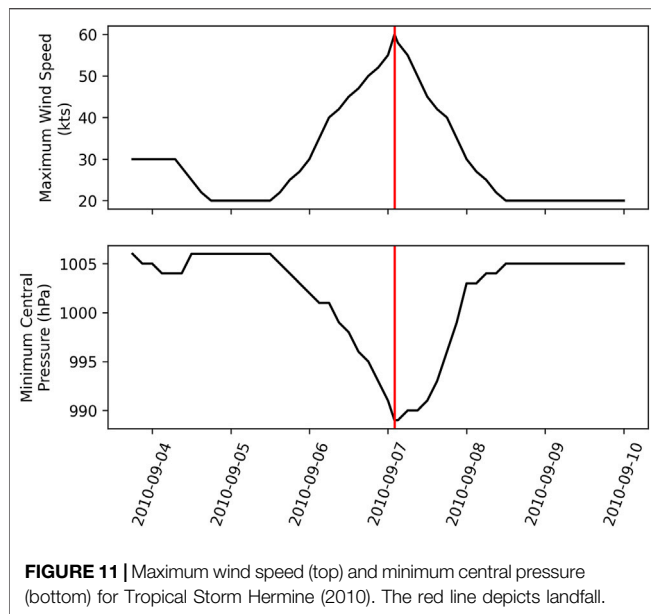


FIGURE 11 | Maximum wind speed (top) and minimum central pressure (bottom) for Tropical Storm Hermine (2010). The red line depicts landfall.

hits. This is one way of discriminating between hits and false positives in the North Atlantic basin.

3.3 Event Analysis

3.3.1 Discussion

Figure 6 shows a geographical distribution of the machine-learning model performance on the testing dataset. The machine-learning model does not predict TCMI events in southern Mexico even though TCMI events do occur in that region. There are several identifiable storms that have and have not undergone TCMI. Specifically, Tropical Storms Erin (2007) and Bill (2015) are storms that were identified by the prototypical machine-learning model, which are published instances of the BOE (Evans et al., 2011; Kellner et al., 2012; Arndt et al., 2009; Brauer et al., 2021). **Table 3** lists other storms that meet the TCMI classification. Below, we examine Tropical Storm Hermine (2010), which followed a similar path to Tropical Storms Erin and Bill, as well as Tropical Storm Dolly (2008), which eventually caused flooding in New Mexico.

3.3.2 Hurricane Dolly (2008)

Hurricane Dolly (2008) was a hurricane that formed in the western Caribbean Sea on 20 July 2008. After experiencing two brief landfalls near Cancun, Mexico and South Padre Island, Dolly experienced a final landfall on Texas on 23 July 2008 at 2000 UTC. **Figure 7** shows the trend in the intensity of Hurricane Dolly. After rapid weakening associated with landfall, Dolly experienced two periods of cyclone maintenance with the first period as a tropical depression and a constant wind speed of 25 kts for 20 h, and the second period as a low pressure with a constant wind speed of 20 kts for 24 h before dissipating. The first period had monotonically increasing pressure, while the pressure decreased two hPa over 12 h, but increased by six hPa over the next 12 h.

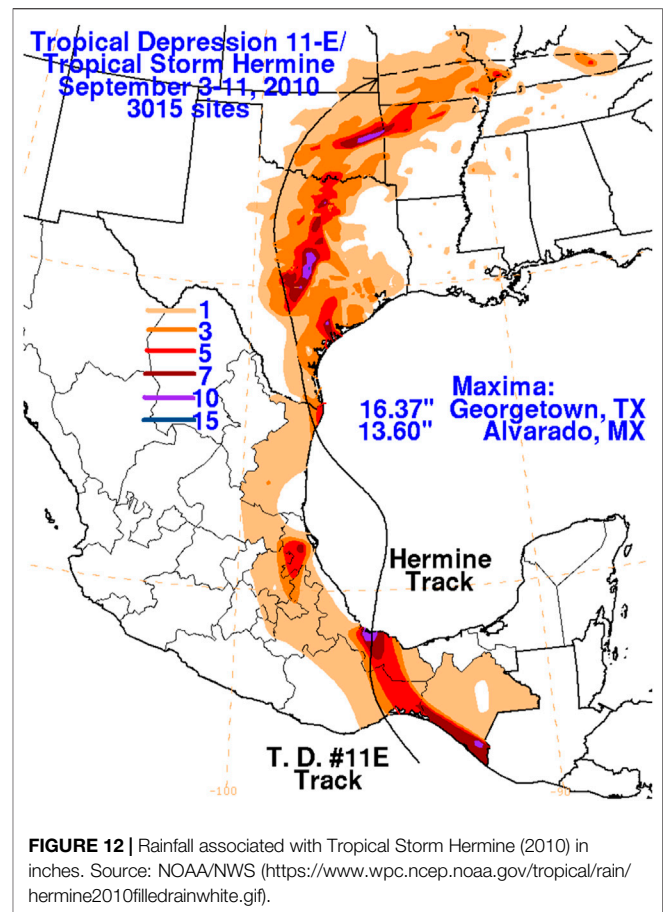


FIGURE 12 | Rainfall associated with Tropical Storm Hermine (2010) in inches. Source: NOAA/NWS (<https://www.wpc.ncep.noaa.gov/tropical/rain/hermine2010filledrainwhite.gif>).

But more than just the characteristic wind speed change, Dolly produced a secondary precipitation maxima (**Figure 8**) in New Mexico, leading to flash flooding and the death of one person and (National Weather Service (NWS) 2018a). It should be noted that widespread floods impacted New Mexico earlier that month, before Hurricane Dolly, which may qualify as a series of predecessor rain events (PRE; Bosart et al., 2012; Galarneau and Davis, 2013). This is supported by **Figure 9**, which shows the time averaged precipitation for the month, prior to final landfall. The machine-learning model did predict a TCMI event. The latent heat flux (shown in **Figure 10**) criteria of 70 W m^{-2} for the BOE, as suggested by AS14, was not sufficient evidence to predict the TCMI of Dolly, indicating that this tool is an improvement on previous criteria.

3.3.3 Tropical Storm Hermine (2010)

Tropical Storm Hermine (2010) developed within the Bay of Campeche and traveled across to the Gulf of Mexico, making landfall in northeast Mexico at 0200 UTC on 7 September 2010 (Avila, 2010). While Hermine lasted only 64 h as a TC after landfall, 30 of those hours were as a tropical depression at a constant wind speed of 20 kts and a constant central pressure of 1,005 hPa. The maximum wind speed and minimum central pressure is summarized in **Figure 11**.

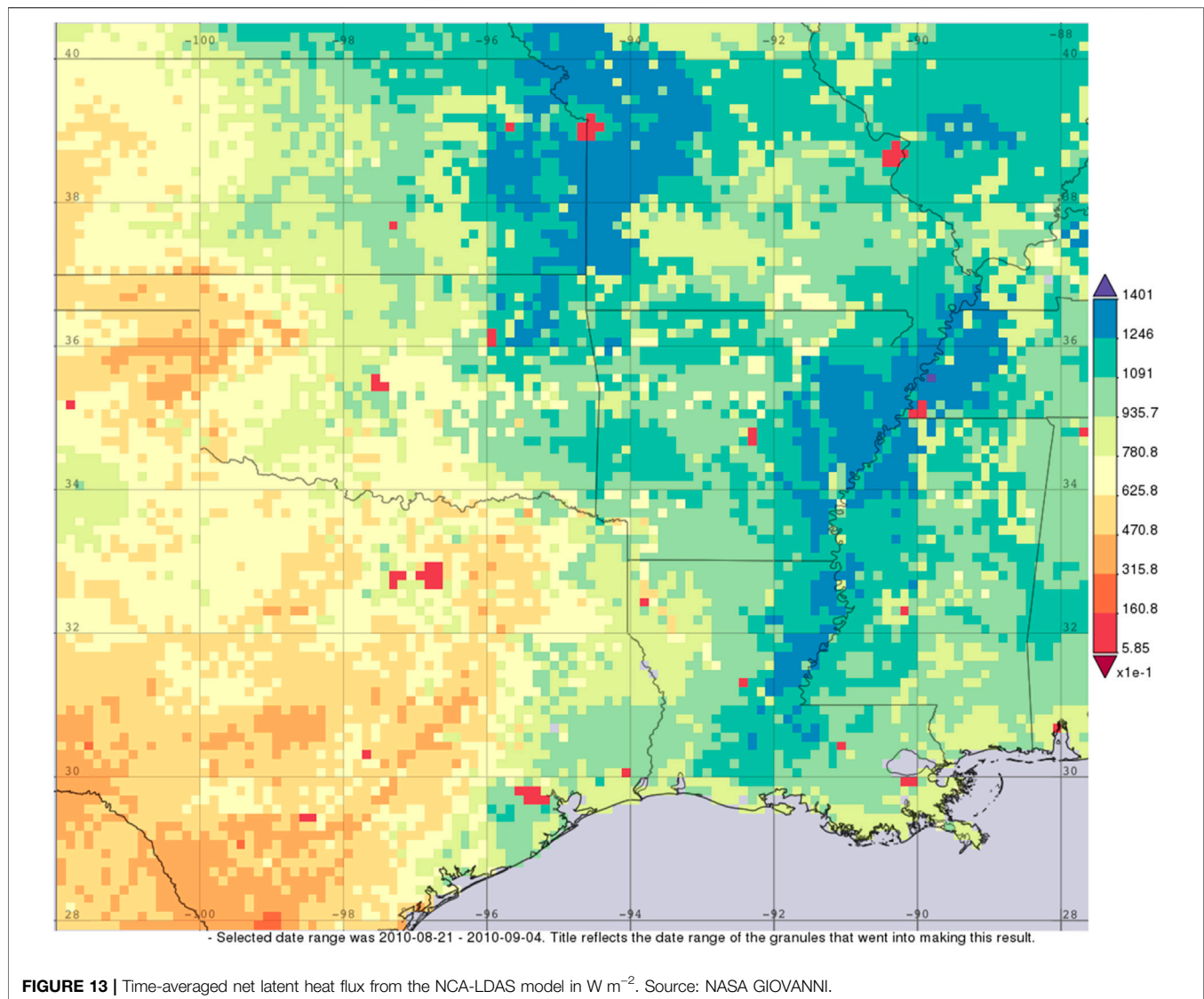


FIGURE 13 | Time-averaged net latent heat flux from the NCA-LDAS model in W m^{-2} . Source: NASA GIOVANNI.

Like Hurricane Dolly, Hermine produced an inland maxima in precipitation, as shown in **Figure 12**. Hermine was a significant precipitation event, despite it qualifying as a TCMI on the basis of the TC dynamics, as it was the only precipitation event for some areas in September 2010. A severe drought began afterwards (National Weather Service (NWS) 2018b). Despite the severe drought, the 2-week averaged latent heat flux, shown in **Figure 13**, was sufficient to produce a BOE storm. For reference, a 2 week average 40 W m^{-2} is the criteria value of for the BOE identified by Andersen et al. (2013).

4 CONCLUSION

A prototypical machine learning model has been developed with variables that were chosen to optimize accuracy rather than any given cause of TCMI. Some variables that were important at the time of storm arrival were important the prior day, which

indicates that a TCMI event is a reaction to the environment, namely BSTAR, PBLH, V250, and PRECTOT. Moreover, the variables that were finally selected show a heavy emphasis on land-surface processes, which also indicates that proper modeling of air-land interactions are critical for modeling TCMI events. This supports the idea that the accurate representation of the land surface state is important for accurate diagnosis of TCMI.

One aspect of the final machine-learning prototype model that can be criticized is the inclusion of the wind components (U10M, V250, V250Prev). The machine-learning model was trained on data in both the Northern and Southern Hemisphere, respectively, indicating an opposing bias in each due to the opposite signed Coriolis force and opposing rotation. Moreover, the 1,000 hPa height from the previous day (H1000Prev) is included, even though it is often masked. However, developing the model without the masked variables still yields a similar subset of variables (including V250 and V250Prev) with similarly signed coefficients within the

confidence interval of the original model, though with less accuracy. The role of the shifting meridional wind deserves more study. Moreover, the inclusion of meridional wind shift emphasizes the independence of variable selection without the perceived bias of the TCMI being caused exclusively by the BOE. To clarify, the variables in the final prototype model were chosen not out of preconceived notions of the causes of TCMI but as variables that improve the accuracy of the prototype machine-learning model. This means that variables that are instinctively examined for the BOE were not given priority (such as latent heat flux) but are heavily influenced by those variables.

5 Applicability and Future Use

What has been presented here is a usable prototypical machine-learning model that may diagnose the probability of a TCMI event based on reanalysis data. This probability forecast is effectively a conditional probability of a TCMI event given the inland onset of a TC. If given the probability that an area is to be struck by a hurricane at a given time, this diagnostic method can be applied to determine whether the TC decays or maintains strength/intensifies. This tool may be useful in diagnosing the occurrence of TCMI events in a future climate beyond the simple 70 W m^{-2} latent heat flux threshold suggested by AS14.

Possible future improvements to this statistical model include excluding weaker TCs as well as distinguishing between intensification and maintenance events. Identifying the BOE given a TCMI event through the use of Bayes' Theorem is also a potential avenue of identifying specific TCs that underwent the BOE. Another potential improvement is the inclusion of surrounding grid cells or times but at the cost of additional computations and possibly decreasing the physical interpretability. While observations of rainfall are not included in the IBTrACS dataset, satellite observations of the precipitation rate in space may also be employed in to broaden the definition of TCMI beyond the dynamic criteria.

This study provides a list of candidate TCs to study for TCMI events (see **Table 3**). More TCs can be considered if the range of dates is expanded to the full selection rather than what is limited by MERRA-2 or if the spatial constraints are reduced. This

provides a new set of TCs to be considered as BOE storms for study, instead of morbidly awaiting new TCMI events or questioning any new TC for the potential for the BOE. This study also indicates that, while the BOE is one specific and major cause of TCMI, it is not the only cause.

DATA AVAILABILITY STATEMENT

Publicly available datasets were analyzed in this study. This data can be found here: <https://www.ncei.noaa.gov/data/international-best-track-archive-for-climate-stewardship-ibtracs/v04r00/access/> <https://goldsmr4.gesdisc.eosdis.nasa.gov/data/MERRA2/>.

AUTHOR CONTRIBUTIONS

AMT designed this as an intermediate step for an proposed project for the dissertation, which JMS oversaw. JMS suggested that this be published as new research. AMT made the technical decisions regarding model development, as well as provided the physical interpretation to the model. JMS provided the resources required for completion. AMT wrote the manuscript and JMS, in conjunction with the dissertation committee, suggested modifications to the manuscript. JMS also provided editorial suggestions.

FUNDING

This research was funded under the NASA Modeling, Analysis, and Prediction (MAP) program (16-MAP16-013) grant.

ACKNOWLEDGMENTS

The authors thank Dr. Gabriel Kooperman, Dr. John Knox, and Dr. Joseph Santanello for their contributions to an early version of the manuscript.

REFERENCES

- Acker, J. G., and Leptoukh, G. (2007). *Online Analysis Enhances Use of NASA Earth Science Data*. Washington D.C: Eos 88. doi:10.1029/2007EO020003
- Andersen, T. K., Radcliffe, D. E., and Shepherd, J. M. (2013). Quantifying Surface Energy Fluxes in the Vicinity of Inland-Tracking Tropical Cyclones. *J. Appl. Meteorol. Climatol.* 52, 2797–2808. doi:10.1175/JAMC-D-13-035.1
- Andersen, T. K., and Shepherd, J. M. (2014). A Global Spatiotemporal Analysis of Inland Tropical Cyclone Maintenance or Intensification. *Int. J. Climatol.* 34, 391–402. doi:10.1002/joc.3693
- Arndt, D. C., Basara, J. B., McPherson, R. A., Illston, B. G., McManus, G. D., and Demko, D. B. (2009). Observations of the Overland Reintensification of Tropical Storm Erin (2007). *Bull. Am. Meteorol. Soc.* 90, 1079–1094. doi:10.1175/2009BAMS2644.1
- Avila, L. A. (2010). Tropical Cyclone Report Tropical Storm Hermine (AL102010). Available at: https://www.nhc.noaa.gov/data/tcr/AL102010_Hermine.pdf.
- Berrick, S. W., Leptoukh, G., Farley, J. D., and Rui, H. (2009). Giovanni: A Web Service Workflow-Based Data Visualization and Analysis System. *IEEE Trans. Geosci. Remote Sens.* 47, 106–113. doi:10.1109/TGRS.2008.2003183
- Bosart, L. F., Cordeira, J. M., Galarneau, T. J., Moore, B. J., and Archambault, H. M. (2012). An Analysis of Multiple Predecessor Rain Events Ahead of Tropical Cyclones Ike and Lowell: 10–15 September 2008. *Mon. Weather Rev.* 140, 1081–1107. doi:10.1175/MWR-D-11-00163.1
- Brauer, N. S., Basara, J. B., Kirstetter, P. E., Wakefield, R. A., Homeyer, C. R., Yoo, J., et al. (2021). The Inland Maintenance and Re-intensification of Tropical Storm Bill (2015) Part 2: Precipitation Microphysics. *J. Hydrometeorol.* 22, 2695–2711. doi:10.1175/jhm-d-20-0151.1
- Brier, G. W. (1950). Verification of Forecasts Expressed in Terms of Probability. *Mon. Weather Rev.* 78, 1–3. doi:10.1175/1520-0493(1950)078<0001:VOFEIT>2.0.CO;2
- Clayton, H. H. (1927). A Method of Verifying Weather Forecasts. *Bull. Am. Meteorol. Soc.* 8, 144–146. Available at: <http://www.jstor.org/stable/26262138>.
- Clayton, H. H. (1934). Rating Weather Forecasts. *Bull. Am. Meteorol. Soc.* 15, 279–283. doi:10.1175/1520-0477-15.12.279
- Coch, N. K. (2020). Inland Damage from Hurricanes. *J. Coastal Res.* 36, 1093–1105. doi:10.2112/JCOASTRES-D-20A-00002.1
- Doswell, C. A., Davies-Jones, R., and Keller, D. L. (1990). On Summary Measures of Skill in Rare Event Forecasting Based on Contingency Tables. *Weather Forecast* 5, 576–585. doi:10.1175/1520-0434(1990)005<0576:OSMOSI>2.0.CO;2

- Evans, C., Schumacher, R. S., and Galarneau, T. J. (2011). Sensitivity in the Overland Reintensification of Tropical Cyclone Erin (2007) to Near-Surface Soil Moisture Characteristics. *Mon. Weather Rev.* 139, 3848–3870. doi:10.1175/2011mwr3593.1
- Evans, C., Wood, K. M., Aberson, S. D., Archambault, H. M., Milrad, S. M., Bosart, L. F., et al. (2017). The Extratropical Transition of Tropical Cyclones. Part I: Cyclone Evolution and Direct Impacts. *Mon. Wea. Rev.* 145, 4317–4344. doi:10.1175/MWR-D-17-0027.1
- Franklin, J. L., Avila, L. A., Beven, J. L., Lawrence, M. B., Pasch, R. J., and Stewart, S. R. (2001). Atlantic hurricane Season of 2000. *Mon. Wea. Rev.* 129, 3037–3056. doi:10.1175/1520-0493(2001)129<3037:ahso>2.0.co;2
- Franklin, J. L., Pasch, R. J., Avila, L. A., Beven, J. L., Lawrence, M. B., Stewart, S. R., et al. (2006). Atlantic hurricane Season of 2004. *Mon. Weather Rev.* 134, 981–1025. doi:10.1175/MWR3096.1
- Galarneau, T. J., and Davis, C. A. (2013). Diagnosing Forecast Errors in Tropical Cyclone Motion. *Mon. Weather Rev.* 141, 405–430. doi:10.1175/MWR-D-12-00071.1
- Gelaro, R., McCarty, W., Suárez, M. J., Todling, R., Molod, A., Takacs, L., et al. (2017). The Modern-Era Retrospective Analysis for Research and Applications, Version 2 (MERRA-2). *J. Clim.* 30, 5419–5454. doi:10.1175/JCLI-D-16-0758.1
- Gilbert, G. K. (1884). Finley's Tornado Predictions. *Am. Meteorol. Journal. A Mon. Rev. Meteorol. Allied Branches Study* 1, 166. Available at: <https://search.proquest.com/scholarly-journals/finleys-tornado-predictions/docview/124374084/se-2?accountid=14537>.
- Heidke, P. (1926). Berechnung des Erfolges und der Güte der Windstärkevorhersagen im Sturmwarnungsdienst. *Geogr. Ann.* 8, 301. doi:10.2307/519729
- Jones, S. C., Harr, P. A., Abraham, J., Bosart, L. F., Bowyer, P. J., Evans, J. L., et al. (2003). The Extratropical Transition of Tropical Cyclones: Forecast Challenges, Current Understanding, and Future Directions. *Wea. Forecast.* 18, 1052–1092. doi:10.1175/1520-0434(2003)018<1052:tetotc>2.0.co;2
- Kaplan, J., and Demaria, M. (2001). On the Decay of Tropical Cyclone Winds after Landfall in the New England Area. *J. Appl. Meteorol.* 40, 280–286. doi:10.1175/1520-0450(2001)040<0280:otdotc>2.0.co;2
- Keller, J. H., Grams, C. M., Riemer, M., Archambault, H. M., Bosart, L., Doyle, J. D., et al. (2019). The Extratropical Transition of Tropical Cyclones. Part II: Interaction with the Midlatitude Flow, Downstream Impacts, and Implications for Predictability. *Mon. Weather Rev.* 147, 1077–1106. doi:10.1175/mwr-d-17-0329.1
- Kellner, O., Niyogi, D., Lei, M., and Kumar, A. (2012). The Role of Anomalous Soil Moisture on the Inland Reintensification of Tropical Storm Erin (2007). *Nat. Hazards* 63, 1573–1600. doi:10.1007/s11069-011-9966-6
- Knapp, K. R., Kruk, M. C., Levinson, D. H., Diamond, H. J., and Neumann, C. J. (2010). The International Best Track Archive for Climate Stewardship (IBTrACS). *Bull. Amer. Meteorol. Soc.* 91, 363–376. doi:10.1175/2009BAMS2755.1
- Knapp, K. R., Kruk, M. C., Levinson, D. H., Diamond, H. J., and Neumann, C. J. (2018). *International Best Track Archive for Climate Stewardship (IBTrACS) Project, Version 4*. Accessed 02 January 2021. doi:10.25921/82ty-9e16
- Manzato, A. (2007). A Note on the Maximum Peirce Skill Score. *Weather Forecast.* 22, 1148–1154. doi:10.1175/WAF1041.1
- Miller, C., Gibbons, M., Beatty, K., and Boissonnade, A. (2013). Topographic Speed-Up Effects and Observed Roof Damage on Bermuda Following Hurricane Fabian (2003). *Weather Forecast.* 28, 159–174. doi:10.1175/WAF-D-12-00050.1
- Monteverdi, J. P., and Edwards, R. (2010). The Redevelopment of a Warm-Core Structure in Erin: A Case of Inland Tropical Storm Formation. *E-journal Sev. Storms Meteorol.* 5, 1–18. Available from: <http://ejssm.org/ojs/index.php/ejssm/article/viewArticle/65>.
- Nair, U. S., Rappin, E., Foshee, E., Smith, W., Pielke, R. A., Mahmood, R., et al. (2019). Influence of Land Cover and Soil Moisture Based Brown Ocean Effect on an Extreme Rainfall Event from a Louisiana Gulf Coast Tropical System. *Sci. Rep.* 9, 17136. doi:10.1038/s41598-019-53031-6
- O'Brien, R. M. (2007). A Caution Regarding Rules of Thumb for Variance Inflation Factors. *Qual. Quant.* 41, 673–690. doi:10.1007/s11135-006-9018-6
- Peirce, C. S. (1884). The Numerical Measure of the success of Predictions. *Science (80-)* ns-4, 453–454. doi:10.1126/science.ns-4.93.453-a
- Seabold, S., and Perktold, J. (2010). “Statsmodels: Econometric and Statistical Modeling with Python,” in Proceedings of the 9th Python in Science Conference, 92–96. doi:10.25080/majora-92bf1922-011
- Shen, W., Ginis, I., and Tuleya, R. E. (2002). A Numerical Investigation of Land Surface Water on Landfalling Hurricanes. *J. Atmos. Sci.* 59, 789–802. doi:10.1175/1520-0469(2002)059<0789:aniols>2.0.co;2
- Shepherd, M., Thomas, A., Santanello, J., Lawston, P. M., and Basara, J. (2021). Evidence of Warm Core Structure Maintenance over Land: A Case Study Analysis of Cyclone Kelvin. *Environ. Res. Commun.* 3, 045004. doi:10.1088/2515-7620/abf39a
- Stephenson, D. B. (2000). Use of the “Odds Ratio” for Diagnosing Forecast Skill. *Weather Forecast.* 15, 221–232. doi:10.1175/1520-0434(2000)015<0221:UOTORF>2.0.CO;2
- Wilks, D. S. (2006). *Statistical Methods in the Atmospheric Sciences*. Academic press.
- Yoo, J., Santanello, J. A., Shepherd, M., Kumar, S., Lawston, P., and Thomas, A. M. (2020). Quantification of the Land Surface and Brown Ocean Influence on Tropical Cyclone Intensification over Land. *J. Hydrometeorol.* 21, 1171–1192. doi:10.1175/JHM-D-19-0214.1

Conflict of Interest: The authors declare that the research was conducted in the absence of any commercial or financial relationships that could be construed as a potential conflict of interest.

Publisher's Note: All claims expressed in this article are solely those of the authors and do not necessarily represent those of their affiliated organizations, or those of the publisher, the editors and the reviewers. Any product that may be evaluated in this article, or claim that may be made by its manufacturer, is not guaranteed or endorsed by the publisher.

Copyright © 2022 Thomas and Shepherd. This is an open-access article distributed under the terms of the Creative Commons Attribution License (CC BY). The use, distribution or reproduction in other forums is permitted, provided the original author(s) and the copyright owner(s) are credited and that the original publication in this journal is cited, in accordance with accepted academic practice. No use, distribution or reproduction is permitted which does not comply with these terms.



Impact of the Spring North Atlantic Oscillation on the Northern Hemisphere Tropical Cyclone Genesis Frequency

Leying Zhang¹, Xiting Yang¹ and Jiuwei Zhao^{2*†}

¹College of Biology and the Environment, Joint Innovation Center for Modern Forestry Studies, Nanjing Forestry University, Nanjing, China, ²Institute of Climate and Application Research, Nanjing University of Information Science and Technology, Nanjing, China

OPEN ACCESS

Edited by:

Guanghua Chen,
Institute of Atmospheric Physics
(CAS), China

Reviewed by:

Lei Wang,
Guangdong Ocean University, China
Chundi Hu,
Sun Yat-sen University, China

*Correspondence:

Jiuwei Zhao
jiuwei@nuist.edu.cn

†ORCID:

Jiuwei Zhao
0000-0001-9146-7500

Specialty section:

This article was submitted to
Atmospheric Science,
a section of the journal
Frontiers in Earth Science

Received: 06 December 2021

Accepted: 05 January 2022

Published: 07 March 2022

Citation:

Zhang L, Yang X and Zhao J (2022)
Impact of the Spring North Atlantic
Oscillation on the Northern
Hemisphere Tropical Cyclone
Genesis Frequency.
Front. Earth Sci. 10:829791.
doi: 10.3389/feart.2022.829791

A majority of studies have documented basin-dependent factors for predicting interannual variability of tropical cyclone genesis frequency (TCGF) over basins. In this study, we find that the spring North Atlantic Oscillation (NAO) has cross-basin impacts on summer and autumn TCGF over the whole North Hemisphere. The positive NAO suppresses the TCGF in the North Atlantic (NA) but promotes the TCGF in the North Pacific (NP) via modulating the large-scale environment parameters and vice versa. The positive NAO in spring can induce negative sea surface temperature (SST) anomalies in the NA, which persists into summer via the ocean memory. The negative SST anomalies cool the overlying atmosphere and damp the precipitation, leading to a low-level anti-cyclonic circulation and thereby counteracting the TCGF over the NA in summer and autumn. The southerly anomaly west of the anti-cyclonic circulation increases the SST and precipitation over the northeast Pacific in summer. Accordingly, a cyclonic circulation appears western NP via Gill response and sustains by the warm advection via the air–ocean positive feedback, which devotes the NP TCGF in summer and autumn. The composite results in high-resolutions numerical model from Coupled Model Intercomparison Project Phase 6 further verify the relationship between the spring NAO and TCGF.

Keywords: North Atlantic oscillation, tropical cyclones genesis frequency, north hemisphere, preceding influence, high-resolutions numerical model

INTRODUCTION

Tropical cyclone (TC) often associates with destructive weather, resulting in enormous death and property damage (Kossin et al., 2016; Peduzzi et al., 2012; Schultz and Cecil, 2009). Thus, numerous efforts are directed to monitor and predict the TC genesis frequency (TCGF) variability. The TCGF exhibits a distinct interannual variation (Chan and Xu, 2009), extensively associated with the local sea surface temperature (Li, 2012; Zhao and Wang, 2019). Li (2012) showed that the TCGF in the western North Pacific (NP) tends to increase during the summer of a developing El Niño, while it decreases during the summer of a decaying El Niño. Mei et al. (2019) revealed that a 1°C increase in SST of the main TC development region produces 7.05 ± 1.39 more hurricanes in the North Atlantic (NA) from 100 ensembles of high-resolution atmospheric simulations. Besides the local SST, remote tropical SST forcing can also modulate the interannual variability of TCGF (Cao et al., 2016; Du et al., 2011; Tao et al., 2012; Wang et al., 2014; Yu et al., 2021). Patricola et al. (2016) suggested that Atlantic

tropical cyclones are suppressed during El Niño. Zhan et al. (2011) reported that warm eastern Indian Ocean SST anomaly suppresses the TCGF in the western NP through the large-scale atmospheric circulation and barotropic energy conversion in summer. Yu et al. (2016) found that the negative NA SST in summer can induce a local negative heating anomaly and trigger a low-level anomalous westerly in the tropical Indian Ocean. The westerly anomaly cools the SST and suppresses convection *in situ*, inducing anomalous westerlies over the western NP, and thereby increases the TCGF there.

In addition to the tropical forcing, extratropical forcing plays active roles in the TCGF interannual variability. Choi and Byun (2010) found that more TCs form over east of 150°E and recurve in the east during a strong summer Arctic Oscillation. Wang and Wang (2021) proposed that during a strong South Asian high year, the related upper-level convergence favors descending motion and low-level divergence in the South China Sea, decreasing mid-level humidity and low-level vorticity and thus suppressing TCGF there. Zhou and Cui (2014) showed that during a strong summer North Atlantic Oscillation (NAO), an anomalous cyclonic circulation appears in the western NP and benefits the TCGF there. This relationship features a significant interdecadal shift, which becomes significant after 1980.

The preceding extratropical forcing could also serve as a prediction on the TCGF. Zhang et al. (2020) indicated that East Asian Jet Stream significantly enhances the subsequent TCGF in the NA through a Rossby wave train. A strong North Pacific Oscillation in spring induces a tripole SST pattern over the NP, which subsequently results in an enhanced western NP monsoon trough, thereby fostering the TCGF (Chen et al., 2015a). A strong positive NP Victoria mode in spring benefits a strengthened western NP monsoon trough and weakened western Pacific subtropical high *via* the wind-evaporation-SST feedback, leading to an enhanced (suppressed) TCGF in the eastern (western) western NP (Pu et al., 2019). Choi and Cha (2017) showed that a positive June NAO indicates that more July–August TCs occurs in the northwestern region of western NP, while the positive April–May NAO also devotes to the June–September TC in the western NP (Zhou and Chen, 2020).

Note that no matter the simultaneous or preceding relationship, previous studies mostly focus on the impact of large-scale circulation on the TC in one specific basin. From a single-factor analysis model, Elsner and Kocher (2000) noted that the NAO has a statistically simultaneous link to the global TCGF. That is, the annual NAO is negatively correlated with the TCGF in Atlantic, while it is positive in other oceanic basin. However, how the NAO influences the global TCGF has not been followed up. The NAO is traditionally characterized by the sea-level pressure difference between Iceland and the Azores (Walker, 1924) and is closely related to the strength and direction of westerly winds and storm tracks at mid-high latitude (Nie et al., 2020; Wettstein and Wallace, 2009). The spring NAO could persist its influence through the memory of SST anomalies (Wu et al., 2009) and modulate the global climate and atmospheric circulation in the following seasons (Du et al.,

2019; Ham et al., 2013; Zuo et al., 2012). What is more, the spring NAO could modulate the following ENSO evolution and western Pacific subtropical high intensity, which are both closely related to the TCGF (Chen et al., 2014; Wang et al., 2013; Wang and Wang, 2021). These strongly suggest that NAO may exert significant influences on the global TCs in the following seasons, which is not clear yet.

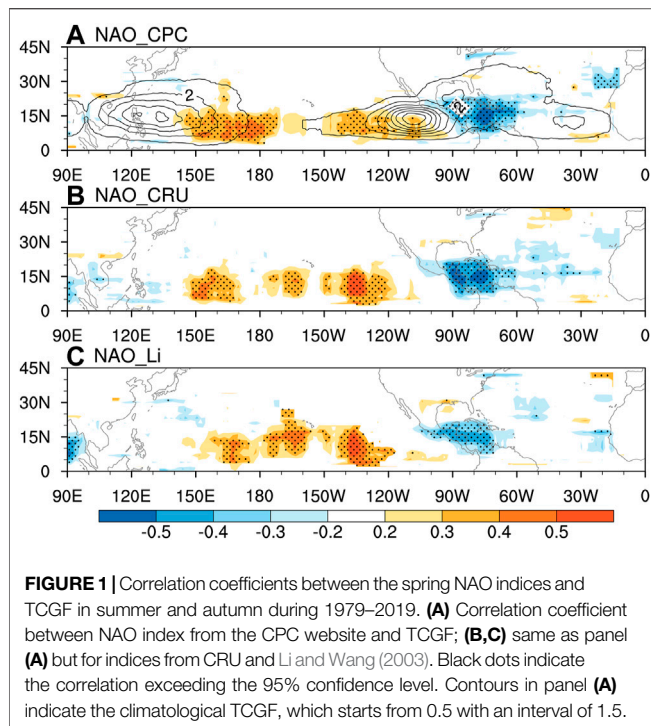
In this study, we aim to ascertain the influence of the spring NAO on the North Hemisphere (NH) TCGF in summer and autumn and explore the associated mechanism. **Section 2** introduces the data and methods. **Section 3** describes the relationship between the spring NAO and North Hemisphere TCGF in the following seasons. The associated mechanism is given in **Section 4**. **Section 5** is a summary and discussion.

DATA AND METHODS

Data

We used the 6-hourly NH TC best-track dataset from the International Best Track Archive for Climate Stewardship version 4 (IBTrACS v4; <https://www.ncei.noaa.gov/data/international-best-track-archive-for-climate-stewardship-ibtracs/v04r00/access/netcdf/>) to obtain TC information, including TC central position (in longitude and latitude) and intensity in terms of maximum sustained near-surface wind speed of each TC. The TC genesis location is defined as the central position where a TC reaches 35 knots for the first time. Since 85% of the TCs form during June–November each year, we focused on the summer and autumn in this study (Murakami et al., 2015). In addition, TCs over the North Indian Ocean mainly form in the pre-monsoon (April and May) and the post-monsoon (October and November) seasons (Chen et al., 2015b); thus, the TCGF over the North Indian Ocean was not included in this study.

The monthly NAO index was downloaded from the National Oceanic and Atmospheric Administration (NOAA) Climate Prediction Center (CPC) website (<https://www.cpc.ncep.noaa.gov/products/precip/CWlink/pna/nao.shtml>; Barnston and Livezey, 1987) for the observational data. The indices from Climate Research Unit (CRU) (<https://crudata.uea.ac.uk/cru/data/nao/nao.dat>; Jones et al., 1997), calculated according to Li and Wang (2003), which is the difference of monthly normalized sea level pressure (SLP) averaged over the longitudes of 80°W–30°E between 35°N and 65°N, are also used to verify the robust relationship between the NAO and TCGF. The spring NAO index is defined as the mean of monthly NAO indices averaged from March to May. The monthly atmospheric reanalysis is from the fifth-generation European Center for Medium-Range Weather Forecasts atmospheric reanalysis of the global climate (ERA5), including sensible heat flux, latent heat flux, SLP, precipitation, winds, vorticity, relative humidity, and air temperature with a 1.0° × 1.0° horizontal resolution (<https://cds.climate.copernicus.eu/cdsapp#!/search?type=dataset>; Hersbach et al., 2020). The monthly SST is obtained from the Hadley Center Global Sea Ice and SST (HadISST) with a resolution of 1.0° × 1.0° (<https://www.metoffice.gov.uk/hadobs/hadisst2/data/download.html>; Rayner, 2003). All the data were

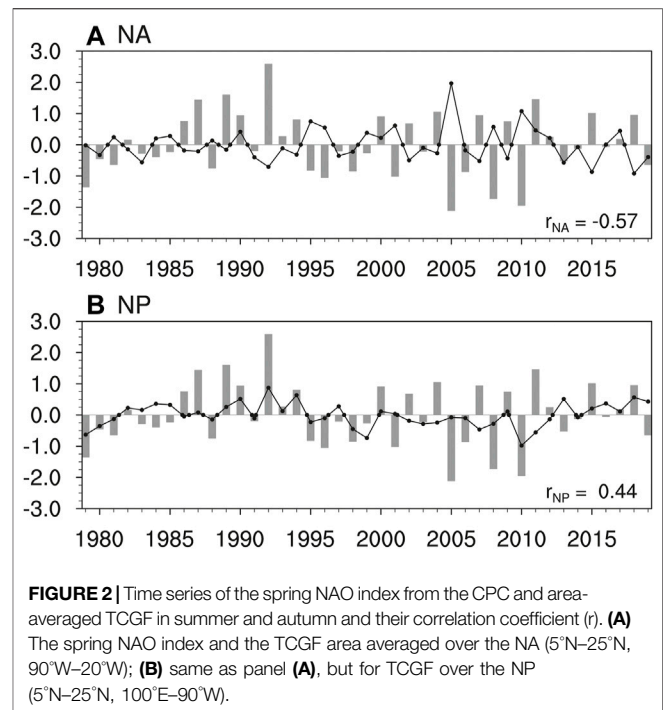


from 1979 to 2019, and their linear trends were removed in advance.

Provided by Coupled Model Intercomparison Project Phase 6 (CMIP6), here, we also used datasets with high spatio-temporal resolutions from the European Centre for Medium-Range Weather Forecasts (ECMWF). The present-day simulation of ECMWF has a spatial resolution of 0.5° and 6-hourly output interval forced by the observed daily SST data from 1979 to 2014, which also contain five members that are integrated with a slight difference of the initial conditions. The five members are from r2i1p1f1, r3i1p1f1, r4i1p1f1, r5i1p1f1, and r6i1p1f1 runs in the ECMWF. The SLP, winds, and relative humidity were used to define the TCGF and verify its relationship with the NAO in the CMIP6. The NAO index in the CMIP6 was calculated according to Li and Wang (2003). Following previous studies (Murakami and Wang, 2010; Zhao et al., 2020a; Zhao et al., 2020b), the TCs were extracted from the high-resolution ECMWF datasets based on criteria below: first, a low pressure center was traced, but the SLP isobars were not necessary to be closed; second, the surface/850-hPa winds were not $<15/17 \text{ m s}^{-1}$ at least one time in its lifespan, and the absolute value of vorticity at 850 hPa was larger than $5 \times 10^{-5} \text{ s}^{-1}$; third, the TC lifetime should be longer than 1.5 days; and last but optional, the warm core of a TC should exist in the range of 1,200–2,400 km at 300–500 hPa. We consider the TC genesis as the winds speed larger than 15 m s^{-1} for the first time in the lifespan of a TC.

Tropical Cyclone Genesis Frequency Definition

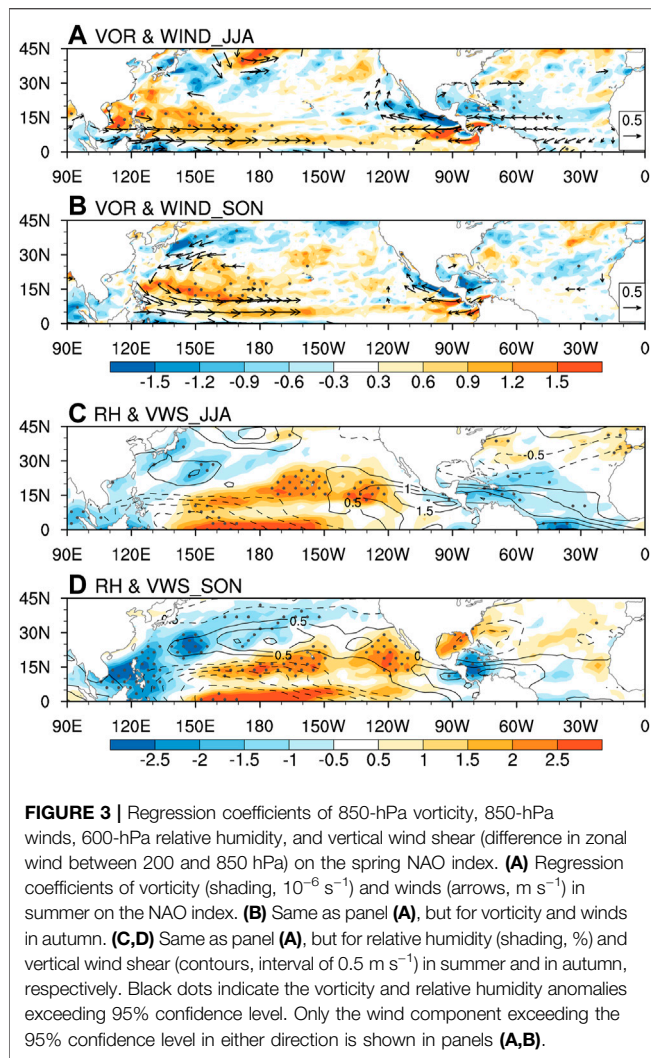
According to the kernel density method of TCGF (Lu and Xiong, 2019), the NH domain is meshed into $1^\circ \times 1^\circ$ grid box, and then,



the TCGF in each grid box is counted as the sum of the TCs formed in an area of 10° in the zonal direction and 5° in the meridional direction centered at this grid box. This method, as a smoother, cannot only reduce the possible uncertainty due to the scattering nature of TC genesis or bias of genesis location in the TC data but also establish a stable relationship between the observed TCGF and the related environmental factors. Since the synoptic waves, such as equatorial Rossby waves, mixed-Rossby-gravity wave, and easterly wave, or other types of synoptic disturbances that trigger TC genesis have scales of about 2,000 km in the zonal direction and e-folded in the meridional direction, we chose a $20^\circ \times 10^\circ$ domain in this study (Chen and Huang, 2009).

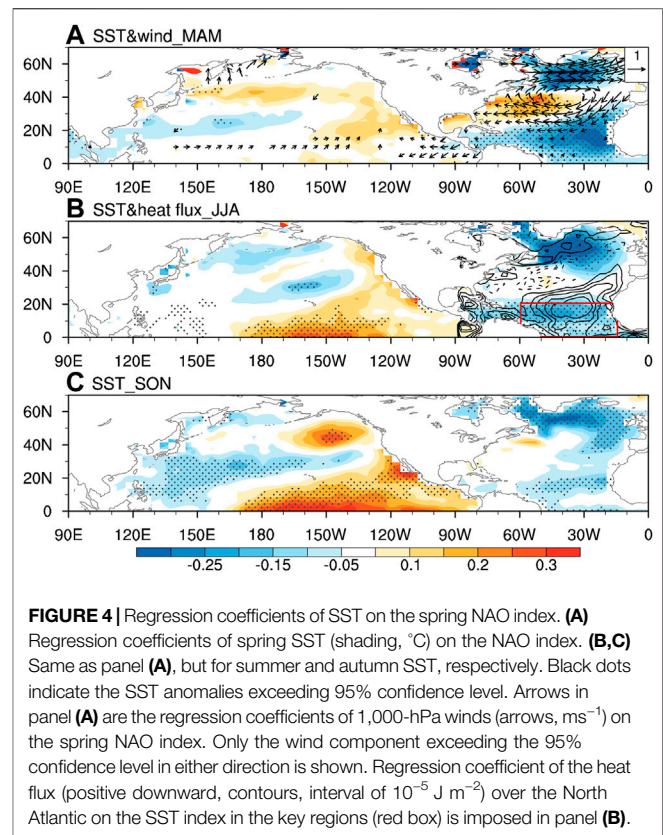
RELATIONSHIP BETWEEN THE NORTH ATLANTIC OSCILLATION AND TROPICAL CYCLONE GENESIS FREQUENCY

Figure 1 displays the correlation coefficients between the spring NAO indices from three definitions and TCGF from observational data in summer and autumn. The high correlation coefficients for all three NAO indices over the NA and NP show that the summer–autumn TCGFs are closely related to the spring NAO. During a positive NAO, the TCGF over the NA is remarkably reduced, while those over the NP could experience a tremendous increase in the following tropical cyclone (hurricane) seasons. This is consistent with the simultaneous correlation between the annual NAO and TCGF in Elsner and Kocher (2000). The out-of-phase relationship between TCGF over the North Atlantic and the North Pacific is also found in the previous studies (Maue, 2009; Wang and Lee, 2009; Wang et al., 2016). Note that the significant coefficient



concentrates on the Gulf of Mexico and Northeast Pacific (Figure 1A). We further calculated the correlation coefficients between the spring NAO index from CPC and TCGF area averaged over the whole tropical NA (90°W – 60°W , 5°N – 25°N) and NP (100°E – 90°W , 5°N – 25°N); they were -0.57 and 0.44 , respectively, all exceeding the 95% confidence level (Figure 2). This confirms the robust relationship between the spring NAO and the TCGF in summer and autumn. Moreover, the 3-month time lag coefficient indicates that the spring NAO could potentially be used to predict the TCGF over the NA and NP.

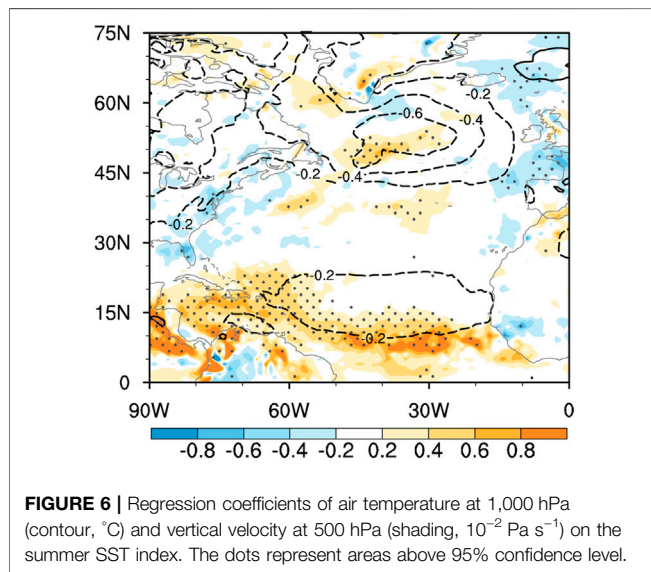
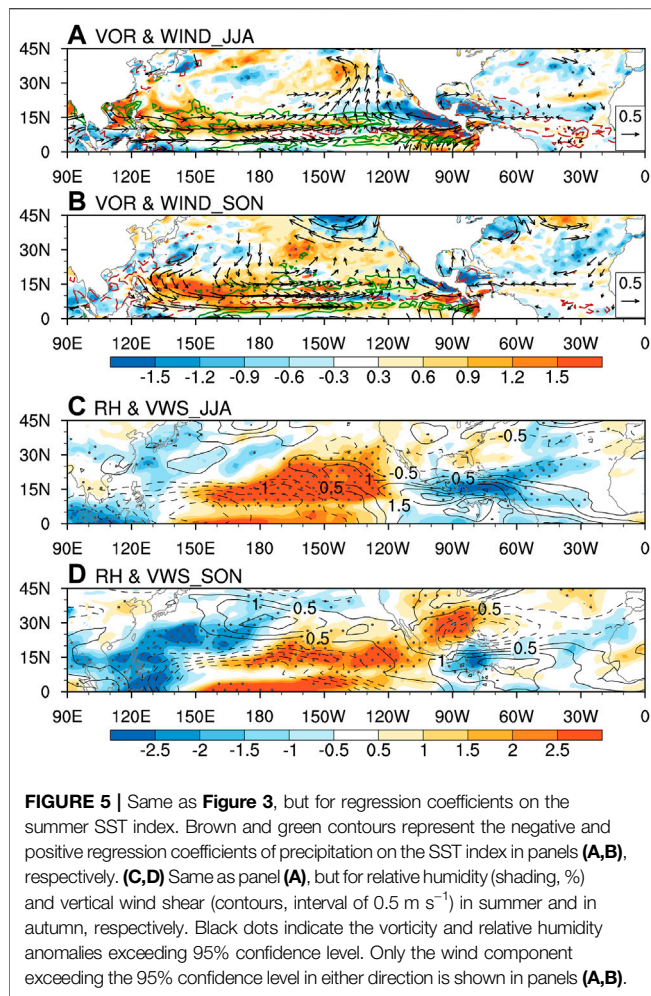
Large-scale environment parameters are considered to make great contributions in the TCGF (Gray, 1979; Wang and Wang, 2021; Zhang et al., 2020). Figure 3 shows the regression coefficients of vorticity, winds, relative humidity, and vertical wind shear on the spring NAO. For NA, the negative vorticity and relative humidity anomalies with the positive anomalous vertical wind shear appearing in summer and autumn during a positive NAO are all unfavorable for the TCGF. In contrary, the positive vorticity, the positive relative humidity, and the negative vertical wind shear anomalies favor the occurrence of the TC in the NP. Thus, the spring NAO could modulate the large-scale



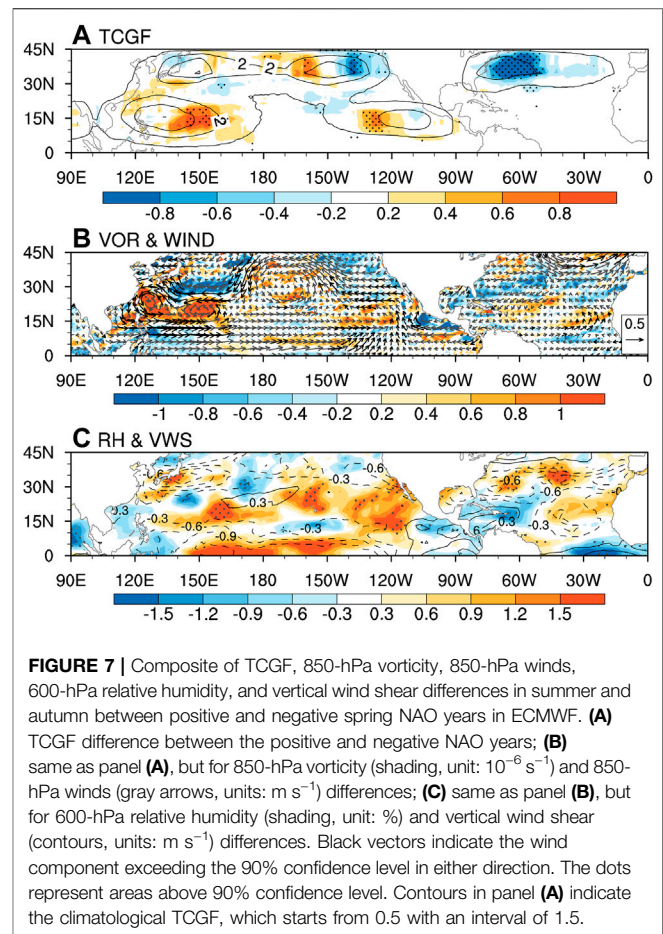
environment parameters in summer and autumn and further influence the TCGF over NA and NP. Next, we aimed to explore how the effect of the spring NAO persists into summer and autumn and plays an important role in the large-scale environment parameters closely associated with the TCGF over the NA and NP.

MECHANISM

A positive spring NAO is featured by an anti-cyclone and a cyclone over the tropical and subpolar Atlantic at 1,000 hPa, respectively (Li and Wang, 2003; Figure 4A). The surface easterly (westerly) wind anomalies south (north) of tropical anti-cyclone enhance the climatological easterly (westerly) wind and increase the heat flux released from the ocean to the atmosphere, leading to the local SST cooling (Zuo et al., 2013; Figure 4A). The negative SST anomalies can persist from spring to summer *via* the ocean memory and cool the atmosphere in summer through the heat flux (Wu et al., 2009; Figure 4B). This suggests that the spring NAO may impose significant influences on the environmental parameters associated with the TCGF *via* the NA SST in summer. Accordingly, the area-averaged negative SST anomalies over (60.5°W – 15.5°W , 0.5°N – 20.5°N), which persist from spring to summer, is defined as the SST index to further analyze how the spring NAO influence the TCGF *via* the summer NA SST. For the convenience of comparison, the sign of the SST index has been reversed. The regression coefficients of

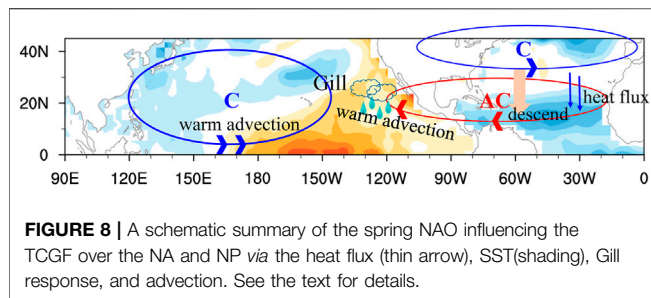


vorticity, winds, relative humidity, and vertical wind shear on the summer SST index bear high similarity to those related to the spring NAO (**Figures 3, 5**). The negative vorticity and relative



humidity with positive wind shear over the NA suppress the TCGF, while the anomalous circulations promote TCGF over the NP, forming a see-saw variability of circulations and TCGF across two basins. These confirm the bridge role of the NA SST between the spring NAO and TCGF in summer and autumn. Now, of our interest is how the SST anomaly in summer modules the large-scale conditions associated with the TCGF over the NA and NP.

Figure 6 shows the regression coefficients of air temperature at 1,000 hPa and vertical velocity at 500 hPa on the summer SST index in the NA. As expected, the negative air temperature appears over the negative SST key regions due to the heat flux anomalies (**Figure 4B**). The negative air temperature over the tropical NA corresponds to the anomalous descent, which benefits the anti-cyclonic circulation at lower troposphere and cyclonic circulation at upper troposphere in summer (Yu et al., 2016). These devote to the negative vorticity and relative humidity anomaly and positive vertical wind shear (**Figures 5A,C**), which counteract the TCGF over the NA. On the other hand, the negative air temperature and anomalous descent damp the convective activity over the tropical NA (**Figure 5A**), in turn forcing anti-cyclonic circulation to its northwest according to the Gill response (Gill, 1980; Ham et al., 2013). It also suppresses the TCGF over the NA and extends the NA anti-cyclonic circulation westward to the eastern Pacific (**Figure 5A**). Meanwhile, the



southerly wind anomaly west of the anti-cyclone increases the local SST (**Figure 4B**) and precipitation over the domain (150°W–120°W, 10°N–15°N; **Figure 5A**) through the warm advection from the equator. The increased diabatic heating associated with the enhanced precipitation triggers an anomalous cyclone to its northwest according to Gill response, which corresponds to the positive vorticity and relative humidity and fosters the TCGF over the NP (**Figure 5A**). The westerly wind south of the anomalous cyclone warms the tropical SST in the NP via transporting warm water from the warm pool (**Figure 4B**), which, in turn, enhances the cyclonic circulation via the Gill response. The anomalous cyclone and warmer SST in the tropical NP are enhanced via this air–ocean positive feedback and persist into autumn (**Figures 4C, 5B**), which benefits the NP TCGF in autumn. Yu et al. (2016) suggested that the cold NA SST anomaly can increase the TCGF in the western NP through the eastward air–sea interaction way across the Indian Ocean. We supplement that it is also feasible through the westward air–sea interaction way directly westward to the NP.

To verify the relationship between the spring NAO and TCs in summer and autumn, 35 (40) positive (negative) NAO years in five ECWMF members are selected according to the ± 0.7 normalized NAO index to composite the TCGF and the associated large-scale environment parameters (**Figure 7**). The composite summer–autumn TCGF and circulation differences reproduce the observational counteracted circulation patterns over the respective NA and NP, leading to the see-saw change in TCGF across basins. The TCs significantly increases in the NP but decreases in the NA (**Figure 7A**). The positive (negative) vorticity and relative humidity with negative (positive) vertical wind shear benefit (suppress) the TCs in the NP (NA, **Figures 7B,C**). Note that the negative TCGF over the NA shifts northward and locates around 30°N compared with the observation (**Figure 1A**), which may be due to the simulation northward bias of the climatological TCGF over the NA.

Thus, the positive NAO in spring can induce negative SST anomalies over the NA, which persist into summer. In summer, the tropical negative SST anomalies lead to a low-level anti-cyclonic circulation through heat fluxes and Gill response, which damps the TCGF over the NA. Meanwhile, the anti-cyclonic circulation benefits its west precipitation; the precipitation anomalies further forced an anomalous cyclonic circulation over the NP via Gill response and devoted the TCGF over the NP. The westerly wind south of the anomalous cyclone warms the tropical SST in the NP and enhances the cyclone via the air–ocean positive feedback, which benefits the TCGF over the NP in autumn.

SUMMARY AND DISCUSSION

This study investigates the influence of spring NAO on the NH TCGF in summer and autumn and finds that positive NAO suppresses (benefits) the TCGF over the NA (NP) through modulating the vorticity, relative humidity, and vertical wind shear. The positive NAO in spring can induce negative SST anomalies over the NA, which persist into summer via ocean memory. The tropical negative SST anomalies cool the overlying atmosphere and damp the precipitation, leading to a low-level anti-cyclonic circulation. The anti-cyclonic circulation devotes negative vorticity, negative relative humidity, and positive vertical wind shear, all counteracting the TCGF over the NA. The southerly west of the anti-cyclonic circulation increases the local SST and precipitation. Accordingly, a cyclonic circulation appears in the western Pacific via Gill response. The cyclonic circulation sustains from summer to autumn via the warm advection by its westerly wind and fosters the TCGF in the NP (**Figure 8**).

The SST anomaly associated with the spring NAO bears some similarities to the ENSO evolution from summer to autumn (**Figure 4**; Chen et al., 2014); we further check the modulation of the ENSO on the relationship between the spring NAO and TCGF. The results are not changed with the preceding winter ENSO signal removed in advanced (not shown). Although the preceding influence of the NAO on the TCGF has been investigated by Choi and Cha (2017) and Zhou and Chen (2020), this study focuses on the NH influence rather than the western NP. More importantly, the NAO index used in this study is averaged over the spring season, which leads the summer and autumn TCGF over the NH. It implies that the NAO could be a good candidate for predicting the TC activity over the specific regions of the NH in the following typhoon season.

DATA AVAILABILITY STATEMENT

The original contributions presented in the study are included in the article/Supplementary Material, further inquiries can be directed to the corresponding author.

AUTHOR CONTRIBUTIONS

LZ and XY contributed to figures included in this manuscript. LZ and JZ wrote the manuscript. All authors contributed to the article and approved the submitted version.

FUNDING

This work was supported by the Natural Science Foundation of China (Grant Nos. 42088101, 42105022 and 42005033).

ACKNOWLEDGMENTS

We thank two reviewers for their insightful suggestions and comments.

REFERENCES

- Barnston, A. G., and Livezey, R. E. (1987). Classification, Seasonality and Persistence of Low-Frequency Atmospheric Circulation Patterns. *Mon. Wea. Rev.* 115, 1083–1126. doi:10.1175/1520-0493(1987)115<1083:csapol>2.0.co;2
- Cao, X., Chen, S., Chen, G., and Wu, R. (2016). Intensified Impact of Northern Tropical Atlantic SST on Tropical Cyclogenesis Frequency over the Western North Pacific after the Late 1980s. *Adv. Atmos. Sci.* 33, 919–930. doi:10.1007/s00376-016-5206-z
- Chan, J. C., and Xu, M. (2009). Inter-annual and Inter-decadal Variations of Landfalling Tropical Cyclones in East Asia. Part I: Time Series Analysis. *Int. J. Climatol.* 35 (11), 3353–3361. doi:10.1002/joc.1782
- Chen, D., Wang, H., Liu, J., and Li, G. (2015a). Why the spring North Pacific Oscillation Is a Predictor of Typhoon Activity over the Western North Pacific. *Int. J. Climatol.* 35, 3353–3361. doi:10.1002/joc.4213
- Chen, X., Wang, Y., and Zhao, K. (2015b). Synoptic Flow Patterns and Large-Scale Characteristics Associated with Rapidly Intensifying Tropical Cyclones in the South China Sea. *Mon. Weather Rev.* 143, 64–87. doi:10.1175/MWR-D-13-00338.1
- Chen, G., and Huang, R. (2009). Interannual Variations in Mixed Rossby-Gravity Waves and Their Impacts on Tropical Cyclogenesis over the Western North Pacific. *J. Clim.* 22, 535–549. doi:10.1175/2008JCLI2221.1
- Chen, S., Yu, B., and Chen, W. (2014). An Analysis on the Physical Process of the Influence of AO on ENSO. *Clim. Dyn.* 42, 973–989. doi:10.1007/s00382-012-1654-z
- Choi, K.-S., and Byun, H.-R. (2010). Possible Relationship between Western North Pacific Tropical Cyclone Activity and Arctic Oscillation. *Theor. Appl. Climatol.* 100, 261–274. doi:10.1007/s00704-009-0187-9
- Choi, J.-W., and Cha, Y. (2017). Possible Relationship between NAO and Tropical Cyclone Genesis Frequency in the Western North Pacific. *Dyn. Atmospheres Oceans* 77, 64–73. doi:10.1016/j.dynatmoce.2016.08.006
- Du, Y., Yang, L., and Xie, S.-P. (2011). Tropical Indian Ocean Influence on Northwest Pacific Tropical Cyclones in Summer Following Strong El Niño*. *J. Clim.* 24, 315–322. doi:10.1175/2010JCLI3890.1
- Du, Y., Zhang, J., Zhao, S., and Chen, H. (2020). Impact of the Eastward Shift in the Negative-phase NAO on Extreme Drought over Northern China in Summer. *J. Geophys. Res. Atmos.* 125, e2019JD032019. doi:10.1029/2019JD032019
- Elsner, J. B., and Kocher, B. (2000). Global Tropical Cyclone Activity: a Link to the North Atlantic Oscillation. *Geophys. Res. Lett.* 27, 129–132. doi:10.1029/1999gl010893
- Gill, A. E. (1980). Some Simple Solutions for Heat-Induced Tropical Circulation. *Q. J. R. Met. Soc.* 106, 447–462. doi:10.1002/qj.49710644905
- Gray, G. M. (1979). “Hurricanes: Their Formation, Structure and Likely Role I the Tropical Circulation,” in *Meteorology over Tropical Oceans*. Editor D. B. Shaw (Bracknell: Royal Meteorological Society), 155–218.
- Ham, Y.-G., Kug, J.-S., Park, J.-Y., and Jin, F.-F. (2013). Sea Surface Temperature in the north Tropical Atlantic as a Trigger for El Niño/Southern Oscillation Events. *Nat. Geosci.* 6, 112–116. doi:10.1038/ngeo1686
- Hersbach, H., Bell, B., Berrisford, P., Hirahara, S., Horányi, A., Muñoz-Sabater, J., et al. (2020). The ERA5 Global Reanalysis. *Q. J. R. Meteorol. Soc.* 146, 1999–2049. doi:10.1002/qj.3803
- Jianping, L., and Wang, J. X. L. (2003). A New North Atlantic Oscillation index and its Variability. *Adv. Atmos. Sci.* 20, 661–676. doi:10.1007/BF02915394
- Jones, P. D., Jonsson, T., and Wheeler, D. (1997). Extension to the North Atlantic Oscillation Using Early Instrumental Pressure Observations from Gibraltar and South-West Iceland. *Int. J. Climatol.* 17, 1433–1450. doi:10.1002/(sici)1097-0088(19971115)17:13<1433:aid-joc203>3.0.co;2-p
- Kossin, J. P., Emanuel, K. A., and Camargo, S. J. (2016). Past and Projected Changes in Western North Pacific Tropical Cyclone Exposure. *J. Clim.* 29, 5725–5739. doi:10.1175/JCLI-D-16-0076.1
- Li, T. (2012). in *Synoptic and Climatic Aspects of Tropical Cyclogenesis in Western North Pacific*. Editors K. Oouchi and H. Fudeyasu, 61–94. Chap. 3.
- Lu, M., and Xiong, R. (2019). Spatiotemporal Profiling of Tropical Cyclones Genesis and Favorable Environmental Conditions in the Western Pacific Basin. *Geophys. Res. Lett.* 46, 11548–11558. doi:10.1029/2019GL084995
- Maue, R. N. (2009). Northern Hemisphere Tropical Cyclone Activity. *Geophys. Res. Lett.* 36, L05805. doi:10.1029/2008GL035946
- Mei, W., Kamae, Y., Xie, S.-P., and Yoshida, K. (2019). Variability and Predictability of North Atlantic Hurricane Frequency in a Large Ensemble of High-Resolution Atmospheric Simulations. *J. Clim.* 32, 3153–3167. doi:10.1175/JCLI-D-18-0554.1
- Murakami, H., Vecchi, G. A., Underwood, S., Delworth, T. L., Wittenberg, A. T., Anderson, W. G., et al. (2015). Simulation and Prediction of Category 4 and 5 Hurricanes in the High-Resolution GFDL HiFLOR Coupled Climate Model*. *J. Clim.* 28, 9058–9079. doi:10.1175/JCLI-D-15-0216.1
- Murakami, H., Wang, B., and Kitoh, A. (2011). Future Change of Western North Pacific Typhoons: Projections by a 20-Km-Mesh Global Atmospheric Model*. *J. Clim.* 24 (4), 1154–1169. doi:10.1175/2010JCLI3723.1
- Nie, Y., Ren, H.-L., and Scaife, A. A. (2020). Enhanced Mid-to-late winter Predictability of the Storm Track Variability in the North Pacific as a Contrast with the North Atlantic. *Environ. Res. Lett.* 15, 094037. doi:10.1088/1748-9326/ab9c4d
- Patricola, C. M., Chang, P., and Saravanan, R. (2016). Degree of Simulated Suppression of Atlantic Tropical Cyclones Modulated by Flavour of El Niño. *Nat. Geosci.* 9, 155–160. doi:10.1038/ngeo2624
- Peduzzi, P., Chatenoux, B., Dao, H., De Bono, A., Herold, C., Kossin, J., et al. (2012). Global Trends in Tropical Cyclone Risk. *Nat. Clim Change* 2, 289–294. doi:10.1038/nclimate1410
- Pu, X., Chen, Q., Zhong, Q., Ding, R., and Liu, T. (2019). Influence of the North Pacific Victoria Mode on Western North Pacific Tropical Cyclone Genesis. *Clim. Dyn.* 52, 245–256. doi:10.1007/s00382-018-4129-z
- Rayner, N. A. (2003). Global Analyses of Sea Surface Temperature, Sea Ice, and Night marine Air Temperature since the Late Nineteenth century. *J. Geophys. Res.* 108 (D14). doi:10.1029/2002JD002670
- Schultz, L. A., and Cecil, D. J. (2009). Tropical Cyclone Tornadoes, 1950–2007. *Mon. Weather. Rev.* 137, 3471–3484. doi:10.1175/2009mwr2896.1
- Tao, L., Wu, L., Wang, Y., and Yang, J. (2012). Influence of Tropical Indian Ocean Warming and ENSO on Tropical Cyclone Activity over the Western North Pacific. *J. Meteorol. Soc. Jpn.* 90, 127–144. doi:10.2151/jmsj.2012-107
- Walker, G. T. (1924). *Everyone's Book of the Weather*. By A. Francon Williams. London (The Sheldon Press), 1923. 16°. Pp. 117. 2s. 6d. Net. *Q. J. R. Meteorol. Soc.* 50, 275. doi:10.1002/qj.49705021136
- Wang, B., Xiang, B., and Lee, J.-Y. (2013). Subtropical High Predictability Establishes a Promising Way for Monsoon and Tropical Storm Predictions. *Proc. Natl. Acad. Sci.* 110, 2718–2722. doi:10.1073/pnas.1214626110
- Wang, C., and Lee, S.-K. (2009). Co-variability of Tropical Cyclones in the North Atlantic and the Eastern North Pacific. *Geophys. Res. Lett.* 36, L24702. doi:10.1029/2009GL041469
- Wang, C., and Wang, B. (2021). Impacts of the South Asian High on Tropical Cyclone Genesis in the South China Sea. *Clim. Dyn.* 56, 2279–2288. doi:10.1007/s00382-020-05586-8
- Wang, H., Long, L., Kumar, A., Wang, W., Schemm, J.-K. E., Zhao, M., et al. (2014). How Well Do Global Climate Models Simulate the Variability of Atlantic Tropical Cyclones Associated with ENSO? *J. Clim.* 27 (15), 5673–5692. doi:10.1175/jcli-d-13-00625.1 Available from: <https://10.1175/JCLI-D-13-00625.1>
- Wang, C., Wang, L., Wang, X., Wang, D., and Wu, L. (2016). North-south Variations of Tropical Storm Genesis Locations in the Western Hemisphere. *Geophys. Res. Lett.* 43, 11367–11374. doi:10.1002/2016GL071440
- Wettstein, J. J., and Wallace, J. M. (2010). Observed Patterns of Month-To-Month Storm-Track Variability and Their Relationship to the Background Flow*. *J. Atmos. Sci.* 67, 1420–1437. doi:10.1175/2009JAS3194.1
- Wu, Z., Wang, B., Li, J., and Jin, F.-F. (2009). An Empirical Seasonal Prediction Model of the East Asian Summer Monsoon Using ENSO and NAO. *J. Geophys. Res.* 114, D18120. doi:10.1029/2009JD011733
- Yu, J., Li, T., Tan, Z., and Zhu, Z. (2016). Effects of Tropical North Atlantic SST on Tropical Cyclone Genesis in the Western North Pacific. *Clim. Dyn.* 46, 865–877. doi:10.1007/s00382-015-2618-x
- Yu, J. H., Ou, L., Chen, L., Li, L., Sun, M., Zhong, X., et al. (2021). Tropical Cyclone Genesis over the Western North Pacific Impacted by SST Anomalies from Other Basins while El Niño Decays. *Q. J. R. Meteorol. Soc.* 147, 2580–2596. doi:10.1002/qj.4042
- Zhan, R., Wang, Y., and Lei, X. (2011). Contributions of ENSO and East Indian Ocean SSTA to the Interannual Variability of Northwest Pacific Tropical Cyclone Frequency*. *J. Clim.* 24, 509–521. doi:10.1175/2010jcli3808.1

- Zhang, W., Villarini, G., and Vecchi, G. A. (2020). The East Asian Subtropical Jet Stream and Atlantic Tropical Cyclones. *Geophys. Res. Lett.* 47, e2020GL088851. doi:10.1029/2020GL088851
- Zhao, H., and Wang, C. (2019). On the Relationship between ENSO and Tropical Cyclones in the Western North Pacific during the Boreal Summer. *Clim. Dyn.* 52, 275–288. doi:10.1007/s00382-018-4136-0
- Zhao, J., Zhan, R., and Wang, Y. (2020a). Different Responses of Tropical Cyclone Tracks over the Western North Pacific and North Atlantic to Two Distinct Sea Surface Temperature Warming Patterns. *Geophys. Res. Lett.* 47 (7), e2019GL086923. doi:10.1029/2019GL086923
- Zhao, J., Zhan, R., Wang, Y., Xie, S.-P., and Wu, Q. (2020b). Untangling Impacts of Global Warming and Interdecadal Pacific Oscillation on Long-Term Variability of North Pacific Tropical Cyclone Track Density. *Sci. Adv.* 6 (41), aba6813. doi:10.1126/sciadv.aba6813
- Zhou, B., and Cui, X. (2014). Interdecadal Change of the Linkage between the North Atlantic Oscillation and the Tropical Cyclone Frequency over the Western North Pacific. *Sci. China Earth Sci.* 57 (9), 2148–2155. doi:10.1007/s11430-014-4862-z
- Zhou, Q., and Chen, W. (2020). Unstable Relationship between spring NAO and Summer Tropical Cyclone Genesis Frequency over the Western North Pacific. *Acta Oceanol. Sin.* 39 (5), 65–76. doi:10.1007/s13131-019-1509-0
- Zuo, J.-Q., Li, W.-J., Ren, H.-L., and Chen, L.-J. (2012). Change of the Relationship between the spring NAO and East Asian Summer Monsoon and its Possible Mechanism. *Chin. J. Geophys.* 55, 23–34. doi:10.1002/cjg2.1697
- Zuo, J., Li, W., Sun, C., Xu, L., and Ren, H.-L. (2013). Impact of the North Atlantic Sea Surface Temperature Tripole on the East Asian Summer Monsoon. *Adv. Atmos. Sci.* 30, 1173–1186. doi:10.1007/s00376-012-2125-5

Conflict of Interest: The authors declare that the research was conducted in the absence of any commercial or financial relationships that could be construed as a potential conflict of interest.

Publisher's Note: All claims expressed in this article are solely those of the authors and do not necessarily represent those of their affiliated organizations, or those of the publisher, the editors, and the reviewers. Any product that may be evaluated in this article, or claim that may be made by its manufacturer, is not guaranteed or endorsed by the publisher.

Copyright © 2022 Zhang, Yang and Zhao. This is an open-access article distributed under the terms of the Creative Commons Attribution License (CC BY). The use, distribution or reproduction in other forums is permitted, provided the original author(s) and the copyright owner(s) are credited and that the original publication in this journal is cited, in accordance with accepted academic practice. No use, distribution or reproduction is permitted which does not comply with these terms.



Risk Assessment of Typhoon Disaster Chains in the Guangdong–Hong Kong–Macau Greater Bay Area, China

Yujie Wang^{1,2}, Yizhou Yin^{3*} and Lianchun Song³

¹Key Laboratory of Meteorological Disaster, Ministry of Education/International Joint Research Laboratory on Climate and Environment Change/Collaborative Innovation Center on Forecast and Evaluation of Meteorological Disasters, Nanjing University of Information Science and Technology, Nanjing, China, ²School of Atmospheric Sciences, Nanjing University of Information Science and Technology, Nanjing, China, ³National Climate Center, China Meteorological Administration, Beijing, China

OPEN ACCESS

Edited by:

Yihong Duan,
Chinese Academy of Meteorological
Sciences, China

Reviewed by:

Shibin Xu,
Ocean University of China, China
Mei Liang,
Guangdong Ocean University, China
Li Dong,
Southern University of Science and
Technology, China

*Correspondence:

Yizhou Yin
yin_yizhou@foxmail.com

Specialty section:

This article was submitted to
Atmospheric Science,
a section of the journal
Frontiers in Earth Science

Received: 20 December 2021

Accepted: 08 February 2022

Published: 11 March 2022

Citation:

Wang Y, Yin Y and Song L (2022) Risk
Assessment of Typhoon Disaster
Chains in the Guangdong–Hong
Kong–Macau Greater Bay Area, China.
Front. Earth Sci. 10:839733.
doi: 10.3389/feart.2022.839733

The typhoon disaster chain is one of the leading climate risks in constructing the Guangdong–Hong Kong–Macau Greater Bay Area (GBA). In this study, the risks of the typhoon disaster chains including typhoon-induced gales, rainstorms, and storm surges in the GBA, as well as the comprehensive risk of typhoon disaster, are investigated at county level by comprehensively analyzing the hazard, exposure, and vulnerability. The results show that the high- and very-high-risk areas of typhoon–gale disaster chain are located in Zhuhai, Zhongshan, Foshan, Dongguan, central-southern Jiangmen, southern Shenzhen, and parts of Huizhou. The high- and very high-risk areas of typhoon–rainstorm disaster chain include Zhuhai, Zhongshan, Shenzhen, central-southern Foshan, northern Dongguan, central Jiangmen, and central Huizhou. Regarding the typhoon–storm surge disaster chain, the areas at high and very high risk are located in Zhuhai, eastern Zhongshan, and the coastal areas of the Pearl River Estuary. In addition, the comprehensive risk of typhoon disaster is very high in Zhuhai and high in Zhongshan, Jiangmen, Dongguan, and Shenzhen. By verifying the spatial correlation between typhoon disaster risk indexes and actual losses, it is found that the comprehensive risk index of typhoon disaster constructed in this study can better reflect the actual losses. Overall, the findings of this study can provide a scientific basis for typhoon disaster prevention and mitigation in the GBA, and it can also serve as a reference for typhoon disaster risk research in other areas.

Keywords: typhoon, disaster chain, risk, guangdong–Hong Kong–Macau Greater Bay Area, hazard

INTRODUCTION

The typhoon disaster chain is a series of disaster phenomena caused by typhoons, and it is composed of gales, rainstorms, and storm surges, as well as a series of secondary disasters induced by them. The spatiotemporal chain reactions of typhoon disaster chains can amplify disaster situations (Shi et al., 1991; Shi et al., 2010; Yu et al., 2014; Shi et al., 2014). In the context of global warming, the intensity and destructiveness of typhoons have increased significantly, and the proportion of super typhoon has grown remarkably (Webster et al., 2005; Emanuel, 2005; Mendelsohn et al., 2012; IPCC 2013), resulting in more frequent catastrophic events. With population growth, urbanization, and climate change in the past decades, the losses of life and property caused by typhoon disaster chains have

risen noticeably (Pielke et al., 2005; Pielke et al., 2008; Fengjin and Ziniu, 2010; Fischer et al., 2015; Chen et al., 2021).

The coastal areas of China have developed economies and dense population. On average, about seven typhoons landed in China per year in recent 30 years. From 2004 to 2015, the direct economic losses and fatalities caused by typhoon disasters respectively accounted for 18.3% and 50.2% of those caused by all meteorological disasters (Wang Y. et al., 2016). Approximately 6.3% of the coastal areas in China have a high-risk level of typhoon-induced disasters, and they mainly concentrate in coastal river delta regions (Yin et al., 2013). Guangdong Province has the longest coastline in China, and its coastal cities have developed socioeconomic and a significantly larger population than other provinces. Simultaneously, it is also one of the provinces suffering from the most severe typhoon disasters in China (Wang R. et al., 2016; Luo et al., 2018). The Guangdong–Hong Kong–Macau Greater Bay Area (GBA), located in the central coastal area of Guangdong, is the most economically developed and densely populated region of Guangdong and is also the region with the highest risk level of typhoon disaster (Yin et al., 2012; Xu et al., 2015). In the past 10 years, the number and intensity of super typhoons affecting the GBA have increased significantly (Wang et al., 2021a). For example, in August 2017, two typhoons directly attacked Jinwan District, Zhuhai City of the GBA during just 4 days. The short time interval of the two typhoons and the high overlap of their landing location set new meteorological records. Specifically, the strong typhoon “Hato (2017)” was one of the most serious typhoons affecting Zhuhai in history, leading to serious economic losses. In summary, the typhoon disaster is one of the main climate risks in the construction of GBA in the future.

Previous studies on typhoons in China mainly focused on the characteristics, causes, and the impacts of typhoon-induced gale and heavy rainfall (Fengjin and Ziniu, 2010; Yin et al., 2013; Deng et al., 2015). Chou et al. (2020) pointed out that the direct economic losses caused by typhoons in China showed a remarkable interdecadal increasing trend, and the losses gradually transferred from the primary industry to the secondary and tertiary industries. In recent years, the disasters caused by typhoons have attracted more and more concerns. Scholars assessed the hazard, vulnerability, exposure, and the risks of typhoon disasters in coastal areas of China (Niu et al., 2011; Ye et al., 2019). Some studies proposed a classification system of typhoon disaster chains, mainly including typhoon–gale chain (a series of disaster phenomena caused by typhoon wind force), typhoon–rainstorm chain (a series of disaster phenomena caused by typhoon rainstorm), and typhoon–storm surge chain (a series of disaster phenomena caused by typhoon storm surge), and they statistically derived the regional characteristics of disaster intensity and types (Chen et al., 2011; Shuai et al., 2012; Wang R. et al., 2016; Shih et al., 2018; Yu et al., 2019; Ye et al., 2014, 2020). In addition, they found that typhoon disasters are related to the track of landing typhoon, and rainstorm is the main factor causing typhoon

disasters. Moreover, some scholars used the geographical information system technology to assess typhoon disaster risk and discussed the causes and laws of typhoon disaster chains at city level of Guangdong (Pan et al., 2002; Tang and Liang, 2006; Zhang et al., 2017). However, these studies did not systematically analyze the influence mechanisms of hazard factors and disaster-pregnant environments for different typhoon disaster chains. Meanwhile, the researches on typhoon disaster risk at county level are insufficient (Gemmer et al., 2011).

Therefore, in this study, based on the disaster data and observation data of typhoons from 2009 to 2020, the hazard, exposure, vulnerability, and the related mechanisms on typhoon disaster chains are analyzed at county level in the GBA. Moreover, the risks of typhoon–gale, typhoon–rainstorm, and typhoon–storm surge disaster chains, as well as the typhoon comprehensive risk, are studied in detail. We hope our results can provide scientific support for typhoon disaster prevention and mitigation in the GBA.

The remainder of this article is organized as follows. **Section 2** briefly introduces the study area, various data and methods used in this study. The results are presented in **Section 3**. Finally, **Section 4** provides the conclusions and discussion.

Study Area, Data, and Methods

Study Area

The GBA is one of the regions with the highest degree of openness and the strongest economic vitality in China, which is located in the subtropical region of South China and composed of nine cities in the Pearl River Delta (Guangzhou, Shenzhen, Zhuhai, Foshan, Huizhou, Dongguan, Zhongshan, Jiangmen, and Zhaoqing) and two Special Administrative Regions (Hong Kong and Macau). The GBA includes 48 counties (districts), with a total area of 56,000 km². By the end of 2020, the permanent resident population in the GBA exceeded 72 million, and the gross domestic product (GDP) was more than 11 trillion yuan.

The GBA is adjacent to the Western Pacific and suffers from great impact of landfall typhoons (Wang et al., 2021a). The river systems in this region are numerous, complex, and staggered, and the river network is densely distributed. Therefore, when superimposed with the flood peaks of rivers, the heavy rainfall brought by typhoons is prone to cause floods and mountain torrents (Zhang et al., 2017). The terrain of GBA is high in the north and low in the south, surrounded by hilly mountains in the west, north, and east. Thus, in the GBA, the geological disasters such as landslide and debris flow often occur under the influence of heavy typhoon rainfall (Zhao et al., 2014). The central-southern GBA is mainly composed of alluvial plains, which are distributed in the main cities in the GBA. Hence, heavy rainfall in this area can easily cause urban waterlogging (Chen et al., 2017). The topography of the GBA plain areas is low and flat, with an average altitude of approximately only 50 m, so the GBA lacks a natural barrier against typhoon-induced gales (Yin et al., 2012). In addition, there are many trumpet-shaped

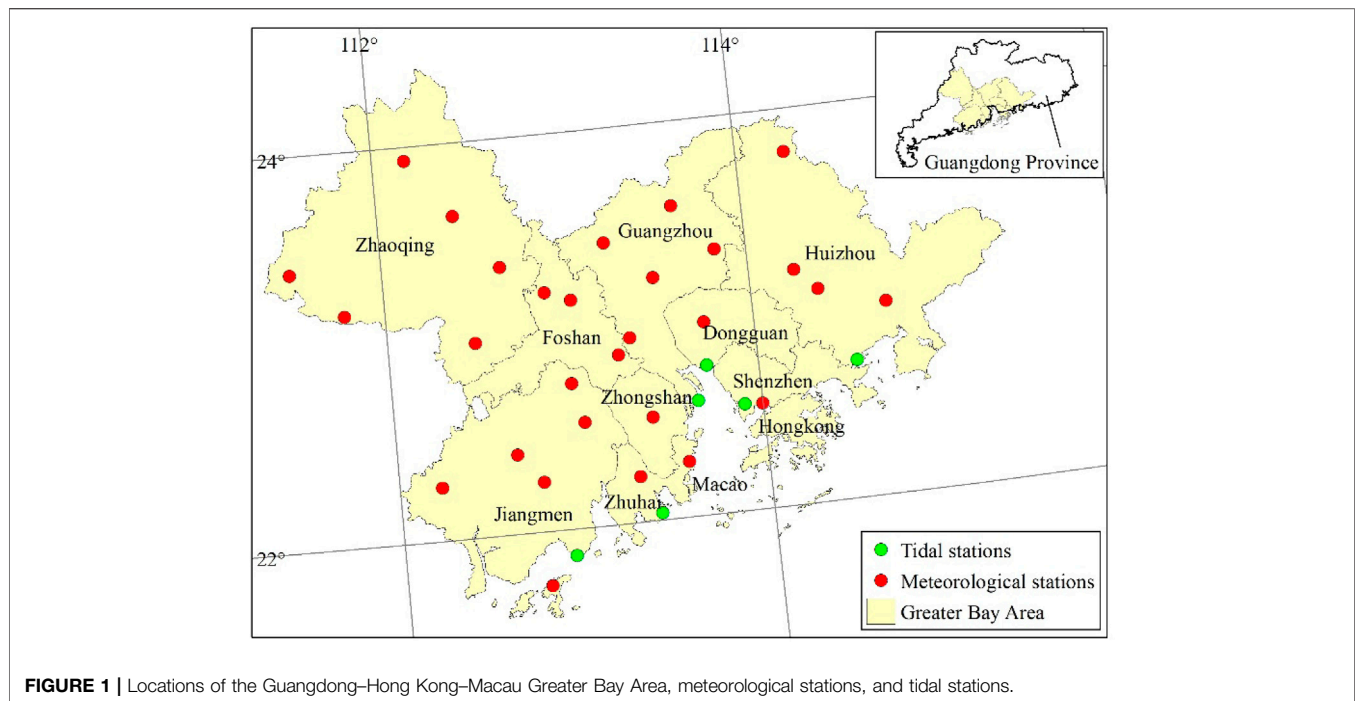


FIGURE 1 | Locations of the Guangdong–Hong Kong–Macau Greater Bay Area, meteorological stations, and tidal stations.

estuaries near shore in the GBA, which exacerbates the impact of storm surge in estuaries and ports. Once superimposed with the astronomical spring tides, the storm surge disasters may aggravate (Pang et al., 2020).

Data

Because of the lack of daily meteorological observation data and typhoon disaster data for Hong Kong and Macau, the study area of this research is mainly the Chinese mainland of GBA. The daily (from previous 20:00 to current 20:00 China Standard Time) precipitation and daily maximum wind speed data from 29 meteorological stations used in this study (Figure 1) are obtained from the Daily Meteorological Dataset of Basic Meteorological Elements of China National Surface Weather Station released by the National Meteorological Information Center of the China Meteorological Administration (China Meteorological Administration, 1991–2018; Ren et al., 2012). The daily values of meteorological observation since the establishment of the meteorological station are included in this dataset. Daily maximum wind speed is the maximum average wind speed of 10 min in 1 day. The historical typhoon data are from the Tropical Cyclone Best Track Dataset issued by the Shanghai Typhoon Institute, CMA, including the longitude, latitude, wind speed, and intensity of the typhoon center every 6 h (Ying et al., 2014). According to the national standard (GB/T 19,201–2006; grade of tropical cyclones) issued by the China Meteorological Administration, 2006, based on the maximum average wind speed of 2 min at the low level near the tropical cyclone center (V_c), tropical cyclones are classified into six grades: tropical depression ($10.8 \text{ m s}^{-1} \leq V_c \leq 17.1 \text{ m s}^{-1}$), tropical storm ($17.2 \text{ m s}^{-1} \leq V_c \leq 24.4 \text{ m s}^{-1}$),

severe tropical storm ($24.5 \text{ m s}^{-1} \leq V_c \leq 32.6 \text{ m s}^{-1}$), typhoon ($32.7 \text{ m s}^{-1} \leq V_c \leq 41.4 \text{ m s}^{-1}$), severe typhoon ($41.5 \text{ m s}^{-1} \leq V_c \leq 50.9 \text{ m s}^{-1}$), and super typhoon ($V_c \geq 51.0 \text{ m s}^{-1}$).

The storm surge data used in this study are derived from the Bulletin of China Marine Disaster (2009–2020) released annually by the Ministry of Natural Resources, 2009–2020, including the daily peak surge (PS) and ultrawarning tidal level (UWT) from five tidal stations, that is, Taishan, Sanzao, Hengmen, Chiwan, and Huizhou stations. UWT refers to the tide level when the warning threshold is exceeded.

The typhoon disaster data are from the annual climate assessment report (2009–2020) released by the National Climate Center, including disaster-affected population, death tolls, missing persons, disaster-affected area, collapsed buildings, and direct economic losses. The economic losses are converted based on the price in 2020. The conversion coefficient is the quotient of the 2020 retail price index and the current year's index. The population and GDP grid data with a resolution of 1 km in 2015 are from the Resource and Environment Science and Data Center of the Institute of Geographic Sciences and Natural Resources Research, Chinese Academy of Sciences (<http://www.resdc.cn/Default.aspx>). The digital elevation model and river data of disaster-pregnant environment with the resolution of 1 km in 2015 are obtained from the 1:250,000 scale topographic database of the National Geomatic Center of China (Wang et al., 2001). The land use data (1-km resolution) in 2015 are obtained from the Institute of Geographic Sciences and Natural Resources Research, Chinese Academy of Sciences (Xu and Gong, 2018). The vegetation coverage in 2015 is calculated based on the Normalized Difference Vegetation Index product (1-km

resolution) from the Moderate Resolution Imaging Spectroradiometer (Didan 2015).

Methods

Standardization

The standardization method of elements is as follows (Eq. 1).

$$D_i = 0.5 + 0.5 \times \frac{A_i - \min_i}{\max_i - \min_i} \quad (1)$$

where D_i denotes the standardized value of the i th element, A_i is the i th element value, \min_i is the minimum of the i th element, and \max_i is the maximum of the i th element.

Hazard Index

The maximum value of the daily maximum wind speed (MW) during a typhoon process is used as the hazard factor of the typhoon–gale disaster chain. The accumulated precipitation (AP) and maximum daily precipitation (MP) during the process are considered as the hazard factors of the typhoon–rainstorm disaster chain.

In this study, the equation for calculating the hazard of typhoon–gale and typhoon–rainstorm disaster chains is as follows (Eq. 2).

$$H = \sum_{l=1}^L (w_l \cdot P_l) \quad (2)$$

where H denotes the hazard factor, l ($l = 1, \dots, L$) represents the level interval of hazard factors, and w_l and P_l are, respectively, the weighting coefficient of the l th interval and the cumulative probability of a hazard factor in this interval. In this study, the probability calculation mainly adopts the information diffusion technology (Huang, 2005) that is mainly used to solve the probability distribution estimation of the small sample with insufficient information and incomplete data. The calculation method of probability is as follows. It is assumed that X ($X = \{x_1, x_2, \dots, x_i, \dots, x_m\}$) is the sample of the hazard factor at a meteorological station, and U ($U = \{u_1, u_2, \dots, u_j, \dots, u_n\}$) is the set of possible values of X and is called the universe of X . In this study, the step size is 1. In addition, for the sample sequence of a hazard factor at all meteorological stations in the GBA, the integral parts of its minimum and maximum values are taken as the starting and ending points, respectively. According to the following equation (Eq. 3), a single-valued observation sample X_i can diffuse its information to every point in the set U .

$$f_i(u_j) = \frac{1}{\delta\sqrt{2\pi}} e^{-\frac{(x_i - u_j)^2}{2\delta^2}} \quad (3)$$

where δ is the diffusion coefficient, which can be determined according to the maximum value b , minimum value a , and the number of samples m in the sample set. The calculation equation of δ is as follows (Eq. 4). The number of samples required to participate in the calculation must be 5 or more. If it is fewer than 5, the final probability value will be 0.

$$\delta = \begin{cases} 0.8146(b-a), m=5 \\ 0.5690(b-a), m=6 \\ 0.4560(b-a), m=7 \\ 0.3860(b-a), m=8 \\ 0.3362(b-a), m=9 \\ 0.2986(b-a), m=10 \\ 2.6851(b-a)/(m-1), m \geq 11 \end{cases} \quad (4)$$

The occurrence probability of u_j is as follows (Eq. 5).

$$P(u_j) = \sum_{i=1}^m \mu_{x_i}(u_j) / \sum_{j=1}^n \sum_{i=1}^m \mu_{x_i}(u_j) \quad (5)$$

where

$$\mu_{x_i}(u_j) = f_i(u_j) / \sum_{j=1}^n f_i(u_j) \quad (6)$$

The cumulative probability P_l in each level interval is obtained by accumulating $P(u_j)$ in the corresponding level interval of a hazard factor.

In this study, one typhoon that brings negative effect to the GBA and leads to disasters is defined as a disaster-causing typhoon. Once a typhoon disaster occurs in a county, a disaster-causing typhoon is recorded in that county. Thus, a total of 186 disaster-causing typhoon samples in all counties of the GBA from 2009 to 2020 are obtained. The MW, AP, and MP values of these samples are extracted to calculate the mean value and standard deviation of the MW, AP, and MP sequences. Typhoons sometimes have a beneficial impact, such as alleviating drought. In order to avoid the “good typhoon” in the risk assessment, we define the assessment starting point, which is similar to the hazard threshold. In this study, disaster-causing typhoons are used to determine the assessment starting point. Based on the difference between the mean value and standard deviation, the starting points of the assessment for the MW, AP, and MP are 13.5 m s^{-1} , 65 and 50 mm, respectively. As long as the values of wind speed and precipitation exceed the assessment starting point, typhoons are regarded as samples of hazard index calculation in the county, even if there is no economic loss. According to different wind speed and precipitation, the MW, AP, and MP can be divided into five levels, as shown in Table 1 (Zhu et al., 2018).

We apply the inverse distance weighted interpolation technique to estimate MW, AP, and MP in 48 counties based on their values at 29 meteorological stations. The linear relationships of the MW, AP, and MP with direct economic losses are shown in Table 2. Taking the MW as an example, the step size is set to 1 m s^{-1} , and the fitting values of the losses corresponding to each interval between 13 and 41 m s^{-1} are calculated based on the linear relationship shown in Table 2. The mean values of the MW fitting values in the first four intervals (rounded) are 5,650, 15,126, 26,971, and 40,395, respectively (Table 1). The proportions of these mean values to the sum of the first four intervals are 0.064, 0.172, 0.306, and 0.458, respectively, which are defined as the weighting coefficients of these four intervals. In addition, the weighting coefficient of the fifth interval is set to 1.

TABLE 1 | Level intervals of the maximum value of daily maximum wind speed (MW), accumulated precipitation (AP), and maximum daily precipitation (MP).

	Level 1	Level 2	Level 3	Level 4	Level 5
MW ($\text{m} \cdot \text{s}^{-1}$)	[13.5, 17.2)	[17.2, 24.5)	[24.5, 32.7)	[32.7, 41.5)	≥ 41.5
AP (mm)	[65, 100)	[100, 200)	[200, 300)	[300, 400)	≥ 400
MP (mm)	[50, 100)	[100, 150)	[150, 200)	[200, 250)	≥ 250

TABLE 2 | Linear relationships of hazard factors for typhoon–gale and typhoon–rainstorm disaster chains with direct economic losses.

	Linear relationship y (LOSS)
x (MW)	$y = 1579.3x - 18039$
x (AP)	$y = 48.236x + 2535.2$
x (MP)	$y = 95.962x + 444.05$

TABLE 3 | Weighting coefficients of each hazard factor in different intervals.

	Level 1	Level 2	Level 3	Level 4	Level 5
MW	0.064	0.172	0.306	0.458	1
AP	0.129	0.194	0.290	0.386	1
MP	0.128	0.209	0.291	0.372	1

TABLE 4 | Level intervals of the daily peak surge (PS) and ultra-warning tidal level (UWT).

	Level 1	Level 2	Level 3	Level 4	Level 5
PS (cm)	[50, 101)	[101, 151)	[151, 201)	[201, 251)	≥ 251
UWT (cm)	[0, 31)	[31, 81)	[81, 151)	≥ 151	—

Similarly, the weighting coefficients of the AP and MP in each interval are obtained, as shown in **Table 3**. These weighting coefficients are substituted into **Eq. 2** to obtain disaster-causing dangerousness of MW, AP, and MP. The disaster-causing dangerousness of MW is standardized according to **Eq. 1** to obtain the hazard index of typhoon–gale disaster chain (H_w). The standardized dangerousness of AP and MP is added with the equal weight to obtain the typhoon–rainstorm hazard index (H_r).

The daily PS and UWT are chosen as the hazard factors of typhoon–storm surge disaster chain. According to Yu et al. (2016), the hazard index of typhoon–storm surge disaster chain (H_s) is obtained by using the following:

$$H_s = 0.4 \times I'_{PS} + 0.6 \times I'_{UWT} \quad (7)$$

where I'_{PS} and I'_{UWT} are the standardized I_{PS} (**Eq. 8**) and I_{UWT} (**Eq. 9**), respectively.

$$I_{PS} = 4 \times N_1 + 8 \times N_2 + 12 \times N_3 + 16 \times N_4 + 20 \times N_5 \quad (8)$$

$$I_{UWT} = 5 \times N_1 + 10 \times N_2 + 15 \times N_3 + 20 \times N_4 \quad (9)$$

where N_1 indicates the frequency of the PS or UWT in the first interval at a tidal station during a certain statistical period, N_2 , N_3 , N_4 , and N_5 , respectively for the second to fifth intervals. The level

intervals of PS and UWT are shown in **Table 4** (China National Standards GB/T 39,418-2020, Grades of Storm Surge).

Exposure Index

The exposure is generally represented by the GDP and population per unit area. After standardizing the population and GDP data of the GBA in 2015 based on **Eq. 1**, the socioeconomic exposure index (E) is calculated by the following:

$$E = 0.5 \times \text{POP} + 0.5 \times \text{GDP} \quad (10)$$

where POP and GDP are the population and GDP at 1-km grid, respectively. According to the expert scoring method, the weighting coefficients of POP and GDP are equal (Wang et al., 2021b). The expert scoring method is mainly based on the results of questionnaires to determine the weight of each evaluation index through the hundred-mark system (He et al., 2016).

Vulnerability Index

The terrain (T), river network (R), and vegetation coverage (C) are selected as the factors of vulnerability index (V_r) for the typhoon–rainstorm disaster chain in the GBA (Wang et al., 2021b). We considered elevation and slope as terrain factors affecting typhoon–rainstorm disasters (Meraj et al., 2015). The degree of topography and flatness is expressed by absolute elevation and the elevation standard deviation at 1×1 -km grids, respectively. T is assigned according to the different combinations of elevation and elevation standard deviation graded by the National Climate Center of China Meteorological Administration, 2009. The lower the elevation, the smaller the elevation standard deviation is; the greater the T , the more sensitive it is to rainstorm disasters. In terms of the Standard DB33/T 2025-2017 (Zhejiang Meteorological Observatory, 2017), the combinations of total length of the river within 1 km and the distance to the water body are used to characterize the river network (National Climate Center of China Meteorological Administration, 2009). The place that has greater drainage density and is closer to water body has a higher risk of suffering from typhoon–rainstorm disasters (Sun et al., 2020). Because vegetation has a strong function of water and soil conservation, greater vegetation coverage means lower risk of typhoon–rainstorm disaster. The vegetation coverage index (C) is calculated according to the meteorological standard QX/T394-2019 (China Meteorological Administration, 2012). After the standardization of T , R , and C (**Eq. 1**), V_r can be calculated by **Eq. 11**. Then, the spatial distribution of the vulnerability index of the disaster-pregnant environment for the typhoon–rainstorm disaster chain at 1-km grid spacing in the GBA in 2015 is obtained.

$$V_r = 0.4 \times T + 0.3 \times R - 0.3 \times C \quad (11)$$

TABLE 5 | Values of the vulnerability index for the typhoon–storm surge disaster chain.

Terrain elevation (m)	Inland distance from shoreline (km)		
	Level 1 (≤5)	Level 2 (5–10)	Level 3 (10–20)
Level 1 (≤50)	1	0.9	0.8
Level 2 (50–100)	0.9	0.8	0.7
Level 3 (100–300)	0.8	0.7	0.6
Level 4 (≥300)	0.7	0.6	0.5

Some studies have pointed out that the lower the elevation and the flatter the terrain, the slower the wind speed weakens, and the more likely to form wind disasters. Conversely, under the same conditions, the higher the vegetation coverage, the greater the corresponding surface roughness, and the smaller the wind speed near the surface (Shuai et al., 2012). In this study, based on the previous research and the topography in the GBA, the terrain and vegetation coverage are regarded as the vulnerability factors for the typhoon–gale disaster chain. After the standardization of the terrain data and vegetation coverage (Eq. 1), the vulnerability index (V_w) of the disaster-pregnant environment at 1-km grid in the GBA in 2015 can be calculated according to Eq. 12. Note that the weighting coefficients are determined by the expert scoring method (He et al., 2016).

$$V_w = 0.5 \times T - 0.5 \times C \quad (12)$$

Referring to previous studies (Yang, 1997; Yu et al., 2016; Pang 2020), the terrain elevation data and inland distance from shoreline are taken as the vulnerability factors for the typhoon–storm surge disaster chain. The values of vulnerability index (V_s) for the typhoon–storm surge disaster chain are shown in Table 5.

Risk Index

According to the disaster risk management framework from the Intergovernmental Panel on Climate Change Fifth Assessment Report (IPCC, 2014), the gridded risk of typhoon disaster chains can be calculated based on hazard, exposure, and vulnerability. The specific calculation formulas are as follows (Eqs. 13–15). All elements are standardized with Eq. 1 before they are combined.

The risk index of typhoon–gale disaster chain:

$$RISK_w = H_w \times E \times V_w \quad (13)$$

The risk index of typhoon–rainstorm disaster chain :

$$RISK_r = H_r \times E \times V_r \quad (14)$$

The risk index of typhoon–storm surge disaster chain:

$$RISK_s = H_s \times E \times V_s \quad (15)$$

The above risk indexes are all standardized. The typhoon comprehensive risk index (RISK_c) is composed of three disaster chain risks, i.e., typhoon–gale, typhoon–rainstorm and typhoon–storm surge disaster chains. The weight coefficients of each disaster chain risk should be assigned according to their contribution to RISK_c. We calculate the correlation

coefficients between economic losses and typhoon–gale risk index, typhoon–rainstorm risk index and typhoon–storm surge risk index at county level, and the correlation coefficients are 0.56, 0.55 and 0.50, respectively ($p < 0.01$). The proportions of the three disaster chain correlation coefficients to the sum are 0.35, 0.34, and 0.31, respectively, and they are the weight coefficients of RISK_c. The RISK_c is then calculated by the weighted average (Eq. 16), and the result values are normalized to the range between 0.5 and 1.

$$RISK_c = 0.35 \times RISK_w + 0.34 \times RISK_r + 0.31 \times RISK_s \quad (16)$$

The natural breakpoint method in ArcGIS is used to classify the risk of typhoon disaster chains. It identifies classification intervals based on the natural grouping inherent in the data, allows for the most appropriate grouping of similar values, and maximizes differences between classes. In this study, we classify the risk of typhoon disaster chains into five levels, including very low risk (level 1), low risk (level 2), moderate risk (level 3), high risk (level 4), and very high risk (level 5). The ranges of risk values at each level are shown in Table 6.

The typhoon risk index for an administrative region is the average of the risk indexes at all grids in this region.

RESULTS

Statistical Characteristics of Disaster-Causing Typhoons

In this study, as long as one of MW, AP, and MP exceeds the assessment starting point in anyone of the 29 meteorological stations during the period of typhoon influence, the typhoon is considered to be an influencing typhoon. From 2009 to 2020, there were 38 influencing typhoons in the GBA, which were regarded as the samples of hazard index calculation in the county. Among them, there were 31 disaster-causing typhoons, with an average of 2.6 per year. Specifically, the largest number of annual disaster-causing typhoons was 6 in 2009, and the fewest was 1 in 2013 (Figure 2A). In terms of the monthly distribution, 31 disaster-causing typhoons occurred from June to October, with relatively more in August and September (9 each month) and relatively fewer (5 or fewer each month) in other months (Figure 2B).

Among the 31 disaster-causing typhoons, 11 landed in the GBA (Figure 3A) and 13 landed in other places of Guangdong Province (Figure 3B). These typhoons mainly moved westward. Four typhoons landed in Taiwan or Fujian and went westward through Guangdong after landing (Figure 3C). Three typhoons

TABLE 6 | The risk levels of typhoon disaster chains.

Risk level	Gale	Rainstorm	Storm surge	Comprehensive
Level 1	[0.50, 0.56)	[0.50, 0.57)	[0.50, 0.72)	[0.50, 0.58)
Level 2	[0.56, 0.60)	[0.57, 0.63)	[0.72, 0.77)	[0.58, 0.64)
Level 3	[0.60, 0.65)	[0.62, 0.67)	[0.77, 0.83)	[0.64, 0.69)
Level 4	[0.65, 0.70)	[0.67, 0.70)	[0.83, 0.90)	[0.69, 0.80)
Level 5	[0.70, 1.0]	[0.70, 1.0]	[0.90, 1.0]	[0.80, 1.0]

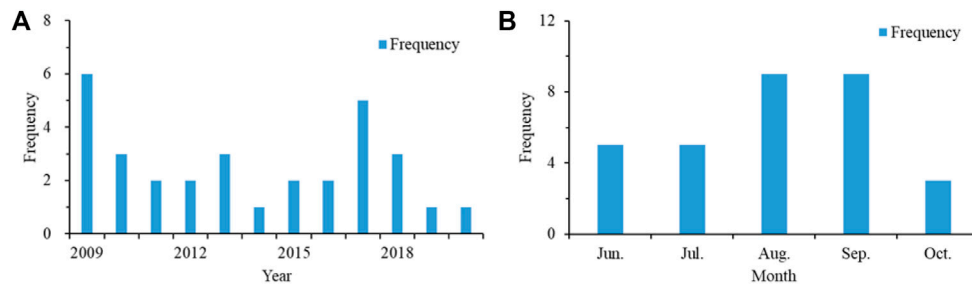


FIGURE 2 | (A) Annual frequency and (B) monthly frequency of disaster-causing typhoons in the GBA from 2009 to 2020.

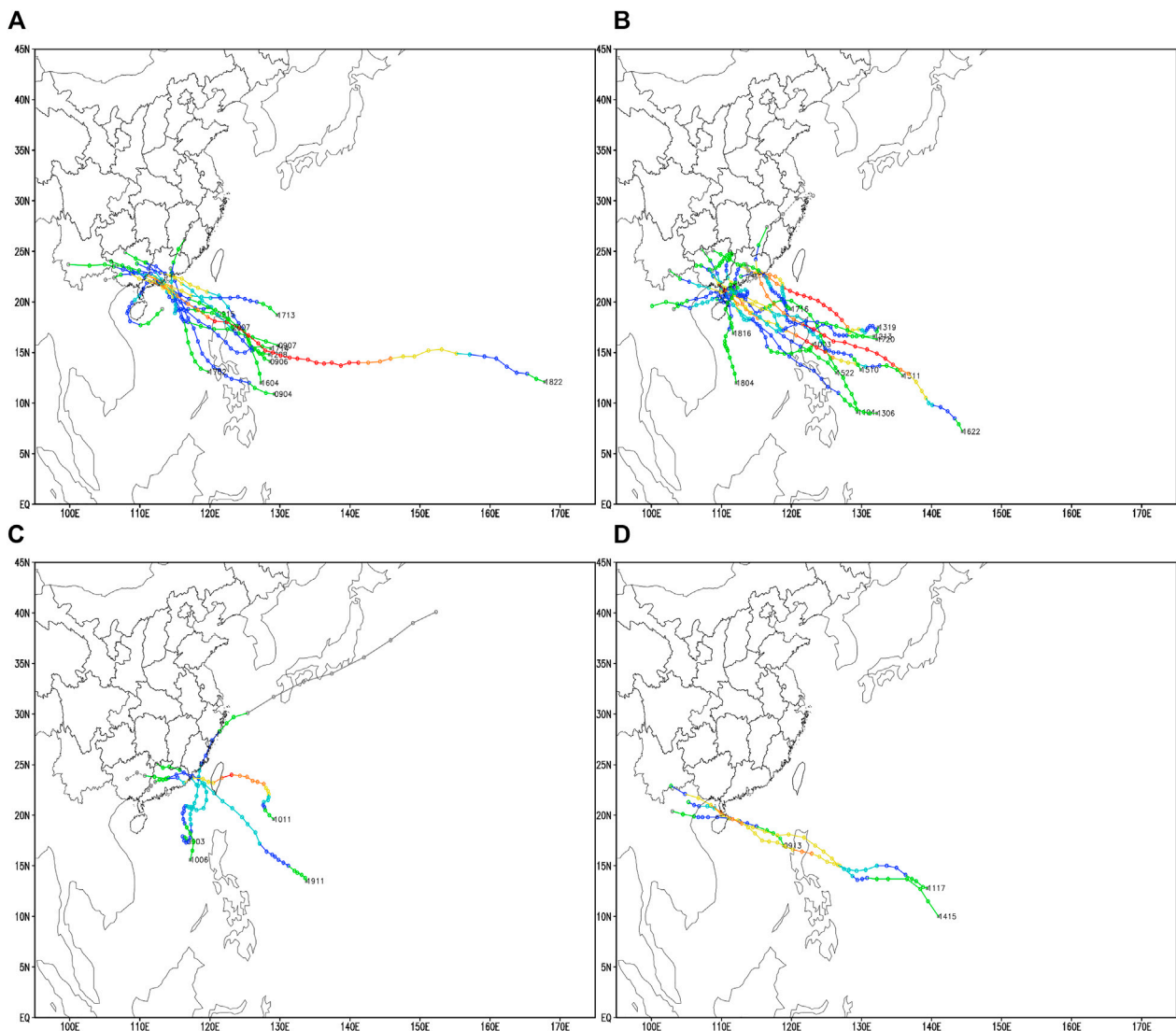
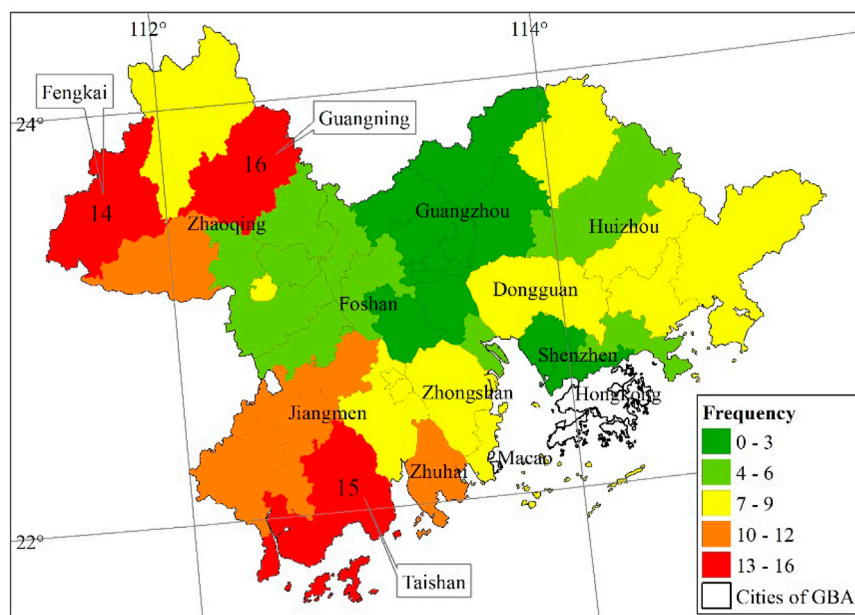


FIGURE 3 | Tracks of disaster-causing typhoons in GBA (A) landfall in GBA; (B) landfall in other places of Guangdong; (C) landfall in Taiwan or Fujian; (D) landfall in Hainan. The colors represent different typhoon levels. Gray means below the intensity of tropical depression, green means tropical depression, blue means tropical storm, cyan means severe tropical storm, yellow means typhoon, orange means strong typhoon, and red means super typhoon. The number indicates the typhoon serial number.

TABLE 7 | Risk, hazard, exposure, and vulnerability of typhoon–gale disaster chain in cities of the GBA.

	Risk index	Hazard index	Exposure index	Vulnerability index
Guangzhou	0.599	0.542	0.518	0.742
Shenzhen	0.644	0.602	0.532	0.756
Zhuhai	0.714	0.731	0.511	0.783
Foshan	0.657	0.581	0.517	0.839
Jiangmen	0.660	0.686	0.504	0.744
Zhaoqing	0.565	0.545	0.502	0.663
Huizhou	0.588	0.579	0.503	0.686
Dongguan	0.655	0.575	0.529	0.822
Zhongshan	0.692	0.647	0.517	0.830

**FIGURE 4** | Frequency distribution of total disaster-causing typhoons at county level in the GBA from 2009 to 2020.

made landfall in Hainan with westward-moving tracks and influenced the GBA (**Figure 3D**).

For the regional distribution of 31 disaster-causing typhoons, the cumulative number of disaster-causing typhoons in Zhaoqing was the largest (24), followed by Jiangmen (15) and Zhuhai (12), and the least in Shenzhen (6), as shown in **Table 9**. Although Zhaoqing is located in the inland area of the central and western parts of Guangdong Province, typhoons landing in Guangdong, Fujian, and Hainan may affect Guangning County of Zhaoqing, resulting in more disaster-causing typhoons (Zhou et al., 2015). Guangning County is located in the northwest of the GBA, and typhoons can affect Guangning County after making landfall from the east and west sides of the GBA.

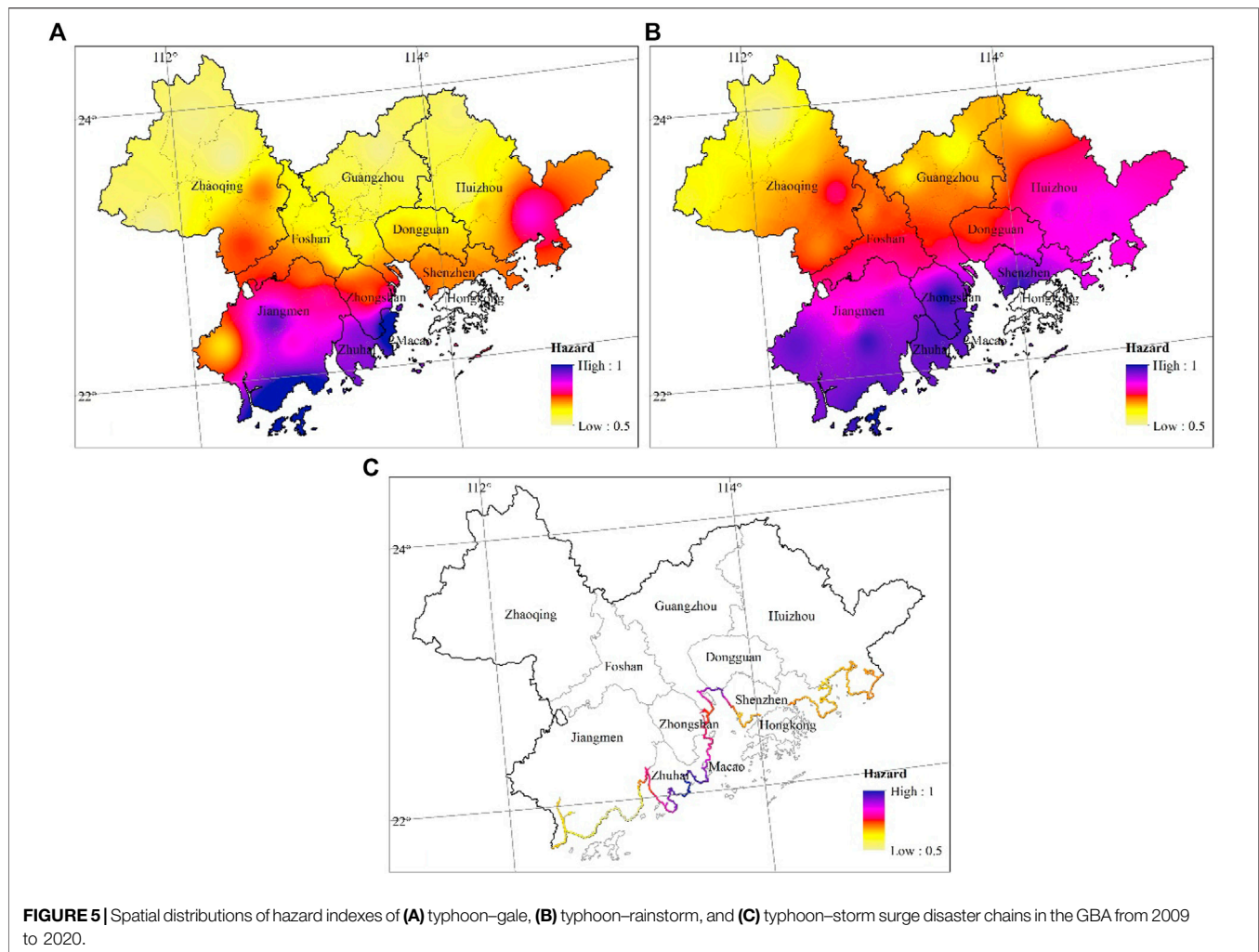
Figure 4 shows the spatial distribution of 186 disaster-causing typhoon samples at county level in the GBA from 2009 to 2020. The results suggest that there are 47 counties (districts) that suffered from disaster-causing typhoons except the Luogang District of Guangzhou. The Guangning County of Zhaoqing

experienced the most (16) disaster-causing typhoons, followed by Taishan City of Jiangmen (15) and Fengkai County of Zhaoqing (14). Liwan, Yuxiu, Haizhu, and Tianhe Districts of Guangzhou and Luohu and Baoan Districts of Shenzhen have experienced only 1 disaster-causing typhoon.

Hazard

The hazard indexes of typhoon–gale, typhoon–rainstorm, and typhoon–storm surge disaster chains in the GBA from 2009 to 2020 are calculated. The ranges of H_w , H_r , and H_s are 0.91–5.0, 1.07–4.96, and 36.8–116.4, respectively. The standardized results are shown in **Figure 5**.

For the typhoon–gale disaster chain, the areas with high and relatively high hazard index are mainly located in Zhuhai, central-southern Jiangmen, southern Zhongshan, and southeastern Huizhou, whereas the hazard index in the central-northern Zhaoqing, northern Foshan, central-northern Guangzhou, and northern Huizhou is low and relatively low (**Figure 5A**). At



county level, the hazard index in Xiangzhou, Jinwan, and Doumen Districts of Zhuhai and Taishan District of Jiangmen is the highest, exceeding 0.7. The hazard index in Fengkai, Guangning and Huaiji Counties of Zhaoqing and Conghua District of Guangzhou is the lowest (<0.53).

In terms of the typhoon-rainstorm disaster chain, the areas with higher hazard index are mainly concentrated in Zhuhai, Zhongshan, Shenzhen, Dongguan, Jiangmen, southern Foshan, and southern Huizhou, whereas areas with lower hazard index are mainly distributed in northern Zhaoqing, northern Guangzhou, and northwestern Huizhou (Figure 5B). At county level, the hazard index in Futian and Nanshan Districts of Shenzhen, Doumen, Xiangzhou and Jinwan Districts of Zhuhai, and Taishan District of Jiangmen is the highest, exceeding 0.94.

Moreover, for the typhoon-storm surge disaster chain, the areas with higher hazard index are distributed in the coastal regions from eastern Jiangmen to northwestern Shenzhen, where the highest hazard index is in the coastal areas of the central Zhuhai and Dongguan (Figure 5C). The index in Dongguan and Zhuhai exceeds 0.85.

In order to verify the rationality of the hazard indexes of typhoon-gale and typhoon-rainstorm, we calculate the cumulative number of typhoon gale days, rainstorm days, and precipitation from 2009 to 2020 as shown in Figure 6. It can be found that the spatial distributions of gale days (Figure 6A) and typhoon-gale hazard index (Figure 5A) are relatively consistent. The spatial correlation coefficient between them reaches 0.98 ($p < 0.01$). The spatial distributions of accumulated rainstorm days (Figure 6B), accumulated precipitation (Figure 6C), and typhoon-rainstorm hazard index (Figure 5B) are also relatively consistent. The spatial correlation coefficients between accumulated rainstorm days and typhoon-rainstorm hazard index, accumulated precipitation, and typhoon-rainstorm hazard index reach 0.96 and 0.98 ($p < 0.01$), respectively.

Exposure

Figure 7 shows the exposure index with a resolution of 1 km in the GBA in 2015. The range of exposure index is 0.5–1.0 in this study. The areas with higher exposure index are the highly populated and economically dense areas of the GBA, especially

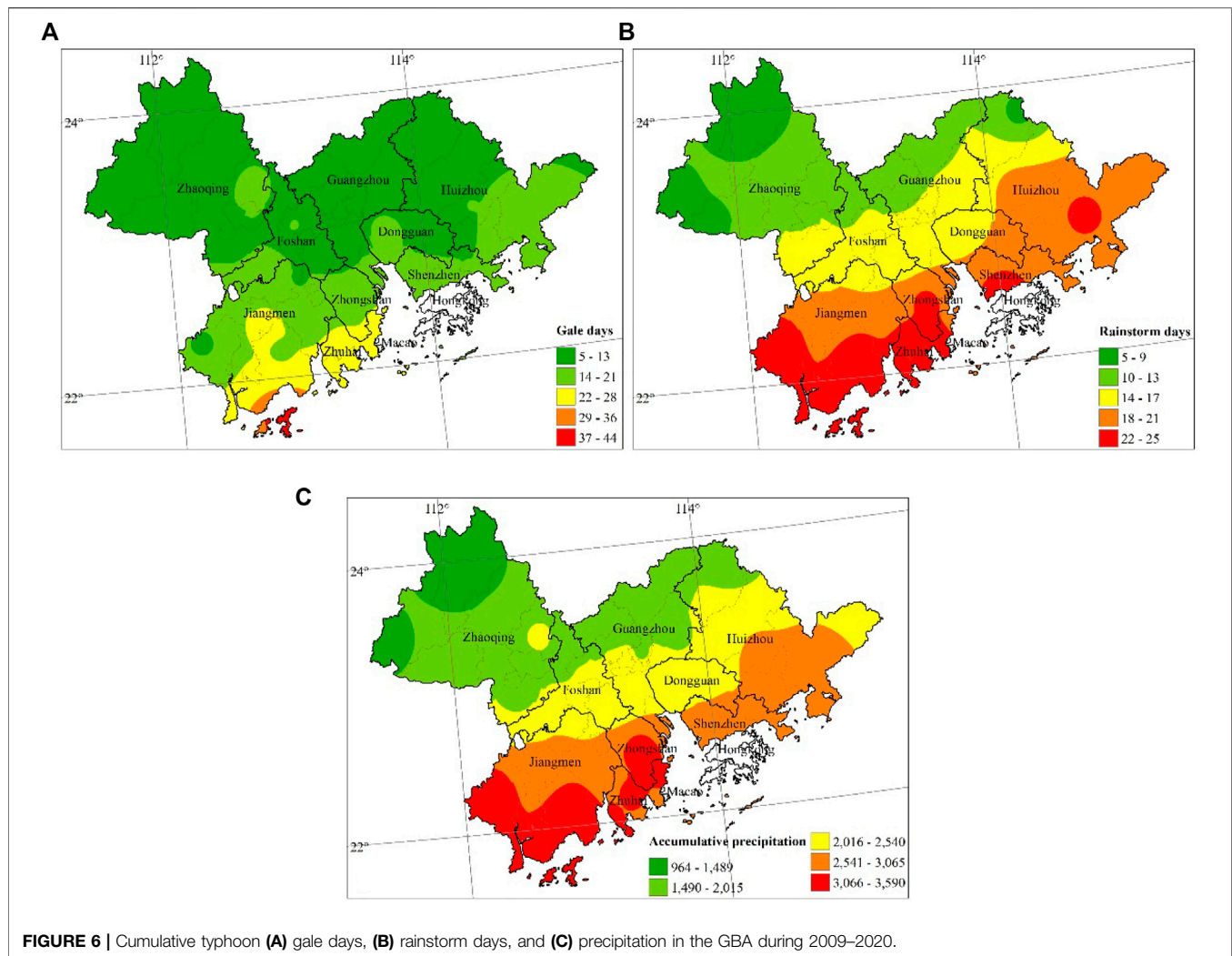


FIGURE 6 | Cumulative typhoon (A) gale days, (B) rainstorm days, and (C) precipitation in the GBA during 2009–2020.

the central part of Guangzhou, central part of Foshan, and southern part of Shenzhen. For example, the statistics show that the population density of Yuexiu District (34,225 people/km²), Haizhu District (17,851 people/km²), Tianhe District (16,046 people/km²), and Liwan District (15,596 people/km²) is much higher than the average of other districts in Guangzhou (1,526 people/km²). Similarly, the GDP per square kilometer in Yuexiu District (7,987 million yuan), Tianhe District (3,569 million yuan), Liwan District (1719 million yuan), and Haizhu District (1,574 million yuan) is much higher than the average of other districts in Guangzhou (203 million yuan) (<http://112.94.72.17/portal/queryInfo/statisticsYearbook/index>). The exposure index in Huizhou, Zhuhai, Jiangmen, and Zhaoqing is relatively lower.

Vulnerability

Based on Eqs. 11 and 12 and Table 5, we calculated V_w , V_r , and V_s , and their ranges are 0.003–0.42, 0.04–0.59, and 0.5–1.0 before standardization, respectively. In terms of the typhoon–gale disaster chain, the vulnerable areas are mainly located in Foshan, Dongguan, northern Zhongshan, central Zhuhai,

central Jiangmen, central Shenzhen, and southern Guangzhou (Figure 8A). For the typhoon–rainstorm disaster chain, the vulnerable areas are mainly distributed in Foshan, northern Dongguan, northern Zhongshan, eastern Zhuhai, southern Guangzhou, central Huizhou, and Zhaoqing along the West River (Figure 8B). Figure 8C presents the vulnerability for the typhoon–storm surge disaster chain. It is indicated that the vulnerability gradually decreases from coastal areas to the boundaries of the buffer zone 20 km away from the coastal lines (Figure 8C). Because of the relatively low altitude and being close to the coastlines, most coastal areas have the relatively high vulnerability against the typhoon-induced storm surge. On the contrary, the vulnerability in coastal areas of eastern Shenzhen and southeastern Jiangmen is relatively low because they are mostly hilly areas.

When the hazard of typhoon disaster is similar, the higher the vulnerability, the higher the typhoon disaster risk. We compare the average vulnerability and comprehensive disaster loss at city level to verify the rationality of vulnerability index. The vulnerability in Dongguan is obviously higher than that in Huizhou, which results in greater typhoon disaster loss

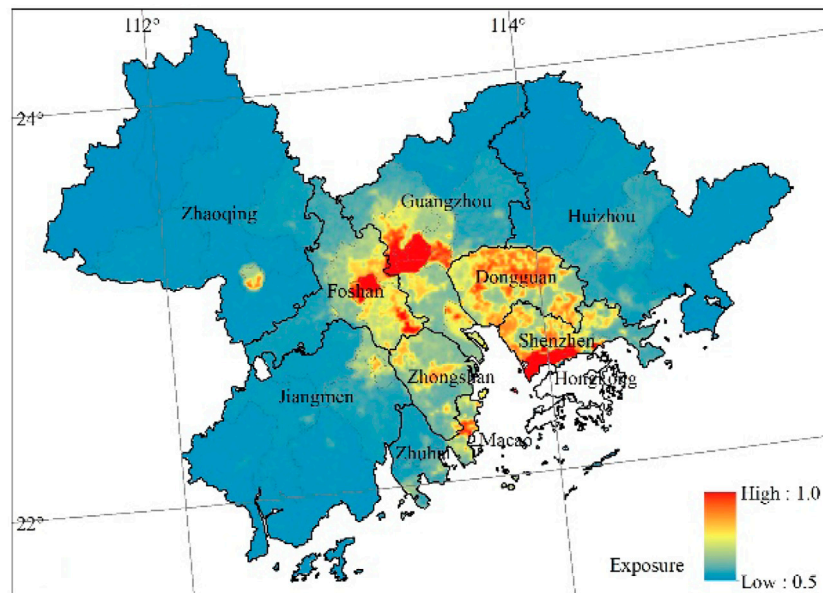


FIGURE 7 | Exposure index distribution of economic society in the GBA in 2015.

(Table 7), whereas they almost have the same hazard index. The same situation happens in Zhongshan and Jiangmen; the higher the vulnerability, the greater the typhoon disaster risk in Zhongshan compared with Jiangmen. Therefore, the vulnerability index constructed in the study is relatively reasonable.

Risk of Disaster Chains

The risks of typhoon–gale, typhoon–rainstorm, and typhoon–storm surge disaster chains are calculated based on Eqs. 13–15 and are classified into five levels according to Table 6. For the typhoon–gale disaster chain, there are 10, 11, 13, 8, and 6 districts or counties with the risk of level 5, level 4, level 3, level 2 and level 1, respectively. Level 5 is found in Xiangzhou, Doumen and Jinwan Districts of Zhuhai, Pengjiang and Jianghai Districts of Jiangmen, Chancheng District of Foshan, Futian District of Shenzhen, and Liwan, Yuexiu and Haizhu Districts of Guangzhou. Level 1 is found in only six districts or counties, that is, Conghua of Guangzhou, Guangning, Huaiji, Fengkai and Deqing of Zhaoqing, and Longmen of Huizhou (Figure 9A). At city level, the top three highest-risk cities are Zhuhai, Zhongshan, and Jiangmen (Table 7). The highest hazard index may result in the highest risk in Zhuhai, although its exposure and vulnerability are not too high compared with other cities. Because the vulnerability index in Zhongshan is higher despite lower hazard index than Jiangmen, its risk is higher than that of Jiangmen.

For the typhoon–rainstorm disaster chain, there are 9, 15, 12, 6, and 6 districts or counties with level 5, level 4, level 3 level, 2 and level 1, respectively. Level 5 is found in Doumen District of Zhuhai, Pengjiang, and Jianghai Districts of Jiangmen, Chancheng District of Foshan, Futian District of Shenzhen, and Liwan, Yuexiu, and Haizhu Districts of Guangzhou and

Zhongshan. Level 1 is found in six districts or counties, that is, Conghua District of Guangzhou, Guangning, Huaiji, Fengkai, and Deqing Counties of Zhaoqing and Longmen County of Huizhou (Figure 9B). At city level, the average risk index in Zhongshan and Zhuhai ranks top two in the GBA because the hazard index in the two cities is greater than 0.9, although their exposure and vulnerability indexes are not too high (Table 8). It can also be seen that the higher risk index in Zhongshan is mainly determined by its higher hazard and vulnerability index. Although the hazard in Jiangmen is relatively high, its exposure and vulnerability are not too high, leading to its low risk.

In terms of the typhoon–storm surge disaster chain, the areas with risk level being high or above are mainly distributed in Zhuhai, eastern Zhongshan, and coastal areas surrounding the Pearl River Estuary (Figure 9C). Moreover, the risk level in Xiangzhou and Jinwan Districts of Zhuhai is the highest, reaching level 5. At county level, the risk levels of typhoon–gale and typhoon–rainstorm disaster chains are comparable, except for the coastal areas where the risk of the typhoon–storm surge disaster chain is relatively higher.

The typhoon comprehensive risk index is calculated based on Eq. 16, as shown in Figure 9D. It can be found that the comprehensive risk level reaches level 4 or above in southern Jiangmen, Zhuhai, Zhongshan, Shenzhen, southern Dongguan, southern Foshan, southwestern Guangzhou, and coastal areas of Huizhou, whereas the risk level is level 2 or below in Zhaoqing, northern Guangzhou, and northern Huizhou. At county level, seven districts have the risk of level 5, including Doumen, Xiangzhou, and Jinwan Districts of Zhuhai, Futian, and Nanshan Districts of Shenzhen and Yuexiu and Nansha Districts of Guangzhou.

Table 9 presents the risk distributions of typhoon disaster chains at city level. For the typhoon–gale disaster chain, the

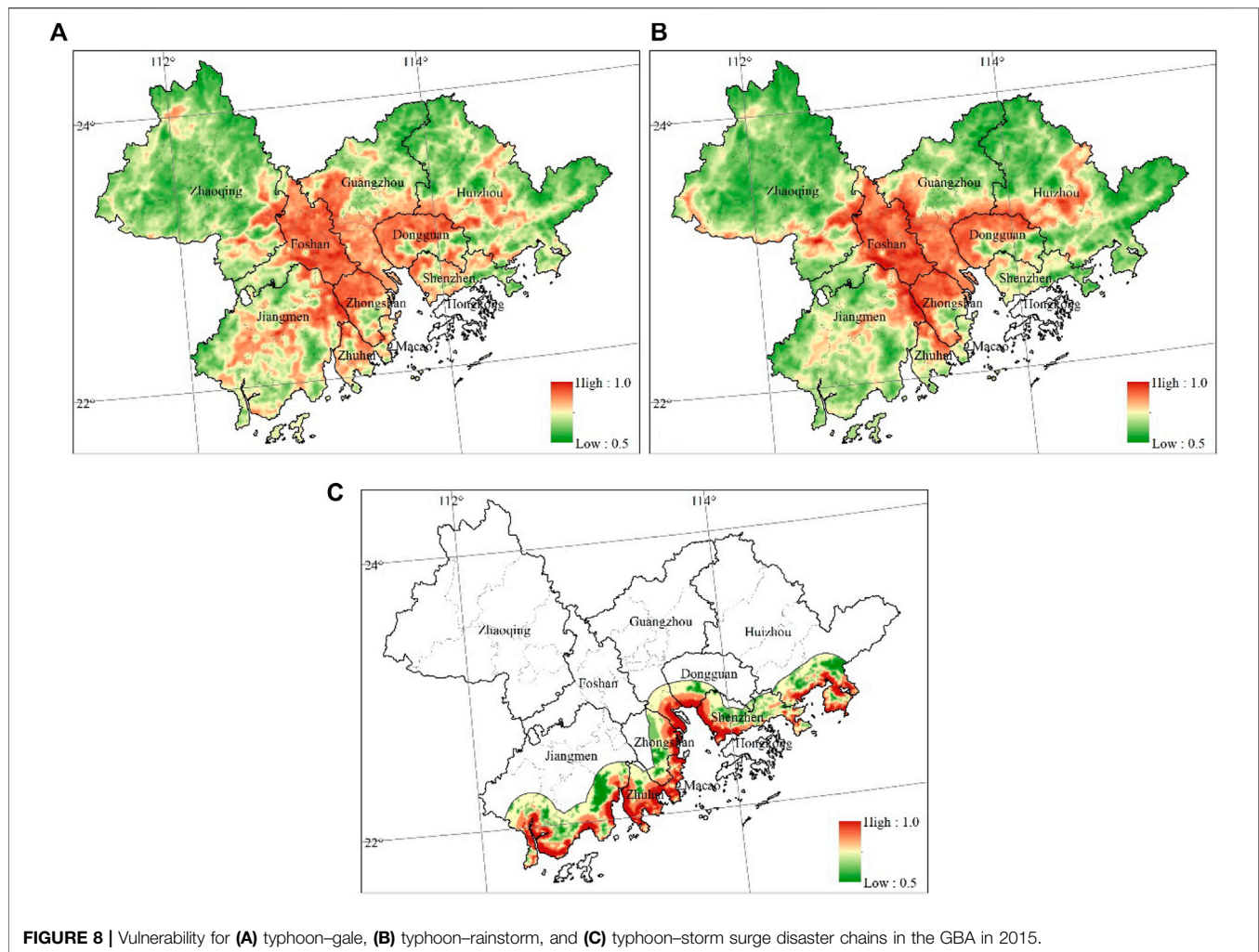


FIGURE 8 | Vulnerability for (A) typhoon-gale, (B) typhoon-rainstorm, and (C) typhoon-storm surge disaster chains in the GBA in 2015.

TABLE 8 | Risk, hazard, and vulnerability of typhoon-rainstorm disaster chain in cities of the GBA.

	Risk index	Hazard index	Vulnerability index
Guangzhou	0.608	0.691	0.688
Shenzhen	0.678	0.886	0.670
Zhuhai	0.710	0.946	0.705
Foshan	0.672	0.749	0.787
Jiangmen	0.662	0.899	0.669
Zhaoqing	0.565	0.646	0.629
Huizhou	0.612	0.780	0.641
Dongguan	0.675	0.778	0.751
Zhongshan	0.740	0.920	0.781

average risk index is level 5 in Zhuhai; level 4 in Foshan, Jiangmen, Dongguan, and Zhongshan; and level 2 in Guangzhou, Zhaoqing and Huizhou. The average risk index of typhoon-rainstorm disaster chain is level 5 in Zhuhai and Zhongshan; level 4 in Foshan, Dongguan, and Shenzhen; and level 1 in Zhaoqing. In terms of the typhoon-storm surge disaster chain, the average risk index is level 4 in Zhuhai,

Zhongshan, and Dongguan and level 1 in Guangzhou, Zhaoqing, and Foshan, because they are far away from the coastlines. For the typhoon comprehensive risk of each city, it can be found that the risk is level 5 in Zhuhai; level 4 in Zhongshan, Jiangmen, Dongguan, and Shenzhen; level 3 in Foshan; level 2 in Guangzhou and Huizhou; and level 1 in Zhaoqing.

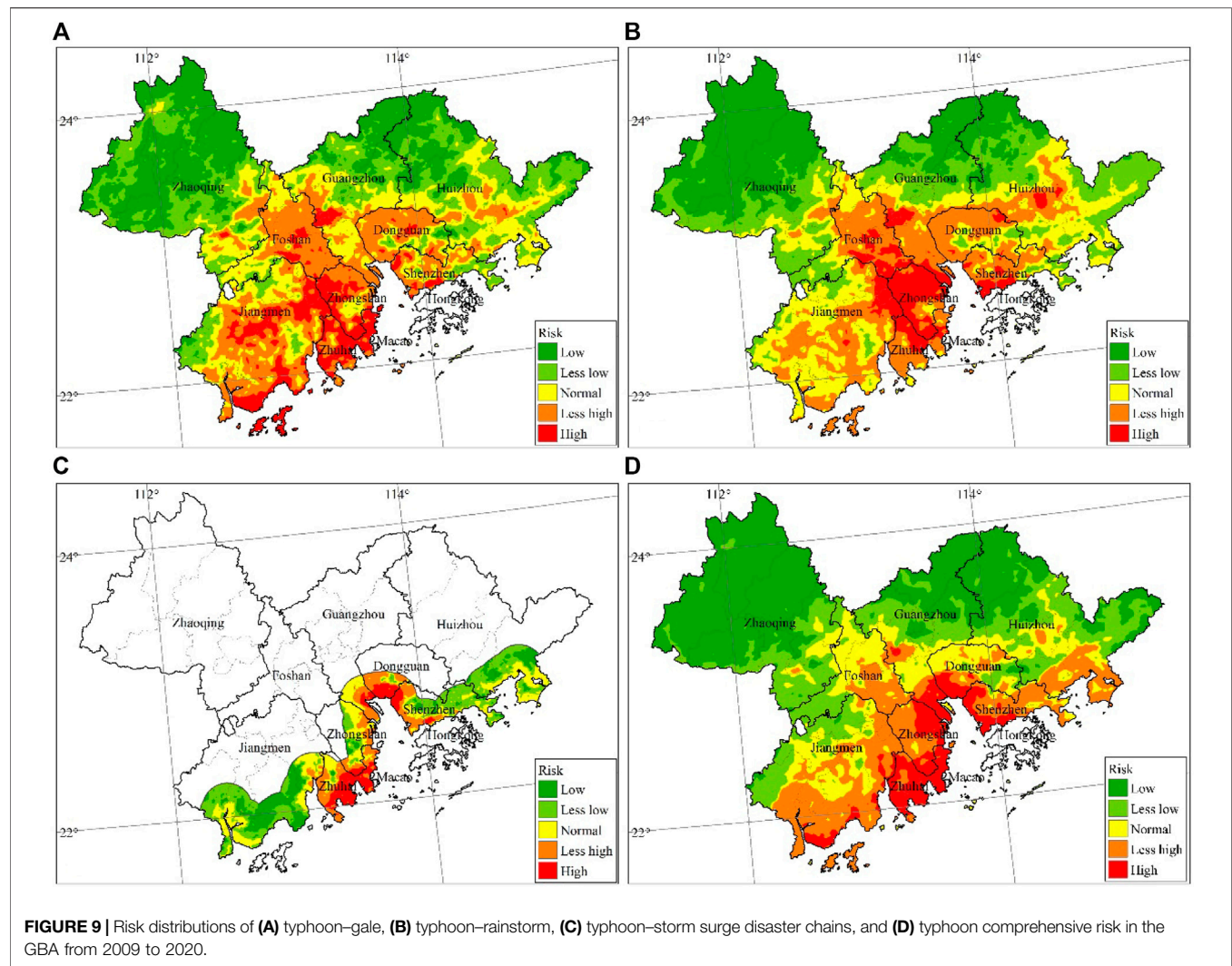


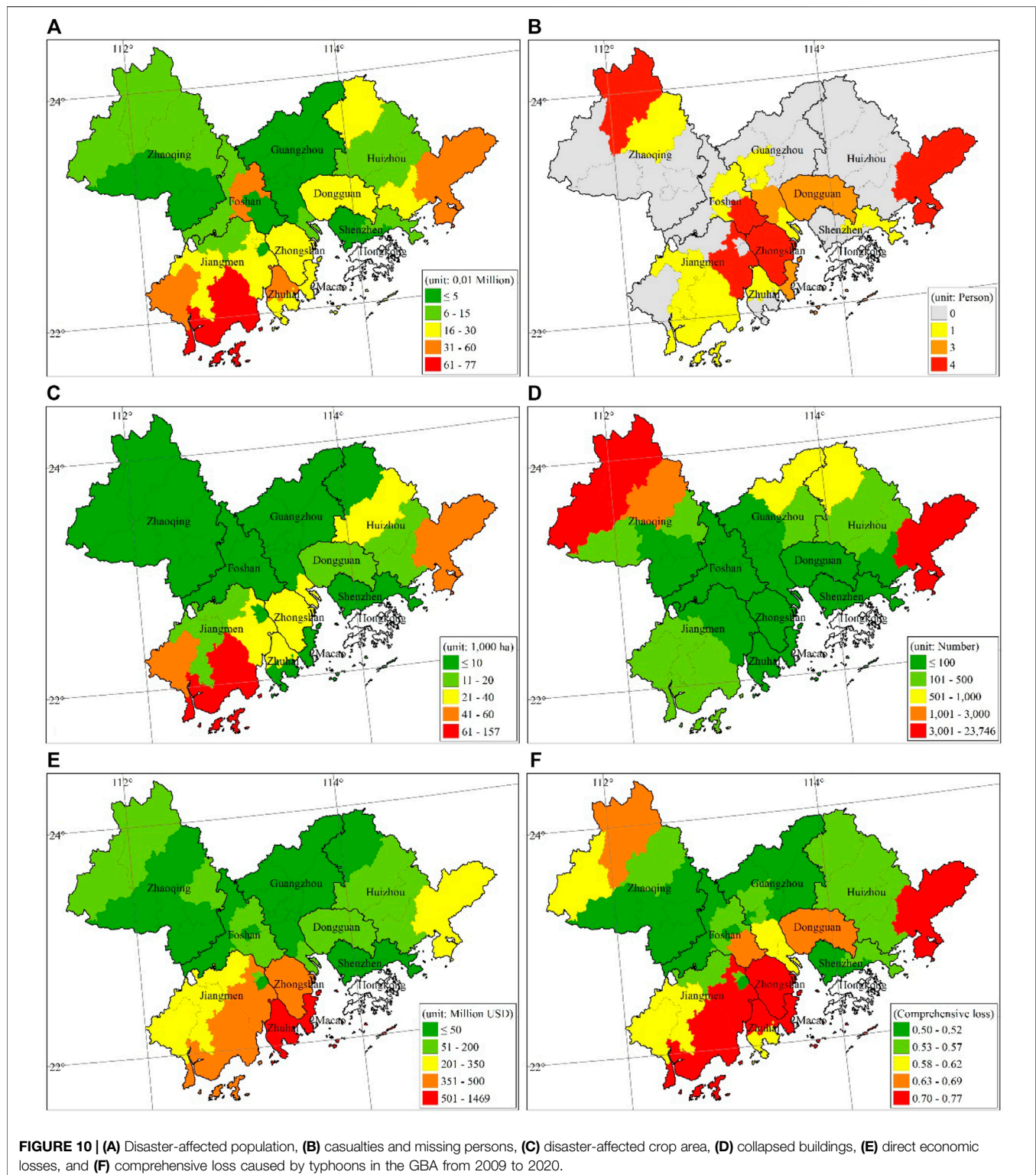
TABLE 9 | The number of disaster-causing typhoons, disaster risk level, and comprehensive loss index in each city of the GBA from 2009 to 2020.

Cities	No. of disaster-causing typhoons	Risk level of typhoon-gale	Risk level of typhoon-rainstorm	Risk level of typhoon-storm surge	Comprehensive risk level	Comprehensive loss index
Guangzhou	8	2	2	1	2	0.53
Shenzhen	6	3	4	3	4	0.51
Zhuhai	12	5	5	4	5	0.70
Foshan	8	4	4	1	3	0.55
Jiangmen	15	4	3	2	4	0.59
Zhaoqing	24	2	1	1	1	0.54
Huizhou	10	2	2	2	2	0.58
Dongguan	9	4	4	4	4	0.64
Zhongshan	7	4	5	4	4	0.72

Verification on the Disaster Risk

The disaster-affected population, casualties and missing persons, disaster-affected crop area, collapsed buildings, and direct economic losses are selected as typhoon disaster indicators, and their distributions in the GBA are shown in **Figure 10**.

From 2009 to 2020, because of typhoon disasters, there were 5.91 million people affected, 39 deaths, and direct economic losses of 50.93 billion yuan in the GBA. The area with the most disaster-affected population was Jiangmen City (2.037 million people). This is because Jiangmen City is



located in the southeast coastal area of GBA, which suffered from more disaster-causing typhoons (15) and had a comprehensive risk level 4. The disaster prevention and mitigation capacity of Jiangmen City is relatively weak (Zhang et al., 2018). Also, the largest disaster-affected crop area was in Jiangmen City

(278,000 ha), which is related to the fact that Jiangmen is the main agricultural base of the GBA. The city with the most collapsed buildings was Zhaoqing City (37,000 buildings), which was associated with mountain torrents and geological disasters caused by the typhoon-rainstorm disaster chain in

the mountain areas of Zhaoqing (https://www.sohu.com/a/153196981_741455). The most direct economic loss was in Zhuhai City (22.91 billion yuan). This is because the comprehensive risk and the risk of typhoon–gale, typhoon–rainstorm, and typhoon–storm surge disaster chains in Zhuhai are the highest among the nine cities.

The typhoon disaster indicators are standardized according to Eq. 1. Based on the expert scoring method, the weight coefficients of disaster-affected population, casualties and missing population, disaster-affected crop area, collapsed buildings, and direct economic losses are determined as 0.1, 0.35, 0.1, 0.1, and 0.35, respectively. The typhoon comprehensive loss index can be obtained through the weighted average of the disaster indicators above (Figure 10F). The results suggest that the comprehensive loss index is the highest in Xiangzhou and Doumen Districts of Zhuhai, Xinhui District of Jiangmen, and Zhongshan City, exceeding 0.7. After calculating the average of comprehensive loss index at all counties (districts) in each city (Table 9), we find the largest value is in Zhongshan City, followed by Zhuhai. This situation is related to the high comprehensive risk level in the two cities. Although the comprehensive risk in Shenzhen is level 4, the loss is the lowest, which may be related to the developed economy and the strong capacity of typhoon disaster prevention and mitigation in Shenzhen. The spatial correlation coefficient between the comprehensive risk index and the comprehensive loss index at county level passes the significance test at 99.9% confidence level, indicating that the typhoon comprehensive risk index constructed in this study can well reflect the potential impact of typhoon disasters.

CONCLUSIONS AND DISCUSSION

In this study, we developed an objective typhoon risk index from the view of disaster chains. This study is a pioneer to assess typhoon–gale, typhoon–rainstorm, and typhoon–storm surge disaster chains at county level of the GBA. The zoning of typhoon disasters chains can help policy-makers better understand typhoon risks in GBA. The main conclusions are as follows.

For the typhoon–gale disaster chain, the areas with risk of level 4 or above are mainly located in Zhuhai, Zhongshan, Foshan, Dongguan, central and southern Jiangmen, southern Shenzhen, and parts of Huizhou. In terms of the typhoon–rainstorm disaster chain, the areas with risk of level 4 or greater are mainly concentrated in Zhuhai, Zhongshan, Shenzhen, central-southern Foshan, northern Dongguan, central Jiangmen, and central Huizhou. Moreover, for the typhoon–storm surge disaster chain, the areas with risk of level 4 or greater are mainly distributed in Zhuhai, eastern Zhongshan and coastal areas surrounding the Pearl River Estuary. In addition, the typhoon comprehensive risk is level 4 or greater in southern Jiangmen, Zhuhai, Zhongshan, Shenzhen, southern Dongguan, southern Foshan, southwestern Guangzhou, and coastal areas of Huizhou.

At city level, the typhoon comprehensive risk reaches level 5 in Zhuhai and level 4 in Zhongshan Jiangmen, Dongguan, and

Shenzhen. At county level, Doumen, Xiangzhou, and Jinwan Districts of Zhuhai, Futian and Nanshan Districts of Shenzhen, and Yuexiu and Nansha Districts of Guangzhou are the areas with very high typhoon comprehensive risk.

Moreover, the validation results of the spatial correlation between the typhoon comprehensive risk index and the comprehensive loss demonstrate that the typhoon comprehensive risk index constructed in this study can better reflect the possible impacts of typhoon disasters.

In this study, the risk indexes of typhoon disaster chains in GBA were constructed based on hazard, exposure, and vulnerability. Because of the numerous and complex factors affecting typhoon disaster risk, the selected indicators have certain subjectivity and may not be comprehensive enough. For the hazard index, we adopted the historical observation data of 29 meteorological stations in GBA, and the disadvantage was the spatial resolution limitation. For the exposure index, we need to try the path polygons approach to recognize regional exposure affected by the typhoon as a whole. To summarize, the exposure values for each census block within the county could be more reasonable (<https://www.fema.gov/sites/default/files/documents>). In the assessment of vulnerability, the weights were mainly to indicate the relative importance of terrain, river network, and vegetation coverage, which could affect the results of vulnerability and risk index. In this study, some weight coefficients were determined by the expert scoring method. Although the invited experts have rich experiences in typhoon disaster assessment, which can help us get relatively reasonable results, it was not an objective method as it depends on each expert's subjective understanding. In order to overcome the subjectivity of the weight coefficients, we need to collect more typhoon disaster samples and determine the weight coefficient based on the actual disaster losses in the future. For the typhoon risk index, we adopted the natural breakpoint method in ArcGIS to classify risk levels, whereas the level interval could affect the risks. For now, it is difficult to find all specific quantifiable factors to evaluate typhoon risk, but it should be considered in future researches.

Under the background of global warming, the severe typhoon and its potential destructive power increased in the Northwest Pacific during the past few decades (Li et al., 2017; Knutson et al., 2019). The increasing trends in rainy days, total precipitation, and maximum 1-h precipitation of per typhoon indicate an enhanced influence of typhoons in South China (Ying et al., 2012). Moreover, sea level rise leads to higher typhoon storm surges along the coast, which can cause severe damage to the GBA. Therefore, climate change detection and attribution for typhoon activity should be further investigated to assist in better understanding of the typhoon disaster risk in the GBA (Lee et al., 2020).

The results of this study have a positive reference for local governments to improve the pertinence of the strategies for the regional typhoon disaster prevention and mitigation. This study reveals that the comprehensive risk of typhoon disaster is very high in Zhuhai and high in Zhongshan, Jiangmen, Dongguan, and Shenzhen. Improving the level of defense against typhoon through engineering measures, increasing green space, and arranging reasonable spatial patterns of impervious surfaces

would provide useful ways to mitigate typhoon disasters in these areas. Meanwhile, different typhoon-resistant strategies should be made based on the typhoon disaster chains, the disaster-pregnant environment and the different characteristics of development planning, so as to improve the disaster prevention and mitigation capacity of cities.

DATA AVAILABILITY STATEMENT

Publicly available datasets were analyzed in this study. This data can be found here: <http://www.resdc.cn/Default.aspx>.

AUTHOR CONTRIBUTIONS

YJ and YZ contributed to conception and design of the study. YJ wrote the first draft of the article. YZ and LC performed the

statistical analysis. YZ and LC revised the article. All authors contributed to manuscript revision, read, and approved the submitted version.

FUNDING

This work was funded by the National Key Research and Development Program of China (2019YFC1510400).

ACKNOWLEDGMENTS

We thank the editor and three reviewers who all made very valuable suggestions for improvement of this manuscript. We thank Nanjing Hurricane Translation for reviewing the English language quality of this paper.

REFERENCES

- Chen, F., Jia, H., Du, E., Wang, L., Wang, N., and Yang, A. (2021). Spatiotemporal Variations and Risk Analysis of Chinese Typhoon Disasters. *Sustainability* 13, 2278. doi:10.3390/su13042278
- Chen, W., Xu, W., and Shi, P. (2011). Risk Assessment of Typhoon Disaster at County Level in the Yangtze River Delta of China. *J. Nat. Disasters* 20 (4), 77–83. (in Chinese with English abstract). doi:10.13577/j.jnd.2012.0306
- Chen, Y., Qin, J., Dong, L., and Zhang, T. (2017). The Formation Regularity and Control Measures of Urban Pluvial Floods in Guangzhou City. *China Flood&Drought Management* 27 (5), 72–76.
- China Meteorological Administration (CMA) (1991–2018). *Annual Bulletin of Meteorological Disasters in China*. Beijing: China Meteorological Press.
- China Meteorological Administration (CMA) (2006). *GBT 19201-2006, Grade of Tropical Cyclones*. Beijing: China Standards Press.
- China Meteorological Administration (CMA) (2012). *Grade of Precipitation (GB/T 28592—2012)*. Beijing: Science Press.
- Chou, J., Dong, W., Tu, G., and Xu, Y. (2020). Spatiotemporal Distribution of landing Tropical Cyclones and Disaster Impact Analysis in Coastal China during 1990–2016. *Phys. Chem. Earth* 115, 102830. doi:10.1016/j.pce.2019.102830
- Deng, Z., Xun, H., Zhou, M., Jiang, B., Wang, S., Guo, Q., et al. (2015). Impacts of Tropical Cyclones and Accompanying Precipitation on Infectious Diarrhea in Cyclone Landing Areas of Zhejiang Province, China. *Ijperph* 12 (2), 1054–1068. doi:10.3390/ijperph120201054
- Didan, K. (2015). MOD13A1 MODIS/Terra Vegetation Indices 16-Day L3 Global 500m SIN Grid V006 [Data Set]. NASA EOSDIS LP DAAC. doi:10.5067/MODIS/MOD13A1.006
- Emanuel, K. (2005). Increasing Destructiveness of Tropical Cyclones over the Past 30 Years. *Nature* 436 (7051), 686–688. doi:10.1038/nature03906
- Fengjin, X., and Ziniu, X. (2010). Characteristics of Tropical Cyclones in China and Their Impacts Analysis. *Nat. Hazards* 54, 827–837. doi:10.1007/s11069-010-9508-7
- Fischer, T., Su, B., and Wen, S. (2015). Spatio-Temporal Analysis of Economic Losses from Tropical Cyclones in Affected Provinces of China for the Last 30 Years (1984–2013). *Nat. Hazards Rev.* 16, 04015010. doi:10.1061/(asce)nh.1527-6996.0000186
- Gemmer, M., Yin, Y., Luo, Y., and Fischer, T. (2011). Tropical Cyclones in China: County-Based Analysis of Landfalls and Economic Losses in Fujian Province. *Quat. Int.* 244, 169–177. doi:10.1016/j.quaint.2011.03.021
- He, C., Li, M., Li, T. T., Peng, X., Li, J., and Zhao, J. (2016). Comparison and Analysis of the Four Methods of Determining Weights in Multi-Objective Comprehensive Evaluation. *J. Hubei Univ. (Natural Science)* 38 (2), 172–178.
- Huang, C. (2005). *Risk Assessment of Natural Disaster Theory & Practice*. Beijing: Science Press, 45–94. (in Chinese).
- IPCC (2013). “Climate Change 2013,” in *The Physical Science Basis* (Cambridge, UK: Cambridge University Press).
- IPCC (2014). “Climate Change 2014,” in *Impacts, Adaptation, and Vulnerability. Part A: Global and Sectoral Aspects. Contribution of Working Group II to the Fifth Assessment Report of the Intergovernmental Panel on Climate Change* (Cambridge: Cambridge University Press), 535–612.
- Knutson, T., Camargo, S. J., Chan, J. C. L., Emanuel, K., Ho, C.-H., Kossin, J., et al. (2019). Tropical Cyclones and Climate Change Assessment: Part I: Detection and Attribution. *Bull Amer Meteorol. Soc* 100, 1987–2007. doi:10.1175/BAMS-D-18-0189.1
- Lee, T.-C., Knutson, T. R., Nakaegawa, T., Ying, M., and Cha, E. J. (2020). Third Assessment on Impacts of Climate Change on Tropical Cyclones in the Typhoon Committee Region - Part I: Observed Changes, Detection and Attribution. *Trop. Cyclone Res. Rev.* 9 (1), 1–22. doi:10.1016/j.tcr.2020.03.001
- Li, R. C. Y., Zhou, W., Shun, C. M., and Lee, T. C. (2017). Change in Destructiveness of Landfalling Tropical Cyclones over China in Recent Decades. *J. Clim.* 30, 3367–3379. doi:10.1175/JCLI-D-16-0258.1
- Luo, W., Hou, M., Liu, X., Huang, S., Chao, H., Zhang, R., et al. (2018). Geological and Geochemical Characteristics of marine-continental Transitional Shale from the Upper Permian Longtan Formation, Northwestern Guizhou, China. *Mar. Pet. Geology* 89 (4), 58–67. doi:10.1016/j.marpetgeo.2017.06.029
- Mendelsohn, R., Emanuel, K., Chonabayashi, S., and Bakkensen, L. (2012). The Impact of Climate Change on Global Tropical Cyclone Damage. *Nat. Clim Change* 2, 205–209. doi:10.1038/nclimate1357
- Meraj, G., Romshoo, S. A., Yousuf, A. R., Altaf, S., and Altaf, F. (2015). Assessing the Influence of Watershed Characteristics on the Flood Vulnerability of Jhelum Basin in Kashmir Himalaya. *Nat. Hazards* 77, 153–175. doi:10.1007/s11069-015-1605-1
- Ministry of Natural Resources (2009–2020). *Bulletin of China marine Disaster*. Beijing.
- National Climate Center of China Meteorological Administration (NCC) (2009). *Technical Specification for Risk Zoning of Rainstorm and Flood Disaster*.
- Niu, H., Liu, M., Lu, M., Quan, R., Wang, J., and Zong, N. (2011). Risk Assessment of Typhoon Disasters in China Coastal Area during Last 20 Years. *Sci. Geogr. Sin* 31 (6), 764–768. (in Chinese with English abstract).
- Pan, A., Tang, X., and Liu, H. (2002). Preliminary Research into the Typhoon Disaster Chain in Guangdong Coastal Area. *J. Guangzhou University(Natural Sci. Edition)* 1 (3), 55–61. (in Chinese with English abstract).
- Pang, G., Huang, Y., He, J., Li, W., and Zhang, L. (2020). Analysis and Assessment of the Characteristics of Typhoon Induced Storm Surge in Zhuhai. *J. Trop. Meteorology* 36 (1), 42–50. (in Chinese with English abstract). doi:10.16032/j.issn.1004-4965.2020.005
- Pielke, R. A., Gratz, J., Landsea, C. W., Collins, D., Saunders, M. A., and Musulin, R. (2008). Normalized Hurricane Damage in the United States: 1900–2005. *Nat. Hazards Rev.* 9, 29–42. doi:10.1061/(asce)1527-6988(2008)9:1(29)

- Pielke, R. A., Landsea, C., Mayfield, M., Layer, J., and Pasch, R. (2005). Hurricanes and Global Warming. *Bull. Amer. Meteorol. Soc.* 86 (11), 1571–1576. doi:10.1175/BAMS-86-11-1571
- Ren, Z., Yu, Y., Zou, F., and Xu, Y. (2012). Quality Detection of Surface Historical Basic Meteorological Data. *J. Appl. Meteorol. Sci.* 23 (6), 739–747. (in Chinese with English abstract).
- Shi, P., Lu, L., Wang, M., and Wang, J. (2014). Disaster System: Disaster Cluster, Disaster Chain and Disaster Compound. *J. Nat. Disaster* 23 (6), 1–12. doi:10.11821/dljy201605003
- Shi, P. (1991). On the Theory of Disaster Research and its Practice. *J. Nanjing Univ. Nat. Sci. Res. Nat. Disasters album*, 37–42. (in Chinese with English abstract).
- Shi, P., Shuai, J., Chen, W., and Liu, L. (2010). Study on Large-Scale Disaster Risk Assessment and Risk Transfer Models. *Int. J. Disaster Risk Sci.* 1 (2), 1–8. doi:10.3974/j.issn.2095-0055.2010.02.001
- Shih, H.-J., Chen, H., Liang, T.-Y., Fu, H.-S., Chang, C.-H., Chen, W.-B., et al. (2018). Generating Potential Risk Maps for Typhoon-Induced Waves along the Coast of Taiwan. *Ocean Eng.* 163, 1–14. doi:10.1016/j.oceaneng.2018.05.045
- Shuai, J., Xu, W., and Shi, P. (2012). Characteristic Analysis of Typhoon Disaster Chains in the Yangtze River Delta Region of China. *J. Nat. Disasters* 21 (3), 36–42. doi:10.13577/j.jnd.2012.0306
- Sun, S., Zhai, J., Li, Y., Huang, D., and Wang, G. (2020). Urban Waterlogging Risk Assessment in Well-Developed Region of Eastern China. *Phys. Chem. Earth, Parts A/B/C* 115, 102824. doi:10.1016/j.pce.2019.102824
- Tang, X., and Liang, M. (2006). The Tropical Cyclones Landed in Guangdong and its Disaster Chains. *J. Catastrophology* 21 (3), 47–53. (in Chinese with English abstract).
- Wang, D., Liu, J., Shan, Y., Ji, J., and Song, H. (2001). The Design and Establishment of 1:250000 Digital Elevation Model of China. *Bull. Surv. Mapp.* 10, 27–29.
- Wang, R., Lian, F., Yu, H., Shi, P., and Wang, J. (2016b). Classification and Regional Features Analysis of Global Typhoon Disaster Chains Based on hazard-formative Environment. *Geographical Res.* 35 (5), 836–850. doi:10.11821/dljy201605003
- Wang, Y., Wen, S., LiThomas, X. F., Thomas, F., Su, B., Wang, R., et al. (2016a). Spatiotemporal Distributions of Influential Tropical Cyclones and Associated Economic Losses in China in 1984–2015. *Nat. Hazards* 84, 2009–2030. doi:10.1007/s11069-016-2531-6
- Wang, Y., Yin, Y., and Song, L. (2021a). Characteristics and Diagnosis of the Landfalling Tropical Cyclones in the Guangdong-Hong Kong-Macao Greater Bay Area of China during 1981–2018. *J. Trop. Meteorology* 27 (3), 246–258. doi:10.46267/j.1006-8775.2021.22
- Wang, Y., Zhai, J., and Song, L. (2021b). Waterlogging Risk Assessment of the Beijing-Tianjin-Hebei Urban Agglomeration in the Past 60 Years. *Theor. Appl. Climatol.* 145, 1039–1051. doi:10.1007/s00704-021-03670-5
- Webster, P. J., Holland, G. J., Curry, J. A., and Chang, H.-R. (2005/2005). Changes in Tropical Cyclone Number, Duration, and Intensity in a Warming Environment. *Science* 309 (5742), 1844–1846. doi:10.1126/science.1116448
- Xu, N., and Gong, P. (2018). Significant Coastline Changes in China during 1991–2015 Tracked by Landsat Data. *Sci. Bull.* 63, 883–886. doi:10.1016/j.scib.2018.05.032
- Xu, X., Sun, D., and Guo, T. (2015). A Systemic Analysis of Typhoon Risk across China. *Nat. Hazards* 77 (1), 461–477. doi:10.1007/s11069-015-1586-0
- Yang, G. (1997). *The Coastal Environments Change and Regional Responses to it in China*. Nanjing: Nanjing Institute of Geography and Limnology, Chinese Academy of Sciences.
- Ye, J., Lin, G., Zhang, M., and Gao, L. (2020). Hazard Analysis of Typhoon Disaster-Causing Factors Based on Different landing Paths: a Case Study of Fujian Province, China. *Nat. Hazards* 100 (2), 811828. doi:10.1007/s11069-019-03843-6
- Ye, J., Lin, G., and Zhang, M. (2014). Spatial Characteristics of Typhoon Disaster Chains in Fujian Province. *J. Fujian Normal Univ. (Natural Sci. Edition)* 30 (2), 99–106. (in Chinese with English abstract).
- Ye, J., Wang, S., and Ding, F. (2019). Analysis of Typhoon Disaster Exposure in Coastal Areas of China Based on Geospatial Parameters. *J. Inst. Disaster Prev.* 21 (1), 82–88. (in Chinese with English abstract).
- Yin, J., Wu, S., and Dai, E. (2012). Assessment of Economic Damage Risks from Typhoon Disasters in Guangdong, China. *J. Resour. Ecol.* 3 (2), 144–150. doi:10.5814/j.issn.1674-764x.2012.02.006
- Yin, J., Yin, Z., and Xu, S. (2013). Composite Risk Assessment of Typhoon-Induced Disaster for China's Coastal Area. *Nat. Hazards* 69, 1423–1434. doi:10.1007/s11069-013-0755-2
- Ying, M., Chen, B., and Wu, G. (2011). Climate Trends in Tropical Cyclone-Induced Wind and Precipitation over mainland China. *Geophys. Res. Lett.* 38, a–n. doi:10.1029/2010GL045729
- Ying, M., Zhang, W., Yu, H., Lu, X., Feng, J., Fan, Y., et al. (2014). An Overview of the China Meteorological Administration Tropical Cyclone Database. *J. Atmos. Ocean. Technol.* 31, 287–301. doi:10.1175/jtech-d-12-00119.1
- Yu, F., Dong, J., and Xu, F. (2016). *Marine Disasters in the Offshore Seas of China*. Beijing: Maritime Press, 46–48.
- Yu, H., Wang, J., Chai, M., and Shi, P. (2014). Review on Research Methods of Disaster Loss Accumulation and Amplification of Disaster Chains. *Prog. Geogr.* 33 (11), 1498–1511. (in Chinese with English abstract). doi:10.11820/dlkxjz.2014.11.007
- Yu, Y.-C., Chen, H., Shih, H.-J., Chang, C.-H., Hsiao, S.-C., Chen, W.-B., et al. (2019). Assessing the Potential Highest Storm Tide hazard in Taiwan Based on 40-year Historical Typhoon Surge Hindcasting. *Atmosphere* 10 (6), 346. doi:10.3390/atmos10060346
- Zhang, X., Wei, B., Yang, H., and He, X. (2018). Risk Assessment of Typhoon Disaster in Guangdong Province Based on GIS. *J. Trop. Meteorology* 34 (6), 783–790. (in Chinese with English abstract).
- Zhang, Y., Li, S., and Chen, H. (2017). Evaluation of Typhoon Disaster Risk in Guangdong Province. *J. Trop. Meteorol.* 33 (2), 281–288. doi:10.16032/j.issn.1004-4965.2017.02.015
- Zhao, H., Liu, X., Yu, C., and Shang, Z. (2014). Risk Assessment and Temporal-Spatial Changes of Collapse, Landslide and Debris Flow in Guangdong. *Trop. Geogr.* 34 (6), 804–813. (in Chinese with English abstract).
- Zhejiang Meteorological Observatory (2017). *Assessment Technical Specification for the Risk Level of Rainstorm Processes*. DB33/T 2025–2017.
- Zhou, J., Zhou, Y., Li, H., and Weng, J. (2015). Statistical Analysis of Tropical Cyclones Affecting the Zhaoqing Prefecture over the Past 15 Years. *Guangdong Meteorology* 37 (2), 45–47. (in Chinese with English abstract).
- Zhu, Z., Yin, Y., and Huang, J. (2018). Analysis on Hazards of the Wind and Rain Factors Associated with Tropical Cyclones in China's Major Coastal Provinces. Part I: Basic Values. *J. Trop. Meteorology* 34 (2), 145–152. (in Chinese with English abstract). doi:10.16032/j.issn.1004-4965.2018.02.001

Conflict of Interest: The authors declare that the research was conducted in the absence of any commercial or financial relationships that could be construed as a potential conflict of interest.

Publisher's Note: All claims expressed in this article are solely those of the authors and do not necessarily represent those of their affiliated organizations, or those of the publisher, the editors, and the reviewers. Any product that may be evaluated in this article, or claim that may be made by its manufacturer, is not guaranteed or endorsed by the publisher.

Copyright © 2022 Wang, Yin and Song. This is an open-access article distributed under the terms of the Creative Commons Attribution License (CC BY). The use, distribution or reproduction in other forums is permitted, provided the original author(s) and the copyright owner(s) are credited and that the original publication in this journal is cited, in accordance with accepted academic practice. No use, distribution or reproduction is permitted which does not comply with these terms.



Sea Surface Height Changes due to the Tropical Cyclone-Induced Water Mixing in the Yellow Sea, Korea

KiRyong Kang^{1*} and Il-Ju Moon^{2*}

¹Operational Systems Development Department, National Institute of Meteorological Sciences/KMA, Jeju, South Korea,

²Typhoon Research Center, Jeju National University, Jeju, South Korea

OPEN ACCESS

Edited by:

Hui Yu,
China Meteorological Administration,
China

Reviewed by:

Ricardo de Camargo,
University of São Paulo, Brazil
Costas A Varotsos,
National and Kapodistrian University of
Athens, Greece

*Correspondence:

KiRyong Kang
krkang@korea.kr
Il-Ju Moon
ijmoon@jejunu.ac.kr

Specialty section:

This article was submitted to
Atmospheric Science,
a section of the journal
Frontiers in Earth Science

Received: 01 December 2021

Accepted: 01 March 2022

Published: 07 April 2022

Citation:

Kang K and Moon I-J (2022) Sea
Surface Height Changes due to the
Tropical Cyclone-Induced Water
Mixing in the Yellow Sea, Korea.
Front. Earth Sci. 10:826582.
doi: 10.3389/feart.2022.826582

Sea surface height changes due to the tropical cyclone (TC)-induced water mixing in the Yellow Sea, Korea, were investigated using temperature and salinity profile data obtained by two Argo floats during the summer and fall of 2018 and 2020. Strong winds and low pressure, which are important characteristics of TCs, caused horizontal and vertical sea surface water movement and induced water mixing. This caused an increase in mixed layer depth, a decrease in water density, and an increase in specific volume. Specific volume changes related to the water steric effect were directly linked to sea surface height changes. During the TC Soulik (1819) period, the thermocline deepened by more than 10 m, and the steric sea level was increased by more than 3 cm. Other TC cases, such as Jebi (1821), Trami (1824), and Kong-Rey (1825), showed sea level increases of 1–2 cm. In 2020, 3 TCs—Bavi (2008), Maysak (2009), and Haishen (2010)—showed minor sea level increases (about 0.5–1 cm) because of weak mixing due to their high moving speeds or weak impacts. As a post-TC impact, the water mixing could cause a rise in sea levels due to the steric effect of seawater.

Keywords: tropical cyclone, Yellow Sea, Argo floats, water mixing, specific volume change, steric sea level

INTRODUCTION

Tropical cyclones (TCs) severely impact oceanic environments in terms of external and internal water bodies (Ginis, 2002; D'Asaro et al., 2011; Pun et al., 2011; Harris, 1963). When a TC moves over the sea, the sea level rises in the central area of the TC, and high waves form around the TC. The sea level rise is directly related to the convergence of wind-induced water transport and to the inverse barometric effect of low pressure, and high waves are related to wind stress on the sea surface. The TC, in turn, is affected by the oceanic environment due to air–sea interactions. Recent research suggests that warm eddies and high ocean heat content areas play an important role in TC intensity fluctuations (Lin et al., 2005; Lin et al., 2008; Lu et al., 2016). These external phenomena occur when a TC approaches and disappear soon after it moves away.

As an internal effect on the ocean, TCs induce vertical mixing of warmer upper waters with colder lower waters due to velocity shear and turbulent flow changes affecting the temperature and salinity profiles, which results in thermocline and halocline layer fluctuations (Mao et al., 2000; Baranowski et al., 2011; Vincent et al., 2012; Kang et al., 2020). Based on Argo float observations, Baranowski et al. (2011) found that water surface cooling was caused by increased entrainment induced by the thermocline due to turbulent mixing and that vertical mixing could result in salinity changes, which eventually led to a greater or fluctuating mixed layer depth. Vincent et al. (2012) used the wind power index to investigate the cooling processes caused by TCs with high energy transfer to the upper ocean

and showed that the cooling process and temperature stratification steepness differed according to the wind's power. Kang et al. (2020) also used daily Argo float observations in the Yellow Sea, Korea, and found that the temperature and salinity profiles during the passage of a typhoon exhibited a sudden deepening of the thermocline and halocline, which then moved 30–50 m up and down in the upper layer.

Many previous studies on the impact of TCs on oceans have focused on the mechanism by which oceans respond to TC conditions (Pei et al., 2015; Zhang et al., 2016; Pei et al., 2019). These studies have shown that most external events occur during the passage of TCs and quickly dissipate afterward. However, internal effects, such as subsurface heat anomalies caused by vertical water mixing, persist over considerably longer periods (Korty et al., 2008; Jansen et al., 2010). Pasquero and Emanuel (2008) studied the global effects of the interplay between TCs and upper ocean heat content and suggested that at least one-third of the heat anomaly could remain in a tropical region for more than 1 year. Mei et al. (2013) used satellite-derived sea surface height to quantify cyclone-induced ocean warming by directly monitoring the thermal expansion of water, and their results suggest that TC-induced mixing is closely related to sea surface height changes and that its effects could be associated with climatological variations.

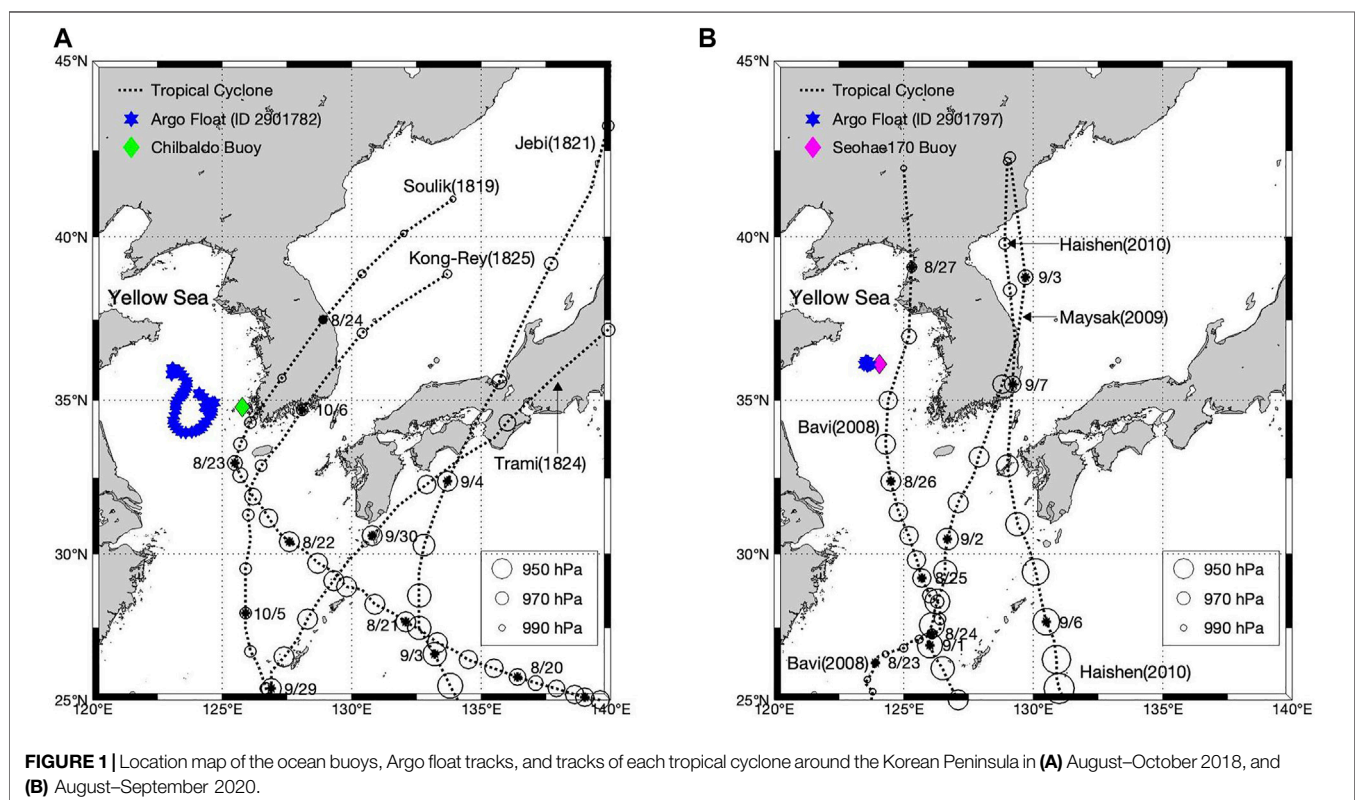
Although sea surface height changes and TC-induced mixing could be related, direct observation-based work of this relationship is lacking. Therefore, this study aimed to investigate how much of sea surface height could be changed by TC-induced water mixing using Argo float-observed

temperature and salinity profiles in the Yellow Sea. The main research question was to what extent height increased due to increased water volume directly related to TC-induced water mixing during the summer and fall of 2018 and 2020.

The data and methods used in this study are described in *Data and Methods*. The buoy data analysis, Argo float-measured temperature and salinity profile changes, and specific volume of water and steric sea level (SSL) changes are reported and discussed in *Results and Discussion*. Finally, *Conclusions* summarizes the results and presents the conclusions.

DATA AND METHODS

The Korea Meteorological Administration (KMA) operates more than 20 ocean buoys around the Korean peninsula to detect and monitor extreme weather phenomena above oceans, since they can be run automatically even under the TC condition in the summer and fall. These buoys provide marine meteorological information, such as wind, sea-level pressure, air and water temperature, and waves, at 30-min or 1-h intervals (<http://www.kma.go.kr>). The buoy data used in this study were obtained from two stations: Chilbaldo buoy, which was established at 34.7933°N, 125.7769°E on 1 July 1997, and Seohae170 buoy, which was established at 36.1333°N, 124.0569°E on 5 November 2019 (**Figure 1**). These stations were selected because they were near Argo float profiling areas and TC tracks. Marine meteorological data (August 15–10 October 2018) from Chilbaldo buoy were mainly investigated for TC cases of



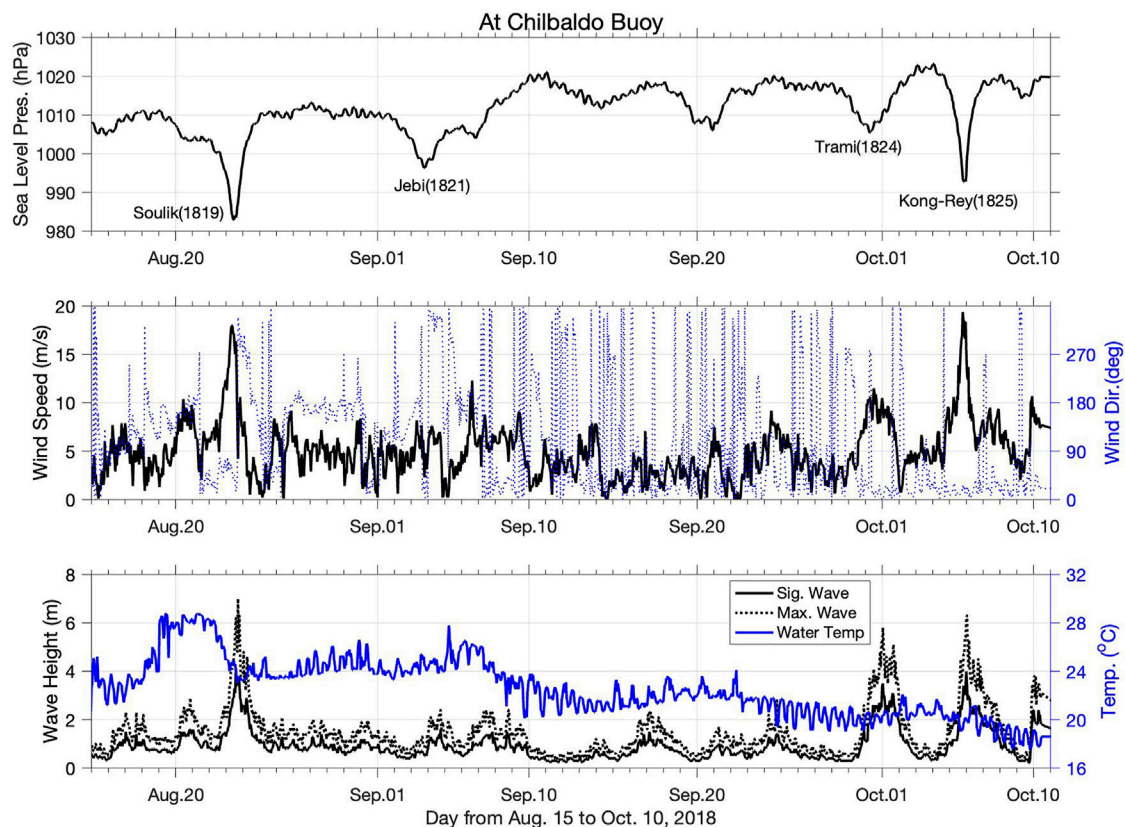


FIGURE 2 | Time series of sea level pressure, wind speeds and direction, and wave height and water temperature obtained by the Chilbaldo buoy station from August 15 to October 10, 2018. Time is in UTC units.

2018, such as Typhoons Soulik (1819), Jebi (1821), Trami (1824), and Kong-Rey (1825), whereas Seohae170 buoy data (August 21–14 September 2020) were used for TCs of 2020, such as Bavi (2008), Maysak (2009), and Haishen (2010). These TCs were selected because they directly or indirectly affected the Yellow Sea in the summer and fall of each year. TC track and intensity information was obtained from the Regional Specialized Meteorological Center, Tokyo (<https://www.jma.go.jp>).

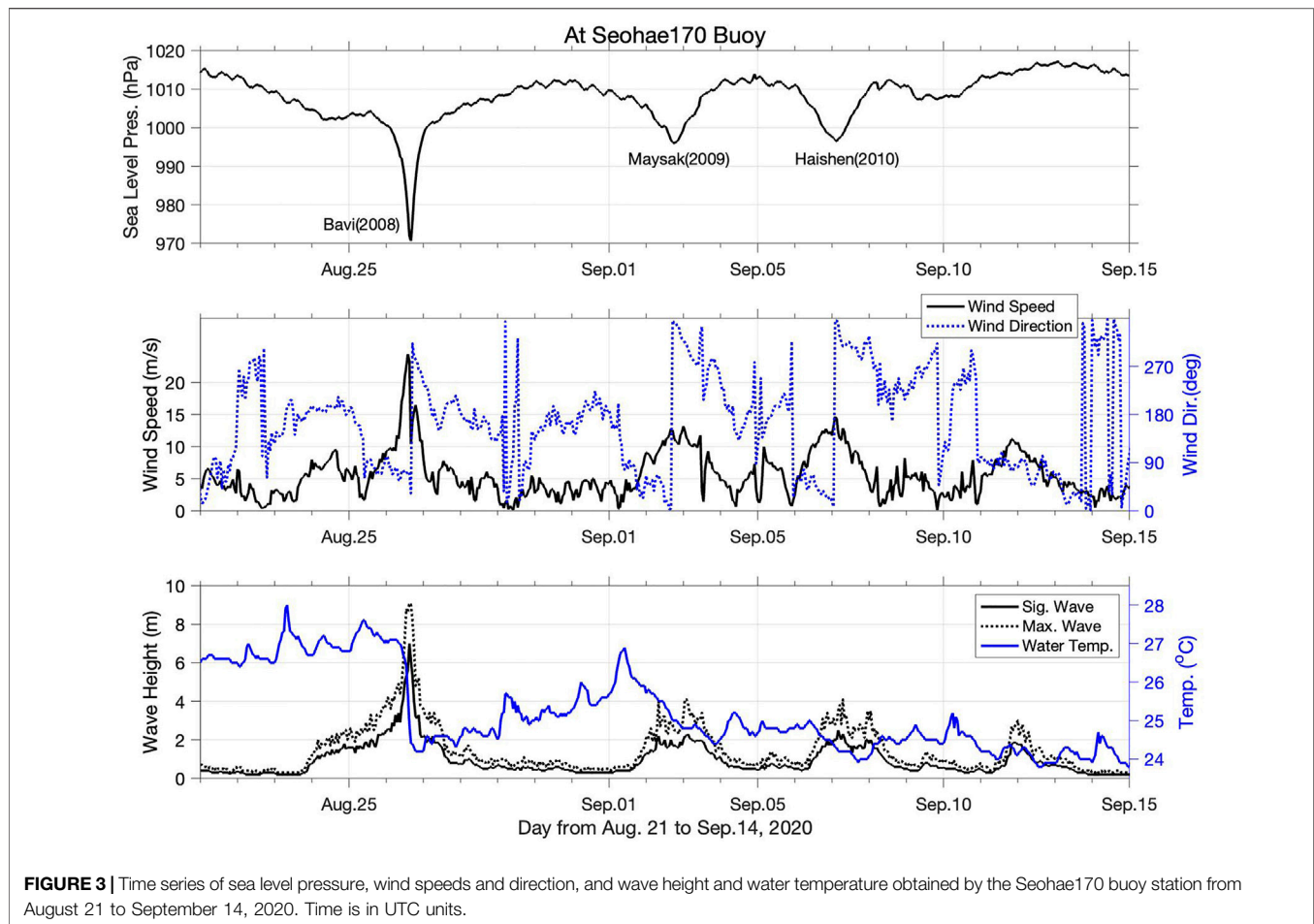
To investigate the internal ocean response during or after the passage of a TC, the water temperature and salinity profiles of the same area are needed. However, manual observations at sea are not possible under such weather conditions. To overcome this observation limitation, Argo floats have been used to determine the ocean temperature and salinity profiles from the surface to a depth of 2000 m in the open ocean in 10-days cycles as part of the integrated global ocean observation program (<https://argo.ucsd.edu>). The National Institute of Meteorological Sciences/KMA first deployed Argo floats in the Yellow Sea in 2017. Since the Yellow Sea is shallower, with a maximum depth of 80 m, and shows greater variation of the ocean characteristics than the open ocean, a different profiling scheme, including one- or 2-day profiling cycles, 1-m vertical resolution, 60-m parking-depth, and stronger buoyant force, was set up prior to deployment. Two Argo floats were deployed

in 2018, and another two were deployed in 2020. In this study, data from one Argo float were used for each year. In **Figure 1A**, the blue stars show the track of Argo float 2901782 from August 15 to 14 October 2018, and in **Figure 1B**, the blue stars show the track of Argo float 2901797 from August 21 to 14 September 2020. During this period, interestingly this float was not moved a lot and it looked like staying at the same point.

Water temperature and salinity changes are directly related to the water density which also causes water volume change. In this study, the international equation of state for seawater, IES80 (UNESCO, 1981), was used to calculate the water density. Since the sea water volume change is inversely related to water density, seawater volume-induced SSL changes can be estimated as:

$$SSL = \frac{1}{g} \int_{p_{surface}}^{p_{bottom}} \frac{1}{\rho(s, t, p)} dp = \frac{1}{g} \int_{p_{surface}}^{p_{bottom}} \alpha(s, t, p) dp \quad (1)$$

where $g = 9.8 \text{ m/s}^2$, ρ is water density, p is pressure, and α is the specific volume of sea water. The water temperature, salinity, and pressure profiles regularly obtained by the Argo floats were used for this calculation. It should be noted that although the profiling locations were not fixed because the floats drifted along the ocean



currents, it was assumed that these data reflected the impact of TCs on the ocean since all profiling locations were in an impacted area during the passage of a TC.

RESULTS AND DISCUSSION

TC Cases and Ocean Status

Figure 1 shows the tracks of the 2018 and 2020 TCs directly or indirectly affecting the area around the Korean Peninsula during August, September, and October. In 2018, 4 TCs—Soulik (1819), Jebi (1821), Trami (1824), and Kong-Rey (1825)—affected the area around the peninsula (**Figure 1A**). Soulik (1819) and Kong-Rey (1825) had direct impacts, whereas Jebi (1821) and Trami (1824) had indirect impacts. In 2020, 3 TCs—Babi (2008), Maysak (2009), and Haishen (2010)—made landfall and directly impacted the study area from August 21 to September 14. As shown in **Figure 1B**, Babi (2008) almost passed over the buoy and Argo float 2901797 on 26 August 2020, with a central pressure of 970 hPa, while the other two were about 100 km away from the buoy and float when they approached the Korean Peninsula on September 2 and 6 September 2020, respectively. According to the KMA's weather stations, the

central pressure of both TCs was 955–960 hPa when it made landfall near Busan City, Korea.

Figure 2 shows the central pressure, wind speed, wave height, and water temperature changes recorded by Chilbaldo buoy from August to October 2018. The sea-level pressure data clearly showed signals from the 4 TCs. Since Soulik (1819) on August 23–24 and Kong-Rey (1825) on 6 October 2018 passed very near the buoy, the sea-level pressure was relatively low, the wind speed exceeded 17–19 m/s, the significant wave height was over 4 m, and the maximum wave height was 6 m. On the other hand, the wind speed in cases of TCs that did not pass near the buoy was 7–12 m/s. In the Trami (1824) case, the wind speed was about 10 m/s, and the maximum wave height was almost 6 m, possibly because of the longer duration of strong winds compared to other TCs, with a wind speed of 9–10 m/s maintained for more than 1 day. Therefore, strong winds and high waves under TC conditions, which cause strong mixing in the upper water layer, resulting in a sudden drop in water temperature, can be expected.

The time series of water temperature shown in the bottom panel of **Figure 2** reveals several phenomena. First, when TCs passed over this area, a sudden decrease in the sea surface temperature (SST) occurred. Especially on August 23–24, 2018, Soulik (1819) caused a water temperature reduction

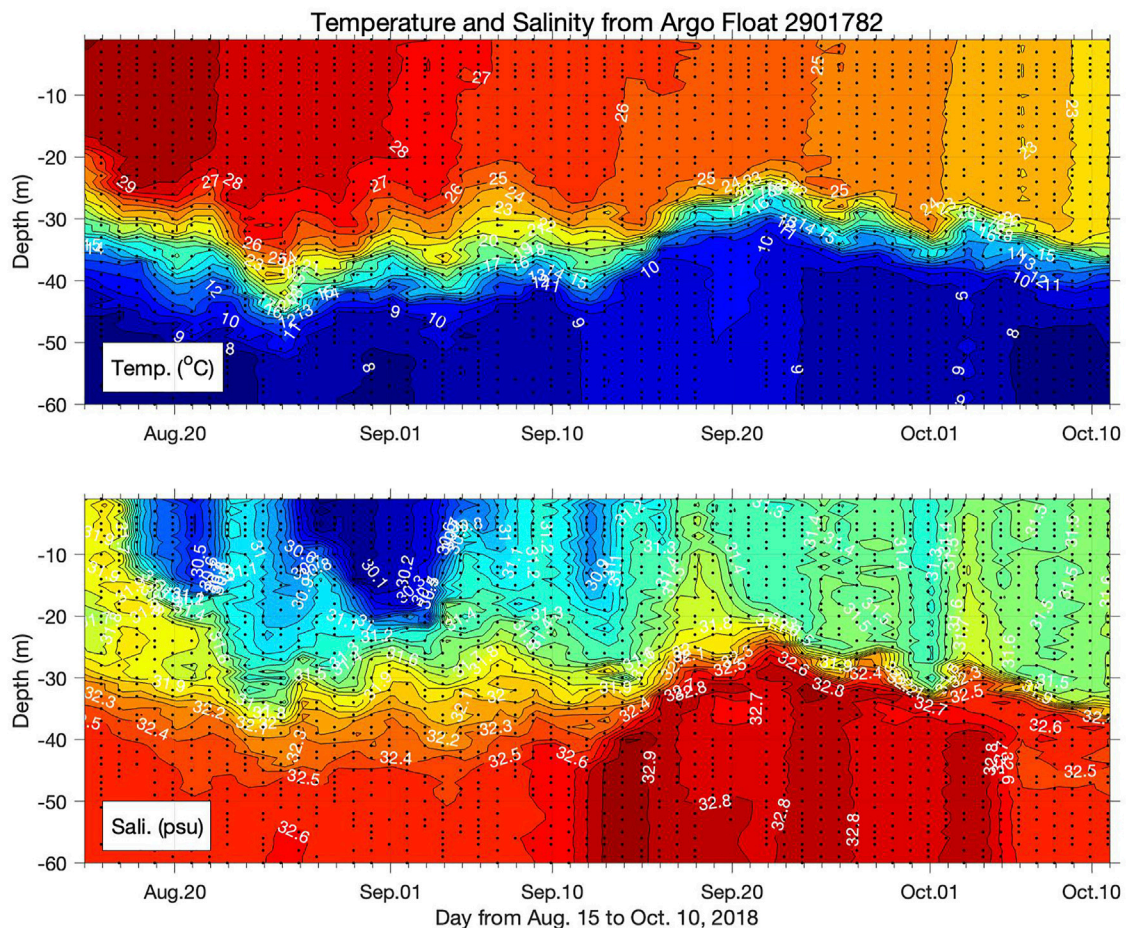


FIGURE 4 | Vertical distribution of water temperature and salinity in the Yellow Sea obtained by Argo float 2901782 from August 15 to October 10, 2018. The black dots indicate the observation depths.

of almost 4 °C. The temperature then started to recover before Jebi (1821)'s approach. This process was repeated in every TC case. It can be concluded that the decrease in water temperature during the summer–fall season was accelerated by TC-induced water mixing. Moreover, there was also tidal variation such as semidiurnal and spring-neap variations, which may also have caused the expansion and contraction of the summer low SST area and temperature front formation along the southwestern coast of Korea (Lie, 1989; Cho et al., 1995; Kang and Lee, 2014).

Figure 3 shows the air–sea situation in the central area of the Yellow Sea in August and September 2020. As mentioned before, there were 3 TCs during this period. Babi (2008) passed over the buoy on 26 August 2020, and the recorded sea-level pressure was almost 970 hPa. The closest proximity of Maysak (2009) and Haishen (2010) to the float was about 100 km, and the sea-level pressure recorded at Seohae170 buoy was about 995 hPa for both TCs. The wind speed was about 25 m/s in the Babi (2008) case and 12–13 m/s in the Maysak (2009) and Haishen (2010) cases, with a rotational direction. Regarding the duration of the wind's impact on the

ocean, the Babi (2008) case was relatively shorter than the other cases. In terms of wave height, the maximum wave height in the Babi (2008) case was about 9 m and the significant wave height was 7 m. This wave height could be developed by the sudden increase in wind speed. In other two cases, the maximum wave height was 4 m, and the significant wave height was 2 m.

The water temperature showed a sudden drop during the passage of TCs, followed by a recovery process. On August 26, September 1, and 6 September 2020, the water temperature decreased by about 3, 2.5, and 1°C, respectively, and then recovered, with some fluctuations. The decrease on August 26 occurred rapidly in the space of a few hours, while that on September 1 was gradual, occurring over a period of almost 3 days, which means that the longer cooling could have a deeper impact on the ocean. In terms of total period, as in 2018, TC activity accelerated the water cooling process from summer to fall. Diurnal water temperature fluctuations were observed in the central Yellow Sea area, while semidiurnal fluctuations were observed in coastal areas (bottom panel of **Figure 2**). It may be speculated that the diurnal variation in

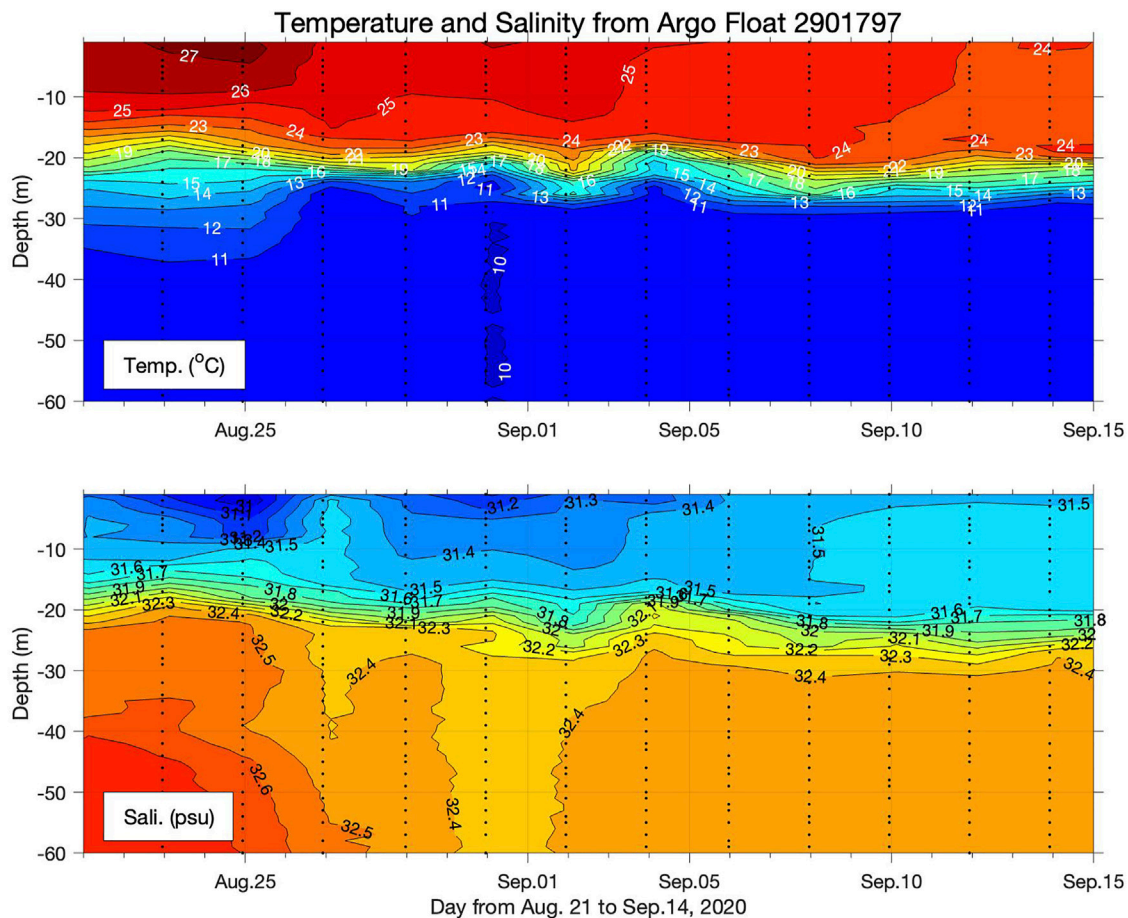


FIGURE 5 | Vertical distribution of water temperature and salinity in the Yellow Sea obtained by Argo float 2901797 from August 21 to September 14, 2020. The black dots indicate the observation depths.

water temperature is caused by tides. However, this topic is beyond the scope of this study.

Vertical Temperature and Salinity Changes

To see what is going on inside the ocean during the passage of a TC, water temperature and salinity profile data are needed. In reality, it is impossible for a ship to perform a CTD cast under such high-risk weather conditions. The deployment of unmanned floats, such as Argo floats, is a solution to this problem. **Figure 4** shows the vertical distribution of water temperature and salinity profiled in 1-day cycles by Argo float 2901782 between August 15 and 14 October 2018. According to the Chilbaldo buoy data presented in **section 3-1**, sudden decreases in pressure was occurred when TCs were approaching. For example, August 23, September 3, September 30, and 6 October 2018 showed inverted peaks in sea-level pressure.

As shown in the water temperature profile in the top panel of **Figure 4**, the thermocline fluctuated between 25 and 45 m, and the upper layer temperature showed a homogeneous vertical distribution. When a TC passes over the sea, the upper layer can be mixed by the strong winds and high waves, resulting in a homogeneous distribution. In this case, however, the upper layer was already mixed, so it is difficult to find evidence of TC-induced

mixing. Nevertheless, the vertical changes in the thermocline could provide such evidence. For example, on August 23, the thermocline started to deepen, reached its maximum depth on August 26, and began to recover until August 27. At this stage, the thermocline moved from 30 m to almost 45 m, and the water temperature change at a depth of 40 m was over 8°C when water mixing was at its peak. Even the water temperature change rate differed due to the external TC conditions. The same process was observed on September 3–5, September 28–October 2, and October 5–6. It is worth noting that the deepening of the thermocline started when a TC was approaching and peaked one or 2 days after the TC had passed. In the Trami (1824) case, it started on September 28, peaked on October 1, and recovered 1 day later.

The salinity distribution showed clearer evidence of TC-induced vertical mixing, even in the upper layer. As shown in the bottom panel of **Figure 4**, the halocline was at a depth of 25–40 m and exhibited a barrier of low salinity in the upper layer and a barrier of high salinity in the deeper layer. The difference between two layers was about 2 psu. Like the thermocline, this layer exhibited depth fluctuations on August 23–27, September 3–5, and September 28–2 October 2018. The profile change showed homogenizing salinity in

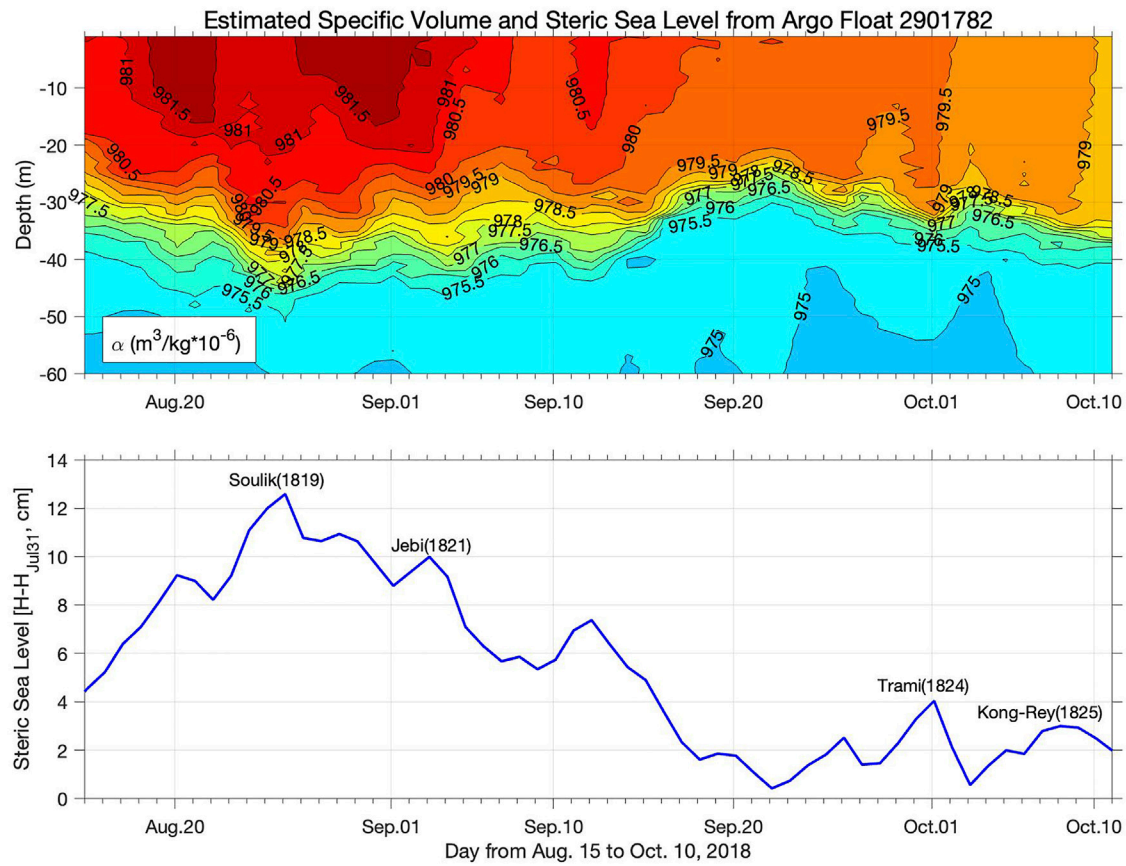


FIGURE 6 | Calculated specific volume of sea water and the steric sea level change from August 15 to October 10, 2018. The steric sea level was calculated as the height relative to the value of 31 July 2018.

the vertical direction in the upper layer during the TC impact period around August 24, September 5, September 29–30, and 6 October 2018. This finding suggests that the water temperature and salinity profiles were affected by the TCs and persisted for several days afterward. Moreover, it can be expected that the water volume may be changed by the steric effect.

Let us consider another TC impact case in the Yellow Sea in 2020. **Figure 5** shows the 2-day cycle of Argo float 2901797, which was deployed in the study area on 11 November 2019, and remained for one and a half years. Between August 21 and 14 September 2020, this float remained in an almost fixed area, so the profile data could represent the water temperature and salinity in the central area of the Yellow Sea. However, since the observation interval was 2 days, the float had certain limitations in recording detailed profile changes in terms of the ocean's response to TCs. Especially in cases of fast-moving TCs, it is difficult to determine the exact ocean response during TC impact periods. TC Bavi (2008) passed near the Argo float with strong winds and low sea-level pressure on 26 August 2020, however the moving speed of every 6 hours was 25.9, 38.9, 38.9, and 53.8 km/h from 06:00 UTC on August 26 to 00:00 UTC on August 27. The moving speeds of Maysak (2009) and Haishen (2010) were 35.5–58.3 km/h and

44.5–51.9 km/h when they were approaching the Korean Peninsula. This means that none of these TCs had enough time to seriously impact the sea.

As shown in the top panel of **Figure 5**, the surface temperature decreased from 27 to 25°C on August 25–26, 2020, and the thermocline was at a depth of 20–30 m. However, as there are no profile data for August 26, it is difficult to know the situation when the TC was passing over the float. On September 1–2 and 7–8, the upper layer water temperature was almost homogeneous. However, the temperature at a depth of 20–30 m slightly increased due to the impact of the TC. The salinity profile in the bottom panel of **Figure 5** shows evidence of upper layer mixing above a depth of 20 m, which resulted in a vertical homogenization process—for example, on August 27, September 2, and 8 September 2020. In summary, although the impacts of TCs moving fast over the sea were not severe, these results provide evidence of vertical mixing, such as thermocline and halocline fluctuations and homogenizing processes in the upper layer.

Seawater Volume and Steric Sea Level

The previous *Vertical Temperature and Salinity Changes* dealt with water temperature and salinity distribution changes caused by TCs during the summer and fall of 2018 and 2020. Based on the

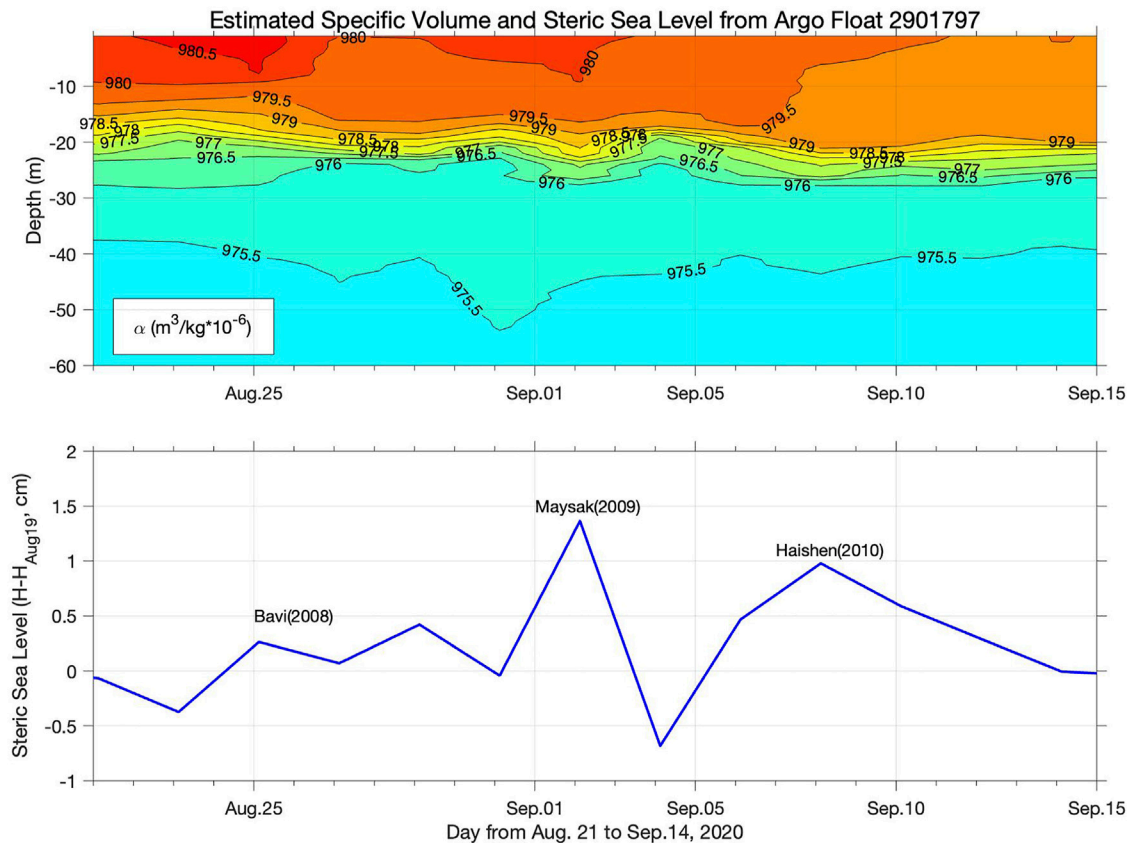


FIGURE 7 | Calculated specific volume of sea water and the steric sea level change from August 21 to September 14, 2020. The steric sea level was calculated as the height relative to the value of 19 August 2020.

temperature and salinity profiles obtained by two Argo floats, the specific volume of water was integrated from the surface and a depth of 60 m using Eq. 1. There are two reasons that we choose 60 m as the bottom. First, most profiles covered from the surface to this depth in common since the parking depth of float was 60 m, and second is that the water depth was deep enough to show almost constant temperature and salinity. And Figures 6, 7 show the specific volume distribution and SSL of each profile in 2018 and 2020. The SSL values during the study period were calculated as the heights relative to the values obtained from specific dates. The reference date was selected just to see the relative sea level changes before and after the TC events during the study period. So it was chosen under this rule arbitrarily to compare the first TC event of each period, i.e. on 31 July 2018 and 19 August 2020.

An examination of the specific volume distribution between August 15 and 14 October 2018 (top panel of Figure 6) shows that two layers were separated from the thermocline, with a high value in the upper layer ($0.9780\text{--}0.9815 \times 10^{-3} \text{ m}^3/\text{kg}$) and a low value in the lower layer ($0.9755\text{--}0.9760 \times 10^{-3} \text{ m}^3/\text{kg}$). As shown in the temperature profile in Figure 4, the barrier layer depth fluctuated with a linearly deepening trend from summer to fall. When the TC-influenced mixed layer depth started to be deepened, as on August 23, September 2, September 28, and 5 October 2018, the high-volume layer thickened and was directly linked to the increase in sea surface

height. The bottom panel of Figure 6 shows a sudden rise in sea surface as the TC passed over the sea. Assuming that the water temperature and salinity changes during the TC impact period mainly depended on TC-induced mixing, the SSL increased by more than 3 cm between August 23 and 26, 2018. September 3, October 1, and October 8 also showed peak SSL values, with increases of about 1–2 cm. A comparison between TC Soulik (1819) and Kong-Rey (1825) shows that although their wind speeds and wave heights recorded at the same buoy were similar, the SSL change differed. This might be because the warm layer depth increase in the water column was considerably larger in the Soulik (1819) case. In addition, it should be noted that salinity could play a big role in the SSL changes. For example, on Sept. 12, 2018, there were no high waves, TC or strong wind, the SSL showed a peak value. Even this is out of our scope, it could be another topic for the future study.

Figure 7 shows the specific volume distribution and SSL variation in the central area of the Yellow Sea between August 21 and 14 September 2020. There were also two layers separated at a depth of 20 m, and the specific volume in the barrier layer was about $0.9770\text{--}0.9780 \times 10^{-3} \text{ m}^3/\text{kg}$. The depth of the barrier layer was increased under the TC's influence and decreased after the TC impact period. This process was evident, for example, on September 2 and 8 September 2020. The SSL (bottom panel of Figure 7) peaked during the TC impact period, and the sea level rose by about 0.5–1 cm. In the

Bavi (2008) case, since it moved very fast over the Argo float area (at over 50 km/h) and there was no float data on September 26, the SSL did not show a peak value on August 25–27, 2020. Considering the analysis results of specific volume changes in 2018 and 2020, it may be concluded that sea surface height changes depend on TCs' intensity and the length of time during which they remain over the sea, as well as water characteristics such as stratification.

CONCLUSION

It is well known that the ocean is affected by interannual and decadal climate variabilities such as El Niño–Southern Oscillation and Pacific Decadal Oscillation ENSO (Varotsos, 2013; Varotsos et al., 2014; Varotsos et al., 2016), as well as short-time scale fluctuations due to air–ocean interactions during the passage of TCs. It is well known that the ocean is greatly impacted by TCs due to air–sea interactions during their passage. In this study, we investigated sea surface height changes due to TC-induced water mixing phenomena in the Yellow Sea using temperature and salinity profile data from August 15 to 14 October 2018 (Argo float 2901782) and from August 21 to 14 September 2020 (Argo float 2901797). We also used data from the Chilbaldo and Seohae170 buoy stations to investigate phenomena at the air–sea boundary layer, such as sea-level pressure, wind, waves, and water surface temperature.

During the study period, a total of 7 TCs directly or indirectly influenced the study area: four in August–October 2018, and three in August–September 2020. We can directly recognize TCs approaching and moving away in the sea-level pressure, wind, wave, and water temperature data obtained by the buoys. TCs Soulik (1819) on August 23–24 and Kong-Rey (1825) on 6 October 2018 passed near the buoy. Compared to the other 2 TCs, which passed far from the observation point, these TCs were associated with a greater decrease in sea-level pressure, stronger winds (17–19 m/s), and higher waves (6–7 m). However, the water temperature decrease associated with these TCs depended on their intensity and impact period and on the vertical water temperature distribution. The 2020 TC cases showed similar characteristics. Bavi (2008) passed very near the observation location, showing a rapid and sharp drop in sea-level pressure, a maximum wind speed of 25 m/s, and a water surface temperature drop of over 3°C. Here we also found that the surface water was cooled a lot, however total volume of water column was a bit increased after the TC passed. To summarize the TC impact on water temperature variation obtained from buoy observations in the central and coastal areas of the Yellow Sea, TC activity played a role in accelerating the water cooling process during the summer–fall season.

Even though the Argo float–obtained water temperature and salinity profiles could not capture the exact sudden drop of temperature like the buoy record due to one or two day-cycle observation, they could reflected the internal differences in seawater properties before and after the passage of TCs (Figures 4, 5). Under TC influence, the thermocline and halocline deepened due to vertical water mixing, especially in the boundary layer between the upper and lower layers. For example, on August 23–26, 2018, the thermocline moved from 30 to 45 m in depth, and the water temperature difference before and after water mixing

was over 8°C at a depth of 40 m. Although the variation in temperature and salinity depended on external, TC-related conditions, such as wind speed, central pressure, and moving speed, thermocline and halocline deepening and shallowing processes were observed in this area during TC impact periods, such as September 3–5, September 28–October 2, and October 5–6, 2018, and September 1–2 and 7–8, 2020. Notably, the thermocline started to deepen when a TC was approaching, reached its maximum depth within one or 2 days, and returned to its previous position after the TC had passed.

The specific volume of water and SSL were calculated to investigate sea surface height changes due to TC-induced water mixing (Figures 6, 7). There were two layers, one with a high specific volume and one with a low specific volume, from August 15 to 14 October 2018. The layer with a high specific volume thickened as the TC impact started and was directly linked to the sea surface height increase. The SSL increased by more than 3 cm between August 23 and 26, 2018, and by about 1–2 cm on September 3, October 1, and 8 October 2018. In the period August 21–14 September 2020, the basic specific volume distribution pattern was similar to that of 2018, showing two layers separated at a depth of 20 m, and the SSL increased by about 0.5–1 cm during the TC impact period. To summarize the analysis result of the specific volume and SSL changes, it can be said that sea surface height change eventually depends on the TC-induced water mixing and volume change resulting from the effect of temperature and salinity variations.

Finally, while most studies on TC–ocean interactions have focused on the ocean's response to TC conditions, this study focused on post-TC processes. Thus, the results provide valuable insights into changes in oceanic environments after TCs.

DATA AVAILABILITY STATEMENT

The data that support the findings of this study are available on request from the corresponding authors.

AUTHOR CONTRIBUTIONS

Conceptualization, methodology, resources, calculation, writing and editing, KK; formal analysis, validation and review, IM. All authors have read and agreed to the published version of the manuscript.

FUNDING

This research was funded by the National Institute of Meteorological Sciences of the Korea Meteorological Administration project titled “Development of Marine Meteorology Monitoring and next-generation Ocean Forecasting System (KMA 2018-00420)”.

ACKNOWLEDGMENTS

The authors would like to thank reviewers for their constructive comments to make the high quality research.

REFERENCES

- Baranowski, D. B., Flatau, P. J., and Malinowski, S. P. (2011). Tropical Cyclone Turbulent Mixing as Observed by Autonomous Oceanic Profilers with the High Repetition Rate. *J. Phys. Conf. Ser.* 318 (section 7), 072001. doi:10.1088/1742-6596/318/7/072001
- Cho, Y. K., Choi, B. H., and Chung, H. W. (1995). Variation of Tidal Front in the Southwestern Sea of Korea. *J. Korean Soc. of Coast Ocean Eng.* 7, 170–175. (in Korean with English abstract).
- D'Asaro, E., Black, P., Centurioni, L., Harr, P., Jayne, S., Lin, I. I., et al. (2011). Typhoon-ocean Interaction in the Western North Pacific: Part 1. *Oceanog.* 24 (4), 24–31. doi:10.5670/oceanog.2011.91
- Ginis, I. (2002). "Atmosphere-Ocean Interaction," in *Advances in Fluid Mechanics Series* (Southampton: WIT Press), 83–114. No. 33.
- Harris, D. L. (1963). *Characteristics of the Hurricane Storm Surge*. Washington, D.C.: U.S. Dept. of Commerce, Weather Bureau, 1–39. Technical Paper, No. 48.
- Jansen, M. F., Ferrari, R., and Mooring, T. A. (2010). Seasonal versus Permanent Thermocline Warming by Tropical Cyclones. *Geophys. Res. Lett.* 37 (3), a–n. doi:10.1029/2009GL041808
- Kang, K., Jo, H. J., and Kim, Y. (2020). Ocean Responses to Typhoon Soulik (1819) Around Korea. *Ocean Sci. J.* 55, 445–457. doi:10.1007/s12601-020-0030-x
- Kang, K., and Lee, S.-R. (2014). Variation of the Summer Low SST Area in the Southwestern Coast of Korea. *Geosci. J.* 18 (2), 231–239. doi:10.1007/s12303-013-0055-6
- Korty, R. L., Emanuel, K. A., and Scott, J. R. (2008). Tropical Cyclone-Induced Upper-Ocean Mixing and Climate: Application to Equable Climates. *J. Clim.* 21 (4), 638–654. doi:10.1175/2007jcli1659.1
- Lie, H.-J. (1989). Tidal Fronts in the southeastern Hwanghae (Yellow Sea). *Continental Shelf Res.* 9, 527–546. doi:10.1016/0278-4343(89)90019-8
- Lin, I.-I., Wu, C.-C., Emanuel, K. A., Lee, I.-H., Wu, C.-R., and Pun, I.-F. (2005). The Interaction of Supertyphoon Maemi (2003) with a Warm Ocean Eddy. *Monthly Weather Rev.* 133, 2635–2649. doi:10.1175/mwr3005.1
- Lin, I.-I., Wu, C.-C., Pun, I.-F., and Ko, D.-S. (2008). Upper-Ocean Thermal Structure and the Western North Pacific Category 5 Typhoons. Part I: Ocean Features and the Category 5 Typhoons' Intensification. *Monthly Weather Rev.* 136, 3288–3306. doi:10.1175/2008mwr2277.1
- Lu, Z., Wang, G., and Shang, X. (2016). Response of a Preexisting Cyclonic Ocean Eddy to a Typhoon. *J. Phys. Oceanogr.* 46, 2403–2410. doi:10.1175/JPO-D-16-0040.1
- Mao, Q., Chang, S. W., and Pfeffer, R. L. (2000). Influence of Large-Scale Initial Oceanic Mixed Layer Depth on Tropical Cyclones*. *Mon. Wea. Rev.* 128, 4058–4070. doi:10.1175/1520-0493(2000)129<4058:iolsio>2.0.co;2
- Mei, W., Primeau, F., McWilliams, J. C., and Pasquero, C. (2013). Sea Surface Height Evidence for Long-Term Warming Effects of Tropical Cyclones on the Ocean. *Proc. Natl. Acad. Sci.* 110 (38), 15207–15210. Available from: www.pnas.org/cgi/doi/10.1073/pnas.1306753110. doi:10.1073/pnas.1306753110
- Pasquero, C., and Emanuel, K. (2008). Tropical Cyclones and Transient Upper-Ocean Warming. *J. Clim.* 21 (1), 149–162. doi:10.1175/2007jcli1550.1
- Pei, Y., Zhang, R., and Chen, D. (2015). Upper Ocean Response to Tropical Cyclone Wind Forcing: A Case Study of Typhoon Rammasun (2008). *Sci. China Earth Sci.* 58, 1623–1632. doi:10.1007/s11430-015-5127-1
- Pei, Y., Zhang, R.-H., and Chen, D. (2019). Roles of Different Physical Processes in Upper Ocean Responses to Typhoon Rammasun (2008)-induced Wind Forcing. *Sci. China Earth Sci.* 62, 684–692. doi:10.1007/s11430-018-9313-8
- Pun, I., Chang, Y.-T., Lin, I. I., Tang, T. Y., and Lien, R.-C. (2011). Typhoon-ocean Interaction in the Western North Pacific: Part 2. *Oceanog.* 24 (4), 32–41. doi:10.5670/oceanog.2011.92
- Unesco (1981). Tenth Report of the Joint Panel on Oceanographic Tables and Standards. *UNESCO Tech. Paper Mar. Sci.* 36, 25.
- Varotsos, C. A., Franzke, C. L. E., Efstathiou, M. N., and Degermendzhi, A. G. (2014). Evidence for Two Abrupt Warming Events of SST in the Last century. *Theor. Appl. Climatol.* 116, 51–60. doi:10.1007/s00704-013-0935-8
- Varotsos, C. A. (2013). The Global Signature of the ENSO and SST-like fields. *Theor. Appl. Climatol.* 113, 197–204. doi:10.1007/s00704-012-0773-0
- Varotsos, C. A., Tzani, C. G., and Sarlis, N. V. (2016). On the Progress of the 2015–2016 El Niño Event. *Atmos. Chem. Phys.* 16, 2007–2011. doi:10.5194/acp-16-2007-2016
- Vincent, E. M., Lengaigne, M., Madec, G., Vialard, J., Samson, G., Jourdain, N. C., et al. (2012). Processes Setting the Characteristics of Sea Surface Cooling Induced by Tropical Cyclones. *J. Geophys. Res.* 117, a–n. doi:10.1029/2011JC007396
- Zhang, H., Chen, D., Zhou, L., Liu, X., Ding, T., and Zhou, B. (2016). Upper Ocean Response to Typhoon Kalmaegi (2014). *J. Geophys. Res. Oceans* 121, 6520–6535. doi:10.1002/2016jc012064

Conflict of Interest: The authors declare that the research was conducted in the absence of any commercial or financial relationships that could be construed as a potential conflict of interest.

Publisher's Note: All claims expressed in this article are solely those of the authors and do not necessarily represent those of their affiliated organizations, or those of the publisher, the editors, and the reviewers. Any product that may be evaluated in this article, or claim that may be made by its manufacturer, is not guaranteed or endorsed by the publisher.

Copyright © 2022 Kang and Moon. This is an open-access article distributed under the terms of the Creative Commons Attribution License (CC BY). The use, distribution or reproduction in other forums is permitted, provided the original author(s) and the copyright owner(s) are credited and that the original publication in this journal is cited, in accordance with accepted academic practice. No use, distribution or reproduction is permitted which does not comply with these terms.



Estimation of Dissipative Heating Properties Above the Internal Boundary Layer in Landfalling Typhoons Using Multi-Layer Tower Observations

Kang Zhou¹, Qingqing Li^{2,3*} and Jie Tang⁴

¹Nanjing University of Information Science and Technology, Nanjing, China, ²Pacific Typhoon Research Center, Key Laboratory of Meteorological Disaster of the Ministry of Education, Nanjing University of Information Science and Technology, Nanjing, China, ³State Key Laboratory of Severe Weather, Chinese Academy of Meteorological Sciences, Beijing, China, ⁴Shanghai Typhoon Institute, China Meteorological Administration, Shanghai, China

OPEN ACCESS

Edited by:

Christos H. Halios,
Public Health England,
United Kingdom

Reviewed by:

John Edwards,
Met Office, United Kingdom
Jia Liang,
Nanjing University of Information
Science and Technology, China
Yuqing Wang,
University of Hawaii at Manoa,
United States

*Correspondence:

Qingqing Li
liqq@nuist.edu.cn

Specialty section:

This article was submitted to
Atmospheric Science,
a section of the journal
Frontiers in Earth Science

Received: 12 December 2021

Accepted: 22 March 2022

Published: 08 April 2022

Citation:

Zhou K, Li Q and Tang J (2022)
Estimation of Dissipative Heating
Properties Above the Internal
Boundary Layer in Landfalling
Typhoons Using Multi-Layer
Tower Observations.
Front. Earth Sci. 10:833994.
doi: 10.3389/feart.2022.833994

Wind observations from a multi-level observation tower are used to estimate the dissipative heating (DH) in three landfalling typhoons. The observations reveal the presence of a stress internal boundary layer (IBL) in the typhoon circulations. The integrated DH values increase with increasing wind speed above the IBL. The integrated DH calculated with the turbulent spectra method increases more rapidly with increasing wind speed than that estimated with the theoretical method. However, the integrated DH estimated using the theoretical method is significantly smaller than that calculated with the turbulent spectra method because dissipative rates with the turbulent spectra method are much larger above the IBL.

Keywords: landfall, tropical cyclone, dissipative heating, multi-layer tower, internal boundary layer

INTRODUCTION

In the presence of friction, viscous dissipation of kinetic energy comes about through molecular processes, and frictional dissipation is expected to furnish tropical cyclones (TCs) with thermodynamic energy. However, in early theoretical frameworks and numerical simulations regarding TC development, the role of dissipative heating (DH) was regularly neglected. For instance, the effect of DH was not considered within the Carnot heat engine mechanism for TCs (Emanuel, 1986).

Recently, an increasing body of studies has documented the importance of DH to TC intensity in numerical modeling. Bister and Emanuel (1998) conducted idealized numerical experiments using a nonhydrostatic model to show that, when DH was included, the maximum surface wind speed of TCs increased by 25%, and the central minimum pressure dropped by 40%. Other numerical experiments also indicated that DH has a significant influence on the intensity and structure of TCs (Zhang and Altshuler, 1999; Jin et al., 2007; Cheng et al., 2012), and they showed consistent amplification of maximum TC intensity with the inclusion of DH. However, Kieu (2015) believed that about 10–30% of the work done by friction would be transferred to the ocean surface waves and ocean mixing layer. Therefore, the hypothesis of Bister and Emanuel (BE) that all the work done by friction is converted into dissipative heating within the boundary layer is likely unreasonable, and the magnitude of DH within the atmospheric boundary layer tended to be overestimated. In addition,

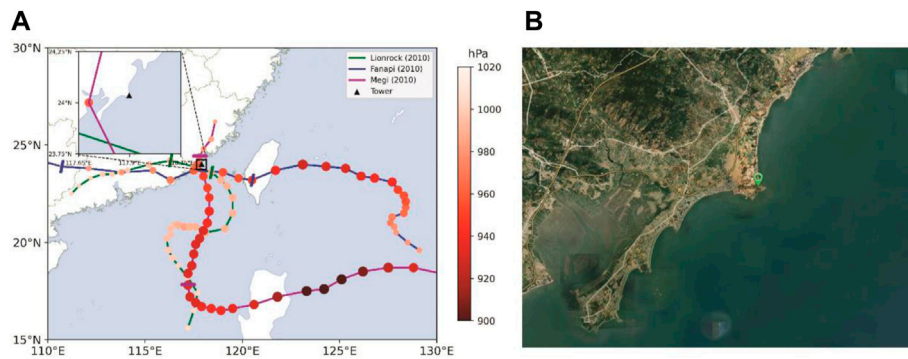


FIGURE 1 | (A) Tracks of Lionrock (green curve), Fanapi (blue curve), and Megi (purple curve). Dots show the storm center positions every 6 h, with the minimum central pressure indicated with colors. The time analyzed is the time encompassed between the two short crosses on each track. The site of the observational tower is indicated by the black triangle. An enlarged view of the tower position is also present in the upper-left corner. **(B)** The ground environment surrounding the tower, with the light green sector symbol marking the tower location.

the inclusion of DH tends to make the surface sensible heat flux less positive, which results in a subtle reduction of maximum wind velocity of TCs (Edwards, 2019).

Several studies have estimated DH values based on a variety of observations. For example, Zhang (2010) reckoned the magnitude of DH in the boundary layer in North Atlantic hurricanes using *in situ* aircraft observations. He found that the DH values estimated with the product of the cubic of the surface wind speed and the drag coefficient, as utilized in BE, significantly exceed the DH values computed by integrating the dissipation rate (i.e., the turbulent spectra method). Zhang et al. (2011) further estimated the DH during TC landfalls using data from portable weather stations, indicating a significant overestimation of DH by the BE method. Ming and Zhang (2018) employed observations from two towers to compare DH evaluations of landfalling typhoons moving over different underlying surfaces. They also found that the surface-layer theory (namely BE method) overestimated the magnitude of DH in contrast to the spectra method. Additionally, the overestimation of DH by the BE method tended to be less over land than over shallow waters.

It is noted that the limited observational studies mainly directly estimated DH within TCs at different near-surface heights. For instance, Zhang (2010) and Zhang et al. (2011) investigated DH at $z = 10$ m over water and land, respectively. By contrast, Ming and Zhang (2018) compared DH in TCs at two close observational heights (i.e., 60 and 70 m) in two towers, one located offshore and the other located on the land near the coastline. For landfalling TCs, when the TC boundary layer is advected over a boundary with varying surface conditions, the near-surface portion of the flow profile significantly changes. The region of the boundary layer adjacent to the surface influenced by these changes, named the internal boundary layer (IBL), can develop (Garratt, 1990; Garratt, 1992). Several studies have documented DH characteristics within the TC IBL (Zhang et al., 2011). However, an unsettled question is what DH properties in landfalling TCs are above the IBL. To address this question, we will estimate integrated DH during typhoon

landfalls above the IBL in this study, using observations from a multi-level observation tower. In section 2, the data and analysis methods used will be briefly introduced. Then, the results will be presented in section 3, and the main findings will be summarized in the last section.

DATA AND ANALYSIS METHODS

Typhoons Lionrock, Fanapi, and Megi

In the current study, the DH of TCs Lionrock, Fanapi, and Megi in 2010 will be estimated during their landfalls in China. According to the China Meteorological Administration best-track data (Ying et al., 2014), Lionrock formed in the eastern South China Sea, followed by poleward movement and then a cyclonic meandering in the track (Figure 1). It made landfall at Zhangpu, Fujian Province, around 2300 UTC 1 September 2010, with a minimum central pressure of 990 hPa. Super Typhoon Fanapi formed on 16 September 2010, approximately 920 km southeast of Taiwan Island. Afterward, it tracked northwestward, followed by a cyclonic turning. Fanapi made its first landfall at Hualien, Taiwan, around 0100 UTC 19 September 2010, before which it had attained a minimum central pressure of 935 hPa. Continuously Moving westward, Fanapi made its second landfall at Zhangpu, Fujian Province, near 2300 UTC 19 September (Figure 1), with an observed maximum surface wind of 35 m s^{-1} . Super Typhoon Megi was the most intense TC in the world in 2010, forming on 13 October 2010, approximately 410 km southwest of Guam. It persistently moved northwestward to the east of the Philippines after genesis. Whereafter, Megi progressed west-southwestward and intensified with a minimum central pressure of 895 hPa before making its first landfall at the northeast coast of Luzon Island near 0300 UTC 18 October. As Megi entered the east South China Sea, its track sharply turned northward (Figure 1). Around 0500 UTC 23 October, this typhoon made its second landfall at Zhangpu, Fujian Province (Figure 1). Because the three TCs made landfall in the vicinity of Zhangpu, Fujian Province, in the 2010 typhoon

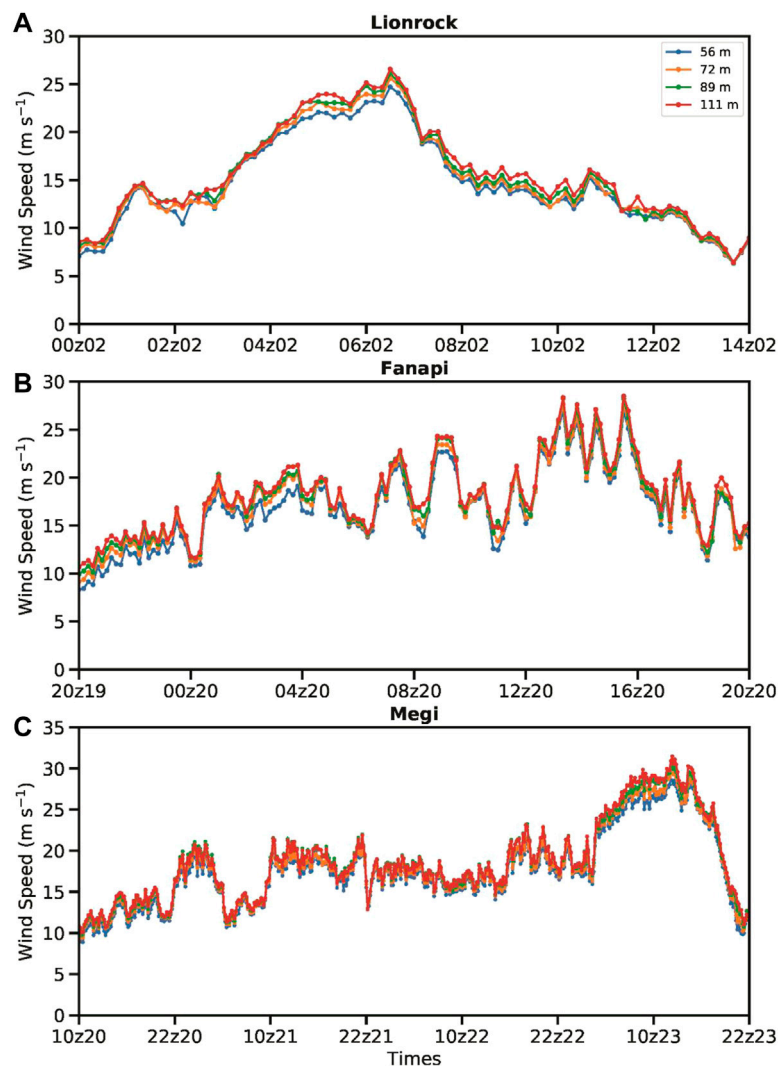


FIGURE 2 | Time series of the 10-min averages of wind velocity observed with the tower in Typhoon **(A)** Lionrock from 11 to 14 UTC 2 September, **(B)** Fanapi from 20 UTC 19 to 20 UTC 20 September, and **(C)** Megi from 10 UTC 20 to 22 UTC 23 October 2010. The blue, orange, green, and red curves represent the averaged wind speed at $z = 56, 72, 89,$ and 111 m, respectively.

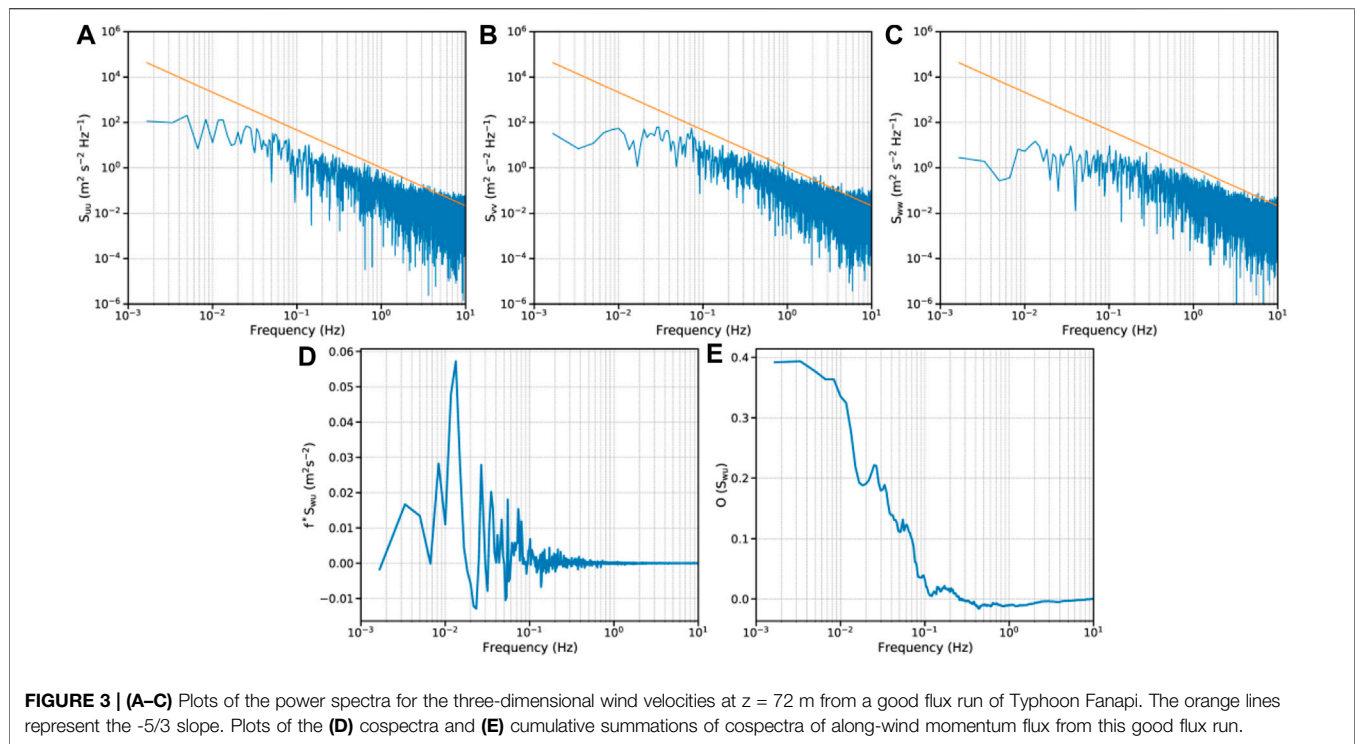
season, we have a decent chance to evaluate the DH traits associated with the TC landfalls using observations from the same tower.

Wind Data From the Tower Observations

The data used in this study are obtained from a multi-level weather tower placed in Chihu Town, Zhangpu, Fujian Province, China, at the 24.036°N latitude and 117.897°E longitude (**Figure 1A**). The minimal distance of the tower from the coastline is about 150 m (**Figure 2B**), and it lies 29 m above sea level. The surface around the tower is mainly rubble soil with scattered shrubs. WindMaster Pro 3D supersonic anemometers manufactured by British Gill are fitted at 27 -, 43 -, 60 -, and 82 -m heights. Correspondingly, the tower's four observational heights are $56, 72, 89,$ and 111 m above sea level. The sampling frequency for the three-dimensional wind

speed is 20 Hz. Quality control for the three-dimensional wind fields is conducted using a spectral analysis method following Zhang et al. (2009) and Ming and Zhang (2018). This data has been utilized to examine the near-surface turbulent cascade features (Tang et al., 2015) and vertical eddy diffusivity and mixing length in the TC boundary layer (Tang et al., 2018).

In this study, we put the spotlight on the wind observations of Lionrock from 1600 UTC 1 September to 0600 on 2 September, Fanapi from 1200 UTC 19 September to 1200 UTC 20 September, and Megi from 0200 UTC 20 October to 1400 UTC 23 October 2010 (**Figure 1A**). These periods are chosen when the horizontal wind velocities averaged in 10 min are above 10 m s^{-1} at the four observational heights. **Figure 2A** shows that the 10-min averaged wind velocities of Typhoon Lionrock gradually increased as the system approached the tower, peaking around 0630 UTC 2 September 2010 and followed by a gradual decrease in speed.



Similar wind speed evolution was observed in Typhoon Fanapi, with the maximum averaged wind speed occurring when the TC center neared the tower around 1500 UTC 20 September 2010 (**Figure 2B**). The maximum wind speed observed by the tower was greater than 30 m s^{-1} in Typhoon Megi near 1100 UTC 23 October 2010 (**Figure 2C**), and it rapidly weakened afterward due to the proximity of the eye.

An IBL can appear in an area of horizontal advection across a discontinuity in varying surface properties (Deaves, 1981; Garratt, 1990). In particular, the IBL should continue to deepen until its depth has adjusted to the underlying surface, dependent on the surface roughness (Savelyev and Taylor, 2015). IBL development was frequently observed at landfalls of TCs, particularly in the land-water transition (Powell, 1982; Knupp et al., 2006; Hirth et al., 2012). Regardless of mesoscale effects, neutral static stability is widely considered to dominate the TC boundary layer (Kepert, 2012), and the velocity IBL height (h_{VIBL}) can be estimated as

$$h_{VIBL} = cZ_R \left(\frac{X}{Z_R} \right)^{0.8}, \quad (1)$$

where Z_R denotes the roughness length, c is a stability constant generally valued at 0.28 for a statistically neutral environment (Simiu and Scanlan, 1996; Wood, 1982), and X indicates the downstream distance. As indicated in Fang et al. (2018), a Z_R value of 0.05 m is selected for the surface featured by rubble soil with scattered shrubs, and a maximum land fetch is about 400 m for onshore winds. Thus, a h_{VIBL} value approximates to be 18.56 m at this land fetch. Moreover, prior studies have revealed that the stress IBL height (h_{SIBL})

approximately doubles h_{VIBL} (Rao et al., 1974; Garratt, 1990). Correspondingly, h_{SIBL} is ~ 37.1 m near the tower (Fang et al., 2018), implying that the surface likely has a striking effect on the local stress above the first observational height but below the second height of the tower. Therefore, given the stress IBL, we limit our focus to the DH properties from the second to the fourth levels that lie in a constant flux layer.

Figures 3A–C show the wind speed spectra of three-dimensional wind speeds at $z = 72$ m for one good flux run in Typhoon Fanapi, which is displayed in the log-log plots of frequency. The spectrum patterns conform to the $-5/3$ slope of Kolmogorov (1941) power law. Correspondingly, the cospectra and cumulative summations of cospectra of the flux run are shown in **Figures 2D,E**, respectively. A good flux run approaches a constant value in both high and low frequencies, which represents stationarity. Such a scenario can be confirmed by the flatness near the high- and low-frequency tails from 0.001 to 10 Hz in **Figure 2E**. Lastly, 106, 116, and 111 good flux runs are validated at the 72-, 89-, and 111-m observational heights, respectively, for the three TCs.

Estimation Methods for Dissipative Heating

As noted in the introduction, two methods have usually been used to estimate DH values associated with TCs. One is proposed by Bister and Emanuel (1998), hereafter referred to as the BE method. In the BE method, DH is estimated by calculating the momentum flux and drag coefficient. According to the eddy correlation method, the momentum flux (τ) is defined as:

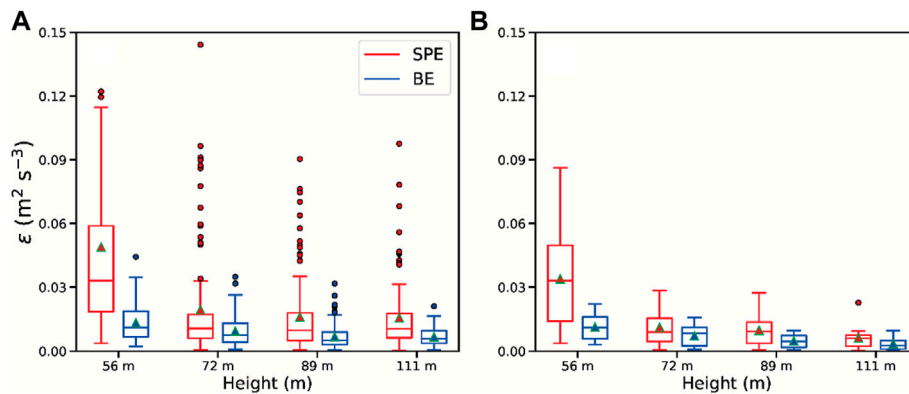


FIGURE 4 | Boxplots of the dissipative rates at the four observational levels using (A) all the good runs and (B) good runs coexisting at all the levels at a given time [with the lower and upper quartiles as the lower and upper limits of the box, respectively; the median (line in the box); the mean (triangles), and outliers (black circles)]. Blue and red colors indicate the BE and turbulent spectra methods, respectively.

$$\hat{\tau} = \rho \left(-\overline{w'u'\hat{i}} - \overline{w'v'\hat{j}} \right), \quad (2)$$

where u' , v' , and w' represent the turbulent fluctuations of longitudinal, lateral, and vertical components of wind speed, and the overbar represents 10-min averaging. ρ is the air density. The momentum flux magnitude in the surface layer can be calculated as follows:

$$\tau = \rho u^{*2} = \rho C_d U^2, \quad (3)$$

where u^* represents the friction velocity, U is the average horizontal wind speed at the given height, and C_d is the drag coefficient. Therefore, the friction velocity can be defined as

$$u^* = \left(\frac{|\hat{\tau}|}{\rho} \right)^{1/2}. \quad (4)$$

Additionally, shear production is assumed to balance dissipation as heat in a weak wind environment (Businger and Businger, 2001). Based on the Monin-Obukhov similarity theory (Monin and Obukhov, 1954), shear production can be estimated using u^* . The dissipation term (ε) can, therefore, be computed by

$$\varepsilon = \frac{u^{*3}}{\kappa z}, \quad (5)$$

where κ is the Von Kármán constant and equals 0.4.

In the absence of an IBL, DH can be calculated by vertically integrating the dissipation rate and can be expressed by

$$DH = \rho \bar{\varepsilon} Z_1 = \rho \frac{u^{*3}}{\kappa} \ln \left(\frac{Z_1}{Z_R} \right), \quad (6)$$

where Z_1 is the observational height and the overbar represents the average value.

However, given the stress IBL in the tower site, it is difficult to directly apply Eq. 6 to calculate DH at the observational levels because when the u^* values within the IBL exceed approximately 0.4 m s^{-1} they are much larger than those above the IBL (Fang

et al., 2018). Therefore, the ε magnitudes estimated by Eq. 5 are significantly larger at $z = 56 \text{ m}$ than at the upper levels (Figures 4A,B). Nevertheless, we can estimate the integrated DH between two levels (for example, at Z_1 and Z_2) above the stress IBL but in the surface layer as follows:

$$\rho \frac{u^{*3}}{\kappa} \ln \left(\frac{Z_2}{Z_1} \right) = \rho u^{*2} U(Z_2) - \rho u^{*2} U(Z_1), \quad (7)$$

if ε decreases linearly with height. Here, based on the Monin-Obukhov similarity theory, the difference in wind speed (U) between the two layers is

$$U(Z_2) - U(Z_1) = \frac{u^*}{\kappa} \ln \left(\frac{Z_2}{Z_1} \right). \quad (8)$$

Figure 4B shows that the mean ε value regarding the sets of concurrent good runs at all the heights indeed decreases with height approximately in a linear manner. Thus, Eq. 7 may be applied herein to assess the integrated DH within the constant flux layer.

The other method for the DH estimation is to directly estimate the dissipation rate of turbulence by spectral analysis and vertically integrating the dissipation rate. According to Zhang (2010) and Ming and Zhang (2018), ε can be estimated from the spectral density of the longitudinal velocity whose spectra show a $f^{-5/3}$ power law, and given by

$$\varepsilon = \alpha_u^{-3/2} \frac{2\pi f}{U} [f S_{uu}(f)]^{3/2}, \quad (9)$$

where α_u is the one-dimensional Kolmogorov constant, being generally equal to 0.5 (Sreenivasan, 1995), S_{uu} is the power spectral density of horizontal wind speed, and f is the frequency. Note that using the direct method involves satisfying an assumption that ε is constant with height. Figures 4A,B show the ε properties calculated by Eq. 9 for all the good run samples and the simultaneous samples at the four observations levels, respectively. The ε values are statistically significantly larger at the first observational level ($z = 56 \text{ m}$)

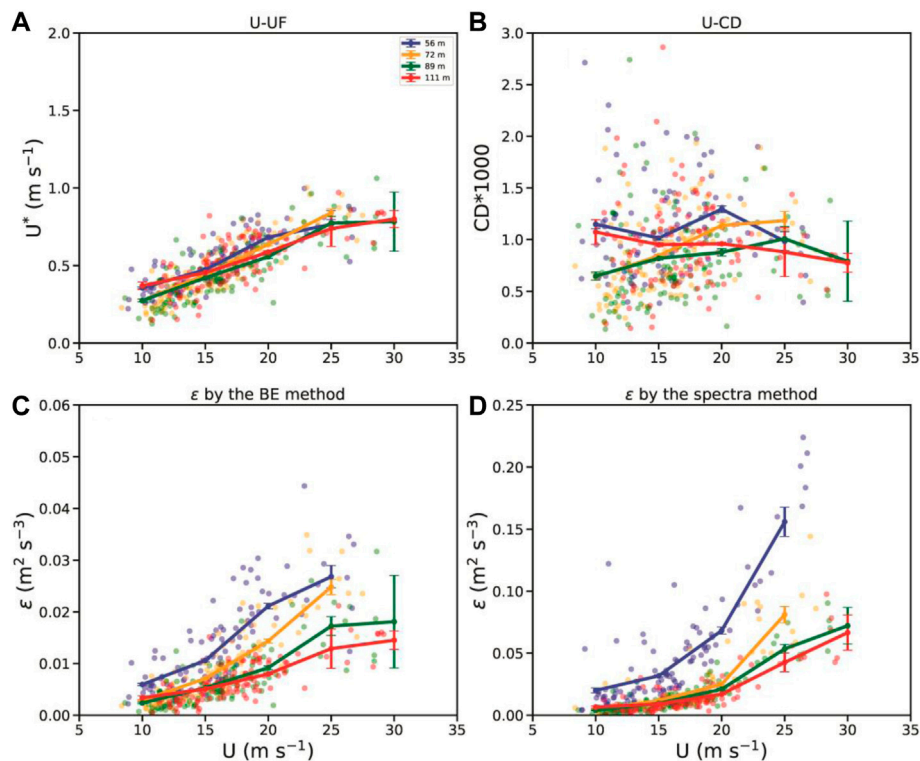


FIGURE 5 | Plots of (A) the friction velocity, (B) drag coefficients, and (C) dissipative rates estimated with the BE method and (D) turbulent spectra method as a function of the mean wind speed. The blue, orange, green, and red solid lines with error bars indicate the bin-averaged values of the two variables at $z = 56, 72, 89$, and 111 m, respectively. The error bars represent the 95% confidence interval.

than at upper levels (Figures 4A,B). Additionally, there are no significant differences in the ε magnitude between the three levels above (at the 95% confidence level based on the permutation test). This result further suggests that the first observational level resides likely within the IBL. Therefore, based on the turbulent spectra method, the integrated DH between two levels above the stress IBL but within the surface layer can be given by

$$\rho \int_{Z_1}^{Z_2} \varepsilon dz = \rho \bar{\varepsilon} (Z_2 - Z_1), \quad (10)$$

with ε being estimated by Eq. 9. Furthermore, Figure 4 also shows that the mean ε values calculated by the theoretical method are less than those directly estimated by the turbulent spectra method at each level.

As noted in previous studies, there are apparent differences in the BE and turbulent spectra methods for estimating the DH value. The former assumes that frictionally dissipated kinetic energy is wholly converted to heat, while the latter directly measures DH considering the turbulent flow characteristics.

RESULTS

As introduced above, the DH estimation with the BE method first involves the computation of friction velocity and the drag

coefficient. Figure 5A portrays the friction velocities measured from the tower observations versus mean wind speed. We can see that the bin-averaged friction velocities tend to linearly increase with wind speed when the wind speed is lower than 25 m s^{-1} , whereas those at $z = 54, 89$, and 111 m level off at wind speeds of 25 m s^{-1} (Figure 5A). This result is slightly smaller than that in Zhao et al. (2015), which indicated that the wind speed threshold for friction velocity level-off was between 26 and 30 m s^{-1} .

Figure 5B shows the drag coefficient as a function of wind speed at different levels. Not surprisingly, at the lowest level ($z = 56$ m), the drag coefficient values are the largest when the wind velocity is smaller than 25 m s^{-1} . The averaged drag coefficient values range between 0.001 and 0.0015 , close to prior results over shallow water (Zhao et al., 2015; Ming and Zhang, 2018). Previous studies indicated that the magnitude of the drag coefficient tended to increase with increasing wind speed when the speed was lower than the critical value (Powell et al., 2003; Jarosz et al., 2007; Holthuijsen et al., 2012). However, such a tendency is not captured at $z = 56$ m, likely because of the limited samples at lower wind speed (Figure 5B). The drag coefficient values go down as the altitude rises (e.g., $z = 72$ and 89 m). At these two levels, the drag coefficients increase with increasing wind speed. In particular, the estimated drag coefficient value at $z = 89$ m turns to lower when the wind speed exceeds 25 m s^{-1} , indicative of saturation of the drag coefficient.

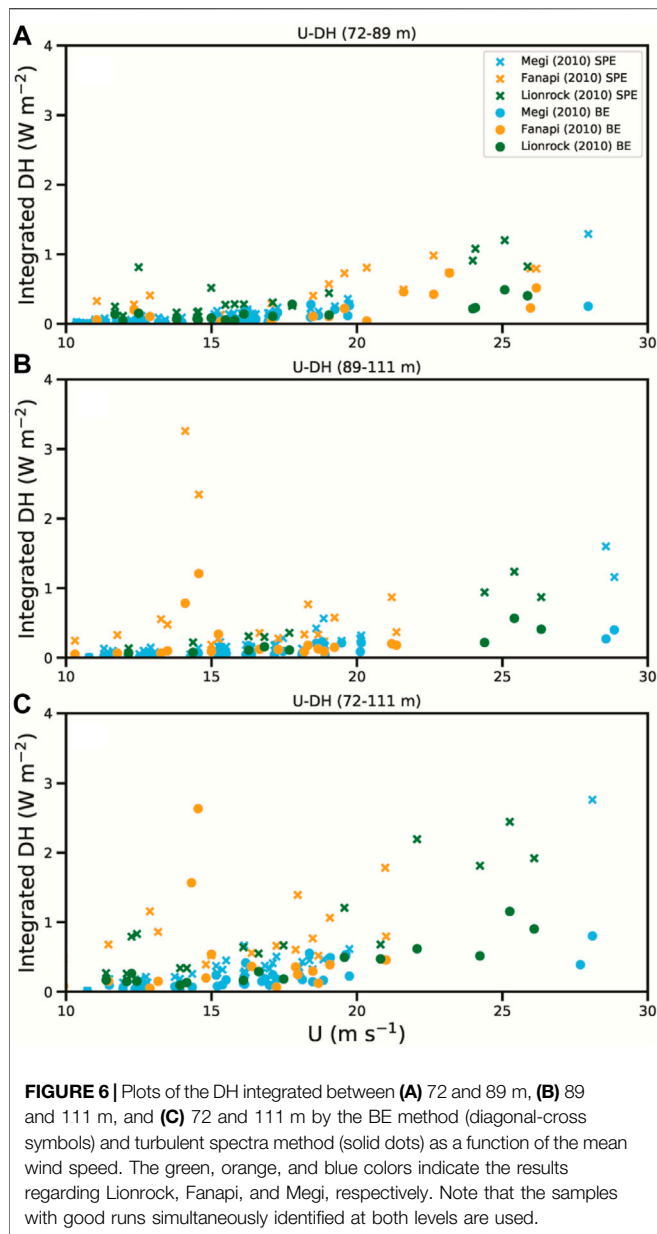


Figure 5C depicts the dissipative rates estimated by **Eq. 5** as a function of the mean wind speed. The dissipative rates estimated by the theoretical method tend to increase with increasing wind speed as the wind velocity is smaller than 25 m s^{-1} , consistent with the finding in **Zhang (2010)**. According to **Eq. 5**, the dissipative rate is predicted to be a smaller magnitude at a higher level. This pattern can be reflected by the bin-averaged values in **Figure 5C**, except at $z = 89$ and 111 m with the wind velocity around 10 m s^{-1} . In contrast, the dissipative rates directly estimated by the turbulent spectra method are indicated in **Figure 5D**. At the levels above the stress IBL, the differences in the mean dissipative rates are minimal when the wind speed is less than 20 m s^{-1} , and they subtly increase when the wind speed exceeds 20 m s^{-1} . Nevertheless, the variation of the dissipative rates with height seems smaller than implied in the BE approach.

In addition, a comparison of **Figures 5C,D** further suggests that the mean dissipative rates estimated by shear production are smaller at relatively high wind speeds than those estimated by the turbulent spectra method, which is also revealed in **Figure 4** and previous findings over ocean conditions (**Zhang, 2010**). It is worth noting that the mean directly-measured dissipative rates at $z = 56 \text{ m}$ are 2–3 times those at the upper levels (**Figure 5D**), indicating that the stress within IBL indeed greatly reinforces the local dissipation.

The DH integrated between two levels above the stress IBL, calculated by the two methods mentioned above as a function of mean wind speed, is depicted in **Figure 6**. Note that the samples with good runs simultaneously identified at both levels are analyzed. The integrated DH values tend to increase with

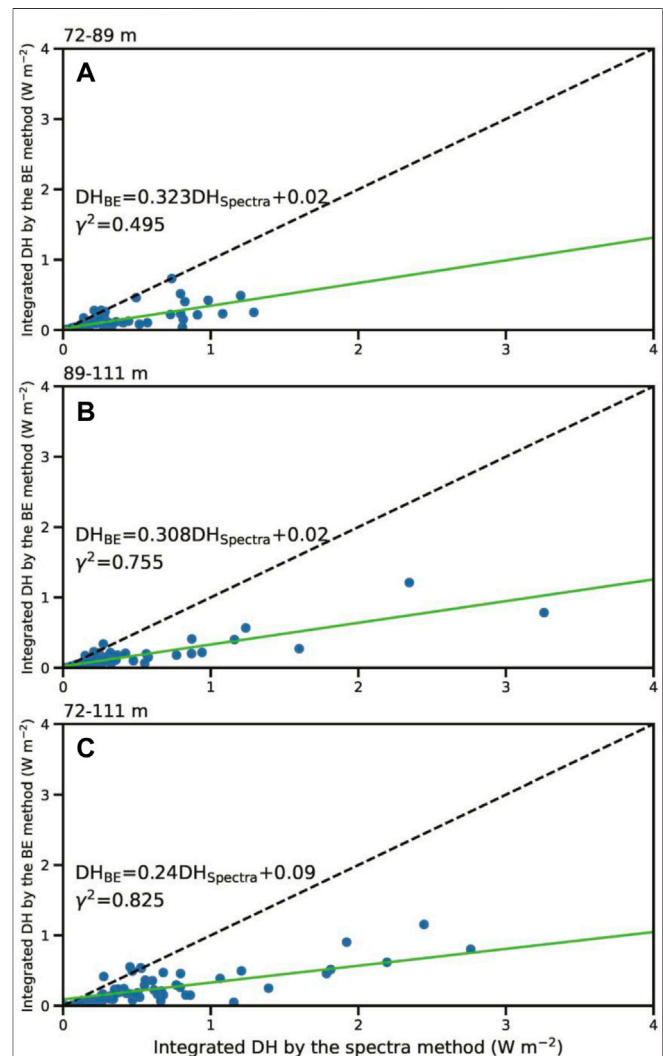


TABLE 1 | The bin-averaged integrated DH values (W m^{-2}) estimated with the turbulent spectra method and the BE method, with the standard deviations included in parentheses.

Method	Layer Range	Wind Speed Bins				
		10 m s^{-1}	15 m s^{-1}	20 m s^{-1}	25 m s^{-1}	30 m s^{-1}
The BE method	72–89 m	0.04 (0.01)	0.06 (0.01)	0.17 (0.01)	0.41 (0.03)	
	89–111 m	0.04 (0.01)	0.14 (0.06)	0.15 (0.01)	0.40 (0.03)	0.34 (0.01)
	79–111 m	0.11 (0.01)	0.28 (0.25)	0.37 (0.03)	0.86 (0.10)	0.60 (0.09)
The turbulent spectra method	72–89 m	0.13 (0.04)	0.18 (0.01)	0.40 (0.04)	0.92 (0.03)	
	89–111 m	0.14 (0.01)	0.19 (0.02)	0.39 (0.04)	1.02 (0.04)	1.38 (0.10)
	72–111 m	0.37 (0.09)	0.37 (0.04)	0.81 (0.27)	2.06 (0.11)	3.41 (0.85)

increasing wind velocities. However, when the wind speed is less than 15 m s^{-1} , the integrated DH increases much slower with increasing wind speed. The integrated DH estimated by the BE method tends to be constant when the wind speed is less than 15 m s^{-1} (Figures 6A–C). When the wind speed is more than 15 m s^{-1} , the integrated DH values significantly increase. Notably, the integrated DH estimated by the turbulent spectra method increases much more rapidly with increasing wind speed than those estimated by the BE method. As a result, the integrated DH values produced by the two methods gradually bifurcate each other when the wind velocity is larger than 20 m s^{-1} , particularly between $z = 72$ and 111 m (Figure 6C).

Figure 7 further compares the integrated DH values estimated with the BE method versus the turbulent spectra method for the good flux runs. In detail, most integrated DH values estimated with the turbulent spectra method are larger than those estimated with the BE method (Figures 7A–C), with the integrated DH estimated with the BE method approximating $1/4$ – $1/3$ of the DH estimated with the turbulent spectra method within the constant flux layer.

The integrated DH properties above the IBL are further quantified with the bin-averaged values in Table 1. As noted above, the integrated DH estimated with the BE method is much smaller than that estimated with the turbulent spectra method above the stress IBL. The integrated DH values estimated with both methods increase with increasing wind speed, and not surprisingly, they also increase with layer depth for each wind speed bin. Table 1 indicates that the integrated DH calculated with the turbulent spectra method grows much more rapidly with increasing wind speed than that calculated with the theoretical method. For instance, the mean DH values integrated between $z = 89$ and 111 m with the turbulent spectra method (BE method) rise dramatically from 0.39 (0.15) to 1.02 (0.40) W m^{-2} for the wind speed bin increasing from 20 to 25 m s^{-1} .

As pointed out in previous studies, the BE method that assumes all the work done by friction converted into DH within the TC boundary layer overestimates DH magnitude (Zhang, 2010; Zhang et al., 2011; Ming and Zhang, 2018). As a result, during TC landfalls, the IBL DH estimated using the BE formula is much larger (even larger than an order of magnitude) than that estimated using the turbulent spectra method (Zhang et al., 2011). In the current study, DH properties within the stress IBL cannot be estimated due to the limited observations within the IBL. Nevertheless, the multi-level observations from the

coastal tower furnish an opportunity to document the DH properties integrated between levels above the stress IBL. Unlike the DH within the IBL, the integrated DH based on the turbulent spectra method is significantly larger than that estimated based on the BE method.

SUMMARY

In this paper, wind observations collected from a multi-level observation tower near the coast are used to estimate the DH properties above the IBL during the landfalls of three typhoons. The main interest is quantifying the vertically integrated DH in landfalling TC conditions. In addition, the integrated DH estimations based on the BE method and turbulent spectra method are also made for comparison.

The results demonstrate that, above the stress IBL, the integrated DH values estimated with the BE method and the turbulent spectra method increase with increasing wind speed. Additionally, the integrated DH calculated with the turbulent spectra method rises more rapidly with increasing wind speed than that estimated with the BE method. However, the integrated DH calculated with the BE method is much smaller than that calculated with the turbulent spectra method, although DH overestimation based on the BE method has been widely recognized. The larger integrated DH with the turbulent spectra method than the BE method is mainly related to greater dissipative rates estimated using the former above the IBL.

An implication of the tower-based observational study results here is assessing the numerically modeled DH and surface layer height in landfalling TC circulation, which may contribute to improvements in surface layer schemes in numerical modeling of TCs. However, one of the limitations of the present study is that the wind speed observed here is under severe tropical storm force. In a region close to the water, how the complex surface state can modulate the vertical variation of DH above the IBL requires further dedicated investigation.

DATA AVAILABILITY STATEMENT

The raw data supporting the conclusions of this article will be made available by the authors, without undue reservation.

AUTHOR CONTRIBUTIONS

KZ: Investigation and Writing—review. QL: Writing—review and editing. JT: Investigation.

FUNDING

This work was jointly supported by the National Key Research and Development Program of China under grant 2017YFC1501601 and the National Natural Science Foundation of China under grants

REFERENCES

- Bister, M., and Emanuel, K. A. (1998). Dissipative Heating and Hurricane Intensity. *Meteorol. Atmos. Phys.* 65, 233–240. doi:10.1007/bf01030791
- Businger, S., and Businger, J. A. (2001). Viscous Dissipation of Turbulence Kinetic Energy in Storms. *J. Atmos. Sci.* 58, 3793–3796. doi:10.1175/1520-0469(2001)058<3793:vdotke>2.0.co;2
- Cheng, X., Fei, J., Huang, X., and Zheng, J. (2012). Effects of Sea spray Evaporation and Dissipative Heating on Intensity and Structure of Tropical Cyclone. *Adv. Atmos. Sci.* 29, 810–822. doi:10.1007/s00376-012-1082-3
- Deaves, D. M. (1981). Computations of Wind Flow Over Changes in Surface Roughness. *J. Wind Eng. Ind. Aerodyn.* 7, 65–94. doi:10.1016/0167-6105(81)90068-4
- Edwards, J. M. (2019). Sensible Heat Fluxes in the Nearly Neutral Boundary Layer: The Impact of Frictional Heating within the Surface Layer. *J. Atmos. Sci.* 76, 1039–1053. doi:10.1175/jas-d-18-0158.1
- Emanuel, K. A. (1986). An Air-Sea Interaction Theory for Tropical Cyclones. Part I: Steady-State Maintenance. *J. Atmos. Sci.* 43, 585–605. doi:10.1175/1520-0469(1986)043<0585:asistf>2.0.co;2
- Fang, P., Zhao, B., Zeng, Z., Yu, H., Lei, X., and Tan, J. (2018). Effects of Wind Direction on Variations in Friction Velocity with Wind Speed under Conditions of strong Onshore Wind. *J. Geophys. Res.* 123, 7340–7353. doi:10.1029/2017jd028010
- Garratt, J. R. (1992). *The Atmospheric Boundary Layer*. UK: Cambridge University Press, 316.
- Garratt, J. R. (1990). The Internal Boundary Layer—A Review. *Boundary-Layer Meteorol.* 50, 171–203. doi:10.1007/bf00120524
- Hirth, B. D., Schroeder, J. L., Weiss, C. C., Smith, D. A., and Biggerstaff, M. I. (2012). Research Radar Analyses of the Internal Boundary Layer over Cape Canaveral, Florida, during the Landfall of Hurricane Frances (2004). *Wea. Forecast.* 27, 1349–1372. doi:10.1175/waf-d-12-00014.1
- Holthuijsen, L. H., Powell, M. D., and Pietrzak, J. D. (2012). Wind and Waves in Extreme Hurricanes. *J. Geophys. Res.* 117, C09003. doi:10.1029/2012jc007983
- Jaros, E., Mitchell, D. A., Wang, D. W., and Teague, W. J. (2007). Bottom-up Determination of Air-Sea Momentum Exchange under a Major Tropical Cyclone. *Science* 315, 1707–1709. doi:10.1126/science.1136466
- Jin, Y., Thompson, W. T., Wang, S., and Liou, C.-S. (2007). A Numerical Study of the Effect of Dissipative Heating on Tropical Cyclone Intensity. *Wea. Forecast.* 22, 950–966. doi:10.1175/waf1028.1
- Keptert, J. D. (2012). Choosing a Boundary Layer Parameterization for Tropical Cyclone Modeling. *Mon. Wea. Rev.* 140, 1427–1445. doi:10.1175/mwr-d-11-00217.1
- Kieu, C. (2015). Revisiting Dissipative Heating in Tropical Cyclone Maximum Potential Intensity. *Q.J.R. Meteorol. Soc.* 141, 2497–2504. doi:10.1002/qj.2534
- Knapp, K. R., Walters, J., and Biggerstaff, M. (2006). Doppler Radar and Profiler Observations of Boundary Layer Variability during the Landfall of Tropical Storm Gabrielle. *J. Atmos. Sci.* 63, 234–251. doi:10.1175/jas3608.1
- 42175005, 41875054, 41730961, 41730960, and 41775065. The observational data in this study were from a field experiment supported by the Experiment of Typhoon Intensity Changes in the Coastal Area (EXOTICCA).
- Kolmogorov, A. N. (1941). The Local Structure of Turbulence in Incompressible Viscous Fluid for Very Large Reynolds Number. *Dokl. Akad. Nauk SSSR* 30, 301–303.
- Ming, J., and Zhang, J. A. (2018). Direct Measurements of Momentum Flux and Dissipative Heating in the Surface Layer of Tropical Cyclones during Landfalls. *J. Geophys. Res. Atmos.* 123, 4926–4938. doi:10.1029/2017jd028076
- Monin, A. S., and Obukhov, A. M. (1954). Basic Laws of Turbulent Mixing in the Ground Layer of the Atmosphere. *Akad. Nauk. SSSR Geofiz. Inst.* 151, 163–187.
- Powell, M. D. (1982). The Transition of the Hurricane Frederic Boundary-Layer Wind Field from the Open Gulf of Mexico to Landfall. *Mon. Wea. Rev.* 110, 1912–1932. doi:10.1175/1520-0493(1982)110<1912:tothf>2.0.co;2
- Powell, M. D., Vickery, P. J., and Reinhold, T. A. (2003). Reduced Drag Coefficient for High Wind Speeds in Tropical Cyclones. *Nature* 422, 279–283. doi:10.1038/nature01481
- Rao, K. S., Wyngaard, J. C., and Coté, O. R. (1974). The Structure of the Two-Dimensional Internal Boundary Layer over a Sudden Change of Surface Roughness. *J. Atmos. Sci.* 31, 738–746. doi:10.1175/1520-0469(1974)031<0738:tsottd>2.0.co;2
- Savelyev, S. A., and Taylor, P. A. (2005). Internal Boundary Layers: I. Height Formulae for Neutral and Diabatic Flows. *Boundary-Layer Meteorol.* 115, 1–25. doi:10.1007/s10546-004-2122-z
- Simiu, E., and Scanlan, R. H. (1996). *Wind Effects on Structures: Fundamentals and Applications to Design*. New York: John Wiley & Sons, 589.
- Sreenivasan, K. R. (1995). On the Universality of the Kolmogorov Constant. *Phys. Fluids* 7, 2778–2784. doi:10.1063/1.868656
- Tang, J., Byrne, D., Zhang, J. A., Wang, Y., Lei, X.-t., Wu, D., et al. (2015). Horizontal Transition of Turbulent cascade in the Near-Surface Layer of Tropical Cyclones. *J. Atmos. Sci.* 72, 4915–4925. doi:10.1175/jas-d-14-0373.1
- Tang, J., Zhang, J. A., Aberson, S. D., Marks, F. D., and Lei, X. (2018). Multilevel Tower Observations of Vertical Eddy Diffusivity and Mixing Length in the Tropical Cyclone Boundary Layer during Landfalls. *J. Atmos. Sci.* 75, 3159–3168. doi:10.1175/jas-d-17-0353.1
- Wood, D. H. (1982). Internal Boundary Layer Growth Following a Step Change in Surface Roughness. *Boundary-Layer Meteorol.* 22, 241–244. doi:10.1007/bf00118257
- Ying, M., Zhang, W., Yu, H., Lu, X., Feng, J., Fan, Y., et al. (2014). An Overview of the China Meteorological Administration Tropical Cyclone Database. *J. Atmos. Ocean. Technol.* 31, 287–301. doi:10.1175/jtech-d-12-00119.1
- Zhang, D.-L., and Altshuler, E. (1999). The Effects of Dissipative Heating on hurricane Intensity. *Mon. Wea. Rev.* 127, 3032–3038. doi:10.1175/1520-0493(1999)127<3032:teodho>2.0.co;2
- Zhang, J. A., Drennan, W. M., Black, P. G., and French, J. R. (2009). Turbulence Structure of the Hurricane Boundary Layer between the Outer Rainbands. *J. Atmos. Sci.* 66, 2455–2467. doi:10.1175/2009jas2954.1
- Zhang, J. A. (2010). Estimation of Dissipative Heating Using Low-Level *In Situ* Aircraft Observations in the hurricane Boundary Layer. *J. Atmos. Sci.* 67, 1853–1862. doi:10.1175/2010jas3397.1
- Zhang, J. A., Marks, F. D., Montgomery, M. T., and Loruso, S. (2011). An Estimation of Turbulent Characteristics in the Low-Level Region of Intense

- Hurricanes Allen (1980) and Hugo (1989). *Mon. Wea. Rev.* 139 (5), 1447–1462. doi:10.1175/2010mwr3435.1
- Zhao, Z.-K., Liu, C.-X., Li, Q., Dai, G.-F., Song, Q.-T., and Lv, W.-H. (2015). Typhoon Air-Sea Drag Coefficient in Coastal Regions. *J. Geophys. Res. Oceans* 120, 716–727. doi:10.1002/2014jc010283

Conflict of Interest: The authors declare that the research was conducted in the absence of any commercial or financial relationships that could be construed as a potential conflict of interest.

The reviewer JL declared a shared affiliation with the authors KZ, QL to the handling editor at the time of review.

Publisher's Note: All claims expressed in this article are solely those of the authors and do not necessarily represent those of their affiliated organizations, or those of the publisher, the editors and the reviewers. Any product that may be evaluated in this article, or claim that may be made by its manufacturer, is not guaranteed or endorsed by the publisher.

Copyright © 2022 Zhou, Li and Tang. This is an open-access article distributed under the terms of the Creative Commons Attribution License (CC BY). The use, distribution or reproduction in other forums is permitted, provided the original author(s) and the copyright owner(s) are credited and that the original publication in this journal is cited, in accordance with accepted academic practice. No use, distribution or reproduction is permitted which does not comply with these terms.



Modulation of Pacific Sea Surface Temperature on Two Types of Tropical Cyclone Tracks Affecting Northeast China

Yiqiu Yu^{1,2}, Yihe Fang^{1,2*}, Chunyu Zhao¹, Yi Lin^{3*}, Yitong Lin¹, Zhiqiang Gong^{4,5} and Yang Li⁶

¹Regional Climate Center of Shenyang, Shenyang, China, ²Key Opening Laboratory for Northeast China Cold Vortex Research, China Meteorological Administration, Shenyang, China, ³Liaoning Provincial Meteorological Service Center, Shenyang, China, ⁴Laboratory for Climate Studies, National Climate Research Center, China Meteorological Administration, Beijing, China, ⁵College of Physics and Electronic Engineering, Changshu Institute of Technology, Suzhou, China, ⁶Shenyang Central Meteorological Observatory, Shenyang, China

OPEN ACCESS

Edited by:

Qingqing Li,
Nanjing University of Information
Science and Technology, China

Reviewed by:

Yipeng Guo,
Nanjing University, China
Chao Wang,
Nanjing University of Information
Science and Technology, China

*Correspondence:

Yihe Fang
49954570@qq.com
Yi Lin
liny_0330@163.com

Specialty section:

This article was submitted to
Atmospheric Science,
a section of the journal
Frontiers in Earth Science

Received: 08 November 2021

Accepted: 25 April 2022

Published: 31 May 2022

Citation:

Yu Y, Fang Y, Zhao C, Lin Y, Lin Y,
Gong Z and Li Y (2022) Modulation of
Pacific Sea Surface Temperature on
Two Types of Tropical Cyclone Tracks
Affecting Northeast China.
Front. Earth Sci. 10:810943.
doi: 10.3389/feart.2022.810943

In this study, the northward-moving tropical cyclones (TCs) that influence Northeast China (NEC) in July–September are identified based on the distance between the TC center and the boundaries of NEC. Then, based on a machine learning algorithm named hierarchical agglomerative clustering, the tracks of northward-moving TCs that influence NEC are classified into the eastern-track type and the turning type. In NEC, the precipitation induced by eastern-track type TCs gradually decreases from east to west, and the precipitation induced by turning-type TCs gradually decreases from south to north. For eastern-track type TCs, negative Niño3 sea surface temperature (SST) anomalies in preceding January–March can induce cyclonic circulation anomalies and positive vorticity anomalies over the Philippine Sea during subsequent July–September, which favors the genesis of TCs. Moreover, the westerly anomaly in the subtropical western north Pacific and the strengthening of cyclonic steering flow over the Philippines jointly steer the TCs to move northward along the northerly airflow on the west of the western Pacific subtropical high, which favors the genesis of eastern-track type TCs. For turning-type TCs, the positive SST anomalies in the West Wind Drift area during preceding May–July cause positive vorticity anomalies from the northern Philippines to Taiwan from July to September. The cyclonic steering flow over the Philippines and the anticyclonic steering flow over the Sea of Japan lead the TCs to move northwestwards and then turn to northeast, which is conducive to the genesis of turning type northward-moving TCs. Finally, the results of numerical experiments have confirmed these findings.

Keywords: machine learning, hierarchical agglomerative clustering, tropical cyclone track, air-sea interactions, West wind drift, steering flow

1 INTRODUCTION

China is severely affected by typhoons, and suffers substantial economic losses and great casualties from typhoons every year. In recent years, northward-moving typhoons have significantly influenced the precipitation in Northeast China (NEC) during the flood season, which may even result in severe flooding. In the summer of 2020, NEC was hit by three strong northward-moving tropical cyclones (TCs)

successively. Frequent northward-moving TCs have attracted considerable attention. Previous studies have mainly analyzed intermonthly characteristics, interannual and interdecadal variations, climate incidents and oscillation period of the TCs influencing northern China. The TCs influencing northern China exhibit remarkable intermonthly and interannual variations. The main TC season in northern China is from July to September (Wang and Liang, 2006). The TCs affecting the Liaodong Peninsula from different source regions have different impacts and disaster distributions (Liang and Chen, 2005). The landing northward-moving and turning TCs are able to bring heavy rainstorm and gale (Zhou et al., 2007; Gao Q. Q. et al., 2017). The position and intensity of the western Pacific subtropical high (WPSH), the middle-latitude westerlies and the South Asian high have an important influence on TC's northward movement (Jin et al., 2006). The influence of northward-moving TCs on NEC can vary significantly with the TC tracks (Gao S. Y. et al., 2017). Therefore, only considering the overall TC intensity or frequency is insufficient for predicting the weather and climate in NEC. It is necessary to classify the northward-moving TCs objectively. Many studies have tried to classify the tracks of TCs and northeast cold vortices. For example, following Nakamura et al. (2009), Zheng et al. (2013) and Peng et al. (2019) used K-means clustering algorithm to classify TC tracks in the western north Pacific based on the location, intensity, track length and moving direction of TCs. Wang et al. (2019) and Fang et al. (2020) also used K-means clustering algorithm to classify the tracks of Madden-Julian Oscillation (MJO) and the northeast cold vortex.

Sea surface temperature (SST) and its distribution can significantly influence the genesis and development of TCs (Huang et al., 2005; Yamasaki, 2007). Air-sea interactions can alter the distribution of atmospheric circulation (Wang et al., 1999; Huang et al., 2011), and then result in the changes of TC tracks (Cheung and Chan, 2010). Therefore, such interactions are the fundamental for TC development. Seasonal-scale movement of TCs is regulated mainly by the large-scale and slowly-moving background fields. El Niño-Southern Oscillation (ENSO) events are the most significant interannual variation signals occurring in tropical oceans, and their relationship with TCs in the western north Pacific has been studied extensively (Zuki and Lupo, 2008; Guo and Tan, 2021). The changes of large-scale circulations in tropical regions caused by ENSO events can be used to explain the relationships between TCs and ENSO, such as the Walker circulation and the western north Pacific monsoon trough (Chen and Huang, 2006a; Feng et al., 2013).

In El Niño years, the western north Pacific monsoon trough deepens towards the east, and TCs are generated in the southeastern areas of the western north Pacific. In La Niña years, the monsoon trough is shallow, and the location of TC genesis is more northwesterly (Chen et al., 1998; Wang and Chan, 2002; Huang and Xu, 2009; Tao and Cheng, 2012). However, the effect of ENSO on the frequency of TCs generated has not reached an agreement by researchers. Some scholars pointed out that the total frequency of TCs generated in an El Niño year is smaller than the climatic mean (Wu and Lau, 1992; Chan, 2000). But some other studies showed that there are no substantial correlations between

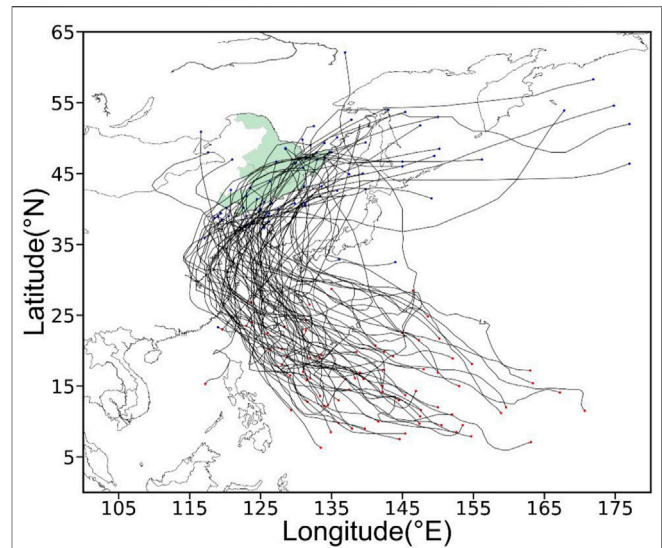
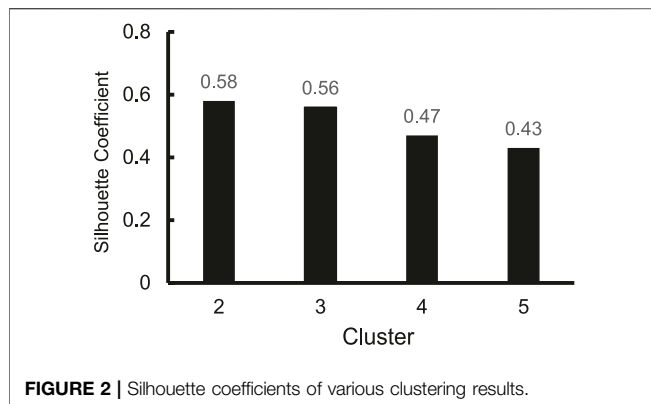


FIGURE 1 | The tracks of TCs that can influence Northeast China (NEC) during 1949 and 2019. The red (blue) dots represent the genesis (dissipation) locations of TCs.

the frequency of TC and the ENSO index (Lander, 1994; Chen et al., 2006). At present, the influence of central Pacific El Niño events on TCs has become a hot topic. Previous studies have indicated that the TC activities during a central Pacific El Niño year are more westward and extend to the northwest part of the western north Pacific, which could affect the coastal areas of East Asia (Kim et al., 2011; Ha et al., 2012). The western Pacific warm pool can also influence TC activity. Specifically, the warm pool is correlated with the onset of the South China Sea summer monsoon and the variation of the WPSH through the East Asia-Pacific (EAP) teleconnection, influencing the TC activities in the western north Pacific. In addition, the western Pacific warm pool influences the genesis and movement of TCs in the western north Pacific through the monsoon trough (Chen and Huang, 2006b; Huang and Chen, 2007; Huang and Wang, 2010; Huang et al., 2016). Moreover, the tropical Atlantic SST anomalies can also regulate the atmospheric circulation over the western north Pacific, affecting TC activities (Huo et al., 2016; Yu et al., 2016). In contrast, the warming of the Indian Ocean Basin negatively correlates with the frequency of TC genesis in the western north Pacific. The Indian SST anomaly can remotely influence the low-level anticyclone circulation anomaly and strengthen the vertical wind shear, resulting in fewer TCs over the western North Pacific (Zhan et al., 2011a, 2011b, 2012; Ha et al., 2015).

The TC activity in the North Indian Ocean is found to correlate well with the Indian Ocean dipole-like SST anomaly. The adjustment of atmospheric circulation caused by such anomaly can influence the genesis environment and movement of TCs (Yuan and Cao, 2013). Related studies were conducted to study the genesis, development and movement of TCs, and provided substantial theoretical support for governmental decision-making in disaster prevention and mitigation plans.



However, relatively few studies have analyzed the different types of northward-moving TCs that affect NEC. Although classifying TC tracks can benefit the prediction of TC track. To this end, this study uses geographic information technology to isolate the northward-moving TCs that affect NEC. Then, based on the precipitation data during the TC influence period, the rationality of the derived TC data is verified. Furthermore, the machine learning method (hierarchical agglomerative clustering) is used to classify the tracks of northward-moving TCs objectively. Then, the influence mechanisms of precedent SST on the tracks of northward-moving TCs are investigated from an air-sea interaction perspective. It is expected to provide an important reference for the refined diagnosis, forecasting and scientific research of northward-moving TCs.

The remainder of this paper is organized as follows. **Section 2** introduces the data and method used in this study. The variation characteristics of two types of northward-moving TCs that affect NEC are detailedly presented in **Section 3**. The relationships between the two types of TCs and SST are analyzed in **Section 4**. **Section 5** discusses the effects of Pacific SST on the two types of northward-moving TCs. In **Section 6**, we conduct some sensitivity experiments and try to explore the influence of SST on atmospheric circulations. **Section 7** presents the discussions and conclusions.

2 DATA AND METHOD

2.1 Observation Data and Statistical Method

The best track dataset of TCs from 1949 to 2019 in the western north Pacific is provided by the Shanghai Typhoon Research Institute of China Meteorological Administration (CMA; Ying et al., 2014; Lu et al., 2021). The daily precipitation data in northeastern China from 1951 to 2019 is obtained from the National Meteorology Information Center of CMA. The monthly SST data from 1951 to 2019 with a horizontal resolution of $1^\circ \times 1^\circ$ are provided by the United Kingdom Met Office Hadley Center (Rayner et al., 2003). The daily and monthly reanalysis data between 1951 and 2019 are obtained from the National Centers for Environmental Prediction (NCEP)/National Center for Atmospheric Research (NCAR; Kalnay et al., 1996) of the United States National Oceanic and Atmospheric

administration (NOAA), with a horizontal resolution of $2.5^\circ \times 2.5^\circ$ and 17 vertical layers. The Niño3 index and the West Wind Drift index are provided by the National Climate Center of CMA.

To analyze the reasons for the anomaly of northward-moving TCs, some statistical methods are used, including composite analysis, regression analysis and partial correlation analysis. The peak season of TC activities is defined as July–September in this study. The pressure-weighted mean airflow method is used to calculate the steering flow. The pressure-weighted mean airflow between 850 and 300 hPa is considered as the steering flow (Holland, 1993) in this study. The formula is as follows:

$$\vec{V} = \frac{\int_{P_1}^{P_2} \vec{V} dp}{P_2 - P_1} \quad (1)$$

where P_1 and P_2 represent geopotential heights of 850 and 300 hPa, respectively.

2.2 Model Introduction

The NCAR atmospheric circulation model (CAM5.3) is used to run the sensitivity experiments. The atmospheric section of the general Earth model (CESM1.2.2) can be operated independently or coupled with ocean, land surface and other models. The model uses the finite volume dynamical core. The horizontal resolution is $1.9^\circ \times 2.5^\circ$, with 96 (meridional) \times 144 (zonal) grid points. In the vertical direction, a δ - p hybrid coordinate system is adopted, and there are 30 vertical layers.

2.3 Judgement Method for Whether Tropical Cyclones Influence Northeast China

TCs that can influence NEC are identified by using an objective method, which can estimate TC's influence on NEC based on the range of strong wind and rainfall caused by TC. Relevant studies have shown that, thunderstorms (Molinari et al., 1999), strong winds (Mueller et al., 2006) and severe precipitation (Lonfat et al., 2007) frequently occur within around 200 km from the TC center. This study evaluates the TC influence radius by applying a cartographic python library (Cartopy, developed by the United Kingdom Met Office). With the help of geographic information technology, the buffer zone (i.e., the influence range) is defined as the circular region with a radius of 2° (about 222 km in the Cartesian coordinate system in middle latitudes) centered on the TC center. Then the spatial relationship between the influence range and the NEC boundary is analyzed. Any intersection between the TC influence range and the NEC boundary indicates that the TC process has influenced NEC. After selection, 81 TC processes are considered to have possible influence on NEC between 1949 and 2019. **Figure 1** shows the tracks of TCs influencing NEC. Most northward-moving TCs influencing NEC are generated in the tropical western Pacific and the adjacent sea areas, and they first move to the northwest and then moves to the northeast, presenting recurving tracks. The centers of most TCs reach the eastern or southern NEC. But a few TCs travel northeastward along the coastal areas of China instead of landfall. The dissipation locations of most TCs are in southern or eastern NEC, the

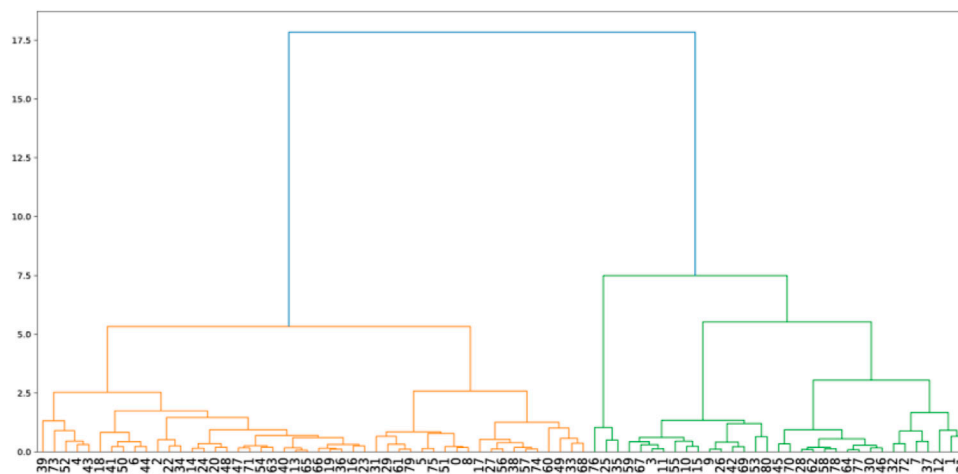


FIGURE 3 | Pedigree chart of hierarchical agglomerative clustering. The x-axis represents 81 samples, and the y-axis is the relative distance between the samples. Green and orange lines represent the clustering results obtained by hierarchical agglomerative clustering for the first and second type of TC tracks, respectively.

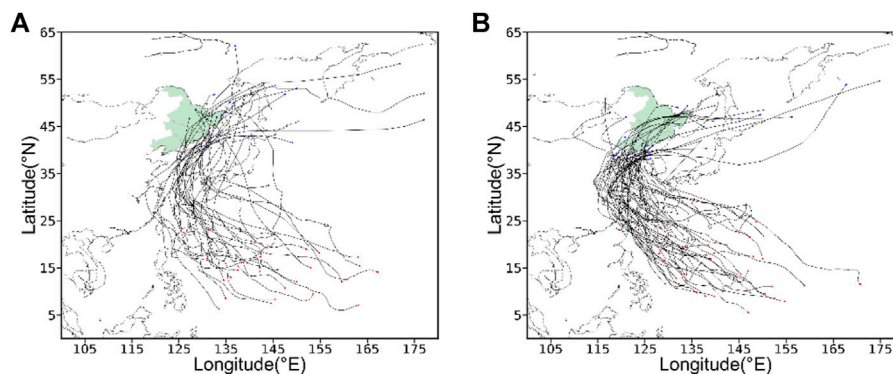


FIGURE 4 | Classification of the tracks of TCs influencing NEC. **(A)** Eastern-track type TCs; **(B)** turning type TCs. The red (blue) dots represent the genesis (dissipation) locations of TCs.

Korean Peninsula, the Sea of Okhotsk and as far as the Bering Sea. Some of the TCs can deeply reach the inland of China and dissipate on the east side of the Mongolian Plateau.

2.4 Classification of the Tracks of Northward-Moving Tropical Cyclones Influencing Northeast China

The northward-moving TCs with different types of tracks have different characteristics and influences. Therefore, based on the machine learning method we perform clustering analysis on the tracks of northward-moving TCs, so as to distinguish the differences among the tracks.

2.4.1 Hierarchical Agglomerative Clustering Method

The hierarchical agglomerative clustering method is used in this study because its advantage that the number of clusters is not predetermined. In this study, scattered adjacent clusters are

merged from bottom to top. The clustering ends when all samples are merged into the same cluster. The hierarchical agglomerative clustering has several methods for calculating the cluster proximity. In this study, the Ward method which is based on the explained sum of squares (ESS) is applied (Ward, 1963):

$$ESS = \sum_{i=1}^n x_i^2 - \frac{1}{n} \left(\sum_{i=1}^n x_i \right)^2 \quad (2)$$

where x_i is the score of the i -th individual cluster. First, the sum of the original ESS of the whole data is calculated by totaling the individual ESS of all clusters. Second, one of the clusters is selected for merging with another one to calculate the ESS. Then, the ESSs of the merged clusters and remained ones are added to obtain the merged ESS value. The difference between the original ESS and merged ESS is the merge cost. The merged cluster corresponds to the minimum value of the $n \times \frac{n-1}{2}$ merge cost.

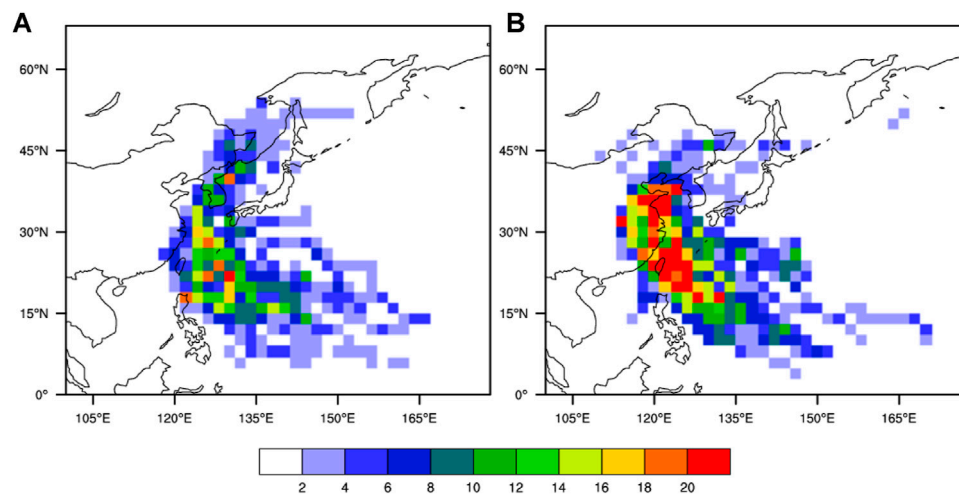


FIGURE 5 | TC Track frequencies at 2° × 2° spatial resolution for (A) eastern-track type TCs, and (B) turning type TCs.

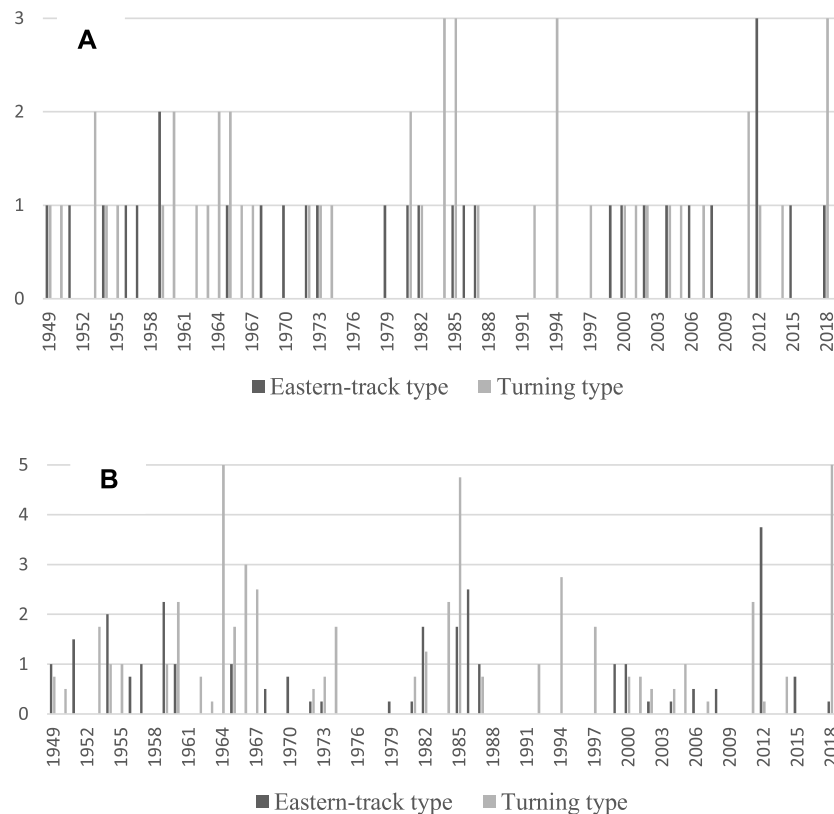


FIGURE 6 | Time series of (A) TC number and (B) influence days of the two types of northward-moving TCs.

2.4.2 Selection Scheme for the Tropical Cyclone Characteristic Parameters

The TC track information is presented as several TC characteristic parameters, and then we perform the

hierarchical agglomerative clustering on these parameters. Because this study focuses on the TCs that can influence NEC, we narrow the scope by setting the tracks when TCs influencing NEC as the characteristic parameter. The initial location of the

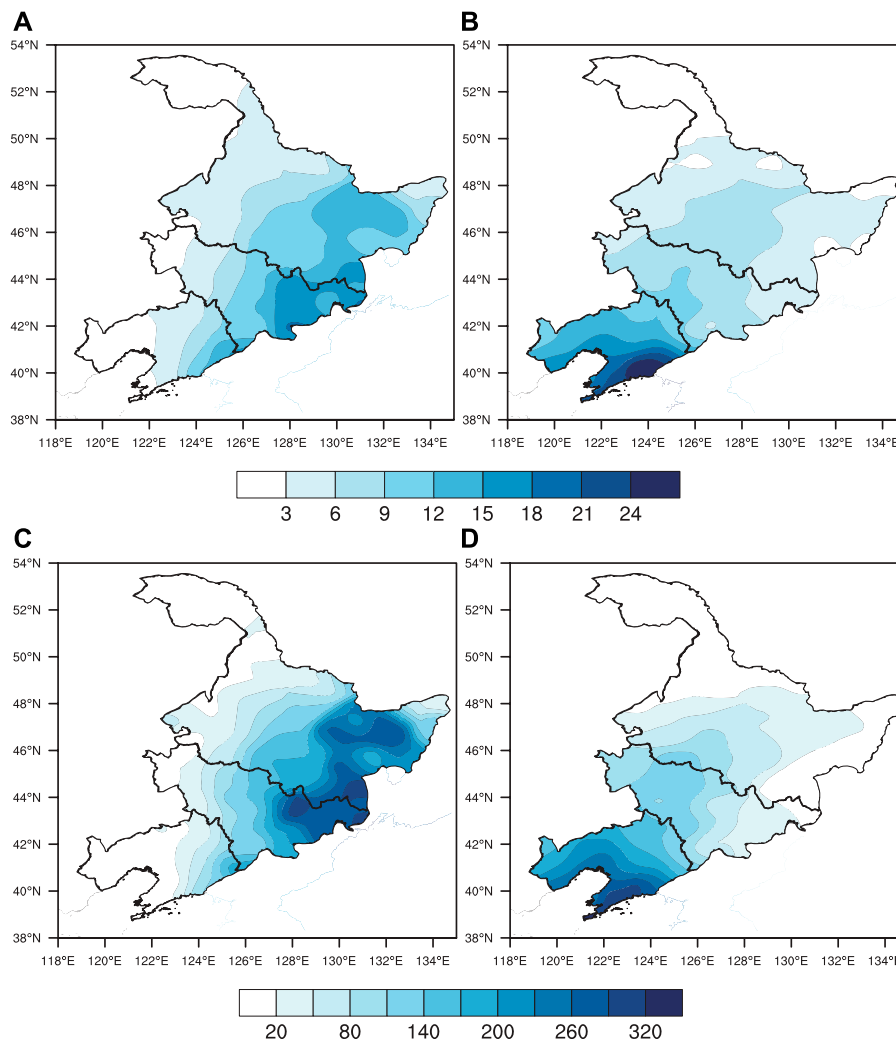


FIGURE 7 | (A,B) Average precipitation in NEC (mm/day) and **(C,D)** precipitation anomaly percentages (%) for the different types of northward-moving TCs. **(A,C)** are for the eastern-track type TCs; **(B,D)** are for the turning type TCs.

TCs influencing NEC is widely distributed in the range of 117°E–134°E and 36.8°N–45°N. The region of TC activities when NEC is influenced is generally in the south of 50°N. In the clustering analysis of TC tracks, the initial location and track characteristics of TCs are considered as the characteristic parameters. The longitude and latitude of the TC center when NEC is firstly influenced by TC are selected as classification parameters for characterizing the initial location of TC. Considering that the TC track when influencing NEC is generally in a southwest-northeast orientation and the meridional span is large, so selecting the average longitude and initial location as the parameters can well cover the information of location and span. Therefore, the average longitude of the TC track when influencing NEC is included in the classification parameters. Before clustering, the characteristic parameters are standardized by the Z-score, and the processed data conform to the standard normal distribution. The conversion function is

$$Z = \frac{x - \mu}{\delta} \quad (3)$$

where Z is the value after Z-score normalization, μ is the average, and δ is the standard deviation. The Z value indicates the relationship between the data and the average. $Z > 0$ means that the data is greater than the average.

2.4.3 Classification Results of Northward-Moving Tropical Cyclones

After comprehensively considering the subsequent classification of TC track characteristics and the circulation characteristics, the hierarchical agglomerative clustering is conducted for all TCs influencing NEC according to the cluster number (from two to five). The silhouette coefficients of the clustering results are shown in **Figure 2**. When the number of clusters is two or three, the silhouette coefficient is obviously greater than that of 4–5 clusters. Further analysis on the classification data shows that, when the number of clusters is 3–5 the number of samples in certain cluster

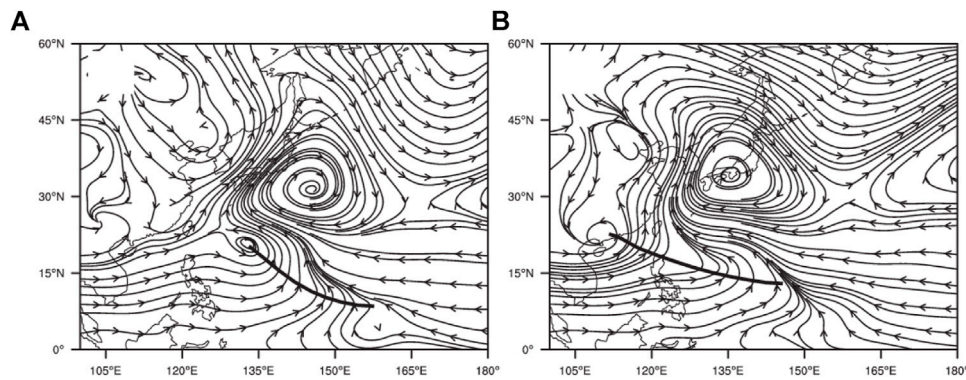


FIGURE 8 | Composite of 850 hPa flow field on the genesis day of the two types of TCs (m/s): **(A)** eastern-track type; **(B)** turning type.

is less than 5, which is too less to be statistically significant. Therefore, considering the silhouette coefficient and sample distribution, the number of clusters is finally set as two. **Figure 3** depicts the detailed process of hierarchical agglomerative clustering. **Figure 4** illustrates the classification of TC tracks. The first type of TC tracks is relatively easterly and is named as the eastern-track type (**Figure 4A**). This type of TCs move northward through the East China Sea and the Yellow Sea, and then travel northeastward in the Korean Peninsula and its east. Most TCs of this type do not pass through mainland China, and a few move eastwards out of China after passing through the southeastern NEC. Generally, the tracks of the eastern-track type TCs are relatively straight. Differently, most of the second type of TCs move northwestwards after their genesis, making landfall in the coastal areas between the southeastern NEC and southern NEC. Afterward, they turn northeastwards and pass through the southern and eastern NEC. This type is named as the turning-type (**Figure 4B**). Most of the turning-type TCs dissipate in the southern NEC or the oceans near the Korean Peninsula, while a few dissipate after moving away from the eastern NEC. **Figure 5** shows the frequency of the two types of northward-moving TCs. It is found that the eastern-track type TCs affect mainly parts of the southeastern and eastern NEC. However, the turning-type TCs influence most parts of NEC. Thus, the turning-type TCs should have more substantial effects on NEC. Accordingly, we should pay more attention to the turning-type TCs when studying the influence of TCs on NEC.

3 VARIATION CHARACTERISTICS OF NORTHWARD-MOVING TROPICAL CYCLONES INFLUENCING NORTHEAST CHINA

The interannual variations of the number and duration of the two types of TCs are presented in **Figure 6**. During 1949–2019, 81 northward-moving TCs have influenced NEC in 45 of the total 71 years, and there are 2–4 TCs in 22 years and 1 TC in 23 years. Specifically, 32 of them belong to the eastern-track type and 49 of them belong to the turning-type, accounting for 39.5% and 60.5%, respectively. In particular, the total days when NEC is influenced by the eastern-track type and turning-type TCs are 30

and 54, respectively, with an average of 0.94 and 1.10, respectively. Therefore, the influence period of the turning-type TCs on NEC is longer. **Figure 7** shows the average precipitation and precipitation anomaly percentage in NEC in the period influenced by the two types of TCs. **Figures 7A,C** show that the NEC precipitation anomaly induced by the eastern-track type TCs gradually decreases from east to west. These TCs mainly affect the eastern part of NEC, particularly the eastern Heilongjiang and the northeastern Jilin. The precipitation amount and the precipitation anomaly percentage reach 12 mm/day and 300%/day, respectively. As is seen from **Figures 7B,D**, the NEC precipitation anomaly induced by the turning-type TCs gradually decreases from south to north. These TCs mainly affect Liaoning Province which is in southern NEC, especially the south-eastern Liaoning. The average precipitation and precipitation anomaly percentage reach 24 mm/day and the 300%/day, respectively. The distribution of the anomalous precipitation in the active days of TCs in the NEC is consistent with the TC track characteristics shown in **Figure 5**. Hence, the obtained TC cases are reasonable.

4 RELATIONSHIP BETWEEN SEA SURFACE TEMPERATURE AND THE TWO TYPES OF NORTHWARD-MOVING TROPICAL CYCLONES

Figure 8 provides the 850 hPa wind on the initiation day of the two types of TCs, and notable differences can be found in the locations of the monsoon trough and western north Pacific subtropical anticyclone. For the eastern-track type TCs, the monsoon trough is located in the south of 15°N, 130°E, while the western north Pacific subtropical anticyclone is located in the eastern and western north Pacific with a center in the southeastern Japan. The western ridge of the WPSH is located around 30°N, 130°E. In the initiation day of the turning-type TCs, the monsoon trough shows a northwestward shift. The center of the western north Pacific subtropical anticyclone is over Japan, and the western end of the WPSH ridge is located at 35°N, 125°E. The location of the western north Pacific subtropical anticyclone on the initiation days of two types of TCs is generally

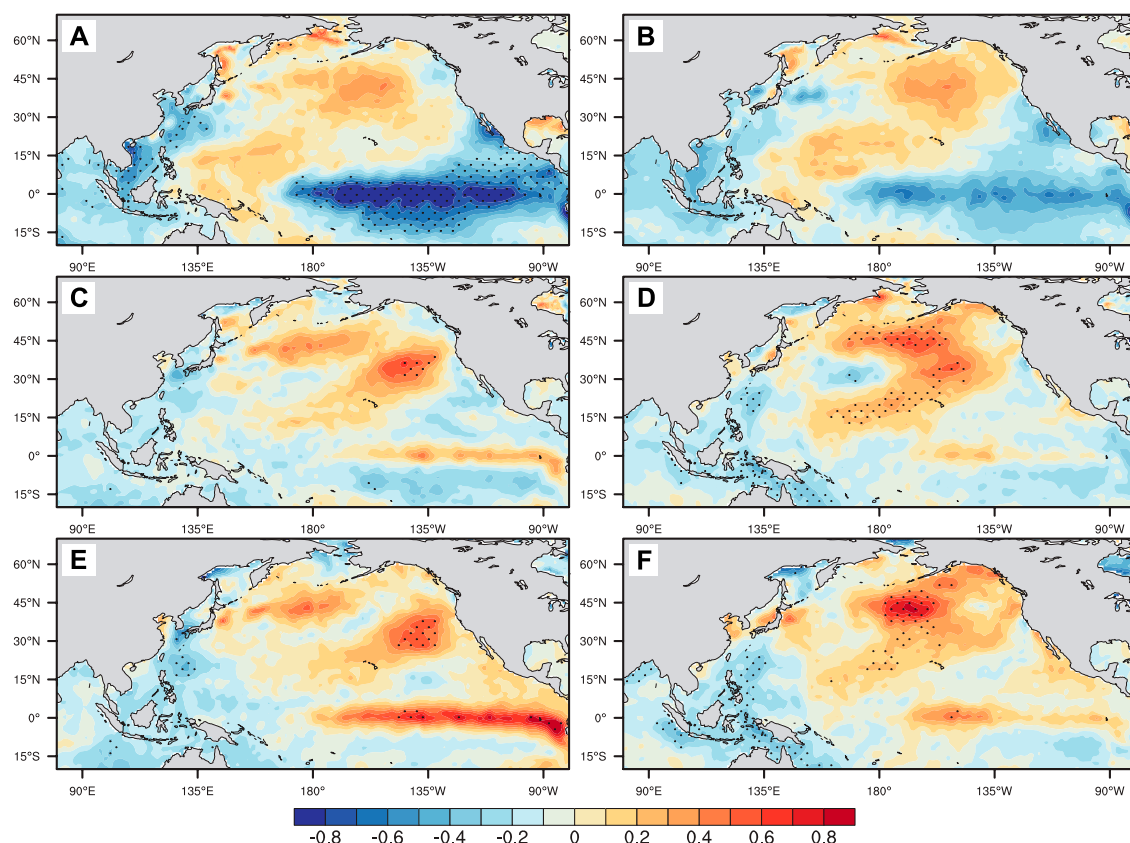


FIGURE 9 | Composite of SST anomalies ($^{\circ}\text{C}$) in (A,B) late winter and early spring (January–March), (C,D) late spring and early summer (May–July), and (E,F) peak season of TC activities (July–September). (A,C,E): eastern-track type; (B,D,F): turning type. The dotted areas indicate the anomalies that are significant at the 95% confidence level.

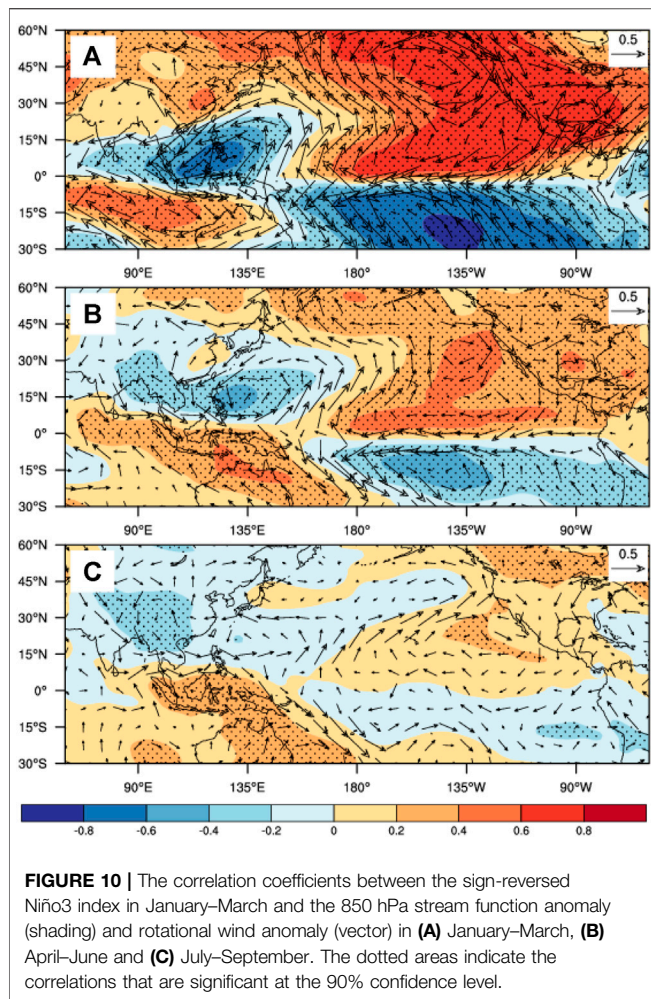
TABLE 1 | List of the years when two types of northward-moving TCs occur independently.

Type	Year
Eastern-track type	1951, 1956, 1957, 1968, 1970, 1979, 1986, 1999, 2006, 2008, 2015
Turning type	1953, 1955, 1960, 1962, 1963, 1964, 1966, 1967, 1974, 1984, 1992, 1994, 1997, 2001, 2005, 2007, 2011, 2014

more eastward, which is conducive to the northward movement of the TCs along the northerly wind on the left side of the anticyclone. Some past studies have indicated that most TCs are generated in the monsoon trough (Wang et al., 2006; Gao et al., 2008). The mean genesis location of eastern-track type TCs is 14.6°N , 144.1°E , while that of the turning-type TCs is 16.5°N , 139°E . The latter is slightly northwestward than that of the eastern-track type, which is consistent with the location of monsoon trough. The locations of the monsoon trough and WPSH are different between the two types of TCs, resulting in the difference in TC tracks.

Figure 9 shows the composite SST anomalies (SSTAs) for the two types of TCs during late winter and early spring (January–March), late spring and early summer (May–July), and the peak season of TC activities (July–September). The selected composite years are listed in **Table 1**. For the eastern-track type TCs, the SSTA distribution corresponds to the La Niña

state during late winter and early spring. Significant negative SSTA appears in the tropical central-eastern Pacific (**Figure 9A**), while positive SSTA appears in the subtropical North Pacific Ocean. During the peak season of TC activities, the SSTA is positive in the tropical central and eastern Pacific (**Figure 9E**). Thus, the eastern-track type TCs are more likely to occur in the decay year of La Niña. For the turning-type TCs, the negative SSTA in January–March is relatively weak in the tropical central-eastern Pacific (**Figure 9B**). In May–July, the composite SST shows a significant positive anomaly in the West Wind Drift area in the subtropical central North Pacific (**Figure 9D**). The composite results suggest that the SSTA is important to the tracks. The Niño3 area (5°S – 5°N , 150°W – 90°W) of the equatorial Central and Eastern Pacific in late winter and early spring (January–March) is the key location for the eastern-track type TCs. Whereas the West Wind Drift area (35°N – 45°N ,



160°E–160°W) in late spring and early summer (May–July) is crucial for the turning-type TCs.

5 EFFECTS OF PACIFIC SEA SURFACE TEMPERATURE ON THE TWO TYPES OF NORTHWARD-MOVING TROPICAL CYCLONES

To understand the mechanisms for the impacts of SST in various key areas on TC tracks, two SST indexes are used. The first is the Niño3 index, which is defined as the area-mean SSTA over 5°S–5°N, 150°W–90°W. The second is the West Wind Drift index, which is defined as the area-mean SSTA over 35°N–45°N, 160°E–160°W. **Figure 10** shows the distribution of correlation coefficients between the January–March mean Niño3 index (multiplied by -1) and the 850 hPa stream function and rotational wind from January to March, from April to June, and from July to September. The negative SSTA in the tropical eastern Pacific can stimulate a Gill type Rossby wave through the diabatic heating (Gill, 1980). An anticyclonic circulation appears in the tropical northeastern Pacific during January–March, and

meanwhile a cyclonic circulation appears on the Northwest Pacific. The southerly wind on the west side of the anticyclonic circulation transports warm air to the subtropical western north Pacific and weakens the atmosphere stability. Additionally, the southerly wind acts to decelerate the trade wind and warm SST in the subtropical western north Pacific. The SST warming and the weakened atmosphere stability favor the convection in the tropical eastern and western north Pacific, further emanating a cyclonic circulation over the western Northwest Pacific. The cyclonic circulation can further sustain and expand to Northeast Asia from July to September through local air-sea interaction or the capacitor effect of the Indian Ocean, which in turn affects the circulation that is important for the genesis and movement of TCs.

To eliminate the influence of West Wind Drift index in the early stage, partial correlation analysis is conducted on the Niño3 index and the atmospheric circulation during the peak season of TC activities. **Figure 11A** shows the distribution of partial correlation coefficients between the sign-reversed January–March mean Niño3 index and the 500 hPa geopotential height and 850 hPa wind during the peak season of TC activities. The negative SSTA in the Niño3 area during January–March is conducive to the decrease of the 500 hPa geopotential height in tropical and subtropical North Pacific. The anomalous cyclonic circulation occurs in the Northwest Pacific, which is conducive to the genesis and development of TCs. **Table 2** lists the correlation coefficients between the sign-reversed January–March mean Niño3 index and the WPSH index in the peak season of TC activities. The sign-reversed Niño3 index shows a significant negative correlation with the area, intensity and the location of the WPSH northern boundary, which is significant at the 99% confidence level. When the Niño3 SST shows negative anomalies during January–March, the area of WPSH is relatively small, and its intensity is relatively weak. The weakened and eastward WPSH is favorable for the northward movement of TCs along the northerly wind to the west of the WPSH and is conducive to the TC landfall in NEC, North Korea, the Republic of Korea, Japan and other subtropical regions. **Figure 11B** shows the partial correlation coefficients between the sign-reversed January–March mean Niño3 index and the 500 hPa zonal wind during the peak season of TC activities. Significant positive correlation coefficients can be found in the tropical western Pacific. Thus, when the Niño3 SST shows negative anomalies during January–March, the WPSH in the peak season of TC activities is weakened and moves eastwards. At the same time, the associated westerly wind anomalies in the tropical western Pacific can weaken the southeasterly wind on the south of the WPSH, which is conducive to the northward movement of TCs to higher latitudes. **Figure 11C** shows that the sign-reversed Niño3 index and the 850 hPa vorticity are significantly positively correlated in the subtropical western north Pacific near 140°E–150°E, which is the main genesis region of eastern-track type TCs (**Figure 8A**). When the Niño3 area SST shows negatively anomalies during January–March, the positive low-level vorticity in the western north Pacific near 150°E during the late stage of the peak season of TC activities is conducive to the genesis of the eastern-track type

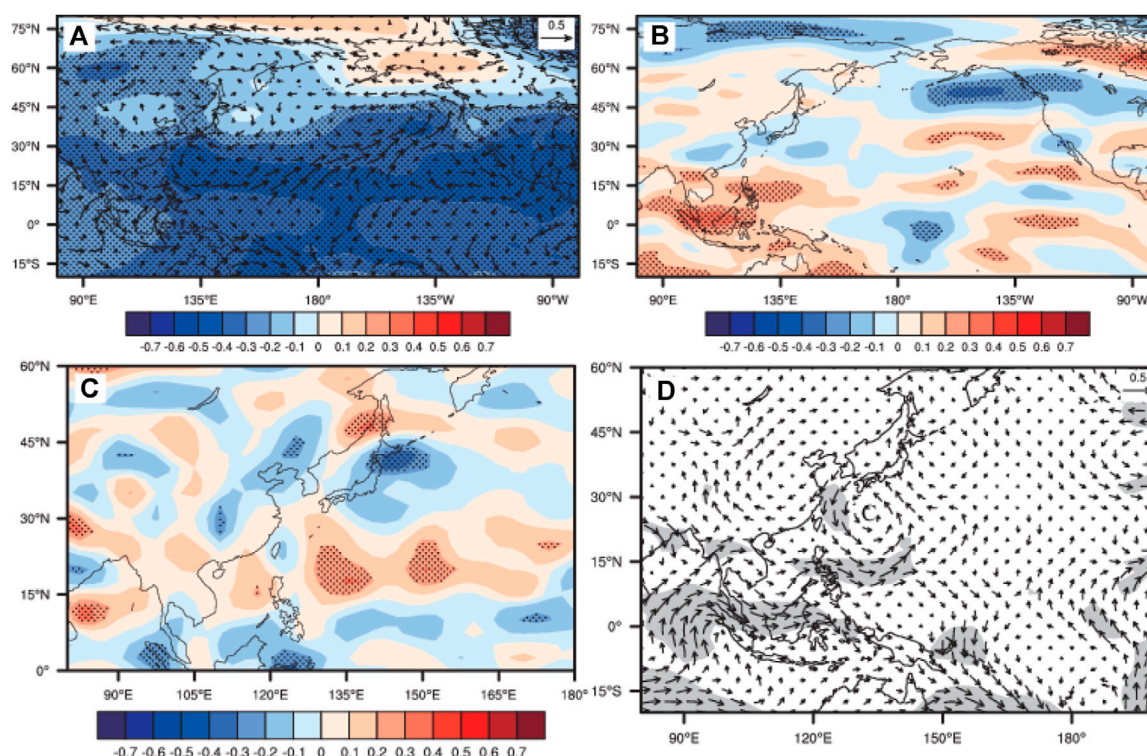


FIGURE 11 | The partial correlation coefficients between the sign-reversed Niño3 index in January–March and the (A) 500 hPa geopotential height anomaly (shading) and 850 hPa wind anomaly (vector), (B) 500 hPa zonal wind anomaly, (C) 850 hPa vorticity anomaly, and (D) steering flow in July–September. Both the dotted areas and shaded areas indicate the correlations that are significant at the 90% confidence level.

TABLE 2 | Correlation/partial correlation coefficients between the SST index and the West Pacific Subtropical high index in different key areas.

Type	Area	Intensity	Ridge position	North boundary location	Western ridge point
Niño3 *−1	−0.52/−0.51	−0.49/−0.49	−0.08/−0.08	−0.40/−0.37	0.04/0.03
West wind drift	−0.15/0.04	−0.10/0.08	−0.08/0.05	−0.02/0.01	−0.16/−0.03

TCs in this area. As shown in **Figure 11D**, the negative Niño3 SST anomaly during January–March generates a cyclonic steering circulation in the vicinity of the Philippine Basin. The anomalous westerly steering flow associated with the cyclonic circulation can weaken the easterly wind on the south of the WPSH. Meanwhile, the northerly steering flow on the east of the cyclonic circulation is conducive to the northward movement of TCs. Therefore, the zonal circulation is weakened and the meridional circulation is strengthened, which is favorable for TC's northward movement along the northerly steering flow rather than moving westwards or turning. As a result, more TCs will influence NEC.

In summary, the negative SSTA in the Niño3 area during January–March can stimulate Gill-type Rossby wave, which can cause atmospheric circulation anomalies that last to the peak season of TC activities. The negative SSTA in the Niño3 area during January–March favors the generation of cyclonic circulations and positive vorticity anomalies in the lower levels in the vicinity of

Philippines during the peak season of TC activities. The anomalous circulation corresponds to an eastward extension of the monsoon trough, facilitating TC genesis in the vicinity of Philippines. In addition, the westerly anomalies associated with the weakened WPSH can weaken the strong easterly wind on the south side of the WPSH, hindering the westward movement of TCs. The cyclonic large-scale steering flow in the vicinity of Philippine Sea further enables the TCs to move northwards along the northerly steering flow on the west of the WPSH.

The upper-level disturbances could propagate downstream along the jet in the mid-high latitudes of the Northern Hemisphere, producing teleconnection wave trains and affecting the atmospheric circulation around the entire Northern Hemisphere (Gong et al., 2006). **Figure 12** shows the distribution of regression coefficients of the 500 hPa height and wave action flux anomalies from July to September against the May–July mean West Wind Drift index. There are anomalous teleconnection wave trains with alternative positive and negative anomalies along the middle

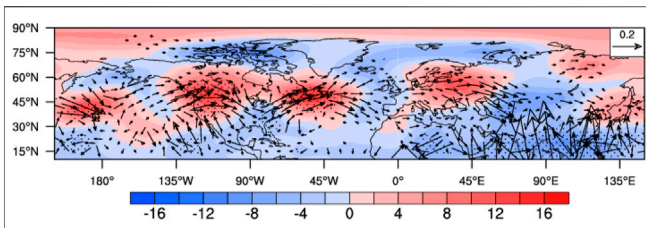


FIGURE 12 | Regression coefficients of West Wind Drift index in May–July with 500 hPa geopotential height anomaly (shading, gpm) and wave activity flux from July to September (vector, m^2/s^2). The dotted areas indicate the coefficients that are significant at the 90% confidence level. Only the part with the regression coefficient of wave activity flux greater than $0.02 \text{ m}^2/\text{s}^2$ is shown.

latitudes of the Northern Hemisphere from the central North Pacific to East Asia. It indicates that the SSTa in the West Wind Drift area may affect the geopotential height and circulations over the Northwest Pacific and East Asia through the teleconnection wave train, and thereby regulating the movement of TCs.

To eliminate the influence of the January–March mean Niño3 index on the atmospheric circulation in the peak season of TC activities, we conduct a partial correlation analysis. **Figure 13A** shows the partial correlation coefficients between the May–July averaged West Wind Drift index and the 500 hPa geopotential height anomaly and 850 hPa wind anomaly in the peak season of TC activities. The

May–July averaged West Wind Drift index shows a negative correlation with the 500 hPa geopotential height in the Northern Hemisphere tropics except a positive correlation to the north of 30°N , with significant anomalies in the Korean Peninsula, Japan, the West Wind Drift area and North America. The partial correlation coefficients between the May–July averaged West Wind Drift index and the 500 hPa zonal wind during the peak season of TC activities are shown in **Figure 13B**. A positive correlation appears in the tropical western Pacific, while a negative correlation appears along the zonal band in 15°N – 30°N . Moreover, a positive correlation occurs in the East Asia to the north of 30°N and the northeastern Pacific. When the SST in the West Wind Drift area is high, the anomalous westerly wind to the north of 15°N is favorable for enabling the TCs to enter the South China Sea. However, the easterly wind anomaly in the zonal band in 15°N – 30°N facilitates northwestward movement of TCs. Moreover, the westerly wind anomaly over East Asia (to the north of 35°N) deflects the northwestward moving TCs and steers the TCs to move eastward. **Figure 13C** shows that the West Wind Drift index and the 850 hPa vorticity anomaly are positively correlated in Taiwan, the Philippines, and the southeastern part of the tropical western north Pacific. When the SSTa in the May–July West Wind Drift area is positive, the positive low-level vorticity anomalies in the western north Pacific during the late stage of the peak season of TC activities facilitate the genesis of turning-type TCs. **Figure 13D** indicates that the positive SSTa in the West Wind Drift area in May–July corresponds to the cyclonic steering flow over the northern Philippines during the peak season of TC activities. The southeasterly

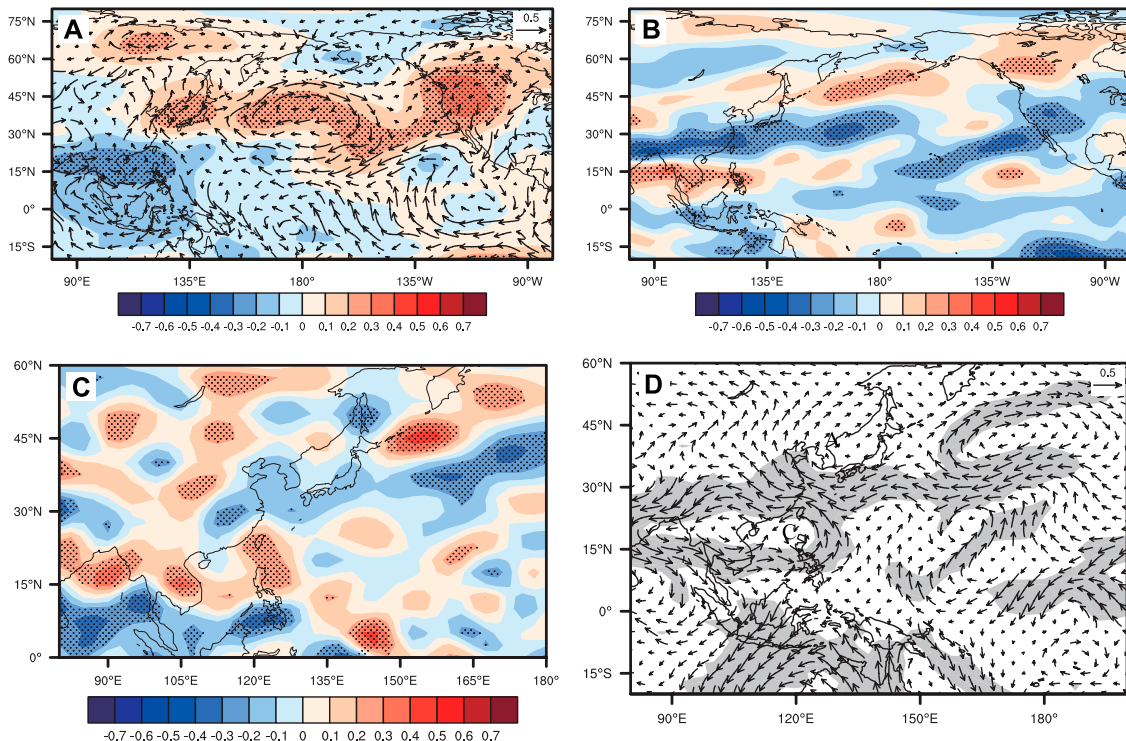
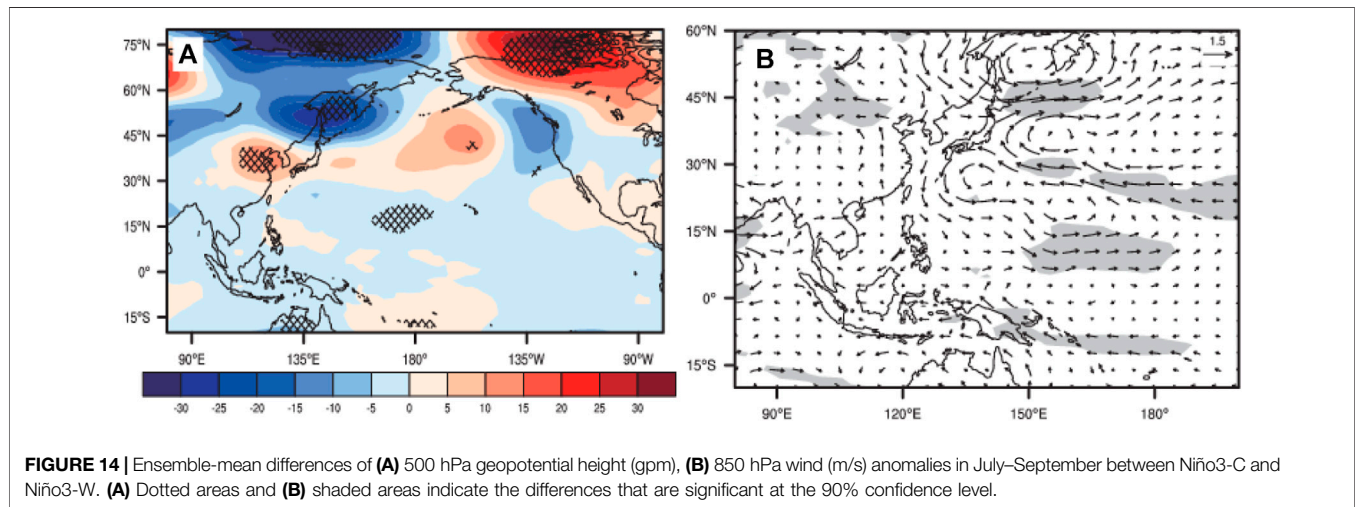


FIGURE 13 | The partial correlation coefficients between the West Wind Drift index in May–July and (A) 500 hPa geopotential height anomaly (shading) and 850 hPa wind anomaly (vector), (B) 500 hPa zonal wind anomaly, (C) 850 hPa vorticity anomaly, and (D) steering flow in July–September. The dotted areas and shaded areas indicate the correlations that are significant at the 90% confidence level.

TABLE 3 | Design of numerical experiments.

Experiments	SSTA condition
Niño3_W	Warm SSTA forcing added to the Niño33 area (5°S–5°N, 150°W–90°W) from January to March
Niño3_C	Cold SSTA forcing added to the Niño33 area (5°S–5°N, 150°W–90°W) from January to March
West wind dirft_W	Warm SSTA forcing added to the West Wind Dirft area (35°N–45°N, 160°E–160°W) from May to July
West wind dirft_C	Cold SSTA forcing added to the West Wind Dirft area (35°N–45°N, 160°E–160°W) from May to July



steering flow on the northeast of the cyclonic circulation steers the TCs generated in the western part of the western north Pacific to move northwestward and eventually make landfall in China. An anticyclonic circulation anomaly appears in the Japan Sea. The southwesterly wind in front of the anticyclonic circulation makes the TCs to turn around and move to the northeast. In summary, the positive SSTA in the West Wind Drift area during May–July is conducive to the formation of the cyclonic circulation anomalies and positive vorticity anomalies over the northern Philippines and Taiwan during the peak season of TC activities, which facilitates TC genesis in this region. In addition, the cyclonic steering flow over the Philippines and the anticyclonic steering flow over Japan Sea steer TCs to move northwestward. Then TCs turn to NEC.

6 NUMERICAL EXPERIMENT VALIDATION ON THE EFFECTS OF SEA SURFACE TEMPERATURE ON ATMOSPHERIC CIRCULATIONS

As discussed above, the SSTA in Niño3 area during January–March influences the geopotential height and circulation in the western Pacific during the peak season of TC activities, and further influences the northward movement of TCs. The SSTA in the West Wind Drift area during May–July results in cyclonic circulation anomalies in the western north Pacific and anticyclonic anomalies in the Japan Sea. The associated steering flow steers TCs to move northwestwards and then northeastward. To verify this proposed mechanism in two key areas, four groups of sensitivity experiments are designed (Table 3).

Each group is continuously integrated for 15 years. To remove the possible influence of the initial condition, we only use the model results of the last 5 years are used to remove the possible influence of the initial condition and spinning up of the model. In the sensitivity experiments, the positive (negative) SSTAs are added to the climatological SST, which is referred to as the warm (cold) phase experiment. Niño3_W (Niño3_C) represents that warm (cold) SSTA forcing is added to the Niño3 area (5°S–5°N, 150°W–90°W) from January to March. The West Wind Dirft_W (West Wind Dirft_C) represents that warm (cold) SSTA forcing is added to the West Wind Dirft area (35°N–45°N, 160°E–160°W) from May to July. Figure 14 shows the differences in the 500 hPa geopotential height and the 850 hPa wind between the cold and warm phase experiments for the Niño3 area in the peak season of TC activities. When the SSTs in January–March are low, a negative anomaly of the 500 hPa geopotential height occurs in the western north Pacific to the south of 30°N. Meanwhile, there is a low-level cyclonic circulation anomaly to the south of Japan and an anticyclonic circulation anomaly to the east of Japan. The simulated low-level wind anomalies are generally consistent with the observed steering flow (Figure 11D). However, compared with the observations, a positive geopotential height anomaly is presented over North China, and the cyclonic circulation in southern Japan is slightly northeastward. Figure 15 shows the differences in 500 hPa geopotential height and the 850 hPa wind between the warm and cold phase experiments in the West Wind Drift area in the peak season of TC activities. As shown in Figure 15, a positive geopotential height anomaly occurs over East Asia. A cyclonic circulation anomaly is presented over the low-level troposphere in the southern part of Japan, and an anticyclonic circulation

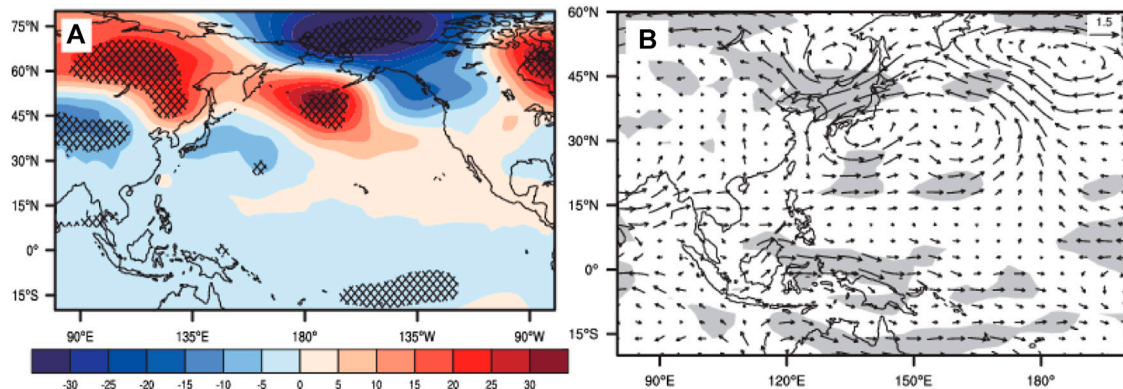


FIGURE 15 | Ensemble-mean differences of (A) 500 hPa geopotential height (gpm), (B) 850 hPa wind (m/s) anomalies in July–September between West Wind Drift_W and West Wind Drift_C. Dotted areas and shaded areas indicate the differences that are significant at the 90% confidence level.

anomaly appears over East Asia. The geopotential height over the western north Pacific and East Asia are in anti-phase, and the anomalous configuration of the cyclonic-anticyclonic circulation anomaly is generally consistent with the observation (Figures 13A,D). However, the locations of the cyclonic circulation in the southern part of Japan and the anticyclonic circulation over East Asia are slightly northeastward than the observation.

Overall, the numerical experiments have generally reproduced the low geopotential height in the middle troposphere over the western north Pacific and the cyclonic circulation anomaly in the lower troposphere during the peak season of TC activities when the SSTA is negative in the Niño3 area in January–March. Moreover, the results well reproduce, the observed anti-phase of geopotential height over the western north Pacific and East Asia during the peak season of TC activities when the SSTA is positive in the West Wind Drift area in May–July. Therefore, the numerical experiments have well confirmed the proposed mechanism.

7 DISCUSSION AND CONCLUSION

A machine learning method is used in this study to objectively classify the selected northward-moving TCs that can influence NEC into eastern-track type and turning type. Then, the possible influences of SST on TC tracks are discussed. In July–September between 1949 and 2019, 81 TCs affecting NEC are identified. For the eastern-track type TCs, the TC induced precipitation in NEC gradually decreases from east to west. Differently, for the turning type TCs the TC induced precipitation in NEC gradually decreases from south to north, which means the southern NEC is more influenced by TCs (i.e., Liaoning).

Notable interannual variabilities are found in the number of TCs and the days with TC influencing NEC. The genesis location of the eastern-track type TCs is relatively southeastward. The genesis location of the turning type TCs is more northward, and the influence time is longer. The interannual variability has a close relationship with the Pacific SST. For the eastern-track type TCs, negative SSTA in the tropical central-eastern Pacific Ocean during

January–March is conducive to development of anti-cyclonic circulation anomalies by stimulating Gill-type Rossby wave. The southerly wind on the west of the anticyclonic circulation transports warm air to the subtropical western north Pacific and weakens the atmospheric stability there. Additionally, the southerly wind can decelerate the trade wind and the warming up of SST in the subtropical western north Pacific. The SST warming and the weakened atmospheric stability favor the convection in the tropical eastern Northwest Pacific, which then further emanates a cyclonic circulation over the western Northwest Pacific. The cyclonic circulation can further sustain and expand to Northeast Asia from July to September and facilitate the TC genesis in that area. Also, the associated westerly wind anomalies in the tropical western Pacific can weaken the southeasterly wind on the south of the WPSH, which is conducive to the northward movement of TCs along the northerly steering flow to the north of the subtropical high. For the turning type TCs, the positive SSTA in the West Wind Drift area in May–July induces positive vorticity anomalies in the northern Philippines and Taiwan from late July to September. The associated cyclonic steering flow over the Philippines and the anticyclonic steering flow over the Japan Sea steer TCs to move northwestward and then turn to northeast, which is favorable for the genesis of the turning type TCs.

The numerical experiments have successfully reproduced the negative SSTA in the Niño3 area in January–March, the low geopotential height in the middle troposphere over the western north Pacific during the peak season of TC activities, and the cyclonic circulation anomaly in the lower troposphere. Moreover, the simulation results have well reproduced the positive SSTA in May–July in the West Wind Drift area. In addition, the observed anti-phase of geopotential height over the Northwest Pacific and East Asia during the peak season of TC activities is also reproduced. The numerical experiments can well confirm the proposed mechanism.

Previous studies have shown that the sea ice out of the tropics (Fan, 2007; Gao Q. Q. et al., 2017; Sato et al., 2018) and the snow cover on the Tibetan Plateau (Lian et al., 2005; Xie and Yan, 2007) also have influences on TC activities over the Northwest Pacific. Their effects will be analyzed in our future studies. In this study,

the influence of SST in different sea areas on the circulation is discussed. But, the year with the simultaneous occurrence of different types of northward-moving TC is not discussed, which will be the focus of our subsequent research.

DATA AVAILABILITY STATEMENT

Publicly available datasets were analyzed in this study. This data can be found here: NCEP/NCAR reanalysis are provided by NOAA/OAR/ESRLPSL, Boulder, Colorado, United States, from their web site at <https://psl.noaa.gov/data/gridded/data.ncep.reanalysis.pressure>. The HadISST data are provided by the Met Office Hadley Centre, from their web site at <https://www.metoffice.gov.uk/hadobs/hadisst/data/download.html>. The tropical cyclones data are provided by the Shanghai Typhoon Research Institute of the China Meteorological Administration, from their web site at https://tcdata.typhoon.org.cn/zjljsjj_zlhq.html.

REFERENCES

- Chan, J. C. L. (2000). Tropical Cyclone Activity over the Western North Pacific Associated with El Niño and La Niña Events. *J. Clim.* 13 (16), 2960–2972. doi:10.1175/1520-0442(2000)013<20.CO;2>10.1175/1520-0442(2000)013<2960:tcaotw>2.0.co;2
- Chen, G. H., and Huang, R. H. (2006b). Research on Climatological Problems of Tropical Cyclone and Typhoon Activity in Western North Pacific. *Adv. Earth Sci.* 21 (6), 610–616. doi:10.3321/j.issn:1001-8166.2006.06.008
- Chen, G. H., and Huang, R. H. (2006a). The Effect of Warm Pool Thermal States on Tropical Cyclone in West Northwest Pacific. *J. Trop. Meteorol.* 22 (6), 527–532. doi:10.3969/j.issn.1004-4965.2006.06.002
- Chen, T.-C., Wang, S.-Y., and Yen, M.-C. (2006). Interannual Variation of the Tropical Cyclone Activity over the Western North Pacific. *J. Clim.* 19 (21), 5709–5720. doi:10.1175/JCLI3934.1
- Chen, T.-C., Weng, S.-P., Yamazaki, N., and Kiehne, S. (1998). Interannual Variation in the Tropical Cyclone Formation over the Western North Pacific. *Mon. Wea. Rev.* 126 (4), 1080–1090. doi:10.1175/1520-0493(1998)126<1080:ivittc>2.0.co;2
- Cheung, K. K. W., and Chan, J. C. L. (2010). Ensemble Forecasting of Tropical Cyclone Motion Using a Barotropic Model. Part I: Perturbations of the Environment. *Mon. Weather Rev.* 127 (6), 2617–2640. doi:10.1175/1520-0493(1999)127<20.CO;2>
- Fan, K. (2007). North Pacific Sea Ice Cover, a Predictor for the Western North Pacific Typhoon Frequency? *Sci. China Ser. D.* 50 (8), 1251–1257. doi:10.1007/s11430-007-0076-y
- Fang, Y., Chen, H., Lin, Y., Zhao, C., and Zhou, F. (2020). Classification of Northeast China Cold Vortex Activity Paths in Early Summer Based on K-Means Clustering and Their Climate Impact. *Adv. Atmos. Sci.* 38 (3), 400–412. doi:10.1007/s00376-020-0118-3
- Feng, T., Huang, R. H., Chen, G. H., Wu, L., Huang, P., and Wang, L. (2013). Progress in Recent Climatological Research on Tropical Cyclone Activity over the Western North Pacific. *Chin. J. Atmos. Sci.* 38 (3), 400–412. doi:10.3878/j.issn.1006-9895.2012.12307
- Gao, J. Y., Zhang, X. Z., and You, L. J. (2008). Anomalous Western North Pacific Monsoon Trough and Tropical Cyclone Activities. *Acta. Oceanol. Sin.* 30 (3), 35–47. doi:10.3321/j.issn:0253-4193.2008.03.005
- Gao, Q. Q., Wu, H. M., Zhu, T. M., Xu, C. S., and Cao, B. (2017). Characteristics of Winter-Spring Arctic Sea-Ice and its Relationship with Tropical Cyclone in the Northwest Pacific. *Chin. J. Polar Res.* 29 (4), 506–512. doi:10.13679/j.jdyj.2017.4.506
- Gao, S. Y., Zhao, T. T., Song, L. L., Meng, Z. X., Luo, J. X., Xu, L. L., et al. (2017). Study of Northward Moving Tropical Cyclones in 1945–2015. *Meteor. Sci. Technol.* 45 (2), 313–323. doi:10.19517/j.1671-6345.20160229
- Gill, A. E. (1980). Some Simple Solutions for Heat-Induced Tropical Circulation. *Q. J. R. Metall. Soc.* 106 (449), 447–462. doi:10.1002/qj.49710644905
- Gong, Y. F., He, J. H., Duan, T. Y., and Pan, P. (2006). Numerical Experiment on the Influences of Minus-SSTA over Mid-latitude Northern Pacific on the Subtropical Anticyclone. *J. Trop. Meteorol.* 22 (4), 386–392. doi:10.3969/j.issn.1004-4965.2006.04.011
- Guo, Y. P., and Tan, Z. M. (2021). Influence of Different ENSO Types on Tropical Cyclone Rapid Intensification over the Western North Pacific. *JGR Atmos.* 126 (11), 033059. doi:10.1029/2020JD033059
- Ha, K.-J., Yoon, S.-J., Yun, K.-S., Kug, J.-S., Jang, Y.-S., and Chan, J. C. L. (2012). Dependency of Typhoon Intensity and Genesis Locations on El Niño Phase and SST Shift over the Western North Pacific. *Theor. Appl. Climatol.* 109 (3), 383–395. doi:10.1007/s00704-012-0588-z
- Ha, Y., Zhong, Z., Yang, X., and Sun, Y. (2015). Contribution of East Indian Ocean SSTA to Western North Pacific Tropical Cyclone Activity under El Niño/La Niña Conditions. *Int. J. Climatol.* 35 (4), 506–519. doi:10.1002/joc.3997
- Holland, G. J. (1993). *Tropical Cyclone Motion. Global Guide to Tropical Cyclone Forecasting. Document WMO/TD 560, Tropical Cyclone Programme Rep.* Geneva Switzerland: World Meteorological Organization Tech.
- Huang, F., and Xu, S. B. (2009). Characteristics of Super Typhoon Activity over Western North Pacific and Its Relationship with ENSO. *Periodical ocean Univ. China* 39 (5), 883–888. doi:10.3969/j.issn.1672-5174.2009.05.009
- Huang, G., Qu, X., and Hu, K. (2011). The Impact of the Tropical Indian Ocean on South Asian High in Boreal Summer. *Adv. Atmos. Sci.* 28 (2), 421–432. doi:10.1007/s00376-010-9224-y
- Huang, L. W., Wu, G. X., and Yu, R. C. (2005). The Effects of Mesoscale Air-Sea Interaction on Heavy Rain in Two Typhoon Progresses. *Acta. Meteorol. Sin.* 63 (4), 455–467. doi:10.3321/j.issn:0577-6619.2005.04.007
- Huang, R. H., and Chen, G. H. (2007). Research on Interannual Variations of Tracks of Tropical Cyclones over Northwest Pacific and Their Physical Mechanism. *Acta. Meteorol. Sin.* 65 (5), 683–694. doi:10.3321/j.issn:0577-6619.2007.05.004
- Huang, R. H., Huangfu, J. L., Liu, Y., Feng, T., Wu, L., Chen, J. L., et al. (2016). Progress in Recent Research on the Processes and Physical Mechanisms Involved in the Influence of the Western Pacific Warm Pool on the Monsoon Trough and Tropical Cyclone Activity over the Western North Pacific. *Chin. J. Atmos. Sci.* 40 (5), 877–896. doi:10.3878/j.issn.1006-9895.1512.15251
- Huang, R. H., and Wang, L. (2010). Interannual Variation of the Landfalling Locations of Typhoons in China and its Association with the Summer East Asia/Pacific Pattern Teleconnection. *Chin. J. Atmos. Sci.* 34 (5), 853–864. doi:10.3878/j.issn.1006-9895.2010.05.01
- Huo, L. W., Guo, P. W., and Zhang, F. Y. (2016). Impact of Summer Tropical Atlantic SST Anomaly on Western North Pacific Tropical Cyclone Genesis. *Trans. Atmos. Sci.* 39 (1), 55–63. doi:10.13878/j.cnki.dqkxxb.20150403002
- Jin, R. H., Gao, S. Z., Gu, H., and Liu, Z. K. (2006). An Analysis on Characteristics of Landing and Going Northward Typhoons and its Causes during 1975–2005. *Meteor. Mon.* 32 (7), 33–39. doi:10.7519/j.issn.1000-0526.2006.7.005

AUTHOR CONTRIBUTIONS

YY and YF conceived the study and wrote the article. CZ and ZG provided critical feedback. Other authors helped the data analysis. All authors contributed to the article and approved the submitted version.

FUNDING

This work was jointly supported by the National Natural Science Foundation of China (Grant No. 42005037); Special Project of Innovative Development, CMA (CXFZ2021J022 and CXFZ2021Z011); Liaoning Provincial Natural Science Foundation Project (Ph.D. Start-up Research Fund 2019-BS214); and Research Project of the Institute of Atmospheric Environment, CMA (2020SYIAE08 and 2021SYIAEKFMS09).

- Kalnay, E., Kanamitsu, M., Kistler, R., Collins, W., Deaven, D., and Gandin, L. (1996). The NCEP/NCAR 40-Year Reanalysis Project. *B. Am. Meteorol. Soc.* 77 (3), 437–472. doi:10.1175/1520-0477(1996)077<0437:tnyrp>2.0.co;2
- Kim, H. M., Webster, P. J., and Curry, J. A. (2011). Modulation of North Pacific Tropical Cyclone Activity by Three Phases of ENSO. *J. Clim.* 24 (6), 1839–1849. doi:10.1175/2010JCLI3939.1
- Lander, M. A. (1994). An Exploratory Analysis of the Relationship between Tropical Storm Formation in the Western North Pacific and ENSO. *Mon. Weather Rev.* 122 (4), 333–360. doi:10.1175/1520-0493(1994)122<0636:aeotr>2.0.co;2
- Lian, X., Yan, T., Pietrafesa, L., Karl, T., and Xu, X. (2005). Relationship between Western North Pacific Typhoon Activity and Tibetan Plateau Winter and Spring Snow Cover. *Geophys. Res. Lett.* 32. doi:10.1029/2005GL023237
- Liang, J., and Chen, L. S. (2005). Motion and Intensity and Impact Characteristics of Tropical Cyclone Affecting the Liaodong Peninsula. *J. Trop. Meteorol.* 21 (4), 410–419. doi:10.3969/j.issn.1004-4965.2005.04.009
- Lonfat, M., Rogers, R., Marchok, T., and Marks, F. D. (2007). A Parametric Model for Predicting Hurricane Rainfall. *Mon. Weather Rev.* 135 (9), 3086–3097. doi:10.1175/MWR3433.1
- Lu, X., Yu, H., Ying, M., Zhao, B., Zhang, S., Lin, L., et al. (2021). Western North Pacific Tropical Cyclone Database Created by the China Meteorological Administration. *Adv. Atmos. Sci.* 38 (4). doi:10.1007/s00376-020-02111-7
- Molinari, J., Moore, P., and Idone, V. (1999). Convective Structure of Hurricanes as Revealed by Lightning Locations. *Mon. Weather Rev.* 127 (4), 520–534. doi:10.1175/1520-0493(1999)127<0520:CSOHR>2.0.CO;2
- Mueller, K. J., Demaria, M., Knaff, J., Kossin, J. P., and Haar, T. V. (2006). Objective Estimation of Tropical Cyclone Wind Structure from Infrared Satellite Data. *Weather Forecast.* 21 (6), 990–1005. doi:10.1175/WAF955.1
- Nakamura, J., Lall, U., Kushnir, Y., and Camargo, S. J. (2009). Classifying North Atlantic Tropical Cyclone Tracks by Mass Moments. *J. Clim.* 22 (20), 5481–5494. doi:10.1175/2009JCLI2828.1
- Peng, Y. H., Yi, D. J., Wang, T., Wang, S., and Liu, B. (2019). Clustering Analysis of Typhoon Track in the North-west Pacific Ocean. *Mar. Forecasts* 36 (5), 63–70. doi:10.11737/j.issn.1003-0239.2019.05.008
- Rayner, N. A., Parker, D. E., Horton, E. B., Folland, C. K., Alexander, L. V., Rowell, D. P., et al. (2003). Global Analyses of Sea Surface Temperature, Sea Ice, and Night Marine Air Temperature since the Late Nineteenth Century. *J. Geophys. Res.-Atmos.* 108 (D14), D14. doi:10.1029/2002JD002670
- Sato, K., Inoue, J., Yamazaki, A., Kim, J. H., Makshtas, A., Kustov, V., et al. (2018). Impact on Predictability of Tropical and Mid-latitude Cyclones by Extra Arctic Observations. *Sci. Rep.* 8 (1). doi:10.1038/s41598-018-30594-4
- Tao, L., and Cheng, S. C. (2012). Impact of Indian Ocean Basin Warming and ENSO on Tropical Cyclone Activities over the Western Pacific. *Chin. J. Atmos. Sci.* 36 (6), 1223–1235. doi:10.3878/j.issn.1006-9895.2012.12031
- Wang, B., and Chan, J. C. L. (2002). How Strong ENSO Events Affect Tropical Storm Activity over the Western North Pacific. *J. Clim.* 15 (13), 1643–1658. doi:10.1175/1520-0442(2002)015<1643:hseat>2.0.co;2
- Wang, B., Chen, G., and Liu, F. (2019). Diversity of the Madden-Julian Oscillation. *Sci. Adv.* 5 (7), 1–8. doi:10.1126/sciadv.aax0220
- Wang, C., Weisberg, R. H., and Virmani, J. I. (1999). Western Pacific Interannual Variability Associated with the El Niño Southern Oscillation. *J. Geophys. Res.-Ocean.* 104 (C3), 5131–5149. doi:10.1029/1998JC900090
- Wang, H., Ding, Y. H., and He, J. H. (2006). Influence of Western North Pacific Summer Monsoon Changes on Typhoon Genesis. *Acta Meteorol. Sin.* 64 (3), 345–356. doi:10.3321/j.issn:0577-6619.2006.03.009
- Wang, X. P., and Liang, J. (2006). Some Climatic Features of Tropical Cyclones Influencing Northern China for Recent 52 Years. *Meteor. Mon.* 32 (10), 76–80. doi:10.3969/j.issn.1000-0526.2006.10.012
- Ward, J. H. (1963). Hierarchical Grouping to Optimize Objective Function. *J. Am. Stat. Assoc.* 69, 236–244. doi:10.1080/01621459.1963.10500845
- Wu, G., and Lau, N. C. (1992). A GCM Simulation of the Relationship between Tropical-Storm Formation and ENSO. *Mon. Weather Rev.* 120 (6), 958. doi:10.1175/1520-0493(1992)120<0958:agsotr>2.0.co;2
- Xie, L., and Yan, T. (2007). West North Pacific Typhoon Track Patterns and Their Potential Connection to Tibetan Plateau Snow Cover. *Nat. Hazards.* 42 (2), 317–333. doi:10.1007/s11069-006-9087-9
- Yamasaki, M. (2007). Numerical Experiment of Tropical Cyclone Formation in the Intertropical Convergence Zone. *J. Meteorol. Soc. Jan.* 67 (4), 529–540. doi:10.2151/jmsj1965.67.4_529
- Ying, M., Zhang, W., Yu, H., Lu, X., Feng, J., Fan, Y., et al. (2014). An Overview of the China Meteorological Administration Tropical Cyclone Database. *Atmos. Ocean. Tech.* 31 (2), 287–301. doi:10.1175/JTECH-D-12-00119.1
- Yu, J., Li, T., Tan, Z., and Zhu, Z. (2016). Effects of Tropical North Atlantic SST on Tropical Cyclone Genesis in the Western North Pacific. *Clim. Dynam.* 46 (3–4), 1–13. doi:10.1007/s00382-015-2618-x
- Yuan, J. P., and Cao, J. (2013). North Indian Ocean Tropical Cyclone Activities Influenced by the Indian Ocean Dipole Mode. *Sci. China Earth Sci.* 56, 855–865. doi:10.1007/s11430-012-4559-0
- Zhan, R., Wang, Y., and Lei, X. (2011a). Contributions of ENSO and East Indian Ocean SSTA to the Interannual Variability of Northwest Pacific Tropical Cyclone Frequency. *J. Clim.* 24 (2), 509–521. doi:10.1175/2010JCLI3808.1
- Zhan, R., Wang, Y., and Wu, C.-C. (2011b). Impact of SSTA in the East Indian Ocean on the Frequency of Northwest Pacific Tropical Cyclones: A Regional Atmospheric Model Study. *J. Clim.* 24 (23), 6227–6242. doi:10.1175/JCLI-D-10-05014.1
- Zhan, R., Wang, Y., and Ying, M. (2012). Seasonal Forecasts of Tropical Cyclone Activity over the Western North Pacific: a Review. *Trop. Cyclone Res. Rev.* 1 (3), 307–324. doi:10.6057/2012TCRR03.07
- Zheng, Y. Q., Yu, J. H., Wu, Q. S., Lin, J. G., and Gong, Z. B. (2013). K-means Clustering Method for Classification of the Northwestern Pacific Tropical Cyclone Tracks. *J. Trop. Meteorol.* 29 (04), 607–615. doi:10.3969/j.issn.1004-4965.2013.04.009
- Zhou, X. S., Yang, Y., Yang, S., and Chen, J. Y. (2007). Climatic Characteristics of North-Going Tropical Cyclone. *J. Meteor. Environ.* 23 (6), 1–5. doi:10.3969/j.issn.1673-503X.2007.06.001
- Zuki, Z. M., and Lupo, A. R. (2008). Interannual Variability of Tropical Cyclone Activity in the Southern South China Sea. *J. Geophys. Res.-Atmos.* 113 (D6). doi:10.1029/2007jd009218

Conflict of Interest: The authors declare that the research was conducted in the absence of any commercial or financial relationships that could be construed as a potential conflict of interest.

Publisher's Note: All claims expressed in this article are solely those of the authors and do not necessarily represent those of their affiliated organizations, or those of the publisher, the editors and the reviewers. Any product that may be evaluated in this article, or claim that may be made by its manufacturer, is not guaranteed or endorsed by the publisher.

Copyright © 2022 Yu, Fang, Zhao, Lin, Lin, Gong and Li. This is an open-access article distributed under the terms of the Creative Commons Attribution License (CC BY). The use, distribution or reproduction in other forums is permitted, provided the original author(s) and the copyright owner(s) are credited and that the original publication in this journal is cited, in accordance with accepted academic practice. No use, distribution or reproduction is permitted which does not comply with these terms.



OPEN ACCESS

EDITED BY

Yihong Duan,
Chinese Academy of Meteorological
Sciences, China

REVIEWED BY

Jinjie Song,
Chinese Academy of Meteorological
Sciences, China
Jingliang Huangfu,
Institute of Atmospheric Physics (CAS),
China

*CORRESPONDENCE

Qinglan Li,
ql.li@siat.ac.cn

SPECIALTY SECTION

This article was submitted to
Atmospheric Science,
a section of the journal
Frontiers in Earth Science

RECEIVED 30 April 2022

ACCEPTED 14 July 2022

PUBLISHED 11 August 2022

CITATION

Li G, Li Q, Zhao W, Zhou G, Qian Q,
Qian C and He L (2022), Enhanced
understanding of changes in tropical
cyclones' landfall frequency over
mainland China.
Front. Earth Sci. 10:932843.
doi: 10.3389/feart.2022.932843

COPYRIGHT

© 2022 Li, Li, Zhao, Zhou, Qian, Qian
and He. This is an open-access article
distributed under the terms of the
[Creative Commons Attribution License
\(CC BY\)](https://creativecommons.org/licenses/by/4.0/). The use, distribution or
reproduction in other forums is
permitted, provided the original
author(s) and the copyright owner(s) are
credited and that the original
publication in this journal is cited, in
accordance with accepted academic
practice. No use, distribution or
reproduction is permitted which does
not comply with these terms.

Enhanced understanding of changes in tropical cyclones' landfall frequency over mainland China

Guangxin Li^{1,2}, Qinglan Li^{1*}, Wei Zhao¹, Guanbo Zhou³,
Qifeng Qian³, Chuanhai Qian³ and Lunkai He^{1,2}

¹Shenzhen Institute of Advanced Technology, Chinese Academy of Sciences, Shenzhen, China,

²University of Chinese Academy of Sciences, Beijing, China, ³National Meteorological Center, Beijing, China

The climatological characteristics and interannual variations of tropical cyclones (TCs) making landfall in mainland China during the peak TC seasons (July–October) from 1980 to 2020 are examined using the China Meteorological Administration (CMA) best-track dataset. There were 270 TCs landfalling in mainland China during the study period, with 226 TCs landfalling in South China (SC) and 44 TCs landfalling in East China (EC). During 1980–2020, the number of TCs affecting mainland China gradually decreased, although the trend is not significant. The number of TCs impacting SC is experiencing a significant decrease, while the number of TC affecting EC is stable. Based on the change-point analysis, the TC landfall frequency in mainland China and SC incurred significant decreases in 1995/1996 and 1996/1997, respectively. The significant reduction in the number of landfalling TCs over SC and the insignificant reduction in the TC landfall frequency over mainland China are mainly due to the great reduction in the TC formation frequency over the western North Pacific (WNP). Meanwhile, the yearly mean of TCs' landfalling latitudes is moving northward slightly, possibly linked to the slight poleward shift of their genesis locations. A large area of negative anomalies in the lower-tropospheric absolute vorticity and positive variations in the vertical wind shear (VWS) over the tropical WNP are possibly responsible for the reduction in TC genesis over the WNP. Moreover, the apparent opposite anomalies of the two variables over the region north of 20°N and south of 20°N might contribute to the slight poleward shift of genesis locations of landfalling TCs during the 41 years. The variations in the large-scale steering flow are favorable for more TCs moving northwestward and making landfall in EC than before. Meanwhile, the decrease in TC landfall frequency over mainland China is found to be significantly correlated to the pronounced warming over the tropical Indian Ocean.

KEYWORDS

tropical cyclone, landfall frequency, mainland China, South China, East China

Introduction

Landfalling tropical cyclones (TCs) bring enormous devastation to people and property in coastal areas (Liu et al., 2020; Wang and Toumi, 2021). China is one of the countries most severely affected by TCs in the world, with an average of 9 TCs making landfall every year (Yin et al., 2010; Dong et al., 2015). The historical data for the 2005–2016 period show that TCs affect 36.7 million people annually in China, leading to a mean annual direct economic loss of 69.5 billion Yuan and 254 deaths (Wang et al., 2019). The socioeconomic losses caused by TCs might become more and more pronounced due to recent population growth and economic development in the coastal region (Wu and Wang, 2004; Li et al., 2017). Therefore, investigating the characteristics and variations in the landfalling TCs' activities and understanding the underlying mechanisms are of great significance.

The frequency of TC landfall is considered to be an essential measure of TC landfall activity in a region, and its changes in China have received considerable attention (Liu and Chan, 2003; Li and Duan, 2010; Chan et al., 2012; Zhang et al., 2012; Lu and Zhao, 2013; Liu and Chan, 2017; Liu and Chan, 2020; Liu et al., 2020). Liu et al. (2020) examined the variability of the number of TCs landfalling over the entire mainland China and reported that there was no apparent trend in the landfall frequency of TCs over mainland China during 1980–2018. More studies have been conducted on the variations of TC landfall frequency in individual regions of China (Liu and Chan, 2003; Li and Duan, 2010; Chan et al., 2012; Zhang et al., 2012; Lu and Zhao, 2013; Liu and Chan, 2017; Liu and Chan, 2020). Liu and Chan (2003) examined the TCs making landfall along the SC coast from 1960 to 1999, and found a large annual variation in the number of landfalling TCs. A strong El Niño event tended to reduce the number of landfalling TCs, while more TC landfalls were found in years associated with La Niña events (Liu and Chan, 2003). Liu and Chan (2020) reanalyzed the interdecadal variations in the frequency of TCs landfalling in SC during the period 1975–2018 and reported that the annual frequency showed a tendency to decrease in 1997 and tended to rise again after 2008, which was closely related to the changes in the number of TCs forming over the WNP and the SCS. Chan et al. (2012) found that the frequency of TCs landing in EC experienced significant variations, with periods ranging from centennial to decadal from 1450 to 1949, which were apparently related to the changes in the planetary-scale atmospheric circulations that went through oscillations on various timescales. Liu and Chan (2017) investigated the changes in TC landfalls in East Asia, and found the TC landfall number in Zhejiang and the Korean Peninsula exhibited upward trends, while the number in Guangdong showed a downward trend during the period 1960–2013 (Liu and Chan, 2017). Previous studies were mainly carried out in specific regions. However, few of them focused on investigating the difference and relationship

between changes in TC landfall frequency in the individual regions of China (Li et al., 2017; Shan and Yu, 2021).

Regarding the background reason for the TCs' landfall frequency changes in different regions of China, Li et al. (2017) reported a noticeable enhancement in TC landfall frequency over EC during the period 1975–2014, which was due to the significant changes in the large-scale steering flow, characterized by a prominent cyclonic circulation centered over southeast China. In contrast, the changes in the landfall frequency of TCs making landfall in SC were less apparent (Li et al., 2017). Shan and Yu (2021) confirmed the increasing trend in landfall frequency of TCs over EC in recent decades, but reported a decreasing trend in the annual TC landfalls in SC. The opposite variations of TC landfalls in the two adjacent regions were further reported to be phenomenally independent (Shan and Yu, 2021). They attributed the variations to the significant changes in the TC genesis induced by the decreased relative vorticity and increased vertical wind shear over the WNP (Shan and Yu, 2021). However, for two adjacent coastal regions in China, it is hard for the variations in TCs' landfalls in EC and SC to be independent. The above studies mainly focus on the changes in the number of TCs making landfall in various regions of China, and rarely on the variations of their landfall positions. Several studies have revealed a poleward shift in TC activity over the WNP in recent decades, including genesis position and location of lifetime maximum intensity. Therefore, it is worth investigating if there is a similar northward migration in TC landfall positions over mainland China.

In addition, much attention has been placed on how climate change affects WNP TC activity (Liu and Chan, 2003; Goh and Chan, 2010; Chan et al., 2012; Liu and Chan, 2013; Mei et al., 2015). Many studies have shown the remote effects of sea surface temperature (SST) variability in the tropical Indian Ocean (TIO) on WNP TC frequency through changes in the East Asian-WNP monsoon circulation and associated atmospheric factors (Du et al., 2011; Zhan et al., 2011; Zhan et al., 2014; Gao et al., 2020). Several recent studies claimed the dominant contribution of tropical North Atlantic (TNA) SST to WNP TC frequency (Gao et al., 2018; Zhang et al., 2018). Despite no connections having been reported between WNP TC frequency and El Niño–Southern Oscillation (ENSO), a strong modulation of ENSO on TC genesis locations has been well documented, with more (fewer) TCs generated in the southeast quadrant of WNP in El Niño (La Niña) years (Wang and Chan, 2002; Camargo and Sobel, 2005). The Pacific decadal oscillation (PDO) has also been shown to be responsible for WNP TC formation (Liu and Chan, 2013). However, few studies have thoroughly explored the comprehensive relationships between the global SST changes, environmental factors, and variations of the TC landfall frequency over mainland China.

Therefore, this study aims to achieve an overview of the characteristics and changes in the landfalling TCs in China. Furthermore, environmental conditions are investigated to explore the reasons contributing to the observed changes in the TCs' landfalls. The factors include SST, potential intensity

(PI), vertical wind shear (VWS), low-level absolute vorticity, mid-tropospheric moisture, and large-scale steering flow, which are considered to be essential conditions influencing TC activity (Gray, 1975; Chan and Gray, 1982; Holland, 1983; Chan, 1985; Emanuel and Nolan, 2004; Camargo et al., 2007; Korty et al., 2012; Yanase et al., 2012; Murakami et al., 2013; Ling et al., 2016; Torn et al., 2018).

The rest of the article is organized as follows. The second section introduces the datasets and methods employed in the study. The third section reveals the characteristics of landfalling TCs over mainland China. The fourth section investigates the changes in the activities of landfalling TCs. The fifth and sixth sections discuss the possible environmental factors and global SST variations contributing to such changes. A summary is given in the final section.

Data and methods

Data

TCs that made landfall over mainland China, including Hainan Island, are investigated in this study. The TC best-track data for these TCs are obtained from the China Meteorological Administration (CMA) (Ying et al., 2014), which includes the latitude and longitude of the TC center, and TC intensity in terms of the maximum sustained wind (MSW) near the TC center over a period of 2 minutes. For the climatic studies related to TCs landfalling in China, the CMA database may be more accurate and complete than other datasets from different administrations, as there are many more *in situ* observations available in CMA (Ying et al., 2014; Shan and Yu, 2021). Genesis is defined as the first position for a particular TC that attains the intensity of tropical depression. The TC's landfall position is defined as the intersection of the TC's tracks with the coastlines, similar to the study of Fudeyasu et al. (2018). Following previous studies (Kim et al., 2008; Li et al., 2017), the territory of China is subdivided into SC and EC by an artificial boundary line along 25°N. As TCs' data are considered more reliable since the introduction of geostationary meteorological satellites in the mid to late 1970s (Kossin et al., 2014), this study focuses on the TCs formed during the peak TC season (July–October) from 1980 to 2020.

The monthly mean reanalysis data of ECMWF Reanalysis v5 (ERA5) at the horizontal resolution of 0.25° × 0.25° from the European Centre for Medium-Range Weather Forecasts (ECMWF) during the period 1980–2020 are used to investigate the large-scale environmental factors surrounding TCs and explore their contributions to the changes in TC activities in this study (Hersbach et al., 2020). The 600-hPa relative humidity is used to represent the mid-tropospheric relative humidity. The sea surface temperature, sea level pressure, temperature, and humidity profiles of the atmosphere are employed to analyze the potential intensity. The wind field is used to calculate the vertical wind shear, absolute vorticity, and

background steering flow. The PDO index, the leading PC of monthly SST anomalies in the North Pacific Ocean, is obtained from <https://psl.noaa.gov/data/climateindices/list/>.

Methods

The PI is a function of environmental conditions that influence the thermodynamic atmosphere-ocean disequilibrium and the TC thermodynamic efficiency, primary sea surface temperatures, and the TC outflow temperatures, and it is the theoretical upper limit of the wind speed of a TC under the current environmental thermodynamic conditions (Emanuel, 1986; Bister and Emanuel, 2002; Gilford et al., 2017). This study explores PI to analyze the thermodynamic environmental reasons for the changes in the TCs' landfall. According to Bister and Emanuel (2002), the computing equation for PI is expressed as follows (equation 1):

$$PI = \alpha \sqrt{\frac{T_s}{T_0} \frac{C_k}{C_D} [CAPE^* - CAPE]} \quad (1)$$

where T_s is SST; T_0 is the outflow temperature; C_k is the exchange coefficient for enthalpy; C_D is the drag coefficient; $CAPE^*$ is the saturation moist static energy at the sea surface; and $CAPE$ is the moist static energy of the free troposphere.

It is well known that some dynamic factors, such as VWS, play an essential role in TC formation and development (Emanuel, 2000; Wang, 2012; Liu and Chan, 2020). This study estimates the VWS by the vector difference of the horizontal winds between 200 hPa and 850 hPa (Gray, 1968). TC movement is primarily determined by the large-scale environmental steering flow (Holland, 1983; Chen et al., 2011). Following Wu and Wang (2004), this study calculates the steering flow as averaged flow between 850 and 300 hPa.

Student's *t* test is applied to estimate the significance of linear trends in TC activity during 1980–2020 and the difference in the environmental variables and TC genesis region between different periods (Park et al., 2014; Liu and Chan, 2020). To detect a regime shift in climate series, the change-point detection method following Pettitt (1979) is employed. The trends and regime shifts with *p*-values less than 0.1 are considered significant. In addition, the correlation between two variables is computed by the Pearson correlation coefficient (Wilks, 2006).

Climatological characteristics of landfalling TCs

During the TC peak seasons of 1980–2020, 270 TCs made landfall in mainland China, of which 171 (63.3%) originated in the WNP, and the rest originated in the South China Sea (SCS). Among the 270 landfalling TCs, 226 TCs (83.7%) affected SC, while 44 TCs (16.3%) hit EC. SC suffered five times as many TCs as EC over the study period. Figures 1A and B show the spatial distribution of the annual mean occurrence frequency of TCs

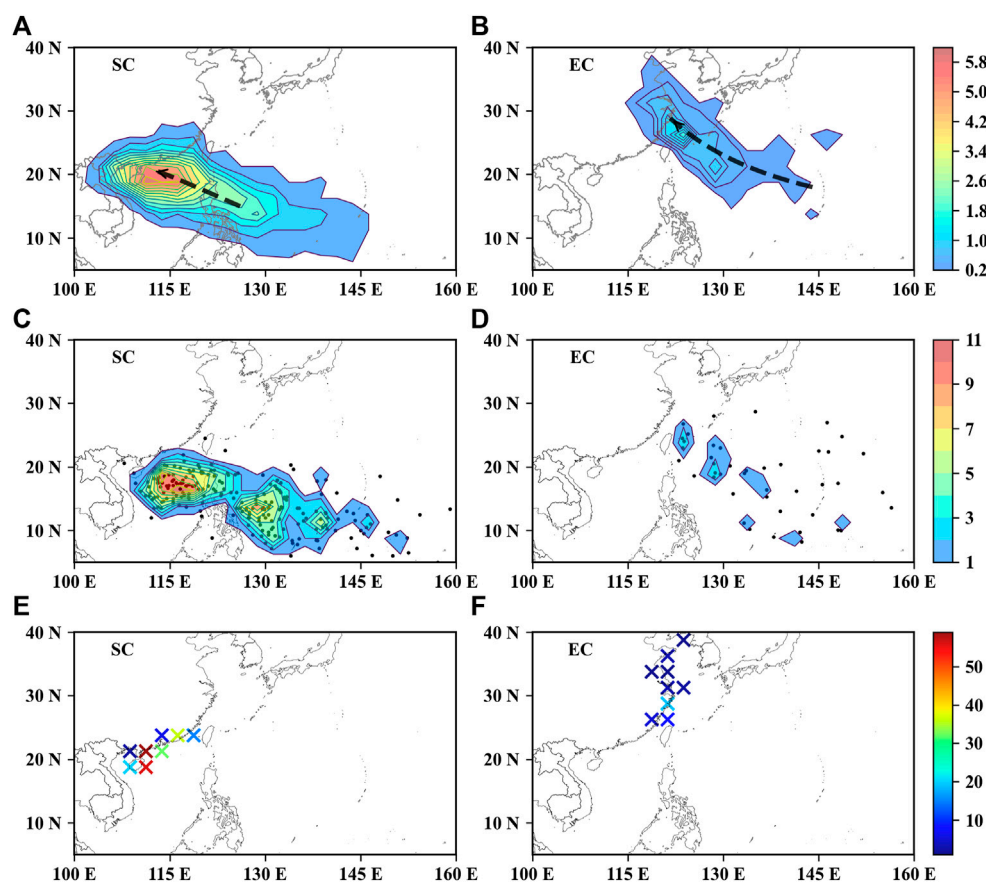


FIGURE 1

Frequency distribution of (A,B) annual mean TC occurrence, (C,D) TC formation, and (E,F) TC landfall over a grid of $2.5^{\circ} \times 2.5^{\circ}$ during the TC peak season (Jul–Oct) from 1980 to 2020. The thick dashed curves with arrows in (A,B) schematically denote the mean regression trajectories of landfalling TCs, and the markers 'x' in (C,D) indicate TC genesis locations. The left column is for TCs landfalling in SC and the right column is for TCs landfalling in EC.

affecting SC and EC during 1980–2020. The frequency is counted at each $2.5^{\circ} \times 2.5^{\circ}$ grid box. As shown in the figure, most of the landfalling TCs in SC originated over the WNP, passed through the Luzon Strait, entered the SCS, and landed on the southern coast of China. The prevailing track of westward-moving TCs is shown in Figure 1A. For the TCs making landfall over the eastern coast of China, the high frequency of occurrence extended from the WNP to east of Taiwan Island and made landfall in EC, indicating a primary northwestward track (Figure 1B).

The TC genesis locations over SC and EC for the 1980–2020 period are depicted in Figures 1C and D. For the TCs making landfall in SC, approximately half of them (43.8%) formed in the northern part of the SCS, and the rest were generated over the WNP (Figure 1C). As shown, most of the observed genesis locations occur in the tropical belt, between 5°N and 20°N . Their frequency distribution exhibits two major centers, in the northern SCS and east of the Philippines. The spatial pattern of the formation frequency (Figure 1C) is similar

to that of the occurrence frequency (Figure 1A). During the study period, the average genesis location of the TCs landfalling in SC is 14.7°N , 126.6°E . In comparison, all TCs landfalling in EC originated in the WNP, and most of them formed in the region of $10^{\circ}\text{N} - 30^{\circ}\text{N}$, $120^{\circ}\text{E} - 160^{\circ}\text{E}$ with a mean value of 18.5°N , 137.2°E (Figure 1D). The mean genesis location of TCs landfalling EC is further north and east than that of TCs landfalling SC. The formation distribution of TCs landfalling in SC (Figure 1C) is more concentrated than that of TCs landfalling in EC (Figure 1D).

The spatial distribution of the TCs' landfall frequency over SC and EC during these 41 years is depicted in Figures 1E and F, respectively. The figures show that the TCs' landfalling locations are distributed unevenly along the China coast. The highest landfalling frequency occurs at the grid with the latitude of $20 - 22.5^{\circ}\text{N}$ and longitude of $110 - 112.5^{\circ}\text{E}$ (denoted simply as: at the grid 21.25°E , 111.25°E ; similar expressions are used hereafter). During the study period, 59 TCs landed at this grid. In SC, the lowest landfalling

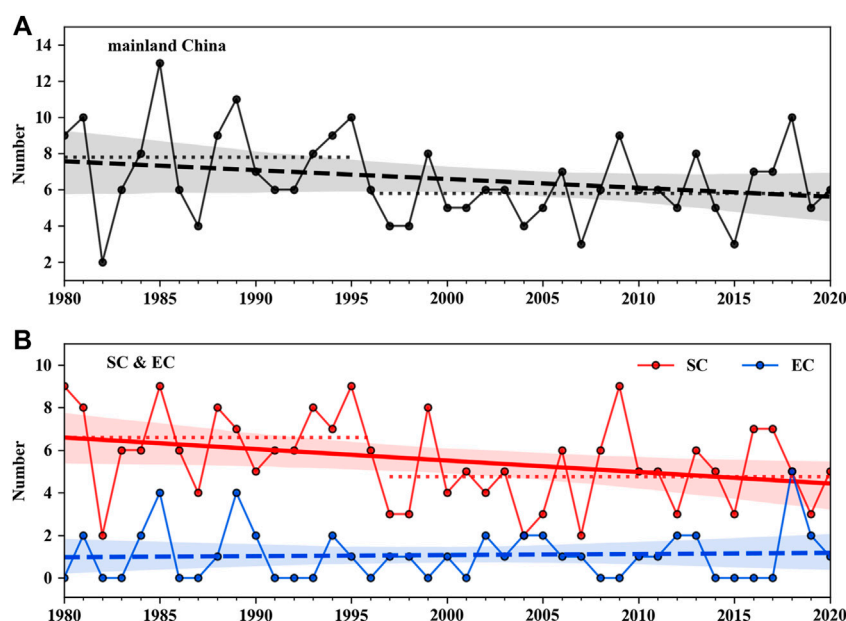


FIGURE 2

The time series and the linear regression fit of the TCs' landfalling frequency over (A) mainland China and (B) SC and EC from 1980 to 2020. The solid (dashed) trend lines represent significant (insignificant) trends at the 90% confidence level by Student's *t* test. Linear trend lines are shown with their 95% two-sided confidence intervals (shaded). The dotted lines indicate the mean landfall frequency over different periods.

TABLE 1 The linear trends and corresponding *p* values for the annual landfall frequency of TCs over mainland China, SC, and EC from 1980 to 2020.

		Mainland China	SC	EC
Landfall frequency	Trend	-0.049	-0.054*	0.005
	<i>p</i> value	0.115	0.045	0.760

Values in boldface with an asterisk denote trends that are statistically significant at the 90% confidence level by Student's *t* test.

frequency is at the grid 21.25°N, 108.75°E, with 2 TCs landfalling during the 41 years. For TCs landfalling in EC, the highest landfalling frequency occurs at the grid 28.75°N, 121.25°E, with 19 TCs landfalling during the study period. In EC, no TC is found landfalling over three grids, which are [36.25°N, 118.75°E], [38.7°N, 118.75°E], and [38.75°N, 121.25°E], respectively.

Changes in the TC activities

TC landfall

The long-term changes in landfall frequency of TCs in mainland China over the 41-year period are depicted in Figure 2 and Table 1. From 1980 to 2020, the annual number of TCs making landfall in mainland China (including SC and EC) presents an annual mean of

6.6, and its time series show a slight downward trend (Figure 2A and Table 1). Out of them, the number of landfalling TCs in EC is stable, while that in SC presents a significant decreasing trend with a rate of -0.054 per year (Figure 2B and Table 1). The annual frequency of TCs making landfall in SC has reduced by 33.8% over the 41 years, which is the main contribution to the decrease of landfalling TCs in mainland China. These results are somewhat different from several previous conclusions (Li et al., 2017; Shan and Yu, 2021), which suggested an increased frequency of TCs making landfall along the eastern coast of China in recent decades. The possible causes for the divergence in TCs' landfall frequency analysis might be the different study periods and the boundary division line for SC and EC used in these studies.

Based on the Pettitt's test results, as presented in Figure 2, it is clearly shown that the frequencies of TC landfall in mainland China and SC were very likely to change significantly in 1995/1996 and 1996/1997, respectively (with a confidence level of 90%). The mean frequency of TC landfalls over mainland China from 1980 to 1995 is 7.8, whereas the mean frequency from 1996 to 2020 is 5.8. That is, the average number of TC landfalls decreased by approximately 2 after 1995. For TCs landfalling over SC, the average numbers for the periods 1980–1996 and 1997–2020 are 6.6 and 4.8, respectively. The difference between the two periods is 2.2. The apparent drop suggests that large-scale climate factors may have a climate regime shift in the late 1990s, which significantly affects the TC activity in China.

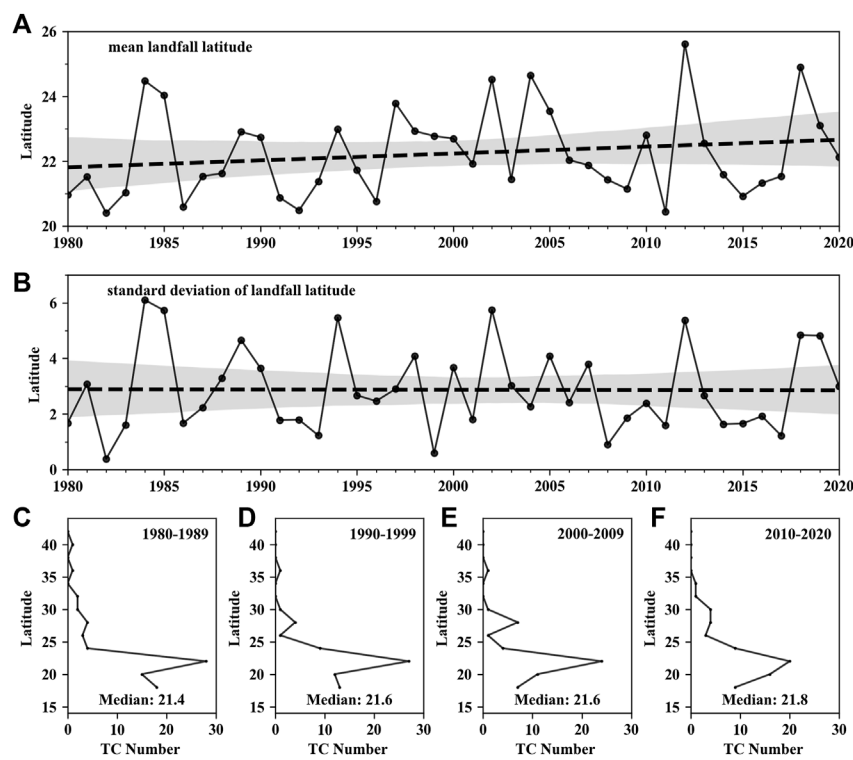


FIGURE 3 The time series and the linear regression fits for (A) the annual mean of TCs' landfalling latitudes and (B) the standard deviation of the yearly TCs' landfalling latitudes over mainland China from 1980 to 2020. The latitudinal distribution of TCs landfalling over mainland China for the periods: (C) 1980–1989, (D) 1990–1999, (E) 2000–2009, and (F) 2010–2020. The medians of the decadal TCs' landfall latitudes are also shown in the corresponding figures.

TABLE 2 The same as Table 1, but for the mean and standard deviation of landfall latitude of TCs over mainland China from 1980 to 2020.

		Mean	Standard deviation
Landfall latitude	Trend	0.021	−0.001
	<i>p</i> value	0.240	0.957

This study further investigates the variation of TCs' landfall locations in terms of the yearly mean of TCs' landfalling latitudes (Figure 3A), the standard deviation (Std) of the yearly TCs' landfalling latitudes (Figure 3B), and the decadal distribution of the TCs' landfalling latitudes over mainland China (Figures 3C–F) from 1980 to 2020. The analysis results are also shown in Table 2. During the study period, the TCs' landfalling latitudes slightly increase (Figure 3A and Table 2), which should be due to the combination of the significant decrease of TC landfalls over SC and unchanged number of TCs affecting EC. As shown in Figures 3B–F, although no obvious changes can be observed in the Std of TCs' landfalling latitude, the latitude range exhibits a decadal decrease during the 41-yr period. The latitudes range for the

period of 1980–1989 is from 18.2 °N to 39.7 °N, while the latitudes range for the period of 2010–2020 is from 18.2 °N to 34.6 °N. Furthermore, the medians of the TCs' landfall latitudes during the 4 decades (Figures 3C–F) also show a tendency to move northward slightly.

TC genesis

Since a TC landfall is generally considered to be directly relevant to its genesis (Wu and Wang, 2004; Camargo and Sobel, 2005; Park et al., 2013; Shan and Yu, 2021), this study investigates the long-term changes in the formation frequency and location of the landfalling TC from 1980 to 2020 (Figures 4 and 5). The trends and the corresponding *p* values are calculated, and the results are tabulated in Table 3. As shown in Figures 4A and B, for the TCs making landfall over mainland China, the annual number of TCs forming in both the WNP and the SCS changed slightly during these 41 years. As discussed in the previous subsection, all the landfalling TCs over EC form in the WNP, and the total number has no trend over the 41-year period (Figures 4C

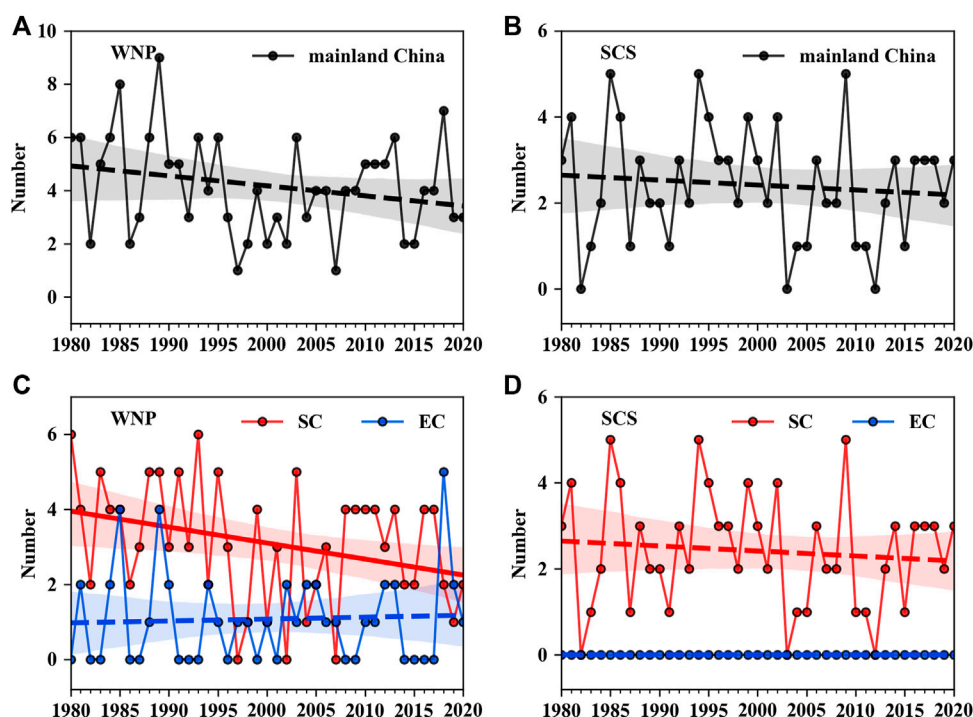


FIGURE 4

The same as Figure 2, but for the annual number of the TCs generated in the WNP (A,C) and SCS (B,D) and made landfall in mainland China, SC, and EC.

and D and Table 3). As mentioned earlier, nearly half of the landfalling TCs over SC come from the WNP, and the rest generate over the SCS. The former show a significant decrease during 1980–2020, with a mean rate of -0.043 per year (Figure 4C and Table 3). The annual genesis number has decreased by 50% over the 41 years (Figure 4C). The latter shows no apparent changes (Figure 4D and Table 3). Thus, the significant reduction in the total number of landfalling TCs over SC during the 41 years results from the corresponding apparent decrease in the number of TCs formed in the WNP. The correlation coefficient between them is 0.76, and this correlation is highly significant ($p < 0.1$). The slight reduction in TC genesis over the WNP (Figure 4A) might also help explain the decrease in the frequency of TC landfalls over mainland China (Figure 2A), although the decline of TC landfall frequency in mainland China is less apparent than those of TCs over SC.

The shift in TCs' genesis locations also has a significant impact on the TCs' landfall activity in the East Asia region (Yonekura et al., 2014; Liu and Chan, 2017). This study further explores the zonal and meridional changes in the TC formation locations. Figures 5A–D are the time series of the annually averaged genesis latitude and longitude of TCs making landfall in mainland China, SC, and EC from 1980 to 2020. The

trends and the corresponding p values for these changes are recorded in Table 4.

Landfalling TCs over mainland China show a slight increment and reduction in their mean genesis latitude and longitude over the 41 years (Figures 5A and B and Table 4). It seems plausible that the increase in genesis latitude of landfalling TCs (Figure 5A) may be one of the reasons for the poleward shift of their landfall positions (Figure 3A). The correlation coefficient between the latitude anomalies of TC landfall and that of TC genesis is 0.6 ($p < 0.1$). From them, the mean genesis latitude of landfalling TCs over SC shows a significant increasing trend, with a rate of 0.041° per year (Figure 5C and Table 4). As shown in Figure 1C, most of the landfalling TCs over SC form in the tropical belt south of 20°N . It indicates that the TC genesis region has a trend away from the equator. Such poleward TC migration is consistent with Studholme et al. (2022), who suggest that more WNP TCs tend to form at higher latitudes, take north-turning tracks, and then occupy a broader range of latitudes. On the other hand, the mean genesis longitude decreases significantly, and the decline rate is -0.133° per year (Figure 5D and Table 4). It suggests that there has been a markedly poleward and westward shift in the genesis region of TCs making landfall over SC during the past 41 years (Figures 5C and D). This might be induced by the

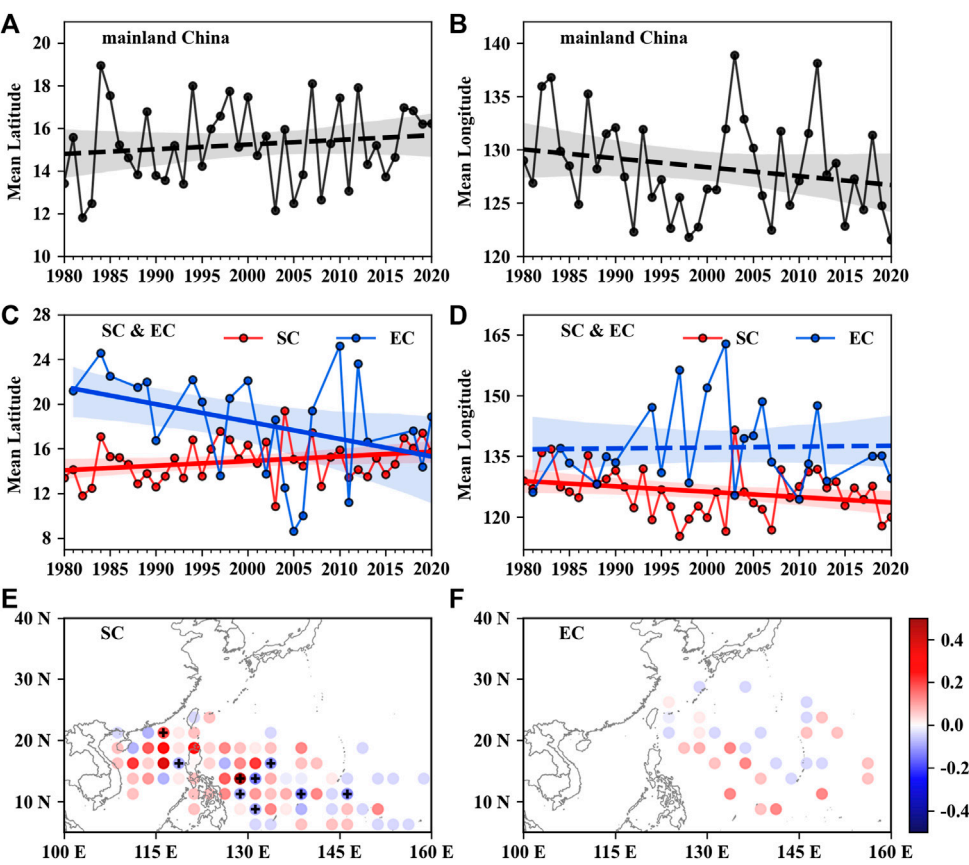


FIGURE 5 The same as Figure 2, but for the annual mean genesis (A,C) latitude and (B,D) longitude for the landfalling TCs over mainland China, SC, and EC. The difference in the genesis frequency for TCs landfalling over (E) SC and (F) EC between 1980–1995 and 1996–2020. The marks ‘+’ indicate where the difference between the two periods is significant at a confidence level of 90%.

TABLE 3 The same as Table 1, but for the number of TCs generated in the SCS and WNP and made landfall over mainland China, SC, and EC from 1980 to 2020.

		Mainland China	SC	EC
SCS TCs	Trend	−0.011	−0.011	nan
	<i>p</i> value	0.523	0.523	nan
WNP TCs	Trend	−0.037	−0.043*	0.005
	<i>p</i> value	0.131	0.044	0.760

Values in boldface with an asterisk denote trends that are statistically significant at the 90% confidence level by Student’s *t* test.

TABLE 4 The same as Table 1, but for the genesis latitude and genesis longitude of TCs over mainland China, SC, and EC from 1980 to 2020.

		Mainland China	SC	EC
Genesis latitude	Trend	0.022	0.041*	−0.156*
	<i>p</i> value	0.383	0.082	0.070
Genesis longitude	Trend	−0.083	−0.133*	0.022
	<i>p</i> value	0.171	0.082	0.908

Values in boldface with an asterisk denote trends that are statistically significant at the 90% confidence level by Student’s *t* test.

significant reduction in the number of TCs forming in the WNP (Figure 4C) and almost no change in the number of TCs forming in the SCS (Figure 4D). In addition, the TCs making landfall in EC tend to generate at a lower latitude significantly (Figure 5C and Table 4), and therefore, these TCs are more likely to land in EC at a lower latitude than before (Figures 3C–F).

As shown in Figure 2, the TC landfall frequency over mainland China experienced a climate shift between 1995 and 1996. We then explore the spatial difference in the TC formation frequency between the two periods: period 1 (1980–1995) and period 2 (1996–2020) (Figures 5E and F). Figure 5E shows that more area (20 grids over the total 26 grids) over the northern SCS experiences an increase in the TCs’ genesis frequency. For the genesis region

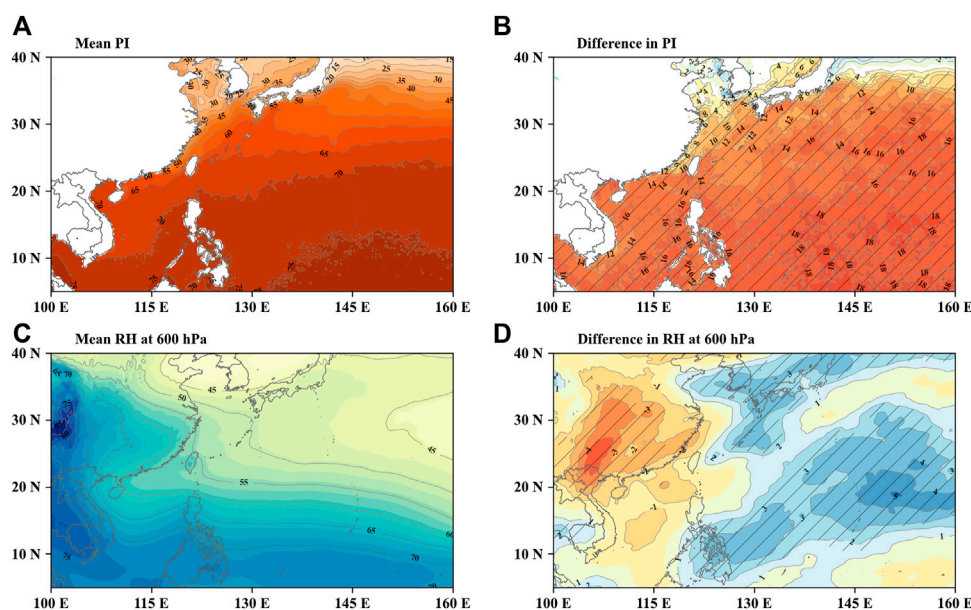


FIGURE 6

The climatological mean from 1980 to 2020 and the difference between 1980–1995 and 1996–2020 for (A,B) PI (m s^{-1}) and (C,D) RH at 600 hPa (%). The stippling indicates where the difference is significant at a confidence level of 90%.

over the WNP south of 20°N , the number of the increasing points (in red) and that of the decreasing points (in blue) are almost the same. However, among those grids for TCs genesis over the WNP (Figure 5E), six points show significant decreasing trends while only one point shows a significant increasing trend. Compared with the anomalies in the SCS, the WNP tends to generate fewer TCs than before. At the same time, a slight increment in the formation frequency of landfalling TCs over EC is observed in the tropical WNP around 10°N (Figure 5F). It indicates that more TCs forming in the tropical zone have opportunities to threaten EC. These results also agree with their long-term temporal changes (Figures 5C and D). Thus, the variation of the TCs' landfalling over mainland China in recent decades is mainly related to the changes in the TCs' genesis. Next, we will discuss the environmental reasons for these variations in detail in the following section.

Environmental factors contributing to changes in TCs' landfalls

The activities of TCs are influenced by several dynamic and thermodynamic parameters, including moist static stability and planetary vorticity (Gray, 1975; Emanuel and Nolan, 2004; Camargo et al., 2007; Kerty et al., 2012; Yanase et al., 2012; Murakami et al., 2013). For TCs' genesis, the low-level vorticity, relative humidity, the magnitude of VWS between 850 and 250 hPa, and PI are reported to be essential (Gray, 1975; Emanuel and Nolan, 2004; Camargo et al., 2007; Kerty et al.,

2012). Large low-level vorticity, weak VWS, high PI, and high mid-tropospheric humidity are favorable for TC formation (Camargo et al., 2007; Yanase et al., 2012). To examine the reasons for the recent changes in TCs' genesis, the mean and difference of the large-scale environments surrounding TCs between 1980–1995 and 1996–2020 are analyzed.

PI is a thermodynamic factor considering the influences of both the SST and moist static instability (Bister and Emanuel, 2002; Yanase et al., 2012). Several studies point out that the changes in SST are strongly similar to that of PI over the WNP in recent years (Park et al., 2013; Zhan and Wang, 2017). So, the variations of SST are not discussed independently in this study, although it is a well-known important thermodynamic factor related to TC genesis and development (Emanuel, 1986; Kerty et al., 2012). Figures 6A and B present the climatological mean PI for the 41 years and the difference in the mean PI between 1980–1995 and 1996–2020. It is found that the PI gradually increases with the decrease of latitude, and it achieves the highest value in the deep tropics, where the water temperature is also the highest (Figure 6A). As shown in Figures 1C and D, the genesis locations of TCs landfalling in SC are distributed over the region closer to the tropics than those of TCs landfalling in EC. In general, higher PI provides more favorable conditions for TC formation (Yanase et al., 2012). It can partly explain that there are more TCs making landfall in SC than those in EC. As shown in Figure 6B, PI increases significantly over the region south of 35°N , covering all the genesis locations of

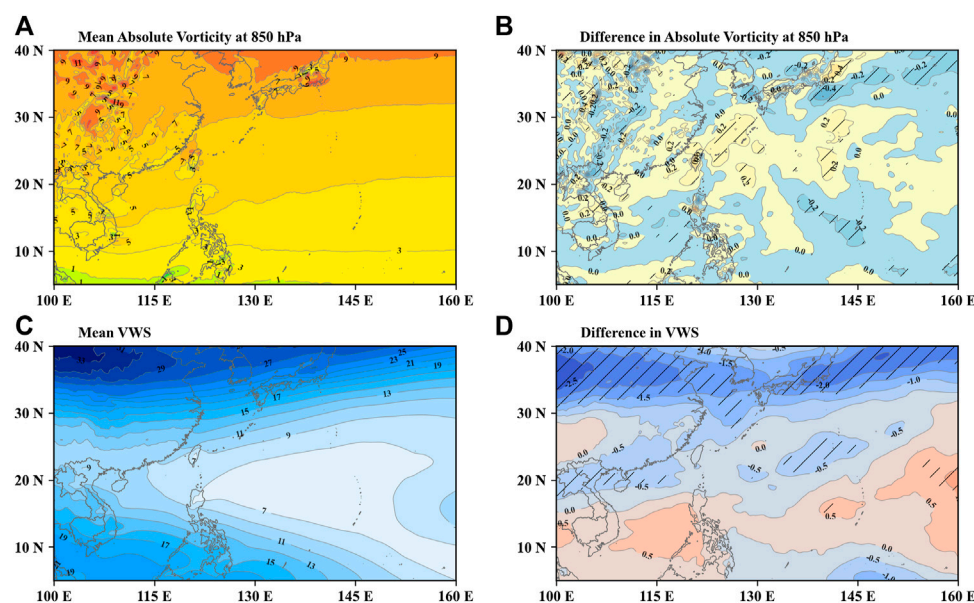


FIGURE 7

The same as Figure 6, but for (A,B) absolute vorticity at 850 hPa (10^{-5} s^{-1}) and (C,D) VWS (m s^{-1}).

TCs making landfall in mainland China (Figures 1C and D). However, the spatial pattern of PI changes (Figure 6B) cannot explain the decline of TC occurrence over the WNP and the difference in frequency between TCs making landfall in SC and EC (Figures 5E and F).

Usually, high relative humidity (RH) in the middle troposphere is favorable for TC genesis by reducing the detrimental effects of convective downdrafts (Gray, 1975; Korty et al., 2012). Figure 6C shows the mean RH at 600 hPa from 1980 to 2020. Similar to the pattern of PI, the middle troposphere RH in the tropical region is generally greater than that in the subtropical region, and it reaches a maximum of 75% in the deep tropics. It may also explain the long-term difference in the frequencies of TCs making landfall in SC and EC. In Figure 6D, a significant increase in the middle troposphere RH is observed over the region of $10^{\circ}\text{N} - 30^{\circ}\text{N}$, $120^{\circ}\text{E} - 160^{\circ}\text{E}$, covering almost all the genesis regions for TCs affecting EC (Figure 1D). Moreover, the midlevel RH decreases slightly over the northern part of the SCS and increases significantly over the area east of the Philippines, which are the two genesis regions for TCs hitting SC (Figure 1C). However, the changing pattern of the midlevel RH cannot explain the genesis changes for TCs making landfall in SC from 1980 to 2020 (Figure 5E), which are relative stability in the TCs genesis number over the SCS and a significant reduction in the WNP. In summary, the variations of thermodynamic factors, PI and midlevel RH, do not contribute clearly to the changes in the genesis of landfalling TCs over mainland China.

Besides thermodynamic factors, TC genesis is also related to dynamic conditions, such as the lower-tropospheric absolute

vorticity and VWS. Many studies stated that the low-level absolute vorticity is necessary for TC genesis, as TCs rarely form within a few degrees of the equator (Gray, 1975; Tippet et al., 2011). Furthermore, most of the cyclogenesis tend to occur around the positive anomaly of absolute vorticity (Gray, 1975; Yanase et al., 2012). Figures 7A and B show the mean absolute vorticity at 850 hPa during the 41 years and the mean absolute vorticity differences between 1980–1995 and 1996–2020. Figure 7A shows that the climatological mean absolute vorticity increases with the latitude, while both RH and PI decrease with the latitude (Figures 6A and C). On average, the largest absolute vorticity values can be found at high latitudes, where few TCs form due to the low SST (Tippet et al., 2011).

To the north of 15°N , the absolute vorticity appears to have slight positive anomalies over the northern part of the SCS (Figure 7B), where approximately half of landfalling TCs in SC form (Figure 1C). According to Gray (1975) and Yanase et al. (2012), these positive changes are conducive to TCs' genesis. It possibly contributes to the increase in the TC genesis frequency over the SCS north of 15°N (Figure 5E). The absolute vorticity over the waters east of Taiwan Island between 20°N and 30°N displays an increasing change, and some sporadic regions west of 145°E increase significantly (Figure 7B). As shown in Figure 1D, a minority of landfalling TCs in EC form in this region, which could provide favorable vorticity conditions. In comparison, a large area of negative anomalies over the tropical WNP and significant decline over the waters southwest of the Mariana Islands with the longitude range of $140^{\circ}\text{E} - 145^{\circ}\text{E}$ are observed, indicating lower absolute vorticity in these areas. These changes

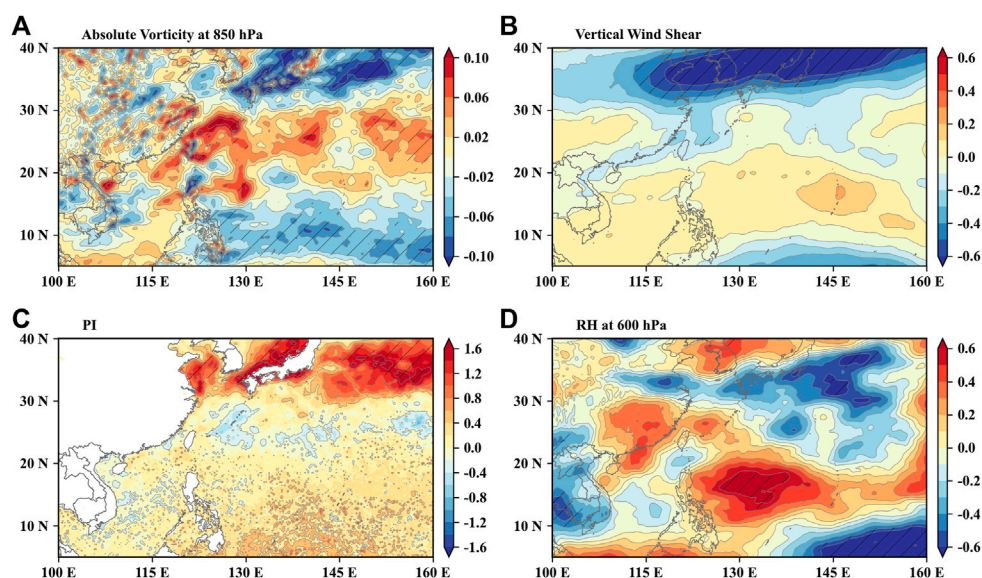


FIGURE 8

Regression of environmental factors with respect to the mean TCs genesis latitudes during 1980–2020. (A) Absolute vorticity at 850 hPa (10^{-5} s^{-1} per latitudinal degree), (B) VWS ($m s^{-1}$ per latitudinal degree), (C) PI ($m s^{-1}$ per latitudinal degree), and (D) RH at 600 hPa (% per latitudinal degree). The stippling indicates the regression exceeding the 90% confidence level.

affect the main region of genesis for TCs landfalling over mainland China (Figures 1C and D, Figures 5E and F) and are possibly responsible for the overall decrease in the formation frequency of TCs over the WNP.

It is known that weak VWS is a necessary dynamic condition for tropical cyclogenesis because strong shear will break the warm core structure of the TCs (Gray, 1975; Yanase et al., 2012). The 41-years' climatological mean and difference in the VWS between the two periods are investigated and shown in Figures 7C and D. As depicted in Figures 1C and D, most of the landfalling TCs tend to form in the tropical WNP in the latitude range of $10^{\circ}N - 25^{\circ}N$ due to relatively small VWS in this region (Figure 7C). However, the VWS increases in the majority of this region and rises significantly in the east of the Mariana Islands around $[20^{\circ}N, 160^{\circ}E]$ after 1995 (Figure 7D). Although the VWS over the northern SCS and the areas east of Taiwan Island present significant decreasing trends, the upward anomalies in VWS over the tropical WNP affect the main genesis region of landfalling TCs and suppress the TCs' formation there.

Comparing Figures 7B and D, the spatial distribution of unfavorable changes in the VWS is similar to that of the decrease in absolute vorticity in the lower troposphere. The reduction in TCs' genesis over the WNP is mainly due to the combination of the increasing VWS and decreasing lower-tropospheric absolute vorticity. Indeed, the thermodynamic factors (PI and RH) over the WNP increased during the 41 years (Figures 6B and D), but the frequency of TC genesis still declined. It means that the dynamic factors are more effective than the thermodynamic conditions in influencing TCs' formation when the

thermodynamic conditions are favorable for TCs' genesis. That is, the dynamic factors played a major role in TC genesis in the WNP during the study period. These results are consistent with the previous conclusions of Murakami et al. (2013), who found that dynamic variables are of primary importance for separating developing and non-developing disturbances for TC formation in the present climate of the WNP.

To further identify the relative contributions of the aforementioned environmental factors to the changes in TC genesis latitude, the factors are regressed onto the mean genesis latitude of landfalling TCs over mainland China during 1980–2020 (Figure 8). As shown in Figure 8A, the regression of the 850-hPa absolute vorticity shows significant positive (negative) correlations at the region north (south) of $20^{\circ}N$, which are favorable (unfavorable) for TC genesis. It suggests that the increase in the mean latitude of TC genesis (Figure 5A) may be related to the variations in the low-level atmospheric absolute vorticity (Figure 7B). Such a result is similar to that found by Wu et al. (2020), who found that the low-level relative vorticity is mainly responsible for the observed increasing variation of mean TC genesis latitude over the WNP. Concurrently, a similar dipole structure can be observed in the regression of VWS (Figure 8B), but the signals are not significant. For the other two environmental conditions (Figures 8C and D), no obvious difference is observed between their regressions at higher and at lower latitudes, or the changes are unfavorable for the poleward shift of TC genesis. In comparison, the low-level atmospheric absolute vorticity and VWS possibly make a relatively more significant contribution to the slight poleward

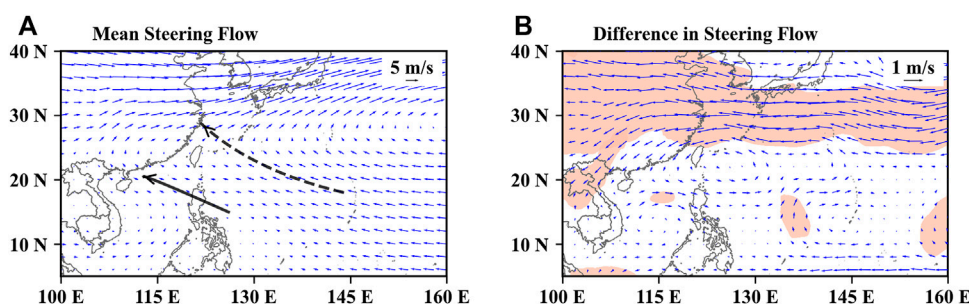


FIGURE 9

The same as Figure 6, but for the Steering Flow (m s^{-1}). The thick black solid (dashed) curves with arrows in (A) schematically denote the mean regression trajectories of TCs making landfall in SC (EC). The shaded area in pink (B) refers to the difference being significant at a confidence level of 90%.

shift in the TCs' genesis locations than other factors. This also confirms the major role of dynamic factors in the TC genesis over the WNP during the study period.

After genesis, the landfall of a TC is determined by its movement, which is mainly controlled by the large-scale environmental steering flow and also affected by other factors, such as beta shift (Chan and Gray, 1982; Holland, 1983; Chan, 1985; Ling et al., 2016; Torn et al., 2018). This section explores the long-term mean background steering flow and the difference in steering flow between the two periods (Figures 9A and B). It can be seen that the higher the latitude, the stronger the mean steering flow. The westward steering flow in the tropics leads most of the TCs formed in the tropical WNP (including the SCS) to move westward and then make landfall in SC. The remaining TCs formed at higher latitudes hit EC under the strong westerly flow in the midlatitudes (Figure 9A). After the TCs' landfall in EC, they may reenter the sea at an even higher latitude, controlled by the steering flow, if they do not dissipate in the mainland (Figure 9A).

In Figure 9B, the large-scale steering flows over the Philippine Sea are characterized by a cyclonic anomaly centered over the waters east of Taiwan Island. This cyclonic anomaly presents an anomalous westerly flow in the latitude band between 10°N and 20°N , suppressing the movement of TCs from the Philippine Sea to the SCS and reducing the chance of TCs making landfall along the SC coast. That means, with the depression of TCs' activity, the number of TCs making landfall along the SC coast is, therefore, reduced. Concurrently, the significant easterly anomaly dominates the midlatitudes, enhancing the chance of a TC striking the EC coast. In other words, the notable reduction in the eastward component of the flow possibly prevents TCs from recurving or moving northeastward to the Japan region. Moreover, Figure 9B shows that the cyclonic anomaly along the EC coast tends to move in a southwest direction at around 30°N , which may prevent those TCs landfalling in EC from moving further north. This can explain why the range of TCs' landfalling latitudes tends to get smaller during the 41 years (Figures 3C–F).

Global SST variations contributing to changes in TCs' landfalls

Previous studies have shown that global SST anomalies can remotely influence WNP TC genesis (Du et al., 2011; Mei et al., 2015; Gao et al., 2018; Zhao et al., 2018; Gao et al., 2020). We then calculate the trends of global SST from 1980 to 2020 (Figure 10A), and the correlations between global SSTs and the number of TC landfalls over mainland China (Figure 10B). The results reveal that the TC landfall frequency over mainland China is significantly negatively correlated to the SSTs over the TIO, the tropical and high-latitude North Atlantic, and the tropical central-eastern Pacific (Figure 10B). Figure 10A shows that the SST has increased significantly in TIO, consistent with a pronounced warming trend over the ocean during the past several decades (Hoerling et al., 2004; Du and Xie, 2008; Roxy et al., 2014), which might be associated with the amplification impact of global warming (Gao et al., 2020). The TIO warming could induce atmospheric anomalies, including suppressed convection and an anomalous surface anticyclone, and further suppress WNP TC activity (Du et al., 2011). Significant negative correlations between the TC landfall frequency and the SSTs over most areas of the TNA (Figure 10B), and significant SST increase over the same ocean area (Figure 10A) can also be observed. This is in line with Gao et al. (2018), who suggested that warm SST anomalies in the TNA might suppress TC landfalls by regulating TC genesis location and frequency associated with modulated environmental conditions. Below-normal SSTs over the tropical central and eastern Pacific may be optimal for above-normal TC activity over the WNP (Figure 10B). However, the SST changes in the tropical central and eastern Pacific are not significant from 1980 to 2020 (Figure 10A). In addition, the number of landfalling TCs over mainland China may be linked to the PDO, as suggested in previous studies (Goh and Chan, 2010; Mei et al., 2015). The correlation between the July–October PDO index and the anomalous TC landfall frequency in mainland

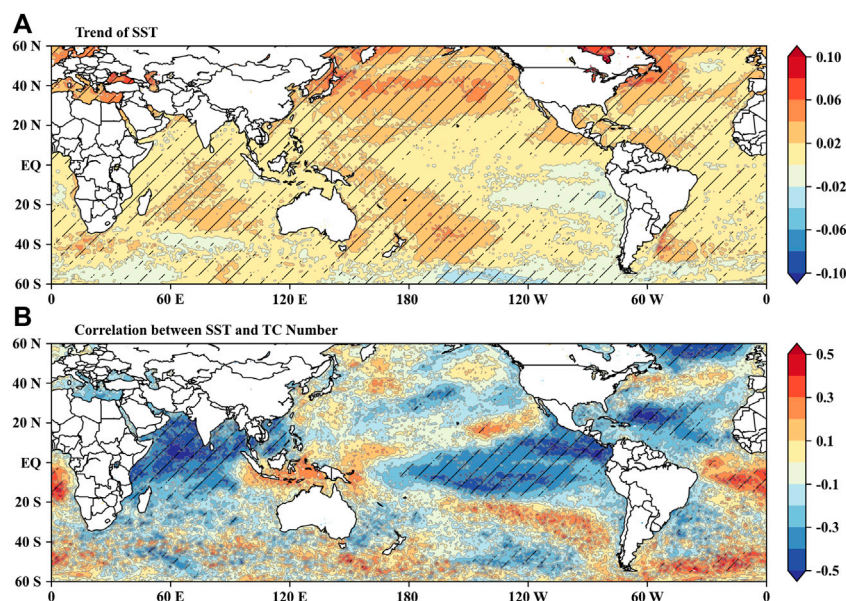


FIGURE 10

(A) Trends of global SST ($^{\circ}\text{C}\cdot\text{yr}^{-1}$) from 1980 to 2020. (B) Correlations between global SSTs and the numbers of TCs making landfall in mainland China from 1980 to 2020. The stripping indicates that the trends and correlations are statistically significant at the 90% confidence level.

China is -0.04 , and it is not significant during the 41 years. It indicates that PDO has no apparent influence on the TCs' landfall frequency over mainland China.

Overall, the SST increases in the TIO, the tropical and high-latitude North Atlantic, and the tropical central and eastern equatorial Pacific may suppress the TC landfalls over mainland China from 1980 to 2020. During this period, the suppressing influence from the TIO may be more significant than the other ocean, due to its strong correlation with the TCs genesis and the consistent and universal SST increase.

Summary

This study examines the characteristics and variability of TC landfalls over mainland China from 1980 to 2020. Artificially, China is divided into SC and EC by the latitude line of 25°N . During the study period, 5.51 TCs land in SC, while 1.07 TCs land in EC annually. The number of TCs impacting mainland China decreases slightly from 1980 to 2020, the number of TCs landfalling in SC experiences a significant decrease, and there is no change in the number of TCs affecting EC. Based on the Pettitt's test results, the frequency of TCs' landfall in mainland China and SC appear to drop significantly in 1995/1996 and 1996/1997, respectively. From 1980 to 1995 (1996), the mean number of TCs landfalling over mainland China (SC) is 7.8 (6.6); from 1996 (1997) to 2020, the mean number of TCs landfalling over mainland China (SC) is 5.8 (4.8). The yearly mean of the TCs' landfalling

latitudes moves northward slightly. Meanwhile, the maximum TCs' latitudes during the 4 decades are found to move southward slightly, leading to a slight decrease in the landfall latitudes range during the study period. All these landfall location shifts are not statistically significant. The significant reduction in the number of landfalling TCs over SC is mainly due to the apparent decrease in the frequency of TCs' formation in the WNP, which also indirectly leads to the markedly northwestward shift of the TC genesis region. The slight northward trend of the yearly mean TCs' landfalling latitude over mainland China is mainly due to the insignificant increase in their genesis latitudes.

The large-scale environments factors, including thermodynamic factors of PI and the middle troposphere RH, and the dynamic factors of lower-tropospheric absolute vorticity, VWS and steering flow, are investigated during the two periods, 1980–1995 and 1996–2020, to explore the environmental background contributing to the observed changes in the landfall and genesis of TCs influencing mainland China. It is found that the dynamic factors play a major role in the TCs' activity changes over the WNP in recent years. A large area of negative anomalies in the lower-tropospheric absolute vorticity and positive variations in the VWS over the tropical WNP, covering the major of the genesis region for TCs landfalling in China, suppresses TC formation over WNP. Concurrently, the opposite changes in both the low-level absolute vorticity and VWS over the northern region (north of 20°N) and southern region (south of 20°N) might contribute to the slight poleward shift of genesis locations of landfalling TCs during the 41 years.

In addition, the variation in the steering flow tends to result in a higher percentage of TCs making landfall along the eastern coast rather than the southern coast than before, with a slight southward shift in the maximum landfall latitudes for TCs. Finally, the SST increases in several ocean basins, the TIO, tropical and high-latitude North Atlantic, and the tropical central-eastern Pacific are found to suppress the formations of TCs that landfall in mainland China from 1980 to 2020. Among these oceans, TIO's influence is the greatest.

Data availability statement

Publicly available datasets were analyzed in this study. This data can be found here: http://tcdata.typhoon.org.cn/en/zjljsjj_zlqh.html <https://cds.climate.copernicus.eu#!/home> <https://psl.noaa.gov/data/climateindices/list/>.

Author contributions

Conceptualization: QL and GL; data collection and analysis: GL; methodology: QL and GL; writing original draft: GL and QL; all the co-authors participated the manuscript review and editing.

References

- Bister, M., and Emanuel, K. A. (2002). Low frequency variability of tropical cyclone potential intensity 1. Interannual to interdecadal variability. *J. Geophys. Res.* 107 (D24), ACL 26-1–ACL 26-15. doi:10.1029/2001JD000776
- Camargo, S. J., Emanuel, K. A., and Sobel, A. H. (2007). Use of a Genesis potential index to diagnose ENSO effects on tropical cyclone Genesis. *J. Clim.* 20 (19), 4819–4834. doi:10.1175/JCLI4282.1
- Camargo, S. J., and Sobel, A. H. (2005). Western North Pacific tropical cyclone intensity and ENSO. *J. Clim.* 18 (15), 2996–3006. doi:10.1175/JCLI3457.1
- Chan, J. C., and Gray, W. M. (1982). Tropical cyclone movement and surrounding flow relationships. *Mon. Weather Rev.* 110 (10), 1354–1374. doi:10.1175/1520-0493(1982)110<1354:TCMASF>2.0.CO;2
- Chan, J. C. (1985). Identification of the steering flow for tropical cyclone motion from objectively analyzed wind fields. *Mon. weather Rev.* 113 (1), 106–116. doi:10.1175/1520-0493(1985)113<0106:IOTSFF>2.0.CO;2
- Chan, J. C., Liu, K. S., Xu, M., and Yang, Q. (2012). Variations of frequency of landfalling typhoons in East China, 1450–1949. *Int. J. Climatol.* 32 (13), 1946–1950. doi:10.1002/joc.2410
- Chen, X., Wu, L., and Zhang, J. (2011). Increasing duration of tropical cyclones over China. *Geophys. Res. Lett.* 38 (2). doi:10.1029/2010GL046137
- Dong, S., Gao, J., Li, X., Wei, Y., and Wang, L. (2015). A storm surge intensity classification based on extreme water level and concomitant wave height. *J. Ocean. Univ. China* 14 (2), 237–244. doi:10.1007/s11802-015-2342-5
- Du, Y., and Xie, S. P. (2008). Role of atmospheric adjustments in the tropical Indian Ocean warming during the 20th century in climate models. *Geophys. Res. Lett.* 35 (8), L08712. doi:10.1029/2008GL033631
- Du, Y., Yang, L., and Xie, S.-P. (2011). Tropical Indian Ocean influence on northwest Pacific tropical cyclones in summer following strong El Niño. *J. Clim.* 24 (1), 315–322. doi:10.1175/2010JCLI3890.1
- Emanuel, K. A. (2000). A statistical analysis of tropical cyclone intensity. *Mon. weather Rev.* 128 (4), 1139–1152. doi:10.1175/1520-0493(2000)128<1139:ASAOTC>2.0.CO;2
- Emanuel, K. A. (1986). An air-sea interaction theory for tropical cyclones. Part I: Steady-state maintenance. *J. Atmos. Sci.* 43 (6), 585–605. doi:10.1175/1520-0469(1986)043<0585:AASITF>2.0.CO;2
- Emanuel, K., and Nolan, D. S. (2004). “Tropical cyclone activity and the global climate system,” in 26th Conference on Hurricanes and Tropical Meteorology, Miami, FL, 2–7 May (United States: American Meteorological Society).
- Fudeyasu, H., Ito, K., and Miyamoto, Y. (2018). Characteristics of tropical cyclone rapid intensification over the Western North Pacific. *J. Clim.* 31 (21), 8917–8930. doi:10.1175/JCLI-D-17-0653.1
- Gao, J., Zhao, H., Klotzbach, P. J., Wang, C., Raga, G. B., Chen, S., et al. (2020). Possible influence of tropical Indian Ocean sea surface temperature on the proportion of rapidly intensifying Western North Pacific tropical cyclones during the extended boreal summer. *J. Clim.* 33 (21), 9129–9143. doi:10.1175/JCLI-D-20-0087.1
- Gao, S., Chen, Z., and Zhang, W. (2018). Impacts of tropical North Atlantic SST on Western North Pacific landfalling tropical cyclones. *J. Clim.* 31 (2), 853–862. doi:10.1175/JCLI-D-17-0325.1
- Gilford, D. M., Solomon, S., and Emanuel, K. A. (2017). On the seasonal cycles of tropical cyclone potential intensity. *J. Clim.* 30 (16), 6085–6096. doi:10.1175/JCLI-D-16-0827.1
- Goh, A. Z. C., and Chan, J. C. (2010). Interannual and interdecadal variations of tropical cyclone activity in the South China Sea. *Int. J. Climatol.* 30 (6), 827–843. doi:10.1002/joc.1943
- Gray, W. M. (1968). Global view of the origin of tropical disturbances and storms. *Mon. Weather Rev.* 96 (10), 669–700. doi:10.1175/1520-0493(1968)096<0669:GVOTOO>2.0.CO;2
- Gray, W. M. (1975). *Tropical cyclone genesis*. Colorado: Colorado State University.
- Hersbach, H., Bell, B., Berrisford, P., Hirahara, S., Horányi, A., Muñoz-Sabater, J., et al. (2020). The ERA5 global reanalysis. *Q. J. R. Meteorol. Soc.* 146 (730), 1999–2049. doi:10.1002/qj.3803

Funding

This study was supported by the Science and Technology Department of Guangdong Province with Grant of 2019B111101002 and the Innovation of Science and Technology Commission of Shenzhen Municipality Ministry with Grants of JCYJ20210324101006016 and GJHZ20210705141403010.

Conflict of interest

The authors declare that the research was conducted in the absence of any commercial or financial relationships that could be construed as a potential conflict of interest.

Publisher's note

All claims expressed in this article are solely those of the authors and do not necessarily represent those of their affiliated organizations, or those of the publisher, the editors, and the reviewers. Any product that may be evaluated in this article, or claim that may be made by its manufacturer, is not guaranteed or endorsed by the publisher.

- Hoerling, M. P., Hurrell, J. W., Xu, T., Bates, G. T., and Phillips, A. (2004). Twentieth century North Atlantic climate change. Part II: Understanding the effect of Indian Ocean warming. *Clim. Dyn.* 23 (3), 391–405. doi:10.1007/s00382-004-0433-x
- Holland, G. J. (1983). Tropical cyclone motion: Environmental interaction plus a beta effect. *J. Atmos. Sci.* 40 (2), 328–342. doi:10.1175/1520-0469(1983)040<0328:TCMEIP>2.0.CO;2
- Kim, J.-H., Ho, C.-H., Kim, H.-S., Sui, C.-H., and Park, S. K. (2008). Systematic variation of summertime tropical cyclone activity in the Western North Pacific in relation to the Madden-Julian oscillation. *J. Clim.* 21 (6), 1171–1191. doi:10.1175/2007JCLI1493.1
- Korty, R. L., Camargo, S. J., and Galewsky, J. (2012). Variations in tropical cyclone Genesis factors in simulations of the Holocene epoch. *J. Clim.* 25 (23), 8196–8211. doi:10.1175/JCLI-D-12-00033.1
- Kossin, J. P., Emanuel, K. A., and Vecchi, G. A. (2014). The poleward migration of the location of tropical cyclone maximum intensity. *Nature* 509 (7500), 349–352. doi:10.1038/nature13278
- Li, Q., and Duan, Y. (2010). Tropical cyclone strikes at the coastal cities of China from 1949 to 2008. *Meteorol. Atmos. Phys.* 107 (1), 1–7. doi:10.1007/s00703-010-0065-0
- Li, R. C., Zhou, W., Shun, C., and Lee, T. C. (2017). Change in destructiveness of landfalling tropical cyclones over China in recent decades. *J. Clim.* 30 (9), 3367–3379. doi:10.1175/JCLI-D-16-0258.1
- Ling, Z., Wang, Y., and Wang, G. (2016). Impact of intraseasonal oscillations on the activity of tropical cyclones in summer over the south China sea. Part I: Local tropical cyclones. *J. Clim.* 29 (2), 855–868. doi:10.1175/JCLI-D-15-0617.1
- Liu, K., and Chan, J. C. (2003). Climatological characteristics and seasonal forecasting of tropical cyclones making landfall along the South China coast. *Mon. Weather Rev.* 131 (8), 1650–1662. doi:10.1175/2554.1
- Liu, K. S., and Chan, J. C. (2013). Inactive period of Western North Pacific tropical cyclone activity in 1998–2011. *J. Clim.* 26 (8), 2614–2630. doi:10.1175/JCLI-D-12-00053.1
- Liu, K. S., and Chan, J. C. (2020). Recent increase in extreme intensity of tropical cyclones making landfall in South China. *Clim. Dyn.* 55, 1059–1074. doi:10.1007/s00382-020-05311-5
- Liu, K. S., and Chan, J. C. (2017). Variations in the power dissipation index in the East Asia region. *Clim. Dyn.* 48 (5), 1963–1985. doi:10.1007/s00382-016-3185-5
- Liu, L., Wang, Y., Zhan, R., Xu, J., and Duan, Y. (2020). Increasing destructive potential of landfalling tropical cyclones over China. *J. Clim.* 33 (9), 3731–3743. doi:10.1175/JCLI-D-19-0451.1
- Lu, X.-q., and Zhao, B.-k. (2013). Analysis of the climatic characteristics of landing tropical cyclones in East China. *J. Trop. Meteorology* 19 (2), 145.
- Mei, W., Xie, S.-P., Zhao, M., and Wang, Y. (2015). Forced and internal variability of tropical cyclone track density in the Western North Pacific. *J. Clim.* 28 (1), 143–167. doi:10.1175/JCLI-D-14-00164.1
- Murakami, H., Li, T., and Peng, M. (2013). Changes to environmental parameters that control tropical cyclone Genesis under global warming. *Geophys. Res. Lett.* 40 (10), 2265–2270. doi:10.1002/grl.50393
- Park, D.-S. R., Ho, C.-H., and Kim, J.-H. (2014). Growing threat of intense tropical cyclones to East Asia over the period 1977–2010. *Environ. Res. Lett.* 9 (1), 014008. doi:10.1088/1748-9326/9/1/014008
- Park, D.-S. R., Ho, C.-H., Kim, J.-H., and Kim, H.-S. (2013). Spatially inhomogeneous trends of tropical cyclone intensity over the Western North Pacific for 1977–2010. *J. Clim.* 26 (14), 5088–5101. doi:10.1175/JCLI-D-12-00386.1
- Pettitt, A. N. (1979). A non-parametric approach to the change-point problem. *Appl. Stat.* 28 (2), 126. doi:10.2307/2346729
- Roxy, M. K., Ritika, K., Terray, P., and Masson, S. (2014). The curious case of Indian ocean warming*, +. *J. Clim.* 27 (22), 8501–8509. doi:10.1175/JCLI-D-14-00471.1
- Shan, K., and Yu, X. (2021). Variability of tropical cyclone landfalls in China. *J. Clim.* 34 (23), 9235–9247. doi:10.1175/JCLI-D-21-0031.1
- Studholme, J., Fedorov, A. V., Gulev, S. K., Emanuel, K., and Hodges, K. (2022). Poleward expansion of tropical cyclone latitudes in warming climates. *Nat. Geosci.* 15 (1), 14–28. doi:10.1038/s41561-021-00859-1
- Tippett, M. K., Camargo, S. J., and Sobel, A. H. (2011). A Poisson regression index for tropical cyclone Genesis and the role of large-scale vorticity in Genesis. *J. Clim.* 24 (9), 2335–2357. doi:10.1175/2010JCLI3811.1
- Torn, R. D., Elless, T. J., Papin, P. P., and Davis, C. A. (2018). Tropical cyclone track sensitivity in deformation steering flow. *Mon. Weather Rev.* 146 (10), 3183–3201. doi:10.1175/MWR-D-18-0153.1
- Wang, B., and Chan, J. C. (2002). How strong ENSO events affect tropical storm activity over the Western North Pacific. *J. Clim.* 15 (13), 1643–1658. doi:10.1175/1520-0442(2002)015<1643:HSEAT>2.0.CO;2
- Wang, H., Xu, M., Onyejuruwa, A., Wang, Y., Wen, S., Gao, A. E., et al. (2019). Tropical cyclone damages in Mainland China over 2005–2016: Losses analysis and implications. *Environ. Dev. Sustain.* 21 (6), 3077–3092. doi:10.1007/s10668-019-00481-7
- Wang, S., and Toumi, R. (2021). Recent migration of tropical cyclones toward coasts. *Science* 371 (6528), 514–517. doi:10.1126/science.abb9038
- Wang, Y. (2012). Recent research progress on tropical cyclone structure and intensity. *Trop. Cyclone Res. Rev.* 1 (2), 254–275. doi:10.6057/2012TCRR02.05
- Wilks, D. S. (2006). *Statistical methods in the atmospheric sciences*. Cambridge: Academic Press.
- Wu, L., and Wang, B. (2004). Assessing impacts of global warming on tropical cyclone tracks. *J. Clim.* 17 (8), 1686–1698. doi:10.1175/1520-0442(2004)017<1686:AIOGWO>2.0.CO;2
- Wu, M., Wang, L., and Chen, B. (2020). Recent weakening in interannual variability of mean tropical cyclogenesis latitude over the Western North Pacific during boreal summer. *J. Meteorol. Res.* 34 (6), 1183–1198. doi:10.1007/s13351-020-0039-1
- Yanase, W., Satoh, M., Taniguchi, H., and Fujinami, H. (2012). Seasonal and intraseasonal modulation of tropical cyclogenesis environment over the Bay of Bengal during the extended summer monsoon. *J. Clim.* 25 (8), 2914–2930. doi:10.1175/JCLI-D-11-00208.1
- Yin, Y., Gemmer, M., Luo, Y., and Wang, Y. (2010). Tropical cyclones and heavy rainfall in Fujian Province, China. *Quat. Int.* 226 (1–2), 122–128. doi:10.1016/j.quaint.2010.03.015
- Ying, M., Zhang, W., Yu, H., Lu, X., Feng, J., Fan, Y., et al. (2014). An overview of the China meteorological administration tropical cyclone database. *J. Atmos. Ocean. Technol.* 31 (2), 287–301. doi:10.1175/jtech-d-12-00119.1
- Yonekura, E., and Hall, T. M. (2014). ENSO effect on East Asian tropical cyclone landfall via changes in tracks and Genesis in a statistical model. *J. Appl. Meteorol. Climatol.* 53 (2), 406–420. doi:10.1175/JAMC-D-12-0240.1
- Zhan, R., Wang, Y., and Tao, L. (2014). Intensified impact of East Indian Ocean SST anomaly on tropical cyclone Genesis frequency over the Western North Pacific. *J. Clim.* 27 (23), 8724–8739. doi:10.1175/JCLI-D-14-00119.1
- Zhan, R., and Wang, Y. (2017). Weak tropical cyclones dominate the poleward migration of the annual mean location of lifetime maximum intensity of Northwest Pacific tropical cyclones since 1980. *J. Clim.* 30 (17), 6873–6882. doi:10.1175/jcli-d-17-0019.1
- Zhan, R., Wang, Y., and Wu, C.-C. (2011). Impact of SSTA in the East Indian ocean on the frequency of northwest pacific tropical cyclones: A regional atmospheric model study. *J. Clim.* 24 (23), 6227–6242. doi:10.1175/JCLI-D-10-05014.1
- Zhang, Q., Zhang, W., Lu, X., and Chen, Y. D. (2012). Landfalling tropical cyclones activities in the South China: Intensifying or weakening? *Int. J. Climatol.* 32 (12), 1815–1824. doi:10.1002/joc.2396
- Zhang, W., Vecchi, G. A., Murakami, H., Villarini, G., Delworth, T. L., Yang, X., et al. (2018). Dominant role of Atlantic multidecadal oscillation in the recent decadal changes in Western North Pacific tropical cyclone activity. *Geophys. Res. Lett.* 45 (1), 354–362. doi:10.1002/2017GL076397
- Zhao, H., Duan, X., Raga, G., and Klotzbach, P. J. (2018). Changes in characteristics of rapidly intensifying Western North Pacific tropical cyclones related to climate regime shifts. *J. Clim.* 31 (19), 8163–8179. doi:10.1175/JCLI-D-18-0029.1

Frontiers in Earth Science

Investigates the processes operating within the major spheres of our planet

Advances our understanding across the earth sciences, providing a theoretical background for better use of our planet's resources and equipping us to face major environmental challenges.

Discover the latest Research Topics

[See more →](#)

Frontiers

Avenue du Tribunal-Fédéral 34
1005 Lausanne, Switzerland
frontiersin.org

Contact us

+41 (0)21 510 17 00
frontiersin.org/about/contact

